Computational Structural Dynamics and Earthquake Engineering

Editors:
Manolis Papadrakakis, Dimos C. Charmpis,
Nikos D. Lagaros & Yiannis Tsompanakis

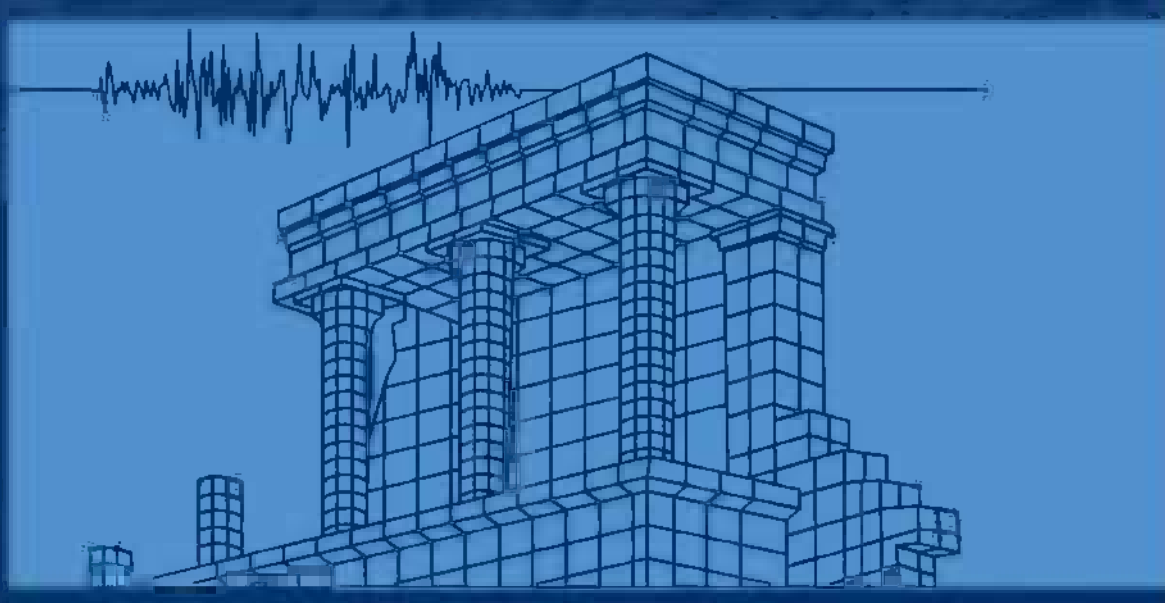

CRC Press
Taylor & Francis Group
A BALKEMA BOOK

Structures and Infrastructures 2

Computational Structural Dynamics and Earthquake Engineering

Structures and Infrastructures Series

ISSN 1747-7735

Book Series Editor:

Dan M. Frangopol
Professor of Civil Engineering and
Fazlur R. Khan Endowed Chair of Structural Engineering and Architecture
Department of Civil and Environmental Engineering
Center for Advanced Technology for Large Structural Systems (ATLSS Center)
Lehigh University
Bethlehem, PA, USA

Volume 2

Computational Structural Dynamics and Earthquake Engineering

Edited by

Manolis Papadrakakis[1],
Dimos C. Charmpis[2],
Nikos D. Lagaros[1] &
Yiannis Tsompanakis[3]

[1]National Technical University of Athens, Athens, Greece
[2]University of Cyprus, Nicosia, Cyprus
[3]Technical University of Crete, Chania, Greece

CRC Press
Taylor & Francis Group
Boca Raton London New York Leiden

CRC Press is an imprint of the
Taylor & Francis Group, an **informa** business

A BALKEMA BOOK

Colophon

Book Series Editor:
Dan M. Frangopol

Volume Editors:
Manolis Papadrakakis, Dimos C. Charmpis, Nikos D. Lagaros & Yiannis Tsompanakis

Cover illustration:
Minoan palace ruins, Knossos, Crete, Greece
Nikos D. Lagaros
September 2006

Taylor & Francis is an imprint of the Taylor & Francis Group,
an informa business

Typeset by Charon Tec Ltd (A Macmillan company), Chennai, India
Printed and bound in Great Britain by Antony Rowe (a CPI Group company),
Chippenham, Wiltshire

British Library Cataloguing in Publication Data
A catalogue record for this book is available from the British Library

Library of Congress Cataloging-in-Publication Data

Computational structural dynamics and earthquake engineering / Manolis Papadrakakis ... [et al.].

p. cm. – (Structures and infrastructures series, ISSN 1747-7735)

Includes bibliographical references and index.

ISBN 978-0-415-45261-8 (hardcover : alk. paper) 1. Structural dynamics–Mathematics. 2. Earthquake engineering–Mathematics. 3. Engineering mathematics–Formulae. I. Papadrakakis, Manolis. II. Title. III. Series.

TA654.C633 2009

624.1′71–dc22

2008044127

Published by: CRC Press/Balkema
P.O. Box 447, 2300 AK Leiden, The Netherlands
e-mail: Pub.NL@taylorandfrancis.com
www.crcpress.com – www.taylorandfrancis.co.uk – www.balkema.nl

ISBN13 978-0-415-45261-8(Hbk)
ISBN13 978-0-203-88163-7(eBook)
Structures and Infrastructures Series: ISSN 1747-7735
Volume 2

Table of Contents

Editorial

Welcome to the New Book Series *Structures and Infrastructures*.

Our knowledge to model, analyze, design, maintain, manage and predict the life-cycle performance of structures and infrastructures is continually growing. However, the complexity of these systems continues to increase and an integrated approach is necessary to understand the effect of technological, environmental, economical, social and political interactions on the life-cycle performance of engineering structures and infrastructures. In order to accomplish this, methods have to be developed to systematically analyze structure and infrastructure systems, and models have to be formulated for evaluating and comparing the risks and benefits associated with various alternatives. We must maximize the life-cycle benefits of these systems to serve the needs of our society by selecting the best balance of the safety, economy and sustainability requirements despite imperfect information and knowledge.

In recognition of the need for such methods and models, the aim of this Book Series is to present research, developments, and applications written by experts on the most advanced technologies for analyzing, predicting and optimizing the performance of structures and infrastructures such as buildings, bridges, dams, underground construction, offshore platforms, pipelines, naval vessels, ocean structures, nuclear power plants, and also airplanes, aerospace and automotive structures.

The scope of this Book Series covers the entire spectrum of structures and infrastructures. Thus it includes, but is not restricted to, mathematical modeling, computer and experimental methods, practical applications in the areas of assessment and evaluation, construction and design for durability, decision making, deterioration modeling and aging, failure analysis, field testing, structural health monitoring, financial planning, inspection and diagnostics, life-cycle analysis and prediction, loads, maintenance strategies, management systems, nondestructive testing, optimization of maintenance and management, specifications and codes, structural safety and reliability, system analysis, time-dependent performance, rehabilitation, repair, replacement, reliability and risk management, service life prediction, strengthening and whole life costing.

This Book Series is intended for an audience of researchers, practitioners, and students world-wide with a background in civil, aerospace, mechanical, marine and automotive engineering, as well as people working in infrastructure maintenance, monitoring, management and cost analysis of structures and infrastructures. Some volumes are monographs defining the current state of the art and/or practice in the field, and some are textbooks to be used in undergraduate (mostly seniors), graduate and

postgraduate courses. This Book Series is affiliated to *Structure and Infrastructure Engineering* (http://www.informaworld.com/sie), an international peer-reviewed journal which is included in the Science Citation Index.

If you like to contribute to this Book Series as an author or editor, please contact the Book Series Editor (dan.frangopol@lehigh.edu) or the Publisher (pub.NL@taylorandfrancis.com). A book proposal form can be downloaded at www.balkema.nl.

It is now up to you, authors, editors, and readers, to make *Structures and Infrastructures* a success.

Dan M. Frangopol
Book Series Editor

About the Book Series Editor

Dr. Dan M. Frangopol is the first holder of the Fazlur R. Khan Endowed Chair of Structural Engineering and Architecture at Lehigh University, Bethlehem, Pennsylvania, USA, and a Professor in the Department of Civil and Environmental Engineering at Lehigh University. He is also an Emeritus Professor of Civil Engineering at the University of Colorado at Boulder, USA, where he taught for more than two decades (1983–2006). Before joining the University of Colorado, he worked for four years (1979–1983) in structural design with A. Lipski Consulting Engineers in Brussels, Belgium. In 1976, he received his doctorate in Applied Sciences from the University of Liège, Belgium, and holds two honorary doctorates (Doctor Honoris Causa) from the Technical University of Civil Engineering in Bucharest, Romania, and the University of Liège, Belgium. He is a Fellow of the American Society of Civil Engineers (ASCE), American Concrete Institute (ACI), and International Association for Bridge and Structural Engineering (IABSE). He is also an Honorary Member of both the Romanian Academy of Technical Sciences and the Portuguese Association for Bridge Maintenance and Safety. He is the initiator and organizer of the Fazlur R. Khan Lecture Series (www.lehigh.edu/frkseries) at Lehigh University.

Dan Frangopol is an experienced researcher and consultant to industry and government agencies, both nationally and abroad. His main areas of expertise are structural reliability, structural optimization, bridge engineering, and life-cycle analysis, design, maintenance, monitoring, and management of structures and infrastructures. He is the Founding President of the International Association for Bridge Maintenance and Safety (IABMAS, www.iabmas.org) and of the International Association for Life-Cycle Civil Engineering (IALCCE, www.ialcce.org), and Past Director of the Consortium on Advanced Life-Cycle Engineering for Sustainable Civil Environments (COALESCE). He is also the Chair of the Executive Board of the International Association for Structural Safety and Reliability (IASSAR, www.columbia.edu/cu/civileng/iassar) and the Vice-President of the International Society for Health Monitoring of Intelligent Infrastructures (ISHMII, www.ishmii.org). Dan Frangopol is the recipient of several prestigious awards including the 2008 IALCCE Senior Award, the 2007 ASCE Ernest Howard Award, the 2006 IABSE OPAC Award, the 2006 Elsevier Munro Prize, the

2006 T. Y. Lin Medal, the 2005 ASCE Nathan M. Newmark Medal, the 2004 Kajima Research Award, the 2003 ASCE Moisseiff Award, the 2002 JSPS Fellowship Award for Research in Japan, the 2001 ASCE J. James R. Croes Medal, the 2001 IASSAR Research Prize, the 1998 and 2004 ASCE State-of-the-Art of Civil Engineering Award, and the 1996 Distinguished Probabilistic Methods Educator Award of the Society of Automotive Engineers (SAE).

Dan Frangopol is the Founding Editor-in-Chief of *Structure and Infrastructure Engineering* (Taylor & Francis, www.informaworld.com/sie) an international peer-reviewed journal, which is included in the Science Citation Index. This journal is dedicated to recent advances in maintenance, management, and life-cycle performance of a wide range of structures and infrastructures. He is the author or co-author of over 400 refereed publications, and co-author, editor or co-editor of more than 20 books published by ASCE, Balkema, CIMNE, CRC Press, Elsevier, McGraw-Hill, Taylor & Francis, and Thomas Telford and an editorial board member of several international journals. Additionally, he has chaired and organized several national and international structural engineering conferences and workshops. Dan Frangopol has supervised over 70 Ph.D. and M.Sc. students. Many of his former students are professors at major universities in the United States, Asia, Europe, and South America, and several are prominent in professional practice and research laboratories.

For additional information on Dan M. Frangopol's activities, please visit www.lehigh.edu/~dmf206/

Foreword

The purpose of this book is to present recent research findings in the fields of computational structural dynamics and earthquake engineering. The first part (Chapters 1 to 14) is devoted to computational structural dynamics, and the second part (Chapters 15 to 35) deals with computational earthquake engineering. To provide the reader with a good overview of pertinent literature, all cited references and additional references on the topics presented are collected in a comprehensive list of references.

The Book Series Editor would like to express his appreciation to the Editors and all Authors who contributed to this book. It is his hope that this second volume in the *Structures and Infrastructures* Book Series will generate a lot of interest in the Computational Mechanics, Structural Dynamics, and Earthquake Engineering Communities.

Dan M. Frangopol
Book Series Editor
Bethlehem, Pennsylvania
August 30, 2008

Preface

The increasing necessity to solve complex problems in Structural Dynamics and Earthquake Engineering requires the development of new ideas, innovative methods and numerical tools for providing accurate numerical solutions in affordable computing times. The purpose of this book is to present the latest research developments in the scientific fields of Computational Dynamics, Stochastic Dynamics, Structural Dynamics and Earthquake Engineering. This volume consists of state-of-the-art contributions. The selected chapters are revised and extended versions of the papers which were presented as plenary, semi-plenary and keynote lectures at the recent thematic Compdyn 2007 Conference.

The book is addressed to people working in universities, engineering practice and industry. It will be useful for academic staff, researchers, post-graduate and research students active in areas of civil, mechanical, naval, aerospace engineering. Furthermore, the book is addressed to professional engineers confronted with complicated problems that need cost-effective designs. The potential readers will extend their knowledge in the aforementioned research fields. They will find this book very helpful in order to enhance their knowledge, to provide a foundation for further study, to indicate novel research areas, or areas where further developments are necessary and to deal with applications of advanced complexity.

This volume is a "multi-collective" book of thirty-five, high-quality and self-contained chapters, which present state-of-the-art theoretical advances and applications in various fields of Computational Structural Dynamics and Earthquake Engineering. The chapters in the first part of the book are focused on Computational Structural Dynamics theory and applications, while the chapters in the second part deal with advances in Earthquake Engineering theory and applications. The communities of Structural Dynamics and Earthquake Engineering will benefit from this publication, since they will be acquainted with advanced computational methods and software tools which can highly assist them in tackling complex problems in dynamic/seismic analysis and design. In addition, the book will also give the Computational Mechanics community the opportunity to become more familiar with very important application areas of great social impact. In the sequence, short descriptions of the chapters are presented.

The aim of the introductory chapter by Schuëller (Chapter 1) is to review some of the most relevant lessons learned for solving reliability problems in structural dynamics. The emphasis is given on studying the effects of dimensionality of a reliability problem as well as the effects of structural nonlinearities when applying different reliability

methods. In particular, a critical appraisal on the role of the design point in estimating failure probabilities is carried out. The range of applicability of approximate methods is examined, as these methods rely to a large extent on the design point for producing reliability estimates. The discussion is based on the observations generated through the resolution of a series of numerical examples rather than from a theoretical point of view, given the inherent complex nature of structural reliability problems involving nonlinearities. The examples addressed show that the design point and its vicinity contribute significantly to the failure probability integral (P_F) for low dimensional problems. In contrast, when the number of random variables is large the design point and its vicinity do not play an important role in estimating P_F. In addition, the examples examined indicate that the shape of the failure region in reliability problems involving structural nonlinearities can be rather involved, thus preventing its approximation by means of the so-called First Order Reliability Method (FORM). In view of the evidence presented in this chapter, the use of techniques such as FORM seems advisable only for problems with few uncertain parameters, involving weak nonlinearities. For high dimensional problems involving weak or strong nonlinearities, simulation techniques like direct Monte Carlo simulation, Subset simulation or Line Sampling should be applied.

Conte, Barbato and Gu (Chapter 2) present the recent developments in finite element (FE) response sensitivity analysis based on the Direct Differentiation Method (DDM) for displacement-based, force-based, and three-field mixed finite elements. First-Order Second-Moment (FOSM) approximations of the first- and second-order statistics of the response of structural systems with random/uncertain parameters and subjected to deterministic quasi-static and/or dynamic loads are obtained using DDM-based FE response sensitivities and compared to Monte Carlo simulation results. The probability of a structural response quantity exceeding a specified threshold level is evaluated using the First-Order Reliability Method (FORM) combined with DDM-based FE response sensitivities in the search for the "design point(s)" (DPs). Both time-invariant and time-variant problems are considered. The geometry of limit-state surfaces near the DP(s) is explored in subspaces defined by planes of major principal curvatures. This geometry explains the lack of accuracy of FORM-based solutions in some cases and suggests the development of new improved solution strategies, e.g., the Design Point – Response Surface – Simulation (DP-RS-Sim) method. The examples presented in this study include both structural systems and soil-foundation-structure interaction systems and are based on two types of analyses which are used extensively in earthquake engineering, namely pushover analysis and time history analysis.

Armero (Chapter 3) describes a new strain finite element formulation (or B-bar method) for the locking-free simulation of nearly incompressible elastic and inelastic solids in the finite deformation dynamic range that also preserves the conservation/dissipation properties of the so-called energy-dissipative momentum-conserving (EDMC) time-stepping algorithms. The general setting of finite strain plasticity is considered, including hyperelastic models as a particular case. The main motivation of this work is to avoid the nonlinear numerical instabilities observed in classical numerical schemes with unbounded growth of the energy (even in the plastic case) by introducing the exact dissipation/conservation of the energy in the discrete system by design. The incorporation of the conservation laws of linear and angular momenta, and the preservation of the associated relative equilibria, is also obtained. The chapter identifies

the conditions that the linearized strain operator has to satisfy for the preservation of these properties in time. These conditions require the definition of the assumed strain operator, originally developed with spatial considerations only, accounting for the temporal discretization in the definition of the associated strain variations. As a result, a fully discrete system in space and time is defined that shows exactly all these conservation/dissipation laws of the underlying physical system, including the exact plastic dissipation of the energy, with exact energy conservation for elastic steps. Numerical simulations are presented to illustrate the performance of the new formulation.

Momentum and energy conserving time integration procedures are receiving increased interest due to the central role of conservation properties in relation to the problems under investigation. However, most problems in structural dynamics are based on models that are first discretized in space, and this often leads to a fairly large number of high-frequency modes, that are not represented well by the model. It is desirable to cure this problem by devising algorithms that include the possibility of introducing algorithmic energy dissipation of the high-frequency modes. The problem is well known from classic collocation based algorithms - notably various forms of the Newmark algorithm where the equation of motion is supplemented by approximate relations between displacement, velocity and acceleration. In the chapter by Krenk (Chapter 4) an efficient adjustment of the algorithmic parameters is used to introduce the so-called damping, and an improved form leading only to high-frequency damping that can be obtained by suitable averaging of the equilibrium equation at consecutive time steps. Conservative time integration algorithms are obtained by use of an integral of the equation of motion and the acceleration therefore does not appear as an independent parameter of these algorithms. Typically they do not contain algorithmic parameters either. Algorithmic damping can then be introduced in two ways: either by introducing artificial damping in terms of the displacement and velocity vectors, or by introducing additional variables to represent damping.

The chapter by Soize, Chen, Durand, Duhamel and Gagliardini (Chapter 5) deals with the robustness of uncertain computational elastoacoustic models in low- and medium-frequency ranges. The elastoacoustic system is made up of a heterogeneous viscoelastic structure coupled with an internal acoustic cavity filled with a dissipative acoustic fluid. A reduced mean elastoacoustic model is deduced from the mean finite element model by using the modal approach with the structural modes of the structure and the acoustic modes of the acoustic cavity. Data uncertainties and model uncertainties are taken into account by using a nonparametric probabilistic approach for the structure, for the acoustic cavity and for the vibroacoustic coupling interface. The main objectives of this paper are (i) to present experimental validation of the nonparametric probabilistic approach of model uncertainties and to propose methods to perform the experimental identification of the probabilistic model parameters, (ii) to analyze the robustness of computational elastoacoustic models with respect to model and data uncertainties, (iii) to study uncertainty propagation through complex elastoacoustic systems. To illustrate the efficiency of their computational stochastic elastoacoustic model the authors analyze various experimental configurations.

The theme of the contribution by Moens, Vandepitte, DeGersem, DeMunck and Desmet (Chapter 6) is structural dynamics design validation and optimization with imprecise parameters using the fuzzy finite element method. After initial research in the field of fuzzy finite elements has started in the middle of the nineties, different aspects

of the problem have been considered, and continuous development has improved not only the capabilities but also the performance of the procedures. The improvement of the performance of fuzzy finite element analysis is still a big challenge. Vertex analysis with n uncertain parameters requires 2^n deterministic analysis runs for each α-level that is considered. Another approach is optimization, which is capable of predicting absolute maxima and minima. Unlike vertex analysis, the performance of optimization procedures is unpredictable. Structural dynamics is a specific type of problem that can also be tackled with interval or fuzzy finite elements and there is currently no generally applicable consistent approach to take into account the effect of parameter uncertainties on Component Mode Synthesis (CMS) reduction schemes. Several approximation procedures have been proposed, but they are sensitive to the particular case that is considered. This chapter presents two recent enhancements to the hybrid optimization and interval arithmetic procedure for fuzzy envelope FRF calculation: a Response Surface Modeling (RSM) method and a new CMS procedure. The result is a highly efficient procedure for interval and especially fuzzy finite element analysis.

De Wilde and Steirteghem (Chapter 7) deal with a number of dimensionless morphological indicators that represent a property of a structure and depend only on a small number of variables. These indicators allow for optimization at the stage of conceptual design. The most important indicators are the indicator of volume, related to the strength of the structure, and the indicator of displacement, related to the stiffness of the structure. These indicators, in their most simple appearance, are functions only of the geometrical slenderness of the structure, under the assumption that the structure is not subjected to second order effects and that shear effects are not predominant. The indicator of volume allows choosing the structural typology with a minimum of volume of material. When using the indicator of volume at the stage of conceptual design, important areas of slenderness appear to bring about problems of resonance. This is particularly the case for structures which have predominant co-vibrating loads, have large spans and are using a material with a small stiffness/strength ratio. To further illustrate this situation, a real-world example is discussed and some general design guidelines are proposed.

In the work by Sapountzakis and Mokos (Chapter 8) a general solution for the dynamic analysis of plates stiffened by arbitrarily placed parallel beams with deformable connection is presented. According to the proposed model, the stiffening beams are isolated from the plate by sections in the lower outer surface of the plate, taking into account the arising tractions in all directions at the fictitious interfaces. These tractions are integrated with respect to each half of the interface width resulting two interface lines. Their unknown distribution is established by applying continuity conditions in all directions taking into account their relation with the interface slip through the shear connector stiffness. Any distribution of connectors in each direction can be efficiently handled. The proposed model permits the evaluation of the shear forces at the interfaces in both directions. Three finite element models using beam, shell or solid finite elements are presented for the verification of the accuracy of the results.

Schiehlen and Seifried (Chapter 9) elaborately describe the impact on beams that results in large rigid body motions and small structural waves. Such mechanical systems are often modeled as multibody systems to describe the large nonlinear motion where the impacts are treated by the coefficient of restitution. The coefficient of restitution is considered as deterministic number depending on the material, the shape and the

velocity of the colliding bodies. However, in experiments and computations it was observed that for a sphere striking a beam the coefficient of restitution is uncertain due to multiple impacts resulting in chaotic behavior. For the evaluation of the numerical and experimental data a statistical approach is proposed providing mean value and dispersion of the coefficient of restitution depending on four classes of the velocity. It is shown that these parameters allow characterizing the uncertainty. The statistical range is increasing with the relative velocity of the impact. However, the mean value or midrange point, respectively, may be used to solve the structural dynamics beam problem.

A rational approach is proposed by Paraskevopoulos, Panagiotopoulos and Talaslidis (Chapter 10) for the time integration of the dynamic equations arising in nonlinear structural problems, which employs a series of innovative concepts, e.g.: independent assumptions for the velocities and momentum type variables, use of different approximations for the test functions and the variables itself, and abandonment of the convention concerning the vanishing of the test functions at the time boundaries. The presented methodology offers a systematic and mathematically consistent procedure for time integration, ensures consistency and stability, and avoids flaws of existing techniques. Conservation properties are examined employing a form of Noether's Theorem. Furthermore, existing integration schemes may be theoretically justified by the present approach. The methodology is applied to the analysis of systems under moving loads and masses. Since this class of problems contains Dirac's delta function and its time derivatives, the effective numerical treatment of the governing equations offers a challenging problem.

Tairidis, Stavroulakis, Marinova and Zacharenakis (Chapter 11) describe how smart structures are incorporated into control schemes that allow them to react against disturbances. In mechanics, suppression of mechanical vibrations with possible applications on noise and vibration isolation is a very important field. Smart structures that include sensors and actuators are able to react to the environment due to coupling with some active control mechanism. The intelligence is introduced by a structural control scheme. A model problem of a smart beam with embedded piezoelectric sensors and actuators is used in this study. Vibration suppression is realized by using active control. Classical mathematical control usually gives good results for linear feedback laws under given assumptions. The design of nonlinear controllers based on fuzzy inference rules is proposed and tested. From the numerical results it can be observed that further vibration reduction can be accomplished. Nevertheless, the problems concerning velocities and accelerations remain. The performance of the fuzzy control system can be further reduced by fine-tuning the parameters of the fuzzy system (membership functions, rules, etc) by using neural networks or a global optimization scheme such as the Particle Swarm Optimization (PSO) method.

The essence of railway dynamics is the transfer of forces at the wheel rail interface. The energy from the motion of the train is taken up as elastic deformation in the track structure consisting of the rail, sleepers, dry crust, ballast and soil. Spatial changes in the material properties of the track and subground may lead to variations in the contact forces at the wheel-rail interface. A shift from one material to another can potentially induce transition radiation vibration modes. The phenomenon has been observed in situations where the train goes onto a bridge. In the chapter by Lane, Kettil and Wiberg (Chapter 12) an advanced numerical model of the entire train-track-subgrade dynamic

system with moving finite elements has been used to study the influence of material stiffness transitions in the subground. While the properties of the ballast and the rail were kept constant, the Young's moduli of the two layers of clay representing the soil underwent a linear change over a short distance. Both transitions from soft to stiff and from stiff to soft soil were considered. The results indicate that the main effect of the transition is a temporary variation followed by a transient low-frequent vibration.

High speed rail transportation is quickly becoming a popular form of mass transit through-out the world. High Speed Trains (HST) pertain to passenger trains traveling in excess of 160 km/h, and as fast as 500 km/h. Potential problems arise when high speed trains travel over soft soils having relatively low wave velocities. In the chapter by Rizos, O'Brien and Leon (Chapter 13) an efficient methodology for the analysis of vibrations in a railroad track system, induced by the passage of conventional and high speed trains, is presented. The methodology is based on an efficient coupling of the Boundary Element method (BEM) with the Finite Element Method (FEM) in the direct time domain. BEM is based on the 4th order B-Spline fundamental solutions for 3-D elastodynamics and the concept of B-Spline impulse response functions. The BEM is used for the modeling of the soil-tie system and the FEM for the modeling of the flexible rail system. Soil-Structure Interaction and traveling wave effects are inherently accounted for and normalizations and scaling procedures are adopted. The proposed methodology allows for selection of different time steps in order to fulfil stability requirements of each solver. Numerical applications demonstrate the accuracy and versatility of the method.

The chapter by De Roeck and Reynders (Chapter 14) gives an overview of the necessary conditions for a successful structural condition assessment by vibration measurements and concentrates on finite element (FE) updating, a versatile method for damage identification. First a critical overview is given about the advantages and disadvantages of the different excitation sources: forced, ambient and impact excitation. At the expense of building an elaborate FE-model of the structure, all acquired data can be used: natural frequencies, scaled or unscaled mode shapes and modal strains. Potential damage is simulated in the finite element model using a parametric representation and a constrained optimization problem is solved with the objective function defined as a sum of squared differences. Two bridge examples illustrate the use of finite element updating for damage assessment. Finally, a detailed set of conclusions are highlighted which can be considered as guidelines for engineering practice in vibration monitoring.

There is a dearth of accurate, efficient and reliable analytical approaches for the inelastic static and dynamic analyses of complex reinforced concrete and composite high-rise buildings under extreme loads taking into account shear-flexure-axial interaction, crack propagation and other detailed features of concrete response. In the work of Ji, Kwon, Elnashai and Kuchma (Chapter 15), a new approach termed Multi-resolution Distributed Finite Element Analysis (MDFEA) is proposed and used to analyze a reference RC high-rise building with a dual core wall-frame system. The features of the new framework are demonstrated through the analysis of a complex 54-story reinforced concrete building. In this distributed analysis framework, the capabilities of a frame analysis tool and a continuum analysis tool are combined using a suitable simulation coordinator software. The static and dynamic responses of the building are predicted using MDFEA and compared with those predicted by conventional frame analysis. The comparisons from both pushover and response history analysis highlight that due

to the influence of shear, the use of the multi-resolution approach is able to capture critical aspects of the behavior more sufficiently than some traditional methodologies performing pure frame analysis. The integrated MDFEA framework is generic, thus it enables the use of the best features of any computational tools so as to accurately and efficiently predict the inelastic static and dynamic response of complex structures subjected to extreme loads.

A simplified method for the probabilistic seismic performance assessment of building structures is presented by Dolšek and Fajfar (Chapter 16). The method is basically the SAC-FEMA approach, in which the most demanding part, i.e. the Incremental Dynamic Analysis (IDA), is replaced by the incremental N2 method, which is based on nonlinear pushover analysis and the response spectrum approach and has been implemented in Eurocode 8. In this work the method is applied to a bare and an infilled reinforced concrete frame, for which pseudo-dynamical laboratory test results are available. The most common analytical modeling technique, which employs compressive diagonal struts for modeling of masonry infill, and one-component lumped plasticity elements for modeling the flexural behavior of beams and columns, was applied. The mathematical models developed are validated by comparing the results of nonlinear dynamic analyses with the test results. The probabilities of exceedance of the near collapse limit state are estimated and discussed. The results of analyses indicate that the infills can completely change the distribution of damage throughout the structure. The probability of failure of the infilled frame is smaller than that of the bare frame, however for both structures the probability of failure is larger than acceptable.

Barbat, Oller, Mata and Vielma (Chapter 17) study the nonlinear dynamic response of reinforced concrete (RC) buildings with energy dissipating devices using advanced computational techniques. A fully geometric and constitutive nonlinear model is used for describing the dynamic behavior of structures. The equations of motion are expressed in terms of cross sectional forces and strains and its weak form is solved using the displacement based finite element method. A suitable version of Newmark's scheme is used in updating the kinematics variables in a classical Newton type iterative scheme. Material points of the cross section are assumed to be composed of several simple materials with their own constitutive laws. The mixing theory is used to treat the resulting composite. A specific finite element based on the beam theory is proposed for the dissipators including constitutive relations. In addition, several numerical tests are carried out to validate the proposed model.

In the contribution by Sibilio, Ciampoli and Beck (Chapter 18), a complete procedure for structural health monitoring, that is, for both damage detection and reliability assessment of a structure subject to seismic excitation, is briefly illustrated and applied to an example case. The problem of damage detection is dealt with by an identification technique with unknown input. A Bayesian model updating procedure is adopted to quantify the damage to the structure based on data from monitoring. Bayesian updating is based on an adaptive Markov Chain Monte Carlo method: the knowledge of the modal quantities of the undamaged and damaged structure is used to update the stiffness parameters that are chosen as the damage indicators. An advanced simulation technique, the so-called Subset Simulation, is then used to assess the probability of exceeding any structural response level, that is, the risk for the damaged structure. The procedure is formulated in a unified probabilistic framework that takes into account

any kind of uncertainty involved in the various phases of the analysis. It is observed that the Bayesian approach is really efficient in characterizing the structural damage and its effects in probabilistic terms. The main reason is that this approach gives as final result the probability density functions of the identified parameters, which in turn can be used in any structural reliability assessment. Moreover, Subset Simulation requires a much smaller number of samples than Monte Carlo simulation; this advantage is essential, especially for structures which exhibit a strongly nonlinear behaviour when subjected to seismic excitation.

A multiphase model including a hypoplastic formulation of the solid phase is presented and its application to earthquake engineering problems is discussed by Meskouris, Holler, Butenweg and Meiners (Chapter 19). This advanced soil model, which is based on the theory of porous media, comprises three distinct phases namely: solid, fluid and gas phase. For each of these phases the compressibility of the respective medium is taken into account in the mathematical formulation of the model. Due to the hypoplastic formulation including intergranular strain, the model is capable of predicting soil behaviour even under cyclic loading and therefore offers a possibility to further investigate complex dynamical phenomena such as ground liquefaction. The presented mutliphase model is capable of simulating consolidation, saturation and drainage processes and can realistically predict permanent ground displacements. Although the compressibilities of fluid and gas phases do not have a strong impact on the flow characteristics and the load bearing capacity of soils, they were still taken into account to provide further application possibilities for the model. Additionally, the model allows the implementation of arbitrary constitutive equations for the solid phase and also allows coupling to existing solid elements. The accuracy of the numerical approximation has been shown by comparison to experimental data. The model is numerically realized by means of the finite element method, it is implemented into the finite element code ANSYS and also allows the simulation of soil-structure interaction problems.

In the chapter by Reinhorn, Sivaselvan, Dargush and Lavan (Chapter 20) a Lagrangian approach is developed for analysis of frame structures near-collapse, which is a mixed method, where in addition to the displacements, the stress-resultants and other variables of state are primary unknowns. This formulation consists of two sets of equations: equilibrium and compatibility of displacement rates (velocities), while its primary unknowns are forces and velocities. For numerical solution, a discrete variational integrator is derived. This integrator inherits the energy and momentum conservation characteristics. The integration of each step is a constrained minimization problem and it is solved using an Augmented Lagrangian algorithm. The presented examples show that this method can provide as good or better information than a widely used displacement based inelastic analysis solution. The results also show that the method is stable and efficient for large structures. However, the power of the method presented herein is in evaluating structures where various elements collapse, and forces and momentum have to be redistributed in the remaining system.

Spacone, Camata and Faggella (Chapter 21) underline the potential of nonlinear models and nonlinear procedures for seismic analysis of reinforced concrete frame structures. Nonlinear methods of analysis for seismic vulnerability assessment of existing structures are attracting increasing attention due to their capacity to predict the actual seismic behavior better than linear methods. Their inclusion in modern design

codes such as Eurocode 8 is a major boost for their use in practical applications. Recent years have also seen steady advances in the modeling capabilities of reinforced concrete frames, particularly in the field of beam and column behavior. Advanced frame modeling tools are included in both research and commercial codes. As research and practicing engineers start applying nonlinear methods to real problems, questions arise regarding the application of the design code-provided procedures and the selection of the appropriate structural model given the objective limitations of the frame modeling capabilities today available. The scope of this chapter is to discuss some of the issues still open regarding the applications of the nonlinear methods of analysis to reinforced concrete structures, with the firm belief that an open discussion on these methods, their advantages and limitations will open the way to a more widespread use of advanced and more accurate methods of analysis. This way, the above issues will become clearer and any major deficiencies will be solved, especially through a strong interaction between practicing engineers and researchers.

Past earthquakes have shown that a common failure mode of reinforced concrete (RC) members is buckling of the longitudinal reinforcement. In order to obtain an accurate prediction of strength and ductility, this effect should be taken into account during analysis. Buckling of the reinforcement is in essence a stability problem and therefore depends both on the geometry of the bar and on the material properties. To deal with this issue, Fragiadakis, Pinho and Antoniou (Chapter 22) propose a uniaxial material model for steel reinforcing bars subjected to a generalized loading history. The model of Monti and Nuti which is based on a set of experimental observations in order to account for buckling of the steel bars is examined. It has been noticed that in the case of partial unloading and then reloading, a common situation when a structure is subjected to seismic actions, the model might greatly overestimate the corresponding stress. An additional memory rule is thus proposed to eliminate this observed shortcoming. With the aid of the proposed modification, the Monti-Nuti model is proved to be capable of simulating accurately the capacity of reinforced concrete members. The rules presented are easy to implement and applicable to any model in the literature where a similar situation is identified. Two case studies are examined where the enhanced model was proven capable to produce realistic numerical results.

Pantelides, Adan and Reaveley (Chapter 23) analyze steel moment-resisting connections using finite element modelling. They stress that in seismic structural design and rehabilitation deviations from the common practice require testing. The AISC seismic provisions for structural steel buildings recommend that usage and sizing of beam flange continuity plates across the column web shall be based on tests. FEMA 350 recommended seismic design criteria state that unless project-specific testing is performed to demonstrate that continuity plates are not required, moment-resisting connections should be provided with continuity plates when the thickness of the column flange is below a minimum value. Similarly, in order to qualify any new connection type for inclusion in the AISC prequalified connections for special and intermediate steel moment frames for seismic applications, testing has to be carried out to validate the design concept and to satisfy minimum performance criteria on strength and interstory drift angle capacity. In this study, nonlinear finite element analyses are performed to establish a correlation between measured and computed responses of two steel connections: (i) the reduced beam section (RBS) moment connection without continuity plates, and (ii) the bolted bracket (BB) moment connection. The connections

were tested using cyclic quasi-static displacements applied at the beam tip and the comparison of measured and computed responses showed good correlation.

Ansal, Kurtulus and Tönük (Chapter 24) present a specialized software to perform earthquake scenarios for estimating structural damage and human casualties. The first stage involves generation of microzonation maps for separately calculated regional seismic hazard. The seismic hazard can be probabilistic or deterministic where PGA and spectral accelerations or acceleration time histories are specified respectively for each cell on the engineering bedrock outcrop. In the second stage, representative soil profiles are defined for each cell and 1D site response analyses are conducted to calculate average PGAs and elastic acceleration response spectra on the ground surface. An envelope NEHRP spectrum is calculated for each cell based on site specific average acceleration spectrum to estimate short ($T = 0.2$ s) and long ($T = 1$ s) period spectral accelerations. In the third stage, vulnerability of the building stock is estimated with respect to number of buildings in each cell. A characteristic case study is discussed to demonstrate the applicability of the software.

In the chapter by Aydınoğlu and Önem (Chapter 25) the Incremental Response Spectrum Analysis (IRSA) procedure is introduced as an advanced multi-mode pushover analysis tool for the performance-based seismic assessment and design of buildings and bridges. The practical version of the procedure works directly with smoothed elastic response spectrum and makes use of the well-known equal displacement rule to scale modal displacement increments at each piecewise linear step, in which the traditional linear Response Spectrum Analysis (RSA) is implemented. Being a general analysis tool, IRSA is completely independent of the type of structure, as in its linear counterpart RSA. In this respect, IRSA is readily applicable to any type of bridge. In the present contribution, IRSA is applied to few types of highway bridges and its performance is checked against the results of the corresponding nonlinear response history analysis (NRHA) performed. It is shown that IRSA is capable of estimating bridge nonlinear demands with an acceptable accuracy for practical purposes.

In the work of Papagiannopoulos and Beskos (Chapter 26) an efficient method is presented for the determination of the maximum structural response through a linear elastic spectrum analysis using equivalent modal damping values instead of the crude strength reduction factor. Geometrical and material non – linear structural effects are converted into equivalent time – invariant modal damping values. These equivalent damping values for the first few modes of the structure are numerically computed by first iteratively forming a frequency response transfer function until certain smoothness criteria are satisfied and then by solving a set of non – linear algebraic equations. A design – oriented scheme is developed in order to apply the equivalent modal damping concept to the seismic response analysis of multi-degree-of-freedom (MDOF) building structures. This scheme involves: a) the quantification of equivalent modal damping of a structure for predefined deformation limits and b) the use of spectrum analysis and modal synthesis for the calculation of the design base shear of the structure. For illustration purposes, curves providing equivalent damping as function of period for the first few modes as well as design acceleration versus period for given equivalent damping are constructed using a large number of steel moment resisting frames excited by various seismic motions. It is concluded that the proposed design scheme can be viewed as an alternative to the force based method of current seismic codes with equivalent modal damping values playing the role of the strength reduction factor.

Beck and Muto (Chapter 27) explain how identification of structural models from measured earthquake response can play a key role in structural health monitoring, structural control and improving performance-based design. System identification using data from strong seismic shaking is complicated by the nonlinear hysteretic response of structures where the restoring forces depend on the previous time history of the structural response rather than on an instantaneous finite-dimensional state. Furthermore, this inverse problem is ill-conditioned because even if some components in the structure show substantial yielding, others will exhibit nearly elastic response, producing no information about their yielding behavior. Classical least-squares or maximum likelihood estimation will not work with a realistic class of hysteretic models because it will be unidentifiable based on the data. In contrast, the combination of Bayesian updating and model class selection provides a powerful and rigorous approach to tackle this problem, especially when implemented using Markov Chain Monte Carlo simulation methods. The emergence of these methods in recent years has led to a renaissance in Bayesian methods across all disciplines in science and engineering because the high-dimensional integrations that are involved can now be readily evaluated. The power of these methods to handle ill-conditioned or unidentifiable system identification problems is demonstrated by using a recently-developed stochastic simulation algorithm, Transitional Markov Chain Monte Carlo, to perform Bayesian updating and model class selection on a class of Masing hysteretic structural models that are relatively simple yet can give realistic responses to seismic loading. Examples are given using deteriorating hysteretic building models with simulated seismic response data.

The chapter by Jeremic and Jie (Chapter 28) focuses on two main topics. Firstly, it describes (in some detail) a parallel finite element computational method that is particularly well suited for elastic-plastic models. The method, named Plastic Domain Decomposition (PDD), dynamically balances computational loads for elastic-plastic finite element computations on distributed memory parallel computers. The PDD method uses the original algorithm with weighted graph partitioning that minimizes wall clock time for parallel, elastic-plastic computations. Excellent scalability of the method is shown on a variety of distributed memory parallel computers (from in house developed clusters to large national supercomputers). Secondly, the developed PDD method is applied to a problem of seismic soil-foundation-structure (SFS) interaction. Detailed 3D models of a prototype bridge (with up to 1.6 million DOFs) were developed and used for scalability studies. In addition to that, those detailed models were used to investigate seismic SFS interaction behavior of a conrete bridge founded on piles in soft and/or stiff soils. Results indicate that the interaction of a triad of dynamic characteristics of earthquake, soil and structure all have very important influence on overall seismic behavior of a soil-structure system. For example, it is shown that a long period earthquake motion has a detrimental effect on a stiff structure founded on soft soil. In contrast a short period earthquake motion has an even more detrimental effect on a stiff structure founded on stiff soil.

Retaining systems, such as cantilever walls, are widely used worldwide for serving various purposes in structures and infrastructures (embankments, bridges, ports, etc). In the chapter by Tsompanakis (Chapter 29) the dynamic interaction of the retaining walls with the retained soil and the retained structures is investigated. This so-called phenomenon of dynamic wall–soil–structure interaction (DWSSI) is a rather

complicated issue that includes: (a) the dynamic interaction between a wall and a retained single soil layer (DWSI), and (b) the "standard" dynamic soil–structure interaction (DSSI) of a structure with its underlying soil. The aforementioned dynamic interaction issues are not properly considered in the modern seismic codes, thus, in the present work, using numerical two-dimensional simulations, the influence of the wall flexibility on the free-field ground shaking behind the wall is investigated. Emphasis is given on the impact of the wall's presence on the amplification of the base acceleration on the retained soil layer, an amplification generally ignored by the seismic design norms. Consequently, a structure founded on the retained soil is included in the numerical models. Numerical results provide a clear indication of the direct interaction between a retaining wall and its retained structures. That fact justifies the necessity for a more elaborate consideration of this interrelated phenomenon on the seismic design, not only of the retaining walls but of the nearby structures as well.

In the chapter by Kim and Lee (Chapter 30) a 3-D transmitting boundary in a cylindrical coordinate system is applied to obtain the earthquake response of a cylindrical liquid storage tank installed in the water-saturated transversely isotropic ground. The effects of the far-field region are represented by the transmitting boundary. Using finite elements, models are developed for the flexible tank wall and the near-field region of the ground. The motion of the contained liquid is modeled using boundary elements. Hybrid time domain-frequency domain analysis is used to obtain direct time-domain representation of the earthquake response of the system. Numerical results are given to illustrate this method of analysis. The results from the numerical analysis show that complex soil-structure interactions in water-saturated transversely isotropic ground can be modeled successfully. A rigorous two-phase transversely isotropic medium model has to be employed to accurately represent the dynamic behavior of a structure on the water-saturated transversely isotropic strata.

In the work by Mitropoulou, Bakas, Lagaros and Papadrakakis (Chapter 31) a number of design approaches for 3D reinforced concrete (RC) buildings are formulated in the framework of structural optimization and they are assessed in terms of structural performance under earthquake loading. This chapter consists of two distinctive parts. In the first part the European seismic design code is evaluated with reference to the behavioral factor q. For each optimum design achieved for the various values of the behavioral factor, fragility curves are developed for four characteristic damage states. The optimum designs are compared based on limit-state probabilities of exceedance encountered for the design earthquake. In the second part, three design approaches for RC buildings are considered aiming at improving the torsional response of RC buildings. It is shown that the optimized designs obtained according to the minimum eccentricity of the rigidity centre behave better in frequent (50/50 hazard level) and occasional (10/50 hazard level) earthquakes, while the designs obtained according to the minimum eccentricity of the strength centre formulation was found better in rare (2/50 hazard level) events.

Hurtado and Aguirre (Chapter 32) focus on the randomness of earthquake ground motions which constitutes one of the main problems in seismic design, as it increases the uncertainty and the effectiveness of design decisions. In advanced earthquake-resistant design an alternative to incorporate ground motion uncertainty is to perform a reliability-based optimization, consisting in minimizing the cost subject to keeping the failure probability less than a certain threshold. The use of structural passive or active

control necessarily implies a severe reduction of the allowable failure probabilities, thus making more expensive the application of reliability-based optimization. In addition, a major problem in applying Linear Quadratic Regulator (LQR) control is that it is subject to arbitrary selection of the relative weights of the story displacements and control forces. For these reasons it is convenient to apply a different strategy than the reliability-based design to overcome these difficulties and drawbacks. The concept of robust optimal design is used, which consists of minimizing the structural cost in such a way that the standard deviations of the responses are less than certain thresholds, thus yielding the optimal values of the weights with due regard to the uncertainties present in the system. The computation of the response standard deviations in view of the large uncertainties of the ground motion parameters is also discussed and the application of a practical procedure is suggested and illustrated for a passive control case.

Marano, Sgobba and Greco (Chapter 33) propose a robust optimization criterion of mechanical parameters in the design of linear Tuned Mass Dampers (TMD) located at the top of a main structural system subject to random base accelerations. The dynamic input is modelled as a stationary filtered white noise random process. The aim is to properly consider non-uniform spectral contents that happen in many real physical vibration phenomena. The main structural system is described as a single linear degree of freedom, and it is assumed that uncertainty affects the system model. The problem parameters treated are described as random uncorrelated variables known only by the estimation of their means and variances. Robustness is formulated as a multi-objective optimization problem in which both the mean and variance of a conventional objective function are minimized simultaneously. Optimal Pareto fronts are obtained and results show a significant improvement in performance stability compared to a standard conventional solution.

Möller, Quiroz, Rubinstein and Foschi (Chapter 34) present an efficient methodology for performing performance-based design in earthquake engineering. They take into account various structural and ground motion uncertainties in optimizing design parameters, satisfying multiple performance criteria with target reliabilities and minimizing an objective. This implies performing nonlinear structural dynamic analyses for earthquakes likely to occur at the site, in order to obtain the demand responses of interest. The responses are represented here via neural networks and used in the performance criteria for estimation of achieved reliabilities by Monte Carlo simulation. An optimization technique is implemented to obtain optimal parameters, using a gradient-free algorithm. A numerical application is presented for a reinforced, multi-story concrete frame. The demand is simulated using artificially generated ground motions, with the peak ground acceleration corresponding to the city of Mendoza, Argentina. Performance requirements (operational, life safety or collapse) are specified in terms of damage severity, using maximum displacements, inter-story drifts, local and global damage indices while optimization objectives are minimum cost, minimum dimensions and/or minimum steel reinforcement.

In the last contribution, Jensen and Valdebenito (Chapter 35) deal with an efficient computational procedure for the reliability-based optimization of uncertain stochastic linear dynamical systems. The reliability-based optimization problem is formulated as the minimization of an objective function for a specified failure probability. The probability that design conditions are satisfied within a given time interval is used as a measure of the system reliability. Approximation concepts are used to construct

high quality approximations of dynamic responses in terms of the design variables and uncertain structural parameters during the optimal design process. The approximations are combined with an efficient simulation technique to generate explicit approximations of reliability measures with respect to the design variables. In particular, an efficient importance sampling technique is used to estimate the failure probability. The effectiveness and feasibility of the suggested approach is demonstrated by a characteristic example problem. Concurrently, the effect of uncertainty in the system parameters on the performance and reliability of the final design is also investigated. Numerical results show that uncertainty in the structural parameters may cause significant changes in the performance and reliability of linear systems subject to stochastic loading. The proposed procedure dramatically reduces the number of exact dynamic analyses as well as reliability estimations required during the design process.

The book editors would like to express their deep gratitude to all contributors for their active participation in the Compdyn07 Conference and for their time and effort devoted to the completion of their contributions for this volume. In addition, we are most appreciative to the Book Series Editor, Professor Dan M. Frangopol, for his kind invitation to edit this volume and for his constructive comments and suggestions offered during the publication process. Finally, the editors would like to thank all the personnel of Taylor and Francis Publishers, especially Germaine Seijger, Richard Gundel, Leon Bijnsdorp and Janjaap Blom, for their most valuable support for the publication of this book.

Manolis Papadrakakis
Dimos C. Charmpis
Nikos D. Lagaros
Yiannis Tsompanakis
August 2008

Brief Curriculum Vitae of the Editors

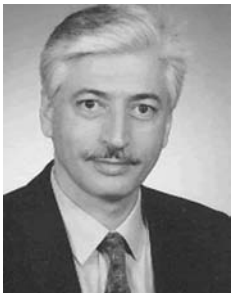

Manolis Papadrakakis is Professor of computational structural mechanics in the School of Civil Engineering at the National Technical University of Athens, Greece. His main fields of interest are: large-scale, stochastic and adaptive finite element applications, nonlinear dynamics, structural optimization, soil-fluid-structure interaction and soft computing applications in structural engineering. He is co-Editor-in-chief of the Computer Methods in Applied Mechanics and Engineering journal, an Honorary Editor of the International Journal of Computational Methods, and an Editorial Board member of a number of other international scientific journals. He is also a member of both the Executive and the General Council of the International Association for Computational Mechanics, Chairman of the European Committee on Computational Solid and Structural Mechanics and Vice President of the John Argyris Foundation. He is also the President of the European Community on Computational Methods in Applied Sciences (ECCOMAS). Professor Papadrakakis has chaired many international conferences and presented numerous invited lectures. He has written and edited various books and published a large variety of scientific articles and book chapters.

Dimos Charmpis is a Lecturer at the Department of Civil and Environmental Engineering of the University of Cyprus. His scientific interests cover various topics of Computational Mechanics and aim in the exploitation of innovative computing systems and numerical methods for the analysis and design of structures under static or dynamic/seismic loading. More specifically, his research work is related with finite element methods, reliability estimation and stochastic analysis, design optimization, soft computing applications and high performance computing. Dr. Charmpis has participated in several research projects funded by national or European Union sources focusing on computational methods for structural engineering applications. He has also experience from working in the private civil engineering sector in Greece. He has authored or co-authored several scientific publications, has served as

board member and special sessions organizer in a number of international conferences and is a reviewer of research articles for international journals.

Nikos D. Lagaros is Lecturer of structural dynamics and computational mechanics in the School of Civil Engineering of the National Technical University of Athens, Greece. His research activity is focused on the development and the application of novel computational methods and information technology to structural and earthquake engineering analysis and design. In addition, Dr. Lagaros has provided consulting and expert-witness services to private companies and federal government agencies in Greece. He also serves as a member of the editorial board and reviewer of various international scientific journals. He has published numerous scientific papers, and is the co-editor of a number of books, one of which is dealing with innovative soft computing applications in earthquake engineering and another is focused on probabilistic structural optimization. Nikos Lagaros is co-organizer and co-editor of COMPDYN 2007 and its selected papers volume.

Yiannis Tsompanakis is Assistant Professor in the Department of Applied Sciences of the Technical University of Crete, Greece, where he teaches structural and computational mechanics as well as earthquake engineering lessons. His scientific interests include computational methods in structural and geotechnical earthquake engineering, structural optimization, probabilistic mechanics, structural assessment and the application of artificial intelligence methods in engineering. Dr. Tsompanakis has published many scientific papers and is the co-editor of several books in computational mechanics. He is involved in the organization of mini-symposia and special sessions in international conferences as well as special issues of scientific journals as guest editor. He serves as a board member in various conferences, co-organized the COMPDYN-2007 conference and acts as a co-editor of the resulting selected papers volume.

Contributors List

Adan Scott M., *Simpson Gumpertz and Heger Inc., San Francisco, USA*
Aguirre Naile, *Universidad Nacional de Colombia, Manizales, Colombia*
Ansal Atilla, *Bogaziçi University, Istanbul, Turkey*
Antoniou Stelios, *SeismoSoft—Software Solutions for Earthquake Engineering, Chalkida, Greece*
Armero Francisco, *University of California, Berkeley, USA*
Aydınoğlu Nuray M., *Bogaziçi University, Istanbul, Turkey*
Bakas Nikos P., *National Technical University of Athens, Athens, Greece*
Barbat Alex H., *Technical University of Catalonia, Barcelona, Spain*
Barbato Michele, *University of California, San Diego, USA*
Beck James L., *California Institute of Technology, Pasadena, USA*
Beskos Dimitri, *University of Patras, Rio, Greece*
Butenweg Christoph, *RWTH Aachen University, Aachen, Germany*
Camata Guido, *University of Chieti-Pescara, Pescara, Italy*
Chen Chahoui, *Universite de Marne la Vallee, Marne la Vallee, France*
Ciampoli Marcello, *Università di Roma, Rome, Italy*
Conte Joel P., *University of California, San Diego, USA*
Dargush Gary F., *University at Buffalo (SUNY), Buffalo, USA*
De Gersem Hilde, *K.U. Leuven, Leuven, Belgium*
De Munck Maarten, *K.U. Leuven, Leuven, Belgium*
De Roeck Guido, *K.U. Leuven, Leuven, Belgium*
De Wilde Willy Patrick, *Vrije Universiteit Brussel, Brussels, Belgium*
Desmet Wim, *K.U. Leuven, Leuven, Belgium*
Dolšek Matjaž, *University of Ljubljana, Ljubljana, Slovenia*
Duhamel Denis, *Ecole des Ponts, Marne la Vallee, France*
Durand Jean-François, *Universite de Marne la Vallee, Marne la Vallee, France*
Elnashai Amr S., *University of Illinois at Urbana-Champaign, Illinois, USA*
Faggella Marco, *University of Chieti-Pescara, Pescara, Italy*
Fajfar Peter, *University of Ljubljana, Ljubljana, Slovenia*
Foschi Ricardo O., *University of British Columbia, Vancouver, Canada*
Fragiadakis Michalis, *National Technical University of Athens, Athens, Greece*
Gagliardini Laurent, *PSA Peugeot-Citroen, Velizy-Villacoublay Cedex, France*
Greco Rita, *Technical University of Bari, Taranto, Italy*
Gu Quan, *University of California, San Diego, USA*

Holler Stefan, *Airbus Deutschland GmbH, Hamburg, Germany*
Hurtado Jorge E., *Universidad Nacional de Colombia, Manizales, Colombia*
Jensen Hector, *Santa Maria University, Valparaiso, Chile*
Jeremić Boris, *University of California Davis, California, USA*
Ji Jun, *Kal Krishnan Consulting Services, Inc., Oakland, USA*
Jie Guanzhou, *Wachovia Corporation, New York, USA*
Kettil Per, *Chalmers University of Technology, Gothenburg, Sweden*
Kim Jae Kwan, *Seoul National University, Seoul, Korea*
Krenk Steen, *Technical University of Denmark, Lyngby, Denmark*
Kuchma Daninal A., *University of Illinois at Urbana-Champaign, Illinois, USA*
Kurtuluş Aslı *Bogaziçi University, Istanbul, Turkey*
Kwon Oh-Sung, *Missouri University of Science and Technology, Missouri, USA*
Lagaros Nikos D., *National Technical University of Athens, Athens, Greece*
Lane Håkan, *Chalmers University of Technology, Gothenburg, Sweden*
Lavan Oren, *Technion - Israel Institute of Technology, Haifa, Israel*
Lee Jin Ho, *Seoul National University, Seoul, Korea*
Leon Evangelia, *Geomech Group Inc., Columbia, USA*
Marano Giuseppe Carlo, *Technical University of Bari, Taranto, Italy*
Marinova Daniela, *Technical University of Sofia, Sofia, Bulgaria*
Mata Pablo, *Technical University of Catalonia, Barcelona, Spain*
Meiners Daniel, *RWTH Aachen University, Aachen, Germany*
Meskouris Konstantin, *RWTH Aachen University, Aachen, Germany*
Mitropoulou Chara C., *National Technical University of Athens, Athens, Greece*
Moens David, *K.U. Leuven, Leuven, Belgium*
Mokos Vasilios G., *National Technical University of Athens, Athens, Greece*
Möller Oscar, *University of Rosario, Rosario, Argentina*
Muto Matthew M., *California Institute of Technology, Pasadena, USA*
O'Brien John, *University of South Carolina, Columbia, USA*
Oller Sergio, *Technical University of Catalonia, Barcelona, Spain*
Önem Göktürk, *Bogaziçi University, Istanbul, Turkey*
Panagiotopoulos Christos, *Aristotle University Thessaloniki, Thessaloniki, Greece*
Pantelides Chris P., *University of Utah, Salt Lake City, USA*
Papadrakakis Manolis, *National Technical University of Athens, Athens, Greece*
Papagiannopoulos George, *University of Patras, Rio, Greece*
Paraskevopoulos Elias, *Aristotle University Thessaloniki, Thessaloniki, Greece*
Pinho Rui, *European School for Advanced Studies in Reduction of Seismic Risk, Pavia, Italy*
Quiroz Laura, *University of Rosario, Rosario, Argentina*
Reaveley Lawrence D., *University of Utah, Salt Lake City, USA*
Reinhorn Andrei M., *University at Buffalo (SUNY), Buffalo, USA*
Reynders Edwin, *K.U. Leuven, Leuven, Belgium*
Rizos Dimitris C., *University of South Carolina, Columbia, USA*
Rubinstein Marcelo, *University of Rosario, Rosario, Argentina*
Sapountzakis Evangelos J., *National Technical University of Athens, Athens, Greece*
Schiehlen Werner, *University of Stuttgart, Stuttgart, Germany*
Schuëller Gerhart I., *University of Innsbruck, Innsbruck, Austria*
Seifried Robert, *University of Stuttgart, Stuttgart, Germany*

Sgobba Sara, *Technical University of Bari, Taranto, Italy*
Sibilio Enrico, *Università di Roma TRE, Rome, Italy*
Sivaselvan Mettupalayam V., *University of Colorado at Boulder, Boulder, USA*
Soize Christian, *Universite de Marne la Vallee, Marne la Vallee, France*
Spacone Enrico, *University of Chieti-Pescara, Pescara, Italy*
Stavroulakis Georgios, *Technical University of Crete, Chania, Greece*
Steirteghem Jan Van, *Besix Belgium, Brussels, Belgium*
Tairidis Georgios, *Technical University of Crete, Chania, Greece*
Talaslidis Demosthenes, *Aristotle University Thessaloniki, Thessaloniki, Greece*
Tönük Gökçe, *Bogaziçi University, Istanbul, Turkey*
Tsompanakis Yiannis, *Technical University of Crete, Chania, Greece*
Valdebenito Marcos A., *University of Innsbruck, Innsbruck, Austria*
Vandepitte Dirk, *K.U. Leuven, Leuven, Belgium*
Vielma Juan C., *Lisandro Alvarado University, Barquisimeto, Venezuela*
Wiberg Nils-Erik, *Chalmers University of Technology, Gothenburg, Sweden*
Zacharenakis Emmanuel, *Technological Educational Institute of Crete, Heraklion, Greece*

Author Data

Scott M. Adan
Simpson Gumpertz and Heger Inc.
The Landmark @ One Market, Suite 600
San Francisco, CA 94105
USA
E-mail: smadan@sgh.com

Naile Aguirre
Universidad Nacional de Colombia
Apartado 127
Manizales
Colombia

Atilla Ansal
Professor
Earthquake Engineering Department
Kandilli Observatory and Earthquake
Research Institute
Bogaziçi University,
Çengelköy, Istanbul 34684, Turkey
E-mail: ansal@boun.edu.tr

Stelios Antoniou
SeismoSoft—Software Solutions for
Earthquake Engineering,
21 Perikleous Stavrou Str, Chalkida, Greece
E-mail: s.antoniou@seismosoft.com

Francisco Armero
Professor
Structural Engineering, Mechanics
and Materials
Department of Civil and Environmental
Engineering
University of California at Berkeley
Berkeley CA 94720

USA
E-mail: armero@ce.berkeley.edu

M. Nuray Aydınoğlu
Professor
Kandilli Observatory and Earthquake
Research Institute
Boğaziçi University
34684 Çengelköy, Istanbul, Turkey
E-mail: aydinogn@boun.edu.tr

Nikos P. Bakas
PhD Student
Institute of Structural Analysis &
Seismic Research
Faculty of Civil Engineering
National Technical University of Athens,
Zografou Campus, Athens 157 80, Greece
E-mail: nibas@central.ntua.gr

Alex H. Barbat
Professor
Structural Mechanics Department,
Civil Engineering School,
Technical University of Catalonia
Edificio C1, Campus Norte UPC,
Jordi Girona 1–3,
Barcelona 08034, Spain
E-mail: alex.barbat@upc.es

Michele Barbato
Assistant Professor
Department of Civil and Environmental
Engineering
Louisiana State University, Baton Rouge
3531 Patrick F. Taylor Hall
Baton Rouge, LA 70803, USA
E-mail: mbarbato@lsu.edu

James L. Beck
Professor
Division of Engineering and Applied Science,
California Institute of Technology
California Blvd,
MC 104-44, 91125, Pasadena (CA), USA
E-mail: jimbeck@caltech.edu

Dimitri Beskos
Professor
Department of Civil Engineering

University of Patras,
Rio 26500, Greece
E-mail: d.e.beskos@upatras.gr

Christoph Butenweg
Senior Lecturer
Institute of Structural Statics and Dynamics,
Faculty of Civil Engineering,
RWTH Aachen University
Mies-van-der-Rohe-Strasse 1,
D-52074 Aachen, Germany
E-mail: butenweg@lbb.rwth-aachen.de

Guido Camata
University of Chieti-Pescara, Dept. PRICOS
viale Pindaro 42, 65127,
Pescara 65127, Italy
E-mail: g.camata@unich.it

Chahoui Chen
Doctoral Student
Université Paris-Est
Laboratoire Modélisation et Simulation
Multi-Echelle
5 Bd Descartes
77 454 Marne-la-Vallée, France

Marcello Ciampoli
Professor
Department of Structural and
Geotechnical Engineering,
Sapienza Università di Roma
Via Eudossiana 18, Roma 00184, Italy
E-mail: marcello.ciampoli@uniroma1.it

Joel P. Conte
Professor
Department of Structural Engineering
University of California, San Diego
9500 Gilman Drive
La Jolla, CA 92093-0085, USA
E-mail: jpconte@ucsd.edu

Gary F. Dargush
Professor and Department Chairman
Department of Mechanical & Aerospace
Engineering

University at Buffalo (SUNY)
Buffalo, NY 14260, USA
E-mail: gdargush@eng.buffalo.edu

Hilde De Gersem
K.U.Leuven
Department of Mechanical Engineering,
Division Production Engineering,
Machine Design and Automation (PMA)
Kasteelpark Arenberg 41, box 2449, B-3001,
Leuven, Belgium

Maarten De Munck
K.U.Leuven
Department of Mechanical Engineering,
Division Production Engineering, Machine
Design and Automation (PMA)
Kasteelpark Arenberg 41, box 2449, B-3001,
Leuven, Belgium

Guido De Roeck
Professor
Department of Civil Engineering,
K.U. Leuven
Division Structural Mechanics
Kasteelpark Arenberg 40
Belgium
E-mail: guido.deroeck@bwk.kuleuven.be

Willy Patrick De Wilde
Vrije Universiteit Brussel
Mechanics of Materials and Constructions,
Pleinlaan 2, B-1050 Brussels, Belgium
E-mail: pdwilde@vub.ac.be

Wim Desmet
K.U.Leuven
Department of Mechanical Engineering,
Division Production Engineering,
Machine Design and Automation (PMA)
Celestijnenlaan 300-B, box 2420, B-3001,
Leuven, Belgium

Matjaž Dolšek
University of Ljubljana
Faculty of Civil and Geodetic Engineering
Jamova 2, SI-1000, Ljubljana

Slovenia
E-mail: mdolsek@ikpir.fgg.uni-lj.si

Denis Duhamel
Professor
Université Paris-Est
Laboratoire Analyse des Matériaux et
Identifications, ENPC
6–8 Avenue Blaise Pascal
77 455 Marne-la-Vallée, France
E-mail: denis.duhamel@univ-paris-est.fr

Jean-François Durand
Doctoral Student
Université Paris-Est
Laboratoire Modélisation et Simulation
Multi-Echelle
5 Bd Descartes
77 454 Marne-la-Vallée, France

Amr S. Elnashai
William J. & Elaine F. Hall Endowed
Professor in Civil & Environmental
Engineering
Dept. of Civil and Environment
Engineering
University of Illinois at Urbana-Champaign,
IL, USA
E-mail: aelnash@uiuc.edu

Marco Faggella
University of Chieti-Pescara, Dept. PRICOS
viale Pindaro 42
Pescara 65127, Italy
also
Department of Structural Engineering
University of Califomia San Diego
9500 Gillllan Drive, MC 0085
La Jolla, Califomia 92093-0085, USA
E-mail: mfaggella@ucsd.edu

Peter Fajfar
Professor
University of Ljubljana
Faculty of Civil and Geodetic Engineering
Jamova 2, SI-1000, Ljubljana
Slovenia
E-mail: pfajfar@ikpir.fgg.uni-lj.si

Ricardo O. Foschi
Department of Civil Engineering
University of British Columbia
Vancouver V6T 1Z4, B.C.
Canada
E-mail: rowfa1@civil.ubc.ca

Michalis Fragiadakis
School of Civil Engineering, National
Technical University of Athens,
Zografou Campus, Athens 15780, Greece
and
Department of Civil Engineering,
University of Thessaly,
Pedion Areos 38334, Volos, Greece
E-mail: mfrag@mail.ntua.gr

Laurent Gagliardini
PSA Peugeot-Citroen
Route de Gisy
78 943 Velizy-Villacoublay, France
E-mail: laurent.gagliardini@mpsa.com

Rita Greco
Assistant Professor
Department of Civil Engineering and
Architectural Science,
Faculty of Architecture
Technical University of Bari,
Via Orabona 4
Bari 70126, Italy
E-mail: r.greco@poliba.it

Quan Gu
Staff Engineer
AMEC Geomatrix
510 Superior Avenue, Suite 200
Newport Beach, CA 92663, USA
E-mail: quan.gu@amec.com

Stefan Holler
Structural Engineer
Passstr. 89
D-52070 Aachen, Germany
E-mail: mail@StefanHoller.de

Jorge E. Hurtado
Professor
Universidad Nacional de Colombia
Apartado 127
Manizales
Colombia
E-mail: jehurtadog@unal.edu.co

Hector Jensen
Professor
Department of Civil Engineering
Santa Maria University
Valparaiso, Chile
E-mail: hector.jensen@usm.cl

Boris Jeremić
Associate Professor
Department of Civil and Environmental
Engineering
University of California
Davis, CA 95616, USA
E-mail: jeremic@ucdavis.edu

Jun Ji
Senior Project Engineer
Kal Krishnan Consulting Services, Inc.
300 Lakeside Drive, Suite 1080
Oakland, CA 94612, USA
E-mail: junji999@gmail.com

Guanzhou Jie
Wachovia Corporation,
375 Park Ave,
New York, NY 10152, USA
E-mail: gjie@ucdavis.edu

Per Kettil
Assistant Professor
Department of Applied Mechanics
Chalmers University of Technology,
Gothenburg 412 80, Sweden
E-mail: Per.Kettil@chalmers.se

Jae Kwan Kim
Professor
Department of Civil and Environmental

Engieering,
Seoul National University,
Seoul 151–744, Korea
E-mail: jkwankim@snu.ac.kr

Steen Krenk
Professor
Department of Mechanical Engineering
Technical University of Denmark
Nils Koppels Allé, Building 403
DK-2800 Kgs. Lyngby
Denmark
E-mail: sk@mek.dtu.dk

Daninal A. Kuchma
Associate Professor
Dept. of Civil and Environment Engineering
University of Illinois at Urbana-Champaign,
IL, USA
E-mail: kuchma@uiuc.edu

Aslı Kurtuluş
Research Associate
Earthquake Engineering Department
Kandilli Observatory and Earthquake
Research Institute
Bogaziçi University,
Çengelköy, Istanbul 34684, Turkey
E-mail: asli.kurtulus@boun.edu.tr

Oh-Sung Kwon
Assistant Professor
Department of Civil, Architectural, and
Environmental Engineering
Missouri University of Science and
Technology (Missouri S&T)
324 Butler-Carlton Hall,
1401 North Pine Street
Rolla, MO 65409-0030, USA
E-mail: kwono@mst.edu

Nikos D. Lagaros
Lecturer
Institute of Structural Analysis &
Seismic Research
Faculty of Civil Engineering

National Technical University of Athens,
Zografou Campus, Athens 157 80, Greece
E-mail: nlagaros@central.ntua.gr

Håkan Lane
Techn. Dr.
Department of Applied Mechanics
Chalmers University of Technology,
Gothenburg 412 80, Sweden

Oren Lavan
Senior Lecturer
Faculty of Civil and Environmental Engineering
Technion - Israel Institute of Technology,
Technion City, Haifa 32000, Israel
E-mail: lavan@tx.technion.ac.il

Jin Ho Lee
Postdoctoral Researcher
Korea Construction Engineering Development
Collaboratory Program
Management Center,
Seoul National University,
Seoul 151–744, Korea
E-mail: ohnij2@ snu.ac.kr

Evangelia Leon
Geotechnical Engineer
The Geomech Group Inc.
1407 Sunbury Lane
Columbia SC 29205, USA
E-mail: lleon@geomechgroup.com

Giuseppe Carlo Marano
Assistant Professor
Department of Environmental Engineering and
Sustainable Development,
II Faculty of Engineering
Technical University of Bari,
Viale del Turismo 10
Taranto 74100, Italy
E-mail: gmarano@poliba.it

Daniela Marinova
Associate Professor
Department of Applied Mathematics and
Informatics,

Technical University of Sofia
Sofia 1756, Bulgaria
E-mail: dmarinova@dir.bg

Pablo Mata
Research Assistent
Structural Mechanics Department,
Civil Engineering School,
Technical University of Catalonia
Edificio C1, Campus Norte UPC,
Jordi Girona 1–3,
Barcelona 08034, Spain
E-mail: pmata@cimne.upc.edu

Daniel Meiners
Structural Engineer
Arup GmbH
Uhlandstrasse 20-25
10623 Berlin, Germany
E-mail: daniel.meiners@arup.com

Konstantin Meskouris
Professor
Institute of Structural Statics and Dynamics,
Faculty of Civil Engineering,
RWTH Aachen University
Mies-van-der-Rohe-Strasse 1,
D-52074 Aachen, Germany
E-mail: fkmeskou@lbb.rwth-aachen.de

Chara Ch. Mitropoulou
PhD Student
Institute of Structural Analysis & Seismic Research
Faculty of Civil Engineering
National Technical University of Athens,
Zografou Campus, Athens 157 80, Greece
E-mail: chmitrop@central.ntua.gr

David Moens
K.U.Leuven
Department of Mechanical Engineering,
Division Production Engineering, Machine
Design and Automation (PMA)
Kasteelpark Arenberg 41, box 2449, B-3001,
Leuven, Belgium
E-mail: david.moens@mech.kuleuven.be

Vasilios G. Mokos
Postdoctoral Researcher
Institute of Structural Analysis &
Aseismic Research
School of Civil Engineering
National Technical University of Athens,
Zografou Campus,
Athens 157 80, Greece
E-mail: vgmokos@central.ntua.gr

Oscar Möller,
Institute of Applied Mechanics and
Structures, IMAE,
University of Rosario, Rosario, Argentina
E-mail: moller@fceia.unr.edu.ar

Matthew M. Muto
Post-doctoral Scholar
Engineering and Applied Science Division
California Institute of Technology
Mail Code 104-44
Pasadena, CA 91125
USA
E-mail: muto@caltech.edu

John O'Brien
Former Graduate Research Assistant
Department of Civil and Environmental
Engineering
300 Main Str.
University of South Carolina,
Columbia SC 29208, USA

Sergio Oller
Professor
Structural Mechanics Department,
Civil Engineering School,
Technical University of Catalonia
Edificio C1, Campus Norte UPC,
Jordi Girona 1–3,
Barcelona 08034, Spain
E-mail: sergio.oller@upc.es

Göktürk Önem
Ph D. Candidate
Kandilli Observatory and Earthquake

Research Institute
Boğaziçi University
34684 Çengelköy, Istanbul, Turkey
E-mail: onemgokt@boun.edu.tr

Christos Panagiotopoulos
PhD Student
Institute of Structural Analysis
Department of Civil Engineering
Aristotle University Thessaloniki,
Thessaloniki 54124, Greece
E-mail: pchr@civil.auth.gr

Chris P. Pantelides
Professor
University of Utah
122 S. Central Campus Drive
Salt Lake City, UT 84112
USA
E-mail: chris@civil.utah.edu

Manolis Papadrakakis
Professor
Institute of Structural Analysis &
Seismic Research
Faculty of Civil Engineering
National Technical University of Athens,
Zografou Campus, Athens 157 80, Greece
E-mail: mpapadra@central.ntua.gr

George Papagiannopoulos
Ph.D. Candidate
Department of Civil Engineering
University of Patras,
Rio 26500, Greece
E-mail: gpapagia@upatras.gr

Elias Paraskevopoulos
Research Assistant
Institute of Structural Analysis
Department of Civil Engineering
Aristotle University Thessaloniki,
Mail Stop 502
Thessaloniki 54124, Greece
E-mail: eapcivil@yahoo.com

Rui Pinho
European School for Advanced Studies in
Reduction of Seismic Risk
(ROSE School)
c/o European Centre for Training and
Research in Earthquake
Engineering (EUCENTRE),
Via Ferrata 1, 27100 Pavia, Italy
E-mail: rui.pinho@eucentre.it

Laura Quiroz
Institute of Applied Mechanics and Structures,
IMAE,
University of Rosario, Rosario, Argentina
E-mail: quiroz@fceia.unr.edu.ar

Lawrence D. Reaveley
University of Utah
122 S. Central Campus Drive
Salt Lake City, UT 84112
USA

Andrei M. Reinhorn
Clifford C. Furnas Eminent Professor
Department of Civil, Structural &
Environmental Engineering
University at Buffalo (SUNY)
Buffalo, NY 14260, USA
E-mail: reinhorn@buffalo.edu

Edwin Reynders
Department of Civil Engineering, K.U. Leuven
Division Structural Mechanics
Kasteelpark Arenberg 40
Belgium
E-mail: edwin.reynders@bwk.kuleuven.be

Dimitris C. Rizos
Associate Professor Structural Engineering
Department of Civil and Environmental
Engineering
300 Main Str.
University of South Carolina,
Columbia, SC 29208, USA
E-mail: rizos@engr.sc.edu

Marcelo Rubinstein
Institute of Applied Mechanics and
Structures, IMAE,
University of Rosario, Rosario, Argentina
E-mail: marub@fceia.unr.edu.ar

Evangelos J. Sapountzakis
Assoc. Professor
Institute of Structural Analysis &
Aseismic Research
School of Civil Engineering
National Technical University of Athens,
Zografou Campus,
Athens 157 80, Greece
E-mail: cvsapoun@central.ntua.gr

Werner Schiehlen
Professor Emeritus
Institute of Engineering and Computational
Mechanics
University of Stuttgart
D-70550 Stuttgart
Germany
E-mail: schiehlen@itm.uni-stuttgart.de

Gerhart I. Schuëller
Professor and Chair
Chair of Engineering Mechanics
University of Innsbruck
Innsbruck, Austria
E-mail: Mechanik@uibk.ac.at

Robert Seifried
Institute of Engineering and Computational
Mechanics
University of Stuttgart
D-70550 Stuttgart
Germany
E-mail: seifried@itm.uni-stuttgart.de

Sara Sgobba
PhD student
Department of Environmental Engineering and
Sustainable Development,
II Faculty of Engineering
Technical University of Bari,
Viale del Turismo 10

Taranto 74100, Italy
E-mail: s.sgobba@poliba.it

Enrico Sibilio
Postdoctoral Fellow
Department of Structures, Università
di Roma TRE
Via Corrado Segre 6, Roma 00146, Italy
E-mail: enrico.sibilio@libero.it

Mettupalayam V. Sivaselvan
Assistant Professor
Department of Civil Environmental &
Architectural Engineering
University of Colorado at Boulder
Boulder, CO 80309, USA
E-mail: siva@colorado.edu

Christian Soize
Professor
Université Paris-Est
Laboratoire Modélisation et Simulation
Multi-Echelle
5 Bd Descartes
77 454 Marne-la-Vallée, France
E-mail: christian.soize@univ-paris-est.fr

Enrico Spacone
Professor
University of Chieti-Pescara, Dept. PRICOS
viale Pindaro 42
Pescara 65127, Italy
E-mail: espacone@unich.it

Georgios E. Stavroulakis
Professor
Institute of Computational Mechanics and
Optimization
Department of Production Engineering and
Management,
Technical University of Crete
Chania 73100, Greece
E-mail: gestavr@dpem.tuc.gr

Jan Van Steirteghem
Besix Belgium
Avenue des Communautés 100,

B - 1200 Brussels, Belgium
E-mail: Jan.Van.Steirteghem@skynet.be

Georgios Tairidis
Graduate Student
Institute of Computational Mechanics and Optimization
Department of Production Engineering and Management,
Technical University of Crete
Chania 73100, Greece
E-mail: tairidis@yahoo.gr

Demosthenes Talaslidis
Professor
Institute of Structural Analysis
Department of Civil Engineering
Aristotle University Thessaloniki,
Mail Stop 502,
Thessaloniki 54124, Greece
E-mail: talaslid@civil.auth.gr

Gökçe Tönük
Research Assistant & Ph.D. Candidate
Earthquake Engineering Department
Kandilli Observatory and Earthquake Research Institute
Bogaziçi University,
Çengelköy, Istanbul 34684, Turkey
E-mail: gokce.tonuk@boun.edu.tr

Yiannis Tsompanakis
Assistant Professor
Division of Mechanics
Department of Applied Sciences
Technical University of Crete
University Campus
Chania 73100, Greece
E-mail: jt@science.tuc.gr

Marcos A. Valdebenito
Research Associate
Institute of Engineering Mechanics,
University of Innsbruck
Technikerstrasse 13
Innsbruck 6020, Austria
E-mail: Marcos.Valdebenito@student.uibk.ac.at

Dirk Vandepitte
K.U.Leuven
Department of Mechanical Engineering,
Division Production Engineering,
Machine Design and Automation (PMA)
Kasteelpark Arenberg 41, box 2449,
B-3001, Leuven, Belgium
E-mail: dirk.vandepitte@mech.kuleuven.be

Juan C. Vielma
Professor
Lisandro Alvarado University,
Departamento de Ingeniería Estructural,
Decanato de Ingeniería Civil
Av. La Salle entre Av. Las Industrias
y Av. Benítez
Barquisimeto 3001, Venezuela
E-mail: jcvielma@ucla.edu.ve

Nils-Erik Wiberg
Professor
Department of Applied Mechanics
Chalmers University of Technology,
Gothenburg 412 80, Sweden
E-mail: Nils-Erik.Wiberg@chalmers.se

Emmanuel Zacharenakis
Professor
Department of Civil Engineering,
Technological Educational Institute of Crete
Heraklion 71306, Greece
E-mail: zacharen@stef.teiher.gr

Part I

Computational Structural Dynamics

Chapter 1

Computational stochastic dynamics – some lessons learned

Gerhart I. Schuëller

University of Innsbruck, Innsbruck, Austria

ABSTRACT: This contribution discusses some of the lessons learned in computational stochastic dynamics. Among them is the role of the design point for calculating failure probabilities of systems involving a large number of random variables and structural non linearities. Several selected numerical examples are carried out. The results obtained allow to identify the range of applicability of the reliability techniques based on the design point. Finally, the properties of the failure domains for non linear systems are discussed.

1 Introduction

It is a well known fact that problems in structural dynamics are considerably more involved that in statics. This is – among other things – due to the fact that the correlation in time must be considered. Moreover, when dealing with reliability problems there are in general several extremes of which only the highest within a particular time span must be counted, etc. In this context, it should be noted that no exact solution for the excursion probability (P_F) is known. Analytical approximations are available for limiting cases. Efficient numerical simulation procedures are available for estimating P_F. While linear, but uncertain systems are still not well explored w.r.t. reliability aspects, even dynamical systems with deterministic geometrical and material properties still need to be explored, particularly when they are high dimensional. This applies even more to the effects of non linearities. This is underlined by a recent benchmark study (Schuëller et al. 2004a).

The aim of structural reliability is to produce rational metrics of the safety of a system with respect to a certain failure criterion (or criteria) by taking into account all possible sources of uncertainty, either in loading or in structural parameters (or in both). To generate such rational metrics, it is necessary to:

- Characterize the aforementioned uncertain parameters by means of a suitable model. For this purpose, a vector of random variables ($\boldsymbol{\theta}$) and its corresponding joint probability density function ($h(\boldsymbol{\theta})$) are considered.
- Define the failure criterion (criteria), i.e. the structural response(s) and the respective threshold level(s) to be controlled. This is achieved by defining appropriate performance function(s) ($g(\boldsymbol{\theta})$), which is (are) equal or smaller than zero if a given realization of $\boldsymbol{\theta}$ causes failure.

Then, the safety of a structure can be expressed in terms of a failure probability (P_F), which is the complement of the reliability.

$$P_F = \int_{g(\boldsymbol{\theta})\leq 0} h(\boldsymbol{\theta})\, d\boldsymbol{\theta} \tag{1}$$

To evaluate Equation 1, it is necessary to compute an integral of d dimensions, where d is the length of the vector of uncertain parameters. In cases of practical interest, the number d is large, i.e. thousands, in order to appropriately account for all the uncertain parameters present in the structural model. Hence, the solution of Equation 1 by means of numerical integration is unfeasible for problems of engineering interest (Schuëller and Stix 1987). On the other hand, closed-form solutions of the aforementioned integral exist only for a few cases. Thus, several alternative methods (other than numerical integration and closed-form solutions) have been developed in order to solve realistic structural reliability problems. These methods can be broadly classified in two categories (Schuëller et al. 2004b):

- Approximate Methods: First and Second Order Reliability Methods (FORM and SORM).
- Simulation Methods: Two subcategories can be distinguished.
  - General Simulation Methods: Monte Carlo Simulation (MCS) and Subset Simulation (SS).
  - Variance Reduction Techniques: Importance Sampling (IS), Line Sampling (LS), etc.

General simulation methods can be regarded as black box techniques, given that they do not require any previous information or assumption about the problem under study and their numerical efficiency does not depend on the number of uncertain parameters or the nature of the structural model (static or dynamic, linear or non linear). On the other side, approximate methods and variance reduction techniques rely on the so-called design point to estimate P_F, where the design point is the realization of the uncertain parameters with highest probability density in the failure region (projected in the standard normal space). Methods which rely on the design point have been successfully used in a number of applications such as in the estimation of the first excursion probability of linear dynamical systems subject to stochastic load (see, e.g. (Au and Beck 2001b; Katafygiotis and Cheung 2006)), in code calibration (see, e.g. (Ditlevsen and Madsen 1996)) or in reliability-based optimization (RBO) problems (see, e.g. (Youn et al. 2005)). In all of the aforementioned applications, either:

- The limit state function(s) (LSF), defined as $g(\boldsymbol{\theta}) = 0$, is(are) linear with respect to the random variables (and these variables are Gaussian distributed).
- The limit state function does not deviate significantly from a hyperplane, i.e. a weakly non linear behavior of $g(\cdot)$ with respect to $\boldsymbol{\theta}$ is expected, and the number of random variables involved in the problem is low, e.g. less than 20.

In structural reliability problems where any of the two conditions above are fulfilled, the information provided by the design point is meaningful for estimating P_F.

Lately, many researchers have tried to extend the range of application of methods based on the design point to highly non linear problems involving a large number of random variables (see, e.g. (Fujimura and Der Kiureghian 2007)), paying much attention in how to determine the design point (see, e.g. (Koo et al. 2005)), which is a challenging task that involves a constrained optimization problem. Nonetheless, the key issue of verifying whether or not the design point provides the appropriate information to estimate P_F for these types of problems has been overlooked in most of the publications in the field of structural reliability (being the exception a recent study carried out by (Au et al. 2007)). Then, the aim of this contribution is to make a critical appraisal of the role of the design point in estimating failure probabilities in structural reliability problems involving a large number of uncertain parameters and non linear behavior, i.e. it is sought to assess the relevance of the design point in view of the non linearities of structural systems. It is expected that such critical appraisal will establish a precedent concerning the range of applicability of reliability methods which rely on the design point. The discussion is carried out based on the observations generated through the resolution of a series of numerical examples rather than from a theoretical point of view, given the inherent complex nature of structural reliability problems involving non linearities. The examples addressed throughout this contribution are rather simple, involving a single failure criterion. Nonetheless, it is seen that even such (apparently) trivial examples may be tremendously challenging in context with structural reliability estimation.

The outline of this contribution is the following: firstly, a brief look on the definition of the design point and some of the aforementioned reliability methods is given. Secondly, the issue of dimensionality in reliability problems is addressed. Thirdly, the issue of structural non linearities in the context of small failure probability estimation is studied. Finally, in the conclusions, the range of applicability of the reliability techniques based on the design point is identified in view of the results obtained in the respective sections.

2 Theoretical background

2.1 *The design point*

To define the design point, it is necessary to transform the problem posed in Equation 1 from the original random variable space $\boldsymbol{\theta} \in \Re^d$ (also known as the physical space) to the standard normal space $x \in \Re^d$. This is, to use a mapping $\boldsymbol{\theta} \leftrightarrow x$ in order to establish a suitable transformation:

$$x = T_{\theta x}(\boldsymbol{\theta}) \tag{2}$$

$$\boldsymbol{\theta} = T_{x\theta}(x) \tag{3}$$

A common means to perform such mapping is to use an approximate method like the Nataf's model (Liu and Der Kiureghian 1986). Once the random variables involved in Equation 1 have been expressed into the standard normal space, it is possible to define the design point ($\boldsymbol{x}^*$) using a geometrical or probabilistic interpretation (see, e.g. (Freudenthal 1956)). In the geometrical interpretation, the design point is defined as the realization in the standard normal space which lies on the limit state function

$(g(T_{x\theta}(\boldsymbol{x}))=0)$ with the minimum Euclidean norm (ρ or β) with respect to the origin. According to the probabilistic interpretation, the design point is the point with highest probability density in the failure region. This means, it is the point that maximizes $p(\boldsymbol{x})$ subject to $g(T_{x\theta}(\boldsymbol{x}))\leq 0$, where $p(\cdot)$ is the standard normal probability density function in $\Re^d$.

The task of finding the design point involves the solution of the following constrained optimization problem:

$$\begin{aligned} &\min \sqrt{x_1^2+x_2^2+\cdots+x_d^2} \\ &\text{subject to } g(T_{x\theta}(\boldsymbol{x}))\leq 0, \quad \boldsymbol{x}\in\Re^d \end{aligned} \tag{4}$$

The value of the objective function in the optimum is the so-called reliability index (β). Closed form solutions for identifying the design point exist only for a few cases, e.g. in the context of non linear stochastic dynamics:

- For certain types of non linear dynamical systems subject to stochastic loading, a method has been proposed based on the free-vibration response of the structure (Koo et al. 2005). In several cases, the output of this method will be a rough approximation of the design point which can be used as a starting point (a so-called *warm solution*) for a specific optimization algorithm.
- For a single degree of freedom (SDOF) elastoplastic system subject to stochastic loading, an efficient method has been formulated based on the parametrization of the design point (see, e.g. (Au 2006a)).

Although the aforementioned approaches can produce estimates of the design point with reduced numerical costs, the range of applicability of these approaches is quite narrow. Hence, when dealing with more general structural reliability problems, it is necessary to apply an optimization algorithm to estimate the design point; nonetheless, such strategy is quite involved numerically, i.e. it is necessary to evaluate repeatedly the performance function and in realistic structural reliability problems this can imply the solution of large FE models.

2.2 *First order reliability method*

The first order reliability method (FORM) is an approximate method for assessing the reliability of a structural system. Its basic assumption is to approximate the limit state function $(g(T_{x\theta}(\boldsymbol{x}))=0)$ of the structural reliability problem by means of a hyperplane which is orthogonal to the design point vector; note that this approximation is constructed in the standard normal space. Thus, the failure probability can be estimated using the Euclidean norm of $\boldsymbol{x}^*$, i.e.

$$P_F\approx\hat{P}_F=\Phi(-|\boldsymbol{x}^*|)=\Phi(-\beta) \tag{5}$$

In equation 5, $\Phi(\cdot)$ is the standard normal cumulative density function. The schematic representation of the FORM method is shown in Figure 1.1.

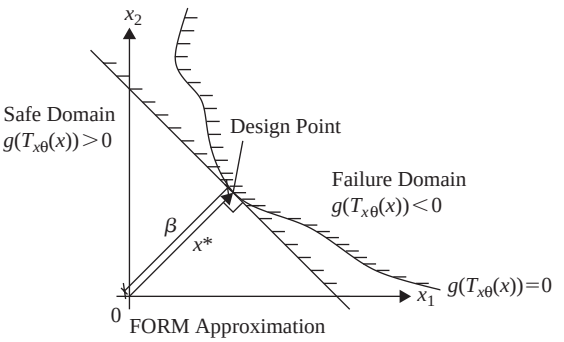

Figure 1 FORM approximation in the standard normal space.

Equation 5 provides an exact estimate of the failure probability provided that the limit state function is linear with respect to the Gaussian distributed vector of uncertain parameters. Under more general conditions, Equation 5 yields only approximate results. Moreover, it should be noted that FORM does not produce any measure of the error introduced by the linearization assumption.

2.3 *Monte Carlo simulation*

The Monte Carlo simulation method (MCS) is a general simulation technique, i.e. it is applicable to linear and non linear problems indifferently. Moreover, its efficiency is independent of the number of random variables involved in the problem under analysis. The basic idea behind MCS is to generate N samples of $\boldsymbol{\theta}$ which are distributed according to $h(\boldsymbol{\theta})$. Then, the failure probability can be estimated as:

$$P_F \approx \hat{P}_F = \frac{1}{N}\sum_{i=1}^{N} I_F(\boldsymbol{\theta}^{(i)}), \quad \boldsymbol{\theta}^{(i)} \text{ i.i.d.} \sim h(\boldsymbol{\theta}) \tag{6}$$

In Equation 6, $I_F(\cdot)$ is the indicator function, which is equal to 1 if $g(\boldsymbol{\theta}) \leq 0$ and 0 otherwise. Moreover, it is possible to estimate the convergence rate of the estimator in Equation 6 by means of the coefficient of variation, i.e.

$$\delta_{MCS} = \sqrt{\frac{1-\hat{P}_F}{N\hat{P}_F}} \tag{7}$$

Despite MCS is the most general simulation technique, it has one major drawback: for calculating low failure probabilities, a large number of samples (proportional to $1/P_F$) is required to generate a reliable estimator, i.e. with sufficient accuracy. Hence, the numerical costs involved in estimating probabilities of occurrence of rare events may be extremely high and even prohibitive, especially when a structural system is modeled using a large FE model.

2.4 *Line sampling*

As method of solution, the application of advanced simulation techniques is most instrumental. Line sampling (LS) for example serves this purpose. It is a variance reduction technique which, basically, reduces a high dimensional problem in the standard normal space to a one dimensional problem (see, e.g. (Schuëller et al. 2004b)). The key issue in performing such transformation is to identify a so-called *important direction* ($\boldsymbol{\alpha}$), which is a unit vector pointing towards the failure region; candidates for such direction are (a) the direction of the design point vector and (b) the opposite of the direction of the gradient of the limit state function evaluated at the origin of the standard normal space.

Once $\boldsymbol{\alpha}$ has been identified, information about the performance function is collected along lines which are parallel to the important direction. Such information allows to estimate the failure probability. More details about the LS procedure can be found in Appendix A.

3 The issue of dimensionality

By definition, the design point is the realization of the uncertain parameters with highest probability density in the failure domain (according to the probabilistic interpretation). Hence, in low dimensional spaces, it is expected that the vicinity of $\boldsymbol{x}^*$ (inside the failure domain) will contribute significantly to P_F. This intuitive concept is based on the interpretation of Equation 1 as a *volume integral*: the region adjacent to $\boldsymbol{x}^*$ contains most of the total volume (i.e. P_F) because the probability density function reaches its maximum. This argument is valid and it justifies the use of approximate methods like FORM or SORM in a number of applications. In such methods, an approximation of the limit state function is constructed precisely in the region which contributes the most to the probability integral. Nonetheless, the intuitive concepts derived in low dimensional spaces may *not* be applicable when dealing with reliability problems involving a large number of dimensions. For a better understanding of the last point, the following performance function is considered:

$$g(\boldsymbol{x}) = 4 - x_1 + \frac{1}{2}\kappa \sum_{i=2}^{d} x_i^2 \tag{8}$$

In Equation 8, κ denotes curvature and $x_i \sim N(0,1),\ i = 1, \ldots, d$.

The design point and reliability index associated with the performance function in Equation 8 can be calculated analytically, i.e.

$$\boldsymbol{x}^* = \langle 4 \ \ 0 \ \ \ldots \ \ 0 \rangle^T \tag{9}$$

$$\beta = |\boldsymbol{x}^*| = 4 \tag{10}$$

Note that the reliability index is constant, independent of the number of dimensions (d) and the curvature (κ). This implies that if an approximate method like FORM is used, i.e. a linear approximation of $g(\cdot)$ is constructed around the design point, the

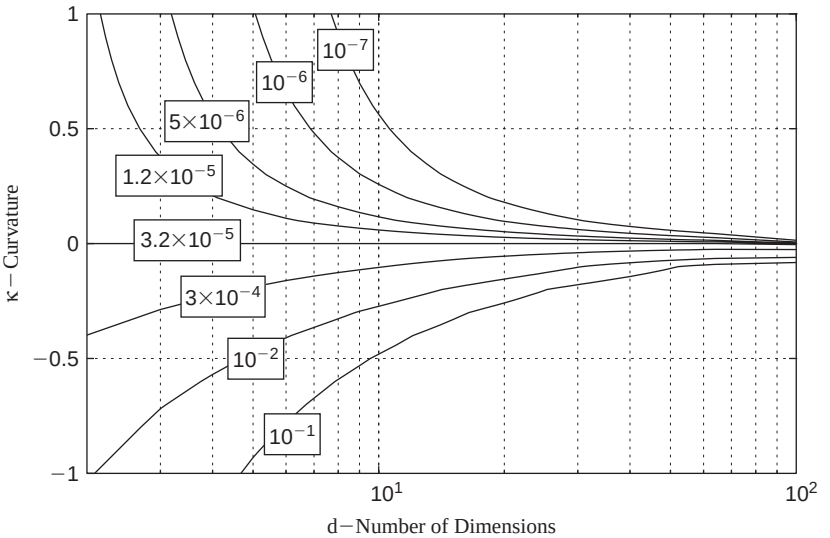

Figure 2 Failure probability as a function of the number of dimensions and curvature.

probability that the performance function is smaller than zero is constant for any given values of κ and d, i.e.:

$$P_F = P\left[4 - x_1 + \frac{1}{2}\kappa\sum_{i=2}^{d} x_i^2 < 0\right] \approx \hat{P}_F = \Phi(-4) = 3.2 \times 10^{-5} \tag{11}$$

In order to verify the accuracy of the FORM approximation, the failure probability described in Equation 11 is calculated exactly over a suitable grid of the parameters κ and d; the results obtained are shown as contour levels of P_F in Figure 1.2.

The results in Figure 1.2 indicate that the estimate of P_F generated using FORM is valid for a certain range of the curvature κ when the number of dimensions is low, i.e. less than 10. Hence, to approximate the limit state function (LSF) by a hyperplane orthogonal to the design point vector is quite reasonable. But when the number of dimensions involved is large, e.g. 100, even the slightest deviation of κ from 0 causes the FORM approximation to be erroneous by *several* orders of magnitude. Thus, taking into account that the reliability index remains constant independent of the number of dimensions, it is clear that the approximation of the LSF around the design point vector may be useful only in low dimensions. For high dimensions, the design point and its vicinity lose their relevance in estimating the failure probability. Naturally, it could be argued that for the specific performance function described in Equation 8, FORM is not the most appropriate method for estimating the failure probability. Although SORM (see, e.g. (Breitung 1994)) could certainly produce better results for this specific example, in more general cases where the LSF is neither linear nor quadratic (nor the random variables are Gaussian distributed), none of the approximate reliability

methods would produce accurate results when the number of uncertain parameters involved is large.

Even though the results presented in Figure 1.2 may be surprising at first glance, the reason why the design point and its vicinity lose relevance in estimating the failure probabilities has been acknowledged a number of times in the literature (see, e.g. (Katafygiotis et al. 2007)). In order to study such reason, consider the following definition:

$$R^2 = x_1^2 + x_2^2 + \cdots + x_d^2 \tag{12}$$

In Equation 12, R represents the Euclidean norm (with respect to the origin) of a point in the standard normal space. Given that $x_i \sim N(0,1), i = 1, \ldots, d$, then R^2 follows a chi-square distribution of d degrees of freedom. This implies that the expected radius will be equal to the square root of the number of dimensions, i.e.:

$$E[R] = \sqrt{d} \tag{13}$$

Hence, the probability density mass of the radius of $\boldsymbol{x}$ will shift away from the origin of the standard normal space as the number of dimensions (uncertain variables) involved in the reliability problem increases. Moreover, if d is large, the design point and its vicinity may be located in the *tail* of the probability density function of R and, thus, the contribution of this region to the total failure probability becomes negligible. To clarify the latter point, the following experiment is carried out: it is calculated which is the probability of drawing a sample of $\boldsymbol{x}$ inside a hypersphere of radius $\beta + \Delta$, where β represents the reliability index, which is taken equal to 4. The results of such experiment are shown in Figure 1.3 as a function of both d and Δ.

The results shown in Figure 1.3 demonstrate that even though the design point *is* the realization of the uncertain parameters with highest probability density in the failure domain, its vicinity is not important for estimating failure probabilities in high dimensions, i.e. if the dimension $d = 100$, then the region around $\boldsymbol{x}^*$ is irrelevant in estimating the failure probability. Hence, it is concluded that the information provided

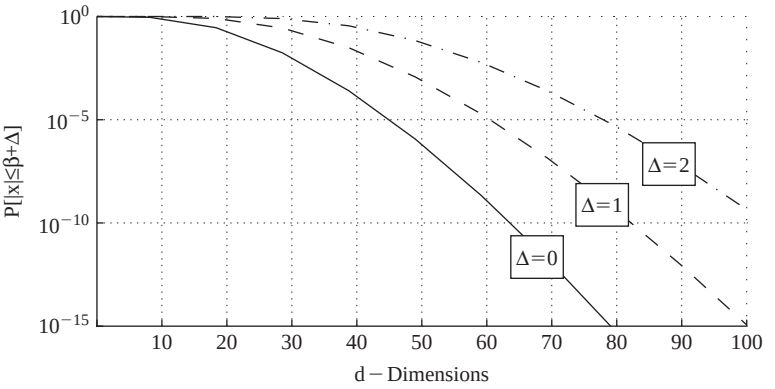

Figure 3 Probability of drawing a sample of x inside a hypersphere of radius $\beta + \Delta$.

by the design point (and the Hessian of the LSF at $\boldsymbol{x}^*$ in case SORM is used) is not helpful in calculating P_F unless the limit state function fulfills some specific conditions, i.e. the performance function is linear or quadratic (without interaction terms) with respect to the Gaussian distributed random variables.

4 The role of the design point in evaluating the failure probability in view of structural non linearities

4.1 *Definition of the reliability problem*

In the previous section, it was shown that the intuitive ideas which are applicable in low dimensional spaces cannot be always extended to problems involving a large number of dimensions. Specifically, it was demonstrated by two examples that the vicinity of the design point in large dimensions may not be as meaningful as in problems that involve a few random variables only. Thus, the next step is to assess how the structural *non linearities* may affect the solution of reliability problems in dynamics, focusing on the role of the design point for estimating failure probabilities. For such purpose, an example taken from (Schuëller et al. 2004a) is studied. The system consists of a 5 DOF non linear shear beam model, which is shown in Figure 1.4. The model has 25 structural parameters characterized as Gaussian independent random variables. The structure is excited by a stochastic ground acceleration of 20 *s* of duration, modeled by 200 independent Gaussian random variables, i.e. the total number of random variables associated to the model is 225. Moreover, the restoring force of the structure is modeled as bilinear hysteretic. The specific details about the model as well as the uncertainty quantification can be found in the aforementioned reference.

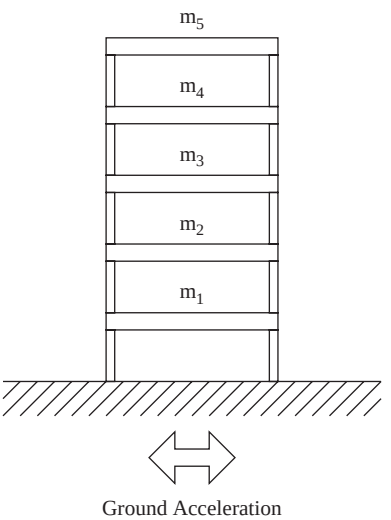

Figure 4 Non linear shear beam model.

The failure event to be analyzed is defined as the relative displacement of the 5th DOF with respect to the 4th exceeding a prescribed threshold level b at 10 s, i.e.

$$F = \{\boldsymbol{x} \in \Re^{225} : g(\boldsymbol{x}) = b - r_{5-4}(\boldsymbol{x}, t = 10\ s) \leq 0\}, \quad x_i \sim N(0,1) \quad i = 1, \ldots, 225 \tag{14}$$

4.2 *Design point search*

To the knowledge of the author, no analytical solution (neither exact nor approximate) exists for finding the design point of the problem posed in Equation 14. Hence, it is necessary to use an optimization technique for determining $\boldsymbol{x}^*$. Numerical validation has shown that a technique which is convenient fur such purpose is the so-called Cross Entropy (CE) optimization method (see, e.g. (Rubinstein 1999)). This method is a gradient-free algorithm and, hence, is suitable for dealing with structural non linearities. It has been applied to a number of optimization problems in different fields and it can be used for rare event simulation as well. For specific details about its theoretical basis and its features, it is referred to the literature (see, e.g. (de Boer et al. 2005) for a comprehensive tutorial).

The CE method is directed towards the solution of unconstrained optimization problems. Thus, in order to find $\boldsymbol{x}^*$, it is necessary to pose the problem in Equation 4 (constrained optimization problem) in an alternative way. This is done by incorporating the constraint as a penalty term in the objective function, i.e.:

$$\min \sqrt{x_1^2 + x_2^2 + \cdots + x_{225}^2} + C \max(0, g(T_{x\theta}(x)))^2, \quad x \in \Re^{225} \tag{15}$$

The formulation presented in Equation 15 is a common method for handling constraints within the context of unconstrained optimization algorithms. The main drawback of such formulation is that there is no general rule for establishing the penalty term C and, hence, it must be calibrated for each specific problem (Coello 2002). Being aware of this particular drawback and the possibility of getting trapped in local minima, the optimization runs used for the design point search are repeated several times in an effort to find the global solution of the problem posed in Equation 15. Such an approach certainly implies enormous numerical costs but, given that the objective of this contribution is to assess the role of the design point in structural reliability and not to propose efficient numerical techniques for finding $\boldsymbol{x}^*$, the chosen scheme for the design point search is considered to be adequate.

The design point search was performed for four different threshold levels, i.e. $b = \{1.2, 1.7, 2.2, 2.7\} \times 10^{-2}\ m$. The results of such search are presented in Table 1.1, where the reliability index (β) associated to each threshold level is shown.

It is most interesting to observe that besides the design points shown in Table 1.1, different runs of the optimization algorithm produced a number of realizations in the standard normal space that belong to the failure domain which are *similar* to the design points found, i.e. for a given threshold level, it is possible to find samples $\boldsymbol{x} \in F$ with an Euclidean norm slightly larger than $\boldsymbol{x}^*$, however with different directions. Thus, although there is a realization of the uncertain parameters that can be identified as the design point (global minimum), there are other realizations that closely resemble

Table 1 Reliability index for different threshold levels

b	β
0.012 m	2.847
0.017 m	3.454
0.022 m	3.932
0.027 m	4.437

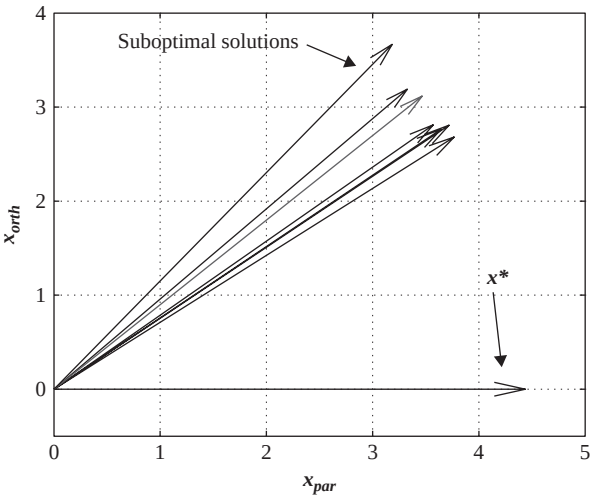

Figure 5 Design Point (x^*) and Suboptimal Solutions for $b = 2.7 \times 10^{-2}$ [m].

the design point (local minima). The existence of such suboptimal solutions has been already acknowledged and studied for an elastoplastic oscillator in (Au 2006a; Au 2006b). Hence, the results obtained for the problem under study concerning the design point search are consistent with those published in the literature.

To provide some insight into the design point and the suboptimal solutions found, the specific results obtained for $b = 0.027\,m$ are presented in the following figures. In Figure 1.5, the design point and 7 suboptimal solutions are shown in a 2 dimensional plot that involves the parallel ($\boldsymbol{x}_{par}$) and orthogonal ($\boldsymbol{x}_{orth}$) directions to the design point; note that although the orthogonal component of the suboptimal solutions is similar, they actually point towards different directions.

In Figure 1.6, the components of the design point and of one suboptimal solution are depicted. It is important to note that the design point and the suboptimal solutions are quite different concerning the components related to the excitation, but rather similar regarding the structural components. This phenomenon has a physical interpretation: while several different excitations can cause the structure to reach a determined level of displacement, the effect of the uncertainty in the structural parameters is *well defined*, e.g. clearly, a smaller stiffness will induce larger displacements.

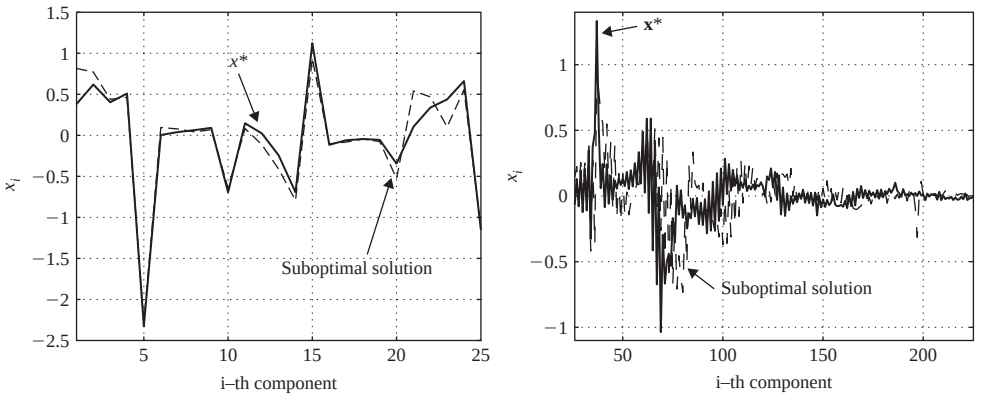

(a) Uncertainty Associated to the Structural Parameters (b) Uncertainty Associated to the Excitation

Figure 6 Component-by-component comparison between design point (x^*) and suboptimal solution for $b = 2.7 \times 10^{-2}$ [m].

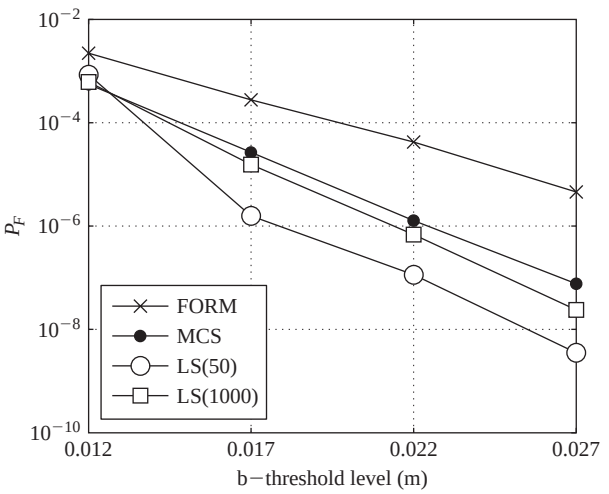

Figure 7 Failure probability of non linear shear beam model.

4.3 *Reliability estimates*

The estimates of $P[r_{5-4}(\boldsymbol{x}, t = 10\,[s]) \geq b]$ for several threshold levels are presented in Figure 1.7. The reliability techniques used for estimating P_F are MCS (reference), FORM and LS. Line Sampling is applied using 50 and 1000 lines and the important direction is chosen equal to the direction of the design point.

The details about the results obtained are discussed below.

- FORM: The results obtained by FORM are off between one and two orders of magnitude when compared to MCS for the different values of the threshold level.

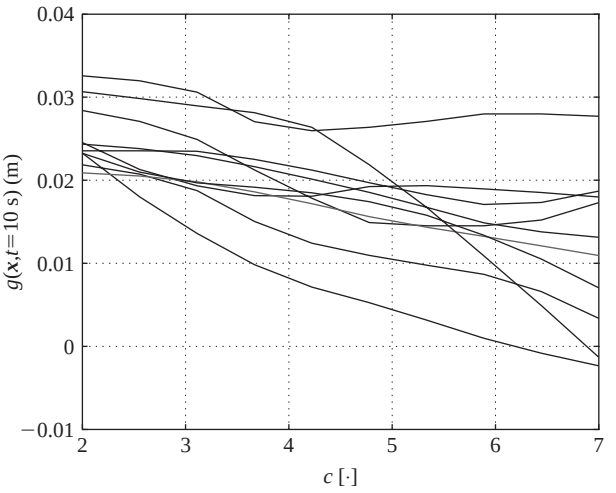

Figure 8 Line sampling: 10 random lines.

- Line Sampling: For a low number of lines, the estimates of P_F produced by LS are rather poor; when the number of lines is increased, the quality of these estimates improve (at the expense of higher numerical costs). To gain insight about the shape of the failure region, 10 random lines of LS are shown in Figure 1.8. The lines present a considerable scatter and they do not have a monotic behavior, which indicates that the failure region associated to the non linear shear beam model is far from being bounded by a hyperplane.

4.4 *The shape of the failure region*

The lack of accuracy in the reliability estimates produced by FORM and the shape of the samples lines of LS suggest that the shape of the failure region may be rather complex. To widen the study of this issue, the following numerical experiment is carried out: it is estimated which is the proportion of failure samples generated by MCS that simultaneously belong to the failure region defined by the FORM hypothesis. The details involved in such experiment are the following:

- The failure event F_{FORM} is defined as:

$$F_{FORM} = \{\boldsymbol{x} \in \Re^d : \boldsymbol{x}^{*T}\boldsymbol{x} \geq \beta\}, \quad x_i \sim N(0,1), \;\; i = 1, \ldots, d \tag{16}$$

  Note that F_{FORM} corresponds to the failure event associated to the FORM hypothesis.
- The sought proportion is calculated using the following formula:

$$P[F_{FORM}/F] = \frac{\sum_{j=1}^{N} I_F(\boldsymbol{x}^{(j)}) \times I_{F_{FORM}}(\boldsymbol{x}^{(j)})}{\sum_{j=1}^{N} I_F(\boldsymbol{x}^{(j)})} \tag{17}$$

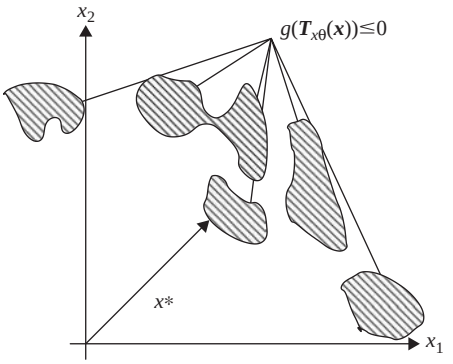

Figure 9 Schematic representation of possible failure region.

where $I_{F_{FORM}}(\cdot)$ is the indicator function associated to the failure event F_{FORM}, $I_F(\cdot)$ is the indicator function associated to the failure event F (see Equation 14) and $\boldsymbol{x}^{(j)}$ are samples drawn following a 225-dimensional standard normal distribution.

- The parameter N is chosen large enough so that the estimate of Equation 17 is accurate; specifically, $N = 800 \times 10^6$.

The results of the numerical simulation indicate that the sought proportion ($P[F_{FORM}/F]$) is for all the threshold levels under study within the range $[0.3, 0.4]$. Such proportion is consistent with the results from Figures 7 and 8, i.e. the failure region may not be appropriately represented by the FORM hypothesis.

Even though the results discussed so far indicate that the failure region of the reliability problem posed in Equation 14 is rather complex, it is difficult to express these results quantitatively. Nonetheless, further numerical experiments carried out in (Valdebenito et al. 2008) suggest that the failure region for strongly non linear systems is by far more complicated than any of the traditional hypotheses proposed in the literature. Thus, the failure region may be composed even by disconnected regions ('*islands*') or '*valleys*' connected by low probability paths, as shown in Figure 1.9. Of course, the representation of the failure region in Figure 1.9 is no more than a guess. But the point of suggesting such representation is to emphasize that the LSF can not be approximated by a hyperplane (FORM) or a paraboloid (SORM).

5 Conclusions

In the first part of this contribution, the relevance of the design point in view of dimensionality was addressed. The examples discussed show that the design point and its vicinity contribute significantly to the failure probability integral for low dimensional problems, i.e. 10 to 20 random variables. But when the number of dimensions involved in the reliability problem is large, the design point and its vicinity do not play an important role in estimating P_F. The design point might be still useful in high dimensions but only when the limit state function has a particular structure, e.g. is linear with respect to the Gaussian distributed random variables.

When dealing with reliability problems involving strong structural non linearities, the knowledge of the design point seems to be of little advantage. The estimates of the failure probabilities calculated using FORM can be off by orders of magnitude and, furthermore, the basic hypothesis of this reliability technique is not representative of the actual failure domain. On the other hand, LS does not benefit from the direction defined by the design point due to the variability of the sampled lines.

In view of the results obtained, it is possible to identify the range of applicability of the reliability techniques based on the design point:

- For low dimensional problems, the design point is certainly relevant in estimating P_F. Techniques like FORM or SORM may produce estimates of the reliability with sufficient accuracy.
- For high dimensional problems involving weak non linearities, the design point might be still relevant but in combination with a simulation technique, e.g. if the design point is readily available, it can be used for determining the important direction required in Line Sampling. The design point (and the Hessian of the LSF at the design point) are of relevance only in very special cases.
- For high dimensional problems involving strong non linearities, none of the reliability methods available seem to benefit from the knowledge of the design point (Au et al. 2007; Valdebenito et al. 2008). In such cases, general simulation techniques like Monte Carlo simulation or Subset simulation (Au and Beck 2001a; Beck and Au 2005; Katafygiotis and Cheung 2007) should be preferred.

In spite of the arguments discussed above, the concept of design point in reliability analysis should not be discarded. Recent advances in the development of variance reduction techniques (Au 2008) have shown that the design point (associated with uncertainty in excitation) can be rather useful when interpreted as the excitation with minimum energy capable of driving the structural reponse towards a prescribed threshold level. But how to estimate the design point efficiently still remains an open issue, except for a small class of reliability problems, where exact or approximate solutions have been proposed.

Acknowledgements

This report has been supported by the Austrian Science Fund (FWF) under the contract P17459–N13 which is gratefully acknowledged by the author. The help of Mr. M.A. Valdebenito and Dr. H.J. Pradlwarter in the preparation of this contribution is deeply appreciated.

A Line sampling

The algorithm to implement LS can be summarized in the following steps.

1. Identify an important direction ($\boldsymbol{\alpha}$) in the standard normal space; $\boldsymbol{\alpha}$ can be chosen based in the information provided by the design point or by the gradient of the performance function, evaluated at the origin of the standard normal space.
2. Generate N random samples ($\boldsymbol{x}^{\perp(j)}$, j=1, …, N) in the standard normal space orthogonal to $\boldsymbol{\alpha}$.

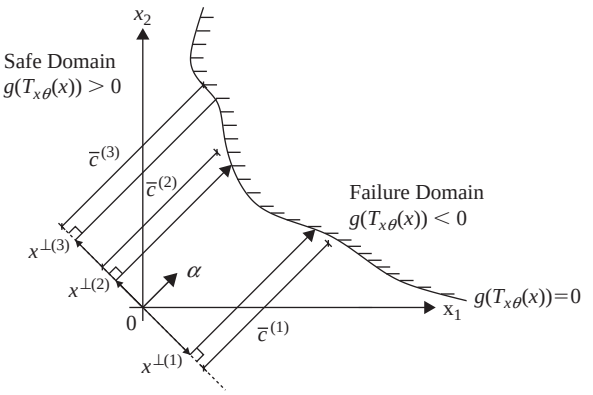

Figure 10 Line sampling procedure.

3. For each of the random samples previously generated, compute $g(T_{x\theta}(\boldsymbol{x}^{\perp(j)} + c_i^{(j)}\boldsymbol{\alpha}))$ where i = 1, … , n and $c_i^{(j)}$ is a factor conveniently chosen such that it is possible to find via interpolation a scalar $\overline{c}^{(j)}$ that complies

$$g(T_{x\theta}(x^{\perp(j)} + \overline{c}^{(j)}\boldsymbol{\alpha})) = 0, \quad c_1^{(j)} \leq \overline{c}^{(j)} \leq c_n^{(j)} \tag{18}$$

As it can be seen from Figure 10, the scalar $\overline{c}^{(j)}$ resembles a *local reliability index* if compared with FORM. Thus, the failure probability associated to the *jth* sample is

$$\overline{p}_{F,\alpha}^{(j)} = \Phi(-\overline{c}^{(j)}) \tag{19}$$

4. Estimate the failure probability and its variance using

$$\overline{P}_F = \frac{1}{N}\sum_{j=1}^{N} \overline{p}_{F,\alpha}^{(j)} \tag{20}$$

$$\sigma_{\overline{P}_F}^2 = \frac{1}{N(N-1)}\sum_{j=1}^{N}\left(\overline{p}_{F,\alpha}^{(j)} - \overline{P}_F\right)^2 \tag{21}$$

The schematic representation of the LS procedure is shown in Figure 10.

One of the advantages of LS over other reliability techniques is that it allows to estimate qualitatively how much does the LSF deviates from a hyperplane. This information is provided by the aspect of the sampled lines: if the lines are almost straight and highly concentrated, then the LSF is close to a hyperplane; if the lines present considerable scatter and are irregular, then the LSF is non linear.

In structural reliability problems where an important direction can be identified, LS provides accurate estimates of the failure probability with high numerical efficiency.

If such direction cannot be identified (or if the direction does not exist at all), LS still provides correct estimates but at higher numerical costs (comparable to MCS). This is the case for structural reliability problems involving strong non linearities (Pradlwarter et al. 2007).

References

Au, S. 2006a. Critical excitation of SDOF elasto-plastic systems. *Journal of Sound and Vibration 296*(4–5), 714–733.

Au, S. 2006b. Sub-critical excitations of SDOF elasto-plastic systems. *International Journal of Non-Linear Mechanics 41*(9), 1095–1108.

Au, S. 2008. First passage probability of elasto-plastic systems by importance sampling with adapted process. *Probabilistic Engineering Mechanics 23*, 114–124.

Au, S. & Beck, J. 2001a. Estimation of small failure probabilities in high dimensions by subset simulation. *Probabilistic Engineering Mechanics 16*, 263–277.

Au, S. & Beck, J. 2001b. First excursion probabilities for linear systems by very efficient importance sampling. *Probabilistic Engineering Mechanics 16*(3), 193–207.

Au, S., Lam, H. & Ng, C. 2007. Reliability analysis of single-degree-of-freedom elastoplastic systems. I: Critical excitations. *Journal of Engineering Mechanics 133*(10), 1072–1080.

Beck, J. & Au, S. 2005. Reliability of dynamic systems using stochastic simulation. In C. Soize and G. I. Schuëller (Eds.), *Structural Dynamics EURODYN 2005 - Proceedings of the 6th International Conference on Structural Dynamics*, Volume 1, Paris, France, pp. 23–30. Millpress, Rotterdam.

Breitung, K. 1994. *Asympotic Approximations for Probability Integrals*. Lecture Notes in Mathematics, vol. 1592. Berlin: Springer.

Coello, C. 2002. Theoretical and numerical constraint-handling techniques used with evolutionary algorithms: a survey of the state of the art. *Computer Methods in Applied Mechanics and Engineering 191*(11–12), 1245–1287.

de Boer, P., Kroese, D., Mannor, S. & Rubinstein, R. 2005. A tutorial on the cross-entropy method. *Annals of Operations Research 134*(1), 19–67.

Ditlevsen, O. & Madsen, O. 1996. *Structural Reliability Methods*. John Wiley and Sons.

Freudenthal, A. 1956. Safety and the probability of structural failure. *ASCE Transactions 121*, 1337–1397.

Fujimura, K. & Der Kiureghian, A. 2007. Tail-equivalent linearization method for nonlinear random vibration. *Probabilistic Engineering Mechanics 22*(1), 63–76.

Katafygiotis, L. & Cheung, S. 2006. Domain decomposition method for calculating the failure probability of linear dynamic systems subjected to Gaussian stochastic loads. *Journal of Engineering Mechanics 132*(5), 475–486.

Katafygiotis, L. & Cheung, S. 2007. Application of spherical subset simulation method and auxiliary domain method on a benchmark reliability study. *Structural Safety 29*(3), 194–207.

Katafygiotis, L., Moan, T. & Cheung, S. 2007. Auxiliary domain method for solving multi-objective dynamic reliability problems for nonlinear structures. *Structural Engineering & Mechanics 25*(3), 347–363.

Koo, H., Der Kiureghian, A. & Fujimura, K. 2005. Design–point excitation for non–linear random vibrations. *Probabilistic Engineering Mechanics 20*(2), 134–147.

Liu, P. & Der Kiureghian, A. 1986. Multivariate distribution models with prescribed marginals and covariances. *Probabilistic Engineering Mechanics 1*(2), 105–112.

Pradlwarter, H., Schuëller, G.I., Koutsourelakis, P. & Charmpis, D. 2007. Application of line sampling simulation method to reliability benchmark problems. *Structural Safety 29*(3), 208–221.

Rubinstein, R. 1999. The cross-entropy method for combinatorial and continuous optimization. *Methodology and Computing in Applied Probability 1*, 127–190.

Schuëller, G.I., Pradlwarter, H. & Koutsourelakis, P. 2004a. *Benchmark Study on Reliability Estimation in Higher Dimensions of Structural Systems*. Chair of Engineering Mechanics, Leopold-Franzens University, Innsbruck, Austria, EU, http://mechanik.uibk.ac.at/Benchmark_Reliability/.

Schuëller, G.I., Pradlwarter, H. & Koutsourelakis, P. 2004b. A critical appraisal of reliability estimation procedures for high dimensions. *Probabilistic Engineering Mechanics 19*(4), 463–474.

Schuëller, G.I. & Stix, R. 1987. A critical appraisal of methods to determine failure probabilities. *Structural Safety 4*, 293–309.

Valdebenito, M., Pradlwarter, H. & Schuëller, G.I. 2008. The Role of the Design Point for Calculating Failure Probabilities – Part 2: in View of Non Linearities. Structural Safety, *Submitted for publication*.

Youn, B., Choi, K. & Du, L. 2005. Adaptive probability analysis using an enhanced hybrid mean value method. *Structural and Multidisciplinary Optimization 29*(2), 134–148.

Chapter 2

Finite element response sensitivity, probabilistic response and reliability analyses

Joel P. Conte

University of California, San Diego, USA

Michele Barbato

Louisiana State University, Louisiana, USA

Quan Gu

AMEC Geomatrix, Newport Beach, USA

ABSTRACT: Efficient and accurate analytical tools are needed in earthquake engineering to propagate uncertainties from the seismic input and finite element (FE) model parameters to a probabilistic estimate of the seismic performance through advanced large-scale nonlinear simulations based on the same FE models as those used in deterministic analysis. Sensitivities of the FE response with respect to both model and loading parameters represent an essential ingredient in studying this complex propagation of uncertainties. This chapter presents recent developments in FE response sensitivity analysis based on the Direct Differentiation Method (DDM) for displacement-based, force-based, and three-field mixed finite elements. First-Order Second-Moment (FOSM) approximations of the first- and second-order statistics of the response of structural systems with random/uncertain parameters and subjected to deterministic quasi-static and/or dynamic loads are obtained using DDM-based FE response sensitivities and compared to Monte Carlo simulation results. The probability of a structural response quantity exceeding a specified threshold level is evaluated using the First-Order Reliability Method (FORM) combined with DDM-based FE response sensitivities in the search for the "design point(s)" (DPs). Both time-invariant and time-variant problems are considered. The geometry of limit-state surfaces near the DP(s) is explored in subspaces defined by planes of major principal curvatures. This geometry explains the lack of accuracy of FORM-based solutions in some cases and suggests the development of new improved solution strategies, e.g., the Design Point – Response Surface – Simulation (DP-RS-Sim) method. The examples presented in this study include both structural systems and soil-foundation-structure interaction systems and are based on two types of analysis which are used extensively in earthquake engineering, namely pushover analysis and time history analysis.

1 Introduction

Providing a structure with the capability of achieving a target performance over its design life-time is a challenging task for structural engineers. In order to complete this task successfully, the engineer must account correctly during the design process for the existing aleatory and epistemic uncertainties. Thus, proper methods are required for propagating uncertainties from model parameters describing the geometry, the material

behaviours and the applied loadings to structural response quantities used in defining performance limit-states. These methods need also to be integrated with methodologies already well-known to practicing engineers, such as the finite element (FE) method.

This study presents recent developments in response sensitivity, probabilistic response and reliability analyses of structural and geotechnical systems in a general-purpose framework for nonlinear FE response analysis. Current advances are highlighted which cover relevant gaps between response sensitivity computation using the Direct Differentiation Method (DDM) and state-of-the-art FE response-only analysis. This work shows extensions of the DDM which were required for efficient computation of FE response sensitivities of structural and Soil-Foundation-Structure-Interaction (SFSI) systems. Response sensitivity analyses are performed and used in application examples to gain insight into the relative importance of model parameters with regard to system response. Response sensitivities are essential tools in studying the propagation of uncertainties in nonlinear dynamic analysis of structural and SFSI systems.

Examples of probabilistic response analysis using the mean-centred First-Order Second-Moment (FOSM) approximation, time-invariant (First- and Second-Order Reliability Methods, FORM and SORM) and time-variant (mean outcrossing rate computation) reliability analyses are provided to illustrate the methodology presented and its current capabilities and limitations.

A new multidimensional visualization technique is introduced to study the topology of limit-state surfaces near their design point(s) (DPs). A hybrid reliability analysis method, developed using the insight gained from this visualization technique, is introduced and illustrated through an application example.

The response sensitivity, probabilistic response and reliability analysis methods presented are based on nonlinear FE quasi-static pushover and time-history analyses, which are used extensively in earthquake engineering and referred to by structural design codes.

2 Finite element response sensitivity analysis

FE response sensitivities represent an essential ingredient for gradient-based optimization methods needed in various subfields of structural engineering such as structural optimization, structural reliability analysis, structural identification, and FE model updating (Ditlevsen & Madsen 1996, Kleiber et al. 1997). Furthermore, FE response sensitivities are extremely useful for gaining deeper insight into the effect and relative importance of system and loading parameters with regard to structural response. The computation of FE response sensitivities to geometric, material and loading parameters requires extension of the FE algorithms for response-only computation. If r denotes a generic scalar response quantity, the sensitivity of r with respect to the geometric, material or loading parameter θ is defined mathematically as the partial derivative of r with respect to parameter θ, considering both explicit and implicit dependencies, evaluated at $\theta = \theta_0$, with $\theta_0 =$ nominal value taken by the sensitivity parameter θ for the FE response analysis.

Response sensitivity computation can be performed using different methods, such as the forward/backward/central Finite Difference Method (FDM) (Kleiber et al. 1997, Conte et al. 2003, 2004), the Adjoint Method (AM) (Kleiber et al. 1997), the Perturbation Method (PM) (Kleiber & Hien 1992), and the Direct Differentiation Method

(DDM) (Kleiber et al. 1997, Conte 2001, Conte et al. 2003, 2004, Gu & Conte 2003, Barbato & Conte 2005, 2006, Zona et al. 2005, 2006, Barbato et al. 2006, 2007, Gu et al. 2007a). The FDM is the simplest method for response sensitivity computation, but is also computationally expensive and can be negatively affected by numerical noise (Haftka & Gurdal 1993, Gu & Conte 2003). The AM is extremely efficient for linear and nonlinear elastic structural systems/models, but is not as efficient computationally as other methods when nonlinear hysteretic material constitutive models are employed (Kleiber et al. 1997). The PM is computationally efficient but generally not very accurate. The DDM, on the other hand, is very general, efficient and accurate and is applicable to any material constitutive model. These advantages can be obtained at the one-time cost of differentiating analytically the space- (finite element) and time- (finite difference) discrete equations governing the structural response and implementing these algorithms for "exact" derivative computation in a FE code.

According to the DDM, the consistent FE response sensitivities are computed at each time step, after convergence is achieved for response computation. Response sensitivity calculation algorithms impact the various hierarchical layers of FE response calculation, namely: (1) the structure level, (2) the element level, (3) the integration point (section for frame/truss elements) level, and (4) the material level. Details on the derivation of the DDM sensitivity equation at the structure level and at the element level for classical displacement-based finite elements, specific software implementation issues, and properties of the DDM in terms of efficiency and accuracy can be found elsewhere (Kleiber et al. 1997, Conte 2001, Conte et al. 2003, Gu & Conte 2003). In this study, some newly developed algorithms and recent extensions are presented which cover relevant gaps between state-of-the-art FE response-only analysis and response sensitivity computation using the DDM.

2.1 *Response sensitivity algorithm for force-based frame elements*

Recent years have seen great advances in nonlinear analysis of frame structures. These advances were led by the development and implementation of force-based elements (Spacone et al. 1996), which are superior to classical displacement-based elements in tracing material nonlinearities such as those encountered in reinforced concrete beams and columns. In the classical displacement-based frame element, the cubic and linear Hermitian polynomials used to interpolate the transverse and axial displacement fields, respectively, are only approximations of the actual displacement fields in the presence of non-uniform beam cross-section and/or nonlinear material behaviour. On the other hand, force-based frame element formulations stem from equilibrium between section and nodal forces, which can be enforced exactly in the case of a frame element. The exact flexibility matrix can be computed for an arbitrary (geometric) variation of the cross-section and for any section/material constitutive law. Thus, force-based elements enable, at no significant additional computational costs, a drastic reduction in the number of elements required for a given level of accuracy in the simulated response of a FE model of a frame structure.

The established superiority of force-based over classical displacement-based frame elements for response-only computation motivated the extension of the DDM to force-based frame elements. The problem is conceptually more complicated for the

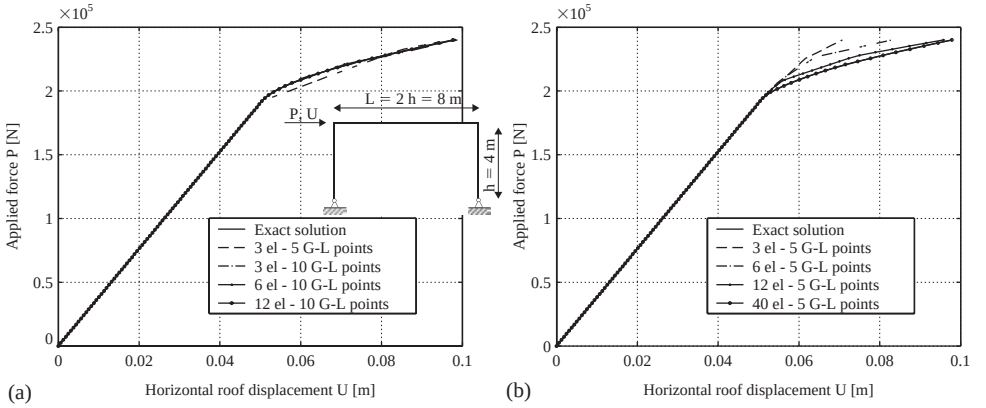

Figure 1 Applied horizontal force versus horizontal roof displacement of different FE meshes: (a) using force-based frame elements and (b) using displacement-based frame elements.

force-based than for the displacement-based element, since in the former no simple direct relation exists between section deformations and the element end deformations. In fact, while equilibrium is enforced in strong form, compatibility is enforced only in weak form over the element. The solution to this problem has been derived and presented elsewhere (Conte et al. 2004). This solution requires solving, at the element level and at each load/time step, a system of linear equations (the size of which depends on the number of integration points for the element) having as unknown the sensitivities of section deformations and element nodal forces. These quantities are necessary for the solution of the sensitivity equation at the structure level. An alternative solution, which does not require solving a system of linear equations at the element level, has been developed and presented in Scott et al. (2004).

The benefit of using force-based instead of displacement-based frame elements has been found even more conspicuous when accurate and efficient computation of structural response sensitivities to material and loading parameters is required in addition to response-only computations (Barbato & Conte 2005). This benefit in terms of improved accuracy and efficiency increases with the complexity of the structural system being analyzed. As application example, a statically indeterminate two-dimensional single-story single-bay steel frame (shown in the inset of Figure 1(a)) with distributed plasticity (modelled by using a Von Mises J_2 plasticity section constitutive law, see Conte et al. 2003) subjected to a horizontal force P at roof level is presented in this work. Details on the mechanical and geometric properties of the structure and on its modelling can be found in Barbato & Conte (2005). For this simple structure, closed-form solutions are available for horizontal roof displacement and its sensitivities to material parameters as functions of P. Figures 1(a) and (b) compare the force-displacement results in the horizontal direction obtained from FE analyses employing different meshes of force-based and displacement-based frame elements, respectively. Similarly, Figures 2(a) and (b) compare the sensitivity to the kinematic hardening modulus of the horizontal displacement obtained from FE analyses employing different meshes of force-based and displacement-based frame elements, respectively. It is

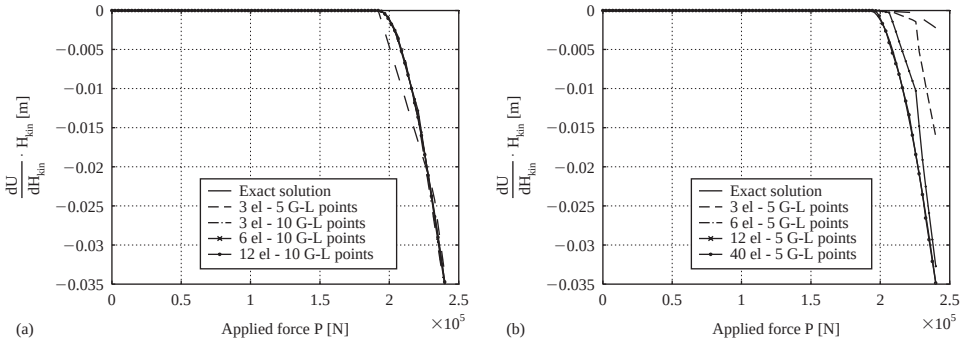

Figure 2 Sensitivities of roof displacement to kinematic hardening modulus for different FE meshes: (a) using force-based frame elements and (b) using displacement-based frame elements.

found that convergence of the FE response to the exact solutions is much faster when force-based elements are employed and this trend is more pronounced for FE response sensitivities.

2.2 *Response sensitivity algorithm for three-field mixed formulation elements*

A large body of research has been devoted to mixed FE formulations in the last 30 years. Several finite elements based on different variational principles have been developed (Washizu 1975, Belytschko et al. 2000) and relationships among them have been established. Accuracy and performance have been thoroughly analyzed and improved and important properties have been recognized and explained, such as equivalence between various stress recovery techniques and ability to eliminate shear-locking effects for specific applications (Belytschko et al. 2000). After more than three decades of research, mixed finite elements are now well established and largely adopted tools in a wide range of structural mechanics applications. Therefore, the advantage of extending the DDM to finite elements based on a mixed formulation is evident.

The DDM algorithm for a three-field mixed formulation based on the Hu-Washizu functional (Washizu 1975) has been derived and presented elsewhere (Barbato et al. 2007). This formulation stems from the differentiation of basic principles (equilibrium, compatibility and material constitutive equations), applies to both material and geometric nonlinearities, is valid for both quasi-static and dynamic FE analysis and considers material, geometric and loading sensitivity parameters. This general formulation has also been specialized to frame elements and linear geometry (small displacements and small strains).

2.3 *Extension of the DDM to steel-concrete composite frame structures*

The last decade has seen a growing interest in FE modelling and analysis of steel-concrete composite structures, with applications to seismic resistant frames and bridges

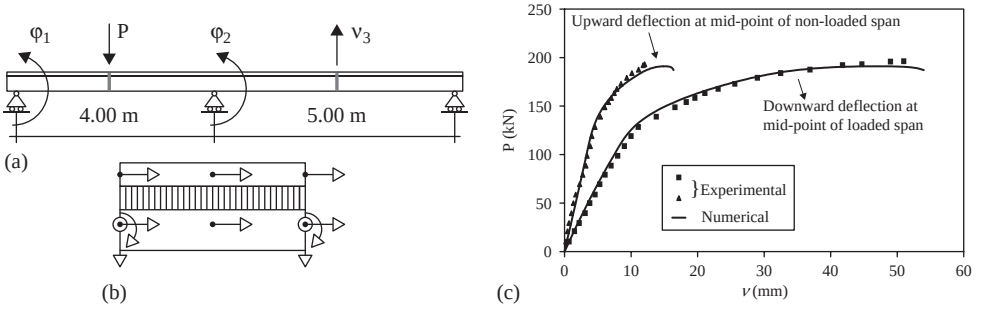

Figure 3 Application example of steel-concrete composite structure: (a) geometry and loading, (b) FE degrees of freedom and (c) comparison of experimental and numerical results.

(Spacone & El-Tawil 2004). The behaviour of composite beams (made of two components connected through shear connectors to form an interacting unit) is significantly influenced by the type of connection between the steel beam and the concrete slab. Flexible shear connectors allow the development of partial composite action. Thus, for accurate analytical response prediction, structural models of composite structures must account for the interlayer slip between the steel and concrete components. A composite beam finite element able to capture the interface slip is therefore an essential tool for model-based response simulation of steel-concrete composite structures.

Compared to common monolithic beams, composite beams with deformable shear connection present additional difficulties. Even in very simple structural systems (e.g., simply supported beams), complex distributions of the interface slip and force can develop. Different finite elements of composite beams with deformable shear connection have been developed and presented in the literature (Spacone & El-Tawil 2004, Dall'Asta & Zona 2004). These elements include suitable models describing section deformations in order to compute the section force resultants of steel-concrete composite members. This requires the use of realistic material constitutive models for beam steel, reinforcement steel, concrete, and shear-slip behaviour of the studs connecting the two structural components (Zona et al. 2005, 2006, Barbato et al. 2007).

The DDM has recently been extended for response sensitivity computation of steel-concrete composite frame structures (Zona et al. 2005, 2006, Barbato et al. 2007). Thus, advanced finite elements incorporating the deformable shear-connection between the two structural components of steel-concrete composite structures can be used for efficient computation of both the response and response sensitivity. Figure 3(a) depicts the configuration and loading condition of a two-span asymmetric continuous steel-concrete composite beam for which experimental data are available. Figure 3(b) shows the degrees of freedom of the frame element (with deformable shear connection) used in modelling this beam structure. Experimental and numerical simulation results are compared in Figure 3(c). It is seen that their agreement is very good.

Figure 4(a) plots the normalized sensitivities (i.e., multiplied by the nominal value of the sensitivity parameter and divided by the current value of the response quantity) of the vertical uplift ν_3 at midpoint of the non-loaded span to several material parameters as function of the normalized vertical uplift (i.e., the ratio between the current vertical

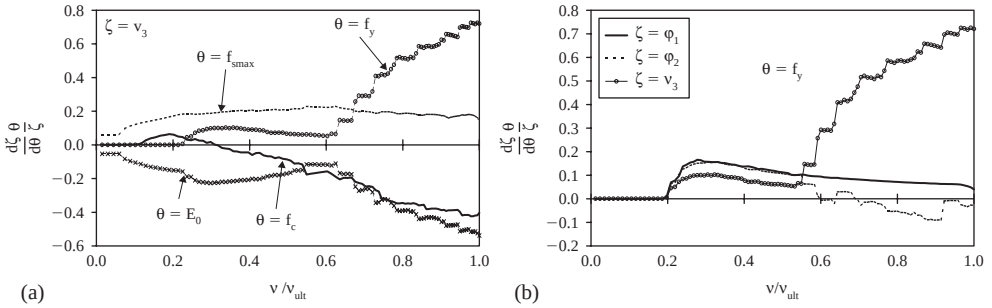

Figure 4 Normalized response sensitivities for steel-concrete composite structure: (a) sensitivities of vertical uplift at midpoint of non-loaded span to several material constitutive parameters and (b) sensitivities of several response quantities to yield strength of the steel of the beam component.

uplift and the maximum uplift which is reached at failure of the beam). The normalized sensitivities can be used directly as importance measures of the sensitivity parameters for the considered response quantity, since they represent the percent change in the response per percent change in the parameter. In the case presented here, the yield strength of the steel of the beam, f_y, is the parameter affecting the most the vertical uplift ν_3. Figure 4(b) plots the normalized sensitivities of several response quantities to parameter f_y as functions of the normalized vertical uplift. The effects of parameter f_y are pronounced for ν_3, but much less so for the rotations of the beam at the left and central supports (φ_1 and φ_2, respectively).

2.4 *Extension of the DDM to Soil-Foundation-Structure-Interaction (SFSI) systems*

The seismic excitation experienced by structures (buildings, bridges, etc.) is a function of the earthquake source (fault rupture mechanism), travel path effects, local site effects, and SFSI effects. Irrespective of the presence of a structure, the local soil conditions (stratification of subsurface materials) may change significantly, through their dynamic filtering effects, the earthquake motion (seismic waves) from the bedrock level to the ground surface. The complex and still poorly understood interactions between subsurface materials, foundations, and the structure during the passage of seismic waves is further significantly complicated by clouds of uncertainties associated with the various components of a SFSI system as well as the seismic excitation.

The DDM has been extended to the analysis of SFSI systems. This extension required development and implementation of response sensitivity algorithms for 2-dimensional (quadrilateral) and 3-dimensional (brick) isoparametric finite elements, soil materials (such as the pressure-independent multi-yield surface plasticity model, see Prevost 1977, Gu et al. 2008b, c) and handling of multipoint constraints (Gu et al. 2008a) required for properly connecting finite elements used in modelling the soil domain with the ones used for the superstructure model (such as frame elements). A benchmark

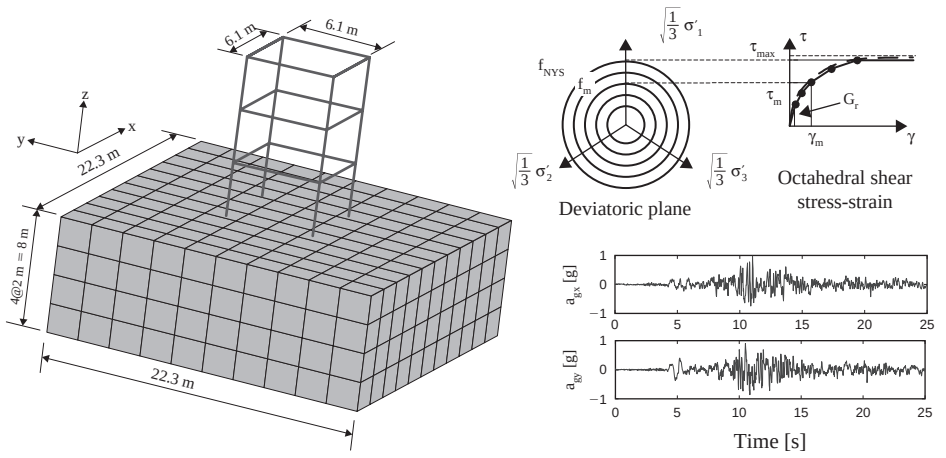

Figure 5 Geometry, input earthquake ground motion and soil material constitutive model for the benchmark SFSI system.

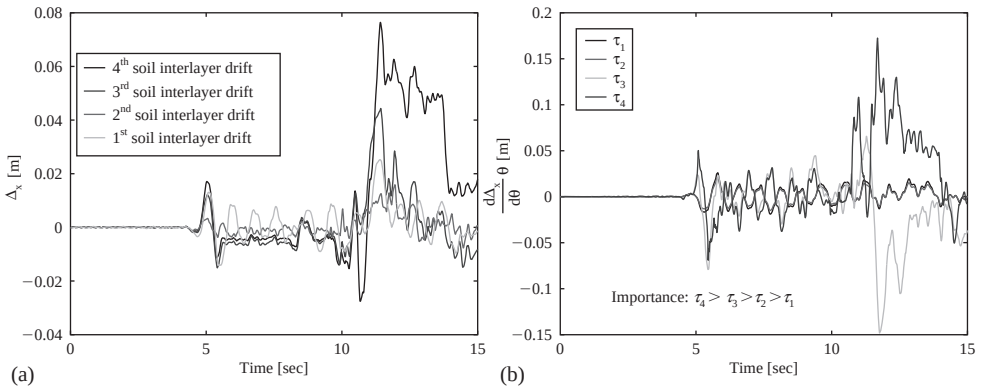

Figure 6 Benchmark SFSI system: (a) time histories of the soil interlayer drifts and (b) sensitivities of the first interstory drift to the shear strengths of the soil layers.

SFSI system is presented in Figure 5. A detailed description of the superstructure can be found in Barbato et al. (2006).

Figure 6(a) plots the time histories of the soil interlayer drifts in the x-direction, while Figure 6(b) shows the first interstory drift in the x-direction, Δ_{1x}, sensitivities (multiplied by the nominal value of the sensitivity parameter) to the shear strength parameter of each of the four soil layers. In this case, the parameters affecting the most Δ_{1x} are the shear strengths of the two deeper soil layers, since they govern the energy transferred into the structure by the soil from the earthquake input at bedrock level.

2.5 *Other computational issues in FE response sensitivity analysis*

The analytical derivation of FE response sensitivities requires a detailed knowledge of the FE algorithms used for response-only computation, while the efficient computation and reliable use of these sensitivities demand a clear understanding of the analytical properties of the computed response and response sensitivities. These properties for response sensitivities have been investigated in the context of specific applications such as design point search in FE reliability analysis. Some of these properties are discussed below.

A first important issue is the equivalence between two methods for computing FE response sensitivities according to the DDM. Response sensitivities can be computed (1) by differentiating analytically with respect to the sensitivity parameters the time- and space-discrete equations of motion of the structural system considered or (2) by obtaining the time-continuous, space-discrete differential equations governing the response sensitivities and discretizing them in time to numerically compute the response gradient. The conditions of equivalence of these two methods are given in Conte et al. (2003). It is emphasized that consistent (or algorithmic) tangent moduli (leading to consistent tangent stiffness matrices) are to be used in the first method instead of continuum tangent moduli. For uniaxial material constitutive laws, consistent and continuum tangent moduli coincide, which is not the case for multidimensional constitutive models. The consistent tangent moduli have been derived and successfully implemented in FE codes for several multidimensional material constitutive models such as the cap-plasticity model (Conte et al. 2003) (for concrete and geological materials) and the multi-yield-surface plasticity model (Gu et al. 2008b) (for soil).

Continuity/smoothness of FE response sensitivities is another issue needing careful examination, particularly when sensitivities are used in gradient-based optimization algorithms. Gradient discontinuities are detrimental to the rate of convergence or can even impair the convergence to a local minimum of gradient-based optimization algorithms (Gill et al. 1981). It has been recognized that non-smooth material constitutive models exhibit discontinuous response sensitivities corresponding to elastic-to-plastic material state transitions (Conte et al. 2003, Haukaas & Der Kiureghian 2004) while linear elastic unloading events do not produce response sensitivity discontinuities (Haukaas & Der Kiureghian 2004). Recent work established a sufficient condition on the smoothness properties of material constitutive models and loading functions to ensure FE response sensitivity continuity (for both loading and unloading) along the time and parameter axes in the case of quasi-static analysis (Barbato & Conte 2006). The same study also recognized that in the case of dynamic analysis, in addition to smoothness conditions on the material constitutive models employed and the loading functions, a sufficiently fine time-discretization (generally finer than the one required for convergence of response-only computations) is required to avoid response sensitivity discontinuities along the parameter axes.

Finally, the properties of FE response sensitivities have been studied in terms of convergence to the response sensitivities corresponding to the (analytically unknown) solution of the time- and space-continuous equations of motions (Gu & Conte, 2003). The results of these studies indicate that convergence in response sensitivities requires stricter conditions (i.e., finer spatial discretization and, to a lower degree, smaller

load or time step size) than the ones required for convergence of response-only calculations. It is noteworthy that gradient-based optimization algorithms require consistent (and not necessarily converged) gradients in order to preserve the asymptotic rate of superlinear convergence of quasi-Newton methods.

3 Simplified finite element probabilistic response analysis

Probabilistic response analysis consists of computing the probabilistic characterization of the response of a specific structure, given as input the probabilistic characterization of material, geometric and loading parameters. An approximate method of probabilistic response analysis is the mean-centred First-Order Second-Moment (FOSM) method, in which mean values (first-order statistical moments), variances and covariances (second-order statistical moments) of the response quantities of interest are estimated by using a mean-centred, first-order Taylor series expansion of the response quantities in terms of the random/uncertain model parameters. Thus, this method requires only the knowledge of the first- and second-order statistical moments of the random parameters. It is noteworthy that often statistical information about the random parameters is limited to first and second moments and therefore probabilistic response analysis methods more advanced than FOSM analysis cannot be fully exploited.

Given the vector of n random parameters $\boldsymbol{\theta}$, the corresponding covariance matrix $\Sigma_{\boldsymbol{\theta}}$ is defined as

$$\Sigma_{\boldsymbol{\theta}} = [\rho_{ij}\sigma_i\sigma_j]; \quad i,j = 1,2,\ldots,n \tag{1}$$

where ρ_{ij} = correlation coefficient of random parameters θ_i and θ_j ($\rho_{ii} = 1$; $i = 1,2,\ldots,n$), and σ_i = standard deviation of random parameter θ_i. The vector $\mathbf{r}$ of m response quantities of interest is approximated by a first-order truncation of its Taylor series expansion in the random parameters $\boldsymbol{\theta}$ about their mean values $\boldsymbol{\mu}_{\boldsymbol{\theta}}$ as

$$\mathbf{r}(\boldsymbol{\theta}) \approx \mathbf{r}_{\text{lin}}(\boldsymbol{\theta}) = \mathbf{r}(\boldsymbol{\mu}_{\boldsymbol{\theta}}) + \nabla_{\boldsymbol{\theta}}\mathbf{r}|_{\boldsymbol{\theta}=\boldsymbol{\mu}_{\boldsymbol{\theta}}} \cdot (\boldsymbol{\theta} - \boldsymbol{\mu}_{\boldsymbol{\theta}}) \tag{2}$$

The first- and second-order statistical moments of the response quantities $\mathbf{r}$ are approximated by the corresponding moments of the above linearized response quantities, i.e.,

$$\boldsymbol{\mu}_{\mathbf{r}} \approx \boldsymbol{\mu}_{\mathbf{r}_{\text{lin}}} = \text{E}[\mathbf{r}_{\text{lin}}(\boldsymbol{\theta})] = \mathbf{r}(\boldsymbol{\mu}_{\boldsymbol{\theta}}) + \nabla_{\boldsymbol{\theta}}\mathbf{r}|_{\boldsymbol{\theta}=\boldsymbol{\mu}_{\boldsymbol{\theta}}} \cdot \text{E}[\boldsymbol{\theta} - \boldsymbol{\mu}_{\boldsymbol{\theta}}] = \mathbf{r}(\boldsymbol{\mu}_{\boldsymbol{\theta}}) \tag{3}$$

$$\Sigma_{\mathbf{r}} \approx \Sigma_{\mathbf{r}_{\text{lin}}} = \text{E}\left[\left(\mathbf{r}_{\text{lin}}(\boldsymbol{\theta}) - \boldsymbol{\mu}_{\mathbf{r}_{\text{lin}}}\right) \cdot \left(\mathbf{r}_{\text{lin}}(\boldsymbol{\theta}) - \boldsymbol{\mu}_{\mathbf{r}_{\text{lin}}}\right)^{\text{T}}\right] = \nabla_{\boldsymbol{\theta}}\mathbf{r}|_{\boldsymbol{\theta}=\boldsymbol{\mu}_{\boldsymbol{\theta}}} \cdot \Sigma_{\boldsymbol{\theta}} \cdot \left(\nabla_{\boldsymbol{\theta}}\mathbf{r}|_{\boldsymbol{\theta}=\boldsymbol{\mu}_{\boldsymbol{\theta}}}\right)^{\text{T}} \tag{4}$$

in which E[...] = mathematical expectation operator.

The approximate response statistics computed through Eqs. (3) and (4) are extremely important in evaluating the variability of the response quantities of interest due to the intrinsic uncertainty of the model parameters and provide information on the statistical correlation between the different response quantities. It is noteworthy that these approximate first- and second-order response statistics can be readily obtained when response sensitivities evaluated at the mean values of the random parameters are

available. Only a single FE analysis is needed in order to perform a FOSM probabilistic response analysis, when the FE response sensitivities are computed using the DDM. Probabilistic response analysis can also be performed using Monte Carlo simulation (MCS). In this study, MCS is used to assess the accuracy of the FOSM approximations in Eqs. (3) and (4) when applied to nonlinear FE response analysis of R/C building structures characterized with random/uncertain material parameters and subjected to quasi-static pushover. The MCS procedure requires:

1. Generation of N realizations of the n-dimensional random parameter vector $\boldsymbol{\theta}$ according to a given n-dimensional joint probability density function (PDF).
2. Computation by FE analysis of N response curves for each component of the response vector $\mathbf{r}$, corresponding to the N realizations of the random parameter vector $\boldsymbol{\theta}$.
3. Statistical estimation of specified marginal and joint moments of the components of response vector $\mathbf{r}$ at each load step of the FE response analysis.

MCS is a general and robust method for probabilistic response analysis, but it suffers two significant limitations: (1) it requires knowledge of the full joint PDF of random parameters $\boldsymbol{\theta}$, which, in general, is only partially known, and (2) it requires performing a usually large number of FE response analyses, which could be computationally prohibitive.

In this study, the Nataf model (Ditlevsen & Madsen 1996) was used to generate realizations of the random parameters $\boldsymbol{\theta}$. It requires specification of the marginal PDFs of the random parameters $\boldsymbol{\theta}$ and their correlation coefficients. It is therefore able to reproduce the given first- and second-order statistical moments of random parameters $\boldsymbol{\theta}$. The same three-dimensional three-story reinforced concrete building presented in Section 2.4, but on rigid supports, is considered as application example. Table 1 provides the marginal distributions and their statistical parameters for the material parameters modelled as correlated random variables. Other details on the modelling of the structure and the statistical correlation of the random parameters can be found in Barbato et al. (2006).

Table 1 Marginal PDFs of material parameters (statistical parameters for lognormal distribution: (1) $\lambda = \mu_{Ln(X)}$, (2) $\zeta = \sigma_{Ln(X)}$; for beta distribution: (1) x_{min}, (2) x_{max}, (3) α_1, (4) α_2).

RV	*Distribution*	*Par. #1*	*Par. #2*	*Par. #3*	*Par. #4*	*Mean*	*c.o.v. [%]*
$f_{c,core}$ [MPa]	Lognormal	3.4412	0.1980	–	–	34.47	20
$\varepsilon_{c,core}$ [−]	Lognormal	−5.3973	0.1980	–	–	0.005	20
$f_{cu,core}$ [MPa]	Lognormal	3.0845	0.1980	–	–	24.13	20
$\varepsilon_{cu,core}$ [−]	Lognormal	−4.0110	0.1980	–	–	0.02	20
$f_{c,cover}$ [MPa]	Lognormal	3.2180	0.1980	–	–	27.58	20
$\varepsilon_{c,cover}$ [−]	Lognormal	−6.3136	0.1980	–	–	0.002	20
$\varepsilon_{cu,cover}$ [−]	Lognormal	−5.2150	0.1980	–	–	0.006	20
f_y [MPa]	Beta	227.53	427.48	3.21	4.28	307.46	10.6
E [MPa]	Lognormal	12.1946	0.0330	–	–	201000	3.3
b [−]	Lognormal	−4.0110	0.1980	–	–	0.02	20

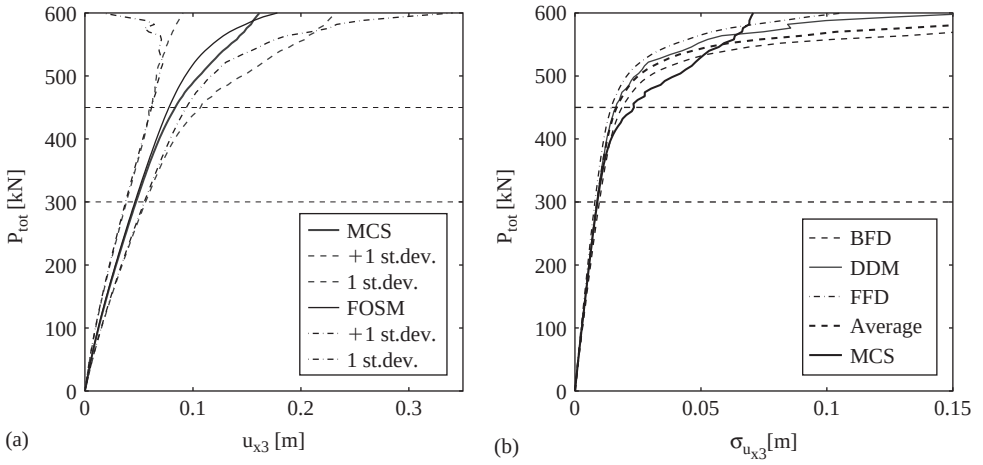

Figure 7 Comparison of probabilistic response analysis results for u_{3x} obtained from FOSM and MCS: (a) mean value ± one standard deviation and (b) standard deviation estimates.

Figure 7(a) compares the estimates of the mean value and mean value ± one standard deviation of the roof displacement in the x-direction, u_{x3}, for a quasi-static pushover analysis with an upper-triangular pattern of applied horizontal forces obtained using FOSM and MCS. Figure 7(b) provides the estimates of the standard deviation of u_{x3} obtained from MCS and FOSM with sensitivities computed through DDM, backward/forward finite differences (BFD and FFD, respectively, using a small perturbation of each parameter), and the average of BFD and FFD. It is found that a DDM-based FOSM analysis can provide, at low computational cost, estimates of the first- and second-order response statistics which are in good agreement with significantly more expensive MCS estimates when the frame structure experiences low-to-moderate material nonlinearities. Further discussions of these results can be found elsewhere (Barbato et al. 2006).

4 Finite element reliability analysis

In general, the structural reliability problem consists of computing the probability of failure P_f of a given structure, which is defined as the probability of exceeding some limit-state (or damage-state) function(s) when the loading(s) and/or structural properties and/or limit-state function parameters are uncertain quantities modelled as random variables. This study focuses on component reliability problems, i.e., single limit-state function (LSF) $g = g(\mathbf{r}, \boldsymbol{\theta})$ where $\mathbf{r}$ = vector of response quantities of interest and $\boldsymbol{\theta}$ = vector of random variables considered. The LSF g is chosen such that $g \leq 0$ defines the failure domain/region. Thus, the time-invariant component reliability problem can be expressed mathematically as

$$P_f = P[g(\mathbf{r}, \boldsymbol{\theta}) \leq 0] = \int_{g(\mathbf{r},\boldsymbol{\theta})\leq 0} p_{\Theta}(\boldsymbol{\theta})\, d\boldsymbol{\theta} \tag{5}$$

where $p_\Theta(\boldsymbol{\theta})$ = joint PDF of random variables $\boldsymbol{\theta}$. For time-variant reliability problems, an upper bound of the probability of failure, $P_f(T)$, over the time interval [0, T], can be obtained as

$$P_f(T) \leq \int_0^T \nu_g(t)\, dt \tag{6}$$

where $\nu_g(t)$ = mean down-crossing rate of level zero of the LSF g and t = time. An estimate of $\nu_g(t)$ can be obtained numerically from the limit form relation (Hagen & Tvedt 1991)

$$\nu_g(t) = \lim_{\delta t \to 0} \frac{P[\{g(\mathbf{r}(\boldsymbol{\theta}, t), \boldsymbol{\theta}) > 0\} \cap \{g(\mathbf{r}(\boldsymbol{\theta}, t + \delta t), \boldsymbol{\theta}) \leq 0\}]}{\delta t} \tag{7}$$

Numerical evaluation of the numerator of Eq. (7) reduces to a time-invariant two-component parallel system reliability analysis. It is clear that the first part of Eq. (5) represents the building block for the solution of both time-invariant and time-variant reliability problems (Der Kiureghian 1996). Using Eq. (7), Poisson approximation to the failure probability, $P_{f,Poisson}(T)$, is obtained as (under the hypothesis that $P[g(\mathbf{r}(\boldsymbol{\theta}, t = 0), \boldsymbol{\theta}) > 0] = 1$)

$$P_{f,Poisson}(T) = 1 - \exp\left(-\int_0^T \nu_g(t)\, dt\right) \tag{8}$$

The problem posed in Eq. (5) is extremely challenging for real-world structures and can be solved only in approximate ways. A well established methodology consists of introducing a one-to-one mapping/transformation between the physical space of variables $\boldsymbol{\theta}$ and the standard normal space of variables $\mathbf{y}$ (Ditlevsen & Madsen 1996) and then computing the probability of failure P_f as

$$P_f = P[G(\mathbf{y}) \leq 0] = \int_{G(\mathbf{y}) \leq 0} \varphi_Y(\mathbf{y})\, d\mathbf{y} \tag{9}$$

where $\varphi_Y(\mathbf{y})$ = standard normal joint PDF and $G(\mathbf{y}) = g(\mathbf{r}(\boldsymbol{\theta}(\mathbf{y})), \boldsymbol{\theta}(\mathbf{y}))$ is the LSF in the standard normal space. Solving the integral in Eq. (9) remains a formidable task, but this new form of P_f is suitable for approximate solutions taking advantage of the rotational symmetry of the standard normal joint PDF and its exponential decay in both the radial and tangential directions. An optimum point at which to approximate the limit-state surface (LSS) $G(\mathbf{y}) = 0$ is the "design point" (DP), which is defined as the most likely failure point in the standard normal space, i.e., the point on the LSS that is closest to the origin. Finding the DP is a crucial step for approximate methods to evaluate the integral in Eq. (9), such as FORM and SORM and importance sampling

(IS) (Breitung 1984, Der Kiureghian 1996, Au et al. 1999). The DP, $\mathbf{y}^*$, is found as solution of the following constrained optimization problem:

$$\mathbf{y}^* = \arg\{\min(0.5\mathbf{y}^T\mathbf{y}) | G(\mathbf{y}) = 0\} \tag{10}$$

The most effective techniques for solving the above constrained optimization problem are gradient-based optimization algorithms (Gill et al. 1981, Liu & Der Kiureghian 1991) coupled with algorithms for accurate and efficient computation of the gradient of the constraint function $G(\mathbf{y})$, requiring computation of the sensitivities of response quantities $\mathbf{r}$ to parameters $\boldsymbol{\theta}$. Using the implicit function theorem together with the chain rule of differentiation for multi-variable functions, $\nabla_y G$ can be obtained as

$$\nabla_y G = (\nabla_r g|_\theta \cdot \nabla_\theta \mathbf{r} + \nabla_\theta g|_r) \cdot \nabla_y \boldsymbol{\theta} \tag{11}$$

where $\nabla_r g|_\theta$ and $\nabla_\theta g|_r$ = gradients of LSF g with respect to its explicit dependency on quantities $\mathbf{r}$ and $\boldsymbol{\theta}$, respectively, and usually can be computed analytically; $\nabla_\theta \mathbf{r}$ = sensitivities of response variables $\mathbf{r}$ to parameters $\boldsymbol{\theta}$, and $\nabla_y \boldsymbol{\theta}$ = gradient of physical space parameters with respect to standard normal space parameters. For probability distribution models defined analytically (with monotonically increasing joint CDF), the gradient $\nabla_y \boldsymbol{\theta}$ can also be derived analytically (Ditlevsen & Madsen 1996).

For real-world problems, the response simulation (computation of $\mathbf{r}$ for given $\boldsymbol{\theta}$) is typically performed using advanced mechanics-based nonlinear computational models developed based on the FE method. FE reliability analysis requires augmenting existing FE formulations for response-only calculation to compute the response sensitivities, $\nabla_\theta \mathbf{r}$, to parameters $\boldsymbol{\theta}$. As already seen in Section 2, an accurate and efficient way to perform FE response sensitivity analysis is through the DDM.

4.1 *Time-invariant reliability analysis*

A time-invariant reliability analysis is performed on the same three-story reinforced concrete building as in Sections 2.4 and 3, with the same probabilistic characterization of the material constitutive parameters as well. In addition, the value of the maximum applied horizontal force (equal to the total base shear) is modelled as lognormal random variable (see Figure 8(d)). A roof displacement $u_{x3} = 0.3$ m (corresponding to a roof drift ratio of 3.1%) is considered as failure condition. First, a DP search is performed (see Figure 8(a)) and a FORM approximation of the probability of failure is obtained. Then, using the DP found in the FORM analysis, a SORM estimate is obtained by computing the first principal curvature at the DP of the LSS and correcting the FORM approximation with Breitung's formula (Breitung 1984). Finally, an IS analysis is performed using as sampling distribution a joint standard normal PDF centred at the DP. It is found that the SORM approximation is distinctly more accurate than the FORM approximation and close to the IS analysis result, which is used here as reference result (Figures 8(b) and (c)).

4.2 *Time-variant reliability analysis*

The methodology presented in Section 4 for time-variant reliability analysis has been tested on simple structures. Mean up-crossing rates are estimated by FORM (Eq. (7)).

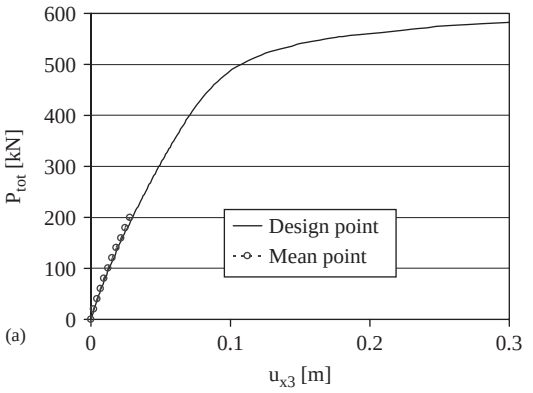

(b)

Type of analysis	P_f
FORM	0.001090
SORM	0.001623
IS	0.001755

(c)

	# samples	c.o.v.
IS	10000	0.023

(d)

P_{tot} [kN]	Mean	St. dev.	DP
Lognormal	200.00	80.00	582.84

Figure 8 Time-invariant reliability analysis of a 3-story R/C building subjected to pushover loads: (a) Mean and DP pushover curves, (b) comparison of analysis results, (c) IS analysis description, and (d) probabilistic and DP characterization of P_{tot}.

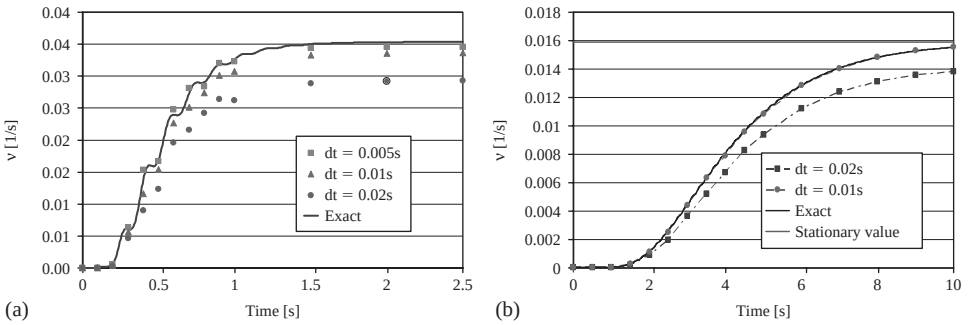

Figure 9 Mean out-crossing computation for linear elastic structures subjected to white noise from at rest initial conditions: (a) SDOF system ($T = 0.31$ s, $\zeta = 0.10$), and (b) 3-DOF steel building model ($T_1 = 0.38$ s, $T_2 = 0.13$ s, $T_3 = 0.09$ s, $\zeta_1 = \zeta_3 = 0.02$, Rayleigh damping).

First, linear elastic SDOF and MDOF structures with at rest initial conditions are subjected to white noise excitation. It is found that the mean up-crossing rates obtained using FORM are in very good agreement with available closed-form solutions (Lutes & Sarkani 1997) as shown in Figures 9(a) and (b) for SDOF and MDOF systems, respectively, when a sufficiently small time-interval, dt, is used in discretizing the white noise excitation process.

The same methodology is used for SDOF systems with a force-deformation relation modelled using a Menegotto-Pinto (MP) constitutive law (Menegotto & Pinto 1973). This constitutive law is calibrated to a shear-type single-story steel frame with height $H = 3.20$ m, bay length $L = 6.00$ m and made of European HE340A steel columns. The system is defined by the following parameters (taken as deterministic): mass $M = 28800$ kg, damping ratio $\zeta = 0.02$, initial stiffness $K = 40.56$ kN/mm,

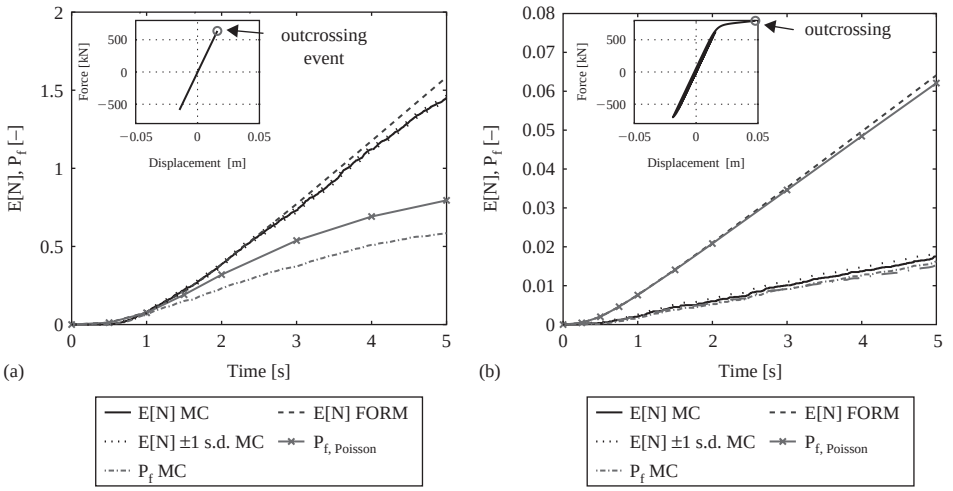

Figure 10 Time-variant reliability analysis results for nonlinear hysteretic SDOF systems: (a) quasi-linear behaviour and (b) significantly nonlinear behaviour.

initial yield force $F_{y0} = 734\,\text{kN}$ and post-yield to initial stiffness ratio $b = 0.05$. This SDOF system is subjected to two different input ground motions modelled as white noises with power spectral density $\phi_0 = 0.035\,\text{m}^2/\text{s}^3$ and $\phi_0 = 0.25\,\text{m}^2/\text{s}^3$, respectively. The expected cumulative number of up-crossings and time-variant failure probability relative to the roof displacement exceeding the threshold $\xi = 0.016\,\text{m}$ (roof drift ratio = 0.5%) and $\xi = 0.048\,\text{m}$ (roof drift ratio = 1.5%), respectively, are computed using FORM and MCS. Figure 10(a) compares the estimates of the expected number of up-crossings obtained using FORM and MCS (with ± one standard deviation interval as well) for the case $\phi_0 = 0.035\,\text{m}^2/\text{s}^3$ and $\xi = 0.016\,\text{m}$, for which the structure behaves quasi-linearly. Figure 10(a) also compares the time-variant failure probability estimates obtained through the FORM-based Poisson approximation and MCS. Figure 10(b) compares the same estimates as in Figure 10(a), but for the case $\phi_0 = 0.25\,\text{m}^2/\text{s}^3$ and $\xi = 0.048\,\text{m}$, for which the structure yields significantly. The insets of Figures 10(a) and (b) provide the DP force-displacement responses for 5.0 s of excitation.

For quasi-linear structural behaviour, the results in terms of expected cumulative number of up-crossings obtained using FORM are in good agreement with the MCS results. In this case, the difference between the FORM-based Poisson approximation and MCS estimate of the time-variant failure probability is mainly due to the relatively high value of P_f, for which the Poisson assumption of statistically independent up-crossing events is not valid. On the other hand, a FORM approximation of the LSS for significantly nonlinear structural behaviour provides a very inaccurate estimate of the expected cumulative number of up-crossings and therefore of the time-variant failure probability. Thus, computationally efficient methodologies are needed to take into account the nonlinear nature of the LSS for mean out-crossing rate computation.

4.3 *Limit-state surface topology and multidimensional visualization*

Knowledge about the topology (in both the physical and standard normal spaces) of the LSSs corresponding to a given reliability problem is extremely valuable in (1) gaining physical and geometrical insight into the structural reliability problem at hand, (2) analyzing the inaccuracies of the FORM/SORM approximations for time-invariant probability of failure and mean out-crossing rate computation, and (3) pointing to more efficient and accurate computational reliability methods for evaluating the probability content of typical failure domains. The study of the topology of LSSs is a challenging task and requires visualization of nonlinear hyper-surfaces in high-dimensional spaces (i.e., physical or standard normal space defined by random parameters representing loading, geometric and material properties).

A new methodology, herein referred to as Multidimensional Visualization in the Principal Planes (MVPP), is proposed for visualizing the shape of LSSs in FE reliability analysis in the neighbourhood of the DP(s). The MVPP requires finding the trace of the LSS in the planes of principal curvatures at the DP(s) (Principal Planes: PPs) in decreasing order of magnitude of the principal curvatures. Each PP is defined by the DP vector $\mathbf{y}^*$ and one of the eigenvectors (Principal Direction: PD) of the following Hessian matrix $\mathbf{A}$ (Der Kiureghian & De Stefano 1991)

$$\mathbf{A} = \frac{\mathbf{H}_{\text{red}}}{\left\| \nabla_{\mathbf{y}} G|_{\mathbf{y}^*} \right\|} \tag{12}$$

in which $[\mathbf{H}_{\text{red}}]_{i,j} = [\mathbf{R} \cdot \mathbf{H} \cdot \mathbf{R}^{\mathrm{T}}]_{i,j}$ is the reduced Hessian, with $i, j = 1, 2, \ldots, N-1$ and $N =$ number of random parameters, $\mathbf{H} = (N \times N)$ Hessian matrix of the LSF at the DP, $\mathbf{R} =$ matrix of coordinate transformation so that the new reference system has the N-th axis oriented as the DP vector $\mathbf{y}^*$, and $\left\| \nabla_{\mathbf{y}} G|_{\mathbf{y}^*} \right\| =$ Euclidean norm of the gradient of the LSF at the DP. The PDs are sorted in decreasing order of magnitude of the corresponding eigenvalues.

In this study, the Hessian matrix is obtained by forward finite difference calculations applied to the DDM-based response sensitivities. For accurate FE models of realistic structural systems with a large number of uncertain model parameters, this approach for computing the Hessian matrix, which is then used to compute the major eigenvalues/eigenvectors, could be computationally prohibitive. Methods are under study for obtaining computationally affordable approximations of the Hessian matrix able to produce sufficiently accurate major eigenvalues/eigenvectors. In addition, the use of an existing algorithm (Der Kiureghian & De Stefano 1991) for computing eigenvalues (and corresponding eigenvectors) in order of decreasing magnitude without having to compute the Hessian matrix is also being considered.

The MVPP methodology provides important information about the topology of the LSS identifying a small number of dimensions which are of interest and thus requiring a limited number of FE simulations to visualize the LSS.

4.4 *New hybrid method for finite element reliability analysis*

As shown in Sections 4.1 and 4.2, FORM approximation of the LSS(s) can provide a very crude estimate of the time-invariant and time-variant (using mean out-crossing

rate computation) failure probability of a structural system exhibiting a strongly nonlinear material behaviour. Information about the topology of the LSS(s) near the DP(s) can be used effectively in order to improve on the FORM approximation accounting for nonlinearities in the LSF.

A currently under development hybrid time-invariant reliability method, referred to herein as DP-RS-Sim method and able to enhance the FORM/SORM estimates of time-invariant and time-variant failure probabilities for structural and/or geotechnical systems, is briefly presented and illustrated below. The DP-RS-Sim method combines (1) the DP search (used in FORM and SORM), (2) the Response Surface (RS) method to approximate in analytical (polynomial) form the LSF near the DP, and (3) a simulation technique (Sim), to be applied on the response surface representation of the actual LSF.

The proposed method is suitable, with minor variations, for both component and system time-invariant reliability problems and for component mean out-crossing rate computations. The main steps of the DP-RS-Sim method for time-invariant component reliability analysis involving a LSS with a single DP are:

1. Search for the DP (step common to FORM, SORM and the MVPP method).
2. Computation of (few) PDs (step common to SORM with curvature fitting and the MVPP method).
3. Use of RS method to approximate analytically the LSF near the DP as the sum of a nonlinear part (in the few transformed variables defined by the DP vector and the computed PDs) and a linear part (in the remaining transformed variables and defined by the gradient at the DP). This step is unique to the proposed DP-RS-Sim method.
4. Estimate of the time-invariant failure probability using crude MCS or any other more advanced simulation technique (e.g., IS) applied on the analytical response surface approximation of the actual LSF.

In time-invariant system reliability analysis, the DP-RS-Sim method requires repeating the first three steps defined above for each of the components (LSFs) and applying the fourth step after forming a Boolean indicator which provides correspondence between failures of the single components and failure of the system. Time-invariant component reliability analysis with a LSS characterized by multiple DPs can be interpreted as a special case of a time-invariant system reliability problem, with the failure domain given by the union of the failure domains defined by the response surfaces approximating the original LSF in the neighbourhood of each of the DPs. Time-variant component reliability analysis is treated using the DP-RS-Sim method to compute the mean out-crossing rate with the limit relation in Eq. (7), in which the two LSSs $\{g(\mathbf{r}(\boldsymbol{\theta}, t), \boldsymbol{\theta}) = 0\}$ and $\{g(\mathbf{r}(\boldsymbol{\theta}, t + \delta t), \boldsymbol{\theta}) = 0\}$ are approximated at their DPs with the RS method.

The use of the DP-RS-Sim method in the case of a time-variant reliability problem is illustrated using the same MP SDOF system defined in Section 4.2 (with deterministic parameters) when subjected to white noise base excitation with power spectral density $\phi_0 = 0.25\ \mathrm{m^2/s^3}$ and displacement threshold $\xi = 0.048$ m (corresponding to the significantly nonlinear behaviour case in Section 4.2). Figures 11(a) and (b) provide visualization of the LSSs at times $t = 1.0$ s and $t + \delta t = 1.001$ s using the MVPP method in the first and second PPs, respectively. The traces of these two LSSs (obtained as the

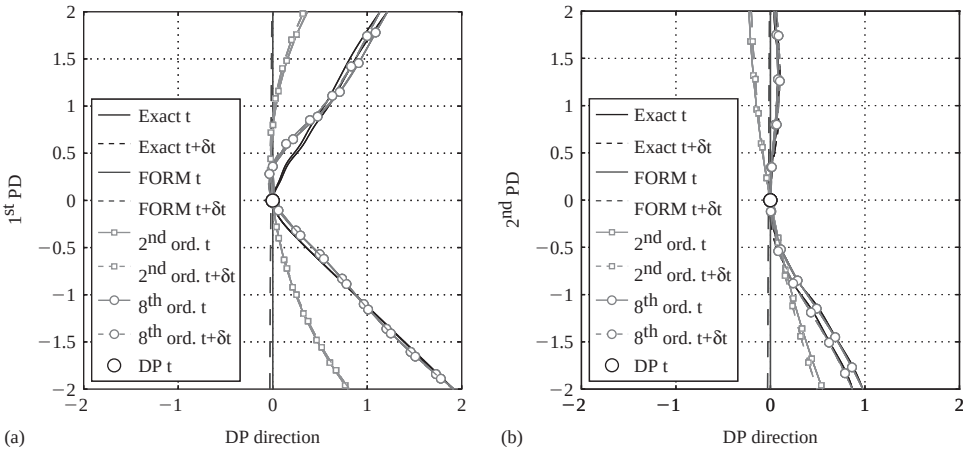

Figure 11 Visualization of LSS by the MVPP method and different response surface approximations for mean up-crossing rate computation at time t = 1.0 s for nonlinear hysteretic MP SDOF system: (a) 1st PP and (b) 2nd PP.

zero level contour lines of the LSF simulated over a fine grid of points in each PP) are compared with different response surface approximations, namely a 1st order (FORM), 2nd order and 8th order polynomial approximation. It is seen that the 8th order response surface approximates the actual LSSs fairly well in the first PP (Figure 11(a)) and very well in the second PP (Figure 11(b)).

The DP-RS-Sim method is applied to compute the time-variant failure probability (for T = 5.0 s) of the inelastic SDOF system defined above. The probability of failure is estimated by integrating numerically the mean out-crossing rate computed at given instants of time (t = 0.25 s, 0.5 s, 0.75 s, 1.0 s, 1.5 s, 2.0 s, 3.0 s, 4.0 s and 5.0 s). The Gaussian white noise excitation is discretized with dt = 0.01 s into 25, 50, 75, 100, 150, 200, 300, 400, and 500 random variables for these instants of time. Each of the LSFs is approximated with a response surface obtained as the sum of an 8th order polynomial in the four transformed variables defined by the DP vector and the first three principal directions and a 1st order polynomial in the remaining variables (i.e., hyperplane tangent to the LSS at the DP). The probability content of the hyper-wedge defined by the intersection of the two component failure domains, see Eq. (7), is estimated via IS with sampling distribution centred at the DP. Figure 12 compares the results obtained through crude MCS for the expected cumulative number of up-crossings, E[N], and the failure probability, P_f, with the upper bound approximation of the failure probability obtained through FORM and DP-RS-Sim. The results obtained show that the error due to the use of the analytical upper-bound to the probability of failure P_f is small, while the error due to the use of a FORM approximation to E[N] is very high (error = 266% at time t = 5.0 s). The DP-RS-Sim method reduces significantly the error by FORM, providing very good estimates of E[N] (error = 16% at time t = 5.0 s) with a reasonable additional computational cost compared to FORM.

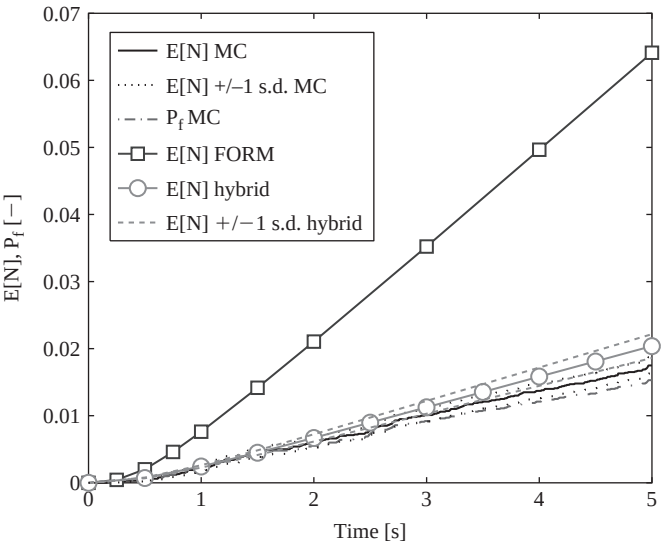

Figure 12 Time-variant reliability analysis of nonlinear hysteretic MP SDOF system: comparison of FORM and DP-RS-Sim (hybrid) method results with Monte Carlo (MC) simulation results.

5 Conclusions

This study presents recent advances in finite element (FE) response sensitivity, simplified probabilistic response and reliability analyses of structural and/or geotechnical systems. These developments are integrated into general-purpose frameworks for nonlinear FE response analysis. The objective is to extend the analytical tools used extensively by practicing engineers in order to propagate uncertainties through nonlinear static and dynamic analyses of actual structural and/or geotechnical systems to obtain probabilistic estimates of their predicted performance. Extensions of the Direct Differentiation Method (DDM) to nonlinear material FE models of structural and/or geotechnical systems are presented.

The mean-centred First-Order Second-Moment (FOSM) method is presented as simplified FE probabilistic response analysis method. The FOSM method is applied to probabilistic nonlinear pushover analysis of a structural system. It is found that a DDM-based FOSM analysis can provide, at low computational cost, estimates of first- and second-order FE response statistics which are in good agreement with significantly more expensive Monte Carlo simulation estimates when the frame structure considered in this study experiences low-to-moderate material nonlinearities.

Time-invariant and time-variant reliability analysis capabilities are also illustrated. The geometry of limit-state surfaces near the design point(s) (DPs) is explored in reduced-dimension spaces defined by planes of major principal curvatures at the DP, following a newly developed technique called Multidimensional Visualization in the Principal Planes. This new geometrical insight explains the lack of accuracy of FORM-based solutions in some cases and suggests the use of existing and development

of new improved solution strategies. In particular, a new hybrid reliability method referred to as the DP-RS-Sim method is presented and illustrated through an example of mean out-crossing rate computation for a nonlinear hysteretic single-degree-of-freedom system. The methodology presented in this work allows, in general, obtaining at reasonable computational cost FE reliability analysis results that are sufficiently accurate for engineering purposes.

Extension of the DP-RS-Sim method to nonlinear hysteretic multi-degree-of-freedom FE models of actual structural and/or geotechnical systems is currently under study by the authors.

Acknowledgements

Supports of this research by the Pacific Earthquake Engineering Research (PEER) Center through the Earthquake Engineering Research Centers Program of the National Science Foundation under Award No. EEC-9701568, the National Science Foundation under Grant No. CMS-0010112, and the main Italian Electricity Company (ENEL) are gratefully acknowledged. Any opinions, findings, conclusions, or recommendations expressed in this publication are those of the authors and do not necessarily reflect the views of the sponsors.

References

Au, S.K., Papadimitriou, C. & Beck, J.L. 1999. Reliability of uncertain dynamical systems with multiple design points. *Structural Safety*, 21(2), 113–133.

Barbato, M. & Conte, J.P. 2005. Finite element response sensitivity analysis: a comparison between force-based and displacement-based frame element models. *Computer Methods in Applied Mechanics and Engineering*, 194(12–16), 1479–1512.

Barbato, M. & Conte, J.P., 2006. Finite element structural response sensitivity and reliability analyses using smooth versus non-smooth material constitutive models. *International Journal of Reliability and Safety*, 1(1–2), 3–39.

Barbato, M., Gu, Q. & Conte, J.P. 2006. Response sensitivity and probabilistic response analyses of reinforced concrete frame structures. *Proceedings of the 8th NCEE, San Francisco, April 18–22*.

Barbato, M., Zona, A. & Conte, J.P. 2007. Finite element response sensitivity analysis using three-field mixed formulation: general theory and application to frame structures. *International Journal for Numerical Methods in Engineering*, 69(1), 114–161.

Belytschko, T., Liu, W.K. & Moran, B. 2000. *Nonlinear Finite Elements for Continua and Structures*. New York: Wiley.

Breitung, K. 1984. Asymptotic approximations for multinormal integrals. *Journal of the Engineering Mechanics Division* (ASCE), 110(3), 357–366.

Conte, J.P. 2001. Finite element response sensitivity analysis in earthquake engineering. In Spencer & Hu (eds), *Earthquake Engineering Frontiers in the New Millennium*, 395–401.

Conte, J.P., Vijalapura, P.K. & Meghella, M. 2003. Consistent finite-element response sensitivity analysis. *Journal of Engineering Mechanics* (ASCE), 129, 1380–1393.

Conte, J.P., Barbato, M. & Spacone, E. 2004. Finite element response sensitivity analysis using force-based frame models. *International Journal for Numerical Methods in Engineering*, 59, 1781–1820.

Dall'Asta, A. & Zona, A. 2004. Comparison and validation of displacement and mixed elements for the non-linear analysis of continuous composite beams. *Computers and Structures*, 82 (23–26), 2117–2130.

Der Kiureghian, A. & De Stefano, M. 1991. Efficient algorithms for second-order reliability analysis. *Journal of Engineering Mechanics* (ASCE), 117(12), 2904–2923.

Der Kiureghian, A. 1996. Structural reliability methods in seismic safety assessment: a review. *Journal of Engineering Structures*, 18(6), 412–424.

Ditlevsen, O. & Madsen, H.O. 1996. *Structural Reliability Methods*. New York: Wiley.

Gill, P.E., Murray, W. & Wright, M.H. 1981. *Practical Optimization*. London: Academic Press.

Gu, Q. & Conte, J.P. 2003. Convergence studies in non-linear finite element response sensitivity analysis. *Applications of Statistics and Probability in Civil Engineering, Proceedings of ICASP9, San Francisco, July 6–9*.

Gu, Q., Barbato, M. & Conte, J.P. 2008a. Handling of constraints in finite element response sensitivity analysis. *Journal of Engineering Mechanics*, (ASCE). Submitted for review.

Gu, Q., Conte, J.P., Yang, Z. & Elgamal, A. 2008b. Consistent tangent moduli for multi-yield-surface J_2 plasticity material model. *International Journal for Numerical Methods in Engineering*. Submitted for review.

Gu, Q., Conte, J.P., Yang, Z. & Elgamal, A. 2008c. Finite element response sensitivity analysis of multi-yield-surface J_2 plasticity model by direct differentiation method. *Computer Methods in Applied Mechanics and Engineering*. Submitted for review.

Haftka, R.T. & Gurdal, Z. 1993. *Elements of Structural Optimization*. Dordrecht: Kluver Academic Publishers.

Hagen, O. & Tvedt, L. 1991. Vector process out-crossing as parallel system sensitivity measure. *Journal of Engineering Mechanics* (ASCE), 117(10), 2201–2220.

Haukaas, T. & Der Kiureghian, A. 2004. Finite element reliability and sensitivity methods for performance-based engineering. *Report PEER 2003/14*, Pacific Earthquake Engineering Research Center, University of California, Berkeley.

Kleiber, M. & Hien, T.D. 1992. *The Stochastic Finite Element Method. Basic Perturbation Technique and Computer Implementation*. New York: Wiley.

Kleiber, M., Antunez, H., Hien, T.D. & Kowalczyk, P. 1997. *Parameter Sensitivity in Nonlinear Mechanics: Theory and Finite Element Computation*. New York: Wiley.

Liu, P.-L. & Der Kiureghian, A. 1991. Optimization algorithms for structural reliability. *Structural Safety*, 9(3), 161–177.

Lutes, L.D. & Sarkani, S. 1997. *Stochastic Analysis of Structural and Mechanical Vibrations*. Upper Saddle River: Prentice Hall.

Menegotto, M. & Pinto, P.E. 1973. Method for analysis of cyclically loaded reinforced concrete plane frames including changes in geometry and non-elastic behavior of elements under combined normal force and bending. *Proceedings, IABSE Symposium*, Lisbon.

Prevost, J.H. 1977. Mathematical modelling of monotonic and cyclic undrained clay behaviour. *International Journal for Numerical and Analytical Methods in Geomechanics*, 1(2), 195–216.

Spacone, E., Filippou, F.C. & Taucer, F.F. 1996. Fibre beam-column element for nonlinear analysis of R/C frames. Part I: formulation. *Earthquake Engineering and Structural Dynamics*, 25(7), 711–725.

Spacone, E. & El-Tawil, S. 2004. Nonlinear analysis of steel-concrete composite structures: state-of-the-art. *Journal of Structural Engineering*, 130(2), 159–168.

Scott, M.H., Franchin, P., Fenves, G.L. & Filippou, F.C. 2004. Response sensitivity for nonlinear beam-column elements. *Journal of Structural Engineering* (ASCE), 130(9), 1281–1288.

Washizu, K. 1975. *Variational methods in elasticity and plasticity*. Oxford: Pergamon Press.

Zona, A., Barbato, M. & Conte, J.P. 2005. Finite element response sensitivity analysis of steel-concrete composite beams with deformable shear connection. *Journal of Engineering Mechanics* (ASCE), 131(11):1126–1139.

Zona, A., Barbato, M. & Conte, J.P. 2006. Finite element response sensitivity analysis of continuous steel-concrete composite girders, *Steel and Composite Structures, an International Journal*, 6(3), 183–202.

Chapter 3

Energy-momentum algorithms for nonlinear solid dynamics and their assumed strain finite element formulation

Francisco Armero

University of California, Berkeley, USA

ABSTRACT: We present in this paper a new assumed strain finite element formulation (or B-bar method) for the locking-free simulation of nearly incompressible elastic and inelastic solids in the finite deformation dynamic range that also preserves the conservation/dissipation properties of the so-called energy-dissipative momentum-conserving (EDMC) time-stepping algorithms. The general setting of finite strain plasticity is considered, including hyperelastic models as a particular case. The main motivation of this work is to avoid the nonlinear numerical instabilities observed in classical numerical schemes with unbounded growth of the energy (even in the plastic case) by introducing the exact dissipation/conservation of the energy in the discrete system by design. The incorporation of the conservation laws of linear and angular momenta, and the preservation of the associated relative equilibria, is also obtained. The paper identifies the conditions that the linearized strain operator (or, simply, the B-bar operator as it is usually known) has to satisfy for the preservation of these properties in time. These conditions require the definition of the assumed strain operator, originally developed by with spatial considerations only, accounting for the temporal discretization in the definition of the associated strain variations. As a result, we arrive to a fully discrete system in space and time that shows exactly all these conservation/dissipation laws of the underlying physical system, including the exact plastic dissipation of the energy, with exact energy conservation for elastic steps. Numerical simulations are presented to illustrate the performance of the new formulation.

1 Introduction

Classical time-stepping algorithms, like the Newmark or HHT schemes, developed originally in the context of linear elastodynamics, are known to lead to severe numerical instabilities in the nonlinear finite deformation range, even for schemes that are unconditionally stable in the linear range; see e.g. Simo & Tarnow (1992); Armero & Romero (2001a), among others, or the results presented here. These instabilities are characterized by an unbounded growth of the energy, and have been observed even in the context of elastoplastic models (Meng & Laursen, 2002; Armero, 2006). This situation, and the lack of the conservation law of angular momentum in many of these classical schemes, has motivated a large amount of recent literature on the formulation

of the so-called energy-momentum schemes. These schemes inherit the conservation laws of energy and momenta of the underlying physical system by design.

We refer to Simo & Tarnow, (1992); Crisfield & Shi (1994); González (2000) for an illustration of energy-momentum methods in nonlinear elastic problems, and to Meng & Laursen (2002); Noels *et al.* (2004); Armero (2006); Armero & Zambrana-Rojas (2007) for formulations considering the elastoplastic range where the goal is to capture the exact plastic dissipation (with exact conservation for elastic steps) while still preserving the momentum conservation laws. Extensions of these methods to incorporate an additional controllable numerical energy dissipation in the high-frequency range in order to handle the characteristic numerical stiffness of typical mechanical and structural system of interest have been proposed in Armero & Romero (2001a, b); for nonlinear continuum elastodynamics and in Romero & Armero (2002); Armero & Romero (2003) in the context of rod and shell Cosserat models of nonlinear structural dynamics. We refer to these time-stepping algorithms as EDMC schemes (for **E**nergy-**D**issipative **M**omentum-**C**onserving). They include, as a particular case, some of the aforementioned energy-momentum schemes.

All these references consider the finite element method for the spatial discretization. The consideration of a nearly incompressible material response, like the one observed in plastically deforming metals and captured by classical elastoplastic models of J_2-flow theory, requires the consideration of finite element formulations more sophisticated than the basic displacement model to avoid the characteristic volumetric locking of this basic formulation. To this end, the so-called assumed strain approach, as developed originally by Nagtegaal *et al.* (1974); Hughes (1980) in the infinitesimal range and Simo *et al.* (1988); Armero (2000) in the finite deformation range (both for static problems), becomes very convenient as it only requires the proper definition of the numerical approximation of the strains and their variations regardless of the material model under consideration. In the continuum nearly incompressible context of interest here, these formulations are also known as "B-bar" methods.

B-bar methods that lead to locking-free finite elements in general configurations are well-known by now, including general linear and quadratic quadrilateral and triangular elements for two dimensional problems, and similarly in 3D. Unfortunately, their direct consideration in the dynamic range of interest here destroys completely the conservation/dissipation properties outlined above when used in combination of the aforementioned energy-momentum or EDMC schemes. These time-stepping algorithms rely on specific incremental properties of the linearized strain operator appearing in the equation of motion for a typical time step, properties that a straightforward evaluation of the B-bar operator, say at the mid-point, does not have. This situation can be traced back to the nonlinear definition of the assumed deformation gradient defining the assumed strain. For the incompressible limit of interest here, the assumed deformation gradient involves a nonlinear scaling with its determinant or Jacobian (another nonlinear operation) and the assumed Jacobian defined through a weighted average over the element.

All these considerations lead to the need of a new B-bar operator if the fundamental conservation laws of energy and momentum are to be preserved. The new operator needs to account not only for the discrete finite element interpolations in space, but also the discrete structure in time of the EDMC time-stepping algorithms, as presented in this paper.

2 The governing equations and their conservation laws

We consider a solid $\mathcal{B} \subset \mathbb{R}^{n_{\text{dim}}}$ ($n_{\text{dim}} = 1, 2$ or 3) and its motions $\boldsymbol{\varphi}(\boldsymbol{X}, t)$ in time t for the material particles $\boldsymbol{X} \in \mathcal{B}$, which satisfy the weak equation

$$\int_{\mathcal{B}} \rho_o \ddot{\boldsymbol{\varphi}} \cdot \delta\varphi \, dV + \int_{\mathcal{B}} \boldsymbol{S} : \underbrace{(\boldsymbol{F}^T \text{GRAD}[\delta\varphi])^s}_{=: \frac{1}{2}\delta \boldsymbol{C}(\boldsymbol{\varphi}, \delta\varphi)} \, dV = \int_{\mathcal{B}} \rho_o \boldsymbol{b} \cdot \delta\varphi \, dV + \int_{\mathcal{B}} \overline{\boldsymbol{T}} \cdot \delta\varphi \, dA, \quad (1)$$

for all admissible variations $\delta\varphi$, that is, $\delta\varphi = 0$ on the part of boundary $\partial_{\boldsymbol{\varphi}}\mathcal{B}$ with imposed deformation $\boldsymbol{\varphi} = \overline{\boldsymbol{\varphi}}$, complementary to the part of the boundary $\partial_t\mathcal{B}$ in (1) where the tractions $\overline{\boldsymbol{T}}$ are imposed. We have introduced in (1) the reference density of the solid ρ_o, the acceleration $\ddot{\boldsymbol{\varphi}} = \partial^2\boldsymbol{\varphi}/\partial t^2$, the specific body force $\boldsymbol{b}$ and the second Piola-Kirchhoff stress tensor $\boldsymbol{S}$, a symmetric tensor in the reference configuration $\mathcal{B}$ of the solid. We observe the appearance of the conjugate variations $\delta\boldsymbol{C}/2$ of the right Cauchy-Green tensor $\boldsymbol{C} = \boldsymbol{F}^T\boldsymbol{F}$ for the deformation gradient $\boldsymbol{F} = \text{GRAD}[\boldsymbol{\varphi}]$.

The particular form of the governing equation (1) leads to a number of physical conservation laws, very characteristic of the motions of solids and structures. In particular, denoting the velocity field by $\boldsymbol{V} = \dot{\boldsymbol{\varphi}}$, we easily obtain for the case of a free solid for brevity (i.e. for $\boldsymbol{b} = 0$, $\overline{\boldsymbol{T}} = 0$ and $\partial_{\boldsymbol{\varphi}}\mathcal{B} = \emptyset$) the conservation laws

$$\boldsymbol{l} := \int_{\mathcal{B}} \rho_o \boldsymbol{V} \, dV = \textit{constant} \quad \text{and} \quad \boldsymbol{j} := \int_{\mathcal{B}} \boldsymbol{\varphi} \times \rho_o \boldsymbol{V} \, dV = \textit{constant}, \quad (2)$$

corresponding to the linear and angular momentum, respectively, after using the crucial properties

$$\delta\boldsymbol{C}(\boldsymbol{\varphi}, \boldsymbol{c}) = 0 \quad \text{and} \quad \delta\boldsymbol{C}(\boldsymbol{\varphi}, \boldsymbol{c} \times \boldsymbol{\varphi}) = 0, \quad (3)$$

for all constant vector fields $\boldsymbol{c} \in \mathbb{R}^{n_{\text{dim}}}$. The relations (3) correspond to the infinitesimal generators of the action of the Euclidean group $\mathbb{R}^{n_{\text{dim}}} \times SO(n_{\text{dim}})$ associated with the symmetry of the governing equations (1) under translations and rotations, respectively; see e.g. Marsden (1992). This leads to the existence of special (dynamic) equilibrium solutions given by the group motion

$$\boldsymbol{\varphi}_{et}(\boldsymbol{X}, t) = \text{EXP}[t \ \text{SPIN}[\boldsymbol{\Omega}_e]] \, \boldsymbol{\varphi}_e(\boldsymbol{X}) + \left(\int_O^t \text{EXP}[\eta \ \text{SPIN}[\boldsymbol{\Omega}_e]] \, d\eta \right) \boldsymbol{V}_e, \quad (4)$$

in terms of two fixed vectors $\boldsymbol{\Omega}_e$ and $\boldsymbol{V}_e$, the angular and translational velocities, respectively, and the relative equilibrium configuration $\boldsymbol{\varphi}_e(\boldsymbol{X})$ satisfying the equilibrium equation

$$\int_{\mathcal{B}} \rho_o \boldsymbol{\Omega}_e \times [\boldsymbol{\Omega}_e \times \boldsymbol{\varphi}_e + \boldsymbol{V}_e] \cdot \delta\boldsymbol{\varphi} \, dV + \int_{\mathcal{B}} \boldsymbol{S}(\boldsymbol{\varphi}_e) : \boldsymbol{F}_e^T \text{GRAD}[\delta\boldsymbol{\varphi}] \, dV = 0, \quad (5)$$

again for all admissible variations $\delta\varphi$; see Simo *et al.* (1991). The existence of these relative equilibria relies again on the critical property of the strain variations

$$\delta\boldsymbol{C}(\boldsymbol{\varphi}_{et}, \delta\varphi) = \delta\boldsymbol{C}(\boldsymbol{\varphi}_e, \text{EXP}[-t \ \text{SPIN}[\boldsymbol{\Omega}_e]] \, \delta\varphi), \quad (6)$$

along the group motion $\boldsymbol{\varphi}_{et}(\boldsymbol{X}, t)$ in (4). Here, SPIN$[\boldsymbol{\Omega}_e]$ denotes the skew tensor with axial vector $\boldsymbol{\Omega}_e$, and EXP[SPIN$[\boldsymbol{\Omega}_e]$] the rotation defined by the exponential map between skew and rotation tensors.

Finally, we note that we always have the relation

$$\frac{d}{dt}\underbrace{\left[\int_{\mathcal{B}}\left[\frac{1}{2}\rho_o\|\mathbf{V}\|^2 + W\right] dV\right]}_{=:H} = -\int_{\mathcal{B}} \mathcal{D}\, dV \quad \text{for } \mathcal{D} = \boldsymbol{S} : \frac{1}{2}\dot{\boldsymbol{C}} - \dot{W}, \tag{7}$$

for a general function W. Crucial again for obtaining the stress power in (7) is the relation

$$\delta \boldsymbol{C}(\boldsymbol{\varphi}, \dot{\boldsymbol{\varphi}}) = \dot{\boldsymbol{C}}, \tag{8}$$

for the strain variations. The interest here is the consideration of material models with W corresponding to the (internal) stored energy (H being the total energy with the kinetic energy) and $\mathcal{D}$ the energy dissipation, a non-negative quantity by the second law of thermodynamics.

In particular, we are interested in the case of finite strain plasticity characterized by the multiplicative decomposition $\boldsymbol{F} = \boldsymbol{F}^e\boldsymbol{F}^p$ of the deformation gradient in an elastic and plastic part; see Armero (2006) and references therein. The stresses are then given in terms of an elastic potential $W^e(\boldsymbol{C}^e)$ for $\boldsymbol{C}^e = \boldsymbol{F}^{e^T}\boldsymbol{F}^e$ as

$$\widetilde{\boldsymbol{S}} = \boldsymbol{F}^p\boldsymbol{S}\boldsymbol{F}^{p^T} = 2\frac{\partial W^e}{\partial \boldsymbol{C}^e}, \tag{9}$$

with the plastic part $\boldsymbol{F}^p$ defined by the plastic evolution equations ($\boldsymbol{L}^p = \dot{\boldsymbol{F}}^p\boldsymbol{F}^{p^{-1}}$)

$$\boldsymbol{D}^p := \operatorname{sym}\left[\boldsymbol{C}^e\boldsymbol{L}^p\right] = \boldsymbol{F}^{p^{-T}}\dot{\boldsymbol{C}}\boldsymbol{F}^{p^{-1}} - \dot{\boldsymbol{C}}^e = \gamma \mathbf{N}_\phi(\widetilde{\boldsymbol{S}}, q), \tag{10}$$

$$\boldsymbol{W}^p := \operatorname{skew}\left[\boldsymbol{C}^e\boldsymbol{L}^p\right] = \gamma \boldsymbol{M}_{\mathbb{W}^p}(\widetilde{\boldsymbol{S}}, q), \tag{11}$$

$$\dot{\alpha} = \gamma n_\phi(\widetilde{\boldsymbol{S}}, q), \tag{12}$$

$$\phi(\widetilde{\boldsymbol{S}}, q) \le 0, \quad \gamma \ge 0, \quad \gamma\phi = 0 \quad \text{and} \quad \gamma\dot{\phi} = 0, \tag{13}$$

for the yield surface $\phi(\widetilde{\boldsymbol{S}}, q)$ characterizing the elastic domain in stress space. We have considered isotropic hardening, modeled by the equivalent plastic strain α and the conjugate stress-like variable $q := -\partial\mathcal{H}/\partial\alpha$ for a hardening potential $\mathcal{H}(\alpha)$. In this setting, the internal energy $W = W^e + \mathcal{H}$ with the plastic dissipation given by $\mathcal{D} = \widetilde{\boldsymbol{S}} : \boldsymbol{D}^p + q\dot{\alpha}$. The hyperelastic case is recovered for a fixed $\boldsymbol{F}^p$, which is the case assumed for the relative equilibria (5) (i.e. vanishing of the plastic evolution or $\gamma = 0$ in (10)–(13)).

3 EDMC time-stepping algorithms

The numerical solution of the governing equations (1) proceeds with the consideration of their spatial and temporal discretizations. The spatial discretization of interest here

starts with the finite element discretizations of the deformation and velocity fields

$$\boldsymbol{\varphi}(\boldsymbol{X}, t_{n+i}) \approx \boldsymbol{\varphi}^h_{n+i}(\boldsymbol{X}) = \sum_{A=1}^{n_{node}} N^A(\boldsymbol{X}) \underbrace{\left(\boldsymbol{X}^A + \boldsymbol{d}^A_{n+i}\right)}_{=:\boldsymbol{x}^A_{n+i}}, \tag{14}$$

and

$$\boldsymbol{V}(\boldsymbol{X}, t_{n+i}) \approx \boldsymbol{V}^h_{n+i}(\boldsymbol{X}) = \sum_{A=1}^{n_{node}} N^A(\boldsymbol{X}) \boldsymbol{v}^A_{n+i}, \tag{15}$$

with $i = 0$, or 1, and for the shape functions $N^A(\boldsymbol{X})$ associated to the n_{node} nodes with nodal (reference) coordinates $\boldsymbol{X}^A$, displacements $\boldsymbol{d}_{n+i}$ and velocities $\boldsymbol{v}_{n+i}$ in a typical time step $[t_n, t_{n+1}]$ with $\Delta t = t_{n+1} - t_n$, not necessarily constant.

Using standard procedures, together with a one-step mid-point interpolation in time $\left(\boldsymbol{v}_{n+\frac{1}{2}} := (\boldsymbol{v}_n + \boldsymbol{v}_{n+1})/2\right)$, we obtain the discrete algebraic system of equations

$$\frac{1}{\Delta t}\boldsymbol{M}(\boldsymbol{v}_{n+1} - \boldsymbol{v}_n) + \int_{\mathcal{B}^h} \overline{\boldsymbol{B}}^T_* \boldsymbol{S}_* \, dV = \boldsymbol{f}_{ext}, \tag{16}$$

$$\boldsymbol{d}_{n+1} - \boldsymbol{d}_n = \Delta t \boldsymbol{v}_{n+\frac{1}{2}}, \tag{17}$$

for a (symmetric) stress approximation $\boldsymbol{S}_*$ to be defined. Here, we have introduced the standard nodal external force $\boldsymbol{f}_{ext}$ and the mass matrix $\boldsymbol{M}$ defined as usual by the assembly of element contributions $\boldsymbol{M} = \mathbf{A}_{e=1}^{n_{elem}} M_e^{AB} \mathbf{1}$ with

$$M_e^{AB} = \int_{\mathcal{B}^h_e} \rho_o N^A N^B \, dV, \quad \text{or} \quad M^{AB} = \int_{\mathcal{B}^h_e} \rho_o N^A \, dV \, \delta_{AB} \text{ (no sum)}, \tag{18}$$

for the consistent or lump forms of the mass. We have also considered an assumed linearized strain operator $\overline{\boldsymbol{B}}_*$ (or, simply, the B-bar operator) defined by the relations

$$\frac{1}{2}\delta \mathbf{C} \approx \frac{1}{2}\delta \overline{\mathbf{C}} \approx \overline{\boldsymbol{B}}_* \delta \boldsymbol{d}, \tag{19}$$

for the nodal variations $\delta \boldsymbol{d}$. Note the approximate signs in this equation, indicating numerically consistent approximations (in fact, second order approximations of the mid-point values). In particular, the stresses are assumed to be given in terms of the assumed strains $\overline{\mathbf{C}} = \overline{\boldsymbol{F}}^T \overline{\boldsymbol{F}}$ for an assumed deformation gradient $\overline{\boldsymbol{F}} \approx \text{GRAD}[\boldsymbol{\varphi}^h]$ as considered in the following section.

The goal is the development of numerical approximations that preserve the conservation/dissipation laws of energy and momenta identified in the previous section for the problem at hand, the so-called EDMC schemes. The conservation laws of linear and angular momenta, defined in this discrete setting

$$\boldsymbol{l}^h_{n+i} = \sum_{A,B=1}^{n_{node}} M^{AB} \boldsymbol{v}^B_{n+i} \quad \text{and} \quad \boldsymbol{j}^h_{n+i} = \sum_{A,B=1}^{n_{node}} M^{AB} \boldsymbol{x}^A_{n+i} \times \boldsymbol{v}^B_{n+i}, \tag{20}$$

(i.e. $\boldsymbol{l}^h_{n+1} = \boldsymbol{l}^h_n$ and $\boldsymbol{j}^h_{n+1} = \boldsymbol{j}^h_n$ for $\boldsymbol{f}_{ext} = 0$), follow easily from the considered mid-point approximation (17), as long as the B-bar operator satisfies the relations

$$\overline{\boldsymbol{B}}_* \widehat{\mathbf{c}} = 0 \quad \text{and} \quad \overline{\boldsymbol{B}}_* \Big(\widehat{c \times \boldsymbol{x}_{n+\frac{1}{2}}} \Big) = 0, \tag{21}$$

for a constant vector $\mathbf{c} \in \mathbb{R}^{n_{\text{dim}}}$ (here, $\widehat{(\cdot)}$ denotes the global vector of nodal values given by $(\cdot)$). We observe that the conditions (21) are the discrete counterparts of the relations (3) for the continuum problem.

The group motion associated to the relative equilibria of the discrete equations (16)–(17) were obtained in Armero & Romero (2001a) and are given by

$$\boldsymbol{x}^A_{en} = \boldsymbol{\Lambda}_n \boldsymbol{\varphi}^{bA}_e + \boldsymbol{u}_n \quad \text{and} \quad \boldsymbol{v}^A_{en} = \boldsymbol{\Lambda}_n [\boldsymbol{\Omega}_e \times \boldsymbol{\varphi}^{bA}_e + \boldsymbol{V}_e], \tag{22}$$

for fixed vectors $\boldsymbol{\Omega}_e$ and $\boldsymbol{V}_e$, and a sequence of rotations $\{\boldsymbol{\Lambda}_n\}$ and displacements $\{\boldsymbol{u}_n\}$ defined recursively by the relations

$$\boldsymbol{\Lambda}_{n+1} = \boldsymbol{\Lambda}_n \text{CAY}[\Delta t \ \text{SPIN}[\boldsymbol{\Omega}_e]] \quad \text{and} \quad \boldsymbol{u}_{n+1} = \boldsymbol{u}_n + \Delta t \ \boldsymbol{\Lambda}_{n+\frac{1}{2}} \boldsymbol{V}_e, \tag{23}$$

for $\boldsymbol{\Lambda}_{n+\frac{1}{2}} := (\boldsymbol{\Lambda}_n + \boldsymbol{\Lambda}_{n+1})/2$ (not a rotation in general) and the Cayley transform

$$\text{CAY}[\Delta t \ \text{SPIN}[\boldsymbol{\Omega}_e]] := \left[\mathbf{1} + \frac{\Delta t}{2} \text{SPIN}[\boldsymbol{\Omega}_e] \right] \left[\mathbf{1} - \frac{\Delta t}{2} \text{SPIN}[\boldsymbol{\Omega}_e] \right]^{-1} \in SO(n_{\text{dim}}), \tag{24}$$

for the discrete relative equilibrium configuration $\boldsymbol{\varphi}^b_e$ given by the equation

$$\boldsymbol{M} \Big(\boldsymbol{\Omega}_e \times (\widehat{\boldsymbol{\Omega}_e \times \boldsymbol{\varphi}^b_e} + \boldsymbol{v}_e) \Big) + \int_{\mathcal{B}^b} \overline{\boldsymbol{B}}^T_e \boldsymbol{S}(\boldsymbol{\varphi}^b_e) \, dV = 0, \tag{25}$$

as long as the condition

$$\overline{\boldsymbol{B}}_{*e} = \overline{\boldsymbol{B}}_e \boldsymbol{\Lambda}^T_{n+\frac{1}{2}}, \tag{26}$$

is satisfied along the group motion (22). We observe that equation (25) is the discrete counterpart of the equilibrium equation (5). Thus the algorithm preserves the relative equilibria of the system as long as the B-bar operator satisfies condition (26), the counterpart of relation (6).

Finally, the counterpart of the energy conservation/dissipation equation (7) is obtained as

$$H_{n+1} - H_n = -\int_{\mathcal{B}} \Delta \mathcal{D} \, dV \quad \text{for} \ \ \Delta \mathcal{D} = \boldsymbol{S} : \frac{1}{2} \Delta \overline{\mathbf{C}} - \Delta W, \tag{27}$$

and

$$H_{n+i} = \frac{1}{2} v_{n+i} \cdot \mathbf{M} v_{n+i} + \int_{\mathcal{B}^h_e} W_{n+i} \, dV \quad i = 0 \text{ or } 1, \tag{28}$$

for the discrete system (16)–(17), as long as we have the relation

$$\overline{B}_*(d_{n+1} - d_n) = \frac{1}{2}\Delta\overline{C}, \tag{29}$$

for the B-bar operator $\overline{B}_*$ and the increment of the assumed strain $\Delta\overline{C}/2$.

Clearly, the interest here lies in the discrete dissipation (27) reproducing exactly the dissipation of the continuum system. For the elastoplastic model (10)–(13), this can be accomplished by considering the elastoplastic decomposition of the assumed deformation gradient $\overline{F} = F^e F^p$ (see Section 4.1 below) and the discrete equations

$$\frac{1}{2}\left([F^p]^{-T}_{n+\frac{1}{2}}\Delta\overline{C}[F^p]^{-1}_{n+\frac{1}{2}} - \Delta C^e\right) = \Delta\gamma\, N_\phi(\widetilde{S}_*, q_*), \tag{30}$$

$$\text{skew}\left[[C^e]_{n+\frac{1}{2}}(F^p_{n+1} - F^p_n)[F^p]^{-T}_{n+\frac{1}{2}}\right] = \Delta\gamma\, M_{W^p}(\widetilde{S}_*, q_*), \tag{31}$$

$$\phi_* := \phi(\widetilde{S}_*, q_*) \leq 0, \quad \Delta\gamma \geq 0, \quad \Delta\gamma\phi_* = 0, \tag{32}$$

as proposed in Armero (2006), with $q_* = -\Delta\mathcal{H}/\Delta\alpha$ and the stresses given by $S_* = F^p_{n+\frac{1}{2}}\widetilde{S}_* F^{p^T}_{n+\frac{1}{2}}$ with

$$\begin{aligned} S_* = {} & 2\frac{\partial W}{\partial C^e}\left([C^e]_{n+\frac{1}{2}}\right) \\ & + 2\frac{W(C^e_{n+1}) - W(C_n) - 2\dfrac{\partial W}{\partial C^e}\left([C^e]_{n+\frac{1}{2}}\right)\colon \Delta C^e}{[C^e]^{-1}_{n+\frac{1}{2}}\Delta C^e\colon \Delta\overline{C}^e\ [C^e]^{-1}_{n+\frac{1}{2}}}[C^e]^{-1}_{n+\frac{1}{2}}\Delta C^e[C^e]^{-1}_{n+\frac{1}{2}}. \end{aligned} \tag{33}$$

Here we have introduced the notation $[(\cdot)]_{n+\frac{1}{2}} = ((\cdot)_n + (\cdot)_{n+1})/2$. The formula (33) corresponds to a conserving approximation of the gradient formula (9) such that $\widetilde{S}\colon \frac{1}{2}\Delta C^e = \Delta W^e$. It is a modification of the the original conserving formula proposed in González (2000) by including the elastic metric $[C^e]^{-1}_{n+\frac{1}{2}}$, as it will become crucial in the construction of the assumed B-bar operator in the following section. Again, the exact plastic dissipation (including exact energy conservation for an elastic step) is obtained by the return mapping algorithm (30)–(32) and the stress formula (33). This situation adds the desired numerical stability to the algorithms as illustrated with the numerical simulation presented in Section (5).

A variation of the return mapping algorithm (30)–(32) that also imposes exactly the isochoric plastic response in isochoric plastic models, like the classical J_2-flow theory of metals, can be found in Armero & Zambrana-Rojas, (2007). Similarly, we refer to Armero & Romero (2001a, b) for variations of the stress formula (33) that incorporate a controllable high-frequency numerical energy dissipation to handle the usual high numerical stiffness in the systems of interest.

4 Conserving assumed strain finite element methods

4.1 *The assumed deformation gradient and its variations*

The interest here is the development of assumed strain finite element methods for the locking-free approximation of nearly incompressible material models, like the plasticity models outlined above combined with a Mises-type deviatoric yield surface, while exhibiting the conservation/dissipation laws obtained in the previous section. This can be accomplished with the now standard scaled deformation gradient (see e.g. Armero 2000; Simo *et al.*, 1988)

$$\overline{F}_{n+i} = \left(\frac{\Theta_{n+i}}{J_{n+i}}\right)^{\frac{1}{3}} \text{Grad}\,[\boldsymbol{\varphi}^h_{n+i}] \quad \text{for } J_{n+i} := \det\left[\text{Grad}\,[\boldsymbol{\varphi}^h_{n+i}]\right], \tag{34}$$

(for $i = 0$, or 1) and the assumed Jacobian $\Theta = \det[\overline{F}]$ defined by the weighted average at the element level

$$\Theta_{n+i}(X) := \boldsymbol{\Gamma}^T(X) H^{-1} \int_{\mathcal{B}^h_e} \boldsymbol{\Gamma}(Y) J_{n+i}(Y)\, dV, \tag{35}$$

for a set of n_θ element interpolation functions $\boldsymbol{\Gamma}(X)$ and the corresponding matrix

$$\boldsymbol{H} := \int_{\mathcal{B}^h_e} \boldsymbol{\Gamma}(Y) \boldsymbol{\Gamma}^T(Y)\, dV \in \mathbb{R}^{n_\theta \times n_\theta}, \tag{36}$$

over a generic element $\mathcal{B}^h_e$. Typical choices are $n_\theta = 1$ and $\boldsymbol{\Gamma} = 1$ in combination with a bilinear quadrilateral or trilinear brick element (Q1/A0), and $n_\theta = 3$ with $\boldsymbol{\Gamma} = [1\ \xi\ \eta]^T$ for the isoparametric coordinates (ξ, η) in plane problems (and similarly for 3D) in combination with quadratic quadrilateral or triangular elements (Q2/A1 or P2/A1).

The consideration of the assumed right Cauchy-Green tensor $\overline{C}_{n+i} = \overline{F}^T_{n+i} \overline{F}_{n+i}$ leads to the variations $\delta \overline{C}_{n+i}/2 = \overline{B}_{n+i} \delta d_{n+i}$ for

$$\overline{B}^A_{n+i} = \left(\frac{\Theta_{n+i}}{J_{n+i}}\right)^{\frac{2}{3}} \left[B^A_{n+i} + \frac{1}{3} C(\boldsymbol{\varphi}^h_{n+i}) \otimes (\overline{g}^A_{n+i} - g^A_{n+i})\right], \tag{37}$$

defining the classical B-bar operator $\overline{B}_{n+i}$ in terms of the standard (displacement) linearized strain operator

$$B^A_{n+i} := \begin{bmatrix} (\boldsymbol{\varphi}^h_{n+i})^T_{,1}\, N^A_{,1} \\ (\boldsymbol{\varphi}^h_{n+i})^T_{,2}\, N^A_{,2} \\ (\boldsymbol{\varphi}^h_{n+i})^T_{,1}\, N^A_{,2} + (\boldsymbol{\varphi}^h_{n+i})^T_{,2}\, N^A_{,1} \end{bmatrix} \quad \text{for } A = 1, n_{node}, \tag{38}$$

for plane problems (similarly for 3D), and the spatial gradients

$$\boldsymbol{g}^A_{n+i} := \boldsymbol{F}^{-T}_{n+i} \boldsymbol{G}^A \quad \text{and} \quad \overline{\boldsymbol{g}}^A_{n+i} := \boldsymbol{\Gamma}^T H^{-1} \int_{\mathcal{B}^h_e} \boldsymbol{\Gamma}\, \boldsymbol{g}^A_{n+i}\, dV, \tag{39}$$

for the material gradients $\boldsymbol{G}^A := \text{GRAD}[N^A] = [N^A_{,1}\ N^A_{,2}]^T$ $(A = 1, n_{node})$ as used in (38). Here we consider $i = 0$, 1/2 or 1, with $i = 1/2$ corresponding to the evaluation of the different quantities above in the mid-point configuration $\boldsymbol{\varphi}^h_{n+\frac{1}{2}} = (\boldsymbol{\varphi}^h_n + \boldsymbol{\varphi}^h_{n+1})/2$.

The standard choice $\overline{\boldsymbol{B}}_{n+\frac{1}{2}}$ in the governing equation (16) does not lead, however, to a conserving approximation. The conditions (21) can be easily seen to be satisfied, but the conditions (26) and (29) for the conservation of the relative equilibria and energy are not. This situation is to be traced to the spatial gradients $\boldsymbol{g}^A_{n+\frac{1}{2}}$ in (39). First, we observe that during the group motion (22) we have $\boldsymbol{F}_n = \boldsymbol{\Lambda}_n \boldsymbol{F}_e$ and $\boldsymbol{F}_{n+1} = \boldsymbol{\Lambda}_{n+1} \boldsymbol{F}_e$ for the equilibrium deformation gradient $\boldsymbol{F}_e$, but

$$\boldsymbol{g}^A_{n+\frac{1}{2}} = \boldsymbol{\Lambda}^{-T}_{n+\frac{1}{2}} \underbrace{\boldsymbol{F}_e^{-T} \boldsymbol{G}^A}_{=:\boldsymbol{g}^A_e} = \boldsymbol{\Lambda}^{-T}_{n+\frac{1}{2}} \boldsymbol{g}^A_e \neq \boldsymbol{\Lambda}_{n+\frac{1}{2}} \boldsymbol{g}^A_e, \tag{40}$$

as required for (26), since $\boldsymbol{\Lambda}_{n+\frac{1}{2}} = (\boldsymbol{\Lambda}_n + \boldsymbol{\Lambda}_{n+1})/2$ is not a rotation in general. Similarly, the condition (29) is not satisfied, in part because

$$\sum_{A=1}^{n_{node}} \boldsymbol{g}^A_{n+\frac{1}{2}} \cdot (\boldsymbol{d}^A_{n+1} - \boldsymbol{d}^A_n) \neq \frac{(J_{n+1} - J_n)}{[J]_{n+\frac{1}{2}}}, \tag{41}$$

for $[J]_{n+\frac{1}{2}} = (J_n + J_{n+1})/2$, as it would be expected from its continuum counterpart $(\dot{J} = J\ \nabla \boldsymbol{v} : \boldsymbol{1}$ for the spatial velocity gradient $\nabla \boldsymbol{v})$.

4.2 *A new conserving B-bar operator*

Faced with the difficulties observed in the previous section, we introduce the new modified spatial gradients

$$\widehat{\boldsymbol{g}}^A_{n+\frac{1}{2}} := \boldsymbol{F}_{n+\frac{1}{2}} [\boldsymbol{C}]^{-1}_{n+\frac{1}{2}} \boldsymbol{G}^A + 2 \frac{\dfrac{J_{n+1} - J_n}{[J]_{n+\frac{1}{2}}} - \frac{1}{2} [\boldsymbol{C}]^{-1}_{n+\frac{1}{2}} : \Delta \boldsymbol{C}}{[\boldsymbol{C}]^{-1}_{n+\frac{1}{2}} \Delta \boldsymbol{C} : \Delta \boldsymbol{C} [\boldsymbol{C}]^{-1}_{n+\frac{1}{2}}} \boldsymbol{F}_{n+\frac{1}{2}} [\boldsymbol{C}]^{-1}_{n+\frac{1}{2}} \Delta \boldsymbol{C} [\boldsymbol{C}]^{-1}_{n+\frac{1}{2}} \boldsymbol{G}^A, \tag{42}$$

for $A = 1, n_{node}$, and their assumed counterparts

$$\overline{\widehat{\boldsymbol{g}}}^A_{n+\frac{1}{2}} = \frac{1}{[\Theta]_{n+\frac{1}{2}}} \boldsymbol{\Gamma}^T \boldsymbol{H}^{-1} \int_{\mathcal{B}^h_e} \boldsymbol{\Gamma}\, [J]_{n+\frac{1}{2}} \widehat{\boldsymbol{g}}^A_{n+\frac{1}{2}}\, dV, \tag{43}$$

where we note the use of the average Jacobian $[J]_{n+\frac{1}{2}} = (J_n + J_{n+1})/2$. We observe that these modified spatial gradients do satisfy, by construction, the relations

$$\sum_{A=1}^{n_{node}} \widehat{\boldsymbol{g}}^A_{n+\frac{1}{2}} \cdot (\boldsymbol{d}^A_{n+1} - \boldsymbol{d}^A_n) = \frac{J_{n+1} - J_n}{[J]_{n+\frac{1}{2}}} \quad \text{and} \quad \sum_{A=1}^{n_{node}} \overline{\widehat{\boldsymbol{g}}}^A_{n+\frac{1}{2}} \cdot (\boldsymbol{d}^A_{n+1} - \boldsymbol{d}^A_n) = \frac{\Theta_{n+1} - \Theta_n}{[\Theta]_{n+\frac{1}{2}}}, \tag{44}$$

and

$$\widehat{\boldsymbol{g}}^{A}_{n+\frac{1}{2}} = \boldsymbol{\Lambda}_{n+\frac{1}{2}} \boldsymbol{g}^{A}_{e} \quad \text{and} \quad \widehat{\overline{\boldsymbol{g}}}^{A}_{n+\frac{1}{2}} = \boldsymbol{\Lambda}_{n+\frac{1}{2}} \overline{\boldsymbol{g}}^{A}_{e}, \tag{45}$$

along the group motion (22), all for $A = 1, n_{node}$. We can observe the similarities with the stress formula (33) and, in particular, the use of the reference (convected) metric $[\boldsymbol{C}]_{n+\frac{1}{2}}$ to arrive at the proper transformation properties for the modified spatial gradients.

With these definitions at hand, we introduce the following new B-bar operator

$$\begin{aligned} \overline{\boldsymbol{B}}^{A}_{*} = & \left[\Theta^{\frac{2}{3}}\right]_{n+\frac{1}{2}} \left[J^{-\frac{2}{3}}\right]_{n+\frac{1}{2}} \boldsymbol{B}^{A}_{n+\frac{1}{2}} + \tfrac{1}{2} \left[\Theta^{\frac{2}{3}}\right]_{n+\frac{1}{2}} D_{J}^{\left(-\frac{2}{3}\right)} [\boldsymbol{C}]_{n+\frac{1}{2}} \otimes \widehat{\boldsymbol{g}}^{A}_{n+\frac{1}{2}} \\ & + \tfrac{1}{2} D_{\theta}^{\left(\frac{2}{3}\right)} \left[J^{-\frac{2}{3}} \boldsymbol{C}\right]_{n+\frac{1}{2}} \otimes \widehat{\overline{\boldsymbol{g}}}^{A}_{n+\frac{1}{2}}, \end{aligned} \tag{46}$$

for $A = 1, n_{node}$ where

$$D^{(a)}_{(\cdot)} := \begin{cases} [(\cdot)]_{n+\frac{1}{2}} \dfrac{((\cdot)_{n+1})^{a} - ((\cdot)_{n})^{a}}{(\cdot)_{n+1} - (\cdot)_{n}} & \text{for } (\cdot)_{n+1} \neq (\cdot)_{n}, \\ a \left([(\cdot)]_{n+\frac{1}{2}}\right)^{a} & \text{for } (\cdot)_{n+1} = (\cdot)_{n}, \end{cases} \tag{47}$$

for a generic quantity $(\cdot)$ and exponent a. By the way, we note that the formulas (33) and (42) are well-defined, with the quotients vanishing when $\boldsymbol{C}^{e}_{n+1} = \boldsymbol{C}^{e}_{n}$ and $\boldsymbol{C}_{n+1} = \boldsymbol{C}_{n}$, respectively. No singularity occurs.

The different terms in the expression (46) can be seen to be second-order approximation of the variations of the assumed $\overline{\boldsymbol{C}}$. Some long algebraic manipulations show that this new B-bar operator satisfies the desired conditions (21), (26) and (29). In particular, the relation (26) for the relative equilibria is satisfied for the assumed B-bar operator

$$\overline{\boldsymbol{B}}^{A}_{e} = \left(\frac{\Theta_{e}}{J_{e}}\right)^{\frac{2}{3}} \left[\boldsymbol{B}^{A}_{e} + \frac{1}{3} \boldsymbol{C}_{e} \otimes \left(\overline{\boldsymbol{g}}^{A}_{e} - \boldsymbol{g}^{A}_{e}\right)\right] \quad \text{for } A = 1, n_{node}, \tag{48}$$

at the equilibrium configuration $\boldsymbol{\varphi}^{h}_{e}$. Hence, the new B-bar operator (46) leads to a fully energy-momentum assumed strain finite element formulation when combined with the EDMC time-stepping algorithms considered in Section 3, obtaining in this way a (energy) stable formulation that avoids volumetric locking.

5 Representative numerical simulations

To illustrate the performance of the algorithms developed in this paper, we present the results obtained in the simulation of a three-dimensional solid in free flight. Figure 1 depicts the initial configuration of the solid. It consists of a rigid cylindrical core of diameter 20.00 and height 16.66, and two arms with dimensions

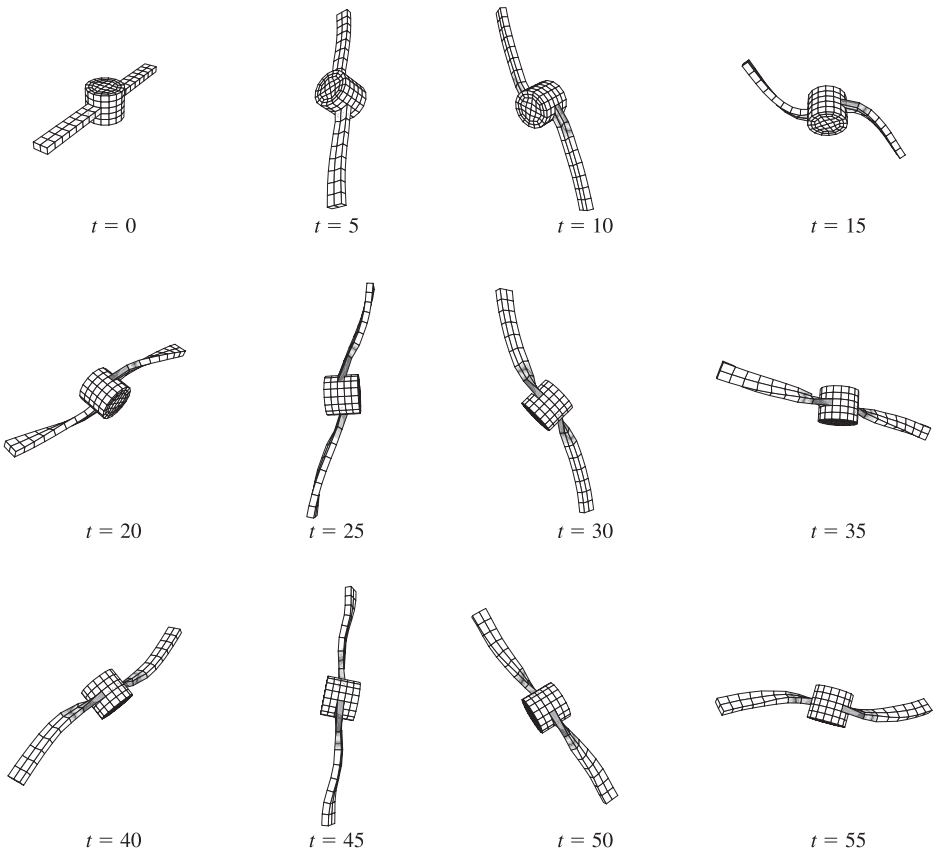

Figure 1 Three-dimensional elastoplastic solid in free flight. Sequence of deformed configurations in the early stages of the motion with the distribution of the equivalent plastic strain α, obtained with the EDMC scheme.

$40.00 \times 7.25 \times 3.33$ each. The rigid core is modeled through a very stiff elastic response, while the arms are elastoplastic.

We consider J_2-flow theory of elastoplasticity, defined by the plastic evolution equations (10)–(13) and the classical von Mises yield surface

$$\phi = \|\boldsymbol{\tau}\| - \sqrt{\frac{2}{3}}(\sigma_o + H\alpha) \leq 0, \tag{49}$$

in the Kirchhoff stresses $\boldsymbol{\tau} = \boldsymbol{F}\boldsymbol{S}\boldsymbol{F}^T = \boldsymbol{F}^e\widetilde{\boldsymbol{S}}\boldsymbol{F}^{e^T}$, with a uniaxial yield limit σ_o and linear hardening with modulus H. The elastic response is governed by the hyperelastic relation (9) with Hencky's stored energy function

$$W^e(\boldsymbol{C}^e) = \frac{1}{2}\kappa(\log(J^e))^2 + \frac{1}{4}\mu\|\log(\boldsymbol{C}^e)\|^2, \tag{50}$$

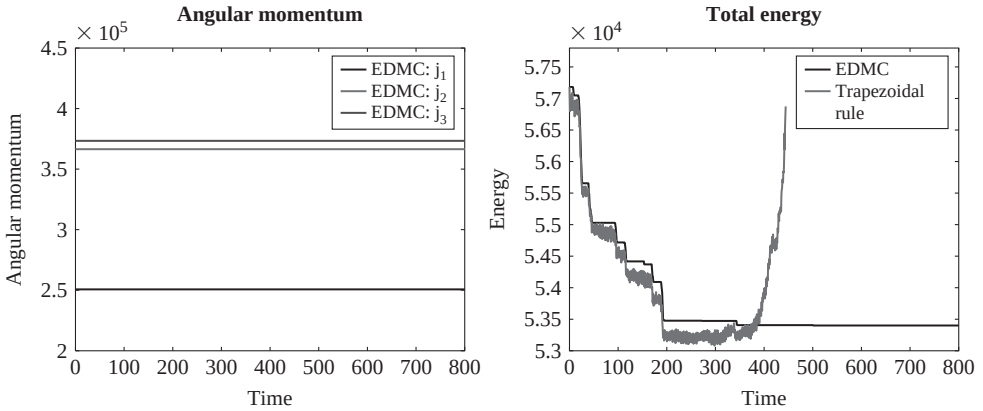

Figure 2 Three-dimensional elastoplastic solid in free flight. Evolution of the three components of the angular momentum $\boldsymbol{j}$ (left) and the total energy (right) obtained with the EDMC scheme, with the latter plot including the evolution of the energy obtained with the classical trapezoidal rule.

for elastic constants κ and μ. The values $\kappa = 58.333$, $\mu = 26.923$, $\sigma_o = 40$, $H = 80$ and reference density $\rho_o = 0.5$ are assumed for the arms, and $\kappa = 17.500 \cdot 10^2$, $\mu = 8.0769 \cdot 10^2$ and $\rho_o = 8.93$ for the central cylindrical core.

A velocity field corresponding to a rotation around the center of mass (see the associated angular momentum in Figure 2) is imposed at $t = 0$ leading to the motion shown in Figure 1 for the early stages. This figure shows the solution obtained with the new B-bar method developed in this work combined with the EDMC return mapping scheme (30)–(32). The motion clearly involves large displacements and strains, for both finite elastic and plastic strains. Figure 1 also shows the distribution of the equivalent plastic strain α superposed to the deformed configuration of the solid.

Figure 2 shows the evolution in time of the three components of the angular momentum $\boldsymbol{j}$ and the total energy H obtained with the EDMC scheme for a constant time step of $\Delta t = 0.5$. The Cartesian reference system is aligned with the axes of the cylindrical core and arms. The exact conservation of the angular momentum for this scheme, including the new B-bar method developed here, is confirmed as it is the non-negative energy dissipation during the solution. Exact energy conservation is observed for elastic steps.

This situation is to be contrasted with the solution obtained with the classical trapezoidal rule (Newmark $\gamma = 1/2$, $\beta = 1/4$) in combination with the standard exponential return map for the evaluation of the stresses. This scheme involves the evaluation of the equation of motion, the stress divergence term in particular, at the end of the time step t_{n+1}. The standard B-bar operator (37) is considered in this case at that time, which leads to the lack of angular momentum conservation. The computed solution is also depicted in the energy plot in Figure 2. A nonlinear instability is observed with an unbounded (non-physical) growth of the energy even though plasticity is occurring.

6 Conclucions

We have presented a new assumed strain finite element method (or B-bar method) that leads to exact energy and momentum conserving formulations when combined with EDMC time stepping schemes for the temporal integration of the equations of motion. The general setting of finite strain plasticity has been considered, requiring the consideration of these assumed formulations to avoid the well-known volumetric locking of basic displacement finite element methods. The new numerical algorithms have shown to avoid, by design, the numerical instabilities that affect standard methods in the nonlinear range of interest.

Acknowledgments

Financial support for this research was provided by the AFOSR under contract no. FA9550-05-1-0117 with UC Berkeley. This support is gratefully acknowledged.

References

Armero, F. 2000. "On the locking and stability of finite elements in finite deformation plane strain problems", Computers & Structures 75:261–290.

Armero, F. 2006. "Energy-dissipative momentum-conserving time-stepping algorithms for finite strain multiplicative plasticity", Comp. Meth. Appl. Mech. Eng., 195:4862–4889.

Armero, F. & Romero, I. 2001a. "On the formulation of high-frequency dissipative time-stepping algorithms for nonlinear dynamics. Part I: Low order methods for two model problems and nonlinear elastodynamics", Comp. Meth. Appl. Mech. Eng., 190:2603–2649.

Armero, F. & Romero, I. 2001b. "On the formulation of high-frequency dissipative time-stepping algorithms for nonlinear dynamics. Part II: High order methods", Comp. Meth. Appl. Mech. Eng., 190:6783–6824.

Armero, F. & Romero, I. 2003. "Energy-dissipative momentum-conserving time-stepping algorithms for the dynamics of nonlinear Cosserat rods", Comp. Mech., 31:3–26.

Armero, F. & Zambrana-Rojas, C. 2005. "Volume–preserving energy–dissipative momentum–conserving algorithms for isochoric multiplicative plasticity", Comp. Meth. Appl. Mech. Eng., 196:4130–4159.

Crisfield, M. & Shi, J. 1994. "A co-rotational element/time-integration strategy for non-linear dynamics", Int. J. Num. Meth. Eng., 37:1897–1913.

González, O. 2000. "Exact energy-momentum conserving algorithms for general models in nonlinear elasticity", Comp. Meth. Appl. Mech. Eng., 190:1763–1783.

Hughes, T.J.R. 1980. "Generalization of selective integration procedures to anisotropic and nonlinear media", Int. J. Num. Meth. Eng., 15:1413–1418.

Marsden, J.E. 1992. Lectures on Mechanics, London Mathematical Society Lecture Note Series, 174: Cambridge University Press.

Meng, X.N. & Laursen, T.A. 2002. "Energy consistent algorithms for dynamic finite deformation plasticity", Comp. Meth. Appl. Mech. Eng., 191:1639–1675.

Nagtegaal, J.C., Parks, D.M. & Rice, J.R. 1974. "On numerically accurate finite element solutions in the fully plastic range", Comp. Meth. Appl. Mech. Eng., 4:153–177.

Noels, L., Stainier, L. & Ponthot, J.P. 2004. "An Energy-Momentum Conserving Algorithm for Non-Linear Hypoelastic Constitutive Models", Int. J. Num. Meth. Eng., 59:83–114.

Romero, I. & Armero, F. 2002. "Numerical integration of the stiff dynamics of geometrically exact shells: an energy-dissipative momentum-conserving scheme", Int. J. Num. Meth. Eng., 54:1043–1086.

Simo, J.C. & Tarnow, N. 1992. "The discrete energy–momentum method. Conserving algorithms for nonlinear elastodynamics", ZAMP 43:757–793.

Simo, J.C., Posbergh, T.A. & Marsden, J.E. 1991. "Stability of relative equilibria. Part II: Application to nonlinear elasticity", Arch. Rational Mech. Anal., 115:61–100.

Simo, J.C., Taylor, R.L. & Pister, K. 1988. "Variational and projection methods for the volume constraint in finite deformation elastoplasticity", Comp. Meth. Appl. Mech. Eng., 57:177–208.

Chapter 4

Energy conservation and high-frequency damping in numerical time integration

Steen Krenk

Technical University of Denmark, Lyngby, Denmark

ABSTRACT: Momentum and energy conserving time integration procedures are receiving increased interest due to the central role of conservation properties in relation to the problems under investigation. However, most problems in structural dynamics are based on models that are first discretized in space, en this often leads to a fairly large number of high-frequency modes, that are not represented well – and occasionally directly erroneously – by the model. It is desirable to cure this problem by devising algorithms that include the possibility of introducing algorithmic energy dissipation of the high-frequency modes. The problem is well known from classic collocation based algorithms – notably various forms of the Newmark algorithm – where the equation of motion is supplemented by approximate relations between displacement, velocity and acceleration. Here adjustment of the algorithmic parameters can be used to introduce so-called α-damping, and an improved form leading only to high-frequency damping can be obtained by suitable averaging of the equilibrium equation at consecutive time steps. Conservative time integration algorithms are obtained by use of an integral of the equation of motion and the acceleration therefore does not appear as an independent parameter of these algorithms. Typically they do not contain algorithmic parameters either. Algorithmic damping can then be introduced in two ways: either by introducing artificial damping in terms of the displacement and velocity vectors, or by introducing additional variables to represent damping. In the present paper it is demonstrated, how damping equivalent to the α-damping of the Newmark algorithm can be introduced directly via displacement and velocity dependent terms. It is furthermore shown, how this damping can be improved by introduction of a new set of variables related to the displacement and velocity vectors by a suitable first order filter with scalar coefficients. By this device an algorithmic damping can be obtained that is of third order in the low-frequency regime. It is an important feature of both algorithms that they can be arranged to require in each time step only the solution of a system of equations of the same size of the corresponding quasi-static problem, followed by one or three vector updates with scalar coefficients – the so-called 'single step – single solve' property.

1 Introduction

Time integration in dynamics of structures and solids has been a very active research area for several decades. The first algorithm to find widespread use was the Newmark family (Newmark 1959), in which approximate relations are used to express the displacement and velocity vectors $\mathbf{u}_{n+1}$ and $\mathbf{v}_{n+1}$ at the new time t_{n+1} in terms of the new acceleration vector and current values of displacements, velocities and

accelerations. These relations permit elimination of $\mathbf{u}_{n+1}$ and $\mathbf{v}_{n+1}$ from the equation of motion at time t_{n+1}, resulting in a system of equations for the acceleration vector at t_{n+1}. The advantage of this scheme is its simplicity and its similarity with the corresponding static problem. However, the Newmark algorithm family has several shortcomings relating to high frequency components, algebraic constraints, and lack of exact conservation properties.

Many models used in structural dynamics involve a spatial discretization, in which the high frequency components do not represent the actual behavior in the original problem. A well known effect is the dispersion introduced in elastic wave propagation by spatial discretization. The limitation of the discretized model to low-frequency components introduces a need for artificial damping of the high-frequency components, so-called algorithmic damping. Ideally, the algorithmic damping shall have filter-like characteristics, leaving the low-frequency response without damping, while imposing a prescribed level of damping on the high frequency response. In the Newmark algorithm family algorithmic damping can be introduced via a slight forward weighting of the acceleration terms used in the representation of the velocity increment, i.e. by increasing the value of the parameter γ slightly beyond the stability limit $\frac{1}{2}$. While this introduces high-frequency damping as desired, it does not leave the low-frequency response unaffected. In fact the algorithmic damping ratio increases linearly with the non-dimensional frequency-timestep parameter $\Omega = \omega h$. This has prompted the development of the so-called α-algorithms, where the equation of motion is satisfied in a weighted average sense, with the weight factor α between present time t_n and forward time t_{n+1}, e.g. Chung & Hulbert (1993) where stiffness and inertia forces are given separate weights. It has recently been demonstrated that the various α-modifications of the Newmark algorithm can all be obtained by introducing additional damping via a first order filter on the response Krenk & Høgsberg (2005).

In many cases, e.g. wave propagation or kinematically non-linear problems, it is preferable to use conservative integration methods, obtained from an integral of the equation of motion, or directly as a finite increment of the momentum, Simo & Tarnow (1992). These algorithms have the advantage that they conserve momentum, and may also conserve total energy. Algorithmic damping can be introduced in these methods by using an unequal weighting of current and forward values of velocity and internal force, Armero & Romero (2001). This leads to damping with frequency dependence like direct α-damping of the Newmark method. In the present paper it is demonstrated, how the idea of representing the damping terms via a special set of variables, introduced by a first order filter, can be used to remove the low frequency damping, while retaining the desired high-frequency damping properties. The proper balance of the terms is obtained by spectral analysis, and the paper therefore concentrates on linear systems. However, the procedure can be extended to non-linear problems in a fairly straightforward manner.

2 Basic equations and the state-space format

The following analysis is concerned with linear systems described by a discretized model in terms of the nodal displacement vector $\mathbf{u}(t)$. The equation of motion is of the form

$$\mathbf{M}\ddot{\mathbf{u}}(t) + \mathbf{C}\dot{\mathbf{u}}(t) + \mathbf{K}\mathbf{u}(t) = \mathbf{f}(t) \tag{1}$$

where the system is described by the mass matrix **M**, the viscous damping matrix **C** and the stiffness matrix **K**, while the external load vector is $\mathbf{f}(t)$. Time differentiation is denoted by a dot, e.g. the velocity $\dot{\mathbf{u}} = d\mathbf{u}/dt$.

The energy balance equation corresponding to the equation of motion (1) is obtained by multiplication with $\dot{\mathbf{u}}^T$, followed by integration,

$$\frac{d}{dt}\left(\frac{1}{2}\dot{\mathbf{u}}^T\mathbf{M}\dot{\mathbf{u}} + \frac{1}{2}\mathbf{u}^T\mathbf{K}\mathbf{u}\right) = \dot{\mathbf{u}}^T\mathbf{f} - \dot{\mathbf{u}}^T\mathbf{C}\dot{\mathbf{u}} \tag{2}$$

The left side is the rate of change of the mechanical energy, consisting of the sum of kinetic and elastic energy, and the right side contains the rate of work of the external load and an energy disssipation term expressed by the viscous damping matrix. In the development of discrete time integration algorithms it is desirable that they satisfy a similar energy balance equation in discretized form, and that the damping term(s) remain representative over the full frequency range in spite of the time discretization.

It is advantageous to recast the second order differential equation of motion into an augmented set of first order differential equations by introduction of a new independent variable representing the velocity, $\mathbf{v} = \dot{\mathbf{u}}$. When this definition is multiplied by the mass matrix **M** the augmented system for the state space variables $[\mathbf{u}^T, \mathbf{v}^T]$ takes the symmetric form,

$$\begin{bmatrix}\mathbf{C} & \mathbf{M}\\ \mathbf{M} & \mathbf{0}\end{bmatrix}\begin{bmatrix}\dot{\mathbf{u}}\\ \dot{\mathbf{v}}\end{bmatrix} + \begin{bmatrix}\mathbf{K} & \mathbf{0}\\ \mathbf{0} & -\mathbf{M}\end{bmatrix}\begin{bmatrix}\mathbf{u}\\ \mathbf{v}\end{bmatrix} = \begin{bmatrix}\mathbf{f}(t)\\ \mathbf{0}\end{bmatrix} \tag{3}$$

While traditional collocation based algorithms like the Newmark family with its various modifications introduce an approximate relation between the displacement, velocity and acceleration, the more recent momentum conserving approach to time integration algorithms is based on an integrated form of the state-space equations. For constant system matrices the first term in the state-space equation integrates exactly, while the second term contains integrals of the displacement and velocity over the time interval $[t_n, t_{n+1}] = [t, t+h]$. If the time mean value over the time interval is denoted by an overbar, e.g. $\bar{\mathbf{f}} = h^{-1}\int_h \mathbf{f}\, d\tau$, the integrated state-space equations take the form

$$\begin{bmatrix}\mathbf{C} & \mathbf{M}\\ \mathbf{M} & \mathbf{0}\end{bmatrix}\begin{bmatrix}\Delta\mathbf{u}\\ \Delta\mathbf{v}\end{bmatrix} + h\begin{bmatrix}\mathbf{K} & \mathbf{0}\\ \mathbf{0} & -\mathbf{M}\end{bmatrix}\begin{bmatrix}\bar{\mathbf{u}}\\ \bar{\mathbf{v}}\end{bmatrix} = \begin{bmatrix}h\bar{\mathbf{f}}\\ \mathbf{0}\end{bmatrix} \tag{4}$$

where $\Delta\mathbf{u}$ and $\Delta\mathbf{v}$ are the finite increments over the time internal. The time integrals of the displacement and velocity vectors are generally unknown, and thus $\bar{\mathbf{u}}$ and $\bar{\mathbf{v}}$ must be represented by an approximation. For linear problems it is suitable to use the arithmetic mean values

$$\bar{\mathbf{u}} = \frac{1}{2}(\mathbf{u}_{n+1} + \mathbf{u}_n), \quad \bar{\mathbf{v}} = \frac{1}{2}(\mathbf{v}_{n+1} + \mathbf{v}_n) \tag{5}$$

While the load can in principle be introduced by its time integral, in practice it is convenient to use the arithmetic mean also for the load vector.

The energy equation corresponding to the discretized equations (4) is obtained by pre-multiplication of this equation with $[\Delta\mathbf{u}^T, -\Delta\mathbf{v}^T]$.

$$\left[\frac{1}{2}\mathbf{v}^T\mathbf{M}\mathbf{v} + \frac{1}{2}\mathbf{u}^T\mathbf{K}\mathbf{u}\right]_n^{n+1} = \Delta\mathbf{u}^T\bar{\mathbf{f}} - \Delta\mathbf{u}^T\mathbf{C}\,\Delta\mathbf{u} \tag{6}$$

This discretized energy relation has a format that reproduces that of its continuous counterpart (2). However, in spite of the similar formats the discretization leads to a non-monotonic dependence of energy dissipation on the frequency of the response. This implies that damping represented via a viscous damping matrix $\mathbf{C}$ will not lead to the desired damping of high-frequency modes outside the range represented by the time increment h.

3 Balanced dissipation

It is easily seen that damping can be obtained by introducing terms in the diagonal of first matrix of the integrated state space equations (4). For a linear system without structural damping introduction of terms of order $O(h)$ this leads to the following form,

$$\begin{bmatrix}\alpha_1 h\mathbf{K} & \mathbf{M} \\ \mathbf{M} & -\alpha_2 h\mathbf{M}\end{bmatrix}\begin{bmatrix}\Delta\mathbf{u} \\ \Delta\mathbf{v}\end{bmatrix} + \begin{bmatrix}\mathbf{K} & 0 \\ 0 & -\mathbf{M}\end{bmatrix}\begin{bmatrix}h\bar{\mathbf{u}} \\ h\bar{\mathbf{v}}\end{bmatrix} = \begin{bmatrix}h\bar{\mathbf{f}} \\ 0\end{bmatrix} \tag{7}$$

The extra diagonal terms are determined by the fact that only the system matrices $\mathbf{K}$ and $\mathbf{M}$ are available, and the extra terms must be of order $O(h)$. The energy balance equation is obtained by pre-multiplication with $[\Delta\mathbf{u}^T, -\Delta\mathbf{v}^T]$.

$$\left[\frac{1}{2}\mathbf{v}^T\mathbf{M}\mathbf{v} + \frac{1}{2}\mathbf{u}^T\mathbf{K}\,\mathbf{u}\right]_n^{n+1} = \Delta\mathbf{u}^T\bar{\mathbf{f}} - \alpha_1\Delta\mathbf{u}^T\mathbf{K}\,\Delta\mathbf{u} - \alpha_2\Delta\mathbf{v}^T\mathbf{M}\,\Delta\mathbf{v} \tag{8}$$

It is seen that both coefficients α_1 and α_2 contribute an energy dissipation term, when they are positive. The optimal balance between these two terms is determined by a spectral analysis.

3.1 *Spectral analysis*

The spectral analysis is performed on the free vibrations associated with the discretized state-space equations (7), which for convenience are written in the generic form

$$\mathbf{B}\Delta\mathbf{w} + \mathbf{A}\bar{\mathbf{w}} = 0 \tag{9}$$

In this equation the matrices $\mathbf{B}$ and $\mathbf{A}$ represent the block matrices of (7), while the vector $\mathbf{w}_n$ contains all state-space variables at time t_n. In practice the spectral analysis is carried out using the mode shapes of the undamped equation of motion together with the non-dimensional modal amplitude vector $\mathbf{w} = [u, hv]^T$. The time step h and the angular modal frequency ω are combined into the non-dimensional frequency parameter $\Omega = h\omega$. When the first equation in (7) is multiplied by h the matrices $\mathbf{B}$ and $\mathbf{A}$ can be represented in non-dimensional form as

$$\mathbf{B} = \begin{bmatrix}\alpha_1\Omega^2 & 1 \\ 1 & -\alpha_2\end{bmatrix}, \quad \mathbf{A} = \begin{bmatrix}\Omega^2 & 0 \\ 0 & -1\end{bmatrix} \tag{10}$$

The free vibrations satisfy the evolution equation

$$\mathbf{w}_{n+1} = \lambda \mathbf{w}_n \tag{11}$$

in terms of the amplification factor λ. Substitution of the free vibration solution (11) into the generic equation of motion (9) leads to the generalized eigenvalue problem

$$(\mathbf{A} + 2z\mathbf{B})\mathbf{w}_n = \mathbf{0} \tag{12}$$

where the eigenvalue z is related to the amplification factor λ by the Möbius transformation

$$z = \frac{\lambda - 1}{\lambda + 1}, \quad \lambda = \frac{1 + z}{1 - z} \tag{13}$$

Stable solutions require the amplification factor to be on or within the unit circle in the complex plane. The Möbius transformation maps the unit circle on the left complex half-plane, and thus in general stability can be analyzed in terms of the variable z by the Routh-Hurwitz criterion.

In the present case the spectral analysis of the algorithm can be carried out explicitly. In order for the solutions z to be separate complex conjugate or at most isolated double roots on the real axis it is necessary that the two damping parameters are equal, and it is convenient to use the common value

$$\alpha_1 = \alpha_2 = \frac{1}{2}\alpha \tag{14}$$

It can be shown that the characteristic equation for the amplification factor λ with damping parameters given by (14) is identical to that of the Newmark algorithm with 'alpha damping' characterized by the parameters $\gamma = \frac{1}{2} + \alpha$ and $\beta = \frac{1}{4}(1 + \alpha)^2$, see e.g. (10) in Krenk & Høgsberg, (2005). While this leads to identical frequency dependence of the amplification factor λ for the method of balanced damping and the alpha damped Newmark method, the spectral analysis of the Newmark method makes use of a non-orthogonal transformation in setting up the eigenvalue problem for λ, and thereby introduces an undesirable bias into the energy balance equation as discovered in Hughes, (1979) and analyzed in detail in Krenk, (2006a). The balanced damping algorithm retains the original energy function, and therefore is not prone to energy oscillations and potential overshoot in connection with rapid transients, as the various forms of damped Newmark algorithms are.

The solution to the characteristic equation with damping parameters given by (14) is

$$\lambda = \frac{1 \pm \frac{1}{2}(1 - \alpha)i\Omega}{1 \mp \frac{1}{2}(1 + \alpha)i\Omega} \tag{15}$$

The two branches of the locus of the complex amplification factor λ are shown in Fig. 1a for $|\lambda_\infty| = 0.6$. They connect the low-frequency limit $\lambda_0 = 1$ with the high-frequency limit

$$\lambda_\infty = -\frac{1 - \alpha}{1 + \alpha} \tag{16}$$

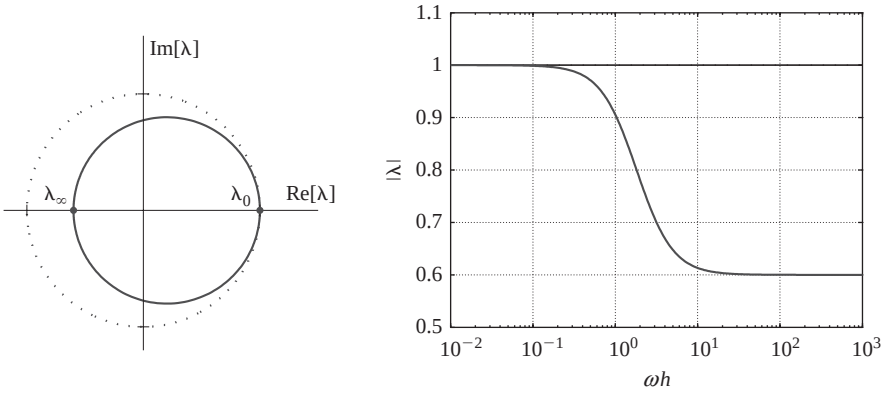

Figure 1 Balanced damping with $\lambda_\infty = 0.6$. a) Amplification factor λ, b) Spectral radius $|\lambda|_{max}$.

for $\Omega \to \infty$. For $\alpha = 0$ there is no damping, and the amplification factor λ traces the unit circle.

The spectral radius $|\lambda|$ is shown as function of the non-dimensional frequency $\Omega = \omega h$ in Fig. 1b for $|\lambda_\infty| = 0.6$. Different values of $|\lambda_\infty|$ lead to similar curves. It is characteristic for all the curves that damping sets in well below $\Omega = 1$. The detailed low-frequency behavior follows from the asymptotic analysis below.

3.2 *Low-frequency asymptotics*

The information to be gained from a discrete numerical time integration is limited by the sampling rate represented by the non-dimensional frequency $\Omega = \omega h$. The Nyquist frequency corresponds to two sampling points per period, and thereby to $\Omega = \pi$. A practical upper frequency limit for representation of a harmonic signal is $\Omega \simeq 1$, corresponding to about 6 points per period. It is of interest to obtain explicit asymptotic expressions for the 'quality' of the time integration algorithm for the low-frequency range. The quality is typically characterized by the amount of damping and the error of the period of an ideal harmonic oscillation.

The damping of the algorithm is characterized by the spectral radius $|\lambda|$. It follows from the solution (15) for the amplification factor that

$$|\lambda| = 1 - \frac{1}{2}\alpha\Omega^2[1 + O(\Omega^2)] \tag{17}$$

It is convenient to express this result in terms of the algorithmic damping ratio ζ, defined by the attenuation of a damped vibration per increase in phase angle, i.e. by $|\lambda| = \exp(-\zeta\varphi)$. The low-frequency algorithmic damping ratio then follows from the asymptotic expression (17) as

$$\zeta = \frac{1}{2}\alpha\Omega[1 + O(\Omega^2)] \tag{18}$$

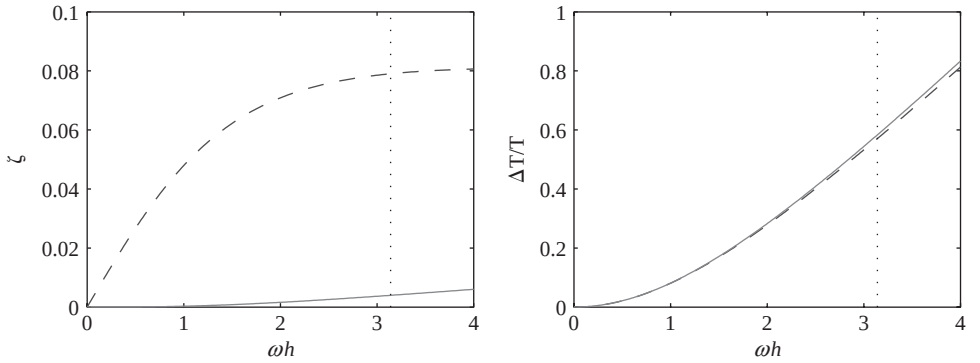

Figure 2 Response parameters for $|\lambda_\infty| = 0.8$. a) Damping ratio, b) Period error.

Thus, the introduction of balanced dissipation into the conservative time integration algorithm introduces a low-frequency damping that increases linearly with the non-dimensional frequency Ω. The behavior of the Newmark algorithm with alpha damping is identical Krenk & Høgsberg (2005). The damping ratio is shown in Fig. 2a by the dashed curve for $|\lambda_\infty| = 0.8$. The linear increase with Ω for low frequencies is clearly seen.

The phase angle φ of the algorithm is determined from damped harmonic response by $\lambda = |\lambda| \exp(\pm i\varphi)$. The low-frequency asymptotic expression can be calculated from (15) as

$$\varphi = \Omega - \frac{1}{12}(1 + 3\alpha^2)\Omega^3 + \mathrm{O}(\Omega^5) \tag{19}$$

From this expression the relative error of the period $T = 2\pi/\omega$ follows as

$$\frac{\Delta T}{T} = \frac{\Omega}{\varphi} - 1 = \frac{1}{12}(1 + 3\alpha^2)\Omega^2 + \mathrm{O}(\Omega^4) \tag{20}$$

It is seen that the period error is positive and that algorithmic damping increases the period error further. Thus, it is desirable to introduce only modest algorithmic damping. The full behavior is shown in Fig. 2b by the dashed curve for $|\lambda_\infty| = 0.8$. The relative period error is seen to take on a very substantial value of around 0.5 before the frequency reaches the Nyquist value $\Omega = \pi$.

3.3 *Balanced dissipation algorithm*

The algorithm with consistent energy dissipation can now be expressed for linear systems including structural damping $\mathbf{C}$. The state space form follows from substitution of the value $\alpha_j = \frac{1}{2}\alpha$ into the state-space equations (7). The formulation takes on a particularly compact form when introducing the parameter

$$\kappa = 1 + \alpha \tag{21}$$

Table 1 Algorithm with balanced energy dissipation.

1.	System matrices $\mathbf{K}, \mathbf{C}, \mathbf{M}$, $\mathbf{K}_* = \kappa \left[\mathbf{K} + \frac{2}{\kappa h}\mathbf{C} + \left(\frac{2}{\kappa h}\right)^2 \mathbf{M} \right]$
2.	Initial conditions: $\mathbf{u}_0, \mathbf{v}_0$.
3.	Increments $n = n + 1$: $\Delta\mathbf{u} = \mathbf{K}_*^{-1} \left\{ \mathbf{f}_{n+1} + \mathbf{f}_n - 2\mathbf{K}\mathbf{u}_n + \frac{4}{\kappa h}\mathbf{M}\mathbf{v}_n \right\}$ $\Delta\mathbf{v} = 2\Delta\mathbf{u}/\kappa h - 2\mathbf{v}_n/\kappa$
4.	Vector updates: $\mathbf{u}_{n+1} = \mathbf{u}_n + \Delta\mathbf{u}, \quad \mathbf{v}_{n+1} = \mathbf{v}_n + \Delta\mathbf{v}$
5.	Return to 3 for new time step, or stop.

The last equation then gives the forward velocity $\mathbf{v}_{n+1}$ by the simple vector relation

$$\Delta\mathbf{v} = \frac{2\Delta\mathbf{u}}{\kappa h} - \frac{2\mathbf{v}_n}{\kappa} \tag{22}$$

while elimination of $\mathbf{v}_{n+1}$ from the first equation leads to

$$\kappa \left[\mathbf{K} + \frac{2}{\kappa h}\mathbf{C} + \frac{4}{(\kappa h)^2}\mathbf{M} \right] \Delta\mathbf{u} = (\mathbf{f}_{n+1} + \mathbf{f}_n) - 2\mathbf{K}\mathbf{u}_n + \frac{4}{\kappa h}\mathbf{M}\mathbf{v}_\mathbf{n} \tag{23}$$

In this equation the displacement increment $\Delta\mathbf{u}$ is determined by the effective stiffness matrix

$$\mathbf{K}_* = \kappa \left[\mathbf{K} + \frac{2}{\kappa h}\mathbf{C} + \frac{4}{(\kappa h)^2}\mathbf{M} \right] \tag{24}$$

It is seen that the terms are scaled as if extending the time increment from h to κh, whereby the dynamic terms get less weight. A similar feature is found in the high-frequency algorithm to be developed below, but now with a different definition of the scaling parameter κ. The balanced dissipation algorithm is summarized in Table 1.

4 High-frequency dissipation

In this section it is demonstrated, how the algorithmic dissipation can be removed from the low-frequency regime by a filter procedure similar to that introduced for the Newmark algorithm in Krenk & Høgsberg (2005). In the balanced dissipation algorithm the energy dissipation is introduced via the diagonal terms containing $\Delta\mathbf{u}$ and $\Delta\mathbf{v}$. In the low and mid-frequency regime these terms are equivalent to $h\dot{\mathbf{u}}$ and $h\dot{\mathbf{v}}$. The idea is to replace these terms expressed by the state-space variables with similar terms using a new set of variables $\mathbf{s}(t)$ and $\mathbf{t}(t)$ defined via first order filters.

$$\nu h\dot{\mathbf{s}} + \mathbf{s} = h\dot{\mathbf{u}}, \quad \nu h\dot{\mathbf{t}} + \mathbf{t} = h\dot{\mathbf{v}} \tag{25}$$

where the non-dimensional parameter ν determines the common time scale of the two filters. At low frequencies the second term in the filter equation will dominate the first, and thus the terms $h\dot{\mathbf{s}}$ and $h\dot{\mathbf{t}}$ used to represent damping will be nearly out of phase with the state space derivatives $\dot{\mathbf{u}}$ and $\dot{\mathbf{v}}$, and thereby only produce a very reduced damping effect.

When the increments $\Delta\mathbf{u}$ and $\Delta\mathbf{v}$ in the damping terms of the balanced algorithm (7) are replaced by the increments $\frac{1}{2}\nu\,\Delta\mathbf{s}$ and $\frac{1}{2}\nu\,\Delta\mathbf{t}$ of the corresponding filtered variables, it takes the form of the state-space equations

$$\begin{bmatrix}\mathbf{C} & \mathbf{M}\\ \mathbf{M} & \mathbf{0}\end{bmatrix}\begin{bmatrix}\Delta\mathbf{u}\\ \Delta\mathbf{v}\end{bmatrix}+h\begin{bmatrix}\mathbf{K} & \mathbf{0}\\ \mathbf{0} & -\mathbf{M}\end{bmatrix}\begin{bmatrix}\bar{\mathbf{u}}\\ \bar{\mathbf{v}}\end{bmatrix}+\frac{1}{4}\nu\alpha h\begin{bmatrix}\mathbf{K} & \mathbf{0}\\ \mathbf{0} & -\mathbf{M}\end{bmatrix}\begin{bmatrix}\Delta\mathbf{s}\\ \Delta\mathbf{t}\end{bmatrix}=h\begin{bmatrix}\bar{\mathbf{f}}\\ \mathbf{0}\end{bmatrix} \tag{26}$$

supplemented by the discretized filter equations

$$\nu\begin{bmatrix}\Delta\mathbf{s}\\ \Delta\mathbf{t}\end{bmatrix}+\begin{bmatrix}\bar{\mathbf{s}}\\ \bar{\mathbf{t}}\end{bmatrix}=\begin{bmatrix}\Delta\mathbf{u}\\ \Delta\mathbf{v}\end{bmatrix} \tag{27}$$

Substitution of the damping terms with the factor $\frac{1}{2}\nu$ leads to an interpretation of the damping parameter α similar to that of the balanced dissipation algorithm of the present paper and the use in the Newmark method and its generalized alpha form. The properties of the present algorithm are characterized by an energy balance equation and a spectral analysis to be described next. The viscous damping matrix $\mathbf{C}$ is indicated in the algorithm to identify its position and weighting but is not included in the energy balance and spectral analysis.

4.1 *Energy balance of extended state-space system*

The energy balance equation of the filter algorithm follows from multiplication of the state-space equations with $[\Delta\mathbf{u}^T, -\Delta\mathbf{v}^T]$.

$$\left[\frac{1}{2}\mathbf{v}^T\mathbf{M}\mathbf{v}+\frac{1}{2}\mathbf{u}^T\mathbf{K}\mathbf{u}\right]_n^{n+1}=\Delta\mathbf{u}^T\bar{\mathbf{f}}-\frac{1}{4}\alpha\nu\left(\Delta\mathbf{u}^T\mathbf{K}\,\Delta\mathbf{s}+\Delta\mathbf{v}^T\mathbf{M}\,\Delta\mathbf{t}\right) \tag{28}$$

In this form of the energy equation the dissipation is represented as the work of the filtered variables through the corresponding displacement and velocity increments. In order to obtain an energy equation in terms of positive definite quadratic terms, the increments $\Delta\mathbf{u}$ and $\Delta\mathbf{v}$ are eliminated in the damping terms by use of the filter equations (27). These two relations are now used to eliminate the coupled damping terms from the energy balance equation (28) that then takes the form

$$\begin{aligned}&\left[\frac{1}{2}\mathbf{v}^T\mathbf{M}\mathbf{v}+\frac{1}{2}\mathbf{u}^T\mathbf{K}\mathbf{u}+\frac{1}{8}\alpha\nu(\mathbf{t}^T\mathbf{M}\mathbf{t}+\mathbf{s}^T\mathbf{K}\mathbf{s})\right]_n^{n+1}\\ &\quad=\Delta\mathbf{u}^T\bar{\mathbf{f}}-\frac{1}{4}\alpha\nu^2(\Delta\mathbf{s}^T\mathbf{K}\Delta\mathbf{s}+\Delta\mathbf{t}^T\mathbf{M}\Delta\mathbf{t})\end{aligned} \tag{29}$$

This is the energy balance equation of the total system consisting of the original state-space variables $\mathbf{u}$ and $\mathbf{v}$ together with the corresponding filter variables $\mathbf{s}$ and $\mathbf{t}$. For $\alpha=0$ the energy conservation equation is recovered, and for $\alpha>0$ and $\nu>0$ the extended energy defined in terms of all variables is positive definite and decreases as determined by a positive definite quadratic form of the increments of the filter variables $\mathbf{s}$ and $\mathbf{t}$.

This secures unconditional stability of the filter algorithm given by (26) and (27) for $\alpha > 0$ and $\nu > 0$.

4.2 *Spectral analysis of the filter algorithm*

The spectral analysis of the extended state-space algorithm is based on the free vibration response of a single mode of the equations (26) and (27). In the non-dimensional generic format (9) this corresponds to the extended modal amplitude vector $\mathbf{w}^T = [u, hv, s, ht]$ and the matrices

$$\mathbf{A} = \begin{bmatrix} \Omega^2 & 0 & 0 & 0 \\ 0 & -1 & 0 & 0 \\ 0 & 0 & 1 & 0 \\ 0 & 0 & 0 & 1 \end{bmatrix}, \quad \mathbf{B} = \begin{bmatrix} 0 & 1 & \frac{1}{4}\alpha\nu\Omega^2 & 0 \\ 1 & 0 & 0 & -\frac{1}{4}\alpha\nu \\ -1 & 0 & \nu & 0 \\ 0 & -1 & 0 & \nu \end{bmatrix} \tag{30}$$

The optimal value of the parameter ν results in equal damping of all the four modes in the high-frequency limit $\Omega \to \infty$, see e.g. the discussion in (26) and (27). In the present case this implies that $\nu = \alpha$, corresponding to the quadruple root at infinity $z_\infty = -1/\alpha$. The corresponding high-frequency limit of the amplification factor λ_∞ follows from the Möbius transformation. It turns out that λ_∞ is given by (16) as for the balanced dissipation algorithm, thus retaining the interpretation of the damping parameter α. In the low-frequency limit $\Omega = 0$ there are two double roots, $z_0 = 0$ and $z_f = -1/2\alpha$, corresponding to the amplification factors

$$\lambda_0 = 1, \quad \lambda_f = -\frac{1 - 2\alpha}{1 + 2\alpha} \tag{31}$$

where the subscript f indicates branches introduced by the filters.

For the particular parameter choice $\nu = \alpha$ the characteristic equation can be solved for z and the amplification factor is obtained by use of the Möbius transformation, Krenk (2008),

$$\lambda = \frac{1 \pm i(1-\alpha)\Omega(\pm)\sqrt{1 \pm 2i\alpha\Omega}}{1 \mp i(1+\alpha)\Omega(\pm)\sqrt{1 \pm 2i\alpha\Omega}} \tag{32}$$

The sign $(+)$ corresponds to the two branches with origin in $\lambda_0 = 1$, whereas the sign $(-)$ corresponds to the two additional branches with origin at λ_f introduced by the filters. The trace of the locus of the amplification factor in the complex plane is illustrated in Fig. 3a for $|\lambda_\infty| = 0.6$. The corresponding result for the balanced alpha-damping is shown as dashed curves. It is seen that the filter damping stays much closer to the unit circle to the left of the imaginary axis. This is in close correspondence with the effect of 'generalized alpha damping' for the Newmark algorithm, illustrated in Krenk & Høgsberg, (2005). The corresponding spectral radius $\max|\lambda|$ is shown in Fig. 3b. It is seen that the spectral radius remains close to unity right up to $\Omega \simeq 1$ before decreasing towards its value $|\lambda_\infty|$. The branches forming the small loop connecting λ_f and λ_∞ are generated by the filter variables. These branches are equivalent to the extra real-valued root appearing in the generalized alpha method (Chung & Hulbert, 1993; Krenk & Høgsberg, 2005). Within the extended state-space formulation they represent the passive response of the filter variables.

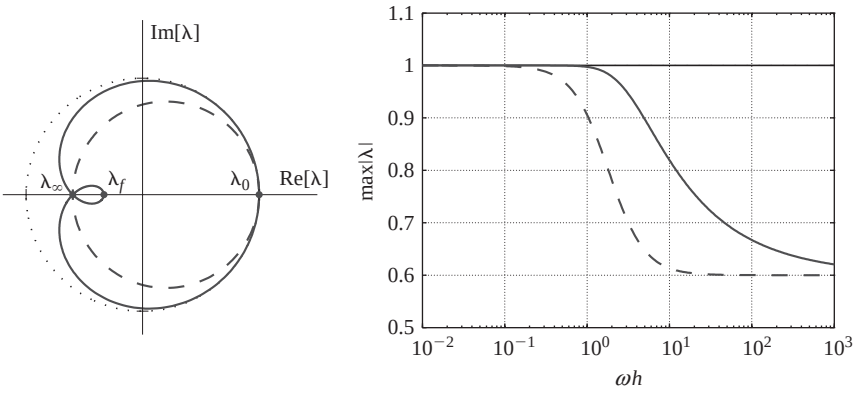

Figure 3 Filter damping with $|\lambda_\infty| = 0.6$. a) Amplification factor λ, b) Spectral radius $|\lambda|_{\max}$.

4.3 *Asymptotic properties*

A more detailed description of the low-frequency behavior of the algorithm is obtained by an asymptotic analysis. In spite of the explicit expression (32) it is probably simpler to obtain a power series representation of z directly from the characteristic equation, see Krenk, (2008). This leads to the asymptotic algorithmic damping ratio

$$\zeta = \frac{1}{4}\alpha^3\Omega^3[1 + \mathrm{O}(\Omega^2)] \tag{33}$$

It is seen that the introduction of the filter variables have changed the leading term of the low-frequency damping from $\frac{1}{2}(\alpha\Omega)$ to $\frac{1}{4}(\alpha\Omega)^3$, i.e. from a linear to a cubic term in $\alpha\Omega$. The full damping behavior is illustrated by the fully drawn curve in Fig. 2a, where the reduction of the damping ratio to order three is clearly seen.

The low-frequency period error remains nearly unaffected unaffected by the extended state-space formulation of the damping as illustrated by the fully drawn curve in Fig. 2b. In fact, the asymptotic behavior is given by (20) also in this case.

4.4 *Extended state-space algorithm*

The high-frequency damping algorithm is given by the system equations (26) and the filter equations (27) with $\nu = \alpha$. It is an important feature of this set of equations that the solution can be advanced one time step by solving only a single set of equations of the sized of the original system matrices $\mathbf{K}$ and $\mathbf{M}$, followed by three simple vector updates without matrix operations. The equation system is obtained by first eliminating the forward values of the filter variables $\mathbf{s}_{n+1}$ and $\mathbf{t}_{n+1}$ from the state-space equations, and then eliminating the forward value of the velocity $\mathbf{v}_{n+1}$. This results in an equation for the incremental displacement vector $\Delta\mathbf{u}$, and the eliminated variables are subsequently recovered by simple vector relations with scalar coefficients.

First the filter equations with $\nu = \alpha$ are written in the form

$$\left(\frac{1}{2} + \alpha\right)\Delta\mathbf{s} = \Delta\mathbf{u} - \mathbf{s}_n, \quad \left(\frac{1}{2} + \alpha\right)\Delta\mathbf{t} = \Delta\mathbf{v} - \mathbf{t}_n \tag{34}$$

Table 2 Extended state-space algorithm.

1. System matrices $\mathbf{K}, \mathbf{C}, \mathbf{M}$,
$$\mathbf{K}_* = \kappa \left[\mathbf{K} + \frac{2}{\kappa h}\mathbf{C} + \left(\frac{2}{\kappa h}\right)^2 \mathbf{M} \right]$$
2. Initial conditions: $\mathbf{u}_0, \mathbf{v}_0$,
$\mathbf{s}_0 = \mathbf{0}, \quad \mathbf{t}_0 = \mathbf{0}$
3. Increments $n = n + 1$:
$$\Delta\mathbf{u} = \mathbf{K}_*^{-1} \left\{ \mathbf{f}_{n+1} + \mathbf{f}_n - \mathbf{K}[2\mathbf{u}_n - (\kappa - 1)\mathbf{s}_n] + \frac{2}{\kappa h}\mathbf{M}[2\mathbf{v}_n - (\kappa - 1)\mathbf{t}_n] \right\}$$
$$\Delta\mathbf{v} = 2\Delta\mathbf{u}/\kappa h - [2\mathbf{v}_n - (\kappa - 1)\mathbf{t}_n]/\kappa$$
$$\Delta\mathbf{s} = (\Delta\mathbf{u} - \mathbf{s}_n)/\left(\tfrac{1}{2} + \alpha\right), \quad \Delta\mathbf{t} = (\Delta\mathbf{v} - \mathbf{t}_n)/\left(\tfrac{1}{2} + \alpha\right)$$
4. Vector updates:
$\mathbf{u}_{n+1} = \mathbf{u}_n + \Delta\mathbf{u}, \quad \mathbf{v}_{n+1} = \mathbf{v}_n + \Delta\mathbf{v}$
$\mathbf{s}_{n+1} = \mathbf{s}_n + \Delta\mathbf{s}, \quad \mathbf{t}_{n+1} = \mathbf{t}_n + \Delta\mathbf{t}$
5. Return to 3 for new time step, or stop.

The increments $\Delta\mathbf{s}$ and $\Delta\mathbf{t}$ are now eliminated from the system equations (26). Here it is convenient to introduce the parameter

$$\kappa = \frac{(1+\alpha)^2}{1+2\alpha} = 1 + \frac{\alpha^2}{1+2\alpha} \tag{35}$$

The last equation contains the mass matrix $\mathbf{M}$ as common factor. When this factor is omitted this equation takes the form of a simple vector relation that is used to express $\Delta\mathbf{v}$ in the form

$$\kappa\,\Delta\mathbf{v} = \left[\frac{2}{h}\Delta\mathbf{u} - 2\mathbf{v}_n\right] + (\kappa - 1)\mathbf{t}_n \tag{36}$$

The variables $\Delta\mathbf{v}$ and $\mathbf{s}_n$ are now eliminated from the first equation by use of the relations (34a) and (36), giving the resulting equation for the displacement increment $\Delta\mathbf{u}$,

$$\kappa \left[\mathbf{K} + \frac{2}{\kappa h}\mathbf{C} + \left(\frac{2}{\kappa h}\right)^2 \mathbf{M} \right] \Delta\mathbf{u}$$
$$= \mathbf{f}_{n+1} + \mathbf{f}_n - \mathbf{K}[2\mathbf{u}_n - (\kappa - 1)\mathbf{s}_n] + \frac{2}{\kappa h}\mathbf{M}[2\mathbf{v}_n - (\kappa - 1)\mathbf{t}_n] \tag{37}$$

It is observed that in this relation the time increment h only appears in the scaled form κh. The form of the two equations (36) and (37) in terms of the parameter κ are identical to (22) and (23) of the balanced dissipation algorithm apart from the contributions from the two variables $\mathbf{s}_n$ and $\mathbf{t}_n$. However, in the filter algorithm the numerical value of κ is typically much smaller. The balanced dissipation algorithm is summarized in Table 2.

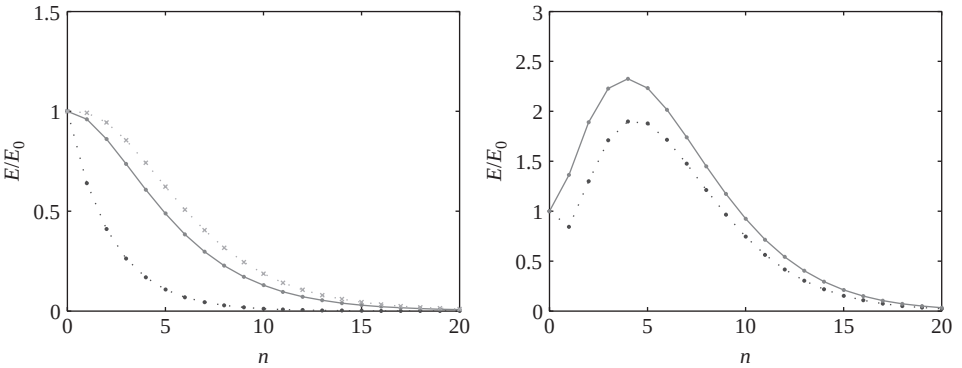

Figure 4 Response from $u_0 = 1, v_0 = 0$ for $h = 10T$. a) Conservative (present), b) Newmark based.

4.5 *Transient high-frequency response*

One of the problems associated with introducing algorithmic damping into the Newmark family of algorithms is, that the known techniques lead to a reinterpretation of the energy as registered by the algorithm, (Hughes, 1979; Krenk, 2006a). Both of the present algorithms keep the basic properties of the energy of the system. As a consequence even very high frequency components leads to monotonically decreasing response when started from unit displacement, zero velocity initial conditions. This is illustrated in Fig. 4, showing the free response to unit displacement initial conditions of a high-frequency component with period $T = h/10$ for $|\lambda_\infty| = 0.8$. Figure 4a shows the performance of the present algorithms. The lower curve is the energy by the balanced dissipation algorithm, the middle curve is the energy by the extended state-space algorithm, while the top curve shows the total energy of the system (29), including the filter variables. Figure 4b shows similar results for the α-damped Newmark method, and the generalized-α method, respectively. It is seen that the algorithms based on integrals of the equation of motion lead to monotonic dissipation of energy, while the Newmark-based collocation algorithms lead to overshoot of the response of the very high frequency components illustrated here.

References

Armero, F. & Romero, I. 2001. On the formulation of high-frequency dissipative time-stepping algorithms for nonlinear dynamics. Part II: Second order methods, *Computer Methods in Applied Mechanics and Engineering*, **190**, 6783–6824.

Chung, J. & Hulbert, G.M. 1993. A time integration algorithm for structural dynamics with improved numerical dissipation: The generalized α method, *Journal of Applied Mechanics*, **60**, 371–375.

Hughes, T.J.R. 1979. A note on the stability of Newmark's algorithm in nonlinear structural dynamics, *International Journal for Numerical Methods in Engineering*, **11**, 383–386.

Krenk, S. 2006a. Energy conservation in Newmark based time integration algorithms, *Computer Methods in Applied Mechanics and Engineering*, **195**, 6110–6124.

Krenk, S. 2006b. State-space time integration with energy control and fourth order accuracy for linear dynamic systems, *International Journal for Numerical Methods in Engineering*, **65**, 595–619.

Krenk, S. 2008. Extended state-space time integration with high-frequency dissipation, *International Journal for Numerical Methods in Engineering*, **73**, 1767–1787.

Krenk, S. & Høgsberg, J.R. 2005. Properties of time integration with first order filter damping, *International Journal for Numerical Methods in Engineering*, **64**, 547–566.

Newmark, N.M. 1959. A method of computation for structural dynamics. *Journal of the Engineering Mechanics Division, ASCE*, **85**, 67–94.

Simo, J.C. & Tarnow, N. 1992. The discrete energy-momentum method. Conserving algorithms for nonlinear elastodynamics, *Zeitschrift für angewandte Mathematik und Physik*, **43**, 757–792.

Chapter 5

Computational elastoacoustics of uncertain complex systems and experimental validation

Christian Soize, Chahoui Chen & Jean-François Durand

Université Paris-Est, Marne-la-Vallée, France

Denis Duhamel

Ecole des Ponts, Marne la Vallee, France

Laurent Gagliardini

PSA Peugeot-Citroen, Velizy-Villacoublay Cedex, France

ABSTRACT: The paper deals with the robustness of uncertain computational elastoacoustic models in low- and medium-frequency ranges. The elastoacoustic system is made up of a heterogeneous viscoelastic structure coupled with an internal acoustic cavity filled with a dissipative acoustic fluid. A reduced mean elastoacoustic model is deduced from the mean finite element model by using the modal approach with the structural modes of the structure and the acoustic modes of the acoustic cavity. Data uncertainties and model uncertainties are taken into account by using a nonparametric probabilistic approach for the structure, for the acoustic cavity and for the vibroacoustic coupling interface. The main objectives of this paper are (1) to present experimental validation of the nonparametric probabilistic approach of model uncertainties and to propose methods to perform the experimental identification of the probabilistic model parameters, (2) to analyze the robustness of computational elastoacoustic models with respect to model and data uncertainties, (3) to study uncertainty propagation through complex elastoacoustic systems. Two experimental configurations are analyzed with the stochastic computational elastoacoustic model. The first experimental configuration is made up of a composite sandwich panel coupled with an acoustic cavity constituted of a simple rigid box. Experimental measurements have been performed for 8 manufactured composite panels. The second experimental configuration is a car made up of a complex heterogeneous structure coupled with a complex acoustic cavity. Experimental measurements have been performed for 22 manufactured cars of the same type with optional extra.

1 Introduction

This chapter is devoted to computational elastoacoustics in low- and medium-frequency ranges of uncertain complex systems made up of a viscoelastic heterogeneous structure coupled with an internal acoustic cavity filled with a dissipative acoustic fluid. Usually, data uncertainties are taken into account by using a parametric probabilistic approach allowing uncertain parameters of the computational model to be

modeled by random variables. The mathematical-mechanical modeling process of the designed elastoacoustic system used to construct the computational model introduces model uncertainties which cannot be taken into account by the parametric probabilistic approach. Consequently, we propose to use the nonparametric probabilistic approach of data and model uncertainties recently introduced (see Soize (2001, 2005). The main objectives of this paper are (1) to present experimental validation of the nonparametric probabilistic approach of model uncertainties and to propose methods to perform the experimental identification of the probabilistic model parameters, (2) to analyze the robustness of computational elastoacoustic models with respect to model and data uncertainties, (3) to study uncertainty propagation through complex elastoacoustic systems. Two experimental configurations are presented and analyzed. The first experimental configuration is made up of a composite sandwich panel (the structure) coupled with an acoustic cavity constituted of a simple rigid box. We are interested in the internal noise produced by the vibration of the structure induced by a point force applied to the structure. Experimental measurements have been performed for 8 manufactured composite panels (see Chen (2006); Chen *et al.* (2006)). The second experimental configuration is a car made up of a very complex viscoelastic heterogeneous structure coupled with a complex acoustic cavity. We are interested in the booming noise which is the internal noise produced by the vibration of the structure induced by engine vibrations. Experimental measurements have been performed for 22 manufactured cars of the same type with optional extra (see Durand (2007); Durand *et al.* (2008)).

2 Uncertainties in the predictive model of a real elastoacoustic system

The designed elastoacoustic system is the system conceived by the designers and analysts. A designed elastoacoustic system, made up of a structure coupled with an internal acoustic cavity, is defined by geometrical parameters, by the choice of materials and by many other parameters. A designed elastoacoustic system such as a car is a very complex elastoacoustic system. The real elastoacoustic system is a manufactured version of the system realized from the designed elastoacoustic system. Consequently, the real elastoacoustic system is a man-made-physical system which is never exactly known due to the variability induced for instance by the process. The objective of a predictive model is to predict the output $(\mathbf{v}^{\exp}, p^{\exp})$ of the real elastoacoustic system to a given input $\mathbf{f}^{\exp}$, in which $\mathbf{v}^{\exp}$ is the response in displacement of the structure and where $p^{\exp}$ is the acoustic pressure inside the acoustic cavity. Such predictive models are constructed by developing mathematical-mechanical model of the designed elastoacoustic system for a given input (see Figure 5.1). Consequently, the mean model has an input $\underline{\mathbf{f}}$ modeling $\mathbf{f}^{\exp}$, an output $(\underline{\mathbf{v}}, \underline{p})$ modeling $(\mathbf{v}^{\exp}, p^{\exp})$ and exhibits a vector-valued parameter $\underline{\mathbf{s}}$ for which data has to be given. The errors are related to the construction of an approximation $(\underline{\mathbf{v}}^n, \underline{p}^n)$ of the output $(\underline{\mathbf{v}}, \underline{p})$ of the mean model for given input $\underline{\mathbf{f}}$ and parameter $\underline{\mathbf{s}}$ and have to be reduced and controlled using adapted methods developed in applied mathematics and in numerical analysis. The mathematical-mechanical modeling process of the designed elastoacoustic system introduces two fundamental types of uncertainties: data uncertainties and model uncertainties. Data uncertainties

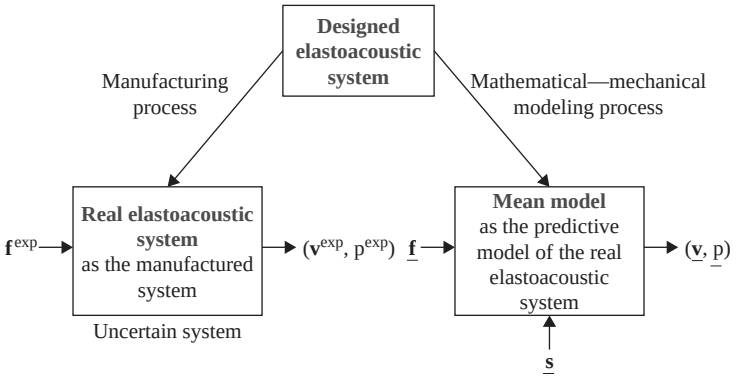

Figure 5.1 Designed elastoacoustic system, real elastoacoustic system and mean model as the predictive model of the real elastoacoustic system.

are input $\underline{\mathbf{f}}$ and parameter $\underline{\mathbf{s}}$ of the mean model. The best approach to take into account data uncertainties is the parametric probabilistic approach consisting in modeling the data of the mean model by random quantities. The mathematical-mechanical modeling process induces model uncertainties with respect to the designed elastoacoustic system. This type of uncertainties is mainly due to the introduction of simplifications in order to decrease the complexity of the mean model which is constructed. For instance, a slender cylindrical elastic structural element will be modeled by using the beam theory, a thick rectangular plate elastic structural element will be modeled by a thick plate theory, a sound proofing scheme between the structure and the acoustic cavity will be modeled by a wall acoustic impedance, the geometry of the acoustic cavity will be simplified, etc. It is clear that the introduction of such simplifications yields a mean model for which all the possible variations of its parameter $\underline{\mathbf{s}}$ do not allow the model uncertainties to be reduced. Model uncertainties have then to be taken into account to improve the predictability of the mean model. As explained above, the parametric probabilistic approach cannot be used. This is the reason why a nonparametric probabilistic approach is proposed. The error between prediction $(\underline{\mathbf{v}}^n, \underline{p}^n)$ calculated with the mean model and the response $(\mathbf{v}^{exp}, p^{exp})$ of the real elastoacoustic system can be measured by $(\|\mathbf{v}^{exp} - \underline{\mathbf{v}}^n\|^2 + \|p^{exp} - \underline{p}^n\|^2)^{1/2}$ in which $\|\,.\,\|$ denotes appropriate norms. Clearly, the mean model can be considered as a predictive model if this error is sufficiently small. In general, due to data uncertainties and model uncertainties, this error is not sufficiently small and has to be reduced by taking into account data uncertainties and model uncertainties.

3 Nonparametric probabilistic approach of model uncertainties

The concept of the nonparametric probabilistic approach of model uncertainties introduced in Soize (2001) is the following (see (Soize (2005)). Let $\mathbf{s} \mapsto \underline{A}(\mathbf{s})$ be a linear mapping from a space $\mathcal{S}$ into a space $\mathcal{A}$ of linear operators. The space $\mathcal{S}$ represents the

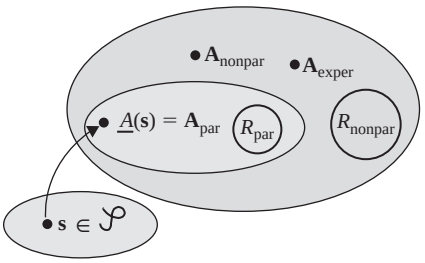

Figure 5.2 Parametric and nonparametric probabilistic approaches of random uncertainties.

set of all possible values of the vector-valued parameter $\mathbf{s}$ of the boundary value problem (for instance, geometric parameters, elastic properties, boundary conditions, etc). For $\mathbf{s}$ fixed in $\mathcal{S}$, operator $\underline{A}(\mathbf{s})$ represents one operator of the boundary value problem (for instance, the stiffness operator of the structure which is assumed to be symmetric and positive, and in this case, any operator in $\mathcal{A}$ will be symmetric and positive). Let $R_{\text{par}} \subset \mathcal{A}$ be the range of the mapping $\mathbf{s} \mapsto \underline{A}(\mathbf{s})$, i.e. the subset of $\mathcal{A}$ spanned by $\underline{A}(\mathbf{s})$ when $\mathbf{s}$ runs through $\mathcal{S}$. The corresponding operator of the real elastoacoustic system system is $\mathbf{A}^{\text{exp}}$ belonging to $\mathcal{A}$. If $\mathbf{s} = \underline{\mathbf{s}}$ is the nominal value, then $\underline{\mathbb{A}} = \underline{A}(\underline{\mathbf{s}}) \in R_{\text{par}}$ is the operator of the mean model.

Parametric probabilistic model of the operator. The parametric probabilistic approach for the operator consists in modeling the parameter $\mathbf{s}$ by a vector-valued random variable $\mathbf{S}$ whose probability distribution $P_{\mathbf{S}}(d\mathbf{s})$ has a support which is $\mathcal{S}$. Then the operator $\underline{\mathbb{A}}$ of the mean model is replaced in the the BVP by the random operator $\mathbf{A}_{\text{par}}$ such that $\mathbf{A}_{\text{par}} = \underline{A}(\mathbf{S})$. The probability distribution $P_{\mathbf{A}_{\text{par}}}$ of the random operator $\mathbf{A}_{\text{par}}$ is $P_{\mathbf{A}_{\text{par}}} = \underline{A}(P_{\mathbf{S}})$ and its support is the set $R_{\text{par}} \subset \mathcal{A}$ (see Figure 5.2). Clearly, the probability $P_{\mathbf{A}_{\text{par}}}$ on R_{par} allows data uncertainties to be taken into account, but $\mathbf{A}^{\text{exp}}$ may not be in R_{par} due to model uncertainties.

Nonparametric probabilistic model of the operator. The nonparametric probabilistic approach for the operator consists in replacing the operator $\underline{\mathbb{A}}$ of the mean model by a random operator $\mathbf{A}_{\text{nonpar}}$ whose probability distribution $P_{\mathbf{A}_{\text{nonpar}}}$ has a support which is $R_{\text{nonpar}} = \mathcal{A}$. Since $\mathbf{A}^{\text{exp}}$ belongs to $\mathcal{A}$ and since the support of $P_{\mathbf{A}_{\text{nonpar}}}$ is also $\mathcal{A}$, model uncertainties can be taken into account by the nonparametric approach (see Figure 5.2). Of course, $P_{\mathbf{A}_{\text{nonpar}}}$ cannot be arbitrary chosen with support R_{nonpar}, but has to be constructed using the available information. Such a methodology has been developed in Soize (2001, 2005) using the information theory.

Methodology. The methodology of the nonparametric probabilistic approach of uncertainties is as follows. (1) Developement of a finite element model of the designed elastoacoustic system. Such a model will be called the mean model (or the nominal model). (2) Construction of a reduced mean model from the mean model. (3) Construction of a stochastic reduced model from the reduced mean model using the nonparametric probabilistic approach which allows the probability distribution of each random generalized matrix to be constructed. (4) Construction and convergence analysis of the stochastic solution.

Experimental identification. The level of uncertainties is controlled by the dispersion parameter of each random matrix introduced in the nonparametric probabilistic approach. In this paper, we present methods for an experimental identification of the dispersions parameters.

4 Stochastic model of uncertain elastoacoustic systems

4.1 *Reduced mean model of the elastoacoustic system*

The elastoacoustic system is made up of a viscoelastic structure coupled with an internal acoustic cavity filled with a dissipative acoustic fluid. The usual formulation in "structural displacement" – "acoustic pressure" is used to construct the mean finite element method of the elastoacoustic system (see for instance Ohayon & Soize (1998)). Let $\underline{\mathbf{u}}(\omega)$ be the $\mathbb{C}^{n_s}$-vector of the n_s DOF of the structure and let $\underline{\mathbf{p}}(\omega)$ be the $\mathbb{C}^{n_f}$-vector corresponding to the the n_f DOF of the acoustic cavity. Let $\{\underline{\varphi}_1, \ldots, \underline{\varphi_{N_s}}\}$ be the N_s first structural modes of the structure in vacuo and calculated at zero frequency (not including rigid body modes if there exist). Let $\{\underline{\psi}_1, \ldots, \underline{\psi_{N_f}}\}$ be the N_f first acoustic modes of the acoustic cavity with rigid fluid-structure coupling interface (including the constant pressure mode if the acoustic cavity is closed). The reduced mean model is obtained by projection of the mean finite element model on the subspace $V_{N_s} \times V_{N_f}$ of $\mathbb{R}^{n_s} \times \mathbb{R}^{n_f}$ in which V_{N_s} is spanned by $\{\underline{\varphi}_1, \ldots, \underline{\varphi_{N_s}}\}$ and V_{N_f} is spanned by $\{\underline{\psi}_1, \ldots, \underline{\psi_{N_f}}\}$. The reduced mean model can then be written as

$$\underline{\mathbf{u}}(\omega) = \sum_{\alpha=1}^{N_s} \underline{q}^s_\alpha(\omega)\underline{\varphi}_\alpha, \quad \underline{\mathbf{p}}(\omega) = \sum_{\beta=1}^{N_f} \underline{q}^f_\beta(\omega)\underline{\boldsymbol{\psi}}_\beta. \tag{1}$$

The $\mathbb{C}^{N_s}$-vector $\mathbf{q}^s(\omega) = (q^s_1(\omega), \ldots, q^s_{N_s}(\omega))$ and the $\mathbb{C}^{N_f}$-vector $\mathbf{q}^f(\omega) = (q^f_1(\omega), \ldots, q^f_{N_f}(\omega))$ are the solution of the following matrix equation

$$\begin{bmatrix} -\omega^2[\underline{M}_s] + i\omega[\underline{D}_s(\omega)] + [\underline{K}_s(\omega)] & [\underline{C}] \\ \omega^2[\underline{C}]^T & -\omega^2[\underline{M}_f] + i\omega[\underline{D}_f] + [\underline{K}_f] \end{bmatrix} \begin{bmatrix} \underline{\mathbf{q}}^s(\omega) \\ \underline{\mathbf{q}}^f(\omega) \end{bmatrix} = \begin{bmatrix} \underline{\mathbf{f}}^s(\omega) \\ \underline{\mathbf{f}}^f(\omega) \end{bmatrix}, \tag{2}$$

in which the $(N_s \times N_s)$ real matrices $[\underline{M}_s]$, $[\underline{D}_s(\omega)]$ and $[\underline{K}_s(\omega)]$ are the generalized mass, damping and stiffness matrices of the structure, where the $(N_f \times N_f)$ real matrices $[\underline{M}_f]$, $[\underline{D}_f]$ and $[\underline{K}_f]$ are the generalized mass, damping and stiffness matrices of the acoustic and where the rectangular $(N_s \times N_f)$ real matrix $[\underline{C}]$ is the generalized vibroacoustic coupling matrix. In Eq. (2) the $\mathbb{C}^{N_s}$-vector $\underline{\mathbf{f}}^s(\omega)$ and the $\mathbb{C}^{N_f}$-vector $\underline{\mathbf{f}}^f(\omega)$ are the generalized force vector of the structure and the generalized acoustic source vector of the acoustic cavity respectively.

4.2 *Stochastic reduced model using the nonparametric probabilistic approach*

The principle of construction of the nonparametric probabilistic approach (see Soize (2001, 2005)) of model uncertainties and data uncertainties in the structure, in the

acoustic cavity and for the vibroacoustic coupling consists (1) in modeling the generalized mass $[\underline{M}_s]$, damping $[\underline{D}_s(\omega)]$ and stiffness $[\underline{K}_s(\omega)]$ matrices of the structure by random matrices $[\mathbf{M}_s]$, $[\mathbf{D}_s(\omega)]$ and $[\mathbf{K}_s(\omega)]$ whose dispersion parameters are δ_{M_s}, δ_{D_s} and δ_{K_s} respectively; (2) in modeling the generalized mass $[\underline{M}_f]$, damping $[\underline{D}_f]$ and stiffness $[\underline{K}_f]$ matrices of the acoustic cavity by random matrices $[\mathbf{M}_f]$, $[\mathbf{D}_f]$ and $[\mathbf{K}_f]$ whose dispersion parameters are δ_{M_f}, δ_{D_f} and δ_{K_f} respectively; (3) in modeling the generalized vibroacoustic coupling matrix $[\underline{C}]$ by a random matrix $[\mathbf{C}]$ whose dispersion parameter is δ_C. The explicit construction of the probability distribution of these random matrices were performed by using the maximum entropy principle and is given in Soize (2001) for random matrices $[\mathbf{M}_s]$, $[\mathbf{D}_s(\omega)]$, $[\mathbf{K}_s(\omega)]$, $[\mathbf{M}_f]$, $[\mathbf{D}_f]$ and $[\mathbf{K}_f]$, and is given in Soize (2005) for random matrix $[\mathbf{C}]$. Let $[\mathbf{A}]$ be anyone of these random matrices. In this theory, the probability distribution of such a random matrix $[\mathbf{A}]$ depends only on its mean value $[\underline{A}] = E\{[\mathbf{A}]\}$ in which E is the mathematical expectation and on its dispersion parameter δ_A which is independent of the matrix dimension. In addition, an algebraic representation of random matrix $[\mathbf{A}]$ has been developed and allows independent realizations to be constructed for a stochastic solver based on the Monte Carlo numerical simulation. It should be noted that when $[\mathbf{A}(\omega)]$ is a symmetric positive real-valued matrix depending on ω, then random matrix $[\mathbf{A}(\omega)]$ is written as $[\mathbf{A}(\omega)] = [\underline{L}_A(\omega)]^T [\mathbf{G}] [\underline{L}_A(\omega)]$ in which $[\underline{A}(\omega)] = [\underline{L}_A(\omega)]^T [\underline{L}_A(\omega)]$ and where the random matrix germ $[\mathbf{G}]$ is independent of ω and dispersion parameter δ_A must be taken independent of ω. Using such an approach, the stochastic reduced model of the uncertain elastoacoustic system for which the reduced mean model is defined by Eq. (2) is written, for all ω fixed in the frequency band of analysis $B = [\omega_0, \omega_1]$ with $0 < \omega_0 < \omega_1$, as

$$\underline{\mathbf{U}}(\omega) = \sum_{\alpha=1}^{N_s} \underline{Q}^s_\alpha(\omega)\underline{\varphi}_\alpha, \quad \underline{\mathbf{P}}(\omega) = \sum_{\beta=1}^{N_f} \underline{Q}^f_\beta(\omega)\,\underline{\boldsymbol{\psi}}_\beta, \tag{3}$$

in which, for ω fixed in B, the $\mathbb{C}^{N_s}$-valued random variable $\mathbf{Q}^s(\omega) = (Q^s_1(\omega), \ldots, Q^s_{N_s}(\omega))$ and the $\mathbb{C}^{N_f}$-valued random variable $\mathbf{Q}^f(\omega) = (Q^f_1(\omega), \ldots, Q^f_{N_f}(\omega))$ are the solution of the following random matrix equation

$$\begin{bmatrix} -\omega^2[\mathbf{M}_s] + i\omega[\mathbf{D}_s(\omega)] + [\mathbf{K}_s(\omega)] & [\mathbf{C}] \\ \omega^2[\mathbf{C}]^T & -\omega^2[\mathbf{M}_f] + i\omega[\mathbf{D}_f] + [\mathbf{K}_f] \end{bmatrix} \begin{bmatrix} \mathbf{Q}^s(\omega) \\ \mathbf{Q}^f(\omega) \end{bmatrix} = \begin{bmatrix} \underline{\mathbf{f}}^s(\omega) \\ \underline{\mathbf{f}}^f(\omega) \end{bmatrix}. \tag{4}$$

4.3 *Construction and convergence of the stochastic solution*

For all ω fixed in B, it can be proven that the probability model constructed for the random matrices is such that Eq. (4) has a unique second-order solution (see the methodology presented in Soize (2001)), i.e., $E\{\|\mathbf{Q}^s(\omega)\|^2\} \le c_1 < +\infty$ and $E\{\|\mathbf{Q}^f(\omega)\|^2\} \le c_2 < +\infty$. Concerning the stochastic solver, for all ω fixed in B, the stochastic solution of Eq. (4) is constructed by using the Monte Carlo numerical simulation with m independent realizations. Using the usual statistical estimator of the mathematical expectation E, the convergence of the stochastic solution with respect

to N_s, N_f and m, is studied in constructing the functions $(N_s, m) \mapsto \text{conv}^s(N_s, m)$ and $(N_f, m) \mapsto \text{conv}^f(N_f, m)$ such that

$$\text{conv}^s(N_s, m) = \left\{ \frac{1}{m} \sum_{k=1}^{m} \int_B \|\mathbf{U}(\omega, \theta_k)\|^2 \, d\omega \right\}^{1/2}, \tag{5}$$

$$\text{conv}^f(N_f, m) = \left\{ \frac{1}{m} \sum_{k=1}^{m} \int_B \|\mathbf{P}(\omega, \theta_k)\|^2 \, d\omega \right\}^{1/2}, \tag{6}$$

in which $\mathbf{U}(\omega, \theta_1), \ldots, \mathbf{U}(\omega, \theta_m)$ and $\mathbf{P}(\omega, \theta_1), \ldots, \mathbf{P}(\omega, \theta_m)$ are m independent realizations of $\mathbf{U}(\omega)$ and $\mathbf{P}(\omega)$ respectively.

5 Identification of the probabilistic model parameters from experiments

The problem to be solved is related to the experimental identification of the vector-valued dispersion parameter $\delta = (\delta_{M_s}, \delta_{D_s}, \delta_{K_s}, \delta_{M_f}, \ldots)$ introduced in the nonparametric probabilistic approach of data and model uncertainties. Let $\mathbf{Y}(\omega, \boldsymbol{\delta}) = (Y_1(\omega, \boldsymbol{\delta}), \ldots, Y_\mu(\omega, \boldsymbol{\delta}))$ be the $\mathbb{R}^\mu$-valued random variable corresponding to μ observations of the stochastic reduced model which will be measured for all ω belonging to frequency band B. This vector-valued random variable depends on the vector-valued dispersion parameter $\boldsymbol{\delta}$ which has to be identified using measurements. Since the manufactured systems have a variability induced by the manufacturing process, the corresponding observations of the real system must be modeled by a $\mathbb{R}^\mu$-valued random variable $\mathbf{Y}^{\text{exp}}(\omega) = (Y_1^{\text{exp}}(\omega), \ldots, Y_\mu^{\text{exp}}(\omega))$. It is assumed that the measurements are performed for ν manufactured real systems. Let $\mathbf{y}^{\text{exp},k}(\omega) = (y_1^{\text{exp},k}(\omega), \ldots, y_\mu^{\text{exp},k}(\omega))$ be the $\mathbb{R}^\mu$-vector of the μ measured observations for manufactured system number k. The mean value $\underline{\mathbf{Y}}(\omega, \boldsymbol{\delta})$ of random vector $\mathbf{Y}(\omega, \boldsymbol{\delta})$ and the mean value $E\{\mathbf{Y}^{\text{exp}}(\omega)\}$ of random vector $\mathbf{Y}^{\text{exp}}(\omega)$ are such that

$$\underline{\mathbf{Y}}(\omega, \boldsymbol{\delta}) = E\{\mathbf{Y}(\omega, \boldsymbol{\delta})\}, \quad E\{\mathbf{Y}^{\text{exp}}(\omega)\} = \underline{\mathbf{y}}^{\text{exp}}(\omega), \quad \underline{\mathbf{y}}^{\text{exp}}(\omega) = \frac{1}{\nu} \sum_{k=1}^{\nu} \mathbf{y}^{\text{exp},k}(\omega), \tag{7}$$

in which $\underline{\mathbf{y}}^{\text{exp}}(\omega)$ is the experimental mean value. Note that random vector $\mathbf{Y}^{\text{exp}}(\omega)$ is constructed such that its mean value is equal to $\underline{\mathbf{y}}^{\text{exp}}(\omega)$. Below, we present two methods which can be used to identify the vector-valued dispersion parameter $\boldsymbol{\delta}$ from experiments. The first one will be called the mean-square identification method and can be used for a vector-valued random variable without any difficulties. This method consists in minimizing, in the mean-square sense, the distance between the computed random response and the experimental response. The second one consists in using the maximum likelihood method and can also be used for a vector-valued random variable. Nevertheless, the computational time required by such a method is prohibitive if the vector-valued random variable has a high dimension. Consequently, we will present this method for a real-valued random variable.

5.1 *Mean-square identification method*

Let $\omega \mapsto \mathbf{X}(\omega) = (X_1(\omega), \ldots, X_\mu(\omega))$ be a $\mathbb{R}^\mu$-valued second-order stochastic process indexed by frequency band B. We introduce the norm $|||\mathbf{X}|||$ of $\mathbf{X}$ such that

$$|||\mathbf{X}|||^2 = E\{||\mathbf{X}||_B^2\}, \quad ||\mathbf{X}||_B^2 = \int_B ||\mathbf{X}(\omega)||^2 \, d\omega, \tag{8}$$

in which $||\mathbf{X}(\omega)||^2 = X_1(\omega)^2 + \cdots + X_\mu(\omega)^2$. The mean square identification of parameter $\boldsymbol{\delta}$ consists in minimizing the cost function $J_0(\boldsymbol{\delta}) = |||\mathbf{Y}(., \boldsymbol{\delta}) - \mathbf{Y}^{\exp}|||^2$ with respect to $\boldsymbol{\delta}$. In order to compute this cost function, we can write $|||\mathbf{Y}(., \boldsymbol{\delta}) - \mathbf{Y}^{\exp}|||^2 = |||\mathbf{Y}(., \boldsymbol{\delta}) - \underline{\mathbf{Y}}(., \boldsymbol{\delta}) - (\mathbf{Y}^{\exp} - \underline{\mathbf{y}}^{\exp}) + \underline{\mathbf{Y}}(., \boldsymbol{\delta}) - \underline{\mathbf{y}}^{\exp}|||^2$. Since $\underline{\mathbf{Y}}(., \boldsymbol{\delta}) - \underline{\mathbf{y}}^{\exp}$ is a deterministic vector and since $\mathbf{Y}(., \boldsymbol{\delta}) - \underline{\mathbf{Y}}(., \boldsymbol{\delta})$ and $\mathbf{Y}^{\exp} - \underline{\mathbf{y}}^{\exp}$ are independent and centered vector-valued random variables, we can write

$$J_0(\boldsymbol{\delta}) = |||\mathbf{Y}(., \boldsymbol{\delta}) - \underline{\mathbf{Y}}(., \boldsymbol{\delta})|||^2 + |||\mathbf{Y}^{\exp} - \underline{\mathbf{y}}^{\exp}|||^2 + ||\underline{\mathbf{Y}}(., \boldsymbol{\delta}) - \underline{\mathbf{y}}^{\exp}||_B^2. \tag{9}$$

In the right-hand side of Eq. (9), the first, the second and the third terms represent the variance of the random response of the stochastic model, the variance of the real system induced by its variability and the bias between the model and the real system, respectively. It should be noted that the second term is independent of $\boldsymbol{\delta}$. Consequently, the cost function $J_0(\boldsymbol{\delta})$ can be replaced by a cost function $J_1(\boldsymbol{\delta})$ obtained by removing this second term. Consequently, the mean square identification of parameter $\boldsymbol{\delta}$ consists in solving the following optimization problem

$$\boldsymbol{\delta}^{\text{opt}} = \arg\min_{\boldsymbol{\delta}} J_1(\boldsymbol{\delta}), \tag{10}$$

in which the cost function $J_1(\boldsymbol{\delta})$ is written as

$$J_1(\boldsymbol{\delta}) = |||\mathbf{Y}(., \boldsymbol{\delta}) - \underline{\mathbf{Y}}(., \boldsymbol{\delta})|||^2 + ||\underline{\mathbf{Y}}(., \boldsymbol{\delta}) - \underline{\mathbf{y}}^{\exp}||_B^2. \tag{11}$$

5.2 *Maximum likelihood method*

For the maximum likelihood method, we introduce the real-valued random variable $Z(\boldsymbol{\delta})$ for which the ν independent realizations $z^{\exp,1}, \ldots, z^{\exp,\nu}$ correspond to the ν manufactured real systems. Let $p_Z(z, \boldsymbol{\delta})\, dz$ be the probability distribution on $\mathbb{R}$ of $Z(\boldsymbol{\delta})$ represented by a probability density function $p_Z(z, \boldsymbol{\delta})$ which depends on dispersion parameter $\boldsymbol{\delta}$. This random variable is defined by

$$Z(\boldsymbol{\delta}) = \int_B \text{dB}(\omega, \boldsymbol{\delta})\, d\omega, \quad \text{dB}(\omega, \boldsymbol{\delta}) = 10 \log_{10}\left(w_{\text{ref}}^2 \frac{1}{\mu} \sum_{j=1}^{\mu} |Y_j(\omega, \boldsymbol{\delta})|^2 \right), \tag{12}$$

in which w_{ref} is a constant of normalization. It should be noted that, for all z fixed in $\mathbb{R}$, probability density function $p_Z(z, \boldsymbol{\delta})$ can easily be estimated with Eqs. (3) and

(4) using the Monte Carlo method and mathematical statistics. For $k = 1, \ldots, \nu$, the corresponding realization $z^{\exp,k}$ is written as

$$z^{\exp,k} = \int_B \mathrm{dB}^{\exp,k}(\omega)\, d\omega, \quad \mathrm{dB}^{\exp,k}(\omega) = 10 \log_{10} \left(w_{\mathrm{ref}}^2 \frac{1}{\mu} \sum_{j=1}^{\mu} |y_j^{\exp,k}(\omega)|^2 \right). \quad (13)$$

The use of the maximum likelihood method (see Serfling (1980)) leads us to the following optimization problem

$$\boldsymbol{\delta}^{\mathrm{opt}} = \arg \max_{\boldsymbol{\delta}} \mathcal{L}(\boldsymbol{\delta}), \quad (14)$$

in which $\mathcal{L}(\boldsymbol{\delta})$ is written as

$$\mathcal{L}(\boldsymbol{\delta}) = \sum_{k=1}^{\nu} \log_{10} (p_Z(z^{\exp,k}, \boldsymbol{\delta})). \quad (15)$$

6 Analyzing experimental configurations

6.1 *First experimental configuration: composite sandwich panel coupled with an acoustic cavity (Chen, 2006; Chen et al., 2006)*

The experimental configuration of the elastoacoustic system is defined in Figure 5.3. The system is made up of a composite sandwich panel coupled with a closed acoustic cavity constituted of an acoustic box with 5 rigid walls. The designed sandwich panel is constituted of five layers made of four thin carbon-resin unidirectional plies and one high stiffness closed-cell foam core. The geometrical and mechanical parameters for the composite sandwich panel and the acoustic box can be found in Chen (2006); Chen *et al.* (2006). Eight sandwich panels have been manufactured from the designed sandwich panel using an identical process and the same materials. All the sandwich panels have been baked in the same batch for suppressing the influences of the different

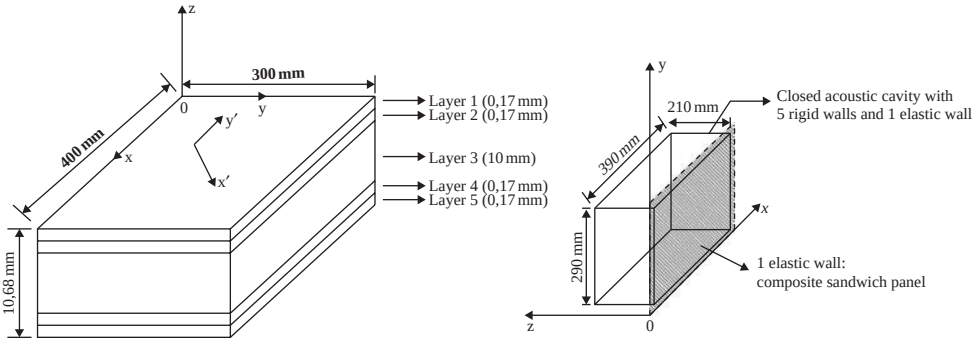

Figure 5.3 Definition of the composite sandwich panel (left figure). Vibroacoustic system made up of the composite sandwich panel and an acoustic cavity (right figure).

baking conditions concerning time and temperature. In addition one acoustic box with 5 rigid walls in the frequency band of analysis has been manufactured. The frequency band of analysis considered is the band $B = [10, 4500]\,Hz$ corresponding to the model validity of the mean finite element model of the vibroacoustic system. The input z-force is a point load applied to the point of coordinates $(0.187, 0.103, 0)$ m. The output z-acceleration at the observation point on the panel is the point of coordinates $(0.337, 0.272, 0)$ m. The mean finite element model of the composite sandwich panel is constituted of 62×46 four-nodes finite elements for laminated plate bending with orthotropic materials. The finite element model of the acoustic cavity is made up of $60 \times 40 \times 30$ eight-nodes solid acoustic finite elements. Consequently, there are $n_s = 8556$ structural DOF and $n_f = 72000$ acoustic DOF. The objective is to analyze the effects of structural uncertainties on the noise produced inside the acoustic cavity by the vibrations of the panel. Consequently, it is assumed that there are uncertainties in the panel but that there are no uncertainties neither in the acoustic cavity nor for the vibroacoustic coupling (this means that $\delta_{M_f} = \delta_{D_f} = \delta_{K_f} = \delta_C = 0$). Convergence of the stochastic reduced model over frequency band B is obtained for $N_s = 117$ structural modes, for $N_f = 630$ acoustic modes and for $m = 1300$ realizations. The experimental estimation of the dispersion parameters δ_{M_s}, δ_{D_s} and δ_{K_s} for the composite panels is performed in Chen (2006); Chen *et al.* (2006) using the method proposed in Soize (2005) and yields $\delta_{M_s} = 0.23$, $\delta_{D_s} = 0.43$ and $\delta_{K_s} = 0.25$. Figures 5.4 and 5.5 are related

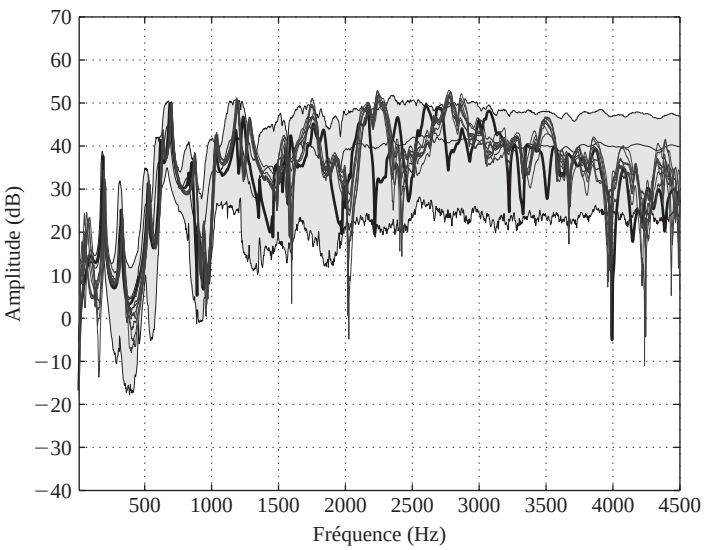

Figure 5.4 Experimental validation of the confidence region prediction for the random cross FRF between the input force applied to the panel and the transversal acceleration at the observation point on the panel for the vibroacoustic system. Horizontal axis: frequency in Hertz. Vertical axis: $\log_{10}$ of the modulus of the transverse acceleration of the panel. Experimental cross FRF corresponding to the 8 panels (8 thin solid lines). Numerical cross FRF calculated with the mean reduced matrix model (thick solid line). Mean value of the random cross FRF calculated with the non parametric probabilistic model (thin solid line). Confidence region of the random cross FRF calculated with the non parametric probabilistic model (grey region).

to the experimental validation of the confidence region prediction for the random cross frequency response functions (FRF) relative to the panel acceleration and to the acoustic pressure, and corresponding to a probability level of 0.96 (grey region). Figure 5.4 shows a good experimental comparison for the confidence region calculated with the stochastic reduced model. It should be noted that the confidence region is relatively narrow in the low-frequency (LF) band [10, 1200] Hz and is broad in the medium-frequency (MF) band [1200, 4500] Hz. These results show that the mean model is robust with respect to data and model uncertainties of the structure in the LF band but is less robust in the MF band. Such a result can also be viewed in comparing the response of the reduced mean model with the mean value of the random response of the stochastic reduced model. In the LF band the mean value of the random response is closed to the response of the mean model while large differences can occur in the MF band. Similarly, Figure 5.5 shows a good experimental comparison for the confidence region of the internal noise. It can be seen that the mean model is robust with respect to data and model uncertainties of the structure not only in the LF band [10, 1200] Hz but also in the low part [1200, 3000] Hz of the MF band while the robustness decreases in the high part [3000, 4500] Hz of the MF band. It can be conclude that the propagation of uncertainties from the structure into the acoustic cavity is weak in the frequency band

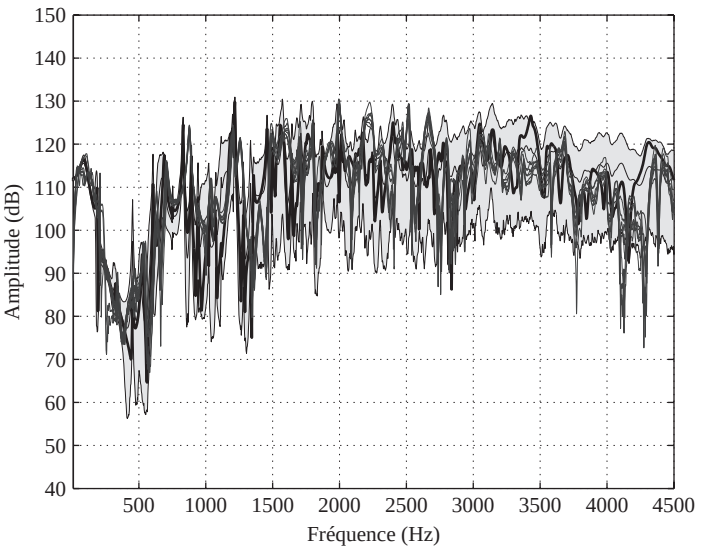

Figure 5.5 Experimental validation of the confidence region prediction for the random cross FRF between the input force applied to the panel and the acoustic pressure at the observation point in the acoustic cavity for the vibroacoustic system. Horizontal axis: frequency in Hertz. Vertical axis: $\log_{10}$ of the modulus of the acoustic pressure inside the acoustic cavity. Experimental cross FRF corresponding to the 8 panels (8 thin solid lines). Numerical cross FRF calculated with the updated mean reduced matrix model (thick solid line). Mean value of the random cross FRF calculated with the non parametric probabilistic model (thin solid line). Confidence region of the random cross FRF calculated with the non parametric probabilistic model (grey region).

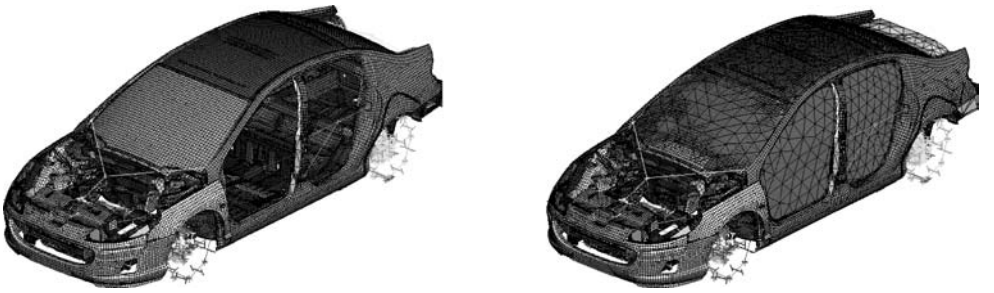

Figure 5.6 Finite element mesh of the structure: 978,733 DOF of displacement (left figure). Finite element mesh of the acoustic cavity: 8,139 DOF of pressure (right figure).

[10, 3000] Hz (LF band and low part of the MF band) and increases in the frequency band [3000, 4500] Hz (high part of the MF band).

6.2 *Second experimental validation: vibroacoustics of cars (Durand, 2007; Durand et al., 2008)*

We present an experimental validation of the numerical prediction of internal noise in a car due to engine excitation applied to the engine supports (booming noise). The mean finite element model is shown in Figure 5.6. The structure is modeled with $n_s = 978,733$ DOF of displacement and the acoustic cavity with $n_f = 8,139$ DOF of pressure. The frequency band of analysis $B = [33, 200]$ Hz corresponding to [1000, 6000] rpm (engine rotation per minute). Convergence of the stochastic reduced model over frequency band B is obtained for $N_s = 1722$ structural modes, for $N_f = 57$ acoustic modes and for $m = 600$ realizations. The experimental identification of the dispersion parameters are performed in three steps as follows (see Durand (2007); Durand *et al.* (2008)). For the first step, acoustic pressure measurements have been performed inside the acoustic cavity for a given acoustic source inside the cavity. Then the maximum likelihood method described in Section 5.2 has been used taking $\delta_{M_f} = \delta_{D_f} = \delta_{K_f}$, where $Y_j(\omega, \boldsymbol{\delta}) = P_{\ell_j}(\omega)$ in which $P_{\ell_1}(\omega), \ldots, P_{\ell_\mu}(\omega)$ are the observed acoustic pressures which are measured inside the cavity, with $w_{\text{ref}} = 1/P_{\text{ref}}$ in which P_{ref} is a reference pressure. For the second step, structural acceleration measurements have been performed in the structure for driven forces applied to the engine supports. Then the mean-square identification method described in Section 5.1 has been used with $Y_j(\omega, \boldsymbol{\delta}) = \log_{10}(w_j\,|U_{\ell_j}(\omega)|)$ in which $U_{\ell_1}(\omega), \ldots, U_{\ell_\mu}(\omega)$ are the observed displacements which are measured and where $w_1, \ldots, w_\mu$ are normalization constants such that $0 < w_j \leq 1$. In a third step, dispersion parameter δ_C of the vibroacoustic coupling operator has been fixed at a given value. Figure 5.7 displays the experimental validation of the numerical prediction of internal noise due to engine excitation with structure, vibroacoustic coupling and acoustic cavity uncertainties. Taking into account the complexity of the vibroacoustic system, there is a good experimental validation of the stochastic elastoacoustic model with model and data uncertainties. The variability of the manufactured real systems is due to the process and to the

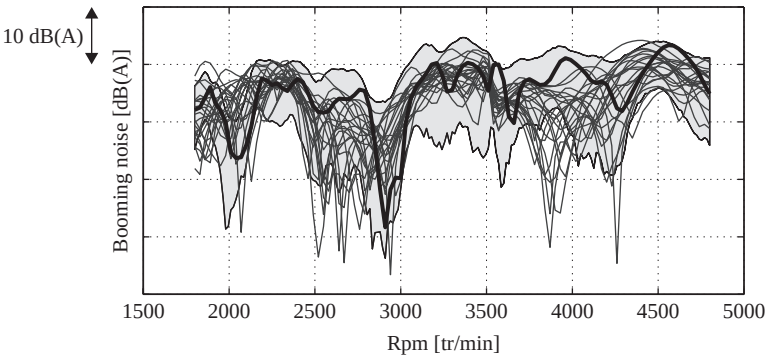

Figure 5.7 Experimental validation of the confidence region prediction for the random cross FRF between the input force applied to engine supports and the acoustic pressure at an observation point in the acoustic cavity for the vibroacoustic system. Horizontal axis: tr/min. Vertical axis: modulus of the acoustic pressure in dBA. 22 experimental measurements for 22 cars of the same type (22 thin solid lines). Numerical prediction of the mean reduced matrix model (thick solid line). Confidence region of the internal noise predicted with the non parametric probabilistic model and for probability level 0.95. (grey region).

extra options. The propagation of uncertainties is significant in the frequency band of analysis.

7 Conclusions

Data and model uncertainties can be taken into account in computational elastoacoustics by using the nonparametric probabilistic approach. Methodologies are proposed to perform an experimental identification of the dispersion parameters controlling the level of uncertainties. This approach has been validated for a simple and for a complex elastoacoustic system.

References

Chen, C. 2006. *Vibration et vibroacoustique des panneaux composites sandwich en présence d'incertitudes – Expérimentation et validation du modèle*. Thesis of the university of Marne la Vallée, Paris, France.

Chen, C., Duhamel, D. & Soize, C. 2006. Probabilistic approach for model and data uncertainties and its experimental identification in structural dynamics: case of composite sandwich panels. *Journal of Sound and vibration*, **294**, 64–81.

Durand, J.-F. 2007. *Modélisation de véhicules automobiles en vibroacoustique numérique avec incertitudes et validation expérimentale*. Thesis of the University of Marne la Vallée, Paris, France.

Durand, J.-F., Soize, C. & Gagliardini, L. 2008. Structural-acoustic modeling of automotive vehicles in presence of uncertainties and experimental identification and validation, *J.* Acoust. Soc. Am., **124**(3).

Lighthill, J. 1978. *Waves in Fluids*. Cambridge University Press, MA.

Ohayon, R. & Soize, C. 1998. *Structural Acoustics and Vibration*. Academic Press, San Diego.
Pierce, A.D. 1989. *Acoustics: An Introduction to its Physical Principles and Applications*. Acoust. Soc. Am. Publications on Acoustics, Woodbury, NY, USA, (originally published in 1981, McGraw-Hill, New York).
Serfling, R.J. 1980. *Approximation Theorems of Mathematical Statistics*, John Wiley & Sons.
Soize, C. 2001. Maximum entropy approach for modeling random uncertainties in transient elastodynamics, *Journal of the Acoustical Society of America*, **109**(5), 1979–1996.
Soize, C. 2005. Random matrix theory for modeling uncertainties in computational mechanics. *Computer Methods in Applied Mechanics and Engineering*, **194**(12–16), 1333–1366.

Chapter 6

Structural dynamics design validation and optimisation of structures with imprecise parameters using the fuzzy finite element method

David Moens, Dirk Vandepitte, Hilde De Gersem, Maarten De Munck & Wim Desmet

K.U. Leuven, Leuven, Belgium

ABSTRACT: After initial research in the field of fuzzy finite elements has started in the middle of the nineties, different aspects of the problem have been considered, and continuous development has improved not only the capabilities but also the performance of the procedures. The improvement of the performance of fuzzy finite element analysis is still a big challenge. Vertex analysis with n uncertain parameters requires 2^n deterministic analysis runs for each α-level that is considered. Another approach is optimisation, which is capable of predicting absolute maxima and minima. Unlike vertex analysis, the performance of optimisation procedures is unpredictable. There is a strong demand to reduce the computation time.

Structural dynamics is a specific type of problem that can also be tackled with interval or fuzzy finite elements. There is currently no generally applicable consistent approach to take into account the effect of parameter uncertainties on CMS reduction schemes. Some approximation procedures have been proposed, but they are sensitive to the particular case that is considered.

Two recent developments in fuzzy dynamic analysis are presented: a Response Surface Modelling method (RSM) and a new Component Mode Synthesis procedure (CMS).

1 Introduction

The fuzzy finite element method (FFEM) has become a most valuable tool for the analysis of structural dynamics problems with imprecise parameters. The present paper gives an overview of the status of development of the FFEM. The paper focuses specifically on the capabilities of the method, especially in early stages of design analysis. The formulation of design criteria in the presence of parameter uncertainties is reviewed and options for early design optimisation are discussed.

The first section presents the terms of reference with respect to the definition of the types of uncertainty and variability. The definitions by Oberkampf are extended with the concepts of intra-variability and inter-variability. The FFEM is most appropriate in early design stages when several problem parameters are only approximately known. In this respect, the FFEM is presented as a complementary alternative to the

well-known and well established probabilistic methods that are very appropriate to handle problems of variability.

The second section deals with the analysis methods that are used in fuzzy finite element analysis. An overview of different approaches is presented first: the transformation method, affine analysis, and global optimisation. The application to dynamic analysis is considered. The core of this section is the presentation of a consistent analysis approach to predict the effect of parameter uncertainties on different characteristics of dynamic behaviour of structures, resonance frequencies and dynamic response levels. A hybrid approach is developed, based on modal superposition and optimisation.

The paper then focusses on 2 recent developments, namely response surface methods (RSM) and component mode synthesis (CMS). The former is a strategy to approximate the real structural behaviour as modelled by repeated finite element calculations by a response surface model that interpolates for structural response between well-chosen settings of uncertain parameters. The latter is an established theory for modelling structural dynamics using superelements. The paper extends the deterministic CMS to models with fuzzy uncertain parameters in the superelements.

A few case studies illustrate the concepts and methods that are discussed.

2 Engineering analysis in early design stages

Engineering design is the activity of design and development of technical products. A technical product is built to fulfil a well specified function under more or less well prescribed conditions of utilisation. The complexity of modern technical products tends to increase systematically, increasing the need for thorough design analysis. This process consists of a number of analysis verifications on a virtual product. A common procedure for design verification is finite element analysis, a numerical method for the simulation of the effect of mechanical or thermal loads on a product. As most product parameters are undetermined in the initial phases of design, a range of uncertainties have to be taken into account. This paper presents a fuzzy finite element approach (FFE) for the analysis of product performance in an early stage of conceptual design.

A number of non-probabilistic approaches for non-deterministic analysis have been developed:

- the Interval FE (IFE) analysis is based on the interval concept for the description of non-deterministic model properties: a finite element model parameter may be represented by an interval number
- the Fuzzy FE (FFE) analysis is basically an extension of the IFE analysis: a finite element model parameter may be represented by a fuzzy number, which consists of an interval and a membership function

2.1 *Definitions*

In literature, the use of the terminology *uncertainty* and *variability* is not unambiguous. Different researchers apply the same terminology but the meaning attached to these is rather inconsistent. This necessitates a profound clarification of the terminology

for each publication which treats uncertainties. The definitions by Oberkampf *et al.* (1999) are found to be most consistent:

certain variability covers *the variation which is inherent to the modelled physical system or the environment under consideration*. Generally, this is described by a distributed quantity defined over a range of possible values. The exact value is known to be within this range, but it will vary from unit to unit or from time to time. Ideally, objective information on both the range and the likelihood of the quantity within this range is available.

In addition to the definitions by OBERKAMPF, variability may further be subdivided in two categories:

intra- variability refers to one product that is considered in different environmental conditions or in different phases of its life cycle

inter- variability refers to different realisations of one nominally identical product

invariable uncertainty is *a potential deficiency in any phase or activity of the modelling process that is due to lack of knowledge*. The word *potential* stresses that the deficiency may or may not occur. This definition basically states that uncertainty is caused by incomplete information resulting from either vagueness, nonspecificity or dissonance. Vagueness characterises information which is imprecisely defined, unclear or indistinct. It is typically the result of human opinion on unknown quantities.

incertain variability is an intermediate category in which model parameters may exhibit scatter within relatively well-known bounds, yet with unknown frequency of occurrence

Figure 1 conceptually compares these categories in the context of the FE methodology. In engineering analysis and design, the interpretation of these categories depends on the stage of development of a product. There generally is an evolution of the type of non-determinism encountered during a typical design process, as formulated by

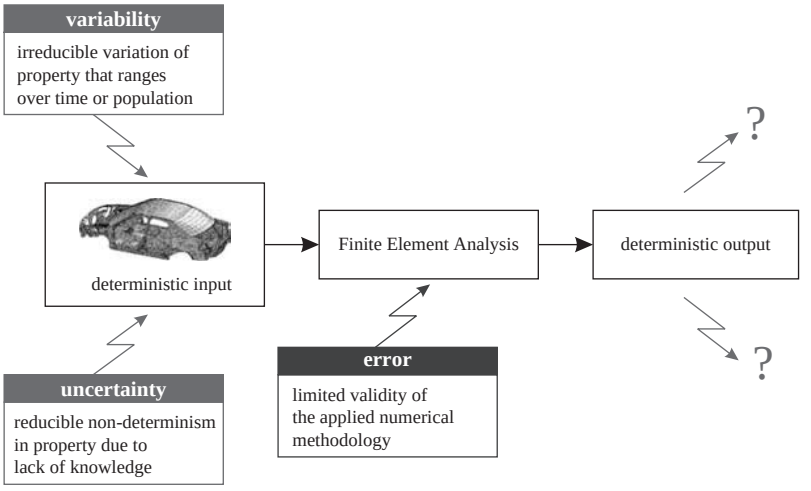

Figure 1 Occurrence of variabilities, uncertainties and errors in the FE procedure.

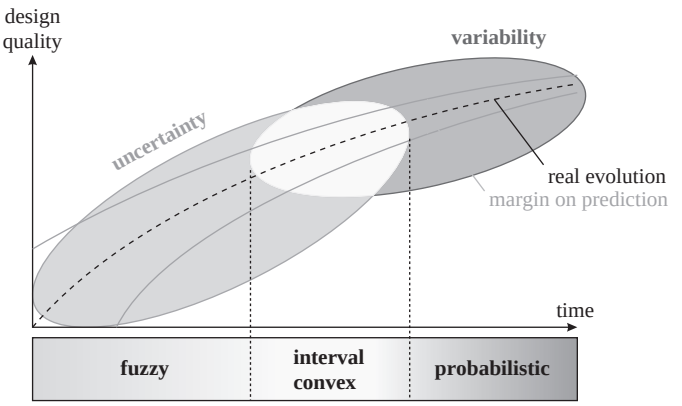

Figure 2 Typical occurrence of non-determinism in the product quality predictions during a design process.

Ross: *as more information about a problem becomes available, the mathematical description of non-determinism can transform from one theory to the next in the characterization of the uncertainty as the uncertainty diminishes or, alternatively, as the information granularity increases and becomes specific.*

2.2 *Interval and fuzzy methods in the evolution of the design process*

Usually more information on a product becomes available as design decisions are taken. The evolution of non-determinism in a typical design process as described above is illustrated in figure 2. The numerical prediction of the actual design quality improves over the design process. In the early stages, the non-determinism in the numerically predicted design quality is mainly driven by invariable model uncertainties, which may in later stages turn into uncertain variability. As the product final design is completed, certain variability may be the appropriate concept for data representation. This figure also indicates the evolution of the numerical concepts that are most appropriate for the dominant class of the occurring non-determinism. Individual model properties are modelled with fuzzy numbers in the initial design stages. This allows the analyst to start the analyst with a subjective interpretation of available data. The interpretation of results inevitably requires reference to the subjective data set. After some design decisions are taken, the property is described by an interval with objective, fixed bounds.

3 Non-probabilistic FE analysis for design purposes

Several strategies have been developed for FE analysis in early stages of engineering design.

3.1 *The interval FE analysis*

The goal of the IFE analysis is to obtain the maximal meaningful information on the possible outcome of the FE analysis when each model parameter is expressed either by an interval or by a crisp number. Numerically, this is equivalent to finding the minimal

and maximal deterministic analysis results taking into account all possible models that lie within the interval uncertainty description. In this section, FE analysis is considered in a black-box form, i.e. a mapping of input properties contained in the FE model to output quantities derived from the FE solution.

3.1.1 *Vertex analysis*

Dong & Shah (1987) first introduced the vertex method. This method approximates the range of the result of a numerical procedure by introducing all possible combinations of the boundary values of the input intervals into the analysis. For n input intervals, there are 2^n vertices for which the analysis has to be performed.

Despite its simplicity, this method have some important disadvantages. The computational cost increases exponentially with the number of input intervals. The main disadvantage of this method, however, is that it cannot identify local optima of the analysis function which are not on the vertex of the input space. It only results in the smallest hypercube if the analysis function is monotonic over the considered input range. This is a strong condition that is difficult to verify for FE analysis because of the complicated relation of analysis output to physical input uncertainties. The approximation obtained when monotonicity is not guaranteed is not necessarily conservative. This fact reduces the validity of this method for design validation purposes.

A more advanced formulation of vertex analysis is the transformation method which was developed by Hanss (2003). The fuzzy problem is converted into a series of deterministic calculations, which are taken to be all possible combinations of bounds on different parameters. The analyst has the option to include additional parameter combinations with intermediate values. This option may be useful when dealing with non-monotonic problems.

Both vertex analysis and the transformation analysis require a large number of deterministic analysis runs. Donders (2005) have derived the so-called short transformation from the original version by Hanss. The method reduces the number of calculations significantly with respect to the basic transformation method, but it suffer seven more from non-monotonicity. In preliminary design analysis however, results may be most valuable.

3.1.2 *The global optimisation strategy*

In essence, calculating the smallest hypercube around the solution set is equivalent to performing a global optimisation, aimed at the minimisation and maximisation of the components of the deterministic analysis results. The deterministic FE analysis is the goal function of the optimisation and the uncertain parameters are the design variables.

An efficient and robust optimisation algorithm is primordial for this solution strategy. Rao & Sawyer (1995) applied Powell's method to tackle the optimisation. Köylüoğlu *et al.* (1995) defined a linear programming solution for this purpose. The input interval vector defines the number of constraints and, therefore, strongly influences the performance of the procedure. Also, because of the required execution of the deterministic FE analysis in each goal function evaluation, the optimisation approach is numerically expensive. Therefore, this approach is best suited for rather small FE models with a limited number of input uncertainties, unless approximate methods can be used that avoid the expensive iterative calculation of the entire FE system of equations.

3.1.3 *The interval arithmetic strategy*

The interval arithmetic approach consists of translating the complete deterministic numerical FE procedure to an interval procedure using the arithmetic operations for addition, subtraction, multiplication and division of interval scalars. The outline of the interval procedure corresponds completely to the deterministic FE analysis.

This method suffers severely from over conservatism, as repeated numerical operations on interval quantities artificially increase the width of the interval. While nearly all literature on IFE is based on the solution phase, the interval matrix assembly phase was shown to have a very important contribution to the conservatism in the final analysis results (Moens & Vandepitte 2005).

3.1.4 *Affine analysis*

The basic formulation of interval arithmetic analysis does not allow to keep track of the relationships between uncertain parameters. The result of this inability is a degree of conservatism that is prohibitively high to be useful in practical applications. Manson (2003) proposes a strategy using affine analysis. The basic idea of affine arithmetic is to keep track of dependency between operands and sub-formulae whilst retaining much of the simplicity of interval arithmetic. As a result, tighter bounds are predicted than with interval arithmetic, especially when multiple iterations are necessary. MANSON has applied this approach on systems with two degrees of freedom where all equations can be written explicitly. For more complicated and less explicit operations like FE analysis, the affine analysis approach is still in development.

3.2 *The fuzzy FE analysis*

The principal goal of the FFE analysis is to obtain the membership function of the output quantities given the membership functions of all input quantities. It basically requires a concept to handle the combination of the fuzzy input sets. The usual practical procedure is by doing IFE analysis runs at each α-sublevel, as shown in figure 3.

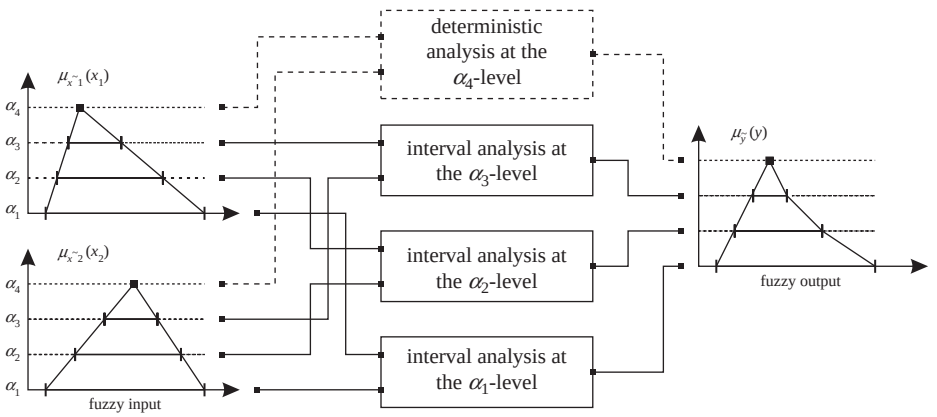

Figure 3 Scheme of the numerical procedure to perform a fuzzy FE analysis using 4 α-sublevels.

4 Deterministic and fuzzy modal superposition

Moens (2002) has developed a hybrid approach for fuzzy *frequency response functions (FRF)* FE analysis. The approach uses the classical concept of modal superposition. This section briefly presents the modal superposition principle, first in a deterministic formulation and then in a fuzzy formulation.

4.1 *Deterministic modal superposition FRF procedure*

For undamped structures, the FRF between degree of freedom (DOF) j and DOF k of an FE model is obtained taking the jth component of the displacement vector U satisfying the dynamic equilibrium equation

$$(K - \omega^2 M)U = F^k \tag{1}$$

with **K** and **M** the FE system matrices, ω the pulsation and F^k the force vector defined as

$$F_i^k = \begin{cases} 1 & \text{if } i = k \\ 0 & \text{if } i \neq k \end{cases} \tag{2}$$

The deterministic modal superposition concept states that, considering the first n modes, this FRF equals:

$$\mathrm{FRF}_{jk} = \sum_{i=1}^{n} \frac{1}{\hat{k}_i - \omega^2 \hat{m}_i} \tag{3}$$

with $\hat{k}_i$ and $\hat{m}_i$ the normalised modal stiffness and the normalised modal mass:

$$\hat{k}_i = \frac{\phi_i^T \mathrm{K} \phi_i}{\phi_{i_j} \phi_{i_k}} \quad \text{and} \quad \hat{m}_i = \frac{\phi_i^T \mathrm{M} \phi_i}{\phi_{i_j} \phi_{i_k}} \tag{4}$$

with ϕ_i the ith eigenvector of the system described by (1) and ϕ_{i_j} the jth component of this eigenvector.

Figure 4(a) gives a graphical overview of this deterministic modal superposition procedure. It introduces the function $\mathcal{D}(\omega) = (\hat{k}_i - \omega^2 \hat{m}_i)$ to express the modal response denominator as a function of the frequency.

4.2 *Interval modal superposition FRF procedure*

For undamped structures with one or more interval inputs, the total envelope FRF can be calculated using a step by step interval translation of the deterministic modal superposition procedure, as shown in figure 4(b).The full mathematical description of this method, developed by Moens, can be found in Moens & Vandepitte (2004). It consists of three major steps:

1. Calculation of the range of modal parameters: The first step in the procedure consists of the calculation of the range of modal parameters for each mode, taking into account the ranges of the input uncertainties. Theoretically, the modal parameters are coupled through the global system. The exact range of the modal parameters of mode i equals

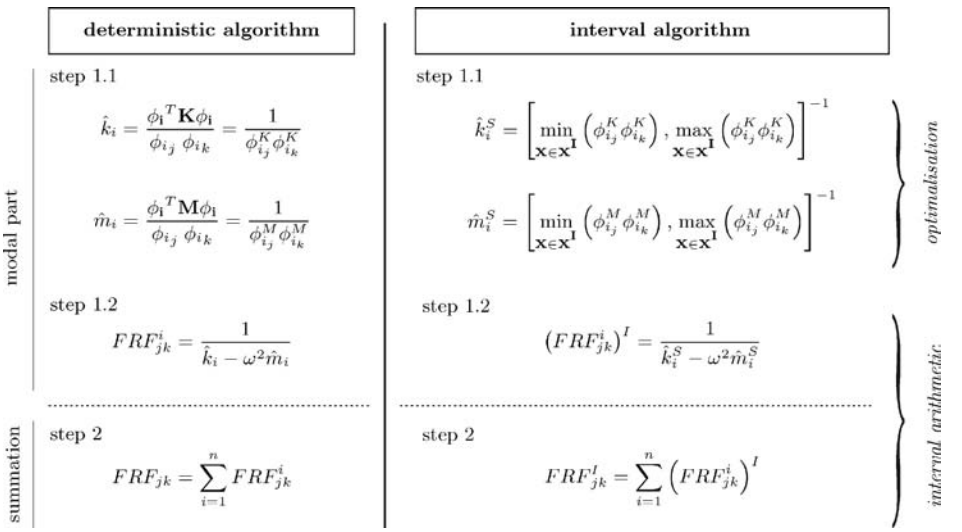

Figure 4 Deterministic and interval modal superposition algorithm.

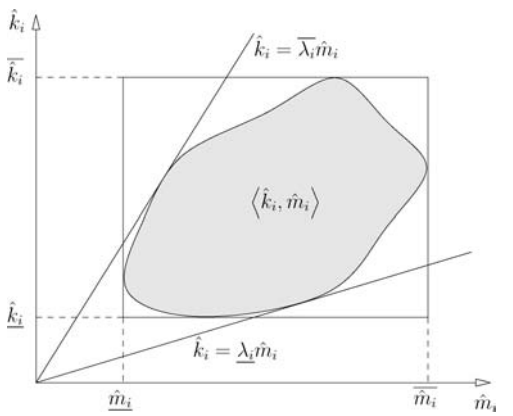

Figure 5 A$\langle \hat{k}_i, \hat{m}_i \rangle$-domain and its MR and MRE approximations.

$$\langle \{\hat{p}_i\} \rangle = \langle \hat{k}_i, \hat{m}_i \rangle = \{(\hat{k}_i, \hat{m}_i) | (\{x\} \in \{x\})\} \tag{5}$$

This can be represented in the modal parameter space of mode i, as illustrated by figure 5. The grey area represents a physically possible locus of $\langle \hat{k}_i, \hat{m}_i \rangle$ combinations. There is no general analytical description of the exact contour of this domain, but there area number of (conservative) numerical approximations:

- The *Modal Rectangle method* (MR) neglects the coupling between the modal stiff-ness and the modal mass. The bounds on the ranges are calculated by minimising and maximising the modal parameters $\hat{k}_i$ and $\hat{m}_i$ over the domain

defined by the input uncertainties. Graphically, this means that the $\langle \hat{k}_i, \hat{m}_i \rangle$-domain is approximated by a conservative rectangle.

- The *Modal Rectangle method with Eigenvalue interval correction* (MRE) aims at a less conservative approximation of the $\langle \hat{k}_i, \hat{m}_i \rangle$-domain through the introduction of the exact eigenvalue intervals $[\underline{\lambda_i}, \overline{\lambda_i}]$ in the procedure. These eigenvalue intervals can be obtained using a global optimisation approach similar to the modal parameter optimisation used in the MR method. Graphically, the MR $\langle \hat{k}_i, \hat{m}_i \rangle$-domain is constrained by two additional lines through the origin.

2. Modal envelope FRF calculation: This step translates the range of the modal parameters into the modal envelope FRF, expressed as the range of the modal frequency response function FRF^i_{jk}:

$$\mathrm{FRF}^i_{jk} = \frac{1}{\hat{k}_i - \omega^2 \hat{m}_i} \tag{6}$$

3. Total envelope FRF calculation: The final step for the computation of the total envelope FRF consists of the summation of all modal envelope FRFs resulting from the previous step:

$$\mathrm{FRF}_{jk} = \sum_{i=1}^{n} FRF^i_{jk} \tag{7}$$

Thus, the three step algorithm results in a hybrid procedure: in the first step, the $\langle \hat{k}_i, \hat{m}_i \rangle$-domain is approximated using a global optimisation approach; in the second and third step, the modal and total envelope FRFs are calculated using interval arithmetic.

5 Fuzzy FRF prediction using response surface methods

5.1 *Optimization algorithms for fuzzy envelope FRF calculation*

As explained in section 3.1.2 an interval FE analysis can be formulated as a numerical optimisation problem, with all uncertain parameters as design variables and the desired output quantity as the objective function. The optimisation procedures then has to be repeated for each individual output quantity of interest. This section presents an efficient approximate approach to reduce the calculation time, while keeping acceptable accuracy.

An MRE analysis requires six optimisations for each mode and – for fuzzy analyses – for each α-level of interest: the minimum and maximum modal stiffness ($\underline{\hat{k}_i}$ and $\overline{\hat{k}_i}$), modal mass ($\underline{\hat{m}_i}$ and $\overline{\hat{m}_i}$) and eigenvalue ($\underline{\lambda_i}$ and $\overline{\lambda_i}$). There are 3 objective functions that have to be evaluated: modal mass, modal stiffness and eigenfrequency. A fuzzy MRE analysis on 5 α-levels, taking into account 10 modes, requires already 300 optimisations. The objective function of these optimisation problems is an modal FE analysis, which can be computationally expensive itself. Thus to analyse anything but very simple models, an efficient optimisation algorithm is absolutely necessary.

Generic non-linear optimisers can solve all optimisation problems independent of each other. Theoretically, the optimisation problems can be non-convex, requiring global optimisation software, but analysis on different industrial sized applications (De Gersem *et al.*, 2005) showed that in practical applications almost all the objective functions are convex or even monotonic, even with large uncertainty intervals. For these problems, local optimisation software gives accurate results, although theoretically there is no guarantee that the results are even close to the exact results. Because local optimisation problems are computationally far less expensive to solve, an efficient local optimiser is the best overall choice, but the results should be examined carefully.

Since an FE solver can calculate all modal parameters for all modes of interest at once, the computational cost to calculate one objective function is equal to the computational cost to calculate all objective functions. Generic non-linear optimisers use only one of these objective functions. Other results however can be useful for other optimisations, for instance to select a suitable start vector. In most cases some optima – especially these located on a vertex – can even be found without performing additional FE analyses. Especially for larger FE models, storing all FE analysis results can cut the computational cost significantly.

By using response surfaces – approximations of the objective functions based on function evaluations in some well chosen points in the input parameter space – it is possible to cut the computational cost even further (Montgomery, 1997; Schuëller *et al.*, 1991a; Schuëller *et al.*, 1991b). Response surface based optimisation techniques prove to be extremely useful in the context of fuzzy analysis. A fuzzy analysis requires the same objective functions to be minimised and maximised on different α-levels or, in optimisation terms, with different bound constraints. Figure 6 shows this for two fuzzy uncertain parameters. The shaded rectangle shows the bound constraints for the optimisation at α-level 0.0. Response surfaces valid at this α-level should approximate the objective functions inside these bounds. The rectangles inside this shaded rectangle

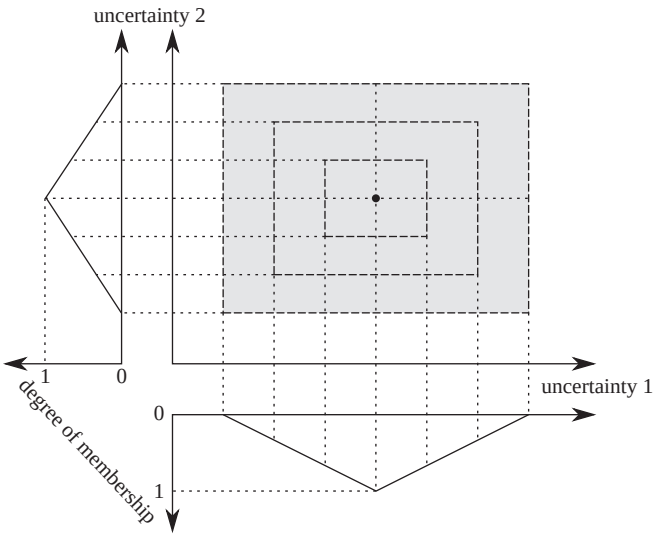

Figure 6 Optimisation bound constraints for an analysis with fuzzy uncertain parameters.

show the bound constraints for the optimisations at higher α-levels. It is clear that the same response surfaces approximate the objective functions at these α-levels too. Since the construction of the response surfaces is by far the computationally most expensive part of the algorithm, the computational cost of a fuzzy analysis is only slightly higher than the computational cost of an interval analysis when using a response surface based optimisation technique.

Also, when using a standard FE solver, the computational cost to evaluate all three objective functions for all modes is equal to the computational cost to evaluate one objective function for one mode. Because of the very low computational cost of a single evaluation of the response surface approximation function, the computational cost of a global optimisation on the response surface is feasible for most practical applications. These properties can be used to develop a very efficient optimisation algorithm for the full fuzzy FE algorithm (Munck *et al.*, 2006).

5.2 *Application: stiffened conical shell structure*

The procedure and the generic implementation are applied on an stiffened conical shell. Figure 7 shows the finite element model (left) and a schematic view on the cross section of the shell (right). The structure consists of five conical shell rings, connected and stiffened by stiffening rings. The finite element model consists of about 38000 nodes (228000 DOFs) and about 28000 elements (quadrilateral plate elements for the skin and five- and six-sided solid elements for the reinforcements). The model is subject to five uncertainties: the thicknesses of the shell structures between the reinforcement rings. These uncertainties are described using fuzzy numbers: (3/4/5) mm, (3/4/6) mm, (3/4/8) mm, (3/4/8) mm and (3/4/10) mm from the lower to the upper side of the structure. $(a/c/b)$ denotes a triangular fuzzy number with support $[a, b]$ and top c. These uncertain parameters and uncertain parameter ranges are specified by the designer of this conical shell structure.

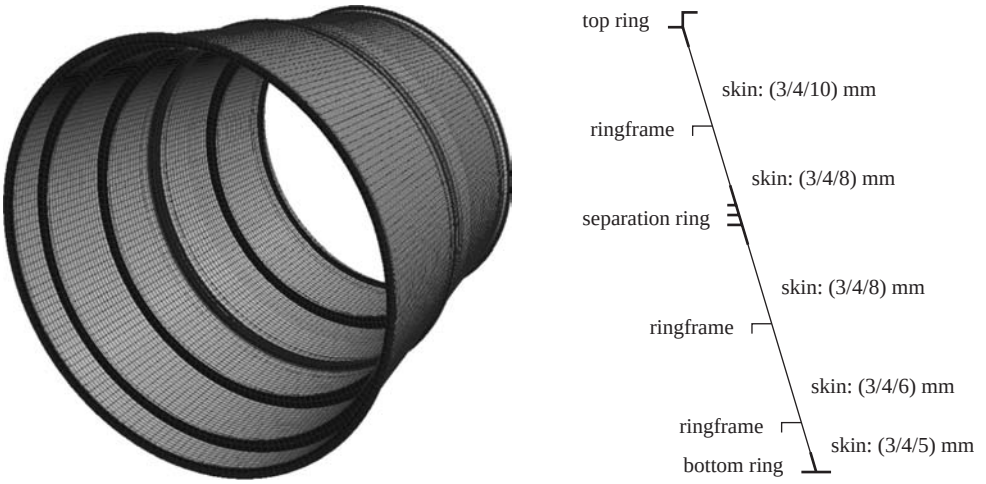

Figure 7 Finite element model (left) and schematic description (right) of the stiffened conical shell structure.

This conical structure serves as a connection between two relatively rigid structures, one rigidly bolted to the bottom ring and the other rigidly bolted to the top ring. Since at this design stage, the exact properties of these structures are unknown, they are modelled as rigid body elements. One is connected to all nodes on the bottom ring, the other one is connected to all nodes on the top ring. The acceleration transmittance FRF between the centres of these rigid body elements in the longitudinal direction is calculated.

The procedure described in sections 4.1 and 4.2 gives the ratio between the displacement in DOF j and the force applied in DOF k as a function of the frequency. If a very large mass m_0, several orders of magnitude larger than the mass of the entire structure, is connected to a DOF, the acceleration caused by a (harmonic) excitation in this DOF is approximately equal to:

$$f = m_0 \cdot a \tag{8}$$

MSC Software Corporation (2002) recommends that the value of m_0 is approximately 10^6 times the mass of the structure for translational DOFs and 10^6 times the moment of inertia for rotational DOFs. For a harmonic excitation $x = \sin(\omega t)$, the relation between the displacement and the acceleration is:

$$a = -\omega^2 \cdot x \tag{9}$$

Thus, the relation between the acceleration transmittance FRF ($\mathrm{FRF_{A/A}}$)and the receptance FRF($\mathrm{FRF_{X/F}}$)is:

$$\mathrm{FRF_{A/A}} = \frac{a_j}{a_k} = \frac{-\omega^2 x_j}{\frac{1}{m_0} f_k} = -\omega^2 m_0 \frac{x_j}{f_k} = -\omega^2 m_0 \cdot \mathrm{FRF_{X/F}} \tag{10}$$

The model is subjected to an MRE analysis using the response surface based optimisation developed by the authors Munck *et al.* (2006) and a vertex (also called two level full factorial design of experiments or transformation method) analysis. Each analysis is done at 6 α-levels(0.0, 0.2,...,1.0).

Based on the magnitude of the modal mass m_i and modal stiffness k_i, only three modes (number 1,2 and 13) contribute to the FRF. Because the contributions of the other modes are negligible compared to the contributions of these three modes, only these three modes are taken into account. Because the order of the modes can change when the uncertain parameters take different values, the modes are tracked using a modal assurance criterion (MAC). The MAC gives the correlation factor between two eigenvectors:

$$\mathrm{MAC_{XY}} = \frac{|X^{*T} W Y|^2}{(Y^{*T} W Y)(X^{*T} W X)} \tag{11}$$

where W is the weighting matrix which is the unity matrix in this case.

The MRE analysis requires 6 optimisations for each mode at each α-level taken into account. Since three modes are considered at five α-levels (the analysis at level 1.0 is a deterministic analysis), 90 optimisations are required. Using the automated

response surface based optimisation procedure, 41 deterministic analyses are required to construct response surfaces for all objective functions. The computational cost of the optimisation using the response surfaces is negligible compared to the computational cost to construct these response surfaces.

The vertex analysis solves the deterministic model for all combinations of minima and maxima of the uncertain parameters. For this model with 5 uncertainties, 32 (2^5) deterministic analysis are required at each α-level, except for α-level 1.0, where only 1 deterministic analysis is required. In total, 161 deterministic analyses are required.

The top graph of Fig. 8 shows the upper bound on the FRF at α-level 0.0, calculated using the MRE and vertex method. Additionally, all vertex samples are plotted. Using the vertex method, 32 deterministic analyses were needed to calculate this upper bound; using the MRE method and the response surface based optimisation technique, 41 deterministic analyses were needed. The bottom graph shows the relative difference between the MRE and vertex results. These results prove that the MRE method using the response surface based optimisation method is able to calculate the bounds on the FRF accurately.

Fig. 9 shows the fuzzy FRF assembled from the interval FRFs at α-levels 0.0,0.2,...,1.0. This FRF shows that the uncertain parameters influence all modes more or less equally, so the uncertainty on the FRF is about equal over the full frequency

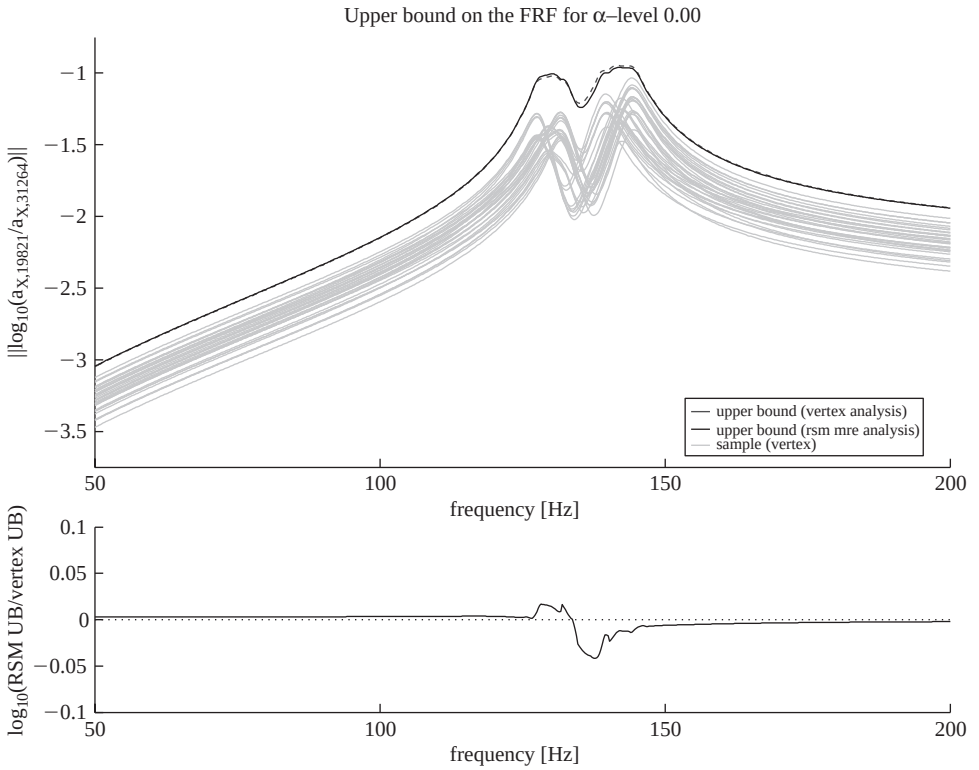

Figure 8 Upper bound on the FRF between the upper and lower ring of the structure.

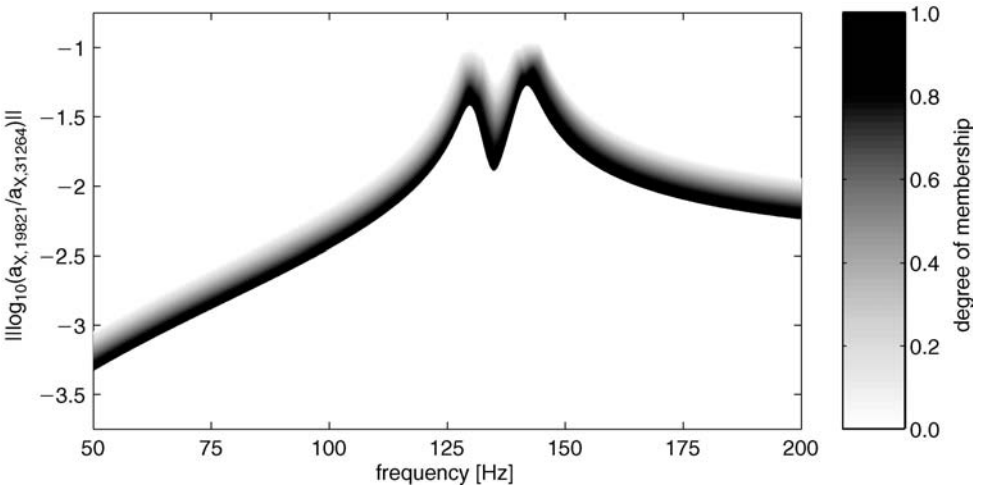

Figure 9 Fuzzy upper bound of the FRF between the upper and lower ring of the structure.

range of interest. 41 deterministic analyses are required to calculate this FRF using the MRE method and the response surface based optimisation technique. Using the vertex method, 161 ($2^5 \cdot 5 + 1$) analyses are required to calculate a similar FRF.

In this case, the RSM approach is 4 times more efficient than the vertex analysis.

6 Component mode synthesis with uncertain sub structures

The aim of the well-known Component Mode Synthesis (CMS) method is to reduce the computational cost of large models and to enable a solution strategy in which individual components can be optimised without the need for the recalculation of the total structure. The CMS technique consists of three global steps. First the structure is divided into a residual structure and a number of components, also referred to as substructures or superelements. For each component, a confined set of component modes is calculated, which represent its static and dynamic behaviour. In the second step, these component modes are used to reduce the component stiffness and mass matrices. In the third step, all reduced superelement models are combined with the non-reduced part of the structure to form the global reduced system, that is further used for global FE analyses.

This section first describes the main steps of the standard CMS approach. Uncertainty is then introduced afterwards.

6.1 *Deterministic CMS*

6.1.1 *Calculation of component modes*

For each component, all unconstrained degrees of freedom (dofs) are assigned to one of two specific sets. The set of boundary degrees of freedom (subscript t) contains all

dofs that connect the considered component to the residual structure or to another component. The remaining dofs are assigned to the set of internal dofs (subscript o, also referred to as "omitted" dofs). The stiffness and mass matrices of each component are assembled, and subsequently partitioned according to these sets (Craig & Bampton, 1968):

$$[K] = \begin{bmatrix} \overline{K_{tt}} & K_{to} \\ K_{ot} & K_{oo} \end{bmatrix} [M] = \begin{bmatrix} \overline{M_{tt}} & M_{to} \\ M_{ot} & M_{oo} \end{bmatrix} \tag{12}$$

For each component, a set of component modes is calculated. In literature, several approaches using different types of component modes for static and dynamic reduction are described. The Craig-Bampton method (Craig & Bampton, 1968) has been widely used and implemented in many finite element codes because the procedure for formulating the component modes is very straightforward, and because the method produces highly accurate results. The basic and most commonly applied version of the Craig-Bampton method uses constraint modes and fixed-interface normal modes to describe the static, respectively the dynamic behaviour of a component. Each constraint mode describes the static deformation of the component when a unit displacement (or rotation) is applied to one boundary degree of freedom, while the other dofs of the t-set are restrained. The static transformation matrix $[G_{ot}]$ with all constraint modes $\{\phi_i^C\}$ as columns, has the following mathematical description:

$$[G_{ot}] = [\{\phi_1^C\}\{\phi_2^C\} \ldots \{\phi_t^C\}] = -[K_{oo}]^{-1}[K_{ot}] \tag{13}$$

The fixed-interface normal modes, which form the columns of the dynamic transformation matrix $[G_{oq}]$, are calculated from the eigenvalue analysis of the component with all boundary dofs fixed:

$$[K_{oo}]\{\phi_i\} = \lambda_i[M_{oo}]\{\phi_i\} \tag{14}$$

$$[G_{oq}] = [\{\phi_1\}\{\phi_2\} \cdots \{\phi_q\}] \tag{15}$$

Each of these modes is assigned to a generalized degree of freedom (q-set). The accuracy of the dynamic reduction step is determined by the number of retained normal modes n_q. As the number of generalized degrees of freedom n_q needed for an accurate description of the dynamic behaviour of the component is usually several orders smaller than the number of internal dofs, the size of the component model is drastically reduced.

6.1.2 *Component reduction*

In the second step, the set of component modes is used for the transformation $[\Gamma]$ of the FE model from the set of physical dofs into the set of reduced dofs:

$$\begin{Bmatrix} x_t \\ x_o \end{Bmatrix} = [\Gamma] \begin{Bmatrix} x_t \\ x_q \end{Bmatrix} = \begin{bmatrix} [I] & [0] \\ [G_{ot}] & [G_{oq}] \end{bmatrix} \begin{Bmatrix} x_t \\ x_q \end{Bmatrix} \tag{16}$$

Using this transformation, the component stiffness and mass matrix are reduced to form the reduced superelement matrices (Craig & Bampton, 1968; MSC Software Corporation, 2001):

$$[K]_{reduced} = [\Gamma]^T[K][\Gamma] = \begin{bmatrix} K_{tt} & 0 \\ 0 & K_{qq} \end{bmatrix} \quad [M]_{reduced} = [\Gamma]^T[M][\Gamma] = \begin{bmatrix} M_{tt} & M_{tq} \\ M_{qt} & M_{qq} \end{bmatrix} \tag{17}$$

with:

$$[K_{tt}] = [\overline{K_{tt}}] + [K_{to}][G_{ot}] \tag{18}$$

$$[K_{qq}] = [G_{oq}]^T[K_{oo}][G_{oq}] \tag{19}$$

$$[M_{tt}] = [\overline{M_{tt}}] + [M_{to}][G_{ot}] + [G_{ot}]^T[M_{ot}] + [G_{ot}]^T[M_{oo}][G_{ot}] \tag{20}$$

$$[M_{tq}] = [M_{to}][G_{oq}] + [G_{ot}]^T[M_{oo}][G_{oq}] \tag{21}$$

$$[M_{qt}] = [M_{tq}]^T \tag{22}$$

$$[M_{qq}] = [G_{oq}]^T[M_{oo}][G_{oq}] \tag{23}$$

These reduced matrices represent the properties of the superelement as seen at its interface with adjacent structures. In case of mass normalised normal modes, the matrices $[K_{qq}]$ and $[M_{qq}]$ simplify to respectively a diagonal matrix with the eigenvalues and a unity matrix:

$$[K_{qq}] = [\Lambda_{qq}][M_{qq}] = [I_{qq}] \tag{24}$$

6.1.3 *Assembly of the reduced structural system*

In a last step, the reduced stiffness and mass matrices of all components are assembled with the non-reduced residual structure, to form the reduced stiffness and reduced mass matrix of the complete structural system. These can then be used to perform finite element analyses (e.g. an eigenfrequency or frequency response function analysis) on the global structure. Data recovery for each superelement is performed by expanding the solution at the attachment points, using the same transformation matrices that were used to perform the original reduction on the superelement.

6.2 *CMS with uncertain components*

For the calculation of the eigenvalue intervals of an uncertain structure with the global optimisation strategy, multiple eigenvalue problems have to be solved. Hence, the interval finite element method for dynamic analysis becomes very time-consuming for large systems. In this paper, the interval finite element method is combined with the component mode synthesis method, in order to reduce the calculation time. Uncertainties in a superelement of a reduced model affect each step of the reduction procedure: the uncertainties generally affect the constraint modes, the normal modes and corresponding eigenfrequencies, the static and dynamic transformation matrices, and the reduced stiffness and mass matrices. The following paragraphs describe several approaches for the implementation of this reduction step influenced by uncertainties: repeated

component reduction, approximative component reduction based on component eigenvalue ranges, non-reduced component matrices updating, and approximative component reduction with the use of deviatoric component modes.

6.2.1 *Repeated component reduction*

A first possible approach to handle uncertainties on the super-element level during an interval eigenfrequency analysis, is to recalculate the component modes, static and dynamic transformation matrices, and reduced matrices of each superelement affected by uncertain parameters, during each evaluation of the goal function of the global optimisation procedure. As in each iteration step all superelements are correctly reduced, this approach does not introduce any approximation, and its results can hence be used as reference. Although the implementation of this approach is straightforward, it limits the efficiency of the substructuring technique as for each eigenvalue analysis of the global structure, one or more superelement reduction steps have to be repeated.

6.2.2 *Approximative component reduction based on component eigenvalue ranges*

Another approach to handle uncertainties on the superelement level, is to approximate the description of an uncertain superelement, such that it can represent the effect of the uncertain parameters on the static and dynamic behaviour adequately, and no component recalculation has to be performed during a global interval or fuzzy analysis of the total reduced structural system.

In literature, the approximation of uncertain superelements is most often carried out by assuming that only the eigenvalues of the superelements are affected by the uncertain parameters, and that the component modes remain unaffected (Lallemand *et al.*, 1999; Mace & Shorter, 2001; Van den Nieuwenhof, 2003). For the Craig-Bampton method with mass normalized modes, this means that only the reduced matrix $[K_{qq}]$ is affected, while all other reduced matrices remain constant, as can be seen in equations (18)–(24). Therefore, in the reduction step of the algorithm, a separate interval eigenfrequency analysis is performed on the superelement in order to calculate the superelement eigenvalue ranges. After this preliminary interval eigenvalue analysis on the uncertain superelement, the reduced component matrix $[K_{qq}(\{s\})]$, containing the uncertainties through the calculated eigenvalue ranges, is included in the global reduced FE model. Hence, the uncertainty originally defined on the superelement is translated towards uncertainty affecting directly the reduced structure, and no further superelement calculations are required during all global interval analyses performed on the total reduced structure, resulting in a decrease of calculation time for these global uncertainty analyses.

6.2.3 *Non-reduced component matrices updating*

The assumption that uncertainties in a superelement only affect its eigenvalue ranges while the component modes and the other reduced matrices remain constant, might be too severe for general cases, e.g. when local geometrical uncertainties affect the component modes, or large stiffness and/or mass changes are present. Therefore, the method using only the eigenvalue ranges of the uncertain superelement might underestimate the real scatter on the output quantities calculated with the approximated reduced model.

Another approach for approximate component reduction is to update the non-reduced substructure matrices and recalculate the reduced matrices, in each iteration step of a global optimisation procedure on the reduced model, while the static and dynamic superelement transformation matrices are kept constant. This leads to a large reduction in calculation time, as on the superelement level only the system matrix assembly has to be performed, and no time-consuming matrix inversions or substructure eigenvalue analyses has to be performed. Mathematically, the approximative method comes down to the recalculation of the matrices in equations (17)–(23). However, care should be taken when calculating the reduced stiffness matrix, as coupling terms $[K_{tq}]$ similar to the mass coupling terms $[M_{tq}]$ arise due to the fact that the deterministic static transformation matrix $[G_{ot}]$ does not necessarily equal the term $-[K_{oo}]^{-1}[K_{ot}]$ with updated system matrices.

6.2.4 *Approximative component reduction using deviatoric component modes*

In case of large influence of the uncertain parameters on the component mode shapes, an expansion of the previous method with an approximation of the static and/or dynamic transformation matrices may be required. This paper proposes new strategy in which the component modes of a substructure are approximated with a summation of the deterministic component modes and some deviatoric mode shapes.

The CMS coordinate transformation is rewritten for explicit inclusion of uncertainties contained in the vector s:

$$\{x(s)\} = ([\Gamma_{det}] + [\Gamma_{dev}(s)])\{p(s)\} \tag{25}$$

In this equation, $\{x(s)\}$ represents the vector containing the physical coordinates of the component, $\{p(s)\}$ is the vector with component generalized coordinates, $[\Gamma_{det}]$ contains the deterministic component modes in its columns, and $[\Gamma_{dev}(s)]$ represents the matrix with deviatoric component modes. Hence, each (constraint/normal) component mode is augmented with a parameter-dependent deviatoric mode shape.

Consider first the case with only one uncertain parameter s, its associated uncertainty interval $[s_{min} - s_{max}]$ and deterministic value s_{det}. The evaluation of all component modes in the deterministic point and the two interval vertices, allows to calculate a second order polynomial approximation of each of the component modes, for brevity of notation here written as $\{\Psi(s)\}$:

$$\{\Psi(s)\} = \{\Psi(s_{det})\} + \{\Upsilon\}\Delta s + \{\Theta\}(\Delta s)^2 \tag{26}$$

with $\{\Upsilon\}$ and $\{\Theta\}$ the linear, respectively the quadratic contribution of the component mode and Δs the relative difference between the specific value for the uncertain parameter s and its deterministic value:

$$\Delta s = \frac{s - s_{det}}{s_{det}} \tag{27}$$

In the case with multiple uncertain parameters contained in the column vector s, a similar procedure can be performed. For each uncertain parameter s_i, two additional

analyses are performed, one in each vertex of the parameter interval with all other uncertain parameters kept at their respective deterministic value. Hence, for each uncertain parameter, the procedure for the one-parameter case is applied, and two deviatoric component mode contributions $\{\Upsilon_i\}$ and $\{\Theta_i\}$ are determined. With the contributions for all uncertain parameters, the approximation of the component mode $\{\Psi(s)\}$ becomes:

$$\{\Psi(s)\} = \{\Psi(s_{det})\} + \{\Upsilon_1\}\Delta s_1 + \{\Theta_1\}(\Delta s_1)^2 + \{\Upsilon_2\}\Delta s_2 + \{\Theta_2\}(\Delta s_2)^2 + \cdots + \{\Upsilon_{n_s}\}\Delta s_{n_s} + \{\Theta n_s\}(\Delta s_{n_s})^2 \quad (28)$$

$$= \{\Psi(s_{det})\} + \sum_{i}^{n_s} (\{\Upsilon_i\}\Delta s_i + \{\Theta_i\}(\Delta s_i)^2) \quad (29)$$

with $\Delta s_i = (s_i - s_{i,det}/s_{i,det})$. The proposed procedure can be interpreted as a quadratic response surface approximation with $1 + 2n_s$ response points, however of a vector function instead of a scalar function. Here, the mutual influence between the uncertain parameters has been ignored, and only two response points per parameter are considered (besides the deterministic case). For some applications, this simple response surface approximation yields good results. However, for other applications, a more sophisticated response surface may be required, with more response points per parameter and/or cross terms to cover part of the coupled parameter influence (De Munck *et al.*, 2006).

6.3 *Uncertainty in substructure matrices and component modes*

Uncertainties in a component of a CMS substructured FE model generally affect the non-reduced component matrices as well as the component modes which are used in the reduction step. Hence, in each iteration step of a global optimisation procedure, performed for the determination of the modal parameter ranges (see section 4.2), component modes and reduced matrices should be recalculated for each uncertain substructure. However, this limits the efficiency of the substructuring technique, as the computationally demanding component mode calculation (constraint modes, normal modes, ...) has to be repeated. Therefore, research has been performed that focusses on the development of approximative methods which enable an adequate uncertainty representation of component modes and/or reduced matrices, such that a large number of recalculations on the substructure level during global FE analyses on the reduced assembly model is avoided.

In literature, the approximation of an uncertain substructure is most often carried out by in the assumption that only the eigenvalues of the substructures are affected by the uncertain parameters, while the component modes remain unaffected (Mace & Shorter, 2001). A separate interval eigenvalue analysis is performed on each uncertain component in order to calculate the component eigenvalue ranges. Hence, the uncertainty originally defined on the substructure is translated towards uncertainty affecting directly the reduced structure, and no further component calculations are required during all global interval analyses performed on the reduced assembly.

The assumption that uncertainties in a substructure only affect its eigenvalue ranges while the component modes remain constant, might be too severe for general cases,

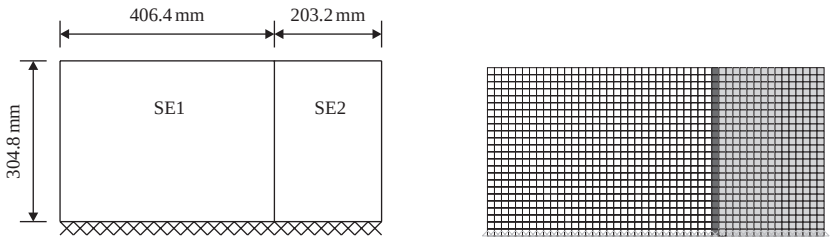

(a) Physical model with dimensions

(b) FE model with the small steel strip in dark gray

Figure 10 Cantilevered plate partitioned into two components.

e.g. when local geometrical uncertainties affect the component modes, or large stiffness and/or mass changes are present. In this context, the authors developed several approximative techniques that take into account uncertainties on component modes and non-reduced matrices (De Gersem *et al.*, 2007a). Recently a novel approach has been developed, in which the component modes of a substructure are approximated with a summation of the deterministic component modes and some deviatoric mode shapes. The accuracy of the results and the computational efficiency are promising (De Gersem *et al.*, 2007b).

6.4 *Numerical example*

A benchmark cantilevered plate model is considered, 609.6 by 304.8 mm (24 by 12 inches), with thickness $t = 3.175$ mm (0.125in.), divided into two unequal substructures, as shown in fig. 10(a). The material of the plate is 2024-T3 aluminium, with Young's modulus $E = 72$ GPa, Poisson's ratio $\nu = 0.33$, and mass density $\rho = 2800\ \text{kg/m}^3$. A finite element mesh of 48×24 square plate elements is used (1 in by 1 in each). The leftmost row of elements of the second substructure (SE2) represents a small steel strip, cf. fig. 10(b). The material properties of the steel are: Young's modulus of 210 GPa, Poisson's ratio of 0.3 and mass density of $7800\ \text{kg/m}^3$. A Craig-Bampton CMS model of the plate was created based on the lowest 5 eigenfrequencies, covering a frequency range of 200 Hz. For the construction of the substructured model, fixed-interface normal modes up to 700 Hz were retained for both substructures: 9 modes for the left hand part (SE1), and 5 for the right hand part (SE2). In addition, there are 150 constraint modes (25 nodes $\times$ 6 dofs), yielding a CMS model with 164 dofs. For reference, it is verified that the first 5 eigenfrequencies of this CMS model are all within 0.1% of the corresponding FEM eigenfrequencies.

The influence of an interval uncertainty on the Poisson's ratio of the aluminium on the eigenfrequencies of the reduced structural system is considered. 4 different methods are used to quantify the effect of the Poisson parameter. The results of the analyses on the 4 lower resonance frequencies are shown in fig. 11:

- vertex analysis (marked with red "+")
- Monte Carlo simulation, with 50 randomly distributed samples in the uncertainty interval [0.25, 0.35]; this analysis is taken as a reference the solid (green) line represents the results of a reference Monte Carlo Simulation

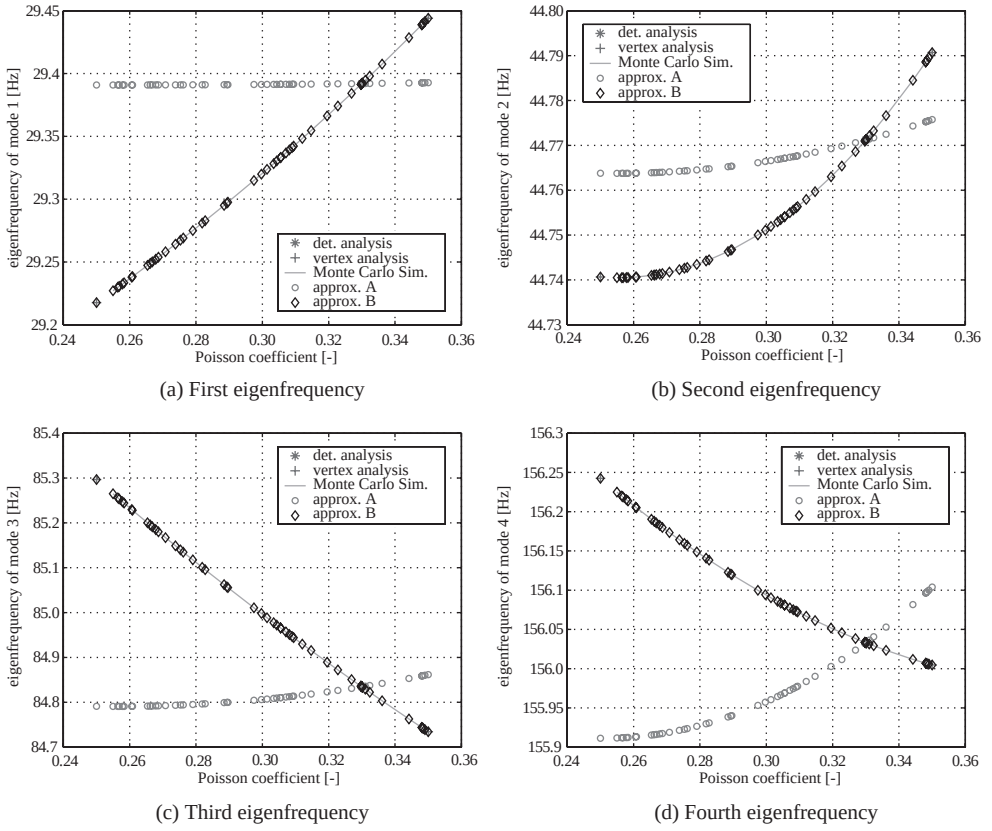

(a) First eigenfrequency

(b) Second eigenfrequency

(c) Third eigenfrequency

(d) Fourth eigenfrequency

Figure 11 Influence of the Poisson coefficient on the first four eigenfrequencies.

- approximation A (marked with magenta "∘"), based on component eigenvalue ranges only
- approximation B (marked with grey " ◇"), using deviatoric component modes

The deterministic analysis ($\nu = 0.33$) is marked at the intersection of the curves. These figures clearly show that the approximative method using only the eigenvalues of the uncertain superelement is not sufficiently accurate for the prediction of the influence of the chosen uncertainty. This can be explained by the fact that the uncertain parameter mainly influences the stiffness of the substructure and the many constraint modes, while the variation of the sub-structure eigenvalues is limited. For the third and fourth eigenfrequencies of the assembly, the general trend is even wrongly predicted by this approximative method. The results of the approach based on the use of deviatoric component modes almost coincide with the reference results.

7 Conclusions

This paper gives an overview of the current state of development of the fuzzy finite element method for dynamic analysis. After a review of definitions and generic analysis

approaches, a hybrid method for FRF prediction is discussed. The paper then presents 2 recent enhancements to the hybrid – optimisation and interval arithmetic – procedure for fuzzy envelope FRF calculation.

The first improvement uses a Response Surface Methodology to reduce the calculation time. It takes advantage of the special properties of the optimisation problems. The result is a highly efficient procedure for interval and especially fuzzy finite element analysis.

The other improvement is in the field of Component Mode Synthesis. A new scheme is developed to take into account the effect of uncertain parameters in the transformation matrices in the component mode reduction phase. It is shown that static and dynamic component modes may change with parameter uncertainties. In order to improve the accuracy of the analysis, it is required that these component mode sensitivities are explicitly taken into account.

Acknowledgement

The authors gratefully acknowledge the support of FWO-Vlaanderen (Flemish Fund for Scientific Research) and the European Commission (Marie Curie Research & Training Network "Maduse").

References

Craig, R.R. & Bampton, M.C.C. 1968. *Coupling of substructures for dynamic analyses*, AIAA Journal, 6(7):1313–1319.

De Munck, M., Moens, D., Desmet, W. & Vandepitte, D. 2006. *An automated response surface based optimisation technique for the calculation of fuzzy envelope FRFs of models with uncertain properties*, Proceedings of the International Conference on Noise and Vibration Engineering ISMA 2006, pages 4091–4103, Leuven, Belgium.

De Munck, M., Moens, D., Desmet, W. & Vandepitte, D. September 2006. *An automated response surface based optimisation technique for the calculation of fuzzy envelope FRFs of models with uncertain properties*, Proceedings of the International Conference on Noise and Vibration Engineering ISMA 2006, Leuven, pp. 4091–4104.

De Gersem, H., Moens, D., Desmet, W. & Vandepitte, D. 2005. *A fuzzy finite element procedure for the calculation of uncertain frequency response functions of damped structures: Part II – numerical case studies*, Journal of Sound and Vibration, 288(3):463–486.

De Gersem, H., Moens, D., Desmet, W. & Vandepitte, D. 2007. *Interval and fuzzy eigenfrequency analysis of uncertain substructured FE models*, Computer Assisted Mechanics and Engineering Sciences (CAMES), in press.

De Gersem, H., Moens, D., Desmet, W. & Vandepitte, D. June 2007. *On the use of deviatoric component modes for the assessment of uncertainty in Component Mode Synthesis*, Proceedings of the 1st International Conference on Uncertainty in Structural Dynamics, Sheffield.

Donders, S., Vandepitte, D., Van de Peer, J. & Desmet, W. 2005. *Assessment of uncertainty on structural dynamic responses with the short transformation method*, Journal of Sound and Vibration, Vol. 288, No.3, pp. 523–549.

Dong, W. & Shah, H. 1987. *Vertex Method for Computing Functions of Fuzzy Variables* Fuzzy Sets and Systems, Vol. 24, pp. 65–78.

Hanss, M. 2003. *The extended transformation method for the simulation and analysis of fuzzy-parameterized models*, International Journal of Uncertainty, Fuzziness and Knowledge-Based Systems, Vol. 11, No.6, pp. 711–727.

Köylüoğlu, U., Çakmak, A. & Nielsen, S. 1995. *Interval Algebra to Deal with Pattern Loading and Structural Uncertainties*, Journal of Engineering Mechanics, Vol. 121, No. 11, pp. 1149–1157.

Lallemand, B., Cherki, A., Tison, T. & Level, P. 1999. *Fuzzy modal finite element analysis of structures with imprecise material properties*, Journal of Sound and Vibration, Vol. 220, No.2, pp. 353–364.

Mace, B.R. & Shorter, P.J. 2001. *A local modal/perturbational method for estimating frequency response statistics of built-up structures with uncertain properties*, Journal of Sound and Vibration, 242(5):793–811.

Manson, G. February 2003. *Sharper eigenproblem estimates for uncertain multi-degree of freedom systems*, Proceedings of IMAC XXI CDrom, Orlando, Florida, USA, pp. 8.

Moens, D. 2002. *A Non-Probabilistic Finite Element Approach for Structural Dynamic Analysis with Uncertain Parameters*, Ph.D. thesis, K.U. Leuven, Leuven.

Moens, D. & Vandepitte, D. 2004. *An interval finite element approach for the calculation of envelope frequency response functions*, International Journal for Numerical Methods in Engineering, Vol. 61, No.14, pp. 2480–2507.

Moens, D. & Vandepitte, D. 2005. *A Survey of Non-Probabilistic uncertainty treatment in Finite Element Analysis*, Computer Methods in Applied Mechanics and Engineering, Vol. 194, Nos. 12–16, pp. 1527–1555.

Montgomery, D.C. 1997. *Design and analysis of experiments*, Wiley, New York, 4th edition.

MSC Software Corporation, 2002. *MSC. Nastran Basic Dynamic Analysis User's Guide*.

MSC Software Corporation, 2001. *MSC. Nastran superelement user's guide*, Los Angeles.

Oberkampf, W., DeLand, S., Rutherford, B., Diegert, K. & Alvin, K. 1999. *A New Methodology for the Estimation of Total Uncertainty in Computational Simulation*, Proceedings of the 40th AIAA/ASME/ASCE/AHS/ASC Structures, Structural Dynamics and Materials Conference, AIAA-99-1612, pp. 3061–3083.

Rao, S. & Sawyer, P. 1995. *Fuzzy Finite Element Approach for the Analysis of Imprecisely Defined Systems*, AIAA Journal, Vol. 33, No. 12, pp. 2364–2370.

Schuëller, G.I., Bucher, C.G. & Pradlwarter, H.J. 1991. *Efficient computational procedures for reliability estimates of mdof systems*, Journal of Nonlinear Mechanics, 26(6):961–974.

Schuëller, G.I., Bucher, C.G. & Pradlwarter, H.J. 1991. *The response surface method – an efficient tool to determine the failure probability of large structural systems*, Proceedings of the International Conference on Spacecraft Structures and Mechanical Testing, pages 247–251, Noordwijk, The Netherlands.

Van den Nieuwenhof, B. 2003. *Stochastic finite elements for elastodynamics: random field and shape uncertainty modelling using direct and modal perturbation-based approaches*, Ph.D. thesis, Université catholique de Louvain, Louvain-La-Neuve, Belgium.

Zadeh, L. 1965. *Fuzzy sets*, Information and Control, 8(3):338–353.

Chapter 7

Morphological indicators and the prediction of the first natural frequency of a lightweight structure

Willy Patrick De Wilde

Vrije Universiteit Brussel, Brussels, Belgium

Jan Van Steirteghem

Besix Belgium, Brussels, Belgium

ABSTRACT: Morphological indicators are dimensionless numbers that represent a property of a structure (e.g. volume, stiffness . . .) and depend only on a small number of variables (Samyn, 1999). These indicators allow for optimization at the stage of conceptual design. The most important indicators are the indicator of volume, related to the strength of the structure, and the indicator of displacement, related to the stiffness of the structure. These indicators, in their most simple appearance, are function only of the geometrical slenderness of the structure, under the assumption that the structure is not subjected to second order effects and that shear effects are not predominant. The indicator of volume allows choosing the structural typology with a minimum of volume of material. When using the indicator of volume at the stage of conceptual design, important areas of slenderness appear to bring about problems of resonance. This is particularly the case for structures which have predominant co-vibrating loads, have large spans and are using a material with a small stiffness/strength ratio. A practical example is discussed and some general design guidelines are proposed.

1 Introduction: morphological indicators

The so-called morphological indicators (MI) were introduced by Samyn (1999). As different papers, both within this conference and in other journals and books (see e.g. a more recent book of Samyn (2004)), have already or will underline the potentials of these dimensionless numbers, we will restrict ourselves to a very short introduction. Samyn (1999, 2000, 2004) essentially introduced two indicators, one related to the minimum volume of material required for a structural typology achieving a fully stressed design, the other related to the maximum displacement in the same structure. The combination of those two indexes, being the volume indicator W and the displacement indicator σ allow the designer to select not only a (sub)optimal typology but also its optimal aspect ratio (defined hereunder as the *slenderness*). The indicators are dimensionless numbers, function of very few parameters, the most important being the so-called *slenderness* of the structure L/H, in which L is the larger and H the lesser dimension of a window, framing the structure.

Samyn (1999) defined them as:

a) $W = (\sigma V/FL)$, in which σ is the admissible stress (in practice we consider the allowable stress in the serviceability limit state (SLS), V the volume of material, F the resultant of (static) forces, loading the structure, and L its span.
b) $\Delta = (E\delta/\sigma L)$, in which E is the elastic modulus and δ the maximum displacement.

He also shows that they can be expressed as a function of L/H: W = W(L/H) and $\Delta = \Delta$(L/H). This allows to draw, either analytically or numerically, diagrams showing the values of the indicators in function of the slenderness, for different typologies of structures. The recent book of Samyn (2004), although not exhaustive, contains an impressive amount of typologies, which can be compared: see Fig. 1 as an example of a comparison of different Warren trusses through the volume indicator: this diagram is taken from Samyn et al. (1998). Similar graphs were developed for the displacement indicator Δ.

It is clear that Samyn (1999) hereby provided the architect with "*a tool allowing to reach a suboptimal design at the stage of the conceptual design*". The fact that he is still using it today, and undoubtedly producing designs of outstanding quality, proves the robustness and the reliability of the tools he introduced.

However, two major objections could be foreseen and they were very soon subject of controversy. Indeed, the two indicators allow for a preliminary design, achieving the required performances of *strength* and *stiffness* with a minimum volume of material (a fully stressed design of statically determinate structures, subject to classical load cases) ... but what about other phenomena like e.g. *(in)stability* and possible *resonance*? Let us state here that we are convinced that conceptual design should take into account the *totality* of the performance criteria to be satisfied by any structure:

- the *strength* of its structural parts is controlled through the *indicator of volume*: $W = (\sigma V/FL)$, as it starts from a fully stressed design (at a stress level σ). In the conceptual design stage, a minimal value of this indicator is aimed at, thus trying to achieve a minimal consumption of material. But, as we shall experience very quickly, a mere choice of the slenderness L/H, corresponding to a minimum of the curve for the chosen typology (see e.g. fig. 1) does not solve the problem! The reason is simple: this simple minimisation does not take into account the stiffness, stability ... and dynamic requirements of the design. In this sense we could say that each of the three other criteria additionally introduce kinds of "*forbidden zones*" in the W = W(L/H) diagrams: a forbidden zone for the excessively flexible structures, one for the unstable structures and eventually one – if relevant – for the unacceptable vibrations.
- the *stiffness* of the structure is evaluated through the *indicator of displacement*: $\Delta = (E\delta/\sigma L)$. As one can see, it is proportional to the ratio Δ/L, which is generally limited by design codes (see e.g. Eurocodes). As we will show later this indicator, originally introduced by P. Samyn will be of primordial importance when evaluating the risk for resonance of a structure.
- through the *buckling indicator* $\Psi = (\mu\sigma L/\sqrt{qEF})$, introduced by Latteur (2000) in his thesis work under the author's supervision, in which σ is the length reduction factor (due to end conditions of the elements), and $q = (I/\Omega^2)$ in which I is the

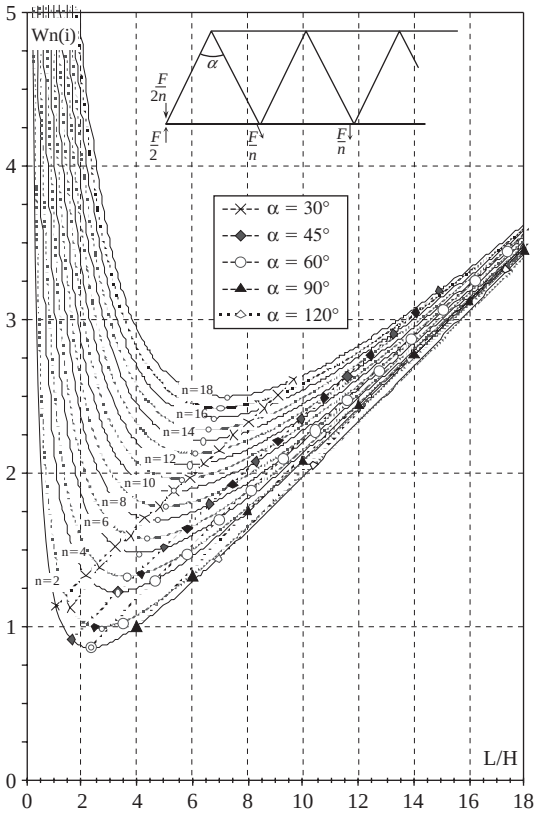

Figure 1 Comparison of different Warren trusses.

(minimal) inertia moment of the section and σ its sectional area, one can evaluate the *sensitivity* of the structure to (*local*) buckling: the higher Ψ, the higher the risk. We are convinced that this instrument should be used in conjunction with the other (W, Δ, Θ), as it gives an excellent estimate of the penalty in material in order to avoid buckling. To be mentioned is that Van Steirteghem (2006) shows in his thesis work that one can also evaluate the risk for *global instability*, starting from this indicator.

Eventually one also has to consider an indicator describing the *dynamic behaviour of the structure*. This is achieved through the use of the indicator of the *first natural frequency* $\Theta = (1/\sqrt{\Delta}) = f((L/H), \Psi)$, extensively discussed by Van Steirteghem (2006). As one sees, there is a direct link with the indicator of displacement σ. This indicator Θ is also directly linked with the buckling indicator, which is not surprising: both resonance and buckling phenomena in elastic systems are related with transformation of energy (compression into bending or torsion for buckling, potential into kinetic for

resonance). An important observation can be made here: if one accepts all the simplifications introduced by the concept of morphological indicators and if one has a closer look at the indicator Θ, one will notice that it is independent on the volume indicator and thus on the mass of the system. This could bring one to the conclusion that – at least, at the stage of conceptual design – there is little hope that one can improve the dynamic behaviour of the structure through simple addition of mass. This has been confirmed when designing e.g. slender footbridges: one quickly comes to the conclusion that the penalty in mass, in order to achieve an acceptable spectrum of resonance frequencies is (very) much higher than the one necessary to control its buckling behaviour.

2 Classification of dynamic loads

When a dynamical analysis of a structure is performed, it is custom to convert the static loads into additional masses. We consider a structure spanning a length L and subjected to a total resultant of static loads F. F includes:

- External live loads F_l, which can further be subdivided in non co-vibrating live loads $F_{l1} = (1 - c)F_m$ and non co-vibrating live loads $F_{l2} = cF_l$,
- External permanent loads F_p,
- Self weight of the structure F_0.

The following combinations can be defined:

- the sum of all permanent loads, i.e. $F_P = F_0 + F_p$,
- the sum of all external loads, i.e. $F_E = F_l + F_p$
- the resultant of all static force, i.e. $F = F_0 + F_E$ or $F = F_P + F_l$

Finally, we define the total co-vibrating load, F_D, combining self weight, external permanent loads and the co-vibrating part of live loads: $F_D = F_P + cF_l$

Herein, c is defined as the share of the live loads that are co-vibrating.

Up to now we considered loads with respect to the ULS. However, the Eurocode [EN1995, EN1992, EN1990] stipulates that the dynamic analysis should be carried out in SLS. Therefore, we convert the loads in order to use them in a SLS–analysis. All quantities with respect to a SLS–analysis are marked with an *. In ULS the partial safety coefficients are 1,35 and 1,5 for the permanent and live loads respectively, in SLS both are equal to 1. Therefore:

$$F_D^* = \frac{F_E}{1{,}35} + c\frac{F_l}{1{,}5}$$

Next, m_D^* is defined as the vibrating mass, in SLS, with respect to the dynamic analysis:

$$m_D^* = \frac{F_D^*}{g}$$

Finally m is defined as the mass of all the loads: $m = F/g$

3 Indicator of natural frequency

We are now able to establish the expression of the indicator of first natural frequency. We start with the general expression for the eigenfrequency of a single degree of freedom (SDOF) system and show that it is possible to use the indicator of displacement, Δ, to establish the expression of an indicator of first natural frequency. By reducing continuous systems to a SDOF system some approximations are made that influence the accuracy of the results. However we show that these approximations are largely acceptable, certainly at the level of conceptual design. Moreover we introduce a correction factor to obtain "exact" results if they are available.

Afterwards we comment on the indicator of first natural frequency by pointing out and discussing the parameters that influence the design decisively and indicate when the dynamic behaviour of structures becomes the dimensioning criterion. We finish by providing some examples that illustrate the use and the scope of the indicator of first natural frequency.

We consider m_{D}^* as the vibrating mass (m_{D}^* must not be confused with the participating mass: $m_p = k/(2\pi f)^2$), in SLS, with respect to the dynamic analysis and k as the static stiffness of the structure. By approximating the structure by an undamped SDOF system. In most textbooks the expressions used for a SDOF system is $f = (1/2\pi)\sqrt{k/m}$. Herein m is the total static mass, this comprises the self weight and added mass as a consequence of the co–vibrating loads in SLS and corresponds therefore with m_D^* as defined previously. The natural frequency associated with mode i can be expressed as: $f_i = (\omega/2\pi) = (c_{cor,i}/2\pi)\sqrt{(k/m_D^*)}$ We add the constant c_{cor} to provide exact analytical solutions if they are available (e.g. beams).

Next, we define z^* as the ratio of the co-vibrating load F_D^* to the total load F_T with respect to SLS or the ratio of the vibrating mass m_D^* to the total mass m: $z^* = (F_D^*/F_T) = (m_D^*/m)$ and thus:

$$f_i = \frac{\omega}{2\pi} = \frac{c_{cor,i}}{2\pi}\sqrt{\frac{k}{z^* m}} = \frac{c_{cor,i}}{2\pi}\sqrt{g\frac{k}{2^* F}}.$$

Since $\delta = F/k$, one finds:

$$f_i = \frac{c_{cor,i}}{2\pi}\sqrt{g\frac{1}{z^*\delta}}$$

or as a function of the indicator of displacement:

$$f_i = \frac{c_{cor,i}}{2\pi}\sqrt{g\beta\frac{E}{z^*\Delta\sigma L}}$$

The indicator of displacement is always determined for the fully stressed design. The parameter β is used to allow a reduced stress level. It is now possible to define an *indicator of natural frequency*:

$$\Theta = \frac{1}{\sqrt{\Delta}} = \frac{2\pi f_i}{c_{cor,i}}\sqrt{g\frac{z^*\sigma L}{\beta E}} = f\left(\frac{L}{H}, \Psi\right)$$

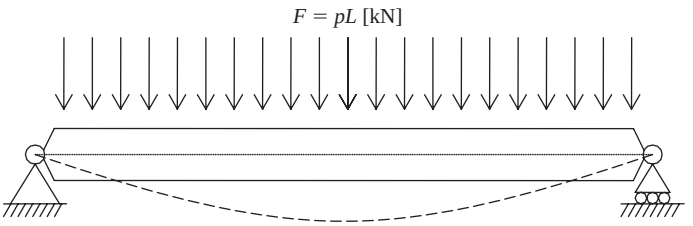

Figure 2 Simple beam example.

The *indicator of first natural frequency* is thus defined as: *The natural frequency of a structure with a unit length* ($L = 1\,m$) *composed of members working at a unit stress* ($\sigma = 1\,Pa$) *and with a unit elastic modulus* ($E = 1\,Pa$) *for which the ratio of the co-vibrating loads to the total load is equal to* z^* *in Serviceability Limit State*.

3.1 *Example: Determining the natural frequency of beams*

This example shows how the indicator of natural frequency can be used to determine the natural frequencies of beams. One considers that all live loads are not co-vibrating and that 60% of the loads arise from self weight and permanent loads.

3.1.1 *Indicator of displacement*

[2] provides the expression of Δ for a fully stressed design:

$$\Delta = 16\frac{5.2}{Z}\frac{H}{L} + \frac{5}{24}\frac{L}{H}$$

3.1.2 *Calculation of* z^*

Since all live loads are not co vibrating:

$$F_l = F_{l1}$$

And 60% of the loads arise from self weight and permanent loads, one obtains F_D in SLS:

$$F_P = 0{,}6F = F_D$$

In ULS this becomes:

$$F_D^* = \frac{0{,}6F}{1{,}35}$$

Therefore:

$$z^* = \frac{F_D^*}{F} = \frac{m_D^*}{m} \approx 0{,}44$$

3.1.3 *Calculation of $c_{cor,1}$*

When establishing the natural frequency of the beams, using $f_i = (c_{cor,i}/2\pi)\sqrt{g(1/z^*\delta)}$, we suppose a SDOF system. In reality, however, the beam is a continuous system and therefore the SDOF results are an approximation. For the SDOF system the result becomes:

$$f_1 = \frac{1}{2\pi}\sqrt{\frac{384}{5}\frac{EI}{m_D^* L^3}} \approx 1{,}39\sqrt{\frac{EI}{m_D^* L^3}}$$

The exact solution can be obtained from [6]:

$$f_1 = \frac{9{,}87}{2\pi}\sqrt{\frac{EI}{m_D^* L^3}} \approx 1{,}57\sqrt{\frac{EI}{m_D^* L^3}}$$

Therefore:

$$c_{cor,1} = \frac{1{,}57}{1{,}39} \approx 1{,}13$$

3.1.4 *Indicator of natural frequency*

We can now draw graphs that allow the determination of the first natural frequency of uniformly loaded beams with $z^* = 0{,}44$.

One considers e.g. a concrete beam ($E = 23\ Gpa, \sigma = 14{,}17$) with a span of 10 m ($L$) and a height of 0,70 m (H) and obtain an overall slenderness of 14,3 (L/H). A concrete beam with a rectangular section has a form factor $Z = 1$, but Figure 3 shows that at $L/H = 14{,}3$, the value of Θ is equal for all values of Z. The first natural frequency of this beam is 6 Hz and the associated mode is a half-sinusoidal bending mode. We observe that the natural frequency for the same beam in timber: 4,1 Hz; S-235 Steel: 4,4 Hz and S-355 Steel: 3,6 Hz.

3.1.5 *Discussion*

The proposed indicator allows an accurate determination of the natural frequency of structures at the stage of conceptual design. Furthermore it allows comparing the behaviour of different materials, the span and the form factor of the section used. We discuss the importance and the scope of the different parameters in the next paragraph.

3.2 *Parameter study*

The example shows convincingly that the natural frequency of structures can be determined at the stage of conceptual design. In this paragraph we study the different parameters that influence the dynamic behaviour of structures. We discuss the influence of loads through z^*, materials, stress level, connections, typology and the correction factor $c_{cor,1}$.

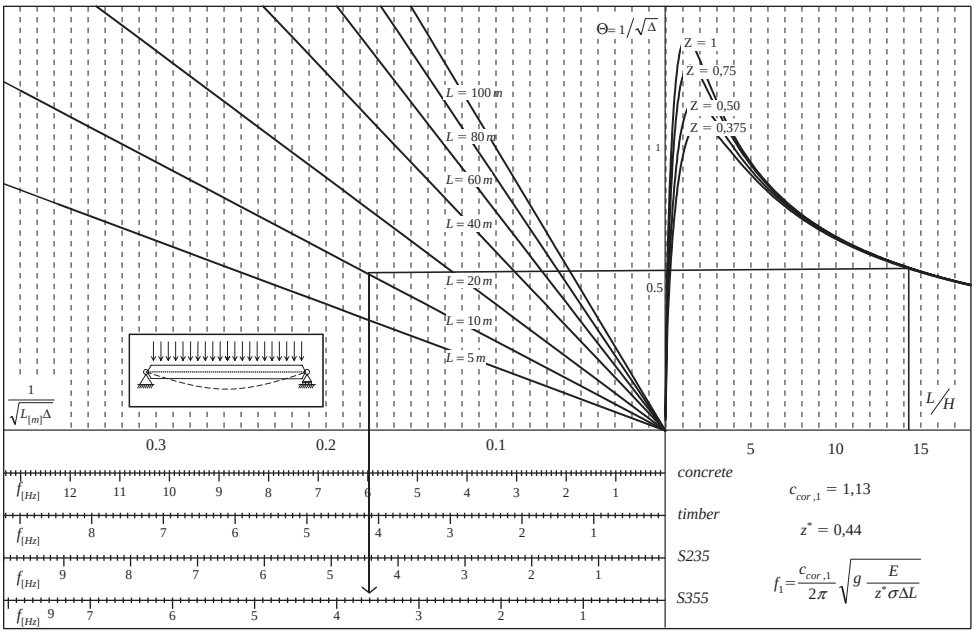

Figure 3 Simple beam example: parametric study results.

3.2.1 *Different values of z**

It is not straightforward to determine the value of z^* at the stage of conceptual design. Therefore we determine the limit values of z^*. The upper bound on F_D^* and z^* occurs when all loads are permanent and as a consequence considered as co-vibrating loads. For that reason:

$$F_l = 0 \quad \text{and} \quad F = F_P = F_0 + F_p.$$

Hence:

$$F_D^* = \frac{F_P}{1{,}35} = \frac{F}{1{,}35}$$

or in terms of vibrating mass:

$$m_D^* = \frac{m}{1{,}35} = \frac{F}{1{,}35\,g}$$

and therefore:

$$z^* = \frac{F_D^*}{F} = \frac{m_D^*}{m} = 0{,}74$$

We note that this is a theoretical situation since we assume that all loads are permanent: none will thus induce vibrations of the structure. Nevertheless this situation determines the upper bound on z^*.

The lower bound on F_D^* and z^* occurs when all external loads are live loads and cannot be considered as co – vibrating. For that reason:

$$F_p = 0, F_E = F_l, F_l = F_{l1} \Rightarrow c = 0.$$

Therefore only self weight should be accounted for the determination of F_D^* and m_D^*. These quantities are not easy to determine. However, the *indicator of self weight* $\Phi = \rho L/\sigma$, introduced by Latteur (2000), provides a tool to determine the percentage of the load originating from self weight:

$$\frac{F_0}{F} = \frac{\rho V}{F} = \frac{\sigma V}{FL}\frac{\rho L}{\sigma} = W\Phi$$

One now expresses F_D^* and M_D^*:

$$F_D^* = \frac{F_0}{1{,}35} = \frac{W\Phi F}{1{,}35} \Rightarrow M_D^* = \frac{W\Phi F}{1{,}35g}$$

and z^*:

$$z^* = \frac{F_D^*}{F} = \frac{m_D^*}{m} = \frac{W\Phi}{1{,}35}$$

Since one considers the natural frequency to be a control calculation W and Φ are already computed and therefore z^* can be determined. In this paper two values are considered to draw the graphs: $W\Phi = 0{,}2$ for lightweight structures (e.g. footbridge) and $W\Phi = 0{,}6$ for structures in which the self weight is important (e.g. railway bridge) resulting in the following values of F_D^* and m_D^* for $\Phi = 0{,}2$ and $\Phi = 0{,}6$ respectively:

$$F_D^* = \frac{F_0}{1{,}35} = \frac{0{,}2F}{1{,}35} \Rightarrow m_D^* = \frac{0{,}2\,m}{1{,}35}$$

$$F_D^* = \frac{F_0}{1{,}35} = \frac{0{,}6F}{1{,}35} \Rightarrow m_D^* = \frac{0{,}6\,m}{1,35}$$

and z^* becomes for $\Phi = 0{,}2$ and $\Phi = 0{,}6$:

$$z^* = \frac{F_D^*}{F} = \frac{m_D^*}{m} = \frac{0{,}2}{1{,}35} = 0{,}15$$

$$z^* = \frac{F_D^*}{F} = \frac{m_D^*}{m} = \frac{0{,}6}{1{,}35} = 0{,}44$$

We consider three values for z^*: $z^* = 0{,}74$; $z^* = 0{,}44$ and $z^* = 0{,}15$.

3.3 *Discussion*

The relation: $f_i = (c_{cor,i}/2\pi)\sqrt{g\beta(E/z^*\Delta\sigma L)}$ indicates that z^* influences the natural frequency of a structure significantly. The designer should therefore carefully assess the

Figure 4 Millenium Bridge.

contribution of the loads in the dynamic analysis of the structure. A very conservative and safe approach would be to consider all loads as co-vibrating ($z^* = 0{,}74$). However, this can lead to an over-conservative design. On the other hand an underestimation of the co-vibrating load may cause unacceptable vibrations of structures. The problem that arose at the opening of the Millenium Bridge in London on June 10th, 2000, illustrates this situation (Figure 4). It is estimated that between 80.000 and 100.000 people crossed the bridge on the first day. Analysis of the video footage showed a maximum of 2.000 people on the deck at the same time, with a maximum of 1,3 to 1,5 people per square metre.

Unexpected movement occurred. The movements were observed to be predominantly lateral and took place mainly on the South span, at a frequency of around 0,8 Hz – the first South lateral mode, and on the central span, at a frequencies just under 0,5 Hz and 0,9 Hz, the first and second lateral modes respectively. More rarely, the movement occurred on the North span at a frequency of just over 1 Hz, the first North lateral mode.

These movements were not continuous; they occurred when a large number of pedestrians were on the bridge and died down if the number of people on the bridge reduced, or if the people stopped walking. From the observation of the amplitude of the movements on the south and central span, the maximum lateral acceleration experienced on the bridge was between 200 and 250 10^{-3} g. At this level of acceleration a significant number of pedestrians have a difficulty in walking and held onto the balustrades for support.

The same phenomenon was not observed with any vertical modes. The bridge behaved vertically as predicted in the design. The vertical movements that took place were within the limits defined by British Standards.

The number of pedestrian allowed onto the bridge was reduced on 11th June, and the movements occurred far more rarely. In the 12th June it was decided to close

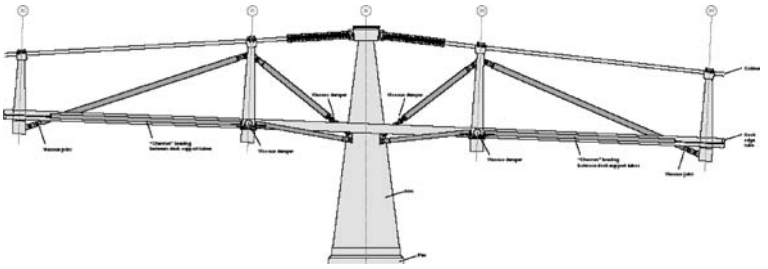

Figure 5 Damping devices to limit the lateral deflections of the bridge.

the bridge in order to fully investigate the cause of movements. Similar phenomena occurred with Auckland Harbour Bridge, Solferino Bridge in Paris and a bridge in Japan but no scientific literature about the phenomenon was then widely available. Moreover, the specific dynamic loads generated by pedestrians when reacting to lateral displacements are difficult to describe mathematically. The authorities (London Port Authority) and the designers (Lord Norman Foster, Arup and Sir Anthony Caro) decided to add damping devices to limit the lateral deflections of the bridge (Figure 5). It is estimated that the original erection cost of the Millenium amounted to 18,6 million £ (27,6 million €). The cost of the adaptation amounted to 5 million £ (7,4 million €) or about 27% of the initial cost. This example shows that it is important to consider all possible vibration modes and dynamic solicitations at every stage of the design.

3.4 *Additional examples and lessons to be drawn*

Van Steirteghem (2006) discussed the dynamic behaviour of trusses and beams. He showed that beams, with standard spans ($5\,m \leq L \leq 10\,m$), have a first natural frequency outside the 0–5 Hz interval and are therefore not subjected to dynamic sollicitations. This result is not surprising but indicates that the theory yields reliable results.

Trusses with important spans, $L \geq 20\,m$, are very sensitive to vibrations. For almost all circumstances one must reduce the stress level in the structure to obtain an acceptable first natural frequency. He showed that this stress reduction is most pronounced if: (i) the co-vibrating load is large, (ii) the span is important and (iii) the stiffness to strength ratio of the material is low.

He showed that Warren trusses are less sensitive to dynamic effects than both Howe and Pratt trusses. Nevertheless, (even) Warren trusses need an important stress reduction to obtain natural frequencies outside the 0–5 Hz interval. Next, he proposed a flow chart that one can use to design structures at the stage of conceptual design. He showed that, even if one considers dynamics, the number of parameters to take into account at the stage of conceptual design is small.

He proposed an example that uses this flow chart to design a 70 m footbridge. He found that dynamics was the dimensioning criterion. If one wants a first natural frequency larger than 5 Hz, one needs to reduce the stress level to an unacceptable level. Therefore one can use a Tuned Mass Damper to attenuate the accelerations in

the structure. Furthermore, one can study the influence of the slenderness and the ratio of the mass of the TMD to the mass of the structure. One can compare the structure in which one does not use a TMD with the damped structure and show that a very important gain in volume can be achieved if one uses a TMD. This example shows clearly that one needs to consider a 'design for stiffness' approach when dynamic loads are important.

4 Conclusions

- This chapter has shown that it is possible to include reasonable estimates of the vibrational behaviour of a structure at the stage of conceptual design. This is achieved by the introduction of an additional morphological indicator: the indicator of *the first natural frequency*

$$\Theta = \frac{1}{\sqrt{\Delta}} = \frac{2\pi f_i}{c_{cor,i}}\sqrt{g\frac{z^*\sigma L}{\beta E}} = f\left(\frac{L}{H}, \Psi\right),$$

  which is depending on the slenderness L/H and the buckling indicator Ψ.
- Trusses with important spans, $L \geq 20$ m, are very sensitive to vibrations. For almost all circumstances one must reduce the stress level in the structure to obtain an acceptable first natural frequency. He showed that this stress reduction is most pronounced if: (i) the co-vibrating load is large, (ii) the span is important and (iii) the stiffness to strength ratio of the material is low.
- A very important gain in volume can be achieved if one uses tuned mass dampers. An example, with parametric analysis, shows clearly that one needs to consider a 'design for stiffness' approach when dynamic loads are important.
- In a subsequent paper, presented in the same conference by T. Vandenbergh et al.[7], one can see that the outlined procedure can be applied to more complex structures, like e.g. trusses.

List of symbols

b = width of cross section [m]
c = constant to indicate the part of the live loads that are co-vibrating [ ]
$c_{cor,i}$ = correction factor to provide exact results if they are available for mode i [ ]
f_i = natural frequency related with mode i [Hz]
F_i = horizontal equivalent load induced by horizontal acceleration in a structure [N]
F = total resultant of the static loads [N]
F_0 = self weight of the structure [N]
$F_D = F_0 + F_p + F_{l_2}$ = resultant of all co-vibrating loads [N]
F_D^* = resultant of all co-vibrating in loads in SLS [N]
F_E = resultant of all external loads [N]
F_l = external live loads [N]
F_{l1} = external live loads that are co-vibrating [N]
F_{l2} = external live loads that are non co-vibrating [N]

F_p = external permanent loads [N]
$F_P = F_0 + F_p$ = resultant of all permanent loads [N]
F_1 = total resultant of static loads [kN]
F_2 = total resultant of static loads [kN]
$g = 9{,}81\, m/s^2$ = gravitational constant [m/s^2]
H_1 = height of structure [m]
H_2 = height of structure [m]
k = stiffness of the structure [N/m]
m_{tot} = total mass of the structure in analysis of structures subjected to vibration [kg]
m_i = mass associated with mode i of the structure [kg]
$m = F/g$ = total mass of all static loads [kg]
$m_D = F_D/g$ = total mass of all co-vibrating loads [kg]
m_D^* = total mass of all co-vibrating loads in SLS [kg]
$m_p = k/(2\pi f_i)^2$ = participating mass associated with a natural frequency [kg]
u_i = eigenmode i of the structure [ ]
u_j = eigenmode j of the structure [ ]
x = constant to indicate the part of the permanent loads that are external [ ]
$z = F_D/F$ = ratio of the co-vibrating load to the total load [ ]
$z^* = F_D^*/F$ = ratio of co-vibrating load to total load in SLS [ ]
α = constant, with respect to response to earthquake, specified by soil [ ]
β = constant providing stress level with respect to allowable stress [ ]
δ = maximum displacement of a structure loaded with F [m]
$\Delta = E\delta/\sigma L$ = indicator of displacement [ ]
$\Phi = \rho L/\sigma$ = indicator of self weight [ ]
ω = first natural pulsation of the structure [rad/s]

References

Latteur, P. 2000. Optimisation des treillis, arcs, poutres et câbles sur base d'indicateurs morphologiques – application aux structures soumises en partie ou en totalité au flambement (3 vol.), Ph. D. thesis, Vrije Universiteit Brussel.

Rao S.S. 1995. Mechanical vibrations, Addison – Wesley Publishing Company, ISBN 0–201–52686–7.

Samyn P., Latteur P. & Van Vooren, J. 1998. Volume of structures: application to classical and harmonic structures, International IASS symposium on Lightweight structures in Architecture, Engineering and Construction, October 5–9, Sydney, Australia.

Samyn, P. 1999. Etude comparée du volume et du déplacement de structures bidimensionnelles, sous charges verticales entre deux appuis – vers un outil d'évaluation et de prédimensionnement des structures (4 vol.), Ph. D. thesis, Université de Liège.

Samyn, P. 2004. Étude de la morphologie des structures à l'aide des indicateurs de volume et de déplacement, Académie royale de Belgique, Classe des Sciences, ISBN 0365–0952.

Van Steirteghem, J. 2006. A Contribution to the Optimisation of Structures Using Morphological Indicators: (In)Stability and Dynamics, Ph.D. thesis, Vrije Universiteit Brussel, Mechanics of Materials and Structures.

Vandenbergh, T., Verbeeck, B. & De Wilde, W.P. 2007. Dynamical analysis and optimisation of statically determinate trusses at conceptual design stage, Compdyn 2007, Rethymnon, June.

Chapter 8

Dynamic analysis of plates stiffened by parallel beams with deformable connection

Evangelos J. Sapountzakis & Vasilios G. Mokos

National Technical University of Athens, Athens, Greece

ABSTRACT: A general solution for the dynamic analysis of plates stiffened by arbitrarily placed parallel beams with deformable connection is presented. According to the proposed model, the stiffening beams are isolated from the plate by sections in the lower outer surface of the plate, taking into account the arising tractions in all directions at the fictitious interfaces. These tractions are integrated with respect to each half of the interface width resulting two interface lines. Their unknown distribution is established by applying continuity conditions in all directions taking into account their relation with the interface slip through the shear connector stiffness. Any distribution of connectors in each direction can be handled. The proposed model permits the evaluation of the shear forces at the interfaces in both directions. Three additional finite element models using beam, shell or solid finite elements are also employed for the verification of the accuracy of the results.

1 Introduction

Structural plate structures stiffened by beams are widely used in buildings, bridges, ships, aircrafts and machines. However, these structures are prone to failure of the bond between the beams and the plate. It is the behavior of this bond that gives composite construction its unique peculiarities, while interface slip can cause significant redistribution of strain and stress.

Although there is an extensive literature on static analysis of these systems to the authors' knowledge a rather limited amount is available on the dynamic one. In all the research efforts the solution of the bending problem of stiffened plates is not general. Only Sapountzakis and Mokos (2007) refining the structural model proposed by Sapountzakis and Katsikadelis (1999) presented a general solution for the static analysis of plates stiffened by parallel beams taking into account tractions in all directions at the fictitious plate – beams interfaces enabling in this way the analysis to include eccentric beams, but in this latter analysis the distribution of the interface transverse shear force is assumed to be constant along the width of the beam flange.

In this paper a general solution for the dynamic analysis of plates stiffened by arbitrarily placed parallel beams of arbitrary doubly symmetric cross section subjected to an arbitrary dynamic loading is presented by improving the employed structural model of Sapountzakis and Mokos (2007) so that a nonuniform distribution of the interface transverse shear force and the nonuniform torsional response of the beams are taken into account. According to the improved model, the stiffening beams are isolated again from the plate by sections in the lower outer surface of the plate, taking into account

the arising tractions in all directions at the fictitious interfaces. These tractions are integrated with respect to each half of the interface width resulting two interface lines, along which the loading of the beams as well as the additional loading of the plate is defined. The utilization of two interface lines for each beam enables the nonuniform torsional response of the beams to be taken into account as the angle of twist is indirectly equated with the corresponding plate slope. The unknown distribution of the aforementioned integrated tractions is established by applying continuity conditions in all directions at the two interface lines taking into account their relation with the interface slip through the shear connector stiffness. Any distribution of connectors in each direction of the interfaces can be handled. The analysis of both the plate and the beams is accomplished on their deformed shape taking into account second-order effects. The method of analysis is based on the capability to establish a flexibility matrix with respect to a set of nodal mass points, while a lumped mass matrix is constructed from the tributary mass areas to these mass points. Six boundary value problems are formulated and solved using the Analog Equation Method (AEM) (Katsikadelis, 2002), a Boundary Element Method (BEM) based method. Both free and forced damped or undamped transverse vibrations are considered and numerical examples with great practical interest are presented. The adopted model permits the evaluation of the shear forces at the interfaces in both directions, the knowledge of which is very important in the design of prefabricated ribbed plates. Three additional finite element models using Bernoulli beam finite elements, 8-noded quadrilateral shell finite elements (parabolic elements) or 8-noded hexahedral solid finite elements (parabolic elements) are also employed for the verification of the accuracy of the results and the validity of the proposed model. The discrepancy in the obtained response of the stiffened plate using the presented analysis and the corresponding one either employing one interface line or ignoring the inplane forces and deformations justifies the analysis based on the proposed model.

2 Statement of the problem

Consider a thin plate of homogeneous, isotropic and linearly elastic material with modulus of elasticity E and Poisson ratio ν, having constant thickness h_p and occupying the two dimensional multiply connected region Ω of the x, y plane bounded by the piecewise smooth $K+1$ curves $\Gamma_0, \Gamma_1, \ldots, \Gamma_{K-1}, \Gamma_K$, as shown in Fig. 1. The plate is stiffened by a set of $i = 1, 2, \ldots, I$ arbitrarily placed parallel beams of arbitrary doubly symmetric cross section of homogeneous, isotropic and linearly elastic material with modulus of elasticity E_b^i and Poisson ratio ν_b^i, which may have either internal or boundary point supports. For the sake of convenience the x axis is taken parallel to the beams. The stiffened plate is subjected to the lateral load $g = g(\mathbf{x}, t)$, $\mathbf{x} : \{x, y\}, t \geq 0$. For the analysis of the aforementioned problem a global coordinate system Oxy for the analysis of the plate and local coordinate ones $O^i x^i y^i$ corresponding to the centroid axes of each beam are employed as shown in Fig. 1.

The solution of the problem at hand is approached by an improved model of that proposed by Sapountzakis and Mokos (2007). According to this model, the stiffening beams are isolated again from the plate by sections in its lower outer surface, taking into account the arising tractions at the fictitious interfaces (Fig. 2). Integration of these tractions along each half of the width of the i-th beam results in line forces

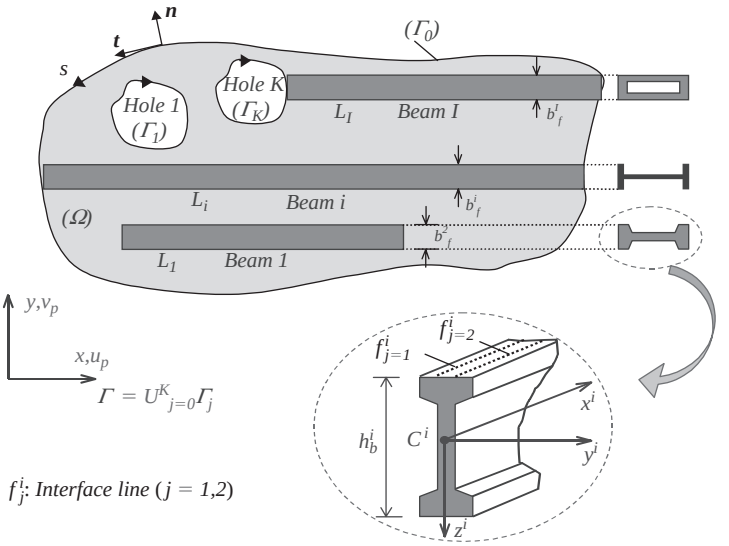

Figure 1 Two dimensional region Ω occupied by the plate.

per unit length in all directions in two interface lines, which are denoted by q^i_{xj}, q^i_{yj} and $q^i_{zj}(j=1,2)$ encountering in this way the nonuniform distribution of the interface transverse shear forces q^i_y, which in the aforementioned model in Sapountzakis and Mokos (2007) was ignored. The aforementioned integrated tractions result in the loading of the i-th beam as well as the additional loading of the plate. Their distribution is unknown and can be established by imposing displacement continuity conditions in all directions along the two interface lines, enabling in this way the nonuniform torsional response of the beams to be taken into account, which in the aforementioned model in Sapountzakis and Mokos (2007) was also ignored.

The arising additional loading at the middle surface of the plate and the loading along the centroid and the shear center axes of each beam can be summarized as follows

a. In the plate (at the traces of the two interface lines j = 1,2 of the i-th plate-beam interface)

(i) A lateral line load q^i_{zj}.

(ii) A lateral line load $\partial m^i_{pyj}/\partial x$ due to the eccentricity of the component q^i_{xj} from the middle surface of the plate. $m^i_{pyj} = q^i_{xj} h_p/2$ is the bending moment.

(iii) A lateral line load $\partial m^i_{pxj}/\partial x$ due to the eccentricity of the component q^i_{yj} from the middle surface of the plate. $m^i_{pxj} = q^i_{yj} h_p/2$ is the bending moment.

(iv) An inplane line body force q^i_{xj} at the middle surface of the plate.

(v) An inplane line body force q^i_{yj} at the middle surface of the plate.

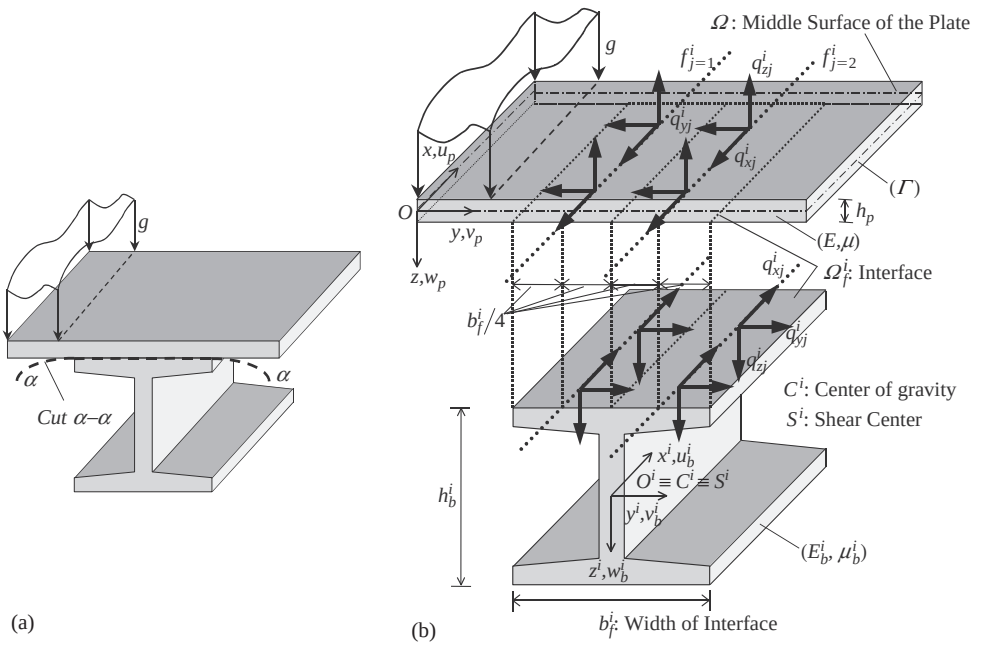

Figure 2 Thin elastic plate stiffened by beams (a) and isolation of the beams from the plate (b).

b. In each (i-th) beam ($O^ix^iy^iz^i$ system of axes)

(i) A perpendicularly distributed line load q^i_{zj} along the beam centroid axis O^ix^i.
(ii) A transversely distributed line load q^i_{yj} along the beam centroid axis O^ix^i.
(iii) An axially distributed line load q^i_{xj} along the beam centroid axis O^ix^i.
(iv) A distributed bending moment $m^i_{byj} = q^i_{xj}e^i_{zj}$ along O^iy^i local beam centroid axis due to the eccentricities e^i_{zj} of the components q^i_{xj} from the beam centroid axis. $e^i_{z1} = e^i_{z2} = -h^i_b/2$ are the eccentricities.
(v) A distributed bending moment $m^i_{bzj} = -q^i_{xj}e^i_{yj}$ along O^iz^i local beam centroid axis due to the eccentricities e^i_{yj} of the components q^i_{xj} from the beam centroid axis. $e^i_{y1} = -b^i_f/4$, $e^i_{y2} = b^i_f/4$ are the eccentricities.
(vi) A distributed twisting moment $m^i_{bxj} = q^i_{zj}e^i_{yj} - q^i_{yj}e^i_{zj}$ along O^ix^i local beam shear center axis due to the eccentricities e^i_{zj}, e^i_{yj} of the components q^i_{yj}, q^i_{zj} from the beam shear center axis, respectively. $e^i_{z1} = e^i_{z1} = -h^i_b/2$ and $e^i_{y1} = -b^i_f/4$, $e^i_{y2} = b^i_f/4$ are the eccentricities.

The structural models and the aforementioned additional loading of the plate and the beams are shown in Fig. 3. On the base of the above considerations the response of the plate and of the beams may be described by the following initial boundary value problems.

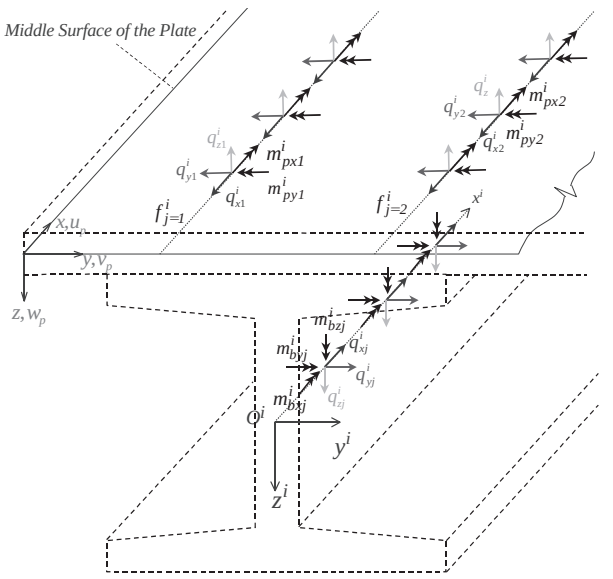

Figure 3 Structural model and directions of the additional loading of the plate and the i-th beam.

a. For the plate.

The plate undergoes transverse deflection and inplane deformation. Thus, for the transverse deflection the equation of motion employing the linearized second order theory can be written as

$$D\nabla^4 w_p + \rho_p \ddot{w}_p + c_p \dot{w}_p - \left(N_x \frac{\partial^2 w_p}{\partial x^2} + 2N_{xy} \frac{\partial^2 w_p}{\partial x \partial y} + N_y \frac{\partial^2 w_p}{\partial y^2} \right) \quad \text{in } \Omega \qquad (1)$$

$$= g - \sum_{i=1}^{I} \left(\sum_{j=1}^{2} \left(q^i_{zj} - \frac{\partial m^i_{pxj}}{\partial y} + \frac{\partial m^i_{pyj}}{\partial x} - q^i_{xj} \frac{\partial w^i_{pj}}{\partial x} - q^i_{yj} \frac{\partial w^i_{pj}}{\partial y} \right) \delta^i_j (y - y_j) \right)$$

the corresponding boundary conditions as

$$\alpha_{p1} w_p + \alpha_{p2} R_{pn} = \alpha_{p3} \qquad \beta_{p1} \frac{\partial w_p}{\partial n} + \beta_{p2} M_{pn} = \beta_{p3} \quad \text{on } \Gamma \qquad (2a,b)$$

and the initial conditions as

$$w_p(\mathbf{x}, 0) = w_{p0}(\mathbf{x}) \quad \dot{w}_p(\mathbf{x}, 0) = \overline{w}_{p0}(\mathbf{x}) \qquad (3a,b)$$

where $w_p(\mathbf{x}, t)$, $\mathbf{x} : \{x, y\}$, $t \geq 0$ = time dependent transverse deflection of the plate; $D = Eh_p^3/12(1 - \nu^2)$ = flexural rigidity; $N_x(\mathbf{x}, t)$, $N_y(\mathbf{x}, t)$, $N_{xy}(\mathbf{x}, t)$ = the membrane

forces per unit length of the plate cross section; $\rho_p = \rho h_p =$ surface mass density of the plate with ρ being the volume mass density; $c_p =$ plate flexural damping constant; $w_{p0}(\mathbf{x})$, $\overline{w}_{p0}(\mathbf{x}) =$ initial deflection and the initial velocity of the points of the middle surface of the plate; $\delta(y - y_i) =$ Dirac's delta function in the y direction; M_{pn} and $R_{pn} =$ bending moment normal to the boundary and the effective reaction along it, respectively, which using intrinsic coordinates n, s are given as

$$M_{pn} = -D\left[\nabla^2 w_p + (\nu - 1)\left(\frac{\partial^2 w_p}{\partial s^2} + \kappa\frac{\partial w_p}{\partial n}\right)\right] \tag{4}$$

$$R_{pn} = -D\left[\frac{\partial}{\partial n}\nabla^2 w_p - (\nu - 1)\frac{\partial}{\partial s}\left(\frac{\partial^2 w_p}{\partial s \partial n} - \kappa\frac{\partial w_p}{\partial s}\right)\right] + N_n\frac{\partial w_p}{\partial n} + N_{nt}\frac{\partial w_p}{\partial s} \tag{5}$$

in which $\kappa(s) =$ curvature of the boundary; $\partial/\partial s$ and $\partial/\partial n$ denote differentiation with respect to the arc length s of the boundary and the outward normal n to it, respectively. Finally, a_{pl}, $\beta_{pl}(l = 1, 2, 3)$ are functions specified on the boundary Γ. In this investigation these functions do not depend on time. In the case that they are time dependent support excitations may be considered.

Since linearized plate bending theory is considered, the components of the membrane forces N_x, N_y, N_{xy} are given as

$$N_x = C\left(\frac{\partial u_p}{\partial x} + \nu\frac{\partial v_p}{\partial y}\right) \quad N_y = C\left(\nu\frac{\partial u_p}{\partial x} + \frac{\partial v_p}{\partial y}\right)$$
$$N_{xy} = C\frac{1 - \nu}{2}\left(\frac{\partial u_p}{\partial y} + \frac{\partial v_p}{\partial x}\right) \tag{6a,b,c}$$

where $C = Eh_p/(1 - \nu^2)$; $u_p(\mathbf{x}, t)$, $v_p(\mathbf{x}, t) =$ displacement components of the middle surface of the plate arising from the line body forces q^i_{xj}, q^i_{yj} $(i = 1, 2, \ldots I)$, $(j = 1, 2)$. These displacement components are established by solving independently the plane stress problem, which is described by the following quasi-static (inplane inertia forces are ignored) boundary value problem (Navier's equations of equilibrium)

$$\nabla^2 u_p + \frac{1 + \nu}{1 - \nu}\frac{\partial}{\partial x}\left[\frac{\partial u_p}{\partial x} + \frac{\partial v_p}{\partial y}\right] - \frac{1}{Gh_p}\sum_{i=1}^{I} q^i_x \delta(y - y_i) = 0 \tag{7a}$$

$$\nabla^2 v_p + \frac{1 + \nu}{1 - \nu}\frac{\partial}{\partial y}\left[\frac{\partial u_p}{\partial x} + \frac{\partial v_p}{\partial y}\right] - \frac{1}{Gh_p}\sum_{i=1}^{I} q^i_y \delta(y - y_i) = 0 \quad \text{in } \Omega \tag{7b}$$

$$\gamma_{p1} u_{pn} + \gamma_{p2} N_n = \gamma_{p3} \qquad \delta_{p1} u_{pt} + \delta_{p2} N_t = \delta_{p3} \quad \text{on } \Gamma \tag{8a,b}$$

in which $G = E/2(1 + \nu)$ is the shear modulus of the plate; N_n, N_t and u_{pn}, u_{pt} are the boundary membrane forces and displacements in the normal and tangential directions to the boundary, respectively; γ_{pl}, $\delta_{pl}(l = 1, 2, 3)$ are functions specified on the boundary Γ.

b. For each (i-th) beam.

Each beam undergoes transverse deflection with respect to z^i and y^i axes, axial deformation along x^i axis and nonuniform angle of twist along x^i axis. Thus, for the transverse deflection with respect to z^i axis the equation of motion employing the linearized second order theory can be written as

$$E_b^i I_{by}^i \frac{\partial^4 w_b^i}{\partial x^{i4}} + \rho_b \ddot{w}_b^i + c_b^i \dot{w}_b^i = \sum_{j=1}^{2} \left(q_{zj}^i - q_{xj}^i \frac{\partial w_b^i}{\partial x^i} + N_{bj}^i \frac{\partial^2 w_b^i}{\partial x^{i2}} - \frac{\partial m_{byj}^i}{\partial x^i} \right) \quad \text{in } L^i, \ \text{i} = 1, 2, \ldots, I \tag{9}$$

the corresponding boundary conditions as

$$a_1^{zi} w_b^i + a_2^{zi} R_{bz}^i = a_3^{zi} \quad \beta_1^{zi} \theta_{by}^i + \beta_2^{zi} M_{by}^i = \beta_3^{zi} \quad \text{at the beam ends } x^i = 0, L^i \tag{10a,b}$$

and the initial conditions as

$$w_b^i(x^i, 0) = w_{b0}^i(x^i) \quad \dot{w}_b^i(x^i, 0) = \overline{w}_{b0}^i(x^i) \tag{11a,b}$$

where $w_b^i(x^i, t)$ = time dependent transverse deflection of the i-th beam with respect to z^i axis; I_{by}^i = moment of inertia with respect to y^i axis; $N_{bj}^i = N_{bj}^i(x^i)$ = axial forces at the x^i centroid axis arising from the line body forces q_{xj}^i; ρ_b = surface mass density of the beams; c_b^i = i-th beam flexural damping constant; $w_{b0}^i(x^i)$, $\overline{w}_{b0}^i(x^i)$ = initial deflection and the initial velocity of the points of the neutral axis of the i-th beam with respect to z^i axis; a_l^{zi}, $\beta_l^{zi} (l = 1, 2, 3)$ = coefficients specified at the boundary of the i-th beam; θ_{by}^i, R_{bz}^i, M_{by}^i = slope, reaction and bending moment at the i-th beam ends, respectively given as

$$\theta_{by}^i = -\frac{\partial w_b^i}{\partial x^i} \tag{12}$$

$$R_{bz}^i = -E_b^i I_{by}^i \frac{\partial^3 w_b^i}{\partial x^{i3}} + \sum_{j=1}^{2} N_{bj}^i \frac{\partial w_b^i}{\partial x^i} \tag{13}$$

$$M_{by}^i = -E_b^i I_{by}^i \frac{\partial^2 w_b^i}{\partial x^{i2}} \tag{14}$$

The $v_b^i = v_b^i(x^i)$ transverse deflection with respect to y^i axis must satisfy the following quasi-static (transverse inertia forces with respect to y^i axis are ignored) boundary value problem

$$E_b^i I_{bz}^i \frac{\partial^4 v_b^i}{\partial x^{i4}} = \sum_{j=1}^{2} \left(q_{yj}^i - q_{xj}^i \frac{\partial v_b^i}{\partial x^i} + N_{bj}^i \frac{\partial^2 v_b^i}{\partial x^{i2}} - \frac{\partial m_{bzj}^i}{\partial x^i} \right) \quad \text{in } L^i, \ \text{i} = 1, 2, \ldots, I \tag{15}$$

$$a_1^{yi} v_b^i + a_2^{yi} R_{by}^i = a_3^{yi} \quad \beta_1^{yi} \theta_{bz}^i + \beta_2^{yi} M_{bz}^i = \beta_3^{yi} \ \text{at the beam ends } x^i = 0, L^i \tag{16a,b}$$

where I^i_{bz} = moment of inertia of the i-th beam with respect to y^i axis; a^{yi}_l, $\beta^{yi}_l (l = 1, 2, 3)$ = coefficients specified at its boundary; θ^i_{bz}, R^i_{by}, M^i_{bz} = slope, reaction and bending moment at the i-th beam ends, respectively given as

$$\theta^i_{bz} = \frac{\partial v^i_b}{\partial x^i} \tag{17}$$

$$R^i_{by} = -E^i_b I^i_{bz} \frac{\partial^3 v^i_b}{\partial x^{i3}} - \sum_{j=1}^{2} N^i_{bj} \frac{\partial v^i_b}{\partial x^i} \tag{18}$$

$$M^i_{bz} = E^i_b I^i_{bz} \frac{\partial^2 v^i_b}{\partial x^{i2}} \tag{19}$$

Since linearized beam bending theory is considered the axial deformation u^i_b of the beam arising from the arbitrarily distributed axial forces q^i_{xj} $(i = 1, 2, \ldots I)$, $(j = 1, 2)$ is described by solving independently the following quasi-static (axial inertia forces are neglected) boundary value problem

$$E^i_b A^i_b \frac{\partial^2 u^i_b}{\partial x^{i2}} = -\sum_{j=1}^{2} q^i_{xj} \quad \text{in } L^i, \ \ i = 1, 2, \ldots, I \tag{20}$$

$$\gamma^{xi}_1 u^i_b + \gamma^{xi}_2 N^i_b = \gamma^{xi}_3 \quad \text{at the beam ends } x^i = 0, L^i \tag{21}$$

where N^i_b = axial reaction at the i-th beam ends given as

$$N^i_b = \sum_{j=1}^{2} N^i_{bj} = E^i_b A^i_b \frac{\partial u^i_b}{\partial x_i} \tag{22}$$

Finally, the nonuniform angle of twist with respect to x^i shear center axis has to satisfy the following quasi-static (torsional and warping inertia moments are ignored) boundary value problem (Sapountzakis and Mokos, 2003)

$$E^i_b I^i_{bw} \frac{\partial^4 \theta^i_{bx}}{\partial x^{i4}} - G^i_b I^i_{bx} \frac{\partial^2 \theta^i_{bx}}{\partial x^{i2}} = \sum_{j=1}^{2} m^i_{bxj} \quad \text{in } L^i, \ \ i = 1, 2, \ldots, I \tag{23}$$

$$a^{xi}_1 \theta^i_{bx} + a^{xi}_2 M^i_{bx} = a^{xi}_3 \quad \beta^{xi}_1 \frac{\partial \theta^i_{bx}}{\partial x^i} + \beta^{xi}_2 M^i_{bw} = \beta^{xi}_3$$
$$\text{at the beam ends } x_i = 0, L_i \tag{24a,b}$$

where $\theta^i_{bx} = \theta^i_{bx}(x^i)$ = variable angle of twist of the i-th beam along the x^i shear center axis; $G^i_b = E^i_b / 2(1 + \nu^i_b)$ = shear modulus; I^i_{bw}, I^i_{bx} = warping and torsion constants of the i-th beam cross section, respectively given as

$$I^i_{bw} = \int_{A^i} (\varphi^P_S)^2 dA^i \quad I^i_{bx} = \int_{A^i} \left((y^i)^2 + (z^i)^2 + y^i \frac{\partial \varphi^P_S}{\partial z^i} - z^i \frac{\partial \varphi^P_S}{\partial y^i} \right) dA^i \tag{25a,b}$$

with $\varphi_S^P(y^i, z^i)$ = primary warping function with respect to the shear center S of the A^i beam cross section; a_l^{xi}, $\beta_l^{xi}(l = 1, 2, 3)$ = coefficients specified at the boundary of the i-th beam; $\dfrac{\partial\theta_{bx}^i}{\partial x^i}$ denotes the rate of change of the angle of twist and it can be regarded as the torsional curvature; M_{bx}^i = twisting moment and M_{bw}^i = warping moment due to the torsional curvature at the boundary of the i-th beam given as (Sapountzakis and Mokos, 2003)

$$M_{bx}^i = M_{bx}^{iP} + M_{bx}^{iS} = G_b^i I_{bx}^i \frac{\partial\theta_{bx}^i}{\partial x^i} - E_b^i I_{bw}^i \frac{\partial^3\theta_{bx}^i}{\partial x^{i3}} \quad M_{bw}^i = -E_b^i I_{xw}^i \frac{\partial^2\theta_{bx}^i}{\partial x^{i2}} \tag{26a,b}$$

Eqns. (1), (7a), (7b), (9), (15), (20), (23) constitute a set of seven coupled partial differential equations including thirteen unknowns, namely w_p, u_p, v_p, w_b^i, v_b^i, u_b^i, θ_{bx}^i, q_{x1}^i, q_{y1}^i, q_{z1}^i, q_{x2}^i, q_{y2}^i, q_{z2}^i. Six additional equations are required, which result from the displacement continuity conditions in the directions of z^i, x^i and y^i local axes along the two interface lines of each (i-th) plate – beam interface. These conditions can be expressed as

In the direction of z^i local axis:

$$w_{p1}^i - w_b^i = -\frac{b_f^i}{4}\theta_{bx}^i \quad \text{along interface line } 1(f_{j=1}^i) \tag{27a}$$

$$w_{p2}^i - w_b^i = \frac{b_f^i}{4}\theta_{bx}^i \quad \text{along interface line } 2\ (f_{j=1}^i) \tag{27b}$$

In the direction of x^i local axis:

$$u_{p1}^i - u_b^i = \frac{h_p}{2}\frac{\partial w_{p1}^i}{\partial x} + \frac{h_b^i}{2}\frac{\partial w_b^i}{\partial x^i} + \frac{b_f^i}{4}\frac{\partial v_b^i}{\partial x^i} + (\phi_S^{iP})_{f1}\frac{\partial\theta_{bx}^i}{\partial x^i} + \frac{q_{x1}^i}{k_{x1}^i}$$
$$\text{along interface line } 1(f_{j=1}^i) \tag{28a}$$

$$u_{p2}^i - u_b^i = \frac{h_p}{2}\frac{\partial w_{p2}^i}{\partial x} + \frac{h_b^i}{2}\frac{\partial w_b^i}{\partial x^i} - \frac{b_f^i}{4}\frac{\partial v_b^i}{\partial x^i} + (\phi_S^{iP})_{f2}\frac{\partial\theta_{bx}^i}{\partial x^i} + \frac{q_{x2}^i}{k_{x2}^i}$$
$$\text{along interface line } 2\ (f_{j=2}^i) \tag{28b}$$

In the direction of y^i local axis:

$$v_{p1}^i - v_b^i = \frac{h_p}{2}\frac{\partial w_{p1}^i}{\partial y} + \frac{h_b^i}{2}\theta_{bx}^i + \frac{q_{y1}^i}{k_{y1}^i} \quad \text{along interface line } 1\ (f_{j=1}^i) \tag{29a}$$

$$v_{p2}^i - v_b^i = \frac{h_p}{2}\frac{\partial w_{p2}^i}{\partial y} + \frac{h_b^i}{2}\theta_{bx}^i + \frac{q_{y2}^i}{k_{y2}^i} \quad \text{along interface line } 2\ (f_{j=1}^i) \tag{29b}$$

where $(\phi_S^{iP})_{fj}$ = value of the primary warping function with respect to the shear center S of the beam cross section at the point of the j-th interface line of the i-th plate – beam

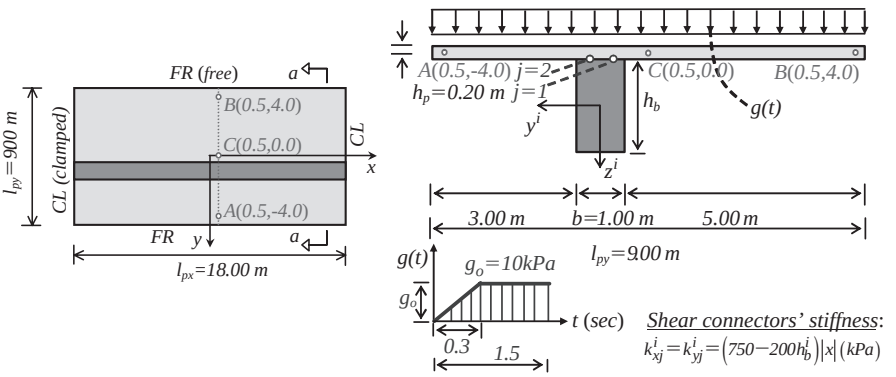

Figure 4 Plan view, section a-a and loading of the stiffened plate of Example 1.

interface f. It is worth here noting that the coupling of the aforementioned equations is nonlinear due to the terms including the unknown q^i_{xj} and q^i_{yj} interface forces.

3 Solution procedure

The numerical solution of the aforementioned problem is achieved employing the method presented by Katsikadelis and Kandilas (1990). According to this method the domain Ω occupied by the plate is discretized by establishing a system of M nodal points on it, corresponding to M mass cells, to which masses are assigned according to the lumped mass assumption. Subsequently, the stiffness matrix, the damping matrix as well as the load vector with respect to these nodal points are established employing the Analog Equation Method (Katsikadelis, 2002), a BEM based method. This procedure leads to the typical equation of motion for the stiffened plate

$$[m]\{\ddot{w}\} + [c]\{\dot{w}\} + [k]\{w\} = \{g\} \tag{30}$$

4 Numerical examples

In all the examples treated $E = E^i_b = 3.00E7$, $\mu = \mu^i_b = 0.20$ and $\rho = \rho^i_b = 2500\, kg/m^3$.

4.1 *Example 1*

A rectangular plate with dimensions $l_{px} \times l_{py} = 18.0 \times 9.0\, m$ stiffened by a rectangular beam of $1.0\, m$ width eccentrically placed with respect to the center line of the plate (Fig. 4) has been studied (damping ratio $\xi = \xi^i_b = 0$). In Table 1 the torsion I^1_{bx} and warping I^1_{bw} constants of the beam cross section and the values of the primary warping function $(\phi^P_S)_{fj}$ $(j = 1, 2)$ at the nodes of the two interface lines for various beam heights are presented. In Table 2 the computed first five eigenfrequencies, in Fig. 5 the fundamental modeshape and in Fig. 6 the deflection time history at point C (Fig. 4) of the stiffened plate for the cases of a partial in both directions and a full shear connection

Table 1 Torsion, warping constants and primary warping function for various beam heights.

h_b (m)	I^I_{bx} (m^4)	I^I_{bw}(m^6)	$(\phi^P_S)_{f1}$ (m^2)	$(\phi^P_S)_{f2}$ (m^2)
0.50	2.8584E−02	3.1760E−04	−4.9366E−02	4.9366E−02
1.00	1.4057E−01	1.3441E−04	−3.5037E−02	3.5037E−02
2.00	4.5733E−01	2.0326E−02	7.5813E−02	−7.5813E−02

Table 2 Dimensionless eigenfrequencies $\Omega_n = \omega_n\sqrt{\rho}$ of the stiffened plate of Example 1.

Ω_n	*Full Connection*				*Partial Conn.*
	AEM *Present study*	*FEM*			*AEM* *Present study*
		Shell–Beam	*Shell–Shell*	*Solid*	
No beam					
1	22.1346	22.1434	22.1092	22.1159	22.1346
2	37.6083	37.1742	37.0602	37.1034	37.6083
3	61.3999	61.0651	60.9110	60.9295	61.3999
4	85.2349	84.1991	83.9974	84.0378	85.2349
5	112.986	109.262	109.5881	109.4903	112.986
$h_b = 100\,cm$					
1	46.9839	48.2654	48.3007	52.6324	42.0545
2	80.8478	86.4500	86.0006	94.2175	58.5281
3	90.9201	89.4149	89.2065	98.2054	89.4929
4	130.2501	135.5596	135.2461	151.5446	111.3646
5	140.2601	146.8720	143.5870	154.1401	130.1845
$h_b = 200\,cm$					
1	51.8608	51.1244	50.9369	56.1035	51.1854
2	92.6791	90.3146	90.0342	95.4062	92.5348
3	102.2650	99.4490	98.6612	118.3639	95.6831
4	148.6789	139.5643	139.0592	153.1325	145.4936
5	152.0960	148.3283	147.8934	162.1458	147.8595

are presented as compared wherever possible with those obtained from FEM solutions using Bernoulli beam finite elements (SAP2000, 2004), 8-noded quadrilateral shell finite elements (parabolic elements) (MSC/NASTRAN, 1999) or 8-noded hexahedral solid finite elements (parabolic elements) (MSC/NASTRAN, 1999). The influence of the shear connectors' stiffness is remarkable while the accuracy of the results and the validity of the proposed model are noteworthy.

4.2 *Example 2*

A rectangular plate with dimensions $l_{px} \times l_{py} = 18.0 \times 9.0\,m$ subjected to an eccentric uniformly distributed dynamic load $g(t)$ and stiffened by three identical I-section beams ($I^i_{bx} = 9.14894\text{E-}3\text{m}^4$, $I^i_{bw} = 6.39132\text{E-}3\text{m}^6$, $I^i_{by} = 1.09333\text{E-}1\text{m}^4$, $I^i_{bz} = 3.06667\text{E-}2\text{m}^4$, $(\phi^P_S)_{f1} = 8.8945\text{E-}2\text{m}^2$, $(\phi^P_S)_{f2} = -8.8945\text{E-}2\text{m}^2$, as shown in Fig. 7 has been studied (damping ratio $\xi = \xi^i_b = 7\%$). In Table 3 the first five eigenfrequencies and in

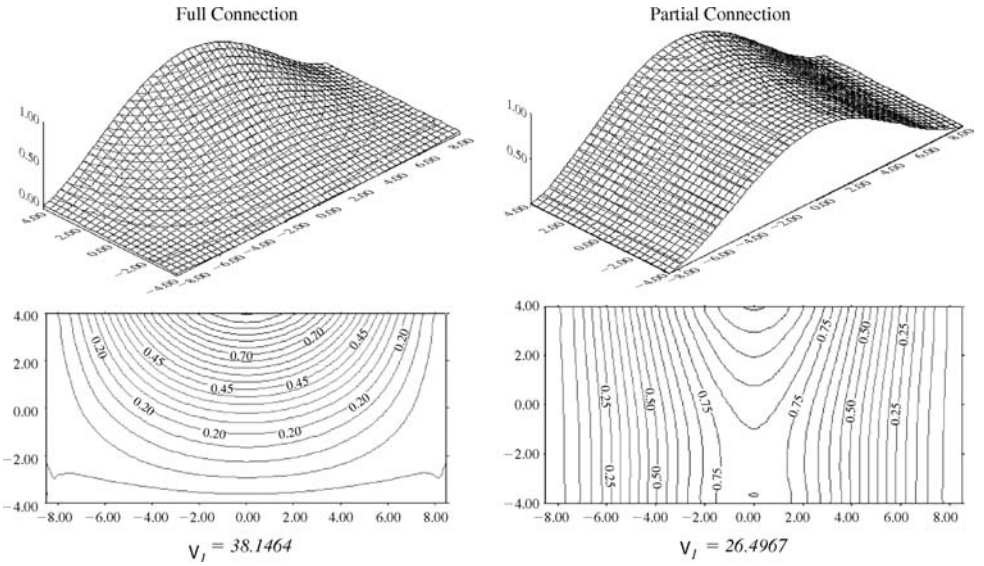

Figure 5 Fundamental mode shape of the stiffened plate of Example 1 for the beam height $h_b = 50$ cm.

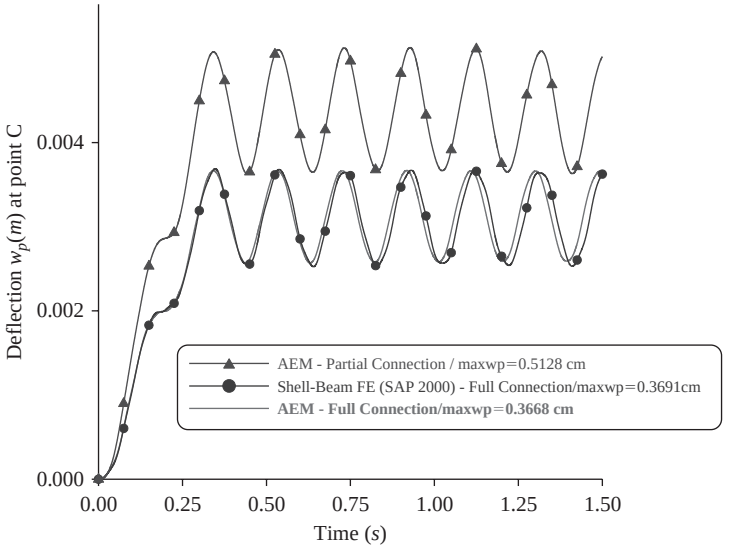

Figure 6 Deflection time history at C of the stiffened plate of Example 1, for the beam height $h_b = 2.0$ m.

Fig. 8 the deflection time history at point C (Fig. 7) of the stiffened plate subjected to the accelerogram of Athens Earthquake at September 7, 1999 for the cases of a partial in both directions and a full shear connection are presented as compared with those obtained from FEM solutions.

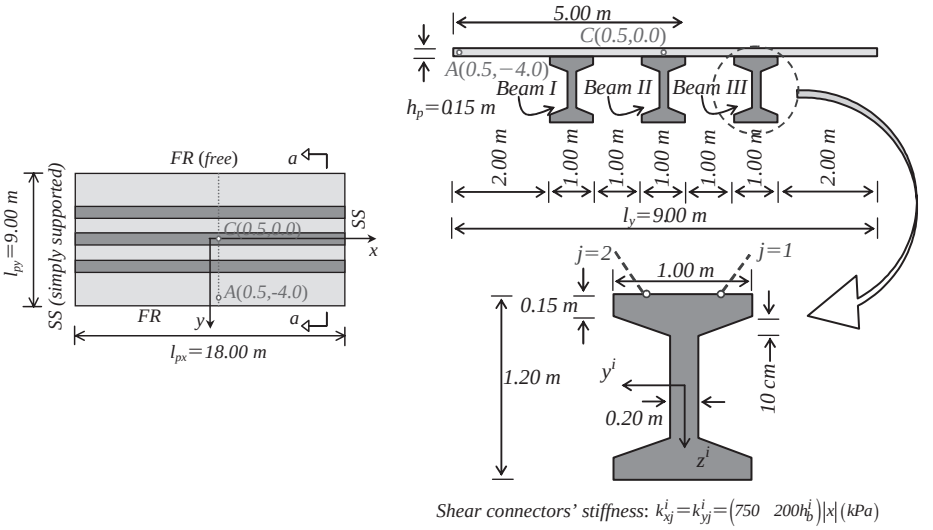

Figure 7 Plan view and section a-a of the stiffened plate of Example 2.

Table 3 Eigenperiods $T_i(s)$ of the stiffened plate of Example 2.

$T_i(s)$	*Full Connection*		*Partial Connection*
	AEM Present study	*FEM Shell–Beam*	*AEM Present study*
1	0.1110	0.1075	0.2564
2	0.1109	0.1068	0.2238
3	0.0694	0.0706	0.1171
4	0.0661	0.0705	0.0787
5	0.0660	0.0637	0.0782

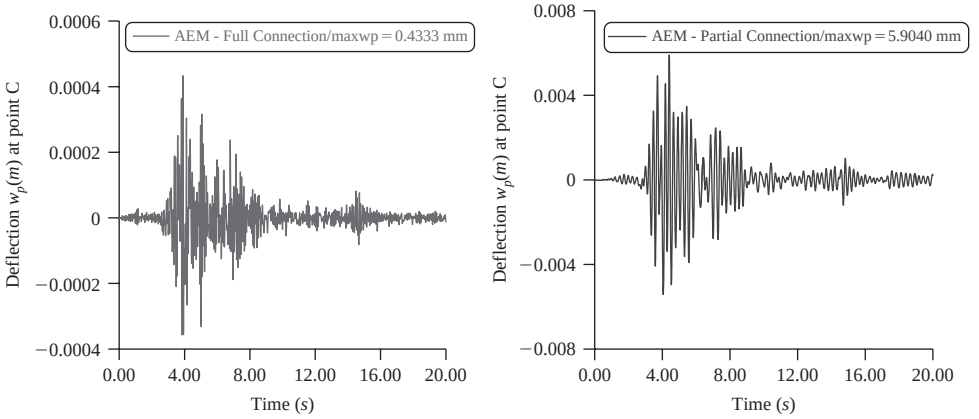

Figure 8 Time history of the deflection at point C for full and partial connection.

5 Concluding remarks

The influence of the interface slip to the behavior of the stiffened plate and the accuracy of the obtained results compared with those obtained from FEM solutions are verified.

References

Katsikadelis, J.T. & Kandilas, C.B. 1990. A Flexibility Matrix Solution of the Vibration Problem of Plates Based on the Boundary Element Method, *Acta Mechanica,* 83: 51–60.

Katsikadelis, J.T. 2002. The Analog Equation Method. A Boundary – only Integral Equation Method for Nonlinear Static and Dynamic Problems in General Bodies, *Theoretical and Applied Mechanics*, 27: 13–38.

MSC/NASTRAN for Windows, 1999. *Finite element modeling and postprocessing system*. Help System Index,Version 4.0, USA.

SAP2000 2004. *Linear and Nonlinear Static and Dynamic Analysis and Design of Three-Dimensional Structures*, Version 9, Computers and Structures, Inc., Berkeley, California, USA.

Sapountzakis, E.J. & Katsikadelis, J.T. 1999. Dynamic Analysis of Elastic Plates Reinforced with Beams of Doubly-Symmetrical Cross Section, *Computational Mechanics*, 23: 430–439.

Sapountzakis, E.J. & Mokos, V.G. 2003. Warping Shear Stresses in Nonuniform Torsion by BEM, *Computational Mechanics,* 30(2): 131–142.

Sapountzakis, E.J. & Mokos, V.G. 2007. Analysis of Plates Stiffened by Parallel Beams, *International Journal for Numerical Methods in Engineering*, 70: 1209–1240.

Chapter 9

Impacts on beams: Uncertainty in experiments and numerical simulation

Werner Schiehlen & Robert Seifried

University of Stuttgart, Stuttgart, Germany

ABSTRACT: Impacts on beams result in large rigid body motions and small structural waves. Such mechanical systems are often modeled as multibody systems to describe the large nonlinear motion where the impacts are treated by the coefficient of restitution. The coefficient of restitution is considered as deterministic number depending on the material, the shape and the velocity of the colliding bodies. However, in experiments and computations it was observed that for a sphere striking a beam the coefficient of restitution is uncertain due to multiple impacts resulting in chaotic behavior. For the evaluation of the numerical and experimental data a statistical approach is proposed providing mean value and dispersion of the coefficient of restitution depending on four classes of the velocity. It is shown that these parameters allow characterizing the uncertainty.

1 Introduction

Beam systems with impacts may be modeled as multibody systems to describe large nonlinear motions while the impacts are treated by the coefficient of restitution, see e.g. (Pfeiffer & Glocker 1996) and (Stronge 2000). Generally, the coefficient of restitution is considered as deterministic number depending on the material, the shape and the velocity of the colliding bodies see e.g. (Goldsmith 1960). However, experiments and simulations show that for a sphere striking a beam the coefficient of restitution is uncertain due to multiple impacts resulting in random behavior, requiring a probabilistic approach as shown in (Schiehlen & Seifried 2006).

2 Impacts in multibody systems

The method of multibody systems allows the dynamical analysis of machines and structures, see e.g. (Schiehlen & Eberhard 2004) and (Schiehlen, Guse & Seifried 2006). More recently contact and impact problems featuring unilateral constraints were considered too, see (Pfeiffer & Glocker 1996). A multibody system is represented by its equations of motion as

$$\mathbf{M}(\mathbf{y})\,\ddot{\mathbf{y}} + \mathbf{k}(\mathbf{y}, \dot{\mathbf{y}}) = \mathbf{q}(\mathbf{y}, \dot{\mathbf{y}}), \tag{1}$$

where $\mathbf{y}(t)$ is the global position vector featuring f generalized coordinates, $\mathbf{M}$ the inertia matrix, $\mathbf{k}$ the vector of Coriolis and gyroscopic forces and $\mathbf{q}$ the vector of the applied forces. The continuous motion of the multibody system might be interrupted by collision. Collisions with non-zero relative velocity result in impacts and impact modeling is required. Using the instantaneous impact modeling the motion of the multibody system is divided into two periods with different initial conditions, see e.g. (Glocker 2001), (Pfeiffer & Glocker 1996) or (Eberhard 2000). During impact the equations of motion (1) have to be extended by the impact force F which is assumed to act in normal direction to the impact points,

$$\mathbf{M}\,\ddot{\mathbf{y}} + \mathbf{k} = \mathbf{q} + \mathbf{w}\,\mathrm{F}. \tag{2}$$

The vector $\mathbf{w}$ projects the impact force from the normal direction of the impact on the direction of the generalized coordinates. Due to the assumption of infinitesimal impact duration, the velocity changes in a jump, whereas the position remains unchanged. The equation of motion during impact is then formulated on velocity level,

$$\lim_{t_e \to t_s} \int_{t_s}^{t_e} (\mathbf{M}\,\ddot{\mathbf{y}} + \mathbf{k} - \mathbf{q} - \mathbf{w}\,\mathrm{F})\mathrm{d}t = \mathbf{M}\,(\dot{\mathbf{y}}_e - \dot{\mathbf{y}}_s) - \mathbf{w}\,\Delta\mathrm{P} = \mathbf{0}, \tag{3}$$

where the indices s and e mark the start and end of the impact, respectively. In the limit case the quantities $\mathbf{M}$ and $\mathbf{w}$ are constant and all but the impact forces vanish due to their limited amplitudes. However, the infinitely large impact force F yields a finite force impulse ΔP which results in the jump of the generalized velocities and the non-smooth behavior. The impact force F and, therefore, the impulse ΔP are still unknown. The coefficient of restitution e provides additional information for the assessment of the impulse. Using the kinetic coefficient of restitution due to Poisson, the impact duration is divided into a compression and a restitution phase. The compression phase starts at time t_s and ends with time t_c, which is marked by the vanishing relative normal velocity. The restitution phase starts at time t_c and ends at t_e. The kinetic coefficient of restitution is defined as the ratio of the impulses $\Delta\,\mathrm{P_c}$ and $\Delta\,\mathrm{P_r}$ during the compression and restitution of the impact, respectively. An impact with $e = 1$ is called elastic and indicates no energy loss, whereas an impact with $e = 0$ is called plastic or inelastic and indicates maximal energy loss, resulting in a permanent contact. However, it should be noted, that the terms 'elastic' and 'plastic' describe here only the impact behavior and have little to do with the material behavior. As shown in (Schiehlen, Seifried & Eberhard 2006) and (Seifried 2005) the impulse during the compression phase reads as

$$\Delta\mathrm{P_c} = \frac{-\dot{g}_s}{\mathbf{w}^{\mathrm{T}}\mathbf{M}^{-1}\,\mathbf{w}}, \tag{4}$$

where $\dot{g}_s$ is the relative normal velocity of the contact points before impact. The total impulse during impact follows as

$$\Delta\mathrm{P} = \Delta\mathrm{P_c} + \Delta\mathrm{P_r} = (1 + \mathrm{e})\Delta\mathrm{P_c} \tag{5}$$

and using Eq. (3) the generalized velocities after impact can be computed. In the case of more than one impact occurring simultaneously or a permanent contact opening due to impact, respectively, the corresponding equations have to be solved simultaneously resulting in linear complementarity problems (LCPs), see (Pfeiffer & Glocker 1996). The impact modeling using Poisson's coefficient of restitution is a very efficient method for treating impacts in multibody systems if the coefficient of restitution is known. The coefficient of restitution is usually found by experiments or it is known from experience. However, the coefficient of restitution may be evaluated numerically by additional simulations on a fast time scale, too, see (Schiehlen & Seifried 2004), (Schiehlen & Seifried 2005) and (Schiehlen, Seifried & Eberhard 2006). This results in a multiscale simulation approach. The simulation on the slow time scale is interrupted by an impact. Then, for the impact, a detailed simulation with deformable bodies is performed on a fast time scale including elastodynamic wave propagation and elastic-plastic material phenomena. The generalized coordinates and velocities before impact are used as initial conditions for the simulations on the fast time scale. These simulations are limited to the impact duration and from the time-continuous impact force F the resulting impulse $\Delta \mathrm{P}$ is computed and the kinetic coefficient of restitution follows as

$$\mathrm{e} = \frac{\Delta \mathrm{P}_\mathrm{r}}{\Delta \mathrm{P}_\mathrm{c}} = \frac{\Delta P - \Delta \mathrm{P}_\mathrm{c}}{\Delta \mathrm{P}_\mathrm{c}} = -\frac{\mathbf{w}^\mathrm{T}\mathbf{M}^{-1}\mathbf{w}\Delta\mathbf{P}}{\dot{g}_\mathrm{s}} - 1. \tag{6}$$

See (Schiehlen, Seifried & Eberhard 2006) and (Seifried 2005) for more details. The coefficient of restitution is now fed back to the slow time scale. Then, the generalized velocities after impact are computed using Eq. (3)–(5).

3 Numerical models

The computation on the fast time scale requires numerical models which include wave propagation within the bodies, and elastic or elastic-plastic deformation of the contact region. First of all, a complete Finite Element (FE) model of the impacting bodies is used. Detailed information and the theoretical background of FE contact is available in the literature e.g. (Bathe 1996), (Kikuchi & Oden 1989), (Papadopoulos & Taylor 1992), (Wriggers 2002) and (Zhong 1993). For modeling impacts, a small overall element length is required to comprise the wave propagation in the bodies and an additional refinement is necessary for the modeling of the contact region, see Reference (Seifried, Hu & Eberhard 2003). Thus, FE-models for impact analysis are excessively time consuming and not suitable for larger impact systems as found in engineering.

Therefore, in a more time efficient numerical approach, impact processes are divided into two parts, a small contact region and the remaining body featuring wave propagation, (Schiehlen, Seifried & Eberhard 2006) and (Seifried 2005). This procedure is also called boundary approach. The contact is a nonlinear problem which is limited to a small region, while the wave propagation is a linear problem encompassing the entire body. Thus, combined models are developed in which the elastodynamic behavior of the impacting bodies is represented by a modally reduced model and the deformation of the contact region is presented by a local contact model based on FE-models of the contact region. The local contact model is than either concurrently computed or

Table 1 Comparison of numerical models for sphere to rod impact.

model	*coeff. of restitution*		*computation time [s]*	
	elastic	*plastic*	*elastic*	*plastic*
A. complete nonlinear FE-model	0.633	0.481	462	937
B. modal model + concurrently-computed FE contact	0.631	0.477	285	354
C. modal model + pr-computed FE contact	0.632	0.477	0.04	0.05

pre-computed and then coupled with the reduced elastodynamic model of the impacting bodies, see (Schiehlen, Seifried & Eberhard 2006), (Seifried, Schiehlen & Eberhard 2005) and (Seifried & Eberhard 2005). The efficiency and consistency of the combined models is demonstrated for the impact of a steel sphere (radius = 15 mm) on aluminum rods (radius = 10 mm, length = 1000 mm) with initial velocity of 0.3 m/s. The rods have elastic and elastic-plastic material behavior, respectively. The computed coefficients of restitution and computation times are summarized in Table 1. For the FE computations the commercial FE code (ANSYS) is used. It turns out clearly that the simulation results obtained from the different models agree very well. It is also obvious that the completely nonlinear FE model is very time consuming, especially when including elastic-plastic material behavior. Using a modal model with concurrently computed FE-contact the computation time is reduced by 40–60%. A tremendous decrease in the computation time is achieved using the modal model with pre-computed FE contact. However, it should be noted that the pre-computation of the force-deformation diagram is time consuming, too, especially for elasto-plastic material behavior. The computation time corresponds to about 15 impact simulations with the nonlinear FE model. Therefore, the benefit of the modal model with pre-computed FE-contact takes place especially when many impacts are investigated.

4 Essential parameters for the coefficient of restitution

The coefficient of restitution depends not only on the material parameters but also strongly on the contact geometry, the body geometry and the initial velocity. Early experimental results for the evaluation of the coefficient of restitution are summarized in (Goldsmith 1960), more recent numerical and experimental results are presented in (Minamoto 2005), (Sondergaard, Chaney & Brennen 1990), (Wu, Li & Thornton 2003), (Zhang & Vu-Quoc 2002) and (Schiehlen & Seifried 2004, 2005, 2006). In Figure 1 the influence of the material properties and the initial velocity on the coefficient of restitution is presented for the impact of a steel sphere (radius = 15 mm) on two different aluminum rods (radius = 10 mm, length = 1000 mm). Rod 1 has a low yield stress of 205 MPa and rod 2 has a high yield stress of 575MPa. The sphere has an initial velocity in the range of 0.05–0.50 m / s, the rods are initially in rest. For the experimental evaluation a test bench with two Laser-Doppler-Vibrometer is used, see (Hu & Eberhard & Schiehlen 2003).

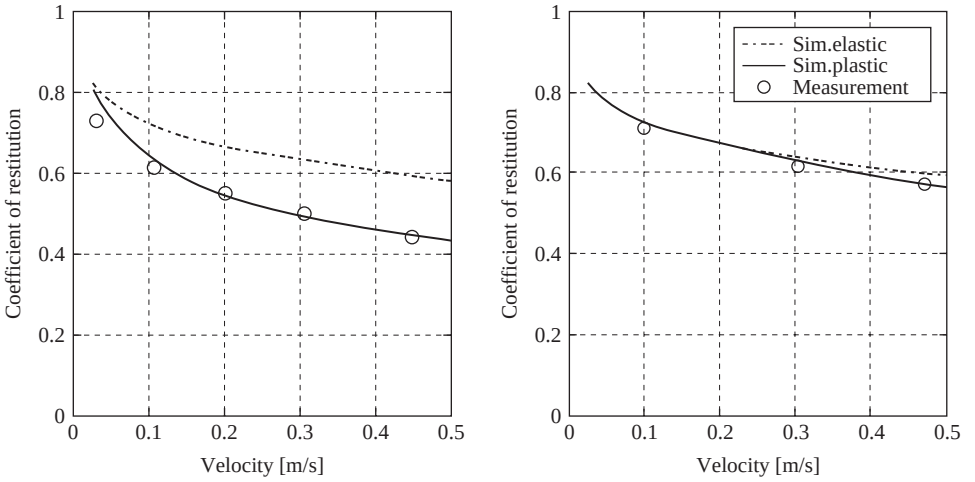

Figure 1 Impact of a hard steel sphere on two aluminum rods (left: rod 1 with low yield stress 205 MPa, right: rod 2 with high yield stress 575 MPa).

It is clearly seen from simulations and experiments that for both impact systems the coefficient of restitution decreases with increasing initial velocity. For rod 1 the measured coefficients and the ones obtained from simulations with elastic-plastic material behavior agree very well. However they are significantly lower than coefficients obtained from simulations with purely elastic material behavior. For rod 2, this has a high yield stress; simulations with elastic and elastic-plastic material behavior show for the investigated velocity range nearly identical behavior and agree well with experimental results. In (Schiehlen, Seifried & Eberhard 2006) and (Seifried, Schiehlen & Eberhard 2005) the influence of plastification on the coefficient of restitution for repeated impacts is investigated for both rods.

The influence of the shape of the bodies on the coefficient of restitution is investigated in (Schiehlen & Seifried 2004) for the impact of a steel sphere on four elastic aluminum bodies with equal mass but different shape. These are a compact cylinder, a half-circular plate, a long rod and a slender beam. Figure 2 shows the computed coefficients of restitution of these impact systems for the velocity range 0.025–0.50 m/s. The computed coefficient of restitution for the cylinder is close to $e = 1$ for the investigated velocity range. For the impact on the cylinder the transformation of initial kinetic energy into waves and vibrations can be neglected. From the simulations for the rod and half-circular plate it is seen that the coefficient of restitution decreases steadily with increasing initial velocity. This indicates an increase of energy transformation from the initial rigid body motion into waves and vibrations with increasing velocity. The transverse impact on the beam excited very strong vibration phenomena in the beam resulting in multiple successive impacts within a very short time period. In sharp contrast to the previous impact systems the beam impact shows no clear pattern but a strong uncertainty, see also (Seifried2005). This phenomenon is discussed in more detail in the next chapter.

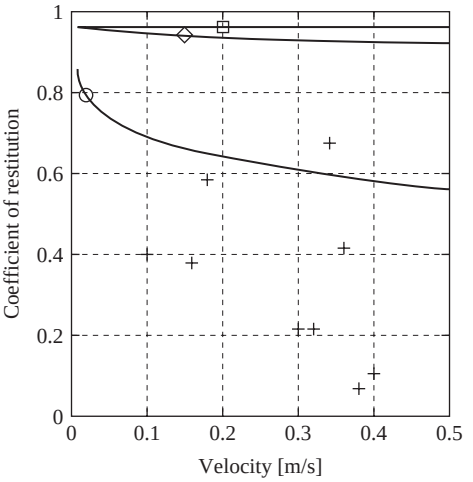

Figure 2 Impact of a hard steel sphere on differently shaped aluminum bodies (□ compact cylinder, ◇ half circular plate, ○ rod, + beam).

5 Uncertainty of the coefficient of restitution

The impact on a beam features multiple impacts which are caused by the strong bending vibrations of the beam, resulting from the first impact. The multiple impacts are the source of the uncertainty of the coefficient of restitution. Since more than one successive impact occur within a short time period efficient numerical methods for impact simulation on the fast time are even more important than for single impacts.

5.1 *Comparison of numerical models*

A comparison of the simulation results using the different numerical models is discussed now. Table 2 summarizes the coefficients of restitution and computation times of the simulations for the impact of a steel sphere (radius = 15 mm) on an elastic aluminum rod (radius = 10 mm, length = 1000 mm) with initial velocity 0.2 m / s. This shows again the good agreement of the modal models with FE-contact and the complete FE-model. It turns out that the complete FE-model is very time consuming. By using modal models the computation times can be reduced significantly. Using the modal model with concurrently computed FE-contact the computation time can be reduced by 97%. Using the modal model with pre-computed FE-contact the computation time can be reduced further, however the computation time for the force-displacement diagram has to be considered, which takes in this case about 1000 s. This shows clearly, that for a larger and complex impact system, such as the transverse impact on a beam, the modal model with pre-computed FE-contact is the most efficient approach.

5.2 *Experimental validation*

For the experimental validation of the simulation results an experimental setup, originally developed by (Hu et al. 2003) and (Hu & Eberhard 1999), was adapted to beam

Table 2 Comparison of numerical models for sphere to beam impact.

	coeff. of restitution	*computation time [s]*
A. complete nonlinear FE-model	0.707	80564
B. modal model + concurrently-computed FE contact	0.700	2422
C. modal model + pr-computed FE contact	0.717	16

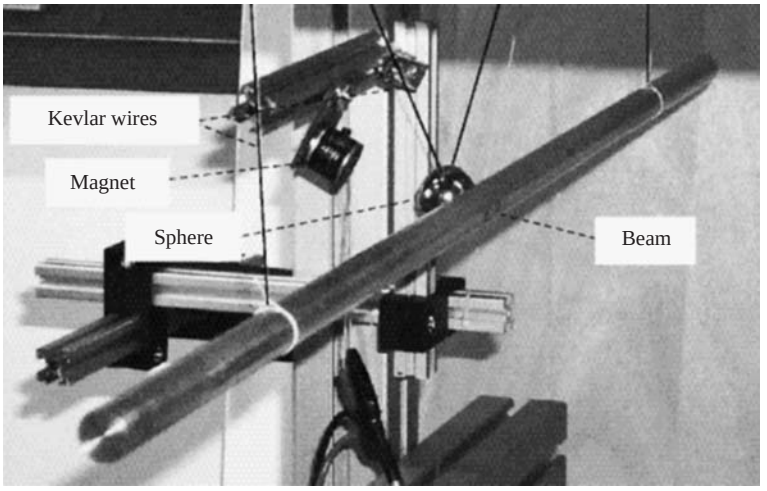

Figure 3 Experimental setup for sphere to beam impact.

impacts, see Figure 3. The sphere and beam are suspended with thin Kevlar wires in a frame as pendula. The sphere is released by a magnet from a predefine height and it impacts on the beam along its symmetry line. Two Laser-Doppler-Vibrometers are used for displacement and velocity measurement of sphere and beam in the central line of impact.

Figure 4 shows for the initial velocity 0.276 m/s the measured and simulated displacement of sphere and beam, as well as the velocity of the sphere. It is obvious from measurement and simulation, that within a few milliseconds several impacts occur.

Figure 4 shows a very good agreement for the first impact as well as consistently a second impact after 4 ms. However, for the successive impacts significant differences may occur resulting in an overall uncertainty. For the impact with an initial velocity 0.276 m/s the second impact yield only to a small velocity change. Therefore, after 5.2 ms a third impact occurs, which results in a large velocity change of the sphere. In this case experiment and simulation agree very well. This is also reflected by the good agreement of the measured and simulated coefficients of restitution which are $e_m = 0.664$ and $e_s = 0.687$, respectively.

However an impact with the initial velocity 0.287 m/s shows in the simulation a much stronger second impact than in the experiment, see Figure 5. This results in a very different behavior of the following motion. Consequently the coefficient of restitution

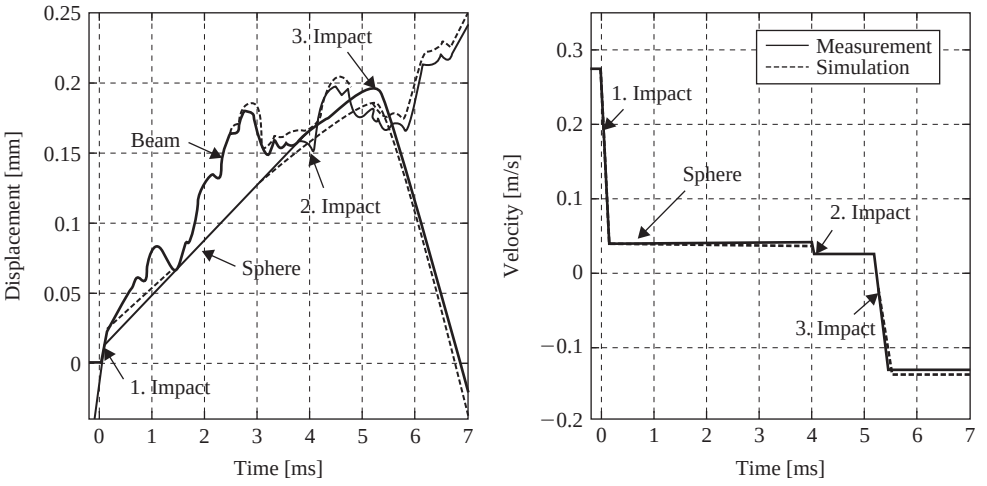

Figure 4 Impact on beam with initial velocity 0.276 m/s.

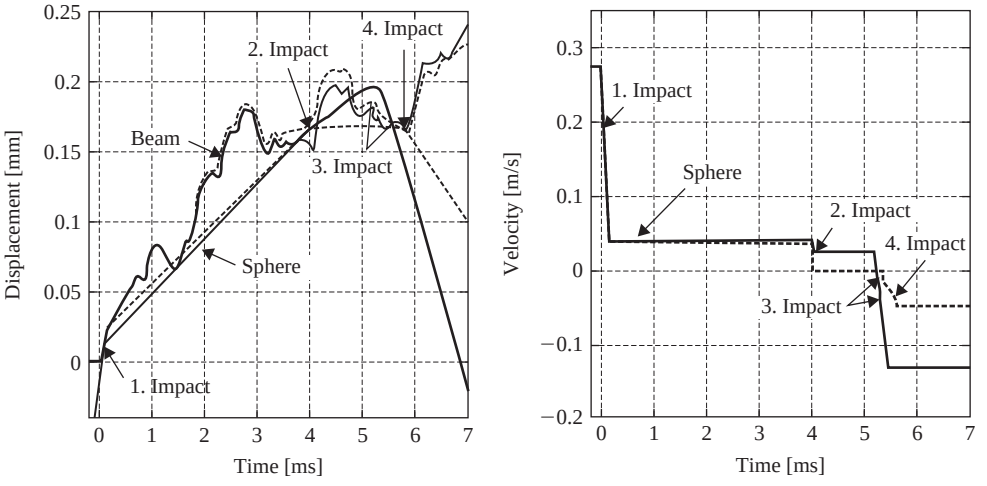

Figure 5 Impact on beam with initial velocity 0.287 m/s.

computed from measurement and simulations differ strongly and are $e_m = 0.620$ and $e_s = 0.334$.

For an impact with initial velocity 0.303 m/s the experiment proves that sphere is in rest after the second impact and a third impact occurs after 5.7 ms. In the simulation the second impact is stronger as the one in the experiment. Thereby the sphere rebounds and no further impact occurs in the simulation. Measurement and simulation yield hereby nearly identical coefficients of restitution of $e_m = 0.230$ and $e_s = 0.243$. The impact on a beam with elastic-plastic material behavior is presented in (Seifried 2007). Thereby a similar behavior with multiple impacts within a short time period is observed.

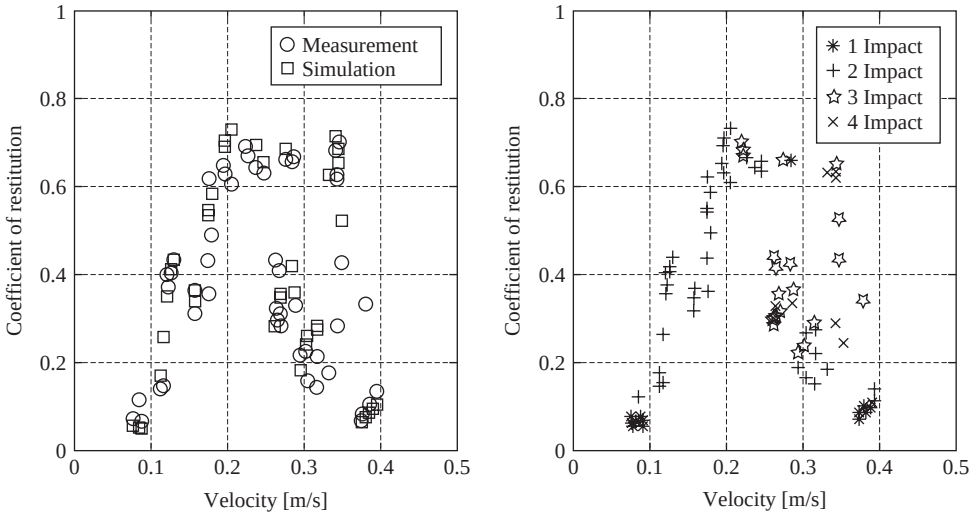

Figure 6 Multiple impacts on an elastic aluminum beam.

5.3 *Analysis of the coefficient of restitution*

In Figure 6 simulated and measured coefficients of restitution are presented for 53 different initial velocities of the sphere. Due to the multiple impacts the coefficient of restitution depends strongly on the initial velocity, however, without showing a clear pattern but strong uncertainty. The coefficients of restitution are in the range $e = 0.07$–0.73. Small differences of the simulated and measured motion of beam and sphere after the first impact result in very different behavior of the successive impacts. As a result, the investigated impacts show significant differences of the measured and simulated coefficients of restitution, for different initial velocities.

In the right plot of Figure 6 the numbers of multiple impacts are indicated for simulation and measurements. It turns out that only for very low velocities one impact occur. For higher velocities 2, 3 or 4 successive impacts occur, however no relationship between the coefficient of restitution and the number of multiple impacts is obvious.

For the discussion of the chaotic behavior statistical methods will be used. The relative cumulative frequency or the probability, respectively, is shown in Figure 7 for four velocity classes, see Table 3. From these data the relative frequency or probability density, respectively, is obtained, see Figure 8. It turns out that the frequency distribution is completely non-Gaussian, and the range characterizing the statistical dispersion is increasing with the relative velocity of the impact, while midrange point and mean value coincide fairly well, see Table 4.

In class 1 one or two impacts occur where the one impact regime results in very strong structural waves corresponding to a very low coefficient of restitution. If a second impact occurs then some of the wave energy is regained and the coefficient of restitution is higher. In class 2 mainly two impacts occur with medium coefficients of restitution. In class 3 three and more impacts take place with a larger range of the

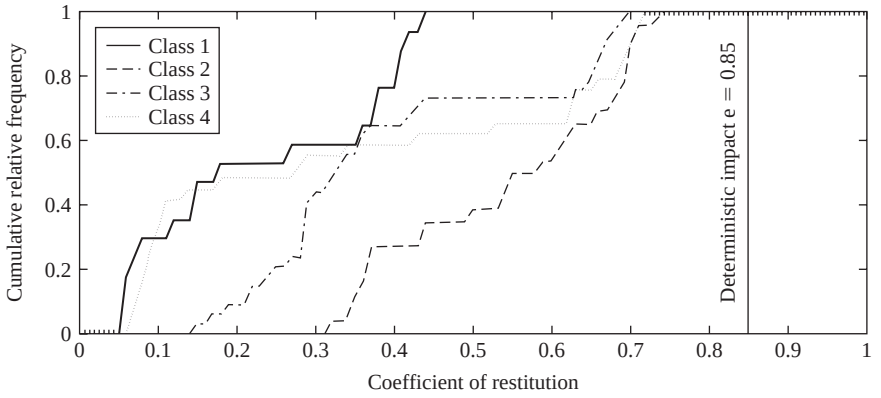

Figure 7 Cumulative relative frequency or probability, respectively.

Table 3 Classification of velocities.

	velocity
class 1	0.05 m/s $\leq$ v $<$ 0.14 m/s
class 2	0.14 m/s $\leq$ v $<$ 0.23 m/s
class 3	0.23 m/s $\leq$ v $<$ 0.32 m/s
4lass 4	0.32 m/s $\leq$ v $<$ 0.41 m/s

Table 4 Statistical evaluation of data of coefficient of restitution.

velocity class	*1*	*2*	*3*	*4*
mean value	0.229	0.543	0.392	0.342
midrange point	0.244	0.522	0.422	0.392
range	0.383	0.417	0.550	0.650

coefficient of restitution. In class 4 the higher velocities result in two impacts, both of them producing very strong structural waves.

The interaction between the rigid sphere and the flexible beam is a mechanical phenomenon characterized by the microscale of the contact and the phase shift of the waves traveling in the beam resulting in an overall chaotic behavior on the macroscale of the impacting bodies.

6 Conclusions

Measurements and simulations for the transverse impact of a steel sphere on an aluminum beam show multiple successive impacts within a very short time period, resulting in a uncertain behavior of the coefficient of restitution. For the evaluation of the numerical and experimental data, a statistical approach using mean value and dispersion of the coefficient of restitution underlines the chaotic behavior of the beam's

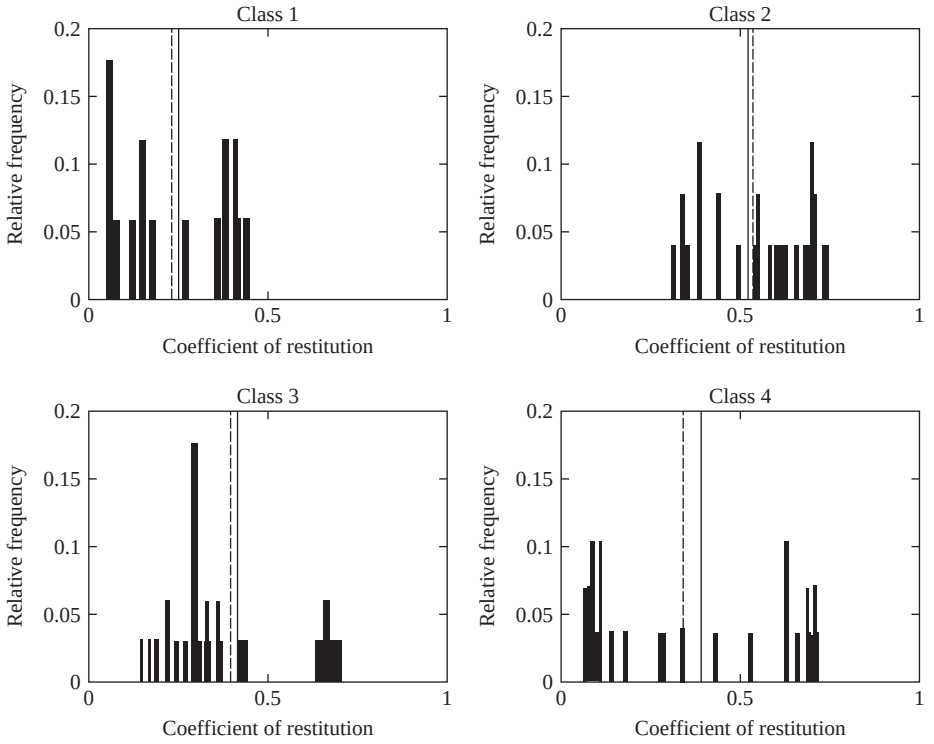

Figure 8 Relative frequency or probability distribution, respectively. (-- mean value, — midrange point).

structural vibrations. The statistical range is increasing with the relative velocity of the impact. However, the mean value or midrange point, respectively, may be used to solve the structural dynamics beam problem.

References

ANSYS Inc. 1997. *ANSYS Theory Reference*, Release 5.4., Canonsburg.

Bathe, K. 2002. *Finite Element Procedures*, Upper Saddle River : Prentice-Hall.

Eberhard, P. 2000. *Kontaktuntersuchungen durch hybride Mehrkörpersystem / Finite Elemente Simulation* (in German), Aachen: Shaker.

Glocker, C. 2001. On frictionless impact models in rigid-body systems. *Philosophical Transactions of the Royal Society of London*, A359: 2385–2404.

Goldsmith, W. 1960. *Impact*, London: Edward Arnold Ltd.

Hu, B. & Eberhard, P. 1999. *Experimental and theoretical investigation of a rigid body striking an elastic rod*. Institutsbericht IB-32, Stuttgart: Institute B of Mechanics.

Hu, B., Eberhard, P. & Schiehlen, W. 2003. Comparison of analytical and experimental results for longitudinal impacts on elastic rods. *Journal of Vibration and Control*, 9: 157–174.

Kikuchi, N. & Oden, J. 1989. *Contact Problems in Elasticity: A Study of Variational Inequalities and Finite Element Methods*, Philadelphia: SIAM.

Minamoto, H. 2005. Elasto/Visco-plastic impact of two equivalent spheres made of SUJ2 (in Japanese). *Transactions of the Japan Society of mechanical Engineers*, C71: 51–57.

Papadopoulos, P. & Taylor, R. 1992. A mixed formulation of the finite element solution of contact problems. *Computer Methods in Applied Mechanics and Engineering,* 94: 373–389.

Pfeiffer, F. & Glocker, C. 1996. *Multibody Dynamics with Unilateral Contacts*, New York: Wiley.

Schiehlen, W. & Eberhard, P. 2004. *Technische Dynamik*, (in German) Wiesbaden: Teubner, 2004.

Schiehlen, W., Guse, N. & Seifried, R. 2006. Multibody dynamics in computational mechanics and engineering Applications. *Computer Methods in Applied Mechanics and Engineering,* 195: 5509–5522.

Schiehlen, W. & Seifried, R. 2004. Three approaches for elastodynamic contact in multibody systems. *Multibody System Dynamics,* 12: 1–16.

Schiehlen, W. & Seifried, R. 2005. Impact mechanics in mechanical engineering. *Proceedings of the International Conference on Mechanical Engineering and Mechanics 2005 (ICMEM),* Nanjing, China, October 26–25: 2–10.

Schiehlen, W. & Seifried, R. 2006. Impact systems with uncertainty. In H. Hu & E. Kreuzer & Z. Wang (eds.), *Proceedings of the IUTAM Symposium on Dynamics and Control of Nonlinear Systems with Uncertainty,* Nanjing, China, September 18–22.

Schiehlen, W., Seifried, R. & Eberhard, P. 2006. Elastoplastic phenomena in multibody impact dynamics. *Computer Methods in Applied Mechanics and Engineering*, 195: 6874–6890.

Seifried, R. 2005. *Numerische und experimentelle Stoßanalyse für Mehrkörpersysteme*, (in German). Dissertation, Schriften aus dem Institut für Technische und Numerische Mechanik der Universität Stuttgart, Band 2, Aachen: Shaker.

Seifried, R. 2007. Effect of body flexibility on impacts studied on rods and beams. *Proceedings of the ASME 2007 International Design Engineering Technical Conferences and Computers and Information in Engineering Conference (IDETC/CIE 2007)*, Las Vegas, USA, September 4.-7, DETC2007-34817.

Seifried, R. & Eberhard, P. 2005. Comparison of numerical and experimental results for impacts. D. van Campen & M. Lazurko & W. van der Oever (eds.). *Proceedings of the ENOC-2005 Fifth EUROMECH Nonlinear Dynamics Conference*, Eindhoven, The Netherlands, August 7–12: 399–408.

Seifried, R., Hu, B. & Eberhard, P. 2003. Numerical and experimental investigation of radial impacts on a half-circular plate. *Multibody Systems Dynamics*, 9: 265–281.

Seifried, R., Schiehlen, W. & Eberhard, P. 2005. Numerical and experimental evaluation of the coefficient of restitution for repeated impacts. *International Journal of Impact Engineering*, 32: 508–524.

Sondergaard, R., Chaney, K. & Brennen, C. 1990. Measurement of solid spheres bouncing off flat plates. *Journal of Applied Mechanics,* 57:694–699.

Stronge, W. 2000. *Impact Mechanics*. Cambridge: Cambridge University Press.

Wriggers, P. 2002. Computational Contact Mechanics, Chichester: Wiley.

Wu, C., Li, L. & Thornton, C. 2003. Rebound behavior of spheres for plastic impacts. *International Journal of Impact Engineering,* 28: 929–946.

Zhang, X. & Vu-Quoc, L. 2002. Modeling of the dependence of the coefficient of restitution on impact velocity in elasto-plastic collisions. *International Journal of Impact Engineering,* 27: 317–341.

Zhong, Z.-H. 1993. Finite Element Procedures for Contact-Impact Problems, New York: Oxford University Press.

Chapter 10

Rational derivation of conserving time integration schemes: The moving-mass case

Elias Paraskevopoulos, Christos Panagiotopoulos & Demosthenes Talaslidis

Aristotle University Thessaloniki, Thessaloniki, Greece

ABSTRACT: A rational approach is proposed for the time integration of the dynamic equations arising in nonlinear structural problems, which employs a series of innovative concepts, e.g.: independent assumptions for the velocities and momentum type variables, use of different approximations for the test functions and the variables itself, and abandonment of the convention concerning the vanishing of the test functions at the time boundaries. The presented methodology offers a systematic and mathematically consistent procedure for time integration, ensures consistency and stability, and avoids flaws of existing techniques. Conservation properties are examined employing a form of Noether's Theorem. Furthermore, existing integration schemes may be theoretically justified by the present approach. The methodology is applied to the analysis of systems under moving loads and masses. Since this class of problems contains Dirac's delta function and its time derivatives, the effective numerical treatment of the governing equations offers a challenging problem.

1 Introduction

In developing time integration techniques for engineering applications, efficiency and accuracy are key features of the algorithm. Moreover, in nonlinear dynamical systems, numerical stability of time integration methods is of profound interest, since unconditional stable algorithms for linear dynamics often lose their stability in the nonlinear case. In other words, unconditional stability in the nonlinear range is manifested through conservation of energy. In this context, representation of the time parameter plays an important role: With regard to the three-dimensional space, the tensorial formulation of the equations of motion ensures frame-invariance under arbitrary transformations. However, with regard to time, invariance is assured only for Galilean transformations. Furthermore, if time is considered as independent variable, a complete description of the dynamic problem requires-additionally to the usual field equations-a condition of conserving the state of energy. Finally, a consistent, covariant formulation can be achieved if space and time are combined into a single entity, known as "spacetime."

Attempts to take into account the aforementioned condition have in common that conservation of properties is considered either explicitly, by including the necessary conditions as constraints, or modifying the algorithms by employing specific

coefficients, or evaluating field variables at specific points according to a posteriori considerations. To be more specific, research efforts followed various paths that led to alternative methods for preserving stability by satisfying appropriate stability criteria: Integration algorithms employing numerical dissipation of energy such as the "generalized alpha-method" (Chung & Hulbert 1993), methods enforcing conservation of energy via Lagrange multipliers, so-called "constraint energy methods" (Hughes et al. 1978), or techniques applying algorithmic preservation of energy ("energy-momentum method" proposed by Simo & Tarnow 1992). Additional approaches are known as "Variational time integrators" (Lew et al. 2004) or "Time discretized operators" (Tamma et al. 2003a, b). For further contributions and alternative schemes, the reader is referred to Kuhl & Ramm (1999). Many of the aforementioned methods are based on intuition or ad hoc techniques, may lead to failure during incremental iterations of equilibrium, or do not guarantee conservation/dissipation of energy for all time integration parameters. The later is a key issue for unconditional stability in the nonlinear range.

In the present paper, a rational approach is proposed for the time integration of the dynamic equations. The development rests upon a series of concepts, e.g.: The velocities and the corresponding momentum type quantities are treated as independent variables and the relationships between weak velocities and derivatives of displacements are introduced in a weak form. Departing from the usual procedure, different approximations are employed for the test functions and the variables itself. Contrary to many existing approaches, the convention concerning vanishing of the test functions at the time boundaries-widely used in the Hamilton's principle family-is not followed in the present approach. Furthermore, the weak formulation of the governing equations is given and the temporal discretization scheme is presented. Conservation properties of total linear and angular momentum as well as of energy are examined employing a form of Noether's Theorem.

The proposed methodology ensures consistency and stability and avoids the flaws of previously proposed schemes. The approach offers a systematic and mathematically consistent procedure for time integration of nonlinear problems. Many existing integration schemes may be theoretically justified by the proposed approach and can be derived as special cases of the presented method (e.g., Simo's discrete energy-momentum method for nonlinear elastodynamics, Simo & Tarnow 1992). Furthermore, the methodology is valid for a large variety of nonlinear dynamic problems.

The presented approach is applied to the dynamic analysis of structural systems (e.g., bridges) under moving vehicles. The vibrations caused by the passage of vehicles and the interaction problem between the moving vehicle and the bridge have attracted much attention and are of importance in civil engineering. The relationships describing such problems differ from the usual equations of motion in structural dynamics due to the presence of the Dirac's delta function and its time derivatives. Therefore, the effective numerical treatment of the equations governing this type of problems and their reliable time integration offer a challenging problem. The weak statement for the moving load/mass problem on an Euler-Bernoulli beam is presented and numerical results for a simple example are shown, which serve to demonstrate characteristic properties of the proposed methodology.

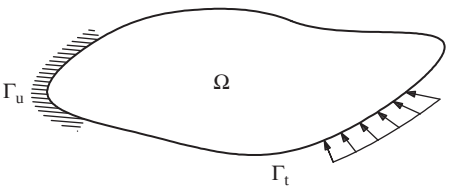

Figure 1 Reference domain.

2 Governing equations

The following hyperbolic, initial boundary-value problem serves as a starting point for the subsequent developments:

$$\rho\ddot{\mathbf{u}} - \frac{\left(\sqrt{g}s^{ij}\mathbf{g}_j\right)_{,i}}{\sqrt{g}} = \mathbf{f}(\mathbf{x},t), \quad (\mathbf{x},t) \in \Omega \times (0,T] \tag{1}$$

$$\mathbf{u}(\mathbf{x},t) = \tilde{\mathbf{u}}(\mathbf{x},t), \quad (\mathbf{x},t) \in \Gamma_u \times (0,T] \tag{2}$$

$$s^{ij}\mathbf{g}_j n_i = \tilde{\mathbf{t}}(\mathbf{x},t), \quad (\mathbf{x},t) \in \Gamma_t \times (0,T] \tag{3}$$

$$\mathbf{u}(\mathbf{x},0) = \tilde{\mathbf{u}}_0(\mathbf{x}), \quad \mathbf{x} \in \Omega \tag{4}$$

$$\dot{\mathbf{u}}(\mathbf{x},0) = \tilde{\mathbf{v}}_0(\mathbf{x}), \quad \mathbf{x} \in \Omega \tag{5}$$

In Eqs. (1–5), the vector $\mathbf{x}$ and the scalar t denote spatial coordinates (x^i) and time, respectively. The vector $\mathbf{u}$ signifies the displacement vector with contravariant components u^i, the components s^{ij} denote the contavariant components of the stress tensor, and the vectors $\mathbf{f}$, $\tilde{\mathbf{u}}_0$, and $\mathbf{v}_0$ are prescribed functions. The vectors $\tilde{\mathbf{u}}(\mathbf{x},t)$ and $\tilde{\mathbf{t}}(\mathbf{x},t)$ represent time dependent prescribed boundary conditions on the parts Γ_u and Γ_t of the boundary Γ, respectively, and ρ denotes mass density. Finally, n_i signify the components of the outward unit normal to Γ_t. It should be noted that this set of equations is supplemented by the equilibrium of angular momentum (a generalized symmetry condition on the stress tensor), the material law, and the kinematic relationships between strains/rigid rotations and the spatial derivatives of displacements.

3 Variational formulation

Multiplying Equation 1 by the arbitrary function

$$\delta\mathbf{u} \in W, \quad W = \{\mathbf{w} \in H^1(\Omega) : \mathbf{w} = \mathbf{0} \text{ on } \Gamma_u\} \tag{6}$$

performing the spatial integration, applying Green's theorem, and employing the natural boundary conditions (Eq. 3), we obtain

$$\iint_{\Omega} \rho \ddot{\mathbf{u}} \cdot \delta \mathbf{u}\, d\Omega + \iint_{\Omega} s^{ij} \mathbf{g}_j \cdot \delta \mathbf{u}_{,i}\, d\Omega - \int_{\Gamma_t} \tilde{\mathbf{t}} \cdot \delta \mathbf{u}\, d\Gamma_t - \iint_{\Omega} \mathbf{f} \cdot \delta \mathbf{u}\, d\Omega = 0 \tag{7}$$

By integrating Equation 7 over the time interval $I \in (0, T]$ and by performing an integration by parts to the first term of the left hand side, yields the following weak formulation of Equation 1: Find

$$\mathbf{u} \in U \quad U = \{\mathbf{u} \in L_2(I, H^1(\Omega)) \,:\, \dot{\mathbf{u}} \in L_2(I, H^1(\Omega))\} \tag{8}$$

satisfying the relationship

$$\begin{aligned} &\int_0^T \left(\iint_{\Omega} -\rho \dot{\mathbf{u}} \cdot \delta \dot{\mathbf{u}}\, d\Omega + \iint_{\Omega} s^{ij} \mathbf{g}_j \cdot \delta \mathbf{u}_{,i}\, d\Omega - \int_{\Gamma_t} \tilde{\mathbf{t}} \cdot \delta \mathbf{u}\, d\Gamma_t \right. \\ &\qquad \left. - \iint_{\Omega} \mathbf{f} \cdot \delta \mathbf{u}\, d\Omega \right) dt + \left[\iint_{\Omega} \rho \dot{\mathbf{u}} \cdot \delta \mathbf{u}\, d\Omega \right]_{t=0}^{t=T} = 0 \\ &\forall\, \delta \mathbf{u} \in W, \quad W = \{\mathbf{w} \in L_2(I, H^1(\Omega)) \,:\, \dot{\mathbf{w}} \in L_2(I, H^1(\Omega)),\, \mathbf{w} = \mathbf{0} \text{ on } \Gamma_u\} \end{aligned} \tag{9}$$

as well as the essential boundary conditions 2, and the initial condition 4. Moreover, in the presence of material nonlinearities, the above system of equations is augmented by the constitutive equations, i.e., the state equations and the flow rule.

4 Introducing weak velocities

A variety of alternative variational formulations may serve as a starting point for the formulation and the subsequent numerical treatment of dynamic problems see, e.g., the monographs by Pars (1965), Lanczos (1974), and Hughes (1976). In the present paper, the relationships between the weak velocities and the strong time derivatives of displacements are introduced via Lagrange multipliers (momentum type variables) in the variational formulation. Thus, velocities and momentum type variables are treated as independent variables. The proposed methodology offers a series of distinct advantages over conventional approaches and has been successfully employed for the development of useful approximating schemes, e.g., for the consistent derivation of diagonal mass matrices (Paraskevopoulos & Talaslidis 2004). As a result, the weak formulation 9 assumes the following form: Find

$$\begin{aligned} &\{\mathbf{u}, \mathbf{v}, \mathbf{p}\} \in U \times V \times V, \\ &U = \{\mathbf{u} \in L_2(I, H^1(\Omega)) \,:\, \dot{\mathbf{u}} \in L_2(I, H^1(\Omega))\},\, V = \{v \in L_2(I, L_2(\Omega))\} \end{aligned}$$

satisfying the relationship

$$\int_0^T \left(\iint_\Omega -\rho \mathbf{v} \cdot \delta \mathbf{v} \, d\Omega + \iint_\Omega s^{ij} \mathbf{g}_j \cdot \delta \mathbf{u}_{,i} \, d\Omega - \int_{\Gamma_t} \tilde{\mathbf{t}} \cdot \delta \mathbf{u} \, d\Gamma_t - \iint_\Omega \mathbf{f} \cdot \delta \mathbf{u} \, d\Omega \right) dt$$
$$+ \int_0^T \left(\iint_\Omega (\mathbf{p} \cdot (\delta \mathbf{v} - \delta \dot{\mathbf{u}}) + \delta \mathbf{p} \cdot (\mathbf{v} - \dot{\mathbf{u}})) d\Omega \right) dt + \left[\iint_\Omega \rho \mathbf{v} \cdot \delta \mathbf{u} \, d\Omega \right]_{t=0}^{t=T} = 0$$
$$\forall \{\delta \mathbf{u}, \delta \mathbf{v}, \delta \mathbf{p}\} \in W \times V \times V,$$
$$W = \{\mathbf{w} \in L_2(I, H^1(\Omega)) \, : \, \dot{\mathbf{w}} \in L_2(I, H^1(\Omega)), \, \mathbf{w} = \mathbf{0} \text{ on } \Gamma_u\} \tag{10}$$

The displacement vector **u** should satisfy the essential boundary conditions 2 and the initial conditions 4. Moreover, the aforementioned system of equations is augmented by the set of constitutive equations. It is mentioned that the constraint between time derivatives of displacements and the weak velocities is enforced in $L_2(\Omega)$ (with respect to space) and that the essential boundary conditions 2 are referred to the displacement variables and their strong time derivatives.

5 Conserved properties of the system

Any dynamical system described by a set of equations possesses some intrinsic properties such as conserved currents. A derived weak statement of the problem should inherit those properties in order to be able to describe the same dynamics. Moreover, its discretized form should reflect the same properties as the initial dynamical system. The celebrated theorem of Emmy Noether provides the basis for the systematic examination of the conserved properties of the weak formulation (Abraham & Marsden 1978, Marsden & Hughes 1983, Arnold 1989). Noether's theorem states that: "*If the Lagrangian function of the system is invariant under a continuous transformation, then there exists an integral of the motion*", i.e., there exist conserved quantities. Invariance of the Lagrangian of the system with respect to a group of transformations means, equivalently, that the basic equations of the system are also form invariant. Recall that in structural mechanics, problems are formulated primarily using the set of Newton's equations, assuming that the space is Euclidian, E, time is one-dimensional, $\mathbb{R}$, and the spacetime is their product, $\mathrm{E} \times \mathbb{R}$. As a consequence, they are form invariant with respect to the group of Galilean transformations, i.e., this group of transformations is the only admissible one.

5.1 *Conservation of energy*

According to Noether's Theorem, for a mechanical system the statement of conservation or dissipation of energy corresponds to invariance under a translation on the time axis. To prove this for the present case, we proceed as follows:

Let us assume that $\{\mathbf{u}_s, \mathbf{v}_s, \mathbf{p}_s, s_s^{ij}\}$ constitute the weak solution of the problem satisfying relationship 10 and the homogeneous essential boundary conditions, and let $(\bar{x}^i, \bar{t})$ denote a selected coordinate system. Furthermore, we assume that the external

loading (traction and body forces) vanish. Consider a second coordinate system (x^i, t) that is related to the former according to the following relations

$$\overline{x}^i = x^i, \quad \overline{t} = t + \varepsilon\tau(x^i, t)$$

where ε is a real continuous parameter and $\tau(x^i, t)$ denotes the generator of the transformation. Therefore, in the coordinate system $(\overline{x}^i, \overline{t})$:

$$\begin{aligned}
&\int_{\overline{t}} \left(\iint_{\overline{\Omega}} -\rho \mathbf{v}_s \cdot \delta\mathbf{v}\, d\overline{\Omega} + \iint_{\overline{\Omega}} s_s^{ij} \mathbf{g}_j \cdot \delta\mathbf{u}_{,i}\, d\overline{\Omega} - \int_{\Gamma_t} \tilde{\mathbf{t}} \cdot \delta\mathbf{u}\, d\Gamma_t - \iint_{\overline{\Omega}} \mathbf{f} \cdot \delta\mathbf{u}\, d\overline{\Omega} \right) d\overline{t} \\
&\quad + \int_{\overline{t}} \left(\iint_{\overline{\Omega}} \left(\mathbf{p}_s \cdot \left(\delta\mathbf{v} - \frac{\partial \delta\mathbf{u}}{\partial \overline{t}} \right) + \delta\mathbf{p} \cdot \left(\mathbf{v}_s - \frac{\partial \mathbf{u}_s}{\partial \overline{t}} \right) \right) d\overline{\Omega} \right) d\overline{t} \\
&\quad + \left[\iint_{\overline{\Omega}} \rho \mathbf{v}_s \cdot \delta\mathbf{u}\, d\overline{\Omega} \right]_{\overline{t}=0}^{\overline{t}=\overline{t}_T} = 0 \\
&\quad \forall \{\delta\mathbf{u}, \delta\mathbf{v}, \delta\mathbf{p}\} \in W \times V \times V
\end{aligned}$$

Performing the change of coordinates and taking into account that $\{\mathbf{u}_s, \mathbf{v}_s, \mathbf{p}_s\}$ is the weak solution of the problem, we obtain,

$$\begin{aligned}
&\int_t \left(\iint_{\Omega} (-\rho \mathbf{v}_s \cdot \delta\mathbf{v}) \varepsilon\dot{\tau}\, d\Omega \right) dt + \int_t \left(\iint_{\Omega} (s_s^{ij} \mathbf{g}_j \cdot \delta\mathbf{u}_{,i}) \varepsilon\dot{\tau}\, d\Omega \right) dt \\
&\quad + \int_t \left(\iint_{\Omega} (\mathbf{p}_s \cdot \delta\mathbf{v}) \varepsilon\dot{\tau}\, d\Omega \right) dt + \int_t \left(\iint_{\Omega} (\delta\mathbf{p} \cdot \mathbf{v}_s) \varepsilon\dot{\tau}\, d\Omega \right) dt = 0
\end{aligned} \tag{11}$$

Realizing that the first and third integral have the opposite sign and are equal in the weak sense, it remains:

$$\int_t \left(\iint_{\Omega} (s_s^{ij} \mathbf{g}_j \cdot \delta\mathbf{u}_{,i}) \varepsilon\dot{\tau}\, d\Omega \right) dt + \int_t \left(\iint_{\Omega} (\delta\mathbf{p} \cdot \mathbf{v}_s) \varepsilon\dot{\tau}\, d\Omega \right) dt = 0 \tag{12}$$

Choosing

$$\begin{aligned}
&\int_t \left(\iint_{\Omega} (\delta\mathbf{p} \cdot \mathbf{f})\, d\Omega \right) dt = \int_t \left(\iint_{\Omega} (\rho \mathbf{v}_s \cdot \mathbf{f})\, d\Omega \right) dt \\
&\int_t \left(\iint_{\Omega} (\mathbf{f} \cdot \delta\mathbf{u})\, d\Omega \right) dt = \int_t \left(\iint_{\Omega} (\mathbf{f} \cdot \mathbf{u}_{s,i})\, d\Omega \right) dt
\end{aligned} \tag{13}$$

where $\mathbf{f}$ denotes an arbitrary vector function and taking into account the integral form of the equilibrium equations, we obtain

$$\left[\iint_{\Omega} (\rho \mathbf{v}_s \cdot \mathbf{v}_s + s_s^{ij} \mathbf{g}_j \cdot \mathbf{u}_{s,i}) \tau(x^i, t)\, d\Omega \right]_{t=0}^{t=T} = 0 \tag{14}$$

Note that in case of the essential inhomogeneous boundary conditions 2, relationships 13 remain valid, if the aforementioned boundary conditions are enforced as

constraints. Setting $\tau(x^i, t) = \text{constant}$, Equation 14 represents the statement of conservation of energy of the system assuming homogeneous boundary conditions, under the assumption of elastic behavior. In case of inhomogeneous boundary conditions, Equation 14 would be augmented by the contribution of the reaction forces. Moreover, in the presence of damping or inelasticity, the same procedure would lead to a statement for the change of the energy of the system, i.e., Equation 14 would be augmented by terms, which represent the energy associated with damping or inelasticity.

5.2 *Conservation of linear and angular momentum*

It is well known that for a continuous mechanical system the statement of the conservation/evolution of linear and angular momentum corresponds, according to Noether's Theorem, to invariance under special changes of the primary variables. More specific, let us assume that the set $\{\overline{\mathbf{u}}_s, \overline{\mathbf{v}}_s, \overline{\mathbf{p}}_s, \overline{s}_s^{ij}\}$ denotes the weak solution of the problem satisfying (Eq. 10). Furthermore, we assume that the external loading (traction and body forces) vanishes. Consider a change of the primary variables that is related to the former according to the following general transformations:

$$\begin{aligned} \overline{\mathbf{u}} &= \mathbf{u} + \boldsymbol{\varepsilon}\boldsymbol{\pi}(x^i, t) \\ \overline{\mathbf{v}} &= \mathbf{v} \\ \overline{\mathbf{p}} &= \mathbf{p} \end{aligned} \tag{15}$$

where ε is a real continuous parameter and $\boldsymbol{\pi}(x^i, t)$ denotes the generator of the transformation. Note that the set $\{\mathbf{u}_s, \mathbf{v}_s, \mathbf{p}_s, s_s^{ij}\}$ is the weak solution with respect to the new representation of the primary variables according to relationships 15. Moreover, the test functions experience no transformation, since this change does not modify the functional spaces of the weak formulation. Therefore, the weak form with respect to $\{\mathbf{u}_s, \mathbf{v}_s, \mathbf{p}_s, s_s^{ij}\}$ assumes the following form:

$$\begin{aligned} &\int_0^T \left(\iint_\Omega -\rho \mathbf{v}_s \cdot \delta\mathbf{v}\, d\Omega + \iint_\Omega s_s^{ij} \mathbf{g}_j \cdot \delta\mathbf{u}_{,i}\, d\Omega - \int_{\Gamma_t} \tilde{\mathbf{t}} \cdot \delta\mathbf{u}\, d\Gamma_t - \iint_\Omega \mathbf{f} \cdot \delta\mathbf{u}\, d\Omega \right) dt \\ &\quad + \int_0^T \left(\iint_\Omega (\mathbf{p}_s \cdot (\delta\mathbf{v} - \delta\dot{\mathbf{u}}) + \delta\mathbf{p} \cdot (\mathbf{v}_s - \mathbf{u}_s))\, d\Omega \right) dt \\ &\quad + \left[\iint_\Omega \rho \mathbf{v}_s \cdot \delta\mathbf{u}\, d\Omega \right]_{t=0}^{t=T} = 0 \\ &\forall \{\delta\mathbf{u}, \delta\mathbf{v}, \delta\mathbf{p}\} \in W \times V \times V \end{aligned}$$

Setting $\mathbf{w} = \varepsilon\boldsymbol{\pi}(x^i, t)$ and all the other test variables equal to zero, we obtain

$$\int_0^T \left(\iint_\Omega -\rho \mathbf{v}_s \cdot \varepsilon\dot{\boldsymbol{\pi}}\, d\Omega + \iint_\Omega s_s^{ij} \mathbf{g}_j \cdot \varepsilon\dot{\boldsymbol{\pi}}\, d\Omega \right) dt + \left[\iint_\Omega \rho \mathbf{v}_s \cdot \varepsilon\boldsymbol{\pi}\, d\Omega \right]_{t=0}^{t=T} = 0 \tag{16}$$

Setting the generator $\boldsymbol{\pi}(x^i, t)$ constant in space and time, the first and second term of the integral in (Eq. 16) vanish and the last term becomes equal to the rate of linear momentum. Moreover, setting $\boldsymbol{\pi}(x^i, t)$ constant in time and equal to $\boldsymbol{\omega} \times \mathbf{r}$ with respect to space, where $\boldsymbol{\omega}$ denotes the rotation vector and $\mathbf{r}$ signifies the position vector, the first two terms in (Eq. 16) vanish again and the last term represents the rate of change of the angular momentum. Note that relationship 16 is valid in the absence of essential boundary conditions. In the opposite case, those conditions are enforced as constraints, thus augmenting (Eq. 16) by an additional term.

5.3 *Some remarks on the implementation of Noether's theorem*

In Subsections 5.1, 5.2, a form of Noether's Theorem has been applied in order to derive the associated weak statements of the conserved currents. This implementation led to Equations 14, 16, which correspond to the conservation of energy and momentum, respectively. These equations express in a clear manner the participation of each primary variable in the statements of conserved currents, a task that proves to be not trivial. To be more specific, in the case of linear and angular momentum-conservation statement 16, only the weak velocities and not, as someone may expect, the momentum type variables enter. Moreover, in the case of energy conservation, it is shown in (Eq. 14) that the weak velocities and not the strong time derivatives of displacement determine the kinetic energy.

6 Temporal discretization scheme

By discretizing in space and time the primary variables $\{\mathbf{u}, \mathbf{v}, \mathbf{p}\}$ and their variations $\{\delta\mathbf{u}, \delta\mathbf{v}, \delta\mathbf{p}\}$, a discrete form of Equation 10 is obtained. Note that for each variable and its variation an arbitrary interpolation scheme may be selected with the restriction that the interpolation is compatible with the functional space to which the variable belongs. Inclusion of the temporal boundary term in the weak form removes the requirement for vanishing of the variation $\delta\mathbf{u}$ at the time boundaries, as it is the case in the class of weak forms based on the classical Hamilton's principle. Moreover, different approximations for the displacements and the weak velocities may be employed that are consistently constrained by the momentum type Lagrange multipliers $\mathbf{p}$. Therefore, by selecting appropriate time approximations, a variety of algorithms can be derived. For example, introducing the simple approximations 17, 18 given below, the integration scheme proposed by Simo & Tarnow (1992) is obtained. Each variable is assumed to vary linearly with respect to time, whereas the variations (test functions) are assumed to be constant. Thus, the basic assumptions for the primary variables and for their variations take the form:

$$\begin{aligned} \mathbf{u} &= \frac{t}{T}\mathbf{u}_{n+1} + \frac{T-t}{T}\mathbf{u}_n \\ \mathbf{v} &= \frac{t}{T}\mathbf{v}_{n+1} + \frac{T-t}{T}\mathbf{v}_n \\ \mathbf{p} &= \frac{t}{T}\mathbf{p}_{n+1} + \frac{T-t}{T}\mathbf{p}_n \end{aligned} \tag{17}$$

and

$$\begin{aligned}\delta\mathbf{u} &= \delta\overline{\mathbf{u}}\\ \delta\mathbf{v} &= \delta\overline{\mathbf{v}}\\ \delta\mathbf{p} &= \delta\overline{\mathbf{p}}\end{aligned} \tag{18}$$

For the spatial discretization, the Finite Element Method is employed. To be more specific, the same spatial interpolation basis has been selected for the whole set of primary variables as well as for their variations, albeit this is not required. In case of linearly elastic constitutive equations, and since variations of the primary variables are independent, the following discrete system of equations is obtained:

$$\begin{aligned}&\delta\widehat{\mathbf{u}}^T\left(\mathbf{M}\left(\widehat{\mathbf{v}}^{n+1}-\widehat{\mathbf{v}}^{n}\right)+\frac{T}{2}\left(\widehat{\mathbf{F}}_{\text{int}}^{n+1}+\widehat{\mathbf{F}}_{\text{int}}^{n}\right)-\frac{T}{2}\left(\widehat{\mathbf{F}}_{ext}^{n+1}+\widehat{\mathbf{F}}_{ext}^{n}\right)\right)\\ &\quad+\delta\widehat{\mathbf{v}}^T\left(\frac{T}{2}\overline{\mathbf{M}}^T\left(\widehat{\mathbf{p}}^{n+1}+\widehat{\mathbf{p}}^{n}\right)-\frac{T}{2}\tilde{\mathbf{M}}\left(\widehat{\mathbf{v}}^{n+1}+\widehat{\mathbf{v}}^{n}\right)\right)\\ &\quad+\delta\widehat{\mathbf{p}}^T\left(\frac{T}{2}\overline{\mathbf{M}}\left(\widehat{\mathbf{v}}^{n+1}+\widehat{\mathbf{v}}^{n}\right)-\overline{\overline{\mathbf{M}}}\left(\mathbf{u}^{n+1}-\mathbf{u}^{n}\right)\right)=0\end{aligned} \tag{19}$$

i.e.,

$$\frac{2}{T}\mathbf{M}\left(\widehat{\mathbf{v}}^{n+1}-\widehat{\mathbf{v}}^{n}\right)+\left(\widehat{\mathbf{F}}_{\text{int}}^{n+1}+\widehat{\mathbf{F}}_{\text{int}}^{n}\right)=\left(\widehat{\mathbf{F}}_{ext}^{n+1}+\widehat{\mathbf{F}}_{ext}^{n}\right) \tag{20}$$

$$\frac{T}{2}\overline{\mathbf{M}}^T\left(\widehat{\mathbf{p}}^{n+1}+\widehat{\mathbf{p}}^{n}\right)-\frac{T}{2}\tilde{\mathbf{M}}\left(\widehat{\mathbf{v}}^{n+1}+\widehat{\mathbf{v}}^{n}\right)=\mathbf{0} \tag{21}$$

$$\frac{T}{2}\overline{\mathbf{M}}\left(\widehat{\mathbf{v}}^{n+1}+\widehat{\mathbf{v}}^{n}\right)-\overline{\overline{\mathbf{M}}}\left(\mathbf{u}^{n+1}-\mathbf{u}^{n}\right)=\mathbf{0} \tag{22}$$

The symbol $(\widehat{\bullet})$ denotes parameters of the spatial discretization. Moreover, matrices $\{\mathbf{M}, \overline{\mathbf{M}}, \tilde{\mathbf{M}}, \overline{\overline{\mathbf{M}}}\}$ contain the space integral of products of the selected spatial interpolation functions. It is worth noting that (Eqs. 20, 22) coincide with those presented in Simo & Tarnow (1992), if we adopt the same spatial interpolation for the whole set of variables and their variations. However, in the present paper, they have been explicitly derived in a rational manner. Furthermore, (Eq. 21), which provides the basis for the consistent computation of the linear momentum of the discrete system, does not appear in the aforementioned publication. Note also that examination of the conserved currents is consistent with the weak form of Noether's Theorem as proposed in Section 5 and justifies the procedures employed by Simo & Tarnow (1992). Moreover, in case of nonlinear constitutive equations, the combination of $\left(\widehat{\mathbf{F}}_{\text{int}}^{n+1}, \widehat{\mathbf{F}}_{\text{int}}^{n}\right)$ in the discrete system of equations is explicitly derived by evaluating the integral, thus avoiding the solution of a nonlinear system as proposed by Simo & Tarnow (1992).

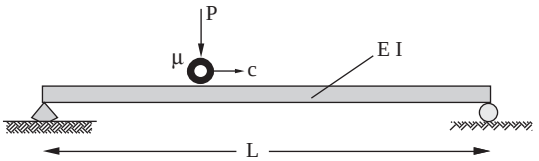

Figure 2 Moving mass problem.

7 Moving mass problem

The framework developed in the previous sections is applied to the problem of a moving mass on an Euler-Bernoulli beam (Fryba 1996, Au et al. 2001). In order to demonstrate the presented methodology, the weak statement of the problem is derived.

7.1 *Strong and weak formulation*

The problem is described by the following set of equations:

$$m\ddot{u} + \frac{\partial^2 M}{\partial x^2} - \boldsymbol{\delta}\left(x - x_0 - \int_0^t c(\tau)\,d\tau\right)(P - \mu\ddot{u}) = 0 \quad (x,t) \in \Omega \times (0,T] \tag{23}$$

$$u(x,t) = 0 \quad (x,t) \in \Gamma \times (0,T] \tag{24}$$

$$M(x,t) = 0 \quad (x,t) \in \Gamma \times (0,T] \tag{25}$$

$$u(x,0) = \tilde{u}(x) \quad x \in \Omega \tag{26}$$

$$\dot{u}(x,0) = \tilde{v}(x) \quad x \in \Omega \tag{27}$$

In (Eqs 23–27), the scalars x and t denote spatial coordinate and time, respectively. The symbols u, M and P signify the transverse displacement, the moment, and the moving load, respectively. Furthermore, m represents the distributed mass of the beam, μ the moving mass, and $c(t)$ its prescribed velocity in time. It has been assumed that the motion of the discrete moving mass begins at a zero initial time and from an initial location x_0 on the beam. Finally, $\boldsymbol{\delta}$ denotes the spatial Dirac's delta function. In order to deal with inelastic behavior, the set of equations 23–27 is supplemented by the state equations and the flow rule.

Multiplying Equation 23 by the arbitrary function δu

$$\delta u \in V, \quad V = \left\{\delta u \in H^1(\Omega) : \delta u = \mathbf{0} \text{ on } \Gamma_u\right\} \tag{28}$$

integrating with respect to space, applying twice Green's theorem, and employing the natural boundary conditions 25, we obtain

$$\int_\Omega m\,\ddot{u}\,\delta u\,d\Omega + \int_\Omega M\frac{\partial^2 \delta u}{\partial x^2}\,d\Omega - \int_\Omega \boldsymbol{\delta}\left(x - x_0 - \int_0^t c(\tau)\,d\tau\right)(P - \mu\ddot{u})\,\delta u\,d\Omega = 0 \tag{29}$$

Integrating (Eq. 29) over the time interval $I \in (0, T]$, performing an integration by parts to the first and the last term of the left hand side, and introducing weak velocities, the following weak form is derived: Find

$$\{u, v, p\} \in U \times V \times V,$$
$$U = \{\mathrm{u} \in L_2(I, H^1(\Omega)) : \dot{\mathrm{u}} \in L_2(I, H^1(\Omega))\}, \quad V = \{v \in L_2(I, L_2(\Omega))\}$$

satisfying the relationship

$$\begin{aligned}
&\int_0^T \left(\int_\Omega -m\,v\,\delta v\,d\Omega + \int_\Omega M\frac{\partial^2 \delta u}{\partial x^2}d\Omega - \int_\Omega \boldsymbol{\delta}\left(x - x_0 - \int_0^t c(\tau)\,d\tau\right) P\,\delta u\,d\Omega \right. \\
&\quad - \int_\Omega \left(\mu\boldsymbol{\delta}\left(x - x_0 - \int_0^t c(\tau)\,d\tau\right) v\,\delta v + \mu\underbrace{\frac{\partial \boldsymbol{\delta}\left(x - x_0 - \int_0^t c(\tau)\,d\tau\right)}{\partial t} v\,\delta u}\right) d\Omega \\
&\quad \left. + \int_\Omega (p(\delta v - \delta\dot{u}) + \delta p(v - \dot{u}))\,d\Omega \right) dt + \left[\int_\Omega \mu\boldsymbol{\delta}\left(x - x_0 - \int_0^t c(\tau)\,d\tau\right) v\,\delta u\,d\Omega \right]_{t=0}^{t=T} \\
&\quad + \left[\int_\Omega m\,v\,\delta u\,d\Omega \right]_{t=0}^{t=T} = 0
\end{aligned}$$

$$\forall\{\delta u, \delta v, \delta p\} \in W \times V \times V,$$
$$W = \{\mathrm{w} \in L_2(I, H^1(\Omega)) : \dot{\mathrm{w}} \in L_2(I, H^1(\Omega)),\ \mathrm{w} = \mathbf{0} \text{ on } \Gamma_u\} \tag{30}$$

the essential boundary conditions 24, and the initial condition 26. The underbraced term of (Eq. 30) is further examined by employing the concept of weak time derivatives

of abstract Bochner functions (Zenisek 1990):

$$\int_0^T \int_\Omega \mu \frac{\partial \boldsymbol{\delta}\left(x - x_0 - \int_0^t c(\tau)\, d\tau\right)}{\partial t} v\, \delta u\, d\Omega\, dt$$
$$= \int_0^T \lim_{\Delta t \to 0} \int_\Omega \frac{\boldsymbol{\delta}\left(x - x_0 - \int_0^{t+\Delta t} c(\tau)\, d\tau\right) - \boldsymbol{\delta}\left(x - x_0 - \int_0^t c(\tau)\, d\tau\right)}{\Delta t} \mu v\, \delta u\; d\Omega\, dt$$
$$= \int_0^T \mu \lim_{\Delta t \to 0} \frac{(v\, \delta u)\big|_{x = x_0 + \int_0^{t+\Delta t} c(\tau) d\tau} - (v\, \delta u)\big|_{x = x_0 + \int_0^t c(\tau) d\tau}}{\Delta t} dt$$
$$= \int_0^T \mu\, c(t) \left.\frac{\partial (v\, \delta u)}{\partial t}\right|_{x = x_0 + c(t)} dt \tag{31}$$

By utilizing relationship 31 and the properties of $\boldsymbol{\delta}$ function, the weak form becomes: Find

$$\{u, v, p\} \in U \times V \times V,$$
$$U = \{\mathrm{u} \in L_2(I, H^1(\Omega)) : \dot{\mathrm{u}} \in L_2(I, H^1(\Omega))\}, \quad V = \{v \in L_2(I, L_2(\Omega))\}$$

satisfying the relationship

$$\int_0^T \left(\int_\Omega -m\, v\, \delta v\, d\Omega + \int_\Omega M \frac{\partial^2 \delta u}{\partial x^2} d\Omega - (P\, \delta u)\big|_{x = x_0 + \int_0^t c(\tau) d\tau} - (\mu\, v\, \delta v)\big|_{x = x_0 + \int_0^t c(\tau) d\tau} \right.$$
$$- \mu\, c \left.\frac{\partial (v\, \delta u)}{\partial x}\right|_{x = x_0 + c(\tau)} + \left. \int_\Omega (p(\delta v - \delta \dot{u}) + \delta p(v - \dot{u}))\, d\Omega \right) dt$$
$$+ \left[\mu (v\, \delta u)\big|_{x = x_0 + \int_0^t c(\tau) d} \right]_{t=0}^{t=T} + \left[\int_\Omega m\, v\, \delta u\, d\Omega \right]_{t=0}^{t=T} = 0$$
$$\forall \{\delta u, \delta v, \delta p\} \in W \times V \times V,$$
$$W = \{\mathrm{w} \in L_2(I, H^1(\Omega)) : \dot{\mathrm{w}} \in L_2(I, H^1(\Omega)),\ \mathrm{w} = \mathbf{0} \text{ on } \Gamma_u\} \tag{32}$$

Introducing the approximations presented in Section 6 and taken into consideration the arbitrariness of the functions, yields the fully discretized problem:

$$\frac{2}{T} (\mathbf{M}_{FEM}) \left(\widehat{\mathbf{v}}^{n+1} - \widehat{\mathbf{v}}^{n} \right) + \frac{2}{T} \mathbf{M}_{1mov} \widehat{\mathbf{v}}^{n+1} - \frac{2}{T} \mathbf{M}_{0mov} \widehat{\mathbf{v}}^{n} + \frac{2}{T} \widehat{\mathbf{F}}_{mov} + \left(\widehat{\mathbf{F}}_{\text{int}}^{n+1} + \widehat{\mathbf{F}}_{\text{int}}^{n} \right)$$
$$= \widehat{\mathbf{F}}_{ext}^{n+1} + \widehat{\mathbf{F}}_{ext}^{n} \tag{33}$$

$$\frac{T}{2} \overline{\mathbf{M}} \left(\widehat{\mathbf{p}}^{n+1} - \widehat{\mathbf{p}}^{n} \right) = \frac{T}{2} \left(\overline{\mathbf{M}}_{FEM} \right) \left(\widehat{\mathbf{v}}^{n+1} + \widehat{\mathbf{v}}^{n} \right) + \overline{\mathbf{M}}_{mov} \tag{34}$$

$$\frac{T}{2} \overline{\mathbf{C}} \left(\widehat{\mathbf{v}}^{n+1} + \widehat{\mathbf{v}}^{n} \right) = \overline{\mathbf{D}} \left(\widehat{\mathbf{u}}^{n+1} - \widehat{\mathbf{u}}^{n} \right) \tag{35}$$

The symbol $(\widehat{\bullet})$ denotes the parameters of the spatial discretization. Moreover the matrices in (Eqs 33–35) are defined by the following relationships:

$$\mathbf{M}_{FEM} = \iint_{\Omega} m N_{\delta u}^T N_v \, d\Omega \tag{36}$$

$$\mathbf{M}_{1mov} = \mu \, N_{\delta u}^T\big|_{x=x_0+\int_0^T c(\tau)d\tau} N_v|_{x=x_0+\int_0^T c(\tau)d\tau}$$

$$\mathbf{M}_{0mov} = \mu \, N_{\delta u}^T\big|_{x=x_0} N_v|_{x=x_0} \tag{37}$$

$$\widehat{\mathbf{F}}_{mov} = -\int_0^T \mu c \left(\frac{\partial N_{\delta u}^T}{\partial x} N_v \widehat{\mathbf{v}} + N_{\delta u}^T \frac{\partial N_v}{\partial x} \widehat{\mathbf{v}} \right)\Bigg|_{x=x_0+\int_0^t c(\tau)d\tau}$$

$$\overline{\mathbf{M}} = \iint_{\Omega} N_{\delta v}^T N_p \, d\Omega \tag{38}$$

$$\overline{\mathbf{M}}_{FEM} = \iint_{\Omega} m N_{\delta v}^T N_v \, d\Omega \tag{39}$$

$$\overline{\mathbf{M}}_{mov} = \int_0^T \mu c (N_{\delta v}^T N_v \widehat{\mathbf{v}})|_{x=x_0+\int_0^t c(\tau)d\tau} \tag{40}$$

$$\overline{\mathbf{C}} = \iint_{\Omega} N_{\delta p}^T N_v \, d\Omega \tag{41}$$

$$\overline{\mathbf{D}} = \iint_{\Omega} N_{\delta p}^T N_{\delta u} \, d\Omega \tag{42}$$

In (Eqs 36–42), the symbol $N_{(\cdot)}$ signifies the generalized spatial interpolation function of the variable $(\cdot)$, respectively. The selection of a common interpolation basis for the variables and their variation leads to a symmetric formulation and to significant simplifications. Nevertheless, the general formulation serves as a powerful tool for tackling nontrivial problems.

7.2 *Numerical examples*

A simply supported beam with elasticity modulus $E = 3.2\,10^7\ kN/m^2$, moment of inertia $I = 10\,m^4$, mass density $m = 16\,t/m$ and total length $L = 45\,m$ has been analyzed assuming a moving mass that travels with constant velocity $c = 90\,km/h$. The weight of moving mass was taken successively equal to 10, 20, 30, and 40 percent of the total mass of the beam. The corresponding time histories of the vertical displacement at the midpoint of the beam are shown in Figure 3. Also, the same simply supported beam has been analyzed assuming a moving mass of $\mu = 72\,t$ for various velocities, i.e., $\mathrm{c} = \{45, 60, 75, 90\}$ km/h. The time histories of the vertical displacement at the midpoint of the beam are shown in Figure 4.

8 Conclusions

In the present paper, a general concept for the time integration of the dynamic equations has been proposed. The development rests upon a series of concepts, e.g.: the velocities

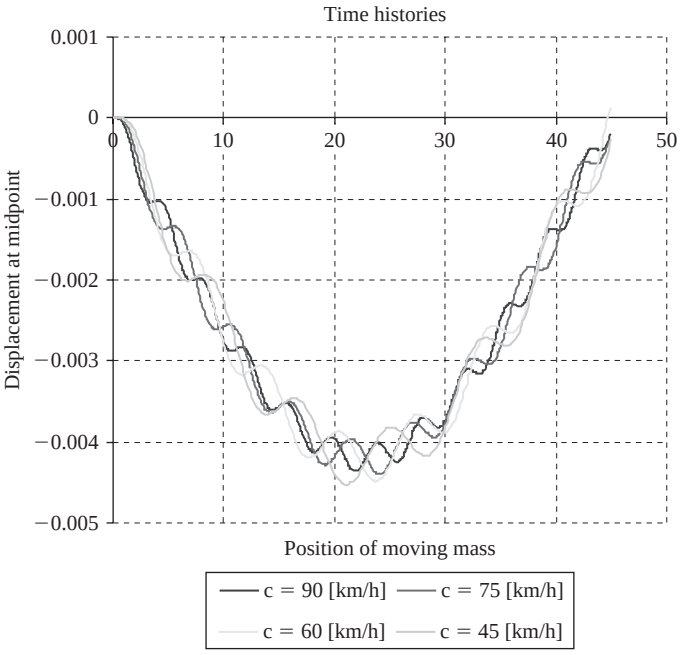

Figure 3 Results at midpoint for various values of mass velocity c.

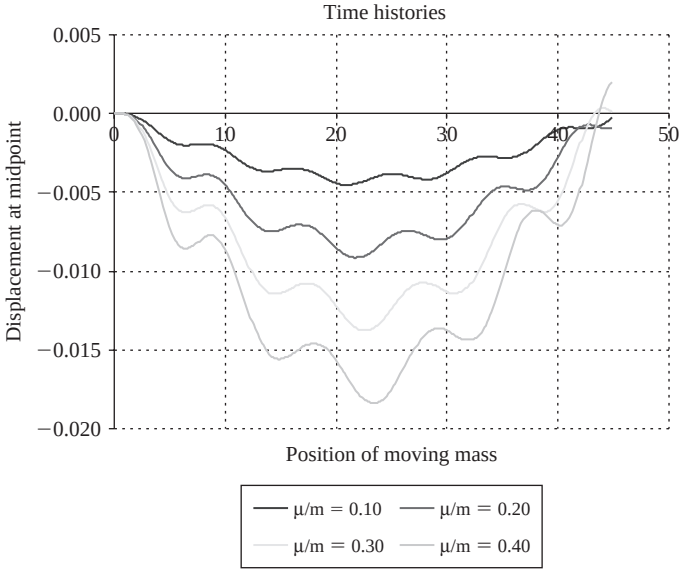

Figure 4 Results at midpoint for various values of ratio μ/m.

are assumed to be independent and the constraint between the velocities and the time derivatives of displacements are enforced in a weak form. Departing from the usual procedure, different approximations are employed for the test functions (variations) and the variables itself. Moreover, we do not impose fixed end conditions at the time boundaries.

The approach provides a systematic and mathematically consistent procedure for the approximation of nonlinear evolution problems and can be easily extended to a variety of nonlinear dynamical problems since it offers an effective strategy for the incorporation of unconventional terms into the weak form. Furthermore, the proposed methodology allows the theoretical justification of existing integration schemes, which can be derived as special cases of the present method.

It is generally accepted that the derived weak statement of the problem and also its discretized form should possess the same conserved properties as the initial dynamical system. The celebrated theorem of Emmy Noether provides the basis for the systematic examination of the conserved properties of the weak formulation as well as of the discrete system. In the present paper we utilize this theorem in a weak sense, as it is more consistent with the whole setting.

The presented approach is applied to the dynamic analysis of structural systems (e.g., bridges) under moving vehicles. The relationships describing such problems differ from the usual equations of motion in structural dynamics due to presence of the Dirac's delta function in terms containing the acceleration of the moving mass. Those terms require special treatment by employing the concept of weak time derivative of abstract Bochner functions.

References

Chung, J. & Hulbert, G.M. 1993. A time integration algorithm for structural dynamics with improved numerical dissipation: the generalized alpha-method. *Journal of Applied Mechanics, Transactions of the ASME* 60: 371–375.

Hughes, T.J.R., Caughey, T.K. & Liu, W.K. 1978. Finite-element methods for nonlinear elastodynamics which conserve energy. *Journal of Applied Mechanics, Transactions of the ASME* 45: 366–370.

Simo, J.C. & Tarnow, N. 1992. The discrete energy-momentum method. Conserving algorithms for nonlinear elastodynamics. *Journal of Applied Mathematics and Physics* 43: 757–792.

Lew, A., Marsden, J.E., Ortiz, M. & West, M. 2004. Variational time integrators. *International Journal for Numerical Methods in Engineering* 60: 153–212.

Tamma, K.K., Sha, D. & Zhou, X. 2003. Time discretized operators. Part 1: towards the theoretical design of a new generation of a generalized family of uncondicionally stable implicit and explicit representations of arbitrary order for computational dynamics. *Computer Methods in Applied Mechanics and Engineering* 192: 257–290.

Sha, D., Zhou, X. & Tamma, K.K. 2003. Time discretized operators. Part 2: towards the theoretical design of a new generation of a generalized family of uncondicionally stable implicit and explicit representations of arbitrary order for computational dynamics. *Computer Methods in Applied Mechanics and Engineering* 192: 291–329.

Kuhl, D. & Crisfield, M.A. 1999. Energy-conserving and decaying algorithms in non-linear structural dynamics. *International Journal for Numerical Methods in Engineering* 45: 569–599.

Pars, L.A. 1965. *A treatise on Analytical Dynamics*. London: Heinemann Educational Books Ltd.

Lanczos, C. 1970. *The Variational Principles of Mechanics, 4th Edition*. Toronto: University of Toronto Press.

Hughes, T.J.R. 1976. Reduction scheme for some structural eigenvalue problems by a variational theorem. *International Journal for Numerical Methods in Engineering* 10: 845–852.

Paraskevopoulos, E.A. & Talaslidis, D.G. 2004. A rational approach to mass matrix diagonalization in two-dimensional elastodynamics. *International Journal for Numerical Methods in Engineering* 61: 2639–2659.

Arnold, V.I. 1989. *Mathematical Methods of Classical Mechanics*. New York: Springer-Verlag.

Marsden, J.E. & Hughes, T.J.R. 1983. *Mathematical Foundations of Elasticity*. Englewood Cliffs, New Jersey: Prentice-Hall, Inc.

Abraham, R. & Marsden, J.E. 1978. *Foundations of Mechanics*. Reading, Mass.: Benjamin/Cummings.

Fryba, L. 1996. *Dynamics of Railway Bridges*. London: Thomas Telford.

Au, F.T.K., Cheng, Y.S. & Cheung, Y.K. 2001. Vibration analysis of bridges under moving vehicles and trains: an overview. *Progress in Structural Engineering and Materials* 3: 299–304.

Zenisek, A. 1990. *Nonlinear Elliptic and Evolution Problems and Their Finite Element Approximations*. London: Academic Press.

Chapter 11

Classical and soft robust active control of smart beams

Georgios K. Tairidis & Georgios E. Stavroulakis

Technical University of Crete, Chania, Greece

Daniela G. Marinova

Technical University of Sofia, Sofia, Bulgaria

Emmanuel C. Zacharenakis

Technological Educational Institute of Crete, Heraklion, Greece

ABSTRACT: Smart structures usually incorporate some control schemes that allow them to react against disturbances. In mechanics we have in mind suppression of mechanical vibrations with possible applications on noise and vibration isolation. A model problem of a smart beam with embedded piezoelectric sensors and actuators is used in this paper. Vibration suppression is realized by using active control. Classical mathematical control usually gives good results for linear feedback laws under given assumptions. The design of nonlinear controllers based on fuzzy inference rules is proposed and tested in this chapter.

1 Introduction

Smart structures include sensors and actuators and are able to react to the environment due to coupling with some active control mechanism. The intelligence is introduced by a structural control scheme. Linear feedback, for which a number of theoretical results are available, is usually applied. Lack of knowledge of the structure due to restricted number of measurements or uncertainty about the structural model itself due, say, to damage or general structural degradation, plastification or other sources of nonlinearities, reduce the performance of the classical control scheme. Moreover for nonlinear feedback controllers the theoretical analysis is usually complicated or not available. Soft computing may be used for the design of the controller algorithm in this case. One of the available tools, tested in this paper, is the fuzzy controller.

Using composite mechanical structures, like beams and plates in bending, with piezoelectric layers that can be used as sensors and actuators we have investigated the performance of robust control algorithms for vibration suppression. Classical robust control based on the H_2 and H_∞ control theories has been considered in previous publications of our group. The considered robust control design methodologies lead to linear time invariant feedback controllers having similarities with the linear feedback laws resulting from the classical *Linear Quadratic Regulator (LQR)* scheme. The controllers are designed to achieve optimal performance for a nominal model and maintain robust stability and robust performance for a given class of uncertainties.

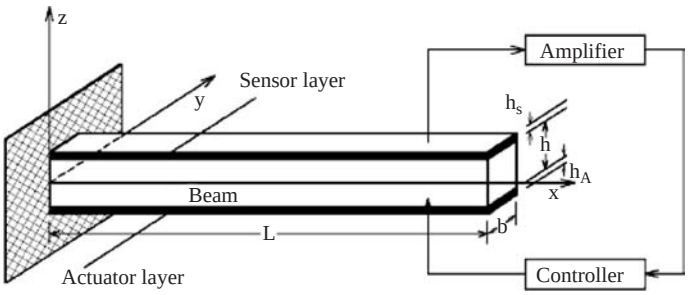

Figure 1 Laminated beam with piezoelectric sensors, actuators and the schematic control system.

This is achieved by the solution of two algebraic Ricatti equations, while in classical structural control one such equation arises.

The design of nonlinear feedback control laws using classical methods is a difficult task. Even the choice of appropriate numerical parameters for the design of an efficient classical robust control, say of the control weights in H_∞ control, is a challenging task. For all these reasons the usage of soft computing techniques, including fuzzy, neural and hybrid control, has been proposed. In this paper the use of control mechanisms based on fuzzy inference control is investigated.

The investigation presented in this paper is relevant for the design of structural control systems for linear and nonlinear structures and can be used, for instance, to solve active control schemes for aseismic design.

2 Models of smart beams and structures

In the smart beam of Figure 1, the control actuators and the sensors are piezoelectric patches symmetrically bonded on the top and the bottom surfaces of the host beam. Both piezoelectric layers are positioned with identical poling directions and can be used as sensors or actuators.

The linear theory of piezoelectricity is employed. Furthermore, quasi-static motion is assumed, which means that the mechanical and electrical forces are balanced at any given instant. It should be emphasized that the fuzzy controller proposed here can be used with more general nonlinear structural models, which may be relevant to other technologies of smart materials and structures (general nonlinear ferroelectric materials etc).

The linear constitutive equations of the two coupled fields read:

$$\{\sigma\} = [Q](\{\varepsilon\} - [d]^T\{E\}) \tag{1}$$

$$\{D\} = [d][Q]\{\varepsilon\} + [\xi]\{E\} \tag{2}$$

where $\{\sigma\}_{6\times1}$ is the stress vector, $\{\varepsilon\}_{6\times1}$ is the strain vector, $\{D\}_{3\times1}$ is the electric displacement, $\{E\}_{3\times1}$ is the strength of applied electric field acting on the surface of the piezoelectric layer, $[Q]_{6\times6}$ is the elastic stiffness matrix, $[d]_{3\times6}$ is the piezoelectric

matrix and $[\xi]_{3\times3}$ is the permittivity matrix. Eq. (1) describes the inverse piezoelectric effect (which is exploited for the design of the actuator). Eq. (2) describes the direct piezoelectric effect (which is used for the sensor). Additional assumptions are used for the construction of the simplified model: (a) Sensor and actuator (S/A) layers are thin compared with the beam thickness. (b) The polarization direction of the S/A is the thickness direction (z axis). (c) The electric field loading of the S/A is uniform uni-axial in the x-direction. (d) Piezoelectric material is homogeneous, transverse isotropic and elastic. Therefore, the set of equations (1) and (2) is reduced as follows:

$$\begin{Bmatrix}\sigma_x\\ \tau_{xz}\end{Bmatrix} = \begin{bmatrix}Q_{11} & 0\\ 0 & Q_{55}\end{bmatrix}\left(\begin{Bmatrix}\varepsilon_x\\ \gamma_{xz}\end{Bmatrix} - \begin{bmatrix}d_{31}\\ 0\end{bmatrix}E_z\right) \tag{3}$$

$$D_z = Q_{11}d_{31}\varepsilon_x + \xi_{33}E_z \tag{4}$$

The electric field intensity E_z can be expressed as:

$$E_z = \frac{V}{h_A} \tag{5}$$

where V is the applied voltage across the thickness direction of the actuator and h_A is the thickness of the actuator layer.

Only strains produced by the host beam, act on the sensor layer and no electric field is applied to it. Thus the output charge from the sensor can be calculated using eq. (4) and is given by:

$$q(t) = \frac{1}{2}\left\{\left(\int_{S_{ef}} D_z\, dS\right)_{z=\frac{h}{2}} + \left(\int_{S_{ef}} D_z\, dS\right)_{z=\frac{h}{2}+h_S}\right\} \tag{6}$$

where S_{ef} is the effective surface of the electrode placed on the sensor layer.

The current on the surface of the sensor is given by:

$$i(t) = \frac{dq(t)}{dt} \tag{7}$$

The current is converted into open-circuit sensor voltage output by:

$$V^S = G_S i(t) \tag{8}$$

where G_S is the gain of the current amplifier.

Furthermore, we suppose that the bending-torsion coupling and the axial vibration of the beam centerline are negligible and that the components of the displacement field $\{u\}$ of the beam are based on the Timoshenko beam theory which, in turn, means that the axial displacement is proportional to z and to the rotation $\psi(x,t)$ of the beam cross section about the positive y-axis and that the transverse displacement is equal to

the transverse displacement $w(x,t)$ of the point of the centroidal axis ($y=z=0$). The strain-displacement relationships read:

$$\varepsilon_x = z\frac{\partial \psi}{\partial x}, \quad \varepsilon_{xz} = \psi + \frac{\partial w}{\partial x} \tag{9}$$

The simpler Euler-Bernoulli theory which considers zero transverse shear deformation γ_{xz} has also been tested. Using Hamilton's principle the equations of motion of the beam are derived. This model has been used in various investigations of our group (see, among others, Stavroulakis et al. 2005, 2007). Further applications of piezoelectric layers in control can be found in the review article (Irschik 2002).

For the finite element discretization beam finite elements are used, with two degrees of freedom at each node: the transversal deflection w_i and the rotation ψ_i. They are gathered to form the degrees of freedom vector $X_i = [w_i \;\; \psi_i]$. After assembling the mass and stiffness matrices for all elements, we obtain the equation of motion in the form:

$$\mathrm{M}\ddot{X} + \Lambda\dot{X} + \mathrm{K}X = F_m + F_e \tag{10}$$

where M and K are the generalized mass and stiffness matrices, F_e is the generalized control force vector produced by electromechanical coupling effects, Λ is the viscous damping matrix and F_m is the external loading vector. It should be mentioned here that bending theories for plates can be constructed analogously.

The main objective is to design robust control laws for the smart beam bonded with piezoelectric S/A subjected to external induced vibrations. For this purpose the following state space representation will be used:

$$\dot{x} = Ax + B_1 w + B_2 u \tag{11}$$

as it is common in control problems for general dynamical systems. Here

$$x = [X \; \dot{X}]^T, \quad A = \begin{bmatrix} 0 & I \\ -M^{-1}\mathrm{K} & -M^{-1}\Lambda \end{bmatrix} \tag{12}$$

where x is the state vector, A is the state matrix, B_1 and B_2 are allocation matrices for the disturbances w (corresponding to external forces F_m) and control u (corresponding to F_e). The initial conditions are assumed to be zero. The identity matrix is denoted by I.

3 Classical active control

Let us consider that the measurements have the following form:

$$y = Cx + Du \tag{13}$$

The control law usually accepted in classical theory is a linear feedback of the form

$$u = Ky \tag{14}$$

where K is the unknown controller gain.

The objective in this study is to determine the vector of active control forces $u(t)$ subjected to some performance criteria and satisfying the dynamical equations of the structure, such that to reduce in an optimal way the external excitations and to meet the above mentioned requirements. The investigations may be implemented in the time domain as well as in the frequency domain. The problem for vibration suppression is solved by both LQR and H_2, H_{inf} optimal performance criteria. These methods actually design the controlled system and do not take into account the external influence (e.g. the loading). The LQR method is only outlined in this paper. Technical details and results of the other control methods can be found in previous publications (Marinova et al. 2005, Stavroulakis et al. 2005, 2007).

3.1 *Linear Quadratic Resulator (LQR)*

In this section the $£_2$ performance problem in the time domain is studied. The following quadratic cost function is minimized

$$J = \frac{1}{2}\int_0^\infty (x^T Q x + u^T R u)dt \rightarrow \min \tag{15}$$

The free parameters Q and R represent weights on the different states and control. They are the main design parameters. $\boldsymbol{J}$ represents the weighted sum of energy of the state and control. This is clearly a compromise between reducing the state vector and the cost of the control effort. We require that Q be symmetric semi-positive definite and R be symmetric positive definite for a meaningful optimization problem. The values of the two weights define the relative importance of effectiveness and cost in the compromise cost function. The arising problem is known as LQR problem and belongs to the powerful machinery of the optimal control.

Assuming full state feedback, the control law is given by

$$U = -K_{LQR}x \tag{16}$$

with constant control gain

$$K_{LQR} = R^{-1}B^T P \tag{17}$$

The constant matrix P is a solution of the Riccati Equation

$$A^T P + PA + Q - PBR^{-1}B^T P = 0 \tag{18}$$

Under technical assumptions existence and uniqueness of the above controller is guaranteed. The closed loop system is the actively controlled structure and is given by

$$\dot{x} = (A - BK_{LQR})x + F_m \tag{19}$$

An advantage of the linear quadratic formulation of the problem is the linearity of the control law, which leads to easy analysis and practical implementation. Another

advantage is good disturbance rejection and good tracking. The gain and phase margins imply good stability.

All these preferences are met when a complete knowledge of the whole state for each time instance is available. If a limited number of measurements are available and they are supposed to be corrupted by some measurement errors the effectiveness of LQR deteriorates. In this case, first the system is reconstructed from the available measurements with the usage of some filter technique (e.g. Kalman filter), and then the optimal control problem is solved based on this reconstructed (estimated) system.

4 Soft computing and control

4.1 *Fuzzy, neural and hybrid techniques in control*

The advantage of classical control theories is the availability of mathematical tools for the design of the controller and the study of it's properties, like stability, robustness etc. Nevertheless, one should mention that most beneficial properties are based on the knowledge of the whole dynamical system. If this is not the case an estimator, like a Kalman-filter, is introduced. The quality and reliability of this estimator defines the effectiveness of the whole control system. Furthermore, a serious disadvantage of classical control is the adoption of a linear feedback. Nonlinear control laws are certainly more flexible. They are also more suitable for nonlinear systems. The tools provided by the classical control for the design of nonlinear controllers are less developed and demand more deep theoretical investigation from the design engineer. Therefore nonlinear controllers are mainly based on intelligent and soft computing tools. In order to fix ideas, we mention several possibilities of using intelligent control in smart structures:

1. *Neural networks* can be trained to approximate every nonlinear mapping. Therefore, they can be used for the approximation of the inverse dynamical mapping of a system. Subsequently the trained network is used to realize a feedback on the system. The arising closed loop system has the ability of vibration suppression. For this application a large number of representative measurements, or data from modeling, is required for the training and testing of the neural network system.
2. *Fuzzy inference* rules systematize existing experience, available in terms of linguistic rules, and can be used for the realization of nonlinear controllers. The feedback is based on fuzzy inference and may be nonlinear and complicated. Knowledge or experience on the controlled system is required for the application of this technique. Since the linguistic rules are difficult to be explained and formulated for multi-input, multi-output systems, most applications are based on multi-input, single-output controllers.
3. *Hybrid and adaptive techniques* that combine elements from both above methods have also been proposed. For example the required details of a fuzzy inference system can be tuned by means of examples and the usage of neural networks or by using some, usually global, optimization.

Further details on fuzzy control can be found in classical monographs like (Driankov et al. 1996). In the area of smart systems the application of neuro-fuzzy control has been adopted by many authors. In particular, it seems to be suitable for the control of

structures with complicated or nonlinear characteristics, like the tuned mass damper systems for aseismic design (Pourzeynali et al. 2007, Wang & Lin 2007) or the semi-active control using active friction devices or electrorheological fluid dampers (Reigles & Symans 2006).

A two-input, single-output fuzzy inference controller is tested in this paper. This configuration is suitable for a feedback control force based on the displacement and velocity at a given point (collocated configuration of the local controller). If needed, several independent and decentralized (local) fuzzy controllers, in general with different characteristics, can be installed on a larger structure. The overall setting of each fuzzy controller (i.e. the fuzzification of the input and output variables, the rules and other variables involved in the fuzzy inference system) are defined from the beginning by the user in this study. Obviously some trial-and-error iterations are required in order to achieve efficient performance of the system. The usage of global optimization tools, like genetic algorithms or evolutionary optimization, can be proposed as an alternative for the optimal tunning of the involved parameters (see, among others, the usage of Particle Swarm Optimization in Marinakis et al. 2008).

4.2 *Fuzzy inference system*

In order to reduce the displacement field of the cantilever beam system discussed in this paper, a non-linear fuzzy controller was constructed by using the Fuzzy Toolbox of Matlab.

More specifically, a Mamdani-type Fuzzy Inference System, consisted of two inputs and one output, was developed. The system receives as inputs the displacement (u) and the velocity ($\dot{u}$), while gives as output the increment of the control force (z). Triangular membership functions (trimf) were chosen both for inputs and output. These are shown in the following figures.

In order to describe the present system-controller 15 rules were used. All rules have weights equal to 1 and use the AND-type logical operator. These rules are presented in the Table 1.

The implication method was set to minimum (min), while the aggregation method was set to maximum (max).

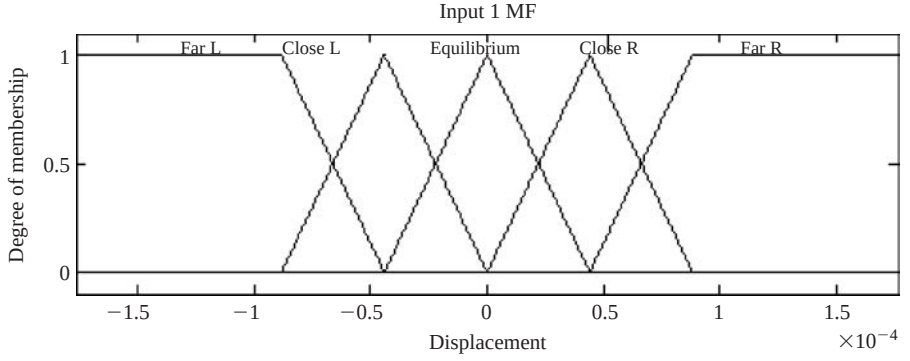

Figure 2 Displacement Membership Function (input 1).

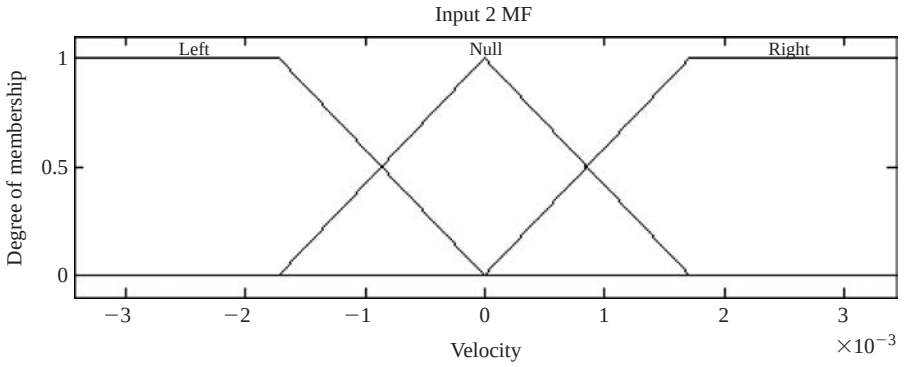

Figure 3 Velocity Membership Function (input 2).

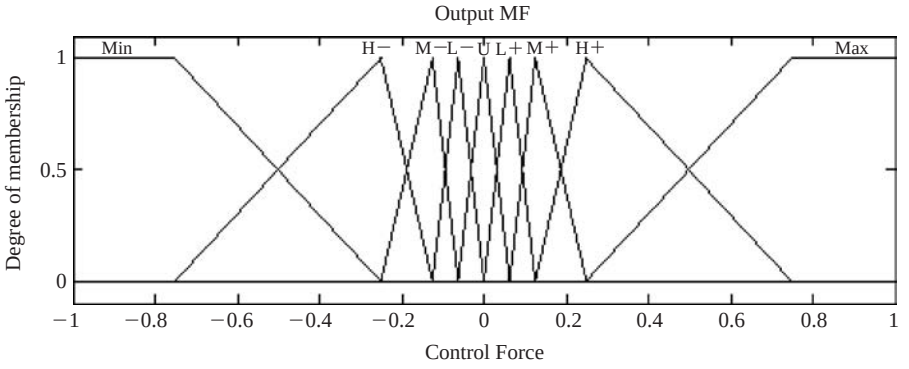

Figure 4 Control Force Membership Function (output).

Table 1 Fuzzy Inference System Rules.

Velocity Displacement	*Far Up*	*Close Up*	*Equilibrium*	*Close Down*	*Far Down*
Up	Max*	Med+	Low+	Null	Med−
Null	Med+	Low+	Null	Low−	High−
Down	High+	Null	Low−	Med−	Min

* If displacement is far up and velocity is up then control force is max.

The defuzzified output value has been created by using the MOM (Mean of Maximum) defuzzification method.

The whole implementation has been programmed within MATLAB, using functions from the fuzzy inference toolbox. Different types of membership functions and defuzzification methods has been tested, with minor changes of the results.

A surface is generated to demonstrate the relation between the inputs (displacement and velocity) and the output (control force) of a fuzzy inference system. The surface arose from the fuzzy controller presented above is shown in the following Figure 5.

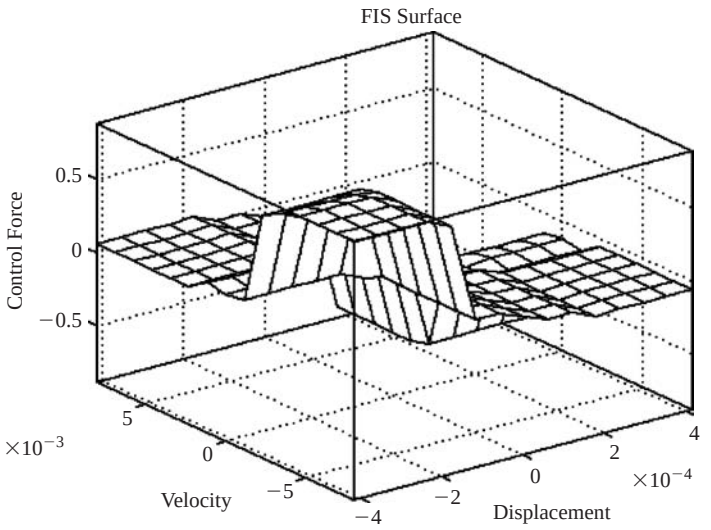

Figure 5 Fuzzy inference system surface.

4.3 *Structural dynamics and fuzzy control*

The Houbolt numerical integration method was chosen in order to integrate the equations of motion:

$$M\ddot{X} + \Lambda\dot{X} + KX = F_m + F_e \tag{20}$$

According to this method, when acceleration is constant, Houbolt factors are set to:

$$\beta = 0.25, \quad \gamma = 0.5 \tag{21}$$

The total integration time was chosen equal to 3 sec, while the time step (Δt) equal to 0.001 sec.

Integration constants are given as:

$$c_1 = \frac{1}{\beta(\Delta t)^2}, \; c_2 = \frac{1}{\beta\Delta t}, \; c_3 = \frac{1}{2\beta}, \; c_4 = \frac{\gamma}{\beta\Delta t}, \; c_5 = \frac{\gamma}{\beta}, \; c_6 = \Delta t\left(\frac{\gamma}{2\beta} - 1\right) \tag{22}$$

In each step (t) of the numerical integration, the fuzzy controller provides a control force (z), according to the given input values (displacement u and velocity $\dot{u}$). Both the control force and the external loads provide the next step's ($t + \Delta t$) values of displacement and velocity.

5 Numerical examples

The problem of a cantilever beam was studied in the present paper. The beam has a total length equal to 0.8 m and a square cross-section with dimensions 0.02×0.02 m. The elasticity modulus is equal to 73×10^9 N/m^2. The mass density is equal to 2700 Kg/m^3.

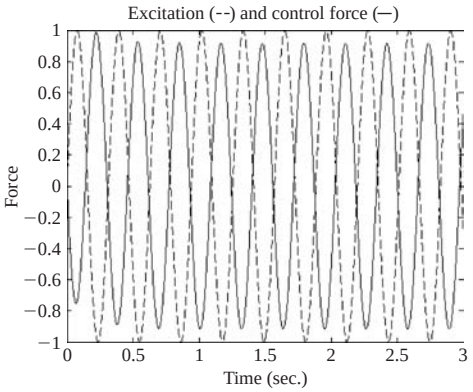

Figure 6 Excitation and control force (LQR).

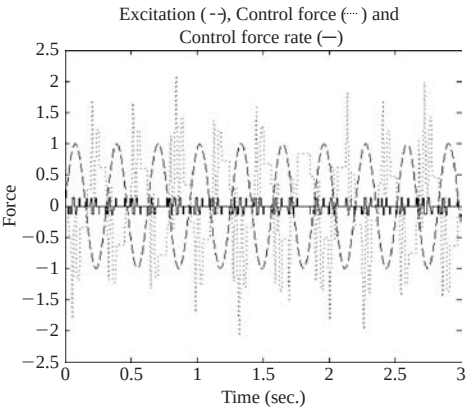

Figure 7 Excitation and control force (fuzzy).

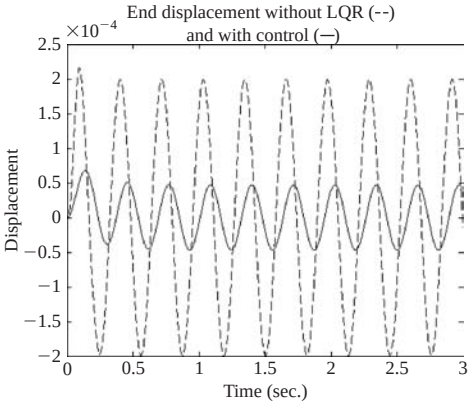

Figure 8 Displacement (LQR).

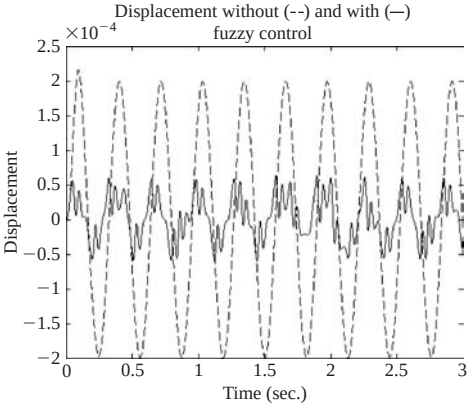

Figure 9 Displacement (fuzzy).

Sinusoidal external excitation concentrated at the free end of the cantilever was chosen. The structure has been discretized with four finite elements resulting in a model with eight degrees of freedom. The purpose of the fuzzy controller is to reduce the oscillation.

First we consider a controller that takes as input the displacement and the velocity of the free end and gives back the control force to be applied at the same point. The results are compared with these that arose from classical control (LQR). In this latter case the whole state of the dynamical system is assumed to be known. Therefore a linear feedback of the sixteen input variables to the one control force has been calculated. Finally the weights Q and R have been taken to be diagonal matrices with appropriate dimensions and values of each element on the diagonal equal to 1 and 1×10^{-5} respectively.

The results are given in Figures 6–11. We observe that displacements can be easily reduced, while velocity and acceleration results of the fuzzy-controlled system are not very satisfactory, due to the nonlinear, impact-like nature of the control force.

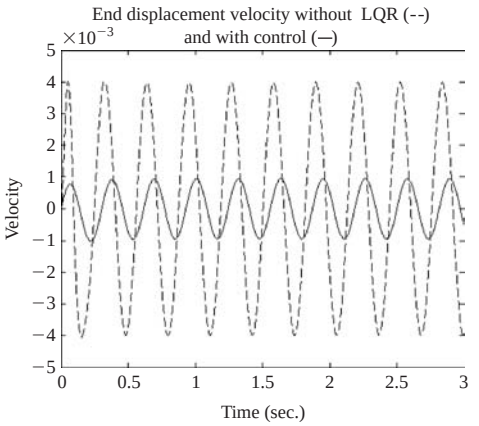

Figure 10 Velocity (LQR).

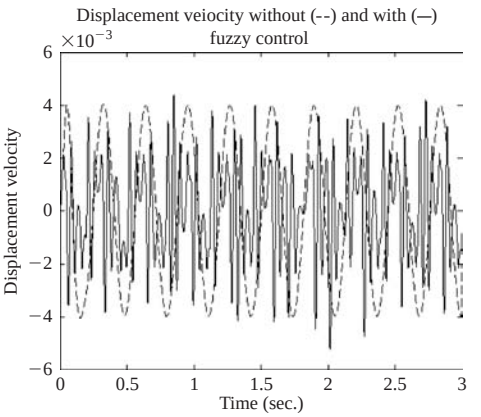

Figure 11 Velocity (fuzzy).

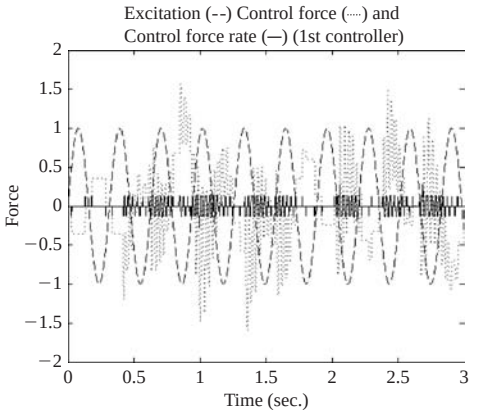

Figure 12 Excitation and control force (1st).

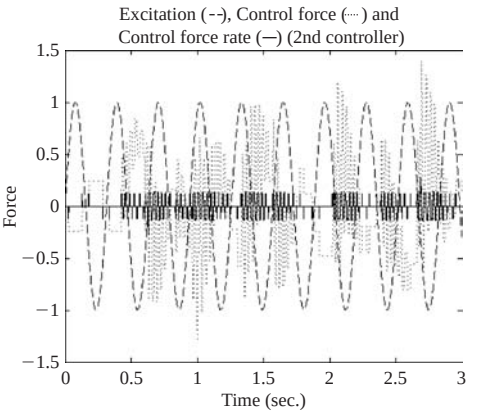

Figure 13 Excitation and control force (2nd).

The second fuzzy controller has two independent fuzzy mechanisms placed at the middle and at the free end of the cantilever beam. Each one of the two controllers can be tunned separately. The results of the two sub-systems are shown in Figures 12–17.

As a matter of fact, from the numerical results one observes that further vibration reduction was accomplished. This is reasonable, as the new system uses four measurements, instead of the previous one that was using only two. Nevertheless the problems concerning velocities and accelerations remain.

The performance of the fuzzy control system can be further enhanced by fine-tunning the parameters of the fuzzy system (membership functions, rules, etc) by using a neural network or a global optimization scheme. First results in this direction, using the Particle Swarm Optimization method, have been presented in Marinakis et al. 2008. Furthermore, from the practical point of view a big deficiency of fuzzy controllers are

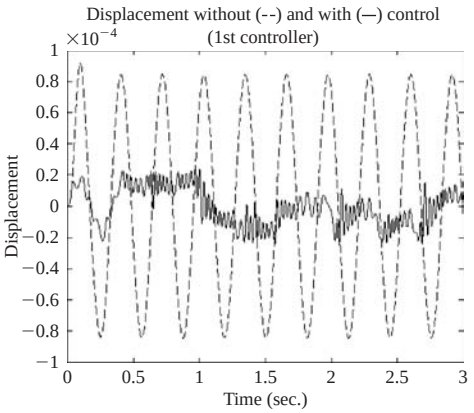

Figure 14 Displacement (1st).

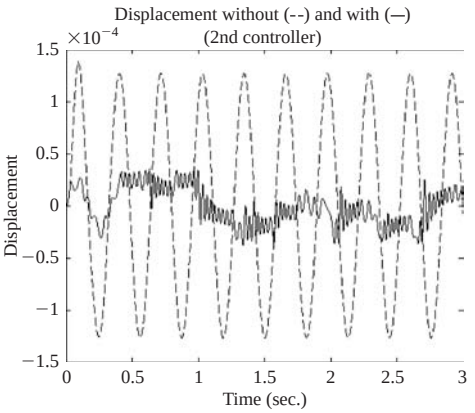

Figure 15 Displacement (2nd).

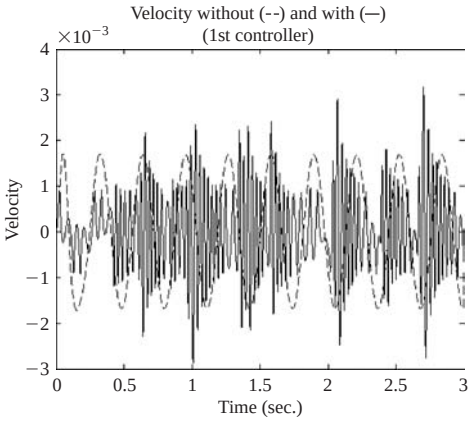

Figure 16 Velocity (1st).

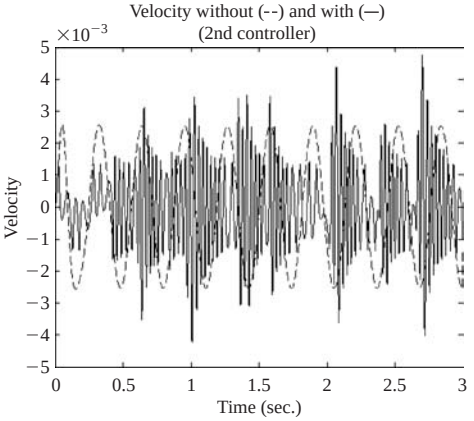

Figure 17 Velocity (2nd).

the discontinuous effect of the induced controlled motion. This effect, which leads to material damage problems, is known in the community and is demonstrated in our results by the bad performance in the velocity and acceleration variables. Optimal tunning of the fuzzy controller in order to reduce this effect is highly desirable. The authors work in this direction and will present their results in the future.

Acknowledgements

The work of the first two authors has been supported by a Grant for Basic Research from the Research Committee of the Technical University of Crete. This support is greatfully acknowledged.

References

Driankov, D. Hellendoorn, H. & Reinfrak, M. 1996. *An introduction to fuzzy control*. 2nd edition, Springer Verlag.

Irschik, H. 2002. A review of static and dynamic shape control of structures using piezoelectric actuation. *Engineering Structures,* **24**(**1**).

Marinakis, Y., Marinaki, M. & Stavroulakis, G.E. 2008. Particle swarm optimization approach for fuzzy control of smart structures. Sixth Intern. Conference on Engineering Computational Technology ECT2008, Athens, Greece, 2–5 September 2008, Civil-Comp Press.

Marinova, D.G., Stavroulakis, G.E. & Zacharenakis, E.C. 2005. Robust control of smart beams in the presence of damage-induced structural uncertainties. *International Conference PhysCon 2005* Saint Petersburg, Russia.

Pourzeynali, S., Lavasani, H.H. & Modarayi, A.H. 2007. Active control of high rise building structures using fuzzy logic and genetic algorithms. *Engineering Structures*, **29**, 346–357.

Reigles, D.G. & Symans, M.D. 2006. Supervisory fuzzy control of a base isolated benchmark building utilizing a neuro-fuzzy model of controllable fluid viscous dampers. *Journal of Structural Control and Health Monitoring,* **13**, 724–747.

Stavroulakis, G.E., Foutsitzi, G., Hadjigeorgiou, V., Marinova, D.G. & Baniotopoulos, C.C. 2005. Design and Robust Optimal Control of Smart Beams with Application on Vibrations Suppression, *Advances in Engineering Software*, **36**, 806–813.

Stavroulakis, G.E., Foutsitzi, G.A., Hadjigeoriou, E.P., Marinova, D.G., Zacharenakis, E.C. & Baniotopoulos, C.C. 2007. Numerical experiments on smart beams and plates. In Miara, B. Stavroulakis, G.E. Valente, V. (eds), *Topics on Mathematics for Smart Systems, European Conference, Roma, 26–28 October 2006*, 218–236, World Scientific Publishers.

Wang, A.P. & Lin, Y.H. 2007. Vibration control of a tall building subjected to earthquake excitation. *Journal of Sound and Vibration*, **299**, 757–773.

Chapter 12

Rail vibrations caused by ground stiffness transitions

Håkan Lane, Per Kettil & Nils-Erik Wiberg

Chalmers University of Technology, Gothenburg, Sweden

ABSTRACT: Spatial changes in the material properties of the track and subground may lead to variations in the contact forces at the wheel-rail interface. A shift from one material to another can potentially induce transition radiation vibration modes. The phenomenon has been observed in situations where the train goes onto a bridge. An advanced numerical model of the entire train-track-subgrade dynamic system with moving finite elements has been used to study the influence of material stiffness transitions in the subground. While the properties of the ballast and the rail were kept constant, the Young moduli of the two layers of clay representing the soil underwent a linear change over a short distance. Both transitions from soft to stiff and from stiff to soft soil were considered. The results indicate that the main effect of the transition is a temporary variation followed by a transient low-frequent vibration. The magnitude is relatively small and does not threat the stability of the system. The shielding track structure with ballast, sleepers and pads evens out the disturbance.

1 Introduction

The essence of railway dynamics is the transfer of forces at the wheel rail interface. The energy from the motion of the train is taken up as elastic deformation in the track structure consisting of the rail, sleepers, dry crust, ballast and soil. The elastic response in the ground depends both in magnitude and characteristics on a number of parameters, e.g. train mass, suspension parameters, train geometry, rail irregularities and soil material characteristics (Ching, 2004).

An advanced numerical application allows for three dimensional analysis of the dynamics of the entire train-track-subgrade system with a high level of detail in the time domain (Lane, 2007). Moving mesh calculations makes computations for a train traveling over longer distances possible (Lane et al., 2007c). By eliminating artificial reflections from the boundaries with a viscoelastic layer technique (Lane et al., 2007b), the finite element computational domain could be reduced to a mesh of 15–25 m in front of and behind the train (Lane, 2007). This paper will use the model to simulate train passage over a domain where the material parameters change. Section 2 presents the moving mesh model integrating rigid body dynamics and finite elements and section 3 the results of some simulations. Section 4 provides the conclusions of the study.

2 Train-track-subgrade system model

We have developed and successively refined an integrated three-dimensional model with an advanced level of detail of all subsystems. The representation of the train is

based on multibody dynamics, incorporating the interplay between the various parts of the train and the suspension system (Lane et al., 2007a). For the soil, there is a full scale finite element grid based on solid eight-node bricks (Ekevid and Wiberg, 2002). Virtual finite elements of viscoelastic materials (Lane et al., 2007b) are added to reduce reflections from the boundaries.

2.1 *Assembling the system*

The solution process and time integration algorithm is based on identifying a common framework for the parts (finite elements, spring/damper connectors, rigid body motion, constraint equations and boundary conditions). The internal force vector $\mathbf{F}_e$ is seeked as:

$$\mathbf{F}_e = \mathbf{M}_e\ddot{\mathbf{u}}_e + \mathbf{C}_e\dot{\mathbf{u}}_e + \mathbf{K}_e\mathbf{u}_e + \boldsymbol{\lambda}_e\frac{\partial\boldsymbol{\Phi}_e}{\partial\mathbf{u}} \tag{1}$$

based on local matrices for mass ($\mathbf{M}_e$), damping ($\mathbf{C}_e$) and stiffness ($\mathbf{K}_e$), a local coordinate vector $\mathbf{u}_e$ and, for constraints and boundary conditions with the expression $\boldsymbol{\Phi}_e$, the local Lagrange multiplier $\boldsymbol{\lambda}_e$. Analysis is based on Lagrangian dynamics (Griffiths, 1985).

2.1.1 *Soil*

For the soil with density ρ, an elastic stress-strain consitutive matrix $\mathbf{D}$ (Samuelsson and Wiberg, 1998) and an analogous stress-strain rate visco-elastic matrix $\mathbf{C}_\eta$, standard FE procedures based on form functions $\mathbf{N}$ and their spatial derivatives $\mathbf{B} = \tilde{\nabla}\,\mathbf{N}$ and a volume integration over the element domain Ω lead to the local matrices as defined in equation (4):

$$\mathbf{M}_e = \int_\Omega \mathbf{N}^T\rho\mathbf{N}\,dV \tag{2}$$

$$\mathbf{C}_e = \int_\Omega \mathbf{B}^T\mathbf{C}_\eta\mathbf{B}\,dV \tag{3}$$

$$\mathbf{K}_e = \int_\Omega \mathbf{B}^T\mathbf{D}\mathbf{B}\,dV \tag{4}$$

It should be noted that the dissipating ($\mathbf{C}_e\dot{\mathbf{u}}_e$) and elastic ($\mathbf{K}_e\mathbf{u}_e$) part of the internal forces are calculated by evaluating form function derivatives, material parameters and statefields in the Gauss points, while the inertial contribution is computed through a volume scalar product.

2.1.2 *Rigid body*

The theory for the application of rigid body equations in a system based on Lagrangian mechanics was presented by Lane *et al.* (2007a). The only points that are included in

the analysis are the *reference points* for each body and the *connected points* in contact with a connector. For the reference points, the inertia matrix equals (Lane et al., 2007a)

$$\mathbf{M_e} = \begin{bmatrix} m\mathbf{I_3} & \\ & \mathbf{J} \end{bmatrix} \tag{5}$$

Here, m equals the body mass, $\mathbf{I_3}$ is the 3×3 unity matrix and $\mathbf{J}$ is the 3×3 rotary inertia tensor.

2.1.3 *Connector*

The characteristics of a Kelvin type connector are assigned as 3×3 matrices for stiffness $\mathbf{K}$ and damping $\mathbf{C}$. While there is no mass contribution, one sets explicitly $\mathbf{K_e} = \mathbf{K}$ and $\mathbf{C_e} = \mathbf{C}$

2.1.4 *Constraint equation*

Each constraint equation $\mathbf{\Phi}_i$ is assigned a Lagrange multiplier λ_i. For a holonomic linear sum

$$\mathbf{A}\mathbf{u_e} = \mathbf{0} \tag{6}$$

application of equation (7) leads to the internal force contributions

$$\boldsymbol{\lambda_e} = \boldsymbol{\lambda}_i \tag{7}$$

$$\frac{\partial \mathbf{\Phi_e}}{\partial \mathbf{u}} = \mathbf{A} \tag{8}$$

2.1.5 *Boundary condition*

A locked boundary condition for a specific degree of freedom is a special type of the general expression for a constraint equation with the expression

$$\boldsymbol{u_k} = \mathbf{0} \tag{9}$$

for a specific degree of freedom k. Again, a Lagrange multiplier λ_j is assigned and the terms in equation (7) are identified as

$$\boldsymbol{\lambda_e} = \lambda_j \tag{10}$$

$$\frac{\partial \mathbf{\Phi_e}}{\partial \mathbf{u}} = 1 \tag{11}$$

The terms from equations (10)–(21) are merged into a tangent left-hand-side matrix

$$\begin{bmatrix} \mathbf{M}_* & \frac{\partial \mathbf{\Phi}}{\partial \mathbf{u}} \\ \frac{\partial \mathbf{\Phi}}{\partial \mathbf{u}} & 0 \end{bmatrix} \tag{12}$$

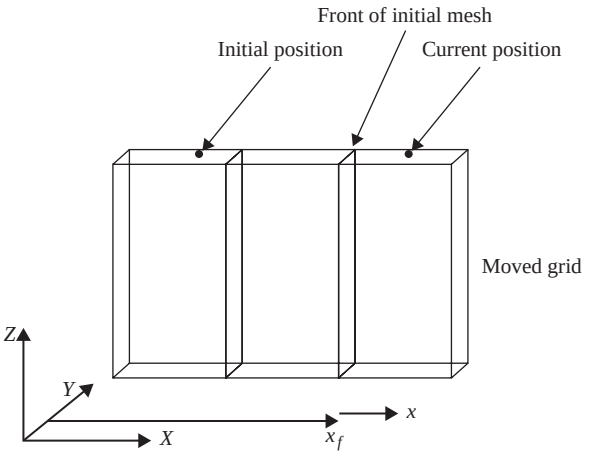

Figure 1 Moving mesh offset.

where the Newmark time integration parameters α and β have been used in a Taylor expansion to generate the dynamic mass matrix

$$\mathbf{M}_* = \mathbf{M} + \alpha\,\Delta t\,\mathbf{C} + \beta\frac{(\Delta t)^2}{2}\mathbf{K} \tag{13}$$

The tangent matrix is then used to find increments to the accelerations ($\boldsymbol{\delta\ddot{u}}$) and Lagrange multipliers ($\boldsymbol{\delta\lambda}$) in a Newmark predictor-corrector scheme.

2.2 *Material parameter transitions*

To achieve transitions with a moving mesh, the Young's moduli will now be a function of the location occupied by the nodes as they are moved forward. The controlling variable is shown in Figure 1.

The simulations will update the elastic properties of some materials during mesh motion, i.e.

$$E = E(x), \quad x = X - x_f \tag{14}$$

2.3 *Dimensions*

The train consists of the X2 power unit, modeled with rigid bodies for the carbody, two bogies and four wheelpairs. The parts are connected through the primary (wheelpair/bogie) and secondary (bogie/carbody) suspensions.The values have been set based on information from the operator SJ or from values used in the GENSYS package (2006). The carbody can move in all directions and rotate around the yaw and roll angles, but is locked in the pitch angle. The bogies and wheels are free to translate, but not to rotate. These settings have been empirically proven to lead to better numerical stability.

The model of the track and subgrade is constructed from solid threedimensional eight-node elements. The diversity of materials in a track structure calls for the creation

Table 1 Locomotive component parameters.

Name	*Mass/kg*
Car body	53600
Bogies	3060
Wheels	1830

Table 2 Suspension spring constants/(N/m).

Level	*Horizontal*	*Lateral*	*Vertical*
Secondary	$600 \cdot 10^3$	$600 \cdot 10^3$	$1000 \cdot 10^3$
Primary	$20 \cdot 10^6$	$20 \cdot 10^6$	$1200 \cdot 10^6$

Table 3 Suspension damper constants/(Ns/m).

Level	*Horizontal*	*Lateral*	*Vertical*
Secondary	$40 \cdot 10^3$	$40 \cdot 10^3$	$40 \cdot 10^3$
Primary	$2 \cdot 10^3$	$2 \cdot 10^3$	$30 \cdot 10^3$

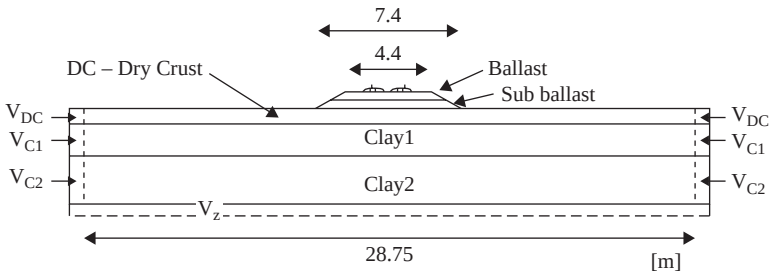

Figure 2 Track-soil-subgrade model dimensions.

of a multi-layer model with different material values. The dimensions are shown in Figure 2. In the horizontal direction, it goes from 13 m behind the rear wheelset to 18 m in front of the front wheels for a total of 43 m. The material characteristics for the two setups are shown in Table 4–6.

The parameters of the visco-elastic absorbing layers in Table 7–9 are found from formulae for non-reflecting boundary conditions (Krenk and Kirkegaard, 2001). As is shown in Figure 3, there are absorbing layers at the boundary at the back of the mesh (and also in the front) as well.

As is apparent from (Lane, 2007), the virtual contact point on the rail is connected to a point on the wheel surface through a special connector. The stiffness of the spring k was chosen based on a linearisation of equation (1) around a force corresponding to equidistribution of normal forces. We found that it was advantageous with a damping value close to *critical damping* in order to maintain numerical stability. The values for a wheel mass of $m_w = 1830$ kg (Table 1) are $k = 1.7321 \cdot 10^8$ N/m and $c = 9.8 \cdot 10^5$ Ns/m.

Table 4 Elastic domain parameters.

Region	*Young's modulus E/pa*	*Poisson ratio ν*	*Density ρ/(kg/m³)*	*Viscous Damping η/pas*	*Rayleigh Damping Parameter*	*Height of layer h/m*
Rail	$206.8 \cdot 10^6$	0.29	7820	–	0.001	0.19
Pads	$69 \cdot 10^6$	0.4995	1185		0.001	0.01
Sleepers	$30 \cdot 10^9$	0.2	2500	–	0.001	0.22*
Ballast	$250 \cdot 10^6$	0.3	1800	$132 \cdot 10^3$	–	0.3
Sub ballast	$300 \cdot 10^6$	0.3	1800	$132 \cdot 10^3$	–	0.5
Dry Crust	$30 \cdot 10^6$	0.45	2000	–	0.001	0.8

* The sleepers are laid out with a length of 0.2 m and a spacing of 0.7 m.

Table 5 Soft clay parameters.

Region	*Young's modulus E/pa*	*Poisson ratio ν*	*Density ρ/(kg/m³)*	*Viscous Damping η/pas*	*Rayleigh Damping Parameter*	*Height of layer h/m*
Clay1	$8 \cdot 10^6$	0.45	1500	–	0.001	1.5
Clay2	$13 \cdot 10^6$	0.45	1600	–	0.001	2.5

Table 6 Stiff clay parameters.

Region	*Young's modulus E/pa*	*Poisson ratio ν*	*Density ρ/(kg/m³)*	*Viscous Damping η/pas*	*Rayleigh Damping Parameter*	*Height of layer h/m*
Clay1	$9000 \cdot 10^6$	0.45	1500	–	0.001	1.5
Clay2	$14000 \cdot 10^6$	0.45	1600	–	0.001	2.5

Table 7 Parameters of lateral viscoelastic zones.

Region	*Young's modulus E/pa*		*Poisson ratio ν*	*Density ρ/(kg/m³)*	*Viscous Damping η/Pas*	
	Soft	*Stiff*			*Soft*	*Stiff*
$\mathbf{V_{DC}}$	$6.2609 \cdot 10^5$	$6.2609 \cdot 10^5$	0.45	1	$3.7731 \cdot 10^4$	$3.7731 \cdot 10^4$
$\mathbf{V_{C1}}$	$1.6696 \cdot 10^5$	$1.8365 \cdot 10^6$	0.45	1	$1.7427 \cdot 10^4$	$5.7800 \cdot 10^4$
$\mathbf{V_{C2}}$	$2.7130 \cdot 10^5$	$2.9843 \cdot 10^6$	0.45	1	$2.2899 \cdot 10^4$	$7.5948 \cdot 10^4$
$\mathbf{V_z}$	$7.2354 \cdot 10^5$	$4.3351 \cdot 10^6$	0.45	1	$2.2899 \cdot 10^4$	$7.5948 \cdot 10^4$

Table 8 Back Absorbing Layers.

Region	*Young's modulus E/pa*		*Poisson ratio ν*	*Density ρ/(kg/m³)*	*Viscous Damping η/Pas*	
	Soft	*Stiff*			*Soft*	*Stiff*
$\mathbf{V_{BCR}}$	$4.7219 \cdot 10^5$	$4.7219 \cdot 10^5$	0.45	1	$3.7731 \cdot 10^4$	$3.7731 \cdot 10^4$
$\mathbf{V_{BC1}}$	$1.2592 \cdot 10^5$	$1.3851 \cdot 10^6$	0.45	1	$1.7427 \cdot 10^4$	$5.7800 \cdot 10^4$
$\mathbf{V_{BC2}}$	$2.0462 \cdot 10^5$	$2.2508 \cdot 10^6$	0.45	1	$2.2899 \cdot 10^4$	$7.5948 \cdot 10^4$

Table 9 Front Absorbing Layers.

Region	*Young's modulus E/pa*		*Poisson ratio* ν	*Density* $\rho/(kg/m^3)$	*Viscous Damping* η*/Pas*	
	Soft	*Stiff*			*Soft*	*Stiff*
$\mathbf{V_{FCR}}$	$3.7799 \cdot 10^5$	$3.7799 \cdot 10^5$	0.45	1	$3.7731 \cdot 10^4$	$3.7731 \cdot 10^4$
$\mathbf{V_{FC1}}$	$1.0080 \cdot 10^5$	$1.1088 \cdot 10^6$	0.45	1	$1.7427 \cdot 10^4$	$5.7800 \cdot 10^4$
$\mathbf{V_{FC2}}$	$1.6380 \cdot 10^5$	$1.8018 \cdot 10^6$	0.45	1	$2.2899 \cdot 10^4$	$7.5948 \cdot 10^4$

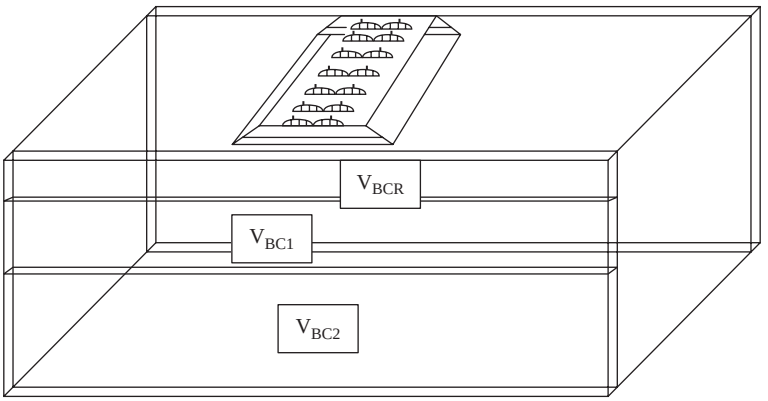

Figure 3 Back Absorbing Layers.

3 Simulations

3.1 *Transition*

The train starts at rest and then travels for a distance of 270 m before it encounters a change in the characteristics of the clay in the subsoil. The Young moduli are shifted from the values in Table 5 to those in Table 6 over a distance of 1.5 m. The transition is illustrated in Figure 4.

3.2 *Results*

The moving mesh method implies that the entire domain is translated as the train moves. This means that all results are presented for locations with constant relative distances from the train, but in a moving frame of reference. The results are presented below.

3.2.1 *Displacements in ballast, sleepers and rail*

Figure 5a–c shows the displacements for respective nodes located:

a. In the lateral mid-plane (between the wheelsets) at the bottom of the ballast region;
b. At the bottom of a sleeper to the left in the running direction;
c. On top of the rail.

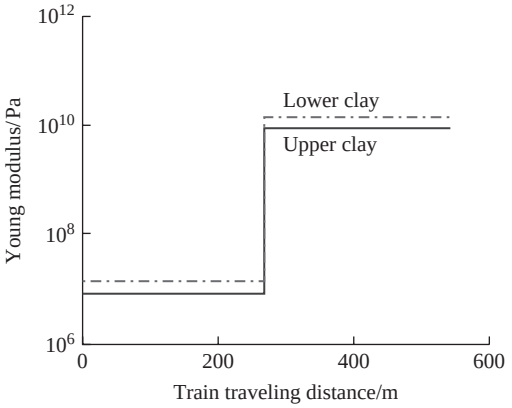

Figure 4 Ground Stiffness Transition.

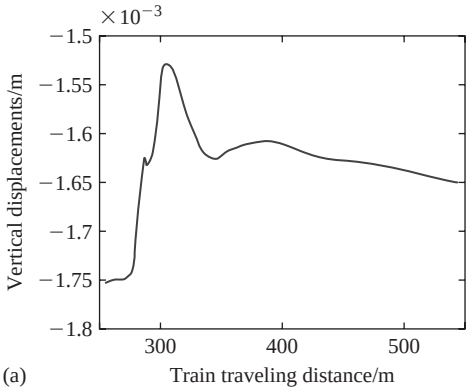

(a)

Figure 5a Displacements in ballast.

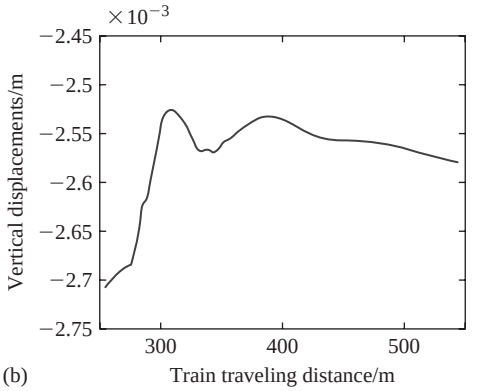

(b)

Figure 5b Displacements in sleeper.

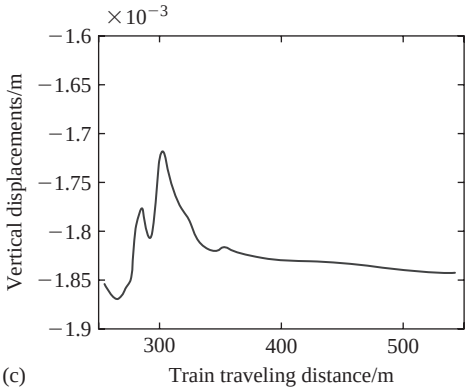

(c)

Figure 5c Displacements in rail.

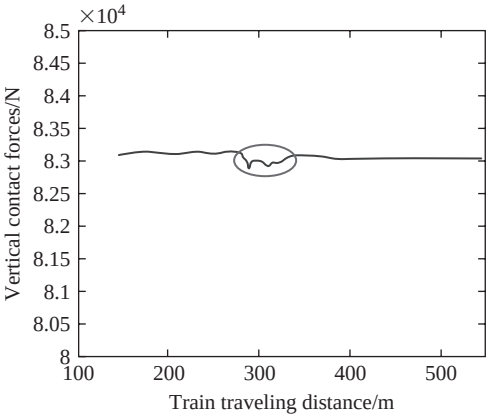

Figure 6 Wheel rail forces.

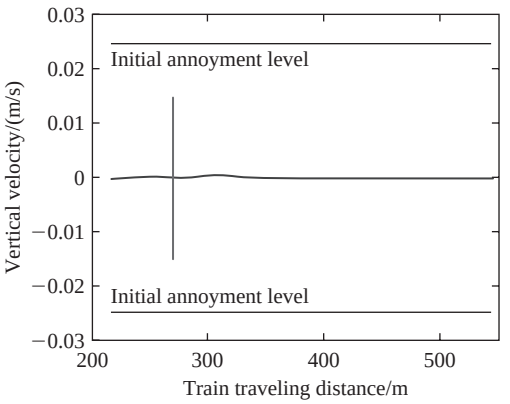

Figure 7 Carbody vertical speed.

3.2.2 *Wheel rail forces*

Figure 6 shows the wheel rail contact forces at for the right front wheels. The transition zone is shown with the circle. The steady state value corresponds to one eighth of the weight of the train.

3.2.3 *Ride discomfort indicator*

Figure 7 shows the vertical velocity of the carbody. A high absolute value can be seen as an indicator of motion discomfort for the passengers. The point of the transition as well as levels for annoyment at 2.5 mm/s have been added to the graph.

3.3 *Comments*

Figure 5a–c shows that there is a small but well-defined effect in the ground and track. The move into a more rigid zone leads to a "bump" followed by a period with

some transient vibrations. The structure settles to a less displaced state after a while. Meanwhile, Figure 6 shows that the vibrations are well shielded from the wheel – rail interface. The two levels of suspension serves to further isolate the coach, as shown in Figure 7.

4 Conclusions

The effect of ground stiffness transitions was simulated with an integrated rigid body – finite element model. By changing material parameters as nodes are moved in a moving mesh scheme, a transition from loose to stiff ground was studied. The model was excited by the passage of an X2 locomotive running at 250 km/h. The effect of transition vibrations were clearly detectable in the ballast, sleepers and rail. The impact at the contact forces and in the train were very modest.

Acknowledgments

Financial support from Banverket (2007), Formas (2007) and Metron Mätteknik (2007) is gratefully received and acknowledged. Inspiration and guidance came from a visit to Professor Tore Dahlberg at the University of Linköping (2007). Colleagues and partners in Banverket and the railway competence centre CHARMEC (2007) gave great technical advice concerning several model parameters.

References

Banverket. 2007. – www.banverket.se. Latest access 19/2-2007.

Charmec. 2007. – www.charmec.chalmers.se Latest access 19/2-2007.

Ching, C.Y.R. 2004. *Finite Element Rail Vibration Dynamics: Multi-body Dynamics of Modern High-speed Trains*. Master Thesis 04:15, Department of Structural Engineering and Mechanics, Chalmers University of Technology, Gothenburg, Sweden.

Ekevid, T. & Wiberg, N.-E. 2002. Computational Wave Propagation – by Adaptive Multigrid FE Technique, Keynote paper at the *Fifth World Congress on Computational Mechanics, Vienna, Austria, July 7–12, 2002*.

Formas. 2007. www.formas.se. Latest access 19/2-2007.

GENSYS. 2006. Vehicle property file: http://www.gensys.se/doc_html/analyse_r_vhe_prop.ins.html – vhe_prop.ins. Latest access 19/11-2006.

Griffiths, J.B. 1985. *The Theory of Classical Dynamics*. Cambridge University Press, Cambridge, United Kingdom.

IKP. 2007. – Division of Solid Mechanics – www.ikp.liu.se/solid/. Latest access 27/2-2007.

Krenk, S. & Kirkegaard, P.H. 2001. Local tensor radiation conditions for elastic waves, *Journal of Sound and Vibration*, **247**, 875–89.

Lane, H., Ekevid, T., Kettil, P., Ching, C.Y. & Wiberg, N.-E. 2007a. Vehicle-track-underground modeling of rail induced wave propagation. *Computers & Structures*, **85**, 1215–1229.

Lane, H., Kettil, P., Enelund, M., Ekevid, T. & Wiberg, N.-E. 2007b. Absorbing Boundary Layers for Elastic Wave Propagation. Presented at the 8th *International Conference on Computational Plasticity, Barcelona, Spain, September 5–8, 2007*.

Lane, H., Kettil, P. & Wiberg, N.-E. 2007c. Moving Finite Elements and Dynamic Vehicle Interaction. Submitted to *European Journal of Mechanics A – Solids*.

Lane, H. 2007. *Computational Railway Dynamics*. Ph. D. thesis, Chalmers University of Technology, Gothenburg, Sweden.

Metron. 2007. – www.metron.se. Latest access 19/2-2007.

Samuelsson, A. & Wiberg, N.-E. 1998. *Finite Element Method – Basics*, Studentlitteratur, Sweden.

Chapter 13

Development and applications of a staggered FEM-BEM methodology for ground vibrations due to moving train loads

Dimitris C. Rizos & John O'Brien

University of South Carolina, Columbia, USA

Evangelia Leon

Geomech Group Inc., Columbia, USA

ABSTRACT: This work presents an efficient methodology for the analysis of vibrations in a railroad track system, induced by the passage of conventional and high speed trains. The methodology is based on an efficient coupling of the Boundary Element (BEM) with the Finite Element Method (FEM) in the direct time domain. The BEM is used for the modeling of the soil-tie system and the FEM for the modeling of the flexible rail system. Soil-Structure Interaction and traveling wave effects are inherently accounted for. The proposed methodology allows for selection of different time steps in order to fulfill stability requirements of each solver.

1 Introduction

High speed rail transportation is quickly becoming a popular form of mass transit through-out the world. High Speed Trains (HST) pertain to passenger trains traveling in excess of 160 km/h (100 mph), and as fast as 300 km/h (186 mph). Potential problems arise when high speed trains travel over soft soils having relatively low wave velocities. In such cases excessive vibrations in the track systems, train suspension, and nearby structures may occur contributing to the passenger discomfort and causing serious damage to the track and train. Additionally, nearby structures experience the effects of the vibrations causing discomfort and a sense of an unsafe environment to the occupants. These potential problems are attributed to a phenomenon equivalent to the "sonic boom" where the wave propagation in the soil is equal or lower than the speed of the moving source. Accurate assessment of vibrations depends on appropriate representation of the wave propagation problem and the dynamic interaction between the soil, track system, and moving train. Tools for vibration prediction in such cases will contribute to the proper design of new and retrofit of existing systems.

Numerical models for Soil-Structure Interaction effects are based on Finite Element Methods (FEM), Boundary Element Methods (BEM) or hybrid techniques. Although FEM are well established procedures, e.g., Bathe (1996) and Cook et al. (2002), they are not free of shortcomings especially when modeling of infinite domains is in order. In such cases special developments are required to satisfy the radiation condition

preventing, thus, spurious vibration modes due to boundary reflections. Alternatively, the infinite soil region can be modeled using BEM methods for wave propagation which are based on Boundary Integral Formulations that implicitly satisfy the radiation. Comprehensive literature reviews on BEM formulations have been reported by Beskos (1997) and Mackerle ((1996),(1998)). BEM models have been coupled to FEM models of structural systems. Such studies have been reported in the literature for problems in dynamic and seismic analysis of coupled soil-structure systems involving stationary loads, Rizos and Wang (2002), von Estorff and Firuziaan (2000), Yazdchi et al. (1999). Coupling the BEM and FEM methods retains the advantages of each method and eliminates their shortcomings.

Availability of experimental data and in-situ measurements on high speed train induced vibrations is limited. Degrande and Shillemans (2001), Kaynia, et al. (2000), Madshus and Kaynia (2000), Hall (2003), and Sheng et al. (2003) have presented in-situ measurements recorded from track sites in Europe. Much of the available research reported in the literature on this topic is based on analytic and numerical techniques, such as in the work of Bode et al. (2002), Hall (2003), Ekevid and Wiberg (2002), Yang et al. (2003), and Ekevid et al. (2001), and recently by the authors (2005), among others.

This work presents an efficient direct time domain solution approach to study the transient response of a soil-track system due to passage of HSTs through computer simulations. To this end, the well established Boundary Element Method and Finite Element Method are coupled in the direct time domain in an efficient manner since it uses impulse response techniques, normalization and scaling procedures, O'Brien and Rizos (2005). Numerical applications demonstrate the accuracy and versatility of the method.

2 Constituent models

2.1 *General*

The physical system under consideration consists of a straight steel track supported on concrete ties, which in turn, rest on the foundation soil. The vehicle dynamics of the HST are ignored in the present study. The present work uses a coupled BEM FEM methodology for the analysis of moving train loads in the direct time domain. The BEM is applied on the soil region and considers the kinematic interaction with the ties, in order to account for the traveling wave effects, and the through the soil interaction of adjacent ties. The FEM method is used for the modeling of the rails. The two solution domains are coupled at their interface, i.e., the tie-rail contact points. A diagram of the system is shown in Figure 1, and the constituent models are discussed next.

2.2 *Soil-Tie model*

The soil region is modeled as homogeneous linear elastic half space with a horizontal free surface. The ballast and subbase are not considered in this model; however, they can be accommodated in the proposed method in a straightforward manner. Hence, ties are assumed to rest directly on the free surface of the halfspace with which they

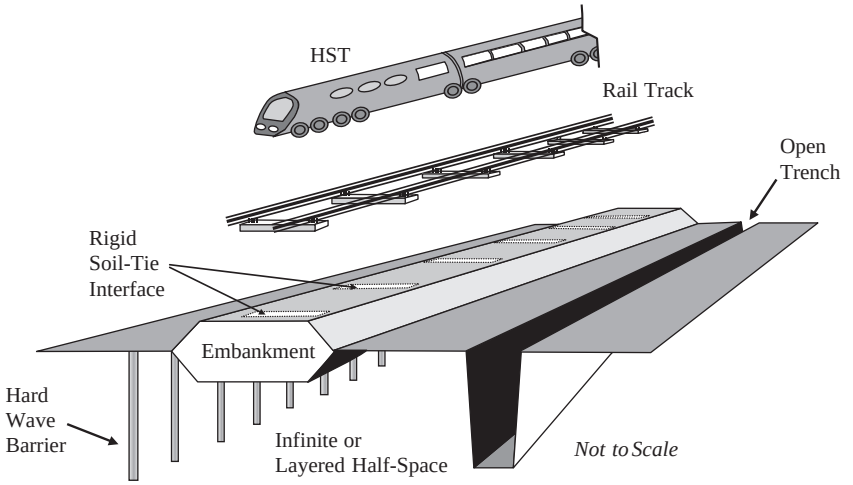

Figure 1 System Idealization.

remain always in contact. The ties are considered to be rigid and only kinematic interaction effects are accounted for in the soil-tie model. Inertia interaction effects due to the tie's mass are accounted for in the track-rail model and the FEM solution. The tie's dimensions are 2.5 m long × 0.285 m wide with center to center spacing of 0.955 meters. The proposed method allows for any number of ties to be accounted for in the soil tie model.

2.3 *Track-Rail model*

The type of rails of the track system considered in this work is the UIC-60 commonly used in European high speed rail applications. Rails are assumed to remain linear elastic and are coupled to the ties in the vertical direction only. Loads applied on the track structure are assumed to be applied equally on each of the two rails. Consequently, the rail model is simplified by using a single rail passing over the center of the ties. The cross sectional area, and the moment of inertia about the x axis of the single rail are both doubled to account for the equivalent stiffness of a two rail track.

2.4 *Train loads*

The train loads applied to the FE model in this work are based on the X-2000 HST consisting of one locomotive and four passenger cars, Kaynia et al. (2000) and Ekevid and Wiberg (2002). Only the vertical bogie loads are used for modeling; this accounts only for the weight of the train and does not include any train dynamics. The supercritical, critical and subcritical train speeds pertain to HST traveling at speeds above, at, or below the shear wave velocity of the soil.

3 Proposed methodology and solution procedure

3.1 *Boundary element solver*

A detailed formulation of the employed 3-D BEM is too extensive and beyond the scope of this paper and can be found in O'Brien and Rizos (2005), Rizos (1993), Rizos (2000), Rizos and Karabalis (1994) and Rizos and Loya (2002). The BEM uses the time domain 4th order B-Spline fundamental solutions of the 3-D full space along with higher order spatial discretization of the boundary. The Boundary Integral Equation associated to the Navier-Cauchy governing equations of motion is expressed in a discrete form yielding a system of algebraic equations at step N relating displacements $\mathbf{u}$ to forces $\mathbf{f}$ at discrete boundary nodes in the BEM model and at discrete time instants t_j and τ_j, as

$$\mathbf{cu}(t_N) = \sum_{n=1}^{N+1} \mathbf{U}(t_n)\, \mathbf{f}(\tau_{N-n+2}) - \mathbf{T}(t_n)\, \mathbf{u}(\tau_{N-n+2}) \quad N = 1, 2, \ldots, N_{end} \tag{1}$$

where $\mathbf{c}$ is a discontinuity term, and $\mathbf{U}$ and $\mathbf{T}$ are the BEM coefficient matrices associated with the fundamental solutions. Equations (1) can be solved in a time marching scheme for N_{end} time steps yielding the B-Spline Impulse Response (BIRF) of the system. In order to derive equivalent, time-dependant flexibility matrices associated with the "loaded part" of the BE model (e.g. points of application of external excitation), a unit B-Spline impulse force $\delta_j = \mathbf{f}$, perturbs each "active" degree of freedom, $j = 1, \ldots, NN$, at a time and successive solutions of Equation (1) yield the B-Spline impulse response vectors, $\mathbf{b}_j^N = \mathbf{u}(t_N)$. These BIRFs can be collected in matrix form as

$$\mathbf{B}^N = [\mathbf{b}_1^N, \mathbf{b}_2^N, \ldots, \mathbf{b}_j^N, \ldots \mathbf{b}_{NN}^N] \tag{2}$$

Matrix $\mathbf{B}$ represents the BIRF associated to the displacements of the BEM nodes due to concentrated unit forces applied in the directions of the degrees of freedom that vary in time according to a B-Spline function, and captures the traveling wave characteristics. Subsequently, the response, $\mathbf{u}^N$, of the elastodynamic system subjected to arbitrary external forces $\mathbf{f} = \mathbf{P}$ applied at the nodes are computed at time step N as:

$$\mathbf{u}^N = \sum_{n=1}^{N+1} \mathbf{B}^n \mathbf{P}^{N-n+2} \tag{3}$$

By separating known from unknown quantities at time step N, and assuming that $\ddot{\mathbf{P}}_{BEM}^N = 0$, Equation (3) can be expressed as:

$$\mathbf{u}_{BEM}^N = \left(\mathbf{B}^1 \mathbf{P}_{BEM}^{N+1} + \mathbf{B}^2 \mathbf{P}_{BEM}^N\right) + \sum_{n=3}^{N+1} \mathbf{B}^n \mathbf{P}_{BEM}^{N-n+2} = \mathbf{F}\mathbf{P}_{BEM}^N + \mathbf{H}^N \tag{4}$$

where

$$\mathbf{F} = 2\mathbf{B}^1 + \mathbf{B}^2$$

$$\mathbf{H}^N = \sum_{n=3}^{N+1} \mathbf{B}^n \mathbf{P}_{BEM}^{N-n+2} - \mathbf{B}^1 \mathbf{P}_{BEM}^{N-1}$$

Matrix **F** represents the flexibility matrix of the loaded BEM region and vector $\mathbf{H}^N$ represents the influence of the response history on the current step. Equation (4) is used for the evaluation of the response at the monitoring points on the ground surface. The flexibility matrix is independent of time, however, vector $\mathbf{H}^N$ needs to be evaluated at every time step. The proposed method is implemented in two major phases. The first phase calculates the BIRF matrices of the boundary of the domain. The evaluation of the BIRF matrices, $\mathbf{B}^N$, is computationally intensive, however, they are independent of the external excitation and need to be evaluated only once for a given model geometry. The second phase calculates the response of the boundary of the domain given a known excitation force time history. The evaluation of Equation (4) for the system response to arbitrary excitation is extremely efficient and can be performed in near real time.

In the presence of rigid bodies in contact with the free surface, such as the case of the railroad ties, the same method can be used along with the Rigid Surface Boundary Element developed by Rizos (2000) to compute the BIRF functions of the soil-tie interface. To this end, the surface of the soil region is discretized with 8-node surface elements and the 4-node rigid surface boundary elements reported in Rizos (2000) are placed at soil-tie interface to represent the ties. The response of each tie is described by three translations and three rotations of the center of the tie. In order to compute the BIRF of the soil-tie system, each of the six degrees of freedom (dof) of the loaded tie is excited by a B-Spline impulse force and the response of all ties in the system is computed following the procedures introduced in O'Brien and Rizos (2005). The computed BIRF are characteristic responses of the system and are expressed symbolically in matrix form as

$$\mathbf{B}^N = [\mathbf{b}_1^N, \mathbf{b}_2^N, \ldots \mathbf{b}_m^N \ldots, \mathbf{b}_M^N] \quad M = \text{total number of ties} \tag{5}$$

Superscript N indicates that quantities are evaluated at time t^N. Each submatrix $\mathbf{b}_m$ in matrix $\mathbf{B}^N$ is of size $6M \times 6$ and pertains to the case where a B-Spline impulse excitation is applied on tie m. Elements in each column, $j = 1, 6$ of $\mathbf{b}_m$ represents the response of all degrees of freedom of all ties at time t^N due to the excitation applied in the direction of degree of freedom j of tie m. Such BIRFs are shown in Figure 2 for a three tie configuration resting on a flat surface elastic halfspace at selected times for the case where the middle tie is loaded by a stationary B-spline impulse in the vertical direction (Figure 2a) and horizontal direction (Figure 2b). With the BIRF matrix, **B**, known, the response, $\mathbf{u}^N$, of a system to an excitation force **P** due to the passage of a train transmitted to the ties through the rail is computed by Equation 3. In this case, **u** is the vector with the time histories of the translations and rotations of the center of all ties in the system. It should be noted that the complete effects of the free field, as well as cross interaction effects between ties, are implicitly accounted for in the response vector **u**. This expression as evaluated for the response of the ties does not monitor the response of the free filed. However, once the response vector **u** is computed, the response of the free field can be computed by the procedures reported in O'Brien and Rizos (2005) in a straightforward manner. Once the displacements are

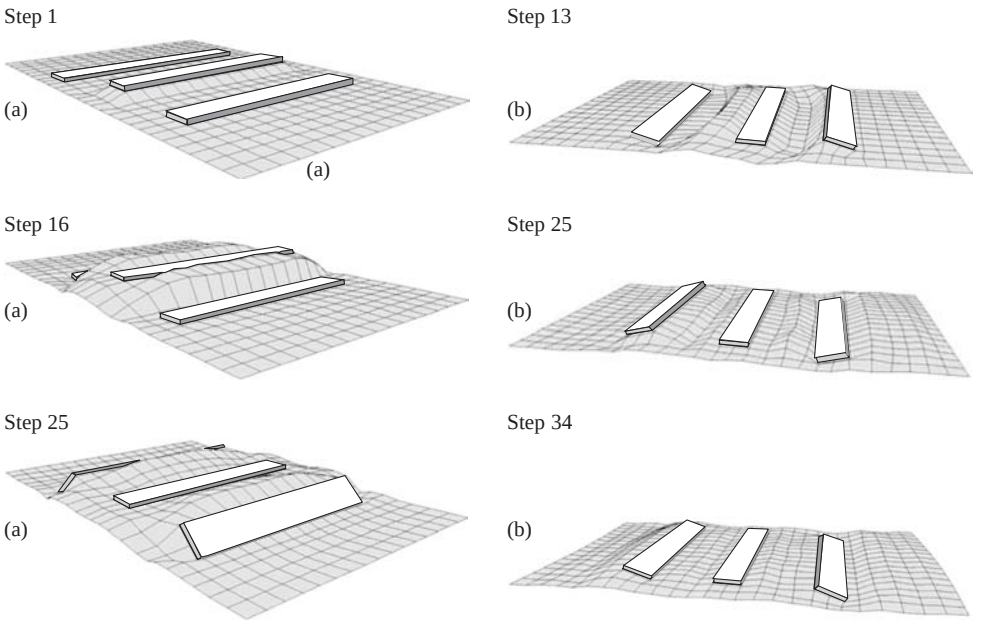

Figure 2 Deformed configurations of BIRF of ground-tie system at selected time steps: (a) vertical excitation, (b) horizontal excitation.

computed, velocities and accelerations are determined in this work through a finite difference approximation, as

$$\dot{\mathbf{u}}^N = \frac{\mathbf{u}^{N+1} - \mathbf{u}^N}{\Delta t} \quad \ddot{\mathbf{u}}^N = \frac{\dot{\mathbf{u}}^{N+1} - \dot{\mathbf{u}}^N}{\Delta t} \tag{6}$$

Equations (3)–(6) represent the BEM solver that is adopted in the proposed methodology for moving loads.

3.2 *Tie superposition*

For the analysis of a real system consisting of a large number of ties where all ties are loaded in an asynchronous pattern due to the moving load, the calculation of the BIRF matrix, Equation (5), is a computationally expensive task if all ties are to be considered simultaneously. In such a complete approach, every tie in the system needs to be loaded by a B-Spline impulse and the response of all ties needs to be computed. Although this approach is an accurate representation of the rail-tie system, it may be simplified by observing that repetitive responses of the ties are expected when a single representative tie is loaded due to the assumption of a straight track. In view of the wave attenuation and the HST speed, only a relatively small number of adjacent ties are expected to have a significant contribution to the response at any given time. Furthermore, depending on the geometry and spacing of ties, cross interaction effects are expected to be important for only the immediate adjacent ties. Therefore, it is feasible to generate BIRF matrices

of a large system based on the analysis of much smaller systems consisting of only a few ties. The details of this technique are too extensive; however they are presented in the work of O'Brien and Rizos (2005). As an example, if a stretch of railroad track contains 5,000 ties, the BIRF matrix of Equation (5) will be of size $30{,}000 \times 30{,}000$ and fully populated. If the proposed technique is adopted and assuming that only 7 ties on each side of the loaded tie contribute significantly to the response, the BIRF matrix of the 15-tie system is of size 90×90 and the BIRF matrix of the 5000-tie system is now a banded matrix of bandwidth 48. As a result increased computational efficiency and optimized storage requirements are achieved without sacrificing accuracy.

3.3 *FEM solver*

As described previously, FE models will be used for the development of the track and train structures. The tracks will be modeled using Timoshenko beams and the trains will be modeled as system with rigid cars and springs and dampers connecting them to the bogies. The behavior of these structures can be modeled using the second order differential equation

$$\mathbf{M}_s\ddot{\mathbf{u}}(t) + \mathbf{C}_s\dot{\mathbf{u}}(t) + \mathbf{K}_s\mathbf{u}(t) = \mathbf{P}^{FEM}(t) \tag{7}$$

where $\mathbf{M}_s$, $\mathbf{C}_s$ and $\mathbf{K}_s$ are the mass, damping and stiffness matrix of the system, $\mathbf{u}(t)$ is the vector of nodal displacements, $\mathbf{P}^{FEM}(t)$ is the vector of applied loads with respect to the time t. Following well established procedures using Newmark's method for direct time integration, Equations (7) can be rearranged in a system of algebraic equations as,

$$\mathbf{D}\mathbf{u}^N = \mathbf{P}^N + \mathbf{H}^N \tag{8}$$

where $\mathbf{D}$ is the dynamic matrix and $\mathbf{H}^N$ is a modification to the nodal force vector, $\mathbf{P}^N$, at step N. In order to develop the FEM solver suitable for the proposed coupled FEM-BEM scheme, Equation (8) is rearranged so a solution can be reached in a single step. To this end, and in view of the free, f, and supported, s, degrees of freedom the system of Equation (8) is partitioned and known from unknown quantities are separated leading to

$$\begin{bmatrix} \mathbf{D}_{ff} & 0 \\ \mathbf{D}_{sf} & -\mathbf{I} \end{bmatrix} \begin{Bmatrix} \mathbf{u}_f \\ \mathbf{R}_s \end{Bmatrix} = \begin{Bmatrix} \mathbf{P}_f \\ 0 \end{Bmatrix} + \begin{Bmatrix} \mathbf{P}_f^{eq} \\ \mathbf{P}_s^{eq} \end{Bmatrix} + \begin{Bmatrix} \mathbf{H}_f \\ \mathbf{H}_s \end{Bmatrix} - \begin{bmatrix} \mathbf{D}_{fs} \\ \mathbf{D}_{ss} \end{bmatrix} \{\mathbf{u}_s\} \tag{9}$$

$\mathbf{P}^{eq}$ are the nodal equivalent forces applied on all degrees of freedom, and $\mathbf{R}_s$ is the vector of unknown support reactions. This equation can now be solved for the unknown displacements and support reactions at step N. Equation (9) represents the FEM solver that is adopted in the proposed coupled BEM-FEM methodology for moving loads, discussed in Section 3.5.

3.4 *Moving loads*

As with any finite element model, loads applied on beam elements must be represented by nodal equivalent forces and moments. For a moving load analysis, the nodal equivalent load vector applied to the structure becomes a function of velocity and time. At

any time step, n, for a single wheel load moving with speed, V, the position of the load on the system is known from

$$x = Vn\,\Delta t \tag{10}$$

where Δt is the analysis time step. Once the global position of the load is determined, the element on which it is located can be found. The nodal equivalent loads for the particular element are then determined based on the position of the load on the element, while the loads on all other elements are zero. At the next time step, the load moves to a new position, the loaded element is determined, and the new equivalent loads are computed. Multiple loads are accounted for by superimposing the time dependant load vectors for each individual load, at every time step.

3.5 *BEM-FEM coupling*

The BEM model of the soil region is coupled to the FEM models of the train, truck and ties at the soil-tie interface and a time marching solution is obtained in a staggered approach. It is assumed that the train is always in contact with the rails, the rail structure is always in contact with the ties and the ties must remain always in contact with the soil. As a result of these contact conditions, forces and displacements at the rails resulting from the traveling train must be introduced to the ties which, in turn, are transmitted to the soil. As the soil is loaded, waves are generated and the resulting displacements due to wave propagation must be applied to the ties which in turn are transmitted to the rails and the train, completing, thus, a single interaction cycle. Coupling of the BEM and FEM models is achieved by considering compatibility of displacements and force equilibrium at the BEM-FEM interface. Therefore, the following relationships must be satisfied at every time step of the solution

$$\mathbf{u}^{BEM} = \mathbf{u}_s^{FEM} \tag{11a}$$

$$\mathbf{P}^{\mathrm{BEM}} + \mathbf{R}_s^{FEM} = 0 \tag{11b}$$

where subscript s pertains to the supported degrees of freedom of the FEM model which, in general, are the tie-rail contact degrees of freedom. The coupling scheme introduced in Rizos and Wang (2002), and adopted in O'Brien and Rizos (2005) and is briefly discussed herein to solve the 3-D Soil Structure Interaction problem for moving loads. A schematic representation of the staggered solution scheme is shown in Figure 3. At each time step of the solution known the moving loads are applied to the structure in the Finite Element portion of the model. Initial velocity and acceleration can also be specified in addition to forces and displacements. The displacements of the interface nodes, $\mathbf{u}_s^{FEM}$, are prescribed as initial conditions at time $t = 0$ or as provided by the Boundary Element solutions along with the compatibility Equation (11a). The interface degrees of freedom are fixed at the new location and the Finite Element Solver, Equations (8), computes the response of the structure as well as the forces, $\mathbf{R}_s^{FEM}$, at the interface nodes. Subsequently, Equation (11b) computes the corresponding forces at the interface nodes in the BE region. Based on these forces, the BEM solver, Equations (4), evaluates the displacements at the interface nodes, which, in view of Equation (11a), become the new initial conditions for the FEM Solver and the solution moves to

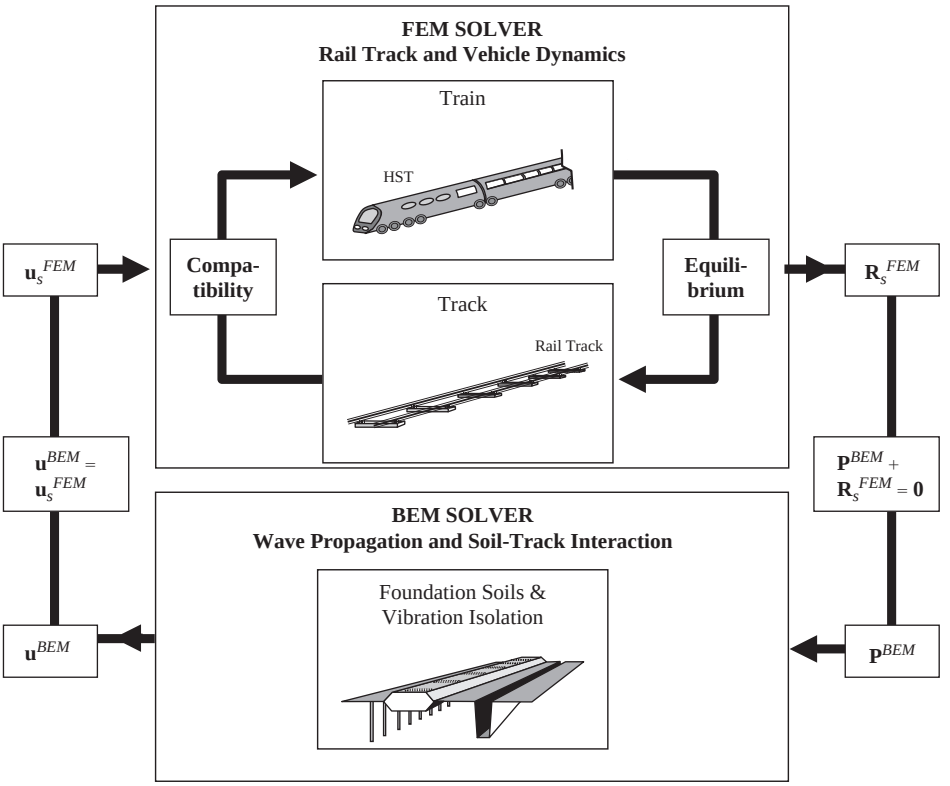

Figure 3 Schematic Representation of the Coupling Scheme.

the next time step. The proposed staggered solution scheme accommodates independent selection of the time step in the FEM and BEM solvers to satisfy any convergence requirements, as discussed in O'Brien and Rizos (2005).

4 Applications

4.1 *Validation study*

This section presents a validation example considering the soil-tie-rail systems along with the full train load moving at speeds V = 19 m/s and V = 51 m/s. Details on the soil and the train loads are listed in O'Brien and Rizos (2005). The BIRF matrices are generated for a 240-tie system in order to accommodate the full length of the train. The results from the proposed method are compared to the field measurements reported by Madshus and Kaynia (2000) and shown in Figures 4 a and b. It should be noted that: (i) only the wheel loads are applied to the rails, (ii) vehicle dynamics are ignored, (iii) train-rail interaction is not considered, (iv) rail imperfections are not accounted for and (v) the assumed soil profile does not account for the ballast and subbase layers found on site. Nevertheless, as evidenced in Figure 4, there is a general agreement between

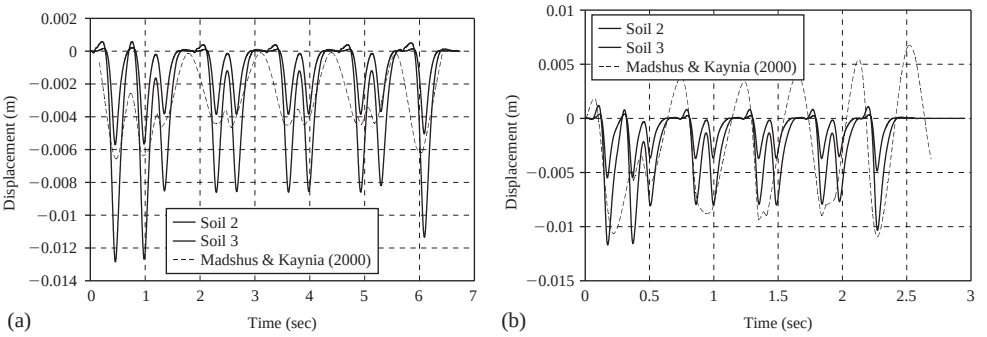

Figure 4 Vertical response of a tie due to a moving train load compared to in-situ measurements for train velocities of (a) $V = 19$ m/s and (b) $V = 51$ m/s. (O'Brien and Rizos 2005).

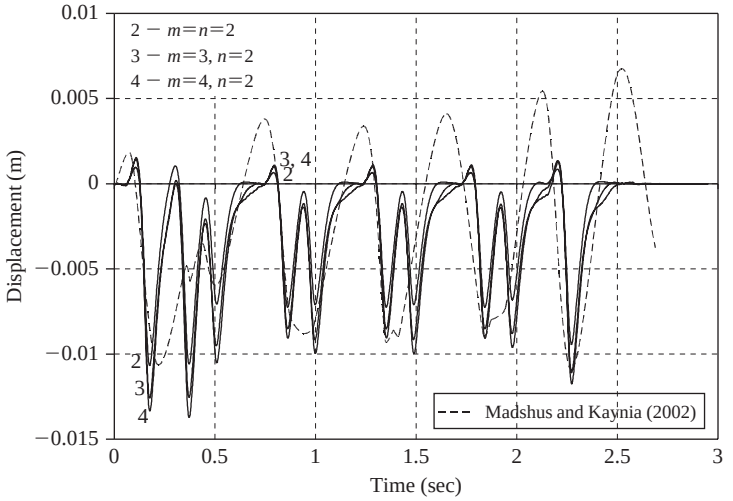

Figure 5 Effects of the number of significant ties in comparison to in-situ measurements. (O'Brien and Rizos 2005).

the computer simulations and the reported in-situ measurements. For the subcritical case, Figure 4a, the observed peak vertical deflections tend to fall between the peak deflections obtained using soils corresponding, respectively, to the ballast material and the free field present in the in-situ conditions. For the supercritical case, Figure 4b, the downward displacements found from this work are once again in a general agreement with the reported values. However, the train is now moving at supercritical speed, and the calculated track uplift is somewhat less than the recorded values. Results of an investigation on the effect of number of significant ties considered in the model are shown in Figure 5. It is observed that increasing the number of significant ties has an effect on the response by increasing both the uplift and peak downward displacements of the ties. Therefore, the number of significant ties becomes a model parameter and depends on the train speed.

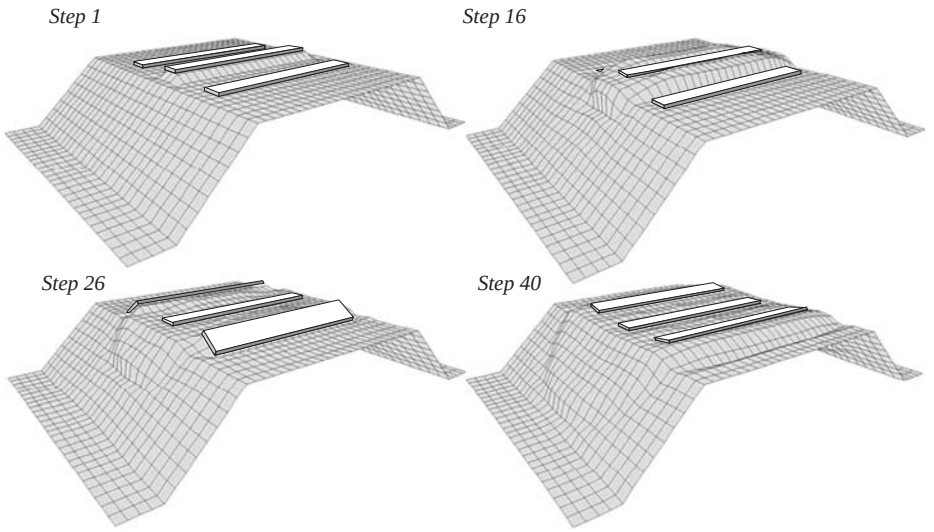

Figure 6 BIRF of a three tie system on an embankment due to a vertical excitation at selected time steps.

4.2 *Effects of embankment*

This section presents a study on the effects of the embankment on the vibration caused by the passage of a moving load at subcritical, critical and supercritical speeds. To this end, it is assumed that the soil medium is a homogeneous semi-infinite medium and the geometry of its free surface considers a typical embankment, Haldankar (2007). A 20-tie system is considered and the geometry and spacing is as described in section 2.2. First the BIRF system response of a three tie system due to a vertical excitation applied at the middle tie is computed. Snapshots of the BIRF response of all nodes at selected times when a vertical excitation is applied at the middle tie is shown in Figure 6.

Subsequently, the BIRF of a 20-tie system is generated as discussed in section 3.2 and the system is subjected to a single concentrated load that moves at speeds $v = 20$ m/sec, 131.6 m/sec and 197.4 m/sec, corresponding to subcritical, critical and supercritical speeds. The horizontal and vertical response of the tenth tie is monitored and plotted in Figure 7 as a function of the dimensionless time defined in O'Brien and Rizos (2005). Figure 7 also shows the response of a system that lies on a flat surface for comparison. It is observed in both cases that the response is prolonged for travel speeds at the critical and supercritical speeds and it lasts long after the passage of the load from the observation point. The effects of travel at critical and supercritical speeds are more pronounced in the horizontal vibration mode that, in addition to higher amplitudes, shows a change in the frequency content. The vertical vibration mode shows a slight amplitude reduction for travel at supercritical speeds, however, uplift starts appearing for travel at critical and supercritical speeds. It is observed that the presence of the embankment affects minimally the vertical response of the system for all three travel speeds. The horizontal mode, however, is considerably affected. In the presence of the

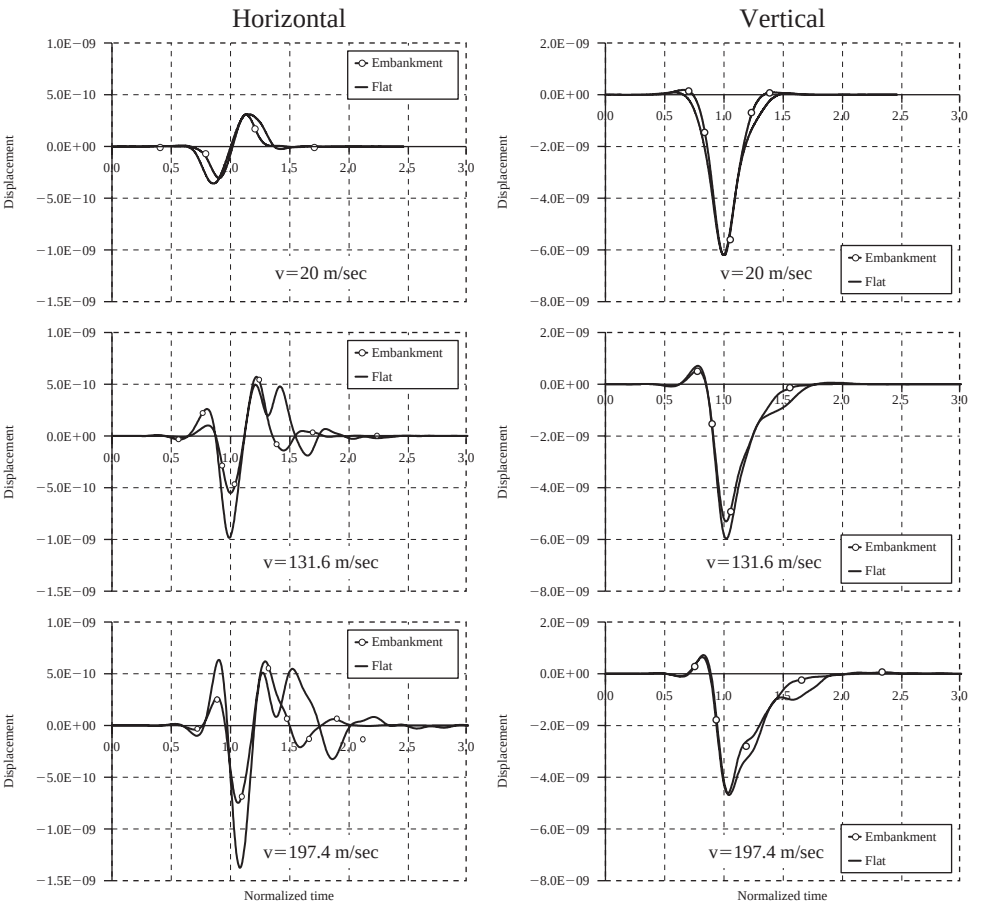

Figure 7 Horizontal and vertical response of the tenth tie in a 20 tie system due to passage of a single concentrated load at speeds v = 20, 131.6 and 197.4 m/sec.

embankment, the amplitude of the vibration is reduced compared to the case of a half-space with flat surface and it appears that the higher frequency components, although present, are dampened out. However, the amplitude still increases with increase of travel speeds to supercritical levels.

5 Conclusions

The present work presents a coupled BEM-FEM procedure suitable for vibration analysis of railroad track systems due to the passage of conventional and high speed trains. The proposed method couples the BEM with the FEM in a staggered approach in the direct time domain. The BEM is used for the modeling of the soil-tie system within the framework of impulse response techniques. The FEM is used to model the rail system.

The two methods are coupled at the tie-rail interface. In view of the discussion in the preceding sections the following conclusions have been reached:

1. The derivation of the B-Spline impulse response matrix of a large soil-tie system can be greatly simplified by observing that: (i) a relatively small number of ties contribute significantly to the response of the system, (ii) cross interaction effects between ties is significant only for a few adjacent ties, (iii) the B-Spline impulse response of the system due to a load applied at an arbitrary tie can be represented by appropriately shifting in space the B-Spline impulse response due to a load applied at a reference tie.
2. The nondimensional B-Spline Impulse Response Function for the soil-tie system is independent of the actual soil conditions and the moving loads. This leads to an efficient implementation of the BEM solver of the proposed methodology.
3. The coupled BEM-FEM scheme allows for selection of different time steps in order to fulfill stability requirements of each solver. In general, it has been observed that the FEM requires smaller time step than the BEM for solution convergence.
4. The number of ties that contribute significantly to the system response depends on the train speed. The number of significant ties should be chosen to balance accuracy and computational efficiency.
5. Dynamic cross interaction effects between adjacent ties need only be considered between immediate adjacent ties regardless of train speed.
6. The horizontal vibration mode is affected more by the passage of high speed trains than the vertical, although the vertical mode shows tie uplift for travel at critical and supercritical speeds. The horizontal vibration mode also shows higher frequency content at critical and supercritical speeds.
7. The effects of an embankment are more pronounced in the horizontal vibration mode.

References

Bathe, K.J. 1996. Finite Element Procedures. Upper Saddle River: Prentice-Hall.

Beskos, D.E. 1997. Boundary element methods in dynamic analysis: Part II 1986–1996. ASME Applied Mechanics Reviews, 50:149–197.

Bode, C., Hirschauer, R. & Savidis, S.A. 2002. Soil-structure interaction in the time domain using halfspace Green's functions. Soil Dynamics and Earthquake Engineering 22:283–295.

Cook, R.D., Malkus, D.S., Plesha, M. & Witt, R.J. 2002. Concepts and Applications of Finite Element Analysis. New York: John Wiley & Sons.

Degrande, G. & Schillemans, L. 2001. Free field vibrations during the passage of a Thalys high-speed train at variable speed. Journal of Sound and Vibration 247:131–144.

Ekevid, T., Li, M.X.D. & Wiberg, N.E. 2001. Adaptive FEA of wave propagation induced by high-speed trains. Computers and Structures 79:2693–2704.

Ekevid, T. & Wiberg, N.E. 2002. Wave propagation related to high-speed train A scaled boundary FE-approach for unbounded domains. Computer Methods in Applied Mechanics and Engineering 191:3947–3964.

Hall, L. 2003. Simulations and analyses of train-induced ground vibrations in Finite Element Models. Soil Dynamics and Earthquake Engineering 2003(23):403–413.

Kaynia, A.M., Madshus, C. & Zackrisson, P. 2000. Ground vibration from high-speed trains: Prediction and countermeasure. Journal of Geotechnical and Geoenvironmental Engineering 126:531–537.

Mackerle, J. 1996. FEM and BEM in geomechanics: Foundations and Soil-Structure Interaction – A bibliography (1992–1994). Finite Elements in Analysis and Design 29:249–263.
Mackerle, J. 1998. Finite element and boundary element analysis of bridges, roads and pavements – A bibliography (1994–1997). Finite Elements in Analysis and Design 29:65–83.
Madshus, C. & Kaynia, A.M. 2000. High-speed railway lines on soft ground: Dynamic behaviour at critical train speed. Journal of Sound and Vibration 231:689–701.
O'Brien, J. & Rizos, D.C. 2005. A 3D BEM-FEM methodology for simulation of high speed train induced vibrations. Soil Dynamics and Earthquake Engineering 25:289–301.
Haldankar, H. 2007. Studies of high speed train induced vibrations. MS Thesis, University of South Carolina.
Rizos, D.C. 1993. An Advanced Time Domain Boundary Element Method for General 3-D Elastodynamic Problems. Ph.D. Dissertation, University of South Carolina.
Rizos, D.C. 2000. A rigid Boundary Element for Soil-Structure Interaction analysis in the direct time domain. Computational Mechanics 26:582–591.
Rizos, D.C. & Karabalis, D.L. 1994. An advanced direct time domain BEM formulation for general 3-D elastodynamic problems. Computational Mechanics 15:249–269.
Rizos, D.C. & Loya, K.G. 2002. Dynamic and seismic analysis of foundations based on free field B-Spline characteristic response histories. Journal of Engineering Mechanics 128:438–448.
Rizos, D.C. & Wang, Z. 2002. Coupled BEM-FEM solutions for direct time domain soil-structure interaction analysis. Engineering Analysis with Boundary Elements 26:877–888.
Sheng, X., Jones, C.J.C. & Thompson, D.J. 2003. A comparison of a theoretical model for quasi-statically and dynamically induced environmental vibration from trains with measurements. Journal of Sound and Vibration 267:621–635.
von Estorff, O. & Firuziaan, M. 2000. Coupled BEM/FEM approach for nonlinear soil/structure interaction. Engineering Analysis with Boundary Elements 24:715–725.
Yang, Y.B., Hung, H.H. & Chang, D.W. 2003. Train-induced wave propagation in layered soils using Finite/Infinite Element simulation. Soil Dynamics and Earthquake Engineering 23:263–278.
Yazdchi, M., Khalili, N. & Valliappan, S. 1999. Dynamic soil-structure interaction analysis via coupled Finite Element-Boundary Element Method. Soil Dynamics and Earthquake Engineering 18:499–517.

Chapter 14

Vibration monitoring as a diagnosis tool for structural condition assessment

Guido De Roeck & Edwin Reynders

K.U. Leuven, Leuven, Belgium

ABSTRACT: The paper gives an overview of the necessary conditions for a successful structural condition assessment by vibration measurements. First a critical overview is given about the advantages and disadvantages of the different excitation sources: forced, ambient and impact excitation. For damage level 1, the advantage of ARX-models, simulating the relation between the histories of eigenfrequencies and the histories of temperatures, over classical regression techniques is enlightened Other new methods like the one based on features extracted from spatial filtering will be presented as well. Many methods have been proposed for damage identification, levels 2 and 3. The paper concentrates on the most versatile of them: finite element updating. At the expense of building a FE-model of the structure, all acquired data can be used: natural frequencies, scaled or unscaled mode shapes and modal strains. Potential damage is simulated in a FE-model of the structure by adopting a parametric representation of this damage. Mathematically, a constrained optimization problem is solved. The objective function is defined as a sum of squared differences. The residual vector contains the differences in the identified modal data (and possibly some derived quantities), such as the natural frequencies, the mode shapes, the modal curvatures, etc. If the objective function contains multiple local minima, a global optimization algorithm should be used, like the Coupled Local Minimisers (CLM) method. Two examples illustrate the use of FE-updating for damage assessment. The first application concerns the well known Z24 bridge in Switzerland. The second example is the Tilff bridge. New in this project was the use of very accurate optical fibers for strain measurements. Finally, a series of conclusions are highlighted which can be considered as guidelines for good practice of vibration monitoring.

1 Introduction

Service loads, environmental and accidental actions may cause damage to structures. Regular inspection and condition assessment of engineering structures are necessary so that early detection of any defect can be made and the structures' updated safety and reliability can be determined. Early damage detection and location allows maintenance and repair works to be properly programmed. This minimizes not only the annual costs of repair (e.g. for bridges estimated at 1.5% of their value) but also avoids a long out of use time which can represent an even higher economic cost (e.g. traffic delay due to major bridge repair). Many civil engineering structures (e.g. bridges, offshore platforms . . .) are 20–30 years old. When just considering the bridge infrastructure of many developed countries, the number of deteriorating bridges is increasing

dramatically, and greatly exceeds the number of new bridges being constructed. Costs for maintenance, repair and rehabilitation are prohibitive and will bear heavily on future national economies.

To avoid high costs of repair, an evaluation method must accurately reveal the present load carrying capacity of the bridge. Vibration monitoring provides a valuable tool to complement other non destructive methods. It directly addresses the performance of the primary load path under service loading. It is a step towards an "intelligent structure (bridge)" – i.e. a structure which knows something of its own life history. Vibration monitoring has distinct advantages over other inspection methods, like e.g. periodic visual check: the state of the structure can be continuously, even remotely, tracked. Moreover, internal damage, otherwise invisible, can be assessed. Nevertheless it is considered to be mainly a global method, which has to be complemented with local non-destructive assessment techniques, like e.g. ultrasonic inspection.

Vibration monitoring of civil engineering structures (e.g. bridges, buildings, dams, wind turbines) has gained a lot of interest over the past decade, due to the relative ease of instrumentation and the development of new powerful system identification techniques, able to extract modal properties from measured accelerations, displacements and/or strains. Special attention is being paid to techniques making use of operational data (service loading testing).

Sometimes it is doubted whether the measured deviations of modal properties are significant enough to be a good indicator of damage or deterioration. The comparison of original and new dynamic properties can also be obscured by natural changes caused by environmental influences (e.g. temperature changes). Also operational conditions can alter the dynamic characteristics. However, by statistical treatment of the vibration data, real damage can be distinguished from environmental and operational effects.

Vibration monitoring can contribute to an extended lifetime, meaning also reduction of waste materials, less consumption of resources like energy for recycling activities. It fits in this way in the idea of promoting durable constructions, sustainable technology. In a number of cases, vibration monitoring can prevent unexpected structural collapses.

Many different schemes/methods for damage detection have been proposed during the last twenty to thirty years. However, the words "damage detection" have been used at random. For clarity the following four levels will be used:

- LEVEL 1: Qualitative indication of the damage (detection or alarm level)
- LEVEL 2: Information about the probable location of the damage (localization)
- LEVEL 3: Information about the size of the damage (assessment)
- LEVEL 4: Information about the actual safety of the structure given a certain damage state (consequence)

Each of the four levels is meaningful to explore. Current research concentrates on levels 1, 2 and 3.

2 Ambient versus forced excitation

The acquisition of high-quality vibration data is essential for a successful damage assessment afterwards. For mechanical engineering applications, exciter-driven forced vibration testing was and still is the most popular testing method for extracting modal properties. Many commercially available systems offer a complete package from sensor

Figure 1 Reaction mass shaker (EMPA).

to analysis software. Systems with several hundred channels have been used successfully with the help of highly automated procedures. However, for heavy civil engineering structures, having often natural frequencies below 1 to 2 Hz, artificial excitation is difficult and costly, if not impossible. Only a few research institutes (e.g. EMPA in Switzerland and ARSENAL in Austria) have developed powerful reaction mass type, hydraulic driven exciters which can be used also in the lower frequency range (Figure 1).

Nevertheless, forced vibration testing requires very costly equipment and much energy, while being logistically complex.

Forced vibration is a test method which can only be applied for periodic inspection. Ambient vibration testing can be used also for continuous monitoring, assuming the availability of robust sensors, cabling and data acquisition equipment. Ambient Vibration Testing (AVT): AVT makes use of the natural vibrations of a structure when in service or due to wind loads, microtremors etc. One of the big advantages is the fact that the excitation is unmeasured. On a bridge, traffic has not to be interrupted, so reducing not only the cost of the test itself, but also the economic impact of closing the bridge. While the structure often remains in service, not all the vibration modes may be sufficiently excited throughout the test by the ambient influences. Essential is the use of sensors with a high sensitivity and a high resolution (a very low internal noise level). A high A/D conversion rate (24 bits) is also recommended to cope with quite different vibration levels during the ambient test. The unfeasibility of measuring accurately the higher modes and the lack of absolute scaling of the mode shapes can reduce the level of detail of the subsequent damage identification. The scaling insufficiency of the mode shapes can be resolved by repeating the test with adding extra masses to the bridge (Parloo et al. 2005).

Drop Weight or Impact Vibration Testing (IVT): IVT is a special form of forced vibration testing in which only a short force impulse acts on the structure. Figure 2 shows the system developed at the K.U. Leuven. Traffic on the bridge has only to be closed for a short time. IVT is a good compromise between AVT and FVT.

Figure 2 Drop Weight (KUL).

Table 1 Characteristics of excitation sources.

Excitation	*investment cost*	*installation cost*	*economic cost*	*measurement time*	*lower eigenfrequencies*	*higher eigenfrequencies*	*quality of lower mode shapes*	*quality of higher mode shapes*	*mass-normalized modes*	*controlled amplitude*
Ambient	++	++	++	−−	++	−	++	−	−/+	−
Shaker	−−	−−	−−	−	o	++	o	++	+	++
Drop Weight	+	+	+	+	+	+	+	+	+	+

Table 1 gives an overview of the advantages and the disadvantages of different excitation sources.

3 System identification

For FVT, well established methods exist, either in frequency or time domain (Maia et al. 1997).

In case of AVT, picking of peaks (PP) observed in frequency spectra was for a long time current practice, at least in civil engineering. Rather recently, more powerful system identification methods are being used, like the enhanced frequency decomposition (EFDD) method (Brincker et al. 2001), stochastic subspace identification (SSI) method (Peeters et al. 2001) and the polymax method (Peeters & De Roeck 2001), offering a good comprise between processing speed and accuracy. With these methods, better results are obtained for the true mode shapes (and not operational deflection shapes as in the case of PP). Besides, closely spaced modes can be more easily separated. A handy tool for finding the correct physical poles of the structure is the so called stabilization diagram, showing the 'stability' of poles at increasing model orders.

4 Damage identification

A vibration monitoring system can be used for periodic or permanent condition assessment. Whatever the case may be, spontaneous changes of modal properties due to variable environmental conditions (e.g. temperature) have to be taken into account!

4.1 *Level 1 damage detection*

For level 1 damage detection – the 'alarm' level – several statistical methods have been proposed. Measurements of the understood environmental disturbances (e.g. temperature) may or may not be included in these methods.

A straightforward method is based on fitting models to the observed time histories of natural frequencies and temperatures. The advantage of this method is that it can be considered a filter for the natural frequencies which can be used in a succeeding step for levels 2 and 3 (damage localization and quantification). For the Swiss Z24-bridge, sophisticated ARX models (Peeters & De Roeck, 2001) have been fitted to the data, acquired over about one year:

$$y_k + a_1 y_{k-1} + \cdots a_{n_a} y_{k-n_a} = b_1 u_{k-n_k} + b_2 u_{k-n_k-1} + \cdots + b_{n_b} u_{k-n_k-n_b+1} + e_k \quad (1)$$

where y_k is the Auto-Regressive output (in casu an eigenfrequency) at time instant k; u_k is the eXogeneous input (in casu a temperature) and e_k is a noise term indicating that the input-output relation is not perfect. It is assumed that e_k is white noise, with zero mean $E[e_k e_{k-i}] = \lambda\delta_i$, where δ_i is the Kronecker symbol ($i = 0 \Rightarrow \delta_i = 1$, $i \neq 0 \Rightarrow \delta_i = 0$). In order to be able to establish confidence intervals, it also assumed that e_k is Gaussian distributed. The ARX model (1) is characterized by 3 numbers: n_a, the auto-regressive order; n_b, the exogeneous order and n_k, the pure time delay between input and output. A regression model is an ARX010 model (with $[n_a, n_b, n_k] = [0,1,0]$).

The advantage of using general ARX models over static regression models is that they include some dynamics: the current output and input are related to outputs and inputs at previous time instants. With a lot of input candidates and the possible choices for n_a, n_b, n_k there are many different ARX models that can be fitted to the data. Hence criteria are needed to assess and compare the quality of the models. The least squares method minimizes the sum of squares of the equation errors e_k.

Table 2 Comparison between SISO models: temperature versus eigenfrequency.

Mode	*ARX model*			*Static regression model*		
	n_a, n_b, n_k	$\hat{\lambda}$	*FPE*	n_a, n_b, n_k	$\hat{\lambda}$	*FPE*
1	2 1 4	0.145	0.145	0 1 0	0.212	0.213
2	3 2 0	0.533	0.536	0 1 0	0.896	0.897
3	2 1 0	0.507	0.509	0 1 0	0.548	0.549
4	2 2 0	0.569	0.572	0 1 0	0.612	0.613

A first quality criterion is the value of the loss function, defined as:

$$\hat{\lambda} = \frac{1}{N}\sum_{k=1}^{N} \varepsilon_k^2(\hat{\theta}) \tag{2}$$

with the estimated equation errors defined as:

$$\varepsilon_k(\hat{\theta}) = \hat{a}(q)y_k - \hat{b}(q)u_k \tag{3}$$

The loss function is also an estimate of the noise covariance 8, what explains the notation. Other criteria include penalties for model complexity like Akaike's final prediction error (FPE) criterion or Rissanen's minimum description length criterion.

After a preliminary selection procedure it turned out that a (SISO) ARX model, based on a temperature at the bridge deck, performed best.

The results are represented in Table 2. The input and output data were normalized before the models were identified. The model for the first mode seems to be much better than the models for the other 3 modes. The static regression results are also represented. Especially for the first 2 modes, the improvements of an ARX model over a static model are spectacular.

An interesting alternative statistical method has recently been proposed (Zhang 2007). It tries to cope with environmental and operational disturbances in a single procedure. It doesn't presume simultaneous measurement of temperatures or traffic density. The assessment procedure involves a 4-step process consisting of data segmentation, data normalization, damage feature extraction as well as statistical diagnosis. A damage index, named damage possibility, is proposed. In the first step, the response time histories are segmented into data samples with a same data length. For the healthy structure, in order to estimate the statistical variability of the extracted damage features, the data are arbitrarily divided into two sets, U and N. For the data recorded on the damaged structure (or better: the structure with unknown status) only one set D is considered. In the second normalisation step, data samples from U and N or U and D are paired. The underlying idea is to search for data samples corresponding to similar environmental and operational conditions. In the practical implementation, AR-models are fitted to the two different samples. Then similarity principles are applied to the AR coefficients and the variance of the error terms, characterizing the samples, to find the best corresponding samples. As a result of step 2, it is assumed that the

paired samples only differ by inherent statistical scatter (case U and N) or occurred damage (case U and D). A third step exists in extracting a damage feature from the previously paired samples. An ARX (n_a, n_b, n_k)-model is first fitted to sample U, taking the error terms of the preceding AR-model as eXogenous inputs. A residual e_x is found. Then this ARX-model is applied to the pairing sample (N or D), resulting in a residual e_y. A damage feature D_F expresses the likeness of the two samples (σ_x is the standard deviation of e_x and σ_y of e_y):

$$D_F = \frac{\sigma_y - \sigma_x}{\sigma_x} \tag{4}$$

D_F equals or is close to zero if the structural conditions are very much alike. If not, e.g. due to occurred damage, D_F will be much greater than zero.

However, in practice, even if the structural condition is not changed, the damage feature D_F can differ from zero due to the nonlinear and time-variant behavior of a bridge, the measurement noise as well as the errors introduced by the AR and ARX processes. Therefore, damage diagnosis is performed in a statistical way on the basis of a large number of data samples. The criterion to evaluate the probability distribution of D_F for the pairs U and D is the comparison with the distribution function for U and N.

However, in practice, even if the structural condition is not changed, the damage feature D_F can differ from zero due to the nonlinear and time-variant behavior of a bridge, the measurement noise as well as the errors introduced by the AR and ARX processes. Therefore, damage diagnosis is performed in a statistical way on the basis of a large number of data samples. The criterion to evaluate the probability distribution of D_F for the pairs U and D is the comparison with the distribution function for U and N.

Another very appealing procedure has recently been presented (Deraemaeker et al. 2008). Two types of features, directly extracted from the measurements, are considered as damage indicators. First, following a traditional approach, eigen properties of the structure are considered, using an automated stochastic subspace identification procedure. To automate the identification, a new process is developed which is based on a new selection criterion of the physical poles, called modal transfer norm (Reynders & Roeck 2008). Starting point is the positive output power spectral density matrix, defined as the Fourier transform of the positive lags of the cross correlations between the measured outputs. Then, modal decomposition is applied to this power spectral density matrix. For each mode i the maximum singular value of the derived modal power spectral density matrix is considered as a measure of the error made when this i-th mode is removed from the full model. A stabilization diagram, showing only the modes with the highest modal transfer norms, is very clear!

A second approach for feature extraction is based on the concept of spatial filtering and peak indicators (Deraemaeker et al. 2006). Spatial filtering consists in combining linearly the outputs of a network of sensors into one single output according to $y = \Sigma\alpha_i y_i$. Upon proper selection of α_i, various meaningful outputs may be constructed, as, for example, modal filters. The idea behind modal filtering is to configure the linear combiner such that it is orthogonal to all N modes of a structure in a frequency band of interest except mode j. The modal filter is then said to be tuned to mode j and all the contributions from the other modes are removed from the signal. Because of spatial aliasing, there are some restrictions on the frequency band where modal filters can be

built, for a given size of the sensor network. When the structure is excited with a white noise input spectrum, the power spectral density of y, tuned to mode j, will reveal only a peak at eigenfrequency ω_j. It has been shown that a local damage produces spurious peaks in the frequency domain output of modal filters, whereas for global changes to the structure (i.e. due to environment), the peak of the modal filter is shifted but the shape remains unchanged. The appearance of new peaks was therefore proposed as a feature for damage detection.

The effects of environment are treated using factor analysis and damage is detected using statistical process control with the multivariate Shewhart-T control charts.

In (Deraemaeker et al. 2008), a numerical example of a three span bridge with temperature dependent material stiffness is presented. Noise is added to the simulated accelerometer responses. Four different damage scenarios are considered. Each set of data studied is made of the undamaged state and one of the damaged states. The noise level is the same for the undamaged and the damaged state. The set is made of 480 samples of output-only time responses on the 29 accelerometers situated at the nodes of the finite element model that have a nonzero displacement. Two kinds of feature extraction are performed: automatic output-only modal analysis using stochastic subspace identification (10 eigenfrequencies and mode shapes for each case) and extraction of peak indicators from the output of the first 9 modal filters.

The following features are considered:

- the first 10 eigenfrequencies;
- mode shapes 1 through 5 extracted using automatic stochastic subspace identification. The mode shapes are normalized with respect to the output of the first accelerometer, which results in 28 features per mode;
- mode shapes 6 through 10, again normalized to the output of the first accelerometer;
- peak indicators extracted from the output of modal filters: 61 features.

The results are summarized in the Table 3 (−− very low, − low, + high, ++ very high):

The numerical results show that if nothing is done in order to remove the effects of environment, eigenfrequencies cannot be used in order to detect damage, whereas mode shapes and peaks from modal filters could be used. On the other hand, if factor analysis is used to remove the effects of environment, all the features considered are able to differentiate between the damaged and the undamaged case. When no noise is present in the measurement, the features can be ranked in terms of increasing

Table 3 Sensitivity of the features to environment, noise, damage, and computation time.

Sensitivity to	*Freq*	*Modes 1–5*	*Modes 6–10*	*Modal filters*
Environment	++	−−	−−	−−
Noise	−−	+	+	++
Damage	−	+	++	++
Comp time	−	−	−	−−

sensitivity: the least sensitive features are the eigenfrequencies, followed by the low frequency mode shapes, the higher frequency mode shapes and the features extracted from modal filters (most sensitive). When noise is added however, the ranking is different. Frequencies have a very low sensitivity to noise while modeshapes have a much higher sensitivity. The present procedure to compute peak indicators is extremely sensitive to noise, so that even for a relatively low level of noise, the damage detection is strongly affected, and these features are the least sensitive to damage. In the example studied, all the features can be extracted in real time and in an automated way (the time to extract the features is smaller than the length of the acquired signals), which makes them suitable for an automated real-time SHM system. For average levels of noise, it seems that modeshapes are the ideal candidate for output-only SHM under changing environmental conditions. However, for real structures with very large arrays of sensors, it may be that the time needed for the identification becomes prohibitively high. Data reduction is therefore necessary in order to perform the identification in real time. Spatial filters could be used for this purpose.

4.2 *Level 2/3 damage identification*

Many methods have been proposed for damage identification, levels 2 and 3.

One of the most versatile is based on finite element updating: at the expense of building a FE-model of the structure, all acquired data can be used: natural frequencies, scaled or unscaled mode shapes and modal strains. Moreover, unlike other methods, FE-updating doesn't require a dense mesh of sensors. Potential damage is simulated in a FE-model of the structure by adopting a parametric representation of this damage. A limited number of unknown updating parameters θ are appearing in this description, which should resemble as close as possible physical damage. Best values of the θ-parameters can be found by minimizing the differences between measured and calculated modal properties.

Mathematically, a constrained optimization problem is solved. The objective function is defined as a sum of squared differences. The residual vector contains the differences in the identified modal data (and possibly some derived quantities), such as the natural frequencies, the mode shapes, the modal curvatures, etc. In order to obtain a unique solution, the number m of residuals should be greater than the number n of unknowns θ.

The relative weighting between the different residual types can be controlled by the definition of the residual functions and by an additional weighting matrix in order to account for the measurement and identification errors.

If the objective function contains multiple local minima, the result of this optimization process might be dependent of the initial choice of θ-parameters. In this case, a global optimization algorithm should be used, like the recently proposed Coupled Local Minimisers (CLM) method (Teughels et al. 2003).

5 Examples

5.1 *The Z24 bridge*

The Swiss Z24 bridge was an intact bridge, slightly skew, with three spans connecting Koppigen to Utzenstorf (Figure 3). The bridge was a highway overpass of the A1,

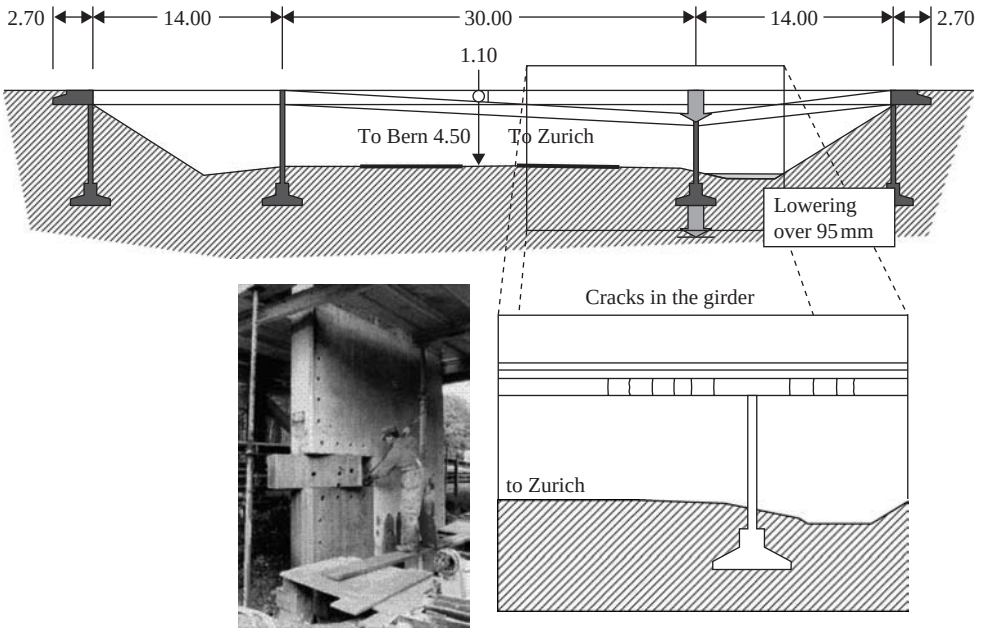

Figure 3 Damage scenario: settlement of pier.

linking Bern and Zurich. It was built in 1963 when the highway A1 was not yet completed. The posttensioned two box cell girder of 14, 30 and 14 meters span rested on four piers. The two central piers were stiffly connected to the girder, while the two triplets of columns at both ends were connected via concrete hinges to the girder. The bridge had to be demolished in 1998 because a new railway, adjacent to the highway, required a new bridge with a larger side-span. To study the influence of varying environmental conditions on the modal properties, a so called environmental monitoring system (EMS) was established. After this continuous monitoring period, several damage scenarios were applied to the bridge. The progressive damage tests (PDT) consisted of lowering one of the two central piers (simulating a settlement) in different stages, tilting the same pier, spalling of concrete (simulating vehicle impact or carbonization), landslide at one of the abutments, failure of anchor heads and rupture of tendons. Before and after applying new damage, a FVT and a AVT test was performed, enabling also a comparison between the two techniques (Peeters et al. 2000).

More details about these tests can be found in (Maeck & De Roeck 2003a,b). A complete description and all data are stored in and available from the Samco database (http://samco.jrc.it/show.gx?_app.page=/research/show_project.htm&object.object_id=SAMCO—0000000000002402).

In what follows, one PDT damage scenario will be investigated in more detail: settlement of one of the central piers (Figure 3).

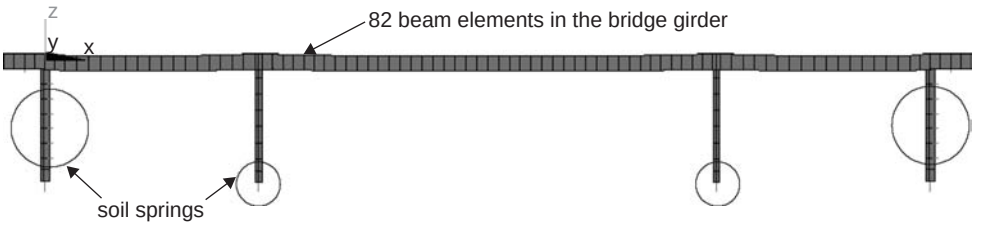

Figure 4 FE model of the bridge Z24. The thickness of the beam elements is displayed. The soil springs at the supports are indicated (circles).

The challenge is to identify damage from observed changes in natural frequencies and mode shapes by FE-updating (Teughels & De Roeck 2004).

The modal data are identified from ambient vibrations, before and after applying the damage. Accelerometers are placed on the bridge deck along 3 parallel measurement lines: at the centreline and along both sidelines. In total 9 measurement setups are used to measure the mode shapes. The first 5 identified mode shapes are used for the updating. The first and the fifth are pure bending modes, the third and fourth are coupled bending and torsional modes – due to the skewness of the bridge – and the second is a transversal mode.

The bridge is modelled with a beam model (6 DOFs in each node, three-dimensional) in Ansys (Figure 4). The bridge girder has higher stiffness values above the supporting piers because of an increased thickness of bottom and top slab. 82 beam elements are used to model the girder. The piers and the columns at the abutments are modeled by 44 beam elements. Mass elements are used for the cross girders and foundations. Concentrated translational mass as well as rotary inertial components are considered. In order to account for the influence of the soil, springs are included at the pier and column foundations, at the end abutments and around the columns.

Two updating processes are performed, in order to model the reference and the damaged state of the bridge, respectively.

The bending as well as the torsional stiffness of the beam elements of the girder are updated since the identified modes contain besides pure bending also coupled bending-torsion modes. They are adjusted by correcting the Young's and the shear modulus, E and G, respectively:

$$a_E^e = -\frac{E^e - E_{ref}^e}{E_{ref}^e} \Rightarrow E^e = E_{ref}^e(1 - a_E^e);$$

$$a_G^e = -\frac{G^e - G_{ref}^e}{G_{ref}^e} \Rightarrow G^e = G_{ref}^e(1 - a_G^e) \tag{5}$$

For the first updating process, the reference values are equal to the initial FE values; in the second updating process, the reference values are substituted with the identified values from the first updating process. In the first updating process, also the vertical soil

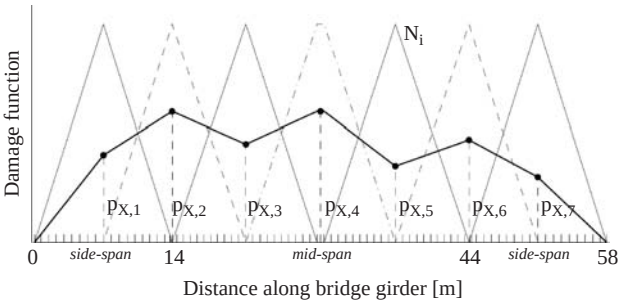

Figure 5 Piecewise linear damage function $N(x, p)$ used for the distribution of both correction factors, a_E and a_G. The mesh of finite elements is also plotted.

stiffness under the supporting piers and the horizontal soil stiffness under the abutments are updated. Since the soil springs are not altered by the damage application, they are not updated in the second updating process.

The major problem in FE model updating is the relatively low information content of the measured data, which results in an ill-conditioned problem if a large number of parameters has to be updated. Therefore, the number of variables is reduced through an additional parameterization by means of damage functions (Teughels et al. 2002). In this approach, the values of the correction factors a_e over the FE model – which define on their turn the updated physical parameters – are determined with prescribed damage functions, instead of determining them independently in all elements, which would result in a large number of updating variables. In particular, the correction factors of a physical parameter are assumed to vary continuously over the model and this continuous function is approximated with a prescribed damage function $N(x, \theta)$.

The bridge girder is subdivided into 8 damage elements: 4 damage elements in the mid-span and 2 damage elements in each side-span (Figure 5).

Two (identical) piecewise linear damage functions are used for identifying the bending and the torsional stiffness distribution, respectively. In the first updating process the optimization problem contains 16 ($= 2 \times 7 + 2$) design variables, corresponding to the multiplication factors of both damage functions, $p_{E,i}$ and $p_{G,i}$, (2×7) and the two correction factors for the soil springs. In the second process only 14 ($= 2 \times 7$) variables have to be identified.

The four vertical modes (bending and bending-torsion) and the transversal mode of the undamaged bridge are used to update the initial FE model to the reference undamaged state of the bridge. The latter mode is included in the process in order to identify the stiffness of the soil springs. The residual vector in the reference updating process contains 5 frequency residuals and 492 mode shape residuals. The vertical displacements along the three measurement lines (3×39 points) and the horizontal displacements along the centreline (31 points) are used for the vertical and transversal modes, respectively. Only the modal displacements which are measured accurately, are selected.

For the identification of the damaged zone only the 4 bending modes are used, measured on the bridge after the pier settlement. The transversal mode is not used

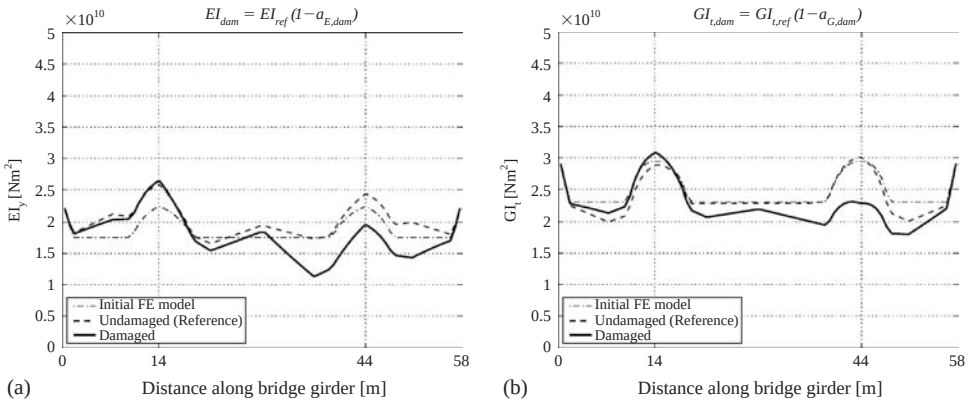

Figure 6 Identified parameters: bending and torsional stiffness distribution, EI and GI_t.

since the soil springs are not updated in this process. The residual vector in the second updating process contains 4 frequency residuals and 451 mode shape residuals. In both processes a weighting factor 1/10 is applied to the mode shape residu.

In the damaged state, a decrease in the girder stiffness above the pier at 44 m is clearly visible. This decrease is due to the lowering of the pier, which induced cracks in the beam girder at that location. The corresponding identified damage pattern, is plotted in figure 6. The bending and the torsional stiffness are reduced with a maximum of 35% and 24%, respectively, located in the expected cracked zone.

5.2 *The Tilff bridge*

This bridge crossing the Ourthe river was built in 1952. It is a three-cell box-girder bridge with variable height (Figure 7). Mid span is 24.75 m, side spans 20.25 m. External posttensioning is applied within the box hollow spaces. The curved path of the strands was realized through the interposition of a number of transverse beams, which create in longitudinal direction 24 partitions. Severe corrosion of prestressing steel occurred due to water accumulation in the cells. Challenge is damage localization (level 2) and quantification (level 3), having only vibration data of the damaged structure. New in this project was also the use of optical fibers of the company Smartec (http://www.smartec.ch/, SOFO Dynamic Reading Unit) for strain measurements in the critical sections.

The measurements were performed by 'Le Ministère wallon de l'Equipement et des Transports' (MET), possessing an acquisition system with 4 channels. One setup consisted of an acceleration measurement in a reference point, a second acceleration measurement by a roving sensor and two axial strain measurements (Figure 8). In total 36 setups were considered, sampling frequency was 200 Hz and measurement time for each setup 5 minutes.

Natural frequencies, mode shapes, modal strains (and derived from them: modal curvatures) were obtained by applying the stochastic subspace method.

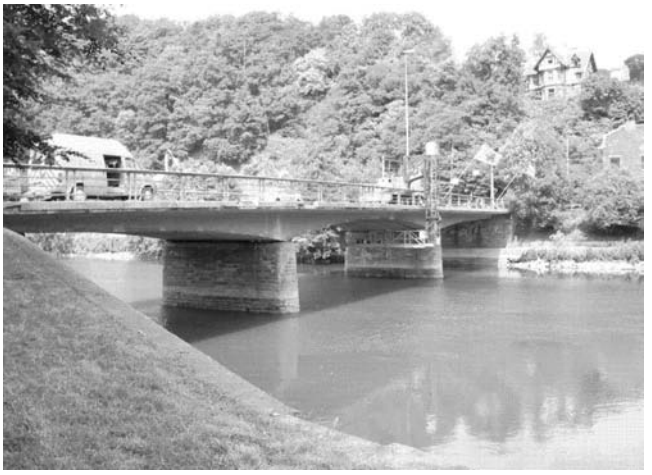

Figure 7 The Tilff bridge.

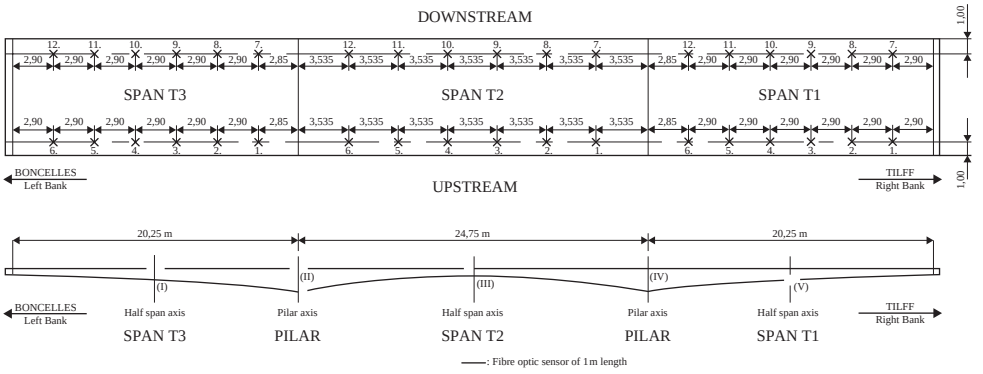

Figure 8 Positions of accelerometers and strain sensors (sections I, II, III, IV,V).

For the damage identification a FE-model was built: the box-girders were modeled with shell elements, the massive bridge ends with volumetric elements and the asphalt layer and non-structural parts with added masses. With regard to the supports: at one of the intermediate pillars, there is a hinge; the other supports are of the pendulum type. At these pendulum supports, the horizontal movement is somewhat restricted due to the reinforcement bars that cross the contact areas.

As updating parameters are selected: the decrease of Young's modulus in 9 distinct zones and the spring stiffness at the pendulum supports. The objective function comprises residuals of 4 natural frequencies and residuals of modal amplitudes and curvatures of the first and second bending modes.

Figures 9 and 10 present the comparison of calculated and measured mode shapes and modal curvatures before and after updating. The apparent lack of anti-symmetry of the second bending mode is well predicted by the updated model. The in-situ use of

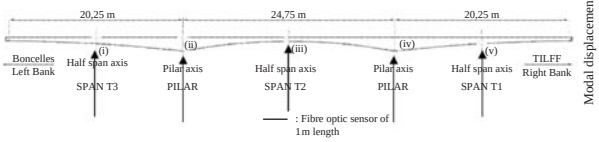

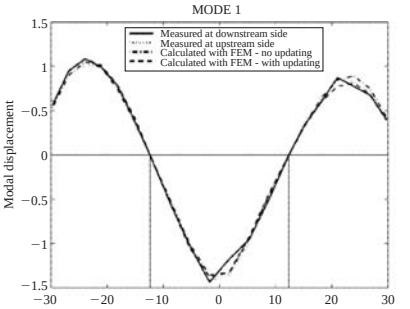

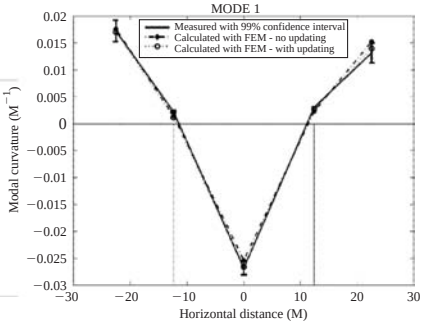

mode 1

section	$\kappa_{measured}$ (mm^{-1})	$\sigma_{measured}$ (mm^{-1})	$\kappa_{calculated}$ (mm^{-1}) (before updating)	$\kappa_{calculated}$ (mm^{-1}) (after updating)
I	17.23	0.78	17.61	17.05
II	2.25	0.07	1.50	1.15
III	−26.79	0.49	−25.37	−26.55
IV	3.06	0.01	2.30	2.72
V	13.17	0.71	15.27	13.99

Figure 9 Comparison modal amplitudes and curvatures (bending mode 1).

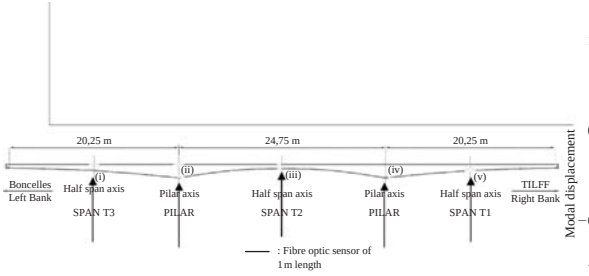

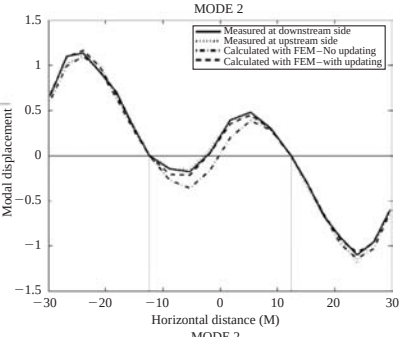

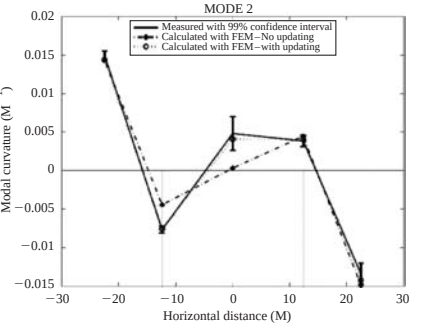

mode 2

section	$\kappa_{measured}$ (mm^{-1})	$\sigma_{measured}$ (mm^{-1})	$\kappa_{calculated}$ (mm^{-1}) before updating	$\kappa_{calculated}$ (mm^{-1}) after updating
I	14.98	0.20	14.31	14.35
II	−7.62	0.17	−4.42	−7.25
III	4.82	0.86	−0.33	4.54
IV	3.84	0.28	4.46	4.09
V	−13.36	0.54	−14.87	−14.19

Figure 10 Comparison modal amplitudes and curvatures (bending mode 2).

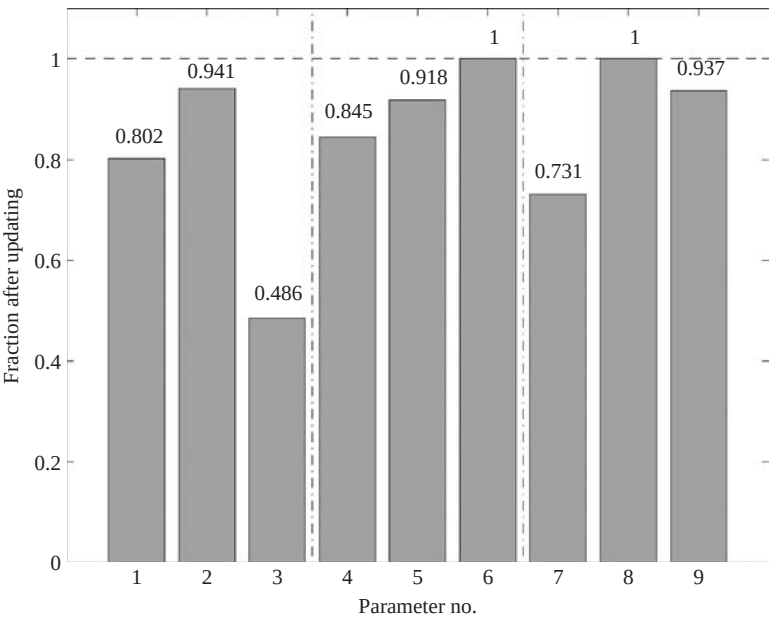

Figure 11 Identified stiffness reduction.

optical fiber strain sensors makes it possible to identify the modal curvatures directly, without an approximate, numerical differentiation procedure.

Figure 11 shows the identified stiffness reduction which resembles well the fraction of broken or strongly corroded cables observed by visual inspection in the box cells.

6 Conclusions

- Reliable modal information can be obtained by output-only dynamic measurements, i.e. accelerations are due to ambient influences. In the case of bridges, traffic under or on top of the bridge, besides wind pressures can be the cause of the induced vibrations. So closing bridges to apply controlled force excitation is not necessary. This makes ambient vibration monitoring suitable for continuous condition assessment.
- Mode shapes, although less accurately determined as eigenfrequencies, can provide useful information about local changes, e.g. of joint or support stiffnesses.
- The variations between eigenfrequencies obtained by different system identification algorithms are rather small. For the mode shapes more substantial differences occur. Because many damage identication methods rely on the accuracy of the experimental mode shapes, the use of state-of-the-art algorithms is important!
- Peak picking on (averaged normalized) Power Spectral Density functions is a quick way to look to eigenfrequencies and mode shapes and can be recommended for an on side quality check of the measurements.
- The most accurate results are obtained with the stochastic subspace identification and the polymax method. With these methods also closely spaced modes can be separated.

- Changes in environmental conditions, mainly temperature, lead to changes in eigenfrequencies. The order of magnitude being similar to that of structural damage, it is important to filter (eliminate) this environmental influence beforehand. It is advisable that the monitoring system includes temperature measurements. The relation between eigenfrequencies and temperatures can be obtained by the measurements of the intact bridge over a period of at least one year. For bridge Z24 the decrease of the first eigenfrequency for a temperature increase from 0° to 30°C is about 3%. When this correction is taken into account, the uncertainty interval is $\pm 0.7\%$ corresponding to the $\pm 95\%$ confidence limits. Depending on its location, damage has a selective influence on eigenfrequencies and mode shapes. Especially those mode shapes will be affected where damage occurs at zones with high modal curvatures. The effect of temperature on these modal properties will be different. This explains why damage detection is possible by statistical treatment of pure vibration measurements without simultaneous temperature measurements.
- Only damage that produce stiffness reductions can be identified. For instance, a loss of prestress will only result in a measurable change in eigenfrequencies if it is accompanied by initiated cracks.
- Mode shapes, although less accurately determined as eigenfrequencies, can provide useful information about local changes, e.g. of support stiffnesses.
- For damage detection (level 1) very promising damage features, based on a statistical treatment of the data, have been recently proposed.
- When FE-updating is used for damage identification, at least eigenfrequencies should be used in the objective function to be minimized: they are crucial, represent absolute quantities, provide global information and can be measured accurately. Mode shapes provide spatial information, are necessary in case of a symmetrical structure, make the global minimum more pronounced but, are difficult to measure accurately. Most often, fewer mode shapes are available than eigenfrequencies. In case of ambient vibrations, mode shapes are not scaled absolutely. Very attractive is the addition of modal strains or curvatures to the objective function. Their advantage is that they are sensitive to damage occurring at the strain gage position. It remains however a challenge to measure accurately the small strains according to the small amplitude dynamic excitation.
- In FE-updating, the choice of updating parameters is crucial. They should represent the physical uncertainties, including the potential damage pattern. The application of regularisation techniques can improve the conditioning of the optimisation problem. Damage functions fulfil the same purpose, while providing at the same time a physical sound solution.
- FE-updating can be categorized as a non-linear least-squares problem which is in turn a special case of general optimisation. It proved to be that the Trust Region Gauss-Newton method is a very robust and reliable algorithm for local optimisation: it uses only first-order derivatives and has fast convergence due to the approximated Hessian. For updating problems with many local minima, making the solution dependent on the chosen start point, a new algorithm (Coupled Local Minimisers) has been developed. Randomly distributed start points are generated. The objective function is enriched with Lagrange and penalty terms, enforcing all the points to come together in the one global minimum.
- If all the previous conditions are met, stiffness reducing damage, that produces shifts of eigenfrequencies more than 1 to 2%, can be detected if the environmental

influences are properly taken into account. For damage detection (level 1), but even more for the localization and quantification of the damage (levels and 3), the choice of sensor type, location and density is crucial, together with the extension of the frequency band in which the modal properties are measured.

References

Parloo, E., Cauberghe, B., Benedettini, F., Alaggio, R. & Guillaume, P. 2005. Sensitivity-based operational mode shape normalisation: Application to a bridge, *Mechanical Systems and Signal Processing* 19(1): 43–55.

Maia, N.M.M., Silva, J.S.M., He, J., Lieven, N.A.J., Lin, R.M., Skingle, G.W., To, W.-M. & Urgueira, A.P.V. 1997. *Theoretical and Experimental Modal Analysis*. Research Studies Press Ltd., Somerset, England.

Brincker, R., Zhang, L.M. & Andersen, P. 2001. Modal identification of output-only systems using frequency domain decomposition. *Smart Materials & Structures* 10(3):441–445.

Peeters, B. & De Roeck, G. 2001. Stochastic system identification for operational modal analysis: A review. *Special Issue on the Identification of Mechanical Systems of the ASME J. of Dynamic Systems, Measurement and Control*, 659–667.

Peeters, B., Van der Auweraer, H., Guillaume, P. & Leuridan, J. 2004. The Polymax frequency-domain method: a new standard for modal parameter estimation? *Shock and Vibration* 11(3–4): 395–409.

Peeters, B. & De Roeck, G. 2001. One-year monitoring of the Z24-bridge: environmental effects versus damage events. *Earthquake Engineering and Structural Dynamics* 30:149–171.

Zhang, Q.W. 2007. Statistical damage identification for bridges using ambient vibration data. *Computers and Structures* 85:476–485.

Deraemaeker, A., Reynders, E., De Roeck, G. & Kullaa, J. 2008. Vibration based Structural Health Monitoring using output-only measurements under changing environment. *Mechanical Systems and Signal Processing*, submitted.

Reynders, E. & De Roeck, G. 2008. Reference-based combined deterministic-stochastic subspace identification for experimental and operational modal analysis. *Mechanical Systems and Signal Processing*, submitted.

Deraemaeker, A. & Preumont, Kullaa, J. 2006. Modeling and removal of environmental effects for vibration based SHM using spatial filtering and factor analysis. *Proc. IMAC XXIV*, S.E.M., St Louis, USA.

Teughels, A., DeRoeck, G. & Suykens, J.A.K. 2003. Global optimization by Coupled Local Minimizers and its application to FE Model Updating. *Computers and Structures* 81 (24–25):2337–2351.

Peeters, B., Maeck, J. & De Roeck, G. 2000. Excitation sources and dynamic system identification in civil engineering. *Proceedings of the European COST F3 Conference on System Identification and Structural Health Monitoring*, Madrid, Spain, 341–350.

Maeck, J. & De Roeck, G. 2003a. Description of Z24 benchmark. *Mechanical Systems and Signal Processing* 71(1):127–131.

Maeck, J. & De Roeck, G. 2003b. Damage assessment using vibration analysis on the Z24-bridge. *Mechanical Systems and Signal Processing* 71(1):133–142.

Teughels, A. & De Roeck, G. 2004. Structural damage identification of the highway bridge Z24 by FE model updating. *Journal of Sound and Vibration* 278(3):589–610.

Teughels, A., Maeck, J. & De Roeck, G. 2002. Damage assessment by FE model updating using damage functions. *Computers and Structures* 80(25):1869–1879.

Part II

Computational Earthquake Engineering

Chapter 15

Multi-resolution distributed FEA simulation of a 54-story RC building

Jun Ji

Kal Krishnan Consulting Services Inc., Oakland, USA

Oh-Sung Kwon

Missouri University of Science and Technology, Missouri, USA

Amr S. Elnashai & Daniel A. Kuchma

University of Illinois at Urbana-Champaign, Illinois, USA

ABSTRACT: A recently developed analysis framework referred to as multi-resolution distributed finite element analysis, MDFEA, is presented in this chapter. The features of the new framework are demonstrated through the analysis of a complex 54-story reinforced concrete building. In this distributed analysis framework, the capabilities of a frame analysis tool, ZEUS-NL, and a continuum analysis tool, VecTor2, are combined using the 'simulation coordinator' program UI-SIMCOR. The static and dynamic responses of the building are predicted using MDFEA and compared with those predicted by conventional frame analysis. The results of this comparison illustrate that frame analysis of high-rise building alone is inadequate to detect the effects of shear-flexure-axial interaction of reinforced concrete continuum members. The integrated MDFEA framework is generic, thus it enables the use of the best features of any number of computational tools so as to accurately and efficiently predict the inelastic static and dynamic response of complex structures subjected to extreme loads.

1 Introduction

The response of low-rise structures to earthquake loading has been extensively studied by employing advanced finite element analyses (FEA), quasi-static experiments, pseudo-dynamic (PSD) simulation of structural components and structural systems. It has also been investigated through shake table tests on models at different scales. On the contrary, reliable estimation of the structural capacity of complex high-rise reinforced concrete (RC) or composite systems under extreme loads has been hindered by the lack of suitable analysis software, computational capacity for refined model analysis, and the impracticality of experimental testing.

The response of complex high-rise buildings has principally been studied using simplified models. Usually wall systems are modeled using frame elements that do not fully account for the effects of shear on deformations and capacity, and the interaction between shear and flexure, as discussed by Ghobarah & Youssef (1999). The latter approach is inadequate since the failure mode of structural walls in high-rise buildings is frequently influenced and controlled by the effects of shear (Paulay & Priestley, 1992). In some instances, the critical components of structural systems have been analyzed using detailed continuum finite element models. However, in doing so, the boundary

and loading conditions imposed on these models are typically idealized or estimated from separate coarse structural models. This non-interacting load and boundary conditions approach is also inadequate since the propagation of failure and redistribution of force demands between components cannot be accurately accounted for. While it may be possible to analyze an entire high-rise structure using detailed FEA, the computational demands of executing this analysis are enormous and render it impractical to conduct adequate parametric studies to account for the uncertainty on loading, modeling and inherent randomness in materials. Furthermore, such a detailed model is a non-starter for probabilistic assessment, where statistically-viable populations of response parameters are sought.

One effective and computationally efficient method to analyze large and complex structures would be to combine different modeling approaches, such as to model the most critical non-slender regions using continuum analysis and to model frames using fiber-based beam elements. Unfortunately, computation platforms seldom provide the most advanced modeling capabilities for all possible elements that would be best to use in the modeling of a complex structural system. The natural solution to this dilemma is to create an analysis framework in which different analysis programs could be combined in one integrated analysis where each program would be selected to make the best use of its merits. Such a framework is developed in this chapter.

The framework for multi-resolution distributed finite element analysis (MDFEA) proposed in this chapter is used to analyze a complex high-rise RC building. The structural walls of this building are modeled with concrete continuum elements while the frames are modeled with fiber-based beam-column elements. The two distinct applications are combined using the MDFEA framework in a step-by-step fashion in the time domain.

The chapter includes brief descriptions of the analysis modules, ZEUS-NL and VecTor2, as well as the simulation coordinator program UI-SIMCOR (Kwon et al., 2005), that was used to combine these analysis tools. The modeling details for the 54-story dual-system high-rise structure used as the reference implementation are presented including the techniques used to model the interface between the two structural models. The influence of different interface assumptions on predicted response is also examined. Using the selected interface boundary conditions, comprehensive comparisons between and discussions of the predicted static and dynamic responses by the MDFEA and by a conventional finite element analysis are presented.

2 Structural analysis software platforms

2.1 *ZEUS-NL: 3D frame FEM analysis software*

Fiber-based frame analysis is one of the most advanced methodologies to model the nonlinear behavior of beams and columns under combined axial and bending loads. The Mid-America Earthquake Center analysis environment ZEUS-NL (Elnashai et al., 2002), is a computational tool for the analysis of two and three dimensional frames. In ZEUS-NL, elements capable of modeling material and geometric nonlinearity are available. The forces and moments at a section are obtained by integrating the inelastic responses of individual fibers. The Eularian approach towards geometric nonlinearity is employed at the element level. Therefore, full account is taken of the spread of

inelasticity along the member length and across the section depth as well as the effect of large member deformations. Since the sectional response is calculated at each loading step from inelastic material models that account for stiffness and strength degradation, there is no need to make assumptions on the moment-curvature response as commonly required by other analysis tools. In ZEUS-NL, conventional pushover, adaptive pushover, Eigen analysis, and dynamic analyses are available and they have been evaluated to be effective and accurately predicting the response of members and structural frames. ZEUS-NL was used to steer a full-scale 3D RC frame testing campaign, and the a priori predictions were shown to be accurate and representative of the subsequently undertaken pseudo-dynamic tests (Jeong & Elnashai, 2004a and 2004b). There have been many other verification examples. Due to scope of this paper, a reference is made to Elnashai et al. (2002) for further information.

2.2 *VecTor2: RC continuum FEM analysis software*

A concrete wall can be modeled as an orthotropic nonlinear inelastic continuum according to Modified Compression Field Theory (MCFT) (Vecchio & Collins, 1986). The MCFT is a rotating angle smeared cracking model that combines equilibrium, compatibility and constitutive relationships. It accounts for the effects of compression softening and tension stiffening. The method includes an evaluation of equilibrium at crack faces that is used to limit field stress levels. The MCFT assumes that the direction of principal stress coincides with that of principal strain. Vecchio (1990) proposed the algorithm for application of MCFT to concrete continuums subjected to plane stress conditions.

In this study, the nonlinear 2D continuum analysis tool VecTor2, Wong & Vecchio (2002), developed at the University of Toronto, is employed for modeling the bottom 10 stories of the structural walls. VecTor2 employs a rotating-angle smeared crack modeling approach and can implement either the Modified Compression Field Theory (MCFT) and Disturbed Stress Field Model (DSFM) by Vecchio (2000). VecTor2 utilizes an iterative secant stiffness algorithm to produce an efficient and robust nonlinear solution technique. The application has been validated by extensive experimental testing to corroborate its ability to predict the load-deformation response of a variety of reinforced concrete structures (Palermo & Vecchio, 2004). VecTor2 is also able to model concrete expansion and confinement, cyclic loading and hysteretic response, construction and loading chronology for repair applications, bond slip, crack shear slip deformations, reinforcement dowel action, reinforcement buckling, and crack allocation processes.

2.3 *UI-SIMCOR: multi-platform distributed analysis framework*

Different state-of-the-art analysis software packages have unique features that other competing packages do not have. The main advantage of multi-platform simulation is the use of the unique features of analytical tools in an integrated fashion. The concept of multi-platform simulation is implemented using the pseudo-dynamic (PSD) simulation approach combined with sub-structuring. In the latter simulation, a structure is subdivided into several modules that can be either physically tested or computationally simulated. UI-SIMCOR (Kwon et al., 2005) was developed for this purpose. The Operator Splitting method in conjunction with the α-modified Newmark scheme

(α-OS method, Combescure & Pegon, 1997) is implemented as a time-stepping analysis scheme. The main feature of UI-SIMCOR is that it is capable of coordinating any number of analysis tools. Interface applications are currently available for ZEUS-NL, FedeasLab (Filippou & Constantinides, 2004), VecTor2, and ABAQUS (Hibbit et al., 2001). Any number of testing sites, or a mixture of analysis tools and testing sites can be incorporated into a pseudo-dynamic multi-platform simulation. It employs software or hardware supporting NEESgrid Teleoperation Control Protocol, NTCP (Pearlman et al., 2004) as well as TCP-IP connections outside of the NEES system. It is also capable of using the same analysis platform while modeling different parts of the system on different processors, thus minimizing computational run time. In this study, UI-SIMCOR is used to combine VecTor2 and ZEUS-NL to model shear-walls and frame elements.

3 Application to reference building

3.1 *Configuration of structure*

A newly constructed high-rise building, Tower C03 of the Jumeirah Beach development in Dubai, United Arab Emirates, was chosen as a reference structure for MDFEA. It has a complex RC dual-core wall system and RC outer frames, as shown in Figure 1, which make it an ideal candidate for MDFEA. Static pushover analyses and dynamic response history analyses were performed for Frame F4 along its strong direction. The main features of this building are as shown in Table 1.

3.2 *Sub-structural modeling*

The selected 2D frame F4 of reference building, Figure 1, is divided into two main structural components, a box-shaped core wall which is Core 1 in Figure 1b and a perimeter moment resisting frame. The core walls from the 1st through 10th stories, which are likely to fail in shear, are modeled using 2D RC continuum elements in VecTor2. Such continuum elements have different thickness values reflecting wall boundary and web geometric characteristics. The core walls from the 11th story and above are approximated with fiber based section elements in ZEUS-NL. The entire structure is subdivided into three modules.

- Module 1: 1st ~ 10th story left wall modeled in VecTor2. This region is modeled in VecTor2. The first 10-stories of the wall is modeled using 2D rectangular elements whose behavior can be captured using the MCFT (Vecchio & Collins, 1986). The mesh size is around 200 mm which is within 10~20 times of aggregate size as recommended (Wong & Vecchio, 2002). Concrete constitutive models are based on Modified Popovics curve by Collins & Porasz (1989), which considers both pre-peak and post-peak concrete behavior. The confinement effects are considered according to Kupfer et al. (1969). The reversed cyclic loading curves of concrete proposed by Palermo & Vecchio (2003) is employed in the analysis.
- Module 2: 1st~10th story right wall in VecTor2. Module 2 is identical to Module 1.
- Module 3: Remaining structural components including all frame members and the core walls from the 11th to the top story.

(a) 3D building frame model in SAP2000

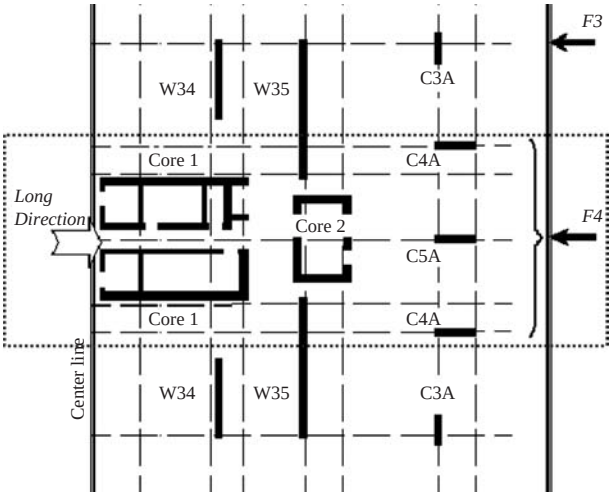

(b) Typical plan view

Figure 1 Reference building structure and half plane view.

Table 1 Main features of reference building.

Features	Description
Height (m)	184
Total Stories	54
Regular Storey Height (m)	3.400
Irregular Storey Height (m)	4.488
Core Walls (m)	9.43 × 3.25 (8.48 × 2.55) (1st∼5th Stories)
(Exterior and Interior Size)	9.33 × 3.15 (8.48 × 2.55) (6th∼20th Stories)
	9.18 × 3.05 (8.48 × 2.55) (21st∼54th Stories)
Concrete f_c' (MPa)	60 (wall); 40 (slab)
Reinforcing Bars f_y (MPa)	421 (Grade 60)

As described earlier, the lower 10 stories of the wall are modeled using 2D continuum elements in VecTor2, while the walls above this level are modeled using beam-column elements in ZEUS-NL. In this approach, there are two types of interfaces: 1) frame elements interfacing with continuum elements at the side of wall, Figure 2; 2) upper-wall modeled with frame elements and lower-wall modeled with continuum elements, Figure 3. The boundary conditions of these two types of interfaces are described in the following.

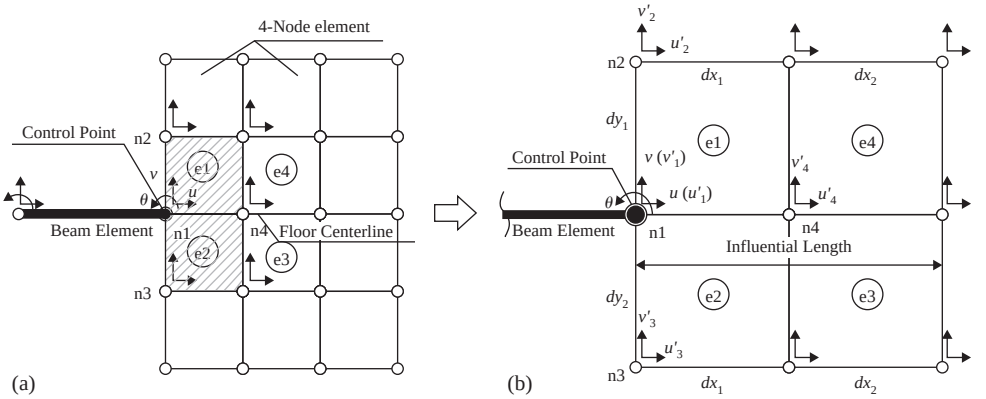

Figure 2 Frame beam element and wall continuum element interface.

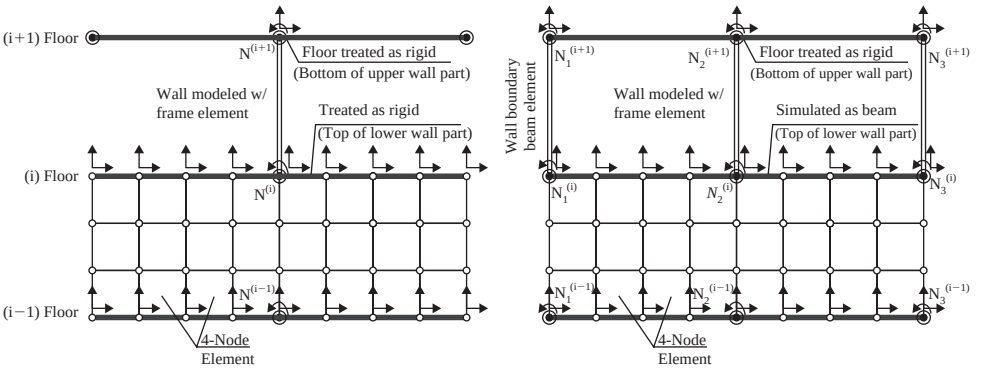

Figure 3 Upper wall beam and lower wall continuum element interface models.

3.2.1 *Interface modeling between beam and wall elements*

UI-SIMCOR (Kwon et al., 2005) uses control points in the sub-structure models. The control points are nodes with lumped masses or nodes which are shared by two or more substructures. These control points need to be defined in order to form the global mass and stiffness matrices necessary in pseudo-dynamic (PSD) algorithm employed in UI-SIMCOR, and to serve as the common interfaces between sub-structures.

There are two ways to simulate the interface between frame elements modeled with Zeus-NL and between continuum elements modeled with Vector2. One method is to use membrane elements for the wall with drilling (out-of-plane rotational) DOFs, but this is not available in VecTor2. The second method and the one used in this study is to simulate displacement and rotational compatibility between nodes of frame elements having three DOFs per node and nodes of 4-noded plane-stress element having two

DOFs per node. To illustrate this approach, consider node n1 in Figure 2 that are common to the beam element and plane-stress elements e1 and e2. In order to satisfy compatibility, constraint equations are added between the nodes of the two models to satisfy compatibility of rotation at these common (control) points.

In UI-SIMCOR, displacements are always imposed at control points and reaction forces are obtained as feedback at the same DOFs. Thus, combining the models requires the calculation of equivalent nodal displacement of continuum elements at the interface connected to control point. The constraint equations for beam-continuum coupling are derived for the interface region shown in Figure 2b, which is formed by elements e1 and e2, and nodes n1 to n4. It is assumed that the left edges of elements e1 and e2 remain straight during deformation.

Hence, the rigid body motion geometric relationships are applied to calculate nodal displacements at left edges as described by Equation (1).

$$\begin{Bmatrix} u_1' \\ v_1' \end{Bmatrix} = \begin{Bmatrix} u \\ v \end{Bmatrix};\ \begin{Bmatrix} u_2' \\ v_2' \end{Bmatrix} = \begin{Bmatrix} u - dy_1 \sin\theta \\ v - dy_1(1-\cos\theta) \end{Bmatrix};\ \begin{Bmatrix} u_3' \\ v_3' \end{Bmatrix} = \begin{Bmatrix} u + dy_2 \sin\theta \\ v + dy_2\,(1-\cos\theta) \end{Bmatrix} \quad (1)$$

where, $[u, v, \theta]$ are the displacements at control point. For the nodes along the beam centerline, not all nodes will be considered as being on an interface. Only those within the influential length (on account of usual anchorage requirements for rebar) are considered and here the middle node n4 in Figure 2 is such a node. For the middle node n4, it is assumed that the horizontal and vertical movements are generated by the control point displacement based on beam shape functions following Equation (2).

$$\begin{Bmatrix} u_4' \\ v_4' \end{Bmatrix} = \begin{bmatrix} (1-\xi) & 0 & 0 & \xi & 0 & 0 \\ 0 & (1-3\xi^2+2\xi^3) & (\xi-2\xi^2+\xi^3)l_e & 0 & (3\xi^2-2\xi^3) & (\xi^3-\xi^2)l_e \end{bmatrix} \begin{Bmatrix} u \\ v \\ \theta \\ 0 \\ 0 \\ 0 \end{Bmatrix} \quad (2)$$

where $\xi = x/l_e$, here the element length $l_e = dx_1 + dx_2$. The feedback control point reactions are computed from the nodal forces at these four nodes through equilibrium conditions described by Equation (3).

$$F_x = \sum_{i=1}^{4} f_{xi};\ \ F_y = \sum_{i=1}^{4} f_{yi};\ \ M_z = \sum_{i=1}^{4} (f_{xi}y_i + f_{yi}x_i) \quad (3)$$

The VecTor2 post-processor can compute and output reaction forces corresponding to the nodes imposed with displacement. MATLAB codes were written as UI-SIMCOR plug-ins to implement functionalities such as receiving commands from UI-SIMCOR

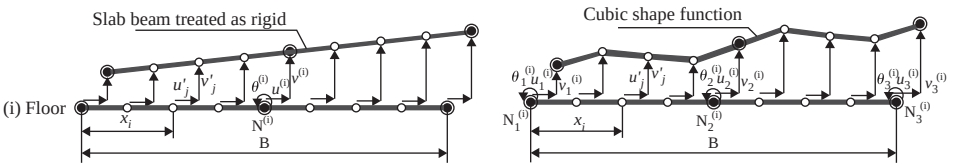

(a) One-control-point approach (b) Three-control-point approach

Figure 4 Wall interface interpolation approaches and DOFs.

through network, calculating interface nodal displacements for VecTor2 model, running VecTor2, and extracting reaction forces.

3.2.2 *Interface modeling between upper wall beam and wall elements*

Wall on 11th story and above can be represented in two ways. The first method is modeling the wall on each floor as a single frame element with large section, Figure 3(a). In this approach, a rigid beam can be placed at the interface of upper wall modeled with frame elements and lower wall with continuum elements to transfer rotational DOF at the interface. The other approach is to model upper wall with multiple elements, Figure 3(b). For instance, the upper-wall frame element can be divided into three components including two boundary regions and a middle web area, all modeled using fiber section elements in ZEUS-NL. The floor slab may strengthen the adjacent region of the wall and at the same time affect wall deformations. Due to the flexibility of the slab-beam and the large attached mass, very significant external loads can be induced in the dynamic analyses. To avoid over-restraining the continuum elements, the floor is considered to have some flexibility as opposed to the full rigidity used in the first method.

The rigid or very stiff beam elements at the interface of upper and lower walls can be represented by constraint equation which constrains relative displacements of DOFs. The shapes of constraint equations for each approach are illustrated in Figure 4. Mathematical expression of the constraint equation is as follows.

One-control-point approach: In this approach, the rigid body motion assumption is made for the floor slab system as shown in Figure 4(a). The rotational DOF at this control point will generate a linear variation in vertical displacement at all nodes along the ith floor. The constraint equations for both upper wall to lower wall and inter-storey lower wall interfaces are derived using Equation (4). The control point reaction forces are computed from the stress resultants at all of the nodes through equilibrium conditions as evaluated by Equation (5).

$$\begin{Bmatrix} u'_j \\ v'_j \end{Bmatrix} = \begin{Bmatrix} u_i + \left(\frac{B}{2} - x_j\right)(1 - \cos\theta_i) \\ v_i - \left(\frac{B}{2} - x_j\right)\sin\theta_i \end{Bmatrix} \tag{4}$$

$$\begin{Bmatrix} F_{xi} \\ F_{yi} \\ M_{zi} \end{Bmatrix} = \begin{Bmatrix} \sum_{j=1}^{Ni} f_{xj} \\ \sum_{j=1}^{Ni} f_{yj} \\ \sum_{j=1}^{Ni} f_{yj} \left(\frac{B}{2} - x_j \right) \end{Bmatrix} \tag{5}$$

where, i – Control point number, $i = 1, 2, \ldots, N_i$, and N_i is the total number of nodes along ith floor in VecTor2 model.

Three-control-point approach: As discussed previously, instead of employing a rigid body motion assumption, beam shape functions are used for the calculation of the equivalent nodal displacements in the VecTor2 model. In the above approach, the interface floor system is divided into two beams connected by three control points. In Figure 4(b), control points N_1, N_2, and N_3 form two beam members with lengths equal to half of the wall width. Cubic shape functions are used for the interpolation of continuum model nodal displacement loads $[u'_j, v'_j]$ from $[u, v, \theta]^i_{1\sim3}$ at these three control points as follows. The shape functions for the two beam members are defined as follows:

$$[N] = \begin{bmatrix} (1-\xi) & 0 & 0 & \xi & 0 & 0 \\ 0 & (1-3\xi^2+2\xi^3) & (\xi-2\xi^2+\xi^3)l_e & 0 & (3\xi^2-2\xi^3) & (\xi^3-\xi^2)l_e \end{bmatrix} \tag{6}$$

where, $\xi = \begin{cases} \dfrac{x}{l_e}, & \text{if } x \le \dfrac{B}{2} \\ \dfrac{(x - B/2)}{l_e}, & \text{if } x > \dfrac{B}{2} \end{cases}$, the element length $l_e = \dfrac{B}{2}$

The nodal displacements at all the nodes along ith floor can then be computed as:

$$\begin{Bmatrix} u'_j \\ v'_j \end{Bmatrix} = \begin{cases} [N]\ [u^i_1\ v^i_1\ \theta^i_1\ u^i_2\ v^i_2\ \theta^i_2]^T, & \text{for } 0 \le x_j \le \dfrac{B}{2} \\ [N]\ [u^i_2\ v^i_2\ \theta^i_2\ u^i_3\ v^i_3\ \theta^i_3]^T, & \text{for } \dfrac{B}{2} \le x_j \le B \end{cases} \tag{7}$$

where, $j = 1, 2, \ldots, N_i$, N_i are the total number of nodes along ith floor in VecTor2 model, and B represents the wall width. The feedback control point reactions are computed from nodal force results from the VecTor2 output using an equivalent nodal force concept for beam elements as expressed in Equations (8)∼(10).

$$[F_{x1}\ F_{y1}\ M_{z1}\ F^1_{x2}\ F^1_{y2}\ M^1_{z2}]^i = \left[\sum_{j=1}^{m1} \left([N]^T \begin{Bmatrix} f_{xj} \\ f_{yj} \end{Bmatrix} \right) \right]^T, \quad \text{for } 0 \le x_j \le \frac{B}{2} \tag{8}$$

$$[F^2_{x2}\ F^2_{y2}\ M^2_{z2}\ F_{x3}\ F_{y3}\ M_{z3}]^i = \left[\sum_{j=m1}^{m2} \left([N]^T \begin{Bmatrix} f_{xj} \\ f_{yj} \end{Bmatrix} \right) \right]^T, \quad \text{for } \frac{B}{2} \le x_j \le B \tag{9}$$

$$[F_{x2}\ F_{y2}\ M_{z2}]^i = [F^1_{x2}\ F^1_{y2}\ M^1_{z2}]^i + [F^2_{x2}\ F^2_{y2}\ M^2_{z2}]^i \tag{10}$$

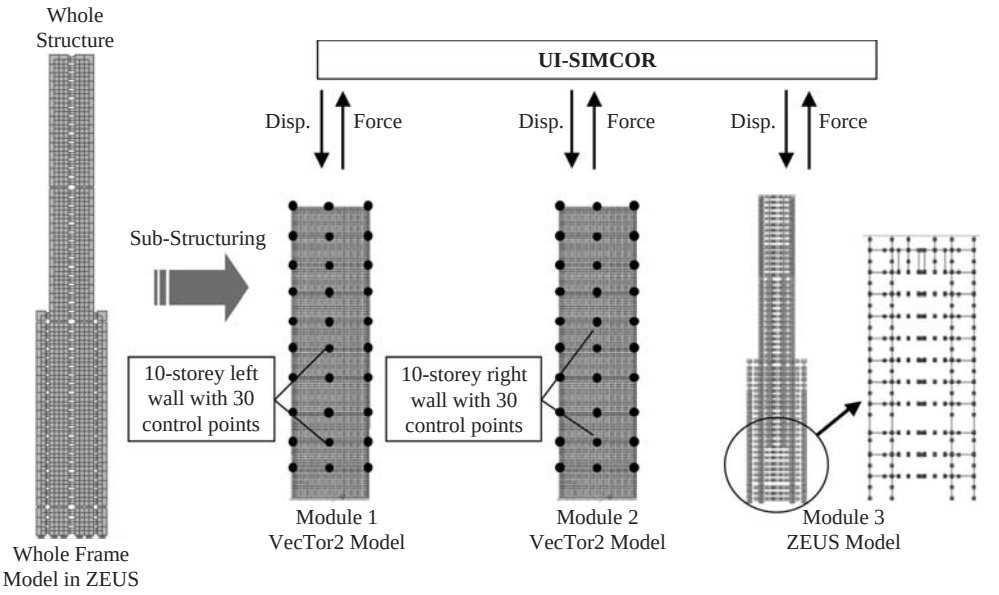

Figure 5 Multi-resolution distributed simulation for reference building combining ZEUS-NL and VecTor2 within UI-SIMCOR.

where, $m1$, $m2$ are the number of nodes at middle and right end of the floor, $[f_{xj}, f_{yj}]$ are the forces at jth node in VecTor2.

Both of these approaches have been investigated and compared on the basis of accuracy, runtime and stability. The three-control-point approach proved to be more realistic by introducing flexibility of the floor as was expected in the real structure. The rigid slab assumptions put severe restraints on the floor nodes and thereby overestimated the stiffness of the lower 10-stories of the walls, which led to smaller flexural deformations of the wall and underestimated the effects on lateral drift. The use of the rigid body motion assumption restricted the development of cracking. The runtime required by one control point approach was somewhat shorter than that with the use of three control points. Based on this evaluation, the accuracy of the results was considered to be more important than runtime and therefore the three-control-point approach was employed for the MDFEA conducted in this study.

3.2.3 *Integrated MDFEA structural modeling*

The MDFEA framework and sub-structuring methodology used for the 54-story case study building is shown in Figure 5. Dynamic response history as well as static pushover analyses are conducted using the distributed simulation approach. The characteristics of the model and control DOFs are described in Table 2.

3.3 *Static pushover analysis*

Static pushover analyses are conducted for the reference building in order to estimate its ultimate strength and ductility capacity. Gravity loads are applied to the building

Table 2 MDFEA model size and control DOFs.

Module No.	*Node Number*	*Element Number*	*Control Node*	*Effective DOF*
1 – Left Wall VecTor2 Model	3640	3502	30	90
2 – Right Wall VecTor2 Model	3640	3502	30	90
3 – Whole Frame ZEUS Model	1160	1672	306	426

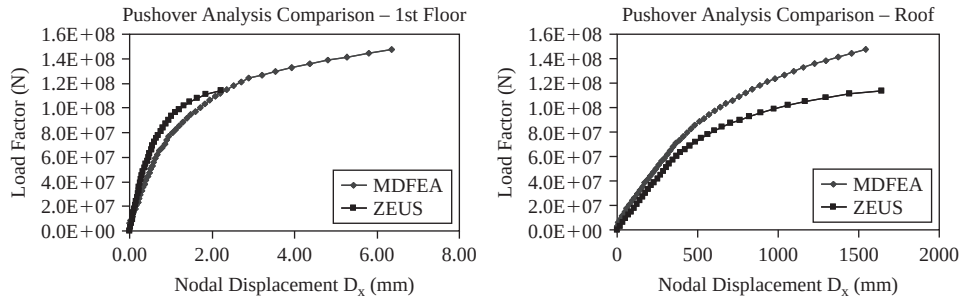

(a) Response at 1st storey (b) Response at roof

Figure 6 Pushover comparisons between results from MDFEA and complete ZEUS-NL.

prior to conducting the static pushover analysis. Two analyses are conducted, one using the MDFEA framework and the other in which the structure is entirely modeled with frame elements in ZEUS-NL. A comparison of the results from these analyses is presented in Figure 6.

This comparison illustrates that the lateral drift in the lower part of the wall has more flexibility and ductility in MDFEA than in the ZEUS-NL analysis. This is mainly due to the much larger shear deformation contributions that are captured in the continuum model of the MDFEA. At higher load levels, the ZEUS-NL model exhibits lower stiffness and ultimately less strength than the MDFEA model. This is mainly because, the plane section assumption in the fiber approach leads to concrete crushing at wall's base earlier than the concrete compressive capacity is reached in the continuum model.

In the MDFEA approach, load redistribution is repeatedly performed at each load step and a confined concrete strength model is applied in the regions of highest compressive stress that follows the Kupfer-Richart Model, Wong & Vecchio (2002), as expressed in Equation (11). This latter feature leads to increased wall capacity and ductility under high load levels even after extensive cracking has been calculated to occur.

$$\beta_l = \left[1 + 0.92\left(\frac{f_{cn}}{f'_c}\right) - 0.76\left(\frac{f_{cn}}{f'_c}\right)^2\right] + 4.1\left(\frac{f_{cl}}{f'_c}\right) \tag{11}$$

where, $f_{cn} = -(f_{c2} - f_{c1}) > 0$, $f_{cl} = -f_{c1} > 0$, $f_{c2} < f_{c1} < 0$

(a) Cracked deformed shape (step 50, scale factor: 20)

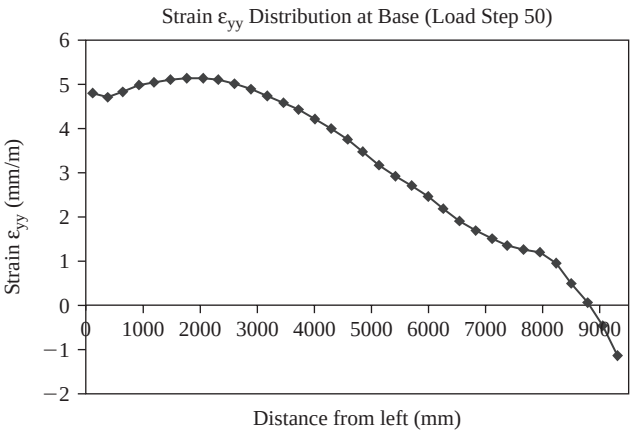

(b) Strain ε_{yy} distribution at wall base section

Figure 7 Results from MDFEA pushover analysis

Table 3 Selected ground motion records for MDFEA.

Earthquake	*Record*	*M*	*Station Data Source*	*Distance (km)*	*Site Soil Condition*	*PGA (g)*
Chi-Chi, Taiwan 1999/09/20	Chi-Chi_close_stiff	7.6	CHY028-N, (CWB)	7.31	Stiff	0.821
Kocaeli, Turkey 1999/08/17	Kocaeli_close_stiff	7.4	SKR090, Sakarya (ERD)	3.1	Stiff	0.376
Kobe, Japan, 1/16/1995	Kobe_close_stiff	6.9	TAZ090 Takarazuka, (CUE)	1.2	Stiff	0.694
Kobe, Japan, 1/16/1995	Kobe_close_soft	6.9	SHI000, Shin-Osaka, (CUE)	15.5	Soft	0.243
Loma Prieta, USA 1989/10/18	Loma_dist_soft	6.9	SFO090 58223, (CDMG)	64.4	Soft	0.329

Figure 7 shows the extent of cracking, the deformed wall shape and vertical strain distribution along the base section at load step 50. It is observed from Figure 7a that the wall deforms and is damaged in flexural-shear mode under the incremental pushover loads. The curved vertical strain distribution over the horizontal cross section also illustrated that plane section assumptions are not really happening inside the wall.

3.4 *Dynamic response history analysis*

Inelastic dynamic response history analyses are conducted using the MDFEA framework for the reference building using selected representative ground motion records. Ground motions were selected to encompass different magnitudes, distance to source, and site soil conditions. The variation of input ground motion shown in Table 3 is

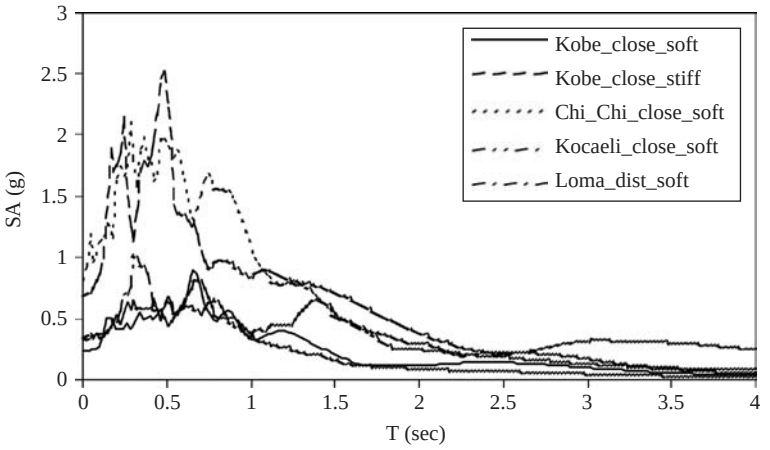

Figure 8 Response spectrum of selected GMs for MDFEA.

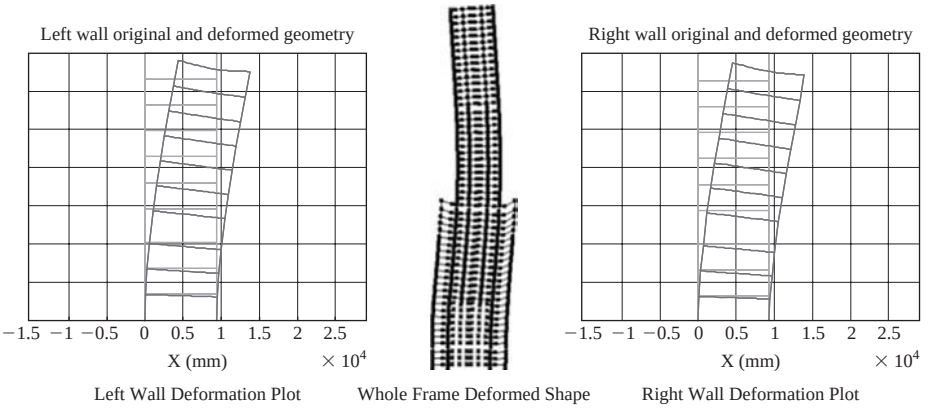

Figure 9 Deformed shapes of three modules from THA using the MDFEA framework.

intended to evaluate the robustness of the MDFEA algorithm for complex structural systems under different types of seismic excitations. The elastic spectrum acceleration diagrams (damping ratio 5%) of the selected GMs are shown in Figure 8.

Figure 9 presents the deformed sub-structure shapes for the reference building during a response time history analysis (THA). The shapes illustrate the synchronized seismic responses of two core walls and the frame as well as the flexibility of the floor and shear deformations in the wall.

In Figure 10, two sets of response history analysis results using both MDFEA framework and the pure frame model using ZEUS-NL are presented. The left wall displacement responses at different height levels are compared between these two models, including total drifts at 1st storey, 10th storey (top of the wall VecTor2 models in modules 1 and 2) and the roof.

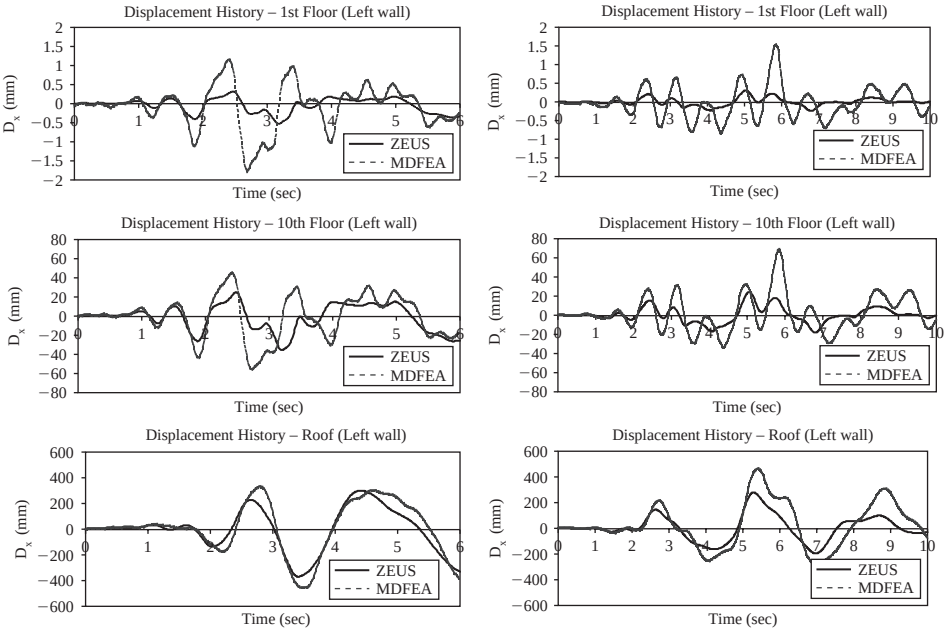

(a) GM record Kobe_close_stiff (b) GM record Kobe_close_soft

Figure 10 Sample displacement histories and comparisons between MDFEA and ZEUS Models.

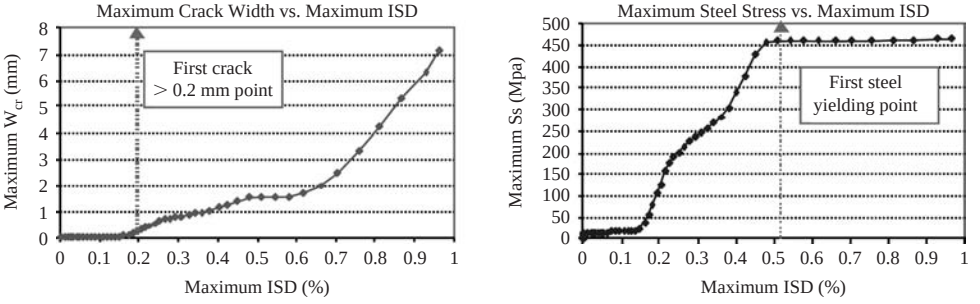

(a) Limit state 1 − Serviceability by considerable cracking ($W_{cr} > 0.2$ mm)

(b) Limit state 2 − Damage control by wall rebar yielding (fy >= 460 MPa)

Figure 11 Quantitative definitions for limit states 1 and 2 using MDFEA results.

The results presented in Figure 11 illustrate that the drift computed from MDFEA at the lower levels is much larger than that from ZEUS-NL pure frame model, while the roof drifts from the two models are relatively close.

The comparisons presented above indicate that pure-frame analyses may not be able to sufficiently predict some important shear deformation features of the response of the 54-story high-rise building.

3.5 *Significance of the MDFEA framework*

With the use of the MDFEA framework proposed herein, it becomes feasible to accurately and efficiently predict the static and dynamic response of complex structures. This framework will help researchers tackle important problems, such as developing performance limit states definitions for seismic risk analysis. The framework is also ideally suited to fragility assessment studies. For RC structures, all the information available from MDFEA, including concrete stress and strain distributions, steel stresses and crack patterns throughout the structural walls, are available for assessing a structures performance. For example, it is now possible to define new limit states for serviceability that consider the state of cracking in the core wall or new limit states for damage control that more accurately consider the yielding of the longitudinal reinforcement. Based on previous pushover analyses, maximum concrete crack width and steel stress can be correlated to global deformation measures including inter-storey drift ratio (ISD) during the loading history, as shown in Figure 11.

3.6 *Computational errors and stability*

With the use of this MDFEA framework, nonlinearities are accounted for in the individual computational modules, such as in ZEUS-NL and VecTor2. The different features of these modules, including finite element model resolutions, theoretical algorithms and numerical techniques, will lead to different accuracy levels and different deviations of strain and stress resultants. Hence, the actual movements and reaction feedbacks at control points will contain errors combined from multiple modules that are difficult to eliminate. Another error source originates from the interface modeling, such as in this case study example in which either rigid or flexible slab assumptions were used.

These errors can be transferred to the next step while the new displacement commands are sent to all modules by UI-SIMCOR based on the calculations from the previous step. Thus, the errors are accumulated along the load history and may lead to numerical divergence. In this study, error monitoring was applied for each step by comparing the imposed displacements and actual movements. This enables an evaluation of the stability of the model and the reliability of the results.

Another computational instability may be caused by numerical divergence within any of the analytical tools being combined. ZEUS-NL will stop the analysis automatically if convergence is not achieved after the predefined multi-level step size reduction technique is used. While for VecTor2, the analysis will be terminated if the convergence limit cannot be satisfied for two consecutive steps. These instabilities are more straightforward to assess since the consecutive divergences are not due to random numerical errors but indicate the occurrence of either global or local structural failures.

4 Conclusions

There is a dearth of accurate, efficient and reliable analytical approaches for the inelastic static and dynamic analyses of complex reinforced concrete and composite high-rise buildings under extreme loads taking into account shear-flexure-axial interaction, crack propagation and other detailed features of concrete response. In this study, a new approach termed multi-resolution distributed finite element analysis (MDFEA) is proposed and used to analyze a reference RC high-rise building with a dual core

wall-frame system. Below, a summary of the features of the study and highlights of its conclusions are given:

- Two advanced analytical platforms ZEUS-NL and VecTor2 were used to effectively model the frame and wall separately, based on the unique algorithms and functionalities of the two programs.
- A 'simulation coordinator' – UI-SIMCOR (Kwon et al., 2005), was used to combine the best features of different FEA software for modeling different components within one system. Through sub-structuring, global integration and network data flow, a distributed FEA simulation was completed.
- A real 54-story high-rise building with a dual core wall-frame structural system was selected as the case study example. By using the MDFEA framework, both static pushover and dynamic response history analyses were conducted. Multiple modules corresponding to frame and wall components were built in UI-SIMCOR and analyzed with frame-wall interaction effects fully considered in a step-by-step manner.
- The comparisons from both pushover and response history analysis highlight that due to the influence of shear, the use of the multi-resolution approach is illustrated to be able to capture critical aspects of the behavior more sufficiently than some traditional methodologies performing pure frame analysis. The use of a MDFEA approach can account for response limit states including shear-flexure-axial interaction.

With the completed and verified functionality of the proposed MDFEA framework, it is practical to extend the application to other high-rise buildings and to other complex structures. This framework is not restricted to combining ZEUS-NL and VecTor2, but rather can be used to integrate the necessary features of any number of FE packages.

Acknowledgement

This study is a product of project EE-3 'Advanced Simulation Tools' of the Mid-America Earthquake Center. The MAE Center is an Engineering Research Center funded by the National Science Foundation under cooperative agreement reference EEC 97-01785. UI-SIMCOR was developed with partial funding from the Network for Earthquake Engineering Simulations (NEES). The contribution of Bill Spencer, University of Illinois, Narutosi Nakata, Johns Hopkins University, and Kyu-sik Park, Research Institute of Industrial Science and Technology, Korea, to the development of UI-SIMCOR as a hybrid distributed simulation platform is gratefully acknowledged.

References

Collins, M.P. & Porasz, A. 1989. Shear Design for High Strength Concrete, Proceeding of Workshop on Design Aspects of High Strength Concrete. *Comité Euro-International du Béton Bulletin d'Information. CEB. Paris.* pp. 77–83.

Combescure, D. & Pegon, P. 1997. α-operator splitting time integration technique for pseudo-dynamic testing, Error propagation analysis. *Soil Dynamics and Earthquake Engineering.* Vol. 16, pp. 427–443.

Elnashai, A.S., Papanikolaou, V. & Lee, D.H. 2002. *Zeus-NL – A System for Inelastic Analysis of Structures*.

Filippou, F.C. & Constantinides, M. 2004. *FEDEASLab – Getting Started Guide and Simulation Examples*. NEESgrid Report 2004-22 and SEMM Report 2004-05, pp. 42.

Ghobarah, A. & Youssef, M. 1999. Modeling of reinforced concrete structural walls. *Engineering Structures*. Vol. 21, pp. 912–923.

Hibbit, Karlsson & Sorensen. 2001. *ABAQUS theory manual*. Version 6.2.

Jeong, S.H. & Elnashai, A.S. 2004a. Analytical assessment of an irregular RC frame for full-scale 3D pseudo-dynamic testing, Part I: Analytical model verification. *Journal of Earthquake Engineering*, Vol. 9, No. 1, pp. 95–128.

Jeong, S.H. & Elnashai, A.S. 2004b. Analytical assessment of an irregular RC frame for full-scale 3D pseudo-dynamic testing, Part II: Condition assessment and test deployment. *Journal of Earthquake Engineering*. Vol. 9, No. 2, pp. 265–284.

Kupfer, H.B., Hilsdorf, H.K. & Rusch, H. 1969. Behavior of Concrete under Biaxial Stress. *ACI Journal*. Vol. 87, No. 2, pp. 656–666.

Kwon, O.S., Nakata, N., Elnashai, A.S. & Spencer, B. 2005. A Framework for Multi-Site Distributed Simulation and Application to Complex Structural Systems. *Journal of Earthquake Engineering*. Vol. 9, No. 5, pp. 741–753.

Palermo, D. & Vecchio, F.J. 2003. Compression Field Modeling of Reinforced Concrete Subject to Reversed Loading: Formulation. *ACI Structural Journal*. Vol. 100, No. 5.

Palermo, D. & Vecchio, F.J. 2004. Compression Field Modeling of Reinforced Concrete Subject to Reversed Loading: Verification. *ACI Structural Journal*. Vol. 101, No. 2.

Paulay, T. & Priestley, M.J.N. 1992. *Seismic design of reinforced concrete and masonry buildings*. John Wiley & Sons, Inc., New York, N.Y.

Pearlman, L., D'Arcy, M., Johnson, E., Kesselman, C. & Plaszczak, P. 2004. *NEESgrid Teleoperation Control Protocol (NTCP)*, NEESgrid TR-2004-23.

Vecchio, F.J. 2000. Disturbed Stress Field Model for Reinforced Concrete: Formulation. *ASCE Journal of Structural Engineering*. Vol. 126, No. 8, pp. 1070–1077.

Vecchio, F.J. 1990. Reinforced Concrete Membrane Element Formulations. *Journal of Structural Engineering*. Vol. 116, No. 3.

Vecchio, F.J. & Collins, M.P. 1986. The modified compression field theory for reinforced concrete elements subjected to shear. *ACI Structural Journal*. Vol. 83(2), pp. 219–231.

Wong, P.S. & Vecchio, F.J. 2002. *VecTor2 & Formworks User's Manual*. University of Toronto.

Chapter 16

Simplified probabilistic seismic performance assessment of buildings

Matjaž Dolšek & Peter Fajfar

University of Ljubljana, Ljubljana, Slovenia

ABSTRACT: A relatively simple approach for the probabilistic seismic performance assessment of building structures has been proposed. It combines the SAC-FEMA method, which is a part of the broader PEER probabilistic framework and enables probability assessment in closed form, with the N2 method. The N2 method, which has been implemented in Eurocode 8, is based on nonlinear pushover analysis and inelastic response spectra. The most demanding part of the PEER probabilistic framework, i.e. the Incremental Dynamic Analysis (IDA), is replaced by the much simpler Incremental N2 (IN2) analysis. Predetermined default values for dispersion measures are needed for the practical implementation of this approach. In the paper, this simplified approach is summarized and applied to two variants of a four storey reinforced concrete frame: a bare frame and the frame with masonry infill with openings. Both structures, representing old building not designed for earthquake resistance, were pseudo-dynamically tested in full-scale in the ELSA laboratory in ISPRA. The most common analytical modeling technique, which employs compressive diagonal struts for modeling of masonry infill, and one-component lumped plasticity elements for modeling the flexural behavior of beams and columns, was applied. The mathematical models were validated by comparing the results of nonlinear dynamic analyses with test results. The probabilities of exceedance of the near collapse limit state are estimated and discussed. The results of analyses indicate that the infills can completely change the distribution of damage throughout the structure. The probability of failure of the infilled frame is smaller than that of the bare frame. As expected, it is larger than acceptable for both structures.

1 Introduction

One of the methods developed for the seismic risk evaluation of structures is the SAC-FEMA method, which enables probability assessment in closed form (Cornell et al. 2002), and represents a part of a broader PEER probabilistic framework (Deierlein 2004). Within the framework of SAC-FEMA method, the relationship between the seismic intensity measure and the engineering demand parameter is usually determined by Incremental Dynamic Analysis (IDA) developed by Vamvatsikos & Cornell (2002). IDA is a powerful tool for estimation of seismic demand and capacity for multiple levels of intensity. However, it requires a large number of inelastic time-history analyses (and corresponding detailed data on ground motion time-histories and hysteretic behavior of structural elements) and is thus very time-consuming. Often it is possible to create summarized IDA curves with less input data, with less effort, but with still acceptable accuracy. One possible approach is to determine seismic demand for multiple levels

of seismic intensity using the N2 method (Fajfar 2000) which is one of the simplified nonlinear methods based on pushover analysis and inelastic response spectrum. Such an approach yields the Incremental N2 (IN2) curve (Dolšek & Fajfar 2004a, 2007) which is intended to approximate a summarized IDA curve.

In this paper, a simplified approach for probabilistic seismic performance assessment is summarized and applied to the example of a four storey reinforced concrete (RC) frame with and without masonry infills. For the determination of an IN2 curve for an infilled frame, the extended N2 method, which is applicable to infilled RC frames, is employed (Dolšek & Fajfar 2004b, 2005).

2 Simplified probabilistic performance assessment

The simplified probabilistic performance assessment analysis combines two procedures, i.e. the N2 method (Fajfar 2000), which is usually employed for deterministic seismic performance assessment, and the probabilistic assessment in closed form, which represents the basis of the SAC-FEMA steel moment frame guidelines (Cornell et al. 2002). In this Section the method for the simplified probabilistic assessment is briefly explained. More detailed explanation can be found elsewhere, e.g. in Dolšek & Fajfar (2007).

The SAC-FEMA method is based on some simplifying assumptions, which allow the formulation of the probabilistic assessment in closed form (Cornell et al. 2002). An additional simplification is introduced by employing the N2 method instead of the IDA analysis for the determination of the relation between the seismic intensity measure and the engineering demand parameter. The curve, which represents this relationship, is usually called an IDA curve (Vamvatsikos & Cornell 2002). In the simplified procedure it is substituted by an IN2 curve (Dolšek & Fajfar 2004a, 2007). An IN2 curve is intended to approximate a summarized IDA curve, and is not calculated for a single ground motion. The term "summarized", when related to IN2 curves, applies only to mean or median curves, since the proposed simplified approach is not intended for the determination of dispersion. Therefore default values for the dispersion measures for randomness and uncertainty in displacement demand and capacity have to be used in order to determine the probabilities of exceedance of a given limit state.

The N2 method (N stands for non-linear analysis, and 2 for two mathematical models) is a relatively simple nonlinear analysis method for deterministic seismic assessment of buildings and bridges, which combines pushover analysis of a multi degree-of-freedom (MDOF) model with the response spectrum analysis of an equivalent single-degree-of-freedom model (SDOF). Although the N2 method has its limitations (Fajfar 2000), it usually provides reasonably accurate predictions of the seismic response of structures, unless vibration in higher modes is important. The N2 method has been mainly used for the seismic assessment of structures where the seismic demand (engineering demand parameter) for a given seismic intensity is compared with the capacity corresponding to a given limit state. (Note that the expression "performance level" used in FEMA 350 (2000) has basically the same meaning as "limit state" according to the Eurocode terminology.) In probabilistic performance assessment the relationship between the seismic demand and the seismic intensity has to be determined for different values of the seismic intensity measure.

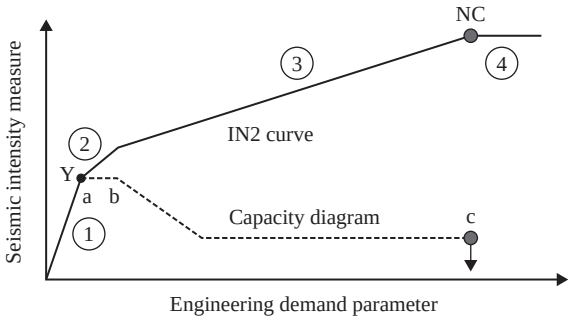

Figure 1 A typical IN2 curve of an infilled RC frame building. Y and NC indicate yield and near collapse points.

The IN2 curve represents the relation between an engineering demand parameter and a seismic intensity measure. Usually, the top displacement is used as the engineering demand parameter and the spectral acceleration, i.e. the value in the elastic acceleration spectrum at the period of the idealized system, represents the intensity measure. Sometimes, it is convenient to use the peak ground acceleration as the seismic intensity measure, especially when IN2 curves for different structures are compared. This was the case in the example presented in this paper. The engineering demand parameter and the corresponding seismic intensity measure will be denoted as $\widetilde{C}$ and $s_a^{\widetilde{C}}$, respectively. The whole IN2 curve can be determined by repeating the N2 approach for increasing ground motion intensity until the "failure" occurs. In the simplest but very common case the "equal displacement rule" applies, i.e. the inelastic displacement is assumed to be equal to the elastic displacement of the system with the same stiffness and mass, but with unlimited strength. In such a case the IN2 curve is a straight line (with its origin at the point (0,0)) until "failure" occurs. It is necessary to determine only the point corresponding to "failure". In general, the shape of the IN2 curve depends on the relation between the reduction factor, ductility and period (R-μ-T relation), which defines the inelastic spectra to be used in the N2 method for the determination of seismic demand. For example, in the case of infilled RC frames, the IN2 curve consists of straight lines, as presented in Figure 1, for which three points have to be evaluated with the N2 method (Dolšek & Fajfar 2004b, 2005) (Figure 1, points at the top displacements a, b and c). The idealized capacity diagram with indicated yield and near collapse points is also shown. It is conservatively assumed that the structure fails after the NC limit state is attained. Thus the IN2 line after the NC limit state is horizontal. Knowing the IN2 curve, the engineering demand parameter, can be easily linked to the corresponding seismic intensity measures.

Once the seismic intensity $s_a^{\widetilde{C}}$, which causes a selected limit state, is determined from the IN2 curve, the x confidence level estimate of the annual probability (mean annual frequency) of exceedance of a given limit state $P_{PL,x}$ can be determined as (Cornell et al. 2002)

$$P_{PL,x} = \widetilde{H}(s_a^{\widetilde{C}})C_H C_f C_x \tag{1}$$

$$C_H = \exp\left[\frac{1}{2}\beta_H^2\right], \quad C_f = \exp\left[\frac{k^2}{2b^2}(\beta_{DR}^2 + \beta_{CR}^2)\right],$$
$$C_x = \exp\left[K_x\sqrt{\frac{k^2}{b^2}(\beta_{DU}^2 + \beta_{CU}^2)}\right] \tag{2}$$

$\widetilde{H}(s_a^{\widetilde{C}})$ is the median value of the hazard function at the seismic intensity $s_a^{\widetilde{C}}$. It provides the median estimate of the annual probability that the seismic intensity will be equal to or exceed the level $s_a^{\widetilde{C}}$, i.e. the seismic intensity "corresponding" to the median displacement capacity $\widetilde{C}$. k is a parameter of the hazard function, whereas b is a parameter of the function relating the engineering demand parameter to the intensity measure, i.e. of the so-called IDA curve, or in the case of the simplified method the IN2 curve. K_x is the standardized normal variate associated with probability x of not being exceeded. For example, $K_x = 0$, 1 and 1.28 are associated with 50%, 84 % and 90 % confidence levels, respectively. β_H is the dispersion measure for hazard. The product $\widetilde{H}(s_a^{\widetilde{C}})C_H$ represents the mean value of the hazard function $\widetilde{H}(s_a^{\widetilde{C}})$. Other β parameters represent the dispersion of the engineering demand parameter (i.e. top displacement) due to ground motion variability (randomness) and due to variability related to structural modeling and analysis (uncertainty). β_{DR} and β_{CR} are the dispersion measures for randomness in top displacement demand and capacity, and β_{DU} and β_{CU} are the dispersion measures for uncertainty in top displacement demand and capacity. For practical applications, predetermined default values for dispersion measures, based on statistical studies of typical structural systems, will be needed. In the example, shown in this paper, some rough preliminary estimates were used.

3 Example: A bare and an infilled reinforced concrete frame

3.1 *Description of the example structures and the mathematical modeling*

A bare and an infilled four-storey plane RC frame have been studied. The buildings had been designed to reproduce the design practice in European and Mediterranean countries about forty to fifty years ago (Carvalho & Coelho 2001). The elevation, the plan and the typical reinforcement in columns are presented in Figure 2. The structure was tested in full scale at ELSA Laboratory in the JRC in Ispra. Detailed description of buildings and results of the experiments can be found in ECOEST2-ICONS Report No.2 (Carvalho & Coelho 2001).

The OpenSees program was employed for all analyses PEER (1999). The elements of the RC frame were modelled by one-component lumped plasticity elements, composed of an elastic beam and two inelastic rotational hinges (defined by the moment-rotation relationship). The moment-rotation relationship of inelastic rotational hinges is bilinear until the maximum moment is attained and has a degrading slope after the maximum moment (Figure 3). The characteristic moments were calculated considering the axial forces which result from the vertical loading on the frame. The characteristic rotations, which describe the moment-rotation envelope of a plastic hinge, were determined according to procedure described in (Fajfar et al. 2006). The zero moment

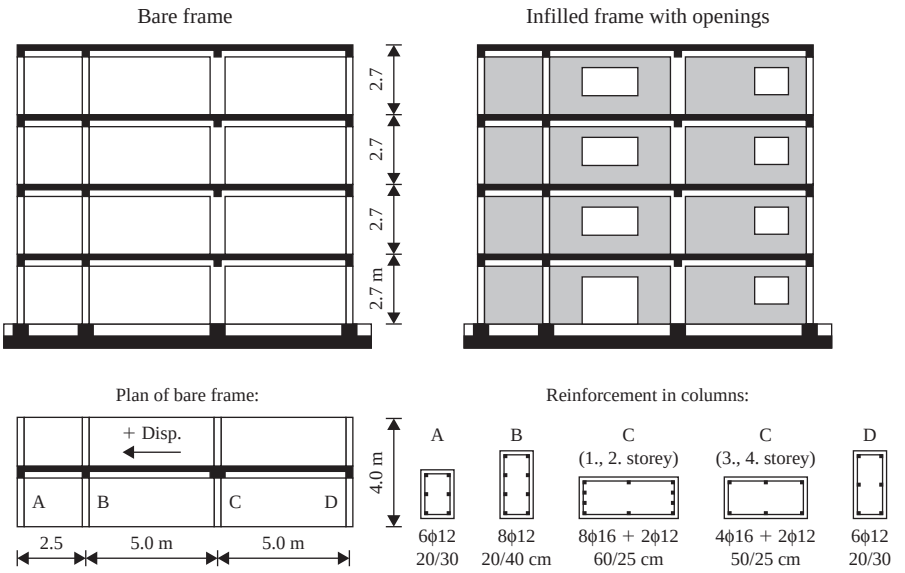

Figure 2 The view, the plan and the typical reinforcement in the columns of the test building.

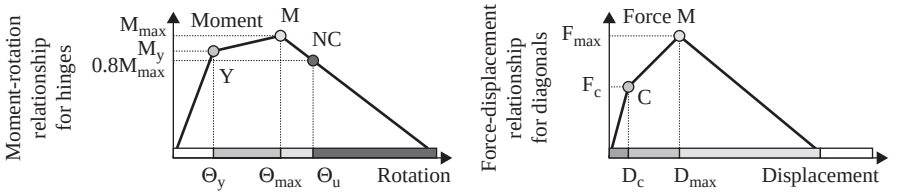

Figure 3 The moment-rotation relationship for a plastic hinge, and the force-displacement relationship of a diagonal representing masonry infill. C represents the cracking of masonry infill, Y the yielding of reinforcement, M the maximum force or moment, and NC the near collapse limit state.

point was assumed at the mid-span of columns and beams. A low value of confinement effectiveness factor $\alpha = 0.1$ and the ratio of transverse reinforcement $\rho_{sx} = 0.02$ were adopted. The rotation Θ_u in columns at the NC limit state, which corresponds to 20% reduction of the maximum moment in the post-capping range ("ultimate" rotation), was estimated with the CAE method (Peruš et al. 2006). For beams, the EC8-3 (CEN 2005) formulas were used, whereas the parameter γ_{el} was taken equal to 1.0 and, due to the absence of seismic detailing, the ultimate rotations were multiplied with factor 0.85. The calculated ultimate rotations vary from 31 mrad to 34 mrad for all columns with exception of the column C for which the ultimate rotation varies from 42 mrad in the first storey to 57 mrad in the top storey. The sign of the moment (tension at the top or tension at the bottom) influences the ultimate rotation in the beams. In general, the ultimate rotation is lower if the tension is at the bottom of the beam. The calculated ultimate rotations in the beams vary from 27 mrad to 43 mrad.

In the case of the infilled frame, the infills were modelled by the diagonal strut elements, which carry loads only in compression and are capable of simulation of the material softening. The diagonals were placed between the beam-column joints. Such a modelling in general underestimates column shear forces, which were not considered in the seismic assessment at this stage of the study. The main problem, which is subject to large uncertainties, is how to determine the characteristics of these diagonals, i.e. their force-displacement envelopes and their hysteretic behaviour. Additional problems arise because of the openings in the infills (Figure 2). In our study, simple empirical formulas were employed for the determination of initial stiffness, the maximum strength of the masonry infill, and the influence of the opening on these quantities. They are described in (Dolšek & Fajfar 2007). A typical force-displacement relationship for a diagonal strut element is presented in Figure 3.

Although rather simple models were used for determination of seismic response, a very good correlation between the calculated and experimental results, which were obtained by pseudo-dynamic tests, were observed. The comparison between calculated and experimental results as well as details of the models are presented and discussed in (Dolšek & Fajfar 2007).

3.2 *Definitions of the NC limit state and acceptable probability*

The European standard EC8-3 (CEN 2005) defines three limit states, i.e. limit states of damage limitation (DL), of significant damage (SD), and of near collapse (NC). The limit states are defined at the element level by the rotations in the moment – rotation relationship of the plastic hinge. In test examples presented in this paper only the probability of the exceedance of the NC limit state was evaluated. The NC limit state at the element level is reached when the rotation in plastic hinge exceeds the ultimate rotation, which corresponds to a 20% drop in strength. At the structure level, there is a lack of definitions of the limit states in codes. In this study, it has been conservatively assumed that the most critical column controls the state of the structure. Consequently, the structure is assumed to attain the NC limit state when the first column attains the NC limit state. Furthermore, it has been conservatively assumed that the NC limit state corresponds to the "failure" of the structure. The collapse of masonry infills does not influence the NC limit state.

In general, in addition to the damage due to flexure, the damage in the joints and the damage due to shear also contribute to the damage and may cause a failure of the reinforced concrete frames. In the example, these sources of potential damage were not considered since the tests and analyses performed on the test structures indicated that the structural behavior was dominated by flexure in the columns.

When performing a probabilistic performance assessment, data on the acceptable probabilities of the exceedance of a given limit state are needed. There are different approaches to define acceptable probabilities of exceedance of a given limit state (Melchers 1999). However, in the earthquake engineering community there are no generally accepted values for acceptable probabilities of exceedance of a given limit state. In the example, the acceptable probability was defined as follows: the probability of exceedance of the NC limit state should not exceed 2% in 50 years (0.0004) with the 90% confidence level. Basically the same definition was used by Yun et al. (2002).

3.3 *Pushover analyses*

The capacities of the structures are determined by pushover analyses. The same masses as in pseudo-dynamic tests (Carvalho & Coelho 2001) were used. They amount to 46 t in the bottom stories and to 40 t in the top storey for both bare and infilled frame. Lateral loads for pushover analysis of the bare and infilled frame were determined based on the first mode shape. For both structures, the effective mass for this mode amounts to more than 80% of the total mass. The pushover curves are presented in Figure 4. It can be seen that the presence of masonry infills substantially increases the stiffness and the strength of the frame. The maximum strength to weight ratio of the infilled frame (0.43) is much larger than that for the bare frame (0.13). However, the maximum strength in infilled frame is reached at a relatively small top displacement, which is equal to 1.5 cm. With a further increase of displacement the masonry infills start to degrade. A substantial reduction of strength occurs after the infills completely collapse in the first storey (Figure 4). The reduction amounts to 57% of the maximum strength.

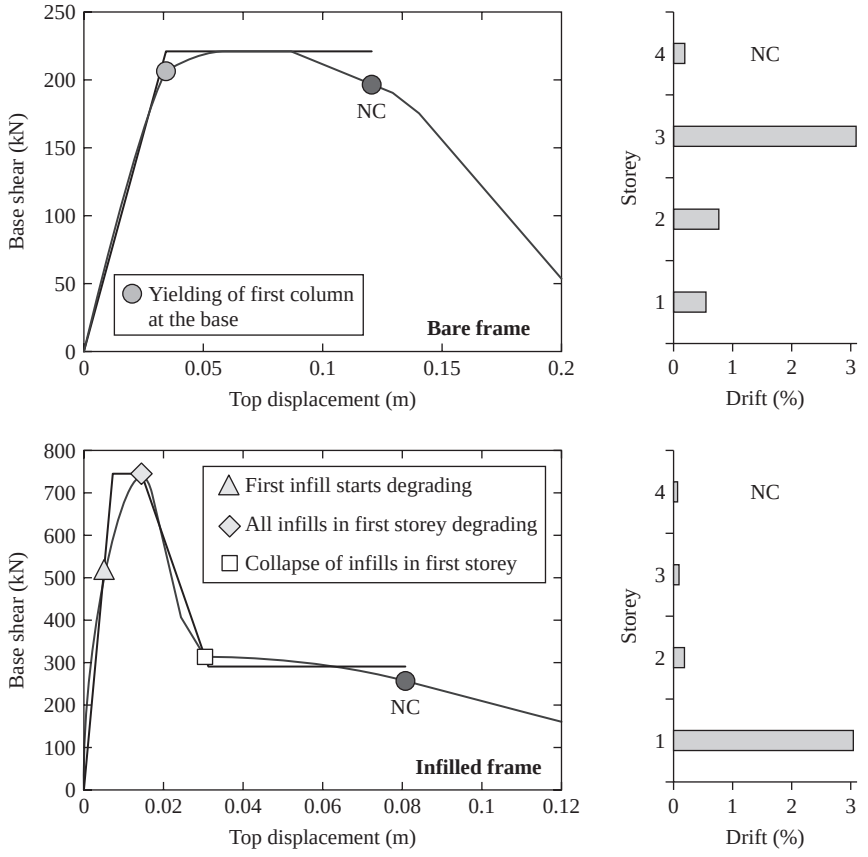

Figure 4 The computed and idealized pushover curves of the bare and infilled frame with indicated selected damage states and the storey drifts at the NC limit state.

The top displacements (capacities) corresponding to the NC limit state and some intermediate damage states are also presented in Figure 4. In general, it can be seen that the top displacement capacity at the NC limit state of the infilled frame is much smaller than that determined for the bare frame. Due to an extreme concentration of damage in the first storey of the infilled frame, the global drift ratio (i.e. the ratio between the top displacement and the height) at the NC limit state amounts to 8.1 cm (0.76%) and it is much smaller than the corresponding value for the bare frame (12.1 cm, 1.14%). The storey drifts at the NC limit state of the infilled frame amount to 3.05%, 0.20%, 0.10% and 0.05% for the bottom to top storey, respectively (Figure 4). At this stage all infills have completely collapsed in the first storey, some of them began to degrade in the second storey, while in the top two stories the infills remain in the elastic range or exceed the cracking point. A similar plastic mechanism had been observed also in the pseudo-dynamic test (Carvalho & Coelho 2001). The distribution of the storey drifts and the damage in the bare frame at the NC limit state is very different from that in the infilled frame. The storey mechanism formed in the third storey is not as explicit as the soft first storey formed in the infilled frame (Figure 4). The maximum drift is observed in the third storey (3.09%). Drifts in the first and second storey amount to 0.52% and 0.72%, respectively.

For further analyses idealized pushover curves will be needed. They are shown in Figure 4. The elastic stiffnesses are determined based on the equal energy concept for the part of the curve before the capping point.

3.4 *Earthquake motion and hazard*

One of the advantages of the N2 method, which will be used for the determination of the IN2 curve of the bare and infilled frame, is the presentation of earthquake motion by an elastic acceleration response spectrum and not by a set of ground motion records, which is required in the IDA analysis. In our example, the EC 8 spectrum for ground type A was used (Figure 5a). For the sake of simplicity it was assumed that the shape of the spectrum does not change with the level of peak ground acceleration. Note, however, that the IN2 curve can be determined also by using the uniform hazard spectra by assuming different shapes for different levels of seismic intensity.

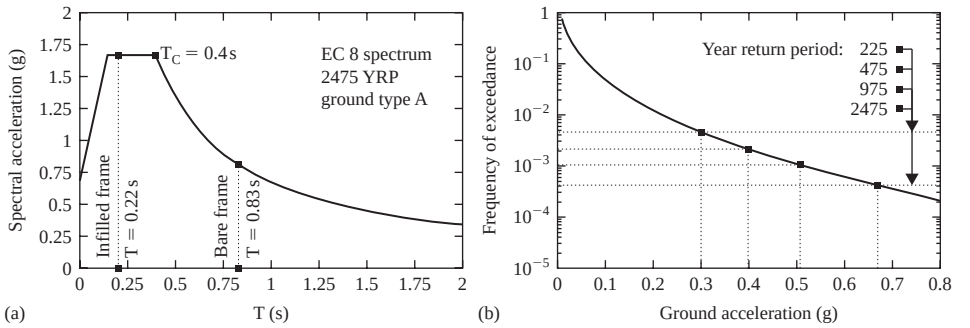

Figure 5 (a) The EC 8 spectrum for 2475 year return period with indicated periods of idealized systems for bare and infilled frame, (b) the hazard curve with some indicated return periods.

In addition to the elastic response spectrum, the hazard curves for the intensity measures are needed for a probabilistic performance assessment. The hazard curve for the peak ground acceleration (Figure 5b) used in the example for both structures corresponds to the city of Reggio Calabria in Southern Italy (in LESSLOSS Subproject 9, 2006). The peak ground accelerations amount to 0.30, 0.40 and 0.67 g for 225 year (20% probability of exceedance in 50 years), 475 year (10%/50 years), and 2475 year (2%/50 years) return periods, respectively, indicating quite a high hazard.

3.5 *IN2 curves*

The top displacement and the peak ground acceleration were selected as the engineering demand parameter and seismic intensity measure, respectively. As explained in Section 2, only a few points of the IN2 curve have to be determined by the N2 method in order to construct the IN2 curve. Idealized systems, as shown in Figure 4, will be used. For the bare frame, only the point at the NC limit state has to be determined, since the period of the idealized system $T = 0.83$ s exceeds the corner period T_C (Figure 5a) and therefore the "equal displacement rule" can be applied for this particular example. The top displacement capacity at the NC limit state was already determined as $D_{NC} = 12.1$ cm (Section 3.3). The corresponding displacement of the equivalent SDOF system, which represents also the spectral displacement, is calculated as $S_{d,NC} = D_{NC}/\Gamma = 12.1/1.29 = 9.4$ cm, where Γ is the transformation factor from the MDOF to the equivalent SDOF system and vice versa. Considering the equal displacement rule, the elastic displacement is equal the inelastic one and the corresponding elastic spectral acceleration $S_{ae,NC}$ is obtained as $S_{ae,NC} = 4\pi^2 S_{d,NC}/T^2 = 0.54$ g. Finally, the peak ground acceleration, which causes the NC limit state, is determined as $a_{g,NC} = 0.54\,\text{g}/1.2 = 0.45$ g, where 1.2 is the ratio between the spectral acceleration $S_{ae}(T = 0.83\,\text{s})$ and peak ground acceleration a_g (Figure 5a). The IN2 curve for the bare frame is then constructed as a straight line from the origin to the point at the NC limit state defined by $S_{d,NC}$ and $a_{g,NC}$. After this point it is assumed that the IN2 curve is horizontal (Section 2). A graphic representation of all relevant quantities of the SDOF system is shown in Figure 6. The IN2 curve for the bare frame is presented in Figure 7a. In addition to the NC point, the point which corresponds to the yielding of the first column at the base is also indicated. For this point the top displacement is already known from pushover analysis and the IN2 curve can be used for the determination of the corresponding ag or spectral acceleration $S_{ae}(T = 0.83$ s) (see the scale on the right hand side of Figure 7a). This is the usual way of using the IN2 curve in probabilistic seismic assessment. In a deterministic assessment, the IN2 curve can be used in an opposite way, i.e. for the determination of the top displacement for a given seismic hazard. The points corresponding to peak ground accelerations with return periods od 225, 475 and 2475 years are also presented in Figure 7a. The figure suggests that for the 2475 year return period the demand exceeds the capacity at the NC limit state, therefore also the probability of exceedance of the NC limit state will exceed the acceptable probability.

In the case of the infilled frame the equal displacement rule is not applicable and only the NC point is not sufficient to construct the IN2 curve. In addition to this point, two other points are needed (Section 2). In this example only the determination of the

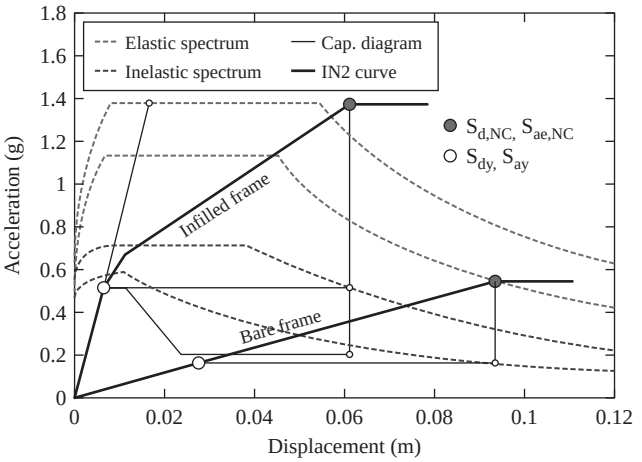

Figure 6 Capacity diagrams, IN2 curves, and elastic and inelastic spectra defining seismic demand at the NC limit state for the bare and infilled frame presented in AD format.

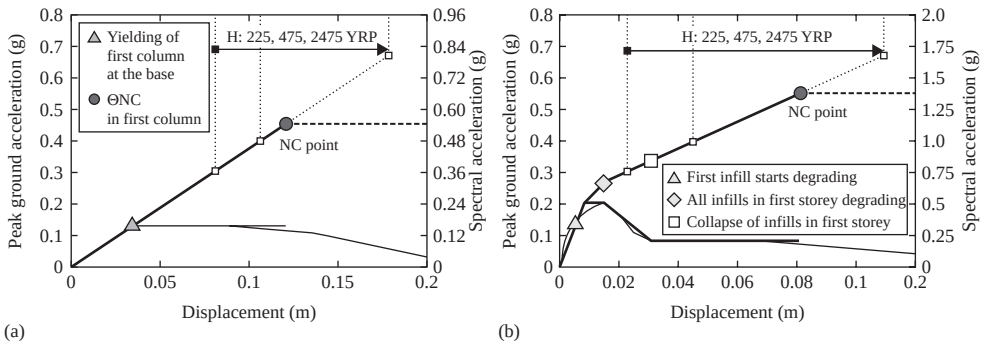

Figure 7 (a) The IN2 curve of the bare and (b) the IN2 curve of the infilled frame.

NC point by using the N2 method applicable to infiled frames (Dolšek & Fajfar 2005) is briefly explained (a graphic presentation is shown in Figure 6).

The pushover curve of the infilled frame was idealized with a four-linear force-displacement relationship as shown in Figure 4. Four parameters defining the idealized pushover curve are needed for further analysis (Dolšek & Fajfar 2005). These are the yield displacement $D_y = 0.81$ cm and the yield force $F_y = 745.4$ kN, the ductility at the beginning of the softening of infills $\mu_s = 1.82$ (i.e. the ratio between the displacement when infills start to degrade and the displacement D_y, and the ratio between the force at which infills completely collapse and the yielding force $r_u = 0.39$. The effective mass m*, the transformation factor Γ and the period of the equivalent SDOF system were determined according to Fajfar (2000) and amount to 112 t, 1.32 and 0.22 s, respectively.

The reduction factor (the ratio between the accelerations in elastic spectrum and the acceleration at the yielding of the idealized system) can be, taking into account

the four parameters of the idealized pushover curve, determined by using formulae for specific inelastic spectra for infilled frames (Dolšek & Fajfar 2004b). For example, the reduction factor R_{NC}, which corresponds to the ductility demand at the NC limit state $\mu_{NC} = D_{NC}/D_y = 8.1\,\text{cm}/0.81\,\text{cm} = 10$, amounts to 2.68. The elastic spectral acceleration $S_{ae,NC} = 1.37\,\text{g}$ corresponding to the NC limit state is then obtained from the definition of the reduction factor by multiplying the reduction factor $R_{NC} = 2.68$ and the acceleration at the yielding of the equivalent SDOF system $S_{ay} = (F_y/\Gamma)/m^* = (745.4\,\text{kN}/1.32)/(112\,\text{t}) = 5.04\,\text{m/s}^2 = 0.51\,\text{g}$. Finally, the peak ground acceleration $a_{g,NC} = S_{ae,NC}/2.5 = 1.37\,\text{g}/2.5 = 0.55\,\text{g}$ is determined from $S_{ae,NC} = S_{ae}(T = 0.22\,\text{s})$ considering the spectral shape (Figure 5a). The NC point of the IN2 curve is indicated in Figure 7a. After this point a horizontal line is assumed (Section 2). The same procedure, as explained for the determination of the NC point, is used for determination of the point, which corresponds to the displacement of the idealized system at the beginning of the degradation of infills (i.e. point b presented in Figure 1). The last point, which is required for the construction of the IN2 curve corresponds to the yielding of the idealized system. It is defined by D_y and $a_{g,y} = S_{ay}/2.5 = 0.2\,\text{g}$.

The IN2 curve of the infilled frame is presented in Figure 7b. Some intermediate damage states are also indicated. For example, the first infill starts to degrade at the ground motion with the peak ground acceleration $a_g = 0.14\,\text{g}$. At $a_g = 0.27\,\text{g}$ all infills in the first storey are in the degrading stage and at $a_g = 0.34\,\text{g}$ all infills in the first storey collapse.

The NC limit state in the bare frame is attained at smaller peak ground acceleration than in the case of the infilled frame (0.45g versus 0.55 g). Nevertheless, the demand based on the seismic hazard for a 2475 year return period still exceeds the capacity at the NC limit state, like in the case of the bare frame.

3.6 *Probabilistic performance assessment*

For a probabilistic assessment the values of dispersion measures have to be known. The dispersion measure β_{DR} was assumed to amount to 0.4 for the bare frame and to 0.7 for the infilled frame. These values may be typical for buildings with moderate to long period and for buildings with short predominant period, respectively (Dolšek & Fajfar 2004b). For β_{CR}, β_{DU} and β_{CU} the value of 0.25 was adopted. Note that the adopted values of dispersion measures for uncertainty are in agreement with the total uncertainty dispersion measure $\beta_{UT} = (\beta_{DU}^2 + \beta_{CU}^2)^{0.5} = 0.35$ used in the SAC-FEMA seismic performance evaluation (FEMA 2000). The dispersion measure for the hazard β_H was arbitrarily assumed to be 0.3.

For the determination of the parameters of the IN2 curve and of the hazard curve b and k (Eq. (2)) (Cornell et al. 2002) the intervals have to be selected, in which a close agreement between the actual and approximates curves is required . Based on a previous study we choose the interval from 0.25 $a_{g,NC}$ to $a_{g,NC}$ for the approximation of the IN2 curve, and the interval from 0.25 $a_{g,NC}$ to 1.25 $a_{g,NC}$ for the approximation of the hazard curve. Therefore, the values of the parameter k are different for the bare and the infilled frame (2.59 versus 2.76) although the same hazard curve is used for both structures. It is obvious that the parameter b of the bare frame is equal to 1.0,

since the IN2 curve is a straight line. In the case of the infilled frame the parameter b amounts to 2.14.

The median value of the hazard function $\widetilde{H}(\widetilde{s_a^C})$ at the peak ground acceleration, which causes the NC limit state, was determined directly from the hazard curve (Figure 5b) and amounts to 1.447E-3 and 7.861E-4 for the bare and infilled frame, respectively. The parameter C_H is equal to 1.05 and C_f amounts to 2.11 and to 1.59 for the bare and infilled frame, respectively. The $P_{PL,x}$ for 50% confidence level was then calculated according to Eq. (1) by taking into account that $C_x = 1$ for $x = 0.5$. The probability of exceedance of the NC limit state for the bare frame amounts to 3.19E-3 (14.7% in 50 years). It is higher than that estimated for the infilled frame (1.30E-3, 6.3% in 50 years). In the case when only 10% chance is accepted that the probability of exceedance of the NC limit state is larger than the estimated probability $P_{PL,x=0.9}$ (i.e. a 90% confidence is required (Section 3.2)), the following values are obtained from Eqs. (2) and (1): $C_x = 3.23$ and $P_{PL,x=0.9} = 1.03\text{E-}2$ (40% in 50 years) for the bare frame, and $C_x = 1.79$ and $P_{PL,x=0.9} = 2.33\text{E-}3$ (11% in 50 years) for the infilled frame. The estimated $P_{PL,x=0.9}$ for the bare and infilled frame exceeds the acceptable (based on the conservative definition presented in Section 3.2) probability of exceedance of the NC limit state (4.04E-4, 2% in 50 years) for a factor of about 25 and 6 for the bare and infilled frame, respectively.

4 Conclusions

A simplified method for the probabilistic seismic assessment of buildings has been summarized. The method is basically the SAC-FEMA approach, in which the most demanding part, i.e. the Incremental Dynamic Analysis (IDA), is replaced by the incremental N2 method, which is based on pushover analysis and response spectrum approach. Default values for dispersion measures are needed for practical applications. The method was applied for a bare and an infilled reinforced concrete frame. The results of analyses indicate that the infills can completely change the distribution of damage throughout the structure. The estimated probability of exceedance of the NC limit state was substantially lower for the infilled frame than for the bare frame. For both structures, however, the estimated probabilities of failure are much larger that the acceptable ones. Such a result was expected because both structures represent old structures not designed for seismic resistance. The large difference between the estimated and acceptable probabilities of failure can be attributed also to conservative assumptions used in the test examples, especially those related to the definition of failure and to the definition of the acceptable probability of failure.

The proposed method has like any other simplified method its limitations which are basically the same as those which apply to the basic N2 method (Fajfar 2000) and to the SAC-FEMA method (Cornell et al. 2002). Additional studies are needed especially for the determination of dispersion measures for randomness and uncertainty.

References

Cornell, C.A., Jalayar, F., Hamburger, R.O. & Foutch, D.A. 2002. Probabilistic basis for 2000 SAC Federal Emergency Management Agency Steel Moment Frame Guidelines. *Journal of Structural Engineering ASCE* 128(4):526–533.

Deierlein, G. 2004. Overview of a comprehensive framework for earthquake performance assessment, *Proceedings of the International Workshop on Performance-Based Seismic Design – Concepts and Implementation*, Bled, Slovenia, Fajfar P., Krawinkler H. eds., PEER Report 2004/05:15–26, Berkeley.

Vamvatsikos, D. & Cornell, C.A. 2002. Incremental Dynamic Analysis. *Earthquake Engineering and Structural Dynamics* 31:491–514.

Fajfar, P. 2000. A nonlinear analysis method for performance-based seismic design. *Earthquake Spectra* 16(3):573–592.

Dolšek, M. & Fajfar, P. 2004a. IN2 – A Simple Alternative for IDA. *Proceedings of the 13th World Conference on Earthquake Engineering*, Vancouver, Canada, paper 3353.

Dolšek, M. & Fajfar, P. 2007. Simplified probabilistic seismic performance assessment of plan-asymmetric buildings. *Earthquake Engineering and Structural Dynamics*, 36:2021–2041.

Dolšek, M. & Fajfar, P. 2005. Simplified non-linear seismic analysis of infilled reinforced concrete frames. *Earthquake Engineering and Structural Dynamics* 34(1):49–66.

Dolšek, M. & Fajfar, P. 2004b. Inelastic spectra for infilled reinforced concrete frames. *Earthquake Engineering and Structural Dynamics* 33(15):1395–1416.

FEMA 350. 2000. *Recommended seismic design criteria for new steel moment frame buildings*. SAC Joint Venture, Federal Emergency Management Agency, Washington (DC).

Carvalho, E.C. & Coelho, E. (Editors). 2001. *Seismic assessment, strengthening and repair of structures*. ECOEST2-ICONS Report No.2, European Commission – "Training and Mobility of Researchers" Programme.

PEER. 1999. *Open System for Earthquake Engineering Simulation (OpenSees)*. Pacific Earthquake Engineering Research Center, University of California, Berkeley, http://opensees.berkeley.edu/

Fajfar, P., Dolšek, M., Marušić, D. & Stratan, A. 2006. Pre- and post-test mathematical modelling of a plan-asymmetric reinforced concrete frame building. *Earthquake Engineering and Structural Dynamics* 35:1359–1379.

Peruš, I., Poljanšek, K. & Fajfar, P. 2006. Flexural deformation capacity of rectangular RC columns determined by the CAE method. *Earthquake Engineering and Structural Dynamics* 35(12):1453–1470.

CEN. 2005. *Eurocode 8: Design of structures for earthquake resistance. Part 3: Strengthening and repair of buildings*. Brussels.

Dolšek, M. & Fajfar, P. 2007. Effects of masonry infills on the seismic response of a four storey reinforced concrete frame – deterministic assessment. *Engineering Structures*, submitted.

Melchers, R.E. 1999. *Structural Reliability Analysis and Prediction*, Second Edition. John Wiley & Sons.

Yun, S.-Y., Hamburger, R.O., Cornell, C.A. & Foutch, D.A. 2002. Seismic performance evaluation for steel moment frames. *Journal of Structural Engineering ASCE* 128(4):534–545.

LESSLOSS. 2006. *Risk Mitigation for Earthquakes and Landslides*. Integrated Research & Development Project of the European Commission. Deliverable 78 – Applications of probabilistic seismic assessment methods to selected case studies. Sub-Project 9 – Probabilistic risk assessment: methods and applications. http://www.lessloss.org.

Chapter 17

Computational simulation of the seismic response of buildings with energy dissipating devices

Alex H. Barbat, Pablo Mata & Sergio Oller

Technical University of Catalonia, Barcelona, Spain

Juan C. Vielma

Lisandro Alvarado University, Barquisimeto, Venezuela

ABSTRACT: In this work, the nonlinear dynamic response of RC buildings with energy dissipating devices is studied using advanced computational techniques. A fully geometric and constitutive nonlinear model is used for describing the dynamic behavior of structures. The equations of motion are expressed in terms of cross sectional forces and strains and its weak form is solved using the displacement based finite element method. A suitable version of Newmark's scheme is used in updating the kinematics variables in a classical Newton type iterative scheme. Material points of the cross section are assumed to be composed of several simple materials with their own constitutive laws. The mixing theory is used to treat the resulting composite. A specific finite element based on the beam theory is proposed for the dissipators including constitutive relations. Finally, several numerical tests are carried out to validate the proposed model.

1 Introduction

Conventional seismic design practice permits designing reinforced concrete (RC) structures for forces lower than those expected from the elastic response on the premise that the structural design assures significant structural ductility Hanson *et al.* (1993). Frequently, the dissipative zones are located near the beam-column joints and, due to cyclic inelastic incursions during earthquakes, several structural members can suffer a great amount of damage. This situation is generally considered economically acceptable if life safety and collapse prevention are achieved.

In the last decades, new techniques based on adding devices to the buildings with the main objective of dissipating the energy exerted by the earthquake and alleviating the ductility demand on primary structural elements have improved the seismic behavior of the structures Soong & Dargush (1997). The purpose is to control the seismic response of the buildings by means of a set of dissipating devices which constitutes the *control system*, adequately located in the structure. In the case of *passive energy dissipating devices* (EDD), an important part of the energy input is absorbed and dissipated; therefore, concentrating the nonlinear phenomenon in the devices without the need of an external energy supply.

Several works showing the ability of EDDs in controlling the seismic response of structures are available; for example, in reference Fu & Kasai (2002) the response of

framed structures equipped with viscoelastic and viscous devices is compared; in reference Kasai *et al.* (1998) an approximated method is used to carry out a comparative study considering metallic and viscous devices. Aiken (1996) presents the contribution of the extra energy dissipation due to EDDs as an *equivalent damping* added to the linear bare structure and gives *displacement reduction factors* as a function of the added damping ratio. A critical review of reduction factors and design force levels can be consulted in reference Lin & Chang (2003). A method for the preliminary design of passively controlled buildings is presented in reference Connor *et al.* (1997). Lin & Chopra (2003) study the accuracy of estimating the dynamic response of asymmetric buildings equipped with EDDs, when they are replaced by their energetic equivalent viscous dampers. Other procedures for the analysis and design of structures with EDDs can be consulted in reference Clark *et al.* (1999).

Today, only a few countries have codes to design RC buildings with EDDs. Particularly, in United States the US *Federal Emergency Management Agency* (FEMA) gives code provisions and standards for the design of EDDs devices to be used in buildings. In Europe, the efforts have been focused on developing codes for base isolation but not for the use of EDDs.

The design methods proposed for RC structures are mainly based on supposing that the behavior of the bare structure remains elastic, while the energy dissipation relies on the control system. However, experimental and theoretical evidence show that inelastic behavior can also occur in the structural elements during severe earthquakes (Shen & Soong 2005). In order to perform a precise dynamic nonlinear analysis of passively controlled buildings sophisticated numerical tools became are necessary for both academics and practitioners, Mata *et al.* (2006).

There is agreement that fully three-dimensional numerical techniques constitute the most precise tools for the simulation of the the seismic behavior of RC buildings. However, the computing time usually required for real structures makes many applications unpractical. Considering that most of the elements in RC buildings are columns and beams, one dimensional formulation for structural elements appear as a solution combining both numerical precision and reasonable computational costs Mata *et al.* (2007b). Experimental evidence shows that inelasticity in beam elements can be formulated in terms of cross sectional quantities, Bayrak *et al.* (2001). Some formulations of this type have been extended for considering geometric nonlinearities, Simo *et al.* (1984). An additional refinement is obtained considering inhomogeneous distributions of materials on arbitrarily shaped beam cross sections, Kumar *et al.* (2004). In this case, the constitutive relationship at cross sectional level is deduced by integration and, therefore, the mechanical behavior of beams with complex combinations of materials can be simulated.

Formulations for beams considering both constitutive and geometric nonlinearity are rather scarce; most of the geometrically nonlinear models are limited to the elastic case, Ibrahimbegovic (1995) and the inelastic behavior has been mainly restricted to plasticity, Simo *et al.* (1984). Recently, Mata *et al.* (2007b, 2008a) have extended the geometrically exact formulation for beams due to Reissner-Simo (Reissner 1973, Simo 1985, Simo & Vu-Quoc 1988) to an arbitrary distribution of composite materials on the cross sections for the static and dynamic cases.

From the numerical point of view, EDDs usually have been described in a global sense by means of force–displacement or moment–curvature relationships, Soong & Dargush

(1997), which attempt to capture appropriately the energy dissipating capacity of the devices (see Mata *et al.* 2007a and 2008b). The inclusion of EDDs in software packages for the seismic analysis of RC structures is frequently done by means of linking elements equipped with the mentioned nonlinear relationships. The relative displacement and/or rotation between the anchorage points activate the dissipative mechanisms of the device.

In this work, a fully geometric and constitutive nonlinear formulation for beam elements is developed. A fiber–like approach is used for representing arbitrary distributions of composite materials on the plane beam cross sections. EDDs are considered as beam elements without rotational degrees of freedom. Thermodynamically consistent constitutive laws are used for concrete, longitudinal and transversal steel reinforcements and EDDs. The mixing rule is employed for the treatment of the resulting composite. A brief description of the damage indices capable of estimate the remaining load carrying capacity of the buildings is also given. Finally, the results obtained from numerical simulations showing the ability of the proposed formulation in simulating the static and dynamic inelastic response of RC buildings with and without EDDs are provided.

2 Finite deformation formulation for structural elements

2.1 *Beam model*

The original geometrically exact formulation for beams due to Simo & Vu Quoc (1986) is expanded here for considering an intermediate curved reference configuration according to Ibrahimbegovic (1995). The geometry and the kinematics of the beams are developed in the nonlinear differential manifold[1] $\mathbb{R}^3 \times SO(3)$. Let $\{\hat{\mathrm{E}}_i\}$ and $\{\hat{\mathrm{e}}_i\}$ be the spatially fixed *material* and *spatial* frames[2], respectively. The straight reference beam is defined by the curve $\hat{\varphi}_{00} = S\hat{\mathrm{E}}_1$, with $S \in [0, L]$ its arc–length coordinate. Beam cross sections are described by means of the coordinates ξ_β directed along $\{\hat{\mathrm{E}}_\beta\}$ and the position vector of any material point is $\hat{X} = S\hat{\mathrm{E}}_1 + \Sigma_\beta\, \xi_\beta\, \hat{\mathrm{E}}_\beta$.

The curved reference beam is defined by means of the spatially fixed curve given by $\hat{\varphi}_0 = \Sigma_i \hat{\varphi}_{0i}(S)\hat{\mathrm{e}}_i \in \mathbb{R}^3$. Additionally, each point on this curve has rigidly attached an orthogonal local frame $\hat{t}_{0i}(S) = \boldsymbol{\Lambda}_0 \hat{\mathrm{E}}_i \in \mathbb{R}^3$, where $\boldsymbol{\Lambda}_0 \in SO(3)$ is the orientation tensor. The beam cross section $A(S)$ is defined considering the local coordinate system ξ_β but directed along $\hat{t}_{0\beta}$. The planes of the cross sections are normal to the vector tangent to the reference curve[3], *i.e.* $\hat{\varphi}_{0,s} = \hat{t}_{01}(S)$. The position vector of a material point on the curved reference beam is $\hat{x}_0 = \hat{\varphi}_{0i} + \Sigma_\beta\, \boldsymbol{\Lambda}_0 \xi_\beta\, \hat{\mathrm{E}}_{0\beta}$. The motion deforms points on the curved reference beam from $\hat{\varphi}_{0,S}$ to $\hat{\varphi}_{S,t}$ (at time t) adding a translational displacement $\hat{u}(S)$ and the local orientation frame is simultaneously rotated together with the beam cross section, from $\boldsymbol{\Lambda}_0(S)$ to $\boldsymbol{\Lambda}(S,t)$ by means of the *incremental rotation tensor* as $\boldsymbol{\Lambda} = \boldsymbol{\Lambda}_n \boldsymbol{\Lambda}_0 \equiv \Sigma_i\, \hat{t}_i \otimes \hat{\mathrm{E}}_i \in SO(3)$ (see Figure 1).

[1] The symbol $SO(3)$ is used to denote the finite rotation manifold

[2] The indices i and β range over and {1,2,3} and {2,3}, respectively.

[3] The symbol $(\bullet)_x$ is used to denote partial differentiation of $(\bullet)$ with respect to x.

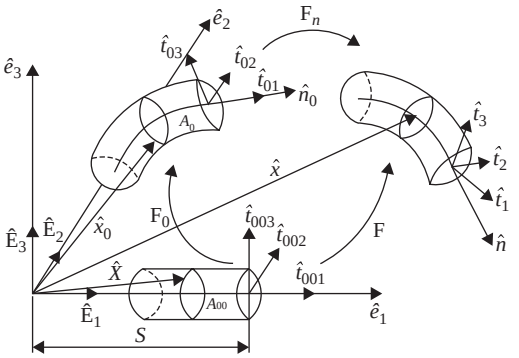

Figure 1 Configurational description of the beam.

In general, the normal vector $\hat{t}_1$ does not coincide with $\hat{\varphi}_{,S}$ because of the shearing, Simo (1985). The position vector of a material point on the current beam is

$$\hat{x}(S,\xi_\beta,t) = \hat{\varphi}_{S,t} + \sum_\beta \xi_\beta \hat{t}_\beta(S,t) = \hat{\varphi} + \sum_\beta \boldsymbol{\Lambda}\xi_{\beta\hat{\mathrm{E}}_\beta} \tag{1}$$

Equation (1) implies that the current beam configuration is completely determined by the pairs $(\hat{\varphi}, \boldsymbol{\Lambda}) \in \mathbb{R}^3 \times SO(3)$. The *deformation gradient* is defined as the gradient of the deformation mapping of Equation (1) and determines the strain measures at any material point of the beam cross section Simo & Vu-Quoc (1986). The deformation gradients of the curved reference beam and of the current beam referred to the straight reference configuration are denoted by $\mathbf{F}_0$ and $\mathbf{F}$, respectively. The deformation gradient $\mathbf{F}_n := \mathbf{F}\mathbf{F}_0^{-1}$ is responsible for the development of strains and can be expressed as, Kapania (2003) and Mata *et al.* (2007).

$$\mathbf{F}_n = \mathbf{F}\mathbf{F}_0^{-1} = \frac{1}{|\mathbf{F}_0|}\left[\hat{\varphi}_{,S} - \hat{t}_1 + \tilde{\boldsymbol{\omega}}_n \sum_\beta \xi_\beta \hat{t}_\beta\right] \otimes \hat{t}_{01} + \boldsymbol{\Lambda}_n \tag{2}$$

where $|\mathbf{F}_0|$ is the determinant of $\mathbf{F}_0$ and $\tilde{\boldsymbol{\omega}}_n = \boldsymbol{\Lambda}_{n,S}\boldsymbol{\Lambda}_n^T$ is the curvature tensor relative to the curved reference beam. In Equation (2) the term defined as $\tilde{\gamma}_n = \hat{\varphi}_{,S} - \hat{t}_1$ corresponds to the reduced strain measure of shearing and elongation, Kapania (2003) and Simo (1985), with material description given by $\hat{\Gamma} = \boldsymbol{\Lambda}^T\tilde{\gamma}$.The material representation of $\mathbf{F}_n$ is obtained as $\mathbf{F}_n^m = \boldsymbol{\Lambda}^T\mathbf{F}_n\boldsymbol{\Lambda}_0$.

Removing the rigid body component from $\mathbf{F}_n$, it is possible to construct the strain tensor $\varepsilon_n = \mathbf{F}_n - \boldsymbol{\Lambda}_n$, which conjugated to the asymmetric *First Piola Kirchhoff* (FPK) stress tensor $P = \hat{P}_i \otimes \hat{t}_{0i}$ referred to the curved reference beam, Simo (1985). $\hat{P}_i$ is the FPK stress vector acting on the *deformed face* in the current beam corresponding to the normal $\hat{t}_{0i}$ in the curved reference configuration. The spatial strain vector acting on the current beam cross section is obtained as $\hat{\varepsilon}_n = \varepsilon_n\hat{t}_{01}$.

By other hand, the spatial form of the *stress resultant* $\hat{n}$ and the *stress couple* $\hat{m}$ vectors can be estimated from the stress vector $\hat{P}_1$ according to

$$\hat{n}(S) = \int_A \hat{P}_1 \, dA; \quad \hat{m}(S) = \int_A (\hat{x} - \hat{\varphi}) \hat{P}_1 \, dA; \tag{3}$$

The material form of $\hat{P}_j$ and ε_n are obtained by means of the pull-back operation as $\hat{\varepsilon}_n = \boldsymbol{\Lambda}^T \varepsilon_n$, $\hat{P}_j^m = \boldsymbol{\Lambda}^T \hat{P}_j$, $\hat{n}^n = \boldsymbol{\Lambda}^T \hat{n}$ and $\hat{m}^n = \boldsymbol{\Lambda}^T \hat{m}$ respectively.

An objective measure of the *strain rate* vector s_n acting on any material point on the current beam cross section can be deduced following the results presented by Mata *et al.* (2008a) and using the definition of the Lie derivative operator $[\overset{\nabla}{\bullet}]$ given in Mata *et al.* (2007b) as follows:

$$s_n = [\overset{\nabla}{\dot{\hat{\varepsilon}}}_n] = [\overset{\nabla}{\dot{\hat{\gamma}}}_n] + [\overset{\nabla}{\dot{\tilde{\boldsymbol{\omega}}}}_n] \sum_\beta \xi_\beta \hat{t}_\beta = \hat{\varphi}_{,S} - \hat{\boldsymbol{\upsilon}}_n \tilde{\varphi}_{,S} + \hat{\boldsymbol{\upsilon}}_{n,S} \sum_\beta \xi_\beta \hat{t}_\beta \tag{4}$$

where $\tilde{\boldsymbol{\upsilon}}_n = \dot{\boldsymbol{\Lambda}}_n \boldsymbol{\Lambda}_n^T$ is the current *spin* or angular velocity of the beam cross section with respect to the curved reference beam. The material form of Equation (4) is $\hat{S}_n = \boldsymbol{\Lambda}^T{}_{\hat{s}_n}$. According to the developments given by Antman (1991), the classical form of the *equations of motion of the Cosserat beam* for the static case are

$$\hat{n}_{,S} + \hat{n}_p = A_{\rho 0} \ddot{\hat{\varphi}} + \underbrace{\tilde{\boldsymbol{\alpha}}_n \hat{S}_{\rho 0} + \tilde{\boldsymbol{\upsilon}}_n \tilde{\boldsymbol{\upsilon}}_n \hat{S}_{\rho 0}}_{D_1} \tag{5a}$$

$$\hat{m}_{,S} + \hat{\varphi}_{,S} \times \hat{n} + \hat{m}_p = \boldsymbol{I}_{\rho 0} \hat{\alpha}_n + \tilde{\boldsymbol{\upsilon}}_n \boldsymbol{I}_{\rho 0} \hat{\upsilon}_n + \underbrace{\hat{S}_{\rho 0} \times \ddot{\hat{\varphi}}}_{D_2} \tag{5b}$$

where $\hat{n}_p$ and $\hat{m}_p$ are the external *body force* and *body moment* per unit of reference length at time t, $A_{\rho 0}$, $\hat{S}_{\rho 0}$ and $I_{\rho 0}$ are the cross sectional mass density, the first mass moment density and the second mass moment density per unit of length of the curved reference beam, respectively; their explicit expressions can be consulted in Kapania (2003) and Simo & Vu-Quoc (1986). $\tilde{\boldsymbol{\alpha}}_n \equiv \ddot{\boldsymbol{\Lambda}}_n \boldsymbol{\Lambda}_n^T - \tilde{\boldsymbol{\upsilon}}_n^2$ is the angular acceleration of the beam cross section and $\hat{\upsilon}_n$ and $\hat{\alpha}_n$ are the axial vectors of $\tilde{\boldsymbol{\upsilon}}_n$ and $\tilde{\boldsymbol{\alpha}}_n$, respectively. For most of the practical cases, the terms D_1 and D_2 can be neglected or added to the external forces and moments.

Considering a kinematically admissible variation[4] $\hat{h} \equiv (\delta\hat{\varphi}, \delta\hat{\theta})$ of the pair $(\hat{\varphi}, \boldsymbol{\Lambda})$, taking the dot product with Eqs. (5a) and (5b), integrating over the length of the curved reference beam and integrating by parts, we obtain the nonlinear functional $G(\hat{\varphi}, \boldsymbol{\Lambda}, h)$ corresponding to the *weak form of the balance equations,* Ibrahimbegovic (1995) and

[4] Supposing that $\boldsymbol{\Lambda}$ is parameterized in terms of the spatial rotation vector and following the results of reference it is possible to show that $\delta\boldsymbol{\Lambda} = \delta\hat{\theta} \times \boldsymbol{\Lambda}$ with $\delta\hat{\theta}$ an admissible variation of the rotation vector.

Simo & Vu-Quoc (1986), which is another way of writing the *virtual work principle*,

$$G(\hat{\varphi}, \boldsymbol{\Lambda}, h) = \int_L [(\delta\hat{\varphi}_{,S} - \delta\hat{\theta} \times \hat{\varphi}_{,S}) \cdot \hat{n} + \delta\hat{\theta}_{,S} \cdot \hat{m}] dS + \int_L [\delta\hat{\varphi} A_{\rho 0} \ddot{\hat{\varphi}} + \delta\hat{\theta} \cdot (I_{\rho 0}\hat{\alpha}_n + \tilde{\boldsymbol{v}}_n I_{\rho 0}\hat{v}_n)] dS - \int_L [\delta\hat{\varphi} \cdot \hat{n}_p + \delta\hat{\theta} \cdot \hat{m}_p] dS - (\delta\hat{\varphi} \cdot \hat{n} + \delta\hat{\theta} \cdot \hat{m})|_0^L = 0 \quad (6)$$

The terms $(\delta\hat{\varphi}_{,S} - \delta\hat{\theta} \times \hat{\varphi}_{,S})$ and $\delta\hat{\theta}_{,S}$ appearing in Equation (6) correspond to the co–rotated variations of the reduced strain measures $\hat{\gamma}_n$ and $\hat{\omega}_n$ in spatial description.

2.2 *Energy dissipating devices*

The finite deformation model for EDDs is obtained from the beam model releasing the rotational degrees of freedom and supposing that all the mechanical behavior of the device is described in terms of the evolution of a unique material point in the middle of the resulting bar.

The current position of a point in the EDD bar is obtained from Equation (1) and considering that $\xi_\beta = 0$ as $\hat{x}(S,t) = \hat{\varphi}(S,t)$. Supposing that the current orientation of the EDD bar of initial length L^* is given by the tensor $\boldsymbol{\Lambda}^*(t)$, ($\boldsymbol{\Lambda}^*_{,S} = 0$, $\dot{\boldsymbol{\Lambda}}^* = 0$), the spatial position of the *dissipative point* in the EDD is obtained as $\hat{\varphi}(L^*/2, t)$ where $L^*/2$ is the arch–length coordinate of the middle point in the bar element and the axial strain and the axial strain rate in the dissipative point are obtained from Eqs. (2) and (4) as

$$\hat{\Gamma}_1(t) = \{(\boldsymbol{\Lambda}^{*T}\hat{\varphi}_{,S}) \cdot \hat{E}_1\}|_{(L^*/2,t)} - 1 \quad (7a)$$

$$\dot{\hat{\Gamma}}_1(t) = \{(\boldsymbol{\Lambda}^{*T}(\hat{\varphi}_{,S} - \tilde{\boldsymbol{v}}_n\hat{\varphi}_{,S})) \cdot \hat{E}_1\}|_{(L^*/2,t)} \approx \frac{d}{dt}\hat{\Gamma}_1(t)\Big|_{(L^*/2,t)} \quad (7b)$$

Finally, the contribution of the EDD bar to the functional of Equation (6), written in the material description, is given by

$$G_{EDD} = \int_{L*} n_1^m \delta\hat{\Gamma}_1 \, dS + \{(\boldsymbol{\Lambda}^{*T}\delta\hat{\varphi})^T [\boldsymbol{M}]_d (\boldsymbol{\Lambda}^{*T}\ddot{\hat{\varphi}})\}|_{(L^*/2,t)} \quad (8)$$

where it was assumed that $I_{\rho 0} \approx 0$, *i.e.* the contribution of the EDDs to the rotational mass of the system is negligible and $[\boldsymbol{M}]_d$ is the EDD's *translational inertia* matrix, *i.e.* the mass of the control system is supposed to be concentrated on the central point of the bar. The term $\delta\hat{\Gamma}_1 = (\boldsymbol{\Lambda}^{*T}(\hat{\varphi}_{,S} - \tilde{\boldsymbol{v}}_n\hat{\varphi}_{,S})) \cdot \hat{E}_1$ corresponds to the material form of the variation of the axial strain in the EDD.

3 Constitutive models

In this work, material points on the cross sections are considered as formed by a *composite material* corresponding to a homogeneous mixture of different simple *components*, each of them with its own constitutive law (see Figure 2). The resulting

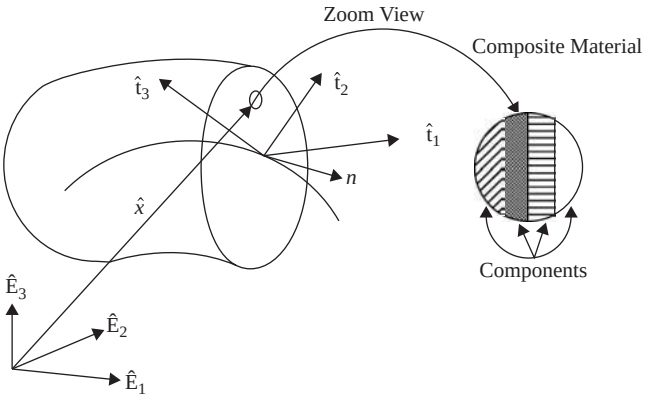

Figure 2 Cross section showing the composite associated to a material point.

behavior is obtained by means of the *mixing theory*. Two kinds of nonlinear constitutive models for simple materials are used: the *damage* and *plasticity* models. The constitutive models are formulated in terms of the material form of the FPK stress and strain vectors, $\hat{P}_1^m$ and $\hat{\varepsilon}_n$, respectively, Mata *et al.* (2007b and 2008a).

3.1 *Degrading materials: damage model*

The damage theory employed in this work is based on a special damage yielding function which differentiates the mechanical response for tension or compression components of the stress vector. The progress of the damage is based on the evolution of a scalar damage parameter Oliver *et al.* (1990). Starting from an adequate form of the free energy density and considering the fulfillment of the Clasius–Plank inequality and applying the Coleman's principle (see Mata *et al.* 2007b and 2008c) the following constitutive relation in material form is obtained:

$$\hat{P}_1^m = (1-d)\boldsymbol{\mathcal{C}}^{me}\hat{\varepsilon}_n = \boldsymbol{\mathcal{C}}^{ms}\hat{\varepsilon}_n = (1-d)\hat{P}_{01}^m \tag{9}$$

where $\boldsymbol{\mathcal{C}}^{me}$ and $\boldsymbol{\mathcal{C}}^{ms} = (1-d)\boldsymbol{\mathcal{C}}^{me}$ is the *secant constitutive tensor*. Equation (9) shows that the FPK stress vector is obtained from its elastic counterpart by multiplying it by the factor $(1-d)$.

The damage yield criterion $\mathcal{F}$, Hanganu *et al.* (2003) and Barbat *et al.* (1997), is defined as a function of the undamaged elastic free energy density and written in terms of the components of the material form of the undamaged principal stresses, $\hat{P}_{01}^m$, as

$$\mathcal{F} = \mathcal{P} - f_c = [1 + r(n-1)]\sqrt{\sum_{i=1}^{3}(P_{\rho 0i}^m)^2} - f_c \leq 0 \tag{10a}$$

where $\mathcal{P}$ is the equivalent stress, r and n are given in function of the tension and compression strengths f_c and f_t and the parts of the free energy density developed

when the tension, $(\Psi_t^0)_L$, or compression, $(\Psi_t^0)_c$, limits are reached; these quantities are defined as

$$(\Psi_{t,c}^0)_L = \sum_{i=1}^{3} \frac{\langle p_{p0i}^m \rangle \varepsilon_{ni}}{2\rho_0}, \quad \Psi_t^0 = (\Psi_t^0)_L + (\Psi_c^0)_L \tag{10b}$$

$$f_t = (2\rho\Psi_t^0 E_0)_L^{\frac{1}{2}}, \quad f_c = (2\rho\Psi_c^0 E_0)_L^{\frac{1}{2}}, \quad n = \frac{f_c}{f_t}, \quad r = \frac{\sum_{i=1}^{3} \langle P_{p0i}^m \rangle}{\sum_{i=1}^{3} |P_{p0i}^m|} \tag{10c}$$

A more general expression equivalent to that given in Equation (10a), Barbat *et al.* (1997), is given by

$$\overline{\mathcal{F}} = \mathcal{G}(\mathcal{P}) - \mathcal{G}(f_c) \tag{11}$$

The function $\mathcal{G}(\mathcal{P})$ has the following general expression Oliver *et al.* (1990):

$$\mathcal{G}(\chi) = 1 - \frac{\overline{\mathcal{G}}(\chi)}{\chi} = 1 - \frac{\chi^*}{\chi} e^{\kappa\left(1-\frac{\chi^*}{\chi}\right)} \tag{12}$$

where the term $\overline{\mathcal{G}}(\chi)$ gives the initial yield stress for certain value of the scalar parameter $\chi = \chi^*$ and for $\chi \to \infty$ the final strength is zero. The parameter κ of Equation (12) is calibrated to obtain an amount of dissipated energy equal to the specific fracture energy of the material $g_f^d = G_f^d / l_c$; where G_f^d is the tensile fracture energy and l_c is the characteristic length of the fractured domain.

The evolution law for the internal damage variable d is given by

$$\dot{d} = \dot{\mu} \frac{\partial \overline{\mathcal{F}}}{\partial \mathcal{P}} = \dot{\mu} \frac{\partial \mathcal{G}}{\partial \mathcal{P}} \tag{13}$$

where $\dot{\mu} = \dot{\mathcal{P}} \geq 0$ is the *damage consistency* parameter Mata *et al.* (2007b). Finally, the Kuhn-Tucker relations: (a) $\dot{\mu} \geq 0$, (b) $\overline{\mathcal{F}} \leq 0$, (c) $\dot{\mu}\overline{\mathcal{F}} = 0$, have to be employed to derive the unloading–reloading conditions *i.e.* if $\overline{\mathcal{F}} < 0$ the condition (c) imposes $\dot{\mu} = 0$; on the contrary, if $\dot{\mu} > 0$ then $\overline{\mathcal{F}} = 0$.

3.1.1 *Viscosity*

The rate dependent behavior is considered by using the Maxwell model. The FPK stress vector $\hat{P}_1^{mt}$ is obtained as the sum of a rate independent part $\hat{P}_1^m$, Equation (9), and a viscous component $\hat{P}_1^{mv}$ as

$$\hat{P}_1^{mt} = \hat{P}_1^m + \hat{P}_1^{mv} = \boldsymbol{\mathcal{C}}^{mv}\hat{\varepsilon}_n + \boldsymbol{\eta}^{sm}\hat{\mathbf{S}}_n = (1-d)\boldsymbol{\mathcal{C}}^{me}\left(\hat{\varepsilon}_n + \frac{\eta}{E_0}\hat{\mathbf{S}}_n\right) \tag{14}$$

where $\boldsymbol{\eta}^{sm} = \eta / E_0 \boldsymbol{\mathcal{C}}^{ms}$ is the *secant viscous* constitutive tensor, $\boldsymbol{\mathcal{C}}^{mv} = (1-d)\boldsymbol{\mathcal{C}}^{me}$, and the parameter η is the viscosity. For the case of a completely damaged material ($d = 1$),

the corresponding stresses are zero. The linearized increment of the FPK stress vector (material and co-rotated forms) are calculated as

$$\Delta\hat{P}_1^{mt} = \boldsymbol{\mathcal{C}}^{mv}\,\Delta\hat{\varepsilon}_n + \boldsymbol{\eta}^{sm}\,\Delta\hat{S}_n, \quad \Delta[\overset{\triangledown}{\hat{P}}_1^{t}] = \boldsymbol{\mathcal{C}}^{sv}\,\Delta[\overset{\triangledown}{\hat{\varepsilon}}_n] + \boldsymbol{\eta}^{ss}\,\Delta[\overset{\triangledown}{\hat{s}}_n] \tag{15}$$

where $\boldsymbol{\mathcal{C}}^{sv} = \boldsymbol{\Lambda}\boldsymbol{\mathcal{C}}^{mv}\boldsymbol{\Lambda}^T$ and $\boldsymbol{\mathcal{C}}^{sv} = \boldsymbol{\Lambda}\boldsymbol{\eta}^{ss}\boldsymbol{\Lambda}^T$. The explicit form of the terms $\Delta\hat{S}_n$ and $[\hat{S}_n]$ can be consulted in reference Mata *et al.* (2008a). Finally, the material description of the tangent constitutive tensor $\boldsymbol{\mathcal{C}}^{mv}$ considering the viscous effect is given by Barbat *et al.* (1997)

$$\boldsymbol{\mathcal{C}}^{mv} = (\mathbf{I} - \mathbf{D}^{me})\boldsymbol{\mathcal{C}}^{me} = \mathbf{I} - \left[\mathbf{I} + \frac{d\mathcal{G}}{d\mathcal{P}^m}(\hat{P}_{01}^m + \hat{P}_1^{mv0}) \otimes \frac{\partial\mathcal{P}^m}{\partial\hat{P}_{01}^m}\right] \tag{16}$$

3.2 *Plastic materials*

In the case of materials which can undergo non-reversible deformations the plasticity model formulated in the material configuration is used for predicting their mechanical response. Assuming small elastic, finite plastic deformations, an adequate form of the free energy density and analogous procedures as those for the damage model we have

$$\hat{P}_1^m = \rho_0 \frac{\partial\Psi(\hat{\varepsilon}_n^e, k_p)}{\partial\hat{\varepsilon}_n^e} = \boldsymbol{\mathcal{C}}^{ms}(\hat{\varepsilon_n} - \hat{\varepsilon}_n^P) = \boldsymbol{\mathcal{C}}^{me}\hat{\varepsilon}_n^e \tag{17}$$

where the $\hat{\varepsilon}_n^e$ is the elastic strain calculated subtracting the plastic strain $\hat{\varepsilon}_n^P$ from the total strain $\hat{\varepsilon}_n$ and ρ_0 is the density in the material configuration.

Both, the yield function, $\mathcal{F}_p$, and plastic potential function, $\mathcal{G}_p$ are formulated in terms of the FPK stress vector $\hat{P}_1^m$ and the plastic damage internal variable k_p as

$$\mathcal{F}_p(\hat{P}_1^m, k_p) = \mathcal{P}_p(\hat{P}_1^m) - f_p(\hat{P}_1^m, k_p) = 0, \;\; \mathcal{G}_p(\hat{P}_1^m, k_p) = \mathcal{K} \tag{18}$$

where $\mathcal{F}_p(\hat{P}_1^m, k_p)$ is the equivalent stress, which is compared with the *hardening* function $f_p(\hat{P}_1^m, k_p)$ and $\mathcal{K}$ is a constant value, Oller *et al.* (1996a). In this work, k_p constitutes a measure of the energy dissipated during the plastic process and, therefore, it is well suited for materials with *softening* and is defined by Oller *et al.* (1996b) as

$$g_f^P = \frac{G_f^P}{l_c} = \int_{t=0}^{\infty} \hat{P}_1^m \cdot \dot{\varepsilon}_n^P \, dt, \quad 0 \leq \left[k_p = \frac{1}{g_f^P}\int_{t=0}^{t} \hat{P}_1^m \cdot \dot{\varepsilon}_n^P \, dt\right] \leq 1 \tag{19}$$

where G_f^P is the specific plastic fracture energy of the material in tension and l_c is the length of the fractured domain defined in analogous manner as for the damage model. The integral term in Equation (19) corresponds to the energy dissipated by means of plastic work.

The flow rules for the internal variables $\hat{\varepsilon}_n^P$ and k_p are defined as

$$\dot{\hat{\varepsilon}}_n^P = \dot{\lambda}\frac{\partial\mathcal{G}_p}{\partial\hat{P}_1^m}, \quad k_p = \dot{\lambda}\hat{\varrho}(\hat{P}_1^m, k_p, G_f^P) \cdot \frac{\partial\mathcal{G}_p}{\partial\hat{P}_1^m} = \hat{\varrho}(\hat{P}_1^m, k_p, G_f^P) \cdot \dot{\hat{\varepsilon}}_n^P \tag{20}$$

where $\dot{\lambda}$ is the plastic consistency parameter and $\hat{\varrho}$ is the *hardening* vector, Oller *et al.* (1996a). Regarding the hardening function of Equation (18), the following evolution equation has been proposed:

$$f_p(\hat{P}_1^m, k_p) = r\sigma_t(k_p) + (1-r)\sigma_c(k_p) \tag{21}$$

where r has been defined in Equation (10c) and the scalar functions $\sigma_t(k_p)$ and $\sigma_c(k_p)$ describe the evolution of the yielding threshold in uniaxial tension and compression tests, respectively.

As it is a standard practice in plasticity, the loading/unloading conditions are derived in the standard form from the Kuhn-Tucker relations formulated for problems with unilateral restrictions, *i.e.* (a) $\dot{\lambda} \geq 0$, (b) $\mathcal{F}_p \leq 0$ and (c) $\dot{\lambda}\mathcal{F}_p = 0$. Starting from the plastic consistency condition $\dot{\mathcal{F}}_p = 0$ and considering the flow rules it is possible to deduce the explicit form of $\dot{\lambda}$, as Oller *et al.* (1996a)

$$\dot{\lambda} = -\frac{\dfrac{\partial \mathcal{F}_p}{\partial \hat{P}_1^m} \cdot (\mathcal{C}^{me}\dot{\hat{\varepsilon}}_n)}{\left\{\dfrac{\partial \mathcal{F}_p}{\partial \hat{P}_1^m}\left(\mathcal{C}^{me}\dfrac{\partial \mathcal{G}_p}{\partial \hat{P}_1^m}\right) - \dfrac{\partial f_p}{\partial k_p}\hat{\varrho} \cdot \dfrac{\partial \mathcal{G}_p}{\partial \hat{P}_1^m}\right\}} \tag{22}$$

The material form of the tangent constitutive tensor is calculated taking the time derivative of Equation (17), considering the flow rule of Equation (20) and the plastic consistency parameter of Equation (22) as Oller *et al.* (1996b)

$$\delta\hat{P}_1^m = \left[\frac{\left(\mathcal{C}^{me}\dfrac{\partial \mathcal{G}_p}{\partial \hat{P}_1^m}\right) \otimes \left(\mathcal{C}^{me}\dfrac{\partial \mathcal{F}_p}{\partial \hat{P}_1^m}\right)}{\dfrac{\partial \mathcal{F}_p}{\partial \hat{P}_1^m} \cdot \left(\mathcal{C}^{me}\dfrac{\partial \mathcal{G}_p}{\partial \hat{P}_1^m}\right) - \dfrac{\partial \mathcal{F}_p}{\partial k_p}\hat{\varrho} \cdot \left(\dfrac{\partial \mathcal{G}_p}{\partial \hat{P}_1^m}\right)}\right] \delta\hat{\varepsilon}_n = \mathcal{C}^{mt}\delta\hat{\varepsilon}_n \tag{23}$$

3.3 *Mixing theory for composites*

Each material point on the beam cross section is treated as a composite material according to the *mixing theory*, Oller *et al.* (1996a). The interaction between all the components defines the overall mechanical behavior of the composite at material point level. Supposing N different components coexisting in a generic material point subjected to the same material strain $\hat{\varepsilon}_n$, we have the following closing equation: $\hat{\varepsilon}_n \equiv (\hat{\varepsilon}_n)_1 = \cdots = (\hat{\varepsilon}_n)_q = \cdots = (\hat{\varepsilon}_n)_N$, which imposes the strain compatibility between components. The free energy density of the composite, $\overline{\Psi}$, is obtained as the weighted sum of the free energy densities of the N components. The weighting factors correspond to the quotient between the volume of the q^{th} component, V_q and the total volume, V, such that $\Sigma_q\, k_q = 1$.

The material form of the FPK stress vector $\hat{P}_1^m$ for the composite, including the participation of rate dependent effects, is obtained in analogous way as for simple materials *i.e.*

$$\hat{P}_1^{mt} = \sum_q k_q(\hat{P}_1^m + \hat{P}_1^{mv})_q = \sum_q k_q\left[(1-d)\mathcal{C}^{me}\left(\hat{\varepsilon}_n + \frac{\eta}{E_0}\hat{S}_n\right)\right]_q \tag{24}$$

where $(\hat{P}_1^m)_q$ and $(\hat{P}_1^{mv})_q$ correspond the strain and rate dependent stresses of each one of the N components. The material form of the secant and tangent constitutive tensors for the composite, $\overline{\mathcal{C}}^{ms}$ and $\overline{\mathcal{C}}^{mt}$, are obtained as, Oller *et al.* (1996a)

$$\overline{\mathcal{C}}^{ms} = \sum_{q=1}^{N} k_q (\mathcal{C}^{ms})_q, \quad \overline{\mathcal{C}}^{mt} = \sum_{q=1}^{N} k_q (\mathcal{C}^{mt})_q \, \delta\hat{\varepsilon}_n \tag{25}$$

where $(\mathcal{C}^{ms})_q$ and $(\mathcal{C}^{mt})_q$ are the material form of the secant and tangent constitutive tensors of the q^{th} component.

3.4 *Constitutive relations for EDDs*

The constitutive law proposed for EDDs is based on a previous work of Mata *et al.* (2007a) which provides a versatile strain–stress relationship with the following general form:

$$\overline{P}^m(\varepsilon_1, \dot{\varepsilon}_1, t) = \overline{P}_1^m(\varepsilon_1, t) = \overline{P}_2^m(\dot{\varepsilon}_1, t) \tag{26}$$

where $\overline{P}^m$ is the average stress in the EDD, ε_1 the strain level, t the time, $\dot{\varepsilon}_1$ the strain rate, $\overline{P}_1^m$ and $\overline{P}_2^m$ are the strain dependent and rate dependent parts of the stress, respectively. The model uncouples the total stress in viscous and non-viscous components, which correspond to a viscous dashpot device acting in parallel with a nonlinear hysteretic spring. The purely viscous component does not requires to be a linear function of the strain rate. Additionally, hardening, and variable elastic modulus can be reproduced. The response of the nonlinear hysteretic spring is obtained solving system of nonlinear differential equations depending on a set of parameters calibrated from experimental data. Details about the determination of the parameters and the integration algorithm can be reviewed in Mata *et al.* (2007a).

4 Numerical implementation

In order to obtain a Newton type numerical solution, the linearized form of the weak form of Equation (6) is required, which can be written as

$$\mathcal{L}[G(\hat{\varphi}_*, \boldsymbol{\Lambda}_*, \hat{h})] = G(\hat{\varphi}_*, \boldsymbol{\Lambda}_*, \hat{h}) = DG(\hat{\varphi}_*, \boldsymbol{\Lambda}_*, \hat{h}) \cdot \hat{p} \tag{27}$$

where $\mathcal{L}[G(\hat{\varphi}_*, \boldsymbol{\Lambda}_*, \hat{h})]$ is the linear part of the functional $G(\hat{\varphi}, \boldsymbol{\Lambda}, \hat{h})$ at the configuration defined by $(\hat{\varphi}, \boldsymbol{\Lambda}) = (\hat{\varphi}_*, \boldsymbol{\Lambda}_*)$ and $\hat{p} \equiv (\Delta\hat{\varphi}, \Delta\hat{\theta})$ is an admissible variation. The term $G(\hat{\varphi}_*, \boldsymbol{\Lambda}_*, \hat{h})$ supplies the *unbalanced force* and it is composed by the contributions of the inertial, external and internal terms; the differential $DG(\hat{\varphi}_*, \boldsymbol{\Lambda}_*, \hat{h}) \cdot \hat{p}$, gives the *tangential stiffness*, Simo & Vu-Quoc (1986).

The linearization of the inertial and external components, $DG_{int} \cdot \hat{p}$ and $DG_{ext} \cdot \hat{p}$ gives the inertial and load dependent parts of the tangential stiffness, K_{1*} and K_{P*},

respectively, and they can be consulted in Simo & Vu-Quoc (1986). The linearization of the internal term is calculated as, Mata *et al.* (2007b and 2008a)

$$DG_{int}(\hat{\varphi}_*, \boldsymbol{\Lambda}_*, \hat{h}) \cdot \hat{p} = \int_0^L \left(\hat{h}^T \underbrace{\begin{bmatrix} 0 & 0 \\ -\widetilde{\boldsymbol{n}}_* \begin{bmatrix} \frac{d}{dS} \end{bmatrix} & 0 \end{bmatrix}}_{[n_{S*}]} \hat{p} + \hat{h}^T [\mathbf{B}_*]^T \begin{bmatrix} \Delta\widehat{n}_* \\ \Delta\widehat{m}_* \end{bmatrix} \right) dS \tag{28}$$

where the skew–symmetric tensor $\widetilde{\boldsymbol{n}}_*$ is obtained from $\hat{n}_*$, $[d/dS]\hat{v} = [\mathbf{I}]\hat{v}_{,S} \; \forall \, \hat{v} \in \mathbb{R}^3$, the operator $[\boldsymbol{n}_{S*}]$ contributes to the geometric part of the tangent stiffness and the operator $[\mathbf{B}_*]$ relates the admissible variation h and the co-rotated variation of the strain vectors. The explicit expression for $[\mathbf{B}_*]$ can be found in Kapania (2003) and Simo & Vu-Quoc (1986).

The estimation of the linearized form of the sectional force and moment vectors appearing in Equation (28) requires taking into account the linearized relation existing between $\hat{P}_1^m$, obtained using the mixing rule, and $\hat{\varepsilon_n}$. After integrating over the beam cross section, the following result is obtained for the linearized relation between cross sectional forces and the reduced strain measures Mata *et al.* (2007b and 2008a)

$$\begin{Bmatrix} \Delta\widehat{n} \\ \Delta\widehat{m} \end{Bmatrix} = \underbrace{\begin{bmatrix} \mathbf{C}_{11}^{SV} & \mathbf{C}_{12}^{SV} \\ \mathbf{C}_{21}^{SV} & \mathbf{C}_{22}^{SV} \end{bmatrix}}_{[\mathbf{C}^{SV}]} \begin{Bmatrix} \Delta[\overset{\triangledown}{\hat{\gamma}}_n] \\ \Delta[\overset{\triangledown}{\hat{\omega}}_n] \end{Bmatrix} + \underbrace{\begin{bmatrix} \boldsymbol{\Upsilon}_{11}^{SS} & \boldsymbol{\Upsilon}_{12}^{SS} \\ \boldsymbol{\Upsilon}_{21}^{SS} & \boldsymbol{\Upsilon}_{22}^{SS} \end{bmatrix}}_{[\boldsymbol{\Upsilon}^{SS}]} \begin{Bmatrix} \Delta[\overset{\triangledown}{\dot{\gamma}}_n] \\ \Delta[\overset{\triangledown}{\dot{\omega}}_n] \end{Bmatrix} - \underbrace{\begin{bmatrix} o & \widetilde{\boldsymbol{n}} \\ o & \widetilde{\boldsymbol{m}} \end{bmatrix}}_{[\widetilde{F}]} \begin{Bmatrix} \Delta\hat{\varphi} \\ \Delta\hat{\theta} \end{Bmatrix} \tag{29}$$

where $\widetilde{m}$ is the skew-symmetric tensor obtained from $\widehat{m}$, $\mathbf{C}_{ij}^{SV}$ and $\boldsymbol{\Upsilon}_{ij}^{SS}$, $(i, j = 1, 2)$ are the spatial forms of the *reduced tangential* and *viscous tangential* constitutive tensors, which are rate dependent and can be consulted in Mata *et al.* (2008a). Finally, Equation (29) allows to rewrite Equation (28) as

$$\begin{aligned} DG_{int} \cdot \hat{p} = & \underbrace{\int_0^L \hat{h}^T [\mathbf{B}_*]^T [\mathbf{C}_*^{\mathrm{st}}][\mathbf{B}_*]\hat{p} \, dS}_{K_{G*}} + \underbrace{\int_0^L \hat{h}^T [\mathbf{B}_*]^T [\boldsymbol{\Upsilon}_*^{\mathrm{st}}][\nu_*]\hat{p} \, dS}_{K_{M*}} \\ & + \underbrace{\int_0^L \hat{h}^T ([\widetilde{\boldsymbol{n}}_{S*}] - [\mathbf{B}_*]^T [\widetilde{\mathbf{F}}_*])\hat{p} \, dS}_{K_{V*}} \end{aligned} \tag{30}$$

where K_{G*}, K_{M*} and $K_{\nu*}$, evaluated at the configuration $(\hat{\varphi}_*, \boldsymbol{\Lambda}_*)$, give the *geometric*, *material* and *viscous* parts of the tangent stiffness, which allows to rewrite Equation (27) as

$$\mathcal{L}[G_*] = G_* + K_{1*} + K_{M*} + K_{V*} + K_{G*} + K_{P*} \tag{31}$$

The solution of the discrete form of Equation (30) by using the FE method follows identical procedures as those described by Simo & Vu-Quoc (1986) for an iterative

Newton-Rapson integration scheme and it will not be included here. Newmark's implicit time stepping algorithm has been chosen as integration method following the development originally proposed by Simo & Vu-Quoc (1986). For the rotation part the time-stepping procedure takes place in $SO(3)$ and the basic steps, as well as the iterative update algorithm for the strain and strain rate vectors are given in Mata *et al.* (2007b and 2008a).

4.1 *Cross sectional analysis*

The cross section analysis is carried out expanding each integration point on the beam axis in a set of integration points located on each fiber on the cross section. The cross section is meshed into a grid of quadrilaterals, each of them corresponding to a fiber oriented along the beam axis. The geometry of each quadrilateral is described by means of normalized bi-dimensional shape functions and several integration points can be specified according to a selected integration rule. The average value of a quantity, $[\bullet]$, for example, the components of FPK stress vector or the tangential tensor existing on a quadrilateral, are

$$[\bullet] = \frac{1}{A_c}\int_{A_c}[\bullet]dA_c = \frac{1}{A_c}\sum_{p=1}^{N_p}\sum_{q=1}^{N_q}[\bullet](y_p, z_p)J_{pq}W_pq \tag{32}$$

where Ac is the area of the quadrilateral, N_p and N_q are the number of integration points in the two directions of the normalized geometry, $[\bullet](y_p, z_q)$ is the value of the quantity $[\bullet]$ existing on a integration point with coordinates (y_p, z_q) with respect to the reference beam axis, J_{pq} is the Jacobian of the transformation between normalized coordinates and cross sectional coordinates and W_{pq} are the weighting factors. Two additional integration loops are required. The first one runs over the quadrilaterals and the second loop runs over each simple material associated to the composite of the quadrilateral. More details can be consulted in Mata *et al.* (2007).

5 Damage indices

A measure of the damage level of a material point can be obtained as the ratio of the existing stress level to its elastic counterpart. Following this idea, it is possible to define the fictitious damage variable $\breve{D}$ as, Barbat *et al.* (1997)

$$\sum_{i=1}^{3}|P_{1i}^m| = (1-\breve{D})\sum_{i=1}^{3}|P_{1i0}^m| \rightarrow \breve{D} = 1 - \frac{\sum_{i=1}^{3}|P_{1i}^m|}{\sum_{i=1}^{3}|P_{1i0}^m|} \tag{33}$$

where $|P_{1i}^m|$ and $|P_{1i0}^m|$ are the absolute values of the components of the existing and elastic stress vectors, respectively. Initially, the material remains elastic and $\breve{D}=0$, but when all the energy of the material has been dissipated $|P_{1i}^m| \rightarrow 0$ and $\breve{D} \rightarrow 1$. Equation (33) can be extended to consider elements or even the whole structure by means of integrating over a finite volume as follows:

$$\breve{D} = 1 - \frac{\int_{V_p}(\Sigma_i|P_{1i}^m|)dV_p}{\int_{V_p}(\Sigma_i|P_{1i0}^m|)dV_p} \tag{34}$$

where V_p is the volume of the part of the structure. Equation (34) is easily implemented in a standard FEM code without requiring large extra memory storage.

6 Numerical examples

6.1 *Experimental–numerical comparative study of a scaled RC building model*

The first example corresponds to the comparison between the numerical simulation obtained by means of the proposed formulation and the experimental data obtained by Lu (2002) for the seismic analysis of a scaled model (1:5.5) of a benchmark regular bare frame (BFR). The structure was designed for a ductility class *medium* in accordance with the Eurocode 8 (2001) with a peak ground acceleration of 0,3 *g* and a soil profile A. Details about loads, geometry, material properties and distribution of steel reinforcements can be consulted in the same publication. In the experimental program, the structure was subjected to several scaled versions of the N–S component of the El Centro 1940 earthquake record. Four quadratic elements with two Gauss integration points were used for each beam and column. Cross sections were meshed into a grid of 20 equally spaced layers. Longitudinal steel reinforcements were included in the external layers as part of a composite material. The fracture energy of the damage model used for concrete was modified to take into account the confining effect of transversal stirrups, Mata *et al.* (2007b). A tension to compression ratio of 10 was used for concrete and 1 for steel. In the numerical simulations, the model is subjected to a push–over analysis. Static forces derived from the inertial contribution of the masses are applied at the floor levels considering an inverted triangular distribution. A relationship between the measured base shear and the top lateral displacement is given by Lu (2002) for each seismic record. This curve is compared in Figure 3 with

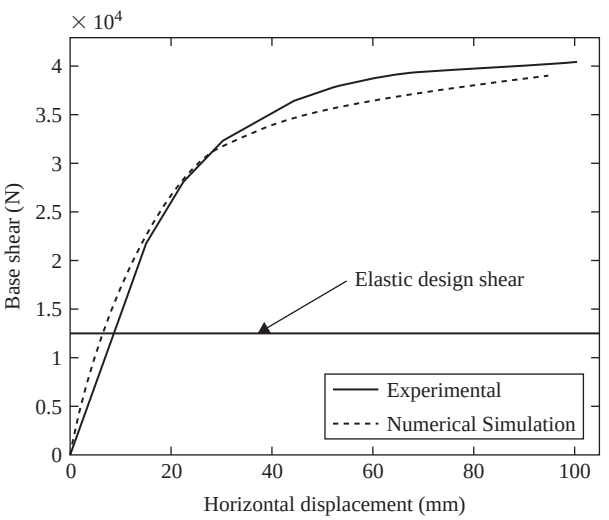

Figure 3 Capacity curves: Comparison between results from numerical pushover and experimental tests.

the capacity curve obtained by using the numerical push–over analysis. It is possible to see that the push– over analysis gives a good approximation for the global maximum response and, therefore, it constitutes a suitable numerical procedure for estimating the expected nonlinear properties of structures subjected lo seismic actions. In the same figure, it is possible to appreciate that in both, the numerical simulation and the experimental cases, the characteristic values of the structure; that is, global ductility level, elastic limit and overstrength, are similar. Figure 4 shows a comparison between the distribution of cross sectional damage predicted numerically and the map of fissures obtained after the application of several shaking table tests.

In this case, the proposed damage index along with the geometric and constitutive formulation used for beams is able to reproduce the general failure mechanism of the structure where dissipation is mainly concentrated in the beam elements.

6.2 *Seismic response of a precast RC building with EDDs*

The nonlinear seismic response of a typical precast RC industrial building shown in Figure 5 is studied. The building has a bay width of 24 m and 12 m of inter–axes length. The story height is 10 m. The concrete of the structure is H-35, (35 MPa, ultimate compression), with an elastic modulus of 29.000 MPa. It has been assumed a Poisson coefficient of 0.2. The ultimate tensile stress for the steel is 510 MPa. This figure also shows some details of the steel reinforcement of the cross sections. The dimensions of the columns are $60 \times 60\,cm^2$. The beam has an initial high of 60 cm on the supports and 160 cm in the middle of the span. The permanent loads considered are $1050\,N/m^2$ and the weight of upper half of the closing walls with 432,000 N. The input acceleration is the same as in example 6.1.

The half part of the building is meshed using 4 quadratic elements with two Gauss integration points for the resulting beam and column. The cross sectional grid of fibers is shown in Figure 6. One integration point is used for each quadrilateral.

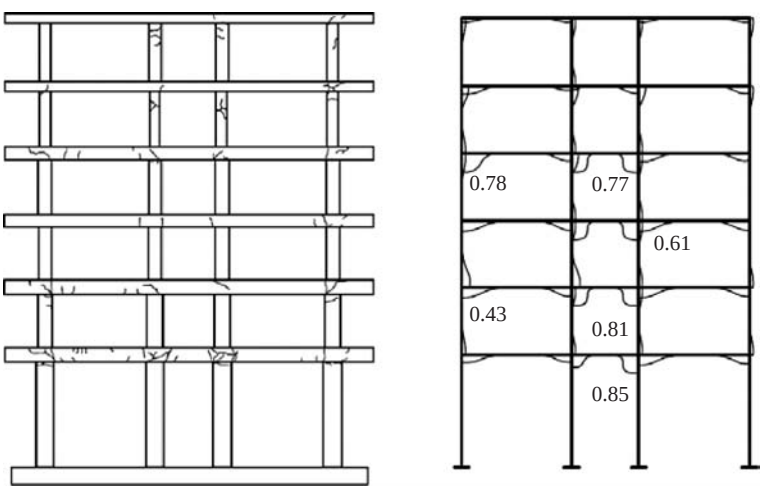

Figure 4 Damage. (a) Experimental: Map of fissures. (b) Numerical: Cross sectional damage index.

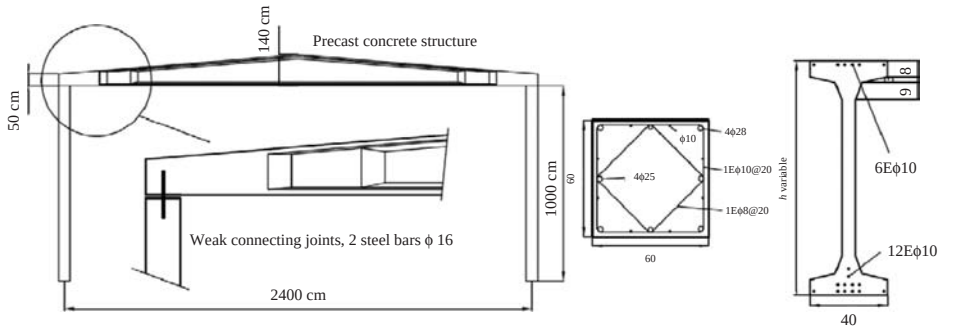

Figure 5 Description of the structure.

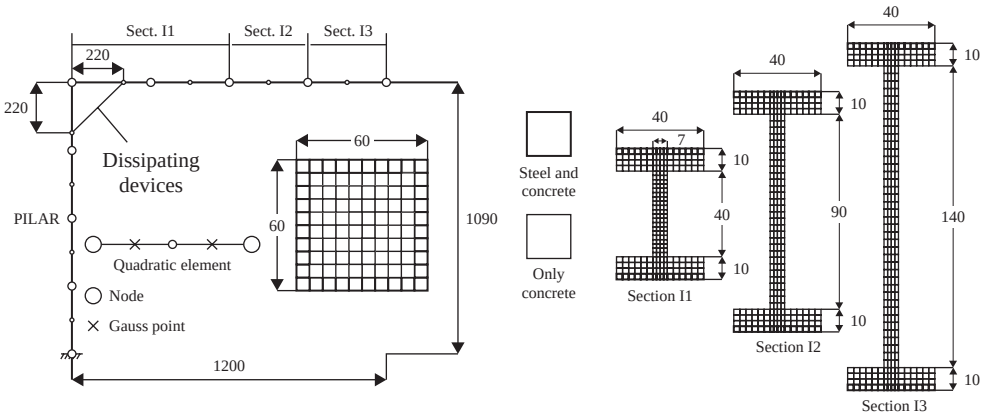

Figure 6 Half part of 2D precast industrial frame. 1: Normal frame 2: Energy dissipating devices incorporated (diagonal elements). 3: Numerical model of column and beam cross sections.

The EED was simulated by means of employing the previously described model reproducing a plastic dissipative mechanism. The properties of the device were designed for yielding with an axial force of 150.000 N and for a relative displacement between the two ending nodes of 1.5 mm. The length of the devices was of 2.0 m. The results of the numerical simulations allow seeing that the employment of plastic EDDs contributes to improve the seismic behavior of the structure for the case of the employed acceleration record. Figure 7a shows the hysteretic cycles obtained from the lateral displacement of the upper beam–column joint and the horizontal reaction (base shear) in the columns for the structure with and without devices. It is possible to appreciate that the non-controlled structure (bare frame) presents greater lateral displacements and more structural damage, (greater hysteretic area than for the controlled case). Figure 7b shows the hysteretic cycles obtained in the EDD, evidencing that part of the dissipated energy is concentrated in the controlling devices, as expected.

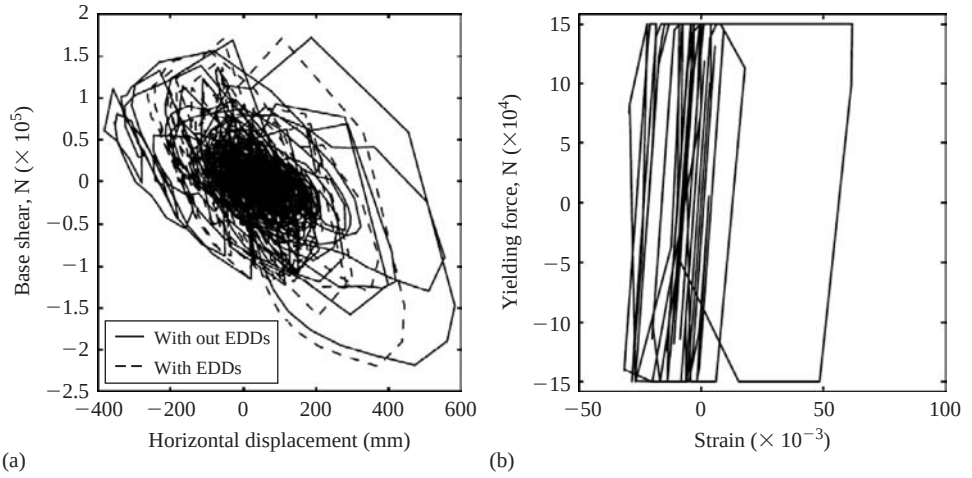

Figure 7 (a) base shear–displacement relationship. (b) Hysteretic cycles in the EDD.

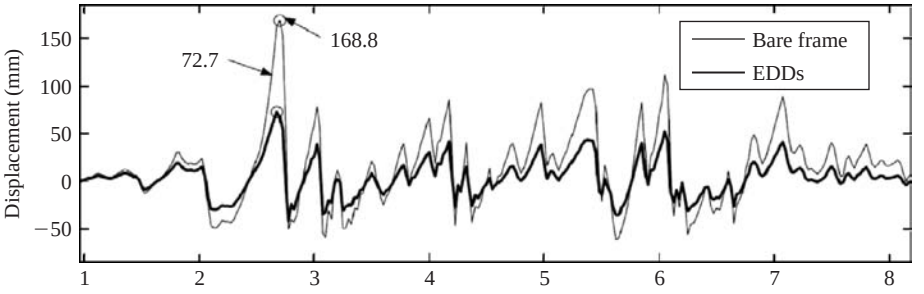

Figure 8 Time history of the top horizontal displacement.

Figure 8 shows the time history response of the horizontal displacement of the upper beam–column joint. A reduction of approximately 40% is obtained for the maximum lateral displacement when compared with the bare frame. Acceleration and velocity are controlled in the same way, but only 10 and 5% of reduction is obtained. A possible explanation for the limited effectiveness of the EDD is that the devices only contribute to increase the ductility of the beam–column joint without alleviating the base shear demand on the columns due to the dimensions of the device and its location in the structure. By other hand, joints are critical points in precast structures and therefore, the employment of EDDs combined with a careful design of the columns can help to improve their seismic behavior.

7 Conclusions

In this work, a geometrically exact formulation for initially curved beams has been extended to consider arbitrary distributions of composite materials on the cross

sections in the seismic case. The consistent linearization of the weak form of the momentum balance equations considers the constitutive nonlinearity with rate dependent effects. The resulting model is implemented in a displacement based FEM code. An iterative Newton-Rapson scheme is used for the solution of the discrete version of the linearized problem. A specific element for EDD is developed, based on the beam model but releasing the rotational degrees of freedom.

Each material point of the cross section is assumed to be composed of several simple materials with their own constitutive laws. The mixing rule is used to describe the resulting composite. Viscosity is included at constitutive level by means of a Maxwell model. Beam cross sections are meshed into a grid of quadrilaterals corresponding to fibers directed along the beam axis. Two additional integration loops are required at cross sectional level in each integration point to obtain the reduced quantities. Local and global damage indices have been developed based on the ratio between the visco-elastic and the nonlinear stresses.

The present formulation is validated by means of two numerical examples, which include the comparison with existing experimental data and the study of the seismic response of a precast reinforced concrete structure with EDDs.

Acknowledgement

This research was partially supported by the European Commission, CEE–FP6 Project FP650544(GOCE) "Risk Mitigation for Earthquakes and Landslides (LESSLOSS)", by the Spanish Government (Ministerio de Educación y Ciencia), project BIA2003-08700-C03-02 "Numerical simulation of the seismic behaviour of structures with energy dissipation devices", project MAT2003-09768-C03-02 "Delamination of reinforced matrix composites (DECOMAR)" project BIA2005-06952 "Study of composite materials for design, reinforcement and retrofit of civil engineering structures (RECOMP)" by the Spanish Government (Ministerio de Fomento) "Numerical simulation methodology for the reinforced concrete behavior structures reinforced with composite materials", and by the collaboration framework between CIMNE and AIRBUS, project PBSO-13-06 "Innovative finite element methods for non linear analysis of composite structures (FEMCOM)". All this support is gratefully acknowledged.

References

Aiken, I. 1996. Passive energy dissipation hardware and applications. *Proceedings, Lo Angeles County and Seaosc Symposium on Passive Energy Dissipation Systems for New and Existing Buildings*, Los Angeles.

Antman, S.S. 1991. *Nonlinear Problems of Elasticity*, Springer-Verlag, 1991.

Barbat, A.H., Oller, S., Hanganu, A. & Oñate, E. 1997. Viscous damage model for Timoshenko beam structures. *International Journal for Solids and Structures*; 34(30):3953–3976.

Bayrak, O. & Sheikh, S.A. 2001. Plastic hinge analysis. *Journal of Structural Engineering*; 127(9):1092–1100.

Clark, P., Aiken, I., Ko, E., Kasai, K. & Kimura, I. 1999. Design procedures for buildings incorporating hysteretic seismic devices. *Proceedings, 68th Annual Convention Santa Barbara, California* Structural Engineering Association of California.

Connor, J.J., Wada, A., Iwata, M. & Huang, Y.H. 1997. Damage-controlled structures. I: Preliminary design methodology for seismically active regions. *Journal of Structural Engineering*; 123(4):423–431.

EC8, Eurocode No 8. 2001. Design of structures for earthquake resistance. European Committee for standardization, 3rd Draft, prEN 1998-1-1.

Federal Emergency Management Agency. 2000. *Prestandard and Commentary for the Seismic Rehabilitation of Buildings*, Report 356, Washington, DC: FEMA.

Federal Emergency Management Agency. *NEHRP Recommended Provisions for Seismic Regulations for New Buildings and Other Structures*. 2000. Report 368, Washington, DC: FEMA.

Fu, Y. & Kasai, K. 1998. Comparative study of frames using viscoelastic and viscous dampers. *Journal of Structural Engineering*; 124(5):513–522.

Hanganu, A., Oñate, E. & Barbat, A.H. 2002. Finite element methodology for local/global damage evaluation in civil engineering structures. *Conputers and Structures*; 80:1667–1687.

Hanson, R.D., Aiken, I.D., Nims, D.K., Ritchter, P.J. & Batchman, R.E. 1993. State of the art and state of the practice in seismic engineering dissipation. *Proceedings, ATC-17-1. Seminar on seismic isolation, passive energy dissipation and active control. Applied Technology Council, San Francisco, California*.

Ibrahimbegovic, A. 1995. On finite element implementation of geometrically nonlinear Reissners beam theory: three-dimensional curved beam elements. *Computer Methods in Applied Mechanics and Engineering*; 122:11–26.

Kapania, R.K. & Li, J. 2003. On a geometrically exact curved/twisted beam theory under rigid cross-section assumption. *Computational Mechanics*; 30:428–443.

Kasai, K., Fu, Y. & Watanabe, A. 1998. Passive control systems for seismic damage mitigation. *Journal of Structural Engineering*; 124:(5):501–512.

Kumar, P., Nukala, V.V. & White, D.W. 2004. A mixed finite element for threedimensional nonlinear analysis of steel frames. *Computer Methods in Applied Mechanic and Engineering*; 193(5):2507–2545.

Lin, W.H. & Chopra, A.K. 2003. Asymmetric one–storey elastic system with non–linear viscous and viscoelastic dampers: Earthquake response. *Earthquake Engineering and Structural Dynamics*; 32:555–577.

Lin, Y.Y. & Chang, K.C. 2003. Study on damping reduction factors for buildings under earthquake ground motions. *Journal of Structural Engineering, JEE*; 129(2):206–214.

Lu, Y. 2002. Comparative study of seismic behavior of multistory reinforced concrete framed structures. *Journal of Structural Engineering, JEE*; 128(2):169–178.

Mata, P., Oller, S., Barbat, A.H. & Boroschek, R. 2006. Numerical code for seismic analysis of structures incorporating energy dissipating devices. *First European Conference on Earthquake Engineering and Seismology, ECEES*, Geneva, Switzerland.

Mata, P., Boroschek, R., Oller, S. & Barbat, A.H. 2007a. High damping rubber model for energy dissipating devices, *Journal of Earthquake Engineering*; 11(2):231–256.

Mata, P., Oller, S. & Barbat, A.H. 2007b. Static analysis of beam structures under nonlinear geometric and constitutive behavior, *Computer Methods in Applied Mechanics and Engineering*; 196:4458–4478.

Mata, P., Oller, S. & Barbat, A.H. 2008a. Dynamic analysis of beam structures considering geometric and constitutive nonlinearity, *Computer Methods in Applied Mechanics and Engineering*; 197:857–878.

Mata, P., Oller, S., Barbat, A.H. & Boroschek, R. 2008b. Computational models for the seismic response of reinforced concrete buildings with energy dissipating devices, *Archives of Computational Methods in Engineering*, (DOI 10.1007/s11831-008-9024-z).

Mata, P., Oller, S., Barbat, A.H. & Boroschek, R. 2008c. Nonlinear seismic analysis of RC structures with energy dissipating devices, *International Journal for Numerical Methods in Engineering*, (Submitted).

Oliver, J., Cervera, M., Oller, S. & Lubliner, J. 1990. Isotropic damage models and smeared crack analysis of concrete. *Proceedings 2nd ICCAADCS, Zell Am See, Austria, Pineridge Press*; 2:945–958.

Oller, S., Oñate, E. & Miquel, J. 1996a. Mixing anisotropic formulation for the analysis of composites, Communications in Numerical Methods in Engineering. 12 471–482.

Oller, S., Oñate, E., Miquel, J. & Botello, S. 1996b. A plastic damage constitutive model for composites materials. *International Journal of Solids and Structures*; 33(17):2501–2518.

Reissner, E. 1973. On one-dimensional large-displacement finite-strain beam theory. *Studies inApplied Mathematics*; LII, 287–295.

Shen, K.L. & Soong, T.T. 2005. Design of energy dissipation devices based on concept of damage control. *Journal of Structural Engineering*; 122(1):76–82.

Simo, J.C. & Vu-Quoc, L. 1986. A three-dimensional finite-strain rod model. Part II: Computational aspects. *Computer Methods in Applied Mechanics and Engineering*; 58:79–116.

Simo, J.C. & Vu-Quoc, L. 1988. On the dynamics in space of rods undergoing large motions – A geometrically exact approach. *Computer Methods in Applied Mechanics and Engineering*; 66:125–161.

Simo, J.C. 1985. A finite strain beam formulation. The three-dimensional dynamic problem. Part I. *Computer Methods in Applied Mechanic and Engineering*, 49:55–70.

Simo, J.C. Hjelmstad, K.D. & Taylor, R.L. 1984. Numerical formulations of elastoviscoplastic response of beams accounting for the effect of shear. *Computer Methods in Applied Mechanics and Engineering*; 42:301–330.

Soong, T.T. & Dargush, G.F. 1997. *Passive Energy Dissipation Systems in Structural Engineering*; John Wiley & Sons Ltda.

Chapter 18

Structural health monitoring by Bayesian updating

Enrico Sibilio

Università di Roma TPE, Rome, Italy

Marcello Ciampoli

Sapienza Università di Roma, Rome, Italy

James L. Beck

California Institute of Technology, Pasadena, USA

ABSTRACT: The problems of structural damage detection and reliability assessment are closely related, and should be dealt with in a unified approach. In fact, the health monitoring of a damaged construction requires both damage detection and the assessment of the effects of damages on the life-cycle reliability. In this paper, a complete procedure for structural health monitoring is briefly illustrated and applied. The problem of damage detection is dealt with by an identification technique with unknown input; a Bayesian model updating procedure, based on an adaptive Markov Chain Monte Carlo method, is adopted to quantify, in probabilistic terms, the structural damage based on data from monitoring. An advanced simulation technique, Subset Simulation, is then used to assess the probability of exceeding any structural response level taking into account the various sources of uncertainty. It is observed that the Bayesian approach is really efficient in characterizing the structural damage and its effects.

1 Introduction

For any structure the problems of life-cycle reliability assessment and damage detection are closely related, and should be dealt with in a unified approach, aimed at structural health monitoring. In fact, according to (Doebling et al. 1996), any structural health monitoring procedure should be articulated in two steps: damage identification that consists of detection, quantification and localization of any damage; and then assessment of the effects of the structural damage on the life-cycle reliability.

The problem of damage detection is often solved by a system identification technique; past research has aimed primarily at implementing efficient solutions for each relevant inverse problem, where the efficiency is usually related to the computational aspects.

The reliability assessment is carried out by using advanced reliability theory; most research in this field has dealt with the issues of the probabilistic characterization of the uncertain quantities, the computational efficiency in case of large dimension problems, and the lack of analytical solutions that occurs, for example, in case of structures that exhibit a strongly nonlinear dynamic behaviour.

However, a global approach to structural health monitoring that consistently takes into account the various sources of uncertainty has been applied only in a few cases. From these studies, it has been concluded that the Bayesian approach is really efficient in characterizing the structural damage and its effects in probabilistic terms; for example, to calculate the probability of damage in various structural elements. The main reason is that this approach gives as final result the probability density functions of the identified parameters, which in turn can be used in any structural reliability assessment.

In this work, the procedure implemented by the authors for the health monitoring of a structure damaged by an earthquake (Sibilio & Ciampoli 2006, Sibilio et al. 2006) is briefly illustrated and applied to an example case. An advanced Markov Chain Monte Carlo simulation technique, known as Subset Simulation (Au & Beck 2001, Au & Beck 2003, Ching et al. 2005a, Ching et al. 2005b), is used to assess the probability of exceeding any response level, that is, to assess the structural risk, for a structure damaged by an earthquake.

2 A procedure for structural health monitoring

The procedure, which is described in detail in (Sibilio & Ciampoli 2006, Sibilio et al. 2006), requires the identification of the structural parameters and the assessment of the seismic reliability of the damaged structure.

2.1 *Structural identification with unknown input*

Consider a structure excited by a seismic ground acceleration $a_g(t)$ which is modeled as a linear dynamic system with N_d degrees of freedom:

$$\mathbf{M}\ddot{\mathbf{x}}(t) + \mathbf{C}\dot{\mathbf{x}}(t) + \mathbf{K}\mathbf{x}(t) = -\boldsymbol{\tau}\mathbf{M}a_g(t) \tag{1}$$

where: **M**, **C** and **K** are the mass, damping and stiffness matrices; $\mathbf{x}(t)$, $\dot{\mathbf{x}}(t)$ and $\ddot{\mathbf{x}}(t)$ are the vectors of displacements, relative velocities and relative accelerations; and $\boldsymbol{\tau}$ is the influence vector which accounts for the degrees of freedom excited by the earthquake.

Consider as a response parameter the absolute acceleration of the j-th degree of freedom $y_j(t)$. Its Fourier transform $Y_j(i\omega)$ is given by the product of the Fourier transform of the ground acceleration $A_g(i\omega)$ and the frequency response function $H_j(i\omega)$:

$$Y_j(i\omega) = A_g(i\omega)H_j(i\omega) \tag{2}$$

The frequency response function $H_j(i\omega)$ depends on the mass, damping and stiffness matrices; it is a function of the natural frequencies $\tilde{\omega}_l$, the modal damping ratios $\tilde{\xi}_l$, and the normalized mode shapes $\boldsymbol{\Phi}$, given by:

$$H_j(i\omega) = \tau_j - \omega^2 \sum_{l=1}^{N_d} \frac{\psi_{jl}}{\omega^2 - 2i\tilde{\omega}_l\tilde{\xi}_l\omega - \tilde{\omega}_l^2} \tag{3}$$

where ψ_{jl} is an element of: $\boldsymbol{\Psi} = diag(\mathbf{p})\boldsymbol{\Phi}$, and: $\mathbf{p} = \boldsymbol{\Phi}^T\mathbf{M}\boldsymbol{\tau}$ is the vector of the modal participation factors.

The ratio $R_{jk}(i\omega)$ between the Fourier transforms of the absolute accelerations of the j-th and k-th degree of freedoms, is given by:

$$R_{jk}(i\omega) = \frac{A_g(i\omega)H_k(i\omega)}{A_g(i\omega)H_j(i\omega)} = \frac{\tau_k - \omega^2 \sum_{l=1}^{N_d} \dfrac{\psi_{kl}}{\omega^2 - 2i\tilde{\omega}_k\tilde{\xi}_k\omega - \tilde{\omega}_k^2}}{\tau_j - \omega^2 \sum_{l=1}^{N_d} \dfrac{\psi_{jl}}{\omega^2 - 2i\tilde{\omega}_l\tilde{\xi}_l\omega - \tilde{\omega}_l^2}} \tag{4}$$

This ratio does not depend on the input, but is only a function of the structural characteristics; therefore, when the input is unknown, it is possible to exploit the information given by any $R_{jk}(i\omega)$ to identify the structural parameters (Capecchi et al. 2004, Sepe et al. 2005).

The Bayesian model updating approach, applied to structural identification in (Beck & Katafygiotis 1998), is used to update the probability density function (PDF) of each model parameter according to measured data. Let $\mathbf{D}_s$ be a set of measured data, M_s the model class, that is, the system of differential equations (Eq. 1), and $\boldsymbol{\theta}_s$ the vector of structural parameters for the chosen model class. Bayes' theorem states that the posterior PDF $p(\boldsymbol{\theta}_s|\mathbf{D}_s, M_s)$ of $\boldsymbol{\theta}_s$ is proportional to the product of the likelihood function $p(\mathbf{D}_s|\boldsymbol{\theta}_s, M_s)$ and the prior PDF $p(\boldsymbol{\theta}_s|M_s)$; the proportionality constant c is given by the inverse of the so-called evidence $p(\mathbf{D}_s|M_s)$.

The structural response is known in terms of the absolute accelerations of some degrees of freedom. According to (Yuen & Katafygiotis 2005, Yuen & Katafygiotis 2006), the vector of structural responses, $\mathbf{y}(t)$, can be divided in two groups, $\mathbf{y}_A(t)$ and $\mathbf{y}_B(t)$. Each vector $\mathbf{y}_A(t)$ and $\mathbf{y}_B(t)$ can be expressed as the sum of the correct structural response, $\mathbf{q}(t)$, and a prediction error, $\boldsymbol{\eta}(t)$, that accounts for the model uncertainty and noise in the signal, and is typically modelled as a Gaussian white noise, as:

$$\mathbf{y}_A(t) = \mathbf{q}_A(t) + \boldsymbol{\eta}_A(t) \quad \mathbf{y}_B(t) = \mathbf{q}_B(t) + \boldsymbol{\eta}_B(t) \tag{5}$$

The same partition can be applied to the measured data $\mathbf{D}_s$. The data collected in $\mathbf{D}_{sA}$ are those that do not add any information on the posterior PDF of the model parameter $\boldsymbol{\theta}_s$ (Yuen & Katafygiotis 2005, Yuen & Katafygiotis 2006). As a consequence of this assumption, the posterior PDF can be written as follows:

$$p(\boldsymbol{\theta}_s|\mathbf{D}_s, M_s) = c\, p(\mathbf{D}_{sB}|\boldsymbol{\theta}_s, \mathbf{D}_{sA}, M_s) p(\boldsymbol{\theta}_s|M_s) \tag{6}$$

The Fourier transform $\mathbf{Y}_B(i\omega)$ of $\mathbf{y}_B(t)$ can be expressed as the function of the Fourier transform $\mathbf{Y}_A(i\omega)$ of $\mathbf{y}_A(t)$, the ratios $\mathbf{R}_{AB}(i\omega, \theta_s)$ and the Fourier transforms of the white noises $\mathbf{N}_A(i\omega)$ and $\mathbf{N}_B(i\omega)$ given by the following Equation 7:

$$\begin{aligned} \mathbf{Y}_B(i\omega) &= \frac{\mathbf{H}_B(i\omega, \boldsymbol{\theta}_s)}{\mathbf{H}_A(i\omega, \boldsymbol{\theta}_s)} \mathbf{Y}_A(i\omega) - \frac{\mathbf{H}_B(i\omega, \boldsymbol{\theta}_s)}{\mathbf{H}_A(i\omega, \boldsymbol{\theta}_s)} N_A(i\omega) + \mathbf{N}_B(i\omega) \\ &= \mathbf{R}_{AB}(i\omega, \boldsymbol{\theta}_s)\, \mathbf{Y}_A(i\omega) + \mathbf{H}(i\omega, \boldsymbol{\theta}_s)\mathbf{N}(i\omega) \end{aligned} \tag{7}$$

Assuming $\mathbf{D}_{sA} = \mathbf{Y}_A(i\omega)$ and $\mathbf{D}_{sB} = \mathbf{Y}_B(i\omega)$ and considering that the values of the transforms at different frequencies are statistically independent, it is possible to

evaluate the likelihood function $p(\mathbf{D}_{sB}|\boldsymbol{\theta}_s, \mathbf{D}_{sA}, M_s)$, and, with the chosen prior PDF $p(\boldsymbol{\theta}_s|M_s)$, to assess the posterior probability up to the constant c.

To identify the posterior PDF of $\boldsymbol{\theta}_s$ by exploiting the information contained in $\mathbf{Y}_A(i\omega)$ and $\mathbf{Y}_B(i\omega)$, samples can be drawn from it. In the implemented procedure (Sibilio & Ciampoli 2006, Sibilio et al. 2006), Markov Chain Monte Carlo simulation is applied: an adaptive Metropolis-Hasting algorithm that is known as the Transitional Markov Chain Monte Carlo (TMCMC) algorithm (Ching & Chen 2007). The results of the TMCMC algorithm are a chain of samples of the model parameters $\boldsymbol{\theta}_s$ asymptotically distributed as the posterior PDF $p(\boldsymbol{\theta}_s|\mathbf{D}_s, M_s)$, obtained from the prior PDF using the information given by the available data. The procedure can successfully identify, quantify and locate the structural damage along with its associated level of uncertainty.

2.2 *Seismic reliability assessment*

Let us consider the seismic reliability assessment of a structure and assume that the site seismic hazard is described by the earthquake magnitude M and the source-to-site distance R. The probability of structural failure $P(F)$, that is, the probability of exceeding a threshold response level, can be expressed by the Theorem of Total Probability as:

$$P(F) = \int_M \int_R P(F|M,R)p(M)p(R)\,dM\,dR \tag{8}$$

or, in a more general framework, as:

$$P(F) = \int_{g(\boldsymbol{\theta})\leq 0} q(\boldsymbol{\theta})\,d\boldsymbol{\theta} = \int_{R^d} I_F(\boldsymbol{\theta})\,q(\boldsymbol{\theta})\,d\boldsymbol{\theta} \tag{9}$$

where: $\boldsymbol{\theta} \in R^d$ is the vector of the d uncertain parameters; $g(\boldsymbol{\theta})$ is a performance function such that: $g(\boldsymbol{\theta}) \leq 0$ defines the failure domain $F \subset R^d$; $g(\boldsymbol{\theta}) > 0$ defines the safe domain. The function $I_F(\boldsymbol{\theta})$ is the indicator function, that assumes the values 1 or 0, that is: $I_F(\boldsymbol{\theta}) = 1$ if $\boldsymbol{\theta} \in F$; $I_F(\boldsymbol{\theta}) = 0$ if $\boldsymbol{\theta} \notin F$.

In what follows, a robust reliability procedure is applied, and the terms of the reliability integral are characterized by means of a Bayesian structural identification approach (Papadimitriou et al. 2001).

Let $\boldsymbol{\theta}_s$ be the vector of structural parameters, $\mathbf{D}_s$ the data gathered by the analysis of the structural response (in the considered case, the measured accelerations), and M_s the class of models representing the structure. By using the Bayesian Model Updating approach, the posterior PDF $p(\boldsymbol{\theta}_s|D_s, M_s)$ can be estimated and the probability of failure $P(F|M, R)$ evaluated as:

$$P(F|M,R) = \int_{\boldsymbol{\theta}_s} P(F|\boldsymbol{\theta}_s, M, R)\,p(\boldsymbol{\theta}_s|\mathbf{D}_s, M_s)\,d\boldsymbol{\theta}_s \tag{10}$$

Substituting Equation 10 into Equation 8 and considering the uncertainty of the excitation to be completely defined by the PDFs of the magnitude $p(M)$ and the source-to-site distance $p(R)$, the probability of failure becomes:

$$P(F) = \int_M \int_R \int_{\boldsymbol{\theta}_s} P(F|\boldsymbol{\theta}_s, M, R)\, p(\boldsymbol{\theta}_s|\mathbf{D}_s, M_s)\, p(R)\, p(M)\, d\boldsymbol{\theta}_s\, dR\, dM \tag{11}$$

Comparing Equation 9 and Equation 11, the distribution $q(\boldsymbol{\theta}) = p(\boldsymbol{\theta}_s|\mathbf{D}_s, M_s)\, p(M)\, p(R)$, is the product of the PDFs of three independent sets of parameter, that is, $\boldsymbol{\theta}_s$, M and R.

The structural response is evaluated in the time domain and the excitation is given in terms of a stochastic model of the input ground acceleration time history. In what follows, the model by (Atkinson & Silva 2003) is implemented. The site seismic hazard is expressed as a function of M and R for given local soil conditions; a further PDF $p(\mathbf{Z})$ is introduced, to model the uncertainty in the ground motion time history for a given M and R. Therefore $q(\boldsymbol{\theta})$ is given by $q(\boldsymbol{\theta}) = p(\boldsymbol{\theta}_s|\mathbf{D}_s, M_s)\ p(M)\, p(R) p(\mathbf{Z})$ and the integral in Equation 11 can be written as:

$$P(F) = \int_M \int_R \int_Z \int_{\boldsymbol{\theta}_s} P(F|\boldsymbol{\theta}_s, M, R, Z)\, p(\boldsymbol{\theta}_s|D_s, M_s)\, p(R)\, p(M)\, p(Z)\, d\boldsymbol{\theta}_s\, dR\, dM\, dZ \tag{12}$$

In order to solve the reliability integral (Eq. 12), Monte Carlo simulation involves selecting N samples $\boldsymbol{\theta}_k$ from $q(\boldsymbol{\theta})$; the indicator function $\mathrm{I}_F(\boldsymbol{\theta}_k)$ is then evaluated for each sample by structural analysis, and the probability of failure approximated by the estimator:

$$P(F) \approx \frac{1}{N} \sum_{k=1}^{N} I_F\left(\boldsymbol{\theta}^{(k)}\right) \tag{13}$$

The assessment of *P(F)* by Eq. (13) is inefficient in case of low probability events. Therefore, *Subset Simulation* (Au & Beck 2001, Au & Beck 2003, Ching et al. 2005a, Ching et al. 2005b) has been applied to assess $P(F)$ by Equation 13.

The basic idea of Subset Simulation is to express the failure probability as the product of the conditional probabilities of some intermediate failure events F_i. Each event must have a larger probability of occurrence $P(F_i)$ than $P(F)$, so that it can be efficiently evaluated. Au & Beck (2001) have proposed to define a decreasing sequence of failure events: $F_1 \supset F_2 \supset \cdots \supset F_m = F$, such that:

$$F_k = \bigcap_{i=1}^{k} F_i \quad k = 1, \ldots, m \tag{14}$$

According to the definition of conditional probability, the probability of failure $P(F)$ can be evaluated as the product of the conditional probabilities $\{P(F_{i+1}|F_i)$:

$i = 1, \ldots, m-1\}$ and of $P(F_1)$. The probability $P(F_1)$ can be obtained by Monte Carlo simulation:

$$P(F_1) \approx \hat{P}_i = \frac{1}{N} \sum_{k=1}^{N} I_{F_1}(\theta^{(k)}) \tag{15}$$

where $\{\boldsymbol{\theta}^{(k)} : k = 1, \ldots, N\}$ are independent and identically distributed samples derived from the PDF of the uncertain parameters $q(\boldsymbol{\theta})$. In order to evaluate $P(F_{i+1}|F_i)$ an estimator similar to (15) can be applied: samples are obtained from the conditional distribution $q(\boldsymbol{\theta}|F_i)$, assuring that any $\boldsymbol{\theta}^{(k)}$ lies in the failure region F_i, by implementing a Metropolis-Hastings algorithm (Au & Beck 2001, Au & Beck 2003). Finally, P(F) is estimated by:

$$\hat{P}(F) \approx \prod_{i=1}^{m} \hat{P}_i \tag{16}$$

Details about the statistical properties of the estimator in Equation 16 can be found in (Au & Beck 2001).

3 A case example

A shear-type planar frame (Fig. 1a) is considered to illustrate the procedure for structural health monitoring. The elements of the stiffness and mass matrices are set equal to: $k_1 = k_2 = k_3 = 100\,\text{kN/m}$; $k_4 = k_5 = k_6 = 80\,\text{kN/m}$; $m_1 = m_2 = m_3 = m_4 = m_5 = m_6 = 100\,\text{kg}$. The natural frequencies are equal to: $f_1 = 1.18\,\text{Hz}$; $f_2 = 3.32\,\text{Hz}$; $f_3 = 5.39\,\text{Hz}$; $f_4 = 7.07\,\text{Hz}$; $f_5 = 8.28\,\text{Hz}$; $f_6 = 9.39\,\text{Hz}$. The modal damping ratios are set equal to: $\xi_1 = \xi_2 = \xi_3 = \xi_4 = \xi_5 = \xi_6 = 0.02$. The vector of modal participation factors is equal to: $\mathbf{p} = [22.61\ -7.81\ -4.00\ 2.81\ 1.45\ -1.27]^T$, and the percentage of the total mass excited for each mode is given by: $\mathbf{m}_{\%} = [85.22\%,\ 10.17\%,\ 2.67\%,\ 1.32\%,\ 0.35\%,\ 0.27\%]^T$. A sampling time step: $\Delta t = 0.005\,\text{s}$ is taken, for a total simulation time of $T = 100\,\text{s}$; so $N_t = 20000$ data points are obtained for each response time history.

The stiffness matrix $\mathbf{K}$ is decomposed according to the FE approach into storey substructure matrices $\mathbf{K}_1, \ldots, \mathbf{K}_6$ and scaling factors $\theta_1, \ldots, \theta_6$ are introduced as follows:

$$\mathbf{K} = \sum_{i=1}^{N_d=6} \theta_i \mathbf{K}_i \tag{17}$$

Let us consider the absolute acceleration of the first, third and sixth floor, $y_1(t)$, $y_3(t)$ and $y_6(t)$ (Fig. 1b) as the available recorded data $\mathbf{D}_s$; the data set D_{sA} is represented by the Fourier transform $Y_1(i\omega)$ of $y_1(t)$, and the data set $\mathbf{D}_{sB}$ by the Fourier transforms $Y_3(i\omega)$ and $Y_6(i\omega)$ of $y_3(t)$ and $y_6(t)$. The noise level is set equal to 5% of the rms of each noise-free response over the interval [0, T], where T = 100 s; the noise is modeled as Gaussian white noise. The parameters to be identified are the stiffness parameters,

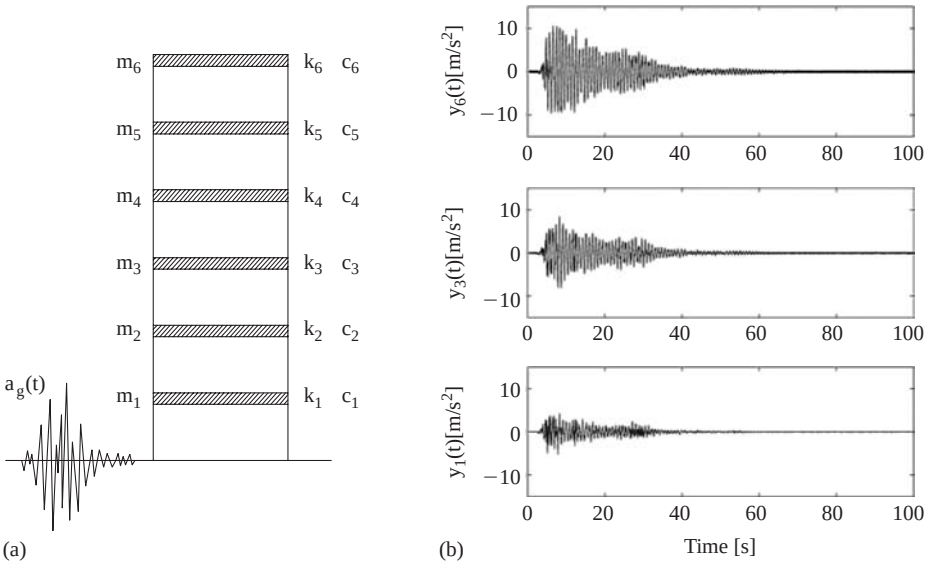

Figure 1 (a) Shear-type frame; (b) absolute accelerations y_1, y_3 and y_6 considered in the identification procedure.

the damping ratios and the standard deviation of the prediction errors $\boldsymbol{\eta}(t)$, and are gathered in the vector $\boldsymbol{\theta}_s = [\theta_1\ \theta_2\ \theta_3\ \theta_4\ \theta_5\ \theta_6\ \xi_1\ \xi_2\xi_3\ \xi_4\ \xi_5\ \xi_6\ \sigma_{\eta 1}\ \sigma_{\eta 3}\ \sigma_{\eta 6}]^T$.

The identification of the parameters for the cases of undamaged structure and five cases of damaged structure are carried out by a pseudo-experimental procedure, that is, by simulating the response for the actual cases, adding the noise and performing the structural identification.

The ground acceleration record of the 1940 El-Centro earthquake is used as input. For the undamaged structure, UD, the vector of stiffness parameters is set equal to: $[\theta_1\ \theta_2\ \theta_3\ \theta_4\ \theta_5\ \theta_6]^T = [1\ 1\ 1\ 1\ 1\ 1]^T$; the five damaged cases (DM1, DM2, DM3, DM4, DM5) correspond to a reduction of 10% of the first, second, third, fourth and fifth floor stiffness, respectively.

To apply the Bayesian model updating procedure, prior distributions with large standard deviations are selected for the model parameters. Lognormal (LN) distributions with mean 1 and standard deviation of the logarithm equal to 1 are adopted for the stiffness parameters; LN distributions with mean 0.02 and standard deviation of the logarithm equal to 1 are adopted for the damping ratios; LN distributions with mean -1.651 and standard deviation of the logarithm equal to 1 are adopted for the prediction-error variances for the structural accelerations.

The results of the structural identification are reported in Table 1 for the case of the undamaged (UD) structure and one case (DM1) of a damaged structure. It is evident that the procedure can accomplish all phases of damage detection, that is, damage identification, localization and quantification. The uncertainty of the identified parameters is sufficiently low in most cases; the model parameters are thus identifiable on the basis of the available data.

Table 1 Actual and identified (optimal) values of parameter $\boldsymbol{\theta}_s$ for the undamaged (UD) and damaged (DM1) structure; coefficient of variation (COV) of the optimal values.

Parameter	*UD*			*DM1*		
	Actual value	*Optimal value*	*COV*	*Actual value*	*Optimal value*	*COV*
θ_1	1.0	1.0510	0.094	0.9	0.9074	0.141
θ_2	1.0	1.0005	0.006	1.0	1.0015	0.006
θ_3	1.0	0.9989	0.006	1.0	0.9978	0.007
θ_4	1.0	1.0019	0.056	1.0	1.0016	0.008
θ_5	1.0	0.9989	0.006	1.0	1.0036	0.007
θ_6	1.0	1.0001	0.007	1.0	0.9914	0.009
ξ_1	0.02	0.0199	0.028	0.02	0.0201	0.034
ξ_2	0.02	0.0203	0.045	0.02	0.0197	0.049
ξ_3	0.02	0.0221	0.129	0.02	0.0217	0.143
ξ_4	0.02	0.0193	0.318	0.02	0.0209	0.288
ξ_5	0.02	0.0234	0.228	0.02	0.0202	0.205
ξ_6	0.02	0.0193	0.175	0.02	0.0219	0.191
$\sigma_{\eta 1}$	0.0034	0.0051	0.245	0.0037	0.0050	0.298
$\sigma_{\eta 3}$	0.0071	0.0187	0.068	0.0079	0.0193	0.052
$\sigma_{\eta 6}$	0.0114	0.0082	0.207	0.0124	0.0112	0.177

However, the precision of the identification is not the same for all parameters. In fact, the stiffness parameter θ_1 is identified with a coefficient of variation (COV) that is significantly greater than the other stiffness parameters, whereas the first two damping ratios ξ_1 and ξ_2 are identified with a lower uncertainty than the others. These differences, which occur also when the other damage scenarios are considered, can be explained by a sensitivity analysis.

A first estimate of the importance of a model parameter can be obtained by varying its value and introducing a measure of the error between the values of the ratios $R_{AB}(i\omega_r, \boldsymbol{\theta}_s)$ corresponding to the actual and the varied model parameters. The error ε_l can be defined as:

$$\varepsilon_l = \sum_{r=r_1}^{r_2} (|R_{AB}(i\omega_r, \boldsymbol{\theta}_s^*)| - |R_{AB}(i\omega_r, \boldsymbol{\theta}_{sl}^*)|)^2 \tag{18}$$

Here $\boldsymbol{\theta}_s^*$ is the vector of the actual model parameters and $\boldsymbol{\theta}_{sl}^*$ is the vector with the varied l–th parameter.

In order to measure the sensitivity of each parameter, a variation of $\pm 20\%$ has been considered for both stiffness parameters and modal damping ratios. In Table 2 the values of the error ε_l are listed. It is seen that a variation of the parameter θ_1 implies the lowest values of ε_l among the stiffness parameters; this is also the case for ξ_3, ξ_4, ξ_5, and ξ_6 among the damping ratios. Therefore, a larger uncertainty is to be expected when these parameters are identified.

A probabilistic sensitivity analysis confirms this conclusion. For the ratios $R_{AB}(i\omega)$ that are considered in the identification, the complex quantity h_{AB}:

$$h_{AB} = \Delta_{R_{AB}}(i\omega_r, \boldsymbol{\theta}_s) = |R_{AB}(i\omega_r, \boldsymbol{\theta}_s)| - |R_{AB}(i\omega_r)| \tag{19}$$

Table 2 Error ε_l for the stiffness θ_l and damping ratios ξ_l parameters.

Error	$R_{13}(20\%)$	$R_{16}(20\%)$	$R_{13}(-20\%)$	$R_{16}(-20\%)$
$\varepsilon_1(\theta_1)$	0.659E00	1.764E00	1.369E00	4.152E00
$\varepsilon_2(\theta_2)$	1.248E03	2.541E03	1.887E03	4.160E03
$\varepsilon_3(\theta_3)$	6.389E02	1.480E03	9.375E02	2.664E03
$\varepsilon_4(\theta_4)$	6.129 E02	1.415E03	9.923 E02	2.583E03
$\varepsilon_5(\theta_5)$	1.055E03	1.001E03	1.597E03	1.812E03
$\varepsilon_6(\theta_6)$	5.237 E02	5.363E02	1.061E03	1.111E03
$\varepsilon_7(\xi_1)$	3.300E01	1.422 E02	5.878E01	2.525E02
$\varepsilon_8(\xi_2)$	3.767 E01	3.092E01	6.430 E01	5.265E01
$\varepsilon_9(\xi_3)$	2.156 E00	6.032 E00	3.219 E00	8.930E00
$\varepsilon_{10}(\xi_4)$	0.628 E00	1.298 E00	0.785 E00	1.597E00
$\varepsilon_{11}(\xi_5)$	0.579 E00	0.847 E00	0.798 E00	1.259E00
$\varepsilon_{12}(\xi_6)$	3.745 E00	0.107 E00	6.013 E00	0.155E00

can be evaluated, which accounts for the difference between the theoretical and the measured ratios, for all frequencies involved in the simulation.

A probabilistic measure of the sensitivity is represented by the variance of the error h_{AB} due to the variation of a model parameter θ_{sl}. This quantity may be seen as the *total* effect of θ_{sl}, which measures the uncertainty in h_{AB} that is unexplained after having learnt everything except θ_{sl}. The variances σ_0^2 and σ_1^2 of the error, corresponding to prior and posterior samples, are evaluated for each ratio $R_{AB}(i\omega_r, \theta_s)$, by replacing the vector $\boldsymbol{\theta}_s$ with $\boldsymbol{\theta}_{sl}$, and then are used to assess the relative influence of each parameter. As indicated in (Sibilio & Ciampoli 2006, Sibilio et al. 2006), σ_0^2 can be interpreted as a global sensitivity index and the total effect of the considered parameter; σ_1^2 can be interpreted as a local sensitivity index.

In Figures 2–5, the global σ_0^2 and the local σ_1^2 sensitivity indices of the error, evaluated for the stiffness parameters θ_1, θ_2, θ_3, θ_4, θ_5, and θ_6, by sampling respectively from the prior distribution $p(\boldsymbol{\theta}_s|M_s)$ and the posterior distribution $p(\boldsymbol{\theta}_s|D_s, M_s)$, are reported. It is clear that, for any stiffness parameter, the value of σ_0^2 is larger than σ_1^2. It can also be observed that both σ_0^2 and σ_1^2 assume very low values for the parameter θ_1 over the whole interval of frequencies; therefore, the parameter θ_1 has a scarce influence on the ratio R_{13}. An analogous result can be obtained for the ratio R_{16}. It can be argued that θ_1 will be identified with higher uncertainty. Similar considerations can be done with regard to the low sensitivities of the parameters ξ_3, ξ_4, ξ_5, and ξ_6 according to the results in Table 2.

The effects of damage on the structural reliability are examined by using Subset Simulation. In order to solve the reliability integral, a time history of the ground acceleration is generated for each sample $\boldsymbol{\theta}$ for a given pair of values of M and R.

The PDF for magnitude M is modeled based on the Gutenberg-Richter law, with a minimum value $M_{min} = 5$ and a maximum value $M_{max} = 8$. This also provides the mean annual rate of a seismic event with magnitude between M_{min} and M_{max} at a specific site (Kramer 1996). The PDF for the source-to-site distance R is based on an earthquake being equally likely to occur anywhere in a circular area of radius equal to 50 km. Sampling from these distributions has been carried out by the inverse transform method (Robert & Casella 2004).

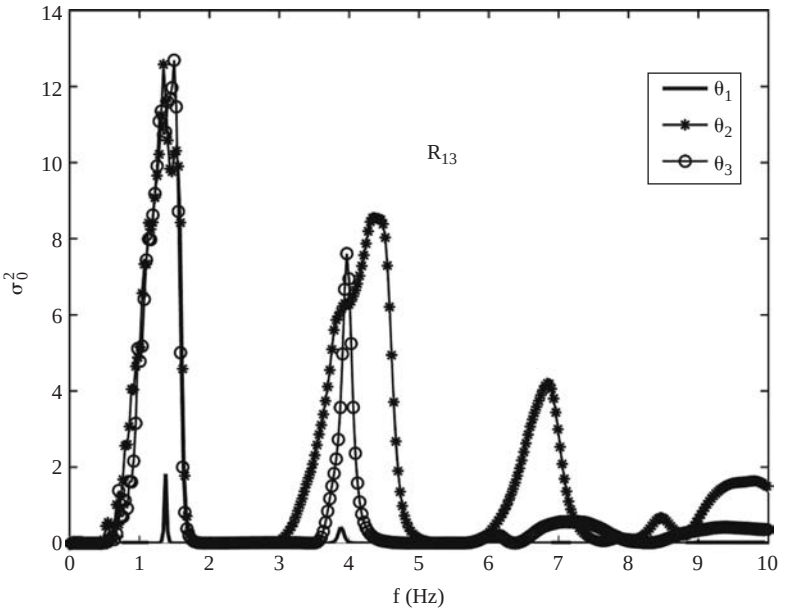

Figure 2 Sensitivity measures σ_0^2 of the error Δ_{R13}, for the stiffness parameters θ_1, θ_2 and θ_3, evaluated by sampling from the prior distribution $p(\boldsymbol{\theta}_s|M_s)$.

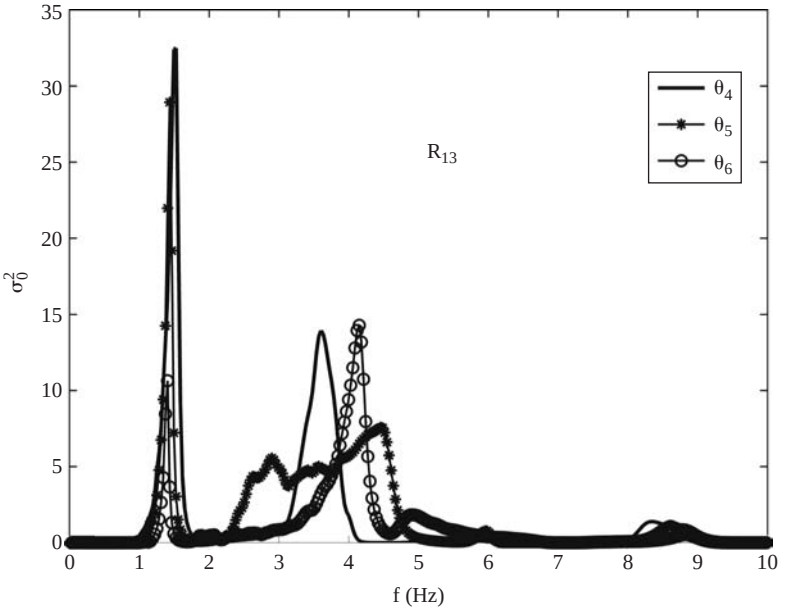

Figure 3 Sensitivity measures σ_0^2 of the error Δ_{R13}, for the stiffness parameters θ_4, θ_5 and θ_6, evaluated by sampling from the prior distribution $p(\boldsymbol{\theta}_s|M_s)$.

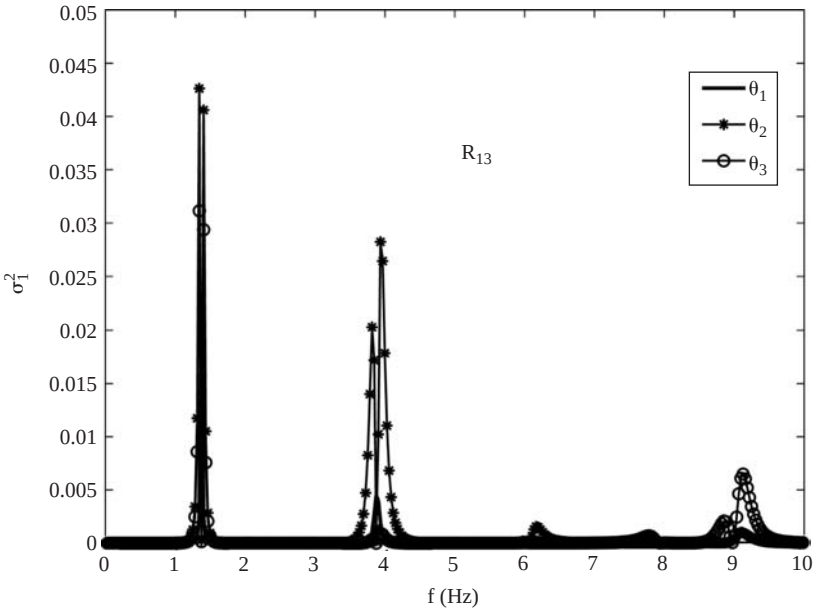

Figure 4 Sensitivity measures σ_1^2 of the error Δ_{R13}, for the stiffness parameters θ_1, θ_2 and θ_3, evaluated by sampling from the posterior distribution $p(\boldsymbol{\theta}_s|D_s, M_s)$.

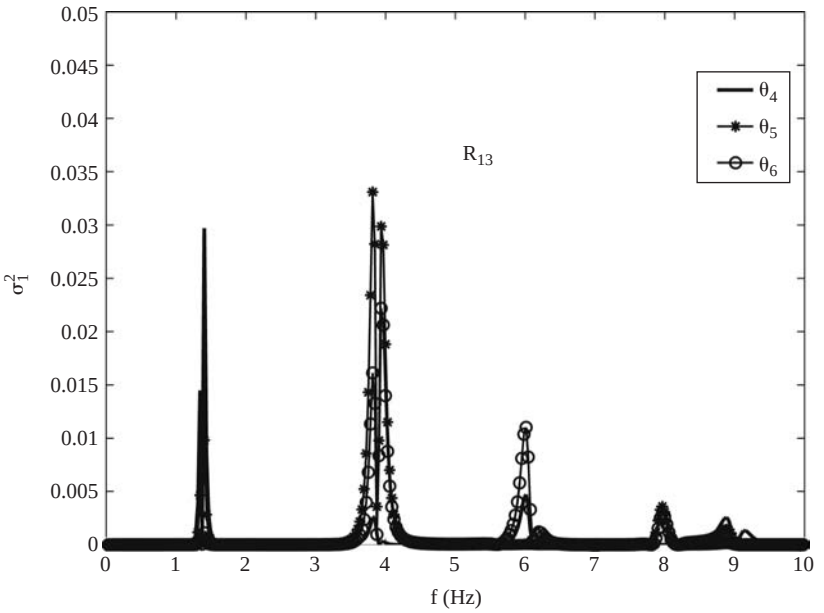

Figure 5 Sensitivity measures σ_1^2 of the error Δ_{R13}, for the stiffness parameters θ_4, θ_5 and θ_6, evaluated by sampling from the posterior distribution $p(\boldsymbol{\theta}_s|D_s, M_s)$.

The considered uncertain parameters are: M; R; the parameters of the white noise in the ground motion record, grouped in the vector $\mathbf{Z}$; the stiffness parameters $[\theta_1\ \theta_2\ \theta_3\ \theta_4\ \theta_5\ \theta_6]^{\mathrm{T}}$; and the modal damping ratios $[\xi_1\ \xi_2\ \xi_3\ \xi_4\ \xi_5\ \xi_6]^{\mathrm{T}}$. The selected structural response parameter is the maximum inter-storey drift b; Subset Simulation thus gives the exceedance probability of b computed for the whole time history and for all the stories of the structure.

Three simulation levels are implemented for Subset Simulation, in addition to the first level, using Monte Carlo simulation. For each level, 500 samples of the uncertain parameters $\boldsymbol{\theta}$ are considered. The value of the probability p_0 for each intermediate failure domain is taken equal to 0.1 (Au & Beck 2003). This means that the threshold value of the maximum inter-storey drift d_i ($i = 1, \ldots, m-1$) defining the intermediate failure domain F_i is the 450-th value of the ranked values of the drift corresponding to each of the 500 samples. There are 50 samples corresponding to the next failure level; so only 450 additional samples are obtained for that level. The total number of samples required for the simulation is: $N_T = 500 + 450 + 450 + 450 = 1850$. With these choices, it is possible to assess a probability of failure greater than or equal to 10^{-4}.

A major advantage of Subset Simulation is that it provides the probability of exceeding any response level over a specified range using only a single run. It is thus possible to evaluate the probability P_{LS} of exceeding any specified limit state LS by choosing the corresponding value of the structural capacity b_c. The capacity b_c may be described in probabilistic terms through its PDF $p(b_c)$. The probability P_{LS} and its approximation are thus given by:

$$P_{LS} = P(b > b_c) = \int P(b > b_c|b_c)p(b_c)\,db_c \approx \frac{1}{N_c}\sum_{i=1}^{N_c} P(b > b_{c_i}|b_{c_i}) \tag{20}$$

The probability $P(b > b_c|b_c)$ is directly estimated by Subset Simulation; the samples b_{ci} are obtained by sampling from the distribution $p(b_c)$.

In this example, three limit states have been considered: $LS1$, $LS2$ and $LS3$, corresponding to three different values of the capacity: $b_c^{(1)} = 0.3\%$, $b_c^{(2)} = 0.7\%$ and $b_c^{(3)} = 1.3\%$. The uncertainty in the limit state has been taken into account by introducing three distributions $p(b_c^{(1)})$, $p(b_c^{(2)})$ and $p(b_c^{(3)})$. Three Lognormal distributions have been taken, with mean value and standard deviation of the logarithm equal, respectively, to -1.20 and 0.1 for $LS1$, -0.36 and 0.05 for $LS2$, and 0.26 and 0.03 for $LS3$. For any group of uncertain parameters, the acceptance rate in the Subset Simulation algorithm has been taken in the range 20% to 50%.

In Figure 6 the probabilities P_{LS} for the cases of undamaged and damaged structure with deterministic capacity parameters (UDa, DM1a, DM2a, DM3a, DM4a, and DM5a) are plotted. For the cases DM1a and DM5a, the response level b for a given value of P_{LS} is higher than that for the case UDa, for each P_{LS} lower than 10^{-1}, while for cases DM2a, DM3a and DM4a, the response level is lower than that for case UDa, for each P_{LS} lower than 0.005.

In Figure 7 the probabilities P_{LS} for the cases of undamaged and damaged structure with uncertain capacity parameters (UDb, DM1b, DM2b, DM3b, DM4b, and DM5b), are plotted. The maximum inter-storey drift b for the damaged structure is higher than that for the undamaged case UDb, for any P_{LS} lower than 10^{-1}.

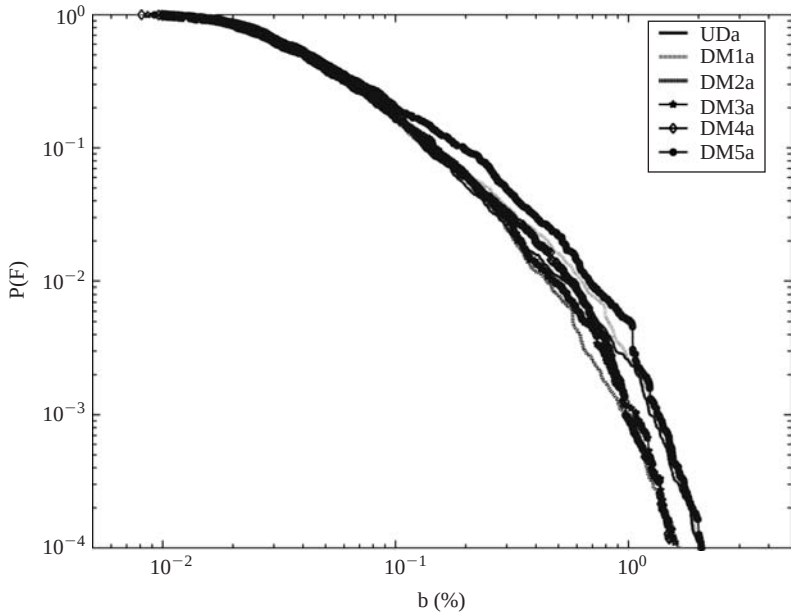

Figure 6 Probability of failure P_{LS} for the structure with deterministic capacity parameters for different damage scenarios.

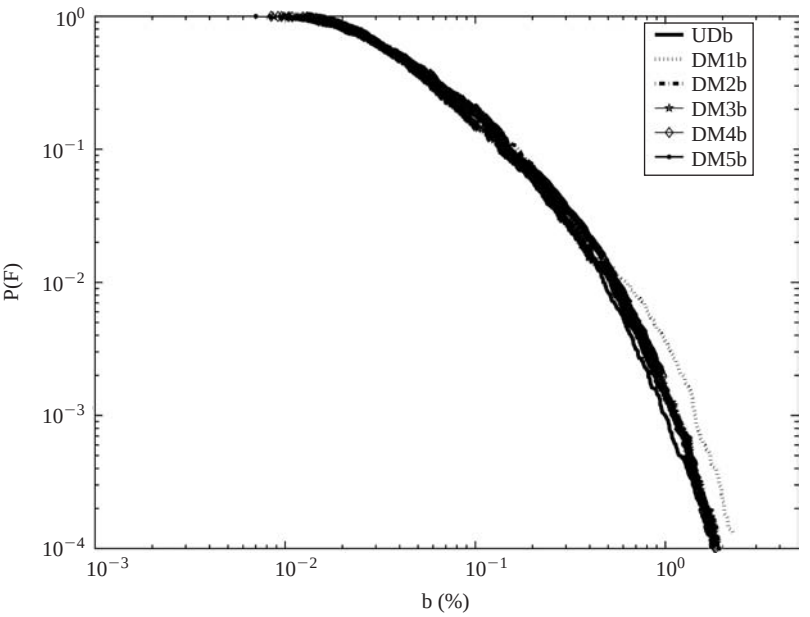

Figure 7 Probability of failure P_{LS} for the structure with uncertain capacity parameters for different damage scenarios.

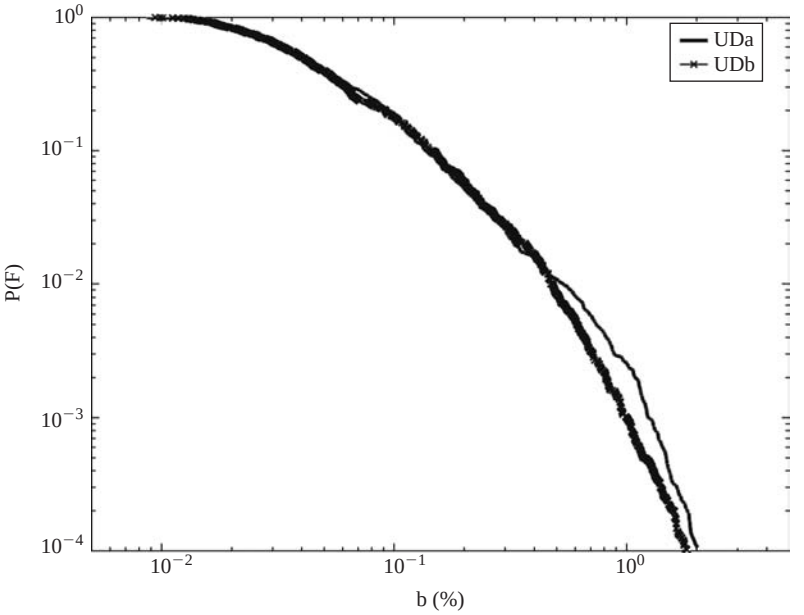

Figure 8 Probability of failure P_{LS} for (a) the undamaged structure with deterministic (UDa) and uncertain capacity parameters (UDb).

Table 3 Probability P_{LS} of exceeding the considered limit states for different damage scenarios and deterministic capacity parameters.

Limite state	*Model UDa*	*Model DM1a*	*Model DM2a*	*Model DM3a*	*Model DM4a*	*Model DM5a*
LS1a	0.02560	0.03580	0.02400	0.03000	0.03240	0.04760
LS2a	0.00580	0.00778	0.00254	0.00442	0.00528	0.00918
LS3a	0.00086	0.00114	0.00028	0.00034	0.00033	0.00114
LS1b	0.02550	0.03651	0.02556	0.02867	0.03261	0.04999
LS2b	0.00580	0.00787	0.00255	0.00428	0.00535	0.00941
LS3b	0.00088	0.00110	0.00027	0.00036	0.00035	0.00114

The comparison of the probabilities of failure between the deterministic and the uncertain models is illustrated in Figures 8–9 for the cases UD and DM1, respectively. For the undamaged structure (UDa, UDb), the uncertainty in the model parameters yields a decreasing level of the structural response b, at least for a probability of failure lower than 10^{-2}. This is probably due to the identified mean value of the parameter θ_1 which is slightly higher than the actual value. For cases DM1a, DM1b, there is no evidence of differences between the deterministic and uncertain models, at least for values of P_{LS} greater than 0.005, whereas for lower probability values the uncertainty plays a more significant role.

The probability of exceeding the limit states *LS*1, *LS*2 and *LS*3 are listed in Tables 3–4; *LS*1*a*, *LS*2*a* and *LS*3*a* and *LS*1*b*, *LS*2*b* and *LS*3*b* refer to deterministic

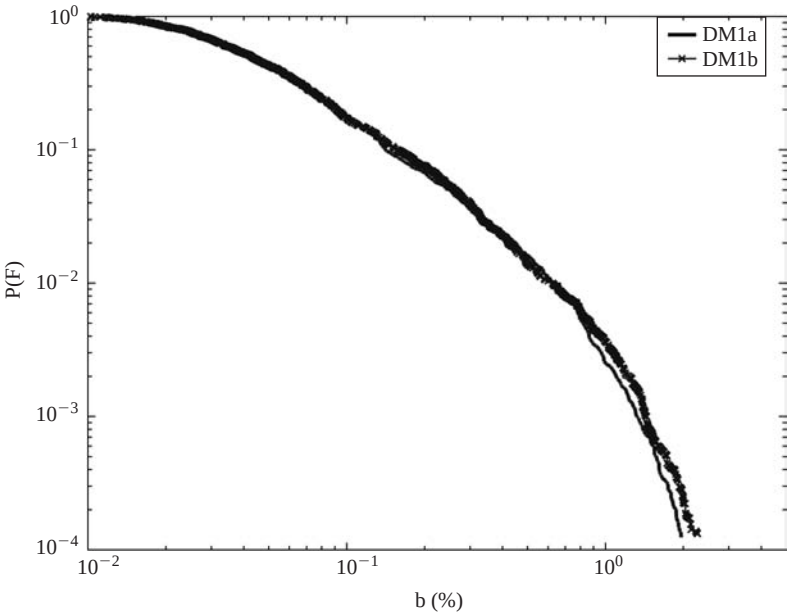

Figure 9 Probability of failure P_{LS} for one case of damaged structure with deterministic (DM1a) and uncertain capacity parameters (DM1b).

Table 4 Probability P_{LS} of exceeding the considered limit states for different damage scenarios and probabilistic capacity parameters.

Limite state	*Model UDb*	*Model DM1b*	*Model DM2b*	*Model DM3b*	*Model DM4b*	*Model DM5b*
LS1a	0.02820	0.03920	0.03220	0.02900	0.03540	0.03020
LS2a	0.00314	0.00784	0.00522	0.00452	0.00512	0.00476
LS3a	0.00040	0.00168	0.00046	0.00067	0.00060	0.00058
LS1b	0.02819	0.03905	0.03207	0.02996	0.03746	0.02949
LS2b	0.00323	0.00805	0.00531	0.00446	0.00518	0.00472
LS3b	0.00040	0.00169	0.00047	0.00062	0.00060	0.00058

and probabilistic structural capacities, respectively. By reading along the rows, one can see the case that corresponds to the highest probability P_{LS} for the corresponding limit state. In each column, as expected, the probability of failure decreases for the limit states associated with higher response levels.

In general, the uncertainty in the definition of the limit state does not produce a large difference in the failure probability P_{LS}. Comparing the values of the probability P_{LS} for deterministic and uncertain capacity parameters, it can be observed that the uncertainty of the parameters plays a significant role for the damage scenarios UD, DM2 and DM5.

4 Conclusions

A general procedure for structural health monitoring that includes both damage detection and reliability assessment of a structure subject to seismic excitation is briefly illustrated and applied to an example case. The procedure is formulated in a unified probabilistic framework that can take into account any kind of uncertainty involved in the various phases of the analysis.

A Bayesian model updating approach is used to identify the structural parameters and their associated uncertainty. An advanced stochastic simulation method, Subset Simulation, is then applied to assess the seismic reliability of the damaged structure. This method can include the effect of the uncertainties identified through the Bayesian model updating in the assessment of the failure probability. Furthermore, the uncertainty of the structural capacity can be considered. Although the approach is applied here to a linear dynamic model, the Bayesian model updating and the seismic reliability assessment can be extended to nonlinear models [see, for example, Beck & Muto (2007) and Au & Beck (2003)]. It is concluded that the proposed probabilistic framework is a powerful one for handling all the uncertainties in any structural health monitoring procedure.

References

Au, S-K. & Beck, J.L. 2001. Estimation of small failure probabilities in high dimensions by Subset Simulation. *Probabilistic Engineering Mechanics* 16: 263–277.

Au, S-K. & Beck, J.L. 2003. Subset Simulation and its application to seismic risk based on dynamic analysis. *Journal of Engineering Mechanics* 129(8): 901–917.

Beck, J.L. & Katafygiotis, L.S. 1998. Updating models and their uncertainties. I: Bayesian statistical framework. *Journal of Engineering Mechanics* 124(4): 455–461.

Beck, J.L. & Muto, M. 2007. Bayesian updating and model class selection of deteriorating hysteretic structural models using seismic response data. *ECCOMAS Thematic Conference on Computational Methods in Structural Dynamics and Earthquake Engineering*, Rethymno, Crete, Greece.

Boore, D.M. 2003. Simulation of ground motion using the stochastic method. *Pure and Applied Geophysics* 160: 635–676.

Capecchi, D., De Angelis, M. & Sepe, V. 2004. Modal model identification with unknown nonstationary base motion. *Meccanica* 39: 31–45.

Ching, J. & Chen, Y-J. 2007. Transitional Markov Chain Method for Bayesian model updating, model class selection and model averaging. *Journal of Engineering Mechanics* 133: 816–832.

Ching, J., Au, S-K. & Beck, J.L. 2005a. Reliability estimation for dynamical systems subject to stochastic excitation using Subset Simulation with splitting. *Computational Methods in Applied Mechanics and Engineering* 194: 1557–1579.

Ching, J., Au, S-K. & Beck, J.L. 2005b. Hybrid Subset Simulation method for reliability estimation of dynamical systems subject to stochastic excitation. *Probabilistic Engineering Mechanics* 20: 199–214.

Doebling, S.W., Farrar, C.R., Prime, M.B. & Shevitz, D.W. 1996. *Damage indication and health monitoring of structural and mechanical systems from change in their vibrations characteristics: A literature review*. Technical Report LA-13070-MS. Los Alamos National Laboratory.

Kramer, S.L. 1996. *Geotechnical Earthquake Engineering*. Prentice Hall, New Jersey.

Papadimitriou, C., Beck, J.L. & Katafygiotis, L.S. 2001. Updating robust reliability using structural test data. *Probabilistic Engineering Mechanics* 16: 103–113.

Robert, C.P. & Casella, G. 2004. *Monte Carlo Statistical Methods*. Springer Texts in Statistics, 2nd edition, Springer and Verlag, New York, 2004.

Sepe, V., Capecchi, D. & De Angelis, M. 2005. Modal model identification of structures under unmeasured seismic excitations. *Earthquake Engineering and Structural Dynamics* 34: 807–824.

Sibilio, E. & Ciampoli, M. 2006. Valutazione dell'affidabilità strutturale attraverso tecniche di simulazione Monte Carlo: "Subset Simulation" e "Bayesian Updating". *Proc. CRASC'06, Messina, CDRom*.

Sibilio, E., Ciampoli, M. & Beck, J.L. 2006. Seismic reliability assessment of structures via Subset Simulation and Bayesian updating. *3rd International Conference on Advances in Mechanical Engineering and Mechanics*, *Hammamet, Tunisia, CDRom*.

Yuen, K-V. & Katafygiotis, L.S. 2005. Model updating using noisy response measurements without knowledge of the input spectrum. *Earthquake Engineering and Structural Dynamics* 34: 167–187.

Yuen, K-V. & Katafygiotis, L.S. 2006. Substructure identification and health monitoring using noisy response measurement only. *Computer-Aided Civil and Infrastructure Engineering* 21: 280–291.

Chapter 19

A multiphase model with hypoplastic formulation of the solid phase and its application to earthquake engineering problems

Konstantin Meskouris

RWTH Aachen University, Aachen, Germany

Stefan Holler

Airbus Deutschland GmbH, Hamburg, Germany

Christoph Butenweg & Daniel Meiners

RWTH Aachen University, Aachen, Germany

ABSTRACT: In the present paper a multiphase model including a hypoplastic formulation of the solid phase is presented and its application to earthquake engineering problems discussed. The macroscopic soil model, which is based on the theory of porous media, comprises three distinct phases namely, solid, fluid and gas phase. For each of these the compressibility of the respective medium is taken into account in the mathematical formulation of the model. The solid phase is modelled using the hypoplastic constitutive equation including intergranular strain to allow for a realistic description of material behaviour of cohesionless soils even under cyclic loading. The model was implemented into the finite element package ANSYS via the user interface and also allows the simulation of soil-structure interaction problems.

1 Introduction

Numerical simulation of heterogeneous materials is of major interest for a wide range of engineering applications. In biomechanical engineering, for instance, multiphase models provide a valuable approach for modelling tissues, cartilage and bones. In civil engineering, they can be used in material research, e.g. for determining moisture penetration in reinforced concrete and therefore estimating the risk of corrosion of the reinforcement. In geotechnical engineering, multiphase modelling is of paramount importance in order to obtain realistic predictions for the soil's behaviour under loading and unloading, since the load bearing capacity of soil is significantly dependent on the degree of water saturation, i.e. on the composition of its distinct phases. Typical applications encompass seepage problems for dams, installation of sheet pile walls by vibration or hydraulic hammer and slope stability problems.

In extension to that, experiences from past earthquakes have shown that ground liquefaction poses a serious hazard to all kinds of structures. During the Loma Prieta earthquake 1989 in San Francisco bay and the 1999 earthquake in Izmit, Turkey,

earthquake-induced loss of shear strength for partially or fully saturated cohensionless soils, i.e. liquefaction, caused major damage to numerous structures. These experiences revealed the deficiencies of existing models with regard to cyclic loading conditions and have manifested the need for accurate numerical models to describe and predict dynamical soil behaviour.

To overcome these problems, a multiphase model considering a hypoplastic approach including intergranular strain for the solid phase has been developed in this work. Due to its implementation into the finite element program ANSYS it also allows for soil-structure-interaction analyses within the existing finite element framework. In Holler & Meskouris (2006), presented the application of the model to a soil-structure interaction analysis of silos under dynamic excitation.

2 Numerical model

2.1 *Multiphase media*

One of the main difficulties in many geotechnical problems is the mathematical representation of the materials involved. Soil and rock are highly complex, inhomogeneous materials whose behaviour is strongly influenced by their distinct phases. Thus, factors such as water saturation and pore pressure have a strong impact on the distribution of loads among these phases. The theory of porous media, which extends the classical approach of continuum mechanics to multiphase media, offers a convenient way to describe materials consisting of several distinct phases by means of two entirely different concepts, namely the microscopic and the macroscopic approach. The microscopic description is based on the movement and deformation of each discrete particle and requires the equilibrium equations to be formulated for all particles separately in order to account for particle interaction, i.e. contact and frictional forces. Due to the irregular particle shape and pore distribution commonly encountered in soils, however, prediction of the behaviour of distinct particles is almost impossible, i.e. the microscopic approach is not suitable for most geotechnical applications. Rather, a macroscopic approach is followed which results in a smeared description of the soil behaviour and basically consists of a homogenization process over a representative volume element. The concept of volume fractions is utilised to formulate the equilibrium equations for each phase separately and to account for phase interaction. The presented model comprises a porous solid skeleton as well as a fluid and a gas phase and takes compressibility for each of those into account. Following the concept of volume fractions, the entire volume of the representative volume element consists of the solid fraction V_s and the pore volume V_p which again is composed of the water saturated and air saturated pore volume, V_w and V_g respectively, as stated in equation 1.

$$V = V_s + V_p = V_s + V_w + V_g \tag{1}$$

Defining the porosity n, the void ratio e and the degree of water and air saturation S_w and S_g respectively as

$$n = \frac{V_p}{V} \tag{2}$$

$$e = \frac{V_p}{V_s} \tag{3}$$

$$S_w = \frac{V_w}{V_p} \tag{4}$$

$$S_g = \frac{V_g}{V_p} \tag{5}$$

the volume fractions of each component can be defined. Upon loading, stress develops not only within the solid skeleton of the multiphase medium but also in the water and gas phases. The total stress results from the difference of the effective stress σ', i.e. stress causing deformations of the solid skeleton, and the averaged pressure surrounding the particles (equation 6).

$$\boldsymbol{\sigma} = \boldsymbol{\sigma'} - \mathbf{m}^T(S_w p_w + S_g p_g) \tag{6}$$

Here $\mathbf{m}^T$ is

$$\mathbf{m}^T = [1\ 1\ 1\ 0\ 0\ 0]^T. \tag{7}$$

If volumetric deformation of the soil particles due to stationary water and air pressures is also taken into account, equation 6 must be modified with Biot's constant (Biot 1957) as follows.

$$\boldsymbol{\sigma} = \boldsymbol{\sigma'} - \alpha\mathbf{m}^T(S_w p_w + S_g p_g) \tag{8}$$

Here Biot's constant α is

$$\alpha = 1 - \frac{K_T}{K_S} \leq 1 \tag{9}$$

In most geotechnical applications, however, the correction introduced by α is negligible since the bulk modulus of the solid skeleton K_T is significantly smaller than the bulk modulus of a single particle K_S.

Flow through a porous medium is described by Darcy's law, which, in its basic form, is only valid for a single fluid flow and was extended to a second fluid by Wyckoff & Botset (1936). This yields equation 10 for the flow velocity of the fluid and gas phase, respectively.

$$\mathbf{v}_{xs} = \frac{\mathbf{k}k_{rx}}{nS_x\eta_x}(-\nabla_{p_x} + \rho_x(\mathbf{g} - \ddot{\boldsymbol{u}}_s)); \quad x = w, g \tag{10}$$

The temporal variation of density for the solid, fluid, and gas phases is taken into account through equations 11 and 12, respectively.

$$\frac{1}{\rho_s}\frac{\partial \rho_s}{\partial t} = \frac{1}{1-n}\left[(\alpha - n)\frac{1}{K_S}\frac{\partial p_s}{\partial t} - (1-\alpha)\nabla \mathbf{v}_s\right] \tag{11}$$

$$\frac{1}{\rho_{x0}}\frac{\partial \rho_x}{\partial t} = \frac{1}{K_x}\frac{\partial p_x}{\partial t}; \quad x = w, g \tag{12}$$

Finally, the balance of mass for the three distinct phases yields a system of equations in terms of the unknown variables displacement, pore water-, and pore air pressure. The continuity equations for the solid, fluid, and gas phases are given in equations 13, 14 and 15, respectively.

$$-\frac{\partial n}{\partial t} + \frac{(1-n)}{\rho_s}\frac{\partial \rho_s}{\partial t} + (1-n)\nabla \mathbf{v}_s = 0 \tag{13}$$

$$\begin{aligned}&\left[\frac{nS_w}{K_w} + (\alpha - n)\frac{S_w}{K_s}\left(S_w + p_c\frac{\partial S_w}{\partial p_c}\right) - n\frac{\partial S_w}{\partial p_c}\right]\frac{\partial p_w}{\partial t}\\ &\quad + \left[\frac{S_w}{K_s}(\alpha - n)\left(S_g - p_c\frac{\partial S_w}{\partial p_c}\right) + n\frac{\partial S_w}{\partial p_c}\right]\frac{\partial p_g}{\partial t}\\ &\qquad + \alpha S_w \nabla \mathbf{v}_s + \frac{1}{\rho_w}\nabla\left[\rho_w\frac{\mathbf{k}k_{rw}}{\eta_w}(-\nabla p_w + \rho_w(\mathbf{g} - \ddot{\boldsymbol{u}}_s))\right] = 0\end{aligned} \tag{14}$$

$$\begin{aligned}&\left[\frac{nS_g}{K_g} + (\alpha - n)\frac{S_g}{K_s}\left(S_g - p_c\frac{\partial S_w}{\partial_c}\right) - n\frac{\partial S_w}{\partial p_c}\right]\frac{\partial p_g}{\partial t}\\ &\quad + \left[\frac{S_g}{K_s}(\alpha - n)\left(S_w + p_c\frac{\partial S_w}{\partial p_c}\right) + n\frac{\partial S_w}{\partial p_c}\right]\frac{\partial p_w}{\partial t}\\ &\qquad + \alpha S_g \nabla \mathbf{v}_s + \frac{1}{\rho_g}\nabla\left[\rho_g\frac{\mathbf{k}k_{rg}}{\eta_g}(-\nabla_g + \rho_g(\mathbf{g} - \ddot{\boldsymbol{u}}_s))\right] = 0\end{aligned} \tag{15}$$

Equations 14 and 15 describe the development of pore water and pore air pressure in a de-formable solid skeleton. The deformation of the solid phase, in turn, depends on the effective stress σ' and will be described in section 2.2 on hypoplasticity. For a more detailed derivation of the multiphase model see Holler (2006).

2.2 *Hypoplasticity*

The hypoplastic material law describes the stress rate as a function of stress, strain rate and void ratio and is well-suited for cohensionless, granular materials. It reliably predicts the non-linear and inelastic behaviour of soil due to its rate-type formulation which ensures a realistic modelling of loading and unloading paths. Also, by virtue of the rate-type formulation, numerical implementation of the hypoplastic material law is significantly simplified. The hypoplastic constitutive equation by von Wolffersdorff (1996) is given in equation 16.

$$\Delta\sigma'_{ij} = L_{ijkl}\,\Delta\varepsilon_{ij} + N_{ij}\sqrt{\Delta\varepsilon_{kl}\,\Delta\varepsilon_{kl}} \tag{16}$$

Here L_{ijkl} is a fourth order tensor describing the linear relation between strain rate and stress rate and N_{ij} represents the nonlinear part.

$$L_{ijkl} = f_s \frac{1}{\hat{\sigma}_{mn}\hat{\sigma}_{mn}}(F^2 I_{ijkl} + a^2 \hat{\sigma}_{ij}\hat{\sigma}_{kl}) \tag{17}$$

$$N_{ij} = f_s f_d \frac{Fa}{\hat{\sigma}_{kl}\hat{\sigma}_{kl}}(\hat{\sigma}_{ij} + \hat{\sigma}^*_{ij}) \tag{18}$$

With

$$\hat{\sigma}_{ij} = \frac{\sigma'_{ij}}{\sigma_{mn}\delta_{mn}} \tag{19}$$

$$\hat{\sigma}^*_{ij} = \hat{\sigma}'_{ij} - \frac{1}{3}\delta_{ij} \tag{20}$$

$$I_{ijkl} = \delta_{ik}\delta_{jl} \tag{21}$$

$$a = \frac{\sqrt{3}(3 - \sin\varphi_c)}{2\sqrt{2}\sin\varphi_c} \tag{22}$$

$$F = \sqrt{\frac{1}{8}\tan^2\psi + \frac{2 - \tan^2\psi}{2 + \sqrt{2}\tan\psi\cos 3\Theta}} - \frac{1}{2\sqrt{2}}\tan\psi \tag{23}$$

$$\tan\psi = \sqrt{3}\sqrt{\hat{\sigma}^*_{kl}\hat{\sigma}^*_{kl}} \tag{24}$$

$$\cos 3\Theta = -\sqrt{6}\frac{\hat{\sigma}^*_{ij}\hat{\sigma}^*_{jk}\hat{\sigma}^*_{ki}}{(\hat{\sigma}^*_{mn}\hat{\sigma}^*_{mn})^{\frac{3}{2}}} \tag{25}$$

and

$$f_s = \frac{h_s}{n}\left(\frac{e_i}{e}\right)^{\beta}\frac{1 + e_i}{e_i}\left(-\frac{\sigma_{ij}\delta_{ij}}{h_s}\right)^{1-n} \times \left[3 + a^2 - \sqrt{3}\left(\frac{e_{i0} - e_{d0}}{e_{c0} - e_{d0}}\right)^{\alpha}\right]^{-1} \tag{26}$$

$$f_d = \left(\frac{e - e_d}{e_c - e_d}\right)^{\alpha} \tag{27}$$

The actual void ratios e_x are obtained with the initial void ratios e_{x0}, the stress state σ'_{ij} and the parameters h_s and n from equation 28.

$$\frac{e_i}{e_{i0}} = \frac{e_c}{e_{c0}} = \frac{e_d}{e_{d0}} = \frac{e}{e_0} = \exp\left[-\left(-\frac{\sigma'_{ij}\,\delta_{ij}}{h_s}\right)^n\right] \tag{28}$$

The parameters of the hypoplastic constitutive equation φ_c, h_s, n, e_{d0}, e_{c0}, e_{i0}, α, and β can be determined from soil mechanics standard tests Herle (1997).

Although von Wolffersdorff's hypoplastic constitutive equation reliably predicts the nonlinear inelastic behaviour of soil, there are some drawbacks with respect to its application to cyclic stress conditions. The most severe shortcoming is an excessive accumulation of deformations for small stress cycles, a phenomenon called ratcheting.

To overcome these drawbacks, Niemunis & Herle (1997) presented an extension of the hypoplastic constitutive equation by introducing the concept of intergranular strain. In addition to the deformations of the granular structure by grain rearrangement they also take the deformations of the contact area between the distinct grains into account. This results in the introduction of an initial resistance for small strains before deformation of the granular structure takes place and it effectively avoids ratcheting, i.e. the build-up of excessive strains for small amplitude cyclic loading. The modified version of equation 16 is then transformed to the form of equation 29.

$$\Delta\sigma'_{ij} = M_{ijkl}\,\Delta\varepsilon_{kl} \tag{29}$$

with

$$\begin{aligned} M_{ijkl} &= [\rho^{\varkappa} m_T + (1-\rho^{\varkappa}) m_R] L_{ijkl} \\ &\quad + \begin{cases} \rho^{\varkappa}(1-m_T) L_{ijmn}\hat{S}_{mn}\hat{S}_{kl} + \rho^{\varkappa} N_{ij}\hat{S}_{kl} & \text{for } \hat{S}_{ij}\,\Delta\varepsilon_{ij} > 0 \\ \rho^{\varkappa}(m_R - m_T) L_{ijmn}\hat{S}_{mn}\hat{S}_k l & \text{for } \hat{S}_{ij}\,\Delta\varepsilon_{ij} \le 0 \end{cases} \end{aligned} \tag{30}$$

Here S_{ij} is an additional variable representing the intergranular strain. Its rate of change is determined from equation 31.

$$\Delta S_{ij} = \begin{cases} (I_{ijkl} - \rho^{\beta_R}\hat{S}_{ij}\hat{S}_{kl})\Delta\varepsilon_{kl} & \text{for } \hat{S}_{ij}\,\Delta\varepsilon_{ij} > 0 \\ \Delta\varepsilon_{ij} & \text{for } \hat{S}_{ij}\,\Delta\varepsilon_{ij} \le 0 \end{cases} \tag{31}$$

$\hat{S}_{ij}$ is the direction of the intergranular strain and equals

$$\hat{S}_{ij} = \begin{cases} \frac{S_{ij}}{\sqrt{S_{kl}S_{kl}}} & \text{for } S_{ij} \neq 0 \\ \Delta\varepsilon_{ij} & \text{for } S_{ij} = 0. \end{cases} \tag{32}$$

The mechanism of intergranular strain can best be explained with the *brick analogy* by Simpson (1992). Consider a man walking about with a brick attached to his legs by a string of the length R. In case the brick is dragged along the ground, this represents the plastic strain rate. If on the other hand the brick remains in place, the relative movement between man and brick represents the intergranular strain.

2.3 *Finite element implementation*

In the present work Gallerkin's method of weighted residuals is used to derive the weak form of the equilibrium equations. Hence, the first step towards finite element discretisation of the governing equations is the definition of shape functions for the domain variables, i.e. displacement, pore water pressure and pore air pressure. Introducing these shape functions into equations 13, 14 and 15 the governing equations are approximated with a certain accuracy. The approximation errors, termed

residuals, are multiplied with weighting functions and then minimized over the entire problem domain. Gallerkin's method of weighted residuals implies taking the element shape functions, used to interpolate the domain variables throughout the element, as weighting funtions for the residuals, thereby ensuring satisfaction of all boundary conditions. Obviously, the choice of appropriate shape functions is crucial with regard to the quality of the finite element approximation.

From the resulting system of equations (equation 33) the mass, damping and stiffness matrices for the finite element can be obtained.

$$\begin{bmatrix} \mathbf{M} & 0 & 0 \\ \mathbf{M}_w & 0 & 0 \\ \mathbf{M}_g & 0 & 0 \end{bmatrix} \begin{bmatrix} \ddot{\overline{\boldsymbol{u}}} \\ 0 \\ 0 \end{bmatrix} + \begin{bmatrix} \mathbf{C} & 0 & 0 \\ \mathbf{C}_{ws} & \mathbf{P}_{ws} & \mathbf{C}_{wg} \\ \mathbf{C}_{gs} & \mathbf{C}_{gw} & \mathbf{P}_{gg} \end{bmatrix} \begin{bmatrix} \dot{\overline{\boldsymbol{u}}} \\ \dot{\overline{p}}_w \\ \dot{\overline{p}}_g \end{bmatrix} + \begin{bmatrix} 0 & -\mathbf{C}_{ws}^T & -\mathbf{C}_{gs}^T \\ 0 & \mathbf{H}_{ww} & 0 \\ 0 & 0 & \mathbf{H}_{gg} \end{bmatrix} \begin{bmatrix} \overline{\boldsymbol{u}} \\ \overline{p}_w \\ \overline{p}_g \end{bmatrix} + \int \boldsymbol{\sigma}' \, d\Omega \begin{bmatrix} 1 \\ 0 \\ 0 \end{bmatrix} = \begin{bmatrix} \mathbf{f}_u^{\Omega} \\ \mathbf{f}_{pw}^{\Omega} \\ \mathbf{f}_{pag}^{\Omega} \end{bmatrix} + \begin{bmatrix} \mathbf{f}_u^{\Gamma} \\ \mathbf{f}_{pw}^{\Gamma} \\ \mathbf{f}_{pg}^{\Gamma} \end{bmatrix} \tag{33}$$

with the mass matrices $\mathbf{M}$, $\mathbf{M}_w$ and $\mathbf{M}_g$,

$$\mathbf{M} = \int \mathbf{N}_u [\rho_s (1-n) + n S_w \rho_w + n S_g \rho_g] \mathbf{N}_u \, d\Omega \tag{34}$$

$$\mathbf{M}_x = \int \nabla \mathbf{N}_p^T \frac{\mathbf{k} k_{rx}}{\eta_x} \rho_x \mathbf{N}_u \, d\Omega; \quad x = w, g \tag{35}$$

coupling matrices $\mathbf{C}_{ws}$, $\mathbf{C}_{sw}$, $\mathbf{C}_{gs}$, $\mathbf{C}_{sg}$, $\mathbf{C}_{wg}$ and $\mathbf{C}_{gw}$,

$$\mathbf{C}_{ws} = \mathbf{C}_{sw}^T = \int \mathbf{N}_p^T \alpha S_w \mathbf{m}^T \mathbf{L} \mathbf{N}_u \, d\Omega \tag{36}$$

$$\mathbf{C}_{gs} = \mathbf{C}_{sg}^T = \int \mathbf{N}_p^T \alpha S_g \mathbf{m}^T \mathbf{L} \mathbf{N}_u \, d\Omega \tag{37}$$

$$\mathbf{C}_{wg} = \int \mathbf{N}_p^T \left[\frac{S_w}{K_s} (\alpha - n) \left(S_g - p_c \frac{\partial S_w}{\partial p_c} \right) + n \frac{\partial S_w}{\partial p_c} \right] \mathbf{N}_p \, d\Omega \tag{38}$$

$$\mathbf{C}_{gw} = \int \mathbf{N}_p^T \left[\frac{S_g}{K_s} (\alpha - n) \left(S_w + p_c \frac{\partial S_w}{\partial p_c} \right) + n \frac{\partial S_w}{\partial p_c} \right] \mathbf{N}_p \, d\Omega \tag{39}$$

compressibilty matrices $\mathbf{P}_{ww}$ and $\mathbf{P}_{gg}$,

$$\mathbf{P}_{ww} = \int \mathbf{N}_p^T \left[\frac{n S_w}{K_w} + (\alpha - n) \frac{S_w}{K_s} \left(S_w + p_c \frac{\partial S_w}{\partial p_c} \right) - n \frac{\partial S_w}{\partial p_c} \right] \mathbf{N}_p \, d\Omega \tag{40}$$

$$\mathbf{P}_{gg} = \int \mathbf{N}_p^T \left[\frac{n S_g}{K_g} + (\alpha - n) \frac{S_g}{K_s} \left(S_g - p_c \frac{\partial S_w}{\partial p_c} \right) - n \frac{\partial S_w}{\partial p_c} \right] \mathbf{N}_p \, d\Omega \tag{41}$$

permeability matrices $\mathbf{H}_{ww}$ and $\mathbf{H}_{gg}$,

$$\mathbf{H}_{xx} = \int \nabla \mathbf{N}_p^T \frac{\mathbf{k} k_{rx}}{\eta_x} \nabla \mathbf{N}_p \, d\Omega; \quad x = w, g \tag{42}$$

and domain forces $\mathbf{f}_u^{\Omega}$, $\mathbf{f}_{pw}^{\Omega}$ and $\mathbf{f}_{pg}^{\Omega}$.

$$\mathbf{f}_u^{\Omega} = \int \mathbf{N}_u [\rho_s (1-n) + n S_w \rho_w + n S_g \rho_g] \mathbf{g} \, d\Omega \tag{43}$$

$$\mathbf{f}_{px}^{\Omega} = \int \mathbf{N}_p^T \frac{\mathbf{k} k_{rx}}{\eta_x} \rho_x \mathbf{g} \, d\Omega; \quad x = w, g \tag{44}$$

The boundary conditions are directly imposed via the boundary forces $\mathbf{f}_u^{\Gamma}$, $\mathbf{f}_{pw}^{\Gamma}$ and $\mathbf{f}_{pg}^{\Gamma}$ of equations 45 and 46.

$$\mathbf{f}_u^{\Gamma} = \int \mathbf{N}_u \boldsymbol{\sigma} \, d\Gamma \tag{45}$$

$$\mathbf{f}_{px}^{\Gamma} = -\int \mathbf{N}_p^T \left[\frac{\mathbf{k} k_{rx}}{\eta_x} (-\nabla \mathbf{N}_p \bar{\boldsymbol{p}}_x + \rho_x \mathbf{g}) \right] d\Gamma; \quad x = w, g \tag{46}$$

The generic formulation of the integral of the effective stress over the domain Ω in equation 33 allows the use of arbitrary nonlinear constitutive equations through the term

$$\int \boldsymbol{\sigma}' \, d\Omega \begin{bmatrix} 1 \\ 0 \\ 0 \end{bmatrix}.$$

The actual implementation of the element in ANSYS was carried out as a plane rectangular element via the user element interface. The element allows the simulation of partially saturated soils under plane strain as well as under rotationally symmetric stress states.

Integration in the time domain was carried out using Newmark's integration method for the solid phase and the generalized trapezoidal method for the fluid and gas phases. The solution in the spatial domain was obtained utilising Gaussian quadrature as integration method. Generally, 3×3 integration points were used to compute the element solution. In the transition phase between unsaturated and fully saturated soils, however, 7×7 integration points were used to improve the accuracy of the solution.

3 Model verification/validation

Various tests, that are documented in detail in Holler (2006), have been performed to validate and verify the presented model. Among these were a simulation of air flow through dry sand, a drainage test after Liakopoulos, and a simulation of soil layer consolidation. In this section, the consolidation problem will be discussed. A fully-saturated soil layer of thickness $h = 1\,m$ was subjected to a surface load of $q0 = 10\,kN/m^2$ and width $2a = 2\,m$ at time $t = 0\,s$. The solution of the given example was carried out analytically and by means of numerical simulation. Figure 1 shows

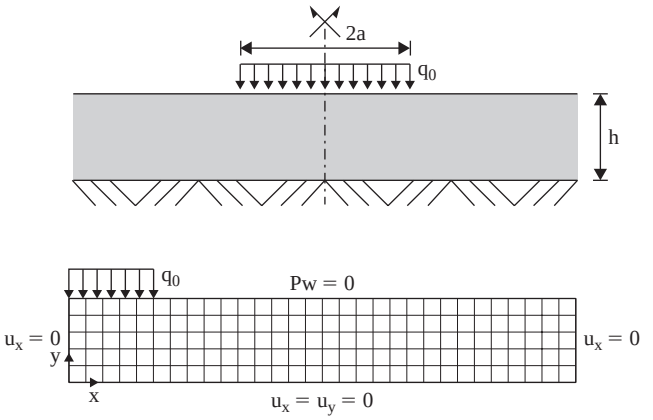

Figure 1 Model setup and finite element mesh.

Table 1 Parameters of consolidation test.

Parameter	*Symbol*	*Unit*	*Value*
Young's modulus	E	*kPa*	5000
Poisson's ratio	μ	–	0.25
Permeability	k	m^2	$1.31 \cdot 10^{-10}$
Water density	ρ_w	t/m^3	1.0
Degree of water saturation	S_w	t/m^3	$1.2 \cdot 10^{-3}$
Bulk modulus solid particle	K_s	*kPa*	$1.0 \cdot 10^9$
Bulk modulus water phase	K_w	*kPa*	$2.0 \cdot 10^6$
Dynamic viscosity water	η_w	kNs/m^2	$1.31 \cdot 10^{-6}$

the initial conditions as well as the finite element model and the imposed boundary conditions.

The material parameters are given in Table 1. Young's modulus of elasticity E as well as the permeability k were chosen arbitrarily. Density ρ_w, bulk modulus K_w and dynamic viscosity η_w of water are constants which were chosen for a reference temperature of $T = 10°C$. The bulk modulus of a solid particle K_s for sand is almost infinite when compared to the compressibility of water and is therefore set to $K_s = 1.0 \cdot 10^9\, kPa$.

The analytical solution was obtained following Booker (1974). Taking advantage of symmetry, the numerical solution was performed on one half of the original system. The width of the considered soil layer is set to $b = 6.0\, m$.

On both the left and right hand side of the model the displacements are restricted in the x-direction. At the bottom displacements are fully constrained. On the free surface at the top the water pressure is set to $p_w = 0$. The simulation is conducted with 60 time steps between $10^{-4}\, s$ and $2\, s$.

For the displacements, biquadratic shape functions have been used. Bilinear and bi-quadratic shape functions have been used for the pore water pressure in Simulation

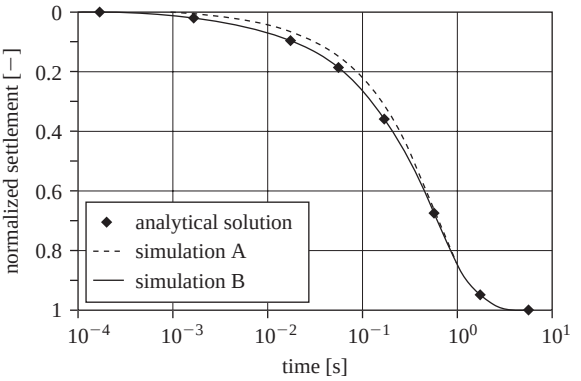

Figure 2 Comparison of analytical and numerical solutions of consolidation problem.

A and B, respectively. Figure 2 shows a comparison of the numerical results to the analytical solution.

For simulation A, i.e. linear approximation of pore water pressure, the normalized settlement is slightly overestimated in the central time period. In the case of biquadratic shape functions for the pore water pressure (Simulation B), however, a very good approximation of the analytical solution can be achieved with the chosen discretization. Of course, better results can be obtained for linear shape functions by simply decreasing the element size to obtain a finer mesh.

4 Example: dam under seismic loading

The phenomenon of ground liquefaction aroused increasing interest during the last decade due to its devastating impact on structures under seismic loading. Numerical models that can predict soil behaviour under cyclic conditions are, however, still rare. Also, laboratory tests are rather complex and difficult to conduct. Some model experiments to investigate ground liquefaction have been reported in C-Core Earthquake Induced Damage Mitigation (2004). Therein, a scaled model (factor 70) of a dam was subjected to an artificial earthquake which was generated by means of a centrifuge.

In the present work, these experiments have been simulated numerically. The simulation was performed with the finite element model of Figure 6. Zero displacements in x-directions were imposed on both the right and left hand side of the model. The bottom layer of the model is fully constrained. The water pressure is applied to the model via equivalent boundary forces. A comparison of the experimental results and those obtained from numerical simulation is given in Figure 4.

The results are generally in good agreement with the experimental data. The increase in pore water pressure at the beginning of the seismic loading is correctly mirrored by the numerical simulation. The maximum change in pore water pressure, however, is overestimated in the time period $15\,s < t < 25\,s$. With progress in time and decrease of loading the pore pressure approaches the initial static state. The decrease of pore pressure is in good agreement at some measuring points but differs significantly in points P1, P5 and P6.

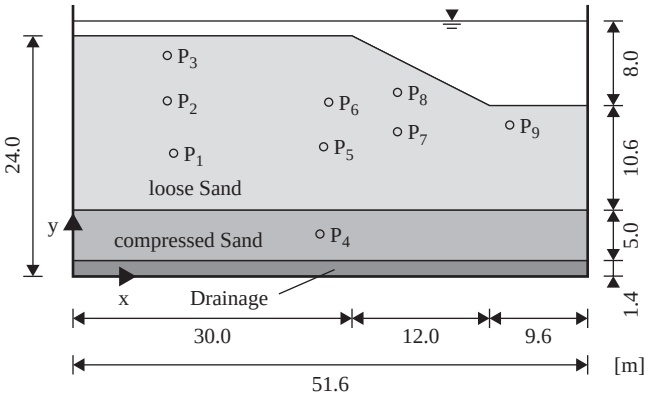

Figure 3 Model of test specimen (scale factor 70) (C-Core Earthquake Induced Damage Mitigation, 2004).

This is a result of the chosen initial boundary conditions, since the sand layers are considered as homogeneous with constant initial conditions. Hence, neither the compaction of the sand due to the increase in vertical acceleration of the centrifuge nor the increase of compaction due to the linear increase of self-weight with depth are taken into account in the numerical simulation.

Also, the void ratio decreases with depth due to the increase in self-weight and the resulting increase of compaction. The change in void ratio in turn influences the permeability which was considered constant during the numerical simulation.

In a second simulation (B) some modification have been applied to the boundary conditions. To realistically mirror the initial conditions of the experiments, the initial void ratio is linearly decreased over the depth in the numerical model and the permeability is defined as a function of the void ratio (equation 47). This way, compaction of the sand layers due to self-weight is accounted for.

$$k = -4.2 \cdot 10^{-11} + e \cdot 1.22 \cdot 10^{-10} \tag{47}$$

The results of the simulation B are given in Figure 5. In comparison to simulation A they show a better approximation of the experimental data due to the improved description of the boundary conditions. Still, pore water pressures in time period $15\,s < t < 25\,s$ are slightly overestimated when compared to the measured data.

The time evolution of water pressure and displacements is shown in Figure 7. At time $t = 0$, i.e. when the dam is subjected only to self-weight, the pressure distribution varies linearly over depth. The increase of pore water pressure within the entire domain yields a decrease of the effective stress acting upon the solid skeleton and an increase of the void ratio e. When reloading the solid skeleton, plastic deformations, which are shown on the right hand side of Figure 7, develop. The simulated deformations were in good agreement with the experimental data.

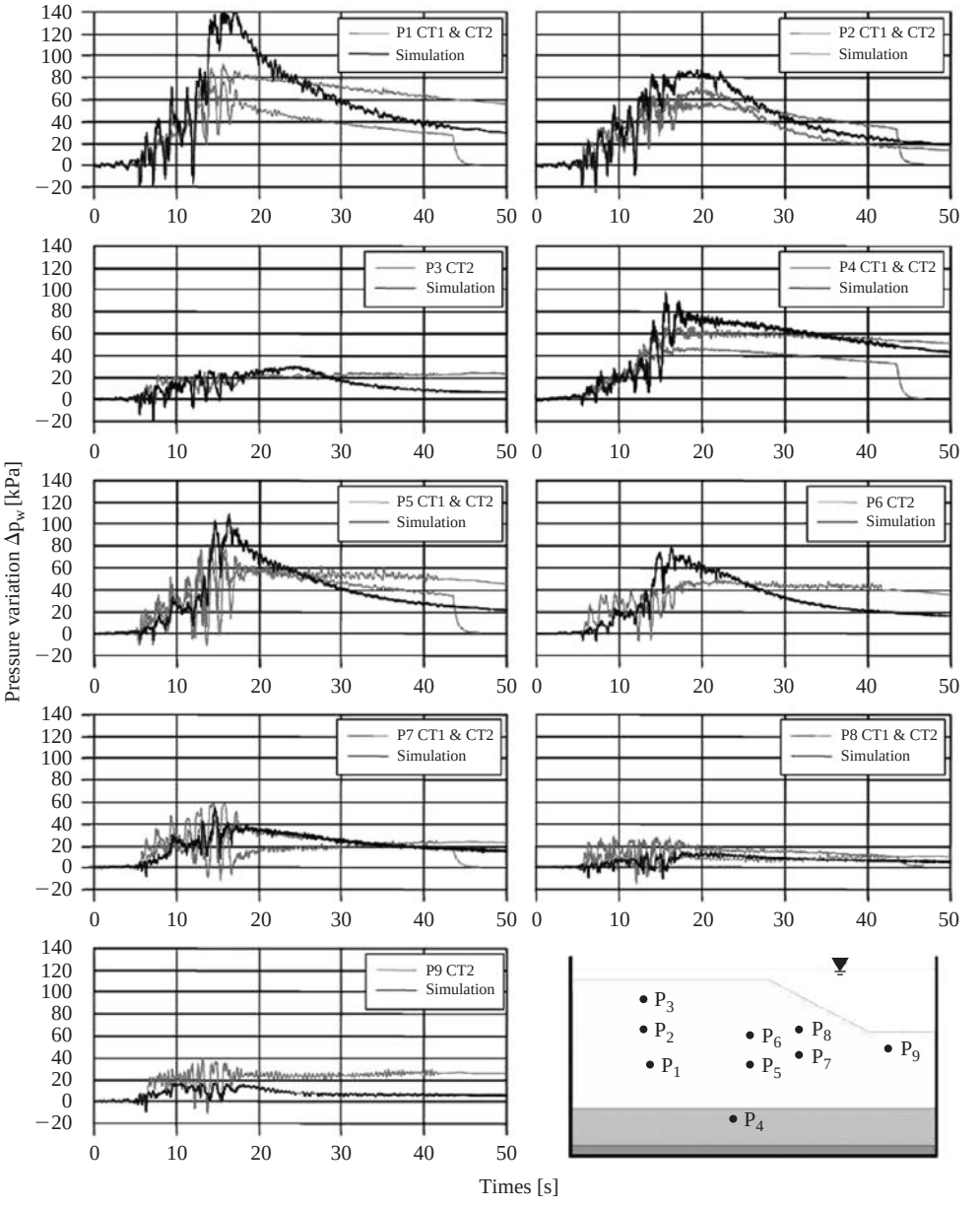

Figure 4 Comparison of results (A) (C-Core Earthquake Induced Damage Mitigation, 2004).

5 Summary and conclusions

In the present work, a dynamic multiphase model including a hypoplastic formulation of the solid phase was developed and realised numerically by means of the finite element

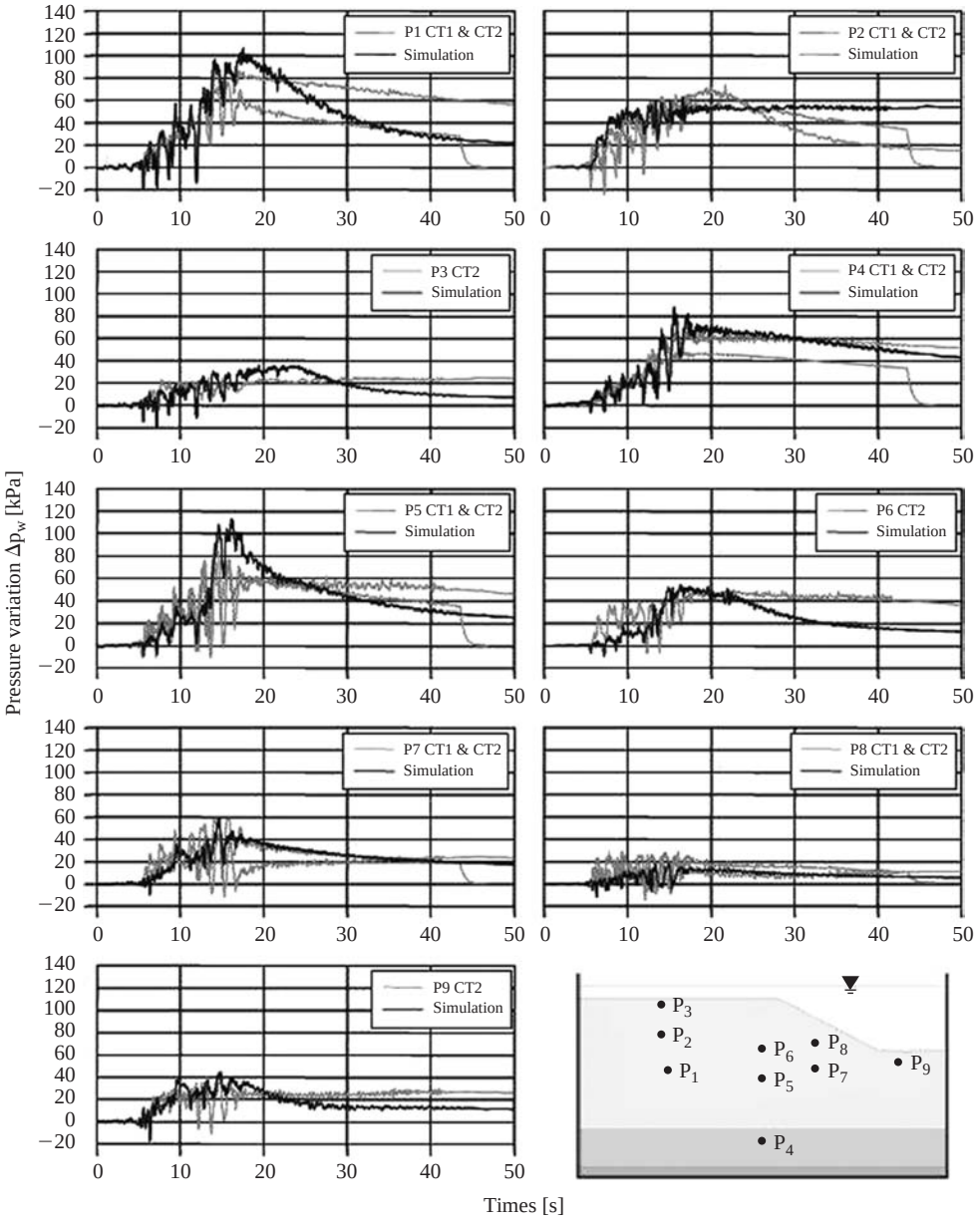

Figure 5 Comparison of results (B) (C-Core Earthquake Induced Damage Mitigation, 2004).

method. The model was implemented into the finite element code ANSYS and verified on the basis of several examples.

Due to the hypoplastic formulation including intergranular strain, the model is capable of predicting soil behaviour even under cyclic loading and therefore offers

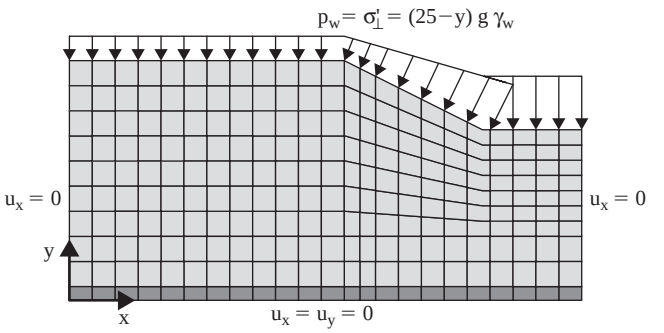

Figure 6 Finite element model of the dam.

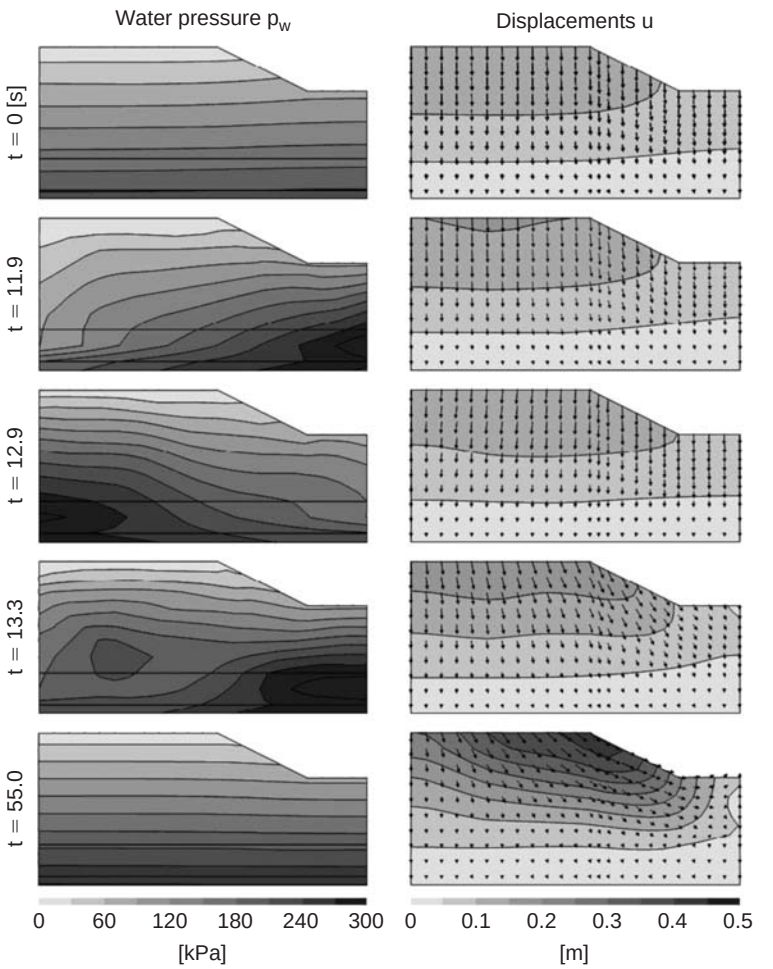

Figure 7 Pore water pressure and displacements (B).

a possibility to further investigate dynamical phenomena such as ground liquefaction. The accuracy of the numerical approximation has been shown by comparison to experimental data.

The presented mutliphase model is capable of simulating consolidation, saturation and drainage processes and can realistically predict permanent ground displacements. Although the compressibilty of fluid and gas phase do not have a strong impact on the flow characteristics and the load bearing capacity of soils, they were still taken into account to provide further application possibilities for the model. Additionally, the model allows the implementation of arbitrary constitutive equations for the solid phase and also allows coupling to existing solid elements.

References

Biot, M.A. 1957. The elastic coefficients of the theory of consolidation, *Journal of Applied Mechanics*, **24**, 594–601.

Booker, J.R. 1974. The consolidation of a finite layer subject to surface loading, *International Journal of Soils and Structures*, **10**, 1053–1065.

C-Core, 2004. Earthquake Induced Damage Mitigation from Soil Liquefaction, Centre for Cold Ocean Resources Engineering, Data Report of Centrifuge Test CT1 and CT2, Canada.

Fredlund, D.G. & Rahardjo, H. 1993. *Soil Mechanics for Unsaturated Soils*. John Wiley & Sons.

Herle, I. 1997. *Hypoplastizität und Granulometrie einfacher Korngerüste*, Dissertation, Institut für Bodenmechanik und Felsmechanik der Universität Karlsruhe, **142**.

Holler, S. 2006. *Dynamisches Mehrphasenmodell mit hypoplastischer Formulierung der Feststoffphase*, Mitteilungen des Lehrstuhls für Baustatik und Baudynamik, RWTH Aachen, **11**.

Holler, S. & Meskouris, K. 2006. Granular Material Silos under Dynamic Excitation: Numerical Simulation and Experimental Validation, *Journal of Structural Engineering*, **132**, 1573–1579.

Niemunis, A. & Herle, I. 1997. Hypoplastic model for cohesionless soils with elastic strain range. *Mechanics of Cohesive-Frictional Materials*, **2**, 279–299.

Öttl, G. 2003. *A Three-Phase FE-Model for Dewatering of Soils*. Innsbruck University press.

Simpson, B. 1992. Retaining Structures: displacement and design. *Geotechnique*, **42**, 541–576.

Wyckoff, R.D. & Botset, H.G. 1936. The flow of Gas-liquid Mixtures through Unconsolidated Sands. *General and Applied Physics*, **7**, 325–345.

von Wolffersdorff, P.-A. 1996. A hypoplastic relation for granular materials with a predefined limit state surface. *Mechanics of Cohesive-Frictional Materials*, **1**, 251–271.

Chapter 20

Mixed Lagrangian formulation in analysis of collapse of structures

Andrei M. Reinhorn

University at Buffalo (SUNY), Buffalo, USA

Mettupalayam V. Sivaselvan

University of Colorado at Boulder, Boulder, USA

Gary F. Dargush

University at Buffalo (SUNY), Buffalo, USA

Oren Lavan

Technion – Israel Institute of Technology, Haifa, Israel

ABSTRACT: A Lagrangian approach was developed, which is a mixed method, where in addition to the displacements, the stress-resultants and other variables of state are primary unknowns. This formulation consists of two sets of equations: equilibrium and compatibility of displacement rates (velocities), while its primary unknowns are forces and velocities. For numerical solution, a discrete variational integrator is derived starting from the weak formulation. This integrator inherits the energy and momentum conservation characteristics. The integration of each step is a constrained minimization problem and it is solved using an Augmented Lagrangian algorithm. In this chapter, details of the formulation and computational algorithms are presented, as well as the examples of a simple structure and a sixteen-story building emphasizing on convergence and computational efficiency issues.

1 Introduction

Nonlinear analyses of structural response to hazardous loads such as earthquake and blast forces should include (i) the effects of significant material and geometric nonlinearities (ii) the phenomenological models describing the behavior of structural components and (iii) the energy and momentum transfer to different parts of the structure when structural components fracture. Computer analysis of structures has traditionally been carried out using the displacement method, combined with an incremental iterative scheme for nonlinear problems wherein the displacements in the structure are treated as the primary unknowns. In this paper, an alternative method is proposed for the analysis of structures considering both material and geometric nonlinearities. The formulation attempts to solve problems using a force-based approach in which momentum appears explicitly and can be potentially used to deal with structures where deterioration and fracture occur before collapse. In conventional formulations, the response of the structure is considered as the solution of a set of differential equations in time. Since the differential equations hold at a particular instant of time, they

provide a temporally local description of the response and are referred to as the strong form. In contrast, in this chapter, a time integral of functions of the response over the duration of the response is considered. Such an approach presents a temporally global picture of the response and is referred to as the weak form. The kernel of the integral mentioned above consists of two functions – the Lagrangian and the dissipation functions – of the response variables that describe the configuration of the structure and their rates. The integral is called the action integral. In elastic systems, the configuration variables are typically displacements. It is shown here, however, that in considering elastic-plastic systems it is natural to also include the time integrals of internal forces in the structure as configuration variables. The Lagrangian function is energy-like and describes the conservative characteristics of the system, while the dissipation function similar to a flow potential describes the dissipative characteristics. In a conservative system, the action integral is rendered stationary (maximum, minimum or saddle point) by the response. In analytical mechanics, this is called Hamilton's principle or more generally the principle of least action. For non-conservative systems such as elastic-plastic systems, such a variational statement is not possible, and only a weak form which is not a total integral is possible. It is shown moreover that the form of the Lagrangian is invariant under finite deformations. Such a weak formulation enables the construction of numerical integration schemes.

2 Simple phenomenological models of reciprocal structures

A complex structural system, such as frame structures representing buildings, bridges or mechanical systems, can be assembled from components which are formulated as reciprocal structures. Reciprocal structures are those structures characterized by convex potential and dissipation functions (Stern, 1965). In this section, the concept of reciprocal structures is explained using simple spring-mass-damper-slider models shown in Figure 1. Mixed Lagrangian and Dissipation functions of such systems are derived for various structural components.

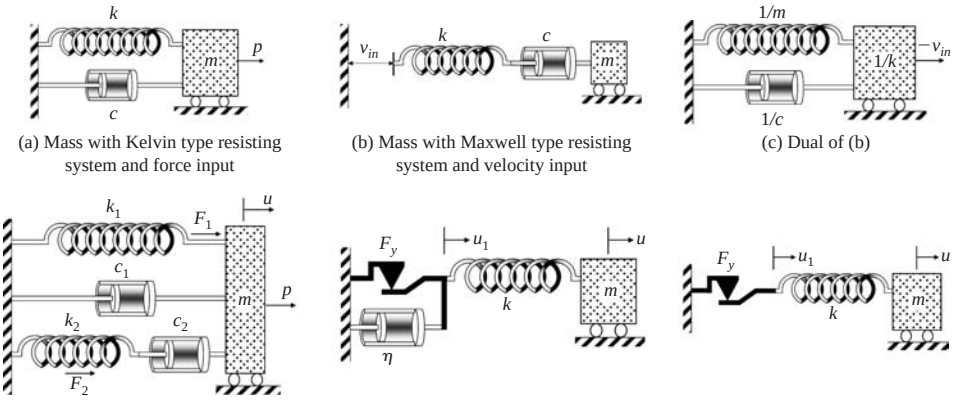

Figure 1 Simple phenomenological models.

(a) Mass with Kelvin type Resisting System: Consider a spring-mass-damper system with the spring and the damper in parallel (Kelvin Model shown in Figure 1(a)) subjected to a time-varying force input P(t). The equation of motion is given by:

$$m\ddot{u} + c\dot{u} + ku = P \tag{1}$$

where m is the mass, k is the modulus of the spring, c is the damping constant, u is the displacement of the mass and a superscripted "." denotes derivative with respect to time. The well known approach in Analytical Mechanics is to multiply equation (1) by a virtual displacement function δ_u, integrate over the time interval [0,T] by parts to obtain the action integral, $\mathcal{I}$, in terms of the Lagrangian function, $\mathcal{L}$ and the dissipation function, φ, as shown below (see for example, José and Saletan (1998)):

$$\delta\mathcal{I} = -\delta\int_0^T \mathcal{L}(u,\dot{u})\,dt + \int_0^T \frac{\partial\varphi(\dot{u})}{\partial\dot{u}}\delta u\,dt - \int_0^T P\delta u\,dt = 0 \tag{2}$$

where δ denotes the variational operator, and the Lagrangian function, $\mathcal{L}$, and the dissipation function, φ, of this system are given by:

$$\mathcal{L}(u,\dot{u}) = \frac{1}{2}m\dot{u}^2 - \frac{1}{2}ku^2 \quad \text{and} \quad \varphi(\dot{u}) = \frac{1}{2}c\dot{u}^2 \tag{3}$$

Notice that due to the presence of the dissipation function and because the force P(t) can in general be non-conservative, equation (2) defines $\delta\mathcal{I}$ and not $\mathcal{I}$ itself.

(b) Mass with Maxwell type Resisting System: Consider on the other hand, a spring-mass-damper system with the spring and the damper in series (Maxwell Model – shown in Figure 1(b)) subjected to a time varying base-velocity input, $v_{in}(t)$. The formulation requires obtaining a Lagrangian function and a dissipation function for this system that determine the equations of motion as above. Formulation of compatibility of deformations results in:

$$v_{in} + \frac{\dot{F}}{k} + \frac{F}{c} = \dot{u} \tag{4}$$

where F is the force in the spring and damper. Writing the equation of equilibrium of the mass, $m\ddot{u} + F = 0$, solving for the velocity and substituting in equation (4), we have:

$$\frac{1}{k}\dot{F} + \frac{1}{c}F + \frac{1}{m}\int_0^t F\,d\tau = -v_{in} - v_0 \tag{5}$$

where v_0 is the initial velocity of the mass. Defining $J = \int_0^t F\,d\tau$ (as suggested by El-Sayed et al. 1991), the impulse of the force in the spring and damper, equation (5) can be written as:

$$\frac{1}{k}\ddot{J} + \frac{1}{c}\dot{J} + \frac{1}{m}J = -v_{in} - v_0 \tag{6}$$

From the correspondence between equations (6) and (1), we conclude that the Lagrangian function, $\mathcal{L}$, the dissipation function, $\boldsymbol{\phi}$ and the action integral, $\delta\mathcal{I}$ of this system are given by:

$$\mathcal{L}(J,\dot{J}) = \frac{1}{2}\frac{1}{k}\dot{J}^2 - \frac{1}{2}\frac{1}{m}J^2 \quad \varphi(\dot{J}) = \frac{1}{2}\frac{1}{c}\dot{J}^2$$

$$\text{and} \quad \delta\mathcal{I} = -\delta\int_0^T \mathcal{L}(J,\dot{J})\,dt + \int_0^T \frac{\partial\varphi(\dot{J})}{\partial\dot{J}}\delta J\,dt + \int_0^T [v_{in}(t) + v_0]\delta J\,dt \tag{7}$$

(c) Mass with Combined Kelvin and Maxwell Resisting Systems: Consider now the combined Kelvin-Maxwell system shown in Figure 1(d) subject to a Force Input. (Note that the velocity input has been excluded for the sake of simplicity). The forces in the springs are denoted by F_1 and F_2 respectively and their impulses by J_1 and J_2. If we define the flexibilities of the springs as $a_1 = 1/k_1$ and $a_2 = 1/k_2$, then the Lagrangian function can be given by

$$\mathcal{L}(J_1,J_2,\dot{u},\dot{J}_1,\dot{J}_2) = \frac{1}{2}m\dot{u}^2 + \frac{1}{2}a_1\dot{J}_1^2 + \frac{1}{2}a_2\dot{J}_2^2 + (J_1+J_2)\dot{u} \tag{8}$$

or in matrix notation:

$$\mathcal{L}(\mathbf{J},\dot{u},\dot{\mathbf{J}}) = \frac{1}{2}m\dot{u}^2 + \frac{1}{2}\dot{\mathbf{J}}^{\mathrm{T}}\mathbf{A}\dot{\mathbf{J}} + \mathbf{J}^{\mathrm{T}}\mathbf{B}^{\mathrm{T}}\dot{u} \tag{9}$$

where $\mathbf{J} = [J_1\ J_2]^{\mathrm{T}}$, $\mathbf{A} = \mathrm{diag}(a_1,a_2)$, the flexibility matrix and $\mathbf{B} = [1\ 1]$, the equilibrium matrix. The equilibrium matrix operates on the vector of internal forces to produce the vector of nodal forces. The compatibility matrix, $\mathbf{B}^{\mathrm{T}}$, operates on the velocity vector to produce the rate of change of deformation. As a consequence of the Principle of Virtual Work, the transpose of the compatibility matrix is the equilibrium matrix, $\mathbf{B}$. The dissipation function is given by:

$$\overline{\varphi}(\dot{u},\dot{J}_2) = \frac{1}{2}c_1\dot{u}^2 + \frac{1}{2}\frac{1}{c_2}\dot{J}_2^2 \tag{10}$$

The Euler-Lagrange equations are:

$$\begin{aligned}
&\frac{d}{dt}\left(\frac{\partial\mathcal{L}}{\partial\dot{u}}\right) - \left(\frac{\partial\mathcal{L}}{\partial u}\right) + \frac{\partial\overline{\varphi}}{\partial\dot{u}} = P \Rightarrow m\ddot{u} + c\dot{u} + \mathbf{B}\dot{\mathbf{J}} = P \\
&\frac{d}{dt}\left(\frac{\partial\mathcal{L}}{\partial\dot{\mathbf{J}}}\right) - \left(\frac{\partial\mathcal{L}}{\partial\mathbf{J}}\right) + \frac{\partial\overline{\varphi}}{\partial\dot{\mathbf{J}}} = 0 \Rightarrow \mathbf{A}\ddot{\mathbf{J}} + \frac{\partial\overline{\varphi}}{\partial\dot{\mathbf{J}}} - \mathbf{B}^{\mathrm{T}}\dot{u} = 0
\end{aligned} \tag{11}$$

The mixed Lagrangian of equation (9) and the Dissipation function of equation (10) form the basis of further developments in this chapter. It should be noted that the Lagrangian does not contain the displacement, u explicitly; therefore the momentum, $\partial\mathcal{L}/\partial u$, is conserved (see for example Scheck, 1994), which leads to the idea of the generalized momentum, $p_u = \partial\mathcal{L}/\partial u = m\dot{u} + J_1 + J_2$.

(d) Elastic-viscoplastic Dynamic System: Consider the elastic-viscoplastic dynamic system of Figure 1(e). This is in fact a viscoplastic representation of the elastic-ideal-plastic system of Figure 1(f). Let the yield force of the slider be F_y, so that that force F_{slider} in the slider is such that $|F_{slider}| = F_y$. If the force in the spring is F and its impulse J, then the rate of deformation of the slider-dashpot combination is:

$$\dot{u}_1 = \frac{1}{\eta}\langle |F| - F_y \rangle sgn(F) = \frac{1}{\eta}\langle |\dot{J}| - F_y \rangle sgn(\dot{J}) \tag{12}$$

where <x> is the Macaulay Bracket, equal to the value of x for positive quantities and equal to zero for negative values of x. and sgn(x), the signum function. The above constitutive equation can be obtained from the following:

$$\mathcal{L}(\dot{u}, \dot{J}) = \frac{1}{2} m\dot{u}^2 + \frac{1}{2} a\dot{J}^2; \quad \varphi(\dot{J}) = \frac{1}{2\eta}\langle |\dot{J}| - F_y \rangle^2;$$

$$\text{and } \delta\mathcal{I} = -\delta \int_0^T \mathcal{L}(J, \dot{u}, \dot{J})\, dt \; + \; \int_0^T \frac{\partial \varphi(\dot{J})}{\partial \dot{J}} \delta J \, dt \; - \; \int_0^T P\, \delta u \, dt \tag{13}$$

(e) Elastic-Ideal Plastic Dynamic System: Figure 1(f) shows an elastic-ideal plastic dynamic system. As noted above, this system is obtained from the viscoplastic one in the limit of the representative viscous coefficient, η, in Equation 18 going to zero. The dissipation function φ of equation (13) then becomes:

$$\varphi(\dot{J}) = \begin{cases} 0 \text{ if } & |\dot{J}| \le F_y \\ \infty \text{ if } & |\dot{J}| > F_y \end{cases} \tag{14}$$

i.e., $\varphi(\dot{J}) = \cup_C(\dot{J})$ where $\cup_C$ is an indicator function of the set C which is the elastic domain, $C = \{x : |x| < F_y\}$. The Lagrangian formulation of the elastic-ideal plastic system is then the same as that of the elastic viscoplastic system, i.e. Equations (13), with the dissipation function suitably interpreted using Equations (21).

3 Governing equations of skeletal structures

The governing equations of the structure consist of the equilibrium equations, the compatibility equations and the constitutive equations. The equilibrium equations including momentum effects are:

$$\mathbf{M}\ddot{\mathbf{u}} + \mathbf{C}\dot{\mathbf{u}} + \mathbf{B}\dot{\mathbf{J}} - \mathbf{F} = \mathbf{0} \tag{15}$$

where **M**, **C** and **B** are the mass, damping and equilibrium matrices respectively **F** is the vector of element internal forces and **J**, its impulse. Let **A** be the block diagonal assembly of the element elastic flexibility matrices. The compatibility equation is similar to Equation (24):

$$\mathbf{A}\ddot{\mathbf{J}} + \frac{\partial \varphi(\dot{\mathbf{J}})}{\partial \dot{\mathbf{J}}} - \mathbf{B}^{\mathrm{T}}\dot{\mathbf{u}} = \mathbf{0} \tag{16}$$

Internal imposed displacements within elements, such as resulting from pre-stressing or thermal loads have been neglected here for the sake of simplicity. However, the forcing term in equations (25) and (16) can be adjusted to include such effects. The action integral for the entire structure is obtained as:

$$\delta\mathcal{I} = -\delta\int_0^T \mathcal{L}(\mathbf{J},\dot{\mathbf{u}},\dot{\mathbf{J}})\,dt + \int_0^T \delta\mathbf{u}^{\mathrm{T}}C\dot{\mathbf{u}}\,dt + \int_0^T \delta\mathbf{J}^{\mathrm{T}}\frac{\partial\varphi(\dot{\mathbf{J}})}{\partial\dot{\mathbf{J}}}\,dt - \int_0^T \delta\mathbf{u}^{\mathrm{T}}\mathbf{P} = \mathbf{0} \tag{17}$$

with the Lagrangian and the dissipation function given by:

$$\mathcal{L}(\mathbf{J},\dot{\mathbf{u}},\dot{\mathbf{J}}) = \frac{1}{2}\dot{\mathbf{u}}^{\mathrm{T}}\mathbf{M}\dot{\mathbf{u}} + \frac{1}{2}\dot{\mathbf{J}}^{\mathrm{T}}\mathbf{A}\dot{\mathbf{J}} + \mathbf{J}^{\mathrm{T}}\mathbf{B}^{\mathrm{T}}\dot{\mathbf{u}} \quad \text{and} \quad \overline{\varphi}(\dot{\mathbf{u}},\dot{\mathbf{J}}) = \frac{1}{2}\dot{\mathbf{u}}^{\mathrm{T}}C\dot{\mathbf{u}} + \varphi(\dot{\mathbf{J}}) \tag{18}$$

4 Effect of geometric nonlinearity on the Lagrangian function

Having examined the structural dynamic problem under small deformations, it is now desired to consider equilibrium in the deformed configuration with large deformations. The effect of large structural displacements is considered, while that of large deformations within the corotational frames of elements is ignored. This seems to be justified for elastic-plastic frame elements where significant displacements occur after yielding when hinges form, thus not accompanied by large deformations within the element corotational frame. The effect of the change of length on the flexibility coefficients of beam-column members is neglected since this is a higher order effect. Large deformations may be included by proceeding from the Lagrangian of an infinitesimal element and performing spatial discretization such as by Finite Element Method. Some remarks on this formulation are presented in the next section. The difference in formulation of the large displacement case from the previous case is only the fact that the equilibrium matrix, **B**, is a function of displacement, **B**(u). However, the equilibrium equations (15) being in global coordinates and the compatibility equations (16) being incremental (compatibility of deformation and displacement rates) must both remain unchanged by this additional consideration. It is demonstrated (see Sivaselvan and Reinhorn, 2004) that the spatially pre-discretized Lagrangian of equation (18) holds in the deformed configuration as well:

$$\mathcal{L}(\mathbf{u},\mathbf{J},\dot{\mathbf{u}},\dot{\mathbf{J}}) = \frac{1}{2}\dot{\mathbf{u}}^{\mathrm{T}}\mathbf{M}\dot{\mathbf{u}} + \frac{1}{2}\dot{\mathbf{J}}^{\mathrm{T}}\mathbf{A}\dot{\mathbf{J}} + \mathbf{J}^{\mathrm{T}}[\mathbf{B}(\mathbf{u})]^{\mathrm{T}}\dot{\mathbf{u}} \tag{19}$$

Since all other terms of the Euler-Lagrange equations remain unaffected, it is sufficient to examine the resulting generalized equilibrium equations obtained from the above Lagrangian:

$$\begin{aligned}\frac{d}{dt}\left(\frac{\partial\mathcal{L}}{\partial\dot{\mathbf{u}}}\right) - \left(\frac{\partial\mathcal{L}}{\partial\mathbf{u}}\right) &= \mathbf{M}\ddot{\mathbf{u}} + \frac{d}{dt}\left(\mathbf{B}^{\mathrm{T}}\mathbf{J}\right) - \frac{\partial}{\partial\mathbf{u}}\left(\dot{\mathbf{u}}^{\mathrm{T}}\mathbf{B}^{\mathrm{T}}\mathbf{J}\right)\\ &= \mathbf{M}\ddot{\mathbf{u}} + \mathbf{B}^{\mathrm{T}}\dot{\mathbf{J}} + \left[\left(\frac{d\mathbf{B}^{\mathrm{T}}}{dt}\right) - \frac{\partial}{\partial\mathbf{u}}\left(\dot{\mathbf{u}}^{\mathrm{T}}\mathbf{B}^{\mathrm{T}}\right)\right]\mathbf{J}\end{aligned} \tag{20}$$

It can be shown (Sivaselvan and Reinhorn, 2006) that $\left(d\mathbf{B}/dt\right) - \partial_{\mathbf{u}}\left(\dot{\mathbf{u}}^{\mathrm{T}}\mathbf{B}\right) = \mathbf{0}$. Having recognized the symmetry in $\mathbf{B}$, the above result may also be proved using index notation as follows:

$$\left(\frac{d\mathbf{B}}{dt}\right) - \partial_{\mathbf{u}}\left(\dot{\mathbf{u}}^{\mathrm{T}}\mathbf{B}\right) = \dot{B}_{ij} - B_{ij,p}\dot{u}_p = B_{ij,p}\dot{u}_p - B_{ij,p}\dot{u}_i = B_{pj,i}\dot{u}_p - B_{ij,p}\dot{u}_i = 0 \quad (21)$$

Thus the formulation remains unchanged when geometric nonlinearity is included.

5 Extension to continuum formulation

Sivaselvan and Reinhorn (2004) have shown that weak formulations analogous to equations (17) through (18) can be obtained for continua. The final formulation derived elsewhere (Sivaselvan and Reinhorn, 2004) is presented below. For a three dimensional continuum, the Lagrangian formulation is given by:

$$\mathcal{L} = \frac{1}{2}\dot{u}_k\dot{u}_k + \frac{1}{2}A_{ijkl}\dot{J}_{ij}\dot{J}_{kl} + \frac{1}{\rho_0}J_{ij}B^*_{ijk}\dot{u}_k; \quad \varphi(\dot{\mathbf{J}}, \dot{\mathbf{u}}) = \cup_C(\dot{\mathbf{J}}) + \frac{1}{2}c_{ij}\dot{u}_i\dot{u}_j$$

$$\begin{aligned}\delta\mathcal{I} = &-\delta\int_0^T\int_\Omega \rho_0\mathcal{L}\,d\Omega\,dt + \int_0^T\int_\Omega \rho_0\frac{\partial\varphi}{\partial\dot{u}_k}\delta u_k\,d\Omega\,dt \\ &+\int_0^T\int_\Omega \rho_0\frac{\partial\varphi}{\partial\dot{J}_{ij}}\delta J_{ij}\,d\Omega\,dt - \int_0^T\int_\Omega \rho_0 f_k\,\delta u_k\,d\Omega\,dt - \int_0^T\int_\Gamma \tau_k\,\delta u_k\,d\Gamma\,dt \end{aligned} \quad (22)$$

The analogy with equations (17) and (18) is seen easily.

6 Time discretization – discrete calculus of variations

The numerical integration of the Lagrangian equations by discrete variational integrators is developed next for the time integration of the governing equations (15) and (16) of the structure. This development consists of two stages: (1) The action integral of equation (17) is discretized in time to obtain an action sum. Using discrete calculus of variations (Cadzow, 1970), finite difference equations are obtained, which are the discrete counterparts of the Euler-Lagrange equations. (2) The task in each time step is shown to be the solution of a constrained minimization problem for which an Augmented Lagrangian algorithm is developed. The action integral of equation (17) is discretized using the midpoint rule and a time step h, using central differences. It is assumed in this process, that the $\mathbf{J}$ and $\mathbf{u}$ are twice continuously differentiable functions and $\mathbf{P}$ is a once continuously differentiable function of time, and that the dissipation function is continuously differentiable with respect to $\dot{\mathbf{J}}$. It is shown in Simo and Govindjee (1991) using geometric arguments, that the $O(h^2)$ accuracy holds in the limiting case of rate-independent plasticity when the viscous coefficient $\eta \to 0$. Starting from action sum, and performing a series of summation by parts (Marsden and West, 2001),

we obtain (Sivaselvan and Reinhorn, 2006):

$$\mathbf{M}\left(\frac{\mathbf{u}_{k+1}-2\mathbf{u}_k+\mathbf{u}_{k-1}}{h^2}\right)+\mathbf{C}\left(\frac{\mathbf{u}_{k+1}-\mathbf{u}_{k-1}}{2h}\right)+\mathbf{B}\left(\frac{\mathbf{J}_{k+1}-\mathbf{J}_k}{2h}\right)=\left(\frac{\mathbf{P}_{k+\frac{1}{2}}+\mathbf{P}_{k-\frac{1}{2}}}{2}\right)$$

$$\mathbf{A}\left(\frac{\mathbf{J}_{k+1}-2\mathbf{J}_k+\mathbf{J}_{k-1}}{h^2}\right)+\frac{1}{2}\left(\left.\frac{\partial\varphi}{\partial\dot{\mathbf{J}}}\right|_{k+\frac{1}{2}}+\left.\frac{\partial\varphi}{\partial\dot{\mathbf{J}}}\right|_{k-\frac{1}{2}}\right)-\mathbf{B}^{\mathrm{T}}\left(\frac{\mathbf{u}_{k+1}-\mathbf{u}_{k-1}}{2h}\right)=\mathbf{0} \tag{23}$$

Using Discrete Variational Calculus results in an integrator with vastly better performance. It is also seen in the following that this results in a form similar to the classical Newmark family of integration schemes. Such variational integrators are symplectic and momentum preserving and often have excellent global energy behavior (Kane et al. 2000).

7 Time-step solution

Introducing the notation, $\mathbf{v}_n$ and $\mathbf{F}_n$ as the Central Difference approximations of the velocity and the internal force respectively, Eq. (23) then becomes:

$$\mathbf{M}\left(\frac{\mathbf{v}_{n+1}-\mathbf{v}_n}{h}\right)+\mathbf{C}\left(\frac{\mathbf{v}_{n+1}+\mathbf{v}_n}{2}\right)+\mathbf{B}\left(\frac{\mathbf{F}_{n+1}+\mathbf{F}_n}{2}\right)=\left(\frac{\mathbf{P}_{n+1}+\mathbf{P}_n}{2}\right) \tag{24}$$

$$\mathbf{A}\left(\frac{\mathbf{F}_{n+1}-\mathbf{F}_n}{h}\right)+\frac{1}{2}\left(\left.\frac{\partial\varphi}{\partial\mathbf{F}}\right|_{n+1}+\left.\frac{\partial\varphi}{\partial\mathbf{F}}\right|_{n}\right)-\mathbf{B}^{\mathrm{T}}\left(\frac{\mathbf{v}_{n+1}+\mathbf{v}_n}{2}\right)=0 \tag{25}$$

where $\mathrm{n}=k-1/2$, $\mathbf{v}_n=\left(\mathbf{u}_{n+(1/2)}-\mathbf{u}_{n-(1/2)}\right)/h$ and $\mathbf{F}_n=\left(\mathbf{J}_{n+(1/2)}-\mathbf{J}_{n-(1/2)}\right)/h$. It is common in modeling frame structures for dynamic analyses to use a lumped mass matrix and to ignore rotational inertia. Hence the mass matrix could in general be singular. Similarly, the damping matrix could also be singular, for example when using mass proportional damping. Thus, consistent with the convexity assumptions and without loss of generality, equation (24) can be rearranged and partitioned as follows:

$$\frac{2}{h}\begin{bmatrix}\mathbf{M}&0&0&0\\0&0&0&0\\0&0&0&0\\0&0&0&0\end{bmatrix}\begin{Bmatrix}\mathbf{v}_1\\\mathbf{v}_2\\\mathbf{v}_3\\\mathbf{v}_4\end{Bmatrix}+\begin{bmatrix}\mathbf{C}_{11}&\mathbf{C}_{12}&0&0\\\mathbf{C}_{12}^{\mathrm{T}}&\mathbf{C}_{22}&0&0\\0&0&0&0\\0&0&0&0\end{bmatrix}\begin{Bmatrix}\mathbf{v}_1\\\mathbf{v}_2\\\mathbf{v}_3\\\mathbf{v}_4\end{Bmatrix}+\begin{bmatrix}\mathbf{B}_1^{\mathrm{T}}\\\mathbf{B}_2^{\mathrm{T}}\\\mathbf{B}_3^{\mathrm{T}}\\\mathbf{B}_4^{\mathrm{T}}\end{bmatrix}^{\mathrm{T}}\mathbf{F}=\begin{Bmatrix}\mathbf{P}_1\\\mathbf{P}_2\\\mathbf{P}_3\\\mathbf{P}_4\end{Bmatrix}+\frac{2}{h}\begin{Bmatrix}\mathbf{M}\mathbf{v}_{1,n}\\0\\0\\0\end{Bmatrix} \tag{26}$$

where the partitions 1 through 4 represent respectively (i) degrees of freedom with mass, (ii) those with damping but no mass, (iii) those with prescribed forces and (iv) those

with prescribed displacements (or velocities). Following some algebraic manipulations, we obtain:

$$\begin{aligned} &\text{Minimize } \Pi\left(\mathbf{F}_{n+1}\right) = \frac{1}{2}\mathbf{F}_{n+1}^{\mathrm{T}}\overline{\mathbf{A}}\mathbf{F}_{n+1} - \mathbf{F}_{n+1}^{\mathrm{T}}\overline{\mathbf{b}} \\ &\text{Subject to (i) } \mathbf{B}_3\mathbf{F}_{n+1} = \mathbf{P}^3 \\ &\quad \text{and (ii) } \frac{\mathrm{h}}{2}\phi_i\left(\mathbf{F}_{n+1}\right) \le 0 \quad i = 1, 2, \ldots, N_y \end{aligned} \tag{27}$$

where

$$\overline{\mathbf{A}} = \mathbf{A} + \frac{h}{2}\mathbf{B}_2^{\mathrm{T}}\mathbf{C}_{22}^{-1}\mathbf{B}_2 + \frac{h^2}{4}\overline{\mathbf{B}}_1^{\mathrm{T}}\overline{\mathbf{M}}^{-1}\overline{\mathbf{B}}_1 \tag{28}$$

$$\begin{aligned} \overline{\mathbf{b}} = &\left[\left(\mathbf{A} - \frac{h}{2}\mathbf{B}_2^{\mathrm{T}}\mathbf{C}_{22}^{-1}\mathbf{B}_2 - \frac{h^2}{4}\overline{\mathbf{B}}_1^{\mathrm{T}}\overline{\mathbf{M}}^{-1}\overline{\mathbf{B}}_1\right)\mathbf{F}_n + \frac{h^2}{2}\overline{\mathbf{B}}_1^{\mathrm{T}}\overline{\mathbf{M}}^{-1}\overline{\mathbf{P}}_1\right. \\ &\left. + h\mathbf{B}_2^{\mathrm{T}}\mathbf{C}_{22}^{-1}\mathbf{P}_2 + h\overline{\mathbf{B}}_1^{\mathrm{T}}\overline{\mathbf{M}}^{-1}\mathbf{M}\mathbf{v}_{1,n} + \frac{h}{2}\left.\frac{\partial\varphi}{\partial\mathbf{F}}\right|_n\right] \\ \overline{\mathbf{M}} = &\mathbf{M} + \frac{h}{2}\overline{\mathbf{C}}_{11}, \overline{\mathbf{C}}_{11} = \mathbf{C}_{11} - \mathbf{C}_{12}\mathbf{C}_{22}^{-1}\mathbf{C}_{12}^{\mathrm{T}}, \\ \overline{\mathbf{B}}_1 = &\mathbf{B}_1 - \mathbf{C}_{12}\mathbf{C}_{22}^{-1}\mathbf{B}_2 \quad \text{and} \quad \overline{\mathbf{P}}_1 = \mathbf{P}_1 - \mathbf{C}_{12}\mathbf{C}_{22}^{-1}\mathbf{P}_2 \end{aligned} \tag{29}$$

This is the Principle of Minimum Incremental Complementary Potential Energy which can be stated as: Of all the forces at step n+1, $\mathrm{F_{n+1}}$, satisfying equilibrium with prescribed external forces at the un-damped quasi-static degrees of freedom and satisfying the yield conditions, the one that minimizes the incremental complementary potential energy Π is the one that satisfies equilibrium and compatibility in the other degrees of freedom.

An Augmented Lagrangian algorithm is used for the solution of the minimization problem (27). For a detailed treatment of the Augmented Lagrangian formulation, the reader is referred to Glowinski and Tallec (1989). The problem (27) is reduced to a sequence of linearly constrained sub-problems using the Augmented Lagrangian regularization:

$$\begin{aligned} &\underset{\mathbf{F}_{n+1}}{\text{Minimize}}\ \Pi_{AL}\left(\mathbf{F}_{n+1}, \boldsymbol{\lambda}\right) = \frac{1}{2}\mathbf{F}_{n+1}^{\mathrm{T}}\overline{\mathbf{A}}\mathbf{F}_{n+1} - \mathbf{F}_{n+1}^{\mathrm{T}}\overline{\mathbf{b}} + \frac{h}{2}\sum_{i=1}^{N_y}\left[\boldsymbol{\lambda}_i\phi_i\left(\mathbf{F}_{n+1}\right) + \frac{\nu}{2}\langle\phi_i\left(\mathbf{F}_{n+1}\right)\rangle^2\right] \\ &\text{Subject to } \mathbf{B}_3\mathbf{F}_{n+1} = \mathbf{P}^3 \end{aligned} \tag{30}$$

where $\{\lambda = \lambda_1, \lambda_2, \ldots, \lambda_{Ny}\}^{\mathrm{T}}$ is the vector of plastic multipliers, ν is a penalty parameter and $< >$ denotes the Macaulay Bracket. The Augmented Lagrangian regularization is a combination of the usual Lagrangian term, $\lambda_i\phi_i(\mathbf{F}_{n+1})$ and the penalty function $\nu/2 < \phi_i(\mathbf{F}_{n+1}) >^2$. The latter helps accelerate convergence while the former eliminates the need for the penalty parameter to be large, which leads to numerical ill-conditioning. Both terms vanish at a feasible point. The solution is obtained in

two nested stages. In the inner stage or primal stage, the dual variables, i.e. the plastic multipliers λ are held fixed and the primal variables, i.e. the forces $\mathbf{F}_{n+1}$ are obtained by solving the above equality constrained problem. In the outer, or dual stage, the forces are held fixed and the plastic multipliers are updated using the formula:

$$\lambda_i^{new} = \left\langle \lambda_i^{old} + \nu\phi\left(\mathbf{F}_{n+1}\right) \right\rangle \tag{31}$$

The superscripts new and old have been used, rather that iteration indices, to denote values at the beginning and at the end of an iteration, to avoid the proliferation of subscripts and superscripts. Due to the Central Difference approximation, $(h/2)\lambda_i(\partial\phi_i(\mathbf{F}_{n+1})/\partial\mathbf{F}_{n+1})$ is the plastic strain increment. In physical terms, therefore, the Augmented Lagrangian process is equivalent to relaxing the regularizing dashpot and allowing the frictional slider to incrementally develop plastic strain in each iteration. A dense matrix algorithm for the solution of equation (30) is presented in Sivaselvan and Reinhorn (2001). When considering large displacements, as stated above when describing the effect of geometric nonlinearity, the equilibrium matrix **B** depends on displacement. It is therefore updated at every step using the newly computed displacements. Strictly, this requires an iterative procedure because the matrix **B** has to be evaluated at time $n+1/2$.

8 Numerical example

The example structure is shown in Figure 2. It is a portal frame consisting of three elements. The connections are assumed rigid. The stress-strain curve of the material is assumed bilinear with the following properties: E = 199955 kN/mm2 and $\sigma_y = 248.2$ kN/mm2. In order to show the feasibility of this formulation as an alternative to existing programs, the results are compared with the program DRAIN-2DX (Allahabadi and Powell, 1988). The example although very simple, is used to illustrate the method and its applicability to collapse simulations.

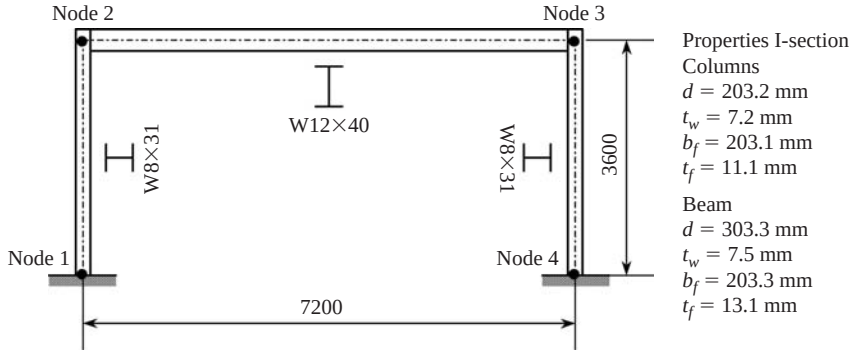

Figure 2 Portal frame Example

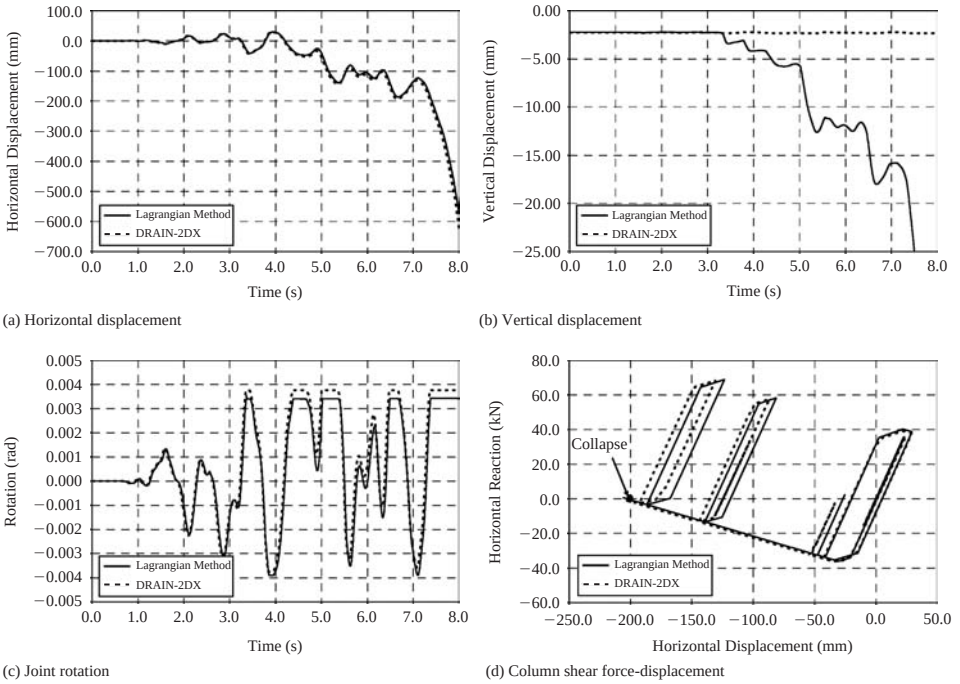

Figure 3 Results with external axial force.

A dynamic analysis is performed with an axial force of 731.05 kN on each column, corresponding 50% of the yield force. In this case there is significant geometric nonlinearity. Figure 3(a) and Figure 3(b) show that the horizontal and vertical displacements continue to grow. Figure 3(c) shows the joint rotation. The point marked "collapse" in Figure 3(d) is the point beyond which an external horizontal force is required to pull the structure back to keep displacements from growing autonomously under the vertical loads acting on it. During a dynamic analysis, when this point is crossed, displacements continue to grow without reversal even when the input reverses; the analysis is terminated at this point. It is also noticed that under load reversal, the yield force in the opposite direction is higher than the original yield force.

Dynamic analyses were made on large frame structures exceeding 2,500 degrees of freedom (see Figure 4a) and up to 30,000 DOF subjected to ElCentro 1940 accelerogram. The results in Figure 4b show stable response under large deformations in presence of material and geometric nonlinearities.

9 Concluding remarks

The evolution of the elastic-plastic structural state in time is provided a weak formulation using Hamilton's principle. It is shown that a certain class of structures called reciprocal structures has a mixed weak formulation in time involving Lagrangian and dissipation functions. The new form of the Lagrangian developed in this work involves

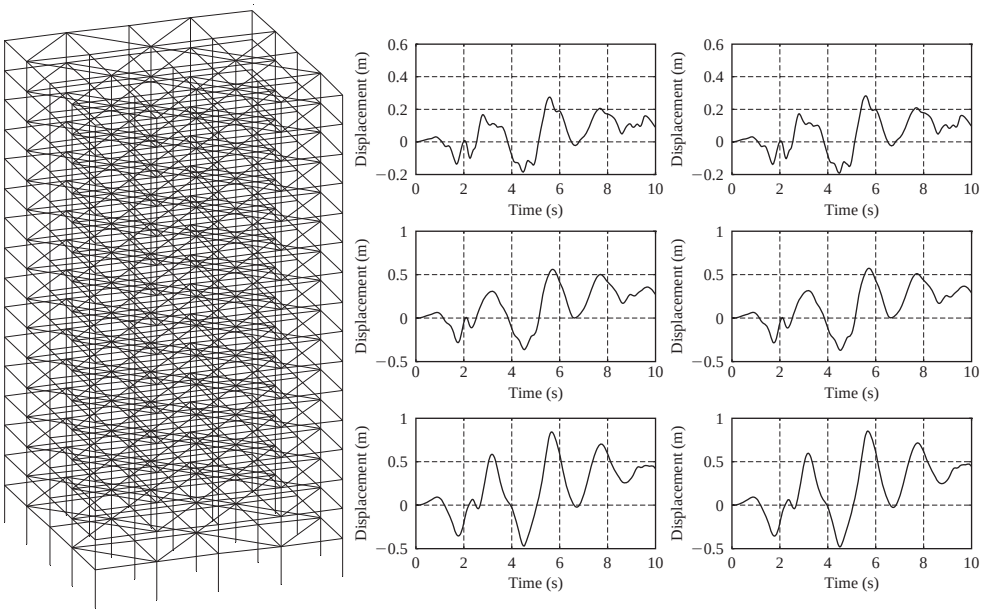

(a) Structural Model (b) Displacement histories of selected nodes

Figure 4 Application of the Lagrangian formulation to a large-scale structure.

not only displacements and velocities but also internal forces and their impulses leading to the concept of the generalized momentum for framed structures. The derivative of the compatibility operator with respect to displacements possesses a symmetry that renders the Lagrangian invariant under finite displacements. The formulation can therefore be used in geometric nonlinear analysis. A discrete time integrator has been derived starting from a weak formulation. The integration of each step has been shown to be a constrained minimization problem – the principle of incremental minimum complementary potential energy. An Augmented Lagrangian algorithm and a dense matrix implementation have been derived for the solution of this problem. Since the matrix of the minimization problem of Eq. 27 is positive definite, the solution is globally convergent, allowing for larger time steps for computation. The examples show that this method can provide as good or better information than a widely used displacement based inelastic analysis solutions. The examples also show that the method is stable and efficient for large structures. However, the power of the method presented herein is in evaluating structures where various elements collapse, and forces and momentum have to be redistributed in the remaining system.

References

Allahabadi, R. & Powell, G.H. 1988. *Drain-2DX user guide*, University of California at Berkeley.

Cadzow, J.A. 1970. Discrete Calculus of Variations. *International Journal of Control*, 11(3): 393–407.

El-Sayed, M.E.M., Marjadi, D. & Sandgren, E. 1991. Force Method Formulations Based on Hamilton Principle. *Computers & Structures*, 38(3): 301–316.

Glowinski, R. & Le Tallec, P. 1989. *Augmented Lagrangian and operator-splitting methods in nonlinear mechanics*, Society for Industrial and Applied Mathematics.

Kane, C., Marsden, J.E., Ortiz, M. & West, M. 2000. Variational integrators and the Newmark algorithm for conservative and dissipative mechanical systems. *International Journal for Numerical Methods in Engineering*, 49: 1295–1325.

José, J.V. & Saletan, E.J. 1998. *Classical dynamics : a contemporary approach*, Cambridge University Press.

Marsden, J.E. & West, M. 2001. Discrete mechanics and variational integrators. *Acta Numerica*, 10: 357–514.

Scheck, F. 1994. *Mechanics : from Newton's laws to deterministic chaos*, *ed. 2nd corr. and enl.*, Springer Verlag.

Simo, J.C. & Govindjee, S. 1991. Non-linear B-stability and symmetry preserving return mapping algorithms for plasticity and viscoplasticity. *International Journal for Numerical Methods in Engineering*, 31(1): 151–176.

Sivaselvan, M.V. & Reinhorn, A.M. 2004. *Nonlinear structural analysis towards collapse simulation – a dynamical systems approach*, Technical Report, Multidisciplinary Center for Earthquake Engineering Research.

Sivaselvan, M.V. & Reinhorn, A.M. 2006. Lagrangian approach to structural collapse simulation. *Journal of Engineering Mechanics-ASCE*, 132(8): 795–805.

Stern, T.E. 1965. *Theory of nonlinear networks and systems; an introduction*, Addison-Wesley.

Chapter 21

Nonlinear models and nonlinear procedures for seismic analysis of reinforced concrete frame structures

Enrico Spacone & Guido Camata

University of Chieti-Pescara, Pescara, Italy

Marco Faggella

University of Chieti-Pescara, Pescara, Italy
University of California San Diego, California, USA

ABSTRACT: Nonlinear methods of analysis for seismic vulnerability assessment of existing structures are attracting increasing attention for their capacity to predict the actual seismic behavior better than linear methods. Their inclusion in modern design codes such as Euro-code 8 is a major boost for their use in practical applications. Recent years have also seen steady advances in the modeling capabilities of reinforced concrete frames, particularly in the field of beam and column behavior. Advanced frame modeling tools are included in both research and commercial codes. As research and practicing engineers start applying nonlinear methods to real problems, questions arise regarding the application of the design code-provided procedures and the selection of the appropriate structural model given the objective limitations of the frame modeling capabilities today available. The scope of this paper is to discuss some of the issues still open regarding the applications of the nonlinear methods of analysis to reinforced concrete structures, with the firm belief that an open discussion on these methods, their advantages and limitations will open the way to a more widespread use of advanced and more accurate methods of analysis.

1 Introduction

Modern seismic design codes allow engineers to use nonlinear methods of analysis to compute design forces and design displacements. In particular, two nonlinear methods are considered: simplified nonlinear pushover analysis and full nonlinear time-history analysis. These methods refer to the design and analysis of frame structures, mainly buildings and bridges. Nonlinear methods are of particular interest for the seismic vulnerability assessment of existing structures, where the modern concepts of capacity design have not been used, and therefore the application of linear methods of analyses cannot be easily justified.

There is no doubt that nonlinear analyses are more accurate than linear analyses in reproducing the actual structural behavior up to the Ultimate and Collapse Limit States, but there still lacks the necessary experience to make nonlinear methods of analyses routine methods for existing structures. The two nonlinear methods require advanced models and advanced nonlinear procedures in order to be fully applicable

by design engineers. Furthermore, reinforced concrete (RC) structures show a highly nonlinear behavior that is not easily modeled with frame elements. Concrete and steel nonlinear response, concrete cracking, bond-slip, re-bar debonding, rebar buckling, shear failure, joint deformations, joint failure, progressive damage are some of the main sources of nonlinearities during a moderate or strong seismic event. Due to the relatively recent introduction of the nonlinear methods, the nonlinear procedures are not yet fully applicable and not many nonlinear programs are available to run them. This paper intends to summarize the two nonlinear procedures contained in Eurocode 8 (2003) (EC8), to highlight some of the open issues related to their applications, and to discuss them with the aid of two applications, one to a RC building, the other to a RC bridge.

2 Overview of nonlinear methods of analysis

This brief overview deals mainly with the nonlinear procedures in EC8. Other seismic codes contain similar approaches (ATC 40, 1996; FEMA 356, 2000). Two nonlinear methods of analysis are considered in EC8: the nonlinear pushover analysis (NPO) and the nonlinear time history analysis (NTH).

The initial steps of both nonlinear procedures are identical: construction of the nonlinear frame model and application of the gravity loads. The gravity loads remain constant during the nonlinear analysis. This initial step is quite important because it changes the initial state of the structure. In a RC building the gravity loads typically induce cracking in the beams and apply high axial forces to the columns.

2.1 *Nonlinear Pushover Analysis*

The NPO consists of applying monotonically increasing constant-shape lateral load distributions to the structure under consideration. The model can be planar or three-dimensional, depending on the plan irregularity of the structure. For buildings conforming with the regularity criteria of EC8 the analysis NPO may be performed using two planar models, one for each principal horizontal direction. For plan-irregular buildings, two independent analyses with lateral loads applied in one direction only are performed, and the results are then combined. Plan irregularity is typical of older structures.

The NPO procedure in EC8 follows the N2 method developed by Prof. Fajfar (2002). The N2 method was based on rigid frames, where the floor beams are rigid. The N2 method consists of applying two load distributions $\mathbf{P} = \mathbf{M}\boldsymbol{\Phi}$ (where $\mathbf{M}$ is the mass matrix and $\boldsymbol{\Phi}$ the load shape array):

a. a "modal" (or "triangular") pattern with $\boldsymbol{\Phi} = \boldsymbol{\Phi}_1$, that is $\mathbf{P}^1 = \mathbf{M}\boldsymbol{\Phi}_1$, where $\boldsymbol{\Phi}_1$ is the first mode shape in the load direction considered;
b. a "uniform" or "mass proportional" pattern with $\boldsymbol{\Phi} = \mathbf{R}$, that is $\mathbf{P}^2 = \mathbf{M}\mathbf{R}$, where $\mathbf{R}$ is the influence vector.

In the N2 method $\boldsymbol{\Phi}_1$ is normalized so that the top floor (n) displacement is 1, i.e. $\boldsymbol{\Phi}_{1,n} = 1$.

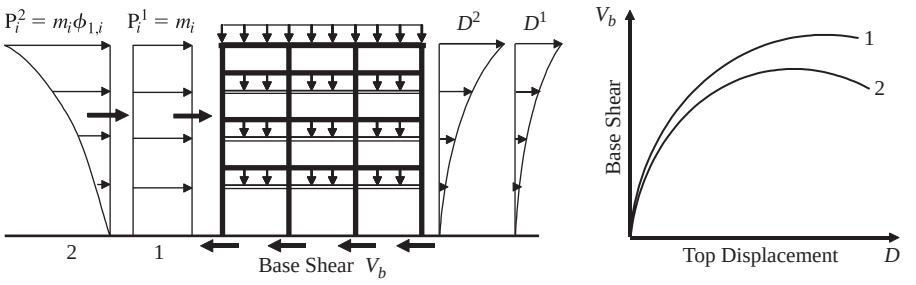

Figure 1 Load distribution for pushover analysis according to EC8 and pushover response curves.

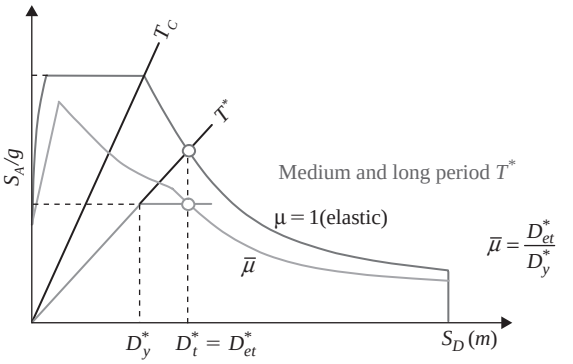

Figure 2 Capacity and Demand spectra for medium and long period T^*: determination of the target displacement for SDOF.

The two load distributions are schematically shown in Figure 1. The applied lateral load distributions are increased and the response is plotted in terms of base shear V_b vs. top floor displacement D (for example center of mass of the top floor). This is the so-called pushover curve or capacity curve (also shown schematically in Figure 1). The above load patterns are supposed to reproduce static loads equivalent to the seismic action. The two load patterns correspond to a first-mode dominated behavior and to a bottom soft-story response. Other distributions can be used but are typically non considered.

The N2 procedure transforms the response of the MDOF system into the response of an equivalent SDOF system, with force-displacement curve $F^* - D^*$, with $F^* = V_b/\Gamma$, $D^* = D/\Gamma$ and $\Gamma = (\mathbf{\Phi}^T\mathbf{M}\mathbf{R})/(\mathbf{\Phi}^T\mathbf{M}\mathbf{\Phi})$. This is necessary in order to compare the building capacity curve of Figure 1 with the demand, expressed in the design codes by the design spectra, which refer to SDOF systems Fajfar (1999, 2002).

In order to compare elastic design spectrum (demand) and capacity curve, first the capacity curve is transformed into an energy equivalent elastic-perfectly plastic system, then the ADRS (Acceleration Displacement Response Spectrum) representation is used, as shown in Figure 2.

Approximate nonlinear demand spectra are obtained using simplified formulas (Eurocode 8, 2003). The design point is given by the intersection between the capacity

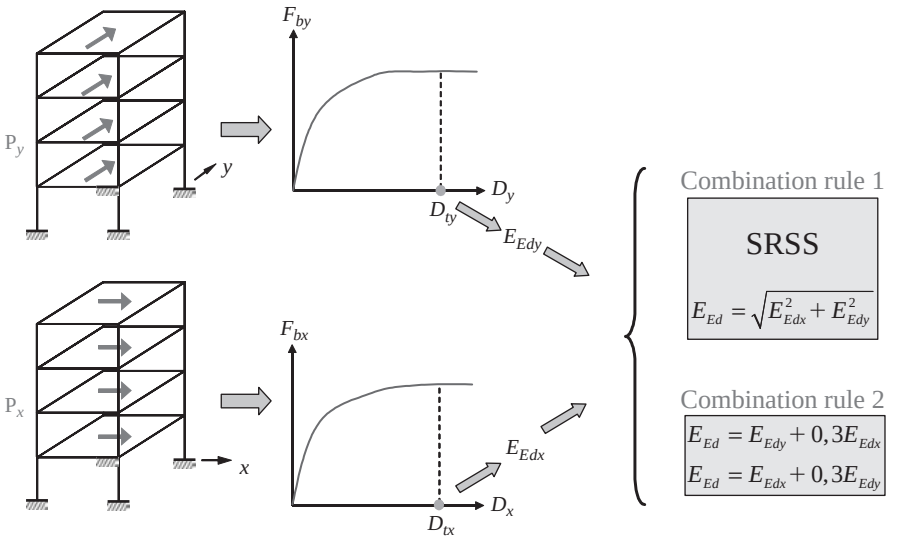

Figure 3 EC8 Combination rules for horizontal seismic forces.

curve and the inelastic response spectrum of equal ductility. Once the target displacement D_t^* for the SDOF system is determined, the target displacement for the MDOF is computed as $D_t = \Gamma D_t^*$. All the design verifications for the given Limit State are performed at the top floor displacement $D = D_t$.

For non symmetric buildings, two different pushover analysis should be performed for each seismic input direction, in the positive and negative directions. For structures that are torsionally flexible, EC8 suggests to account for the torsional effects by following a simplified procedure where the frame displacements are increases based on a modal response spectrum analysis. This approach is based on the modified N2 procedure (Fajfar *et al.*, 2005).

The pushover procedure described so far refers to the application of the ground motion in a single direction. When the ground motion is applied in the two horizontal directions *x* and *y*, (this is the case of plan irregular buildings, i.e. the great majority of existing buildings in southern Europe) EC8 gives two alternatives for the combination, the SRSS method or the 100/30 Combination rule (Figure 3).

In nonlinear analysis, the action effects (as they are called in EC8) may be either forces or deformations. For ductile mechanisms (such as flexure in beams) the action effects are the deformations (for flexure, plastic hinge rotations or curvatures), while for brittle mechanisms (such as shear) the action effects are forces (shear forces in the structural elements). EC8 gives some indications on how to check the seismic performance of a building based on nonlinear analysis results, but studies are still under way and a clear checking procedure is still missing.

The above combination appears as an extension of the directional combination rules in linear procedures. It remains to be proven that they can be extended to the nonlinear case. It seems more logical to apply the two load patterns at the same time, but this

topic is still to be studied. The N2 method was originally developed for plane frame. Its extension to space, plan-irregular buildings with mixed translational-torsional modes, modeled with advanced modeling tools (see later) is a challenge.

Another important issue with the N2 methods stems from the fact that the applied load shapes remain constant during the load history, thus the progressive damage of the structure does not affect the applied seismic loads.

One alternative pushover method is the so called *adaptive pushover*. One example is the method developed by Elnashai (2002); Antoniou & Pinho (2004). The method adapts the form of the applied load to the inelastic evolution of the structure, given by the instantaneous stiffness matrix of the structure. In other words, at given points along the pushover curve, the applied load shape is updated based on the instantaneous mode shapes. This is typically done using either total or incremental updating. In total updating, the total load vector is changed based on the new mode shapes. In the incremental updating form, only the increment of lateral loads includes the change in stiffness and thus the instantaneous mode shapes. This method is an improvement on the N2 method, but the changes in loading function cannot fully reflect the cyclic damage state the structure can have in the actual dynamic motion.

Another method is the so-called *modal pushover* developed by Chopra & Goel (2002). The idea is to extend the modal analysis from the elastic to the inelastic range. It is assumed that the response of the system can still be expressed in terms of n uncoupled nonlinear equations of motion. If the excitation is proportional to the i mode, it is assumed that the response is still dominated by the same mode. That is, if the load is proportional to $\mathbf{\Phi}_i$, the displacement response is dominated (and thus proportional) to $\mathbf{\Phi}_i$. This allows modal decomposition. The global response is obtained combining the modal responses. The pushover procedure is repeated for each mode, and the resulting target displacements are found for each mode. The maximum seismic effects are found using the SRSS or the CQC modal combination rules. The procedure is obviously approximate, but the results published so far show improved results when compared with the N2 method of EC8. The main criticism to this method is that it combines responses of totally independent structures (the single bilinear SDOF systems) and thus lacks a sound physical interpretation. Another problem, common to other nonlinear pushover procedures, is the modal combination based on SRSS or CQC, where the sign of the action is lost.

An alternative nonlinear static procedure was proposed by Aydinoglu (2003). The procedure, called Incremental Response Spectrum Analysis (IRSA) does not properly belong to the pushover methods. The procedure is displacement-based, it uses the equal displacement rule and the structure nonlinear behavior is modeled as piece-wise linear. The initial modes are computed and the elastic response spectrum for the initial structure is carried out. In the first stop the spectral ordinates are scaled to the formation of the first plastic hinge, which corresponds in the piece-wise linear capacity curve, to the first change of stiffness. The updated modal quantities are computed and additional spectral ordinates are computed up to the formation of the second plastic hinge. The procedure continues until the entire spectral ordinates are applied. The method does not require any transformation to an equivalent SDOF system.

Other pushover procedures have been proposed in the published literature, but no general consensus has been reached on the best possible procedure. It appears that

at this stage the N2 method represents a good compromise between simplicity and precision. A number of studies are however under way in this field.

2.2 *Nonlinear Time History (NTH) analysis*

The nonlinear time-history analysis is the most general nonlinear method of analysis. It is deemed unpractical by some because of the computational length of the analysis, but as computer speeds increase, NTH becomes increasingly feasible. Time-history analysis is a general dynamic method of analysis and there are no computational peculiarities related to earthquake engineering analysis. The input force is the input ground motion, expressed in the form of one or more accelerograms. The dynamic equations of motion are:

$$\mathbf{M}\ddot{\mathbf{U}} + \mathbf{C}\dot{\mathbf{U}} + \mathbf{F}(\mathbf{U}) = -\mathbf{M}\mathbf{R}\ddot{\mathbf{u}}_g \tag{1}$$

where $\mathbf{C}$ is the damping matrix, $\ddot{\mathbf{u}}_g$ is a vector containing accelerograms and depends on time, i.e. $\ddot{\mathbf{u}}_g(t)$. In the most general case, $\ddot{\mathbf{u}}_g = \{\ddot{u}_{g,x}\ \ddot{u}_{g,y}\ \ddot{u}_{g,z}\}$, that is the input ground motion, consists of three simultaneously acting accelerograms in three orthogonal directions. For buildings, the z component of the ground motion is typically neglected. Thus, for a 3D structural model, only the horizontal components are considered and $\ddot{\mathbf{u}}_g = \{\ddot{u}_{g,x}\ \ddot{u}_{g,y}\}$.

There are still a few unresolved issues related to NTH analysis: the selection of the appropriate structural model (this problem applies to NPO analyses too), the selection of the ground motions, the selection of a correct damping matrix, the heavy computational effort, the large volume of output quantities to be analyzed.

As for the selection of the ground motions for the NTH analyses, EC8 states that:

a. a minimum of 3 different pairs of accelerograms $\ddot{\mathbf{u}}_g = \{\ddot{u}_{g,x}\ \ddot{u}_{g,y}\}$ should be used. If 3 to 6 ground motions are used, then the maximum of the response quantities from all the analyses should be used as the design value of the action effect E_d in the relevant verifications;
b. if 7 or more different ground motions are used, i.e. if 7 different pairs of accelerograms $\ddot{\mathbf{u}}_g = \{\ddot{u}_{g,x}\ \ddot{u}_{g,y}\}$ are used, then the average of the response quantities from all the analyses should be used as the design value of the action effect E_d in the relevant verifications.

Depending on the nature of the application and on the information actually available, the description of the seismic motion may be made by using *artificial*, *recorded* or *simulated* accelerograms [Eurocode 8, 2003]. EC8 establishes rules with regard to obtaining spectrum-compatible accelerograms.

Though no extensive study is yet available and discussions are under way in those countries that have started employing nonlinear methods of analysis, it is generally recognized that recorded accelerograms, if well selected, are less demanding on the structure, because each single accelerogram does not match well the elastic response spectrum, and the frequency content of each single accelerogram is limited with respect to the elastic response spectrum. On the other hand, generated accelerograms are more

demanding, because each single accelerogram has a response spectrum close to the elastic response spectrum. Some claim that generated or simulated accelerograms should be used at the research level for the refinement of the nonlinear methods of analysis, while recorded accelerograms should be used for the actual design of structures. No general consensus has yet been reached, though. A few computer programs are freely available on the internet for generated and simulated accelerograms.

As for recorded accelerograms, there are databases available (such as the European Strong Motion Database (http://www.isesd.cv.ic.ac.uk), the PEER Strong Motion Database (http://peer.berkeley.edu/smcat/index.html), the Strong Motion Database of SeismoLinks (http://www.seismolinks.com/Strong_Motion_Databases/) to mention just a few. The elaboration of these databases of recorded ground motions and the selection of the appropriate accelerograms that satisfy the EC8 requirements is not trivial. An effort to extract and filter the accelerograms of the European Strong Motion Database is underway in the Italian project Re-luis (Iervolino *et al.*, 2006). Groups of accelerograms compatible (according to EC8 criteria) with the elastic response spectra for different a_g and soil type are available at http://www.reluis.unina.it/ (in Italian).

EC8 does not contain any specific procedure for the estimation of the torsional effects. In principle, the general procedure for accidental torsional effects should be applied. However, this would imply applying the ground motions at 4 different locations, with a considerable increase in computational costs. At this stage it appears reasonable to neglect the torsional effects when performing nonlinear dynamic analyses.

Another important issue related to NTH analyses is the selection of the damping matrix **C** in Eq. (1). The commonly used rule of employing Rayleigh damping with 5% damping in the principal modes cannot be applied here. First of all, the stiffness matrix changes at every instant. Some programs allow for updating of the Rayleigh damping **C** matrix as **K** changes. But the biggest issue concerns which modal damping ratio values to use. Several analyses have shown that 5% is too high a damping for an inelastic structure, as is easily understood since viscous damping $\mathbf{C}\dot{\mathbf{U}}$ accounts already for some nonlinearity in the structure. If the material nonlinearities are accounted for in the nonlinear static term $\mathbf{F}(\mathbf{U})$, then the damping ratio should be reduced. The more accurate the nonlinear structural model is, the lower the damping ratios should be (Panagiotou *et al.*, 2007). It appears that a damping coefficient between 2% and 3% is suggested by most analysts. The issue is however very important (and difficult to solve) because for very low damping, small changes in damping imply large variations in the results.

NTH analyses typically produce large amounts of output data. This problem is related to the fact that there is no consensus yet on the verification procedures. Once the verification procedures are well established, it will be a lot easier for commercial and research software to contain automatic design checks.

3 Overview of current nonlinear models

There are two main sources of nonlinearities; material and geometric. Material nonlinearities have received more attention in earthquake engineering analyses, but geometric

nonlinearities may be quite important when dealing with the ultimate and collapse limit states.

EC8 does not have any specific guidelines on how to model *material nonlinearities*, except for general considerations on the concrete and steel constitutive laws (Eurocode 8, 2003). Material properties should be based on mean values of the mechanic characteristics for existing structures.

EC8 provides some guidelines on *geometric nonlinearities*, but only on when and how to account for them in an approximate way. Second-order, or P-Δ effects, need not be taken into account if the following condition is satisfied:

$$\theta = \frac{P_{tot}\, d_r}{v_{tot}\, h} \leq 0,10 \tag{2}$$

where θ is the interstorey drift sensitivity coefficient, P_{tot} is the total gravity load at and above the storey considered in the seismic design situation, d_r is the design interstorey drift, V_{tot} is the total seismic storey shear, h is the interstorey height. If $0{,}1 < \theta \leq 0{,}2$, then nonlinear geometric effects may approximately be taken into account by multiplying the relevant seismic action effects by a factor equal to $1/(1-\theta)$, $\theta > 0,30$ is not accepted. This is obviously an approximate, code-oriented approach to geometric nonlinearities, while inclusions of the second-order effects typically depends on the capabilities of the nonlinear program used.

Material nonlinearities are typically modeled with either lumped or spread plasticity models. Lumped plasticity models model beams and columns as linear elastic, except in given points where plastic hinges can form. Plastic hinges can be specified in many different forms, using ad hoc plastic laws or more advanced fiber-based section models. In order to model the plastic hinge behavior, it is necessary to assess the length of the plastic hinge L_{pl}, though no general formula or procedure exists. The plastic hinge length is important to transform plastic rotations into plastic curvatures, and vice-versa. In some programs it is also possible to include plastic hinges that describe shear failure (plastic hinge is not probably the right label in this case!). This is important for shear deficient structures. Most commercial software includes lumped plasticity models. For inexperienced analysts, plastic hinges are probably easier to handle than spread plasticity models. The main shortcoming is that structures are assumed mostly elastic, thus approximations are needed for capturing the member elastic stiffness.

Spread-plasticity models are classical finite elements where material nonlinearities are modeled at each integration point. Besides the classical two-node displacement-based beam elements, force-based two-node force-based elements have seen a widespread use both in research and commercial software (McKenna, 1997; MIDAS, 2006; Zimmermann, 1985–2007). The assumed force fields in a two-mode force-based element are exact within classical beam theories, such as the Euler-Bernoulli and Timoshenko theories (Marini & Spacone, 2006; Spacone *et al.*, 1996). This implies that only one element per structural member is used. The element implementation is not trivial and it implies element iterations, but these steps are transparent to the user. The section constitutive law is the source of material nonlinearities.

In principle, the same section constitutive laws can be used for either spread-plasticity elements (at the integration point level) o in lumped models (at the plastic hinges). Fiber section models are considered state-of-the-art at present, because they automatically

account for the interaction between axial and bending forces and can thus effectively describe biaxial bending in RC columns. Shear effects are also easily modeled in two-node force-based elements. The formulation of a force-based Timoshenko beam is very similar to that of an Euler-Bernoulli beam. At the section level, different approaches can be used. The most general one is to couple axial, bending and shear deformations at the section level, but this requires sophisticated cyclic material laws. Petrangeli et al. [OPCM 3431, 2005] have proposed a fiber element with shear deformations for the uniaxial bending case. An alternate formulation decouples the section shear force from the bending and axial forces in the section constitutive law (that is an independent, uncoupled shear V-γ law is assigned to the section), and equilibrium at the section level couples bending and shear responses. In other words, when the shear strength is reached, bending cannot increase to equilibrium between shear forces and bending moments (Marini & Spacone, 2006). It can however be stated that a section model that accounts for full nonlinear coupling between axial, biaxial bending, shear and torque is not yet available for beam elements.

Different uniaxial constitutive laws are available for concrete and steel. For concrete, different properties can be assigned for confined and unconfined concrete. Modifications of the steel bar laws can also account for buckling and for slip, but calibration is a key issue in this case.

At present, no readily available models are yet available for the beam-column joints, which are commonly neglected or assumed rigid in current practice. Another important issue is modeling the effects of the frame infills. It is well known that masonry infills influence the behavior of RC frames, but modeling the interaction is not easy. Strut elements have been proposed, but the selection of the material properties is not straightforward.

As for nonlinear geometric models, there is little experience on their use in nonlinear frame analysis, even though many think it is important as the damage induced by the ground motions leads to larger lateral drifts. For displacement-based elements, treatment of the P-Δ effects or even of the large-displacements and moderate rotations is a well established field. For force-based elements, the problem has been recently solved (Neuenhofer, 1998; Scott & Filippou, 2007) within the general co-rotational framework.

Spread plasticity models are no doubt more precise and accurate than lumped-plasticity models, However, they are somehow more delicate to use. For section behaviors that exhibit softening (reinforced concrete columns, local buckling etc.) spread plasticity elements localize the deformations in the extreme sections and the solution loses objectivity (Coleman & Spacone, 2001). Several solutions have been proposed, all based on the knowledge of the actual plastic hinge length L_{pl}. This is however a central point to the entire nonlinear procedure. The analyses are based (for both lumped and spread plasticity models) on the notion of a plastic hinge length. Yet, there does not yet exist a unified definition of this characteristic length, because the problem is not totally understood or described from a mechanical viewpoint. In other words, nonlinear analyses describe a process, the formation and evolution of the plastic hinge, that is not fully understood. It is therefore difficult to give reliable formulas for L_{pl}. Though EC8 provides some indications on how to compute the plastic hinge lengths, these definitions seem to apply for new buildings where the rebar splicing is placed away from the member ends and the end regions are well confined

by the transverse reinforcement. For existing buildings, the plastic hinge length may be lower.

The application of more advanced methods of analysis such as the fiber elements is sometimes incompatible with the nonlinear procedures specified by the design codes. This is precisely the case of the N2 method in EC8. In this case, for plan-irregular buildings, one has to perform two different pushover curves in the principal x and y directions of the building. The results are then combined using the combination rules of Figure 3. When using the fiber element, though, a problem arises. Both pushover analyses are performed after application of the gravity loads. But the gravity loads cannot be accounted for twice, thus the procedure of Figure 3 can only be rationally applied with section laws that consider axial and bending forces uncoupled. The problem is more general. The combination rules developed for linear methods do not readily extend to nonlinear methods, because the principle of superposition no longer applies. The main problem here is that the N2 method was developed for 2d models, and its extension to 3D models is quite difficult and is becoming unrealistic.

Another problem that arises when using fiber element has to do with the selection of the control point. The original N2 method was developed for shear frames and can be easily applied to frames with floor diaphragms which are rigid in their plane. When the beams are modeled with fiber elements, floor diaphragms cannot be used, because they introduce artificial compression due to the fact that the beams cannot freely extend. Because the beams are normally axially stiffer, almost any point can be selected. However, in older buildings with few beams and thin slabs the floor can become quite flexible in its plane and thus some differences can be expected in the horizontal displacements over a floor. Also, slabs have to be modeled with either shell elements or with equivalent bar elements (which ignore the flexural stiffness of the slabs).

NTH analyses appear to be more reliable than NPO analyses, but some problems exist in their case too. Slowness of the analysis was already mentioned. Another issue that is sometimes neglected is the direction along which the ground motion is applied. Design codes typically apply the ground motions (either in the form of design spectra or of input accelerograms) along the structure principal directions. Such directions may be difficult to identify for older, plan irregular buildings or for skewed bridges. The problem does not exist for linear analysis, where the directional combination rules (CQC3, SRSS, 100/30 etc.) cover the possibility of different ground motion direction. No thorough studies have been completed for nonlinear analyses of plan-irregular structures.

4 Examples

Some of the previously highlighted issues are now discussed through the nonlinear analyses of a RC building and a RC bridge. The RC building is a 3-story structure that was damaged during the 2002 Molise earthquake in Italy. It is a typical residential building with a semi-open ground level. The scope of the study, conducted jointly between the University of Chieti-Pescara, Italy and the University of California, San Diego, USA, is to assess the effects of different modeling details on the structural response of the building model.

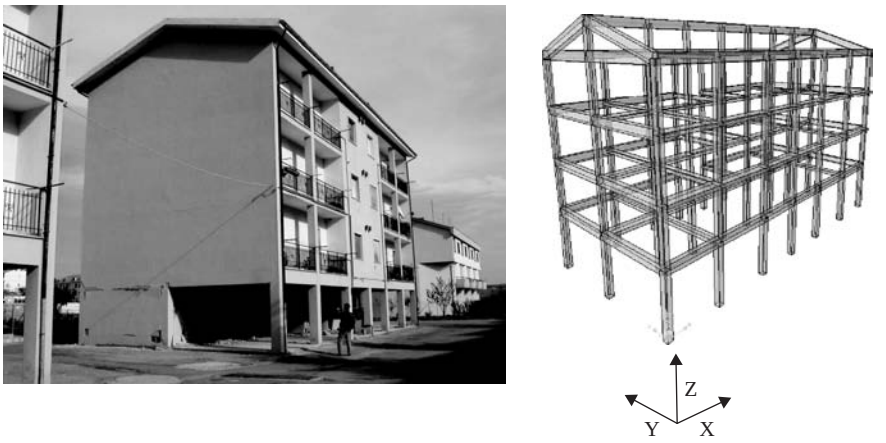

Figure 4 Bonefro building.

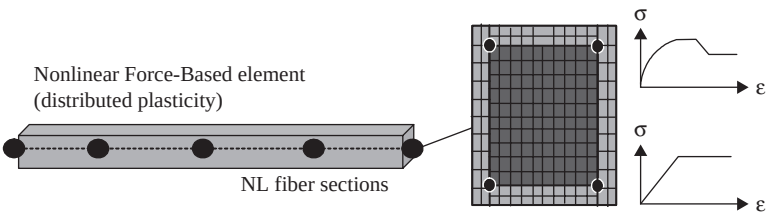

Figure 5 Frame element, fiber section and fiber steel and concrete laws used.

The building is analyzed using OpenSEES (McKenna, 1997; Fenves *et al.*, 2004). The basic frame is modeled with force-based, fiber-section distributed plasticity beam elements (schematically shown in Figure 5. The general section model uses the section aggregator in OpenSEES, where shear is coupled with bending only at the element level. In the applications described in this paper, only linear shear and linear torque were used. One element per structural element is used, unless there is a change in section reinforcement. The bare frame response is shown in Figure 7. The bare frame is in this case loaded in the global Y direction only. The structure is particularly flexible in the Y direction because the central frames have no beams. A 1.18sec fundamental period of the frame structure in the Y direction is found from a modal analysis after the application of the gravity loads.

As previously noted, it is not clear how the N2 Pushover procedure can be applied in this case where a fiber section model is used. The application of the procedure of Figure 3 implies two pushovers in the X and Y plan principal directions. Does that imply that the gravity loads are applied twice? If they are applied twice, then the resulting axial loads will be overestimated, if the gravity loads are applied only once, before say the pushover in the X direction, then the N-M interaction in the pushover in the Y direction is not very meaningful. It appears that in the current format the

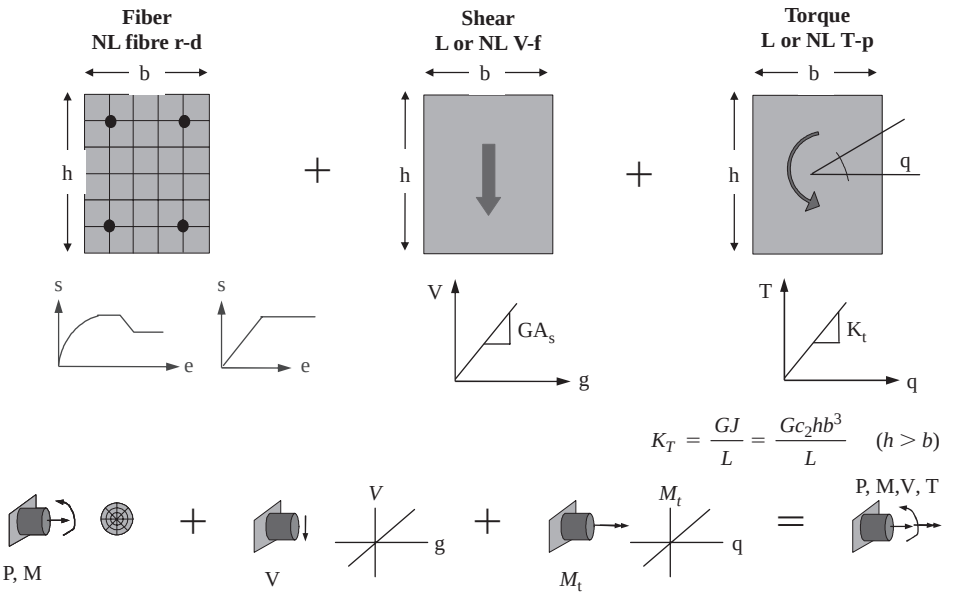

Figure 6 Extended section model (section aggregator in OpenSEES (McKenna, 1997).

N2 procedure cannot be applied to irregular buildings where the structure has to be loaded in two orthogonal directions.

The bare frame of Figure 7 was studies using both modal and uniform pushover according to EC8, modal pushover and nonlinear time history analysis using seven generated accelerograms. The green curves in Figure 7 indicate the responses to the seven accelerograms, while TH indicates the average value of the maximum response quantity, as prescribed by EC8. The results of the pushover analyses are in good agreement with the average time history displacement response, while some inaccuracy appears in the upper floors drift response. The MPA analysis results show that the higher modes have some participation, but their contributions remain essentially elastic. The SRSS combination rule used in this case leads to a total MPA response slightly greater than the mode 1 only PO response. It is noteworthy that all three methods agree in finding a floor mechanism at the second story. Due to the long fundamental period of the structure, the total response has a large elastic component. The plastic hinge inelastic demand varies from column to column depending on the presence of adjacent beams and on the height of the beams.

The floor is typically modeled as a diaphragms rigid in its plane. This may not be a good choice in the present example because: a) the absence of beams in the central frames makes the floor flexible; b) the rigid diaphragms impose artificial prestressing in the fiber-section beams by blocking their extension. A 2x2 mesh of 40 mm-thick elastic 4-node concrete shell elements is used for each slab field (Figure 11).

Similarly to the previous case, the average TH response and the first mode PO analysis match quite well in terms of absolute displacements, while the PO drift demand

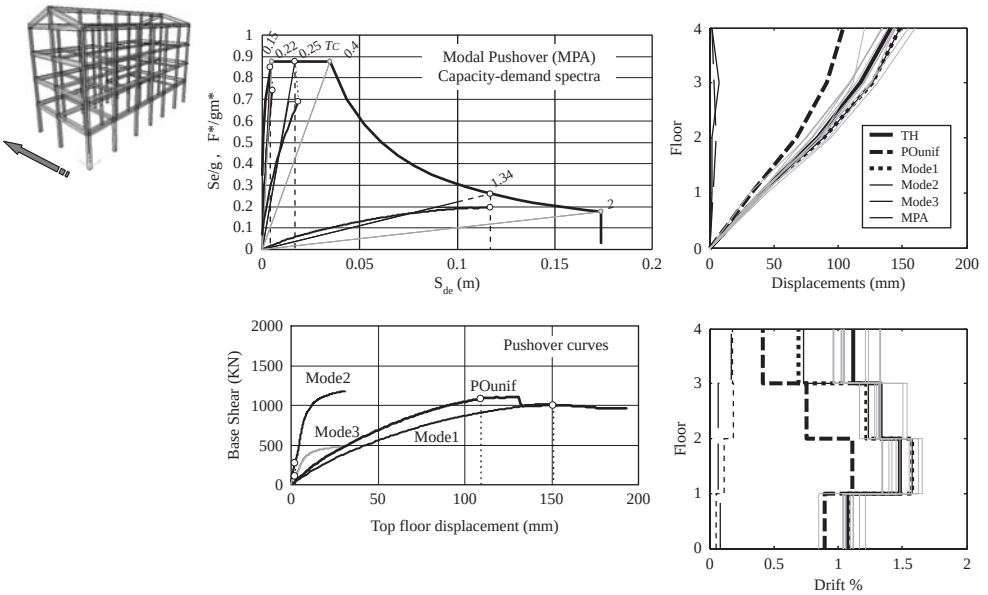

Figure 7 Results of NPO on Bonefro building (bare frame).

is still lower. There is also some increased scatter among drift responses obtained with different ground motions at the floor where the maximum drift occurs. As far as the structural behavior is concerned, the presence of the floor slabs unloads the beams with respect to the previous case. The additional floor bending stiffness produces lower elastic deformations in the columns. The elastic configuration of the floor slab somehow bounds the slab behavior since slabs are expected to crack.

The next element to be added are the infills. The infill panels are modeled as double inelastic no-tension struts, with thickness $t_w = 200$ mm, equivalent width $d_w = d/10$, using a uniaxial elastic, softening law similar to that of concrete. Two cases are considered. In the first, the struts connect the structural joints, in the second, at the ground level the struts are connected to the columns at a distance of approximately 500 mm from the beam-column joint (Figure 9).

The first effect is to increase the stiffness of the building and the base shear in the building, but to decrease the total displacement demand. The pushover response is in good agreement with the time history average results in terms of maximum top displacements. Some differences are found in the maximum drift response at the upper floors. For the case of the eccentric struts, the base column shear behavior was modeled with a nonlinear shear law. The overall response does not change significantly, but the central column of the lateral frames fail in shear. The shear failure is considered using the model of Figure 6 with a nonlinear shear behavior. The central base column response is shown in Figure 10. When the shear strength is reached (upper right plot), by equilibrium the bending moment (still mostly elastic, lower right plot) cannot increase.

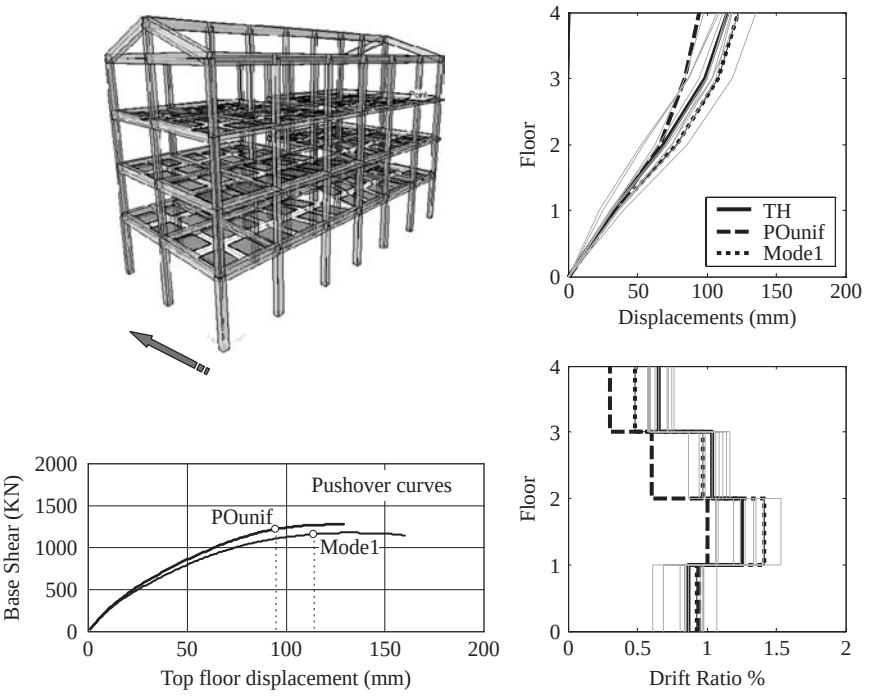

Figure 8 Results of NPO on Bonefro building (bare frame plus flexible floors).

Finally, the bare frame was studied using two accelerograms applied in the X and Y directions. Figure 11 shows the bending moment response at the base section of the highlighted columns for one accelerogram applied in the Y direction only, while Figure 12 shows the same response due to simultaneous accelerograms in the X and Y directions. The section responses change, mainly due to the change in axial load due to the application of the accelerogram in the orthogonal direction. In general, the change in axial load significantly affects the bending response. The outer column is more loaded because there are no beams in the Y direction.

The second example is a RC bridge located in Vasto Marina (south of Pescara, Abruzzo, Italy) along the major north-south Adriatic Highway 16. It is a two-lane bridge built in the 1960s. The bridge, shown in Figure 13, has a sharp bent about 1/3 from the south end. The supporting piers are multi-column bents. The bridge is located near the Adriatic seacoast and some of the steel reinforcement is badly rusted. The bridge is irregular in plan and height.

The superstructure is partly continuous, with Gerber beams connecting the continuous sections of the bridge. The bridge has an irregular geometry. Its complex dynamic response cannot be captured by analyzing separate subsystem. Furthermore, the Gerber supports are rollers in the longitudinal direction only, while they block the transversal displacements. For these reasons, a global model of the entire bridge was created placing particular care in the definition of joints and the nodes. The pier bents

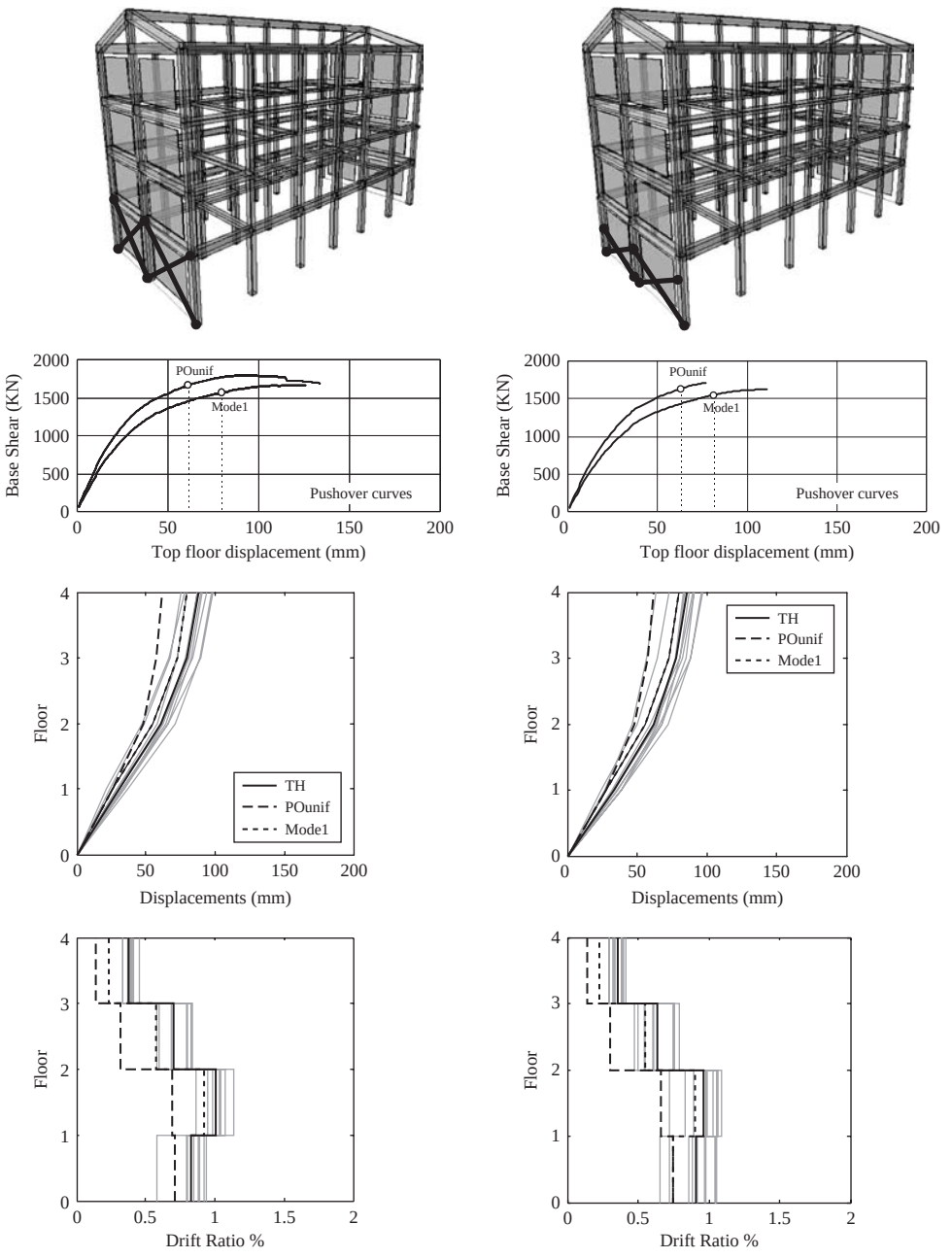

Figure 9 Results of NPO on Bonefro building (bare frame plus infills).

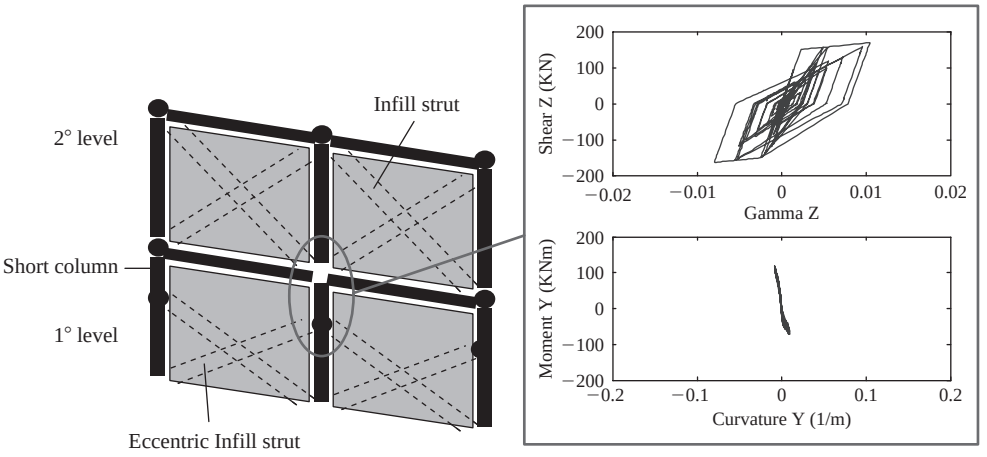

Figure 10 Response of the central base columns with eccentric infills.

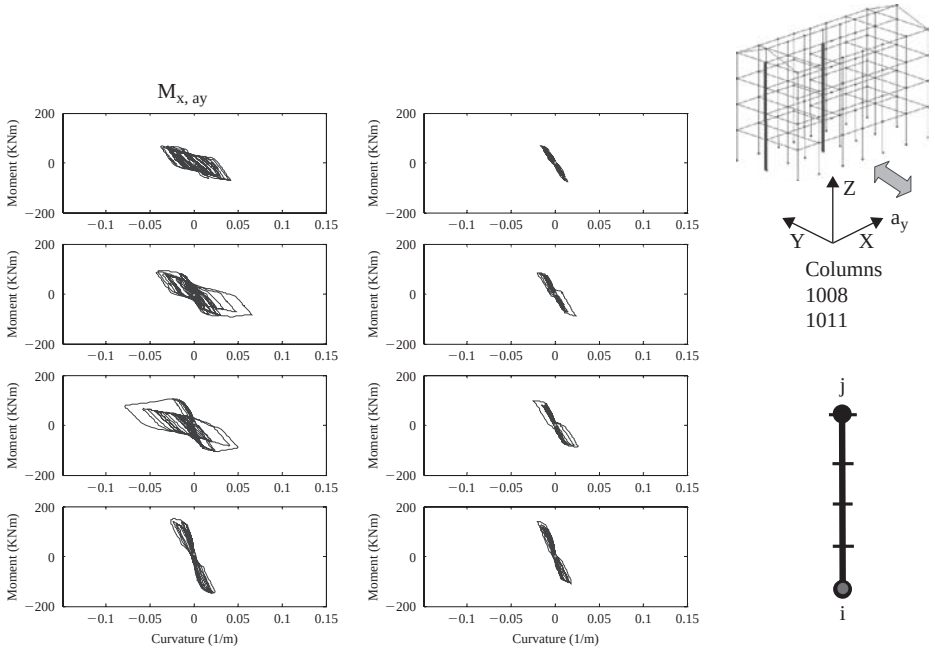

Figure 11 Results of NTH on Bonefro building (bending moment M_x due to accelerogram a_y only).

are modeled with beam elements, whereas the deck is modeled with shell elements as shown in Figure 14.

The Gerber support joints are modeled with two overlapping nodes connected with equal displacement constrains in the x, y and z direction (equal constraints). The roller joints are modeled in a similar manner but the x direction is not constrained. To

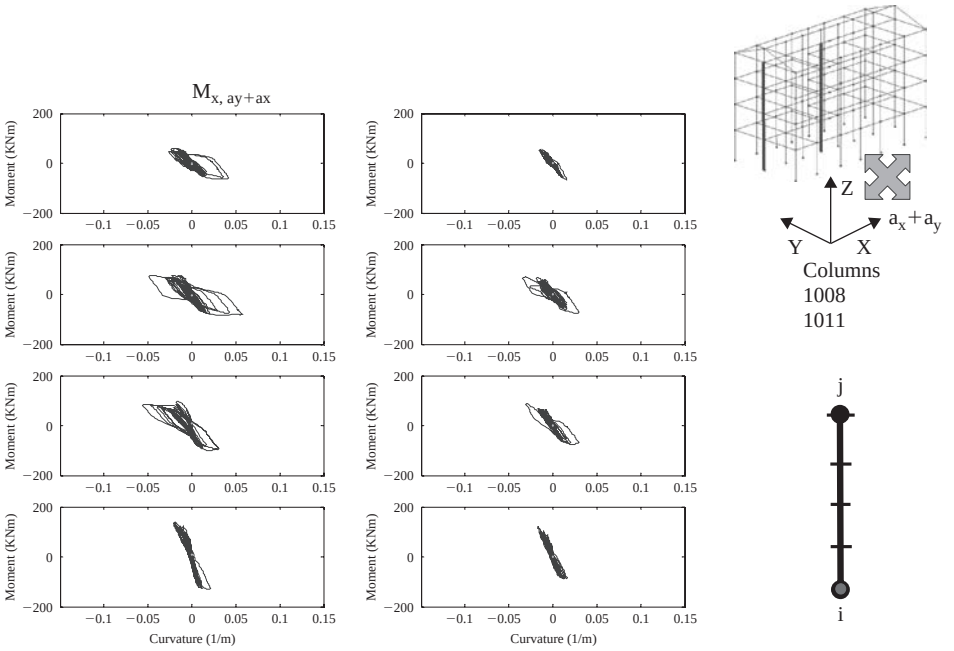

Figure 12 Results of NPO on Bonefro building bending moment M_x due to accelerograms a_x and a_y).

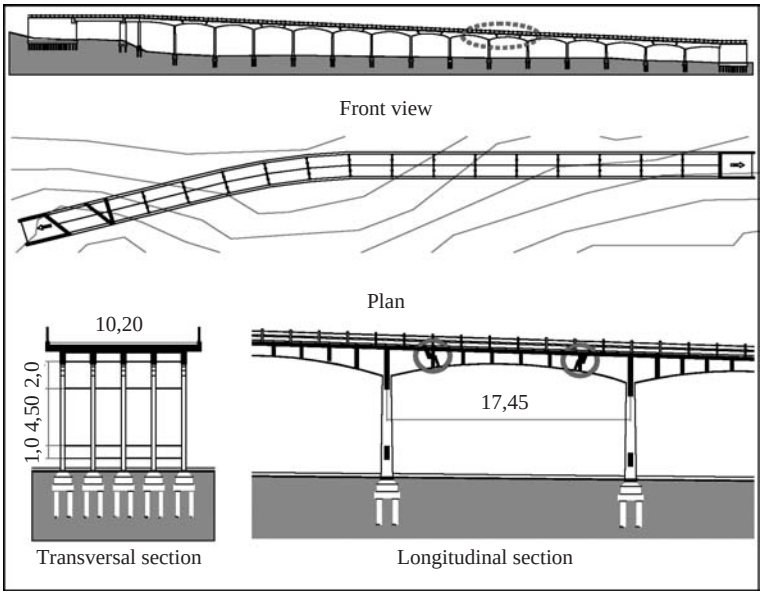

Figure 13 Vasto Marina, Italy Viaduct.

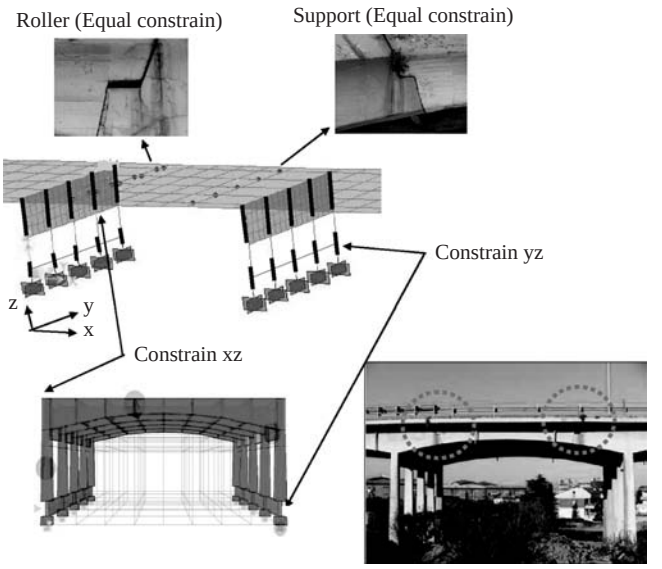

Figure 14 Bridge details and analytical model.

simulate correctly the flexural behavior of the piers in the longitudinal and transversal direction, constrains are inserted in the nodes as shown in Figure 14.

The bridge is studied with linear and nonlinear dynamic analyses, using the Italian draft guidelines for the seismic vulnerability assessment of existing bridges, prepared in the framework of the Reluis project, funded by the Italian Civil Protection Department in support of the new seismic design guidelines [OPCM 3431, 2005]. The linear analysis is the classical response spectrum analysis (RSA) according to EC8. The nonlinear static analysis is performed with lumped plastic hinges and the response time histories (RTH) are performed with fiber force based elements. The results of the RTH performed with the program Midas Civil Fenves *et al.* (2004) are reported here. To perform the analysis, 2 accelerograms are selected. The accelerograms are part of a suite of ground motions that comply with the requirements of the new Italian seismic codes, OPCM 3431 [OPCM 3431, 2005], They can be found at the website: http://reluis.rdm-web.com/pagine/Accelerogrammi_europei.htm.

The structure sits on type C soil (OPCM 3431 [OPCM 3431, 2005]). The material properties used in the analysis are the following: concrete cylinder strength, $f_c = 20$ MPa, steel yielding strength $f_y = 315$ MPa. The concrete is modeled using the Kent and Park model, whereas the steel is modeled using the Menegotto-Pinto model.

The sections are subdivided into 10x10 fibers. Because program Midas does not included tapered elements, the tapered piers are idealized with two elements and every element is integrated with 3 Gauss-Lobatto points. In the longitudinal direction, the pier height varies between 3 (Bent 1) and 10 (Bent 14) meters, therefore the length of the first Gauss-Lobatto point varies between 250 mm and 837 mm. The

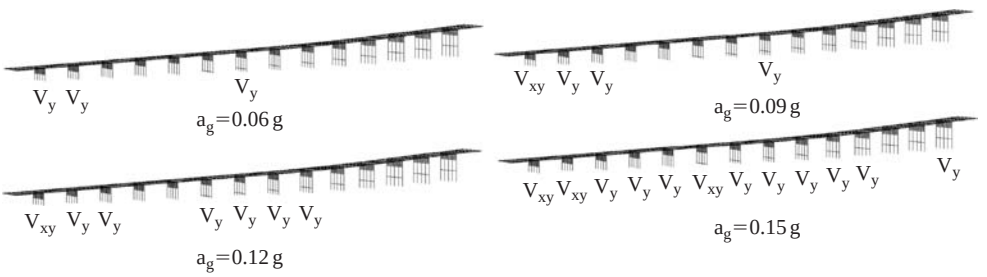

Figure 15 Shear failures for different PGAs.

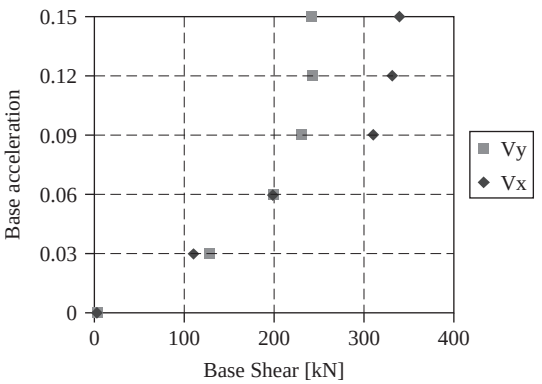

Figure 16 Pier 1 base shear force.

base section dimensions of bent 1 are h = 700 mm and b = 350 mm, whereas the base section dimensions of bent 14 are h = 880 mm and b = 350 mm.

The design base acceleration for the site is $a_g = 0.15$ g. Five incremental dynamic analysis are performed with $a_g = 0.15$ g, 0.12 g, 0.09 g, 0.06 g and 0.03 g. The shear strength is checked using the Eurocode 2 (2005), which uses the modified field theory. The results are represented in Figure 15. The bent are numbered from the left to the right from 1 to 14.

In Figure 15 V_x indicates shear failure in the longitudinal direction and V_y shear failure in the transversal direction. For $a_g = 0.03$ g the piers do not collapse. The first column to collapse in the longitudinal direction is in bent 1 for an acceleration $a_g = 0.06$ g. The base shear of the first column that collapses is depicted in Figure 16 for different levels of the PGA.

For an acceleration of 0.15 g nearly all the elements fail in shear. The members fail in flexure when the ultimate concrete strain is reached. Figure 17 shows the deformed shape when the first column collapse in flexure.

In the Figure 17 F stands for flexural failure and Y indicates yielding of the rebars. The picture clearly indicates that the high torsion of the first bent causes failure of the outmost external column. The base section at failure is shown in Figure 18. There is

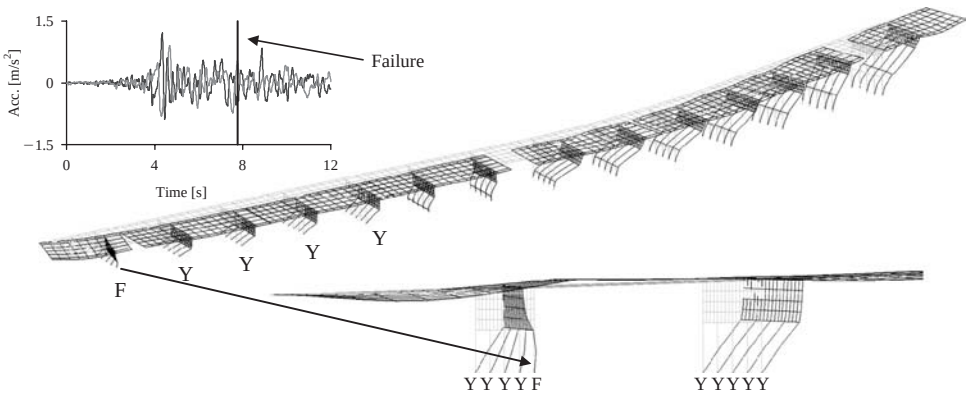

Figure 17 Deformed shape at flexural failure (7.78 seconds).

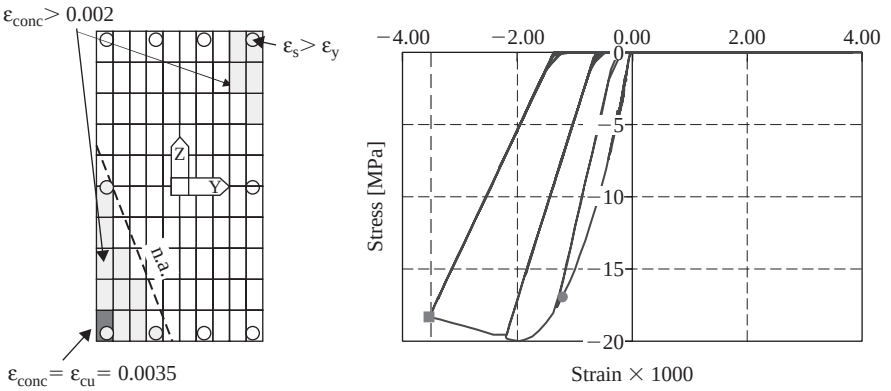

Figure 18 Base section at failure.

a high biaxial bending which causes the neutral axis to rotate. The moment-curvature behavior in the two orthogonal directions is shown in Figure 19.

It is worth noting that in several codes the ultimate capacity is estimated on the basis of the ultimate chord rotation. For example Eurocode 8 uses the following formula:

$$\boldsymbol{\theta}_{p,u} = (\boldsymbol{\Phi}_u - \boldsymbol{\Phi}_y) L_{pl} \left(1 - \frac{L_{pl}}{2L}\right) \tag{3}$$

where $\boldsymbol{\Phi}_u$ is the ultimate curvature, $\boldsymbol{\Phi}_y$ is the yielding curvature, L_{pl} is the plastic hinge length and L is the distance from the end section of the plastic hinge to the point of zero moment in the pier (shear span length). The plastic hinge length L_p can be found as:

$$L_{pl} = 0,10 L_V + 0,015 f_{yk} d_{bL} \tag{4}$$

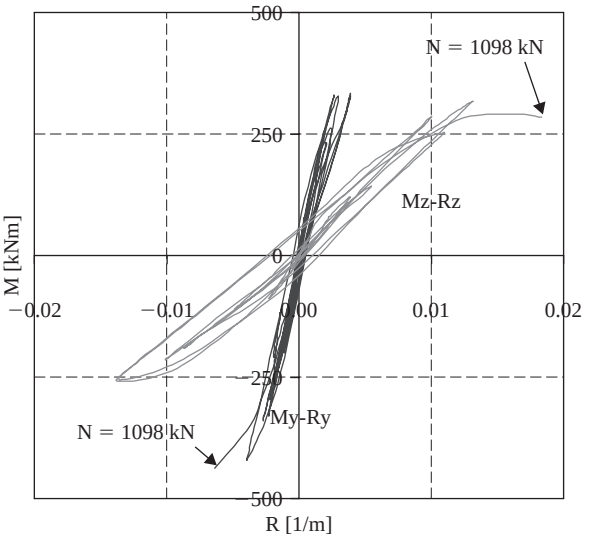

Figure 19 Moment-Curvature at the bottom point.

The formula was calibrated on the basis of simple bending tests. Is it reliable for biaxial bending? Moreover, how can L_V be defined in the case of biaxial bending? It appears that the literature published and the guidelines available at present do not investigate in depth this problem. Also Eq. (4) is applicable to well confined sections only, thus it may not be readily extended to unconfined sections, as is the case of the given example.

5 Conclusions

It is recognized that nonlinear methods of analyses are the rational procedures for predicting the response of structures under moderate and strong earthquakes. Much work and progress have been achieved in recent years, in terms of both model and nonlinear procedure developments, but nonlinear methods of analyses, as proposed by EC8, are not yet routinely used in either research or practice. The following is a partial list of issues that still need clarification:

- The nonlinear pushover procedure is not readily applicable to plan irregular buildings or structures. This simplified and quick method of analyses was originally developed for plane frame and its extension to space frame is not straightforward and may not be achievable;
- The selection of the ground motions for nonlinear dynamic analyses is key to these analyses but no clear procedure is yet in place. Another issue that needs further investigation is the amount of viscous damping that can be assigned. Finally, the directions along which the ground motions are applied to plan-irregular buildings is easily identified;

- The differences found with different modeling assumptions need to be fully understood by the analysts. Floor flexibility, infill effects, shear response are some of the effects that the analyst may want to consider;
- Not all nonlinear phenomena (such as joint failures, frame-infill interaction and shear–bending interaction) are modeled correctly by present nonlinear computer codes, either research or commercial;
- The amount of output produced by nonlinear computer codes is very large. Though graphic post-processing tools are available (mainly in commercial codes) the design checks required by EC8 need further testing before they are fully applicable. Once clear procedures are identified, then post-processing of the results will be easily implemented in the nonlinear codes.

As more and more structures are analyzed with nonlinear procedures, the above issues will become clearer and the problems will be solved, especially through a strong interaction between practicing engineers and researchers.

References

ATC 40. 1996. Seismic Evaluation and Retrofit of Concrete Buildings, *Applied Technology Council*.

Antoniou, S. & Pinho, R. 2004. Advantages and Limitations of Adaptive and Non-adaptive Force-Based Pushover Procedures, *Journal of Earthquake Engineering*, **8**(4), 497–522.

Aydinoglu, M.N. 2003. An Incremental Response Spectrum Analysis Procedure Based on Inelastic Spectral Deformation for Multi-Mode Seismic Performance Evaluation, *Bulletin of Earthquake Engineering*, **1**, 3–36.

Chopra, A.K. & Goel, R.K. 2002. A modal pushover analysis procedure for estimating seismic demands for buildings, *Earthquake Engineering and Structural Dynamics*, **31**, 561–582.

Coleman, J. & Spacone, E. 2001. Localization Issues in Nonlinear Force-Based Frame Elements, *ASCE Journal of Structural Engineering,* **127**(11), pp. 1257–1265.

Elnashai, A.S. 2002. Do we really need Inelastic Dynamic Analysis?, *Journal of Earthquake Engineering*, **6**, Special Issue 1, 123–130.

Eurocode 8. 2003. *Design of Structures for Earthquake Resistance*, European Committee for Standardization.

Fajfar, P. 1999. Capacity Spectrum Method Based on Inelastic Demand Spectra, *Earthquake Engineering and Structural Dynamics*, **28**, 979–993.

Fajfar, P. 2002. Structural Analysis in Earthquake Engineering – A Breakthrough of Simplified Non-Linear Methods, *12th European Conference on Earthquake Engineering*, London, United Kingdom, Paper 843.

Fajfar, P., Kilar, V., Marusic, D. & Perus, I. 2005. The extension of the N2 method to asymmetric buildings, *4th European Workshop on the Seismic Behaviour of Irregular and Complex Structures*, Paper No. 41, Thessaloniki, Greece.

FEMA 356. November 2000. Prestandard and Commentary for the Seismic Rehabilitation of Buildings, Prepared by *American Society of Civil Engineers*, Washington, D.C. (U.S.A.).

Fenves, G., McKenna, F., Scott, M.H. & Takahashi, Y. 1–6 August 2004. An Object-Oriented Software Environment for Collaborative Network Simulation, 13th World Conference on Earthquake Engineering, Paper 1492, Vancouver, B.C. (Canada).

Gupta, B. & Kunnath, S.K. 2000. Adaptive Spectra-Based Pushover Procedure for Seismic Evaluation of Structures, *Earthquake Spectra*, **16**(2), 367–391.

Iervolino, I., Maddaloni, G. & Cosenza, E. 2006. Unscaled real record sets compliant with Euro-code 8. *First European Conference on Earthquake Engineering and Seismology*, Geneva, Switzerland.

Marini, A. & E. Spacone, E. 2006. "Analysis of R/C Elements Including Shear Effects." *ACI Structural Journal*, **103**(5), 645–655.

McKenna, F. 1997. *Object-oriented finite element analysis: frameworks for analysis, algorithms and parallel computing*. Ph.D. dissertation, University of California, Berkeley.

MIDAS. 2006. *Civil Analysis Reference Manual*, Civil 2006 (v7.12 Release No. 1) Midas Information Technology Co. Ltd.

Neuenhofer, A., & Filippou, F.C. 1998. Geometrically Nonlinear Flexibility-Based Frame Finite Elements, *ASCE Journal of Structural Engineering*, **124**(6), 704–711.

OPCM 3431. Ulteriori modifiche ed integrazioni all'OPCM3274, 2005 (*in Italian, Technical Norms for design, evaluation and seismic rehabilitation of buildings*).

Panagiotou, M. & Restrepo, J. 2007. Computational model for the UCSD 7-story structural wall building slice, *SSRP 07-09 Report*, Department of Structural Engineering, University of California San Diego, (in press).

Petrangeli, M., Pinto, P.E. & Ciampi, V. 1999. Fiber element for cyclic bending and shear of R/C structures. I: theory, *ASCE Journal of Engineering Mechanics*, **125**(9), 994–1001.

Scott, M.H. & Fenves, G.L. 2006. Plastic Hinge Integration Methods for Force-Based Beam-Column Elements, *ASCE Journal of Structural Engineering*, **133**(2), 244–252.

Scott, M.H. & Filippou, F.C. 2007. Response Gradients for Nonlinear Beam-Column Elements under Large Displacements, *ASCE Journal of Structural Engineering*, **133**(2), 155–165.

Spacone, E., Filippou, F.C. & Taucer, F.F. 1996. Fiber Beam-Column Model for Nonlinear Analysis of R/C Frames. I: Formulation, II: Applications. *Earthquake Engineering and Structural Dynamics*, **25**(7), 711–742.

Zimmermann, Th., Truty, A., Urbanski, A. & Podles, K. 1985–2007. Z-Soil user manual, Zace Services Ltd.

Chapter 22

Modelling inelastic buckling of reinforcing bars under earthquake loading

Michalis Fragiadakis

National Technical University of Athens, Athens, Greece
University of Thessaly, Volos, Greece

Rui Pinho

European School for Advanced Studies in Reduction of Seismic Risk (ROSE School), Pavia, Italy

Stelios Antoniou

SeismoSoft—Software Solutions for Earthquake Engineering, Chalkida, Greece

ABSTRACT: This study focuses on the modelling of steel reinforcing bars subjected to a generalized loading history. The model of Monti and Nuti which is based on a set of experimental observations in order to account for buckling of the steel bars is examined. It has been noticed that in the case of partial unloading and then reloading, a common situation when a structure is subjected to seismic actions, the model might greatly overestimate the corresponding stress. An additional memory rule is thus proposed to eliminate this observed shortcoming. With the aid of the proposed modification, the Monti-Nuti model proved to be capable of simulating accurately the capacity of reinforced concrete members. The rules presented are easy to implement and applicable to any model in the literature where a similar situation is identified. Two case studies are examined where the enhanced model was proven capable to produce realistic numerical results.

1 Introduction

Past earthquakes have shown that a common failure mode of reinforced concrete (RC) members is buckling of the longitudinal reinforcement. In order to obtain an accurate prediction of strength and ductility, this effect should thus be taken into account during analysis. Buckling of the reinforcement is in essence a stability problem and therefore depends both on the geometry of the bar and on the material properties. However, treating the problem as a second-order problem would require a detailed FE modelling approach. In practice, in order to allow for an easier modelling of RC structures, phenomenological constitutive laws where buckling is taken into consideration through the material properties are commonly adopted.

The interest of this study is on uniaxial stress-strain relationships, which can be used in the framework of a fiber beam-column element and also can capture accurately the response of a linear element with minor bending stiffness such as a reinforcing bar. In particular, special attention is paid on the model proposed by Monti and Nuti (1992).

This model incorporates a set of experimental observations regarding the response of steel reinforcement into the widely-used stress-strain relationship of Menegotto and Pinto (1973).

Experience has shown that a stress-strain relationship may fail to predict correctly the response when small reversals in the strain history occur; this is the case when the structural model is subjected to a ground motion record. Initially this problem was identified in the model of Menegotto and Pinto (1973) by Filippou et al. (1983), who pointed out that, in order to avoid such an undesirable behaviour, the memory of the analytical model should extent over all previous branches of the stress-strain history. In terms of implementation this would be impractical and thus Filippou et al. (1983) proposed to limit the memory of the model to four controlling curves, which warrant that, at least at the structural level, this numerical problem is almost fully eliminated.

The aforementioned numerical difficulty strongly manifests itself when the Monti-Nuti buckling rules (1992) are implemented on the model of Menegotto and Pinto (1973), even if the Filippou et al. (1983) modifications are adopted; the response may be heavily distorted, thus limiting the applicability of the model to non-earthquake engineering applications. In this work, an additional memory rule that enables more accurate handling of a generalized load history is proposed. The methodology proposed is general in scope since it can be applied almost to any constitutive law of a $\sigma = f(\varepsilon)$ type, including the Menegotto-Pinto and the Monti-Nuti models. Emphasis is placed on the Monti-Nuti relationship, where the problem is more critical and also because the Menegoto-Pinto model does not feature modelling of re-bar buckling.

2 General specifications

2.1 *Description of the physical problem*

During load reversals, concrete in compression zone prevents the development of high compressive strain in the compressive steel. Only when concrete loses its resistance, as in the case of concrete spalling, the development of high compressive strain in reinforcing steel is likely. After spalling of the concrete cover the longitudinal bars are exposed and if the amplitude of the cyclic loading is significant the bars will buckle outwards. The only factor contributing against buckling is the existence of stirrups, that should be sufficiently spaced and detailed, particularly in those parts of the member where heavy inelasticity excursion is likely to take place.

Several parameters are involved in the phenomenon of buckling such as the slenderness of the rebar, the stiffness and the rigidity of the hoops and the strain hardening of steel. The most important is probably the slenderness of the rebars. A measure of slenderness is given by the ratio between the length of the stirrups over the diameter of the bar, L/D. The failure modes usually observed are, primarily, buckling between two consecutive stirrups and, less commonly, along a larger length when fracture of more than one stirrup occurs.

Only the monotonic behaviour has been thoroughly investigated when it comes to buckling, while the cyclic behaviour is still under investigation. According to Mander et al. (1984) buckling takes place at or near the yielding load, which is also verified by the recent study of Bae et al. (2005). The monotonic post-buckling path varies for different slenderness ratios of the bar. Mau and El-Mabsout (1989) presented

monotonic curves for different, L/D ratios, where it is concluded that the higher the values of the ratio L/D, the lower the post-buckling peak stress. They have also verified numerically that the transition point between elements that are subjected to buckling phenomena and those that are not, is for L/D values close to five. For ratio values smaller than this threshold, the stress-strain relationship remains similar to that in tension. Monti and Nuti (1992) and Cosenza and Prota (2006) both presented results where the above threshold was justified experimentally, while Bae et al. (2005) concluded, on the basis of extended experiments, that this threshold value may vary also according to the yield strength of the bar. Moreover, Cosenza and Prota (2006) showed that for L/D ratio values greater than 20, elastic buckling is more likely to occur.

2.2 *State-of-the-art in modelling of steel bars*

Few attempts to capture buckling of the longitudinal bars can be found in the literature. Among them, the proposals of Gomes and Appleton (1997) and Monti and Nuti (1992) are based on modifications of the Menegotto-Pinto model (1973). Monti and Nuti (1992) proposed a set of rules based on experimental observations of buckling of reinforcement bars. The stress-strain relationship adopted was that of Menegotto-Pinto, though any given constitutive law may be used, if expressed accordingly. The parameters of the Monti-Nuti model are updated after each load reversal, with such updating being performed by means of the two classical (*i*) isotropic and (*ii*) kinematic hardening rules, (*iii*) a memory rule to account for the material's memory of the plastic path followed and (*iv*) a saturation rule to account for the asymptotic character of the hardening phenomena. These four rules are defined both in the absence and in the presence of buckling. A detailed description of the model is provided by Monti and Nuti (1992), where experiment-based values are used in order to calibrate the model; different values can be easily adopted on the basis of alternative experiments (e.g. Bae et al. (2005), Gomes and Appleton (1997)). A brief description of the Monti-Nuti model is given in the following paragraphs.

The backbone of the Monti-Nuti model is that of the Menegotto-Pinto relationship:

$$\sigma^* = b\varepsilon^* + \frac{(1-b)\varepsilon^*}{(1+\varepsilon^{*R})^{\frac{1}{R}}} \tag{1}$$

where the normalised strain and stress are obtained by:

$$\varepsilon^* = \frac{\varepsilon - \varepsilon_r}{\varepsilon_0 - \varepsilon_r} \quad \text{and} \quad \sigma^* = \frac{\sigma - \sigma_r}{\sigma_0 - \sigma_r} \tag{2}$$

Equation (1) represents a curved transition from a straight-line asymptote with slope E_0 to another asymptote with slope bE_0 (Figure 1 lines (α) and (β) respectively). σ_0 and ε_0 are the stress and the strain at the point where two asymptotes of the branch under consideration meet (Figure 1, point A), while σ_r and ε_r denote the stress and the strain at the point where the last strain reversal with stress of equal sign took place (Figure 1, point B). The shape of the transition curve allows a good representation of the Baushinger effect. This is a function of the curvature parameter R and depends on the strain difference between the current asymptote intersection point and the previous

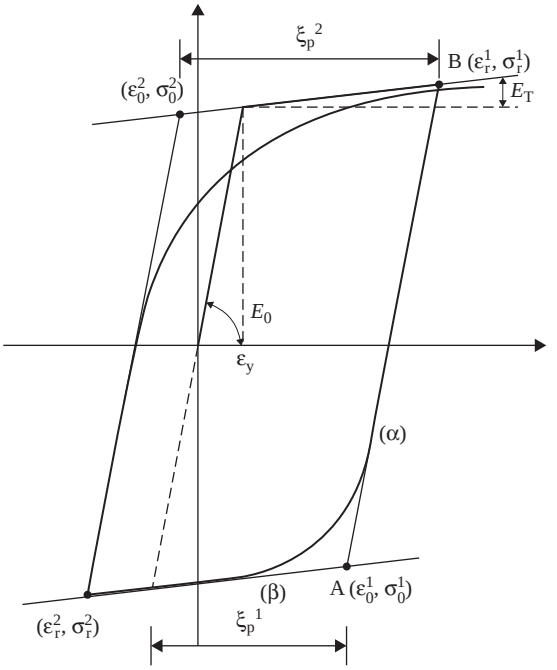

Figure 1 Stress-strain relationship of the Menegotto-Pinto model.

load reversal point with maximum or minimum strain depending on the corresponding steel stress (Filippou et al. (1983)).

The expression for R takes the form: $R^n = R_0 - (a_1\xi_p^n/(a_2 + \xi_p^n))$, where ξ_p^n is the plastic excursion at the current semicycle, defined as: $\xi_p^n = \varepsilon_r^n - \varepsilon_y^n$. Also, R_0 is the value of the parameter R during the first loading and a_1, a_2 are experimentally determined parameters to be defined together with R_0. The hardening rules are functions of four independent parameters: yield stress σ_y, elastic modulus E_0, hardening ratio b_{0p} and a weighting coefficient P. In absence of buckling, experimental tests have shown that no isotropic hardening is developed in half-cycles with plastic excursion equal to or lower than the maximum previous one. In the presence of buckling a complementary phenomenon occurs, in this case no kinematic hardening is developed in half-cycles with plastic excursion equal to or lower than the maximum previous one. These phenomena are modelled through a memory rule based on the additional plastic excursion γ_p^n:

$$\gamma_p^n = \langle|\xi_p^n| - \xi_p^{\max}\rangle \cdot \text{sign}\,\{\xi_p^n\} \tag{3}$$

where $\langle a\rangle = a$ if $a > 0$ and $\langle a\rangle = 0$ if $a \leq 0$ and $\xi_p^{max} = max(|\xi_p^n|)$ is the maximum plastic excursion. The half-cycle plastic work is defined as:

$$\Phi_p^n = \frac{1}{2}(\sigma_r^n - \sigma_y^n)\xi_p^n \tag{4}$$

Φ_p^n in absence of buckling is positive both in tension and in compression, while in the presence of buckling it is positive in tension and negative in compression. The hardening ratio b_{0p} for post-yield hardening branches in tension is defined as the ratio between the post-yield modulus in tension and the initial elastic modulus. The curvature of the branch is defined as in the Menegotto-Pinto model. Some additional parameters are determined in order to account for buckling. The hardening ratio for post-yield softening branches in compression is defined as:

$$b_{0n} = 0.003((L/D)^* - L/D) \tag{5}$$

which decreases with increasing L/D and is not related to the positive hardening ratio b_{0p}. In Equation (5), $(L/D)^*$ denotes the threshold ratio beyond which inelastic buckling is expected to occur, usually taken equal to five. The curvature of the post-yield loading branches in compression follows the rule:

$$R_b = R_{0b} + \frac{a_{1b} \cdot \xi_p^{\max}}{a_{2b} + \xi_p^{\max}} < R_{1b} \tag{6}$$

where $R_{0b} = 0.2(L/D - (L/D)^*)$, $a_{1b} = a_1 + 1$, $a_{2b} = 1000a_2$, and $R_{1b} = R_0 - 2(L/D - (L/D)^*)$. The elastic modulus after reversal from compression varies according to:

$$E = E_0(a_5 + (1 - a_5) \cdot \exp(-a_6\xi_p^2)) \tag{7}$$

where $a_5 = 1 + ((L/D)^* - L/D)/7.5$, and $a_6 = 1000$. The modulus decreases with increasing cycle amplitude, due to the bar axial stiffness degradation that takes place after buckling.

The total hardening is obtained by means of a mixed rule consisting of both a kinematic and an isotropic component. A linear combination of two of the hardening types is assumed using a weighing coefficient P, which is calibrated experimentally:

$$\Delta\sigma_{KI}^n = P \cdot \Delta\sigma_K^n + (1 - P) \cdot \Delta\sigma_I^n \cdot \text{sign}(-\xi_p^n) \tag{8}$$

A value of $P = 0.9$ is suggested for common mild steel. The two hardening components are developed based on a memory rule. In the absence of buckling this rule is applied to the isotropic hardening, while in the presence of buckling it is applied to the kinematic hardening instead. In the absence of buckling the stress variation is due to the plastic excursion and the additional plastic excursion is given as follows:

$$\textit{Kinematic hardening}: \quad \Delta\sigma_K^n = \sum_{i=1}^{n} b_{0n} \cdot E_0 \cdot \xi_p^n \tag{9}$$

$$\textit{Isotropic hardening}: \quad \Delta\sigma_I^n = \sum_{i=1}^{n} \left| b_{0n} \cdot E_0 \cdot \gamma_p^n \right| \cdot \text{sign}(\Phi_p^n) \tag{10}$$

On the contrary, in the presence of buckling the stress variation is due to the additional plastic excursion which is defined as:

$$\textit{Kinematic hardening}: \quad \Delta\sigma_K^n = \sum_{i=1}^{n} b_{0n} \cdot E_0 \cdot \gamma_p^n \tag{11}$$

$$\textit{Isotropic hardening}: \quad \Delta\sigma_I^n = \sum_{i=1}^{n} \left| b_{0n} \cdot E_0 \cdot \xi_p^n \right| \cdot \text{sign}(\Phi_p^n) \tag{12}$$

The updated stress σ_0^n (or σ_y^{n+1}) of Equation (1) becomes:

$$\sigma_y^{n+1} = \sigma_y^0 \cdot \text{sign}(-\xi_p^n) + \Delta\sigma_{KI}^n \tag{13}$$

3 Response under a generalized load history

When a ground motion is used to perform timehistory analysis, relatively small loading-unloading excursions of the material strains are frequent. Reinforcing bar numerical models, however, tend to be verified only under loading conditions such as that of Figure 2(a) where the loading scheme consists of large stable symmetric cycles. As a result, spurious numerical behaviour such as that illustrated in Figure 2(b), that arise from random unsymmetrical loading cycles, might be overlooked.

The severity of the problem depends on the formulation of the material model used. In particular, the Monti-Nuti model was found to be very sensitive to this situation, since a tiny notch in the stress-strain path may lead to a very large overestimation of the corresponding stress (Fig. 2(b)). This is due to the fact that the bilinear envelope, defined by the Menegotto-Pinto model adopted by Monti and Nuti, becomes too narrow and the curves are not capable of "fitting" within it. Therefore, this spurious behaviour is generated because the same algebraic expression used for the skeleton curve is also used when a small unloading and loading back takes place. Consequently, the spurious branches of Figure 2(b) are developed, with a shape that depends on the ratio between tie spacing and bar diameter L/D. As shown in sections to follow, such

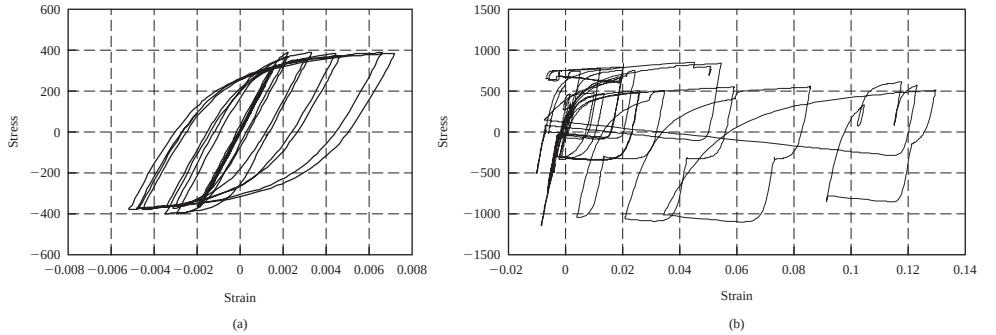

Figure 2 (a) Response under stable cyclic strain history; (b) Spurious branches on the σ-ε level produced by the M–N model when the member is subjected to earthquake loading.

overestimations may affect the accuracy of the overall analysis, for which reason it was deemed necessary to address them accordingly, as discussed subsequently.

4 Proposed modifications

In order to tackle difficulties such as those discussed in the previous section, Dodd and Restrepo-Posada (1995) introduced the idea of major, minor and simple reversals, whilst Balan et al. (1998) distinguished reversals into complete and incomplete, with a value of $2f_y$ being adopted as a threshold parameter. For the Monti-Nuti model, Attolico et al. (2000) proposed that whenever small strain variations take place, the model should follow the backbone curve before the last strain reversal.

In the current work, an alternative corrective measure is proposed for the Monti-Nuti model, where the stress-strain curve is forced to join tangentially the branch defined during the previous strain reversal. In order to determine whether an unloading branch is small or not, a strain interval denoted as $\hat{\varepsilon}$ is introduced. The latter is defined as a proportion of the strain value of the point of the last strain reversal ε_r. Typical efficient values vary between 2.5 or 5 percent of ε_r, though larger values may be used if higher "filtering" is deemed necessary (Fragiadakis (2001)).

All loading and reloading that take place inside the interval $\hat{\varepsilon}$ are assumed to be linear elastic. Figure 3(a) shows that when reloading beyond this interval (from point 4 to 5), the skeleton curve of the last loading branch is followed instead of updating the model parameters that would define a new loading branch. Otherwise, if unloading does not go beyond $\hat{\varepsilon}$, point 5 is obtained elastically (Fig. 3(b)). Loading in the opposite direction, beyond point 4, will follow the previously defined branch 3–4 (Fig. 3(b)). Figure 4 shows two cases where reloading starts from points that have been previously obtained elastically. A strain step that results in a strain value outside the $\hat{\varepsilon}$ interval will follow the previously defined skeleton branch curve (Fig. 4(*a*)). Figure 4(*b*) shows that all load reversals inside $\hat{\varepsilon}$ are considered linear elastic. In Figure 5, the uncorrected and the corrected stress-strain histories for different L/D ratios are shown. Figures 6 and 7,

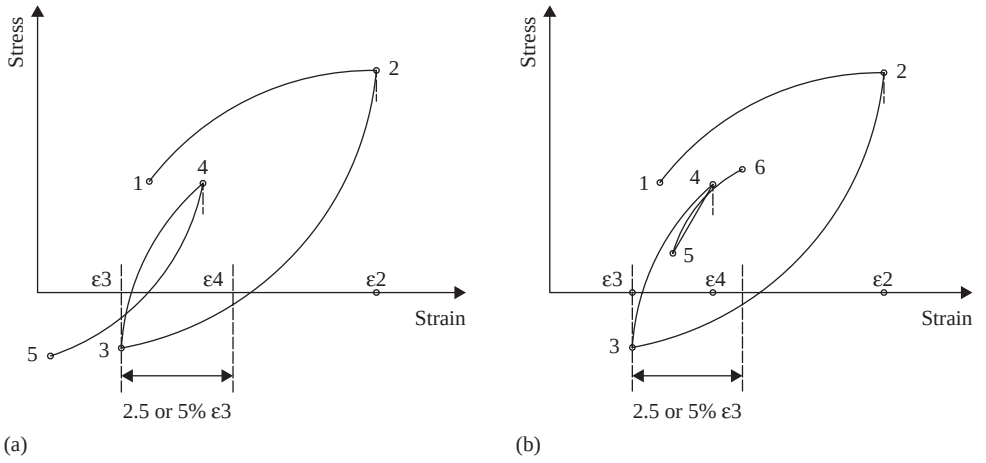

Figure 3 Reversal modelling in the $\hat{\varepsilon}$ interval.

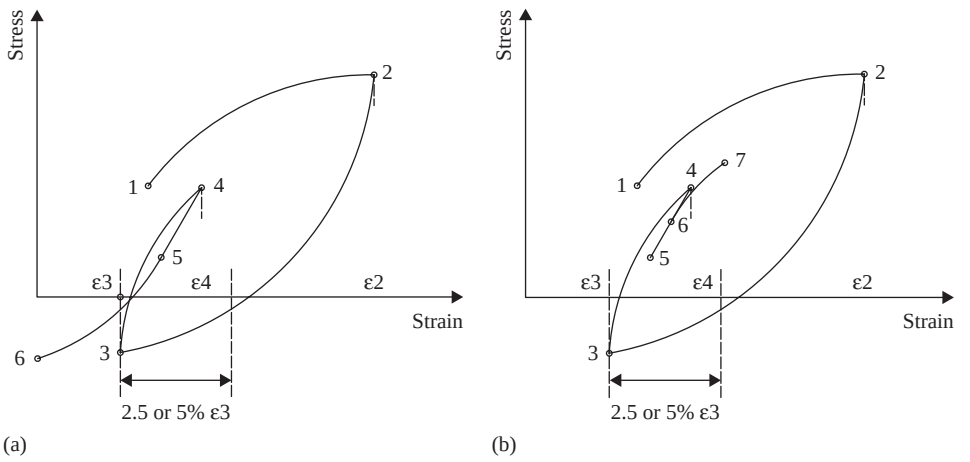

Figure 4 Reversal modelling in the $\hat{\varepsilon}$ interval, when reloading points obtained elastically.

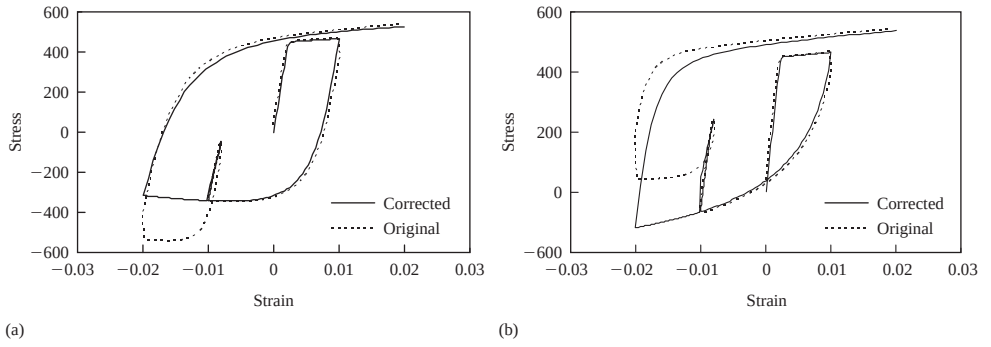

Figure 5 Corrected and uncorrected stress-strain paths; (a) $L/D = 12$, (b) $L/D = 6$.

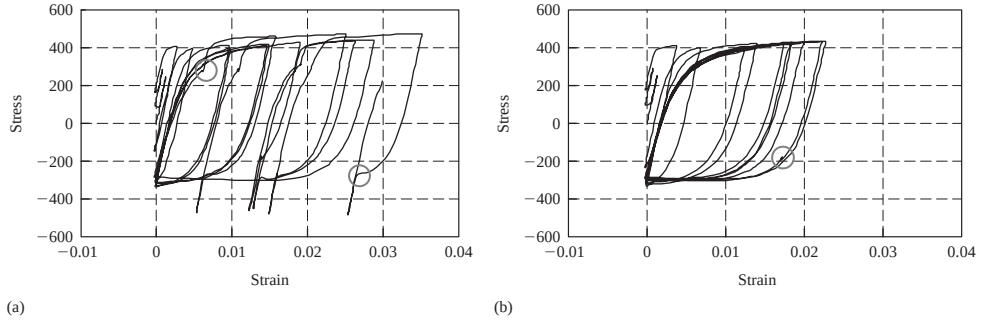

Figure 6 Comparison at the stress-strain level under seismic excitation; (a) without the proposed modifications, (b) with the proposed modifications.

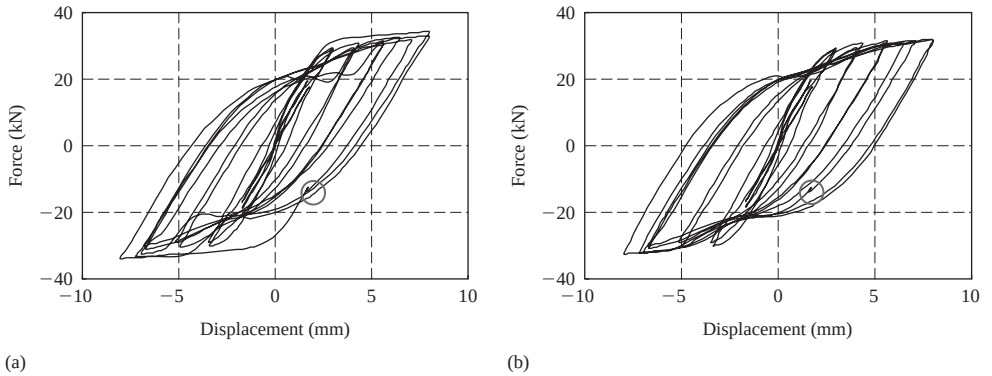

Figure 7 Comparison at the structural level under seismic excitation; (a) without the proposed modifications (b) with the proposed modifications.

Table 1 Material model parameters – Range of values.

	R_0	A_1	a_2	a_3	a_4	P
Men.- Pinto	20	18.5	0.05–**0.15**	0.01–**0.025**	**2**–7	–
Monti-Nuti	20	18.5	0.05–**0.15**	–	–	0.50–**0.90**

on the other hand, demonstrate the effectiveness of the algorithm at the stress-strain and the structural level, respectively, when the structure is subjected to a ground motion record.

5 Calibration of the model

The applicability of a material model depends largely on the values that the user/engineer will choose for the parameters of the model. In most cases in order to select appropriate values, calibration of the model and hence experimental results are required. Usually this sort of information is not available and therefore default values have to be used. When the law employed is sensitive to its parameters, lack of experimental results may narrow considerably its applicability. For both the Monti-Nuti and the Menegotto-Pinto models, suggested values can be obtained from various publications. A typical range for the model parameters are listed in Table 1. Bold letters denote the values that have been found appropriate for a wide range of applications by the authors.

All the parameters of Table1 have a clear physical meaning as described in the original publications. The curvature parameters R_0, a_1 and a_2 affect the shape of the hysteretic curve and hence the representation of the Bauschinger effect and the pinching of the hysteretic loops. Parameters a_3 and a_4 quantify isotropic hardening. Usually the contribution of isotropic hardening is significantly smaller than that of kinematic and hence the set of values adopted would not affect considerably the response. In Figure (8)

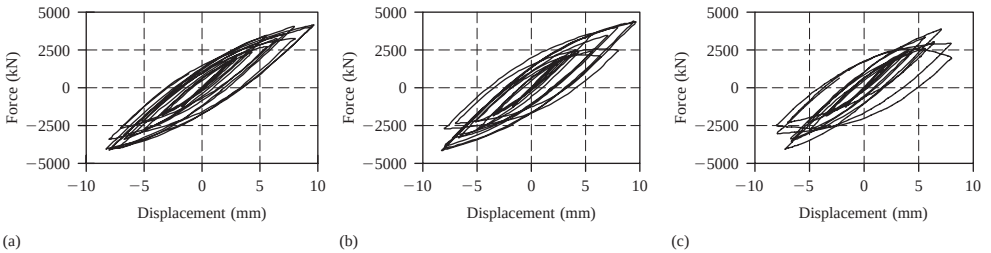

Figure 8 Effect of the weight parameter P on the performance of the Monti-Nuti model; (a) $P = 50\%$, (b) $P = 75\%$ and (c) $P = 90\%$.

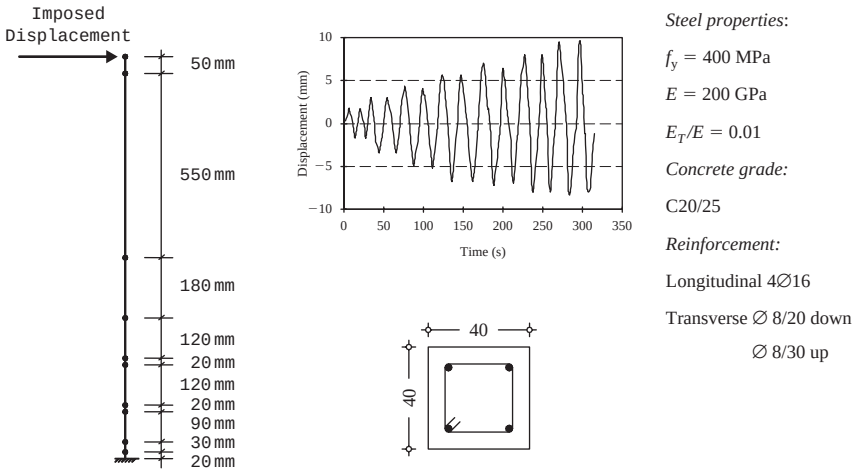

Figure 9 Geometry, FE model, loading scheme and properties of the column.

the parameter P is varied thus demonstrating the influence of isotropic over kinematic hardening. A simple calibration procedure for this parameter that consists of single cycle tests is suggested in the original paper of Monti and Nuti.

6 Numerical studies

6.1 *Column under Cyclic Loading Conditions*

The first case study consists of a cantilever column subjected to a displacement of constantly increasing amplitude on its top. The loading program for the specimen consisted of a displacement-controlled cyclic loading scheme, where two cycles of displacement are applied at each deformation level with 2 mm/step increments. The displacement of the tip of the column, the FE model and the properties of the column are shown in Figure 9.

The response obtained using three different reinforcing steel models is shown in Figure 10. The widely used bilinear model with kinematic hardening and the model

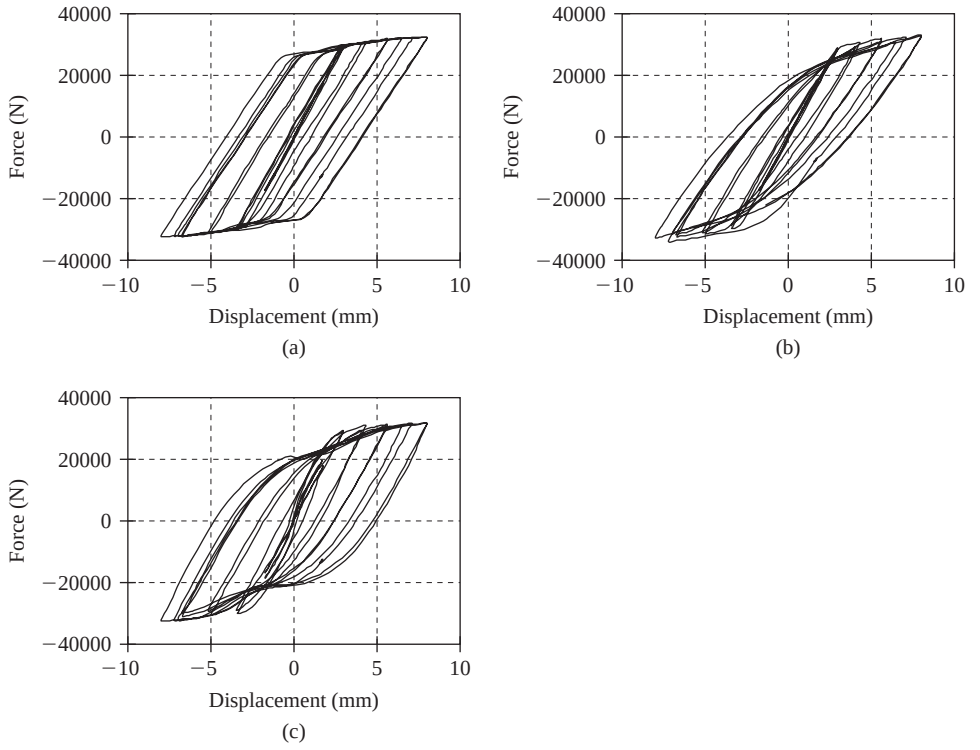

Figure 10 Response of a cantilever beam; (a) bilinear kinematic hardening (b) M–P and (c) M–N.

of Menegotto and Pinto do not show degradation in the capacity of the column as opposed to the Monti-Nuti model where the envelope of the hysteretic loops shows clearly the reduction in the capacity of the column. It is also observed that, dissipation of energy and pinching of the hysteretic loops is not fully captured by the first two models.

6.2 *Wall under Dynamic Loading Conditions*

The second case study is part of a series of shaking table tests carried out at the Centre for Earthquake Studies and Equipment at LNEC (Lisbon, Portugal). Details concerning the project and the actual test set up are reported by Pinho et al. (2000). Ductility class 'L' was adopted to determine section size and longitudinal reinforcement requirements. The wall element with thickness of 200 mm and its height and width are indicated in Figure 11. Both the longitudinal and shear reinforcement are also shown in Figure 11. A combination of two artificial (AR) and two natural records (NR) was applied to generate the input ground motion shown in Figure 12 (Pinho et al. (2000)). The resulting ground motion guarantees that the wall will be damaged progressively. The record was split into four stages, using scaled up and scaled down accelerograms in succession, without pause, mixing both natural and artificial records. The records, in

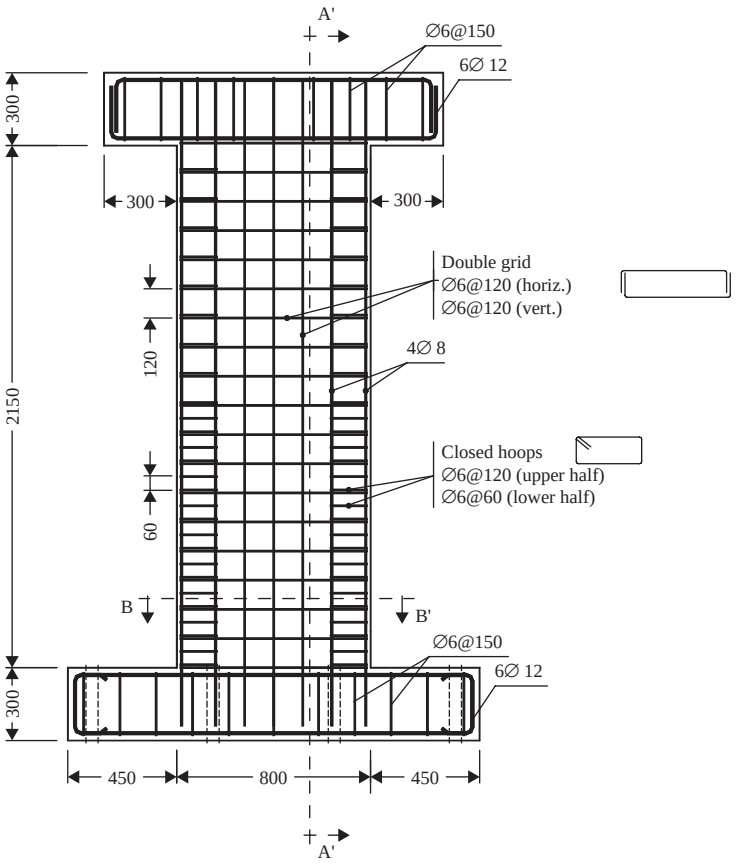

Figure 11 Dimensions and detailing of the test specimen.

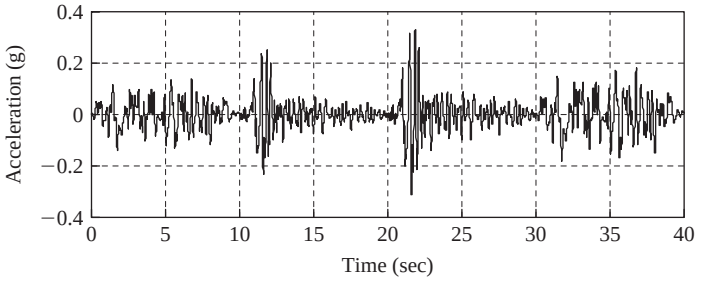

Figure 12 Acceleration ground motion record.

order applied, were AR(0.14), NR(0.25), NR(0.33) and AR(0.18). The second portion of the nomenclature indicates the peak ground acceleration of each record.

The transverse reinforcement used consists of Ø6/60 for the lower half and Ø6/120 for the upper half, while Ø8 bars were used for the longitudinal reinforcement. Therefore,

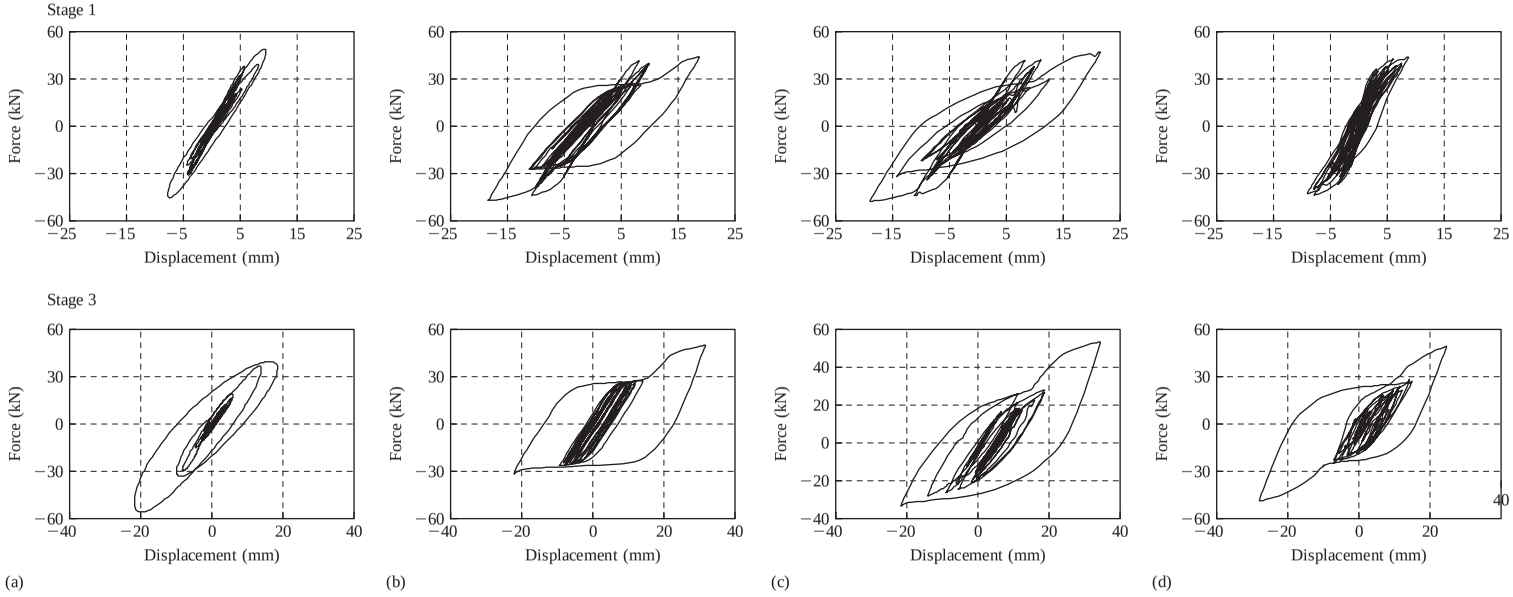

Figure 13 Wall under Dynamic Loading Conditions, first and third stage; (a) experimental, (b) bilinear kinematic hardening model, (c) M–P model and (d) M–N model.

the *L/D* ratios of the wall are 7.5 and 15, respectively. Thus, buckling of the longitudinal reinforcement is expected to take place and therefore considerable improvement of the results is expected when the Monti and Nuti rules are taken into consideration during analysis. The default model parameters are used (see Table 1), while the corrective algorithm was adopted with 2.5% filtering of ε_r.

The data acquired during the test had to be filtered so that high-frequency content, associated to parasitic vibrations in the table and electromagnetic interference, could be removed. The smooth shape of the experimental curve is therefore associated to the filtering of the records. For succinctness, stage one (time $= 0 \div 10$) and three (time $= 20 \div 30$) of the loading phase are presented in Fig. 13, see previous page.

Three models, the bilinear kinematic hardening, the Menegotto-Pinto and the Monti-Nuti were used for comparison. Clearly, the first fails to produce realistic hysteretic plots although the capacity and the displacements are in some cases sufficiently estimated. The Menegotto-Pinto model although it provides hysteretic curves closer to the experimental, still does not fully reproduce the experimental results. This can be attributed to some extent to the buckling of the longitudinal bars. Substantial improvement is achieved with the Monti-Nuti model. A better overall agreement is reached despite the lack of proper calibration of the model and to some particularities present during the test set up that the FE model adopted was not able to capture.

7 Concluding remarks

Buckling of the longitudinal reinforcement may affect considerably the response of RC members, especially when they are subjected to large displacements. This behaviour can be captured if the constitutive model of the reinforcement is enhanced with the experimental observations of Monti and Nuti (1992). Monti and Nuti introduced into the Menegotto-Pinto model a set of rules for buckling of the longitudinal reinforcement. Their model, although conceptually correct, features a not necessarily unconditioned accuracy when predicting stress-strain response under a generalized load history. An additional memory rule is presented in order to tackle this shortcoming. The rule proposed is based on a relatively simple concept, and thus can also be applied in models other than that of Monti and Nuti. In the case-studies examined, improved representation of the response was obtained, though the results could still be bettered if ad-hoc model calibrations would be carried out (the latter was however outside of the scope of this work).

References

Filippou, F.C., Popov, E.P. & Bertero, V.V. 1983. Effects of bond deterioration on hysteretic behaviour of reinforced concrete joint, *Report No. UCB/EERC-83/19, University of California*, Berkeley.

Mander, J.B., Priestley, M.J.N. & Park, R. 1984. Seismic design of bridge piers. *Res. Rep. 84–2, Dept. of Civ. Engrg., Univ. of Canterbury, Christchurch*, New Zealand.

Menegotto, M. & Pinto, P.E. 1973. Method of analysis for cyclically loaded RC plane frames including changes in geometry and nonelastic behaviour of elements under combined normal force and bending. *Proc. IABSE Symposium, Lisbon*, Portugal.

Monti, G. & Nutti, C. 1992. Nonlinear behaviour of Reinforcing Bars Including Buckling. *Journal of Structural Engineering* 118(12): 3268–3284.

Bae, S., Miesses, A.M. & Bayrak, O. 2005. Inelastic Buckling of Reinforcing Bars. *Journal of Structural Engineering* 131(2): 314–321.

Mau, E.T. & El-Mabsout, M. 1989. Inelastic buckling of reinforcing bars. *Journal of Engineering Mechanics* 115(1): 1–17.

Cosenza, E. & Prota, A. 2006. Experimental Behaviour and Numerical Modelling of Smooth Steel Bars under Compression. *Journal of Earthquake Engineering* 10(3): 313–329.

Gomes, A. & Appleton, J. 1997. Nonlinear cyclic stress-strain relationship of reinforcing bars including buckling. *Engineering Structures* 19(10): 822–826.

Dodd, L.L & Restrepo-Posada, J.I. 1995. Model for Predicting Cyclic Behaviour of Reinforcing Steel. *Journal of Structural Engineering* 121(3): 433–445.

Balan, T.A., Filippou, F.C. & Popov, E.P. 1998. Hysteretic model of ordinary and high-strength reinforcing steel. *Journal of Structural Engineering* 124(3): 288–297.

Attolico, A., Biondi, S., Nuti, C. & Petrangeli, M. 2000. Influence of Buckling of Longitudinal Rebars in Finite Element Modelling of Reinforced Concrete Structures Subjected to Cyclic loading: Two Case Studies, *Proc. of Workshop on "Seismic Protection of Existing and New Construction Buildings by means of Unconventional Systems, Prin 97*, Naples, 12–13 May.

Fragiadakis, M. 2001. Nonlinear Material Modelling of Reinforcement Steel Bars Under Transient Loading, *MSc Dissertation, Department of Civil Engineering, Imperial College London*, UK.

Pinho R., Elnashai, A.S. & Vaz, C.T. 2000. Experimental observations from shaking-table tests on selective techniques for repair and strengthening of RC walls, *Proc. Twelfth World Conference on Earthquake Engineering*, Auckland, New Zealand, Paper No. 2245.

Chapter 23

Analyzing steel moment-resisting connections using finite element modeling

Chris P. Pantelides & Lawrence D. Reaveley

University of Utah, Salt Lake City, USA

Scott M. Adan

Simpson Gumpertz & Heger Inc., San Francisco, USA

ABSTRACT: In seismic structural design and rehabilitation deviations from the common practice require testing. The AISC Seismic Provisions for Structural Steel Buildings (American Institute of Steel Construction 2005) recommend that usage and sizing of beam flange continuity plates across the column web shall be based on tests. The FEMA 350 Recommended Seismic Design Criteria (Federal Emergency Management Agency 2000) state that unless project-specific testing is performed to demonstrate that continuity plates are not required, moment-resisting connections should be provided with continuity plates when the thickness of the column flange is below a minimum value. Similarly, in order to qualify any new connection type for inclusion in the AISC Prequalified Connections for Special and Intermediate Steel Moment Frames for Seismic Applications (American Institute of Steel Construction 2006), testing has to be carried out to validate the design concept and to satisfy minimum performance criteria on strength and interstory drift angle capacity. In this paper, nonlinear finite element analyses are performed to establish a correlation between measured and computed responses of two steel connections: (1) the reduced beam section (RBS) moment connection without continuity plates, and (2) the bolted bracket (BB) moment connection. The connections were tested using cyclic quasi-static displacements applied at the beam tip. Comparisons of measured and computed responses showed good correlation. Further nonlinear finite element analyses resolved the issue of when continuity plates are necessary for RBS connections, and whether the bottom-only BB connection is an efficient retrofit scheme.

1 Introduction

In seismic structural design and rehabilitation deviations from the common practice require testing. For example, Post-Northridge studies have shown that when continuity plates of substantial thickness are used in reduced beam section (RBS) moment connections, inelastic strains across the weld of the connected beam flange are considerably higher opposite the column web than they are at the flange tips. The disproportionate strains can cause the weld stress at the center of the flange to exceed the tensile strength prematurely based on a uniform average stress distribution through the entire weld (American Institute of Steel Construction 2005).

When considering the elimination of continuity plates, AISC *Seismic Provisions for Structural Steel Buildings* (American Institute of Steel Construction 2005) recommends

that usage and sizing of continuity plates be based on tests. In addition, FEMA 350 *Recommended Seismic Design Criteria* (Federal Emergency Management Agency 2000) states that unless project-specific testing is performed to demonstrate that continuity plates are not required, RBS moment connections should be provided with continuity plates when the column flange thickness is below a minimum value. The required minimum thickness is based primarily on the beam flange width and thickness.

Similarly, in order to qualify any new connection type for inclusion in the AISC *Prequalified Connections for Special and Intermediate Steel Moment Frames for Seismic Application* (American Institute of Steel Construction 2006), testing is required to validate the design concept and to satisfy minimum performance criteria on strength and interstory drift angle capacity. Qualifying tests performed on the bolted bracket (BB) moment connection have demonstrated that a BB retrofit can restore capacity to a damaged pre-Northridge connection with high reliability and low installation cost (Kasai & Bleiman 1996).

In an effort to gain additional insight into the behavior of both RBS and BB connections, a study was performed using nonlinear finite element modeling. The study utilized a general-purpose finite element modeling program, ANSYS/Multiphysics (2005), to perform a series of nonlinear finite element analyses. The models were able to correlate both nonlinear behavior and lateral-torsional buckling as observed during testing of specimens in the laboratory.

2 RBS moment Connection

2.1 *Experimental investigation of RBS moment connections*

Four full-scale tests were performed at the University of Utah (Pantelides et al. 2004) using the RBS moment connection, following the protocols established for stepwise increasing cyclic tests published by the SAC Steel Project (Clark et al. 1997). The beam-column connections were tested using cyclic quasi-static displacements applied at the beam tip. All tests were performed with a beam size of W30 × 132. Two of the connections used W14 × 283 columns (SP1 and SP2) and the other two used W18 × 211 columns (SP3 and SP4). Details of the connections and the RBS section are shown in Fig. 1. The RBS cutouts reduced the beam flanges to 48 percent of the initial width. The beam web and flanges were connected to the column flange with qualified complete joint penetration groove welds. No continuity plates were installed. To simulate floor slab bracing, the top flanges of the beams were braced by two sets of bracing columns.

The failure modes were different between the specimens with the W14 × 283 and W18 × 211 columns. The failure sequence for specimens with the W18 × 211 columns was as follows: (1) localized buckling of the beam web at the column side of beam plastic hinge; (2) torsional buckling of the bottom beam flange in the RBS section coupled with twisting of the column flange; (3) kinking of the beam bottom flange in the RBS section; and (4) fracture of the beam bottom flange where previous kinking had occurred, during the next cycle of loading. The failure sequence for the W14 × 283 columns differed from that of the W18 × 211 columns in two respects: (1) column flange twisting was insignificant and (2) additional buckling of the beam top flange was observed near the end of the test. No evidence of weld failure was observed in any of the tests.

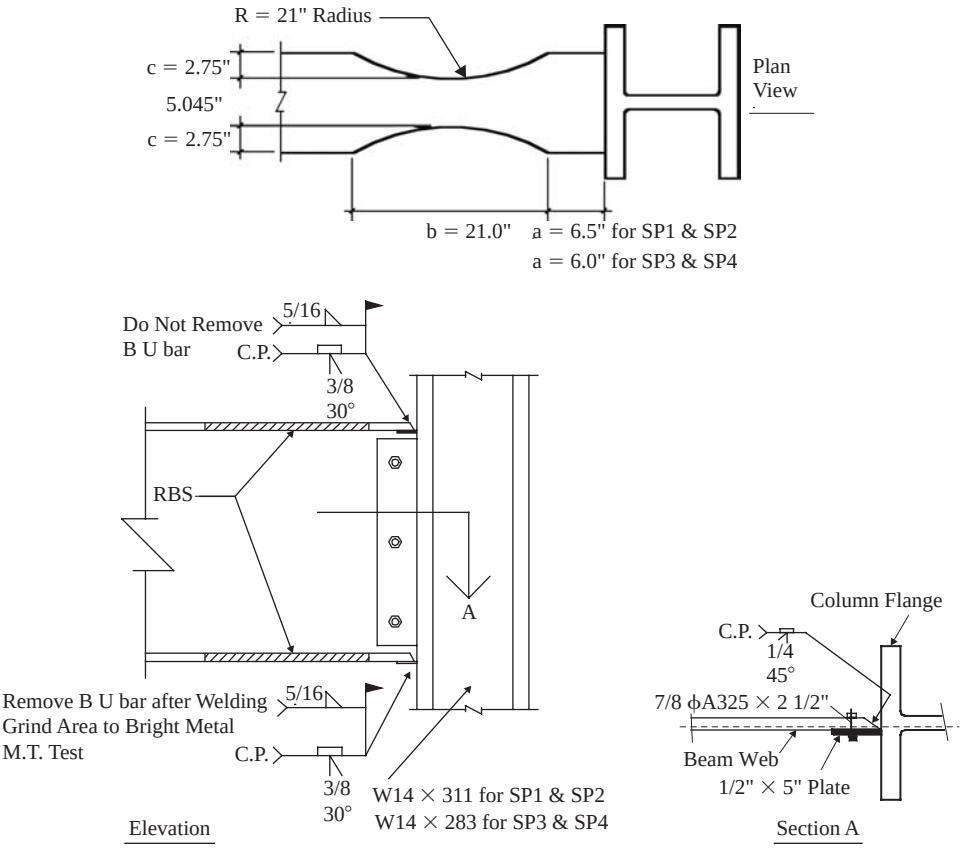

Figure 1 Details of connection and RBS section.

Figure 2 shows the observed localized beam web buckling and the beam bottom flange lateral movement that occurred at higher cycles of inelastic drift. The hysteresis curves of moment versus interstory drift in Fig. 3 show stable performance with no degradation in strength. All specimens reached a total interstory drift angle of 0.05 radians, which satisfies the AISC (American Institute of Steel Construction 2005) requirements for a special moment frame of a total interstory drift angle of 0.04 radians, without significant strength degradation. The pinched responses of specimens SP3 and SP4 indicate local instability at high levels of interstory drift; that was attributed to lateral-torsional buckling of the beam bottom flange coupled with local twisting of the connected column flange.

The column web thickness-to-depth ratio, t_{cw}/T_c influences the column flange rotation. The column web stiffness, when an idealization of the column cross section is made, as shown in Fig. 4, is proportional to the ratio, $(t_{cw})^3/T_c$. The greater the column web stiffness, the greater the torsional resistance provided to restrain column flange rotation, θ_c, and beam lateral-torsional buckling. In the case of the W14 × 283

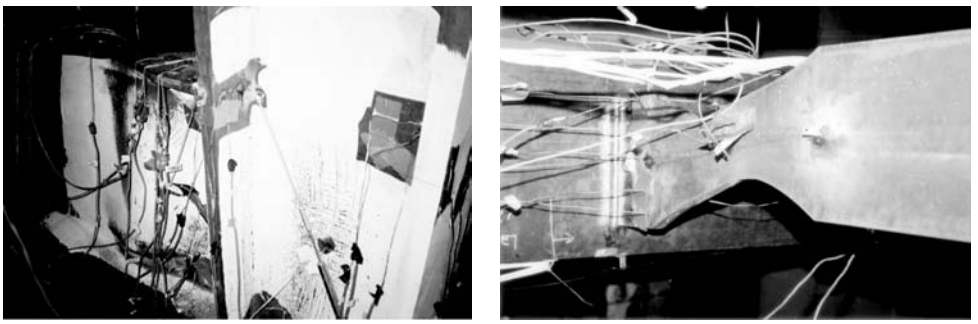

Figure 2 Beam web buckling and beam bottom flange lateral movement of RBS connection.

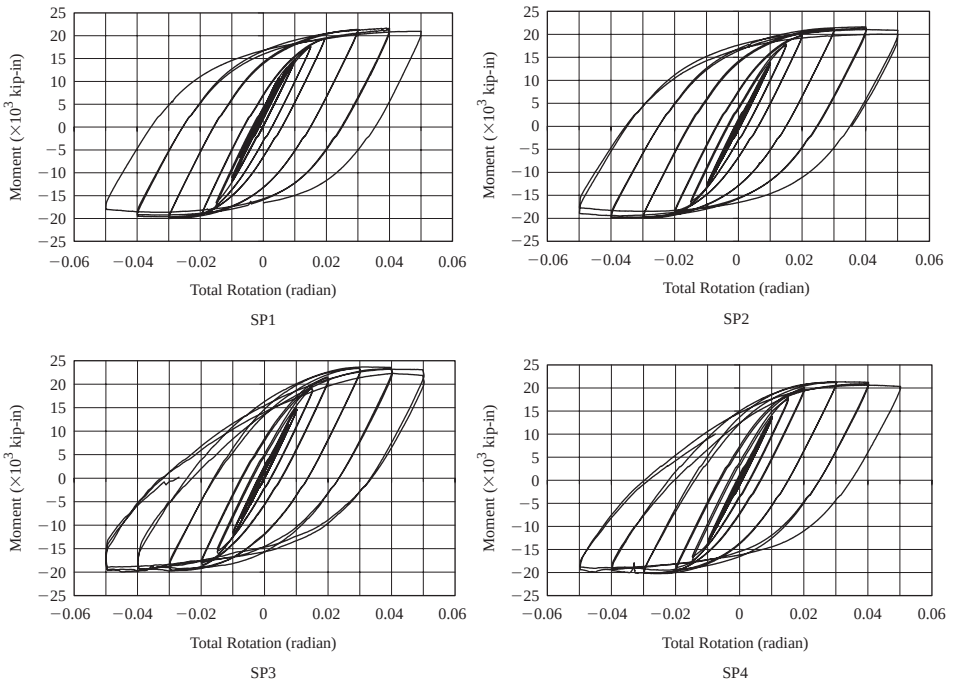

Figure 3 Column centerline moment versus total interstory drift angle for RBS connections.

column, the column web stiffness was equal to 0.191, and for the W18 × 211 column it was equal to 0.077, which is only 40 percent of the W14 × 283 column. The tests demonstrated that column web stiffness influences the requirement for the continuity plate. However, additional full-scale experiments would have been necessary to determine the critical column web stiffness beyond which continuity plates would not be required for satisfactory performance. Experimental evidence of the idealization of Fig. 4 is shown in Fig. 5 for specimens SP1/SP2 and SP3/SP4. Figure 5 shows the displacement measured at the tip of the column flange divided by half the column

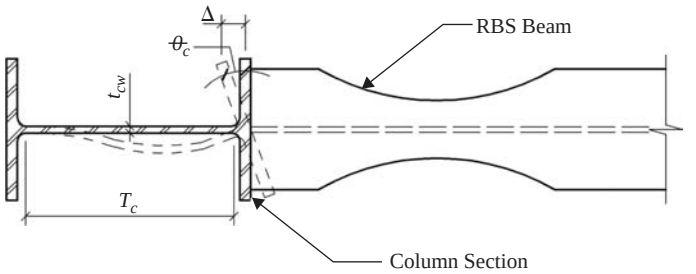

Figure 4 Idealization of RBS column web stiffness and flange rotation.

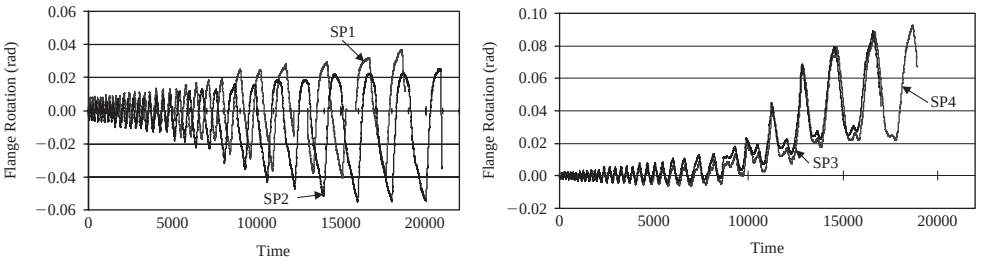

Figure 5 Measured RBS column flange rotation.

flange width in each case. It is clear that specimens SP1 and SP2 have a more stable and symmetric performance compared to specimens SP3 and SP4, which indicate that the column flange has rotated.

2.2 *Finite element investigation of RBS moment connections*

In lieu of performing additional full-scale experiments to determine the critical column web stiffness beyond which continuity plates are not required, finite element analyses were conducted. Finite element models of the connections were constructed from a quadrilateral mesh of four node nonlinear shell finite elements. The shell elements have plasticity, creep, stress stiffening, large deflection, and large strain capabilities (ANSYS 2005). The modeling considers beam web buckling which was shown to trigger lateral movement of the beam bottom flange (Fig. 2). Boundary conditions were applied to the finite element models to match that of the tested connections. The beam top flange was laterally restrained at two locations where lateral bracing was used. Vertical displacement was applied at the end of the beam to simulate the actuator attachment. The computer model was subjected to the same incremental loading history as the tested connections, although the number of cycles in each load step was limited to one. The computer analysis accounts for material nonlinearities through classical metal plasticity theory based on linear isotropic elasticity, the von Mises yield function and the associated flow rule. Geometric nonlinearities are accounted for through a small strain, large displacement formulation.

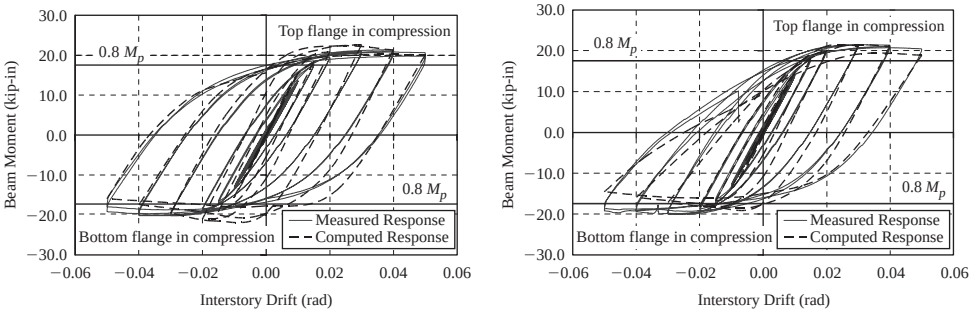

(a) W14 × 283 column and W30 × 132 beam

(b) W18 × 211 column and W30 × 132 beam

Figure 6 RBS connection measured and computed interstory drift response.

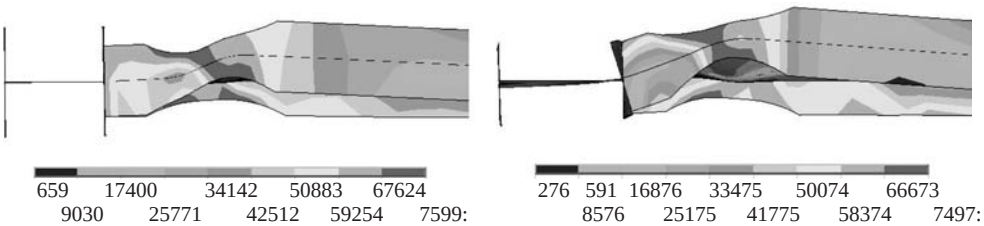

(a) W14 × 283 column and W30 × 132 beam

(b) W18 × 211 column and W30 × 132 beam

Figure 7 Computed RBS connection deformed von Mises stress contours at 0.05 radians of interstory drift (psi).

The finite element model was verified by comparing the measured cyclic responses of the tested specimens with the computed response. Figure 6 shows that the computed response correlated with the measured response envelope of the specimens. Figures 6(a) and 6(b) show comparisons of the beam moment versus interstory drift for the W14 × 283 and W18 × 211 column specimens, respectively. Figures 7(a) and 7(b) show the bottom view of the computed deformed shape with von Mises stress contours at 0.05 radians of interstory drift for the W14 × 283 and W18 × 211 column respectively. As is indicated in Fig. 2, the deformations shown in Fig. 7 are similar to those observed in the tested specimens. During higher cycles of inelastic drift, the beams experienced local buckling in the web and then lateral movement in the RBS bottom flange (Pantelides et al. 2004). As indicated in Fig. 7, the mode of the beam buckled shape is influenced by the restraining boundary condition of the column flange. In Fig. 7(a) this condition appears fully fixed, while in Fig. 7(b) the condition appears hinged. The von Mises contours shown in Fig. 7 indicate the highest regions of stress occur in the web and flanges of the RBS, which would be likely to facilitate fracture if a flaw or other irregularity were introduced. The tested specimens ultimately fractured in these same high stress regions.

By reanalyzing the computer models with continuity plates, the study determined that continuity plates did not improve connection performance for the W14 × 283 column. Therefore, column sections lighter than a W14 × 283 were investigated

to determine which sections would require continuity plates when paired with a W30 × 132 beam. The same modeling technique determined continuity plates improved the connection performance for the W18 × 211 column. Therefore, column sections larger than a W18 × 211 were investigated to determine which sections would not need continuity plates when paired with a W30 × 132 beam. Overall, the study determined that continuity plates improved performance in connections with inadequate column web stiffness.

All seismically compact W14 and W18 column sections were subsequently studied parametrically; Fig. 8 illustrates the relationship developed between column web stiffness and seismic demand for W14 and W18 column sections. An equation for determining the need for continuity plates was formulated by applying a regression analysis to the column data and solving for the web thickness, t_{cw} (Adan 2006). Continuity plates are required in W14 columns if the web thickness is less than the value given by:

$$t_{cw} < \left\{ \frac{0.0026(F_{yf} t_f b_f)^{1.69}}{F_{yc}} \right\}^{\frac{1}{3}} \tag{1}$$

where, t_{cw} is the minimum column web thickness when no continuity plates are provided (in.), t_f is the beam flange thickness (in.), b_f is the beam flange width (in.), and F_{yf}/F_{yc} are the minimum specified yield stress of the beam flange/column web (ksi). The study concluded that Eq. (1) safely limits local web yielding and column flange twist even at higher levels of inelastic drift. A similar equation was developed for W18 column sections.

3 Bolted bracket moment connection

3.1 *Experimental investigation of BB moment connections*

An experimental program was undertaken at Wyle Laboratories to investigate the performance of the bolted bracket connection using high strength steel castings in lieu of fabricated steel plates. The brackets were cast in a variety of sizes and configurations to suit a number of potential connection applications. The bracket sizes were proportioned to develop the full moment capacity of the connected beam and were configured to be either welded or bolted to the beam flange. The testing was performed to qualify both configurations of bracket for use insteel moment frames. The bolted configurations were primarily intended for the retrofit of connections damaged in the 1994 Northridge California earthquake. The welded configurations were intended for new construction. Fig. 9 shows the welded bracket configuration used in specimen HH-8 of the experimental program. The N2.1 bracket was fillet welded to the beam flange and bolted to the column flange with four high strength bolts. The bracket proportions were as follows: $a = 18.0$ in., $a' = 4$ in., $b = 8.75$ in., $b' = 2.5$ in., $c = 9.5$ in., $c' = 3.0$ in., $r = 16.0$ in., $t_v = 2.5$ in., $t_h = 1.0$ in., $t_s = 2.0$ in., $s_e = 2.25$ in., $s = 3.5$ in., and $g_c = 6.5$ in.

The connection was comprised of a W14 × 233 column, a W30 × 108 beam, and a pair of N2.1 brackets. The connection was tested using cyclic quasi-static displacements applied at the beam tip as shown in Fig. 10. The columns were

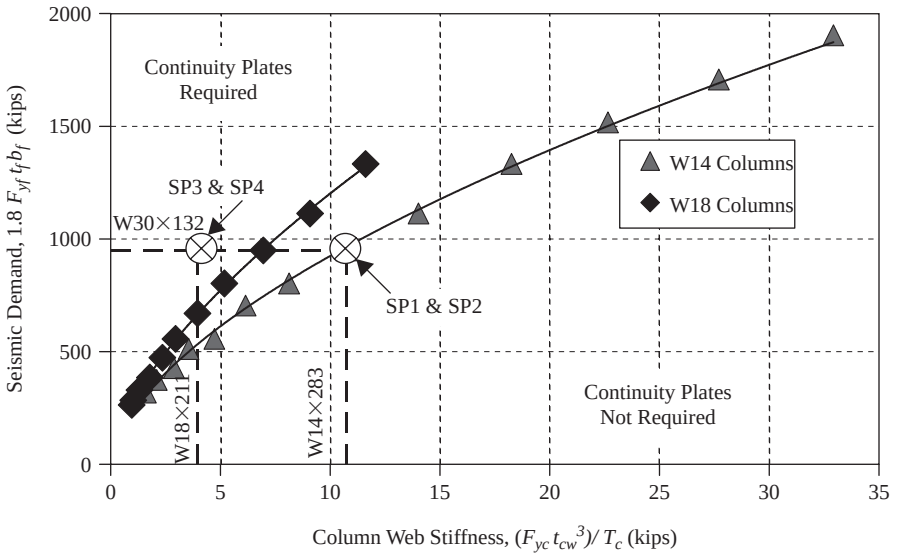

Figure 8 Column web stiffness and seismic demand of RBS connections.

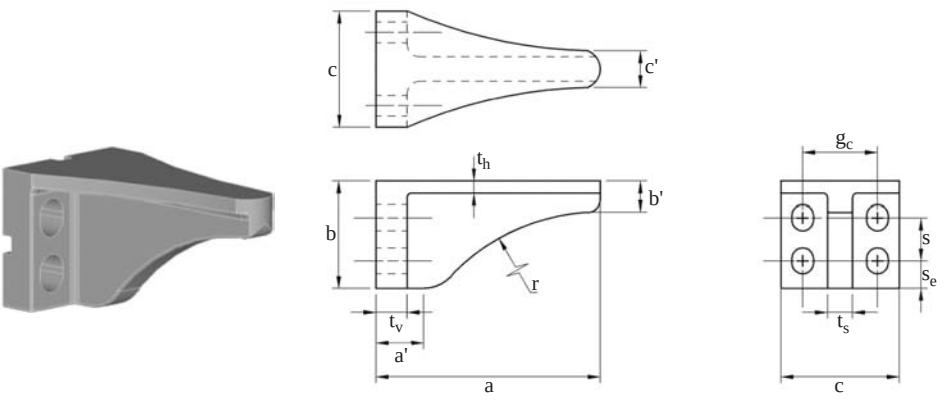

Figure 9 Bolted bracket N2.1 configuration.

held in place with pivots, top and bottom; the pivots were positioned 7.0 ft. above and below the beam centerline. The beams were loaded with a hydraulic actuator 15.0 ft. from the column centerline. To provide lateral stability, bracing was provided at each column pivot and at each beam 3 ft. from the actuator. A total of seven connections were tested (Adan & Gibb 2006). Fillet welding of the bracket to the beam was performed in strict conformance with weld procedure specifications required in the Structural Welding Code (American Welding Society 2006). To attach the bracket to the beam, the beam and brackets are clamped together, preheated, and fillet-welded under controlled conditions.

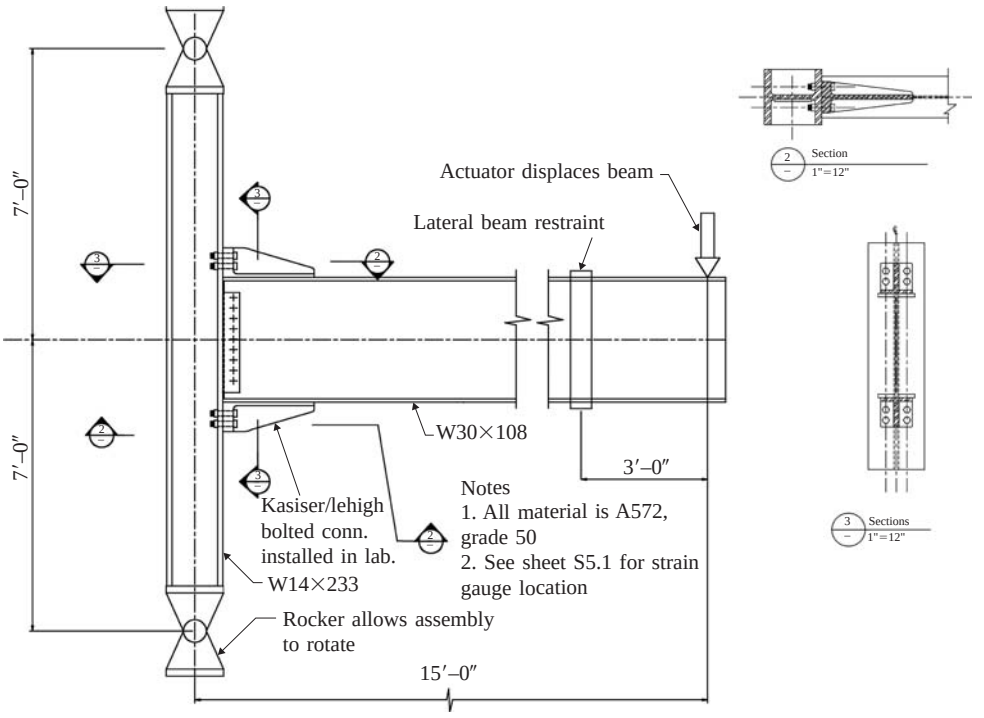

Figure 10 Test subassemblage elevation for BB connection specimen HH-8.

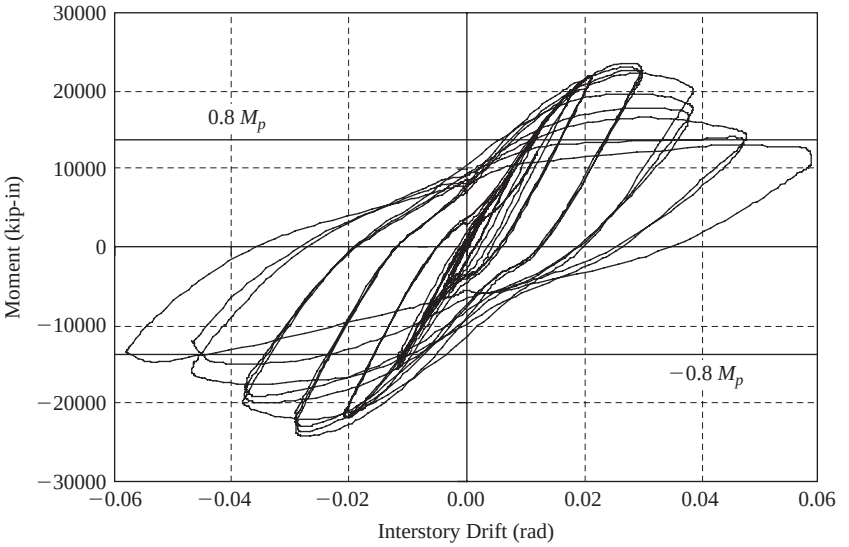

Figure 11 Beam moment vs. interstory drift for BB specimen HH-8.

(a) (b)

Figure 12 BB specimen HH-8: (a) local flange and web buckling; (b) beam plastic hinge formation at end of the bracket.

Each beam and bracket assembly was then erected and connected to the column shear tab. The connection to the shear tab was made with high strength bolts. The bracket-to-column holes were over-sized to provide adequate tolerance for the bracket installation. The bolts were tightened using the AISC calibrated torque wrench procedure (American Institute of Steel Construction 2005). The test specimens were subjected to the cyclic loading sequence specified by ATC (Applied Technology Council 1992). Figure 11 shows a plot of the beam moment versus interstory drift, computed with respect to the centerline of the column, for specimen HH-8. At approximately 0.025 radians of interstory drift, localized buckling of the beam flange and web was observed as a plastic hinge formed near the end of the bracket. As shown in Fig. 12(a), the hinge was approximately 18 in. from the face of the column. At 0.055 radians of interstory drift, extreme localized buckling of the beam flange and web was observed in the plastic hinge. As shown in Fig. 12(b), plastic hinge formation was the controlling failure mode of the connection. As with specimen HH-8, all the tested specimens were able to exceed the AISC moment connection prequalification requirements (American Institute of Steel Construction 2005). The study concluded that when adequately proportioned, the bolted bracket can satisfy prescribed requirements for use in special moment frame (SMF) and intermediate moment frame (IMF) systems.

3.2 *Finite element investigation of BB moment connections*

The testing described in Section 3.1 and elsewhere (Adan & Gibb 2006) for bolted bracket connections was intended to investigate whether the connection would satisfy the AISC prequalification requirements (American Institute of Steel Construction 2005). The question arises as to the suitability of the connection for seismic rehabilitation; in this case, it is desirable to retrofit an existing pre-Northridge beam-to-column connection with a bottom-only bracket. In lieu of performing more experiments to determine the suitability of a bottom-only bracket retrofit, finite element analyses were conducted. As a first step, finite element analysis of the bolted bracket specimen HH-8 described in Section 3.1 was conducted using the ANSYS Multi-Physics

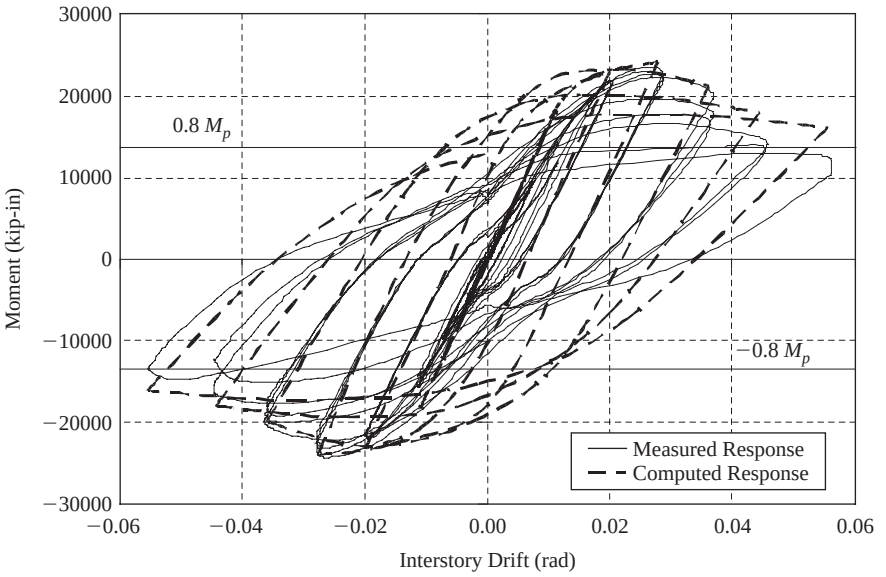

Figure 13 Measured and computed response for BB specimen HH-8.

platform (2005). For simplicity, bracket-to-column connections were modeled as rigid (no bolting). Other applied boundary conditions matched those applied to the tested specimen HH-8. An idealized multi-linear stress-strain relationship with strain hardening was utilized for all the materials in the model including the bracket. The model for specimen HH-8 was subjected to the same incremental loading history as that of the tested specimen, although the number of cycles in each load step was limited to one. When compared with a single monotonic load, the incremental loading history has a significant impact on behavior and performance. The finite element model was verified by comparing the computed response with that of the measured response. Figure 13 indicates that the computed response correlates reasonably well with that of the tested specimen. There are some noticeable discrepancies in the unloading and reloading regions, particularly at higher inelastic deformation levels. The apparent softening of the measured response can be attributed to the controlled actuator motion in the unloading and reloading phases of the test.

The computed von Mises stress contours shown in Fig. 14, indicate the highest regions of stress occur in the web and flanges of the beam. The finite element modeling indicates initial yielding at 0.02 radians of interstory drift, which was similar to that of the tested specimen. In Fig. 14, the computed response indicates beam local flange and web buckling at 0.04 radians of interstory drift. Fig. 14(a) shows the response for downward loading and Fig. 14(b) shows the response for upward loading. The issue of whether the bottom-only bracket connection configuration is an effective retrofit scheme was further investigated using finite element analyses. The computed deformed shape for the upward response of the bottom-only connection at 0.04 radians of interstory drift is shown in Fig. 15; yielding and plastic hinge formation remain within the

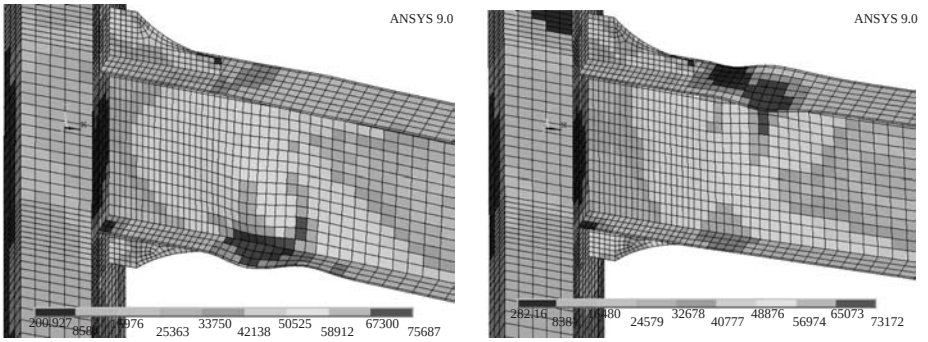

(a) (b)

Figure 14 Computed response showing local flange and web buckling with von Mises stress contours (psi) at 0.04 radians of interstory drift: (a) downward loading, (b) upward loading.

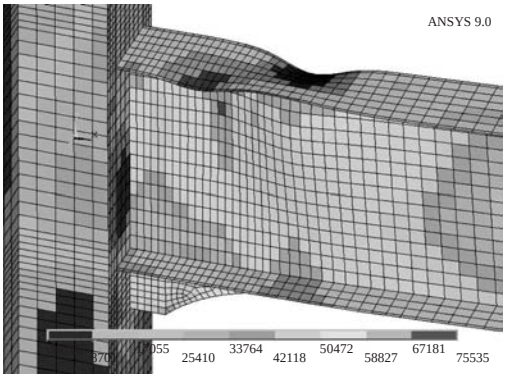

Figure 15 Retrofit bottom-only bracket upward response showing local flange and web buckling with von Mises stress contours (psi) at 0.04 radians of interstory drift.

beam and away from the column interface. Figure 16 shows the computed response for the bottom-only bracket configuration. The computed response predicts that the revised configuration would exceed the AISC prequalified connection requirements (American Institute of Steel Construction 2005). However, in full-scale experimental testing where the bottom flange was modified with a bracket, and the top flange pre-Northridge weld was not modified, the connection performed poorly (American Institute of Steel Construction 1999). The pre-Northridge test specimens developed early fractures in the top flange weld. Unfortunately, the finite element models do not address the issue of fracture propagation. The models can only address the potential for cracking through the development of stress and strain states that would facilitate fracture if a flaw or other irregularity were introduced. Considering the possibility of such flaws to exist, the computed stresses in the top flange indicate that the weld

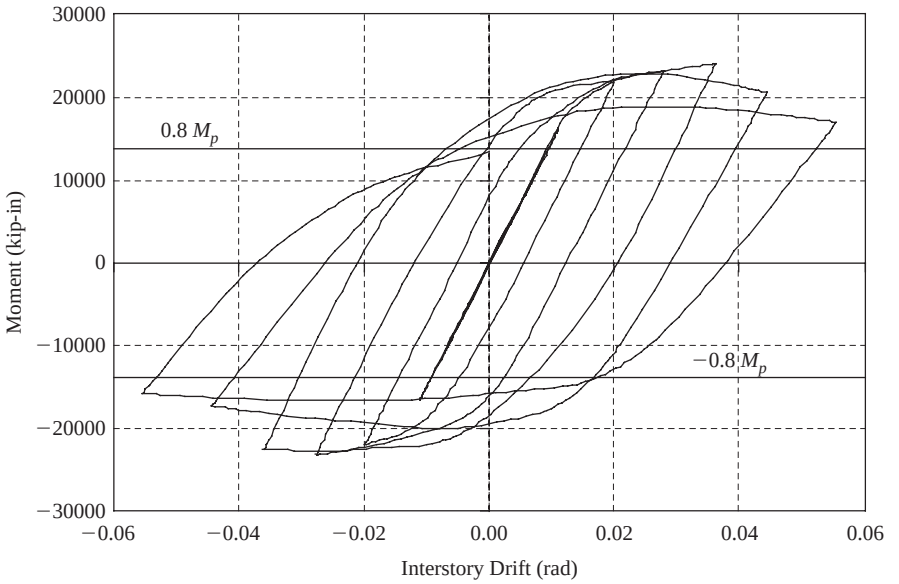

Figure 16 Computed response for retrofit bottom-only bracket.

could be susceptible to premature fracture. Hence, the bottom-only bracket configuration was deemed an ineffective retrofit alternative when combined with a top flange pre-Northridge weld.

4 Conclusions

A limited number of experiments have shown that for reduced beam section moment connections with strong panel zones and columns with sufficiently thick flanges, connections without continuity plates behave as well as those with continuity plates. Finite element analyses verified the experimental results and established a design equation for determining the need for continuity plates by applying a regression analysis and solving for the minimum column web thickness. Another experimental study concluded that when adequately proportioned, the bolted bracket moment connection can satisfy prescribed requirements for use in special moment frame and intermediate moment frame systems. This was verified using finite element analyses. The question arises as to the suitability of the bolted bracket connection for seismic rehabilitation; in this case, it is desirable to retrofit an existing pre-Northridge beam-to-column connection with a bottom-only bracket. In lieu of performing more experiments to determine the suitability of a bottom-only bracket retrofit, finite element analyses were conducted. The predicted von Mises stresses in the top flange of the connection indicated that the weld could be susceptible to premature fracture. Therefore, the bottom-only bracket configuration was deemed an ineffective retrofit alternative when combined with a top flange pre-Northridge weld.

References

American Institute of Steel Construction. 2005. *Seismic Provisions for Structural Steel Buildings*. Chicago, Illinois.

Federal Emergency Management Agency. 2000. *Recommended Seismic Design Criteria For New Steel Moment-Frame Buildings, FEMA 350*. Washington, D.C.

American Institute of Steel Construction. 2006. *Prequalified Connections for Special and Intermediate Steel Moment Frames for Seismic Applications*. Chicago, Illinois.

Kasai, K. & Bleiman, D. 1996. Bolted brackets for repair of damaged steel moment frame Connections. *7th US-Japan Workshop on the Improvement of Structural Design and Construction Practices: Lessons Learned from Northridge and Kobe*, Kobe, Japan.

ANSYS. 2005. *User Manual Version 9.0*. ANSYS, Inc., Canonsburg, Pennsylvania.

Pantelides, C.P., Okahashi, Y. & Reaveley, L.D. 2004. Experimental investigation of reduced beam section moment connections without continuity plates. *Earthquake Spectra*. 20(4):1185–1209.

Clark, P., Frank, K., Krawinkler, H. & Shaw, R. 1997. *Protocol for fabrication, inspection, testing and documentation of beam-column connection tests and other experimental specimens*. Report No. SAC/BD-97/02, Sacramento, California.

Adan, S.M. 2006. *Reduced beam section moment connections without continuity plates*. Ph.D. Dissertation, University of Utah, Salt Lake City, Utah.

Adan, S.M. & Gibb, W. 2006. *Cyclic behavior of the Kaiser bolted bracket steel moment-resisting connection*. Technical Report, KPFF Consulting Engineers, Seattle, Washington.

American Welding Society. 2006. *Structural Welding Code Steel, ANSI/AWS D1.1:12006*. Miami, Florida.

American Institute of Steel Construction. 2005. *Specification for Structural Steel Buildings*. Chicago, Illinois.

Applied Technology Council. 1992. *Guidelines for the Cyclic Seismic Testing of Components of Steel Structures*. Publication No. 24, Redwood City, California.

American Institute of Steel Construction. 1999. *Steel Design Guide Series 12 – Modification of existing welded steel moment frame connections for seismic resistance*, Chicago, Illinois.

Chapter 24

Earthquake damage scenario software for urban areas

Atilla Ansal, Aslı Kurtuluş & Gökçe Tönük

Bogaziçi University, Istanbul, Turkey

ABSTRACT: A software package is developed to perform earthquake scenarios for estimating structural damage and human casualties. The first stage involves generation of microzonation maps for separately calculated regional seismic hazard. The seismic hazard can be probabilistic or deterministic where PGA and spectral accelerations or acceleration time histories are specified respectively for each cell on the engineering bedrock outcrop. In the second stage, representative soil profiles are defined for each cell and 1D site response analyses are conducted to calculate average PGAs and elastic acceleration response spectra on the ground surface. An envelope NEHRP spectrum is calculated for each cell based on site specific average acceleration spectrum to estimate short ($T = 0.2$ s) and long ($T = 1$ s) period spectral accelerations. In the third stage, vulnerability of the building stock is estimated with respect to number of buildings in each cell. A case study for Zeytinburnu, a district in Istanbul, Turkey is conducted to demonstrate the applicability of the software package.

1 Introduction

Estimation of losses in urban areas from future earthquakes is essential for disaster preparedness and decision making at the local, regional and national levels of government. The process of loss estimation due to earthquakes involves different analyses, such as seismic hazard assessment, estimation of earthquake characteristics on the ground surface, vulnerability and fragility analyses of structures and human casualties. Various numerical and empirical methods have been developed over the past years to perform each of these analyses; yet, few attempts have been made to combine the whole process into a single computer code.

The European project SERGISAI developed a software tool where seismic risk assessments at regional, sub regional and local scales are implemented using a combination of Geographical Information Systems (GIS) and Artificial Intelligence (AI) techniques (Zonno et al., 2003). At the local scale of the application, a simplified 3D geotechnical model of the study area is generated in the GIS environment and used together with regional probabilistic or deterministic seismic hazard information to perform 1D site response analyses with Shake91 (Idriss & Sun, 1992). The horizontal peak acceleration obtained at ground level is combined with the vulnerability index map of the study area through available acceleration-vulnerability-damage empirical relationships, to obtain damage scenarios in terms of economical losses.

National Laboratory for Civil Engineering in Portugal (LNEC) developed a procedure (LNECLoss) where human and economic losses due to a deterministic scenario earthquake are computed through a series of software modules (Sousa et al., 2004). Local site effects are taken into account using soil amplification factors evaluated for specific soil profiles estimated for the region. The so-called 'capacity-spectrum method' ATC-40 (1996) and Hazus (1999) is used as reference for evaluating structural damage.

NORSAR (Norway) and the University of Alicante (Spain) have developed a Matlab based tool named SELENA (Seismic Loss Estimation using a Logic Tree Approach) (Molina-Palacios & Lindholm, 2006). SELENA, uses probabilistic or deterministic seismic hazard information and estimates the ground motion at a specific site using 1997 NEHRP provisions. The software computes building damages based on capacity-spectrum method of Hazus (1999).

The software package KoeriLoss2 described in this work provides an alternative loss estimation tool, where local site effects are taken into account by performing 1D site-specific ground response analyses, Shake91 (Idriss & Sun, 1992) and capacity-spectrum methodology developed based on Hazus (1999) is used to perform damage estimations.

2 Methodology for developing earthquake damage scenarios

The methodology developed is composed of two main stages: The first stage involves generation of microzonation maps with respect to earthquake ground shaking parameters for the selected regional earthquake hazard scenario. In the second stage, the vulnerability of the building stock is estimated based on the calculated earthquake ground shaking parameters and the expected casualties are estimated based on the calculated building damage.

The regional earthquake hazard scenario can be probabilistic or deterministic. The variation of earthquake ground shaking parameters (peak ground accelerations, PGA and spectral accelerations, SA at $T = 0.2$ s and 1 s at the engineering bedrock outcrop) are determined independently within the investigated area for a specified level of exceedance probability or based on deterministic simulations.

The study area is divided into cells by a grid system. Site characterization is performed based on available borings and other relevant information by defining one representative soil profile for each cell with shear wave velocities extending down to the engineering bedrock ($Vs \geq 750$ m/s). Earthquake characteristics on the ground surface are calculated using one-dimensional site response analyses, Shake91 (Idriss & Sun, 1992) for each representative soil profile. Hazard compatible acceleration time histories (in terms of expected fault type, fault distance, and earthquake magnitude) are selected from appropriate real earthquake acceleration records or by simulation of spectra compatible synthetic acceleration time histories (Papageorgiou et al., 2000; Deodatis, 1996). In case of using real acceleration time histories PGA scaling is adopted (Durukal et al., 2006, Ansal et al., 2006a) and site response analyses are performed at least for three selected acceleration time histories.

Variations of PGA and acceleration response spectra at the ground surface are determined. The average acceleration response spectrum for each cell is calculated in order to determine the spectral accelerations for the short period (Ss) corresponding to 0.2 s

and for the long period (S1) corresponding to 1 s. An optimization algorithm is utilised to determine the NEHRP (BSSC, 2001) envelope spectrum that mathematically fits best to the calculated average acceleration response spectra (Ansal et al., 2005, 2006b). The two independent variables in the optimization algorithm are (Ss) and (S1). The NEHRP design spectrum is preferred because of its flexibility in defining short period spectral accelerations and for vulnerability assessment of the building stock (Erdik & Fahjan, 2005). The short and long period spectral accelerations estimated based on these NEHRP envelopes are used to generate microzonation maps for the investigated area.

In the second stage, building stock inventory determined with respect to B_{ijk} matrix and site specific spectral accelerations (short and long period) are used to assess the vulnerability of each building. The "i" in the B_{ijk} matrix shows the construction type as: (1) Reinforced concrete frame building, (2) Masonry building, (3) Reinforced concrete shear wall building, (4) Precast building. The number of stories ("j" dimension of the matrix) is defined as: (1) Low rise (1–4 stories, including basement), (2) Mid rise (5–8 stories, including basement), (3) High-rise (more than 8 stories, including basement). The construction date ("k" dimension of the matrix) is defined as: (1) Construction year: Pre-1979 (included) and (2) Construction year: Post-1980 (included). Capacity and vulnerability curves in terms of spectral accelerations are used to estimate the building response due to the earthquake ground shaking. A displacement-based approach is adopted to evaluate the building damage level. Damage levels are defined with respect to five levels (none, slight, moderate, extensive damage and collapsed). Human casualties are estimated based on the damage level, building type and estimated occupancy (Erdik et al., 2002).

3 Earthquake damage scenario software

The methodology described above is automated into a Visual Basic application where loss estimation for an urban area is computed and displayed in maps. The application utilises Excel and Fortran codes for calculations and uses GIS based software – MapInfo to map the estimated ground shaking and the damage distribution for the investigated area. The flow chart composed of several steps involved in the software procedure (KoeriLoss2) is schematically illustrated in Figure 1. Explanation for each step is given in the following paragraphs.

3.1 *Site response analyses*

Given the seismic hazard on the engineering bedrock outcrop (in terms of PGA and a suite of hazard compatible acceleration time histories) and local soil conditions (in terms of shear wave velocity profile down to engineering bedrock, soil stratification, groundwater level and dynamic soil properties), acceleration time histories and elastic acceleration response spectra are calculated on the ground surface for each cell using Shake91 (a Fortran program for equivalent linear one dimensional site response analysis).

3.2 *Optimization for the best fit NEHRP envelope*

Using the elastic acceleration response spectra calculated as output of site response analyses for each cell, the module calculates the average acceleration response spectrum

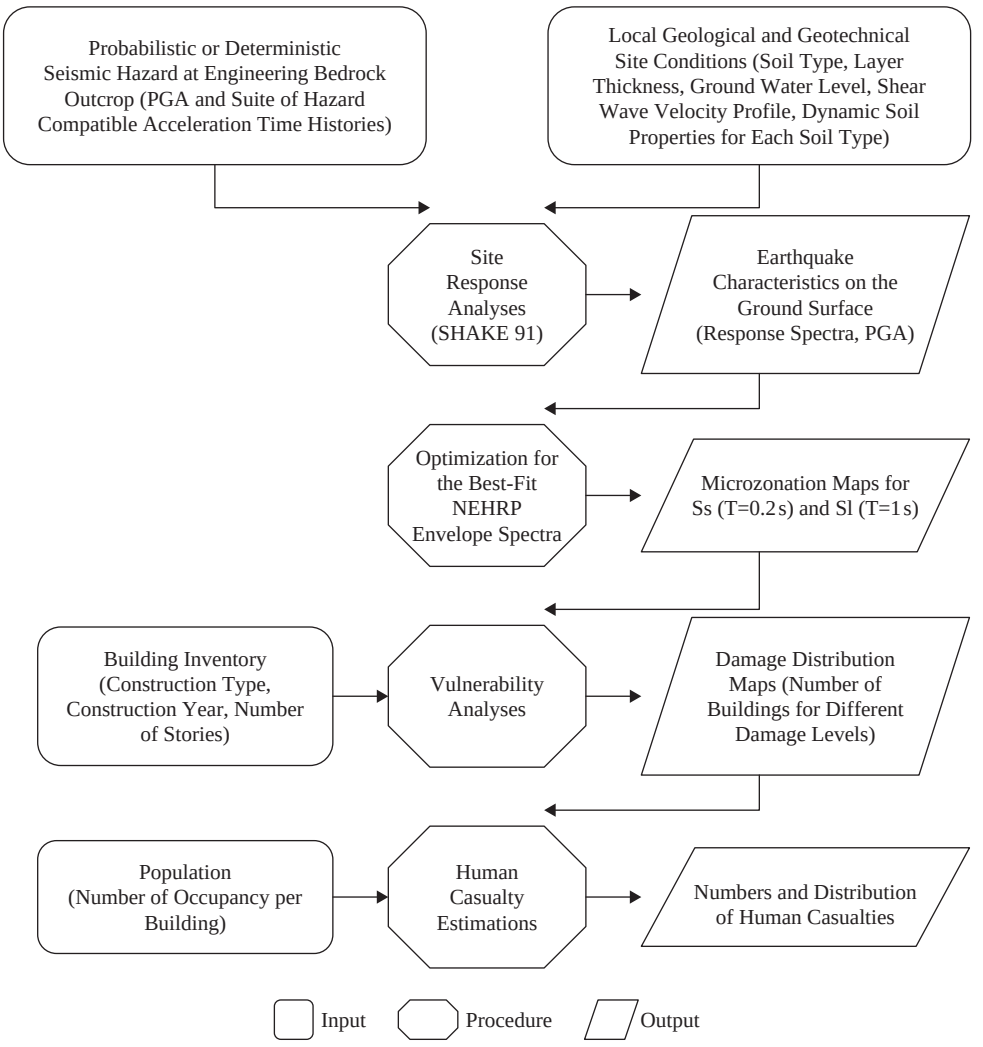

Figure 1 Schematic illustration of KoeriLoss2 software procedures for loss estimation in urban areas.

(average of all spectra calculated by site response analysis with different input motions for each cell) and finds the best fit NEHRP envelope spectra for each cell. At the end of this step, microzonation maps in terms of short period (Ss) and long period (Sl) spectral accelerations can be generated using MapInfo (a GIS based program for mapping and geographic analysis).

3.3 *Vulnerability analyses*

Using the ground shaking parameters (in terms of spectral accelerations Ss and Sl obtained from best-fit NEHRP envelopes) and building inventory in the investigated

area (in terms of building type, number of stories and construction year), the vulnerability of all buildings in each cell is computed based on the fragility curves with respect to building damage levels. At the end of this step, maps showing the distribution of damage for all building types are generated using MapInfo.

3.4 *Casualty estimations*

Given the building type and estimated occupancy, expected human casualties are calculated for each building.

The information that should be provided by the user for operation of the software involves the following data files:

1. Text files for input motions (acceleration time histories) including header lines describing the necessary format information to read acceleration values in the file.
2. A text file that includes PGA values at engineering bedrock outcrop determined from seismic hazard analyses.
3. An excel spreadsheet that requires user to enter information about geotechnical site conditions at each cell in the grid system. The information that should be provided by the user includes soil type, soil layer thickness, ground water level and shear wave velocity profile down to the engineering bedrock ($V_s \geq 750$ m/s) for each cell.
4. A text file that includes dynamic soil properties (shear modulus reduction and material damping ratio curves) for each soil type.
5. An excel spreadsheet that requires user to enter information about building inventory in terms of B_{ijk} building matrix. Number of human occupancy (population) per building type should also be included in this spreadsheet.

The software operates as a single executable file within Excel using Visual Basic (VBA) environment. Given the data files described above, the software procedure calculates the loss estimations for building stock and human casualties and utilizes MapInfo to display the results in maps. Microzonation maps with respect to ground shaking parameters, damage distribution maps for all building types and maps for distribution of human casualty are produced as outputs of the software package.

4 Zeytinburnu case study in Istanbul, Turkey

The demonstration of the methodology was performed for the Zeytinburnu Municipality in Istanbul, Turkey as a part of a European Project – LessLoss (Spence et al., 2005, 2006a, 2006b). Zeytinburnu is one of the older towns established outside the walls of the historic city centre. The area is approximately 14 km^2 and is relatively densely populated (approximately 200,000) with mostly low to middle income residential buildings and some small industrial buildings. Most of the buildings in the area are expected to be lacking the sufficient earthquake resistance and therefore, in the case of a near field strong earthquake, most likely it will be one of the areas with high degree of damage. The base geological units in the Marmara region are Palaeozoic aged formations. These formations are mostly composed of sandstone, siltstone and claystone. The detailed geology of the Zeytinburnu region was determined based on the local geological and geotechnical site investigations and available soil borings conducted in the

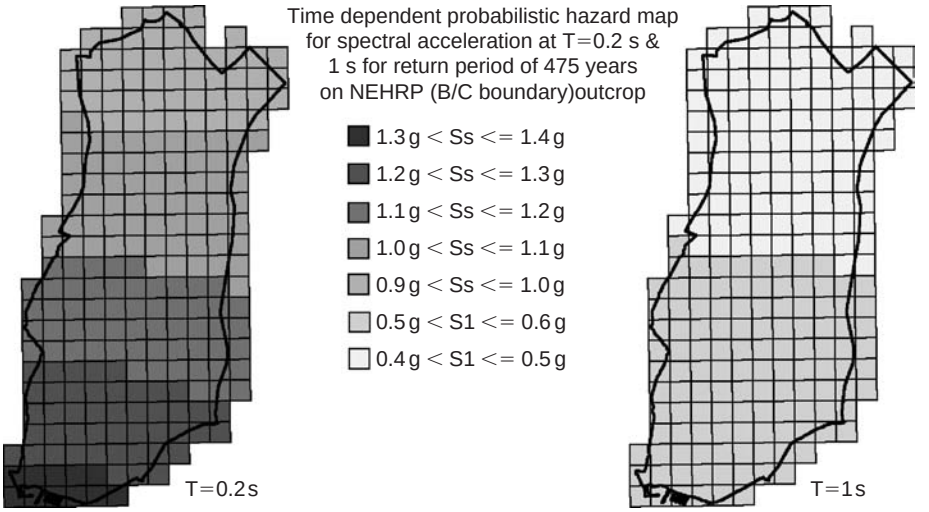

Figure 2 Variation of spectral accelerations at T = 0.2 s and 1 s obtained from probabilistic earthquake hazard assessment for NEHRP B/C boundary.

Table 1 Hazard compatible acceleration time histories selected for site response analyses in Zeytinburnu.

Earthquake	*Station*	*Magnitude*	*Component*	*PGA (g)*
Duzce 11/12/99	Lamont Station 1062	7.1	1062EW	0.26
Kocaeli 08/17/99	Gebze	7.4	GBZ000	0.24
Duzce 11/12/99	Lamont Station 375	7.1	375EW	0.51

region by different agencies. The findings indicate that Neocene aged young sediments are surfacing in the area. The thickness of these (Gürpınar and Bakırköy) formations that can be considered as soil layers over the engineering bedrock are between 40–60 m in the north and increase in the south-southwest direction, reaching the thickness of 200 m along the coastline (Ozaydin et al., 2004).

4.1 *Seismic hazard and site response analyses*

A grid system with cells of 250 m × 250 m was adopted for the damage scenario computations. The regional seismic hazard was evaluated based on a time dependent Poisson model for the return period of 475 years that corresponds approximately to 10% probability of exceedance in 50 years (Erdik et al., 2004, 2005). PGAs and spectral accelerations at T = 0.2 s and T = 1 s were calculated for each cell on the engineering bedrock outcrop (Figure 2).

Three real acceleration time histories compatible with the regional seismic hazard were selected as input motion as summarised in Table 1. These records were scaled

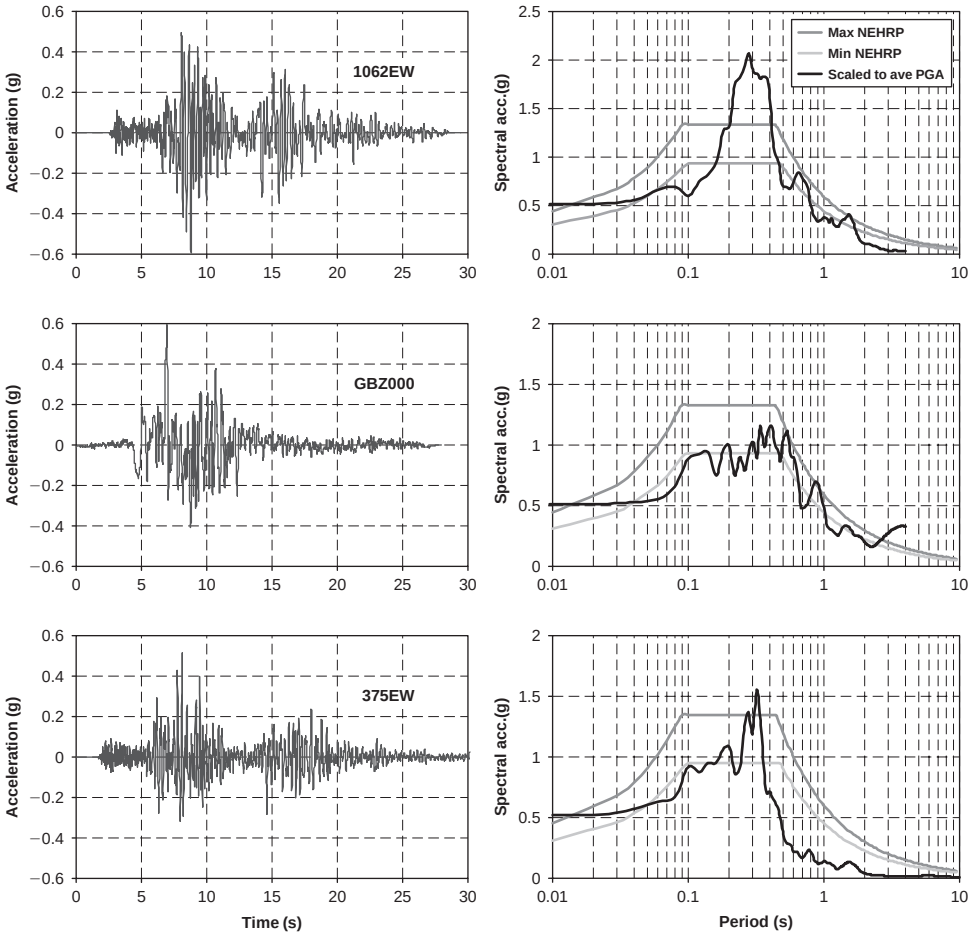

Figure 3 Acceleration time histories scaled with respect to PGA and their respective acceleration response spectra used as input motion in the site response analysis.

with respect to PGAs estimated from the seismic hazard analyses for each cell and were used as outcrop motions in site response analyses.

In order to evaluate the spectrum compatibility, the acceleration response spectra of the selected acceleration time histories scaled to average PGA for the area were calculated and compared with the lowest and highest NEHRP spectra obtained from the earthquake hazard study conducted for the area as shown in Figure 3.

The local site characteristics and soil stratifications were determined based on the available soil borings and insitu seismic wave measurements conducted in the area (Kılıc et al., 2006). The shear wave velocities with depth were estimated using in-hole PS-Logging and surface seismic wave measurements when available and/or using the empirical relationship proposed by Iyisan (1996) in terms of standard penetration blow counts. Shear wave velocity profiles were established down to the engineering bedrock

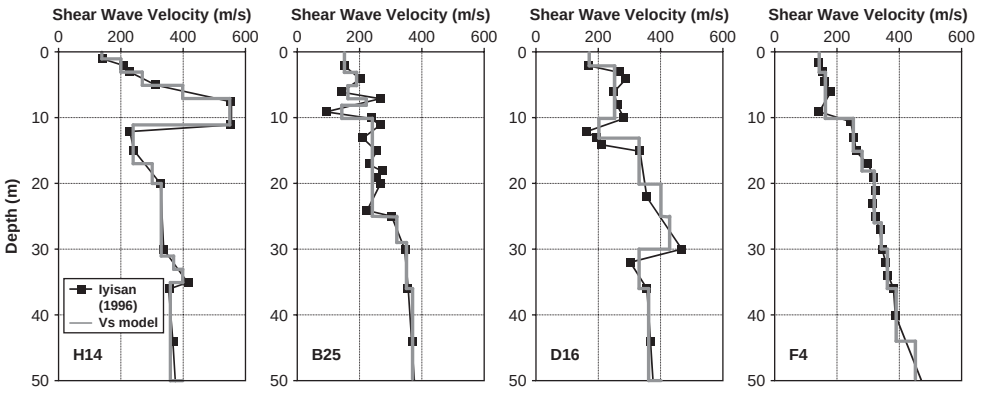

Figure 4 Typical shear wave velocity profiles for the top 50 m of soil in Zeytinburnu.

(Vs $\geq$ 750 m/sec). Typical soil profiles from the study area are shown in Figure 4. Empirical shear modulus and material damping ratio curves that are available in the literature were used to define dynamic soil properties of soil types.

The software was executed using probabilistic seismic hazard parameters to perform site response analyses. The software utilizes Shake91 (Idriss & Sun, 1992) to calculate elastic response spectra (as many as the number of input motions) on the ground surface at each cell location and computes the average of all ground response spectra for that cell. Best-fit NEHRP envelope curve for each average response spectrum was determined using the optimization algorithm. Examples of the best fitting envelope curves obtained in this procedure are shown in Figure 5. Short and long period spectral acceleration values determined from the envelope curves were used to generate microzonation maps. Microzonation maps of the area with respect to short and long period spectral accelerations, based on probabilistic seismic hazard approach are presented in Figure 6.

4.2 *Damage and human loss estimations*

The building inventory of the area was composed of 15738 independent buildings compiled based on street surveys (Aydınoglu et al., 2004; Aydınoglu & Polat, 2004). The inventory was classified with respect to twelve groups based on three parameters: construction type, number of stories and construction date. Results of inventory study indicated that almost all of the buildings in Zeytinburnu are reinforced concrete frame buildings and most of the buildings fall into the mid rise building group. Many buildings have important deficiencies concerning seismic response such as soft stories and short columns.

Five descriptive damage states were defined to grade the damage in buildings: none, slight, moderate, extensive damage and collapsed. Region-specific vulnerability relationships (Erdik et al., 2002) that relate the ground shaking parameters to building damage for each damage state were determined from analytical computations by following a simplified method. The displacement-based methodology described in Hazus

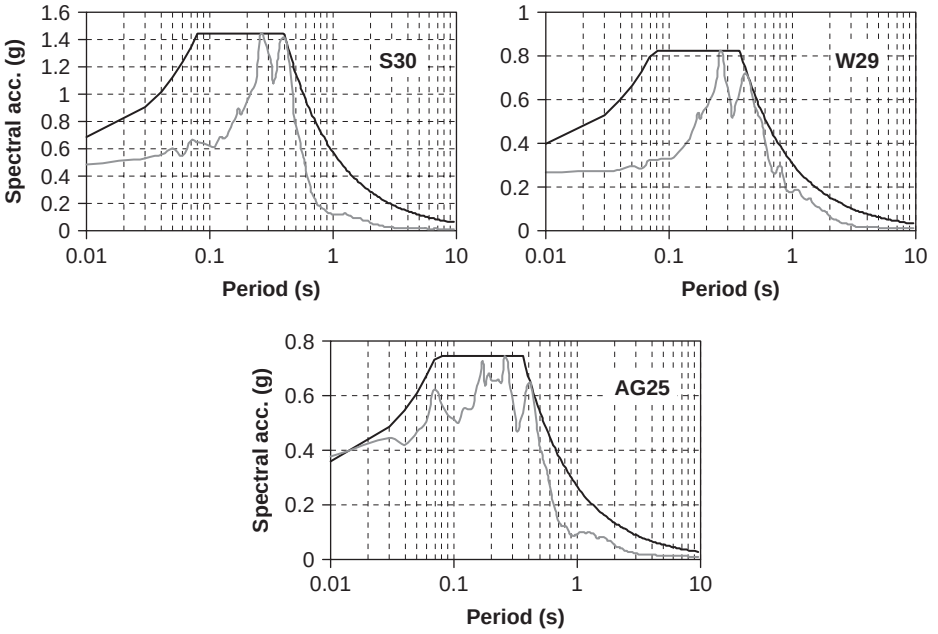

Figure 5 Examples of best-fit NEHRP spectra for the average elastic acceleration response spectra.

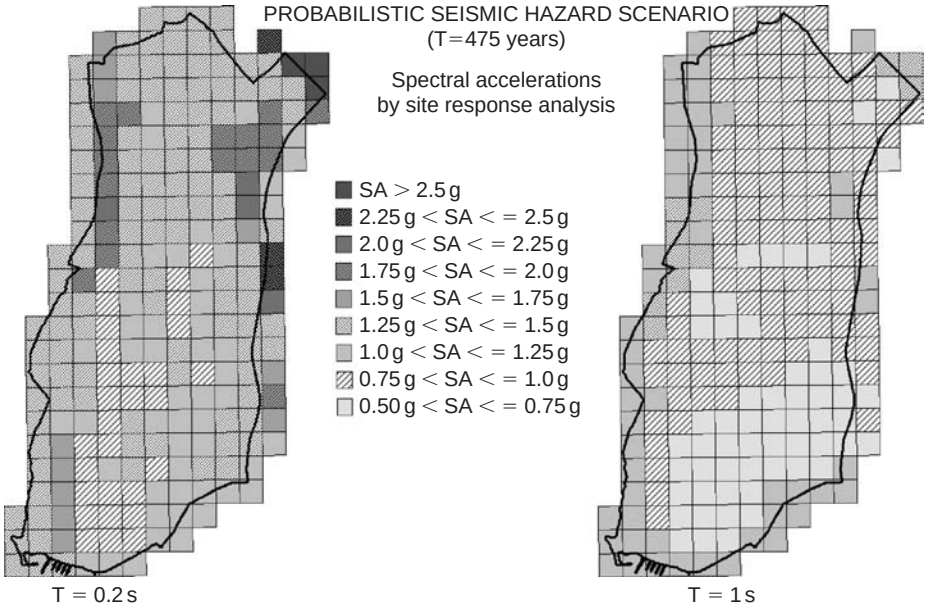

Figure 6 Variation of short and long period (T = 0.2 s and T = 1 s) spectral accelerations on the ground surface in Zeytinburnu determined from site response analysis.

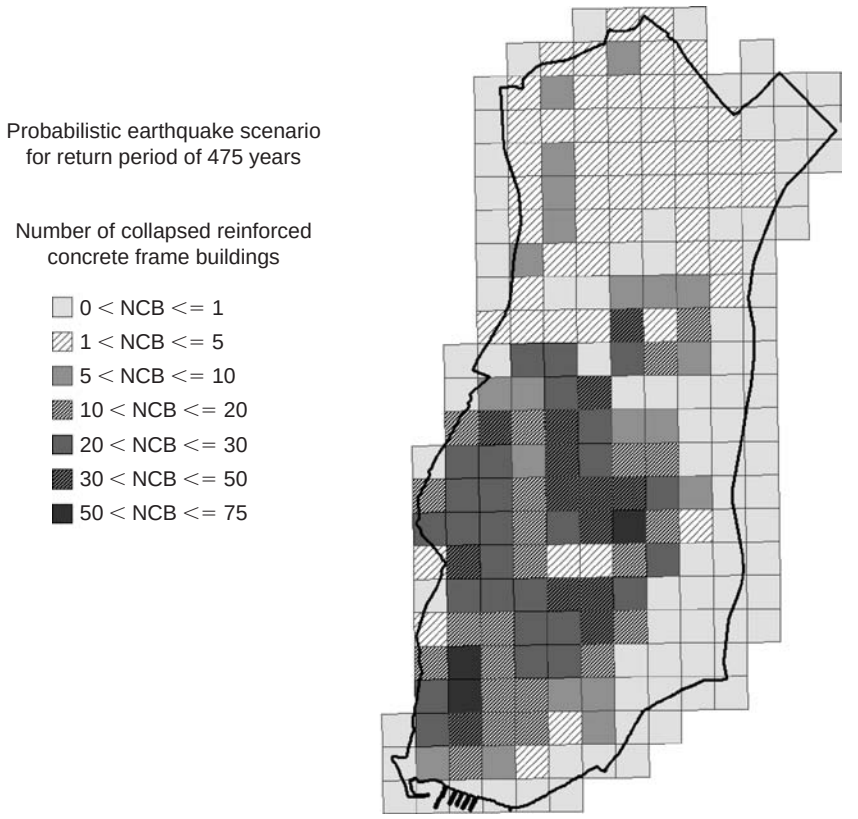

Figure 7 Damage distribution in Zeytinburnu based on PGA scaled real acceleration time histories in accordance with probabilistic seismic hazard analyses.

(1999) was used as reference in developing the so-called 'spectrum demand' and 'spectral capacity curves'. Spectrum demand curve estimates the spectral displacement of the building when subjected to a certain level of spectral acceleration. Spectral capacity curve defines the spectral displacement that the building can sustain for a given spectral acceleration. In the simplified method, the intersection of spectrum demand curve with capacity curve gives the expected median response of the building.

The distribution of number of buildings at each damage state for all building types in Zeytinburnu were computed for probabilistic earthquake scenario. Damage distribution map for this scenario that was obtained as output from the software is presented in Figure 7.

One of the major inputs necessary for earthquake casualty estimation is a correlation between the number and severity of injuries and the damage level of the structures. This is not easily attainable due to the limited quality and lack of information in earthquake casualty data. Several studies that proposed casualty rates with respect to various building types and damage levels are available in the literature (e.g. Coburn and Spence 1992). However, casualty rates derived for other regions of the world

Table 2 Casualty rates for Reinforced Concrete Structures used in this study.

Injury severity	*Casualty rates for RC structures (%)*				
	Slight damage	*Moderate damage*	*Extensive damage*	*Collapsed*	
				Partial	*Total*
Severity 1	0.05	0.2	1	10	50
Severity 2	0.005	0.02	0.5	8	15
Severity 3	0	0	0.01	4	10
Severity 4	0	0	0.01	4	10

(e.g. those available in HAZUS99 for US) are not directly applicable to Turkey as observed by past experience. Erdik et al., (2002) proposed an earthquake casualty model by applying the existing methodologies and by revising the casualty rates with the help of existing data on Turkish earthquakes. According to this approach casualty for any given structure type, building damage level and injury severity level can be calculated as:

$$K = \text{Population per Building} * \text{Number of Damaged Building} * \text{Casualty Rate} \quad (1)$$

The casualties are computed for four injury severity levels as defined in HAZUS 99. Severity 1 is for injuries requiring basic medical aid without requiring hospitalization. Severity 2 is for injuries requiring a greater degree of medical care and hospitalization, but not expected to progress into a life threatening status. Severity 3 is for injuries that pose an immediate life threatening condition if not treated adequately and expeditiously. The majority of these injuries result because of structural collapse and subsequent collapse or impairment of the occupants. Severity 4 is for instantaneously killed or mortally injured.

Casualty data in urbanized areas from Turkish earthquakes indicate higher fatalities in very heavily damaged (partial and total collapse) multi-storey RC buildings. The resulting casualty rates proposed by Erdik et al. (2002) for Turkey are given in Table 2.

The casualties were calculated based on the number of damaged buildings determined from the damage scenarios. The same damage classification was used for both the damage assessment of the buildings and to calculate the casualties. However, based on the damage data and casualty rates from the previous earthquakes in Turkey, it was observed that the fatality is much higher for total collapse (pancake type). Thus, collapse category was divided in to two sub categories as "partial collapse" and "total collapse". It was assumed that total collapse would be encountered in the 10% of the buildings that are calculated as collapsed while 90% were classified as partial collapse with significantly different casualty rates as observed in 1999 in Turkey (Petal 2003).

Average population numbers were adopted for calculating the casualties for different building types. The average population per unit (3 persons) was calculated as the ratio of district populations and number of units in the districts (Erdik et al., 2002). It would have been difficult and not very reliable to make estimates based on a more detailed configuration. The population distribution in the Census is given with respect

Table 3 Population for different building types.

Building type	*Number of floors*	*Number of units (flats)*	*Population*
LOW RISE:	1–4	3	9
MID RISE:	5–8	12	36
HIGH RISE:	>=9	32	96

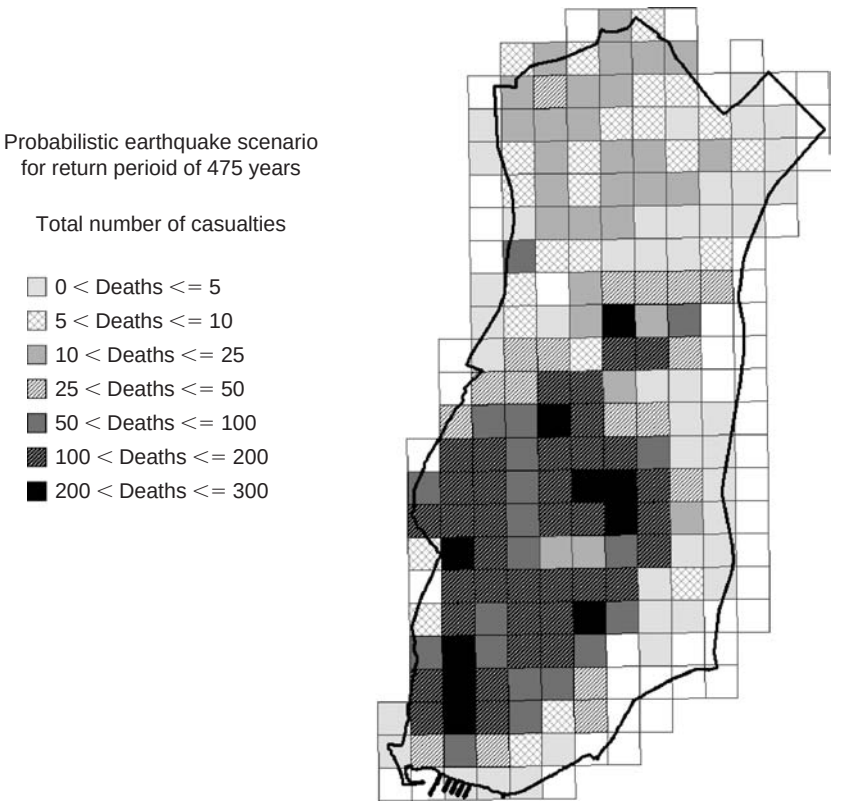

Figure 8 Causality distribution in Zeytinburnu based on PGA scaled real acceleration time histories in accordance with probabilistic seismic hazard analyses.

to districts ("mahalle") as the smallest unit. The damage distributions are based on the number of buildings in each cell. It was assumed that the causality rates can be estimated based on average numbers as given in Table 3. The results are calibrated for the population density determined based on the Census results, thus it could be assumed as casualty estimates for night time population distribution. It would be necessary to conduct a more comprehensive evaluation as proposed in Erdik et al., (2002) to estimate the difference in casualties for daytime population distribution.

5 Conclusions

A software package (KoeriLoss2) is developed to perform detailed urban earthquake scenarios for estimating structural damage and human casualties during an earthquake. The first stage of the procedure involves generation of microzonation maps for the investigated area and for the selected grid system using separately calculated regional seismic hazard data. In the second stage, the effects of local geological and geotechnical site conditions are taken into account based on the representative soil profiles selected for each cell. 1D site specific ground response analyses are conducted using Shake91 to calculate an average site specific PGA and elastic acceleration response spectrum on the ground surface. In the third stage of the procedure, vulnerability of the buildings are estimated based on detailed building inventory and based on the short and long period spectral accelerations obtained from the best fit NEHRP envelopes. A case study for Zeytinburnu Municipality is conducted to demonstrate the application of KoeriLoss2.

Acknowledgments

The earthquake damage scenario software (KoeriLoss2) is developed as a part of the LessLoss FP6 Project on "Risk Mitigation for Earthquakes and Landslides", for SP10 on "Earthquake disaster scenario predictions and loss modelling for urban areas". The Authors would like to acknowledge the significant contributions of Prof. M. Erdik, E. Durukal, M. Demircioglu, and K. Sesetyan during all related projects conducted at Kandilli Observatory and Earthquake Research Institute who supplied the necessary input data and technical support especially on hazard studies.

References

Ansal, A., Özaydın, K., Erdik, M., Yıldırım, M., Kılıç, H., Adatepe, S., Özener, P.T., Tonaroglu, M., Sesetyan, K. & Demircioglu, M. 2005. Seismic Microzonation for Urban Planning and Vulnerability Assessment. *Proceedings of the International Symposium of Earthquake Engineering (ISEE2005)*, Geotechnical Session, Awaji Island, Japan.

Ansal, A., Durukal, E. & Tönük, G. 2006a. Selection and Scaling of Real Acceleration Time Histories for Site Response Analyses. *Proc. of ISSMGE ETC12 Workshop*, Athens, Greece.

Ansal, A., Tönük, G., Demircioglu, M., Bayrakli, Y., Sesetyan, K. & Erdik, M. 2006b. Ground Motion Parameters for Vulnerability Assessment. *Proceedings of the First European Conference on Earthquake Engineering and Seismology*, Geneva, Paper Number: 1790.

ATC & SSC. 1996. *ATC-40 Seismic Evaluation and Retrofit of Concrete Buildings*. Report SSC 96-01, California, USA.

Aydinoglu, A. & Polat, Z. 2004. *First Level Evaluation and Assessment of Building Earthquake Performance*. Report for the Istanbul Master Plan Zeytinburnu Pilot Project, Metropolitan Municipality of Istanbul, Planning and Construction Directorate (in Turkish).

Aydinoglu, A., Polat, Z., Celep, Z., Hancıoglu, B., Kırçıl, M., Önem, G. & Tüzün, C. 2004. *Second level evaluation and assessment of building earthquake performance*. Report for the Istanbul Master Plan Zeytinburnu Pilot Project, Metropolitan Municipality of Istanbul, Planning and Construction Directorate (in Turkish).

BSSC-Building Seismic Safety Council. 2001. *NEHRP (National Earthquake Hazards Reduction Program) Recommended Provisions for Seismic Regulations for new buildings and other structures*, 2000 Edition, Part 1: Provisions (FEMA 368), Ch. 4, Washington, D.C.

Coburn, A. & Spence, R. 1992. *Earthquake Protection,* John Wiley, ISBN 0 471 91833 4.

Deodatis, D. 1996. Non-stationary Stochastic Vector Processes: Seismic Ground Motion Applications. Probabilistic Engineering Mechanics 11:145–168.

Durukal, E., Ansal, A. & Tönük, G. 2006. Effect of Ground Motion Scaling and Uncertainties in Site Characterisation on Site Response Analyses. *Proceedings of the 100th Anniversary Earthquake Conference Commemorating the 1906 San Francisco Earthquake*, San Francisco, USA.

Erdik, M. & Fahjan, Y. 2005. System Analysis and Risk. *Assessing and Managing Earthquake Risk – Geoscientific and Engineering Knowledge for Earthquake Risk Mitigation: developments, tools, techniques*, Part 3, Book Series: Geotechnical, Geological, and Earthquake Engineering, V2, Oliveira CS, Roca A, Goula X (Eds.).

Erdik, M., Aydınoglu, M.N., Barka, A., Yüzügüllü, Ö., Siyahi, B., Durukal, E., Fahjan, Y., Akman, H., Birgören, G., Biro, Y., Demircioğlu, M., Özbey, C. & Sesetyan, K. 2002. *BU-ARC, Earthquake Risk Assessment for Istanbul Metropolitan Area, Project Report*, Bogazici University Publication.

Erdik, M., Demircioğlu, M., Sesetyan, K. & Durukal, E. 2005. *Assessment of earthquake hazard for Bakirköy, Gemlik, Bandırma, Tekirdağ and Körfez*, WB MEER Project -A3 Component, Microzonation and Hazard Vulnerability Studies For Disaster Mitigation in Pilot Municipalities, Bogazici University, Kandilli Observatory and Earthquake Engineering Research Institute.

Erdik, M., Demircioğlu, M., Sesetyan, K., Durukal, E. & Siyahi, B. 2004. Earthquake Hazard in Marmara Region, Soil Dynamics and Earthquake Engineering 24:605–631.

HAZUS. 1999. *Earthquake Loss Estimation Methodology.* Technical Manual, Federal Emergency Management Agency and National Institute of Buildings Sciences, Washington, D.C., USA.

Idriss, I.M. & Sun, J.I. 1992. *Shake91, A Computer Program for Conducting Equivalent Linear Seismic Response Analysis of Horizontally Layered Soil Deposits Modified based on the original SHAKE program Published in December 1972 by Schnabel, Lysmer and Seed.*

Iyisan, R. 1996. Correlations between Shear Wave Velocity and In-situ Penetration Test Results, Technical Journal of Turkish Chamber of Civil Engineers, 7(2):1187–1199 (in Turkish).

Kılıç, H., Özener, P.T., Ansal, A., Yıldırım, M., Özaydın, K. & Adatepe, S. 2006. Microzonation of Zeytinburnu Region with respect to Soil Amplification: A Case Study. Journal of Engineering Geology 86: 238–255.

Molina-Palacios, S. & Lindholm, C.D. 2006. *SELENA V1.0 User and Technical Manual.* NORSAR, Norway (http://www.norsar.no/seismology/selena.html)

Özaydın, K., Ansal, A., Erdik, M., Yıldırım, M., Kılıç, H., Adatepe, S., Özener, P.T., Tonaroglu, M., Sesetyan, K. & Demircioglu, M. 2004. *Earthquake Master Plan for Istanbul, Zeytinburnu Pilot Project, Report on Geological and Geotechnical Evaluation for Seismic Microzonation and Seismic Microzonation for Ground Shaking*, Yıldız Technical Uni., Civil Eng. Geotechnical Dep. (In Turkish).

Petal, M. 2003. Research Report: Causes of Deaths and Injuries in the August 17th, 1999 3:02 a.m. Mw 7.4 Kocaeli Earthquake, Bogazici University, Disaster Preparedness Education Project, Istanbul, Turkey.

Papageorgiou, A., Halldorsson, B. & Dong, G. 2000. *Target Acceleration Spectra Compatible Time Histories*. University of Buffalo, Dept. of Civil, Structural and Environmental Engineering. NY, http://civil.eng.buffalo.edu/engseislab/

Sousa, M.L., Campos Costa, A., Carvalho, A. & Coelho, E. 2004. An Automatic Seismic Scenario Loss Methodology Integrated on a Geographic Information System. 13th World Conference on Earthquake Engineering, Vancouver, B.C., Canada, August 1–6, Paper No. 2526.

Spence, R., Pitilakis, K., Kakderi, K., Ansal, A., Erdik, M., Costa, A.C. & Sousa, M.L. 2006b. *Revised Loss Estimates Based on Alternative Mitigation Actions and Evaluation*, Deliverable

115, Project LessLoss on Risk Mitigation for Earthquakes and Landslides, Sub-Project 10 – Earthquake disaster scenario predictions and loss modelling for urban areas, Sixth Framework Programme.

Spence, R., Pitilakis, K., Kakderi, K., Ansal, A., Erdik, M., Costa, A.C. & Sousa, M.L. 2006a. *Report for each city containing reference loss estimates*, Deliverable 85, Project LessLoss on Risk Mitigation for Earthquakes and Landslides, Sub-Project 10 – Earthquake disaster scenario predictions and loss modelling for urban areas, Sixth Framework Programme.

Spence, R., Pitilakis, K., Kakderi, K., Ansal, A., Erdik, M., Costa, A.C. & Sousa, M.L. 2005. *Report on Building Stock Inventory and Vulnerability Data for each case study*, Deliverable 84, Project LessLoss on Risk Mitigation for Earthquakes and Landslides, Sub-Project 10 – Earthquake disaster scenario predictions and loss modelling for urban areas, Sixth Framework Programme.

Zonno, G., Garcia-Fernandez, M., Jimenez, M.J., Menoni, S., Meronil, F. & Petrini, V. 2003. The SERGISAI procedure for seismic risk assessment. Journal of Seismology **7**:259–277.

Chapter 25

Nonlinear performance assessment of bridges with Incremental Response Spectrum Analysis (IRSA) procedure

M. Nuray Aydınoğlu & Göktürk Önem

Boğaziçi University, İstanbul, Turkey

ABSTRACT: The Incremental Response Spectrum Analysis (IRSA) procedure is introduced as an advanced multi-mode pushover analysis tool for the performance-based seismic assessment and design of buildings and bridges (Aydınoğlu 2003). The practical version of the procedure (Aydınoglu 2004) works directly with smoothed elastic response spectrum and makes use of the well-known equal displacement rule to scale modal displacement increments at each piecewise linear step, in which the traditional linear Response Spectrum Analysis (RSA) is implemented. Being a general analysis tool, IRSA is completely independent of the type of structure, as in its linear counterpart RSA. In this respect, IRSA is readily applicable to any type of bridge. In the present contribution, IRSA is applied to few types of highway bridges and its performance is checked against the results of the corresponding nonlinear response history analysis (NRHA) performed. It is shown that IRSA is capable of estimating bridge nonlinear demands with an acceptable accuracy for practical purposes.

1 Introduction

Nonlinear static procedure (NSP) has been widely recognized and used in engineering practice as an inelastic analysis tool in the framework of performance based seismic evaluation (ATC 1996, FEMA 2000). NSP, which is essentially based on single-mode pushover analysis, has the main advantage of utilizing elastic response spectrum in estimating the inelastic demand as compared to rather time consuming nonlinear response history analyses with an ensemble of acceleration records. However, single-mode pushover analysis can be reliably applied to only two-dimensional response of low-rise building structures regular in plan or simple regular bridges, where the seismic response is essentially governed by the fundamental mode. Application of single-mode pushover to high-rise buildings or any building irregular in plan as well as to irregular bridges involving three-dimensional response would lead to incorrect, unreliable results. Therefore, a number of improved pushover analysis procedures have been offered in recent years in an attempt to take higher mode effects into account. Yet, it is rather surprising that among those only two procedures, i.e., Modal Pushover Analysis (MPA) introduced by Chopra & Goel (2002) and Incremental Response Spectrum Analysis (IRSA) developed by Aydınoğlu (2003, 2004), are able estimate the seismic demand under a given earthquake input. Others actually dealt with structural capacity estimation only, i.e., they cannot estimate the seismic demand, although this important limitation has been generally overlooked (Aydınoğlu 2007).

It is worth noting that Modal Pushover Analysis (MPA) method (Chopra & Goel 2002) ignores the contributions of different modes to the section forces in the formation of plastic hinges. Development of nonlinear response is estimated independently for each mode with a single-mode pushover analysis based on an invariant load pattern proportional to initial linear elastic mode shape. Since modal coupling is ignored, peak response quantities are obtained independently for each mode from a SDOF system analysis (or from a given inelastic response spectrum) and then combined (exactly as in the linear response spectrum analysis) with an appropriate modal combination rule. MPA procedure has been generally applied to multi-story buildings, however recently applications to bridges have emerged in the literature (Isakovic & Fischinger 2006, Paraskeva et al. 2006).

Multi-mode pushover analysis procedure IRSA (Incremental Response Spectrum Analysis) has been introduced by the first author to enable the two and three dimensional nonlinear analyses of buildings and bridges (Aydınoğlu 2003). The practical version of the procedure (Aydınoğlu 2004, 2007) works directly with smoothed elastic response spectrum and makes use of the well-known equal displacement rule to scale modal displacement increments at each piecewise linear step of an incremental application of linear Response Spectrum Analysis (RSA). In this paper, main steps of IRSA are summarized and its performance is evaluated on two example bridges under three different ground motions.

2 Summary of Incremental Response Spectrum Analysis (IRSA) for multi-mode pushover analysis

Incremental Response Spectrum Analysis (IRSA) is a multi-mode pushover procedure, in which the incremental response is assumed *piecewise linear* at each pushover step in between the formation of two consecutive plastic hinges. The key point in IRSA is modal scaling, which is applied at each step to modal displacement increments, $\Delta d_{\mathrm{n}}^{(\mathrm{i})}$, to identify their proportions in different modes (Aydınoğlu 2003, 2007).

$$\Delta d_{\mathrm{n}}^{(\mathrm{i})} = \Delta \tilde{F}^{(\mathrm{i})} S_{\mathrm{den}}^{(1)} \tag{1}$$

where (n) refers to mode number and $\Delta \tilde{F}^{(\mathrm{i})}$ is an *incremental scale factor*, which is applicable to all modes at the (i)'th pushover step. $S_{\mathrm{den}}^{(1)}$ represents n'th mode *initial elastic spectral displacement* defined at the first step (see Fig. 1). According to the well-known *equal displacement rule*, it is assumed equal to the *inelastic spectral displacement* associated with the *instantaneous* configuration of the structure at any pushover step. Cumulative modal displacement at the end of the same pushover step can then be written as

$$d_{\mathrm{n}}^{(\mathrm{i})} = d_{\mathrm{n}}^{(\mathrm{i}-1)} + \Delta d_{\mathrm{n}}^{(\mathrm{i})};\ d_{\mathrm{n}}^{(\mathrm{i})} = \tilde{F}^{(\mathrm{i})} S_{\mathrm{den}}^{(1)} \tag{2}$$

in which $\tilde{F}^{(\mathrm{i})}$ represents the *cumulative scale factor* with a maximum value of unity:

$$\tilde{F}^{(\mathrm{i})} = \tilde{F}^{(\mathrm{i}-1)} + \Delta \tilde{F}^{(\mathrm{i})} \leq 1 \tag{3}$$

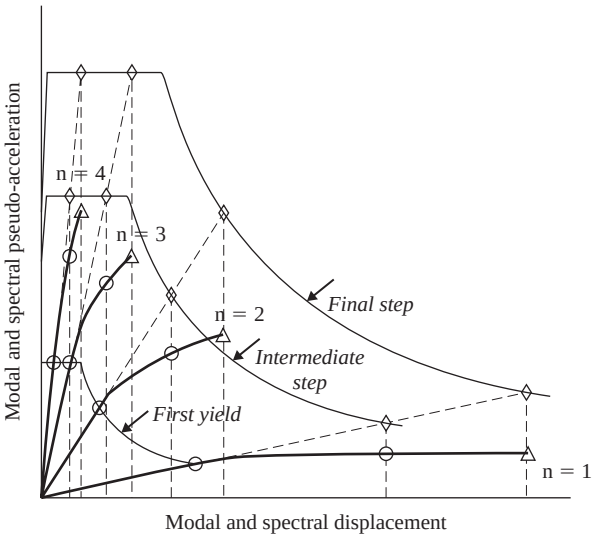

Figure 1 Scaling of modal displacements through monotonic scaling of response spectrum.

Note that modal scaling expressions given above correspond to a monotonic increase of the elastic response spectrum progressively at each step with a cumulative scale factor starting from zero until unity. Physically speaking, the structure is being pushed such that at every pushover step modal displacements of all modes are increased by increasing elastic spectral displacements defined at the first step ($i=1$) in the same proportion according to *equal displacement rule* until they simultaneously reach the target *spectral displacements* on the response spectrum. Shown in Fig. 1 are the scaled spectra corresponding to the first yield, to an intermediate pushover step ($\tilde{F}^{(i)} < 1$) and to the final step ($\tilde{F}^{(i)} = 1$), which are plotted in ADRS (Acceleration-Displacement Response Spectrum) format and superimposed onto modal capacity diagrams.

Main stages of IRSA can now be described as follows:

1. A standard linear response spectrum analysis (RSA) is performed at each (i)'th incremental pushover step for the unit value of the unknown incremental scale factor ($\Delta\tilde{F}^{(i)} = 1$) by considering *instantaneous* mode shapes that are compatible with the current distribution of plastic hinges and the *initial elastic spectral displacements* $S_{den}^{(1)}$ taken as seismic input. Such a linear response spectrum analysis (RSA) effectively corresponds to *adaptive pushover analyses*, which are *simultaneously performed* in each mode followed by the application of an appropriate modal combination rule. Thus, any response quantity of interest, which is represented by a generic response quantity, $\tilde{r}^{(i)}$, is obtained for the unit value of the unknown incremental scale factor. Now, the increment of the generic response quantity, $\Delta r^{(i)}$, is expressed as

$$\Delta r^{(i)} = \tilde{r}^{(i)}\,\Delta\tilde{F}^{(i)} \tag{4}$$

and the generic response quantity at the end of the (i)'th pushover step can be written as

$$r^{(i)} = r^{(i-1)} + \Delta r^{(i)} = r^{(i-1)} + \tilde{r}^{(i)}\,\Delta\tilde{F}^{(i)} \tag{5}$$

in which $r^{(i)}$ and $r^{(i-1)}$ are the generic response quantities to develop at the end of current and previous pushover steps, respectively. In the first pushover step ($i = 1$), response quantities due to gravity loading are considered as $r^{(0)}$.

2. Eq. (5) is specialized for the internal force components defining the yield surfaces of potential plastic hinges to develop in the structural system. The minimum $\Delta\tilde{F}^{(i)}$ identifies the location of the new hinge developed at the end of (i)'th pushover step.
3. Cumulative scale factor $\tilde{F}^{(i)}$ is calculated from Eq. (3) and checked if it exceeded unity. If unity is not exceeded, the remainder of this stage can be skipped and the analysis proceeds with the next stage. If exceeded, incremental scale factor in the last step, $\Delta\tilde{F}^{(p)}$, is re-calculated as

$$\Delta\tilde{F}^{(p)} = 1 - \tilde{F}^{(p-1)} \tag{6}$$

and in the last pushover step modal displacement increment is redefined as

$$\Delta d_n^{(p)} = C_{Rn}\, S_{den}^{(1)}\, \Delta\tilde{F}^{(p)} \tag{7}$$

where C_{Rn} represents n'th mode *spectral displacement amplification factor*, which may be greater or smaller than unity in higher modes depending on the initial period and secondary slopes of the modal capacity diagrams. For detailed information on this particular point, the reader is referred to Aydınoğlu (2007). In the following applications C_{Rn} is assumed to be unity in all cases.
4. All response quantities of interest developed at the end of the pushover step are calculated from the generic expression of Eq. 5. If the final pushover step has been reached, the analysis is terminated. If not, it is continued with the next stage.
5. The current stiffness matrix is modified by considering the last yielded hinge identified at Stage (2) and it is returned to Stage (1) for the next pushover step. Note that second-order (P-Delta) effects can be readily considered in IRSA by adding the so-called *geometric stiffness matrix* to the first order stiffness matrix at each pushover step.

3 Performance of IRSA on seismic assessment of bridges

In order to test the performance of IRSA on bridges structures, two bridge models were selected. The first model represents an existing long viaduct with a moderately irregular configuration located on Trans-European Motorway in Istanbul, which was constructed by Incremental Launching Method in mid 1980's. The second model is artificially generated from the first one to put IRSA on a severe test with a highly irregular configuration. Longitudinal profiles of the two selected models as well as the cross-section of the deck and a typical single-pier are illustrated in Figure 2. All piers are single column bents with varying heights between 8.6 m and 47.0 m in Model 1 and between 17.5 m and 47 m in Model 2.

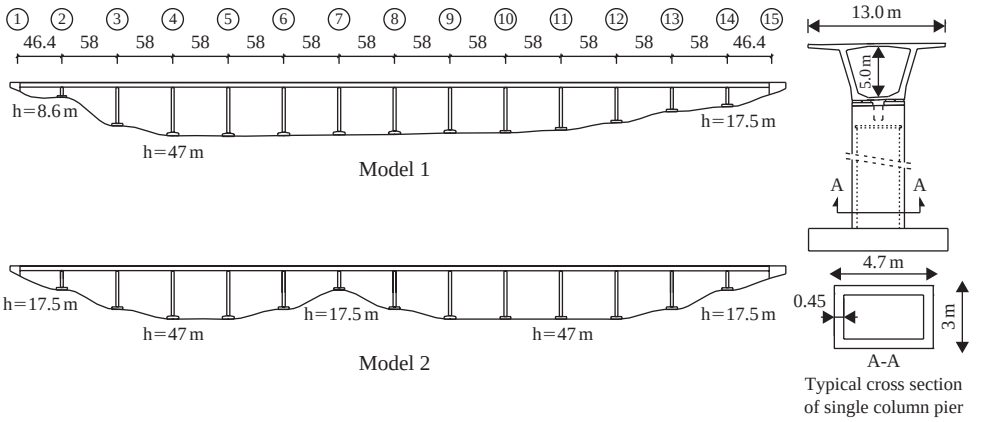

Figure 2 Configuration of selected bridge models and typical cross section.

Table 1 Characteristics of earthquake records.

No.	*Earthquake*	*Magnitude*	*Station No*	*Distance km*	*Site Cond.*	*PGA g*	*PGV cm/s*	*PGD cm*
1	Chalfant Valley	6.2	54429	18.7	D	0.4	44.5	8.56
2	Mammoth Lakes	6	54214	19.7	A	0.48	14.2	1.77
3	Whittier Narrows	6	24461	13.2	B	0.33	22	2.42

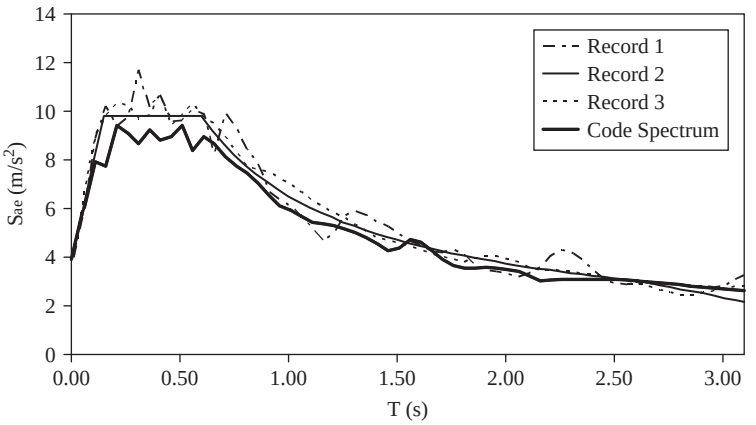

Figure 3 Acceleration response spectra of scaled records and code spectrum.

For nonlinear response history analyses (NRHA), three different earthquake records are employed with characteristics listed in Table 1. These records are appropriately scaled to match a smoothed elastic response spectrum as shown in Figure 3. In the analysis PERFORM-3D structural analysis program (CSI 2006) has been utilized.

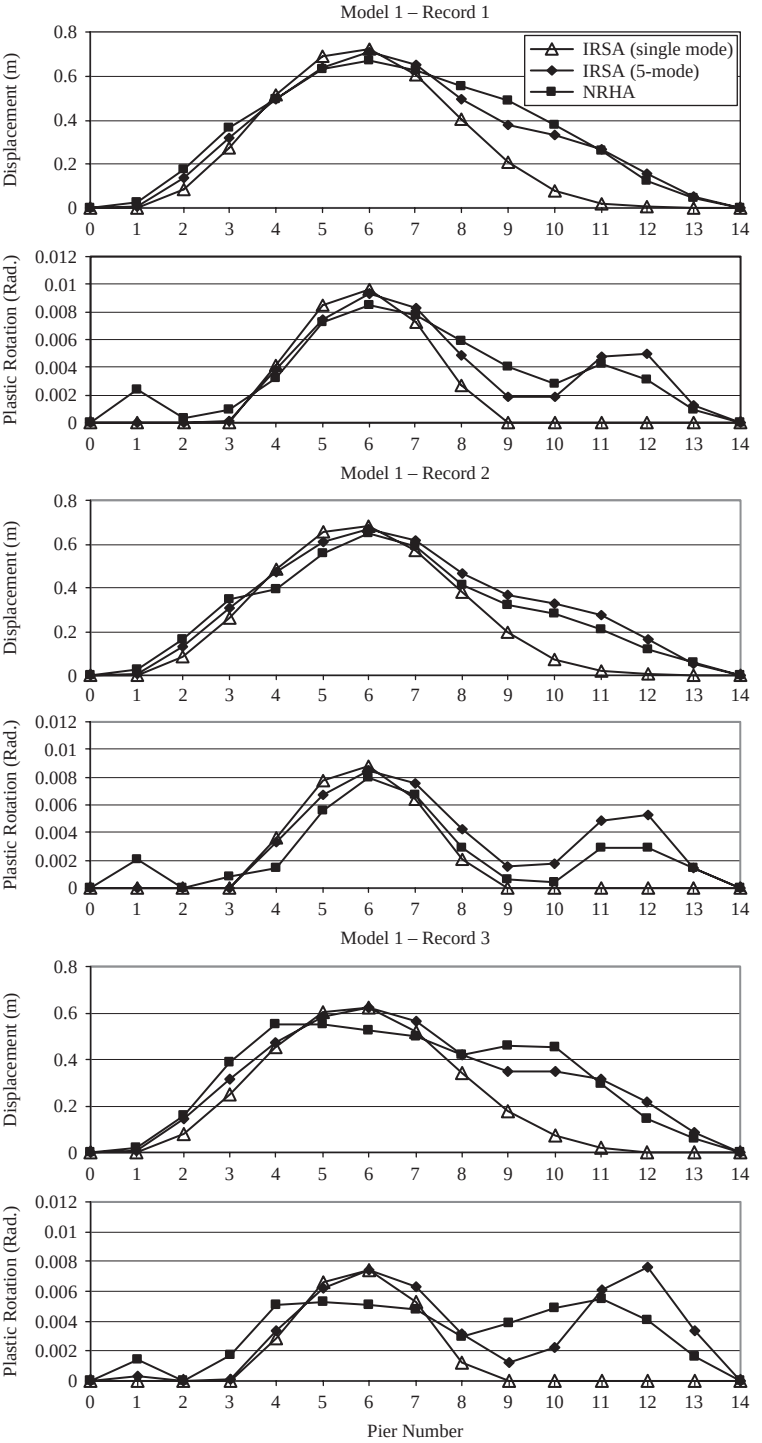

Figure 4 Pier top displacements and plastic rotations at the base of piers calculated from IRSA (five mode), IRSA (single mode) and NRHA of *Bridge Model 1* for three ground motion records.

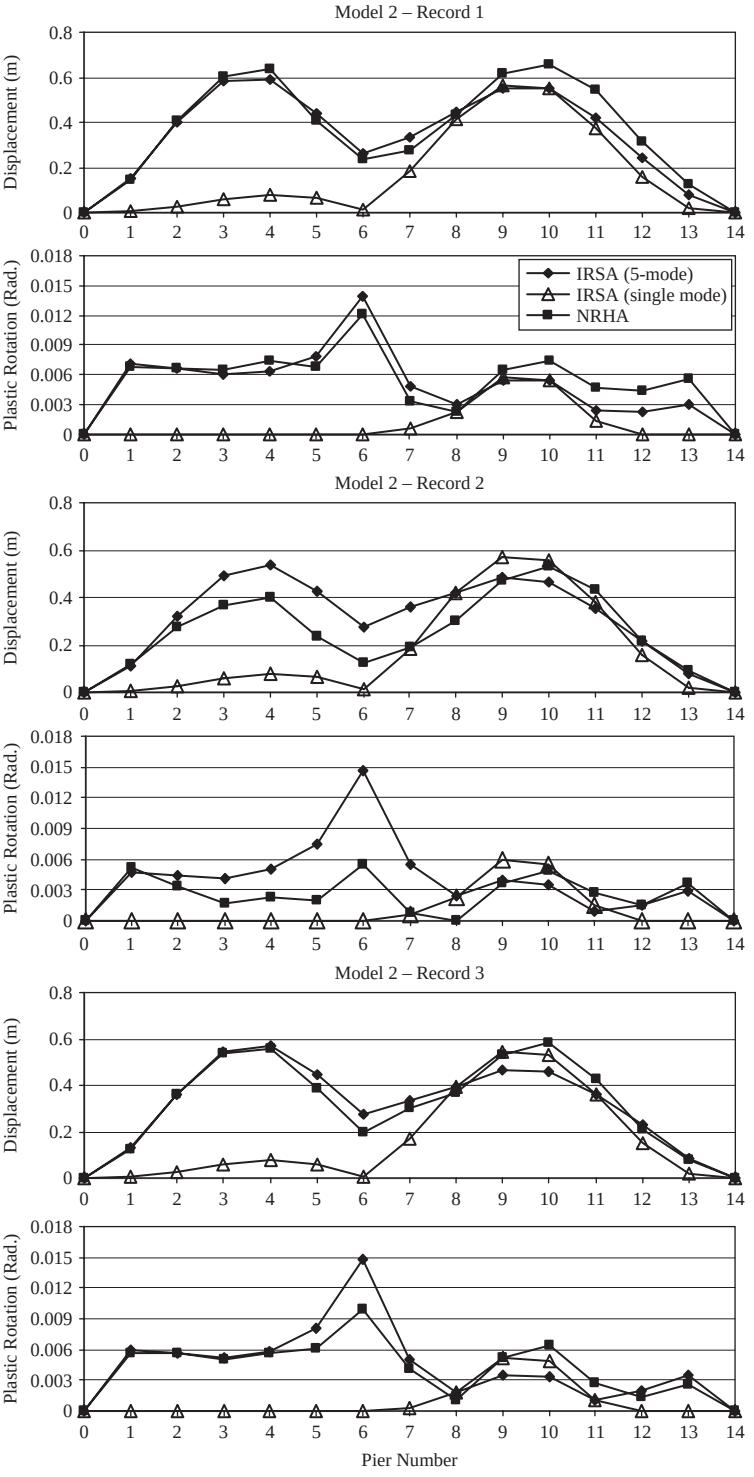

Figure 5 Pier top displacements and plastic rotations at the base of piers calculated from IRSA (five mode), IRSA (single mode) and NRHA of *Bridge Model 2* for three ground motion records.

Plastic hinges are modeled at the bases of piers with an elasto-plastic force-deformation behavior.

Both models are also analyzed with IRSA by an in-house analysis software by taking into account five modes and a single mode. The latter has been intended to identify the significance of higher mode contributions and hence the effectiveness of IRSA in capturing the multi-mode response behavior.

4 Results and conclusions

Pier top displacements and plastic rotations at the base of piers calculated from five-mode IRSA, single-mode IRSA and NRHA are presented in Figure 4 and Figure 5 for Model 1 and Model 2, respectively, under three selected earthquake ground motions. A remarkable agreement between five-mode IRSA and NRHA is observed for both bridge models. It is clear that IRSA results are closer to NRHA results in moderately regular Model 1, however agreement is also very satisfactory for Model 2 under ground motions Record 1 and Record 3. Results divert in Model 2 only for Records 2. Poor performance of single-mode IRSA in both models indicates that the use of traditional pushover analysis for such type of bridges is prohibitive.

Based on limited observations made above, it appears that approximate Incremental Response Spectrum Analysis (IRSA) procedure, which is the natural extension of the traditional Response Spectrum Analysis (RSA), proves to be a reliable analysis tool for deformation-based seismic assessment and design of bridges in the general framework of performance-based design.

References

ATC. 1996. Applied Technology Council. *Seismic evaluation and retrofit of concrete buildings (ATC-40)*. Redwood City, California.

Aydınoğlu, M.N. 2003. An incremental response spectrum analysis based on inelastic spectral displacements for multi-mode seismic performance evaluation. *Bulletin of Earthquake Engineering* 1(1):3–36.

Aydınoğlu, M.N. 2004. An improved pushover procedure for engineering practice: Incremental Response Spectrum Analysis (IRSA). *International Workshop on "Performance-based Seismic Design: Concepts and Implementation"*. Bled, Slovenia.PEER Report 2004/05: 345–356.

Aydınoğlu, M.N. 2007. A Response Spectrum-Based Nonlinear Assessment Tool for Practice: Incremental Response Spectrum Analysis (IRSA). *Special Issue: Response Spectra (Guest Editor: M.D. Trifunac), ISET Journal of Earthquake Technology* 44(1), No. 481.

Chopra, A.K. & Goel, R.K. 2002. A modal pushover analysis for estimating seismic demands for buildings. *Earthquake Engineering and Structural Dynamics* 31(3): 561–582.

CSI. August 2006. Computers and Structures Inc. 2006. *PERFORM-3D: Nonlinear Analysis and Performance Assessment for 3D Structures, User Guide*. Version 4.

FEMA. 2000. Federal Emergency Management Agency. *Prestandard and commentary for the seismic rehabilitation of buildings (FEMA-356)*. Washington D.C.

Isakovic, T. & Fischinger, M. 2006. Higher modes in simplified inelastic seismic analysis of single column bent viaducts. *Earthquake Engineering and Structural Dynamics* 35: 95–114.

Paraskeva, T.S., Kappos, A.J. & Sextos, A.G. 2006. Extension of modal pushover analysis to seismic assessment of bridges. *Earthquake Engineering and Structural Dynamics* 35: 1269–1283.

Chapter 26

The equivalent modal damping concept and its use in seismic design of steel structures

George A. Papagiannopoulos & Dimitri E. Beskos

University of Patras, Rio, Greece

ABSTRACT: A method is presented for the determination of the maximum structural response through a linear elastic spectrum analysis using equivalent modal damping values instead of the crude strength reduction factor. Geometrical and material non – linear structural effects are converted into equivalent time – invariant modal damping values. These equivalent damping values for the first few modes of the structure are numerically computed by first iteratively forming a frequency response transfer function until certain smoothness criteria are satisfied and then by solving a set of non – linear algebraic equations. A design – oriented scheme is developed in order to apply the equivalent modal damping concept to the seismic response analysis of multi-degree-of-freedom (MDOF) building structures. This scheme involves a) the quantification of equivalent modal damping of a structure for predefined deformation limits and b) the use of spectrum analysis and modal synthesis for the calculation of the design base shear of the structure. For illustration purposes, curves providing equivalent damping as functions of period for the first few modes as well as design acceleration versus period for given equivalent damping are constructed using a large number of steel moment resisting frames excited by various seismic motions. The whole design procedure is illustrated by means of a steel moment resisting framed structure. It is concluded that the proposed design scheme can be viewed as an improvement to the force based method of current seismic codes with equivalent modal damping values playing the role of the strength reduction factor.

1 Introduction

Dynamic non – linear (with respect to geometry and material) analysis of structures by the finite element method in conjunction with a stepwise time integration of the equations of motion is the only direct and reliable way for obtaining their response to seismic excitations (Chopra, 2001). However, when a structure is to be seismically designed, this approach is usually not practical since the structure has to be modeled very carefully and excited by a number of seismic excitations. To avoid the need of performing several non – linear dynamic analyses, earthquake engineering has been focused over the past 40 years or so on the computation of seismic demands by various indirect (simplified) procedures of varying degrees of simplicity and accuracy. Most of these procedures at the end make use of the most versatile tool in earthquake engineering, the elastic response spectrum. In general, these simplified approaches can be separated in four major categories: a) those based on equivalent linearization, b) those based on inelastic response spectra – reduction factor, c) those based on non – linear modal superposition and d) those based on transform techniques. A brief review of the most important methods of each category is given in (Papagiannopoulos & Beskos, 2008a).

In this work, an equivalent linear, with respect to geometry and material, multi-degree-of-freedom (MDOF) structure that can substitute the original geometrically and materially non – linear MDOF structure for seismic response applications is constructed. The goal is the determination of the maximum structural response through a linear elastic modal analysis using the equivalent modal damping values instead of the crude strength reduction factor used by modern codes. The proposed equivalent linear structure: a) retains the mass and initial stiffness of the original non – linear structure and takes into account non – linearities in the form of equivalent time – invariant modal damping values; b) is obtained through an iterative formation of a frequency response transfer function until this function satisfies certain smoothness criteria. Equivalent damping values for the first few modes are then numerically computed by solving a set of non – linear algebraic equations. Thus, the proposed method for seismically analyzing non – linear MDOF structures by simplified linear methods belongs to the category of equivalent linearization methods. However, the equivalent linear structure remains here a MDOF structure and it is not reduced to a single-degree-of-freedom (SDOF) one, as it is usually the case in the literature, with obvious gains in modeling accuracy. Furthermore, this equivalent structure here is characterized only by equivalent damping ratios and not by equivalent stiffness and damping as it is usually the case in the literature.

A design – oriented scheme is developed based on the application of the equivalent structure with modal damping to the seismic response calculation of MDOF building structures. This scheme involves a) the quantification of equivalent modal damping of a structure for predefined deformation limits and b) the use of spectrum analysis and modal synthesis for the calculation of the design base shear of the structure. For illustration purposes, curves providing equivalent damping as function of period for the first few significant modes as well as design acceleration versus period for given equivalent damping are constructed using a number of steel moment resisting frames excited by various seismic motions (Papagiannopoulos & Beskos, 2008b). The whole design procedure is illustrated by means of a steel moment resisting framed structure. It is concluded that the proposed design scheme can be viewed as an improvement to the force based method of current seismic codes with equivalent modal damping values playing the role of the strength reduction factor.

2 The equivalent structure with damping

In order to reproduce the seismic response of a non – linear structure, the aim is to construct a MDOF linear structure with the effects of non – linearities (both geometric and material) being taken care of by appropriately quantified modal damping ratios. Since damping is the only parameter that controls the proposed linearization procedure it is very important to realize that if a structure with such a value of viscous damping is to remain in the linear region, non – linear work should not be produced. Therefore, viscous damping is fed into the original non – linear MDOF structure in order to prevent members from being stressed in the non – linear region. Consequently, a critical condition will be reached at which the non – linear MDOF structure will start behaving as linear. This means that the non – linear MDOF structure can be theoretically substituted by an equivalent linear MDOF structure with the same mass and initial stiffness properties as the original non – linear one. Thus, only one parameter of the

equivalent structure needs to be defined, that of the equivalent modal damping with such values so as to maintain the behavior of the structure linear.

The abovementioned thoughts can be interpreted as an effort to balance the work done by non – linearities and viscous damping. This balance is practically realized as follows. It is assumed that the original non – linear MDOF structure possesses well separated classical normal modes and zero initial viscous damping. Damping is added to the structure, by assigning it to each of its normal modes following Rayleigh formula (Chopra, 2001; Papagiannopoulos & Beskos, 2008a), and its non – linear seismic response is then computed via direct stepwise time integration of the equations of motion. The roof to basement frequency response transfer function $R_r(\omega)$ of a linear MDOF plane structure subjected to a horizontal seismic excitation is defined in the frequency domain as the ratio of the absolute roof acceleration response $\overline{\ddot{y}}_r$ of the structure over the seismic excitation $\overline{\ddot{u}}_g$ (Papagiannopoulos & Beskos, 2008a)

$$R_r(\omega) = \frac{\overline{\ddot{y}}_r(\omega)}{\overline{\ddot{u}}_g(\omega)} = 1 + \sum_{k=1}^{N} \left[\frac{\omega^2 \cdot \phi_{rk} \cdot \Gamma_{rk}}{(\omega_k^2 - \omega^2) + i(2 \cdot \xi_k \cdot \omega_k \cdot \omega)} \right] \tag{1}$$

where ϕ_{rk} denotes the roof component of mode k, while ξ_k, Γ_{rk}, ω_k are the damping ratio, the participation factor and the modal frequency in mode k, respectively and N is the total number of modes of the structure. If it is assumed that both participation factors and mode shapes of the structure are a priori known, then the calculation of modal damping can be obtained on the basis of the modulus of the transfer function $|R_r(\omega)|$, which reads as

$$|R_r(\omega)|^2 = 1 + 2 \cdot \sum_{k=1}^{N} Re(z_k) + \sum_{k=1}^{N} |z_k|^2 + 2 \cdot \sum_{k \neq j, j>k}^{N} Re(z_k \cdot z_j^*) \tag{2}$$

where

$$z_k = \frac{[\phi_{rk} \cdot \Gamma_{rk} \cdot \omega^2 \cdot (\omega_k^2 - \omega^2) - 2 \cdot \xi_k \cdot \omega_k \cdot \omega \cdot i]}{[(\omega_k^2 - \omega^2)^2 + (2 \cdot \xi_k \cdot \omega_k \cdot \omega)^2]} \tag{3}$$

with the asterisk (*) denoting the conjugate of the corresponding complex number. Equation (2) for known $|R_r(\omega)|$, ϕ_{rk}, Γ_{rk} and ω_k, represents a set of non – linear algebraic equations, the solution of which leads to the calculation of modal damping ratios of all modes that appear in the transfer function. On the basis of the results presented in (Papagiannopoulos & Beskos, 2006), a linear structure exhibits a smooth transfer function modulus with well defined visible peaks. These peaks correspond to the resonant frequencies of the structure. Modal damping ratios can then be calculated from Eq. (2) by using the modulus of the transfer function as well as the resonant frequencies and the participation factors of the structure as obtained by modal analysis. When the structure ceases to behave linearly, non – linearities begin to take place and the abovementioned transfer function modulus looses its smoothness. This lack of smoothness in the transfer function is depicted by multiple peaks or a jagged (distorted) shape.

The distortion (jaggedness) of the transfer function modulus is exhibited as spurious peaks to the right or left side of the resonant peaks. The number and the position of the

spurious peaks as well as the visibility of the resonant ones depend on the magnitude of non – linear deformation of the structure. Since the goal here is to construct a linear structure equivalent to the original non – linear one, it is important to realize that when the shape of the transfer modulus of the equivalent linear structure follows a smooth (undistorted) pattern, the corresponding calculated equivalent modal damping ratios will reflect the work done due to geometrical and material non – linearities.

Assuming that the non – linear absolute acceleration time history of a structure under a known seismic excitation can be obtained, the construction of its transfer function modulus using Eq.(2) is straightforward. This transfer function modulus can be very jagged (unsmoothed) or it can depict only light jaggedness. The existence or lack of jaggedness depends on the inherent damping of the structure. In case that inherent damping of the structure balances or surpasses the work done due to non – linearities, the transfer function modulus will be smooth. On the other hand, if the inherent damping of the structure cannot balance this work, the transfer function modulus will be jagged. By adjusting (increasing) the inherent damping of the structure until it balances exactly the non – linear work done, one obtains a linear structure that exhibits a smooth transfer function modulus and possesses such modal damping values that take care of all non – linear effects. These are the equivalent modal damping values.

On the basis of the developments in (Papagiannopoulos & Beskos, 2008a), the smooth pattern of the transfer function modulus of a MDOF structure is ensured when certain monotonicity criteria between all its peaks (maximum points) are established. This is the case depicted in Fig. 1. To obtain the increasing and the decreasing branches of a transfer function modulus initial damping is assigned to all modes of the structure according to Rayleigh damping formula. The transfer function modulus of a MDOF structure has more than one resonant peaks corresponding to those structural modes excited by the seismic input used. The satisfaction of the smoothness (monotonicity) criteria does not occur simultaneously for all modes, except in some cases.

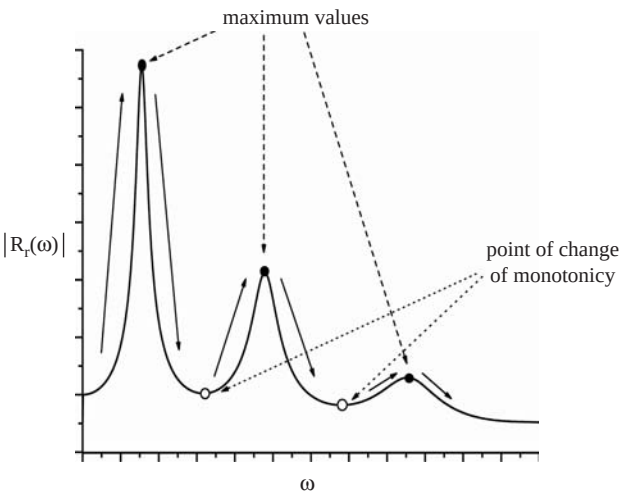

Figure 1 Transfer function modulus for a MDOF structure and its peaks at resonant frequencies (↑ strictly increasing; ↓ strictly decreasing).

Consequently, when the satisfaction of the monotonicity criteria is accomplished for one or more modes, the values of the function $|R_r(\omega)|$ and the corresponding frequencies at its peaks (modes) are not allowed to alter. If additional damping is assigned to the modes that had already satisfied the criteria, their participation in the total response will be overestimated. Therefore, using Rayleigh's formula, initial damping is increased as long as the rest of the modes manage to satisfy the criteria. The damping increase for the mode(s) that have already satisfied the criteria is taken to be zero as long as the iterative procedure continues towards its final goal, i.e., the satisfaction of the monotonicity criteria of for all modes. In other words, these monotonicity criteria for various parts of the transfer function modulus can be satisfied in different cycles of its iterative formation. However, there are cases where one should also check the derivative of $|R_r(\omega)|$ to ensure accurate calculation of the equivalent modal damping values (Papagiannopoulos & Beskos, 2008a).

When all modes manage to satisfy the criteria, the transfer function modulus will attain a very smooth shape corresponding to a linear elastic MDOF structure. Then, Eq. (2) is numerically solved in order to obtain the modal damping values of the equivalent linear elastic MDOF structure. For the calculation of the modal damping ratios one uses: a) the modulus of the transfer function at the peaks, b) the frequencies that correspond to these peaks and c) the participation factors as calculated from the classical eigenvalue problem involving the mass and initial stiffness of the given structure.

3 Application of equivalent damping to seismic design

The proposed technique by means of the iterative formation of the frequency response transfer function modulus leads to equivalent modal damping values that take into account geometrical non – linearities, cyclic inelastic deformations, number of yield excursions and yield reversals because the non – linear seismic response of the structure is successively used till it becomes linear. Therefore, the equivalent modal damping values keep all deformations as well as the base shear of the structure to values that correspond to those just before its first time yielding. Consequently, equivalent modal damping ratios can be viewed as playing the role of the strength reduction factor in seismic design because the non – linear seismic demands posed by a given seismic motion against a given structure are quantified. In contrast to the strength reduction factor, the determination of equivalent modal damping values is more rational. Thus, by using the equivalent modal damping ratios in conjunction with spectrum analysis and modal synthesis, one can easily compute the maximum base shear of a building structure. However, there are two important things that demand further investigation. The first is related to the determination of deformation dependent equivalent modal damping ratios and the second concerns the effect of higher modes.

According to the developments of the previous section, the equivalent modal damping values are derived numerically but no reference is made regarding loss of stability of the structure. Thus, the equivalent modal damping values obtained by using Eq. (2), are found under no restriction concerning the deformability state of the structure. Therefore, it should be checked if these damping values are realistic by posing a limit to the deformation of the structure under consideration.

Deformation limits are expressed herein in terms of interstorey drift ratios that should not surpass predefined limit values, even though other deformation measures

could have been used as well. The calculation of the equivalent modal damping values follows the procedure described in (Papagiannopoulos & Beskos, 2008a) but this time the roof response and the earthquake excitation time signals used in the formation of the roof to base transfer function are modified. More specifically, the structure is assumed to have very light damping, e.g., 0.1% and the earthquake time signal is considered just up to the time step that the violation of the predefined interstorey drift limit occurs. A band of zeros then replaces the values of the rest of the earthquake signal that follows (Papagiannopoulos & Beskos, 2008a). The non – linear response of the roof is obtained by using the part of the earthquake time signal up to the time where violation of the interstorey drift occurs with the rest of the signal having zero values. Therefore, equivalent modal damping values calculated by using part of the earthquake time signal will be different from the ones found by considering the whole earthquake time signal. This procedure enables the calculation of deformation dependent equivalent modal damping ratios and is justified by current efforts in earthquake engineering to control the displacements of the structure.

On the other hand, equivalent modal damping value can be assigned only to these modes that appear in the transfer function. Modes that do not appear in the transfer function cannot be considered in the solution of Eq. (2) used for the quantification of the equivalent modal ratios but as it has been proven in (Papagiannopoulos & Beskos, 2006) they have to be taken into account for accurate response purposes. These higher modes that essentially correspond to high frequencies are not excited, behave statically and thus, a high damping value (100%) has to be taken into account for them (Papagiannopoulos & Beskos, 2008a, 2006). Regarding the proposed design scheme, a simple yet accurate solution is adopted for treating this issue of modal truncation. The number of modes taken into account in order to apply the modal combination rule is derived by considering the first modes that ensure 95% of modal mass participation in the response. Equivalent damping is considered for the modes that appear in the transfer function, while for the rest of the modes needed to satisfy the aforementioned modal mass participation requirement a very high value of damping (100%) is used.

4 Design curves

The proposed method to evaluate equivalent damping is applied to twenty MDOF steel moment resisting framed structures with periods varying between 0.5 and 3.0 sec. The time domain non – linear response of the MDOF structures for the long duration seismic excitations of Table 1 (Papagiannopoulos & Beskos, 2008b) was obtained by means of the computer program DRAIN – 2DX (Prakash, Powell & Campbell, 1993).

Table 1 Long duration seismic excitations.

Earthquake, Country	*Station*	*Date*
Tokachi Oki, Japan	HAC1, HAC2	16/05/1968
Valparaiso, Chile	LLO, LLA, ISI,VDM	03/03/1985
Michoachan, Mexico	SCT	19/09/1985
Manjil, Iran	AT2	20/06/1990
El Salvador, El Salvador	OB, ST	13/01/2001
Tokachi Oki, Japan	HKD 092, HKD 100	25/09/2003
Ica Pisca, Peru	ICA2	15/08/2007

Both geometrical and material non – linearities have been taken into account while the limit of allowable interstorey drift ratio (IDR) for the structures under study has been considered not to exceed the values of 0.6, 1.5 and 2.0% of their storey height for the limit states of fully operational, operational and life safety, respectively and the damage of structural elements cannot exceed acceptable values of plastic hinge rotations (Papagiannopoulos & Beskos, 2008b). Initial assumed damping was computed by Rayleigh's formula (Chopra, 2001), using the first mode and the last mode needed to obtain participation of modal mass greater than 95%.

Figures 2–4 illustrate the variation of equivalent damping with period for the case of 1.5% (IDR) and damage $\theta_p = \theta_y$, where θ_y stands for the yield rotation, and the first

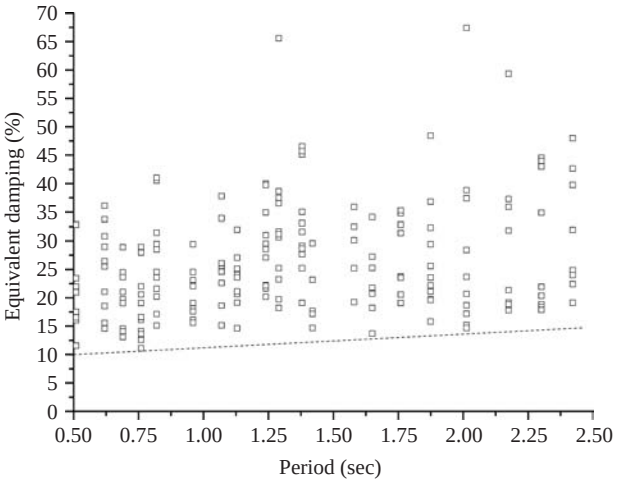

Figure 2 Design values for equivalent damping for 1.5% IDR and damage $\theta_p = \theta_y$ (1st mode).

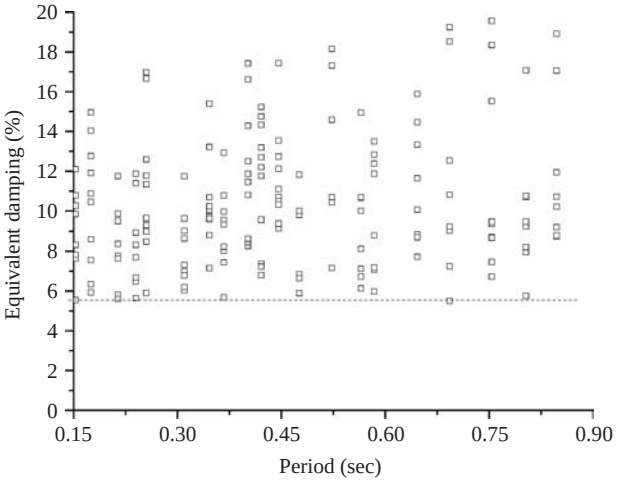

Figure 3 Design values for equivalent damping for 1.5% IDR and damage $\theta_p = \theta_y$ (2nd mode).

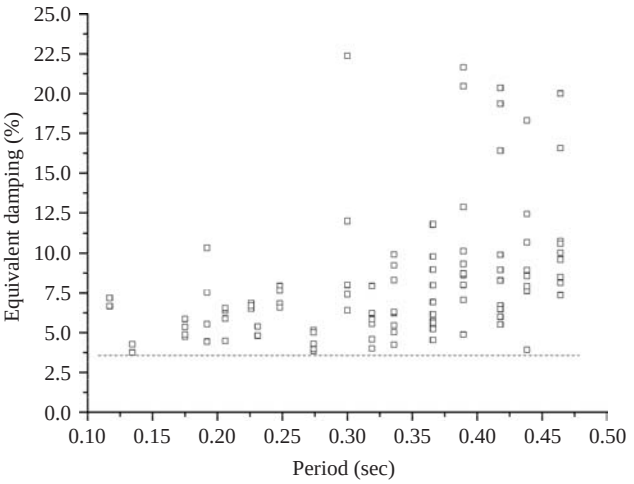

Figure 4 Design values for equivalent damping for 1.5% IDR and damage $\theta_p = \theta_y$ (3rd mode).

Table 2 Modal damping ξ as function of period T, IDR and damage.

Mode	*IDR* = *1.5%* and $\theta_p = \theta_y$	*IDR* = 2.0% and $\theta_p = 3.5\theta_y$
1	$\xi = 0.025 \cdot (T - 0.5) + 0.1$ for $0.5 \leq T \leq 2.5$ sec	$\xi = 0.47$ for $0.5 \leq T \leq 2.5$ sec
2	$\xi = 0.055$ for $0.15 \leq T \leq 0.85$ sec	$\xi = 0.11$ for $0.15 \leq T \leq 0.85$ sec
3	$\xi = 0.035$ for $0.11 \leq T \leq 0.48$ sec	$\xi = 0.10$ for $0.32 \leq T \leq 0.48$ sec
4	$\xi = 0.035$ for $0.11 \leq T \leq 0.27$ sec & $\xi = 0.8 \cdot (T - 0.27) + 0.035$ for $0.27 \leq T \leq 0.32$ sec	–
5	$\xi = 0.929 \cdot (T - 0.17) + 0.035$ for $0.17 \leq T \leq 0.24$ sec	–

three modes, respectively. The dashed lines in these figures indicate the design values for $IDR = 1.5\%$ and damage $\theta_p = \theta_y$. Design equations for equivalent modal damping for the cases of $IDR = 1.5\%$ and damage $\theta_p = \theta_y$ and $IDR = 2.0\%$ and damage $\theta_p = 3.5\theta_y$ are tabulated in Table 2 for the first five modes. In this table a dash is used for the modes that do not appear in the transfer function and implies that an equivalent damping of 100% has to be considered for them.

5 Numerical example

A moment resting framed structure having twelve stories and four bays is used to illustrate how Figs. 2–4 or Table 2 can be used for seismic design. HEB profiles are

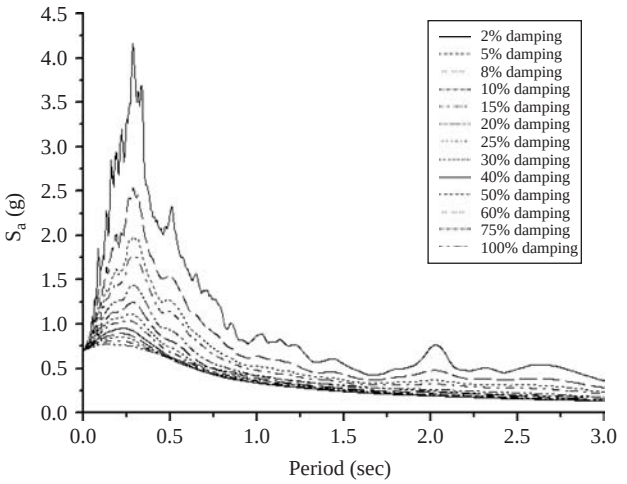

Figure 5 Elastic design spectrum for several damping values.

used for columns and IPE for beams. Each bay of the steel frame has 4.0 m span and each storey 3.0 m height. The dead plus live load on beams is equal to 27.5 KN/m. Interstorey drift is not allowed to surpass 1.5% of storey height and damage is limited to $\theta_p = \theta_y$. The structure has been designed according to EC3 (1992) and seismic hazard is defined by means of the mean plus one standard deviation damped elastic design spectrum of Fig. 5, which has been constructed using the seismic motions of Table 1 for several damping ratios (Papagiannopoulos & Beskos, 2008b).

Performing eigenvalue analysis one first obtains the mode shapes and the natural periods of the given structure. To ensure modal participation mass of 95%, five modes need to be taken into account. Equivalent damping for modes 1 to 5 comes from Table 2, while design acceleration from Fig. 5. The initial value for viscous modal damping of 2% in the elastic region was subtracted from the equivalent modal damping values for reasons of consistency (Papagiannopoulos & Beskos, 2008b). Equivalent modal damping ratios read as: $\xi_1 = 0.133$, $\xi_2 = 0.055$, $\xi_3 = 0.035$, $\xi_4 = 0.035$ and $\xi_5 = 0.05$. One finally has the following sections: 340/340/340/340/340-360 (1-5) & 320/320/320/320/320-360 (6-9) & 320/320/320/320/320-330 (10-12). The above notation, e.g., for the first set of numbers means that for the first five stories the column sections in each bay of the same storey are the same, i.e., sections HEB340, and all beams have IPE360 section.

Non – linear dynamic analyses are executed using the accelerograms of Table 1, in order to check if the designed frame satisfies the target performance criteria. The results from non – linear dynamic analyses (assuming an initial value for viscous modal damping of 2%) regarding median and maximum value for interstorey drift and plastic hinge rotation have as follows: $IDR_{med} = 1.45\%$, $IDR_{\max} = 1.49\%$, $\theta_{pl,med} = 1.01\theta_y$ and $\theta_{pl,\max} = 1.08\theta_y$. On the basis of these results, it is concluded that the proposed method of employing modal damping ratios results in good accuracy regarding values of seismic deformation and damage levels for the case examined.

The frame is now designed according to EC3 (1992) by employing the 2% damped acceleration spectrum of Fig. 5 and a common value for all modes for the reduction factor, i.e., $q = 4$. On the basis of the equal displacement rule for target $IDR = 1.5\%$ one finally finds the sections to be: 400/400/400/400/400-360 (1-5) & 360/360/360/360/320-330 (6-9) & 320/320/320/320/320-330 (10-12). Non – linear dynamic analyses are executed using the accelerograms of Table 1 in order to check if the designed frame satisfies the target performance criteria. The results from non – linear dynamic analyses (assuming an initial value for viscous modal damping of 2%) regarding median and maximum value for interstorey drift lead to $IDR_{med} = 1.27\%$, $IDR_{\max} = 1.32\%$. It is concluded that the conventional seismic design approach using a common value for all modes for the strength reduction factor results in overestimated values of seismic deformation for the considered seismic motions.

On the basis of the above results and similar results provided elsewhere (Papagiannopoulos & Beskos, 2008b), it can be said that the conventional method of employing a single modal value for the strength reduction factor leads to overestimation or underestimation of seismic deformation and damage levels, depending on the frame and the seismic motion expected, because it does not recognize the fact that each mode contributes in a different way to the final seismic response and design results. The proposed approach of using equivalent modal damping ratios leads to more accurate seismic response and design results in a more rational way.

6 Conclusions

On the basis of the preceding developments, the following conclusions can be stated:

- An equivalent linear MDOF structure has been proposed in order to determine the earthquake response of the original non – linear MDOF structure in an approximate yet of satisfactory accuracy way.
- This equivalent linear MDOF structure is constructed by retaining the mass and initial stiffness of the original non – linear MDOF structure and expressing material and geometrical non – linearities in the form of time – invariant modal damping values. These values can be viewed as playing the role of the strength reduction factor in code – based seismic design.
- Curves providing equivalent damping versus period for the first few modes as well as design acceleration for given equivalent damping are constructed. Thus, one can establish a seismic design method on the basis of modal synthesis and spectrum analysis.
- The proposed seismic design scheme can be viewed as an improvement to the force based method of current codes with equivalent modal damping values playing the role of the strength reduction factor.

Acknowledgements

The authors acknowledge the support provided by the European Social Fund (ESF), Operational Program for Educational and Vocational Training I (EPEAEK I), through the Greek Program PYTHAGORAS I of the Greek Ministry of Education and Religious Affairs.

References

Chopra, A.K. 2001. *Dynamics of structures*. New Jersey: Prentice Hall.

EC3. 1992. *Eurocode 3, Design of steel structures, Part 1.1: General rules for buildings, European Prestandard ENV 1993-1-1/1992*. European Committee for Standardization (CEN): Brussels.

Papagiannopoulos, G.A. & Beskos, D.E. 2006. On a modal damping identification model for building structures. *Archive of Applied Mechanics* 76: 443–463.

Papagiannopoulos, G.A. & Beskos, D.E. 2008a. Use of equivalent modal damping for seismic design of steel structures, Part I: Theoretical aspects. *Earthquake Engineering and Structural Dynamics (submitted)*.

Papagiannopoulos, G.A. & Beskos, D.E. 2008b. Use of equivalent modal damping for seismic design of steel structures, Part II: Applications. *Earthquake Engineering and Structural Dynamics (submitted)*.

Prakash, V., Powell, S. & Campbell, S. 1993. *DRAIN 2DX – Base Program Description and User Guide, Version 1.10*. Report No.UCB/SEMM-93/17: University of California at Berkeley.

Chapter 27

Bayesian updating and model class selection of deteriorating hysteretic structural models using recorded seismic response

James L. Beck & Matthew M. Muto

California Institute of Technology, Pasadena, USA

ABSTRACT: Identification of structural models from measured earthquake response can play a key role in structural health monitoring, structural control and improving performance-based design. System identification using data from strong seismic shaking is complicated by the nonlinear hysteretic response of structures where the restoring forces depend on the previous time history of the structural response rather than on an instantaneous finite-dimensional state. Furthermore, this inverse problem is ill-conditioned because even if some components in the structure show substantial yielding, others will exhibit nearly elastic response, producing no information about their yielding behavior. Classical least-squares or maximum likelihood estimation will not work with a realistic class of hysteretic models because it will be unidentifiable based on the data. On the other hand, the combination of Bayesian updating and model class selection provides a powerful and rigorous approach to tackle this problem, especially when implemented using Markov Chain Monte Carlo simulation methods such as the Metropolis-Hastings, Gibbs Sampler and Hybrid Monte Carlo algorithms. The emergence of these stochastic simulation methods in recent years has led to a renaissance in Bayesian methods across all disciplines in science and engineering because the high-dimensional integrations that are involved can now be readily evaluated. The power of these methods to handle ill-conditioned or unidentifiable system identification problems is demonstrated by using a recently-developed stochastic simulation algorithm, Transitional Markov Chain Monte Carlo, to perform Bayesian updating and model class selection on a class of Masing hysteretic structural models that are relatively simple yet can give realistic responses to seismic loading. Examples are given using deteriorating hysteretic building models with simulated seismic response data.

1 Introduction

Current methods for developing finite-element models can produce structural responses that are consistent qualitatively with behavior observed during strong earthquake shaking, but there has long been an interest in using system identification methods for quantitative assessment of structural models using recorded seismic response. The objective may be to improve the predictive capabilities of structural models for dynamic design or for the design of structural control systems, or to implement structural health monitoring. System identification based on updating of finite-element models using measured seismic response is challenging, however, because the large

number of uncertain parameters associated with realistic structural models makes the inverse problem extremely ill-conditioned.

Simplified models can be used in the identification procedure but the selection of an appropriate class of models to employ is complicated by the nonlinear response of structures under strong seismic loading; in particular, the structural restoring forces are hysteretic, depending on the previous time history of the structural response rather than on an instantaneous finite-dimensional state. Although some research into the identification of hysteretic systems has been carried out (Jayakumar 1987, Jayakumar & Beck 1988, Cifuentes & Iwan 1989, Thyagarajan 1989, Benedettini et al. 1995, Smyth et al. 1999, Yang & Lin 2004, Ashrafi et al. 2005, Ashrafi & Smyth 2007), this previous work did not quantify the modeling uncertainties and did not properly deal with the ill-conditioning inherent in this inverse problem. However, the uncertainty associated with structural model predictions can have a significant impact on the decision-making process in structural design, control and health monitoring. Furthermore, classical estimation techniques such as least-squares and maximum likelihood do not usually work properly when applied to hysteretic model classes because they are nearly always unidentifiable based on the available data.

The Bayesian updating approach treats the probability of all models within a set of candidate models for a system, and consequently has the advantage of being able to quantify all of the uncertainties associated with modeling of a system and to handle ill-conditioned identification problems. Note that the probability of a model will not make sense if one interprets probability as a long-run frequency of an event, but it does when probability is interpreted as a multi-valued logic that expresses the degree of plausibility of a proposition conditioned on the given information (Jaynes 2003). Although Bayesian methods are widely used in many fields, their application to identification of dynamic hysteretic dynamic models seems to be very limited.

Many applications of Bayesian methods to model updating and model class selection for systems using dynamic response measurements have primarily used the Laplace asymptotic approximation (Beck & Katafygiotis 1991, 1998, Papadimitriou et al. 2001, Katafygiotis & Lam 2002, Beck & Yuen 2004). However, this approximation is most useful when there is a large amount of data and the model class is globally identifiable (described later); furthermore, in high-dimensional systems, optimization to find the required most probable parameter vectors can be computationally challenging. To avoid these difficult optimizations and to more readily treat cases where the model class is not globally identifiable, in recent years attention has been focused on stochastic simulation methods for Bayesian updating and prediction, especially Markov Chain Monte Carlo methods, such as the Metropolis-Hastings (e.g. Hastings 1970, Beck & Au 2002, Ching & Chen 2007), Gibbs Sampler (e.g. Ching et al. 2005, 2006) and Hybrid Monte Carlo algorithms (e.g. Robert & Casella 1999). The emergence of these stochastic simulation methods has led to a renaissance in Bayesian methods across all disciplines in science and engineering because the high-dimensional integrations involved can now be readily evaluated.

2 Bayesian model updating

A Bayesian statistical framework for model updating and predictions for linear or nonlinear dynamic systems that explicitly treats prediction-error and other model

uncertainties has been presented (Beck 1989, Beck & Katafygiotis 1991, 1998). A basic concept in this framework is that any set of possible deterministic dynamic models for a system can be embedded in a set of predictive probability models for the system by specifying a probability distribution for the uncertain prediction error, which is the difference between the actual system output and the deterministic model output; in particular, modeling the prediction error as a zero-mean, stationary, white-noise Gaussian stochastic process is supported by the Principle of Maximum Differential Entropy (Jaynes 2003). Each predictive probability model is assumed to be uniquely specified by assigning a value to a model parameter vector. Therefore, a probability distribution over the set of possible predictive models that specifies the plausibility of each such model is equivalent to a probability distribution over a corresponding set of possible values for the model parameter vector. When dynamic data is available from the system, a chosen initial (prior) probability distribution over the parameters can be updated using Bayes' Theorem to give a posterior probability distribution, as follows.

Consider a *Bayesian model class* $\mathcal{M}$, which is characterized by: (i) a set of *predictive* PDFs (probability density functions), $p(\mathcal{D} \mid \theta, \mathcal{M})$, for system response $\mathcal{D}$ that is parameterized by N_p model parameters $\theta \in \Theta \subset \mathbb{R}^{N_p}$; and (ii) a chosen *prior* PDF $p(\theta \mid \mathcal{M})$ that can incorporate additional knowledge of the system. The prior PDF is chosen to express the initial plausibility of each model in the class $\mathcal{M}$ defined by the value of the parameter vector θ.

Now suppose a set of data $\mathcal{D}$ from the system is available. The goal of Bayesian updating is to use $\mathcal{D}$ to update the probability distribution over the parameters to give the posterior PDF $p(\theta|\mathcal{D}, \mathcal{M})$ based on Bayes' Theorem:

$$p(\theta|\mathcal{D}, \mathcal{M}) \propto p(\mathcal{D}|\theta, \mathcal{M})\, p(\theta|\mathcal{M}) \tag{1}$$

Here, $p(\mathcal{D}| \theta, \mathcal{M})$ as a function of θ is called the *likelihood function*. The constant of the proportionality is the reciprocal of $p(\mathcal{D}|\mathcal{M})$, the *evidence* for model class $\mathcal{M}$, and it is discussed later. The posterior PDF gives the updated plausibility of each model in $\mathcal{M}$ when the information in the data $\mathcal{D}$ is incorporated.

For a given model class $\mathcal{M}$ and data $\mathcal{D}$, it is useful to characterize the topology of the posterior PDF as a function of the model parameter vector by whether it has a global maximum at a single most probable parameter value, at a finite number of them, or at a continuum of most probable parameter values lying on some manifold in the parameter vector space. These three cases may be described as globally identifiable, locally identifiable, and unidentifiable model classes based on given dynamic data from the system.

3 Bayesian model class selection

Bayesian model class selection (or model comparison) is essentially Bayesian updating at the model class level to make comparisons between alternative candidate model classes for predicting the response of a system. It has long been recognized that comparisons between model classes should factor in not only the quality of the data fit, but also the complexity of the model. Jeffreys referred to the need for a "simplicity postulate," that is, simpler models that are consistent with the data should be preferred over more complex models which offer only slight improvements in the fit to the data

(Jeffreys 1939). Early quantitative forms for a Principle of Model Parsimony utilized a penalty term against using a larger number of uncertain (adjustable) parameters in combination with a quantification of the model data-fit based on the log likelihood of the optimal model in the model class (Akaike 1974); however, the form of this penalty term did not have a very rigorous basis. Subsequent work made it clear that Bayes' Theorem at the model class level automatically enforces model parsimony without ad-hoc penalty terms (Gull 1989, Mackay 1991, Beck & Yuen 2004).

Consider a set $\mathbf{M} \equiv \{\mathcal{M}_j : j = 1, \ldots, N_M\}$ of N_M candidate model classes for representing a system. Given data $\mathcal{D}$, the posterior probability of each model class $P(\mathcal{M}_j \mid \mathcal{D},\mathbf{M})$, $j = 1, \ldots, N_M$, is:

$$P(\mathcal{M}_j|\mathcal{D}, \mathbf{M}) = \frac{p(\mathcal{D}|\mathcal{M}_j)P(\mathcal{M}_j|\mathbf{M})}{\sum_{i=1}^{N_M} p(\mathcal{D}|\mathcal{M}_i)P(\mathcal{M}_i|\mathbf{M})} \tag{2}$$

If all model classes are treated as equally plausible a priori, then the probability of model class $\mathcal{M}_j$ is proportional to its evidence,

$$p(\mathcal{D}|\mathcal{M}_j) = \int p(\mathcal{D}|\theta_j, \mathcal{M}_j)p(\theta_j|\mathcal{M}_j)\, d\theta_j \tag{3}$$

3.1 *Information-theoretic interpretation*

Further insight into the form of this penalty against complexity can be obtained by considering the evidence from an information-theoretic point of view (Ching et al. 2005). Consider the log of the evidence:

$$\begin{aligned} \ln[p(\mathcal{D}|\mathcal{M}_j)] &= \int \ln\left[\frac{p(\mathcal{D}|\theta_j, \mathcal{M}_j)\, p\,(\theta_j|\mathcal{D}, \mathcal{M}_j)}{p(\theta_j|\mathcal{D}, \mathcal{M}_j)}\right] p(\theta_j|\mathcal{D}, \mathcal{M}_j)\, d\theta_j \\ &= \int \ln[p(\mathcal{D}|\theta_j, \mathcal{M}_j)]p(\theta_j|\mathcal{D}, \mathcal{M}_j)\, d\theta_j \\ &\quad - \int \ln\left[\frac{p(\theta_j|\mathcal{D}, \mathcal{M}_j)}{p(\theta_j|\mathcal{M}_j)}\right] p(\theta_j|\mathcal{D}, \mathcal{M}_j)\, d\theta_j \end{aligned} \tag{4}$$

This formulation for the log evidence for model class $\mathcal{M}_j$ shows that it is the difference between two terms: the first term is the posterior mean of the log-likelihood function, which is a measure of the average data fit for model class $\mathcal{M}_j$, while the second term is the relative entropy between the prior and posterior distributions, which is a measure of the information gained about the parameters θ_j from the data $\mathcal{D}$. Therefore, the log evidence is comprised of a data-fit term and a term which provides a penalty against more "complex" models that extract more information from the data. This gives an intuitive understanding of why the application of Bayes' Theorem at the model class level automatically enforces Ockham's razor: "Pluralitas non est ponenda sine neccesitate" ("entities should not be multiplied unnecessarily"). Although this information-theoretic interpretation was initially presented in Beck & Yuen (2004),

it was derived there using a large-sample Laplace asymptotic approximation that depended on global identifiability of the model classes.

4 Applying Bayesian methods using stochastic simulation

The goal of the stochastic simulation methods is to generate samples which are distributed according to the posterior probability density function (PDF) described in Equation 1. In this work, we focus specifically on Markov Chain Monte Carlo (MCMC) methods that are most useful for Bayesian updating. One advantage of these methods is that non-normalized PDFs can be sampled, so that samples may be drawn from the posterior PDF without evaluating the normalizing constant (the evidence) that usually requires evaluating a high-dimensional integral over the parameter space. A remaining challenge associated with model updating by stochastic simulation is the fact that, unless the data is very sparse, the posterior PDF occupies a much smaller volume in the parameter space than the prior PDF over the parameters. This fact makes it difficult to draw samples from the posterior PDF.

Commonly-implemented MCMC methods, such as the Metropolis-Hastings (M-H) algorithm, are difficulty to apply in higher-dimensional parameter spaces since it is often difficult to draw samples that cover all regions of high-probability content. An alternative sampling algorithm (Beck & Au 2002) proposed gradual updating of the model, using the M-H algorithm to sample from a sequence of target PDFs, each target PDF being the posterior PDF based on an increasing fraction of the available data. In this manner, the target PDF gradually converges from the broad prior PDF to the final concentrated posterior PDF. The Transitional Markov Chain Monte Carlo (TMCMC) method used in this study is a modified version of this approach (Ching & Chen 2007). This technique also uses a sequence of intermediate PDFs. The novel feature of this algorithm is that, rather than applying updating with part of the available data, the entire data set is used but its full effect is diluted by taking the target PDF for the mth level of the sampler to be proportional to $p(\mathcal{D}|\theta, \mathcal{M})^{\beta_m} p(\theta|\mathcal{M})$, where $0 \leq \beta_m \leq 1$; here, $\beta_0 = 0$ gives the initial target distribution proportional to the prior PDF and $\beta_M = 1$ for the final level of the sampler gives a target distribution proportional to the posterior PDF. The TMCMC algorithm can also be used to estimate the evidence for a model class (Ching & Chen 2007).

5 Masing hysteretic models

Modeling hysteretic force-deformation relations for structural members and assemblages of members from constitutive equations ("plasticity models") is a difficult task, due to factors such as complex stress distributions, material inhomogeneities and the large number of structural elements. An alternative approach is to develop simplified models that capture the essential features of the hysteretic force-deformation relationship but then, lacking a fundamental theoretical basis, these models should be validated against the observed behavior of structures. An example of this type of model is the well-known Bouc-Wen model (Wen 1976). While these models are mathematically convenient, especially for random vibration studies using equivalent linearization, when subjected to asymmetric cyclic loading, they can exhibit an unphysical "drifting"

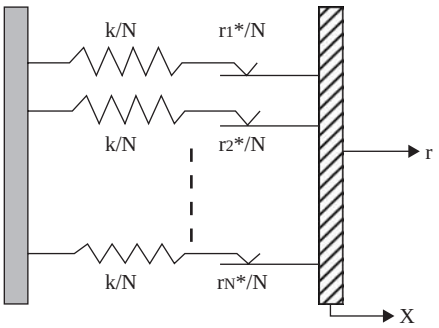

Figure 1 Conceptual sketch for the Distributed Element Model (DEM) (taken from Chiang 1992).

behavior (Jayakumar 1987). This makes them unsuitable as a class of identification models for strong seismic response where this type of irregular loading occurs.

A simplified hysteretic model with a physical basis was presented by Masing (1926), based on the hypothesis that a one-dimensional hysteretic system may be viewed as a collection of ideal elasto-plastic elements (a linear spring in series with a Coulomb damper) with the same elastic stiffness but with a distribution of different yield strengths. This idea was used in structural dynamics by Iwan (1966) to form the Distributed Element Model (DEM), which consists of a collection of N ideal elasto-plastic elements connected in parallel with a common stiffness k/N for the springs but different yield strengths $r_i^*/N, i = 1, \ldots, N$, as shown in Figure 1. The restoring force r of a single-degree of freedom DEM subjected to a displacement x under initial loading is given by:

$$r = \sum_{i=1}^{n} \frac{r_i^*}{N} + kx\frac{N-n}{N} \tag{5}$$

where n is the number of yielded elements. Infinite collections of elasto-plastic elements can be considered by introducing a yield strength distribution function $\varphi(r^*)$ such that the restoring force $r(x)$ is given by:

$$r(x) = \int_0^{kx} r^*\phi(r^*)\,dr^* + kx\int_{kx}^{\infty} \phi(r^*)\,dr^* \tag{6}$$

Because there is an underlying physical basis for the model, DEMs with a finite number of elements have been shown to give good representations of the hysteretic behavior of some structures, and do not exhibit the previously-discussed drifting behavior. However, DEMs with an infinite number of elements are difficult to implement directly, in contrast to the finite case where the state of each element is tracked, although there have been recent advances in this area (Ashrafi et al. 2005, Ashrafi & Smyth

2007). Fortunately, the class of Masing hysteretic models exactly describes the behavior of DEMs without needing to keep track of the internal behavior of the elements. Jayakumar showed that the hysteretic behavior under arbitrary loading is completely described by the initial loading curve, described by the function $f(x, r)$ and a relatively simple set of rules (Jayakumar 1987). Chiang (1992) later demonstrated the inverse relationship, that is, given an initial loading curve for a Masing model, one can find the yield strength distribution, $\varphi(r^*)$ in Equation 6, for the equivalent DEM.

5.1 *Masing shear building model*

Jayakumar and Beck (1988) modeled an n-story shear building in 2-D by applying the Masing model to the relationship between story shear forces and the inter-story drifts. Consider a structural model where the vector of relative floor displacements $x(t)$ is related to the ground acceleration $\ddot{y}(t)$ as follows:

$$M\ddot{x} + C\dot{x} + R = -Mb\ddot{y}(t) \tag{7}$$

where M is the mass matrix, C is the viscous damping matrix, and R is the vector of restoring forces. The inter-story shear force at the ith story is given by:

$$R_i = r_i - r_{i+1} \tag{8}$$

In this work, the initial loading curve relating story shear forces and inter-story drifts is specified by choosing a generalized Rayleigh distribution for the yield strength distribution function (Chiang 1992). The resulting backbone curve is defined by following differential equation:

$$\dot{r}_i = K_i(\dot{x}_i - \dot{x}_{i-1}) \exp\left[-\left(\Gamma\left(1 + \frac{\eta_i + 1}{\eta_i}\right) \frac{K_i\,(x_i - x_{i-1})}{r_{u,i}} \right)^{\eta_i} \right] \tag{9}$$

where K_i is the small-amplitude inter-story stiffness, $r_{u,i}$ is the story ultimate strength, η_i controls the smoothness of the transition from elastic to plastic and $\Gamma(.)$ is the Gamma function. Figure 2 shows how the shape of the initial loading curve is influenced by η_i. Note that for $i = n$ in Equation 8, $r_{n+1} = 0$, and for $i = 1$ in Equation 9, $x_0 = 0$.

A potentially important advantage of the Masing shear building model is that all model parameters, except η_i, correspond to actual physical properties (initial stiffness, ultimate strength) and initial estimates can be calculated from material properties and structural drawings.

5.2 *Deteriorating Masing model*

A modified version of the DEM was developed for modeling deteriorating systems (Cifuentes & Iwan 1989). The model again consists of a collection of linear springs and slip elements, however, in this case an element is allowed to "break" if a certain maximum displacement is exceeded, defined as $\mu x_{y,i}$, where $x_{y,i}$ is the yield displacement of the ith element and μ is the breaking ductility ratio, which for simplicity is assumed to be the same for all elements.

The deteriorating DEM was successfully applied to system identification and damage detection of real structures using earthquake data (Cifuentes & Iwan 1989). However,

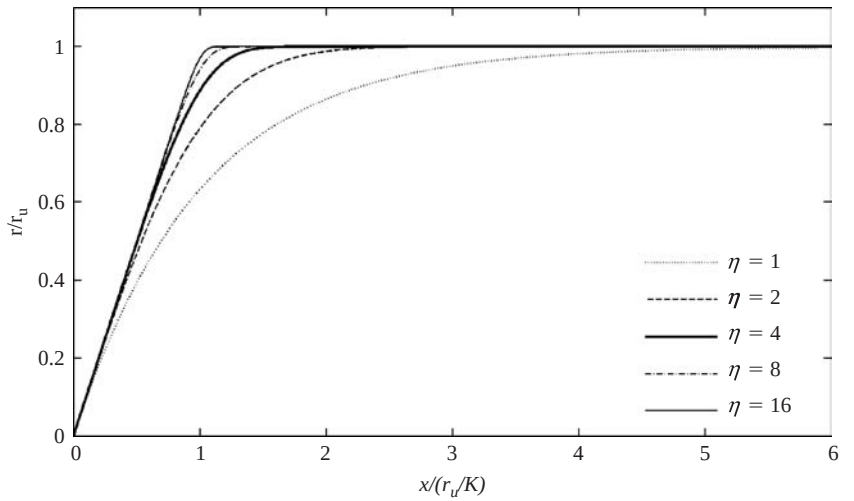

Figure 2 Initial loading curves for different values of the elastic-to-plastic transition parameter η.

as in the case of non-deteriorating DEMs, there are restrictions in terms of the number of parameters that limit the applicability of the model. Chiang (1992) developed a general formulation for deteriorating Masing models, determined the specific form for a Masing model equivalent to the displacement-controlled DEM, and developed expressions for the initial loading, unloading and reloading curves given a backbone curve $f(x, r)$ and the breaking ductility ratio μ. Figure 3 shows how the monotonic loading curve for a deteriorating Masing model, whose non-deteriorating form is shown in Figure 2 for $\eta = 4$, is influenced by μ.

6 Example

To illustrate the application of Bayesian methods to ill-conditioned systems, we consider a three-story deteriorating Masing shear building model with parameters as given in Table 1. The system is subjected to two different ground motion excitations, both recorded during the 1994 Northridge, California earthquake ($M_w = 6.7$). The first record was obtained at the Coldwater Canyon School in North Hollywood, 12.5 km from the fault, with a peak acceleration of 3.13 m/s^2. The second was recorded at Olive View Hospital in Sylmar, 9.9 km from the fault, with a peak acceleration of 5.92 m/s^2. The first ten seconds of each record are used to generate acceleration responses for the system. The data sets generated from the Coldwater Canyon and Olive View records will be referred to as $\mathcal{D}_{CC}$ and $\mathcal{D}_{OV}$, respectively. The viscous damping matrix C in Equation 7 is omitted, as this study is primarily concerned with identifying properties associated with large structural deformations, while viscous damping is generally used to model small-amplitude energy dissipation.

For each ground-motion record, 500 time-steps of simulated acceleration are "measured" at each floor. To provide a realistic level of prediction error, Gaussian discrete white noise with a standard deviation of 1 m/s^2, corresponding to approximately 40%

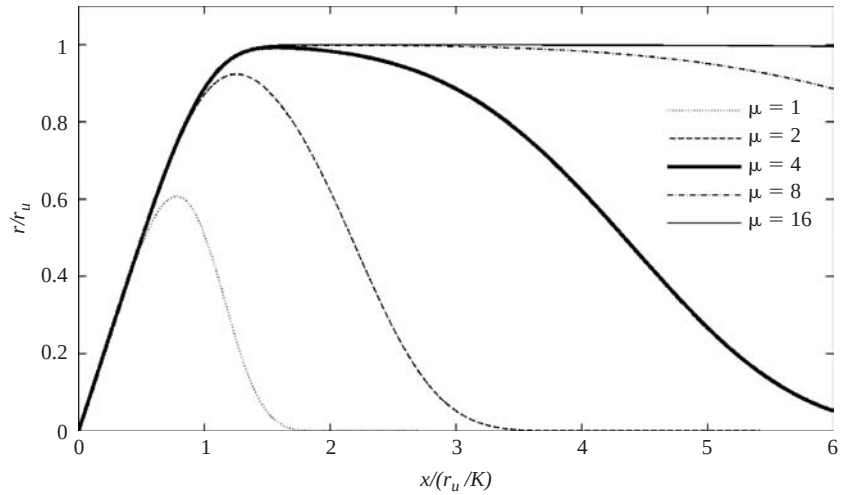

Figure 3 Monotonic loading curves for a deteriorating Masing hysteretic model for different values of the breaking ductility ratio μ.

Table 1 Parameters for Masing shear building system used to generate data.

Story	*Mass (kg)*	*K (N/m)*	r_u *(N)*	η	μ
1st	1.25×10^5	2.50×10^8	1.75×10^6	2	6.5
2nd	1.25×10^5	2.50×10^8	1.75×10^6	2	6.5
3rd	1.25×10^5	2.00×10^8	1.40×10^6	2	6.5

of the RMS value of the acceleration data, is added to each channel of data. Two identification model classes are considered, both of which are Masing hysteretic shear-building models as defined by Equations 7-9. These model classes are used to generate vectors of predicted floor accelerations $a_t^{(i)}$, $i = 1, 2, 3$, $t = 1, \ldots, 500$. The prediction-error for the system output is modeled as Gaussian with a variance of σ^2 for each measurement, so the likelihood function is given by:

$$p(\mathcal{D}|\theta, \mathcal{M}) = \frac{1}{(2\pi\sigma^2)^{\frac{1500}{2}}} \exp\left[-\frac{1}{2\sigma^2}\sum_{i=1}^{3}\sum_{t=1}^{500}(a_t^{(i)}(\theta) - \hat{a}_t^{(i)})^2\right] \tag{10}$$

where $\hat{a}_t^{(i)}$ is the measurement for channel i at time-point t and θ is the vector of parameters to be updated. Model class $\mathcal{M}_1$ is a non-deteriorating model with ten free parameters, the small-amplitude stiffness K_i, ultimate strength $r_{u,i}$ and elastic-to-plastic transition parameter η_i for each story, $i = 1,2,3$, and the prediction-error variance σ^2. Model class $\mathcal{M}_2$ is a deteriorating model with the same ten free parameters included in $\mathcal{M}_1$ and one additional parameter, the breaking ductility ratio μ, which is constrained such that $\mu_i = \mu$, $i = 1,2,3$. For both model classes, the mass matrix M is assumed to be

Table 2 Sample means for posterior samples generated by updating with $\mathcal{D}_{CC}$ (standard deviations in parentheses) compared to values obtained by optimization of posterior PDF.

Model		K_1 (10^8 N/m)	K_2 (10^8 N/m)	K_3 (10^8 N/m)	$r_{u,1}$ (10^6 N)	$r_{u,2}$ (10^6 N)	$r_{u,3}$ (10^6 N)	η_1	η_2	η_3	μ	σ (m/s^2)
Sim	$\mathcal{M}_1$	2.54	2.45	2.00	1.78	2.00	1.60	1.90	1.81	2.15	–	1.00
		(0.03)	(0.04)	(0.02)	(0.04)	(0.22)	(0.51)	(0.10)	(0.21)	(0.59)	–	(0.02)
Opt	$\mathcal{M}_1$	2.53	2.46	2.00	1.75	1.87	1.64	1.96	1.87	1.86	–	1.00
Sim	$\mathcal{M}_2$	2.58	2.47	1.98	1.80	2.04	1.79	1.79	1.69	2.18	8.04	1.00
		(0.04)	(0.05)	(0.02)	(0.04)	(0.20)	(0.81)	(0.10)	(0.19)	(0.66)	(1.68)	(0.02)
Opt	$\mathcal{M}_2$	2.57	2.48	1.99	1.80	1.97	1.47	1.81	1.71	2.03	7.53	1.00

Table 3 Sample means for posterior samples generated by updating with $\mathcal{D}_{OV}$ (standard deviations in parentheses) compared to values obtained by optimization of posterior PDF.

Model		K_1 (10^8 N/m)	K_2 (10^8 N/m)	K_3 (10^8 N/m)	$r_{u,1}$ (10^6 N)	$r_{u,2}$ (10^6 N)	$r_{u,3}$ (10^6 N)	η_1	η_2	η_3	μ	σ (m/s^2)
Sim	$\mathcal{M}_1$	2.24	2.77	2.07	1.75	2.51	2.45	2.22	1.00	1.32	–	1.08
		(0.02)	(0.07)	(0.02)	(0.02)	(0.23)	(0.62)	(0.10)	(0.01)	(0.21)	–	(0.02)
Opt	$\mathcal{M}_1$	2.23	2.79	2.08	1.75	2.47	2.72	2.20	0.98	1.20	–	1.08
Sim	$\mathcal{M}_2$	2.46	2.54	2.01	1.76	1.81	1.60	2.01	1.79	1.98	6.56	0.98
		(0.03)	(0.04)	(0.03)	(0.02)	(0.05)	(0.37)	(0.07)	(0.12)	(0.67)	(0.13)	(0.02)
Opt	$\mathcal{M}_2$	2.46	2.53	2.01	1.74	1.75	1.67	2.08	1.88	1.72	6.53	0.97

known, which is a reasonable assumption since the masses can be accurately computed from structural drawings.

Prior PDFs for the inter-story stiffness, strength, and breaking ductility ratios, were taken to be independent lognormal distributions with logarithmic means of $\ln(2.50 \times 10^8)$, $\ln(1.75 \times 10^8)$ and $\ln(8)$, respectively, and a lognormal standard deviation of 0.5. The prior PDFs for each of the elastic-to-plastic transition parameters were also lognormal, with a logarithmic mean of $\ln(2)$ and a logarithmic standard deviation of 1. The prior PDF for the prediction-error variance was taken to be a uniform distribution between 0 and 3.

Samples from the posterior PDF were generated using the TMCMC algorithm. Three runs were performed for updating with each data set, with 600 samples generated per run. Tables 2 and 3 show the sample means for each parameter for updating with data sets $\mathcal{D}_{CC}$ and $\mathcal{D}_{OV}$, respectively, compared with the parameter values obtained by direct numerical optimization of the posterior PDF. Convergence of the optimization algorithm was slow and only achieved when the initial parameter estimates were based on the stochastic simulation results.

For updating with the smaller-amplitude data set, $\mathcal{D}_{CC}$, estimates of inter-story stiffnesses are fairly well-constrained, and close to the actual values. However, since there is relatively little non-linear behavior, there are larger uncertainties associated with the strength and elastic-to-plastic transition parameters, and especially the breaking ductility ratio in model class $\mathcal{M}_2$, since there is very little deterioration in the actual system. Figure 4 shows the posterior samples obtained by updating model class $\mathcal{M}_2$

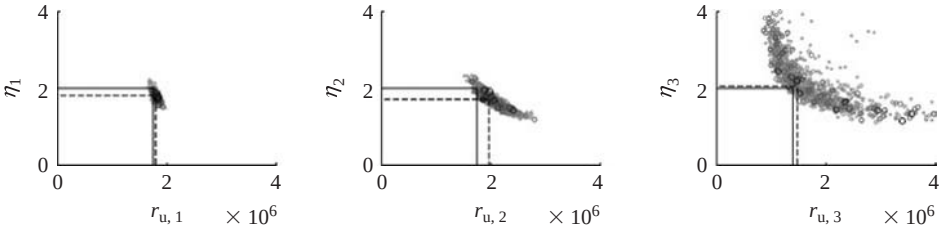

Figure 4 Samples generated by updating the deteriorating model class $\mathcal{M}_2$ with $\mathcal{D}_{CC}$, projected onto the $\{r_{u,i}, \eta_i\}$ sub-spaces. Dashed lines indicate results of numerical optimization of the posterior and solid indicate the actual values used to generate the data.

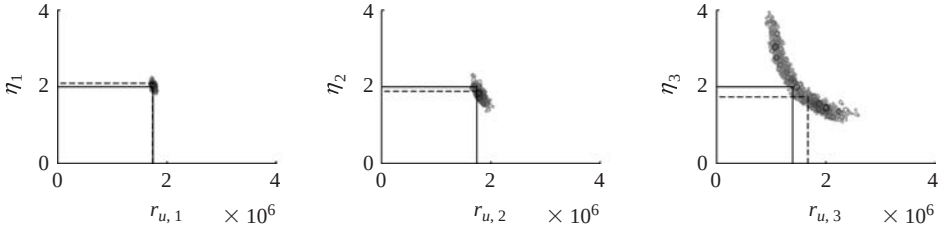

Figure 5 Samples generated by updating the deteriorating model class $\mathcal{M}_2$ with $\mathcal{D}_{OV}$, projected onto the $\{r_{u,i}, \eta_i\}$ sub-spaces. Dashed lines indicate results of numerical optimization of the posterior and solid indicate the actual values used to generate the data.

with data set $\mathcal{D}_{CC}$, projected onto the $\{r_{u,i}, \eta_i\}$ sub-space for each story. Note that the parameters for the first story, where the greatest inter-story shear forces and displacements occur, are fairly well-constrained, despite the 40% RMS noise. However, for the parameters for the second and third stories, where there is much less inelastic response, the samples are distributed over a broad region of the parameter space.

For updating model class $\mathcal{M}_1$ with the large-amplitude data set, $\mathcal{D}_{OV}$, estimates of many of the parameters, including some inter-story stiffnesses, are substantially different from the actual values, because there is significant deterioration involved in the response of the structure, which cannot be accounted for in $\mathcal{M}_1$. As expected, the identified parameter values for model class $\mathcal{M}_2$, which contains the system used to generate the data, are much closer to the actual values. However, there is still some uncertainty associated with the third-story yielding parameters, as shown in Figure 4, which shows the posterior samples obtained by updating model class $\mathcal{M}_2$ with data set $\mathcal{D}_{OV}$, projected onto the $\{r_{u,i}, \eta_i\}$ sub-space for each story. Note that the samples are distributed in a more concentrated region than those obtained by updating with $\mathcal{D}_{CC}$ (shown in Figure 4).

Table 4 summarizes the results for Bayesian model class selection. The log-evidence and average log-likelihood for each model class are estimated using the samples generated from stochastic simulation. The information gain is then calculated from these quantities using Equation 4. For data set $\mathcal{D}_{CC}$, the deteriorating model class $\mathcal{M}_2$ is preferred, but there is significant probability for the non-deteriorating model class $\mathcal{M}_1$. However, for data set $\mathcal{D}_{OV}$, model class $\mathcal{M}_2$ is overwhelmingly preferred. The

Table 4 Bayesian model class selection results.

Data	*Model Class*	*Log Evidence*	*Log Likelihood*	*Information Gain*	$P(\mathcal{M}\|\mathcal{D})$
$\mathcal{D}_{CC}$	$\mathcal{M}_1$	−2158.8	−2132.7	26.1	0.162
$\mathcal{D}_{CC}$	$\mathcal{M}_2$	−2157.2	−2130.9	26.3	0.838
$\mathcal{D}_{OV}$	$\mathcal{M}_1$	−2272.2	−2242.7	29.5	0.000
$\mathcal{D}_{OV}$	$\mathcal{M}_2$	−2137.9	−2098.9	39.0	1.000

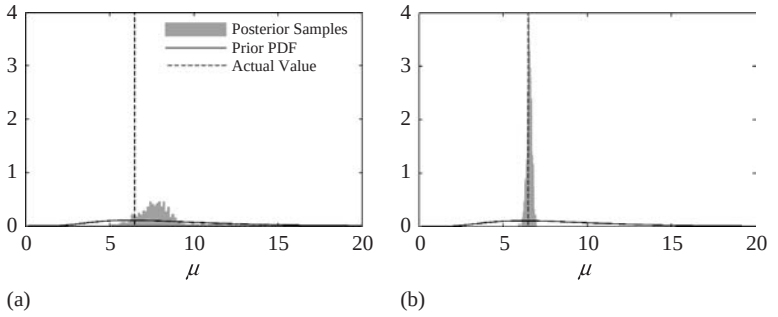

Figure 6 Prior PDFs for the breaking ductility ratio plotted against normalized histograms of posterior samples for updating model class $\mathcal{M}_2$ with (a) data set $\mathcal{D}_{CC}$ and (b) data set $\mathcal{D}_{OV}$.

difference in the accuracy of the two model classes, as expressed by the average log-likelihood, is large enough to more than compensate for the extra information extracted by model class $\mathcal{M}_2$.

The difference in the information gained for the two data sets is illustrated by Figure 6, which shows normalized histograms of the posterior samples for the breaking ductility ratio μ in model class $\mathcal{M}_2$, plotted with the prior PDF. Updating with data set $\mathcal{D}_{CC}$, which features little deterioration, results in a broad posterior PDF that is fairly similar to the prior PDF. However, updating with $\mathcal{D}_{OV}$ results in a very peaked posterior PDF for μ that indicates more information has been extracted from the data.

7 Concluding remarks

Bayesian methods for model updating and model class selection can be used to study systems which are essentially unidentifiable using classical system identification approaches. Additionally, viewing the problem of model class selection in a Bayesian context allows for a quantitative form for a Principle of Model Parsimony with an information-theoretic interpretation of model complexity (it relates to the amount of information extracted from the data by the model class).

Stochastic simulation is an effective tool for the application of Bayesian methods. In the presented example of a deteriorating hysteretic system, it is used to generate samples for a posterior PDF with a complex geometry in the parameter space that is based on very noisy data. These samples may be used for understanding the topology of the posterior PDF and estimating its moments, as well as estimating the evidence for each

model class in a set of proposed candidates for representing the system behavior, which can then be used to compute the posterior probability of each candidate model class. The samples from the posterior PDF may also be used to make robust probabilistic predictions of the system's response based on each model class or the whole set of candidate model classes (Muto & Beck 2008).

References

Akaike, H. 1974. A new look at the statistical identification model, *IEEE Transactions on Automatic Control*, 19, 716–723.

Ashrafi, S.A., Smyth, A.W. & Betti, R. 2005. A parametric identification scheme for non-deteriorating and deteriorating non-linear hysteretic behavior, *Structural Control and Health Monitoring*, 13, 108–131.

Ashrafi, S.A. & Smyth, A.W. 2007. Generalized Masing approach to modeling hysteretic deteriorating behavior, *Journal of Engineering Mechanics*, 133, 495–505.

Beck, J.L. 1989. Statistical system identification of structures, 5th *International Conference on Structural Safety and Reliability*, San Francisco, California.

Beck, J.L. & Au, S.-K. 2002. Bayesian updating of structural models and reliability using Markov Chain Monte Carlo simulation, *Journal of Engineering Mechanics*, 128, 380–391.

Beck, J.L. & Katafygiotis, L.S. 1991. Updating of a model and its uncertainties utilizing dynamic test data, 1st *International Conference on Computational Stochastic Mechanics*, Corfu, Greece.

Beck, J.L. & Katafygiotis, L.S. 1998. Updating models and their uncertainties – Bayesian statistical framework, *Journal of Engineering Mechanics*, 124, 455–461.

Beck, J.L. & Yuen, K.-Y. 2004. Model selection using response measurements: Bayesian probabilistic approach, *Journal of Engineering Mechanics*, 130, 192–203.

Benedettini, F., Capecchi, D. & Vestroni, F. 1995. Identification of hysteretic oscillators under earthquake loading by nonparametric models, *Journal of Engineering Mechanics*, 121, 606–612.

Chiang, D.-Y. 1992. *Parsimonious modeling of inelastic systems*, Technical Report EERL 92–02, California Institute of Technology, Pasadena, CA.

Ching, J. & Chen, Y.-J. 2007. Transitional Markov Chain Monte Carlo method for Bayesian model updating, model class selection and model averaging, *Journal of Engineering Mechanics*, 133, 816–832.

Ching, J., Muto, M. & Beck, J.L. 2005. Bayesian linear structural model updating using Gibbs sampler with modal data, 9th *International Conference on Structural Safety and Reliability*, Rome, Italy.

Ching, J., Muto, M. & Beck, J.L. 2006. Structural model updating and health monitoring with incomplete modal data using Gibbs sampler, *Computer-Aided Civil and Infrastructure Engineering,* 21, 242–257.

Cifuentes, A.O. & Iwan, W.D. 1989. Nonlinear system identification based on modeling of restoring force behavior, *Soil Dynamics and Earthquake Engineering*, 8, 2–8.

Gull, S.F. 1989. Bayesian inductive inference and maximum entropy. J. Skilling ed. *Maximum entropy and Bayesian methods*. Kluwer.

Hastings, W.K. 1970. Monte Carlo sampling methods using Markov chains and their applications, *Biometrika*, 57, 97–109.

Iwan, W.D. 1966. A distributed-element model for hysteresis and its steady-state dynamic response, *Journal of Applied Mechanics*, 33, 893–900.

Jayakumar, P. 1987. *Modeling and identification in structural dynamics*, Technical Report EERL 87–01, California Institute of Technology, Pasadena, CA.

Jayakumar, P. & Beck, J.L. 1988. System identification using nonlinear structural models. H.G. Natke, J.T.P. Yao eds. *Structural safety evaluation based on system identification approaches*, Vieweg and Sons.

Jaynes, E.T. 2003. *Probability theory: the logic of science*. Cambridge University Press.

Jeffreys, H. 1939. *Theory of probability*. Clarendon Press.

Katafygiotis, L.S. & Lam, H.-F. 2002. Tangential-projection algorithm for manifold representation in unidentifiable model updating problems, *Earthquake Engineering and Structural Dynamics*, 31, 791–812.

MacKay, D.J.C. 1991. *Bayesian methods for adaptive models*, Ph.D. thesis, California Institute of Technology, Pasadena, CA.

Masing, G. 1926. Eigenspannungen und verfestigung beim messing (Self-stretching and hardening for brass), 2nd *International Congress on Applied Mechanics*, Zurich, Switzerland.

Muto, M. & Beck, J.L. 2008. Bayesian updating and model class selection for hysteretic structural models using stochastic simulation, *Journal of Vibration and Control*, 14, 7–34.

Papadimitriou, C., Beck, J.L. & Katafygiotis, L.S. 2001. Updating robust reliability using structural test data, *Probabilistic Engineering Mechanics*, 16, 103–113.

Robert, C.P. & Casella, G. 1999. *Monte Carlo statistical methods*. Springer.

Smyth, A.W., Masri, S.F., Chassiakos, A.G. & Caughey, T.K. 1999. On-line parametric identification of MDOF non-linear hysteretic systems, *Journal of Engineering Mechanics*, 125, 133–142.

Thyagarajan, R.S. 1989. *Modeling and analysis of hysteretic structural behavior,* Technical Report EERL 89–03, California Institute of Technology, Pasadena, CA.

Yang, J.N. & Lin, S. 2004. On-line identification of non-linear hysteretic structures using an adaptive tracking technique, *International Journal of Non-Linear Mechanics*. 39, 1481–1491.

Wen, Y.-K. 1976. Method for random vibration of hysteretic systems, *Journal of Engineering Mechanics*, 102, 249–263.

Chapter 28

Parallel soil–foundation–structure interaction computations

Boris Jeremić
University of California Davis, California, USA

Guanzhou Jie
Wachovia Corporation, New York, USA

ABSTRACT: In this work the Plastic Domain Decomposition (PDD) Method is implemented for parallel elastic-plastic finite element computations related to Soil–Foundation–Structure Interaction (SFSI) problems. The PDD provides for efficient parallel elastic-plastic finite element computations steered by an adaptable, run-time repartitioning of the finite element domain. The adaptable repartitioning aims at balancing computational load among processing nodes (CPUs), while minimizing inter–processor communications and data redistribution during elasto-plastic computations. The PDD method is applied to large scale SFSI problem. Presented examples show scalability and performance of the PDD computations. A set of illustrative example is used to show efficiency of PDD computations and also to emphasize the importance of coupling of the dynamic characteristics of earthquake, soil and structural (ESS) on overall performance of the SFS system. The aforementioned ESS coupling can only be investigated using detailed models, which dictates the use of parallel simulations.

1 Introduction

Parallel finite element computations have been developed for a number of years mostly for elastic solids and structures. The static domain decomposition (DD) methodology is currently used almost exclusively for decomposing such elastic finite element domains in subdomains. This subdivision has two main purposes, namely (a) to distribute element computations to CPUs in an even manner and (b) to distribute system of equations evenly to CPUs for maximum efficiency in solution process.

However, in the case of inelastic (elastic–plastic) computations. The static DD is not the most efficient method since some subdomains become computationally slow as the elastic–plastic zone propagates through the domain. This propagation of the elastic–plastic zone (extent of which is not know a–priori) will in turn slow down element level computations (constitutive level iterations) significantly, depending on the complexity of the material model used. Propagation of elastic–plastic zone will eventually result in some subdomains becoming significantly computationally slow while others, that are still mostly elastic, will be more computationally efficient. This discrepancy in computational efficiency between different subdomains will result in inefficient parallel performance. In other words, subdomains (and their respective CPUs) with mostly elastic elements will be finishing their local iterations much faster (and idle afterward) than subdomains (and their respective CPUs) that have many elastic–plastic elements.

This computational imbalance motivated development of the Plastic Domain Decomposition (PDD) method described in this paper. Developed PDD is applied to a large scale seismic soil–foundation–structure (SFS) interaction problem for bridge systems. It is important to note that the detailed analysis of seismic SFSI described in this paper is made possible with the development of PDD as the modeling requirements (finite element mesh size) were such that sequential simulations were out of questions.

1.1 *Soil–structure interaction motivation*

The main motivation for the development of PDD is the need for detailed analysis of realistic, large scale SFSI models. This motivation is emphasized by noting that currently, for a vast majority of numerical simulations of seismic response of bridge structures, the input excitations are defined either from a family of damped response spectra or as one or more time histories of ground acceleration. These input excitations are applied simultaneously along the base of a structural system, usually without taking into account its dimensions and dynamic characteristics, the properties of the soil material in foundations, or the nature of the ground motions themselves. Ground motions applied in such a way neglect the soil–structure interaction (SSI) effects, that can significantly change used free field ground motions. A number of papers in recent years have investigated the influence of the SSI on behavior of bridges. McCallen and Romstadt performed a remarkable full scale analysis of the soil–foundation–bridge system. The soil material (cohesionless soil, sand) was modeled using equivalent elastic approach (using Ramberg–Osgood material model through standard modulus reduction and damping curves developed by Seed et al., 1984). The two studies by Chen and Penzien (1977) and by Dendrou et al. (1985) analyzed the bridge system including the soil, however using coarse finite element meshes which might filter out certainly, significant higher frequencies. Jeremic et al. attempted a detailed, complete bridge system analysis. However, due to computational limitations, the large scale pile group had to be modeled separately and its stiffness used with the bridge structural model. In present work, with the development of PDD (described in some details), such computational limitations are removed and high fidelity, detailed models of Earthquake–Soil–Structure systems can be performed. It is very important to note that proper modeling of seismic wave propagation in elastic–plastic soils dictates the size of finite element mesh. This requirement for proper seismic wave propagation will in turn results in a large number of finite elements that need to be used.

1.2 *Parallel computing background*

The idea of domain decomposition method can be found in an original paper from 1870 by H.A. Schwarz (Rixena and Magoulès, 2007). Current state of the art in distributed computing in computational mechanics can be followed to early works on parallel simulation technology. For example, early endeavors using inelastic finite elements focused on structural problems within tightly coupled, shared memory parallel architectures. We mention work by Noor et al. (1978), Utku et al. (1982) and Storaasil and Bergan (1987) in which they used substructuring to achieve distributed parallelism. Fulton and Su (1992) developed techniques to account for different types of elements used in

the same computer model but used substructures made of same element types which resulted in non–efficient use of compute resources. Hajjar and Abel (1988) developed techniques for dynamic analysis of framed structures with the objective of minimizing communications for a high speed, local grid of computer resource. Klaas et al. (1994) developed parallel computational techniques for elastic–plastic problems but tied the algorithm to the specific multiprocessor computers used (and specific network connectivity architecture) thus rendering it less general and non-useful for other types of grid arrangements. Farhat (1987, 1991) developed the so–called Greedy domain partitioning algorithm, which proved to be quite efficient on a number of parallel computer architectures available. However, most of the above approaches develop loss of efficiency when used on a heterogeneous computational grid, which constitutive currently predominant parallel computer architecture. More recently Farhat and Roux (1991) proposed FETI (Finite Element Tearing and Interconnecting) method for domain decomposition analysis. In FETI method, Lagrange multipliers are introduced to enforce compatibility at the interface nodes.

Although much work has been presented on domain decomposition methods, the most popular methods such as FETI-type are based on subdomain interface constraints handling. It is also interesting to note promising efforts on merging of iterative solving with domain decomposition-type preconditioning (Pavarino, 2007; Li and Widlund, 2007). From the implementation point of view, for mesh-based scientific computations, domain decomposition corresponds to the problem of mapping a mesh onto a set of processors, which is well defined as a graph partitioning problem (Schlegel et al.). Graph based approach for initial partitioning and subsequent repartitioning forms a basis for PDD method.

1.3 *Simulation platform*

Developed parallel simulation program is developed using a a number of numerical libraries. Graph partitioning and repartitioning is achieved using parts of the ParMETIS libraries (Karypis et al., 1998). Parts of the OpenSees framework (McKenna, 1997) were used to connect the finite element domain. In particular, Finite Element Model Classes from OpenSees (namely, class abstractions Node, Element, Constraint, Load and Domain) where used to describe the finite element model and to store the results of the analysis performed on the model. In addition to that, an existing Analysis Classes were used as basis for development of parallel PDD framework which is then used to drive the global level finite element analysis, i.e., to form and solve the global system of equations in parallel. Actor model (Agha, 1984; Hewitt et al., 1973) was used and with addition of a Shadow, Chanel, MovableObject, ObjectBroker, MachineBroker classes within the OpenSees framework (McKenna, 1997) provided an excellent basis for our development. On a lower level, a set of Template3Dep numerical libraries (Jeremic and Yang, 2002) were used for constitutive level integrations, nDarray numerical libraries (Jeremi and Sture, 1997; 1998) were used to handle vector, matrix and tensor manipulations, while FEMtools element libraries from the UCD CompGeoMech toolset (Jeremic, 2004) were used to supply other necessary components. Parallel solution of the system of equations has been provided by PETSc set of numerical libraries (Balay et al., 2001; 2004).

Most of the simulations were carried out on our local parallel computer GeoWulf. Only the largest models (too big to fit in GeoWulf system) were simulated on TeraGrid machine (at SDSC and TACC). It should be noted that program sources described here are available through Author's web site.

2 Plastic domain decomposition method

Domain Decomposition (DD) approach is one of the most popular methods that is used to implement and perform parallel finite element simulations. The underlying idea is to divide the problem domain into subdomains so that finite element calculations will be performed on each individual subdomain in parallel. The DD can be overlapping or non-overlapping. The overlapping domain decomposition method divides the problem domain into several slightly overlapping subdomains. Non-overlapping domain decomposition is extensively used in continuum finite element modeling due to the relative ease to program and organize computations and is the one that will be examined in this work. In general, a good non-overlapping decomposition algorithm should be able to (a) handle irregular mesh of arbitrarily shaped domain, and (b) minimize the interface problem size by delivering minimum boundary conductivities, which will help reducing the communication overheads. Elastic–plastic computations introduce a number of additional requirements for parallel computing. Those requirements are described below.

2.1 *The elastic–plastic parallel finite element computational problem*

The distinct feature of elastic-plastic finite element computations is the presence of two iteration levels. In a standard displacement based finite element implementation, constitutive driver at each integration (Gauss) point iterates in stress and internal variable space, computes the updated stress state, constitutive stiffness tensor and delivers them to the finite element functions. Finite element functions then use the updated stresses and stiffness tensors to integrate new (internal) nodal forces and element stiffness matrix. Then, on global level, nonlinear equations are iterated on until equilibrium between internal and external forces is satisfied within some tolerance.

2.1.1 *Elastic computations*

In the case of elastic computations, constitutive driver has a simple task of computing increment in stresses ($\Delta\sigma_{ij}$) for a given deformation increment ($\Delta\epsilon_{kl}$), through a closed form equation ($\Delta\sigma_{ij} = E_{ijkl}\,\Delta\epsilon_{kl}$). It is important to note that in this case the amount of work per Gauss point is known in advance and is the same for every integration point. If we assume the same number of integration points per element, it follows that the amount of computational work is the same for each element and it is known in advance.

2.1.2 *Elastic-plastic computations*

For elastic-plastic problems, for a given incremental deformation the constitutive driver iterate in stress and internal variable space until consistency condition is satisfied. Number of implicit constitutive iterations is not known in advance. Similarly, if explicit

constitutive computations are done, the amount of work at each Gauss point is much higher that it was for elastic step. Initially, all Gauss points are in elastic state, but as the incremental loads are applied, the elastic–plastic zones develops. For integration points still in elastic range, computational load is light. However, for Gauss points that are elastic–plastic, the computational load increases significantly (more so for implicit computations than for explicit ones). This computational load increase depends on the complexity of material model. For example, constitutive level integration algorithms for soils, concrete, rocks, foams and other granular materials can be very computationally demanding. More than 70% of wall clock time during an elastic-plastic finite element analysis might be spent in constitutive level iterations. This is in sharp contrast with elastic computations where the dominant part is solving the system of equations which consumes about 90% of run time. The extent of additional, constitutive level computations is not known before the actual computations are over. In other words, the extent of elastic-plastic domain is not known ahead of time.

The traditional pre–processing type of Domain Decomposition method (also known as topological DD) splits domain based on the initial geometry and mesh connectivity and assigns roughly the same number of elements to every computational node while minimizing the size of subdomain boundaries. This approach might result in serious computational load imbalance for elastic–plastic problems. For example, one subdomain might be assigned all of the elastic–plastic elements and spend large amount of time in constitutive level computations. The other subdomain might have elements in elastic state and thus spend far less computational time in computing stress increments. This results in program having to wait for the slowest subdomain (the one with large number of elastic-plastic finite elements) to complete constitutive level iterations and only proceed with global system iterations after that.

The two main challenges with computational load balancing for elastic–plastic computations are that they need to be:

- Adaptive, dynamically load balancing computations, as the extent of elastic and elastic-plastic domains changes dynamically and unpredictably during the course of the computation.
- Multiphase computations, as elastic-plastic computations follow up the elastic computations and there is a synchronization phase between those two. The existence of the synchronization step between the two phases of the computation requires that each phase be individually load balanced.

2.2 *PDD algorithm*

The Plastic Domain Decomposition algorithm (PDD) provides for computational load balanced subdomains, minimizes subdomain boundaries and minimizes the cost of data redistribution during dynamic load balancing. The PDD optimization algorithm is based on dynamically monitoring both data redistribution and analysis model regeneration costs during program execution in addition to collecting information about the cost of constitutive level iterations within each finite element. A static domain decomposition is used to create initial partitioning, which is used for the first load increment. Computational load (re–)balancing will (might) be triggered if, during elastic–plastic

computations in parallel, one computations on one of compute nodes (one of subdomains) becomes slower than the others compute nodes (other subdomains). Algorithm for computational load balancing (CLB) is triggered if the performance gain resulting from CLB offsets the extra cost associated with the repartitioning. The decision on whether to trigger repartitioning or not is based on an algorithm described in some details below.

We define the global overhead associated with load balancing operation to consist of two parts, data communication cost T_{comm} and finite element model regeneration cost T_{regen},

$$T_{overhead} := T_{comm} + T_{regen} \tag{1}$$

Performance counters are setup within the program to follow both. Data communication patterns characterizing the network configuration can be readily measured (T_{comm}) as the program runs the initial partitioning. Initial (static) domain decomposition is performed for the first load step. The cost of networking is inherently changing as the network condition might vary as simulation progresses, so whenever data redistribution happens, the metric is automatically updated to reflect the most current network conditions. Model regeneration cost (T_{regen}) is a result of a need to regenerate the analysis model whenever elements (and nodes) are moved between computational nodes (CPUs). It is important to note that model (re-) generation also happens initially when the fist data distribution is done (from the static DD). Such initial DD phase provides excellent initial estimate of the model regeneration cost on any specific hardware configurations. This ability to measure realistic compute costs allows developed algorithm (PDD) to be used on multiple generation parallel computers.

For the load balancing operations to be effective, the $T_{overhead}$ has to be offset by the performance gain. T_{gain}. Finite element mesh for the given model is represented by a graph, where each finite element is represented by a graph vertex. The computational load imposed by each finite element (FE) is represented by the associated vertex weight. $vwgt[i]$. If the summation SUM operation is applied on every single processing node, the exact computational distribution among processors can be obtained as total wall clock time for each CPU

$$T_j := \sum_{i=1}^{n} vwgt[i], \quad j = 1, 2, \ldots, np \tag{2}$$

where n is the number of elements on each processing domain and np is the number of CPUs. The wall clock time is controlled by T_{max}, defined as

$$T_{sum} := sum(T_j), \quad T_{max} := max(T_j), \quad \text{and} \quad T_{min} := min(T_j), \quad j = 1, 2, \ldots, np \tag{3}$$

Minimizing T_{max} becomes here the main objective. Computational load balancing operations comprises delivering evenly distributed computational loads among processors. Theoretically, the best execution time is,

$$T_{best} := T_{sum}/np, \quad \text{and} \quad T_j \equiv T_{best}, \ j = 1, 2, \ldots, np \tag{4}$$

if the perfect load balance is to be achieved.

Based on definitions above, the best performance gain T_{gain} that can be obtained from computational load balancing operation as,

$$T_{gain} := T_{max} - T_{best} \tag{5}$$

Finally, the load balancing operation will be beneficial if

$$T_{gain} \geq T_{overhead} = T_{comm} + T_{regen} \tag{6}$$

Previous equation is used in deciding if the re–partitioning is triggered in current incremental step. It is important to note that PDD will always outperform static DD as static DD represents the first decomposition of the computational domain. If such decomposition becomes computationally unbalanced and efficiency can be gained by repartitioning, PDD be triggered and the T_{max} will be minimized.

2.3 *Solution of the system of equations*

A number of different algorithms and implementations exists for solving unsymmetric systems of equations in parallel. Non-associated elasto–plasticity results in a non-symmetric stiffness tensors, which result in non–symmetric system of finite element equations. Non–symmetry can also result from the use of consistent stiffness operators as described by Jeremic and Sture (1997, 1998). In presented work, use was made of both iterative and direct solvers as available through the PETSc interface (Balay et al. 2001; 2004). Direct solvers, including MUMPS, SPOOLES, SuperLU, PLAPACK have been tested and used for performance assessment. In addition to that, iterative solvers, including GMRES, as well as preconditioning techniques (Jacobi, inconsistency LU decomposition and approximate inverse preconditioners) for Krylov methods have been also used and their performance assessed.

Some of the conclusions drawn are that, for our specific finite element models (non–symmetric, using penalty method for some connections, possible softening behavior), direct solvers outperform the iterative solver significantly. As expected direct solver were not as scalable as iterative solvers, however, specifics of our finite element models (dealing with soil–structure interaction) resulted in poor initial performance of iterative solvers, that, even with excellent performance scaling, could not catch up with the efficiency of direct solvers. IT is also important to note that parallel direct solvers, such as MUMPS and SPOOLES provided the best performance and would be recommended for use with finite element models that, as ours did, feature non–symmetry, are poorly conditioned (they are ill–posed due to use of penalty method) and can be negative definite (for softening materials).

2.4 *PDD scalability study*

The developed PDD method was tested on a number of static and dynamic examples. Presented here are scalability (speed–up) results for a series of soil–foundation–structure model runs. A hierarchy of models, described later in section 3, was used in

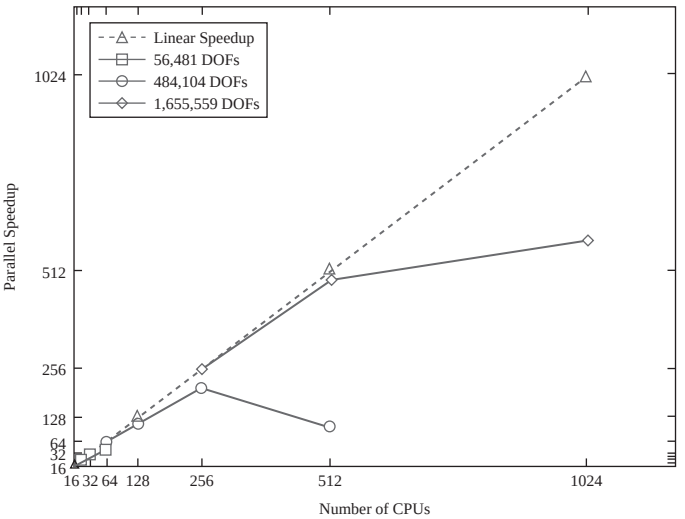

Figure 1 Scalability Study on 3 Bent SFSI Models, DRM Earthquake Loading, Transient Analysis, ITR = 1e-3, Imbal Tol 5%.

scaling study for dynamic runs. Finite element models were subjected to recorded earthquakes (two of them, described in section 4), using DRM for seismic load application (Bielak et al. and Yoshimura et al.).

Total wall clock time has been recorded and used to analyze the parallel scalability of PDD, presented in Figure 1. There is a number of interesting observations about the performance scaling results:

- the scalability is quite linear for small number of DOFs (elements),
- there is a link, relation between number of DOFs (elements) and number of CPUs which governs the parallel efficiency. In other words, there exists certain ratio of the number of DOFs to number of CPUs after which the communication overhead starts to be significant. For example for a models with 484,104 DOFs in Figure 1, the computations with 256 CPUs are more efficient that those with 512 CPUs. This means that for the same number of DOFs (elements) doubling the number of CPUs does not help, rather it is detrimental as there is far more communication between CPUs which destroys the efficiency of the parallel computation. Similar trend is observable for the large model with 1,655,559 DOFs, where 1024 CPUs will still help (barely) increase the parallel efficiency.
- Another interesting observation has to do with the relative computational balance of local, element level computations (local equilibrium iterations) and the system of equations solver. PDD scales very nicely as its main efficiency objective is to have equal computational load for element level computations. However, the efficiency of the system of equations solver becomes more prominent when element level computations are less prominent (if they have been significantly optimized with a large efficiency gain). For example, for the model with 56,481 DOFs it

is observed that for sequential case (1 CPU), elemental computation amount for approx. 70% of wall clock time. For the same model, in parallel with 8 CPUs, element level computation accounts for approx. 40% of wall clock time, while for 32 CPUs the element level computation account for only 10% of total wall clock time. In other words, as the number of CPUs increase, the element level computations are becoming very efficient and the main efficiency gain can then be made with the system of equations solver. However, it is important to note that parallel direct solver are not scalable up to large number of CPUs (Demmel et al., 1999) while parallel iterative solver are much more scalable but difficult to guarantee convergence. This observation can be used in fine tuning of parallel computing efficiency, even if it clearly points to a number of possible problems.

3 Finite element SFSI model development

The finite element models used in this study have combined both elastic–plastic solid elements, used for soils, and elastic and elastic–plastic structural elements, used for concrete piles, piers, beams and superstructure. In this section described are material and finite element models used for both soil and structural components. In addition to that, described is the methodology used for seismic force application and staged construction of the model.

3.1 *Soil and structural model*

3.1.1 *Soil models*

Two types of soil were used in modeling. First type of soil was based on stiff, sandy soil, with limited calibration data (Kurtulus et al., 2005) available from capitol Aggregates site (south–east of Austin, Texas). Based on the stress-strain curve obtained from a triaxial test, a nonlinear elastic–plastic soil model has been developed using Template Elastic plastic framework (Jeremic and Yang, 2002). Developed model consists of a Drucker-Prager yield surface, Drucker–Prager plastic flow directions (potential surface) and a nonlinear Armstrong-Frederick (AF) (rotational) kinematic hardening rule (Armstrong & Frederick, 1966). Initial opening of a Drucker–Prager cone was set at 5° only while the actual deviatoric hardening is produced using AF nonlinear kinematic hardening with hardening constants $a = 116.0$ and $b = 80.0$.

Second type of soil used in modeling was soft clay (Bay Mud). This type of soil was modeled using a total stress approach with an elastic perfectly plastic von Mises yield surface and plastic potential function. The shear strength for such Bay Mud material was set at $C_u = 5.0\,\text{kPa}$. Since this soil is treated as fully saturated and there is not enough time during shaking for any dissipation to occur, the elastic–perfectly plastic model provides enough modeling accuracy.

3.1.2 *Soil element size determination*

The accuracy of a numerical simulation of seismic wave propagation in a dynamic SFSI problem is mainly controlled the spacing of the nodes of the finite element model. In order to represent a traveling wave of a given frequency accurately, about 10 nodes per wavelength are required. In order to determine the appropriate maximum grid spacing the highest relevant frequency f_{max} that is to be simulated in the model needs

Table 1 Variation in model size (number of elements and element size) as function of frequency, stiffness and shear deformation.

model size (# of elements)	*element size*	f_{cutoff}	*min.* G/G_{max}	*shear def.* γ
12 K	1.0 m	10 Hz	1.0	<0.5%
15 K	0.9 m	3 Hz	0.08	1.0%
150 K	0.3 m	10 Hz	0.08	1.0%
500 K	0.15 m	10 Hz	0.02	5.0%

to be decided upon. Typically, for seismic analysis one can assume $f_{max} = 10$ Hz. By choosing the wavelength $\lambda_{min} = v/f_{max}$, where v is the (shear) wave velocity, to be represented by 10 nodes the smallest wavelength that can still be captured with any confidence is $\lambda = 2\Delta h$, corresponding to a frequency of $5f_{max}$. The maximum grid spacing Δh should therefore not be larger than

$$\Delta h \leq \frac{\lambda_{min}}{10} = \frac{v}{10 f_{max}} \tag{7}$$

where v is the smallest wave velocity that is of interest in the simulation (usually the wave velocity of the softest soil layer). In addition to that, mechanical properties of soil will change with (cyclic) loadings as plastification develops. Moduli reduction curve (G/G_{max}) can then used to determine soil element size while taking into account soil stiffness degradation (plastification). Using shear wave velocity relation to shear modulus

$$v_{shear} = \sqrt{\frac{G}{\rho}} \tag{8}$$

one can readily obtain the dynamic degradation of wave velocities. This leads to smaller element size required for detailed simulation of wave propagation in soils which have stiffness degradation (plastification). Table 1 presents an overview of model size (number of elements and element size) as function of cutoff frequencies represented in the model, material (soil) stiffness (given as G/G_{max}) and amount of shear deformation for given stiffness reduction.

It is important to note that 3D nonlinear elastic–plastic finite element simulations were performed, while stiffness reduction curves were used for calibration of the material model and for determining (minimal) finite element size. It should also be noted that the largest FEM model had over 0.5 million elements and over 1.6 million DOFs. However, most of simulations were performed with smaller model (with 150 K elements) as it represented mechanics of the problem with appropriate level of accuracy. Working FEM model mesh is shown in Figure 2. The model used, features 484,104 DOFs, 151,264 soil and beam–column elements, and is intended to model appropriately seismic waves of up to 10 Hz, for minimal stiffness degradation of. $G/G_{max} = 0.08$, maximum shear strain of $\gamma = 1\%$ and with the maximal element size

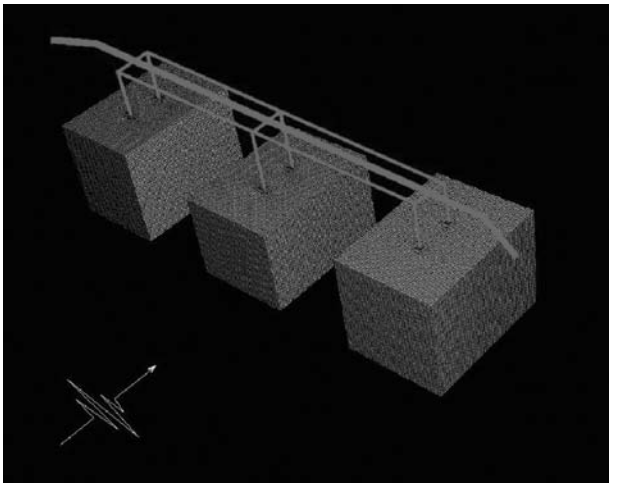

Figure 2 Detailed Three Bent Prototype SFSI Finite Element Model, 484,104 DOFs, 151,264 Elements used for most simulation in this study.

$\Delta h = 0.3$ m. The largest model (1.6 million DOFs) was able to capture 10 Hz motions, for $G/G_{\max} = 0.02$, and maximum shear strain of $\gamma = 5\%$ (see Table 1).

3.1.3 *Structural models*

The nonlinear structure model (the piers and the superstructure) used in this study were initially developed by Fenves and Dryden. This original structural (only) model was subsequently updated to include piles and surrounding soil, and zero length elements (modeling concentrated plastic hinges) were removed from the bottom of piers at the connection to piles. Concrete material was modeled using Concrete01 uniaxial material as available in OpenSees framework (Fenves and Dryden). Material model parameters used for unconfined concrete in the simulation models were $f'_{co} = 5.9$ ksi, $\epsilon_{co} = 0.002$, $f'_{cu} = 0.0$ ksi, and $\epsilon_{cu} = 0.006$. Material parameters for confined concrete used were $f'_{co} = 7.5$ ksi, $\epsilon_{co} = 0.0048$, $f'_{cu} = 4.8$ ksi, and $\epsilon_{cu} = 0.022$.

Hysteretic uniaxial material model available within OpenSees framework was selected to model the response of the steel reinforcement. The parameters included in this model are $F_1 = 67$ ksi, $\epsilon_1 = 0.0023$, $F_2 = 92$ ksi, $\epsilon_2 = 0.028$, $F_3 = 97$ ksi, and $\epsilon_3 = 0.12$. No allowance for pinching or damage under cyclic loading has been made ($pinchX = pinchY = 1.0$, $damage1 = damage2 = 0.0$, $beta = 0$).

The finite element model for piers and piles features a nonlinear fiber beam–column element (Spacone et al. 1996). In addition to that, a zero-length elements is introduced at the top of the piers in order to capture the effect of the rigid body rotation at the joints due to elongation of the anchored reinforcement. Cross section of both piers and piles was discretized using 4×16 subdivisions of core and 2×16 subdivisions of cover for radial and tangential direction respectively. Additional deformation that can develop at the upper pier end results from elongation of the steel reinforcement

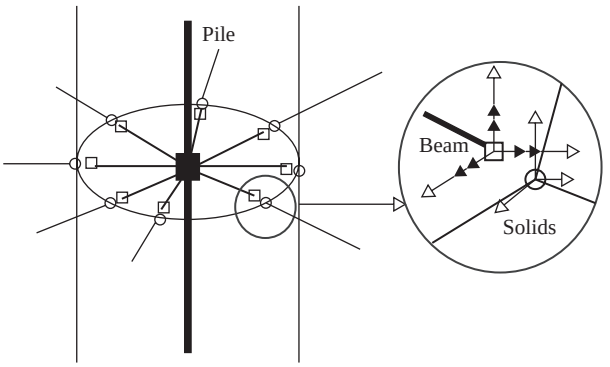

Figure 3 Schematic description of coupling of structural elements (piles) with solid elements (soil).

at beam–column joint with the superstructure and is modeled using a simplified hinge model (Mazzoni). Parameters used for steel–concrete bond stress distribution were $u_e = 12\sqrt{f'_c}$ and $u_e = 6\sqrt{f'_c}$ (Lehman & Moehle, 1998).

The bent cap beams were modeled as linear elastic beam-column elements with geometric properties developed using effective width of the cap beam and reduction of its stiffness due to cracking. The superstructure consists of prismatic prestressed concrete members and was also modeled as linear elastic beam–column element.

3.1.4 *Coupling of structural and soil models*

In order to create a model of a complete soil–structure system, it was necessary to couple structural and soil (solid) finite elements. Figure 3 shows schematics of coupling between structural (piles) and solid (soil) finite elements.

The volume that would be physically occupied by the pile is left open within the solid mesh that models the foundation soil. This opening (hole) is excavated during a staged construction process (described later). Beam–column elements (representing piles) are then placed in the middle of this opening. Beam–column elements representing pile are connected to the surrounding solid (soil) elements be means of stiff short elastic beam–column elements. These short "connection" beam–column elements extend from each pile beam–column node to surrounding nodes of solids (soil) elements. The connectivity of short, connection beam–column element nodes to nodes of soil (solids) is done only for translational degrees of freedom (three of them for each node), while the rotational degrees of freedom (three of them) from the beam–column element are left unconnected.

3.2 *Application of earthquake motions*

Seismic ground motions were applied to the SSI finite element model using Domain Reduction Method (DRM, Bielak et al., 2003; Yoshimura et al., 2003). The DRM is an excellent method that can consistently apply ground motions to the finite element model. The method features a two-stage strategy for complex, realistic three

dimensional earthquake engineering simulations. The first is an auxiliary problem that simulates the earthquake source and propagation path effects with a model that encompasses the source and a free field (from which the soil–structure system has been removed). The second problem models local, soil-structure effects. Its input is a set of effective forces, that are derived from the first step. These forces act only within a single layer of elements adjacent to the interface between the exterior region and the geological feature of interest. While the DRM allows for application of arbitrary, 3D wave fields to the finite element model, in this study a vertically propagating wave field was used. Using given surface, free field ground motions, de-convolution was done for this motions to a depth of 100 m. Then, a vertically propagating wave field was (re–) created and used to create the effective forces for DRM. Deconvolution and (back) propagation of vertically propagating wave field was performed using closed form, 1D solution as implemented in Shake program (Idriss & Sun, 1992).

3.3 *Staged simulations*

Application of loads in stages is essential for elastic–plastic models. This is especially true for models of soil and concrete. Staged loading ensures appropriate initial conditions for each loading stage. Modeling starts from a zero stress and deformation state. Three loading stages, described below, then follow.

3.3.1 *Soil self–weight stage*

During this stage the finite element model for soil (only, no structure) is loaded with soil self–weight. The finite element model for this stage excludes any structural elements, the opening (hole) where the pile will be placed is full of soil. Displacement boundary conditions on the sides of the three soil blocks are such that they allow vertical movements, and allow horizontal in boundary plane movement, while they prohibit out of boundary plane movement of soils. All the displacements are suppressed at the bottom of all three soil blocks. The soil self weight is applied in 10 incremental steps.

3.3.2 *Piles, columns and superstructure self–weight stage*

In this, second stage, number of changes to the model happen. First, soil elements where piles will be placed are removed (excavated), then concrete piles (beam–column elements) are placed in the holes (while appropriately connecting structural and solids degrees of freedom, as described above), columns are placed on top of piles and finally the superstructure is placed on top of columns. All of this construction is done at once. With all the components in place, the self weight analysis of the piles–columns–superstructure system is performed.

3.3.3 *Seismic shaking stage*

The last stage in our analysis consists of applying seismic shaking, by means of effective forces using DRM. It is important to note that seismic shaking is applied to the already deformed model, with all the stresses, internal variables and deformation that resulted from first two stages of loading.

4 Simulation results

Bridge model described above was used to analyze a number of cases of different foundation soils and earthquake excitations. Two sets of ground motions were used for the same bridge structure. Variation of foundation soil, namely (a) all stiff sand and (b) all soft clay. One of the main goals was to investigate if free field motions can be directly used for structural model input (as is almost exclusively done nowadays), that is, to investigate how significant are the SFSI effects. In addition to that, investigated were differences in structural response that result from varying soil conditions. Ground motions for Northridge and Kocaeli earthquakes (free field measurement, see Figures 4a,b) were used in determining appropriate wave field (using DRM). Since the main aim of the exercise was to investigate SFS system a set of short period motions were chosen among Northridge motions records, while long period motions from Kocaeli earthquakes were used for long period example.

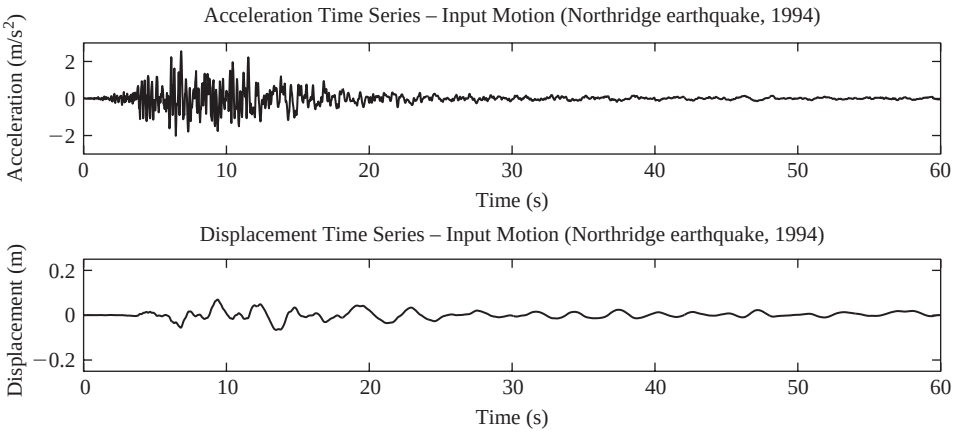

Figure 4a Input motions: short period (Northridge).

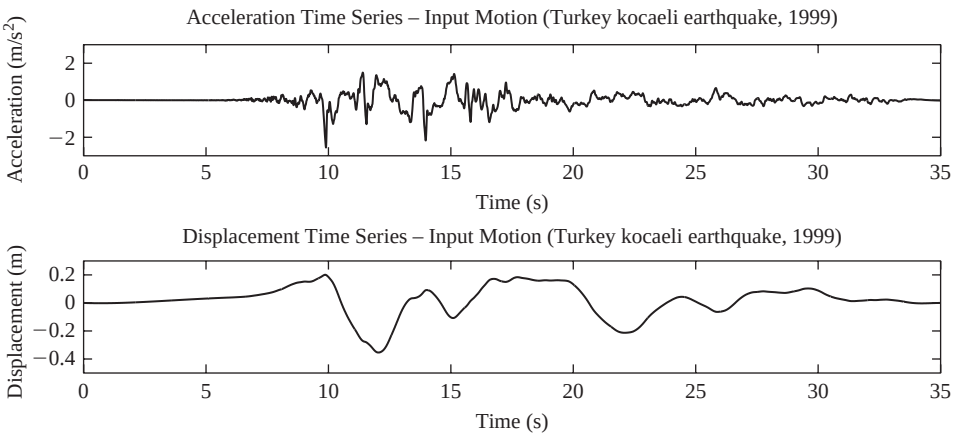

Figure 4b Input motions: long period (Kocaeli).

A number of very interesting results were obtained and are discussed below.

4.1 *Free field vs. SSI motions*

A very important aspect of SFSI is the difference between free field motions and the motions that are changed (affected) but the presence of the structure. Figure 5 shows comparison of free field short period motions (obtained by vertical propagation of earthquake motions through the model without the presence of bridge structure and piles) and the ones recorded at the base of column of the left bent in stiff and soft soils.

It is immediately obvious that the free field motions in this case do not correspond to motions observed in bridge SFS system with stiff or soft soils. In fact, both the amplitude and period are significantly altered for both soft and stiff soil and the bridge structure. This quite different behavior can be explained by taking into account the fact that the short period motions excite natural periods of stiff soil and can produce (significant) amplifications. In addition to that, for soft soils, significant elongation of period is observed.

On the other hand, as shown in Figure 6 the same SFS system (same structure with stiff or soft soil beneath) responds quite a bit different to long period motions.

The difference between free field motions and the motions measured (simulated) in stiff soils is smaller in this case. This is understandable as the stiff soil virtually gets carried away as (almost) rigid block on such long period motions. For the soft soil one of the predominant natural periods of the SFS system is excited briefly (at 12–17 seconds) but other than that excursion, both stiff and soft soil show fair matching with free field motions. In this case the SFS effects are not that pronounced, except during the above mentioned period between 12 and 17 seconds.

4.2 *Bending moments response*

Influence of variable soil conditions and of dynamic characteristic of earthquake motions on structural response is followed by observing bending moment response.

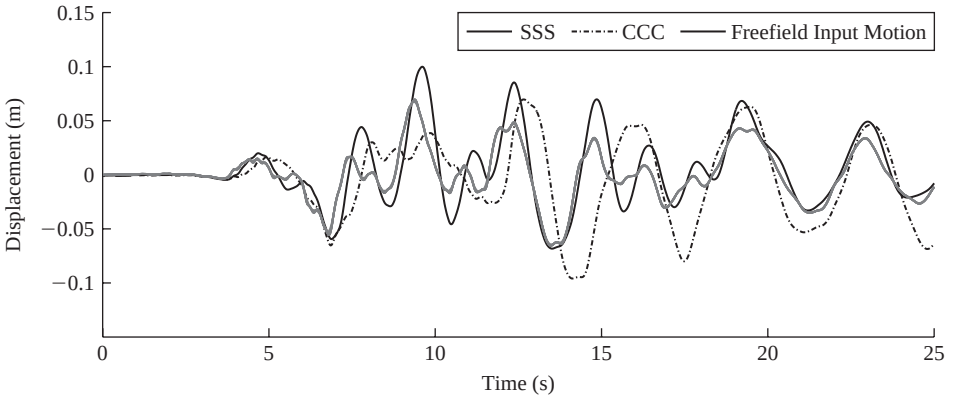

Figure 5 Comparison of free field versus measured (prototype model) motions at the base of left bent for the short period motions (Northridge) for all clay (CCC) and all sand (SSS) soils.

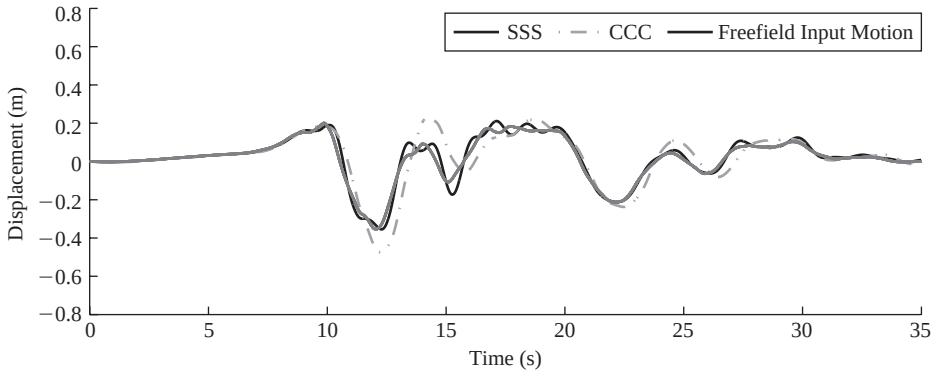

Figure 6 Comparison of free field versus measured (prototype model) motions at the base of left bent for the long period motions (Kocaeli) for all clay (CCC) and all sand (SSS) soils.

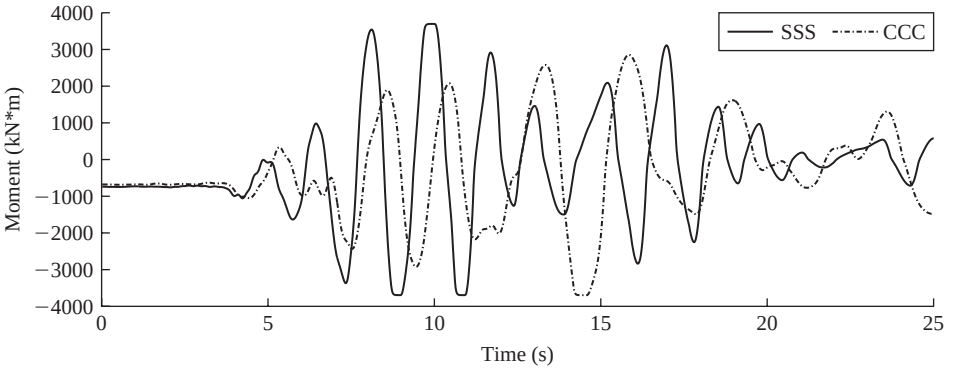

Figure 7 Simulated bending moment time series (top of left pier) for short period motion (Northridge), for all clay (CCC) and all sand (SSS) soils.

For this particular purpose, a time history of bending moment at the top of one of the piers of bent # 1 (left most in Figure 2) is chosen to illustrate differences in behavior.

Figure 7 shows time history of the bending moment at top of left most pier of bent # 1 for all sand (SSS) and all clay (CCC) cases for short period motion (Northridge).

Similarly, Figure 8 shows time history of the bending moment for same pier, for same soil conditions, but for long period motion (Kocaeli).

Time histories of bending moments are quite different for both types of soil conditions (SSS and CCC) and for two earthquake motions. For example, it can be seen from Figure 7 that short period motion earthquake, in stiff soil (SSS) produces (much) larger plastic deformation, which can be observed by noting flat plateaus on moment – time diagrams, representing plastic hinge development. Those plastic hinge development regions are developing symmetrically, meaning that both sides of the pier have yielded and full plastic hinge has formed. On the other hand, the short period earthquake in soft soil (CCC) produces very little damage, one side of a plastic hinge is (might be) forming between 14 and 15 seconds.

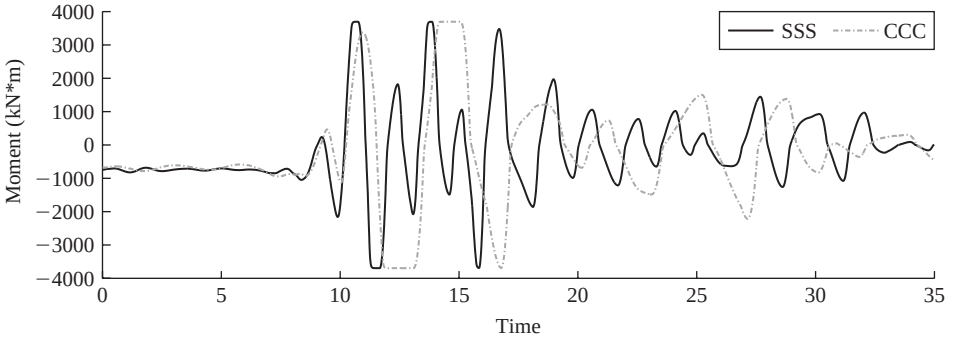

Figure 8 Simulated bending moment time series (top of left pier) for long period motion (Kocaeli), for all clay (CCC) and all sand (SSS) soils.

Contrasting those observation is time history of bending moments in Figure 8, where, for a long period motion, stiff soil (SSS) induces small amount of plastic yielding (hinges) on top of piers. However, soft soil (CCC) induces a (very) large plastic deformations. Development of plastic hinges for a structure in soft soil also last very long (more than two seconds, see lower plateau for CCC case in Figure 8) resulting in significant damage development in thus formed plastic hinges. Observed behavior also somewhat contradicts common assumption that soft soils are much more detrimental to structural behavior. It is actually the interaction of the dynamic characteristic of earthquake, soil and structure (ESS) that seem to control the ultimate structural response and the potential damage that might develop.

5 Conclusions

In this paper, an algorithm, named the Plastic Domain Decomposition (PDD), for parallel elastic–plastic finite element computations was presented. Presented was also a parallel scalability study, that shows how PDD scales quite well with increase in a number of compute nodes. More importantly, presented details of PDD reveal that scalability is assured for inhomogeneous, multiple generation parallel computer architecture, which represents majority of currently available parallel computers.

Presented also was an application of PDD to soil–foundation–structure interaction problem for a bridge system and Earthquake–Soil–Structure (ESS) interaction effects were emphasized. The importance of the (miss–) matching of the ESS characteristics to the dynamic behavior of the bridge soil–structure system was shown on an example using same structure, two different earthquakes (one with short and one with long predominant periods) and two different subgrade soils (stiff sand and soft clay).

The main goal of this paper is to show that high fidelity, detailed modeling and simulations of geotechnical and structural systems are available and quite effective. Results from such high fidelity modeling and simulation shed light on new types of behavior that cannot be discovered using simplified models. These high fidelity models tend to reduce modeling uncertainty, which (might) allow practicing engineers to use simulations tools for effective design of soil–structure systems.

Acknowledgment

The work presented in this paper was partially supported by a grant from the Civil and Mechanical System program, Directorate of Engineering of the National Science Foundation, under Award NSF–CMS–0337811 (cognizant program director Dr. Steve McCabe).

References

Agha, G. 1984. *Actors: A Model of Concurrent Computation in Distributed Systems*. MIT Press.

Armstrong, P.J. & Frederick, C.O. 1966. A mathematical representation of the multiaxial bauschinger effect. Technical Report RD/B/N/ 731, C.E.G.B.

Balay, S., Buschelman, K., Eijkhout, V., Gropp, W.D., Kaushik, D., Knepley, W.G., Curfman McInnes, L., Smith, B.F. & Zhang, H. 2004. PETSc users manual. Technical Report ANL-95/11 – Revision 2.1.5, Argonne National Laboratory.

Balay, S., Buschelman, K., Gropp, W.D., Kaushik, D., Knepley, W.G., Curfman McInnes, L., Smith, B.F. & Zhang, H. 2001. PETSc Web page, http://www.mcs.anl.gov/petsc.

Balay, S., Gropp, W.D., Curfman McInnes, L. & Smith, B.F. 1997. Efficient management of parallelism in object oriented numerical software libraries. In E. Arge, A. M. Bruaset, and H. P. Langtangen, editors, *Modern Software Tools in Scientific Computing*, pages 163–202. Birkhäuser Press.

Bielak, J., Loukakis, K., Hisada, Y. & Yoshimura, C. 2003. Domain reduction method for three–dimensional earthquake modeling in localized regions. part I: Theory. *Bulletin of the Seismological Society of America*, 93(2):817–824.

Chi Chen, M. & Penzien, J. 1977. Nonlinear soil–structure interaction of skew highway bridges. Technical Report UCB/EERC-77/24, Earthquake Engineering Research Center, University of California, Berkeley, August.

Demmel, J.W., Eisenstat, S.C., Gilbert, J.R., Li, X.S. & Liu, J.W.H. 1999. A supernodal approach to sparse partial pivoting. *SIAM J. Matrix Analysis and Applications*, 20(3): 720–755.

Dendrou, B., Werner, S.D. & Toridis, T. 1985. Three dimensional response of a concrete bridge system to traveling seismic waves. *Computers and Structures*, 20:593–603.

Dryden, M. 2006. Validation of simulations of a two-span reinforced concrete bridge. Submitted in partial satisfaction of the requirements for degree od Ph.D.

Farhat, C. 1987. *Multiprocessors in Computational Mechanics*. PhD thesis, University of California, Berkeley.

Farhat, C. 1991. Saddle-point principle domain decomposition method for the solution of solid mechanics problems. In *Fifth International Symposium on Domain Decomposition Methods for Partial Differential Equations*, Norfolk, VA, USA, May 6–8.

Farhat, C. & Geradin, M. 1992. Using a reduced number of lagrange multipliers for assembling parallel incomplete field finite element approximations. *Computer Methods in Applied Mechanics and Engineering*, 97(3):333–354.

Farhat, C. & Roux, F-X. 1991. Method of finite element tearing and interconnecting and its parallel solution algorithm. *International Journal for Numerical Methods in Engineering*, 32(6):1205–1227.

Fenves, G. & Dryden, M. 2005. Nees sfsi demonstration project. NEES project meeting, TX, Austin, August.

Fulton, R.E. & Su, P.S. 1992. Parallel substructure approach for massively parallel computers. *Computers in Engineering*, 2:75–82.

Hajjar, J.F. & Abel, J.F. 1988. Parallel processing for transient nonlinear structural dynamics of three–dimensional framed structures using domain decomposition. *Computers & Structures*, 30(6):1237–1254.

Hewitt, C., Bishop, P. & Steiger, R. 1973. A Universal Modular ACTOR Formalism for Artificial Intelligence. In *Proceedings of the 3rd International Joint Conference on Artificial Intelligence*, Stanford, CA, August.

Idriss, I.M. & Sun, J.I. 1992. *Excerpts from USER'S Manual for SHAKE91: A Computer Program for Conducting Equivalent Linear Seismic Response Analyses of Horizontally Layered Soil Deposits*. Center for Geotechnical Modeling Department of Civil & Environmental Engineering University of California Davis, California.

Jeremic, B. 2004. Lecture notes on computational geomechanics: Inelastic finite elements for pressure sensitive materials. Technical Report UCD-CompGeoMech–01–2004, University of California, Davis, 2004. available online: http://sokocalo.engr.ucdavis.edu/~jeremic/CG/LN.pdf.

Jeremic, B. & Yang, Z. 2002. Template elastic–plastic computations in geomechanics. *International Journal for Numerical and Analytical Methods in Geomechanics*, 26(14):1407–1427, 2002.

Jeremic, B., Kunnath, S. & Xiong, F. 2004. Influence of soil–structure interaction on seismic response of bridges. *International Journal for Engineering Structures*, 26(3): 391–402.

Jeremic, B. & Sture, S. 1997. Implicit integrations in elasto–plastic geotechnics. *International Journal of Mechanics of Cohesive–Frictional Materials*, 2:165–183.

Jeremic, B. & Sture, S. 1998. Tensor data objects in finite element programming. *International Journal for Numerical Methods in Engineering*, 41:113–126.

Kappos, A.J., Manolis, G.D. & Moschonas, I.F. 2002. Seismic assessment and design of R/C bridges with irregular configuration, including SSI effects. *International Journal of Engineering Structures*, 24:1337–1348.

Karypis, G., Schloegel, K. & Kumar, V. 1998. *ParMETIS: Parallel Graph Partitioning and Sparse Matrix Ordering Library*. University of Minnesota.

Klaas, O., Kreienmeyer, M. & Stein, E. 1994. Elastoplastic finite element analysis on a MIMD parallel–computer. *Engineering Computations*, 11:347–355.

Kurtulus, A., Lee, J.J. & Stokoe, K.H. 2005. Summary report – site characterization of capital aggregates test site. Technical report, Department of Civil Engineering, University of Texas at Austin.

Lehman, D.E. & Moehle, J.P. 1998. Seismic performance of well-confined concrete bridge columns. Technical report, Pacific Earthquake Engineering Research Center.

Li, J. & Widlund, O.B. 2007. On the use of inexact subdomain solvers for BDDC algorithms. *Computer Methods in Applied Mechanics and Engineering*, 196(8):1415–1428.

Makris, N., Badoni, D., Delis, E. & Gazetas, G. 1994. Prediction of observed bridge response with soil–pile–structure interaction. *ASCE Journal of Structural Engineering*, 120(10): 2992–3011.

Mazzoni, S., Fenves, G.L. & Smith, J.B. 2004. Effects of local deformations on lateral response of bridge frames. Technical report, University of California, Berkeley.

McCallen, D.B. & Romstadt, K.M. 1994. Analysis of a skewed short span, box girder overpass. *Earthquake Spectra*, 10(4):729–755.

McKenna, F.T. 1997. *Object Oriented Finite Element Programming: Framework for Analysis, Algorithms and Parallel Computing*. PhD thesis, University of California, Berkeley.

Noor, A.K., Kamel, A. & Fulton, R.E. 1978. Substructuring techniques – status and projections. *Computers & Structures*, 8:628–632.

Pavarino, L.F. 2007. BDDC and FETI-DP preconditioners for spectral element discretizations. *Computer Methods in Applied Mechanics and Engineering*, 196(8):1380–1388.

Rixena, D. & Magoulès, F. 2007. Domain decomposition methods: Recent advances and new challenges in engineering. *Computer Methods in Applied Mechanics and Engineering*, 196(8):1345–1346.

Schloegel, K., Kaypis, G. & Kumar, V. 1999. Graph partitioning for high performance scientific simulations. Technical report, Army HPC Research Center, Department of Computer Science and Engineering, University of Minnesota.

Seed, H.B., Wong, R.T., Idriss, I.M. & Tokimatsu, K. 1984. Moduli and damping factros for dynamic analysis of cohesionless soils. Earthquake Engineering Research Center Report UCB/EERC 84/14, University of California Berkeley.

Spacone, E., Filippou, F.C. & Taucer, F.F. 1996. Fibre beam-column model for non-linear analysis of r/c frames 1. formulation. *Earthquake Engineering and Structural Dynamics*, 25:711–725.

Storaasli, O.O. & Bergan, P. 1987. Nonlinear substructuring method for concurrent processing computers. *AIAA Journal*, 25(6):871–876.

Sweet, J. 1993. A technique for nonlinear soil–structure interaction. Technical Report CAI-093-100, Caltrans, Sacramento, California.

Utku, S., Melosh, R., Islam, M. & Salama, M. 1982. On nonlinear finite element analysis in single– multi– and parallel processors. *Computers & Structures*, 15(1):39–47.

Yoshimura, C., Bielak, J. & Hisada, Y. 2003. Domain reduction method for three–dimensional earthquake modeling in localized regions. part II: Verification and examples. *Bulletin of the Seismological Society of America*, 93(2):825–840.

Chapter 29

Dynamic interaction of retaining walls and retained soil and structures

Yiannis Tsompanakis

Technical University of Crete, Chania, Greece

ABSTRACT: In engineering practice retaining walls are very frequently used to support, apart from soil layers, structures founded on the retained soil layers. Thus, it is evident that the dynamic response of each component of this complex system (wall, soil, and structure) may affect substantially the response of the rest, and vice versa, during a seismic event. This phenomenon, which could be adequately described as "dynamic wall–soil–structure interaction" (DWSSI), is a rather complicated issue that combines: (a) the dynamic interaction between the wall and the retained soil layers, and (b) the "standard" dynamic interaction of a structure with its underlying soil layers. In the present study the influence of the wall flexibility on the free-field ground shaking behind the wall is investigated using finite element numerical simulations. Subsequently, a simple structure founded on the retained soil is included in the numerical models. A parametric study is being performed in order to examine at what extend the presence of the wall may affect the inertial accelerations imposed on the structure (with respect to its position and its fundamental eigen-period). In addition, it is investigated how the location and/or the characteristics of the structure may affect the dynamic earth pressures induced on the retaining wall. Despite the fact that there exist many "open issues" in DWSSI, the numerical results of the current study provide a clear indication of the direct dynamic interaction between a retaining wall and its retained soil layers and structures.

1 Introduction

Retaining systems are extensively used worldwide for serving various purposes in structures and infrastructures. Deep excavations, bridge abutments, or harbor quay-walls are some of the cases where a rigid gravity or a flexible cantilever retaining wall is constructed. Despite their structural simplicity, the seismic response of a wall (that retains even a single soil layer) is a rather complicated problem. What makes that response so complicated is the dynamic interaction between the wall and the retained soil, especially when material and/or geometry nonlinearities are present (Kramer 1996; Iai 1998; Wu & Finn 1999). Consequently, the performance of retaining walls during earthquakes is a subject being still examined by many researchers, experimentally, analytically, or numerically (Veletsos & Younan 1997; PIANC 2001; Psarropoulos et al. 2005). Depending on the expected material behavior of the retained soil and the possible mode of the wall displacement, there exist two main categories of analytical methods used in the design of retaining walls against earthquakes: (a) the pseudo-static limiting-equilibrium Mononobe–Okabe type solutions which assume yielding walls resulting to plastic behavior of the retained soil (Okabe 1926; Mononobe & Matsuo

1929; Seed & Whitman 1970), and (b) the elasticity-based solutions that regard the retained soil as a visco-elastic continuum (Scott 1973; Wood 1975; Veletsos & Younan 1997).

However, in many real cases retaining walls are used to support, apart from soil layers, structures founded on the retained soil. It is evident that during a seismic event the dynamic response of each component of this complex system (wall, soil layer, structure) may affect substantially the response of the rest. In other words, the presence of a retaining wall will affect not only the ground surface shaking of the retained soil, but the dynamic response of any type of retained structure as well. In addition, the existence of a structure behind the wall is expected to alter the dynamic earth pressures developed on the wall. Therefore, the phenomenon of *dynamic wall–soil–structure interaction* (*DWSSI*) is a rather complicated issue that includes: (a) the dynamic interaction between a wall and a retained soil layers, and (b) the "standard" dynamic soil–structure interaction of a structure with its underlying soil (Tsompanakis et al. 2006). The aforementioned dynamic interaction issues are not considered with the proper realism in the current seismic norms used in modern engineering practice, like the Eurocode 8 (EC8 2004) or the Greek Seismic Code (EAK 2000). Regarding the design of retaining structures, the dynamic interaction between a retaining wall and the retained soil is ignored; while on the other hand, the issue of *dynamic soil–structure interaction* taken into consideration in a simplistic way is considered a-priori to be beneficial for a structure, which seems not to be always the case (Mylonakis & Gazetas 2000).

The objective of the present study is to examine more thoroughly the phenomenon of *dynamic wall–soil–structure interaction*. For this purpose, two-dimensional numerical simulations are performed, utilizing the finite-element method, in order to investigate some of the most important aspects of this complex phenomenon. Firstly, the influence of the wall flexibility on the ground surface shaking behind the wall is investigated (Figure 1(a)), while emphasis is given on the amplification of the base acceleration, a fact generally ignored by the seismic norms. Subsequently, a simple structure founded on the retained soil is included in the numerical models (Figure 1(b)). A parametric study has been performed in order to examine how the location of the structure may affect the earth pressures induced on the retaining wall. In addition, the parametric study investigates at what extent the presence of the wall may affect the inertial forces imposed on the structure with respect to its position. In all cases, the wall is characterized by its height H, its relative flexibility d_w, and its relative compliance of the foundation d_θ, while the soil material is considered as visco-elastic with shear-wave velocity V_S, density ρ, and critical damping ratio ξ.

In general, dynamic response of any system depends on the seismic excitation characteristics (both in the time and in the frequency domain). In a recent preliminary investigation of *DWSSI* by Tsompanakis et al. (2006), both real earthquake records and pulses were used. In the present numerical study, in order to understand more clearly various aspects of the complex phenomena incorporated in the *DWSSI*, the excitations were limited to harmonic and simple pulses. Results provide a clear indication of the direct dynamic interaction between a retaining wall and its retained structures. That fact justifies the necessity for a more elaborate consideration of this interrelated phenomenon on the seismic design, not only of the retaining walls, but of the nearby structures as well.

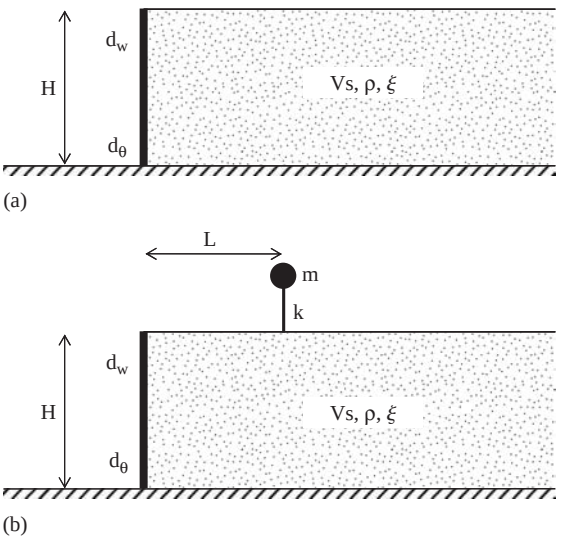

Figure 1 The retaining systems examined in this study: (a) a wall retaining a single soil layer, (b) a wall retaining a soil layer on which a simple structure is founded at distance L.

2 Numerical modelling

In order to examine more efficiently the DWSSI phenomenon, numerical analyses were based on the study of Veletsos & Younan (1997) who developed an analytical approach for evaluating the magnitude and distribution of the dynamic displacements, pressures, and forces induced by horizontal ground shaking on walls that are both flexible and elastically constrained against rotation at their base. Their analytical methodology permitted the assessment of the effects and the relative importance of the factors involved. In their model the soil was considered to act as a uniform, infinitely extended viscoelastic stratum of height H. The properties of the soil were regarded constant, defined by the density ρ, the shear modulus G, and Poisson's ratio ν. The material damping was presumed to be of the constant hysteretic type and was defined by the critical damping ratio ξ. The layer was retained by a vertical, flexible wall, elastically constrained against rotation at its base; it was free at its upper surface and it was fixed on a rigid base (thus no radiation damping was expected). The properties of the wall were described by its thickness t_w, mass per unit of surface area μ_w, modulus of elasticity E_w, Poisson's ratio ν, and critical damping ratio ξ_w. The base of both the wall and the soil stratum were considered to be excited by a space-invariant horizontal motion, assuming an equivalent force-excited system.

In the present study, in order to examine the effects of DWSSI on both retaining wall and retained structures, two-dimensional (2-D) numerical simulations of the two retaining systems depicted in Figure 1 were conducted. The simulations were performed utilizing the ABAQUS (Version 6.4, 2003) finite-element code, which is capable of performing dynamic linear analyses using Rayleigh type of material damping (resulting to a critical damping ratio of ξ for the frequencies of interest). Although soil nonlinearities

are expected to have a significant impact on the DWSSI, it was not examined in this preliminary investigation of this complex phenomenon. An introductory study on this important issue was performed in a recent work by Tsompanakis et al. (2007). The structure was modelled as a lumped mass m on top of a weightless column discretized with beam elements of flexural stiffness k. The wall was discretized also using beam elements of unit longitudinal dimension and thickness equal to $t_w = 0.20$ m. The main parameters that affect the response of the system are: (a) the relative (with respect to the retained soil) flexibility of the wall, defined by:

$$d_w = \frac{GH^3}{D_w} \tag{1}$$

and (b) the relative (with respect to the retained soil) flexibility of the rotational base constraint, defined by:

$$d_\theta = \frac{GH^2}{R_\theta} \tag{2}$$

where D_w in Equation (1) denotes the flexural rigidity per unit of length of the wall:

$$D_w = \frac{E_w t_w^3}{12(1 - \nu_w^2)} \tag{3}$$

while R_θ in Equation (2) is the stiffness of the rotational base constraint.

Three cases were examined in this study: (a) a rigid fixed-base wall ($d_w = 0$, $d_\theta = 0$), (b) a flexible fixed-base wall ($d_w = 5$, $d_\theta = 0$), and (c) a flexible wall with rotational compliance ($d_w = 5$, $d_\theta = 5$). Given the value of d_w, the modulus of elasticity of the wall E_w is evaluated using Equations (1) and (2), while the Poisson's ratio ν_w is taken as 0.2. The wall mass per unit of surface area is presumed to be 2.5 t/m^2. The simplifying assumptions that no de-bonding or relative slip is allowed to occur at the wall-soil and the structure-soil interfaces were used.

In general, the soil material properties (G, γ) and the wall height alone do not affect the dynamic pressures on the wall, as the wall flexibility is examined in relation to soil stiffness and the earth pressures are normalized with γ and H (see Veletsos and Younan 1997; Psarropoulos et al. 2005). Taking that point into account, all the analyses were performed considering an 8m-high wall. The retained soil layer is characterized by a relatively low shear-wave velocity V_S equal to 100 m/s and a unit weight γ of 18 kN/m^3. The retained soil was discretized using four-node quadrilateral plain-strain elements. Horizontal and vertical viscous dashpots were used at the right-hand side of the model in order to simulate the radiation of energy from P and S waves, respectively. We have to mention that although the efficiency of the viscous dashpots is in general quite acceptable, it depends strongly on the angle of incidence of the impinging wave. Therefore, the dashpots were placed far away from the wall in order to simulate the semi-infinite stratum more accurately.

As mentioned before, apart from harmonic excitations, simple pulses have also been used. A simple Ricker pulse with central frequency $f_o = 4$ Hz has been selected as pulse excitation (Ricker 1960). Despite the simplicity of its waveform, this wavelet covers a

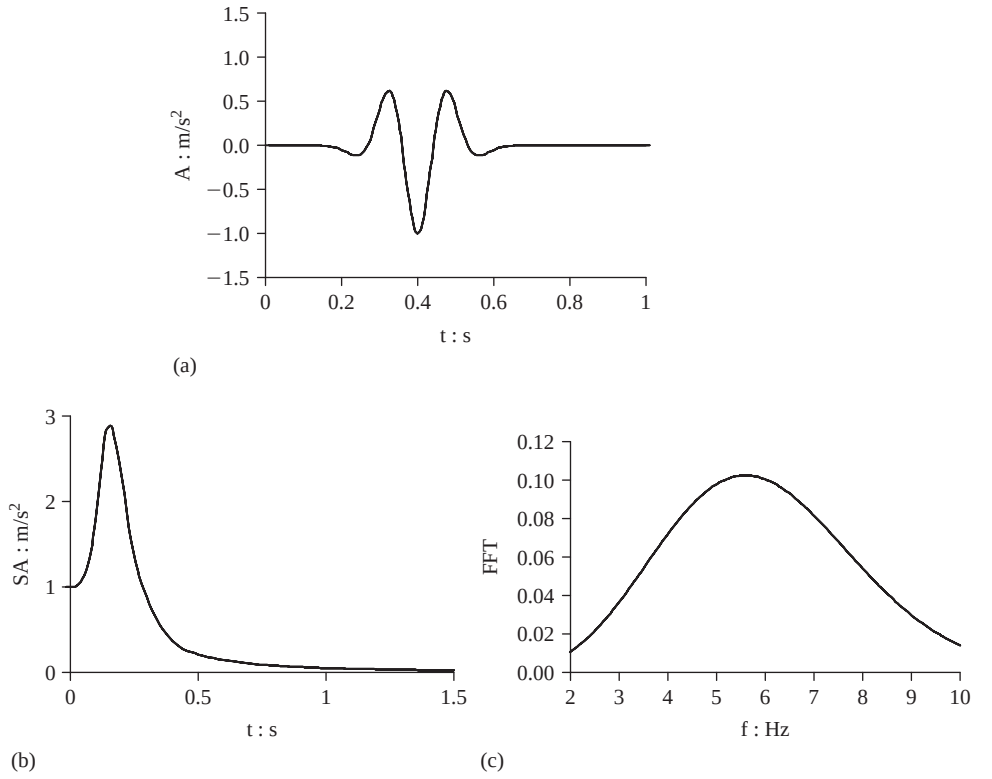

Figure 2 Acceleration time-history (a), response spectrum (b), and Fourier spectrum (c) of the Ricker pulse excitation.

broad range of frequencies up to nearly $3f_o$. The acceleration time-history (scaled to 0.10 g) and the corresponding response and Fourier spectra of the pulse are shown in Figure 2.

3 Effects of the wall on the retained-soil response

The dynamic response of a single soil layer under 1-D conditions has been studied by many researchers and analytical solutions for harmonic excitation can be found in the literature (Roesset 1977; Kramer 1996). In the case of the harmonic excitation the response is controlled by the ratio T/T_{SOIL}, where T is the dominant period of the excitation, and T_{SOIL} the fundamental period of the soil layer. For the case of one-dimensional (1–D) conditions T_{SOIL} is given by Kramer (1996):

$$T_{SOIL} = \frac{4H}{V_S} \tag{4}$$

in which H is the height of the soil layer, and V_S its shear-wave velocity. In this case the fundamental period of the soil layer is $T_{SOIL} = 0.32$s (or equivalently, the fundamental

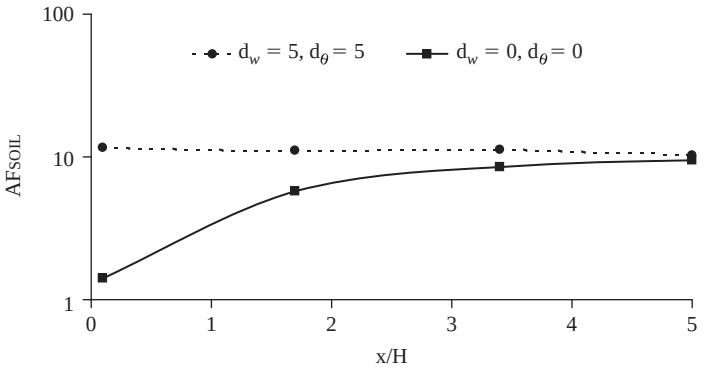

Figure 3 Distribution of the soil amplification factor (AF_{SOIL}) along the surface of the backfill in the case of the harmonic excitation at resonance ($T = T_{SOIL}$) for the two extreme cases of wall flexibility ($d_w = d_\theta = 0$, and $d_w = d_\theta = 5$). Note that vertical axis is in logarithmic scale.

frequency of the soil layer is $f_{SOIL} \approx 3.1$ Hz). The duration of the sinusoidal pulse was such that steady state conditions were reached. In that case the maximum soil amplification factor (AF_{SOIL}) is given by:

$$AF_{SOIL} = \frac{2}{\pi\xi}\frac{1}{2n+1} \tag{5}$$

where ξ is the critical damping ratio and n is the mode number. For the 1st mode ($n = 0$) and $\xi = 5\%$, thus, $AF_{SOIL} \approx 12.5$.

The presence of a retaining wall essentially imposes a vertical boundary condition, leading thus to a two-dimensional (2-D) dynamic response. In this study the response of the soil layer under 1-D conditions is compared with the corresponding 2-D due to the existence of the wall (see Figure 1a). The distribution of the amplification factor (AF_{SOIL}) on the surface of the backfill in the case of the harmonic excitation at resonance ($T = T_{SOIL}$) is plotted in Figure 3. It is evident that, for the rigid fixed-base wall case ($d_w = d_\theta = 0$), the motion in the vicinity of the wall is practically induced by the wall itself, and therefore no amplification is observed ($AF_{SOIL} \approx 1$). The amplification factor converges to its maximum value ($AF_{SOIL} \approx 12.5$) at a distance longer than $4H$ from the wall, since at that distance 1-D conditions are present (*free-field motion*). In contrast the flexible wall system ($d_w = d_\theta = 5$) permits shear deformations and consequently, higher levels of acceleration are developed behind the wall. Thus, the response of the retained soil layer resembles the 1-D conditions. Figure 4 depicts the acceleration time-histories on the surface of the retained soil layer for the rigid and the flexible wall excited with the Ricker pulse. It is obvious that the increased wall flexibility permits the soil layer to behave similarly to 1-D conditions, as in the case of the harmonic excitation, while on the other hand In contrast, in the vicinity of the rigid wall the amplification remains low. Moreover, as shown in Figure 5, the trends of AF_{SOIL} distribution along the surface in the case of Ricker pulse excitation are similar, despite the substantial decrease in amplification levels.

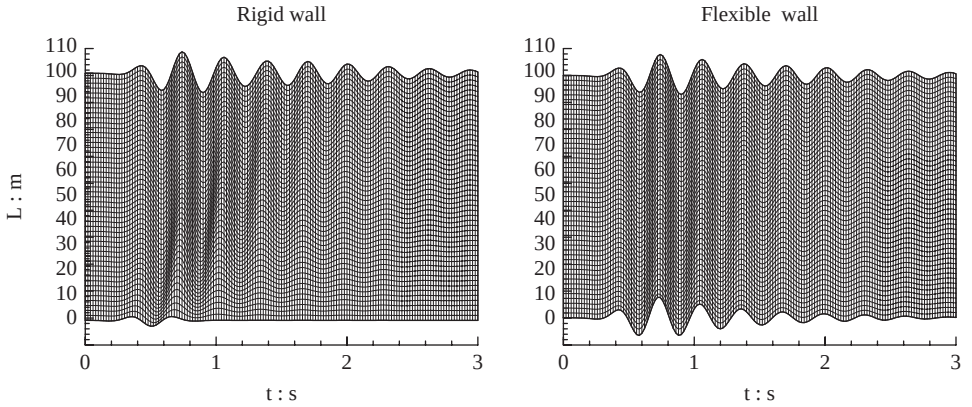

Figure 4 Distribution of acceleration along backfill surface (Ricker pulse excitation).

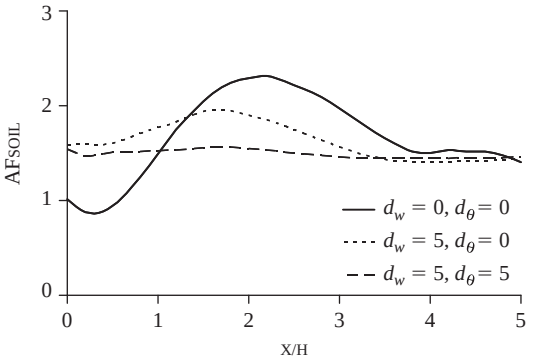

Figure 5 Distribution of the soil amplification factor (AF_{SOIL}) along the surface of the backfill in the case of the high-frequency Ricker pulse excitation.

Figure 6 depicts the Transfer Functions (*TF*) calculated for the response of point B which is located just behind the wall. Each *TF* is defined as:

$$TF = \frac{FFT_B}{FFT_A} \tag{6}$$

where FFT_B is the Fourier spectrum of the acceleration time history calculated at point B and FFT_A is the Fourier spectrum of the acceleration time history of the Ricker pulse excitation that is applied at the base of the model (point A). The Fourier spectrum of the acceleration time history of the Ricker pulse excitation has been given in Figure 2(b) and it is evident that it covers smoothly the frequency range between 2 and 10Hz. Therefore it is clear that *TF* actually comprises the soil amplification AF_{SOIL} at a specific point in the frequency domain. This observation is justified in Figure 6, where the soil amplification factors are depicted for a series of harmonic excitations of the model. As

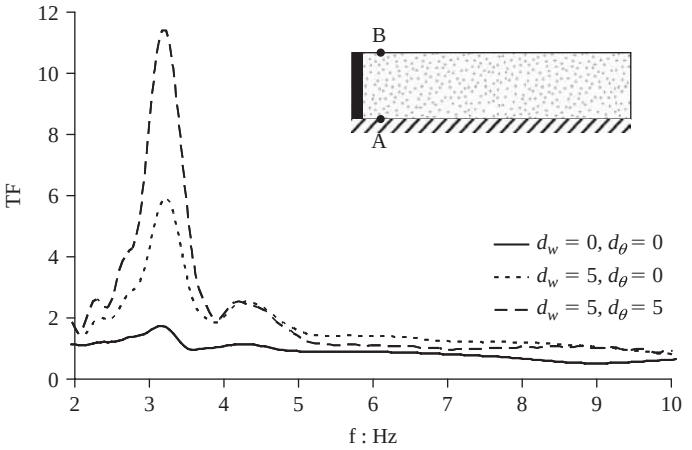

Figure 6 Transfer Functions (TF) calculated for the response of point B, which is just behind the wall, for a series of harmonic excitations. All three cases of wall flexibility are presented.

it was expected, for frequencies close to the fundamental frequency of the soil layer f_{SOIL}, resonance phenomena take place, and *TF* converges to its maximum possible value. This value is close to 12 in the case of the flexible wall ($d_w = d_\theta = 5$), whereas it is close to 1 for the case of rigid fixed-base wall ($d_w = d_\theta = 0$). Note that these values of AF_{SOIL} can also be observed in Figure 3, at the point located just behind the wall.

In addition, in order to investigate the effect of the angle of incidence θ of the imposed seismic motion, two additional dynamic loading cases were examined: Ricker pulse excitation was imposed under an angle of 30° and 45°, respectively. As the flexible wall resembles almost the 1-D conditions, only the rigid wall case was considered. The distribution of the amplification of the acceleration levels on the backfill surface is shown in Figure 7, both in horizontal and vertical directions. It is evident that as the angle θ increases the amplification of the horizontal acceleration is decreased, while the opposite occurs for the vertical acceleration. In Figure 7b the maximum vertical accelerations are normalized with the maximum horizontal base acceleration for $\theta = 0°$, so that the comparison of the acceleration levels in the two directions is meaningful. It has to be noted that for $\theta = 0°$ parasitic vertical accelerations are developed in a certain distance (approximately from $2H$ to $6H$) behind the wall.

4 Effects on the response of the structure

As it was previously mentioned, prescriptive seismic norms are not capable of taking realistically into consideration the main "components" of the dynamic wall-soil-structure interaction: (a) the dynamic interaction between a retaining wall and the retained soil layer, and (b) the "standard" 1-D dynamic soil-structure interaction, e.g. the foundation of a structure on a soil layer and the related kinematic or inertial interaction with it. The first is coped with in a very simplistic way, while the latter

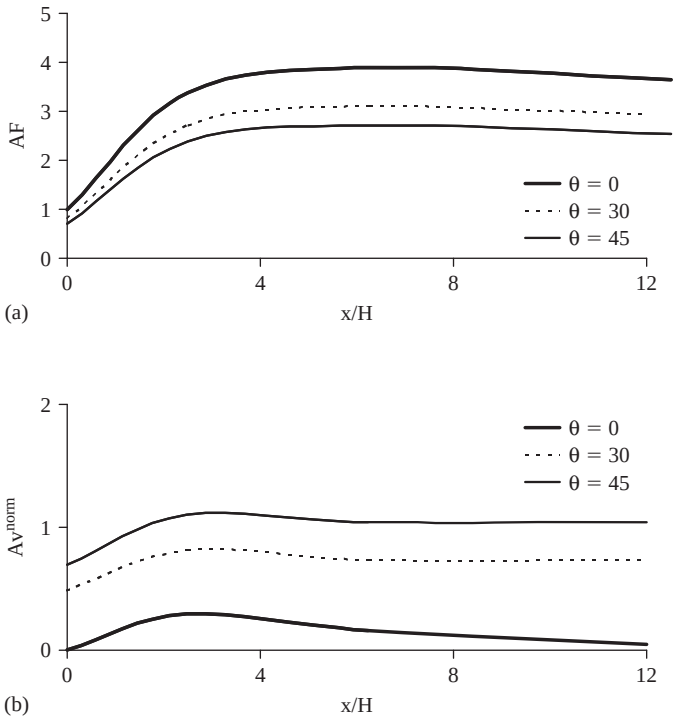

Figure 7 Effects of angle of incidence θ on the amplification of: (a) the horizontal acceleration (AF), and (b) the maximum vertical acceleration normalized with the maximum horizontal base acceleration (AV^{norm}) for Ricker pulse excitation.

is usually considered to be either neutral or even beneficial. However, this is not always the case, since dynamic soil-structure interaction may also be detrimental, depending on the circumstances (see Mylonakis & Gazetas 2000). Therefore, in a case of a complex wall-soil-structure system, elaborate numerical modelling of the whole problem is unavoidable, as it is not realistic to study the wall-soil system and the soil-structure system independently.

In this study the impact of a potential simple structure has been also examined. The simplified model of the structure is shown in Figure 1(b) and it consists of a concentrated mass m located on the top of a single column that provides the stiffness k of the structure. Since the structure can be realized as a fixed-base single-degree-of-freedom (SDOF) system, its eigen-period $T_{STR.}$ could be easily calculated by:

$$T_{STR.} = 2\pi\sqrt{\frac{m}{k}} \tag{7}$$

Figure 8 shows the horizontal acceleration time-histories calculated on the top of the SDOF structure normalized with the base acceleration (AH_{norm}). The response refers

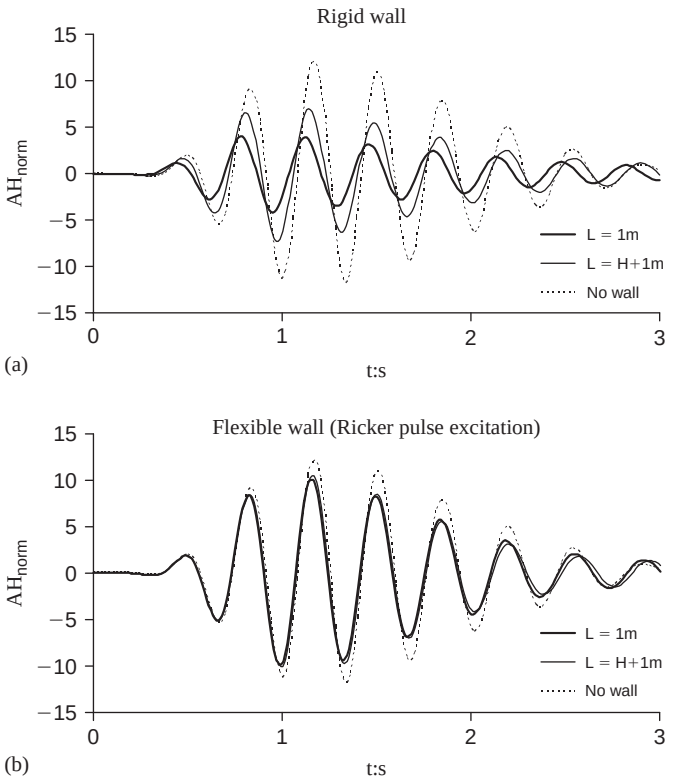

Figure 8 Normalized response of the SDOF structure under the Ricker pulse excitation. Various distances L behind the wall are examined in the case of (a) rigid wall, and (b) flexible wall. Note that for comparison purposes the response of the SDOF under 1-D conditions ("no wall" case) is also included in the graphs.

to the Ricker excitation in the two extreme cases examined (rigid wall and very flexible wall). The distance L behind the wall was considered to be equal to 1 m or 9 m. Note that for comparison purposes the response under 1-D conditions (no wall) is included in the graphs as well. It is obvious that in the case of the rigid wall the response of the structure depends substantially on its distance from the wall, and differs considerably from the corresponding response under 1-D when there is no wall. Conversely, for the case of the flexible wall the location of the structure does not alter its response and the SDOF behaviour is very similar to the 1-D conditions.

In addition, as the relation between T_{SOIL} and $T_{STR.}$ was expected to play a significant role on the overall response, two cases of this ratio were compared. For the first case, T_{SOIL} coincides with $T_{STR.}$ (implying a kind of resonance), while in the second case T_{SOIL} is three times higher than $T_{STR.}$ (representing a relatively stiff structure). In Figure 9 the soil amplification factors AF_{SOIL} (without the structure) and AF'_{SOIL} (with the structure) are compared for three surface points B_i behind the wall: $L/H = 0.2$, 0.7, 1.2, or $L = 1.6$, 5.6, 9.6m, respectively. It is obvious that in the case

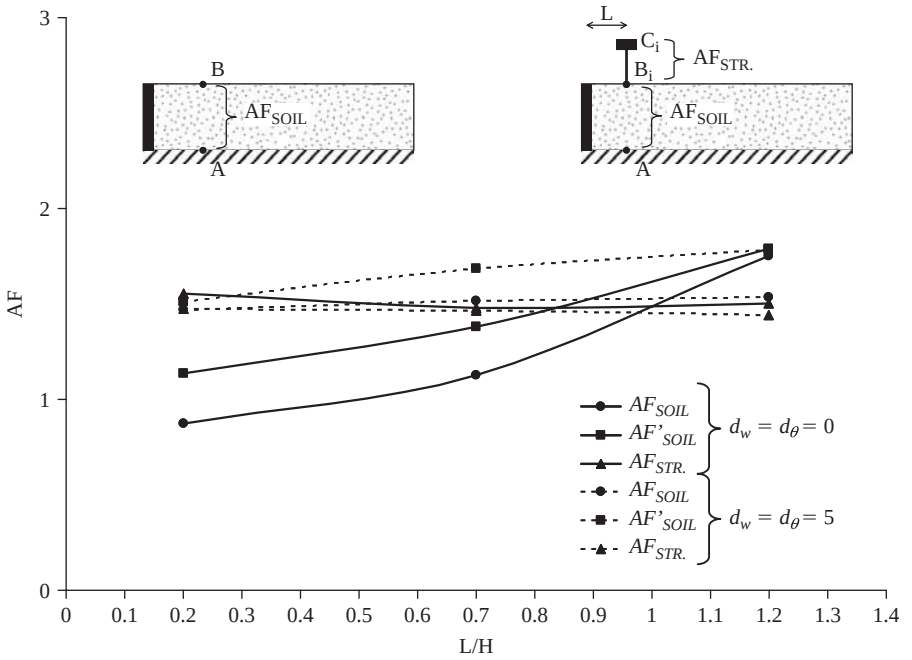

Figure 9 Ricker pulse excitation: Comparison between the soil amplification factors calculated at three points B_i at the surface behind the wall ($L/H = 0.2, 0.7, 1.2$) without the structure (AF_{SOIL}) or with the structure (AF'_{SOIL}). The amplification factor of the structure ($AF_{STR.}$) is also included.

of the rigid fixed-base wall ($d_w = d_\theta = 0$) the difference between AF_{SOIL} and AF'_{SOIL} decreases, while moving away from the wall. In contrast, for the case of the flexible wall ($d_w = d_\theta = 5$) that difference between AF_{SOIL} and AF'_{SOIL} seems to increase.

As it was expected, in the case of the rigid wall the response of the structure depends substantially on its distance from the wall, and differs considerably from the corresponding response of the structure under 1-D conditions (i.e., when there is no wall). On the other hand, for the case of the flexible wall the location of the structure does not alter the response and the behaviour of the structure is affected only by the 1-D conditions. In the same figure the amplification of the structure alone, $AF_{STR.}$, is also included for comparison. This factor represents the amplification of acceleration between the top of the structure and its base. It is evident that the wall flexibility and the distance of the structure from the wall L have no substantial effect on its response.

Finally, in order to examine the effect of the absolute value of the mass of the structure on the amplification factor of the structure $AF_{STR.}$, a structure with five times more mass was incorporated in the models. However, since $T_{STR.}$ should be kept constant in order to make the comparison feasible, the ratio between m and k was kept unchanged, thus the second structure was also five times more stiff. According to Figure 10, this substantial increase of mass seems to have certain influence on the response of the structure that follows the same trend for both cases of wall's flexibility.

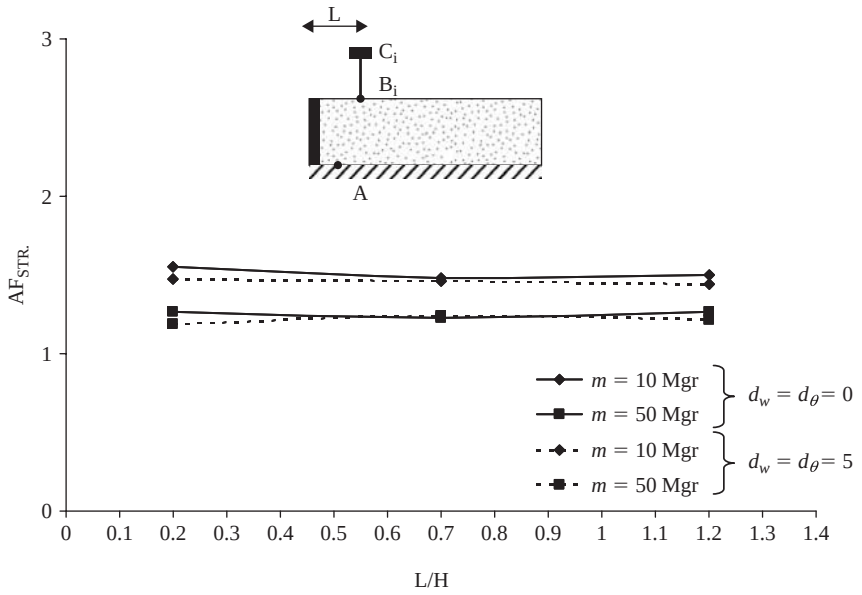

Figure 10 Ricker pulse excitation: Effect of the absolute value of the mass of the structure on the amplification factor of the structure ($AF_{STR.}$). Note that $T_{STR.}$ is kept constant.

5 Effect of the structure on the wall distress

Numerical results have proven that the existence of a structure may increase or reduce the dynamic earth pressures developed on the wall. For that purpose, Figure 11 shows the height-wise distribution of the normalized induced earth pressures for systems with different wall flexibilities and base excitations. It can be observed that the existence of a structure may reduce the dynamic earth pressures developed on the wall, especially when the structure is close to the wall. This phenomenon may be attributed to the impact of the structure on the eigen-frequencies of the whole system. It is evident that the phenomenon is more intense in the case of the flexible wall.

Moreover, Figure 12 presents the height-wise distribution of the normalized induced dynamic earth pressures for the two ratios of soil and structure periods previously mentioned, when the structure is located close to the wall. The observed height-wise stress distributions may be attributed to the impact of the structure on the eigen-frequencies of the whole system, and can be explained by the results plotted in Figure 13, which shows the *Pressure Amplification Factor (PAF)* as a function of frequency which can be defined using the following expression:

$$PAF = \frac{FFT[P(t)]}{FFT_A} \tag{8}$$

where $FFT[P(t)]$ is the Fourier spectrum of the normalized induced dynamic earth force time history P(t), and FFT_A is the Fourier spectrum of the acceleration time history of the Ricker pulse excitation that is applied at the base of the model (point A). It is

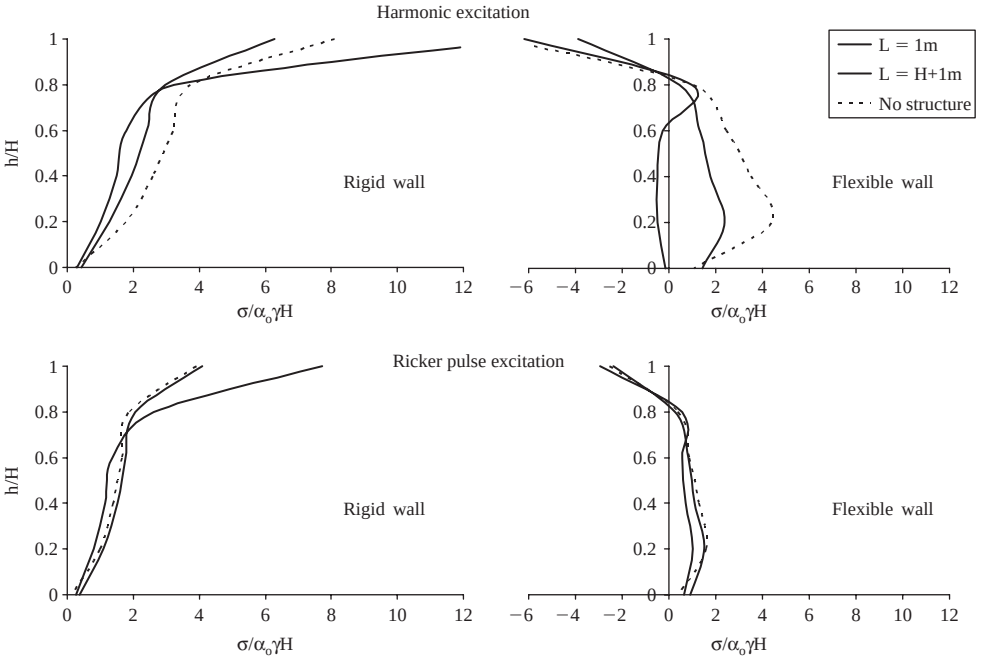

Figure 11 Height-wise distribution of the normalized induced earth pressures for systems with different wall flexibilities and base excitations.

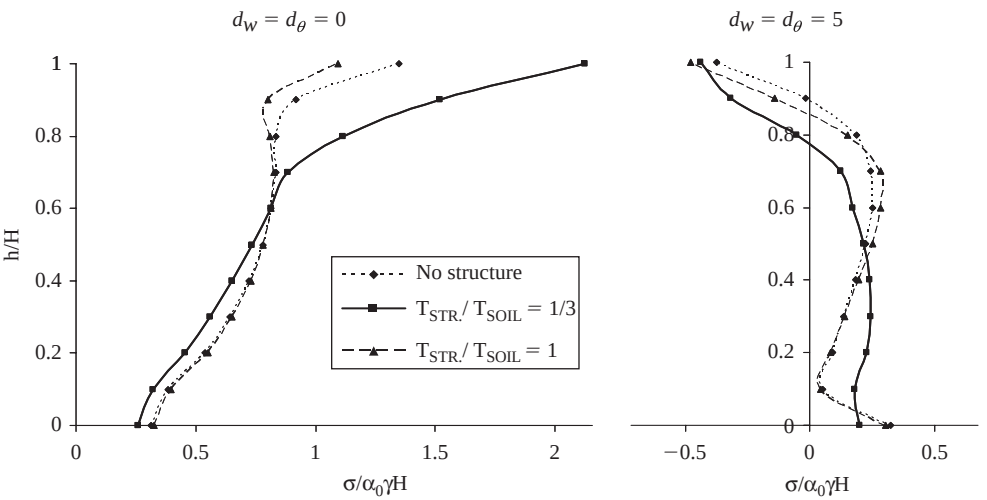

Figure 12 Ricker pulse excitation: Height-wise distribution of the normalized induced dynamic earth pressures for the two extreme cases of wall flexibility examined.

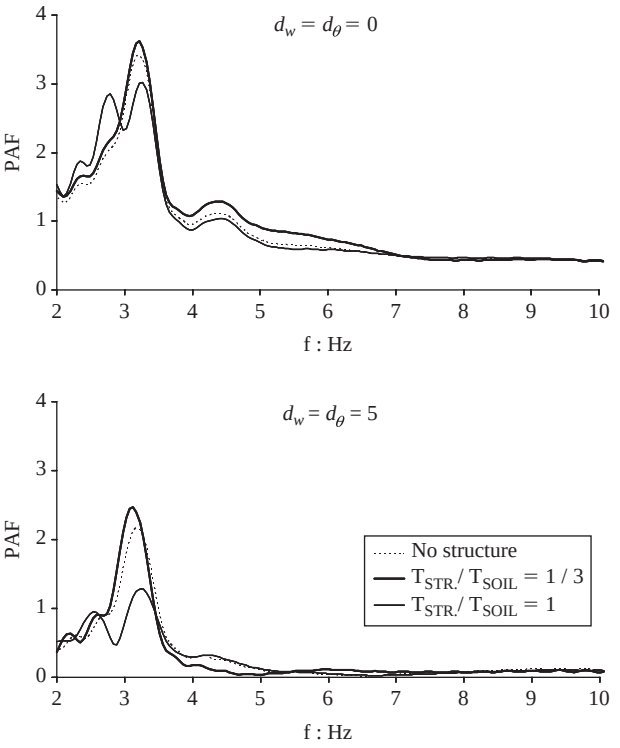

Figure 13 Ricker pulse excitation: Pressure Amplification Factors (PAF) calculated for the two extreme cases of wall flexibility examined.

evident that in the case of low-frequency excitations the values of *PAF* converge to the values proposed by Veletsos & Younan (1997) and Psarropoulos et al. (2005). However, the presence of the structure behind the wall has an impact not only on the amplitude of the developed dynamic earth but on its frequency content. This impact however seems to depend strongly on the characteristics of the structure.

6 Conclusions

The scope of the present study was to investigate the dynamic interaction between retaining walls, retained soil and retained structures. In all cases examined it was proven that the characteristics of the wall as well as the seismic excitation affect substantially the dynamic behaviour of the whole system. The rigid wall imposes a boundary that clearly alters the 1-D conditions of the backfill, while the flexible wall does not transform the model into 2-D. Furthermore, it has been shown that the amplification of the acceleration levels on the retained soil and structure depends also on the seismic motion. In addition, it has been presented that the existence of a retaining wall may alter considerably the dynamic response of a structure founded on the retained soil. Moreover, the distress of the wall may be affected significantly by the presence of retained structures.

The results of the present investigation provide a clear indication of the direct dynamic interaction between the wall, the retained soil, and the retained structures. That fact justifies the necessity for a more elaborate consideration, both in seismic codes and engineering practice, of this interrelated phenomenon during the seismic design, not only of the retaining walls but of the nearby structures as well.

References

ABAQUS. 2003. *Analysis user's manual, Version 6.4*, ABAQUS Inc., USA.

EAK. 2000. *Greek seismic code*, Greek Ministry of Public Works, Athens, Greece.

EC8. 2004. *Eurocode 8: Design of structures for earthquake resistance-Part 1*, European standard CEN-ENV-1998-1, European Committee for Standardization, Brussels.

Iai, S. 1998. Seismic analysis and performance of retaining structures, in Dakoulas, P., Yegian, M. & Holtz, R.D. (Eds.), *Proceedings of Geotechnical Earthquake Engineering and Soil Dynamics III*, Geotechnical Special Publ. No. 75, Vol. 2, ASCE, Reston, Va., pp. 1020–1044.

Kramer, S. 1996. *Geotechnical earthquake engineering*, Prentice Hall.

Mononobe, N. & Matsuo, H. 1929. On the determination of earth pressures during earthquakes, *Proceedings of the World Engineering Congress*, Tokyo, Japan, Vol. 9, Paper 388.

Mylonakis, G. & Gazetas, G. 2000. Seismic soil-structure interaction: beneficial or detrimental? *Journal of Earthquake Engineering*, **4**(3): 277–301.

Okabe, S. 1926. General theory of earth pressures, *Journal of the Japan Society of Civil Engineering*, **12**(1).

PIANC. 2001. *Seismic design guidelines for port structures*, International Navigation Association (PIANC), Balkema Publishers, Netherlands.

Psarropoulos, P.N., Klonaris, G. & Gazetas, G. 2005. Seismic earth pressures on rigid and flexible retaining walls, *Soil Dynamics and Earthquake Engineering*, **25**(7–10): 795–809.

Ricker, N. 1960. The form and laws of propagation of seismic wavelets, *Geophysics*, **18**, 10–40.

Roesset, J.M. 1977. Soil amplification of earthquakes, in Desai, C.S. & Christian, J.T. (Eds.), *Numerical Methods in Geotechnical Engineering*, McGraw-Hill, pp. 639–682.

Scott, R.F. 1973. Earthquake-induced pressures on retaining walls, *Proceedings of the 5th World Conference on Earthquake Engineering*, Vol. 2, pp. 1611–1620.

Seed, H.B. & Whitman, R.V. 1970. Design of earth retaining structures for dynamic loads, *Proceedings of the Special Conference on Lateral Stresses in the Ground and Design of Earth Retaining Structures*, ASCE, pp. 103–147.

Veletsos, A.S. & Younan, A.H. 1997. Dynamic response of cantilever retaining walls, *ASCE Journal of Geotechnical and Geoenvironmental Engineering*, **123**(2): 161–172.

Wood, J.H. 1975. Earthquake–induced pressures on a rigid wall structure, *Bulletin of New Zealand National Earthquake Engineering*, **8**: 175–186.

Wu, G. & Finn, W.D.L. 1999. Seismic lateral pressures for design of rigid walls, *Canadian Geotechnical Journal*, **36**(3): 509–522.

Tsompanakis, Y., Avrana, V., Zania, V. & Psarropoulos, P.N. 2006. Dynamic interaction between retaining walls and retained structures/geostructures, *Proceedings of the 1st European Conference on Earthquake Engineering and Seismology (ECEES 2006)*, September 3–8, Geneva, Switzerland.

Tsompanakis, Y., Psarropoulos, P.N., Zania, V. & Tsimpourakis, S. 2007. Effects of soil nonlinearity on the seismic response of rigid non-sliding retaining walls, *Proceedings of the 4th International Conference on Earthquake Geotechnical Engineering (ICEGE 2007)*, June 25–28, Thessaloniki, Greece.

Chapter 30

Earthquake response of liquid tanks installed in saturated transversely isotropic soil

Jae Kwan Kim & Jin Ho Lee

Seoul National University, Seoul, Korea

ABSTRACT: A 3-D transmitting boundary in a cylindrical coordinate system is applied to obtain the earthquake response of a cylindrical liquid storage tank installed in the water-saturated transversely isotropic ground. The effects of the far-field region are represented by the transmitting boundary. Using finite elements, models are developed for the flexible tank wall and the near-field region of the ground. The motion of the contained liquid is modeled using boundary elements. Hybrid time domain-frequency domain analysis is used to obtain direct time-domain representation of the earthquake response of the system. Numerical results are given to illustrate the results of this method of analysis. A rigorous two-phase transversely isotropic medium model has to be employed to accurately represent the dynamic behaviors of a structure on the water-saturated transversely isotropic strata.

1 Introduction

The effects of soil-structure interaction can be evident in the dynamic response of massive structures installed in relatively flexible ground. In past studies on dynamic soil-structure interactions, the ground was assumed to be either a layered half-space or layered strata over a rigid bedrock. The far-field region of the ground, where elastic waves radiate out to an infinite boundary, was modeled as a homogeneous medium either in the radial or the horizontal direction. The behavior of rigid foundations in the layered strata over a rigid bedrock has been widely studied, partly due to the relative ease of the mathematical modeling and analysis.

A 3-D transmitting boundary in a cylindrical coordinate system is used for modeling the elastic waves radiating out to an infinite boundary in water-saturated transversely isotropic soil strata overlaying rigid bedrock. The saturated soil strata is assumed to consist of a porous material and modeled as a transversely isotropic two-phase medium, based on the $u-U$ formulation of the hybrid mixture theory (Lewis & Schrefler 1998). The transmitting boundary is combined with the finite-elements model of the near-field region, using the same $u-U$ formulation.

The transmitting boundary is applied to obtain the earthquake response, as a direct time-domain representation, of a cylindrical liquid storage tank installed in the ground saturated with water. The soil strata are modeled as a transversely isotropic saturated media. The flexible tank wall is modeled using axisymmetric shell finite elements and the tank is assumed to be anchored to a rigid circular footing. The contained liquid is assumed to be inviscid incompressible ideal fluid, whose motion is modeled using boundary elements to obtain the added mass and sloshing stiffness matrices.

The direct time-domain solution of the system's earthquake response is obtained using hybrid time domain-frequency domain analysis.

2 3-D transmitting boundary in a cylindrical coordinate system

2.1 *Governing equations for a water-saturated transversely isotropic medium*

Using the hybrid mixture theory (Lewis & Schrefler 1998), governing equations for a water-saturated transversely isotropic porous medium can be derived based on the $u-U$ formulation.

$$\begin{aligned}&\nabla\cdot(\mathbf{D}:\nabla\mathbf{u})+Q[(\boldsymbol{\alpha}-n\mathbf{I})\nabla][(\boldsymbol{\alpha}-n\mathbf{I})\nabla]\cdot\mathbf{u}+Q(n\nabla)[(\boldsymbol{\alpha}-n\mathbf{I})\nabla]\cdot\mathbf{U}\\&\quad-(1-n)\rho_s\ddot{\mathbf{u}}-n^2\mathbf{f}(\dot{\mathbf{u}}-\dot{\mathbf{U}})=0\\&Q(n\nabla)[(\boldsymbol{\alpha}-n\mathbf{I})\nabla]\cdot\mathbf{u}+Q(n\nabla)(n\nabla)\cdot\mathbf{U}-n\rho_w\ddot{\mathbf{U}}-n^2\mathbf{f}(\dot{\mathbf{U}}-\dot{\mathbf{u}})=0\end{aligned}\tag{1}$$

where $\mathbf{u}$ and $\mathbf{U}$ denote the displacement of the solid and fluid phases, respectively; ρ_s and ρ_w the density of the solid and fluid phases, respectively; $\mathbf{D}$ the elastic constitutive tensor for a transversely isotropic medium (Chen & Saleeb 1994); n the porosity; $\mathbf{f}=\boldsymbol{\kappa}^{-1}$, in which $\boldsymbol{\kappa}$ is the permeability tensor; and $\mathbf{I}$ represents the second order identity tensor. The generalized Biot's constant $\boldsymbol{\alpha}$ and the bulk modulus Q of the mixture are defined as follows:

$$\begin{aligned}&\boldsymbol{\alpha}=\mathbf{I}-\mathbf{D}:\mathbf{I}\frac{1}{3K_s}=\mathbf{I}-\mathbf{I}:\mathbf{D}\frac{1}{3K_s}\\&\alpha=\frac{1}{3}\mathbf{I}:\boldsymbol{\alpha}=\frac{1}{3}\boldsymbol{\alpha}:\mathbf{I}=1-\frac{K_T}{K_s}\end{aligned}\tag{2}$$

$$\frac{1}{Q}=\frac{\alpha-n}{K_s}+\frac{n}{K_w}\tag{3}$$

where K_s, K_w and K_T are the bulk modulus of solid grain, water, and solid skeleton, respectively. These equations can be derived from the generalized Biot's theory (Zienkiewicz et al. 1999).

On the boundary $\partial\Omega=\Gamma$ of the medium Ω, the boundary conditions for the solid phase can be expressed as follows:

$$\begin{aligned}\boldsymbol{\sigma}\boldsymbol{\nu}&=\widetilde{\boldsymbol{\sigma}}_{\mathbf{n}}\quad\text{on }\Gamma=\Gamma_t\\\mathbf{u}&=\widetilde{\mathbf{u}}\quad\text{on }\Gamma=\Gamma_u\end{aligned}\tag{4}$$

where $\boldsymbol{\nu}$ denotes the outward unit normal vector on the boundary Γ and $\Gamma=\Gamma_t\cup\Gamma_u$. The boundary conditions for the fluid phase can be written on the boundary Γ as follows:

$$\begin{aligned}p&=\widetilde{p}\quad\text{on }\Gamma=\Gamma_p\\\boldsymbol{\nu}\cdot\dot{\mathbf{w}}&=\widetilde{w}_n\quad\text{on }\Gamma=\Gamma_w\end{aligned}\tag{5}$$

where $\mathbf{w} = n(\mathbf{U} - \mathbf{u})$ denotes the 'pseudo-displacement' of the fluid phase with respect to the solid phase so defined that $\dot{\mathbf{w}}$ is the average relative velocity of seepage and $\Gamma = \Gamma_p \cup \Gamma_w$.

2.2 *Eigenvalue problems for the Rayleigh and Love wave modes*

The governing equations can be decoupled into equations of the Rayleigh and Love wave modes (Kim et al. 2000, Lee 2007, Lee & Kim 2008) and the eigenvalue problems for each mode can be defined in the layered strata overlaying a rigid bedrock. In the layered strata shown in Figure 1, there is no traction on the ground surface, no pore pressure on the ground water surface, and no soil displacements at the bedrock. Furthermore, ground water cannot flow perpendicular to the bedrock. With these conditions, the decoupled equations constitute eigenvalue problems for the Rayleigh and Love wave modes, respectively. The finite-element technique (Waas 1972, Kausel 1974, Tassoulas 1981) is employed to calculate eigenvalues and eigenfunctions. The following algebraic equations can be obtained for the Rayleigh and Love wave modes.

$$\begin{aligned} [k^2\mathbf{A}_R + ik\mathbf{B}_R + \mathbf{G}_R - \omega^2\mathbf{M}_R + i\omega\mathbf{C}_R]\boldsymbol{\Delta}_R = 0 \quad & \text{for Rayliegh wave mode} \\ [k^2\mathbf{A}_L + \mathbf{G}_L - \omega^2\mathbf{M}_L + i\omega\mathbf{C}_L]\boldsymbol{\Delta}_L = 0 \quad & \text{for Love wave mode} \end{aligned} \tag{6}$$

where k are eigenvalues and $\boldsymbol{\Delta}_R$ and $\boldsymbol{\Delta}_L$ the corresponding eigenvectors. The matrices $\mathbf{A}_R$, $\mathbf{B}_R$, $\mathbf{G}_R$, $\mathbf{M}_R$, $\mathbf{C}_R$, $\mathbf{A}_L$, $\mathbf{G}_L$, $\mathbf{M}_L$, and $\mathbf{C}_L$ are defined in Lee (2007) and Lee & Kim (2008).

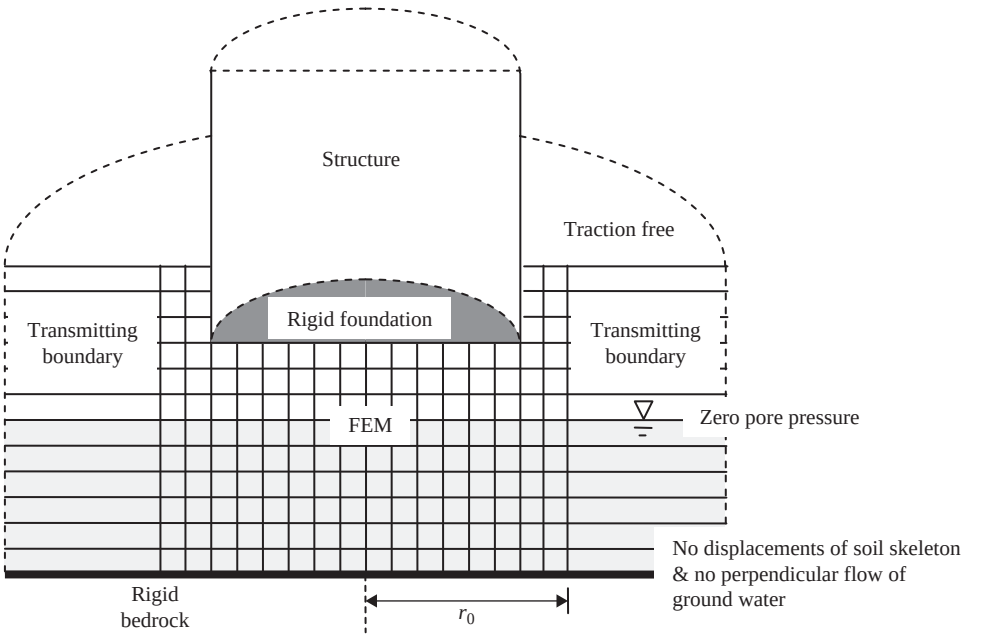

Figure 1 Layered strata overlaying a rigid bedrock.

2.3 *3-D transmitting boundary in a cylindrical coordinate system*

The modes of vibration in a cylindrical coordinate system can be obtained through the method of separation of variables (Kausel 1974; Tassoulas 1981). Using the modes of vibration, equivalent nodal loads and nodal displacements can be evaluated at the cylindrical boundary $r = r_0$ of the region $r \geq r_0$ and the dynamic stiffness of the transmitting boundary in the water-saturated transversely isotropic layered strata can be obtained. The amplitudes of the equivalent nodal loads are given as follows:

$$\mathbf{F} = r_0 \left\{ \mathbf{A}_{TB} \mathbf{\Psi} \mathbf{K}^2 + (\mathbf{D}_{TB} - \mathbf{E}_{TB} + m\mathbf{N}_{TB}) \mathbf{\Phi} \mathbf{K} - \left[\frac{m(m+1)}{2} \mathbf{L}_{TB} + m\mathbf{Q}_{TB} \right] \mathbf{\Psi} \right\} \mathbf{\Gamma} \quad (7)$$

where $\mathbf{\Psi}$ and $\mathbf{\Phi}$ are the modal matrices for the Fourier number m (Lee 2007, Lee & Kim 2008), $\mathbf{K}$ the diagonal matrix of the eigenvalues of the Rayleigh and Love wave modes, and $\mathbf{\Gamma}$ the modal participation factor vector. The matrices $\mathbf{A}_{TB}$, $\mathbf{D}_{TB}$, $\mathbf{E}_{TB}$, $\mathbf{N}_{TB}$, $\mathbf{L}_{TB}$, and $\mathbf{Q}_{TB}$ are defined in Lee (2007) and Lee & Kim (2008). The nodal amplitudes of the displacements can be expressed as the linear combination of the modes of vibration.

$$\mathbf{\Delta} = Y\mathbf{\Gamma} \quad (8)$$

where Y is the modal matrix for the Fourier number m (Lee 2007, Lee & Kim 2008). By eliminating $\mathbf{\Gamma}$ from Equations 7 and 8, the dynamic stiffness $\mathbf{R}$ of the transmitting boundary in the water-saturated transversely isotropic layered strata can be obtained.

$$\mathbf{F} = \mathbf{R}\mathbf{\Delta}$$

$$\mathbf{R} = r_0 \left\{ \mathbf{A}_{TB} \mathbf{\Psi} \mathbf{K}^2 + (\mathbf{D}_{TB} - \mathbf{E}_{TB} + m\mathbf{N}_{TB}) \mathbf{\Phi} \mathbf{K} - \left[\frac{m(m+1)}{2} \mathbf{L}_{TB} + m\mathbf{Q}_{TB} \right] \mathbf{\Psi} \right\} \mathbf{Y}^{-1} \quad (9)$$

The far-field region of the water-saturated transversely isotropic ground in a cylindrical coordinate system can be represented by this transmitting boundary.

2.4 *Finite elements for the near-field region*

The near-field region is modeled by conventional finite elements (Zienkiewicz et al. 1999). Discretized equations of motion can be obtained using the Galerkin method.

$$\begin{bmatrix} \mathbf{M}_{ss} & \\ & \mathbf{M}_{ww} \end{bmatrix} \begin{Bmatrix} \ddot{\mathbf{u}} \\ \ddot{\mathbf{U}} \end{Bmatrix} + \begin{bmatrix} \mathbf{C}_{ss} & -\mathbf{C}_{sw} \\ -\mathbf{C}_{ws} & \mathbf{C}_{ww} \end{bmatrix} \begin{Bmatrix} \dot{\mathbf{u}} \\ \dot{\mathbf{U}} \end{Bmatrix} + \begin{bmatrix} \mathbf{K} + \mathbf{K}_{ss} & \mathbf{K}_{sw} \\ \mathbf{K}_{ws} & \mathbf{K}_{ww} \end{bmatrix} \begin{Bmatrix} \mathbf{u} \\ \mathbf{U} \end{Bmatrix} = \begin{Bmatrix} \mathbf{f}_s \\ \mathbf{f}_w \end{Bmatrix} \quad (10)$$

where subscript s refers to the degrees of freedom of the solid phase and subscript w to those of the fluid phase, respectively.

3 Numerical model of the cylindrical liquid storage tank

3.1 *Finite-elements model for the flexible wall of a cylindrical tank*

The cylindrical tank wall is modeled using axisymmetric shell finite elements (Fig. 2). Shape functions of the 2nd order polynomials are used for the axial and circumferential displacements $\overline{u}_z(\xi)$ and $\overline{u}_\theta(\xi)$. However, those of the 4th order Hermitian polynomials

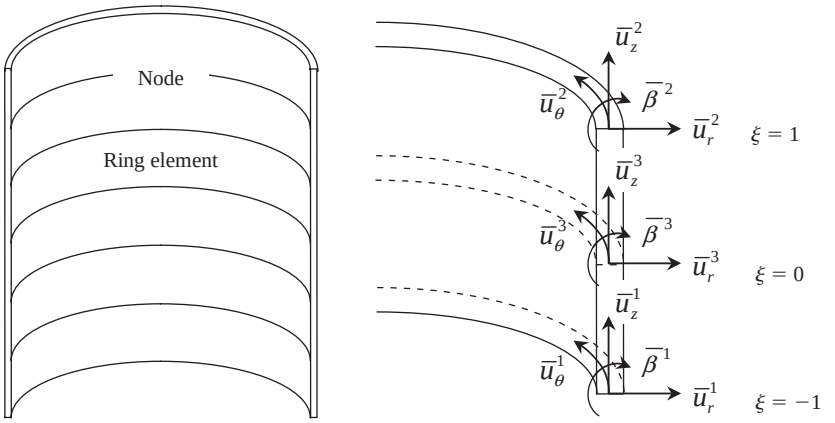

Figure 2 Finite-elements modeling of the flexible wall of a cylindrical tank.

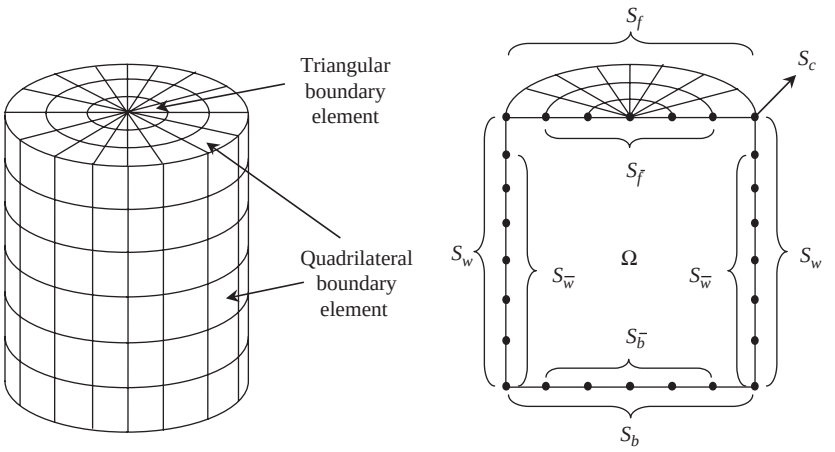

Figure 3 Boundary-elements modeling of the stored liquid.

are used for the radial displacement $\overline{u}_r(\xi)$ to assure the continuity of slope at the nodes. Following the standard finite-element procedures, the mass and stiffness matrices of the cylindrical tank wall can be obtained. The damping matrix is constructed based on the Rayleigh damping after combining the added mass and sloshing stiffness matrices of the liquid stored in the tank.

3.2 *Boundary-elements model for the stored liquid*

An equation of motion for the sloshing height of the liquid surface and the hydrodynamic pressure of the liquid on the wall of the cylindrical tank are obtained using the boundary-elements. The boundary integral equation for the inviscid incompressible liquid (Fig. 3) can be expressed using the velocity potential function ϕ.

$$\phi(\xi, t) = -\int \phi(\mathbf{x}, t)\frac{\partial G(\mathbf{x}, \xi)}{\partial n}ds + \int \frac{\partial \phi(\mathbf{x}, t)}{\partial n}G(\mathbf{x}, \xi)\,ds \quad \text{in } \Omega \tag{11}$$

where $\boldsymbol{\xi}$ is the position vector of the source point, $\mathbf{x}$ the position vector of the field point, n the outward normal vector, and $G(\mathbf{x}, \xi)$ the fundamental solution. The hydrodynamic pressure p can be expressed as follows:

$$p = -\rho_l \frac{\partial \phi(\mathbf{x}, t)}{\partial t} \quad \text{in } \Omega \tag{12}$$

The conditions of the boundary on the free surface of the liquid and of the boundary in contact with the structure can be expressed, respectively, as follows:

$$\begin{aligned} \frac{\partial \phi(\mathbf{x}, t)}{\partial t} + g\eta(\mathbf{x}, t) &= 0 && \text{on } S_f \\ \frac{\partial \phi(\mathbf{x}, t)}{\partial z} &= \frac{\partial \eta(\mathbf{x}, t)}{\partial t} && \text{on } S_f \\ \frac{\partial \phi(\mathbf{x}, t)}{\partial n} &= \dot{u}_n && \text{on } S_w \quad \text{and} \quad S_b \end{aligned} \tag{13}$$

where g is the gravitational acceleration, η the sloshing height of the free surface, and $\dot{u}_n$ the outward normal velocity.

Using 3D boundary elements and applying Equations 12 and 13, discretized algebraic equations can be obtained from Equation 11 as follows:

$$\frac{1}{\rho_l}\left[\begin{array}{c|cc} \mathbf{H}_{ff} & \mathbf{H}_{f\overline{w}} & \mathbf{H}_{f\overline{b}} \\ \hline \mathbf{H}_{\overline{w}f} & \mathbf{H}_{\overline{w}\overline{w}} & \mathbf{H}_{\overline{w}\overline{b}} \\ \mathbf{H}_{\overline{b}f} & \mathbf{H}_{\overline{b}\overline{w}} & \mathbf{H}_{\overline{b}\overline{b}} \end{array}\right]\left\{\begin{array}{c} -\rho_l g \boldsymbol{\eta} \\ -\mathbf{p}_{\overline{w}} \\ -\mathbf{p}_{\overline{b}} \end{array}\right\} - \left[\begin{array}{c|cc} \mathbf{G}_{ff} & \mathbf{G}_{fw} & \mathbf{G}_{fb} \\ \hline \mathbf{G}_{\overline{w}f} & \mathbf{G}_{\overline{w}w} & \mathbf{G}_{\overline{w}b} \\ \mathbf{G}_{\overline{b}f} & \mathbf{G}_{\overline{b}w} & \mathbf{G}_{\overline{b}b} \end{array}\right]\left\{\begin{array}{c} \ddot{\boldsymbol{\eta}} \\ \ddot{\mathbf{u}}_{wn} \\ \ddot{\mathbf{u}}_{bn} \end{array}\right\} = \left\{\begin{array}{c} 0 \\ 0 \\ 0 \end{array}\right\} \tag{14}$$

It should be noted that the corner boundary S_c is included in the surface boundary S_f. The hydrodynamic pressure can be obtained from the second and third equations of Equation 14 and eliminated from the first equation of Equation 14.

The equation of motion for the sloshing height can be obtained.

$$[\mathbf{M}_{\eta\eta}]\{\ddot{\boldsymbol{\eta}}\} + [\mathbf{M}_{\eta w} \quad \mathbf{M}_{\eta b}]\left\{\begin{array}{c} \ddot{\mathbf{u}}_{wn} \\ \ddot{\mathbf{u}}_{bn} \end{array}\right\} + [\mathbf{K}_{\eta\eta}]\{\boldsymbol{\eta}\} = \{0\} \tag{15}$$

where

$$[\mathbf{M}_{\eta\eta}] = -[\mathbf{G}_{ff}] + [\mathbf{H}_{f\overline{w}} \quad \mathbf{H}_{f\overline{b}}]\begin{bmatrix} \mathbf{H}_{\overline{w}\overline{w}} & \mathbf{H}_{\overline{w}\overline{b}} \\ \mathbf{H}_{\overline{b}\overline{w}} & \mathbf{H}_{\overline{b}\overline{b}} \end{bmatrix}^{-1}\begin{bmatrix} \mathbf{G}_{\overline{w}f} \\ \mathbf{G}_{\overline{b}f} \end{bmatrix}$$

$$[\mathbf{M}_{\eta w} \quad \mathbf{M}_{\eta b}] = -[\mathbf{G}_{fw} \quad \mathbf{G}_{fb}] + [\mathbf{H}_{f\overline{w}} \quad \mathbf{H}_{f\overline{b}}]\begin{bmatrix} \mathbf{H}_{\overline{w}\overline{w}} & \mathbf{H}_{\overline{w}\overline{b}} \\ \mathbf{H}_{\overline{b}\overline{w}} & \mathbf{H}_{\overline{b}\overline{b}} \end{bmatrix}^{-1}\begin{bmatrix} \mathbf{G}_{\overline{w}w} & \mathbf{G}_{\overline{w}b} \\ \mathbf{G}_{\overline{b}w} & \mathbf{G}_{\overline{b}b} \end{bmatrix}$$

$$[\mathbf{K}_{\eta\eta}] = -\rho_l g[\mathbf{H}_{ff}] + \rho_l g[\mathbf{H}_{f\overline{w}} \quad \mathbf{H}_{f\overline{b}}]\begin{bmatrix} \mathbf{H}_{\overline{w}\overline{w}} & \mathbf{H}_{\overline{w}\overline{b}} \\ \mathbf{H}_{\overline{b}\overline{w}} & \mathbf{H}_{\overline{b}\overline{b}} \end{bmatrix}^{-1}\begin{bmatrix} \mathbf{H}_{\overline{w}f} \\ \mathbf{H}_{\overline{b}f} \end{bmatrix}$$

The liquid-structure interaction effects in a liquid storage tank can be analyzed using the equation of motion for the sloshing height of Equation 15 and the hydrodynamic pressure which can be obtained from Equation 14. However, the effects of

the hydrodynamic pressure on boundary S_c can not be taken into account explicitly in this formulation. In this study, a new approach is developed to consider these effects.

A new partition of Equation 14 is adopted by the inclusion of the corner boundary S_c into the wall boundary S_w as follows:

$$\frac{1}{\rho_l}\left[\begin{array}{c|cc} \mathbf{H}_{\bar{f}\bar{f}} & \mathbf{H}_{\bar{f}w} & \mathbf{H}_{\bar{f}\bar{b}} \\ \hline \mathbf{H}_{w\bar{f}} & \mathbf{H}_{ww} & \mathbf{H}_{w\bar{b}} \\ \mathbf{H}_{\bar{b}\bar{f}} & \mathbf{H}_{\bar{b}w} & \mathbf{H}_{\bar{b}\bar{b}} \end{array}\right]\left\{\begin{array}{c} -\rho_l g\bar{\boldsymbol{\eta}} \\ -\mathbf{p}_w \\ -\mathbf{p}_{\bar{b}} \end{array}\right\} - \left[\begin{array}{c|cc} \mathbf{G}_{\bar{f}\bar{f}} & \mathbf{G}_{\bar{f}w} & \mathbf{G}_{\bar{f}\bar{b}} \\ \hline \mathbf{G}_{w\bar{f}} & \mathbf{G}_{ww} & \mathbf{G}_{wb} \\ \mathbf{G}_{\bar{b}\bar{f}} & \mathbf{G}_{\bar{b}w} & \mathbf{G}_{\bar{b}\bar{b}} \end{array}\right]\left\{\begin{array}{c} \ddot{\boldsymbol{\eta}} \\ \ddot{\mathbf{u}}_{wn} \\ \ddot{\mathbf{u}}_{bn} \end{array}\right\} = \left\{\begin{array}{c} 0 \\ 0 \\ 0 \end{array}\right\} \tag{16}$$

The hydrodynamic pressure can be obtained from the second and third equations of Equation 16.

$$\left\{\begin{array}{c} -\mathbf{p}_w \\ -\mathbf{p}_{\bar{b}} \end{array}\right\} = \left[\begin{array}{c} \widetilde{\mathbf{G}}_{wf} \\ \widetilde{\mathbf{G}}_{\bar{b}f} \end{array}\right]\{\ddot{\boldsymbol{\eta}}\} + \left[\begin{array}{cc} \widetilde{\mathbf{G}}_{ww} & \widetilde{\mathbf{G}}_{wb} \\ \widetilde{\mathbf{G}}_{\bar{b}w} & \widetilde{\mathbf{G}}_{\bar{b}b} \end{array}\right]\left\{\begin{array}{c} \ddot{\mathbf{u}}_{wn} \\ \ddot{\mathbf{u}}_{bn} \end{array}\right\} + \left[\begin{array}{c} \widetilde{\mathbf{H}}_{wf} \\ \widetilde{\mathbf{H}}_{\bar{b}f} \end{array}\right]\{\boldsymbol{\eta}\} \tag{17}$$

where

$$\left[\begin{array}{c} \widetilde{\mathbf{G}}_{wf} \\ \widetilde{\mathbf{G}}_{\bar{b}f} \end{array}\right] = \rho_l\left[\begin{array}{cc} \mathbf{H}_{ww} & \mathbf{H}_{w\bar{b}} \\ \mathbf{H}_{\bar{b}w} & \mathbf{H}_{\bar{b}\bar{b}} \end{array}\right]^{-1}\left[\begin{array}{c} \mathbf{G}_{wf} \\ \mathbf{G}_{\bar{b}f} \end{array}\right]$$

$$\left[\begin{array}{cc} \widetilde{\mathbf{G}}_{ww} & \widetilde{\mathbf{G}}_{wb} \\ \widetilde{\mathbf{G}}_{\bar{b}w} & \widetilde{\mathbf{G}}_{\bar{b}b} \end{array}\right] = \rho_l\left[\begin{array}{cc} \mathbf{H}_{ww} & \mathbf{H}_{w\bar{b}} \\ \mathbf{H}_{\bar{b}w} & \mathbf{H}_{\bar{b}\bar{b}} \end{array}\right]^{-1}\left[\begin{array}{cc} \mathbf{G}_{ww} & \mathbf{G}_{wb} \\ \mathbf{G}_{\bar{b}w} & \mathbf{G}_{\bar{b}b} \end{array}\right]$$

$$\left[\begin{array}{c} \widetilde{\mathbf{H}}_{wf} \\ \widetilde{\mathbf{H}}_{\bar{b}f} \end{array}\right] = \rho_l g\left[\begin{array}{cc} \mathbf{H}_{ww} & \mathbf{H}_{w\bar{b}} \\ \mathbf{H}_{\bar{b}w} & \mathbf{H}_{\bar{b}\bar{b}} \end{array}\right]^{-1}\left[\begin{array}{c|c} \mathbf{H}_{w\bar{f}} & 0 \\ \mathbf{H}_{\bar{b}\bar{f}} & 0 \end{array}\right]$$

The effects of the hydrodynamic pressure on the boundary S_c can now be incorporated explicitly into Equation 17. Using the equation of motion for the sloshing height of Equation 15 and the hydrodynamic pressure of Equation 17, the liquid-structure interaction effects in a liquid storage tank can be analyzed.

The equivalent nodal forces from the hydrodynamic pressure can be evaluated from Equation 17 as follows:

$$\left\{\begin{array}{c} \mathbf{F}_w^{hyd} \\ \mathbf{F}_b^{hyd} \end{array}\right\} = [\mathbf{L}]\left\{\begin{array}{c} \mathbf{p}_w \\ \mathbf{p}_{\bar{b}} \end{array}\right\} = -\left[\begin{array}{c} \mathbf{M}_{w\eta} \\ \mathbf{M}_{b\eta} \end{array}\right]\{\ddot{\boldsymbol{\eta}}\} - \left[\begin{array}{cc} \mathbf{M}_{ww} & \mathbf{M}_{wb} \\ \mathbf{M}_{bw} & \mathbf{M}_{bb} \end{array}\right]\left\{\begin{array}{c} \ddot{\mathbf{u}}_{wn} \\ \ddot{\mathbf{u}}_{bn} \end{array}\right\} - \left[\begin{array}{c} \mathbf{K}_{w\eta} \\ \mathbf{K}_{b\eta} \end{array}\right]\{\boldsymbol{\eta}\} \tag{18}$$

where

$$\left[\begin{array}{c} \mathbf{M}_{w\eta} \\ \mathbf{M}_{b\eta} \end{array}\right] = [\mathbf{L}]\left[\begin{array}{c} \widetilde{\mathbf{G}}_{wf} \\ \widetilde{\mathbf{G}}_{\bar{b}f} \end{array}\right]$$

$$\left[\begin{array}{cc} \mathbf{M}_{ww} & \mathbf{M}_{wb} \\ \mathbf{M}_{bw} & \mathbf{M}_{bb} \end{array}\right] = [\mathbf{L}]\left[\begin{array}{cc} \widetilde{\mathbf{G}}_{ww} & \widetilde{\mathbf{G}}_{wb} \\ \widetilde{\mathbf{G}}_{\bar{b}w} & \widetilde{\mathbf{G}}_{\bar{b}b} \end{array}\right]$$

$$\left[\begin{array}{c} \mathbf{K}_{w\eta} \\ \mathbf{K}_{b\eta} \end{array}\right] = [\mathbf{L}]\left[\begin{array}{c} \widetilde{\mathbf{H}}_{wf} \\ \widetilde{\mathbf{H}}_{\bar{b}f} \end{array}\right]$$

where **L** is the transformation matrix converting the surface tractions into the equivalent nodal forces. After the equivalent nodal forces in the Cartesian coordinate system are transformed to those in the cylindrical coordinate system, the forces are applied to the axisymmetric finite-elements model of the cylindrical tank wall as external forces.

3.3 *Coupling of the stored liquid with the flexible tank wall*

Equations of motion for the flexible tank wall can be obtained from the finite-elements model as follows:

$$\begin{bmatrix} \mathbf{M}_{11}^s & \mathbf{M}_{12}^s \\ \mathbf{M}_{21}^s & \mathbf{M}_{22}^s \end{bmatrix} \begin{Bmatrix} \ddot{\mathbf{u}}_1^t(t) \\ \ddot{\mathbf{u}}_2^t(t) \end{Bmatrix} + \begin{bmatrix} \mathbf{K}_{11}^s & \mathbf{K}_{12}^s \\ \mathbf{K}_{21}^s & \mathbf{K}_{22}^s \end{bmatrix} \begin{Bmatrix} \mathbf{u}_1(t) \\ \mathbf{u}_2(t) \end{Bmatrix} = \begin{Bmatrix} 0 \\ \mathbf{F}_2^{hyd}(t) \end{Bmatrix} \tag{19}$$

where subscript 1 refers to the degrees of freedom of the tank wall not in contact with the stored liquid and subscript 2 to those in contact with the stored liquid. Superscript t refers to the total displacement. $\mathbf{F}_2^{hyd}$ denotes the hydrodynamic force applied to the tank wall by the stored liquid, which can be constructed from Equation 18. By incorporating Equation 18 into Equation 19, equations of motion can be rewritten as follows:

$$\begin{bmatrix} \mathbf{M}_{11}^s & \mathbf{M}_{12}^s & 0 \\ \mathbf{M}_{21}^s & \mathbf{M}_{22}^s + \mathbf{M}_{22}^l & \mathbf{M}_{2\eta}^l \end{bmatrix} \begin{Bmatrix} \ddot{\mathbf{u}}_1^t(t) \\ \ddot{\mathbf{u}}_2^t(t) \\ \ddot{\boldsymbol{\eta}}(t) \end{Bmatrix} + \begin{bmatrix} \mathbf{K}_{11}^s & \mathbf{K}_{12}^s & 0 \\ \mathbf{K}_{21}^s & \mathbf{K}_{22}^s & \mathbf{K}_{2\eta}^l \end{bmatrix} \begin{Bmatrix} \mathbf{u}_1(t) \\ \mathbf{u}_2(t) \\ \boldsymbol{\eta}(t) \end{Bmatrix} = \begin{Bmatrix} 0 \\ 0 \end{Bmatrix} \tag{20}$$

The equations of motion for the whole liquid-structure interaction system can be obtained by combining the equation of motion for the sloshing height (Equation 15) with Equation 20.

$$\begin{bmatrix} \mathbf{M}_{11}^s & \mathbf{M}_{12}^s & 0 \\ \mathbf{M}_{21}^s & \mathbf{M}_{22}^s + \mathbf{M}_{22}^l & \mathbf{M}_{2\eta}^l \\ 0 & \mathbf{M}_{\eta 2}^l & \mathbf{M}_{\eta\eta}^l \end{bmatrix} \begin{Bmatrix} \ddot{\mathbf{u}}_1^t(t) \\ \ddot{\mathbf{u}}_2^t(t) \\ \ddot{\boldsymbol{\eta}}(t) \end{Bmatrix} + \begin{bmatrix} \mathbf{K}_{11}^s & \mathbf{K}_{12}^s & 0 \\ \mathbf{K}_{21}^s & \mathbf{K}_{22}^s & \mathbf{K}_{2\eta}^l \\ 0 & 0 & \mathbf{K}_{\eta\eta}^l \end{bmatrix} \begin{Bmatrix} \mathbf{u}_1(t) \\ \mathbf{u}_2(t) \\ \eta(t) \end{Bmatrix} = \begin{Bmatrix} 0 \\ 0 \\ 0 \end{Bmatrix} \tag{21}$$

The damping effects can be represented using the Rayleigh damping and the final equations of motion can be obtained in terms of relative displacements.

$$\begin{bmatrix} \mathbf{M}_{11}^s & \mathbf{M}_{12}^s & 0 \\ \mathbf{M}_{21}^s & \mathbf{M}_{22}^s + \mathbf{M}_{22}^l & \mathbf{M}_{2\eta}^l \\ 0 & \mathbf{M}_{\eta 2}^l & \mathbf{M}_{\eta\eta}^l \end{bmatrix} \begin{Bmatrix} \ddot{\mathbf{u}}_1(t) \\ \ddot{\mathbf{u}}_2(t) \\ \ddot{\boldsymbol{\eta}}(t) \end{Bmatrix} + \begin{bmatrix} \mathbf{C}_{11}^s & \mathbf{C}_{12}^s & 0 \\ \mathbf{C}_{21}^s & \mathbf{C}_{22}^s & 0 \\ 0 & 0 & \mathbf{C}_{\eta\eta}^l \end{bmatrix} \begin{Bmatrix} \dot{\mathbf{u}}_1(t) \\ \mathbf{u}_2(t) \\ \dot{\boldsymbol{\eta}}(t) \end{Bmatrix}$$
$$+ \begin{bmatrix} \mathbf{K}_{11}^s & \mathbf{K}_{12}^s & 0 \\ \mathbf{K}_{21}^s & \mathbf{K}_{22}^s & \mathbf{K}_{2\eta}^l \\ 0 & 0 & \mathbf{K}_{\eta\eta}^l \end{bmatrix} \begin{Bmatrix} \mathbf{u}_1(t) \\ \mathbf{u}_2(t) \\ \boldsymbol{\eta}(t) \end{Bmatrix} = - \begin{bmatrix} \mathbf{M}_{11}^s & \mathbf{M}_{12}^s & 0 \\ \mathbf{M}_{21}^s & \mathbf{M}_{22}^s + \mathbf{M}_{22}^l & \mathbf{M}_{2\eta}^l \\ 0 & \mathbf{M}_{\eta 2}^l & \mathbf{M}_{\eta\eta}^l \end{bmatrix} \{\mathbf{r}\} \ddot{u}_g(t) \tag{22}$$

where

$$\begin{bmatrix} \mathbf{C}_{11}^s & \mathbf{C}_{12}^s \\ \mathbf{C}_{21}^s & \mathbf{C}_{22}^s \end{bmatrix} = \alpha_i \begin{bmatrix} \mathbf{M}_{11}^s & \mathbf{M}_{12}^s \\ \mathbf{M}_{21}^s & \mathbf{M}_{22}^s + \mathbf{M}_{22}^l \end{bmatrix} + \beta_i \begin{bmatrix} \mathbf{K}_{11}^s & \mathbf{K}_{12}^s \\ \mathbf{K}_{21}^s & \mathbf{K}_{22}^s \end{bmatrix}$$
$$[\mathbf{C}_{\eta\eta}^l] = \alpha_s [\mathbf{M}_{\eta\eta}^l] + \beta_s [\mathbf{K}_{\eta\eta}^l] \tag{23}$$

in which α_i and β_i are the Rayleigh damping factors for the interaction mode and α_s and β_s for the sloshing mode. **r** denotes the influence vector.

4 Hybrid time domain-frequency domain analysis of soil-structure interaction

The earthquake response, as a direct time-domain representation, of the cylindrical liquid storage tank installed in the water-saturated transversely isotropic soil strata can be obtained by employing the numerical models of the cylindrical tank structure, the stored liquid, the near-field region of the ground, and the transmitting boundary. The equations of motion for the tank structure, the stored liquid, and the near-field region of the ground can be written in the time domain as follows:

$$\begin{bmatrix} \mathbf{M}_{ss} & \mathbf{M}_{sg} \\ \mathbf{M}_{gs} & \mathbf{M}_{gg} \end{bmatrix} \begin{Bmatrix} \ddot{\mathbf{u}}_s(t) \\ \ddot{\mathbf{u}}_g(t) \end{Bmatrix} + \begin{bmatrix} \mathbf{C}_{ss} & \mathbf{C}_{sg} \\ \mathbf{C}_{gs} & \mathbf{C}_{gg} \end{bmatrix} \begin{Bmatrix} \dot{\mathbf{u}}_s(t) \\ \dot{\mathbf{u}}_g(t) \end{Bmatrix} + \begin{bmatrix} \mathbf{K}_{ss} & \mathbf{K}_{sg} \\ \mathbf{K}_{gs} & \mathbf{K}_{gg} \end{bmatrix} \begin{Bmatrix} \mathbf{u}_s(t) \\ \mathbf{u}_g(t) \end{Bmatrix} = \begin{Bmatrix} \mathbf{R}_s(t) \\ \mathbf{R}_g(t) \end{Bmatrix} + \begin{Bmatrix} 0 \\ \mathbf{R}_g^i(t) \end{Bmatrix} \tag{24}$$

where $\mathbf{R}_s(t)$ and $\mathbf{R}_g(t)$ denote the load vectors including the seismic force and $\mathbf{R}_g^i(t)$ the interaction force between the near-field and the far-field regions. Subscript s refers to the nodes for the tank structure, the sloshing surface, and the near-field region; subscript g refers to those on the boundary between the near-field and far-field regions. The equations of motion for the far-field region of the ground can be obtained in the frequency domain using the developed 3-D transmitting boundary.

$$[\mathbf{S}_{gg}^f(\omega)]\{\mathbf{u}_g(\omega)\} = \{\mathbf{R}_g^f(\omega)\} - \{\mathbf{R}_g^i(\omega)\} \tag{25}$$

where $\mathbf{R}_g^f(\omega)$ denotes the effective seismic force generated by the motion of the bedrock.

Using the convolution integral, $\mathbf{u}_g(t)$ can be obtained from Equation 25.

$$\{\mathbf{u}_g(\omega)\} = [\mathbf{S}_{gg}^f(\omega)]^{-1}\{\mathbf{R}_g^f(\omega)\} - [\mathbf{S}_{gg}^f(\omega)]^{-1}\{\mathbf{R}_g^i(\omega)\} = \{\mathbf{u}_g^f(\omega)\} - [\mathbf{F}_{gg}^f(\omega)]\{\mathbf{R}_g^i(\omega)\}$$

$$\{\mathbf{u}_g(t)\} = \{\mathbf{u}_g^f(t)\} - \int_0^t [\mathbf{F}_{gg}^f(t-\tau)]\{\mathbf{R}_g^i(\tau)\}\, d\tau \tag{26}$$

By subdividing the interval of integration $0 \le \tau \le t$ into N subintervals of equal size Δt, and assuming constant physical quantities in each of the subintervals, $\mathbf{R}_g^i(t_N)$ can be expressed as follows:

$$\begin{aligned} \{\mathbf{R}_g^i(t_N)\} = &-\frac{4}{\Delta t}[\tilde{\mathbf{F}}_{gg}^f(t_{1/2})]^{-1}(\{\mathbf{u}_g(t_N)\} - \{\mathbf{u}_g^f(t_N)\}) - \{\mathbf{R}_g^i(t_{N-1})\} \\ &- \sum_{i=1}^{N-1} [\tilde{\mathbf{F}}_{gg}^f(t_{1/2})]^{-1}[\tilde{\mathbf{F}}_{gg}^f(t_{N-i+1/2})]\{\mathbf{R}_g^i(t_{i-1})\} \\ &- \sum_{i=1}^{N-1} [\tilde{\mathbf{F}}_{gg}^f(t_{1/2})]^{-1}[\tilde{\mathbf{F}}_{gg}^f(t_{N-i+1/2})]\{\mathbf{R}_g^i(t_i)\} \end{aligned} \tag{27}$$

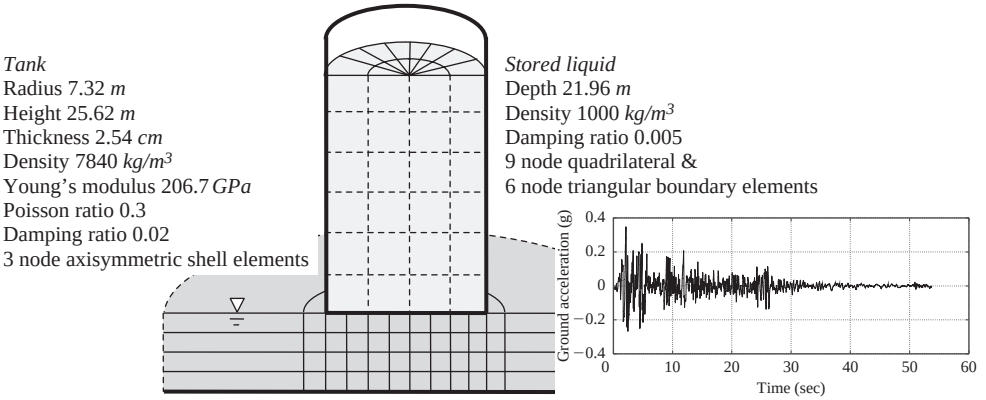

Figure 4 Tall tank on water-saturated transversely isotropic ground.

where $\widetilde{\mathbf{F}}^f_{gg}(t_{N-i+1/2}) = \mathbf{F}^f_{gg}(t_{N-i}) + \mathbf{F}^f_{gg}(t_{N-i+1})$. From Equations 24 and 27, earthquake responses of the total system can be obtained as a direct time-domain representation using an appropriate integration algorithm such as the Newmark method.

5 Numerical example

A tall tank bonded to a water-saturated transversely isotropic ground is examined to illustrate the results of this method of analysis. The tank has a height to radius ratio of 3:1. The ratios of Young's modulus E_v/E_h and the permeability κ_v/κ_h of the ground are 1.5:1 and 0.01:1, respectively. The mesh and material properties are as shown in Figure 4. The input motion is the El Centro earthquake ground motion (Figure 4 inset).

The dynamic stiffness of the foundation for horizontal and rocking motions is obtained using the developed transmitting boundary. The dynamic stiffness for the rocking motion is compared in Figure 5 with the results from a model in which the water-saturated ground is assumed to be an equivalent single-phase medium (Mei & Foda 1981). It is observed that the approximate equivalent single-phase medium model cannot represent the damping effects of the water-saturated ground accurately. The damping coefficients of the foundation on the water-saturated layered strata are no

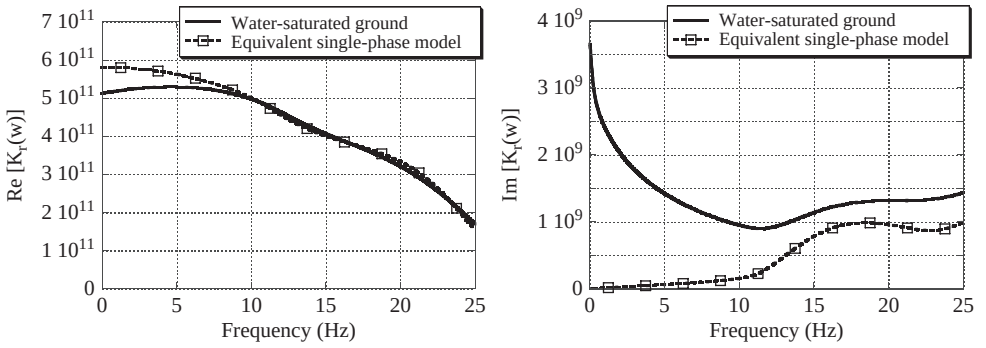

(a) Real part (b) Imaginary part

Figure 5 Dynamic stiffness for rocking motion.

Table 1 Natural frequencies of tall tank (*Hz*).

	Interaction mode	*Sloshing mode*
Rigid tank	–	0.250
Flexible tank (no SSI)	5.217	0.250
SSI (dry ground)	3.748	0.244
SSI (equivalent single-phase model)	3.931	0.244
SSI (2-phase isotropic ground)	3.796	0.244
SSI (2-phase transversely isotropic ground)	3.967	0.244

longer zero at zero frequency due to the effects of the seepage force. Consequently, more energy can be dissipated in low frequency through the internal friction between the solid and fluid phases of a water-saturated medium.

The natural frequencies of the interaction mode and the sloshing mode are obtained for various soil conditions and compared in Table 1. For the interaction mode, the effects of soil-structure interaction are obvious. However, the effects on the sloshing mode are not significant because the stored liquid can be treated as a very flexible system compared to the tank structure or the soil. Therefore, earthquake response of the sloshing height can be obtained with the assumption of a rigid tank on rigid base.

The effects of the modeling of water-saturated ground as a rigorous two-phase medium can be observed in this study. In the equivalent single-phase medium, the assumption of the equal displacements in the solid and fluid phases functions as a constraint. As a result, when the water-saturated ground is modeled as a single phase medium, the resulting numerical model becomes stiffer. Therefore, the natural frequency of the interaction mode from the equivalent single-phase model is larger when compared with that of the two-phase isotropic model.

The effects of the transversely isotropy of the ground can also be identified. Since the behavior of a structure on flexible ground is influenced mainly by rocking motion, the effects of the transversely isotropy of the ground is distinctly noticeable for such a structure. In this numerical example, the ratio of Young's modulus E_v/E_h is 1.5:1. The

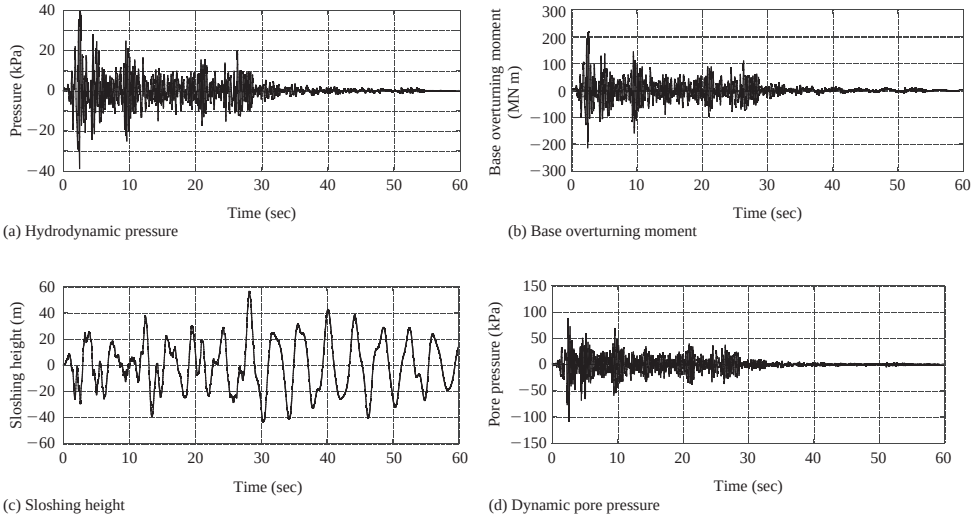

Figure 6 Earthquake response of tall tank.

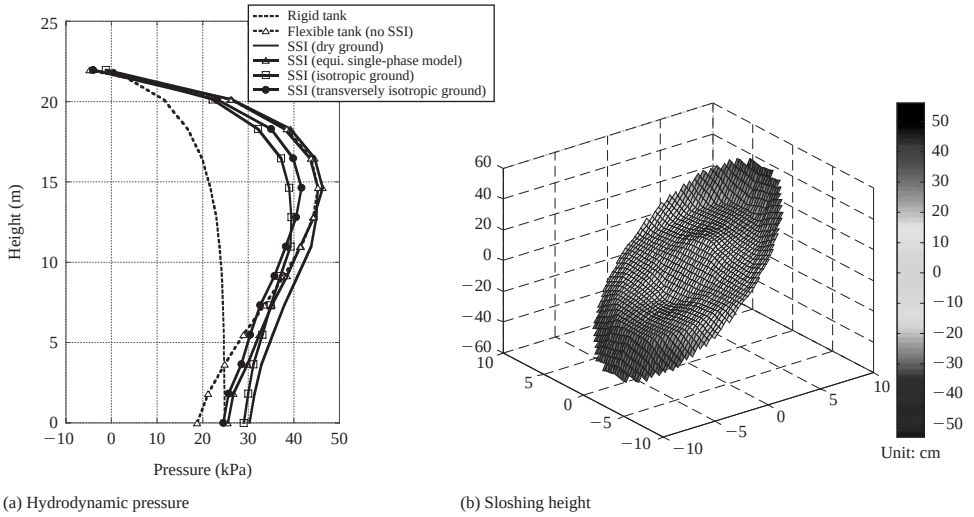

Figure 7 Profiles of maximum responses.

natural frequency of the interaction mode for the tank on the transversely isotropic ground is larger than that of the tank on the isotropic ground.

The time histories of the hydrodynamic pressure at the height of 14.64 *m* from the tank base, the base overturning moment, the sloshing height at the point in contact with the wall, and the dynamic pore pressure at the outermost point just under the tank base are shown in Figure 6. The profiles of the hydrodynamic pressure and the sloshing height at the moment when maximum value occurs are presented in Figure 7. The maximum values of the base overturning moment and the sloshing height are compared

Table 2 Maximum responses of tall tank.

	Base overturning moment (MN·m)	*Sloshing height (cm)*
Rigid tank	106.0 at 2.14 sec	54.1 at 28.26 sec
Flexible tank (no SSI)	246.1 at 3.22 sec	54.3 at 28.30 sec
SSI (dry ground)	226.0 at 2.62 sec	56.5 at 28.24 sec
SSI (equivalent single-phase model)	236.9 at 2.60 sec	56.8 at 28.22 sec
SSI (2-phase isotropic ground)	197.1 at 2.62 sec	56.4 at 28.24 sec
SSI (2-phase transversely isotropic ground)	214.7 at 2.60 sec	56.3 at 28.22 sec

in Table 2 for various soil conditions. When additional damping effects of the water-saturated ground are introduced into the system by the rigorous two-phase medium model, the responses of the tank on the two-phase ground are lower than the responses in the equivalent single-phase model. However, it can be observed that there is little effect on the response of the sloshing height irrespective of the models of the system.

6 Conclusions

A 3-D transmitting boundary in a cylindrical coordinate system is applied to obtain the earthquake response of a cylindrical liquid storage tank installed in the water-saturated transversely isotropic ground. The effects of the far-field region are represented by the transmitting boundary in the frequency domain. Using standard finite-element procedures in the time domain, models are developed for the flexible tank wall and the near-field region of the ground. The motion of the contained liquid is modeled using the boundary elements in the time domain. The direct time-domain representation of earthquake response of the total system is obtained using hybrid time domain-frequency domain analysis.

The results from the numerical analysis show that complex soil-structure interactions in water-saturated transversely isotropic ground can be modeled successfully. The rigorous model using the two-phase transversely isotropic medium has to be employed to accurately represent the dynamic behaviors of a structure on water-saturated transversely isotropic strata

Acknowledgements

This work is a part of a research project supported by the Korea Ministry of Land, Transport and Maritime Affairs (MLTM) through the Korea Bridge Design & Engineering Research Center (KBRC) and the Korea Construction Engineering Development Collaboratory Program Management Center (KOCED PMC) at Seoul National University. The authors wish to express their gratitude for all financial support.

References

Bougacha, S., Tassoulas, J.L. & Roësset, J.M. 1993. Analysis of foundations on fluid-filled poroelastic stratum. *Journal of Engineering Mechanics* 119(8): 1632–1648.

Chen, W.-F. & Saleeb, A.F. 1994. *Constitutive equations for engineering materials, volume 1: elasticity and modeling*. Elsevier.

Kausel, E. 1974. *Forced vibrations of circular foundations on layered media*. Research Report R74-11, Department of Civil Engineering, Massachusetts Institute of Technology, Cambridge, Massachusetts.

Kim, J.K., Koh, H.M., Kwon, K.J. & Yi, J.S. 2000. A three-dimensional transmitting boundary formulated in Cartesian co-ordinate system for the dynamics of non-axisymmetric foundations. *Earthquake Engineering and Structural Dynamics* 29: 1527–1546.

Lee, J.H. 2007. *3-D Transmitting Boundary in Cylindrical and Cartesian Coordinate Systems for Soil-Structure Interaction Analysis in Water-Saturated Transversely Isotropic Layered Ground*. PhD dissertation, Seoul National University, Seoul, Korea (in Korean).

Lee, J.H. & Kim, J.K. 2008. Transmitting boundary for water-saturated transversely isotropic strata based on the u-U formulation. Soil Dyn Earthquake Eng, doi:10.1016/j.soildyn.2008.08.003.

Lewis, R.W. & Schrefler, B.A. 1998. *The finite element methods in the static and dynamic deformation and consolidation of porous media*. John Wiley & Sons.

Mei, C.C. & Foda, M.A. 1981. Wave-induced response in a fluid-filled poroelastic solid with a free surface – a boundary layer theory. *Geophysical Journal of the Royal Astronomical Society* 66: 597–631.

Tassoulas, J.L. 1981. *Elements for the numerical analysis of wave motion in layered media*. Research Report R81-2, Department of Civil Engineering, Massachusetts Institute of Technology, Cambridge, Massachusetts.

Waas, G. 1972. *Linear two-dimensional analysis of soil dynamics problems in semi-infinite layered media*. PhD dissertation, University of California, Berkeley, California.

Zienkiewicz, O.C., Chan, A.H.C., Pastor, M., Schrefler, B.A. & Shiomi, T. 1999. *Computational geomechanics with special reference to earthquake engineering*. John Wiley & Sons.

Chapter 31

Advances in design optimization of reinforced concrete structural systems

Chara C. Mitropoulou, Nikos P. Bakas, Nikos D. Lagaros & Manolis Papadrakakis

National Technical University of Athens, Athens, Greece

ABSTRACT: In this work a number of design approaches for 3D reinforced concrete (RC) buildings are formulated in the framework of structural optimization problems and they are assessed in terms of structural performance under earthquake loading. In particular, this Chapter consists of two distinctive parts. In the first part the European seismic design code is assessed with reference to the behavioral factor q. For each optimum design, achieved for the various values of the behavioral factor, fragility curves are developed in four damage states. The optimum designs are compared based on limit-state probabilities of exceedance encountered for the design earthquake. In the second part three design approaches for RC buildings are considered aiming at improving the torsional response of RC buildings. It is shown that the optimized designs obtained according to the minimum eccentricity of the rigidity centre behave better in frequent (50/50 hazard level) and occasional (10/50 hazard level) earthquakes, while the designs obtained according to the minimum eccentricity of the strength centre formulation was found better in rare (2/50 hazard level) events.

1 Introduction

In the past the requirements and provisions of the seismic design codes for buildings have been based on experience and limited experimental data and they were periodically revised after disastrous earthquakes. Most of the current seismic design codes define a single design earthquake that is used for assessing the structural performance against earthquake hazard. These codes have many inherent assumptions built in the design procedure regarding the behaviour of the structure against earthquake loading. Severe damages caused by recent earthquakes made the engineering community questioning the effectiveness of the current seismic design codes (Xue, 2000; Browning, 2002; Panagiotakos and Fardis, 2004). Given that the primary goal of contemporary seismic design is the protection of human life, it is evident that additional performance targets and earthquake intensities should be considered in order to assess the structural performance in many hazard levels. Most of the current seismic design codes belong to the category of the limit state design procedures, where if a number of checks, expressed in terms of forces, are satisfied the structure is considered safe and not collapse is likely to occur. A typical limit state based design can be viewed as one (i.e. ultimate strength) or two limit state approach (i.e. serviceability and ultimate strength). All modern seismic design procedures are based on the principal that a structure will avoid collapse if it is designed to absorb and dissipate the kinetic energy that is imparted in it during the seismic excitation. Most of the modern seismic codes express the ability of

the structure to absorb energy through inelastic deformation using the reduction or behaviour factor q. The capacity of a structure to resist seismic actions in the nonlinear range generally permits lower seismic loads for its design than those corresponding to a linear elastic response. The seismic loads are reduced using the behaviour factor q. The numerical verification of the behaviour factor became a subject of research work during the past decade (Mazzolani and Piluso, 1996; Fajfar, 1998) in order to check the validity of design theory assumptions and to make structural performance more predictable from engineering point of view.

Designing earthquake resistant structures has been the subject of intensive research among engineers and scientists. Two schools of thought have prevailed in this area: (i) isolate the structure from any excitation propagated through the soil (Naeim and Kelly, 1999; Goel, 2005) and (ii) design the structure in such a way that would acceptably resist the seismic excitation (Duan and Chandler, 1997; Guerra, 2005; Lagaros et al., 2006b). In a number of studies (Paulay, 1998; Tso and Myslimaj, 2003) it has been shown that the rigidity centre is meaningful only when the system behaves elastically. Once the system response enters the inelastic domain the elements stiffness becomes insignificant and it is the strength centre that is important in this deformation stage.

The main objectives of this study are twofold: (i) In the first objective, the behaviour factor q that the Eurocode 8 (2003) suggests for the design of RC building structures is studied and critically assessed. This is achieved in the framework of the optimum design of RC buildings. The optimum designs obtained for the seven values of the behaviour factor considered are compared with respect to the limit-state probabilities of exceedance calculated for the design earthquake in four damage states. (ii) In the second objective, optimized structures obtained through the three design approaches are assessed with respect to the minimum seismic torsional effect and their performance against three earthquake hazard levels. According to the first design concept the initial construction cost is considered as the main objective. In the second design approach, performance criteria are implemented, where the eccentricity of the rigidity and the strength centres with respect to the mass centre is minimized. In the third design approach, both cost minimization and performance criteria are applied. All three design concepts are formulated as a combined topology-sizing optimization problem. The location and the size of the columns and the shear walls of the structure at each storey, constitute the design variables. Apart from the constraints imposed by the design codes on the seismic loading and structural performance, architectural restrictions are also taken into account in all formulations of the optimization problems. The optimum designs obtained through the three approaches are compared with respect to the total life-cycle cost, which is the sum of the initial and the limit state cost. The limit state cost, as considered in this study, represents monetary-equivalent losses due to seismic events that are expected to occur during the design life of the structure.

2 Progress on structural design optimization of RC structures

A number of studies have been published in the past dealing with structural optimization of RC structures. One of the earliest studies on this subject is the work by Frangopol (1986) where the general formulation of the deterministic optimization problem is reviewed and some of the main features of two general purpose deterministic

optimization programs are presented in developing the reliability-based optimization approach for the design of both steel and RC framed structures. In Kanagasundaram and Karihaloo (1991) it is demonstrated how the design process can be simulated mathematically to achieve designs of RC structures which conform to the requirements of the Australian Standard AS3600-1988 by minimizing the construction cost. In the work by Moharrami and Grierson (1993), a computer-based method for the optimal design of RC buildings is presented, where the width, depth and longitudinal reinforcement of member sections are considered as design variables.

The optimization of 3D RC frames is discussed by Balling and Yao (1997), where the validity of the assumption that optimum concrete-section dimensions are insensitive to the number, diameter, and longitudinal topology of reinforcing bars is investigated. In a work by Koskisto and Ellingwood (1997) a decision model is presented for minimizing the life-cycle cost of prefabricated concrete elements and structures. The decision model utilizes principles of engineering economic analysis under uncertainty in considering costs and benefits of construction, maintenance, repair, and consequences of failure. A review of papers on cost optimization of concrete structures can be found in the work by Sarma and Adeli (1998), where it was concluded that there is a need to perform research on cost optimization of realistic three-dimensional structures, especially large structures with hundreds of members where optimization can result in substantial savings.

Performance-based optimum design of reinforced concrete buildings is a relatively new field of research. The performance criteria are imposed as constraints that affect the initial construction cost that has to be minimized. Based on this approach Ganzerli et al. (2000) proposed an optimization methodology for seismic design considering performance-based constraints. Lagaros et al. (2006) proposed an automated procedure for the minimization of the eccentricity between the mass center and the rigidity center. Furthermore, in the work by Li and Cheng (2001), the optimal decision model of the target value of performance-based structural system reliability of RC frames is established according to the cost-effectiveness criterion.

Chan and Wang (2006) presented a numerical approach based on a nonlinear cracking analysis methods in the framework of an optimization algorithm for the stiffness-based optimum design of tall RC buildings. A general approach to the multi-objective reliability-based optimum designs of prestressed concrete beams is presented in the work by Barakat et. al (2004), where all behavior and side constraints specified by the American Concrete Institute code for prestressed concrete are incorporated. In the work by Chan and Zou (2004) an optimization technique is presented for the elastic and inelastic drift performance-based design of reinforced concrete buildings. While Lagaros and Papadrakakis (2007) assessed the design of 3D reinforced concrete buildings obtained according to the European seismic design code, versus a performance-based design procedure, in the framework of a multi-objective optimization problem.

3 Designing against the seismic hazard

The majority of the seismic design codes belong to the category of the prescriptive building design codes, which include: site selection and development of conceptual, preliminary and final design stages. According to a prescriptive design code the strength

of the structure is evaluated at one limit state between life-safety and near collapse, using a response spectrum corresponding to one design earthquake (Eurocode 8, 2003). In addition, serviceability limit state is usually checked in order to ensure that the structure will not deflect or vibrate excessively during its functioning. On the other hand, Performance-Based Design (PBD) is a different seismic design approach which includes, apart from the site selection and the development of the design stages, the construction and maintenance of the building in order to ensure reliable and predictable seismic performance over its life.

According to the Eurocodes a number of checks must be considered in order to ensure that the structure will meet the design requirements. Each candidate design is assessed using these constraints. All Eurocode 2 (2002) checks must be satisfied for the gravity loads using the following load combination

$$S_d = 1.35\sum_j G_{kj}"+"1.50\sum_i Q_{ki} \tag{1}$$

where "+" implies "to be combined with", the summation symbol "Σ" implies "the combined effect of", G_{kj} denotes the characteristic value "k" of the permanent action j and Q_{ki} refers to the characteristic value "k" of the variable action i. If the above constraints are satisfied, multi-modal response spectrum analysis is performed, according to Eurocode 8 (2003), and earthquake loading is considered using the following load combination

$$S_d = \sum_j G_{kj}"+"E_d"+"\sum_i \psi_{2i}Q_{ki} \tag{2}$$

where E_d is the design value of the seismic action for the two components (longitudinal and transverse) respectively and ψ_{2i} is the combination coefficient for the quasi-permanent action i, here taken equal to *0.30*.

The main philosophy of Eurocode 8, is to design structural systems based on energy dissipation and on ductility in order to control the inelastic seismic response. Designing a multistory RC building for energy dissipation comprises the following features: (i) fulfillment of the strong column/weak beam rule, (ii) member verification in terms of forces and resistances for the ultimate strength limit state under the design earthquake (with return period of 475 years, probability of exceedance 10% in 50 years), with the elastic spectrum reduced by the q-factor equal to 3.0, (iii) damage limitation for the serviceability limit state and (iv) capacity design of beams and columns against shear failure.

4 Structural optimization

At the heart of a PBD procedure is the formulation of a structural optimization problem, which constitutes the basis for the vulnerability as well as the performance evaluation of different designs.

4.1 *Formulation*

In the design procedures that will be implemented in this chapter the design variables are divided in two categories: (i) Topology design variables, corresponding to the topology or layout of the columns and shear walls of the building. (ii) Sizing design variables,

corresponding to the dimensions of their cross sections. The mathematical formulation of the optimization problem for the initial construction cost of RC buildings can be stated as follows:

$$\begin{aligned} &\min && C_{IN}(s) = C_b(s) + C_{sl}(s) + C_{cl}(s) \\ &\text{subject to} && g_k(s) \le 0, \qquad k = 1,2,\ldots,m \text{ (behavioral)} \\ &&& \left.\begin{aligned} t^i_{lb,j} \le r^i_j \le t^i_{ub,j}, \quad j = 1,2,\ldots,n_{columns} \\ s^i_{lb,j} \le h^i_j \le s^i_{ub,j}, \quad j = 1,2,\ldots,n_{columns} \end{aligned}\right\} \text{ (architectural)} \\ &&& i = 1,2,\ldots,n\_g_{storeys} \end{aligned} \tag{3}$$

where **s** represents the design vector corresponding to the dimensions of the columns' cross-sections, $\mathcal{F}$ is the feasible region where all the constraint functions (behavioural and/or architectural) are satisfied. The objective function considered is the initial construction cost $C_{IN}(\mathbf{s})$ that refers to the total initial construction cost of the structure, while $C_b(\mathbf{s})$, $C_{sl}(\mathbf{s})$, $C_{cl}(\mathbf{s})$ and $C_{ns}(\mathbf{s})$ refer to the total initial construction cost of beams, slabs, columns and non structural elements, respectively. The term "initial cost" of a new structure refers to the final cost just after construction. The initial cost is related to both material cost, which includes concrete, steel reinforcement, infills, as well as labour cost for the construction of the building.

The behavioural constraints $g_k(s)$ are imposed by the design codes, r^i_j is the distance of the j-th column/shear wall mass centre in the i-th group of storeys from its corresponding AC2 point (see Figure 1b, where for simplicity the superscript i and subscript j are omitted). $n\_g_{storeys}$ is the total number of groups of storeys having the same layout in plan. $t^i_{lb,j}, t^i_{ub,j}$ are the lower and upper bounds of the topology design variables imposed by the architectural constraints, while h^i_j is the largest edge of the j-th column/shear wall in the i-th group of storeys, corresponding to the sizing design variables (Figure 1a). $s^i_{lb,j}, s^i_{ub,j}$ are the lower and upper bounds of the sizing design variables imposed by the architectural constraints. As it will be seen in the following subsection, there is a relation between the two kinds of design variables in topology and sizing optimization, as well as in their corresponding bounds.

4.2 *Solving the optimization problem*

Evolutionary Algorithms (EA) are population based, probabilistic, direct search optimization algorithms gleaned from principles of Darwinian evolution. Starting with an initial population of μ candidate designs, an offspring population of λ designs is created from the parents using variation operators. Depending on the manner in which the variation and selection operators are designed and the spaces in which they act, different classes of EA have been proposed. In the EA algorithm employed in this study (Papadrakakis et al., 1998 and 2001; Lagaros et al., 2002), each member of the population is equipped with a set of parameters:

$$\begin{aligned} &\mathbf{a} = [(\mathbf{s}_d, \boldsymbol{\gamma}), (\mathbf{s}_c, \boldsymbol{\sigma}, \boldsymbol{\alpha})] \in (I_d, I_c) \\ &I_d = D^{n_d} \times R_+^{n_\gamma} \\ &I_c = R^{n_c} \times R_+^{n_\sigma} \times [-\pi, \pi]^{n_a} \end{aligned} \tag{4}$$

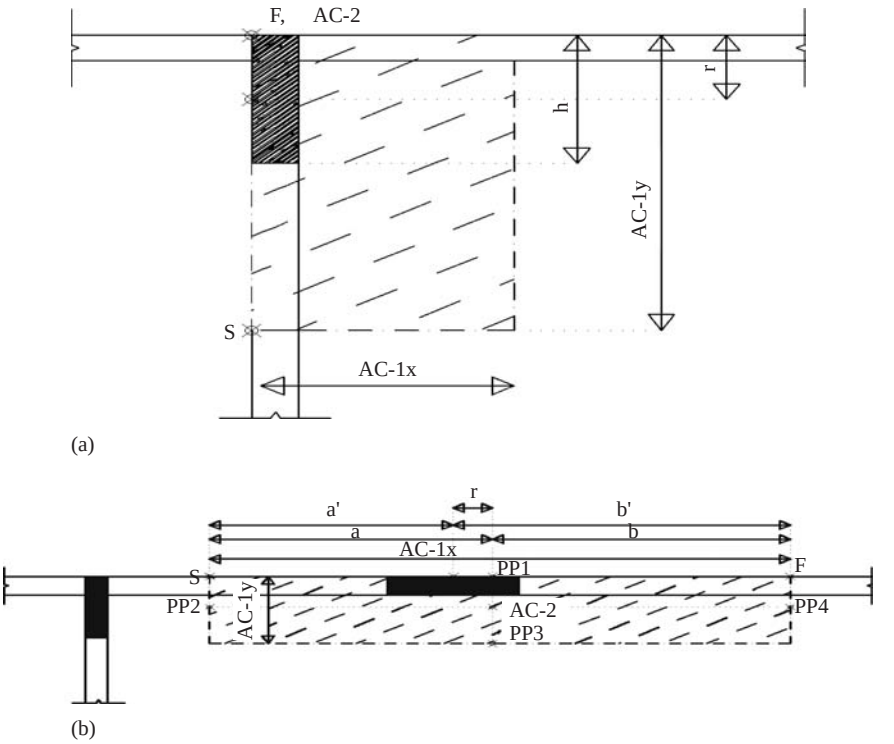

Figure 1 (a) Sample column Type I with its architectural constraints AC1 and AC2, (b): Sample column Type II with its architectural constraints AC1 and AC2.

where $\mathbf{s}_d$ and $\mathbf{s}_c$ are the vectors of discrete and continuous design variables defined in the discrete and continuous design sets D^{n_d} and R^{n_c}, respectively. Vectors $\boldsymbol{\gamma}$, $\boldsymbol{\sigma}$ and $\boldsymbol{\alpha}$ are the distribution parameter vectors taking values in $R_+^{n_\gamma}$, $R_+^{n_\sigma}$ and $[-\pi, \pi]^{n_a}$, respectively. Vector $\boldsymbol{\gamma}$ corresponds to the variances of the Poisson distribution. Vector $\boldsymbol{\sigma} \in R_+^{n_\sigma}$ corresponds to the standard deviations ($1 \leq n_\sigma \leq n_c$) of the normal distribution. Vector $\boldsymbol{\alpha} \in [-\pi, \pi]^{n_a}$ is related to the inclination angles ($n_\alpha = (n_c - n_\sigma/2)(n_\sigma - 1)$) defining linearly correlated mutations of the continuous design variables $\mathbf{s}_c$, where $n = n_d + n_c$ is the total number of design variables.

Let $P(t) = \{a_1, \ldots, a_\mu\}$ denotes a population of individuals at the t-th generation. The genetic operators used in the EA method are denoted by the following mappings:

$$\begin{aligned} &\text{rec} : (I_d, I_c)^\mu \rightarrow (I_d, I_c)^\lambda \text{ (recombination)} \\ &\text{mut} : (I_d, I_c)^\lambda \rightarrow (I_d, I_c)^\lambda \text{ (mutation)} \\ &\text{sel}_\mu^k : (I_d, I_c)^k \rightarrow (I_d, I_c)^\mu \text{ (selection, } k \in \{\lambda, \mu + \lambda\}) \end{aligned} \tag{5}$$

A single iteration of the EA, which is a step from the population $P_p^{(t)}$ to the next parent population $P_p^{(t+1)}$ is modelled by the mapping

$$\text{opt}_{EA} : (I_d, I_c)_t^\mu \rightarrow (I_d, I_c)_{t+1}^\mu \tag{6}$$

1. Begin
2. $t := 0$
3. initialize $\left(P_P^{(0)} := \left\{ \left(P_P^{(0)}, s_m^{(0)}, F\left(s_m^{(0)}\right)\right),\ m = 1,....,\mu \right\}\right)$
4. Repeat
5. For $l := 1$ To λ Do Begin
6. $D_l := \text{marriage}\left(P_P^{(t)}\right)$
7. $s_l := \text{s\_recombination}\left(D_l\right)$
8. $y_l := \text{y\_recombination}\left(D_l\right)$
9. $\tilde{s}_l := \text{s\_mutation}\left(s_l\right)$
10. $\tilde{y}_l := \text{y\_mutation}\left(y_l\right)$
11. $\tilde{F}_l := F\left(\tilde{s}_l\right)$
12. End
13. $P_o^{(t)} := \left\{ \left(y_l^{(t)}, s_l^{(t)}, F\left(s_l^{(t)}\right)\right), l = 1,....,\lambda \right\}$
14. Case selection_type of
15. (μ,λ) : $P_o^{(t+1)} := \text{selection}\left(P_o^{(t)}, \mu\right)$
16. $(\mu+\lambda)$: $P_P^{(t+1)} := \text{selection}\left(P_o^{(t)}, P_P^{(t)}, \mu\right)$
17. End
18. $t := t + 1$
19. Until termination_criterion
20. End

Figure 2 Pseudo-code of the Evolutionary Algorithm (EA) optimization procedure.

In Figure 2 a pseudo-code of the EA algorithm is depicted. At the beginning of the procedure in generation t = 0 the initial parent population $P_p^{(t)}$, composed by μ design vectors, is generated randomly (step 3 of the pseudo-code). Steps 5 to 12 correspond to the main part of the EA algorithm, where in every generation λ offspring vectors are generated by means of recombination and mutation. D_l is a sub-population with two members selected from the parent population of the current generation $P_p^{(t)}$ (Step 6) which is used by the recombination operator. Recombination and mutation operators, described in steps 7 to 10, act on both design variable vectors s_l and distribution parameter vectors (distribution parameter vectors are denoted as y_l in the pseudo-code). In step 11 the objective and constraint functions are calculated in order to assess the design vectors in terms of the objective function value and feasibility.

5 Conceptual topology design optimization of RC structures

The main objective in the seismic resistant design of structural systems, like reinforced concrete buildings, is the proper conceptual design of the seismically resistant structural components and the appropriate arrangement in plan of the vertical structural elements. It is obvious that the architectural layout of the structure imposes the principal restrictions related to the position of the structural elements of the building. The cooperation between the designer and the architect at the structural conceptual level might be crucial in the subsequent design stages. There are two general guidelines for the design engineer to take into account at the early stages of the design of a concrete building: (i) Guidelines related to the mass and stiffness distribution among the storeys

of the structure and (ii) guidelines related to the plan arrangement of the vertical structural elements of the building where a rule of a minimum distance between the mass and the elastic centers for each storey (mass eccentricity) should be followed.

Eccentric structures, which are characterized by the non coincidence of the mass centre with the rigidity centre, develop a coupled lateral-torsional response when subjected to dynamic excitation. A high percentage of building damages, or even collapses, has been attributed to the wrong plan arrangement of the columns and the shear walls, due to the activation of the combined torsional-translational vibration of the structural system (Bachmann, 2002; Bertero, 1995; Wong and Tso, 1995; Rosenblueth and Meli, 1986). For this reason a number of studies have been published in the past where the seismic response of the structure is examined under the framework of coupling the lateral-torsional response (Kan and Chopra, 1977; Tso, 1990; Rutenberg, 2002; De-la-Colina, 2003; Fajfar et al., 2005; Pettinga et al., 2007; Jeong and Elnashai, 2006).

According to the Federal Emergency Management Agency (FEMA-310, 1998) it is suggested that, in order to minimize the influence of the torsion, the distance between the story centre of mass and the story centre of rigidity must be less than 20% of the building width in either plan dimension for Life Safety (LS) and Immediate Occupancy (IO) design states of the building. In most cases of building layouts it is not easy, even through a trial and error procedure, to define the plan arrangement of the columns and shear walls so that the distance of the rigidity center to be within an acceptable distance from the mass center. This is because the possible values of the topology and size variables are extremely large which make their combination very complicated. What is needed is an automatic optimization procedure specially tailored for the solution of such a problem.

The optimum design of steel reinforced concrete 3D frames is formulated in this study on the basis of the FEMA-310 (1998) recommendation where the torsional response demands is to be reduced during a seismic event and thus implicitly enhance the seismic resistance of the structure. In this study, based on the work of Bertero (1995), response demands are reduced by minimizing the mass eccentricity, which is defined as the distance between the mass and the rigidity centers in each storey.

5.1 *Definitions*

There are some definitions that have to be provided in order to facilitate the description of the problem and its handling by the adopted optimization algorithm.

Torsionally balanced: A structural system is defined as torsionally balanced when the mass centre coincides or almost coincides with the rigidity centre at any storey of the structure.

Centre of rigidity (CR): Only in a special class of multi-storey structures can the centres of rigidity be defined in the strict sense (Garcia et al., 2007). The inability in defining the centres of rigidity has led to the following approximate approaches: (i) Decomposition of the multi-storey structural system into single independent storey systems. (ii) Using only the centre of gravity of the shear walls. (iii) Replacing the elastic axis with an axis defined by the geometrical locus of the rigidity centres of the storeys (Garcia et al., 2007). In the present study, approach (iii) is considered, which has been adopted by the Eurocode 8 (2003) and the National Building Code of Canada (1995).

Centre of resistance or strength (CV): This centre can be defined as follows

$$x_{CV} = \frac{\sum_i x_i V_{n,i}}{\sum_i V_{n,i}} \tag{7}$$

where x_{CV} is the x-coordinate of the CV, $V_{n,i}$ is the nominal strength of the i-th vertical structural element and xi is the distance of the i-th element from the centre of mass.

For every column and shear wall, two architectural constraints are defined: *Architectural constraint 1*: The first architectural constraint (AC1) is related to the boundaries in plan where a column or shear wall should be located. It is implemented as a rectangle with dimensions $AC1_x \times AC1_y$. A design is considered feasible, with respect to AC1 constraint, when the cross sections of the columns and shear walls are contained in the corresponding rectangles. In Figures 1a and 1b two AC1 rectangles are shown for a typical plan view of a concrete building. *Architectural constraint 2*: The second architectural constraint (AC2) is related to the topological position of the beams in conjunction with their supporting columns and/or shear walls. This constraint is implemented through a point located within the rectangle AC1. The AC2 constraint, shown in Figures 1a and 1b, is essential in assisting the optimization procedure to reach layouts where the beams and their cross points are supported by columns or shear walls. In any feasible design the AC2 point should correspond to a joint of horizontal (beam) and vertical (column/shear wall) elements. *Column type*: Two types of columns/shear walls are considered. Type I is defined as the column/shear wall where the AC2 point corresponds to one of the corners of the rectangle AC1 labeled as F (see Figure 1a); Type II is defined as the column/shear wall where the AC2 point is located inside the rectangle AC1 (see Figure 1b).

5.2 *Minimum torsional response optimization problem*

In the minimum torsional response optimization problem the basic goal is to formulate an optimization procedure that could lead to designs with improved earthquake resistance and in particular to create designs having minimum torsional response. In this work two separate formulations of this problem have been considered. The first one is formulated as a minimization problem of the eccentricity e_{CM-CR} between the mass centre and the rigidity centre of each storey, while the second formulation is stated as a minimization problem of the eccentricity e_{CM-CV} between the mass centre and the centre of strength. Both formulations are subjected to the behavioural constraints imposed by the design codes as well as to the architectural constraints.

The two optimization formulations can be stated as follows:

$$\begin{aligned}
&\text{(i)} \quad \min \qquad e_{CM-CR} = \sqrt{(x^i_{CM} - x^i_{CR})^2 + (y^i_{CM} - y^i_{CR})^2}, \quad i = 1,2,\ldots,n_g_{storeys} \\
&\qquad \text{subject to} \quad g_k(\mathbf{s}) \le 0, \qquad k = 1,2,\ldots,m \text{ (behavioral)} \\
&\qquad\qquad \left.\begin{aligned} t^i_{lb,j} \le r^i_j \le t^i_{ub,j}, \quad & j = 1,2,\ldots,n_{columns} \\ s^i_{lb,j} \le h^i_j \le s^i_{ub,j}, \quad & j = 1,2,\ldots,n_{columns} \end{aligned}\right\} \text{ (architectural)}
\end{aligned} \tag{8a}$$

$$\text{(ii)} \quad \min \quad e_{CM-CV} = \sqrt{(x^i_{CM} - x^i_{CV})^2 + (y^i_{CM} - y^i_{CV})^2}, \quad i = 1,2,\ldots,n_{storeys}$$

$$\begin{aligned} \text{subject to} \quad & g_k(\mathbf{s}) \le 0, && k = 1,2,\ldots,m \text{ (behavioral)} \\ & \left.\begin{aligned} t^i_{lb,j} \le r^i_j \le t^i_{ub,j}, \quad & j = 1,2,\ldots,n_{columns} \\ s^i_{lb,j} \le h^i_j \le s^i_{ub,j}, \quad & j = 1,2,\ldots,n_{columns} \end{aligned}\right\} && \text{(architectural)} \end{aligned} \tag{8b}$$

where (x^i_{CM},y^i_{CM}), (x^i_{CR},y^i_{CR}) and (x^i_{CV},y^i_{CV}) are the coordinates of the mass centre, the rigidity centre and the centre of strength, respectively. It has to be noted that both centres CR and CV are defined for each storey.

5.3 *The combined optimization problem*

In the third optimization formulation both objectives considered previously are combined through a weighted sum. The mathematical formulation for the combined optimization problem can be stated as follows:

$$\begin{aligned} \min \quad & F(\mathbf{s}) = w \cdot C^*_{IN} + (1-w) \cdot \max(e^*_{CM-CR}, e^*_{CM-CV}) \\ \text{subject to} \quad & g_k(\mathbf{s}) \le 0, && k = 1,2,\ldots,m \text{ (behavioral)} \\ & \left.\begin{aligned} t^i_{lb,j} \le r^i_j \le t^i_{ub,j}, \quad & j = 1,2,\ldots,n_{columns} \\ s^i_{lb,j} \le h^i_j \le s^i_{ub,j}, \quad & j = 1,2,\ldots,n_{columns} \end{aligned}\right\} && \text{(architectural)} \end{aligned} \tag{9}$$

where C^*_{IN}, e^*_{CM-CR} and e^*_{CM-CV} are the normalized values of the three objectives, i.e. the initial construction cost and the two eccentricities, respectively, while w is the weight coefficient.

5.4 *Type of design variables*

In this study the columns/shear walls are of rectangular shape with dimensions $h \times b$, where $h \ge b$, while the smallest column that is permitted to be allocated is $30 \times 30\,cm^2$. The sizing design variables of the columns and shear walls depend on the topology design variables which are defined first.

5.4.1 *Topology design variables*

As mentioned above (see Figure 1) the columns are divided in two categories. For Type I column/shear wall: if $AC1_x > AC1_y$ the final position of the individual element centre of the column/shear wall will be allocated along the edge $AC1_x$, otherwise along the edge $AC1_y$. In the case of a square architectural constraint with $AC1_x = AC1_y$, the selection of the edge is random. For Type I column/shear wall the lower bound of the topology design variable depends on the indicative minimum column size

$$t^i_{lb,j} = \frac{h_{min}}{2} \tag{10}$$

where h_{min} is the minimum column size of 30 cm as imposed by the design codes. The above mentioned lower bound constraint is imposed in order to avoid obtaining

columns with dimensions less than h_{min}. The upper bound is equal to half the size of the corresponding architectural constraint edge ($AC1_x$ or $AC1_y$)

$$t^i_{ub,j} = \frac{1}{2}\sqrt{(x_S - x_F)^2 + (y_S - y_F)^2} \tag{11}$$

In Figure 1a the largest edge of AC1 architectural constraint is $AC1_y$ which will be selected as the edge to which the individual element centre of the column/shear wall will be allocated. Furthermore, S (x_S, y_S) is the starting point and F (x_F, y_F) is the finishing point of the $AC1_y$ edge, where the AC2 point coincides with the finishing point F.

In Type II column/shear wall the edge of the AC1 architectural rectangle, to which the individual element centre of the column will be allocated, has either already been selected or it will be selected by the smallest distance of the projection of the AC2 point to the four edges of the AC1 rectangle. The four projections points PPi, $i = 1, \ldots, 4$ are shown in Figure 1b. It can be seen that the distance between the points AC2 and PP1 is the smallest one, so the edge AC1x of the corresponding architectural constraint is selected for the allocation of the individual element centre of the column/shear wall and the PP1 projection point is renamed to AC2. Point S (x_S,y_S) is the starting point and F (x_F,y_F) is the finishing point of this edge. The allocation of the mass centre of the column/shear wall is either on the left or on the right side of the renamed projection point PP1.

Irrespectively to the side to which the individual element centre will be allocated, the lower bound is defined to be equal to zero

$$t^i_{lb,j} = 0 \tag{12}$$

The definition of the upper bound depends on which side of the projected AC2 point the column mass centre will be allocated:

$$t^i_{ub,j} = \frac{a}{2} \text{ (if on the left side)}$$
$$t^i_{ub,j} = \frac{b}{2} \text{ (if on the right side)} \tag{13}$$

where "a" is the distance of the new position of AC2 point from the point S and "b" is the distance of the new position of AC2 point from the point F (see Figure 1b).

5.4.2 *Sizing design variables*

As mentioned previously, topology design variables are satisfied first followed by the sizing design variables which are related to the topology design variables. In the case of Type I columns/shear walls there is a direct relation between topology and sizing design variables for each column/shear wall. This sizing design variable is defined as inactive:

$$h^i_j = 2r^i_j \tag{14}$$

In the case of Type II column/shear wall there is an indirect relation between the two types of design variables defined by

$$\begin{aligned} s^{i}_{lb,j} &= 2r^{i}_{j} \\ s^{i}_{ub,j} &= 2\min(a',b') \end{aligned} \tag{15}$$

where a' and b' refer to the distance of the individual element centre of the column/shear wall from points S and F, respectively (see Figure 1b). This sizing design variable is defined as active. In this case the sizing design variable is active, since their dimensions have to be defined by the optimizer and not by the topology design variables as in the case of Type I column/shear wall. The bounds of the size of the column/shear wall are dependant on the topological design variable r^{i}_{j}.

6 Life cycle cost analysis

The total cost C_{TOT} of a structure, may refer either to the design life period of a new structure or to the remaining life period of a retrofitted structure. This cost can be expressed as a function of the time and the design vector as follows (Wen and Kang 2001a):

$$C_{TOT}(t, \boldsymbol{s}) = C_{IN}(\boldsymbol{s}) + C_{LS}(t, \boldsymbol{s}) \tag{16}$$

where C_{IN} is the initial cost of a new or retrofitted structure, C_{LS} is the limit state cost; $\boldsymbol{s}$ is the design vector corresponding to the design loads, resistance and material properties, while t is the time period. The term "initial cost of a new structure" refers to the cost just after construction. The initial cost is related to the material and the labor cost for the construction of the building which includes concrete, steel reinforcement, labor cost for placement as well as the nonstructural components cost. The term "limit state cost" refers to the potential damage cost from earthquakes that may occur during the life of the structure. It accounts for the cost of the repairs after an earthquake, the cost of loss of contents, the cost of injury recovery or human fatality and other direct or indirect economic losses. The quantification of losses in economical terms depends on several socio-economic parameters.

The limit state cost (C_{LS}), for the i−th limit state, can thus be formulated as follows:

$$C^{i}_{LS} = C^{i}_{dam} + C^{i}_{con} + C^{i}_{ren} + C^{i}_{inc} + C^{i}_{inj} + C^{i}_{fat} \tag{17}$$

where C^{i}_{dam} is the damage repair cost, C^{i}_{con} is the loss of contents cost, C^{i}_{ren} is the loss of rental cost and C^{i}_{inc} is the income loss cost, C^{i}_{inj} is the cost of injuries and C^{i}_{fat} is the cost of human fatality. Details about the calculation formula for each limit state cost along with the values of the basic cost for each category can be found in Table 1 (Wen and Kang 2001b). The values of the mean damage index, loss of function, down time, expected minor injury rate, expected serious injury rate and expected death rate used in this study are based on (Wen and Kang, 2001b; Ellingwood and Wen, 2005; ATC-13, 1985; FEMA-227, 1992).

It is generally accepted that interstorey drift can be used to determine the expected damage. The relation between the drift limit ratios with the damage state, employed

Table 1 Limit state costs – calculation formula (Ellingwood and Wen, 2005).

Cost Category	*Calculation Formula*	*Basic Cost*
Damage/repair (C_{dam})	Replacement cost × floor area × mean damage index	640 €/m^2
Loss of contents (C_{con})	Unit contents cost × floor area × mean damage index	215 €/m^2
Rental (C_{ren})	Rental rate × gross leasable area × loss of function	4.40 €/month/m^2
Income (C_{inc})	Rental rate × gross leasable area × down time	700 €/year/m^2
Minor Injury ($C_{inj,m}$)	Minor injury cost per person × floor area × occupancy rate × expected minor injury rate	700 €/person
Serious Injury ($C_{inj,s}$)	Serious injury cost per person × floor area × occupancy rate × expected serious injury rate	7×10^3 €/person
Human fatality (C_{fat})	Death cost per person × floor area × occupancy rate × expected death rate	7×10^5 €/person

*Occupancy rate 2 persons/100 m^2

Table 2 Damage state drift ratio limits and cost based on HAZUS (2003).

Performance level	*Damage State*	*Interstorey Drift (%)*
1	None	$\theta < 0.5$
2	Slight	$0.5 < \theta < 1.0$
3	Moderate	$1.0 < \theta < 3.0$
4	Major	$3.0 < \theta < 8.0$
5	Destroyed	$8.0 < \theta$

Table 3 Damage state drift ratio limits and cost based on the work of Ghobarah (2004).

Performance level	*Damage State*	*Interstorey Drift (%)*
1	None	$\theta < 0.1$
2	Slight	$0.1 < \theta < 0.2$
3	Light	$0.2 < \theta < 0.4$
4	Moderate	$0.4 < \theta < 1.0$
5	Heavy	$1.0 < \theta < 1.8$
6	Major	$1.8 < \theta < 3.0$
7	Destroyed	$3.0 < \theta$

in this study (Tables 2 and 3), is based on the HAZUS (2003) project for low-rise RC moment resisting frames for moderate-code design, and on the work of Ghobarah (2004) for ductile moment resisting frames. Based on analytical and experimental data Ghobarah (2004) examined the correlation between drift and damage of various structural elements and systems and determined the relation between the interstorey drift and various damage levels of different reinforced concrete elements and structural systems, as given in Table 3.

Based on a Poisson process model of earthquake occurrences and an assumption that damaged buildings are immediately retrofitted to their original intact conditions

after each major damage-inducing seismic attack, Wen and Kang (2001a) proposed the following formula for the limit state cost function considering N damage states:

$$C_{LS}(t,s) = \frac{\nu}{\lambda}(1 - e^{-\lambda t})\sum_{i=1}^{N} C_{LS}^{i} P_i \tag{18}$$

where

$$P_i = P_i(\theta > \theta_i) - P_{i+1}(\theta > \theta_{i+1}) \tag{19}$$

and

$$P_i(\theta > \theta_i) = (-1/t) \cdot \ln[1 - \overline{P}_i(\theta - \theta_i)] \tag{20}$$

P_i is the probability of the ith damage state being violated given the earthquake occurrence and C_{LS}^{i} is the corresponding limit state cost; $\overline{P}_i(\theta - \theta_i)$ is the annual exceedance probability of the maximum interstorey drift value θ_i; ν is the annual occurrence rate of significant earthquakes modeled by a Poisson process and t is the service life of a new structure or the remaining life of a retrofitted structure. The first component of Eq. (18), with the exponential term, is used in order to express C_{LS} in present value, where λ is the annual monentary discount rate. The calculation of the limit state cost C_{LS} is based on the assumption that after the occurrence of an earthquake the structure is fully restored to its initial state. In this work the annual monentary discount rate λ is taken to be constant, since considering a continuous discount rate is accurate enough for all practical purposes (Rackwitz 2006, Rackwitz et al. 2005). Various approaches yield values of the discount rate λ in the range of 3 to 6% (Wen and Kang 2001b), in this study it was taken equal to 5%.

Each damage state is defined by drift ratio limits, listed in Tables 2 and 3. When one of those drift values is exceeded the corresponding limit state is assumed to be reached. The annual exceedance probability $\overline{P}(\theta > \theta_i)$ is obtained from a relationship of the form:

$$\overline{P}_i(\theta > \theta_i) = \gamma(\theta_i)^{-k} \tag{21}$$

The above expression is obtained by best fit of known $\overline{P}_i(\theta > \theta_i)$ pairs. These pairs correspond to 2, 10 and 50 percent in 50 years earthquakes that have known probabilities of exceedance $\overline{P}_i$. The corresponding maximum interstorey drift limit values θ_i, for these three earthquakes, are obtained using the pushover analysis. According to Poisson's law the annual probability of exceedance of an earthquake with a probability of exceedance p in t years is given by the formula:

$$\overline{P} < \theta < P = (-1/t) \cdot \ln(1 - p) \tag{22}$$

which means that the 2/50 earthquake has a probability of exceedance equal to $\overline{P}_{2\%} = -\ln(1 - 0.02)/50 = 4.04 \times 10^{-4}$ ($4.04 \times 10^{-2}\%$).

7 Fragility analysis

Earthquake risk assessment of building structures requires the calculation of limit-state probabilities for a series of limit-states of monotonically increasing severity. The target is to obtain the limit-state probabilities of exceedance that serve as a hazard curve for structural damage. The mean annual frequency of maximum interstory drift $\theta_{\max}$ exceeding a value y is obtained as:

$$\lambda_{\theta>y} = \int P(\theta_{\max} \geq y / IM = x) \left| d\lambda_{\mathrm{IM}}(x) \right| \tag{23}$$

where $\lambda_{\theta>y}$ is the rate of $\theta_{\max}$, exceeding the value y and $\lambda_{IM}(x)$ is the mean annual frequency of the chosen intensity measure exceeding x or, in other words is the hazard curve and $\mathrm{d}\lambda_{IM}(x)$ is its slope. The absolute value is used in eq. (23) because the slope has a negative value.

Fragilities were introduced in the probabilistic analysis of nuclear power plants, with the purpose of distinguishing the task of the structural engineer from that of the seismologist. According to equation (23) the seismic fragility F_R is defined as the limit-state probability, conditioned on a measure of seismic intensity IM, which may be expressed as peak ground acceleration, spectral acceleration, spectral velocity, or any other control variable that is consistent with the specification of seismic hazard. Thus the seismic fragility is defined as:

$$F_R = P(\theta_{\max} \geq y / IM = x) \tag{24}$$

Assuming that seismic data are lognormally distributed (Benjamin and Cornell 1970), $F_R(\mathrm{x})$ can be calculated analytically.

8 Numerical results

In this chapter two test cases have been considered. In the first one structural optimization is used for performing a critical assessment of the behaviour factor, while in the second one a design procedure is proposed for defining torsionally balanced layouts.

8.1 *A critical assessment of the behaviour factor q*

A two-storey 3D RC building, regular in elevation and plan has been examined for the assessment of the European seismic design code with respect to the behaviour factor q. The plan and the elevation of the two storey 3D RC building are depicted in Figure 3 and Figure 4, respectively. The structure consists of eight columns and eighteen beams while the effect of the infill walls is not considered.

In the framework of this study, the RC building has been optimally designed to meet the Eurocode (EC2 and EC8) or the PBD requirements. According to EC8 the lateral forces were derived from the design response spectrum (5%-damped elastic spectrum divided by the behaviour factor q) at the fundamental period of the building. Concrete of class C20/25 (nominal cylindrical strength of 20 MPa) and class S500 steel (nominal yield stress of 500 MPa) are assumed. The base shear is obtained from the response spectrum for soil type A (stiff soil $\theta = 1.0$, with characteristic periods $T1 = 0.10$ sec and $T2 = 0.40$ sec) and a PGA of 0.31 g. Moreover, the importance factor γ_1 was taken

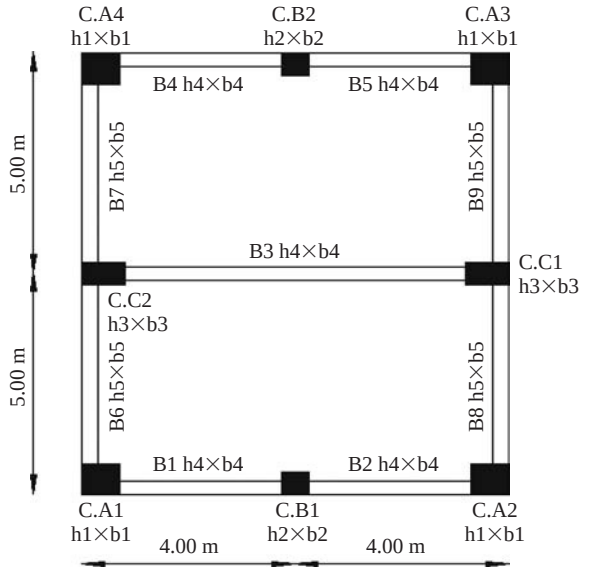

Figure 3 Plain view of the two-storey 3D RC building.

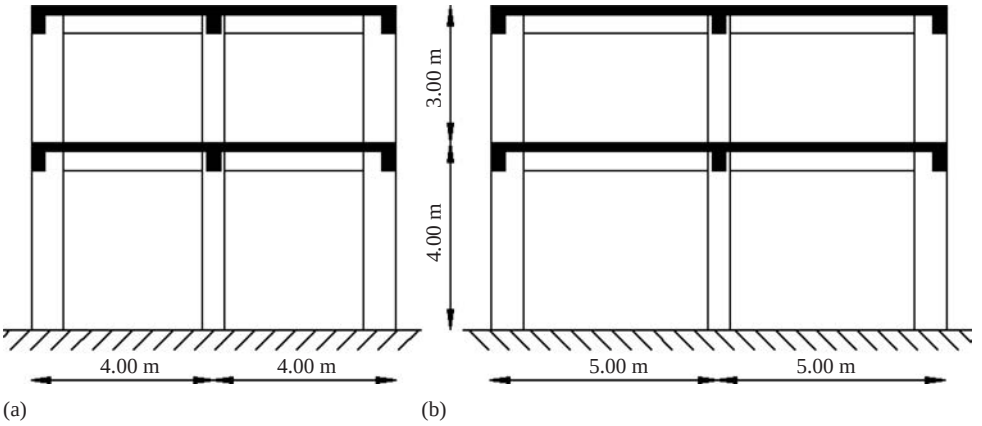

Figure 4 2-storey 3D RC building: (a) Front view and (b) side view.

equal to 1.0, while damping correction factor is equal to 1.0, since a damping ratio of 5% has been assumed.

The slab thickness is equal to 15 cm and is considered to contribute to the moment of inertia of the beams with an effective flange width. In addition to the self weight of the beams and the slab, a distributed dead load of 2 kN/m^2, due to floor finishing and partitions and imposed live load with nominal value of 1.5 kN/m^2, is considered, in the combination with gravity loads ("persistent design situation"). Nominal dead and live loads are multiplied by load factors of 1.35 and 1.5, respectively (Eq. 1). Following EC8, in the seismic design combination, dead loads are taken with their nominal value, while live loads with 30% of their nominal value (Eq. 2).

Table 4 Optimum designs obtained with six behavioral factors q.

	Design					
	$D_{q=1.0}$	$D_{q=1.5}$	$D_{q=2.0}$	$D_{q=2.5}$	$D_{q=3.0}$	$D_{q=3.5}$
h1 × b1 (m^2)	0.45 × 0.55	0.35 × 0.40	0.35 × 0.40	0.35 × 0.40	0.40 × 0.40	0.40 × 0.35
h2 × b2 (m^2)	0.45 × 0.60	0.45 × 0.55	0.45 × 0.50	0.45 × 0.45	0.45 × 0.40	0.45 × 0.40
h3 × b3 (m^2)	0.55 × 0.75	0.50 × 0.65	0.50 × 0.60	0.50 × 0.55	0.45 × 0.45	0.45 × 0.40
h4 × b4 (m^2)	0.55 × 0.30	0.60 × 0.25	0.60 × 0.25	0.60 × 0.25	0.50 × 0.30	0.50 × 0.30
h5 × b5 (m^2)	0.55 × 0.35	0.50 × 0.25	0.50 × 0.25	0.45 × 0.25	0.45 × 0.25	0.45 × 0.25

Table 5 The initial cost for the six optimum designs in €.

Design	*Steel*	*Concrete*	*Initial Cost*
$D_{q=1.0}$	6750	10588	35881
$D_{q=1.5}$	5535	9825	32671
$D_{q=2.0}$	4752	9760	31205
$D_{q=2.5}$	4329	9643	30339
$D_{q=3.0}$	3834	9565	29488
$D_{q=3.5}$	3834	9483	29399

The main objective of this study is to assess the design obtained with the behaviour factor q that the Eurocode 8 (2003) suggests for the design of RC building structures. This is achieved in the framework of the optimum design of RC buildings where the optimum designs obtained for different values of the behaviour factor are compared. The optimum designs (D_q) obtained for six values of the behaviour factor considered are compared with respect to the initial cost, and limit-state probabilities of exceedance. The optimization problem considered is defined as follows:

$$C_{IN} = C_{con}\sum_{i=1}^{ne} V_{con}^{i} + C_{steel}\sum_{i=1}^{ne} W_{steel}^{i} \tag{25}$$

where V_{con} is the volume of the concrete, W_{steel} is the mass of the steel reinforcement, $C_{con} = 120$ €/m^3, $C_{steel} = 0.9$ €/kgr are the unit costs for concrete and steel, respectively and *ne* refers to the number of elements. The initial cost is related to material and the construction of the building which includes concrete, steel reinforcement, placement and the non-structural components cost. The dimensions of the cross section of the beam and the columns have been considered as the design variables of the optimization problem.

Six optimum designs are obtained solving the optimization problem of Eq. (25) where the initial cost is the objective function to be minimized and the cross sections of the columns and beams are the design variables considered. The provisions of the Eurocode 2 and Eurocode 8 are imposed as constraints to the formulation of the optimization problem. The six designs and the respective dimensions are presented in Table 4.

The objective function values (C_{IN}) of the six optimum designs are shown in Table 5 along with the cost of the concrete and steel reinforcement. As it can be seen from

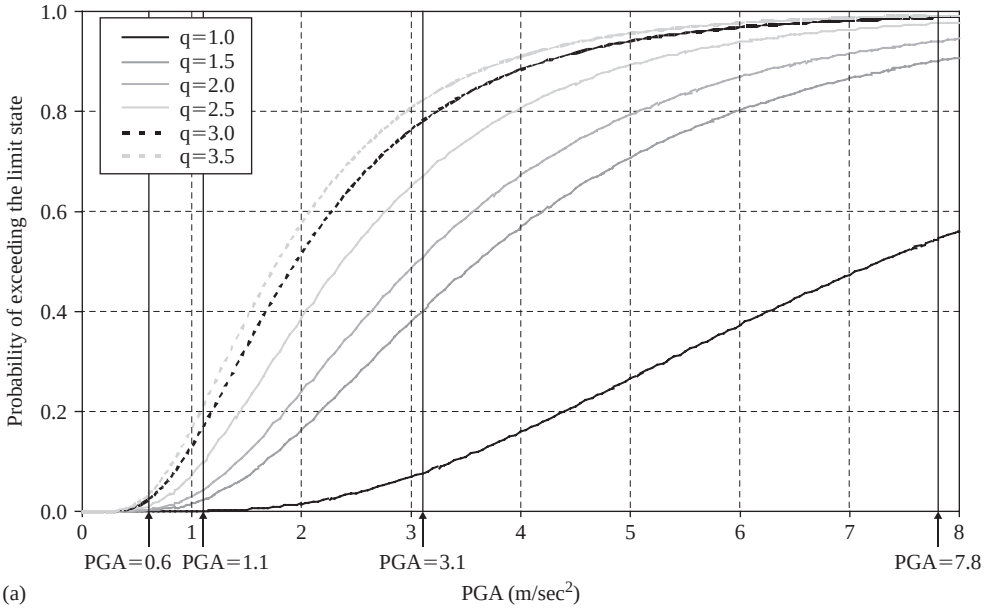

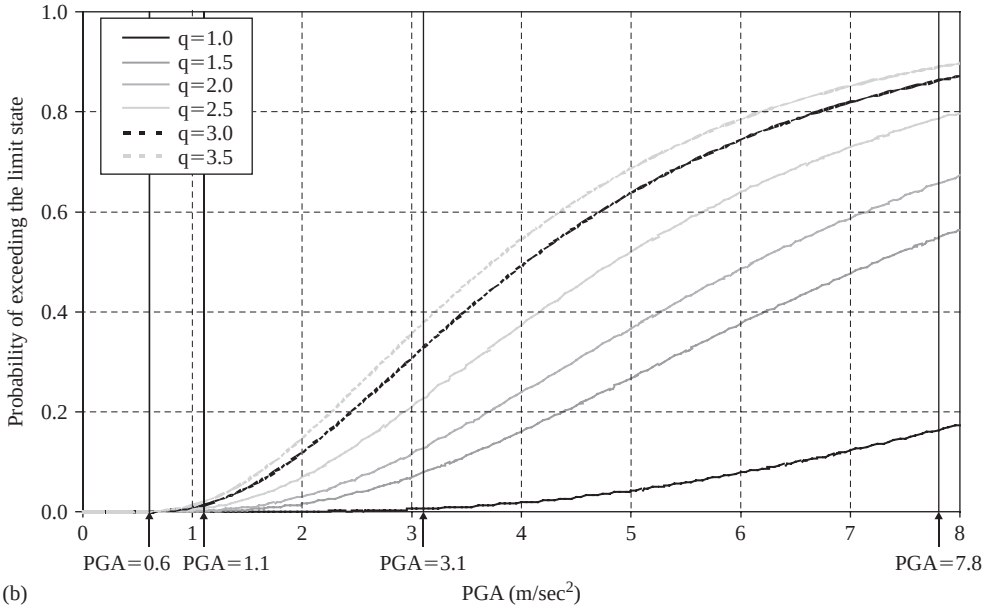

Figure 5 Fragility curves (a) Slight, (b) Moderate, (c) Extensive and (d) Complete structural damage states.

Table 5, the optimum design obtained for q = 1.0 by 20% more expensive compared to the q = 3.0 design. This confirms previous works where it was proved that designing a structure with q = 1.0 is not prohibited by the construction cost (Lagaros et al., 2006a).

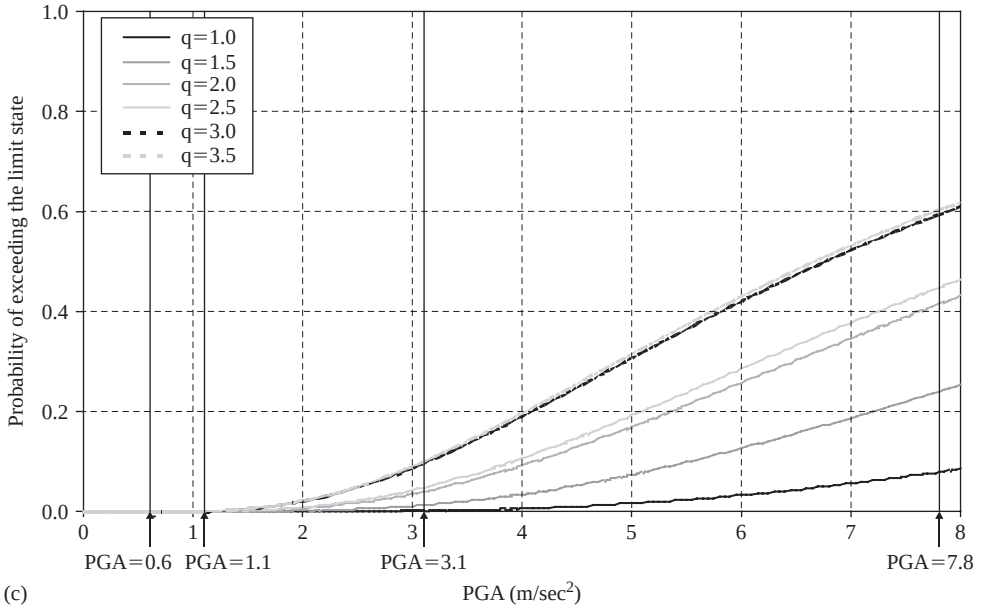

(c)

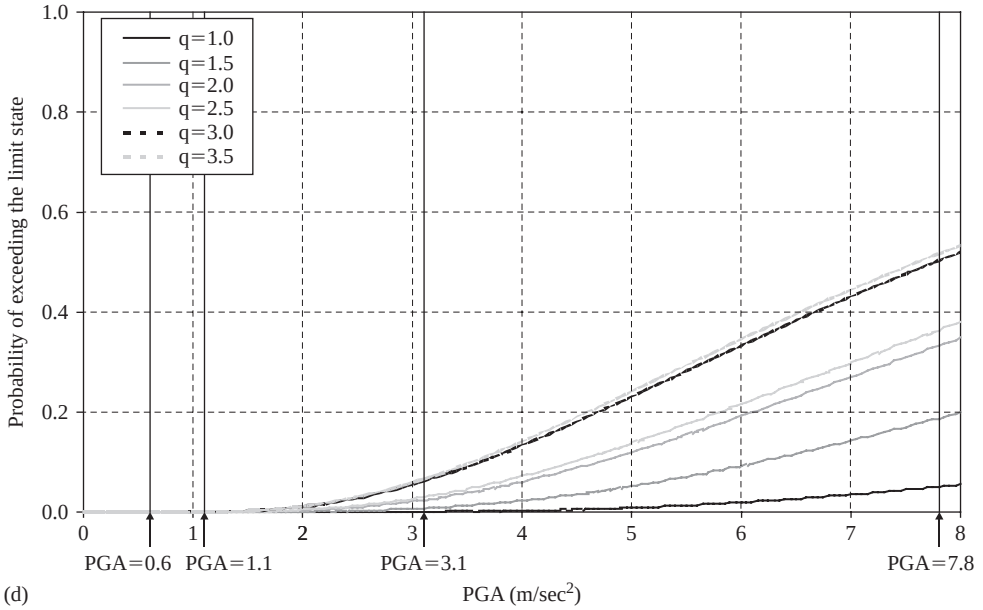

(d)

Figure 5 (Continued)

In the second part of this test case the performance of the six optimum designs is demonstrated in terms of limit state fragilities. Figures 5a to 5d depict the limit state fragility curves for low-rise RC buildings for the High Code Design Level of the earthquake loss estimation methodology (Table 2, HAZUS, 2003) for the Slight, Moderate,

Table 6 Limit state Probabilities of exceedance (%).

Limit state	$D_{q=1.0}$	$D_{q=1.5}$	$D_{q=2.0}$	$D_{q=2.5}$	$D_{q=3.0}$	$D_{q=3.5}$
PGA = 0.6 m/sec^2						
Slight	1.53E−03	1.38E−01	3.24E−01	1.08E+00	2.48E+00	3.50E+00
Moderate	7.06E−06	1.59E−03	5.22E−03	2.41E−02	7.26E−02	1.14E−01
Extensive	6.21E−07	3.00E−05	3.44E−04	5.08E−04	2.64E−03	2.92E−03
Complete	1.62E−07	1.17E−05	1.20E−04	1.82E−04	9.65E−04	1.13E−03
PGA = 1.1 m/sec^2						
Slight	7.99E−02	2.38E+00	4.37E+00	9.91E+00	1.71E+01	2.12E+01
Moderate	1.06E−03	8.22E−02	2.07E−01	6.60E−01	1.49E+00	2.08E+00
Extensive	1.42E−04	3.46E−03	2.46E−02	3.35E−02	1.22E−01	1.32E−01
Complete	4.63E−05	1.61E−03	1.06E−02	1.48E−02	5.56E−02	6.28E−02
PGA = 3.1 m/sec^2						
Slight	7.70E+00	4.01E+01	5.08E+01	6.71E+01	7.82E+01	8.24E+01
Moderate	5.85E−01	7.82E+00	1.28E+01	2.27E+01	3.29E+01	3.79E+01
Extensive	1.58E−01	1.23E+00	3.96E+00	4.73E+00	9.67E+00	1.01E+01
Complete	7.45E−02	7.60E−01	2.42E+00	2.95E+00	6.30E+00	6.74E+00
PGA = 7.8 m/sec^2						
Slight	5.46E+01	9.02E+01	9.41E+01	9.76E+01	9.90E+01	9.93E+01
Moderate	1.63E+01	5.49E+01	6.57E+01	7.86E+01	8.64E+01	8.91E+01
Extensive	7.92E+00	2.40E+01	4.15E+01	4.48E+01	5.95E+01	6.04E+01
Complete	5.10E+00	1.88E+01	3.33E+01	3.64E+01	5.04E+01	5.18E+01

Extensive and Complete structural damage states. The damage states, defined with respect to the drift limits according to HAZUS for this type of structure, are equal to 0.5%, 1.0%, 3.0% and 8.0% for Slight, Moderate, Extensive and Complete structural damage states, respectively. In these Figures, the PGA value for the frequent (PGA = 0.6 m/sec^2), occasional (PGA = 1.1 m/sec^2), rare (PGA = 3.1 m/sec^2) and the very rare (PGA = 7.8 m/sec^2) earthquake hazard levels design which are defined based on the work by Papazachos et al. (1993) are denoted with a bold vertical lines and the corresponding probabilities of exceedance of the four damage states are given in Table 6.

It can be seen from Table 6 that the limit state probabilities of exceedance for the design $D_{q=1.0}$ is one to four orders of magnitude less compared to the Eurocode 8 design $D_{q=3.0}$. Worth mentioning the observation for the rare hazard level (PGA = 3.1 m/sec^2) which is the design earthquake for the structure that, although, the probability of exceedance of the $D_{q=1.0}$ for the Slight damage state is one order of magnitude less than the corresponding probability for the $D_{q=3.0}$ design, the probability of exceedance for the Complete damage state of the $D_{q=1.0}$ design is two orders of magnitude less than the corresponding probability of the $D_{q=3.0}$ design. Consequently, $D_{q=1.0}$ obtained by slightly increasing the construction cost (20%) compared to the design obtained according to the EC8 provisions ($D_{q=3.0}$), results in much better the structural performance with reference to the limit-state probabilities of exceedance.

8.2 *Improving the torsional response of RC buildings*

A two storey 3D RC building has been considered as benchmark test for assessing the design approaches discussed. The material properties are the same with those of

Table 7 Natural records (Somerville and Collins, 2002).

Earthquake	*Station*	*Distance*	*Site*
Records in 50/50 hazard level			
Honeydew (PT)	Cape Mendocino	20	rock
17 August 1991	Petrolia	17	soil
Cape Mendocino (CM)	Rio Dell	13	soil
25 April 1992	Butler Valley	37	rock
Cape Mendocino (C2)	Fortuna	43	soil
aftershock, 4/26/92	Centerville	28	soil
Records in 10/50 hazard level			
Tabas (TB)	Dayhook	14	rock
16 September 1978	Tabas	1.1	rock
Cape Mendocino (CM)	Cape Mendocino	6.9	rock
25 April 1992	Petrolia	8.1	soil
Chi-Chi (CC), Taiwan	TCU101	4.9	soil
20 September 1999	TCU102	3.8	soil
Records in 2/50 hazard level			
Valparaiso (VL), Chile	Vina del Mar	30	soil
3 May 1985	Zapaller	30	rock
Michoacan (MI),	Caleta de Campos	12	rock
Mexico	La Union	22	rock
19 September 1985	La Villita	18	rock
	Zihuatenejo	21	rock

the previous test example. The design spectrum that has been used has the following characteristics: A=0.16g, ground type B and behaviour factor q = 3.0 according to EC8 (2003). The cross section of the beams is $25 \times 60\,\text{cm}^2$. The columns have been considered as fully fixed and no uncertainties in the foundation conditions have been taken into account.

The following four formulations of the optimization problem have been considered in the numerical study: (i) Minimum initial construction cost; (ii) minimum CM-CR eccentricity; (iii) minimum CM-CV eccentricity; and (iv) five combined formulations where two values of the weight coefficient of Eq. (5) have been examined (0.1 and 0.9). The five combined formulations can be described as follows:

$$\begin{aligned}
&\text{Min}\{0.1 \cdot C^*_{IN} + 0.9 \cdot e^*_{CM-CR}\} && \text{Comb(1)}\\
&\text{Min}\{0.1 \cdot C^*_{IN} + 0.9 \cdot e^*_{CM-CV}\} && \text{Comb(2)}\\
&\text{Min}\{0.1 \cdot C^*_{IN} + 0.9 \cdot \max(e^*_{CM-CR}, e^*_{CM-CV})\} && \text{Comb(3)}\\
&\text{Min}\{0.9 \cdot C^*_{IN} + 0.1 \cdot e^*_{CM-CR}\} && \text{Comb(4)}\\
&\text{Min}\{0.9 \cdot C^*_{IN} + 0.1 \cdot e^*_{CM-CV}\} && \text{Comb(5)}
\end{aligned} \tag{26}$$

Three different criteria have been used in order to assess the optimum designs achieved through the above mentioned formulations: The initial construction cost; the total life-cycle cost; and the torsional response criterion. For the second and third assessment criteria, ground motions chosen from the Somerville and Collins (2002) database, belonging to 50/50, 10/50 and 2/50 hazard levels (see Table 7), were used.

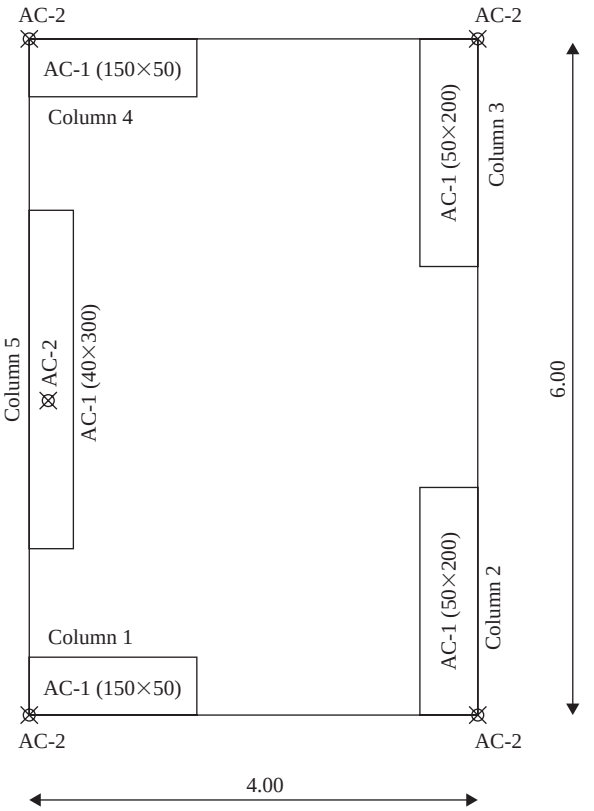

Column/ Shear walls	AC1	
	AC1x	AC1y
C1	150	50
C2	50	200
C3	50	200
C4	150	50
C5	40	300

Figure 6 Architectural constraints of a typical storey.

In the test example considered there is one group of storeys since the plan layout of the columns/shear walls is the same for both storeys.

In Figure 6 both architectural constraints (AC_1 rectangles and AC_2 points) are presented for all columns/shear walls. It has to be noted that all designs obtained from the different formulations fulfil the requirements of EC2 and EC8 design codes. In Table 8 the optimum designs, obtained through the various formulations examined are shown with respect to the cross-sectional dimensions and the two types of eccentricities.

The dimensions of the columns/shear walls are denoted as dim_x and dim_y corresponding to x and y axis, respectively. The formulation of the minimum initial construction cost leads to designs with eccentricities (e_{CM-CR}, e_{CM-CV}) larger than one meter. The two formulations implemented for minimizing the torsional response improve only the associated eccentricity defines the objective function of the problem: When the e_{CM-CR} is minimized, e_{CM-CV} is increased, and vice versa. In Table 8 the cross-sections of the columns/shear walls for all optimum solutions are given. It is clear that the sizes of the cross-sections for those formulations that C_{IN} is the dominant criterion are smaller the smallest ones.

Table 8 Optimum designs obtained through the formulations examined.

Column	$Min\{0.1C_{IN}+0.9e_{CM-CR}\}$		$Min\{0.1C_{IN}+0.9e_{CM-CV}\}$		$Min\{0.1C_{IN}+0.9max(e_{CM-CR}, e_{CM-CV})\}$		$Min\{0.9C_{IN}+0.1e_{CM-CR}\}$		$Min\{0.9C_{IN}+0.1e_{CM-CV}\}$		$Min\{e_{CM-CR}\}$		$Min\{e_{CM-CV}\}$		$Min\{C_{IN}\}$	
	$e_{CM-CR}=0.63$ cm		$e_{CM-CR}=47.3$ cm		$e_{CM-CR}=9.01$ cm		$e_{CM-CR}=141$ cm		$e_{CM-CR}=68.9$ cm		$e_{CM-CR}=0.04$ cm		$e_{CM-CR}=150.2$ cm		$e_{CM-CR}=179.6$ cm	
	$e_{CM-CV}(1)=86.1$ cm		$e_{CM-CV}(1)=5.43$ cm		$e_{CM-CV}(1)=12.7$ cm		$e_{CM-CV}(1)=74.9$ cm		$e_{CM-CV}(1)=54.1$ cm		$e_{CM-CV}(1)=99.7$ cm		$e_{CM-CV}(1)=4.15$ cm		$e_{CM-CV}(1)=118$ cm	
	$e_{CM-CV}(2)=94.8$ cm		$e_{CM-CV}(2)=5.33$ cm		$e_{CM-CV}(2)=10.4$ cm		$e_{CM-CV}(2)=72.4$ cm		$e_{CM-CV}(2)=63.6$ cm		$e_{CM-CV}(2)=97.6$ cm		$e_{CM-CV}(2)=4.26$ cm		$e_{CM-CV}(2)=114$ cm	
	dim_x	dim_y	dim_x	dim_y	dim_x	dim_y	dim_x	dim_y	dim_x	dim_y	dim_x	dim_y	dim_x	dim_y	dim_x	dim_y
C1	110	30	50	30	40	30	30	30	30	30	150	30	30	30	30	30
C2	30	130	30	120	30	130	30	30	30	30	30	90	30	150	30	30
C3	30	110	30	160	30	110	30	30	30	30	30	130	30	170	30	30
C4	110	30	40	30	40	30	30	30	30	30	150	30	70	30	30	30
C5	30	150	30	150	30	150	30	70	30	130	30	140	30	150	30	40

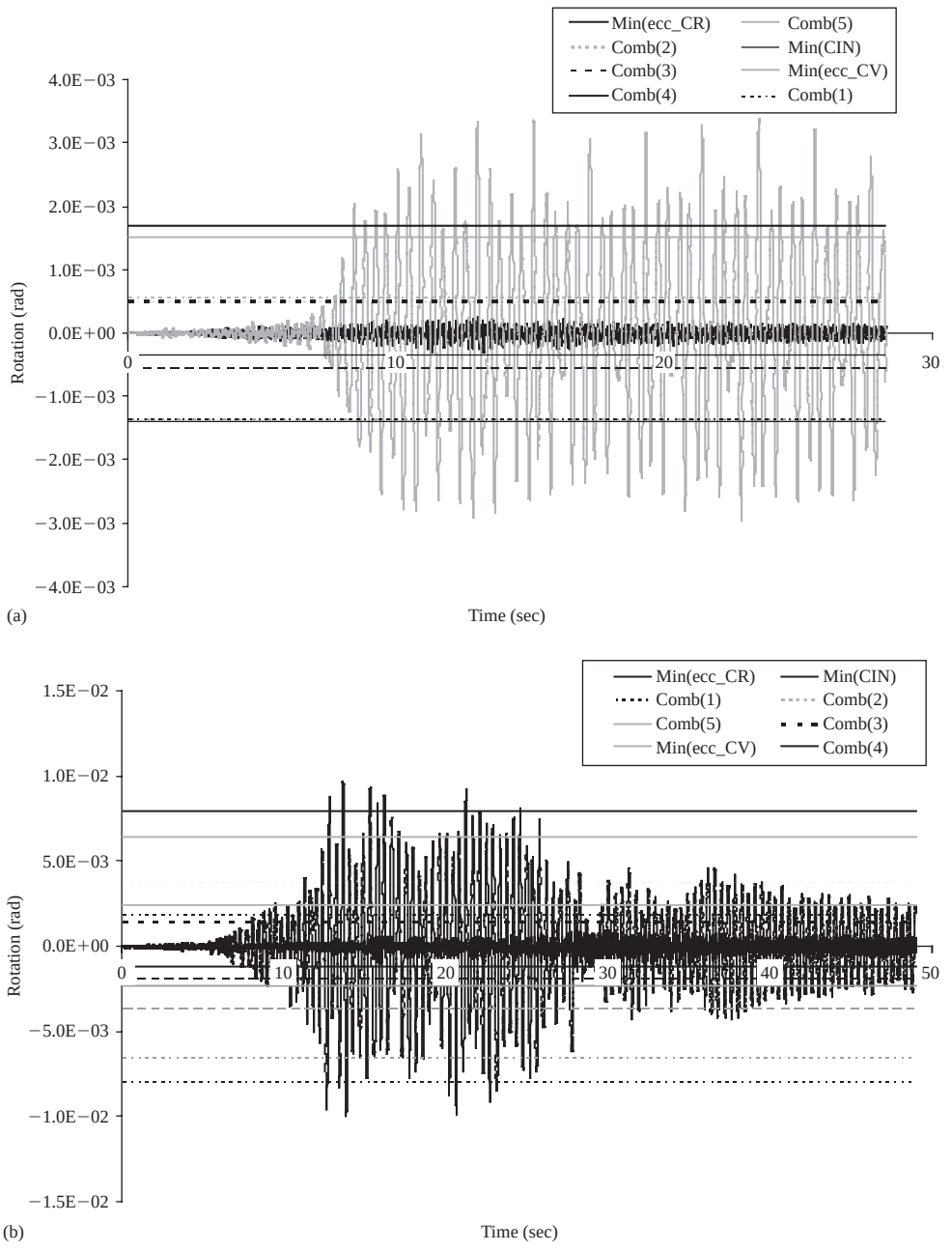

Figure 7 Rotation time histories of second floor for three hazard levels (a) 50/50, (b) 10/50 and (c) 2/50.

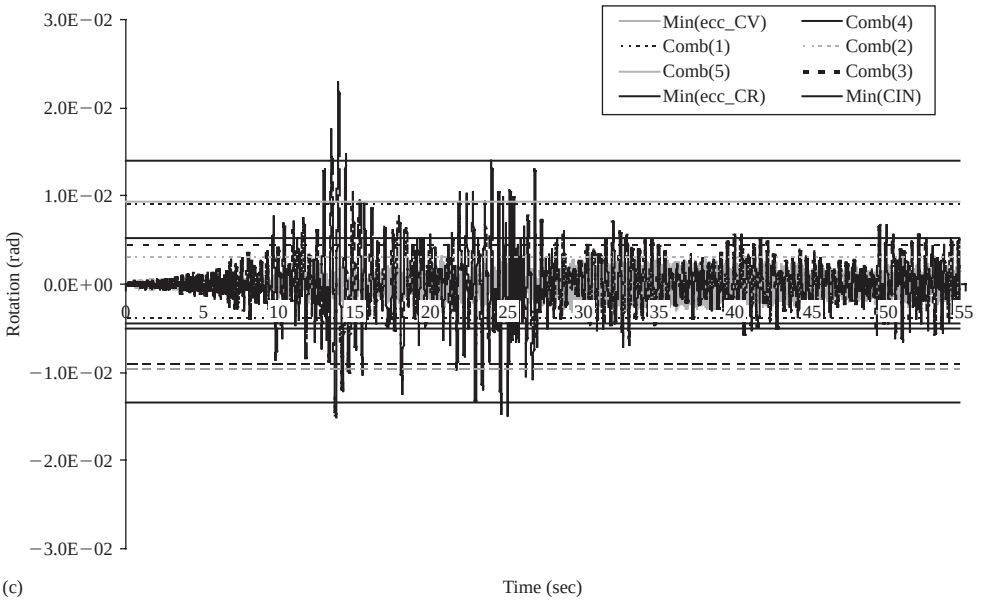

(c)

Figure 7 (Continued)

Table 9 Mean values of the torsional response in three hazard levels.

Design philosophy	*Hazard Level*					
	50/50		*10/50*		*2/50*	
	max (10^{-3} *rad*)	*min* (10^{-3} *rad*)	*max* (10^{-3} *rad*)	*min* (10^{-3} *rad*)	*max* (10^{-3} *rad*)	*min* (10^{-3} *rad*)
$\text{Min}\{0.1C_{IN}+0.9e_{CM-CR}\}$	0.509	−0.543	1.87	−1.84	9.14	−9.02
$\text{Min}\{0.1C_{IN}+0.9e_{CM-CV}\}$	0.569	−0.533	3.20	−3.64	3.77	−3.71
$\text{Min}\{0.1C_{IN}+0.9\max(e_{CM-CR}, e_{CM-CV})\}$	0.505	−0.351	1.43	−1.20	4.46	−4.42
$\text{Min}\{0.9C_{IN}+0.1e_{CM-CR}\}$	2.29	−1.83	9.72	−9.92	23.10	−15.00
$\text{Min}\{0.9C_{IN}+0.1e_{CM-CV}\}$	3.47	−2.94	6.39	−6.53	9.31	−9.45
$\text{Min}\{e_{CM-CR}\}$	0.254	−0.293	0.953	−1.28	5.26	−5.05
$\text{Min}\{e_{CM-CV}\}$	1.51	−1.40	2.46	−2.33	3.50	−5.05
$\text{Min}\{C_{IN}\}$	1.69	−1.34	7.90	−7.91	13.90	−13.40

In order to assess the structural performance of the optimum designs, nonlinear timehistory analyses are performed for the seismic records considered. The results of this investigation performed are shown in Figures 7(a) to 7(c) where the torsional response of the diaphragm of the second storey of the structure for the first record of each hazard level of Table 7 are compared. Table 9 depicts the maximum and minimum values of the diaphragm rotation, for each hazard level among the records of Table 7. It can be seen that the maximum rotation of the diaphragm is encountered when C_{IN}

Table 10 Comparison of the designs with respect to the cost.

		Min{*0.1*C_{IN}+ *0.9*e_{CM-CR}}	*Min*{*0.1*C_{IN}+ *0.9*e_{CM-CV}}	*Min*{*0.1*C_{IN}+ *0.9max*(e_{CM-CR}, e_{CM-CV})}	*Min*{*0.9*C_{IN}+ *0.1*e_{CM-CR}}	*Min*{*0.9*C_{IN}+ *0.1*e_{CM-CV}}	*Min*{e_{CM-CR}}	*Min*{e_{CM-CV}}	*Min*{C_{IN}}
	C_{IN} (in €1,000)	51.92	50.33	49.23	43.13	46.15	52.80	51.24	43.81
HAZUS (2003)	C_{LS}/C_{IN}	0.83	0.45	0.41	4.68	4.38	0.81	0.82	3.88
	C_{TOT} (in €1,000)	94.97	73.12	69.56	245.11	248.49	95.92	93.21	213.93
Ghobarah (2004)	C_{LS}/C_{IN}	3.53	18.57	7.19	22.53	23.56	3.65	13.07	29.18
	C_{TOT} (in €1,000)	235.46	984.92	403.31	1015.01	1133.73	245.61	721.32	1322.33

was the dominant criterion for all three hazard levels. On the other hand, in frequent (50/50) and occasional (10/50) hazard levels, the Min{e_{CM-CR}} formulation behaves better, while in rare (2/50) hazard levels the formulations where the e_{CM-CV} is the dominant criterion gives better designs. This observation is in accordance with the findings of Paulay (1998 and 2001) and Tso and Myslimaj (2003).

In Table 10, the optimum designs are compared with respect to the initial, limit state and total life-cycle costs. Through this comparison it can be seen that minimizing C_{IN} does not lead to the best design in terms of the life-cycle cost. The best design in terms of the total life-cycle cost depends on the drift limits used for calculating the limit state cost. When HAZUS (2003) drift limits are employed the formulation defined with the minimization of e_{CM-CR} and/or e_{CM-CV} leads to the best design. On the other hand, when the drift limits given by Ghobarah (2004) are used, the minimization of the eccentricity e_{CM-CR} leads to the best design. For both groups of drift limits employed it can be seen that although the design formulations, where C_{IN} is the dominant criterion (i.e. Cases (4), (5) and Min{C_{IN}}), lead to the minimum initial construction cost, the corresponding total life-cycle cost is the maximum one. For the HAZUS drift limits, Comb(3) leads to the best design with respect to the total life-cycle cost, while for the drift limits given by Ghobarah, Comb(1) leads to the best design.

9 Conclusions

In this chapter, structural optimization is considered for the assessment of (i) the behaviour factor q with respect to limit state fragilities and (ii) the minimum torsional response of RC buildings under different design considerations in three hazard levels (frequent, occasional and rare). The designs were assessed with respect to the initial as well as to the total life-cycle cost. From the present study the following conclusions can be drawn:

i. The probability of exceedance of the slight damage state for the $D_{q=1}$ design is up to three orders of magnitude less than that of the $D_{q=3}$ design, while for the complete damage state the probability of exceedance for the $D_{q=1}$ design is one and four orders of magnitude less than the corresponding probability for $D_{q=3}$ design. Consequently, $D_{q=1.0}$ obtained by slightly increasing the construction cost (20%) compared to the design obtained according to the EC8 provisions ($D_{q=3.0}$) resulted in much better structural performance with reference to the limit-state probabilities of exceedance.
ii. The rigidity centre eccentricity plays an important role mainly when the structural system behaves linearly. When the structure starts to behave nonlinearly the strength centre eccentricity becomes more important. These observations are verified in a more rigorous and generalized framework provided by structural optimization procedures where a number of recommendations for designing RC buildings are incorporated and critically assessed.

Acknowledgements

The first author acknowledges the financial support of the John Argyris Foundation.

References

ATC-13. 1985. Earthquake Damage Evaluation Data for California. Applied Technology Council: Redwood City, CA.

Bachmann, H. 2002. Seismic Conceptual Design of Buildings – Basic principles for engineers, architects, building owners, and authorities. Order Number: 804.802e, *Swiss Federal Office for Water and Geology, Swiss Agency for Development and Cooperation*. BWG, Biel.

Balling, R.J. & Yao, X. 1997. Optimization of reinforced concrete frames. *Journal of Structural Engineering*: 123(2): 193–202.

Barakat, S., Bani-Hani, K. & Taha, M.Q. 2004. Multi-objective reliability-based optimization of prestressed concrete beams. *Structural Safety* 26(3): 311–342.

Benjamin, J.R. & Cornell, C.A. 1970. *Probability, Statistics, and Decision for Civil Engineers*, McGraw-Hill. New York.

Bertero, R.D. 1995. Inelastic torsion for preliminary seismic design. *Journal of Structural Engineering* 121(8): 1183–1189.

Browning, J. 2002. Proportioning earthquake-resistant RC frames in central/eastern U.S. *Earthquake Engineering & Structural Dynamics* 31(6): 1267–1280.

Chan, C.-M. & Wang, Q. 2006. Nonlinear stiffness design optimization of tall reinforced concrete buildings under service loads. *Journal of Structural Engineering* 132(6): 978–990.

Chan, C.-M. & Zou, X.-K. 2004. Elastic and inelastic drift performance optimization for reinforced concrete buildings under earthquake loads. *Earthquake Engineering & Structural Dynamics 2004* 33(8): 929–950.

De-la-Colina, J. 2003. Assessment of design recommendations for torsionally unbalanced multi-storey buildings. *Earthquake Spectra* 19: 47–66.

Duan, X.N. & Chandler, A.M. 1997. An optimized procedure for seismic design of torsionally unbalanced structures. *Earthquake Engineering & Structural Dynamics* 26: 737–757.

EC2. 2002. Eurocode 2: Design of Concrete Structures. Part 1: General rules and rules for buildings. CEN, EN 1992-1-1:2002. European Committee for Standardization. Brussels.

EC8. 2004. Eurocode 8: Design of structures for earthquake resistance- Part 1. European standard. CEN-ENV-1998-1, European Committee for Standardization. Brussels.

Ellingwood, B.R. & Wen, Y-K. 2005. Risk-benefit-based design decisions for low-probability/high consequence earthquake events in mid-America. *Progress in Structural Engineering and Materials* 7(2):56–70.

Fajfar, P. 1998. Towards nonlinear methods for the future seismic codes. In Booth (ed.), *Seismic design practice into the next century*. Balkema.

Fajfar, P., Marusšicì, D., & Perusš, I. 2005. Torsional effects in the pushover-based seismic analysis of buildings. *Journal of Earthquake Engineering*. 9(6): 831–854.

FEMA 227. 1992. A Benefit–Cost Model for the Seismic Rehabilitation of Buildings. Federal Emergency Management Agency, Building Seismic Safety Council. Washington, DC.

FEMA-310. 1998. Handbook for the Seismic Evaluation of Buildings-A Prestandard, prepared by the American Society of Civil Engineers for the Federal Emergency Management Agency, Washington, DC.

FEMA-National Institute of Building Sciences. HAZUS-MH MR1. 2003. *Multi-hazard Loss Estimation Methodology Earthquake Model*. Washington, DC.

Frangopol, D.M. 1986. Computer-automated design of structural systems under reliability-based performance constraints. *Engineering Computations*. 3(2): 109–115.

Ganzerli, S., Pantelides, C.P. & Reaveley, L.D. 2000. Performance-based design using structural optimization. *Earthquake Engineering & Structural Dynamics*. 29(11): 1677–1690.

Garcia, M., de la Llera, J.C. & Almazan, J.L. 2007. Torsional balance of plan asymmetric structures with viscoelastic dampers. *Engineering Structures*. 29(6): 914–932.

Ghobarah, A. 2004. On drift limits associated with different damage levels. *International Workshop on Performance-Based Seismic Design*, *28 June – 1 July 2004*.

Goel, R.K. 2005. Seismic response of linear and non-linear asymmetric systems with non-linear fluid viscous dampers. *Earthquake Engineering & Structural Dynamics* 34(7): 825–846.

Guerra, F. 2005. Optimum layout of building subjected to geometric constraints. *Practice Periodical on Structural Design and Construction* 10(4): 239–245.

Jeong, S.-H. & Elnashai, A.S. 2006. New three-dimensional damage index for RC buildings with planar irregularities. *Journal of Structural Engineering* 132(9): 1482–1490.

Kan, C.L. & Chopra, A.K. 1977. Effect of torsional coupling on earthquake forces in buildings, *Journal of Structural Division ASCE* 103(4): 805–819.

Kanagasundaram, S. & Karihaloo, B.L. 1991. Minimum cost design of reinforced concrete structures. *Computers & Structures* 41(6): 1357–1364.

Koskisto, O.J. & Ellingwood, B.R. 1997. Reliability-based optimization of plant precast concrete structures. *Journal of Structural Engineering* 123(3): 298–304.

Lagaros, N.D., Fotis, A.D. & Krikos, S.A. 2006a. Assessment of seismic design procedures based on the total cost, *Earthquake Engineering Structural Dynamics*. 35(11): 1381–1401.

Lagaros, N.D. & Papadrakakis, M. 2007. Seismic design of RC structures: a critical assessment in the framework of multi-objective optimization. *Earthquake Engineering & Structural Dynamics*. 36(12): 1623–1639.

Lagaros, N.D., Papadrakakis, M. & Bakas, N. 2006b. Automatic minimization of the rigidity eccentricity of 3d reinforced concrete buildings. *Journal of Earthquake Engineering* 10(4): 533–564.

Lagaros, N.D., Papadrakakis, M. & Kokossalakis, G. 2002. Structural optimization using evolutionary algorithms. *Computer & Structures* 80(7-8): 571–587.

Li, G. & Cheng, G. 2001. Optimal decision for the target value of performance-based structural system reliability. *Structural & Multidisciplinary Optimization* 22(4): 261–267.

Mazzolani, F.M. & Piluso, V. 1996. The theory and design of seismic resistant steel frames. E & FN Spon.

Moharrami, H. & Grierson, D.E. 1993. Computer-automated design of reinforced concrete frameworks. *Journal of Structural Engineering* 119(7): 2036–2058.

Naeim, F. & Kelly, J.M. 1999. *Design of seismic isolated structures – From theory to practice*. New York: Wiley.

National Building Code of Canada. Part 4 Structural Design. *Issued by the Canadian Commission on building and fire codes, Federal Publications Inc*. Toronto, 1995.

Panagiotakos, T.B. & Fardis, M.N. 2004. Seismic performance of RC frames designed to Eurocode 8 or to Greek Codes 2000. *Bulletin of Earthquake Engineering*. 2: 221–259.

Papadrakakis, M., Lagaros, N.D., Thierauf, G. & Cai, J. 1998. Advanced solution methods in structural optimization based on evolution strategies. *Journal of Engineering Computations* 15(1): 12–34.

Papadrakakis, M., Lagaros, N.D., Tsompanakis, Y. & Plevris, V. 2001. Large scale structural optimization: Computational methods and optimization algorithms. *Archives of Computational Methods in Engineering (State of the art reviews)* 8(3): 239–301.

Papazachos, B.C., Papaioannou, Ch.A. & Theodulidis, N.P. 1993. Regionalization of seismic hazard in Greece based on seismic sources. *Natural Hazards* 8(1): 1–18.

Paulay, T. 2001. Some design principles relevant to torsional phenomena in ductile buildings. *Journal of Earthquake Engineering* 5: 273–308.

Paulay, T. 1998. A mechanism-based design strategy for torsional seismic response of ductile buildings. *European Earthquake Engineering* 2: 33–48.

Pettinga, J.D., Priestley, M.J.N., Pampanin, S. & Christopoulos, C. 2007. The role of inelastic torsion in the determination of residual deformations. *Journal of Earthquake Engineering* 11(1): 133–157.

Rackwitz, R. 2006. The effect of discounting, different mortality reduction schemes and predictive cohort life tables on risk acceptability criteria. *Reliability Engineering & System Safety* 91(4): 469–484.

Rackwitz, R., Lentz, A. & Faber, M. 2005. Socio-economically sustainable civil engineering infrastructures by optimization. *Structural Safety* 27(3): 187–229.

Rosenblueth, E. & Meli, R. 1986. The 1985 earthquake: causes and effects in Mexico City. *Concrete International ACI*. 23–34.

Rutenberg, A. 2002. EAEE Task Group (TG) 8: Behaviour of irregular and complex structures asymmetric structures-progress since 1998. *Proceedings of the 12th European Conference on Earthquake Engineering, London*. Elsevier: Oxford, Paper no. 832.

Sarma, K.C. & Adeli, H. 1998. Cost optimization of concrete structures. *Journal of Structural Engineering* 124(5): 570–578.

Somerville, P. & Collins, N. 2002. Ground motion time histories for the Humboldt bay bridge. Pasadena, CA, URS Corporation, www.peertestbeds.net/humboldt.htm.

Tso, W.K. & Myslimaj, B. 2003. A yield displacement distribution-based approach for strength assignment to lateral force-resisting elements having strength dependent stiffness. *Earthquake Engineering & Structural Dynamics* 32: 2319–2351.

Tso, W.K. 1990. Static eccentricity concept for torsional moment estimations. *Journal of Structural Engineering* 116(5): 1199-1212.

Wen, Y.K. & Kang, Y.J. 2001a. Minimum building life-cycle cost design criteria. I: Methodology. *Journal of Structural Engineering* 127(3): 330–337.

Wen, Y.K. & Kang, Y.J. 2001b. Minimum building life-cycle cost design criteria. II: Applications. *Journal of Structural Engineering* 127(3):338-346.

Wong, C.M. & Tso, W.K. 1995. Evaluation of seismic torsional provisions in uniform building code. *Journal of Structural Engineering* 121(10): 1436–1442.

Xue, Q. 2000. Need of performance-based earthquake engineering in Taiwan: a lesson from the Chichi earthquake. *Earthquake Engineering & Structural Dynamics* 29(11): 1609–1627.

Chapter 32

Robust stochastic optimal control of seismically excited buildings

Jorge E. Hurtado & Naile Aguirre

Universidad Nacional de Colombia, Manizales, Colombia

ABSTRACT: The large randomness of earthquake ground motions is one of the main problems for aseismic design, as it makes uncertain the effectiveness of design decisions. In advanced earthquake-resistant design an alternative to incorporate ground motion uncertainty is to perform a reliability-based optimization, consisting in minimizing the cost subject to keeping the failure probability less than a certain threshold. The use of structural passive or active control necessarily implies a severe reduction of the allowable failure probabilities, thus making rather more expensive the application of reliability-based optimization. In addition, a major problem in applying LQR control is that it is subject to arbitrary selection of the relative weights of the story displacements and control forces. For these reasons it is convenient to apply a different strategy than the reliability-based design to overcome these difficulties and drawbacks. In this chapter, the concept of robust optimal design is used. It consists in minimizing the structural cost in such a way that the standard deviations of the responses are less than certain thresholds, thus yielding the optimal values of the weights with due regard to the uncertainties present in the system. The adequate computation of the response standard deviations in view of the large uncertainties of the ground motion parameters is also discussed and the application of a practical procedure is suggested and illustrated for a passive control case.

1 Introduction

In structural engineering one can distinguish two main trends for incorporating uncertainties into design. They are the reliability-based design optimization (RBDO) and the robust design optimization (RDO). The former consists in minimizing the structural cost $C(\boldsymbol{y})$, considered as a function of design parameters $\boldsymbol{y}$, while keeping the probabilities of exceeding critical values lower than certain thresholds. This can be expressed as follows (Rosenblueth and Mendoza 1971; Gasser and Schuëller 1997; Frangopol 1995; Royset et al. 2001; Royset and Polak 2004):

$$\begin{aligned} \text{find}: &\quad \boldsymbol{y} \\ \text{minimizing}: &\quad C(\boldsymbol{y}) \\ \text{subject to}: &\quad \mathbf{P}[f_i(\underline{\boldsymbol{x}}, \boldsymbol{y}) > F_i] \le P_i, \quad i = 1, 2, \ldots \\ &\quad \boldsymbol{y}^- \le \boldsymbol{y} \le \boldsymbol{y}^+ \end{aligned} \tag{1}$$

where $\underline{\boldsymbol{x}}$ is a set of random variables, $\mathbf{P}[A]$ the probability of the random event A and P_i its upper bound. The function $g_i(\underline{\boldsymbol{x}}, \boldsymbol{y}) = F_i - f_i(\underline{\boldsymbol{x}}, \boldsymbol{y})$ is the limit state function defining any reliability problem (Melchers 1999; Hurtado 2004).

On the other hand, RDO is aimed at a reduction of the uncertainty of the response as represented by the low order statistical moments, in order to make it as insensitive to large variations of the input as possible. This problem can be expressed as (Doltsinis and Kang 2004; Doltsinis et al. 2005; Zang et al. 2005; Beyer and Sendhoff 2007)

$$\begin{aligned} \text{find}: \quad & \boldsymbol{y} \\ \text{minimizing}: \quad & C(\boldsymbol{y}) = (1-\alpha)\mathrm{E}[f(\boldsymbol{y})]/\mu^* + \alpha\sqrt{\mathrm{Var}[f(\boldsymbol{y})]}/\sigma^* \\ \text{subject to}: \quad & \mathrm{E}[g_i(\boldsymbol{y})] + \beta_i\sqrt{\mathrm{Var}[g_i(\boldsymbol{y})]} \le 0, \quad i = 1,2,\ldots \\ & \sqrt{\mathrm{Var}[h_j(\boldsymbol{y})]} \le \sigma_j^+, \quad j = 1,2,\ldots \\ & \boldsymbol{y}^- \le \boldsymbol{y} \le \boldsymbol{y}^+ \end{aligned} \tag{2}$$

where $f(\boldsymbol{y})$ is a performance function, $0 < \alpha < 1$ is a factor weighting the minimization of its mean and standard deviation, $\beta_i > 0$ is a factor defining the control of the response $g_i(\boldsymbol{y})$ in the tail of its distribution, σ_j^+ an upper bound to the standard deviation of response $h_j(\boldsymbol{y})$ and μ^*, σ^* are normalizing factors. Other formulations are, however, possible.

The choice between these two approaches depends on many factors, such as the risk consequences of the failure, the availability of statistical information, the feasibility of computing probabilities with sufficient accuracy, the computational cost, etc.

The present chapter deals with the consideration of uncertainties in passive and active control design of linear and nonlinear structures subject to earthquake forces. In this case there are some specific issues that should be considered.

The application of passive and active structural control to reduce the displacements and stresses caused by earthquake forces in buildings is a topic of increasing interest among the engineering community. In fact, structural control opens up the possibility of overcoming the disastrous effects of earthquakes, either by adding external forces intended to maintain the structural vibration within reduced bounds (active control) or by introducing devices that increase the period or the damping of the structure (passive control). However, a mayor risk in using active structural control is that the safety of the structure entirely depends control system, because no significant ductility capacity is given (or is expected to be given) to the structural members. Therefore, the design of the control strategy must be decided judiciously upon consideration of the uncertainties present in the system.

The application of reliability-based design in earthquake engineering imply the computation of first passage probabilities under dynamic loads. Using established random vibration theories, this is accurate only in case of Gaussian loads and responses, because there are explicit formulas for the first passage solution almost exclusively in this case. Despite the seismic action can be reasonably well modeled as a Gaussian stochastic process, as it is the result of a large accumulation of random factors, the nonlinearity of the response makes it decidedly non-Gaussian, thus leading as the only alternative the use of Monte Carlo simulation. This reports the advantage of being a method of absolute generality and accuracy. However, in structural dynamics applications it demands a large computational effort. In addition, when using active control the failure probabilities are expected to be much smaller than in conventional aseismic design, rendering the use of Monte Carlo methods extremely expensive in that case.

For structural systems of significant size, the only, non Monte Carlo method that yields good estimates of the second order statistical responses is the stochastic equivalent linearization technique (Roberts and Spanos 1990; Casciati and Faravelli 1991; Schenk and Schuëller 2005). Upon this basis it is possible obtain very rough estimates of the failure probability using the theory of first-passage and level crossing by stochastic processes. However, it would be very risky to base the selection of the parameters of a structural control upon such estimates. This suggests that the consideration of the large uncertainties posed by earthquake forces in structural control can be most practically carried out using a robust control strategy, based upon second-order, equivalent linearization methods of random vibration. Upon the availability of such second order estimates, an optimization strategy can be applied in order to assure the accomplishment of certain second-order constraints or minima, as shown in the sequel.

Considering the difficulty in estimating with accuracy the failure probability of nonlinear structures subject to seismic actions, the research reported herein concerns a methodology for robust design, requiring estimation of low order statistical moments, which are henceforth used in an optimization programme aimed at the constrained minimization of the cost in the manner explained above. Accordingly, the methodology comprises the following components:

- A method for accurately estimating the second-order statistical responses required for robust design optimization in case of nonlinear response. This is accomplished by a modified method of stochastic equivalent linearization, especially purported to take into account the actual non Gaussian behavior of hysteretic oscillators proposed by the author in (Hurtado and Barbat 1996; Hurtado and Barbat 2000).

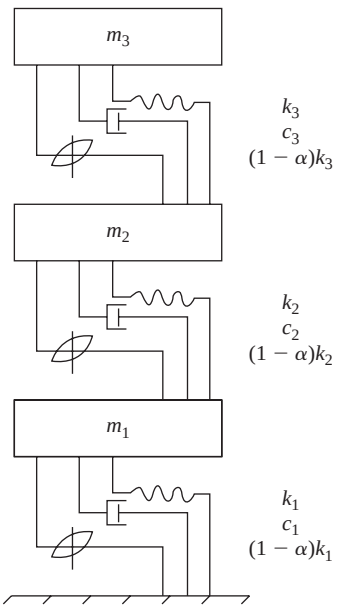

Figure 1 Nonlinear shear beam model.

- An active control strategy. In this case the classical linear-quadratic control (Soong 1990) has been selected.
- A method for optimizing the control parameters, which are normally decided without regard to the uncertainties implied in the system. In present research use was made of the method of particle swarm optimization (Kennedy and Eberhart 2001).
- A method for considering the randomness of the parameters defining the stochastic model of the seismic action used in the preceding steps.

The components of the methodology are described in detail in the next sections.

2 Stochastic linearization

Consider a building modeled as a nonlinear shear beam in the following form:

$$m_i \left[\sum_{j=1}^{i} \ddot{x}_j + p(t) \right] + c_i \dot{x}_i(t) - c_{i+1} \dot{x}_{i+1}(t) + g_i - g_{i+1} = 0 \tag{3}$$

where x_i, x_{i+1}: are the relative displacements, or drifts, between stories i, $i+1$. $i = 1 \ldots s$; m_i, c_i and g_i are respectively the mass, damping coefficient and restoring force of story i and $p(t)$ is the external exciting force. For each story, the nonlinear restoring force corresponds to the Bouc-Wen model (Wen 1976)

$$g(\dot{x}, x, t) = \alpha k x + (1 - \alpha) k z \tag{4}$$

in which k is the stiffness, α is a value that controls the nonlinearity of the system and z is a nonlinear function having displacement units, given by

$$\dot{z} = h(\dot{x}, z) = A\dot{x} - \beta |\dot{x}| |z|^{n-1} z - \gamma \dot{x} |z|^n \tag{5}$$

where A, β, γ and n are parameters controlling the width of hysteretic cycles, the level of energy dissipation, the hardening or softening of the system and the transition from the linear to the nonlinear phases, respectively. The system of equations can be written in state-space form as

$$\begin{aligned} \dot{X}_1 &= X_2 \\ \dot{X}_2 &= -M^{-1} C X_2 - M^{-1} \alpha K X_1 - M^{-1} G X_3 + M^{-1} p(t) \\ \dot{X}_3 &= A X_2 - \beta |X_2| |X_3|^{n-1} X_3 - \gamma X_2 |X_3|^n \end{aligned} \tag{6}$$

with

$$M = \begin{bmatrix} m_1 & & & & \\ & m_2 & & & \\ & & m_3 & & \\ & & & \ddots & \\ & & & & m_n \end{bmatrix}_{n \times n} \qquad C = \begin{bmatrix} c_1 & & & & \\ & c_2 & & & \\ & & c_3 & & \\ & & & \ddots & \\ & & & & c_n \end{bmatrix}_{n \times n} \tag{7}$$

$$\alpha K = \begin{bmatrix} \alpha_1 k_1 & -\alpha_2 k_2 & & & \\ & \alpha_2 k_2 & -\alpha_3 k_3 & & \\ & & \ddots & & \\ & & & \alpha_{n-1} k_{n-1} & -\alpha_n k_n \\ & & & & \alpha_n k_n \end{bmatrix}_{n \times n} \tag{8}$$

$$G = \begin{bmatrix} (1-\alpha_1)k_1 & -(1-\alpha_2)k_2 & & & \\ & (1-\alpha_2)k_2 & -(1-\alpha_3)k_3 & & \\ & & \ddots & & \\ & & & (1-\alpha_{n-1})k_{n-1} & -(1-\alpha_n)k_n \\ & & & & (1-\alpha_n)k_n \end{bmatrix}_{n \times n} \tag{9}$$

$$p(t) = M_d \cdot r \cdot a \tag{10}$$

$$M_d = \begin{bmatrix} m_1 & & & & \\ m_2 & m_2 & & & \\ m_3 & m_3 & m_3 & & \\ \vdots & \vdots & \vdots & \ddots & \\ m_n & m_n & m_n & \cdots & m_n \end{bmatrix}_{n \times n} \qquad r = \begin{bmatrix} 1 \\ 1 \\ \vdots \\ 1 \end{bmatrix}_{n \times 1} \tag{11}$$

where n is the number of degrees of freedom.

In conventional building systems, the structural damping is a result of friction among the particles of the structural members. In the present case it is increased by adding viscous dampers in each story having a damping coefficient c_d to the diagonal elements.

The main principle of stochastic linearization is the minimization of the expected value of the difference between the original nonlinear Bouc-Wen (Eq. 5) and its linear surrogate

$$\hat{\dot{z}} = c_e \dot{x} + k_e z \tag{12}$$

where c_e and k_e are coefficients determined by minimizing the expected value of the squared error given by

$$\epsilon = h(\dot{x}, z) - (c_e \dot{X} + k_e X) \tag{13}$$

Upon the assumption that the responses x, $\dot{x}$ and z are Gaussian, closed form expressions for the coefficients c_e and k_e are obtained. They are (Wen 1976)

$$c_e = \mathrm{E}\left[\frac{\partial h}{\partial \dot{X}}\right] = \mathrm{E}\left[A - \beta \frac{\partial |\dot{X}|}{\partial \dot{X}} |Z|^{n-1} Z - \gamma |Z|^n\right] \tag{14}$$

$$k_e = \mathrm{E}\left[\frac{\partial h}{\partial Z}\right] = \mathrm{E}\left[-\beta |\dot{X}| \frac{\partial}{\partial Z} |Z|^{n-1} Z - \gamma \dot{X} \frac{\partial}{\partial Z} |Z|^n\right] \tag{15}$$

which, after calculating the expectations with the Normal density function yield

$$c_e = A - \beta F_1 - \gamma F_2 \tag{16}$$

$$k_e = A - \beta F_3 - \gamma F_4 \tag{17}$$

with

$$F_1 = \frac{\sigma_z^n}{\pi}\Gamma\left(\frac{n+2}{2}\right)2^{n/2}I_s \tag{18}$$

$$F_2 = \frac{\sigma_z^n}{\sqrt{\pi}}\Gamma\left(\frac{n+1}{2}\right)2^{n/2} \tag{19}$$

$$F_3 = \frac{n\sigma_{\dot{x}}\sigma_z^{n-1}}{\pi}\Gamma\left(\frac{n+2}{2}\right)2^{n/2}\left(2\left(1-\rho_{\dot{x}z}^2\right)^{n+1/2} + \rho_{\dot{x}z}I_s\right) \tag{20}$$

$$F_4 = \frac{n\rho_{\dot{x}z}\sigma_{\dot{x}}\sigma_z^{n-1}}{\sqrt{\pi}}\Gamma\left(\frac{n+1}{2}\right)2^{n/2} \tag{21}$$

$$I_s = 2\int_l^{\pi/2}\sin^n\theta\, d\theta \qquad \Gamma(n) = \int_0^{\infty}x^{n-1}e^{(-x)}dx \tag{22}$$

$$\sigma_x = \sqrt{\mathrm{cov}_{xx}} \qquad \rho_{xy} = \frac{\mathrm{cov}_{xy}}{\sigma_x\sigma_y} \tag{23}$$

$$l = \tan^{-1}\left(\frac{\sqrt{1-\rho_{\dot{x}z}^2}}{\rho_{\dot{x}z}}\right) \tag{24}$$

Eq. (6) can be expressed in state-space form as

$$\dot{y}(t) = A_e(t)y(t) + f(t) \tag{25}$$

where $y(t)$ is the state vector including the degrees of freedom of the Kanai-Tajimi filter U_g y $\dot{U}_g$ used for modeling the earthquake ground motion:

$$y(t) = \begin{bmatrix} X & \dot{X} & Z & U_g & \dot{U}_g \end{bmatrix}^T_{(3n+2)\times 1} \tag{26}$$

On the other hand A_e is the system matrix obtained after linearization:

$$A_e(t) = \begin{bmatrix} \underline{0} & \underline{I} & \underline{0} & \underline{0} & \underline{0} \\ -\underline{M}^{-1}\alpha\underline{K} & -\underline{M}^{-1}\underline{C} & -\underline{M}^{-1}\underline{G} & -\underline{M}^{-1}\underline{M_d}\underline{r}\omega_g^2 & -\underline{M}^{-1}\underline{M_d}\underline{r}2\nu_g\omega_g \\ \underline{0} & \underline{C_e}(t) & \underline{K_e}(t) & \underline{0} & \underline{0} \\ \underline{0} & \underline{0} & \underline{0} & 0 & 1 \\ \underline{0} & \underline{0} & \underline{0} & -\omega_g^2 & -2\nu_g\omega_g \end{bmatrix}_{(3n+2)\times(3n+2)} \tag{27}$$

where the underlines represent matrices for clarity. Here ω_g and ν_g are the parameters of the Kanai-Tajimi filter and C_e y K_e are the matrices containing the linearization coefficients:

$$C_e = \begin{bmatrix} c_{e_1} & & & & \\ & c_{e_2} & & & \\ & & c_{e_3} & & \\ & & & \ddots & \\ & & & & c_{e_n} \end{bmatrix}_{n\times n} \qquad K_e = \begin{bmatrix} k_{e_1} & & & & \\ & k_{e_2} & & & \\ & & k_{e_3} & & \\ & & & \ddots & \\ & & & & k_{e_n} \end{bmatrix}_{n\times n} \tag{28}$$

Finally $f(t)$ is the external force vector, whose only non-zero entry is the white noise exciting the Kanai-Tajimi filter:

$$f(t) = W(t)\xi(t) \begin{bmatrix} \underline{0} \\ \underline{0} \\ \underline{0} \\ 0 \\ -1 \end{bmatrix}_{(3n+2)\times 1} \tag{29}$$

The linear equation 12 can then be easily included in the state-space formulation. After operating upon the state-space equation of the extended system, i.e. that including the linearized equation, and assuming Gaussian behavior of all the responses, one obtains the following differential equation for the evolution of the covariance matrix of the responses:

$$\dot{\Sigma}(t) = A(t)\Sigma(t) + \Sigma(t)A^T(t) + 2\pi S_f(t) \tag{30}$$

where

$$\Sigma(t) = E\left[y(t)\cdot y^T(t)\right] \tag{31}$$

$$S_f(t) = \begin{bmatrix} \underline{0} & \underline{0} & \underline{0} & \underline{0} & \underline{0} \\ \underline{0} & \underline{0} & \underline{0} & \underline{0} & \underline{0} \\ \underline{0} & \underline{0} & \underline{0} & \underline{0} & \underline{0} \\ \underline{0} & \underline{0} & \underline{0} & 0 & 0 \\ \underline{0} & \underline{0} & \underline{0} & 0 & 1 \end{bmatrix} \xi(t)^2 G_0 \tag{32}$$

In this equation G_0 is the spectral power of the white noise $W(t)$ and $\xi(t)$ is a modulating function used for given a non-stationary shape to the seismic model. The solution of equation (30) affords the second-order moments of the responses needed to calculate the linearization coefficients in each time step. However, in case of hysteretic oscillators such as the Bouc Wen model, it has been observed that the Gaussian hypothesis is not satisfactory, because the internal forces are bound in the negative an positive sides by the respective strengths. This imposes the use of a non Gaussian approach, as the

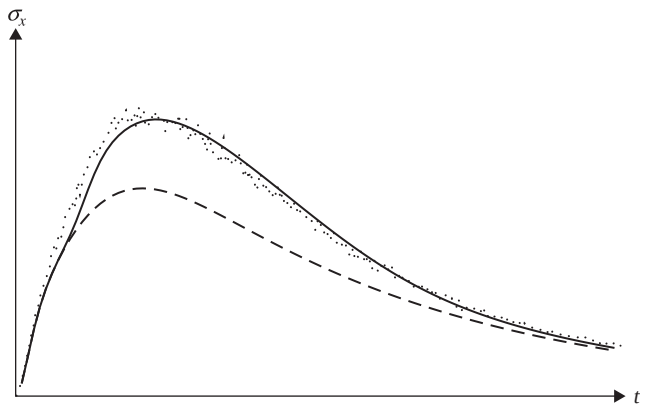

Figure 2 Comparison of Gaussian (dashed line) and non-Gaussian stochastic equivalent linearization (solid line) for an hysteretic oscillator using Monte Carlo results (dotted line).

following proposed by the author (Hurtado and Barbat 1996; Hurtado and Barbat 2000). It consists in using the modified set of coefficients

$$[\widetilde{c}_{\mathrm{e}} \quad \widetilde{k}_{\mathrm{e}}] = ((1-2p)[c_{\mathrm{e}} \quad k_{\mathrm{e}}] + 2p[c_{\mathrm{d}} \quad k_{\mathrm{d}}]S^{-1} \tag{33}$$

where p is a parameter that weights the relative importance of Gaussian and Dirac-delta densities in the internal force variable, S is the 3×3 matrix of covariance responses for each hysteretic degree of freedom and $c_{\mathrm{d}}, k_{\mathrm{d}}$ are respectively the damping and stiffness linearization coefficients corresponding to Dirac pulses located at the strength bounds of the restoring forces. The details can be found in the quoted references. As an illustration, figure (2) shows a comparison of the standard deviation of the displacement of an hysteretic Bouc-Wen oscillator subject to a seismic excitation using the Gaussian and non Gaussian approaches. It can be observed that the accuracy of the non Gaussian method is much higher.

3 Active control strategy

One of the classical strategies developed in control science and technology that has deserved attention in the field of structural control is the Linear Quadratic Regulator strategy (LQR), in which the external control force $u(t)$ is expressed by

$$u(t) = -\frac{1}{2}R^{-1}B^{T}P(t)\, y(t) \tag{34}$$

where B is a matrix whose non-zero entries indicate the location of the control forces, $y(t)$ is the state vector in the state space formulation of the structural dynamics problem. In Eq. (34) R is a matrix of coefficients denoting the relative weight of the control force with respect to the structural displacements. On the other hand, $P(t)$ is the solution of

$$A^T P + PA - 0.5PBR^{-1}B^T P + 2Q = 0 \tag{35}$$

known as the Ricatti matrix equation. Similarly to R, Q denotes the relative weight of the displacements with respect to the control force. In fact, Eq. (34) is the solution of minimizing the compound cost function

$$J = \int_0^{t_f} \{y^T(t)Qy(t) + u^T(t)Ru(t)\} \tag{36}$$

where t_f is the total duration of the earthquake motion. See (Soong 1990) for the details.

For applying the LQR control to the problem at hand an approximation is applied, consisting in linearizing the system about the equilibrium point $y = 0$. Thus, taking into account that $\dot{z} = 0$ when $\dot{x} = 0$, one obtains the system

$$\dot{\bar{y}}(t) = \Lambda_0 \bar{y}(t) + \overline{B}U(t) + \overline{f}(t) \tag{37}$$

with

$$\Lambda_0 = \left.\frac{\partial A_e y(t)}{\partial y(t)}\right|_{y=0} \tag{38}$$

$$\Lambda_0 = \begin{bmatrix} \underline{0} & \underline{I} & \underline{0} & \underline{0} \\ -\underline{M}^{-1}\alpha\underline{K} & -\underline{M}^{-1}\underline{C} & -\underline{r}\omega_g^2 & \underline{r}2\nu_g\omega_g \\ \underline{0} & \underline{0} & 0 & 1 \\ \underline{0} & \underline{0} & -\omega_g^2 & -2\nu_g\omega_g \end{bmatrix}_{(2n+2)\times(2n+2)} \tag{39}$$

$$\bar{y}(t) = \begin{bmatrix} X & \dot{X} & U_g & \dot{U}_g \end{bmatrix}^T_{(2n+2)\times 1} \tag{40}$$

$$\overline{B} = \begin{bmatrix} \underline{0}_{n\times r} \\ \underline{M}^{-1}\underline{H} \\ \underline{0}_{2\times r} \end{bmatrix}_{(2n+2)\times r} \tag{41}$$

$$H = \begin{bmatrix} \underline{I}_{r\times r} \\ \underline{0} \end{bmatrix}_{n\times r} \tag{42}$$

$$\overline{f}(t) = W(t)\xi(t) \begin{bmatrix} \underline{0} \\ \underline{0} \\ 0 \\ -1 \end{bmatrix}_{(2n+2)\times 1} \tag{43}$$

The control force vector is therefore

$$U(t)_{r\times 1} = -\frac{1}{2}R^{-1}\overline{B}^{T}P(t)\,\overline{y}(t) \tag{44}$$

where $P(t)$ is a Riccati matrix satisfying

$$\Lambda_0^T P + P\Lambda_0 - 0.5P\overline{B}R^{-1}\overline{B}^{T}P + 2Q = 0 \tag{45}$$

$$P = \begin{bmatrix} \underline{P_{11}}_{2n\times 2n} & \underline{P_{12}}_{2n\times 2} \\ \underline{P_{21}}_{2\times 2n} & \underline{P_{22}}_{2\times 2} \end{bmatrix}_{(2n+2)\times(2n+2)} \tag{46}$$

$$Q = q\begin{bmatrix} \underline{I}_{n\times n} & \underline{0} \\ \underline{0} & \underline{0} \end{bmatrix}_{(2n+2)\times(2n+2)} \tag{47}$$

$$R = k\,\underline{I}_{r\times r} \tag{48}$$

According to Eq. (44), $U(t)$ can be expressed as a linear function of $\overline{y}(t)$:

$$U(t) = D\overline{y}(t) \tag{49}$$

where

$$D = \begin{bmatrix} \underline{G_1} & \underline{G_2} \end{bmatrix}_{r\times(2n+2)} \tag{50}$$

$$[G_1]_{r\times 2n} = -\frac{1}{2}R^{-1}\overline{B}^{T}P_{11} \tag{51}$$

$$[G_2]_{r\times 2} = -\frac{1}{2}R^{-1}\overline{B}^{T}P_{12} \tag{52}$$

With the aim of deriving a compact formulation of the controlled system, equation (49) can be written as

$$U(t) = \overline{D}y(t) \tag{53}$$

with

$$\overline{D} = \begin{bmatrix} \underline{G_1} & \underline{0} & \underline{G_2} \end{bmatrix}_{r\times(3n+2)} \tag{54}$$

so that upon replacement we have

$$\dot{y}(t) = [A_e(t) + B\overline{D}]y(t) + f(t) \tag{55}$$

Thus, the linearization matrix for the controlled case, A_{ec}, is defined as

$$A_{ec}(t) = A_e(t) + B\overline{D} \tag{56}$$

Finally, Eq. (55) becomes

$$\dot{y}(t) = A_{ec}(t)y(t) + f(t) \tag{57}$$

and the covariance evolution of the controlled system is

$$\dot{\Sigma}(t) = A_{ec}(t)\Sigma(t) + \Sigma(t)A_{ec}^{T}(t) + 2\pi S_f(t) \tag{58}$$

A drawback of the LQR control strategy is the arbitrariness of the selection of matrices Q and R. Taking into consideration the high randomness of earthquake forces and the high cost of active structural control, such an arbitrariness is obviously a matter of concern. this suggest applying an optimization approach to select values. A method for performing this step is summarized in the next section.

4 Artificial life optimization

In recent years several optimization techniques inspired in biological processes have been proposed. This comprises genetic algorithms, evolution strategies, ant-colony optimization, particle swarm optimization and others. In the research reported herein the last method has been adopted, as limited research indicates it presents advantages over other methods.

Particle swarm optimization (PSO) (Kennedy and Eberhart 2001) is based on the observation that flocks of birds, schools of fishes and other population swarms are capable of finding optimum locations upon relying on their distributed intelligence. Accordingly, the optimization algorithm is not based on the Darwinian ideas on evolution, as in genetic or evolution strategies, but on the social behavior of the species. Some applications of this technique in structural engineering have been reported (Elegbede 2005; Hurtado 2006; Fourie and Groenwold 2002).

The essential idea of the algorithm is as follows: Given a population of individuals randomly distributed, the population displaces over the search space keeping in mind the best situation ever found by the population and the best current position found by any member of it. Each individual i moves from the current position in step k to that in step $k+1$, in the dimension d of the search space, according to

$$X(i,d,k+1) = X(i,d,k) + V(i,d,k) \tag{59}$$

where $V(i,d,k)$ is the so-called velocity, which changes as follows:

$$\begin{aligned} V(i,d,k+1) = \chi[&wV(i,d,k) + c_1U_1(B(i,d) - X(i,d,k)) \\ &+ c_2U_2(G(d) - X(i,d,k))] \end{aligned} \tag{60}$$

where $B(i,d)$ is the best position of particle i, along dimension d, in the entire history of the search; $G(d)$ is the best historical position of the group in dimension d; c_1 and c_2 are the so-called social and cognitive parameters, U_1 and U_2 are random variables

uniformly distributed in $[0, 1]$, χ is a parameter controlling the velocity for assuring convergence and w is a parameter of inertia, controlling the effect of previous over updated velocities. Figure 3 illustrate the vectorial composition of the iteration for each particle. The algorithm for unconstrained optimization is as follows:

Initialization:

Set $k = 0$;
for $i = 1 : N$
  Set $\bar{C}(i, k) \Rightarrow \infty$
  for $d = 1 : M$
    Generate random position $X(i, d, k)$
  end
end
while $k \leq K$
  for $i = 1 : N$
    Calculate particle's cost $C(i, k)$
    $\bar{C}(i, k) \Leftarrow \min(\bar{C}(i, k), C(i, k))$
  end

  Find best particle's position and best current global position:

  $$l(i) = \arg\min_{\forall j: j=1:k} \left[\bar{C}(i, k)\right]$$
  $$g = \arg\min_{i} \left[\bar{C}(i, k)\right]$$
  for $d = 1 : M$
    $B(i, d) = X(l(i), d, k)$
    $G(d) = X(g, d, k)$
  end

  Calculate new positions:

  for $i = 1 : N$
    for $d = 1 : M$
      $$V(i, d, k+1) \Leftarrow \chi\left[wV(i, d, k) + c_1 U_1(B(i, d) - X(i, d, k)) + c_2 U_2(G(d) - X(i, d, k))\right]$$
      $$X(i, d, k+1) \Leftarrow X(i, d, k) + V(i, d, k)$$
    end
  end
end

Select best solution from end iteration:

$$b = \arg\min_{i} \left[\bar{C}(i, K)\right]$$
Return $X(b, d, K), d = 1 : M$

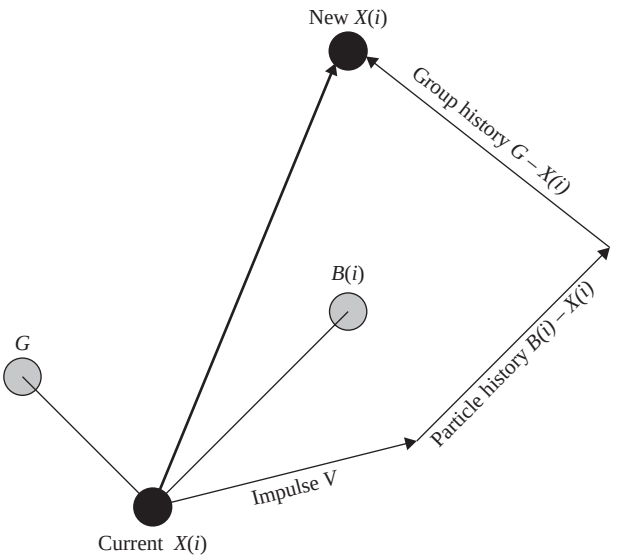

Figure 3 Elements of Particle Swarm step.

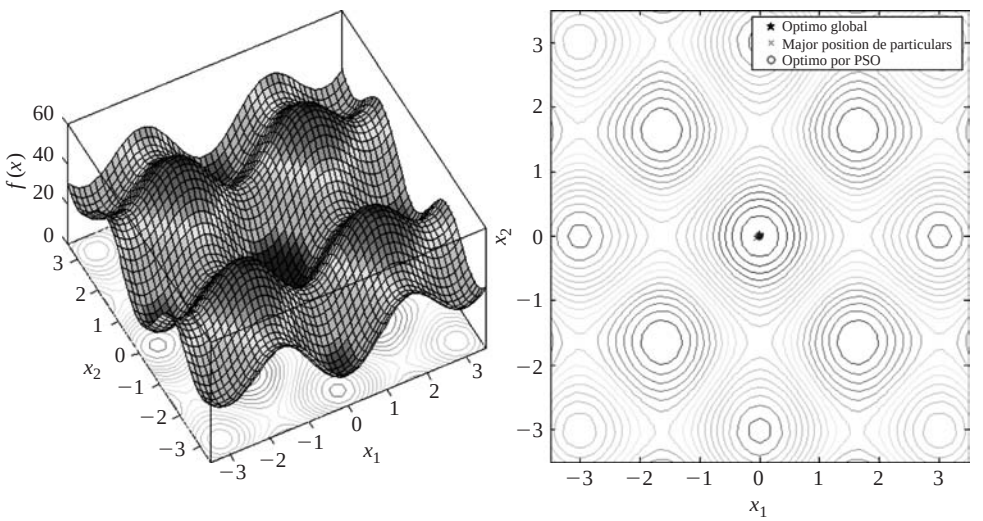

Figure 4 Minimization of eggcrate function using PSO.

The algorithm can be modified to include penalizations for excessive velocities and other effects (Parsopoulos and Vrahatis 2001). As an illustration of the application of the PSO algorithm figure 4 shows the so-called eggcrate function, given by

$$f(x_1, x_2) = x_1^2 + x_2^2 + 25(\sin^2 x_1 + \sin^2 x_2) \tag{61}$$

Notice that the function exhibits many local minima besides the global minimum located at (0,0). The PSO parameters are as follows: $c_1 = c_2 = 1.5$ and $\chi = 0.7$. The inertia parameter w was linearly adjusted from 1.5 to 0.5 along $K = 25$ steps. To do this use was made of $N = 10$ particles. The right panel of the figure shows that the global minimum was successfully found by the algorithm without being trapped in local minima.

4.1 *Application example*

The above methods have been combined to solve the following robust optimization problem of a one-story building:

Find the weighting matrices for the control force and displacement such that the standard deviation of the control force is a minimum subject to the standard deviation of the displacement of the first floor in the controlled case (CC) be less than 80% of the same value in the non-controlled case (NCC). Formally,

$$\textit{Find } Q \textit{ and } R \textit{ such that } \sigma_u \Rightarrow \textit{minimum subject to } \sigma_{x_{CC}} \leq 0.8\sigma_{x_{NCC}}$$

The search space has been defined as (800, 1,500) and (0.001, 0.009) for Q and R, respectively. The parameters used are as follows:

- Particle swarm algorithm parameters: $c_1 = 2.0$ $c_2 = 2.0$.
- Bouc-Wen model parameters: $\alpha = 0$ $\beta = 0.5$ $\gamma = 0.5$ $A = 1$ $n = 1$.
- Structural parameters: $m = 5$ Ton $k = 250$ KN/m $c = 2$ KNs/m $c_d = 3$ KNs/m.
- The evolutionary power spectral density function was modeled as a Kanai-Tajimi filter with a Shinozuka-Sato (Shinozuka and Sato 1967) modulating function.

The trial population was composed by 20 individuals and the number of steps of the PSO algorithm was set to 50. The best solution obtained is:

$$0.0083 \leq R \leq 0.0085$$
$$830 \leq Q \leq 840$$

5 Stochastic model uncertainties

5.1 *Discussion*

In order to assure the robustness of the structural system under the action of earthquake loads it is not sufficient to use a stochastic model of the ground motion as done in the preceding. This is due to the fact that some of the parameters defining the model are highly random. Therefore, in order to correctly estimate the statistical moments of the response it is necessary to incorporate such a randomness in a satisfactory manner. The relevance of this consideration is illustrated in Figure 5. In this section a discussion on the practical ways of performing this extension for assuring structural robustness under random dynamic loads by means of the methods exposed in the preceding is presented.

Table 1 shows the stochastic definition of the parameters ω_g and ν_g defining the Kanai-Tajimi random model used in the preceding, after the survey reported in (Vanmarcke and Lai 1980; Lai 1982). On the other hand the table also includes a

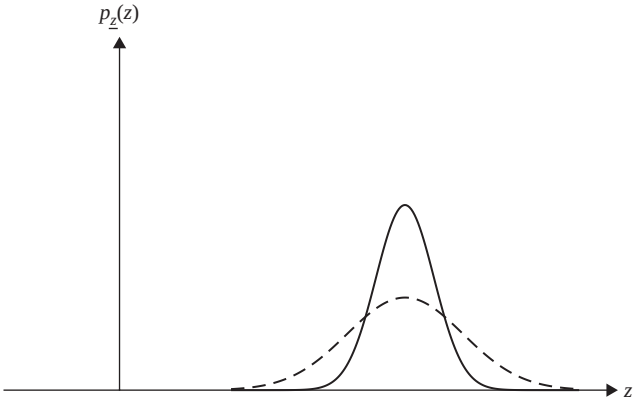

Figure 5 On the consideration of stochastic model uncertainties. The solid and dashed lines respectively represent the probability density function of the response of the system with and without them.

Table 1 Probabilistic definition of independent spectral random variables.

Parameter	*Distribution*	*Mean*	*c.o.v.*
ω_g	Gamma	20.3 rad/s	0.448
ν_g	Lognormal	0.32	0.421
A_g	Lognormal	—	0.6

probabilistic model for the peak ground acceleration A_g having a 10% probability of being exceeded in 50 years, which is modeled as a Lognormal variable with a coefficient of variation of 0.6, according to (Ahmed et al. 1996). Note, however, that there is a proposal suggesting that the parameter has an even larger spread, i.e. in the range from 0.56 to 1.38 (Bertero and Bertero 2002). (The mean value of A_g depends on the seismicity of the region under consideration).

Upon this basis it is possible to derive the probabilistic model for the white noise intensity G_0 needed in Eq. (32), by means of the expression (Moayyad and Mohraz 1982; Sues et al. 1985)

$$G_0 = 2\left(\frac{A_g}{28.4}\right)^2 \tag{62}$$

According to the information given in (Lai 1982), the correlation among all these variables is close to zero, so that the covariance matrix can be taken as diagonal. Notice that the three variables have very large spread. This imposes a discussion on the methods for incorporating this information into the evaluation of the robustness, as follows:

- *Perturbation methods* In first place one could apply perturbation approaches which are based on the Taylor expansion of the response vector $y(t)$. Considering

it a function of the vector of parameters $\theta = \{\omega_g, \nu_g, A_g\}$, the first order expansion for the covariance response yields (Socha 1986; Sues et al. 1985)

$$\frac{\partial \dot{\Sigma}(t)}{\partial \theta} = \frac{\partial A(t)}{\partial \theta}\Sigma(t) + A(t)\frac{\partial \Sigma(t)}{\partial \theta} + \frac{\partial \Sigma(t)}{\partial \theta}A^T(t) + \Sigma(t)\frac{\partial A^T(t)}{\partial \theta} + 2\pi\frac{\partial S_f(t)}{\partial \theta} \quad (63)$$

The matrix $\partial\Sigma(t)/\partial\theta$ contains the sensitivities of the second order responses with respect to the seismic parameters, with which the increase of the statistical moments due to the parameters' spread can be estimated. However, perturbation methods in general are accurate only for parameters having a coefficient of variation of, say, less than 0.1. Since all the seismic parameters considered herein have a much larger spread, this technique should be discarded.

- *Monte Carlo simulation*. Considering the difficulties in applying the perturbation method when the vector of parameters has large spreads as in the present case, it seems necessary to consider the possibility of using Monte Carlo simulation by solving repeatedly Eq. (30) using a random realization of vector θ in each analysis and then computing the average of the variances and covariances of the structural responses. To this end the use of techniques oriented to lower moment estimation with a small number of samples, such as the Latin Hypercube sampling (Florian 1992), seems to be only amenable Monte Carlo solution to the problem in hand.
- *Point estimate method*. This method was originally proposed in (Rosenblueth 1975) and has been applied in several areas of structural engineering research (Zhao et al. 1999; Hurtado 2007). Its main difference with respect to the perturbation approach is that it is intended to cancel the higher order terms in the Taylor expansion instead of disregarding them. There are several proposals for applying this concept (Rosenblueth 1975; Ordaz 1988; Christian and Baecher 1998; Harr 1989; Hong 1998). In this section the simplest variant proposed in (Hong 1998) will be evaluated.

For uncorrelated parameters, which is the case considered herein, the method postulates a linear equation for the moments of the system response $g(\theta)$, regarded as a function of each parameter θ, in the form

$$\mathrm{E}[g^j(\theta)] = \sum_{k=1}^{n}\sum_{i=1}^{m} w_{k,i}\, g(\theta_{k,i})^j \quad j = 1, 2, \ldots \quad (64)$$

in which n is the number of variables and m is the number of concentration points. The function $g(\cdot)$ is evaluated at points $\theta_{k,i} = \mu_\theta + \xi_{k,i}\sigma_\theta, i = 1, 2$, where μ_θ and σ_θ are respectively the mean and standard deviation of the random parameters. For each variable k the values of the weights w_i and the normalized evaluation coordinates ξ_i are (Hong 1998)

$$\xi_i = \frac{\gamma_3}{2} + (-1)^{3-i}\sqrt{n + \left(\frac{\gamma_3}{2}\right)^2}$$
$$w_i = \frac{1}{n}(-1)^i \frac{\xi_{3-i}}{\zeta} \quad (65)$$

Table 2 Values for the application of the Point Estimate method with stochastic Kanai-Tajimi spectrum.

Parameter	θ_1	w_1	θ_2	w_2
ω_g	8.1852	0.2079	40.2275	0.1254
ν_g	0.1601	0.2266	0.6596	0.1067
A_g	0.1006 g	0.2505	0.7018 g	0.0828

with $\zeta = 2\sqrt{n + \gamma_3^2/4}$. Here γ_l is a normalized central moment defined as

$$\gamma_l = \frac{1}{\sigma^l} \int_{-\infty}^{\infty} (x - \mu)^l \, p(\theta) \, \mathrm{d}\theta \tag{66}$$

where $p(\theta)$, μ and σ are respectively the probability density function, the mean and the standard deviation of the variable.

In order to evaluate the accuracy of this approach, the method has been applied to a simple random vibration problem, namely the estimation of the spectrum standard deviation of the displacement of a SDOF linear system with damping ratio $\xi = 0.05$. To this end use is made of the total probability theorem, applied to estimate the unconditional variance of the structural displacement $d(\theta)$, considered as a function of the ground motion parameters $\theta = \{\omega_g, \nu_g, A_g\}$, as follows:

$$\mathrm{Var}(d) = \int \int \mathrm{Var}(d(\theta)|\theta) \, p(\theta) \, \mathrm{d}\theta \tag{67}$$

where $\mathrm{Var}(d(\theta)|\theta)$ is obtained by means of the theory of random vibration as (Clough and Penzien 1993)

$$\mathrm{Var}(d(\theta)|\theta) = \int \frac{1}{(\omega^2 - \Omega^2)^2 + 4\xi^2\Omega^2\omega^2} \cdot G(\Omega, \theta) \, \mathrm{d}\Omega \tag{68}$$

where $G(\Omega, \theta)$ is the power spectral density of the Kanai-Tajimi seismic model:

$$G(\Omega, \theta) = \frac{\omega_g^4 + 4\nu_g^2\omega_g^2\Omega^2}{(\omega_g^2 - \Omega^2)^2 + 4\nu_g^2\omega_g^2\Omega^2} G_0 \tag{69}$$

Taking into account that the mean of the random displacement is zero, the unconditional variance of the response, given by Eq. (67), is estimated with the point estimate technique as

$$\mathrm{Var}(d) = \sum_{k=1}^{n} \sum_{i=1}^{m} w_{k,i} \mathrm{Var} d(\theta_{k,i}) \tag{70}$$

using the probabilistic definition of the parameters θ displayed in Table 1. For the parameter A_g a mean value equal to 0.25 g has been employed. The concentration points and weights are as shown in Table 2.

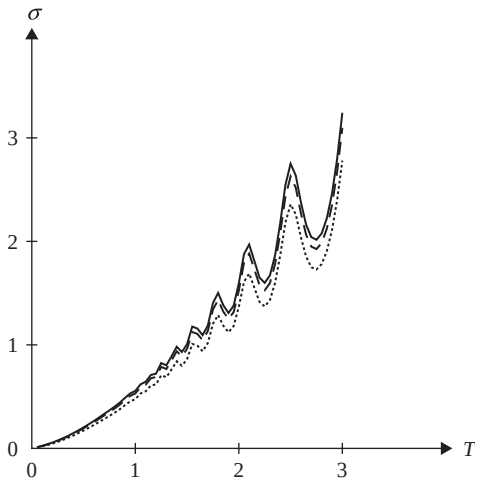

Figure 6 On the accuracy of the Point Estimate technique for calculating the spectrum of the unconditional standard deviation of SDOF displacement. Solid line: Point Estimate method. Dashed line: Monte Carlo simulation (1,000 samples). The dotted line corresponds to the standard deviation without considering uncertainties in the Kanai-Tajimi model and using the mean values of the parameters.

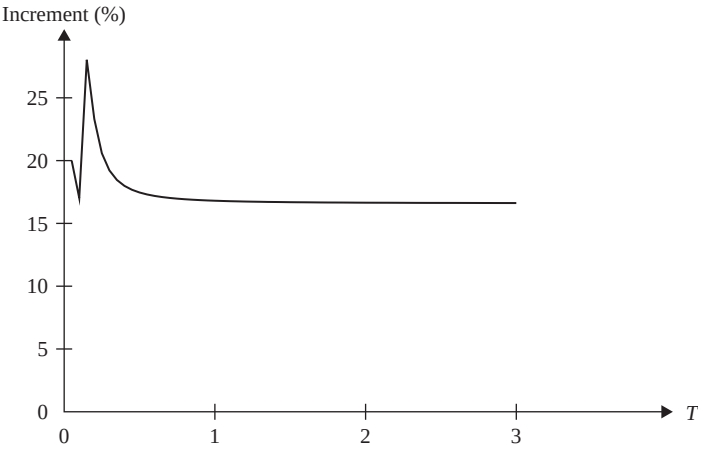

Figure 7 Spectrum of the increment of the standard deviation of the SDOF displacement when considering the uncertainties of the Kanai-Tajimi model parameters.

The results are shown in Fig. 6. Notice that with only six calculation of the SDOF system per period, the results are in excellent agreement with the estimation yielded by Monte Carlo simulation obtained as the average of 1,000 calls of Eq. (68) for each period. The figure also displays the spectrum of the standard deviation without considering the uncertainties of the model parameters. The effect of such a consideration can be better appreciated in Fig. 7, which corresponds to the increment of the standard deviation using the uncertain stochastic model with respect to its use with

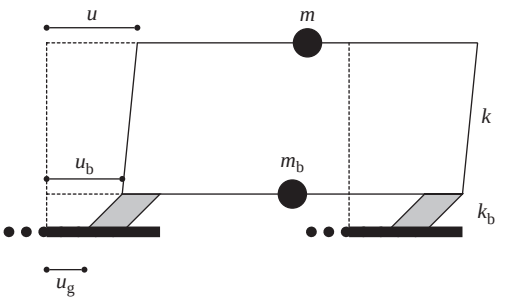

Figure 8 Base isolated building model.

mean values. It can be observed that the impact of the uncertainties is more important at lower periods than at larger ones, for which the increment stabilizes at about 17%. This result points out the relevance of using a full stochastic model for structural robustness computations under earthquake loads.

The above discussion suggests that the Point Estimate method in the version reported in (Hong 1998) constitutes an excellent means to evaluate the unconditional structural robustness in Earthquake Engineering, with or without active control.

5.2 *Application to passive vibration control*

The method presented above is now applied to a passive control of seismic vibrations using base isolation with steel-rubber bearings. Consider the two-floor base isolated building depicted in Figure 8. For the ground, base and structure absolute displacements illustrated in the figure, the relative displacements are

$$\begin{aligned} v_s &= u - u_b \\ v_b &= u_b - u_g \end{aligned} \tag{71}$$

Using these degrees of freedom, the equations of motion are (Kelly 1993)

$$\boldsymbol{M}\ddot{\boldsymbol{v}} + \boldsymbol{C}\dot{\boldsymbol{v}} + \boldsymbol{K}\boldsymbol{v} = -\boldsymbol{M}\boldsymbol{r}\ddot{u}_g \tag{72}$$

with

$$\boldsymbol{M} = \begin{pmatrix} m + m_b & m \\ m & m \end{pmatrix}, \quad \boldsymbol{C} = \begin{pmatrix} c_b & 0 \\ 0 & c \end{pmatrix}, \quad \boldsymbol{K} = \begin{pmatrix} k_b & 0 \\ 0 & k \end{pmatrix}, \quad \boldsymbol{v} = \begin{pmatrix} v_b \\ v_b \end{pmatrix} \quad \boldsymbol{r} = \begin{pmatrix} 1 \\ 0 \end{pmatrix} \tag{73}$$

Here m is the floor mass, m_b, c_b, k_b the base mass, damping and stiffness constants and $\ddot{u}_g$ the horizontal ground acceleration. The damping coefficients and frequencies for base and structural subsystems are given by

$$\omega_s^2 = \frac{k}{m}, \quad \omega_b^2 = \frac{k_b}{m + m_b}, \quad \nu_s = \frac{c}{2m\omega_s}, \quad \nu_b = \frac{c}{2(m + m_b)\omega_b} \tag{74}$$

The first order approximation for the mode shapes is (Kelly 1993)

$$\boldsymbol{\phi}_1 = \begin{pmatrix} 1 \\ \epsilon \end{pmatrix}, \quad \boldsymbol{\phi}_2 = \begin{pmatrix} 1 \\ -\frac{1}{\gamma}(1-\epsilon(1-\gamma)) \end{pmatrix} \tag{75}$$

where

$$\epsilon = \frac{\omega_{\mathrm{b}}^2}{\omega_{\mathrm{s}}^2}, \quad \gamma = \frac{m}{m+m_{\mathrm{b}}} \tag{76}$$

Finally the SRSS estimates of standard deviation of the base and structure relative displacements are

$$\begin{aligned} \sigma_{\nu_{\mathrm{s}}} &= \sqrt{\phi_{1,\mathrm{s}}^2\sigma_1^2 + \phi_{2,\mathrm{s}}^2\sigma_2^2} \\ \sigma_{\nu_{\mathrm{b}}} &= \sqrt{\phi_{1,\mathrm{b}}^2\sigma_1^2 + \phi_{2,\mathrm{b}}^2\sigma_2^2} \end{aligned} \tag{77}$$

where σ_1, σ_2 are respectively the standard deviations of the displacements of the SDOF systems associated to the first and second eigenfrequencies, given by

$$\begin{aligned} \sigma_1 &= L_1\,\sigma(\omega_{\mathrm{b}}', \nu_{\mathrm{b}}') \\ \sigma_2 &= L_2\,\sigma(\omega_{\mathrm{s}}', \nu_{\mathrm{s}}'), \end{aligned} \tag{78}$$

in which the $L_i, i = 1, 2$ are the modal participation factors. Their expressions, together with those of the rest of parameters are as follows.

$$L_1 = 1 - \gamma\epsilon, \qquad L_2 = \gamma\epsilon$$

$$\omega_{\mathrm{b}}' = \omega_{\mathrm{b}}\sqrt{1-\gamma\epsilon}, \qquad \omega_{\mathrm{s}}' = \omega_{\mathrm{s}}\sqrt{\frac{1+\gamma\epsilon}{1-\gamma}} \tag{79}$$

$$\nu_{\mathrm{b}}' = \nu_{\mathrm{b}}\,(1-1.5\gamma\epsilon), \quad \nu_{\mathrm{s}}' = \left(\frac{\nu_{\mathrm{s}}}{\sqrt{1-\gamma}} + \frac{\gamma\nu_{\mathrm{b}}\sqrt{\epsilon}}{\sqrt{1-\gamma}}\right)(1-1.5\gamma\epsilon) \tag{80}$$

Finally, $\sigma(\cdot,\cdot)$ in Eq. (78) is a generic function for the standard deviation of the displacement of a SDOF linear system given (Vanmarcke 1976)

$$\sigma(\omega, \nu) = \left(\frac{1}{\omega^4}\left[\omega G(\omega)\left(\frac{\pi}{4\nu_{\mathrm{s}}} - 1\right) + \int_0^{\omega} G(\Omega)\,\mathrm{d}\Omega\right]\right)^{\frac{1}{2}} \tag{81}$$

where the parameter ν_{s} is a fictitious time dependent damping introduced to consider the transient nature of the response into the stationary random vibration equations for the moments of the response, such as that given by Eq. (68). Its expression is

$$\nu_{\mathrm{s}} = \frac{\nu}{1 - \exp(-2\nu\omega s)} \tag{82}$$

where s is the duration of the strong motion phase of the earthquake, for which the following regression will be applied (Vanmarcke and Lai 1980; Lai 1982):

$$s = 30\exp(-3.254A_g^{0.35}) \tag{83}$$

This problem was solved using the Point Estimate technique with the following set of values (after (Kelly 1993)): $m = 100$ t, $m_b = 66$ t, $\omega_s = 5\pi$ rad/s, $\omega_b = \pi$ rad/s, $\nu_s = 0.02$, $\nu_b = 0.1$. For the peak ground acceleration A_g a mean value equal to 0.25g was employed. The results for the standard deviation of the base and structural displacements are $\sigma_{\nu_b} = 0.0676$ m and $\sigma_{\nu_b} = 0.0135$ m. The solution required only six deterministic calculations of the displacement responses. Finally, the standard deviations of these displacements without regard to parameter uncertainties and using their mean values were found to be 0.0614 m and 0.0123 m, respectively. For both cases the error in omitting the uncertainties in model parameters is 10.2%.

6 Conclusions

- The large uncertainties present in earthquake engineering and the nonlinear behavior imposed by the high intensity of seismic motions demand efforts to develop practical methods that allow reducing the uncertainty about random responses, while keeping them computationally feasible.
- The difficulty in obtaining accurate values of the failure probabilities complicates the application of the reliability-based optimization approaches. A convenient alternative is the robust optimization approach, based on second order statistical information.
- The second-order quantities needed by robust optimization can be obtained with the method of stochastic equivalent linearization, which is the only nonlinear random vibration technique useful for large structures. To this end it is necessary to apply non Gaussian approaches due to the saturation of the restoring forces about the strength values of hysteretic oscillators.
- The application proposed herein is useful for selecting the otherwise arbitrary parameters in designing an active structural control strategy.
- In order to cope with the large uncertainty of the parameters involved in the stochastic description of the seismic ground motion, it is necessary to evaluate the unconditional statistical moments. To this end the method of Point Estimates is a very good alternative. Its use has been demonstrated in a passive control case.

References

Ahmed, K.A., Kanda, J. & Iwasaki, R. 1996. Estimation of uncertainties in the dynamic response of urban soils in japan. In *Proceedings of the Eleventh World Conference on Earthquake Engineering*, Rotterdam. Elsevier Science.

Bertero, R.D. & Bertero, V.V. 2002. Performance-based seismic engineering: the need for a reliable conceptual comprehensive approach. *Earthquake Engineering and Structural Dynamics 31*, 627 – 652.

Beyer, H.G. & Sendhoff, B. 2007. Robust Optimization. A comprehensive survey. Computer *Methods in Applied Mechanics and Engineering doi: 10.1016/j.cma.2007.03.003*.

Casciati, F. & Faravelli, L. 1991. *Fragility Analysis of Complex Structural Systems*. Taunton: Research Studies Press Ltd.

Christian, J.T. & Baecher, G.B. 1998. Point-estimate method and numerical quadrature. *Journal of Geotechnical and Geoenvironmental Engineering 125*, 779–786.

Clough, R.W. & Penzien, J. 1993. *Dynamics of Structures*. New York: McGraw-Hill.

Doltsinis, I. & Kang, Z. 2004. Robust design of structures using optimization methods. *Computer Methods in Applied Mechanics Engineering 193*, 2221–37.

Doltsinis, I., Kang, A. & Cheng, G. 2005. Robust design of non-linear structures using optimization methods. *Computer Methods in Applied Mechanics and Engineering 194*, 1779–1795.

Elegbede, C. 2005. Structural reliability assessment based on particle swarm optimization. *Structural Safety* 27, 171–186.

Florian, A. 1992. An efficient sampling scheme: Updated Latin Hypercube Sampling. *Probabilistic Engineering Mechanics* 7, 123–130.

Fourie, P.C. & Groenwold, A.A. 2002. The particle swarm optimization algorithm in size and shape optimization. *Structural and Multidisciplinary Optimization 23*, 259–267.

Frangopol, D. 1995. Reliability-based structural design. In C. R. Sundararajan (Ed.), *Probabilistic Structural Mechanics Handbook*, pp. 352–387. New York: Chapman & Hall.

Gasser, M. & Schueller, G.I. 1997. Reliability-based optimization of structural systems. *Mathematical Methods of Operations Research 46*, 287–307.

Harr, M. 1989. Probabilistic estimates for multivariate analysis. *Applied Mathematical Modelling 13*, 313 – 318.

Hong, H.P. 1998. An efficient point estimate method for probabilistic analysis. *Reliability Engineering and System Safety 59*, 261–267.

Hurtado, J.E. 2004. *Structural Reliability. Statistical Learning Perspectives*. Heidelberg: Springer.

Hurtado, J.E. 2006. Optimal reliability-based design using support vector machines and artificial life algorithms. In Y. Tsompanakis and N. D. Lagaros (Eds.), *Intelligent Computational Paradigms in Earthquake Engineering*. Hershey: Idea Group Inc.

Hurtado, J.E. 2007. Structural robustness and its relationship to reliability. In Y. Tsompanakis, N. D. Lagaros, and M. Papadrakakis (Eds.), *Structural Design Optimization Considering Uncertainties*. Leiden: Taylor and Francis.

Hurtado, J.E. & Barbat, A. 1996. Improved stochastic linearization method using mixed distributions. *Structural Safety 18*, 49–62.

Hurtado, J.E. & Barbat, A. 2000. Equivalent linearization of the Bouc-Wen hysteretic model. *Engineering Structures* 20, 1121–1132.

Kelly, J.M. 1993. *Earthquake-Resistance Design with Rubber*. London: Springer-Verlag.

Kennedy, J. & Eberhart, R.C. 2001. *Swarm Intelligence*. San Francisco: Morgan Kaufmann.

Lai, S.P. 1982. Statistical characterization of strong ground motions using power spectral density function. *Bulletin of the Seismological Society of America 72*, 259–274.

Melchers, R.E. 1999. *Structural Reliability: Analysis and Prediction*. Chichester: John Wiley and Sons.

Moayyad, P. & Mohraz, B. 1982. A study of power spectral density of earthquake accelerograms. Technical report, Civil and Mechanical Engineering Department, Southern Methodist University, Dallas, TX.

Ordaz, M. 1988. On the use of probability concentrations. *Structural Safety 5*, 317–318.

Parsopoulos, K.E. & Vrahatis, M.N. 2001. Particle swarm optimization method for constrained optimization problems. Technical report, Department of Mathematics, University of Patras, Greece.

Roberts, J.B. & Spanos, P.D. 1990. *Random Vibration and Statistical Linearization*. Chichester: John Wiley and Sons.

Rosenblueth, E. 1975. Point estimates for probability moments. *Proceedings of the National Academy of Sciences of the USA 72*, 3812–3814.

Rosenblueth, E. & Mendoza, E. 1971. Reliability optimization in isostatic structures. *Journal of the Engineering Mechanics Division ASCE 97*, 1625–1640.

Royset, J.O., Kiureghian, A.D. & Polak, E. 2001. Reliability-based optimal structural design by the decoupling approach. *Reliability Engineering and System Safety 73*, 213–221.

Royset, J.O. & Polak, E. 2004. Reliability-based optimal design using sample average approximations. *Probabilistic Engineering Mechanics 19*, 331–343.

Schenk, C.A. & Schuëller, G.I. 2005. *Uncertainty Assessment of Large Finite Element Systems*. Berlin: Springer.

Shinozuka, M. & Sato, Y. 1967. Simulation of nonstationary random processes. *Journal of Engineering Mechanics 93*, 11–40.

Socha, L. 1986. The sensitivity analysis of stochastic non-linear dynamical systems. *Journal of Sound and Vibration 110*, 271–288.

Soong, T.T. 1990. *Active Structural Control: Theory and Practice*. Avon: Longman Scientific, Technical.

Sues, R.H., Wen, Y.K. & Ang, A.H.S. 1985. Stochastic evaluation of seismic structural performance. *Journal of Structural Engineering 111*, 1204–1218.

Vanmarcke, E. 1976. Structural response to earthquakes. In C. Lomnitz and E. Rosenblueth (Eds.), *Seismic Risk and Engineering Decisions*, pp. 287–337. Amsterdam: Elsevier.

Vanmarcke, E.H. & Lai, S.P. 1980. Strong-motion duration and rms amplitude of earthquake records. *Bulletin of the Seismological Society of America 70*, 1293–1307.

Wen, Y.K. 1976. Method for random vibration of hysteretic systems. *Journal of the Engineering Mechanics Division 102*, 248–262.

Zang, C., Friswell, M.I. & Mottershed, J.E. 2005. A review of robust optimal design and its application in dynamics. *Computers and Structures 83*, 315–326.

Zhao, Y.G., Ono, T. & Idota, H. 1999. Response uncertainty and time-variant reliability analysis for hysteretic MDF structures. *Earthquake Engineering and Structural Dynamics 28*, 1187–1213.

Chapter 33

A multi-objective robust criterion for tuned mass dampers optimal design

Giuseppe Carlo Marano, Rita Greco & Sara Sgobba

Technical University of Bari, Taranto, Italy

ABSTRACT: This work proposes a robust optimization criterion of mechanical parameters in the design of linear Tuned Mass Dampers (TMD) located at the top of a main structural system subject to random base accelerations. The dynamic input is modelled as a stationary filtered white noise random process. The aim is to properly consider non-uniform spectral contents that happen in many real physical vibration phenomena. The main structural system is described as a single linear degree of freedom, and it is assumed that uncertainty affects the system model. The problem parameters treated are described as random uncorrelated variables known only by the estimation of their means and variances. Robustness is formulated as a multi-objective optimization problem in which both the mean and variance of a conventional objective function (OF) are minimized simultaneously. Optimal Pareto fronts are obtained and results show a significant improvement in performance stability compared to a standard conventional solution.

1 Introduction

Engineers, physicists and, in general, scientists dealing with real phenomena usually have to deal with uncertainty which often raises serious theoretical and computational difficulties. With the aim of reducing these complications that frequently make many problems irresolvable, standard methods have been developed in structural analysis assuming implicitly that all involved parameters are deterministically known. This remains is an oversimplification of real conditions because parameters are only partially known. Due to economical and technical reasons, only few problem parameter measurements are available if not simply intrinsically uncertain. The uncertainty of structural problems may afflict many involved factors, such as dynamic loads intensity, material mechanical parameters and geometrical configurations, all commonly considered as deterministic in standard analysis.

In some structural dynamics problems, a widely used simplified approach consists in the assumption that loads are considered to be the only source of uncertainty. For example, earthquake or wind actions are modelled as stochastic processes and the standard random vibration theory is used assuming that all other parameters are deterministically defined. Structural response is a stochastic process whose parameters are deterministic (Lutes & Sarkani, 2002). In such a case it is possible to define the "conventional" (with reference to deterministic optimization) OF and restraints concerning the structural response processes or related quantities. This structural design approach

can be defined as "Single Objective Conventional Optimization" (SOCO) and its solution can be obtained by standard numerical methods. Assuming that uncertainties in structural systems have negligible effects on response may prove an unrealistic oversimplification in many real problems. On the contrary, it is reported that structural system parameters uncertainty may have equal or greater influence on response than uncertainty would in case of excitations (Igusa & Der Kiurghian, 1988). This could be particularly significant where the solution is strongly influenced by system parameters variation as in the case of structural optimization. Thus, system parameters must be treated with a suitable description of uncertainty which affects nominal values to obtain a more realistic analysis in optimization problems. Real structures in aeronautics, mechanical or civil engineering are often described by the random variable theory owing to various uncertain factors concerning materials, measurement, manufacturing and installation. For this reason, safe domain and input process parameters, which are parts of a power density spectrum, have to be treated as uncertainty quantities. This means that SOCO may not be achieved or may simply become unfeasible due to the scatter of structural behaviour. Therefore, it is reasonable to explore the effects of uncertainty on the design of structures subject to random vibrations.

In the last twenty years, various non-deterministic methods have been developed to deal with optimum design under environmental uncertainties. These methods can be classified into two main branches, namely reliability-based methods and robust-based methods. The reliability methods, based on the known probability distribution of the random parameters, estimate the probability distribution of the system's response, and are predominantly used for risk analysis by computing the probability of system failure. However, variation is not minimized in reliability approaches (Siddall, 1984) because they concentrate on rare events at the tail of the probability distribution (Doltsinis and Kang, 2004). The robust design methods are commonly based on multiobjective minimization problems. The are commonly indicated as "Multiple Objective Robust Optimization" (MORO) and find a set of optimal solutions that optimise a performance index in terms of mean value and, at the same time, minimize its resulting dispersion due to input parameters uncertainty. The final solution is less sensitive to the parameters variation but eventually maintains feasibility with regards probabilistic constraints. This is achieved by the optimization of the design vector in order to make the performance minimally sensitive to the various causes of variation.

Hence, robust design concentrates on the probability distribution near the mean values. A Structural Robust Design (SRD) solution cannot offer the best possible performance but a low sensitivity to uncertainty. Recently, a robust design of a vibration absorber, with mass and stiffness uncertainty included in the main system, was used to demonstrate the robust design approach in dynamics as proposed by Zang et al. (2005). The design is based on a frequency approach with the assumption that input is a band-limited white noise. Uncertainty is defined by mean and covariance, and concerns main system mass and damping. The maximum over a limited frequency band of the dimensionless displacement transfer function is used as a local performance index. The robust optimisation is obtained by minimizing deviation in mean and variance, through a direct first-order perturbation method based on a Taylor series expansion. A different reliability-robust optimization has also been proposed by Papadimitriou et al. (1997) where the failure probability, related to excessive main system displacement, is adopted as conventional OF.

A multi-objective optimization is performed by using the mean and variance of the main system frequency in order to produce robust optimal Pareto fronts. The mean and variance are evaluated by approximate asymptotic evaluation, and recently different applications were proposed in seismic engineering (Lagaros et al. 2006; Papadrakakis et al. 2004).

In this paper, a stochastic MORO is applied to a TMD, assuming that some structural parameters present an uncertain nature. Parameters are described in a random way, but assuming that they are known only by means and variances. The main structure, described by a single degree of freedom system, is protected by a linear single TMD against base accelerations that are modelled by a general second-order linear filtered white noise stationary process. The design vector collects the two parameters, TMD frequency and damping. The ratio between protected and unprotected standard deviation of the main system displacements is the dimensionless "conventional" OF. The robust optimum solution is obtained by using a multi-objective OF instead of a single conventional one. The mean and standard deviation of conventional OF are estimated by the direct perturbation method with the aim of defining an OF vector. The robust Pareto front in the mean-standard deviation space is obtained by using the NSGAII method (Srinivas & Deb, 1994). Finally, a comparison between SOCO and MORO optimal solutions is analysed for different uncertainty input configurations with some of the following conclusions.

2 Conventional TMD optimum design

A Tuned Mass Damper (TMD) is one of the simplest and the most reliable passive device for vibration control in a wide range of applications, and for this reason many optimization criteria have been proposed for this specific device. Essentially, a TMD consists in an additional mass connected to a main system by a spring and a damper. The main system, excited by a base acceleration, is modelled as a stochastic stationary coloured noise and introducing the global space state vector:

$$Z = (y_T \quad y_S \quad y_f \quad \dot{y}_T \quad \dot{y}_S \quad \dot{y}_f)^T \tag{1}$$

the space state covariance matrix $\boldsymbol{R}_{ZZ}$ becomes the solution of the Lyapunov equation

$$\boldsymbol{A}\boldsymbol{R}_{ZZ} + \boldsymbol{R}_{ZZ}\boldsymbol{A}^T + \boldsymbol{B} = 0 \tag{2}$$

where A is the 6×6 system matrix, and the 6×6 matrix **B** has all null elements except the last on the main diagonal that is $[\mathbf{B}]_{6,6} = 2\pi S_0$ (more details can be found in (Marano et al, 2007).

The system mechanical parameters involved are $\omega_T = \sqrt{(\boldsymbol{k}_T/\boldsymbol{m}_T)}$, $\omega_S = \sqrt{(\boldsymbol{k}_S/\boldsymbol{m}_S)}$, $\xi_T = (c_T/2\sqrt{\boldsymbol{m}_T\boldsymbol{k}_T})$, $\xi_S = (c_S/2\sqrt{m_S k_S})$, $\mu = \frac{m_T}{m_S}$, and S_0 is the Gaussian zero mean white noise process whose intensities, ω_f and ξ_g, are the base filter frequency and damping.

In a similar way, it is possible to obtain the unprotected main structural response covariance matrix $\mathbf{R}_{Z_0Z_0}$ where the space state vector is:

$$Z_0 = \{y_S \quad y_f \quad \dot{y}_S \quad \dot{y}_f\}^T \tag{3}$$

Moreover, previous formulation deals with the assumption that all structural parameters have a deterministic nature, but this is usually an unrealistic assumption if referred to many real cases. The optimization problem for a structure subject to random vibrations can be formulated as the search of a suitable set of variables (design parameters characterizing structural configurations), collected in the so-called *Design Vector* (DV) $\overline{b}$, over a possible admissible domain $\mathbf{\Omega}$. The optimal DV must be able to reduce the induced vibration below an acceptable level, minimizing a given OF (defined by using deterministic or statistic entities) and also satisfying particular constraints expressed in terms of structural reliability. Both reliability constraints and OF must be defined over a given time interval, as the problem regards dynamic structural response.

The conventional optimization problem so defined and first stated for systems subject to random vibrations (Nigam, 1972) can be transformed into a standard nonlinear programming one that is stated as:

$$\text{Find} \quad \overline{b} \in \Omega_b \tag{4}$$

$$\text{Minimize} \quad OF(\overline{b}, t) \tag{5}$$

$$\text{Eventually subject to} \quad g_i(\overline{b}, t) \leq 0 \quad (i = 1, 2, \ldots, k) \tag{6}$$

where the OF can be defined in a standard deterministic manner (total structural weight or elements volume) or stochastically. In the latter case, statistic entities can be used as covariance or spectral moments of the problem variables (for example, displacement, acceleration or structural stress in relevant elements). The optimal mechanical parameters of a TMD are represented by the two-dimensional design vector $\overline{b}$:

$$\overline{b} = (\omega_T, \xi_T)^T \tag{7}$$

having assigned a fixed mass ratio μ and the main system frequency ω_s.

The OF is thus defined in a dimensionless way as being the ratio between the standard deviation of the maximum displacement in the protected structure σ_{X_S} and the unprotected one $\sigma^0_{X_S}$:

$$OF = \frac{\sigma_{X_S}}{\sigma^0_{X_S}} \tag{8}$$

This function represents a direct stochastic *index of vibration protection efficiency* that shows protection effectiveness when its value is smaller than one. At the same time, a value of the OF close to the unit indicates practically negligible effects in vibration control (greater values are for negative TMD effects, increasing main structure displacements). The conventional optimum solution is performed assuming that all parameters involved in the problem are deterministic, and the unrestricted approaches of (6) and (7) are for this specific case:

$$\text{Find the design vector} \quad \overline{b} = (\omega_{TMD}, \xi_{TMD}) \in \Re^2_+ \tag{9}$$

$$\text{Minimize} \quad \frac{\sigma_{X_S}(\overline{b})}{\sigma^0_{X_S}} \tag{10}$$

This approach is able to furnish a global minimum value of OF in the DV space (Marano et al. 2007)

2.1 *Probabilistic characterization of uncertain system parameters*

There are many different ways to treat mathematically uncertainly, but the most common approach used is the probability analysis. It consists in assuming that each uncertain parameter is treated as a random variable characterised by standard probability distribution. This means that structural problems must be solved by knowing the multi-dimensional *Joint Probability Density Function* of all involved parameters. Nevertheless, this approach may offer serious analytical and numerical difficulties. It must also be noticed that it presents some conceptual limitations: the complete uncertainty parameters stochastic characterization presents a fundamental limitation related to the difficulty/impossibility of a complete statistical analysis. The approach cannot be considered economical or practical in many real situations, characterized by the absence of sufficient statistical data. In such cases, a commonly used simplification is assuming that all variables have independent normal or lognormal probability distributions, as an application of the limit central theorem which anyway does not overcome the previous problem. On the other hand the approach is quite usual in real situations where it is only possible to estimate the mean and variance of each uncertainty parameter it being not possible to have more information about their real probabilistic distribution. The case is treated assuming that all uncertainty parameters, collected in the vector $\overline{d}$, are characterised by a nominal mean value μ_{d_i} and a correlation $\gamma_{d_i} = \frac{\sigma_{d_i}}{\mu_{d_i}}$. In this specific case, the structural parameters assumed as uncertain are the main system frequency ω_S and damping ξ_S and the mass ratio η. Moreover, the two *filter parameters* ω_f and ξ_f are also assumed to be potentially afflicted by scatter, so that both are characterised by a variance greater than the nominal value. The uncertainty parameters vector $\overline{d}$ is composed by the following elements:

$$\overline{d} = (\omega_S, \xi_S, \eta, \omega_f, \xi_f)$$

Further in this paper, the mean value of each uncertainty element will be indicated by its nominal symbol $\mu_{d_i} = d_i$ for simplicity.

3 The multi-objective optimization problem

Assuming that some system parameters concern the mechanical problem stated before, a robust approach is more appropriate than a conventional one for TMD optimization. This means that the solution requires the minimization of two indices, performance efficiency and dispersion, instead of a single OF as applied in (10). This is a general topic of structural engineering, where often several objective functions (OFs) are in conflict and it is not possible to define a universally approved criterion of "optimum" as in the case of a single objective optimization problem. Therefore, in MOOP the aim is to produce a set of well compromised solutions from which the decision-maker selects one (Zang et all. 2005). Given that there situations are in contrast with each other, it is not possible to define a universally approved criteria of "optimum" as happens in standard single objective optimization. In fact, a definition is obtained by assuming that

optimization can be obtained when only one "efficiency" index is minimised and the others are considered as problem constraints. Moreover, the definition of the best index to be minimised and that of the indices to be transformed in constraints have no single criterion. The matter depends strongly on designer opinion and experience. On the contrary, the multi-objective optimization approach gives the designer the opportunity to evaluate a set of possible solutions, defined as those able to satisfy best and with different performances all the required efficiency indices defined by designers. The definitions of these solutions are usually known as the *Pareto dominance* and *Pareto optimality* criteria and are a fundamental point in the MOOPs. With reference to the Pareto optimality definition, it is assumed that a design vector $\mathbf{b}^*$ is Pareto optimal if no feasible vector $\mathbf{b}$ exists which could decrease some criterion without causing a simultaneous increase in at least one other criterion. Unfortunately, this concept almost always fails to give a single solution, but rather a set of solutions called the Pareto optimal set. The vectors $\mathbf{b}^*$ corresponding to the solutions included in the Pareto optimal set are called non-dominated. Generally, Pareto concepts ("*Pareto dominance*" and "*Pareto optimality*") constitute very important notions in MOOPs.

Without loss in generalities, a typical minimization-based MOOP is conduced. Given two candidate solution $\{\mathbf{d}_j, \mathbf{d}_k\}$, if:

$$\forall i \in \{1, \ldots, M\}, OF_i(\mathbf{d}_j) \leq OF_i(\mathbf{d}_k) \wedge \exists i \in \{1, \ldots, M\}: OF_i(\mathbf{d}_j) < OF_i(\mathbf{d}_k) \tag{11}$$

the two objective vectors are defined

$$\mathbf{v}(\mathbf{d}_j) = \{OF_1(\mathbf{d}_j), \ldots, OF_M(\mathbf{d}_j)\} \tag{12}$$

$$\mathbf{v}(\mathbf{d}_k) = \{OF_1(\mathbf{d}_k), \ldots, OF_M(\mathbf{d}_k)\} \tag{13}$$

vector $\mathbf{v}(\mathbf{d}_j)$ is said to dominate vector $\mathbf{v}(\mathbf{d}_k)$ (denoted by $\mathbf{v}(\mathbf{d}_j) \prec \mathbf{v}(\mathbf{d}_k)$).

Moreover, if no feasible solution ($\mathbf{v}(\mathbf{d}_k)$) exists that dominates solution $\mathbf{v}(\mathbf{d}_j)$, then $\mathbf{v}(\mathbf{d}_j)$ is classified as a *non-dominated* or *Pareto optimal solution*. More simply, $\overline{b}_j \in \mathbf{\Omega}_{\overline{b}}$ is a *Pareto optimal solution* if there exists no feasible vector $\overline{b}_k \in \mathbf{\Omega}_{\overline{b}}$ which could decrease some criterion without causing a simultaneous increase in at least one other criterion [26].The collection of all Pareto optimal solution are know as the *Pareto optimal set* or *Pareto efficient set*. Instead, the corresponding objective vectors are described as the *Pareto front* or *Trade-off surface*.

Normally, the decision about the "best solution" to be adopted is formulated by the so-called (human) *decision maker* (DM). Extremely rare is the case in which the DM doesn't have any role and a generic *Pareto optimal solution* is considered acceptable (*no–preference based methods*). On the other hand, several *preference–based methods* exist in literature, although this particular aspect of research tends to have been somewhat overlooked. A more general version of the *preference–based method* considers the preference information used to influence the search (Coello 2000). Thus, in *a priori methods*, the DM's preferences are incorporated before the search begins. Therefore, based on the DM's preferences, it is possible to avoid producing the whole *Pareto optimal set*. In *progressive methods*, the DM's preferences are incorporated during the search. This scheme offers the sure advantage of driving the search process, but the DM may be unsure of his/her preferences at the beginning of the procedure

and may be informed and influenced by information that becomes available during the search. A last class of method is *a posteriori*. In this case, the optimiser carries out the *Pareto optimal set* and the DM selects a solution ("search first and decide later"). Many researchers view this approach as standard so that, in many cases, a MOOP is considered resolved once all *Pareto optimal solutions* are individualized. For instance, an extremely diffused *a posteriori approach* is denominated as *Aggregating functions* in which multiple objectives are combined into a single one. A commonly adopted method is the *Weighetd Sum Method*. It consists in a single linear combination of individual objectives and a scalar parameter (so-called weighting coefficient) is used with different values in order to define the *Pareto front*. This method, as well as other Aggregating function techniques, are not efficient for MOOPs because they are not able to find multiple solutions in a single run and multiple runs do not guarantee the definition of the true Pareto front (Kicinger, 2005). Moreover, in the category of *a posteriori approaches*, *Evolutionary Multi-Objective Optimization* is commonly used. In Luh & Chuen (2004), an algorithm for finding constrained Pareto-optimal solutions based on the characteristics of a biological immune system (Constrained Multi-Objective Immune Algorithm, CMOIA) is proposed. In the field of EMOO, the most adopted algorithms are the Multiple Objective Genetic Algorithm (MOGA, Fonseca & Fleming, 1993), and the Nondominated Sorting in Genetic Algorithm (NSGA, Srinivas & Deb, 1994). This work adopts the NSGA-II, which is a new and modified version of the original NSGA method. In the next section, a multi-objective approach is developed for TMD optimal design instead of the conventional method presented in (10).

4 Robust TMD design optimization

The fundamental point developing a MOOP is that of evaluating the mean and variance of a conventional objective function. A widely used solution for this problem, referred to the generic stochastic structural response $R(\overline{d})$ which depends on the uncertainty parameter vector $\overline{d}$, is the linear approximation of the DPM that furnishes the mean value and variance:

$$\mu_{[R]_{lin}} = R(\mu_{\overline{d}}) \tag{14}$$

$$\sigma_{R_{lin}} = \sum_{i=1}^{n_d} \sum_{j=1}^{n_d} (\beta_i \beta_j) \mathrm{cov}[d_i d_j] \tag{15}$$

where n_d is the dimension of the uncertainty element vector and $\beta_i = \left(\frac{\partial R}{\partial d_i}\right)_{\overline{d}=\overline{\mu}_D}$ presents the sensitivity coefficients evaluated for the mean value of vector $\overline{d}$.

This formulation makes considerable simplifications if vector $\overline{d}$ components are assumed as statistically independent (and therefore uncorrelated). Equation (15) becomes:

$$\sigma_{R_{lin}} = \sqrt{\sum_{i=1}^{n_d} \beta_i^2 \, \sigma_{d_i}^2} \tag{16}$$

The application of this method to the OF defined in (10) gives:

$$\mu_{OF}(\overline{d}, \overline{b}) = OF(\mu_{\overline{d}}, \mu_{\overline{b}}) \tag{17}$$

$$\sigma_{OF}(\overline{b}, \overline{d}) = \sqrt{\sum_{i=1}^{n_d} \left\{ \left(\frac{\partial}{\partial d_i} OF(\overline{b}, \overline{d}) \right)^2_{\mu_{\overline{d}}} \sigma^2_{d_i} \right\}} \tag{18}$$

where σ_{d_i} is a problem data, and

$$\left(\frac{\partial}{\partial d_i} OF(\overline{b}, \overline{d}) \right)\Big|_{\mu_d} = \frac{(\sigma_{X_S})_{,d_i} \sigma_{X_S^0} - \sigma_{X_S} (\sigma^0_{X_S})_{,d_i}}{\sigma^2_{X_S^0}} \tag{19}$$

where $(\bullet)_{,d_i} = \frac{d\bullet}{d(d_i)}$.

The two terms that appear in equation (19), the main system standard deviation of displacement and velocity, are directly obtainable from (2):

$$\sigma_{X_S} = \sqrt{[\mathbf{R}_{ZZ}]_{2,2}} \tag{20}$$

$$\sigma_{X_S^0} = \sqrt{[\mathbf{R}_{Z_0 Z_0}]_{1,1}} \tag{21}$$

and the other two, which are their first derivative, are obtainable as

$$(\sigma_{X_s})_{,d_i} = \left(\frac{d\sigma_{X_s}(d, b)}{d(d_i)} \right) = \frac{1}{2} \frac{([\mathbf{R}_{ZZ}]_{22})_{,d_i}}{\sqrt{[\mathbf{R}_{ZZ}]_{22}}} \tag{22}$$

$$(\sigma_{X_s^0})_{,d_i} = \left(\frac{d\sigma_{X_S^0}(d, b)}{d(d_i)} \right) = \frac{1}{2} \frac{([\mathbf{R}_{Z_0 Z_0}]_{22})_{,d_i}}{\sqrt{[\mathbf{R}_{Z_0 Z_0}]_{22}}} \tag{23}$$

Both are obtained by deriving the original (2), so that $\boldsymbol{R}_{,d_i}$ is presented as:

$$\mathbf{A}\mathbf{R}_{ZZ,di} + \mathbf{R}_{ZZ,d_i}\mathbf{A}^T + \mathbf{C}_i = \mathbf{0} \tag{24}$$

where

$$\mathbf{C}_i = \mathbf{A}_{,d_i}\mathbf{R}_{ZZ} + \mathbf{R}_{ZZ}\mathbf{A}^T_{,d_i} + \mathbf{B}_{,d_i} \tag{25}$$

and $\mathbf{A}_{,d_i}$ is the derivative of state matrix $\mathbf{A}$ with respect to each uncertainty parameter. Moreover, $\mathbf{B}_{,d_i}$ is a null matrix for all the vector $\overline{d}$ elements, and so equation (25) can be simplified. This way, all quantities in the equation relative to the generic structural response are known, and it is possible to obtain the linear approximation of the OF mean value and variance in case of system parameters and frequency input content uncertainty. In this last case, a possible way pf getting on with the task of obtaining a robust optimal structural design is to minimize the dispersion of the OF through multi-criteria measures of the goal performance. By adopting this formulation, the

Table 1 Mean $\mu(d_i)$ and variation coeffiecient $\gamma(d_i)$ of system and filter uncertain parameters.

Input Data		*Value*	
Main System period	T_s	0.45 s	
Filter period	T_f	0.35 s	
Power Spectral Density	S_0	1000 cm^2/s^3	
Uncertainty Parameters d_i		$\mu(d_i)$	$\gamma(d_i)$
Main System Parameters	ω_S	13.95	0.15
	ξ_S	0.05	0.20
	η	0.05	0.15
Filter Parameters	ω_f	18.62	0.10
	ξ_f	0.40	0.15

proposed problem becomes a vectorial minimization one in which the two conflicting criteria are the mean value and the variance/standard deviation of the OF, that is:

$$\text{find} \qquad \overline{b} \in \mathbf{\Omega}_b \tag{26}$$

$$\text{that minimize} \quad \{\mu_{OF}(\overline{b}), \sigma_{OF}(\overline{b})\} \tag{27}$$

5 Numerical application of a robust example

In order to solve the multi-objectives optimization problem proposed, several numerical applications have been carried out for specific levels of the main system and filter characteristics. These parameters, stochastically expressed by the mean and the variation coefficient, are considered deterministically known. The principle aim is to incorporate uncertainties in both the load and the structural model parameters. All data with certain and uncertain parameters are listed in Table 1, as above:

Introducing the dimensionless parameter $\rho_{TMD} = (\omega_{TMD}/\omega_s)$, a first analysis concerns the application of the conventional deterministic optimization method to obtain the Objective Function surface. Assuming a given design vector space $\Omega_{\overline{b}}$, in Figure 1 the conventional OF mean and variance are shown. It can be noted that both the mean and standard deviation of the conventional OF present *extreme points*. The points are a single global minimum for the mean and maximum points for the variance. In detail the variance shows not a unique but multiple peaks. Besides, it can also be noted that there is quite perfect agreement between the peak points observed. For example, the global minimum of the mean seems to correspond to the region where maximum points take place in the variance surface. More generally, it can be stated that when the mean of the OF increases, rising from the minimum observed, the standard deviation tends to decrease in relation to the increasing mean. This consideration confirms the impossibility of achieving OF minimization in an absolute sense, both in terms of mean and variance. This is due to the point that when it is possible to reduce the first term, the second one increases, having both counteracting effects with respect to the objective

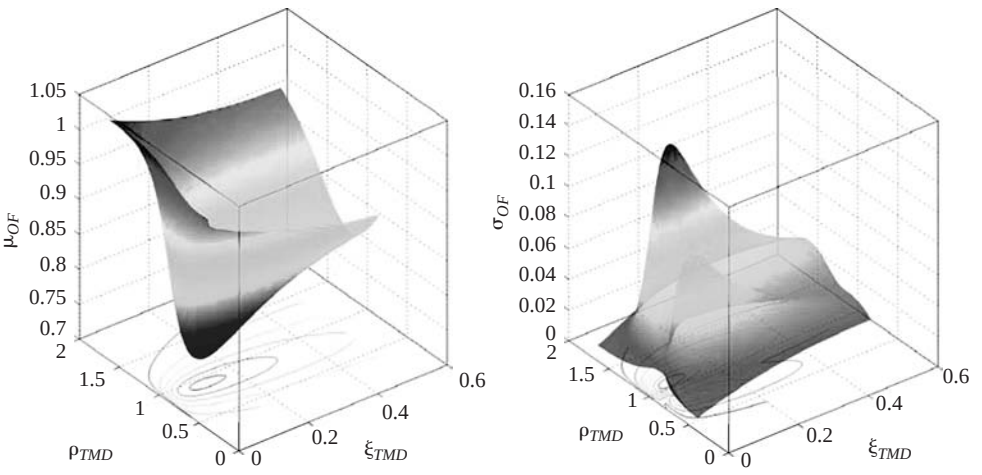

Figure 1 Objective function mean value (a) and variance (b) for different values of ρ_{TMD} and ξ_{TMD}.

function optimization. In fact, a more robust optimal solution can be characterized by a general improvement in structural performance expressed both by the reduction of the OF mean value and by a more stable and less sensitive response to uncertainty sources (i.e. reduction in OF standard deviation).

The above result shows that the optimal solution, obtained by minimizing the expected value of the OF (the mean), is quite sensitive to the fluctuation of the uncertainty parameters, as demonstrated by the corresponding high values of variance.

For this reason, a multi-objective robust design concept must be adopted to overcome this limitation and to provide more pieces of information about the structural optimization problem solution. The previous example demonstrates that the satisfaction of the optimization problem regards two main aspects: the first one concerns the necessity of satisfying critical performance requirements (minimizing the mean of the OF) whereas, the second one involves maximizing the robustness required to deal with uncertainty (minimizing the standard deviation of the OF). Nevertheless, each aspect is in conflict with the other and it is not possible to define a universally approved criterion of "optimum" as in the case of a single objective optimization problem. Therefore, in MOOP the aim is to produce a set of good compromised solutions from which the decision-maker can make a choice. With this aim, a Pareto optimal set for uncertain configurations has been plotted in Figure 2 in a bi-dimensional Pareto domain (in mean μ_{OF} and standard deviation σ_{OF}) for different values of the frequency ratio $\Psi_\omega = (\omega_s/\omega_f)$. In detail, the filter frequency has been changed assuming the same value for the variation coefficient. In Figure 2, it can be noted that Pareto fronts show two main tendencies in function of the frequency ratio.

The first one is for $\Psi_\omega \leq 1$ and represents the situation in which the main system has a frequency lower than the tuned mass. In this case, Pareto fronts appear very close, so there is not much difference between them. In particular, this kind of point distribution is optimal with respect to the other fronts. In fact, the set is characterized

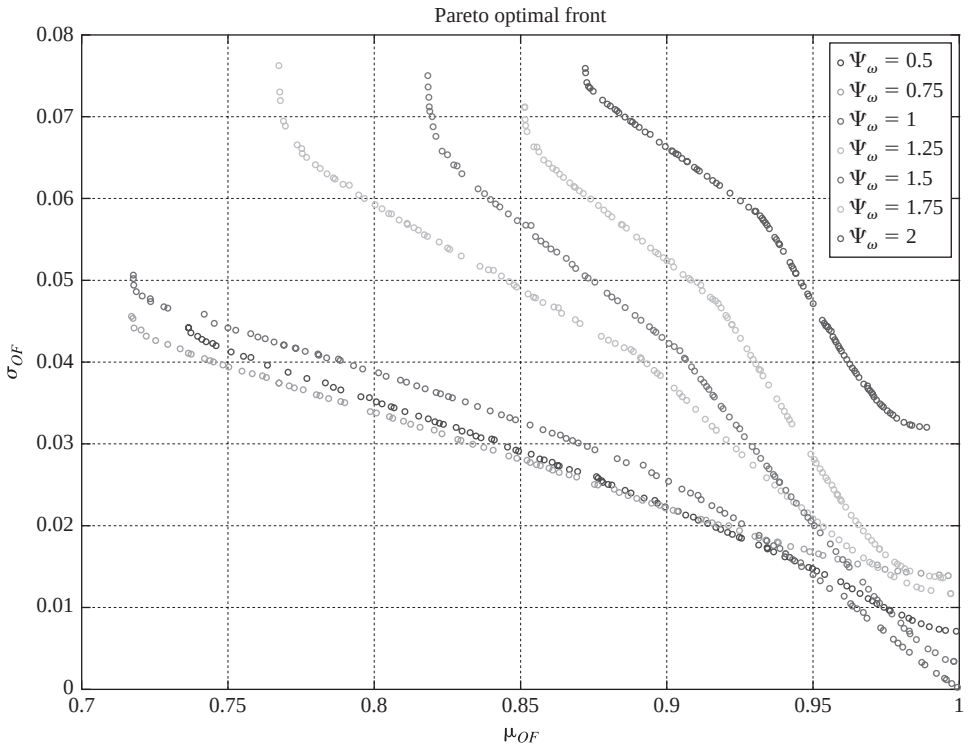

Figure 2 Pareto optimal fronts for different frequency ratios.

by lower values in variance for a fixed mean value if compared with the other ones. The maximum uncertainty achieved, is approximately 50%. The second tendency is for $\Psi_\omega > 1$. This represents the situation in which the main system has a frequency higher than the tuned mass (i.e. condition that departs from the resonance). The performance, expressed in terms of multi-objective structural problem optimization, gets worse. Pareto's fronts are characterized by larger values of variance at a fixed mean value. It can also be noted that all different solutions lie very far from each other because of the more accented sensitivity of optimal points with respect to the uncertainty parameters.

Another consideration concerns the shape of the fronts. They appear convex, and would not be determinable with conventional multi-objective optimization methods like, for example, the Weighted Sum Method. This last method is a linear combination of the objectives, and the application of an Evolutionary optimization problem approach in Pareto's fronts definition would be more appropriate.

Optimal DV distribution referred to OF mean and variance is shown in Figures 3 and 4. Both graphs shows the presence of two very different tendencies depending the frequency ratio, thus confirming the above mentioned trends. For Ψ_ω less then the unit (red, green and blue points), the distribution assumes a characteristic well-located "handle" shape with a limited scatter and quite insensible to being smaller than

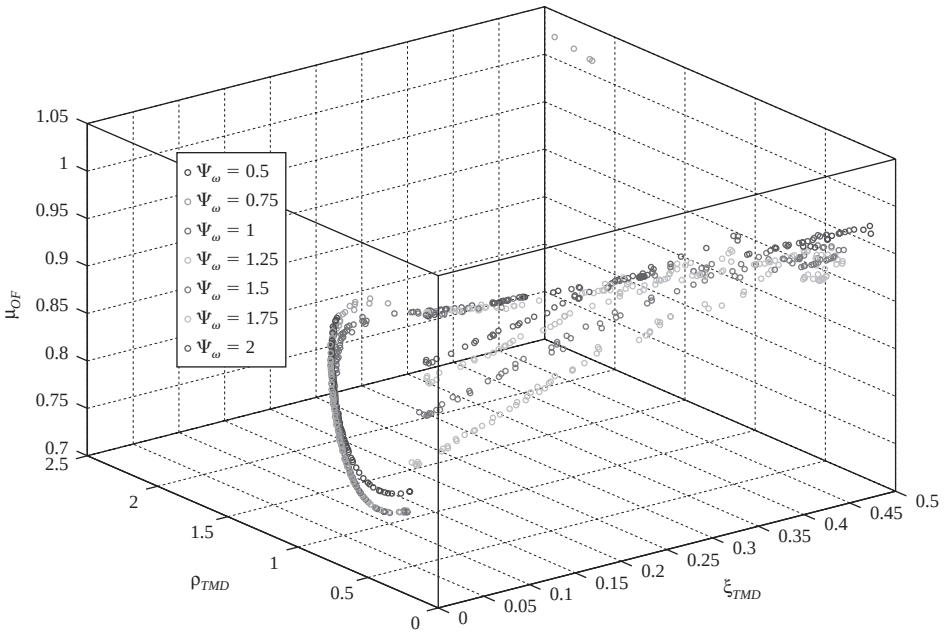

Figure 3 Pareto optimal points in mean value of the OF for different values of ρ_{TMD} and ξ_{TMD}.

the unit. This is evident given that the starting and ending points which represent the extremes of Pareto fronts, are nearly the same, as in the case of the intermediate points. On the contrary, a completely different trend from Pareto optimal solutions is shown regarding cases of $\Psi_\omega > 1$. The starting points are quite different in the OF mean value (Fig. 3), and an appreciable scatter affects the solutions, tending to converge them at a common final volume. Scatter in variance (Fig. 4) is more sensible, and extreme final solutions are sensibly dispersed.

To demonstrate more clearly the alone considerations, Pareto optimal solutions are plotted in Figure 5, where optimal DV solutions of Pareto front in the bi-dimensional design vector domain (i.e. in terms of ρ_{TMD} and ξ_{TMD}) for two different frequency ratios are reported. The first frequency ratio adopted is $\Psi_\omega \leq 1$ and optimal solutions of the Pareto front are reported with green points. The second case is with $\Psi_\omega > 1$ and optimal solutions are reported with red points. In the same figure, the optimal points are plotted together with OF mean (left) and variance (right). This is done with the aim of clearly observing the location of Pareto optimal solutions for two different values of frequency ratio. In the case of mean value distribution (Figure 5, left column), the optimal points start from the global minimum of the OF mean surface whenever Ψ_ω is adopted. On the other hand, in the variance graph (right column), it can be observed that solutions rise from the middle region between the two peaks. The different trend is even more evident in this representation.

Starting from a conventional solution, represented with the minimum of OF mean on the left, the two trends for DV solutions can be observed increasing the variance

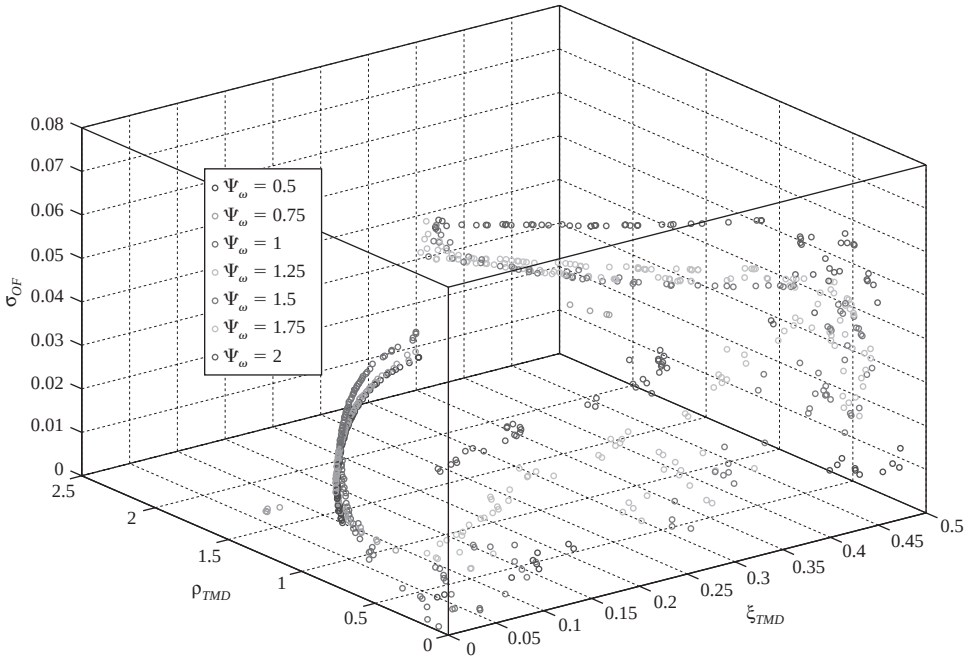

Figure 4 Pareto optimal points and variance of the OF for different values of ρ_{TMD} and ξ_{TMD}.

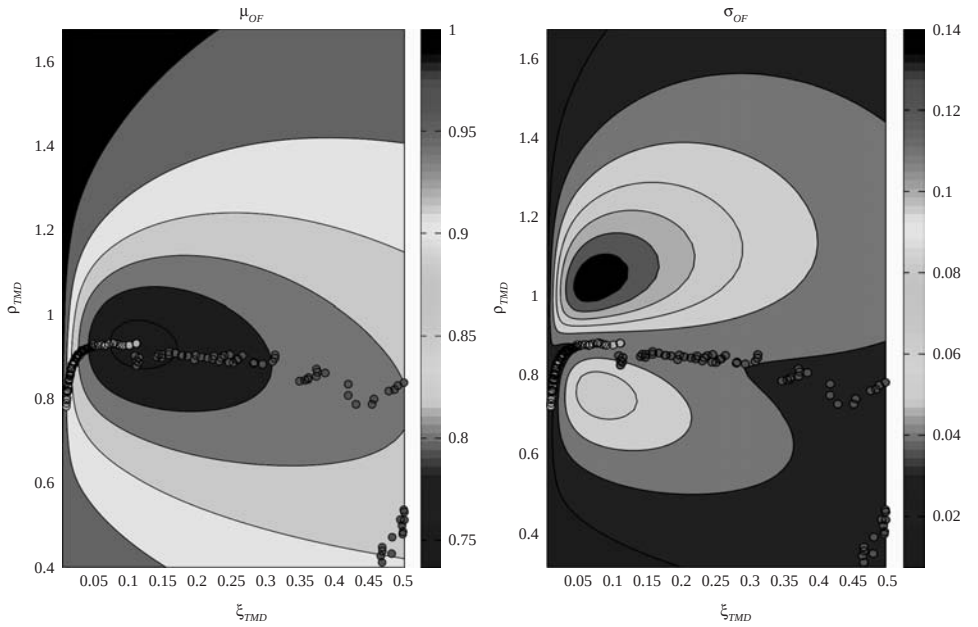

Figure 5 OF mean value (left) and standard deviation (right) and Pareto solutions plotted in the design vector space. Green points are for $\Psi_\omega < 1$ and red ones are for $\Psi_\omega > 1$

control in the optimization criteria, that is moving from the right to the left along the Pareto fronts in Figure 2. For $\Psi_\omega \leq 1$, the optimal solutions (green points) follow a well defined trajectory. The optimization strategy consists in decreasing the tuning effects (decreasing of ρ_{TMD}) with a small reduction of TMD damping. Completely different is the robust optimization strategy obtained for $\Psi_\omega > 1$. Starting from the same conventional point stated before, the optimal solutions in this case move towards the right in the DV space state. This means that for more robust solutions a greater damping is required without variation in the tuning level. These considerations are important in the design choice with regards TMD frequency ratio and damping because the robust optimal solution can be sensitive to these parameter variations, as shown.

6 Conclusions

A robust optimal design criterion for a single TMD device in case of random vibrations is here proposed. This vibration control problem refers to the case of systems subjected to dynamic actions having a stochastic nature that can be modelled by a stochastic process. Robustness is obtained by finding solutions that take into account not only the absolute performance but also consider its sensitivity to system parameters variation due to uncertainty. The dynamic input is represented by a random base acceleration, modelled by a stationary filtered white noise process, to take into account load–structure resonant effects. The main system is described by a single degree of freedom system. It is assumed that main structure stiffness and damping, tuned mass ratio, filter main frequency and damping are affected by uncertainty. They are described by a mean value and a variance, assuming that they are all mutually statistically independent. No other information is considered to assume a given probability densities function. The Objective Function definition is here assumed as main structure covariance displacement.

To perform the robust optimum design, the OF mean and standard deviation are numerically evaluated with a new procedure based on a Lyapunov type equation. Robustness is formulated as a multiobjective optimization problem, in which both the mean and the standard deviation of the deterministic OF are minimized. The results show a significant improvement in performance control and OF real values dispersion limitation if compared with standard conventional solutions. Some interesting conclusions can be reached with reference to the results obtained for the adopted examples. With reference to TMD efficiency in vibration reduction, the real structural performance obtained by using conventional optimization has a reduced efficiency compared to those obtained when system uncertainty parameters is properly considered. With reference to the obtained robust solutions, it can be noted that they can control and limit final OF dispersion by limiting its standard deviation. Moreover, this goal is achieved by finding optimal solutions in terms of DV that induce an increase in OF mean value.

The application of the Pareto concept, in search of the solution of the multiobjective optimization problem, allows to evaluate the optimal choice of the DV that represents a compromise solution which guarantees an acceptable level of relative displacement. An Evolutionary approach by means of a Genetic Algorithm has been used to solve the MOOP and search the population of non-inferior parallel solutions. Illustrated numerical examples show that all assessments and

information drawn by means of this kind of computational model cannot be obtained by the use of a simple conventional optimization technique. In conclusion, the analysis carried out in the present work shows that the optimal design for robust optimization is strongly influenced by environmental parameters, in this case by the frequency ratio Ψ_ω. By changing its value, the optimization strategy may change completely. In the analysed case, the robust TMD optimal solutions are obtained by varying the *damping ratio* using a conventional deterministic optimization method. The result depends on the input frequency content. At the same time, robust TMD optimal solutions are also obtained by varying the *tuned frequency*. With reference to this parameter, the required variation is a function of the input frequency content. For frequency ratio $\psi < 1$ greater than one, the tuned frequency has to decrease, meanwhile it must remain almost constant if $\psi \geq 1$.

References

Coello Coello, C.A. 2000. "Handling Preferences in Evolutionary Multiobjective Optimization: A Survey", IEEE Neural Networks Council (ed.), Proceedings of the 2000 Congress on Evolutionary Computation (CEC 2000) Vol. 1, IEEE Service Center, Piscataway, New Jersey, pp. 30–37.

Doltsinis, I. & Kang, Z. 2004. Robust design of structures using optimization methods. Comput Methods Appl Mech Eng;193:2221–37.

Fonseca, C.M. & Fleming, P.J. 1993. "Genetic Algorithms for Multi-Objective Optimization: Formualtion, Discussion and Generalization", Genetic Algorithms: Proceedings of the 5th International Conference (S. Forrest, ed.) San Mateo, CA: Morgan Kaufmann.

Igusa, T & Kiurghian, AD. 1988. "Response of uncertain systems to stochastic excitation". J Engng Mech, ASCE;114:812–32.

Kicinger, R., Arciszewski, T. & De, Jong, K. 2005. "Evolutionary computation and structural design: A survey of the state-of-the-art", Computers and Structures 83, pp. 1943–1978.

Lagaros, N.D., Fragiadakis, M., Papadrakakis, M. & Tsompanakis, Y. 2006. "Structural optimization: a tool for evaluating seismic design procedures", J. of Engrg. Str., vol. 28, 1623–1633.

Langley, R.S. 2000. "Unified approach to probabilistic and possibilistic analysis of uncertain systems", Journal of Engineering Mechanics, Vol. 126, No. 11, 1163–1172.

Luh, G.C. & Chuen, C.H. 2004. "Multi-Objective optimal design of truss structure with immune algorithm", Computers and Structures, 82, pp. 829–844.

Lutes, L.D. & Sarkani, S. 2001. "*Random Vibrations*", Butterworth-Heinemann, Oxford (UK).

Marano, G.C., Greco, R., Trentadue, F. & Chiaia, B. 2007. "Constrained reliability-based optimization of linear tuned mass dampers for seismic control", International Journal of Solids and Structures, accepted for publication.

Nigam, N.C. 1972. "Structural Optimization in random Vibration Environment" , AIAA, 551–553.

Siddall, JN. 1984. A new approach to probability in engineering design and optimisation. ASME J Mech. Transmiss. Autom Des;106:5–10.

Papadimitriu, C., Beck, J.L. & Katafygiotis, L.S. 1997. "Asymtotic expansion for reliability and moments of uncertainly systems, Journal of Engineering Mechanics (ASCE), Vol 123, No 12, 1219–1229.

Papadrakakis, M., Tsompanakis, Y., Lagaros, N.D. & Fragiadakis, M. 2004. "Reliability based optimization of steel frames under seismic loading conditions using evolutionary computation", Special Issue of the Journal of Theoretical and Applied Mechanics on Computational Intelligence in Mechanics, Vol. 42, No 3, pp. 585–608.

Srinivas, N. & Deb, K. 1994. "Multi-objective Optimization Using Nondominated Sorting in Genetic Algorithms", Journal of Evolutionary Computation, Vol. 2, No. 3, pp. 221–248.

Zang, C., Friswell, M.I. & Mottershead, J.E. 2005. A review of robust optimal design and its application in dynamics, Computers and Structures 83, 315–326.

Chapter 34

Performance-based seismic optimization implementing neural networks

Oscar Möller, Laura Quiroz & Marcelo Rubinstein

University of Rosario, Rosario, Argentina

Ricardo O. Foschi

University of British Columbia,Vancouver, Canada

ABSTRACT: Performance-Based Design in earthquake engineering accounts for structural and ground motion uncertainties in optimizing design parameters, satisfying multiple performance criteria with target reliabilities and minimizing an objective. This implies a nonlinear structural dynamic analysis for earthquakes likely to occur at the site, to obtain the demand responses of interest. The responses are represented here via neural networks and used in the performance criteria for estimation of achieved reliabilities by Monte Carlo simulation. An optimization is finally implemented to obtain optimal parameters, using a gradient-free algorithm. An application is shown for a reinforced, multi-story concrete frame. The demand is simulated using artificially generated ground motions, with the peak ground acceleration corresponding to the city of Mendoza, Argentina. Performance requirements (operational, life safety or collapse) are specified in terms of damage severity, using maximum displacements, inter-story drifts, local and global damage indices. Optimization objectives are minimum cost, minimum dimensions and/or minimum steel reinforcement.

1 Introduction

Performance-Based Design in earthquake engineering (SEAOC Vision 2000 1995, FEMA 273 1997) implies taking into account structural and ground motion uncertainties in order to obtain structural design parameters, satisfying multiple performance criteria with associated minimum reliability levels and (as an option) at a minimum total cost.

The treatment of uncertainties requires the use of probabilistic methods, estimating the probability of exceeding response targets for the different performance requirements, for example, on an annual basis. The dynamic structural responses are highly nonlinear, and their time history must be found by numerical (e.g., finite elements) analysis for the duration of the earthquake. In a thorough analysis, the nonlinearity of the response is further increased when the interactions between the structure and the foundations are included. It is not possible to establish an explicit relationship between the intervening variables and the dynamic responses, and results can only be obtained in a discrete manner, given specific values of the structural variables and a particular earthquake record. Reliability calculations depend on simulations

(e.g., Monte Carlo simulation (MCS) technique), which in turn may require a large number of discrete response evaluations, at great computational cost. The efficiency of the process is greatly improved, however, if the discrete results are represented by a function ("response surface") which would then be used as a substitute (Hurtado 2004) for the actual responses, and which would allow interpolation of the responses for inputs not considered in the original database. Simulation or other reliability estimation technique, using the response surface substitute, requires a much smaller computational effort. Different types of response output substitutes have been used, ranging from analytical functions (Möller 2001, Möller & Foschi 2003), local interpolation of the databases (Foschi et al. 2002), and neural networks (Zhang 2003, Zhang & Foschi 2004, Möller et al. 2006 a, b). It is normally difficult to represent the range of structural response characteristics for different inputs by a simple, global, analytical function. The use of local interpolation of the discrete databases permits a more refined representation. In this regard, however, the use of artificial neural networks, trained with the discrete databases, leads to a superior, more flexible and efficient representation. The computational effort is now shifted from the reliability estimation via simulation to the deterministic calculation of the databases for a strategic choice of the input combinations.

The optimization process involves finding design parameters which lead to a minimum structural volume, or minimum amount of steel, or total construction cost, satisfying also minimum target reliability indices for the different performance requirements. The optimization algorithm implemented in this work does not make use of gradients, thus avoiding numerical problems of convergence or the finding of local minima.

As an illustration, this work presents an application of neural networks to the optimal design of a two-dimensional reinforced concrete frame under seismic excitation. The optimization considers three performance requirements: operational, life safety and collapse. Each, in turn, has an associated minimum target reliability. Three objectives are considered for the optimization: 1) optimum beam and columns dimensions for minimum total structural volume; 2) optimum steel reinforcement ratio for minimum total steel weight; and 3) optimum beam and column dimensions, and steel reinforcement ratio, for minimum total structural construction cost.

2 Nonlinear dynamic response and representation by neural networks

2.1 *Model for nonlinear dynamic analysis*

The structural model used here considers the frame as a set of one-dimensional beam elements (Möller 2001). In order to represent the hysteretic behavior of reinforced concrete members, each contains three sub-elements connected in series: (i) an elasto-plastic sub-element to represent the elastic behavior of the member itself, and including non-linear elements at its extremes, of varying length depending on the load history; (ii) a connection sub-element to characterize the localized relative rotation at the ends of the member as a result of degradation of steel anchorage; (iii) a shear sub-element to describe the distortion at critical regions of the member and the shear slip at the end of the member. The extremes of each member consider nodes of non-negligible

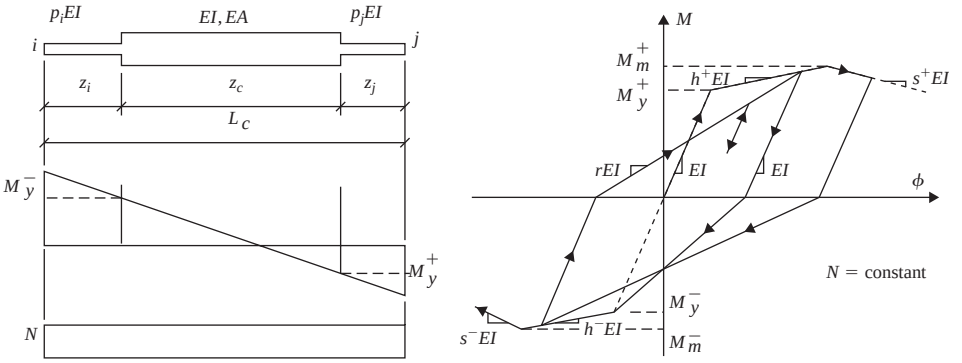

Figure 1 Elasto-plastic sub-element – Moment-curvature relationship.

dimensions. In this work the analysis has considered only the effect of the elasto-plastic sub-elements, as shown in Figure 1.

The plastic behavior during loading and unloading is assumed concentrated at the extremes of the member. Further, the stiffness of these plastic zones is represented by an effective average stiffness *pEI*, which depends on the extreme section. These assumptions imply that the moment-curvature history needs to be traced only at the extremities of the member.

The moment-curvature relationship M-ϕ for a given reinforced concrete cross-section is constructed, for a constant axial force, using the following hypotheses: (a) plane sections remain plane during deformation, and normal to the deformed axis of the member; (b) Mander's models (1984) are utilized as the constitutive relations for concrete and steel. The cross-section is subdivided in strips parallel to the neutral axis and, for each increment in curvature, the position of the deformed (rotated) cross-section is adjusted iteratively until equilibrium is achieved between the internal and external actions, when the corresponding moment is then finally calculated.

The ultimate curvature ϕ_u is determined when, at the end of a pre-determined number of complete cycles to $\pm\phi_u$, one of the following limit states is reached: (a) a 20% reduction in the moment capacity; (b) the transverse steel reinforcement reaches its capacity to absorb energy From the energy balance of the cross-section, the concrete ultimate compression deformation is calculated; (c) the maximum tensile or compression deformation of the longitudinal reinforcement is reached.

In the hysteresis model shown in Figure 1, the factors p_i, p_j have the following values: (a) $p=1$, for elastic behavior, (b) $p=h$ for strain hardening , (c) $p=s$ for strain softening, with $z_i=l_p$ (a characteristic length $\cong 0.75\,d$, d being the cross-sectional depth), (d) $p=1$ for unloading, (e) $p=2/(1/r+1)$ for re-loading, a value obtained from the average of the stiffness corresponding to the extreme section, rEI , and that corresponding to the elastic section EI, at the end of the plastic section. The parameters M_y, M_m, EI, h, s, for the positive and negative directions, are calculated by linearization of the relationship $M-\phi$ obtained in a pre-processing of the cross-section.

The analysis included a consistent mass matrix and viscous damping proportional to mass and stiffness. The system of nonlinear equations is solved by time-stepping direct

integration using Newmark's method, with a Newton-Raphson iteration scheme within each step to achieve equilibrium within each element. The analysis output contains the parameters included in the definitions of the limit states for each of the performance levels considered.

2.2 *Response approximation using neural networks*

Artificial neural networks (Hurtado 2004) are computational devices which permit the approximate calculation of outputs given an input set. The input is organized as a layer of neurons, each corresponding to one of the input variables, and the output is contained in an output layer. Intermediate, hidden layers, contain a number of neurons which receive information from the input layer and pass it on to subsequent layers. Each link in the network is associated with a weight w. The total information received by a neuron is processed by a transfer function h before being sent forward to the neurons in the next layer. For a network with a single hidden layer, the computational process can be expressed as

$$R(\mathbf{X}) \cong F(\mathbf{X}) = h\left(\sum_{k=0}^{J} w_{kj} h\left(\sum_{i=0}^{N} w_{ji} X_i\right)\right) \tag{1}$$

where $R(\mathbf{X})$ is the true value in the relationship being represented by the neural network; $F(\mathbf{X})$ is the neural network output; $h(t)$ is the transfer function associated with the neurons (usually a sigmoid function); w are the weights; X_i are the input variables plus one bias term, making up N neurons in the input layer; and J is the number of neurons in the single intermediate hidden layer plus one additional bias neuron. Figure 2 shows a schematic architecture for a multilayer neural network. In this work only one hidden layer is considered.

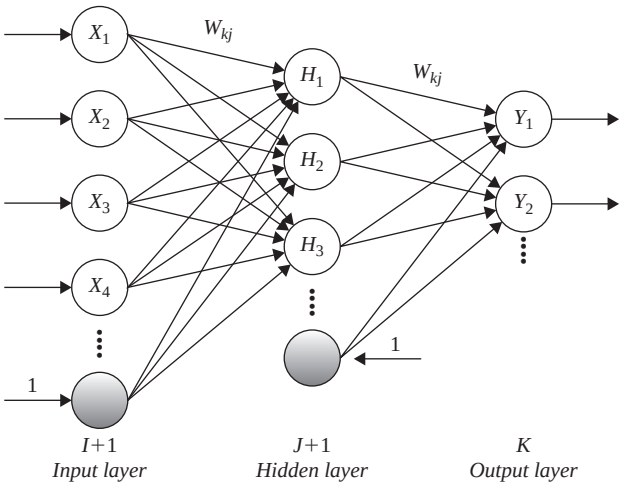

Figure 2 Multilayer neural network.

The transfer of information between neurons in adjacent layers is implemented through the weights w associated with each link and a transfer function h(t). In Figure 2, let the number of neurons in the input, hidden and output layers be, respectively, $I+1$, $J+1$ y K; let X_i^p be the *pth* datum for the *ith* neuron in the input layer, I_j^p the *pth* datum for the *jth* neuron in the hidden layer; H_j^p the *pth* output from the jth neuron in the hidden layer; I_k^p the *pth* datum for the *kth* neuron of the output layer; and Y_k^p the *pth* output from the *kth* neuron in the output layer. Thus, the following relationships correspond to the transfer of information between the input and the output layers:

$$\mathrm{I}_j^p = \sum_i^{\mathrm{I}} w_{ji} X_i^p + w_{j0} \qquad H_j^p = h(\mathrm{I}_j^p) \tag{2}$$

$$\mathrm{I}_k^p = \sum_j^J w_{kj} H_j^p + w_{k0} \qquad Y_k^p = h(\mathrm{I}_k^p) \tag{3}$$

in which w_{ji} is the weight connecting the *ith* neuron in the input layer with the *jth* neuron in the hidden layer; and w_{kj} is the weight between the *jth* neuron and the *kth* in the output layer. The transfer function $h(.)$ used here is the sigmoid

$$h(x) = \frac{1.0}{(1+\exp(-x))} \tag{4}$$

The number of neurons in the hidden layer must be sufficiently large to permit a good representation of the input-output relationship, but not so large that the network may produce inaccurate values for input combinations not in the training set.

The network can be used to represent the relationship $R(\mathbf{X})$ after the weights have been determined by training, that is, by adjusting their values so that the differences between the true values of a training set and the network predictions for that same set are minimized.

The number of neurons in the hidden layer must be related to the number of available input data *NDAT*. Normally, a fraction of the available data is used for training (e.g., 80%), while the rest are used for validation of the neural network predictions. The maximum number of neurons in the hidden layer is thus given by

$$NEUMAX = \frac{0.8\ NDAT - 1}{NINT + 2} \tag{5}$$

in which *NINT* is the number of input variables. The optimum number of neurons is found by evaluating the total error (training + validation) achieved with a varying number of neurons, from 1 to *NEUMAX*, adopting the number corresponding to the least total error. In each case, this error is obtained here by minimization using the back-propagation algorithm (Zhang 2003). Thus, for each choice of the number of

neurons in the hidden layer, the total error corresponds to the minimization, with respect to the weights w, of the expression E:

$$E = \frac{1}{2}\sum_{p}\sum_{k}(Y_k^p(w) - T_k^p)^2 \tag{6}$$

where T_k^p is the true or target value for *kth*-output neuron corresponding to the *pth*-datum.

Training of the network implies minimizing E and thus obtaining the optimum weights w_{ji}, w_{kj}. A common minimization algorithm is called back propagation, based on an updating of the weights, Δw_{ji}, along the direction of steepest descent:

$$w_{ji}(g+1) = w_{ji}(g) + \Delta w_{ji}(g) \quad \text{with } \Delta w(g) = -\eta\,\nabla E(g) + \alpha\,\Delta w(g-1) \tag{7}$$

in which g is the iteration number, η is called the learning rate and α the momentum. In this algorithm, the value used for the learning rate controls the convergence: if chosen too large convergence may not occur, if chosen too small the convergence may be slow. In the applications shown here, the values $\eta = 0.01$ and $\alpha = 0.05$ were utilized.

2.3 *Portal frames*

Figure 3 shows a generic reinforced concrete portal frame, for which the intervening variables considered, with their corresponding bounds, were: number of stories $NS = 3$ to 10; number of bays $NB = 1$ to 4; bay span $XL = 300$ to 600 *cm* (all equal); mass per unit length for each story $m = 2.15 \times 10^{-4}$ to 4×10^{-4} KNs^2/cm^2; characteristic concrete compressive strength $f_c' = 20$ to 40 *MPa*; beam width $b_b = 15$ to 30 *cm*;

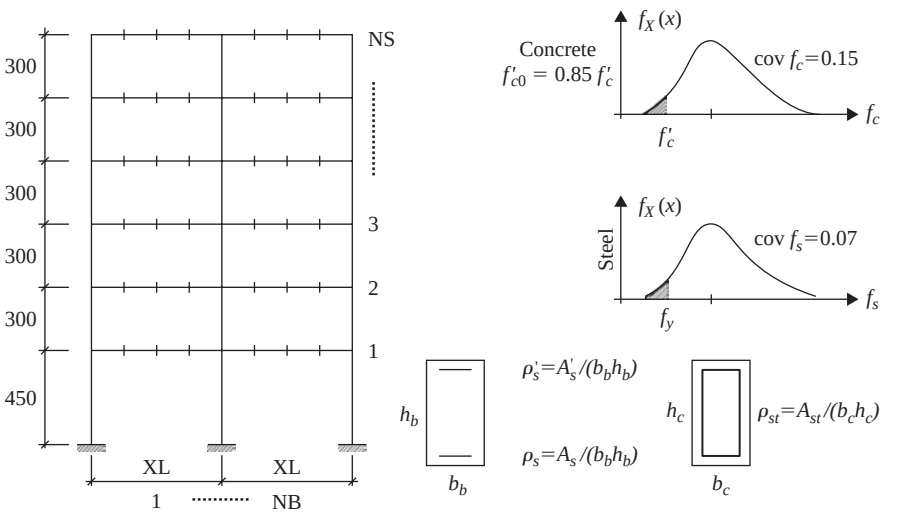

Figure 3 Portal frame geometry and variables.

beam depth $h_b =$ 40 to 70 *cm*; column width $b_c = 20$ to 40 *cm*; column depth $h_c = 40$ to100 *cm*.

The beam and column dimensions, b_b , h_b ,b_c and h_c correspond to the lower stories. Upper stories have reduced dimensions according to the ratios specified in Table 1.

The bounds for the reinforcement ratios are controlled by Norms. Here, the ratio for beams at midspan was from $\rho_{s_{span}} = \sqrt{f'_c} / (4 f_y)$ to $(f'_c + 10)/(6 f_y)$; for beams over their supports, from $\rho'_{s_{end}} = \sqrt{f'_c} / (4 f_y)$ to $(f'_c + 10)/(6 f_y)$; and for columns, from $\rho_{s_t} = 0.008$ to 0.04286. The bounds for normalized confinement pressure were taken as $f_r / f'_{c0} = 0.0$ to 0.15. Furthermore, the reinforcement ratios for beams must supply an adequate bending strength for gravitational loads,

$$\phi \, (M_{span} + M_{end}) \geq \frac{q_u \, XL^2}{8} \tag{8}$$

where $M_{span} = b_b \, h_b \; \rho_{s\,span} \; f_y \; 0.9 \; h_b$, $M_{end} = b_b \, h_b \; \rho'_{s\,end} \; f_y \; 0.9 \; h_b$, with $f_y = 420 \, MPa$, $q_u = 1.2 \; D + 1.6 \; L \cong 1.33 \, (D + L) \cong 1.40 \, mg$, and a strength reduction factor $\phi = 0.9$.

The seismic excitation corresponded to the city of Mendoza, Argentina. The variables associated with the ground motion, and their corresponding bounds, were: the peak ground acceleration, $a_g = 25$ *to* $1200 \, cm/s^2$, and the central frequency for the soil filter, $f_g = 2.0$ *to* $3.0 \, Hz$. Other variables required for the generation of accelerograms were taken either as functions of a_g and f_g, or as constants.

Individual accelerograms were simulated using the method proposed by Shinozuka and Sato (1967):

$$a(t) = I(t) \sum_{n=1}^{NFR} \{4 \, S_{XX}(n \, \Delta f)[1 + \delta_S \, R_N] \Delta f\}^{1/2} \sin(2\pi n \, \Delta f t + \theta_n) \tag{9}$$

in which S_{XX} is the power spectral density function for the process, *NFR* is the number of sine functions or frequencies included, between 0 y f_{max} , such that $NFR \geq f_{max} T_0$, T_0 being the duration of the simulated record. The ordinates of the function S_{XX} are taken to be random, with δ_S being the coefficient of variation and R_N a Standard

Table 1 Number of stories and beam/column dimensions.

NS	*Type G1*	*Type G2*	*Type G3*
3	2	1	
4	2	2	
5	3	2	
6	3	3	
7	3	2	2
8	3	3	2
9	3	3	3
10	4	3	3

Dimensions for different stories:
Type G1: b_b, h_b b_c, h_c
Type G2: $b_b, 0.8h_b$ $b_c, 0.8h_c$
Type G3: $b_b, 0.6h_b$ $b_c, 0.6h_c$

Normal variable. Δf is a frequency step, and θ_n are random phase angles with a uniform distribution between 0 y 2π. The process thus generated is stationary, but non-stationarity is introduced with the modulation function $I(t)$ defined as follows:

$$\begin{aligned} I(t) &= (t/T_1)^d && \text{for } 0 \le t \le T_1 \\ I(t) &= 1 && \text{for } T_1 \le t \le T_2 \\ I(t) &= e^{-c\,(t-T_2)} && \text{for } T_2 \le t \le T \end{aligned} \tag{10}$$

in which t is time, T_1 and T_2 specific times and d and c are constants.

This work used the power spectral density function S_{XX} introduced by Clough and Penzien (1975),

$$S_{XX}(f) = S_0 \frac{1 + 4\,\xi_g^2\,(f/f_g)^2}{[1-(f/f_g)^2]^2 + 4\,\xi_g^2\,(f/f_g)^2} \; \frac{(f/f_f)^4}{[1-(f/f_f)^2]^2 + 4\,\xi_f^2\,(f/f_f)^2} \tag{11}$$

in which S_0 is a constant or the power spectral density corresponding to white noise; f_g, ξ_g are respectively, the characteristic ground frequency and the ground damping ratio; and f_f, ξ_f are parameters for a high-pass filter to attenuate low frequency components.

The baseline of the accelerogram thus generated is further corrected to minimize the mean square value of the corresponding velocities. The record is finally scaled to have a peak acceleration a_G, a random peak value that could occur at the site in case of an earthquake.

A total of 900 combinations of the variables were developed, following techniques of experimental design (Zhang 2003). For each combination, 5 sub-combinations were developed, each corresponding to a different accelerogram and specific parameters in the moment-curvature relationship for the members. Each accelerogram was derived considering a different sequence of random phase angles. A dynamic analysis, as described in 2.1, was carried out for each combination, obtaining the following outputs: maximum total displacement at the top of the frame, u_{max}; the maximum inter-story drift, *DSIM*; the maximum local Park & Ang (1985) damage index, *DILOM*; and the maximum global damage index *DIG*.

For each of these outputs R_i, and for each of the 900 combinations, the corresponding mean value and standard deviation of R_i were calculated over the $N = 5$ sub-combinations,

$$\overline{R}_i = \frac{1}{N}\sum_{k=1}^{N} R_{k_i} \qquad \sigma_{R_i} = \sqrt{\frac{1}{N-1}\sum_{k=1}^{N}(R_{k_i} - \overline{R}_i)^2} \tag{12}$$

Thus, for each output parameter, two databases of 900 data each were assembled, representing an estimate of the mean and the standard deviation of the particular response over the set of ground motions used. These two databases were used to train corresponding neural networks for each of the outputs.

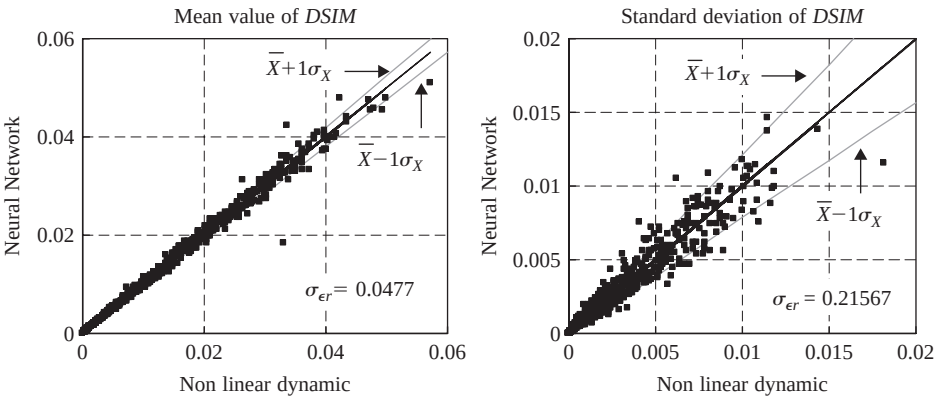

Figure 4 Neural network training, maximum inter-story drift DSIM.

2.4 *Training of the neural networks*

Following the procedures described in 2.2, neural networks were trained to represent the mean value and the standard deviation of the response parameters. Figure 4 shows the result of the training corresponding to the maximum inter-story drift *DSIM*. As shown in this figure, a good representation was achieved.

If the agreement were perfect, all points would lie on the 45° line. A scattering of points around this line is shown, more for the standard deviation than for the mean values. This dispersion can be approximately quantified with the standard deviation of the relative error

$$\sigma_{\varepsilon_r} = \sqrt{\frac{1}{N_E - 1} \sum_{k=1}^{N_E} \left(\frac{T_k - Y_k}{Y_k} \right)^2} \tag{13}$$

in which Y_k is the output from the neural network, T_k is the value obtained with the dynamic analysis and $N_E = 900$ is the number of combinations of the network input parameters.

Adopting a Normal distribution for the training error, the mean response $\overline{R_i}$ and the Standard deviation of the response σ_{Ri} can be expressed as

$$\overline{R}_i = \overline{Y}_i \, (1. + \sigma_{\varepsilon_r} X_N) \quad \sigma_{Ri} = \sigma_{Y_i} (1. + \sigma_{\varepsilon_r} X_N) \tag{14}$$

in which $\overline{Y}_i, \sigma_{Y_i}$ are the mean value and the Standard deviation for the ith response parameter, calculated with the corresponding neural network, σ_{ε_r} is the standard deviation of the relative error from Eq. (13), y X_N is a Standard normal random variable.

3 Evaluating reliability

3.1 *Random variables and performance functions:*

One portal type was considered in the examples. This frame had 6 stories and 3 bays. The reliability levels corresponding to three performance requirements (operational, life safety and collapse) were obtained for seismic conditions corresponding to the city of Mendoza, Argentina. Characteristics of all the intervening random variables are shown in Table 2 and the mean value of those marked with the symbol ? are the design parameters considered in the optimization.

The generic expression for the performance or limit state function $G(\mathbf{X})$ is

$$G(\mathbf{X}) = RLIM - R(\mathbf{X}) \tag{15}$$

in which $RLIM$ is the limiting value for the response parameter $R(\mathbf{X})$ which, in turn, is a function of the set of intervening random variables X_i, $(i = 1, N)$. The value $RLIM$ is also considered a random variable, so that

$$RLIM = \overline{RLIM}\,(1. + COVRL\,X(N-1)) \tag{16}$$

in which the mean values and standard deviation $\overline{R}_i$, σ_{R_i} are obtained from Eq. (14). Assuming a lognormal distribution for the response, this can be expressed as

$$R(\mathbf{X}) = \frac{\overline{R}(\mathbf{X})}{\sqrt{1. + \left(\dfrac{\sigma_R(\mathbf{X})}{\overline{R}(\mathbf{X})}\right)^2}} \exp\left[X(N)\sqrt{\ln\left(1. + \left(\frac{\sigma_R(\mathbf{X})}{\overline{R}(\mathbf{X})}\right)^2\right)}\right] \tag{17}$$

Table 2 Random Variables.

Variable	$\overline{X}$	σ_X	*Type*	*Variable*	$\overline{X}$	σ_X	*Type*
$X(1) = NS$	6	0	Normal	$X(12) = \rho_s$	?	$0.10\,\overline{X}$	Log-Normal
$X(2) = NB$	3	0	Normal	$X(13) = f_r/f'_{c0}$	0.10	0.01	Normal
$X(3) = XL$	450 *cm*	22.5 *cm*	Normal	$X(14) = a_G$	$X(14) = X(16)[1.0 + X(17)]$		
$X(4) = m$	3×10^{-4}	3×10^{-5}	Normal	$X(15) = f_g$	2.50 *Hz*	0.375 *Hz*	Normal
$X(5) = f'_c$	30 *MPa*	3 *MPa*	Log-Normal	$X(16) = \overline{a}_G$	94 *cm/s*^{2}	130 *cm/s*^{2}	Log-Normal
$X(6) = b_b$	20 *cm*	1 *cm*	Normal	$X(17) = \sigma_{\overline{a}G}$	0	0.25	Normal
$X(7) = h_b$	? *cm*	$0.05\,\overline{X}$	Normal	$X(18) = X(N-3)$	0	1	Normal
$X(8) = b_c$	30 *cm*	1.5 *cm*	Normal	$X(19) = X(N-2)$	0	1	Normal
$X(9) = h_c$	? *cm*	$0.05\,\overline{X}$	Normal	$X(20) = X(N-1)$	0	1	Normal
$X(10) = \rho_{s,\,span}$	?	$0.10\,\overline{X}$	Log-Normal	$X(21) = X(N)$	0	1	Normal
$X(11) = \rho'_{s,\,end}$	?	$0.10\,\overline{X}$	Log-Normal				

and

$$\overline{R}(\mathbf{X}) = \overline{Y}(\mathbf{X})\ (1. + \sigma_{\varepsilon_R}\ X(N-3))$$
$$\sigma_R(\mathbf{X}) = \sigma_Y(\mathbf{X})\ (1. + \sigma_{\varepsilon_\sigma}\ X(N-2))$$

The performance functions considered in the analysis were:

Operational:

- Elastic behavior $G_{11}(\mathbf{X}) = u_y(1. + 0.10\,X(N-1)) - u_{\max}(\mathbf{X})$ (18)
- Inter-story drift $G_{12}(\mathbf{X}) = 0.005(1. + 0.10\,X(N-1)) - DSIM(\mathbf{X})$ (19)

Life safety:

- Inter-story drift $G_{21}(\mathbf{X}) = 0.015(1. + 0.10\,X(N-1)) - DSIM(\mathbf{X})$ (20)
- Max. local damage index $G_{22}(\mathbf{X}) = 0.60(1. + 0.10\,X(N-1)) - DILOM(\mathbf{X})$ (21)
- Global damage index $G_{23}(\mathbf{X}) = 0.40(1. + 0.10\,X(N-1)) - DIG(\mathbf{X})$ (22)

Collapse:

- Inter-story drift $G_{31}(\mathbf{X}) = 0.025(1. + 0.10\ X(N-1)) - DSIM(\mathbf{X})$ (23)
- Max. local damage index $G_{32}(\mathbf{X}) = 1.00(1. + 0.10\ X(N-1)) - DILOM(\mathbf{X})$ (24)
- Global damage index $G_{33}(\mathbf{X}) = 0.80(1. + 0.10\ X(N-1)) - DIG(\mathbf{X})$ (25)

In Eq. (18), u_y is the displacement, estimated according to Priestley (1998), below which the structure remains fully elastic.

3.2 *Failure probability*

The failure probability associated with each performance function is calculated as that of the event $G(\mathbf{X}) < 0$,

$$Pf = \text{Prob}\,[G(\mathbf{X}) \leq 0] \tag{26}$$

using a Monte Carlo simulation with 10^6 to 10^7 replications, and working will all performance functions simultaneously. This task is facilitated by the introduction of the neural networks trained for each of the responses $R(\mathbf{X})$.

Considering the arrival of the earthquakes as a Poisson process, with a mean arrival rate of $\nu = 0.20$ for the city of Mendoza for magnitudes $M \geq 5$, the annual probability of failure can be calculated as

$$Pf_{annual} = 1. - \exp\,[-\nu\ Pf_E] \rightarrow \beta_{annual} \cong -\Phi^{-1}(Pf_{annual}) \tag{27}$$

in which Pf_E is the failure probability given that a seismic event has occurred. Pf_E and Pf_{annual} can be expressed in terms of their corresponding reliability indices β, as shown in Eq. (27).

4 Optimization algorithm

4.1 *The problem*

The optimization problem may be described as follows:

a. Given a system with N random variables, X_i $(i = 1, N)$, each of M performance requirements or limit states $G_j(X_i)$, $(j = 1, M)$, must satisfy minimum target reliability indices, β_j.
b. A set of design parameters d_k $(k = 1, L)$ must be found such that, satisfying the reliability requirements, also lead to a minimum of an objective function $F(d_k)$, for example the structural weight or the construction cost.

The design parameters can be defined as the mean value and/or the standard deviation of some of the intervening random variables X_i.

4.2 *The solution approach*

A variety of solution approaches can be used for the optimization problem. This work uses an algorithm that does not require the calculation of gradients of the objective function. The steps in this algorithm are described as follows:

a. A set of random combinations of the design parameters is chosen within specified bounds;
b. The reliability implied by each combination is found via Monte Carlo simulation and the application of the neural networks;
c. For those combinations which satisfy the reliability targets, the objective function is evaluated. The combination associated with a minimum objective is chosen as an "initial anchor point".
d. A new set of combinations is then randomly chosen within a circular neighborhood around the anchor point. Again, for those combinations which satisfy the reliability targets, the objective function is evaluated and compared with the value of the function at the anchor point. Should one of the combinations lead to lower objective that combination becomes the new anchor point.
e. The process is repeated until all combinations within the circular neighborhood show objective functions greater or equal than that corresponding to the anchor point.
f. The entire process is repeated from step a), or from a different initial anchor. The final result corresponds to the minimum among the minima obtained for each of the repetitions.

This process does not require the calculation of gradients, avoiding numerical problems. The calculation of the implied reliabilities, for each combination of the design parameters, is made efficient by the use of the neural networks, as previously described. The optimization process is illustrated in Figure 5.

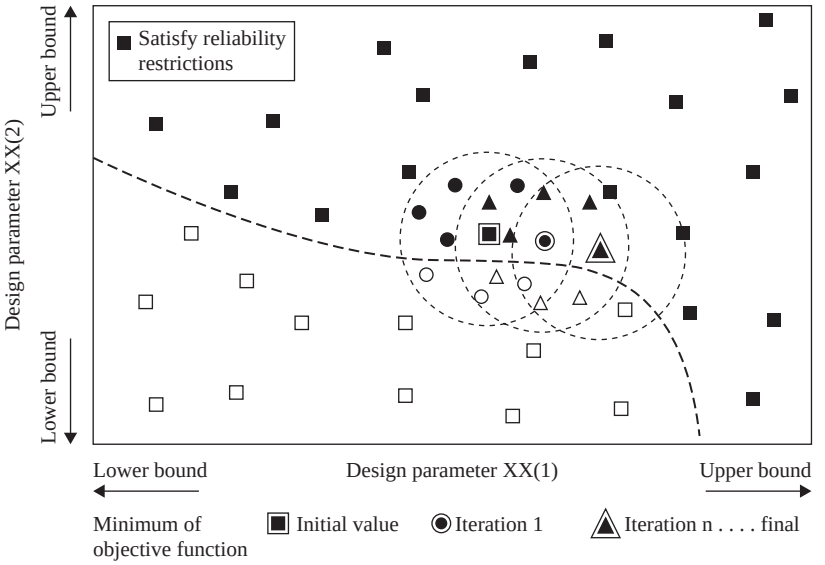

Figure 5 Optimization Process.

5 Applications

5.1 *Optimizing beam and column depths, with the objective of minimum volume*

In this first application, the design parameters are the mean depths of the beams, h_b and the columns h_c, for the frame considered and remaining statistics as shown in Table 2. The design parameters are then as shown in Table 3.

The objective function F to be minimized is the mean volume of the frame, according to:

$$\begin{aligned} Vol &= V_{beams} + V_{columns} \\ F(X_i) &= [\overline{X}(1)\ \overline{X}(2)\ \overline{X}(3)\ \overline{X}(6)\ \overline{X}(7)\ 0.9 \\ &\quad + (150 + 270\ \overline{X}(1))(1 + \overline{X}(2))\ \overline{X}(8)\ \overline{X}(9)]\ 10^{-6}\, m^3 \\ F(d_k) &= [145800 \cdot \overline{X}(7) + 212400 \cdot \overline{X}(9)]\ 10^{-6}\, m^3 \end{aligned} \tag{28}$$

The target minimum annual exceedence probabilities Pf_{annual}, for each performance level, is shown in Table 4. This table also shows the corresponding exceedence probabilities and reliability indices for the seismic event, Pf_E and β_E.

The results of the optimization are shown in Table 5. This table includes the results from three optimization cycles, with final results taken as those of the third cycle. The reliability indices were deemed to satisfy the requirements if they were not less than 0.97 of the targets.

Table 3 Application 1, design parameters.

	$\overline{X}$	σ_X	*Type*
$X(7) = h_b = d_1$	? *cm*	0.05 $\overline{X}$	Normal
$X(9) = h_c = d_2$	? *cm*	0.05 $\overline{X}$	Normal
$X(10) = \rho_{s,\,span}$	0.008	0.0008	Lognormal
$X(11) = \rho'_{s,\,end}$	0.012	0.0012	Lognormal
$X(12) = \rho_s$	0020	0.0020	Lognormal

Table 4 Target minimum reliability levels.

Performance Level	Pf_{annual}	β_{annual}	Pf_E	β_E
Operational	2×10^{-2}	2.054	0.10101	1.276
Life safety	2×10^{-3}	2.878	0.10010×10^{-1}	2.326
Collapse	7×10^{-4}	3.195	0.35012×10^{-2}	2.697

Table 5 Application 1, optimum design parameters.

Cycle	h_b (*cm*)	h_c (*cm*)	*Vol* (m^3)	β_1	β_2	β_3
1	55.1	51.8	19.109	1.310	2.259	2.658
2	56.5	50.7	19.054	1.315	2.257	2.649
3	56.4	50.9	19.030	1.315	2.258	2.651

Each cycle correspond to a different initial random selection. The results from Table 5 show that the three cycles gave very similar optimum dimensions, and, therefore, very similar total volume. This is interpreted as showing that the problem has a single minimum within the prescribed bounds for the design parameters.

5.2 *Optimizing the steel reinforcement, with the objective of minimum steel weight*

In this second application, the objective is to obtain an optimum longitudinal steel reinforcement ratio in order to achieve a minimum steel weight. The design parameters are as shown in Table 6. The frame is the same as in Application 1, with the remaining intervening variables as per Table 2.

The objective function F is the longitudinal steel reinforcement weight, according to:

$$
\begin{aligned}
P &= [V_{beams}(\rho_{s,span} + 0.6\,\rho'_{s,end}) + V_{columns}\ \rho_s]\ 7.85 \cdot 10^{-5}\ KN \\
F(X_i) &= [\overline{X}(1)\ \overline{X}(2)\ \overline{X}(3)\ \overline{X}(6)\ \overline{X}(7)\ 0.9\ (\overline{X}(10) + 0.6\,\overline{X}(11)) \\
&\quad + (150 + 270\ \overline{X}(1))(1 + \overline{X}(2))\ \overline{X}(8)\ \overline{X}(9)\ \overline{X}(12)]\ 10^{-6}\ 7.85 \cdot 10^{-5}\ KN \\
F(d_k) &= [8.019(\overline{X}(10) + 0.6\,\overline{X}(11)) + 12.744\ \overline{X}(12)]\ 7.85 \cdot 10^{-5}\ KN \qquad (29)
\end{aligned}
$$

Table 6 Application 2, design parameters.

Variable	$\overline{X}$	σ_X	*Type*
$X(7) = h_b$	55 *cm*	2.75	Normal
$X(9) = h_c$	60 *cm*	3.00	Normal
$X(10) = \rho_{s,\,span} = d_1$	?	$0.10\,\overline{X}$	Lognormal
$X(11) = \rho'_{s,end} = d_2$	?	$0.10\,\overline{X}$	Lognormal
$X(12) = \rho_s = d_3$	?	$0.10\,\overline{X}$	Lognormal

Table 7 Application 2, optimum design parameters.

Cycle	$\rho_{s,\,span}$	$\rho'_{s,\,end}$	ρ_s	*P*(*KN*)	β_1	β_2	β_3
1	0.005765	0.01132	0.01100	18.91	1.328	2.258	2.628
2	0.006630	0.01053	0.01098	19.13	1.323	2.256	2.636
3	0.006190	0.01079	0.01079	19.14	1.326	2.258	2.634

The minimum target reliabilities are as shown in Table 4. The design parameters must satisfy in this case, additional constraints. The steel reinforcement ratios must provide adequate resistance to gravitational loads, as per Eq. (8), and also provide a minimum ductility for the beam cross-sections, according to

$$0.5\,\rho'_{s,end} \le \rho_{s,span} \le 2\,\rho'_{s,end}$$
$$0.5\,\overline{X}(11) \le \overline{X}(10) \le 2\,\overline{X}(11) \tag{30}$$

The results from three cycles are shown in Table 7, choosing those from the first cycle as the final output. Again, the reliability indices were deemed to satisfy the requirements if they were not less than 0.97 of the targets.

Again, the three cycles used in this example produce very similar results, indicating again the presence of a single minimum. The reinforcement ratios for the columns are almost identical, while cycle 1 and cycle 2 show slight differences between the ratios for the beam at mid-span and over the supports. These differences, however, translate into minor differences in the weight of the steel reinforcement, while the prescribed reliability levels are always satisfied.

5.3 *Optimizing the beam and column depths, and the steel reinforcement, with the objective of minimizing construction cost*

The design parameters are now as shown in Table 8, while the details for the remainder variables are shown in Table 2. The objective is now to minimize the total construction cost.

The objective function F is the direct cost of construction, using $UCC = 288.5\,\text{US\$}/m^3$ as the unit cost of concrete and $USC = 0.80\,\text{US\$}/Kg$ as the unit cost of steel reinforcement.

Table 8 Application 3, design parameters.

Variable	$\overline{X}$	σ_X	*Type*
$X(7) = h_b = d_1$	? *cm*	0.05 $\overline{X}$	Normal
$X(9) = h_c = d_2$	? *cm*	0.05 $\overline{X}$	Normal
$X(10) = \rho_{s,\,span} = d_3$	?	0.10 $\overline{X}$	Lognormal
$X(11) = \rho'_{s,\,end} = d_4$	?	0.10 $\overline{X}$	Lognormal
$X(12) = \rho_s = d_5$	?	0.10 $\overline{X}$	Lognormal

Table 9 Application 3, optimum design parameters.

Cycle	h_b (*cm*)	h_c (*cm*)	$\rho_{s,\,span}$	$\rho'_{s,\,end}$	ρ_s	*C* (US$)	β_1	β_2	β_3
1	56.79	51.36	0.00614	0.00943	0.0188	7445	1.312	2.257	2.655
2	54.84	47.62	0.00733	0.01170	0.0264	7625	1.302	2.259	2.669
3	59.05	53.74	0.00924	0.01310	0.0165	7898	1.328	2.257	2.620

Thus, the total cost is expressed as

$$\begin{aligned} C &= [V_{beams} + V_{columns}]\ UCC + \lfloor P_{beams\ reinfor} + P_{columns\ reinfor} \rfloor\ USC \\ F(d_k) &= [0.1458\ \overline{X}(7) + 0.2124\ \overline{X}(9)]\ UCC \\ &\quad + [0.1458\ \overline{X}(7)\ (\overline{X}(10) + 0.6\,\overline{X}(11)) + 0.2124\ \overline{X}(9)\ \overline{X}(12)]\ 7850\ USC \end{aligned} \tag{31}$$

The target reliabilities are the same as for the previous applications, and the steel reinforcement ratios must also satisfy the same constraints as described by Eq. (8) and (30).

The results, for three cycles, are shown in Table 9. The results for the different cycles are again quite close to each other, and the reliability levels are not less than 0.97 of the targets. The final result is given as that corresponding to the first iteration.

This application, with 5 design parameters, shows clearly that small differences in the design parameters do not result in large cost changes. That is, satisfying all the reliability requirements, the cost function is relatively flat near the optimum values. In this case, the design engineer could opt for one solution or another, considering other construction or architectural issues.

6 Conclusions

- The application of performance-based design within earthquake engineering requires the consideration of all the uncertainties associated with the structure and the ground motion, and that each of the performance requirements be met with specified minimum reliabilities.
- The evaluation of reliability under seismic excitation requires the application of nonlinear dynamic analyses. Thus, the structural response cannot be given an explicit form, and the calculations are made feasible through response surfaces

representation. Of these, neural networks offer an excellent alternative in terms of accuracy and flexibility.

- The major computational effort is transferred to the development of a deterministic response database for neural network training. The networks, acting as a substitute for the nonlinear dynamic analysis, make feasible the reliability estimation through direct Monte Carlo simulation, at a small computational cost.
- Neural networks can be trained for the mean and for the standard deviation of a structural response over a set of ground motions. The input to the networks will then be the remaining random intervening variables.
- The optimization aims at finding a set of design parameters, so that each performance level is met with minimum target reliability, while minimizing an associated objective function. The optimization algorithm used here is a search and does not depend on gradients, and has been shown to be both efficient and robust.
- Three application examples have been shown, all for a 6-story portal frame located in the city of Mendoza, Argentina. The optimization involves the determination of design parameters considering three performance levels and different limit states at each level. Each example involves different design parameters and optimization objectives: depth of beam and columns for a minimum volume, steel reinforcement ratio for a minimum steel weight, and depth of beams and columns, plus steel reinforcement ratio, for a minimum total construction cost.
- This work has shown that the optimization process can be efficiently implemented when the nonlinear dynamic responses are represented by neural networks, which are then used in a direct simulation for the calculation of reliability levels. The work has also used a simple, robust and gradient-free, optimization algorithm.

Acknowledgements

This work was carried out with the support of the National University of Rosario, Argentina, through the research project 1ING142, "Confiabilidad de sistemas estructurales bajo solicitaciones dinámicas". The support from the project "Neural networks for reliability and performance-based design in earthquake engineering", Natural Sciences and Engineering Research Council of Canada, RGPIN 5882-04, University of British Columbia, Vancouver, Canada, is also gratefully acknowledged.

References

Clough, R.W. & Penzien, J. 1975. Dynamics of Structures. Mc Graw Hill.

FEMA. 1997. NEHRP Guidelines for the seismic rehabilitation of buildings. Report 273. *Buildings Seismic Safety Council.*

Foschi, R., Li, H. & Zhang, J. 2002. Reliability and performance-based design: a computational approach and applications. *Structural safety* 24: 205–218.

Hurtado, J. 2004. Structural Reliability – Statistical Learning Perspectives, Lecture Notes in *Applied and Computational Mechanics*. 17. Springer Verlag.

Mander, J.B., Priestley, M.J.N. & Park, R. 1984. Seismic design of bridge piers, *Research Report 84-2*, *Department of Civil Engineering*, University of Canterbury, New Zealand.

Möller, O. 2001. Metodología para evaluación de la probabilidad de falla de estructuras sismorresistentes y calibración de códigos. *Tesis de Doctorado en Ingeniería*, Universidad Nacional de Rosario.

Möller, O. & Foschi, R. 2003. Reliability evaluation in seismic design: a response surface methodology. *Earthquake Spectra*. 19 (3): 579–603.

Möller, O., Foschi, R., Rubinstein, M. & Quiroz, L. 2006a. Momento-curvatura de secciones de hormigón armado sismorresistentes utilizando redes neuronales. *Mecánica Computacional* XXV:2145–2162. AMCA.

Möller, O., Foschi, R., Rubinstein, M. & Quiroz, L. 2006b. Vulnerabilidad sísmica de estructuras: una aproximación probabilística usando redes neuronales. *Memorias XIX Jornadas Argentinas de Ingeniería Estructural*, CD, 050, AIE.

Park, Y.J. & Ang, A.H-S. 1985. Mechanistic seismic damage model for reinforced concrete. *Journal of Structural Engineering*. ASCE. 111 (ST4):722–739.

Priestley, M.J.N. 1998. Brief comments on elastic flexibility of reinforced concrete frames and significance to seismic design. *Bulletin of the New Zealand National Society for Earthquake Engineering*.3 N° 4.

SEAOC Vision 2000 Committee. 1995. Performance based seismic engineering of buildings. *Structural Engineers Association of California, Sacramento, California*, USA.

Shinozuka, M. & Sato, Y. 1967. Simulation of nonstationary random processes. ASCE *Journal of Engineering Mechanics*, 93(1): 11–40.

Zhang, J. 2003. Performance-based seismic design using designed experiments and neural networks. *PhD. Thesis*, Department of Civil Engineering, University of British Columbia, Canada.

Zhang, J. & Foschi, R.O. 2004. Performance-based design and seismic reliability analysis using designed experiment and neural networks. *Probabilistic Engineering Mechanics*. 19: 259–267.

Chapter 35

A very efficient computational procedure for the reliability-based optimization of uncertain stochastic linear dynamical systems

Hector A. Jensen

Santa Maria University, Valparaiso, Chile

Marcos A. Valdebenito

University of Innsbruck, Innsbruck, Austria

ABSTRACT: A very efficient methodology to carry out reliability-based optimization of linear systems with random structural parameters and random excitation is presented. The reliability-based optimization problem is formulated as the minimization of an objective function for a specified failure probability. The probability that design conditions are satisfied within a given time interval is used as a measure of the system reliability. Approximation concepts are used to construct high quality approximations of dynamic responses in terms of the design variables and uncertain structural parameters during the optimal design process. The approximations are combined with an efficient simulation technique to generate explicit approximations of reliability measures with respect to the design variables. In particular, an efficient importance sampling technique is used to estimate the failure probability. The effectiveness and feasibility of the suggested approach is demonstrated by an example problem. At the same time the effect of uncertainty in the system parameters on the performance and reliability of the final design is investigated.

1 Introduction

When a structure is being designed the environmental loads that the built structure will experience in its lifetime are highly uncertain. The load time history needed in the dynamic analysis of a structure subject to environmental loads is an uncertain value function, and it is best modeled by a stochastic process (Lin (1995)). Likewise, response predictions are made during design based on structural models whose parameters are uncertain because the properties that will be exhibited by the structure when completed are not known precisely. Probabilistic methods provide the means for incorporating system uncertainties as random variables with a prescribed joint probability density function. Uncertainties in both loading and structural properties can adversely affect the reliability and performance of the structural system. Therefore, it is necessary to consider their effects explicitly during the optimization process to achieve a balance between cost and safety for the optimal design.

In reliability-based structural optimization the constrains are usually reliability requirements with respect to possible failure modes of the structure. Probability that

design conditions are satisfied within a given time period is commonly used as a measure of system reliability. Then, the first excursion probability that any one of the system response functions of interest exceeds in magnitude some specified threshold level within a given time duration need to be estimated. If the structural characteristics are known, conditional first excursion probabilities can be calculated by efficient simulation techniques (Au (2001)). On the other hand, system reliabilities that account for the uncertainty in the system parameters are given by the total probability theorem as particular multidimensional integrals over the space of uncertain parameters. An efficient technique based on the importance sampling technique has been developed recently for the solution of first excursion problems of uncertain linear dynamical systems (Jensen (2007)). From an optimization point of view, reliability-based optimization problems can be characterized as two-level optimization problems. Level one is the overall optimization in the design variables, and level two is the failure estimates. For realistic systems, these estimates completely dominate the total calculation cost. Therefore, the reliability estimates should be evaluated in an efficient manner and the number of response calculations must be as few as possible during the optimization process. It is the purpose of this paper to develop an efficient computational procedure for the reliability-based optimization of uncertain linear stochastic dynamical systems (SDS).

2 Problem formulation

Let the vectors $\{y\}$, y_i, $i=1,\ldots,n_d$, $\{\theta\}$, θ_i, $i=1,\ldots,n_s$ and $\{z\}$, z_i, $i=1,\ldots,n_T$ represent the vector of design variables, uncertain structural parameters, and random variables that specify the stochastic excitation, respectively. The uncertain system parameters $\{\theta\}$ and the random variables $\{z\}$ are modeled using prescribed probability density functions $q(\{\theta\})$ and $p(\{z\})$, respectively. These functions indicate the relative plausibility of the possible values of the uncertain parameters $\{\theta\} \in \Omega_\theta \subset R^{n_s}$ and random variables $\{z\} \in \Omega_z \subset R^{n_T}$, respectively. The structural synthesis problem considered in the present formulation is written as

$$Min\ C(\{y\}) \tag{1}$$

subject to

$$P_F(\{y\}) \leq P_F^{accept}, \quad \{y\} \in Y \tag{2}$$

where $Y \subset R^{n_d}$ is the set that contains the side constraints for the design variables, $C(\{y\})$ is an objective function which is assumed to be an explicit function of the design variables, $P_F(\{y\})$ is the failure probability, and P_F^{accept} is the target system reliability. Then, the problem consists in the determination of a set of design variables that minimizes an objective function for a specified reliability. The failure probability function $P_F(\{y\})$ accounts for the uncertainties in the system parameters as well as the uncertainties in the excitation. The failure probability is given in terms of the probability that some stochastic dynamic responses exceed in magnitude within a specified time interval $[0, T]$ certain critical threshold levels, that is

$$P_F(\{y\}) = P[\{\max_{i=1,\ldots,n_r} \max_{t\in[0,T]} |r_i(t)| \geq r_i^*] \tag{3}$$

where $P[]$ is the probability that the expression in parenthesis is true, $r_i(t),\ i=1,\ldots,n_r$ are the response functions of interest, and $r_i^*,\ i=1,\ldots,n_r$ are the threshold levels. It is clear that the response functions depend on the design $\{y\}$, the particular set of values $\{\theta\}$ of the uncertain system parameters in Ω_θ, and the particular set of values $\{z\}$ of the random variables in Ω_z that may assume, i.e. $r_i(t)=r_i(t,\{y\},\{\theta\},\{z\})$.

3 Mechanical modeling

The general matrix equation of motion for a damped linear structure is given by

$$[M]\{\ddot{x}(t)\}+\{R(\{x(t)\},\{\dot{x}(t)\})\}=[G]\{f(t)\} \tag{4}$$

where $\{x(t)\}$ is the displacement response vector of dimension n, $\{R(\{x(t)\},\{\dot{x}(t)\})\}=[C]\{\dot{x}(t)\}+[K]\{x(t)\}$ is the linear restoring force, $[M]$, $[C]$ and $[K]$ are the mass, damping and stiffness matrices of dimension $n\times n$, $\{f(t)\}$ is the excitation vector of dimension n_f, and $[G]$ is a $n\times n_f$ dimensional matrix that couples the excitation components of the vector $\{f(t)\}$ to the degrees of freedom of the structure. The dynamic response is represented by a linear combination of mode shapes

$$\{x(t)\}=\sum_{r=1}^{n}\{\phi\}_r\eta_r(t) \tag{5}$$

where $\eta_r(t), r=1,\ldots,n$ are the modal responses, and $\{\phi\}_r,\ r=1,\ldots,n$ are the eigenvectors associated with the eigenproblem of the undamped equation of motion. If the system is classically damped, the response $x_i(t)$ (ith component of the displacement vector) can be written as

$$x_i(t)=\sum_{j=1}^{n_f}\int_0^t h_{ij}(t-\tau)f_j(\tau)\,d\tau,\quad h_{ij}(t)=\sum_{r=1}^{n}\frac{\phi_{ir}\{\phi\}_r^T\{g_j\}}{\{\phi\}_r^T[M]\{\phi\}_r}\frac{1}{\omega_{dr}}e^{-\xi_r\omega_r t}\sin(\omega_{dr}t) \tag{6}$$

where $\omega_r,\ r=1,\ldots,n$ are the natural frequencies of the system, $\xi_r,\ r=1,\ldots,n$ are the corresponding damping ratios, $h_{ij}(t)$ is the unit impulse response function for the response function $x_i(t)$ at time t due to a unit impulse applied at the j^{th} input at time 0, $\{g_j\}$ is the jth column of the $[G]$ matrix, and $\omega_{dr}=\omega_r(1-\xi_r^2)^{1/2}$ is the damped frequency. It is noted that Equation 6 can be interpreted as the modal superposition formula for the impulse response functions. Similar expressions can be derived if other response functions are considered. For example, the structural response $r_i(t)$ is written as

$$r_i(t)=\sum_{j=1}^{n_f}\int_0^t h_{ij}(t-\tau)f_j(\tau)\,d\tau \tag{7}$$

where $h_{ij}(t)$ is the corresponding impulse response function for the response function $r_i(t)$ at time t due to a unit impulse applied at the jth input at time 0.

4 Stochastic excitation

The components of the excitation vector $\{f(t)\}$ are modeled as statistically independent stochastic processes defined as filtered white noise. Each component $f_j(t)$ is defined as$f_j(t) = \{\beta\}_j^T \{u(t)\}$, where $\{\beta\}_j$ is a constant vector, and $\{u(t)\}$ denotes the state-vector of the filter which satisfies a first-order differential equation of the form

$$\{\dot{u}(t)\} = [B]_j \{u(t)\} + \{b\}_j e_j(t) \omega_j(t) \tag{8}$$

where $[B]_j$ denotes the system matrix of dimension $n_F \times n_F$, $\{b\}_j$ is the distribution vector of the filter of dimension n_F, $e_j(t)$ is a deterministic modulating time function, and $\omega_j(t)$ is a zero mean Gaussian white noise excitation. Then, the process $f_j(t)$ can be represented as

$$f_j(t) = \int_0^t h_j^F(t-\tau) e_j(\tau) \omega_j(\tau)\, d\tau, \quad h_j^F(t) = \sum_{s=1}^{n_F} \frac{\{\beta\}_j^T \{\psi\}_{sj} \{\chi\}_{sj}^T \{b\}_j}{\{\chi\}_{sj}^T \{\psi\}_{sj}} e^{\lambda_{sj} t} \tag{9}$$

where $h_j^F(t)$ is the unit impulse response function for the process $f_j(t)$ at time t due to a unit impulse applied at time $t = 0$. The vectors $\{\psi\}_{sj}$ and $\{\chi\}_{sj}$, s = 1, ..., n_F are the complex right and left eigenvectors associated with the right and left eigenproblems of Equation 8, and λ_{sj}, $s = 1, \ldots, n_F$ are the corresponding eigenvalues. Using the representation of the process $f_j(t)$ given by Equation 9, the response function $r_i(t)$ in Equation 7 can be written as (Jensen (2005))

$$r_i(t) = \sum_{j=1}^{n_f} \int_0^t h_{ij}^*(t,\tau) e_j(\tau) \omega_j(\tau)\, d\tau, \quad h_{ij}^*(t,\tau) = \int_\tau^t h_{ij}(t-z) h_j^F(z-\tau)\, dz \tag{10}$$

where $h_{ij}^*(t,\tau)$ is the impulse response function for the system response function $r_i(t)$ at time t due to a unit impulse applied at the jth filter at time τ. Integration of Equation 10 provides an explicit expression for the impulse response functions h_{ij}^*, $j = 1, \ldots, n_f$.These functions are given in terms of the spectral properties of the structural system and the eigenvalues and eigenvectors of the filters' state equation. In practical applications, the input-output relationship given by Equation 10 is often written in a discrete manner. Let the sampling be uniform at time spacing $\Delta t = T/(n_T - 1)$ where T is the duration of the excitation, and n_T the number of time points so that the sampling times are $t_k = (k-1)\Delta t, k = 1, \ldots, n_T$. If $\omega_j(t)$ is modeled as a band-limited Gaussian white noise process with spectral density S_j, that is, $\omega_j(t_k) = (2\pi S_j/\Delta t)^{1/2} z_k^j$, where $z_k^j, k = 1, \ldots, n_T$ are independent, identically distributed standard Gaussian random variables, the discrete-time analog of the input-output relationship in Equation 10 can be written as

$$r_i(t_k) = \sum_{j=1}^{n_f} \sum_{l=1}^{k} \varepsilon_l h_{ij}^*(t_k - t_l) e_j(t_l) \sqrt{2\pi S_j\, \Delta t}\, z_l^j \tag{11}$$

where ε_l is a coefficient that depends on the particular numerical integration scheme used in the evaluation of the convolution integral.

5 Reliability estimation

From the discrete representation of the response functions given in Equation 11, the first excursion problem 3 can be formulated as

$$P_F(\{y\}) = P\left(\bigcup_{i=1}^{n_r}\bigcup_{k=1}^{n_T} |r_i(t_k)| \geq r_i^*\right) = P\left(\bigcup_{i=1}^{n_r}\bigcup_{k=1}^{n_T} F_{ik}\right) \tag{12}$$

where F_{ik} is the conditional elementary failure event that the response $r_i(t)$ at time t_k exceeds in magnitude the threshold level r_i^*. This equation indicates that the probability of failure is given as the probability of the union of a number of elementary failure elements. Then, it is seen that the evaluation of the probability of failure corresponds to a reliability problem of a series system of $n_r \times n_T$ conditional failure elements. Using the linear relations between input and response in terms of the Gaussian random variables $\{z^j\}$, z_i^j, $i=1, \ldots, n_T$, the nearest points to the origin in the standard normal space can be established in a straightforward manner which define uniquely the elementary failure regions F_{ik}, $i=1, \ldots, n_r$, $k=1, \ldots, n_T$. The interaction of the elementary failure events F_{ik} in forming the first excursion failure event is considered by an importance sampling technique (Ang (1992)). In particular, a methodology based on the techniques proposed in references (Au (2001), Jensen (2007)) is adopted in the present formulation. In the reference (Au (2001)) a very efficient importance sampling technique was developed for estimating first excursion probabilities of linear dynamical systems with deterministic structural parameters. The technique was then extended for the case of linear dynamical systems with uncertain structural parameters in reference (Jensen (2007)). The details of the procedures as well as the evaluation of their efficiencies can be found in such references.

6 Approximation concepts

The computation of the failure probability function $P_F(\{y\})$ has to be carried out repeatedly during the optimization process. From the previous formulation it is clear that the estimator of the failure probability is completely determined by the impulse response functions h_{ij}^*, $i=1, \ldots, n_r$, $j=1, \ldots, n_f$. At the same time, the impulse response functions depend on the mode shapes $\{\phi\}_r$, $r=1, \ldots, n$, and the natural frequencies ω_r, $r=1, \ldots, n$. These quantities are implicit functions of the vector of design variables $\{y\}$ and the vector of uncertain structural parameters $\{\theta\}$, and they are available only in a numerical way. For systems of practical interest the repeated evaluation of these quantities can be very costly in terms of computational resources. Hence, in order to increase the efficiency of the implementation an approximation strategy is introduced here.

6.1 *Approximate system responses*

The system responses $r_i(t)$, $i=1, \ldots, n_r$ are characterized in terms of the spectral properties of the structural system. These quantities are approximated with respect

to the design variables and uncertain structural parameters. For example the frequency ω_r is approximated about a particular set of values $\{y^*\},\ y_i^*,\ i=1,\ \ldots,n_d$, and $\{\theta^*\},\ \theta_i^*,\ i=1,\ \ldots,n_s$ of the set of design variables and uncertain structural parameters, respectively, as

$$\tilde{\omega}_r(\{y\},\ \{\theta\}) = \omega_r(\{y^*\},\ \{\theta^*\}) + \sum_{i=1}^{n_d} \frac{\partial \omega_r(\{y^*\},\{\theta^*\})}{\partial y_i} B^i_{\omega_r}(y_i,\ y_i^*) + \sum_{i=1}^{n_s} \frac{\partial \omega_r(\{y^*\},\ \{\theta^*\})}{\partial \theta_i} B^i_{\omega_r}(\theta_i, \theta_i^*) \tag{13}$$

where $B^i_{\omega_r}(y_i,\ y_i^*)$ and $B^i_{\omega_r}(\theta_i,\ \theta_i^*)$ are operators that define the type of approximation for the components y_i and θ_i, respectively. For instance, if $B^i_{\omega}(y_i,\ y_i^*) = y_i - y_i^*$ the quantity is approximated as a linear function of the design variable y_i. A similar approximation is used for the other quantities. It is noted that the evaluation of the partial derivatives used in the approximations requires a classical eigenvalue-eigenvector sensitivity analysis at the point $(\{y^*\},\{\theta^*\})$. An efficient procedure for determining eigenvector derivatives is used in this implementation (Nelson (1976)). Using the earlier approximations of the spectral quantities in the expression of the unit impulse response functions $h^*_{ij},\ i=1,\ \ldots,n_r,\ j=1,\ \ldots,n_f$, equation 11 can be written as

$$\tilde{r}_i(t_k) = \sum_{j=1}^{n_f} \sum_{l=1}^{k} \varepsilon_l \tilde{h}^*_{ij}(t_k - t_l) e_j(t_l) \sqrt{2\pi S_j\, \Delta t}\, z_l^j \tag{14}$$

where $\tilde{h}^*_{ij}$ represents the approximation of h^*_{ij}. Equation 14 provides an explicit approximation of the response process r_i in terms of the design variables $\{y\}$ and uncertain structural parameters $\{\theta\}$. Note that the characterization of the approximate response functions $\tilde{r}_i,\ i=1,\ \ldots,n_r$ requires only one dynamic analysis at the point $(\{y^*\},\ \{\theta^*\})$ (eigenvalue-eigenvector sensitivity analysis).

6.2 *Approximate failure probabilities*

The computational efficiency of the design process is further increased by approximating the failure probability function locally. The probability of failure $P_F(\{y\})$ is approximated locally about a point $\{y^*\}$ as

$$\tilde{P}_F(\{y\}) = \exp(H(\{y\},\ \{y^*\})) \tag{15}$$

where $H(\{y\},\{y^*\})$ is a multivariable polynomial function, and $\{y^*\}$ is a point in the design space (Gasser (1997), Jensen (2005)). A simple linear expansion for the multivariable polynomial function is used in the present implementation, that is $H(\{y\},\ \{y^*\}) = \lambda_0 + \{\lambda\}^T(\{y\} - \{y^*\})$. The polynomial coefficients are obtained by considering an augmented reliability problem where the design variables $y_i i=1,\ldots,n_d$ are artificially considered as uncertain with independent components uniformly distributed. Let $\kappa(\{y\}) = \prod_{i=1}^{n_d} \kappa_i(y_i)$ be the uniform joint probability density function of the design variables and $\kappa_i(y_i)$ the one dimensional uniform density function of y_i. The

probability density function $\kappa(\{y\})$ is defined in the vicinity of the design point $\{y^*\}$, that is, $\Omega_{\{y^*\}}$. The coefficients of the expansion are determined by solving a set of non-linear equations which is defined by considering some statistics of the augmented reliability problem. In particular, the average failure probability $P_F^{average}$ and the first moments of area $m_{P_F}^i,\ i=1,\ldots,n_d$ of the failure probability function $P_F(\{y\})$ over the space $\Omega_{\{y^*\}}$ are given by

$$P_F^{average} = \int_{\Omega_{\{y*\}}} P_F(\{y\})\kappa(\{y\})d(\{y\})$$
$$m_{P_F}^i = \int_{\Omega_{\{y*\}}} y_i P_F(\{y\})\kappa(\{y\})d(\{y\}), \quad i=1,\ldots,n_d \tag{16}$$

Substituting the expression of the approximate failure probability function $\tilde{P}_F(\{y\})$ yields a set of algebraic non-linear equations for the polynomial coefficients (Valdebenito (2007)). The estimates of $P_F^{average}$ and $m_{P_F}^i,\ i=1,\ldots,n_d$ are carried out by the simulation strategy proposed in (Jensen (2007)).

7 Design process

The solution of the stochastic optimization problem proceeds by transforming it into a sequence of explicit approximate subproblems having a simple explicit algebraic structure. Using the characterization of the failure probability function given en Equation 15 the following approximate reliability-based optimization problem is generated

$$Min\ C(\{y\}) \tag{17}$$

subject to

$$\tilde{P}_F^k(\{y\}) \leq P_F^{accept}, \quad \{y\} \in Y^k \tag{18}$$

where Y^k is a domain in the vicinity of the current design where the approximation of the failure probability function is expected to yield reasonable results. The set Y^k is changed at each design cycle in order to protect the quality of the approximations. The actual optimization procedure applied to the sub-problems is executed without any dynamic response calculation and reliability analysis, respectively. Therefore, the solution of the sub-problems can be obtained in an efficient manner by applying any nonlinear optimization algorithm. As previously pointed out, the approximate failure probability function $\tilde{P}_F^k(\{y\})$ is obtained by solving a set of non-linear equations which in turns implies the estimation of $P_F^{average}$ and $m_{P_F}^i,\ i=1,\ldots,n_d$. These estimates are computed using the local approximations of the system responses about the current design $\{y\}^k$ and a particular set of values $\{\theta\}_{ref}$ of the set of uncertain structural parameters. Then, the characterization of the approximate failure probability function $\tilde{P}_F^k(\{y\})$ requires just one dynamic analysis (eigenvalue-eigenvector sensitivity analysis at the point $(\{y\}^k,\ \{\theta\}_{ref})$). The specification of $\{\theta\}_{ref}$, which is called the reference point, is discussed in the following section. The new design, obtained by the solution of the

approximate optimization problem given in equations 17 and 18, is used as the current design for the next design cycle. The process is continued until some convergence criterion is satisfied.

8 Implementation issues

For a given design $\{y\}$ the reference point is selected as the most probable value of the uncertain structural parameters given that failure has occurred, that is,

$$\{\theta\}_{ref} = E_{q|F}(\{\theta\}) = \int_{\Omega_\theta} \{\theta\} q(\{\theta\}/F)\, d\{\theta\} \tag{19}$$

where $q(\{\theta\}/F)$ denotes the distribution of the uncertain structural parameters given that failure has occurred. By using the Bayes' Theorem it can be shown that the reference point corresponds to the centroid of the integrand function $P_F(\{\theta\})q(\{\theta\})$ of the failure probability integral

$$\int_{\Omega_\theta} P_F(\{\theta\}) q(\{\theta\}\, d\{\theta\} \tag{20}$$

where $P_F(\{\theta\})$ is the conditional failure probability function for a given value of the set of uncertain system parameters $\{\theta\}$. Then, it is expected that the main contribution to the failure probability, in terms of the uncertain structural parameters, comes from a domain in the neighborhood of $\{\theta\}_{ref}$. Based on this observation, it is reasonable to approximate the response functions about this point since the approximations are very accurate in the vicinity of the point where the approximations are constructed. For an efficient estimation of the reference point during the optimization process the design variables are, as before, artificially considered as uncertain. At the kth design cycle the reference point is estimated as

$$\{\theta\}_{ref}^{k} \approx \frac{1}{P_F^{average}} \frac{2}{N_s} \sum_{r=1}^{N_s} \{\theta\}_r \frac{q(\{\theta\}_r)}{\varphi(\{\theta\}_r)} \frac{\sum_{i=1}^{n_r} \sum_{k=1}^{n_T} \Phi(-\beta_{ik}(\{y\}_r, \{\theta\}_r))}{\sum_{i=1}^{n_r} \sum_{k=1}^{n_T} \prod_{F_{ik}}(\{y\}_r, \{\theta\}_r, \{z\}_r)} \tag{21}$$

where N_s is the number of samples, $\Phi(\cdot)$ is the cumulative distribution function of the standard Gaussian distribution, $\beta_{ik}(\{y\}, \{\theta\})$ is the reliability index evaluated at the design $\{y\}$ and a particular set of values $\{\theta\}$, and $\prod(\cdot,\cdot,\cdot)$ is the indicator function. The $\{y\}_r$ and $\{z\}_r$ samples are simulated according to the probability density function κ and the importance sampling density proposed in (Au (2001)), respectively. On the other hand, the $\{\theta\}_r$ samples are obtained from the importance sampling density φ which is defined as the original probability density function of the uncertain structural parameters q with most probable value equal to the reference point from the previous design cycle, i.e. $\{\theta\}_{ref}^{k-1}$. It is noted that the same samples used to estimate the average failure probability $P_F^{average}$ and the first moments of area $m_{P_F}^i$, $i = 1, \ldots, n_d$ of the failure probability function can be used to estimate the reference point in Equation 21. Therefore, the estimation of such point is carried out in an efficient manner with a minimum additional computational cost. In summary, each design cycle of

the optimization process involves the approximation of the failure probability function in terms of the design variables (Equation 15), the estimation of the reference point (Equation 21), and the solution of the corresponding approximate optimization problem (Equations 17 and 18). The approximation of the failure probability function requires the estimation of the average failure probability $P_F^{average}$, and the first moments of area $m_{P_F}^i$, $i = 1, \ldots, n_d$ of the failure probability function. Such estimations are computed using local approximations of the system responses which in turns imply one eigenvalue-eigenvector sensitivity analysis at the current design and at a particular set of values of the set of uncertain structural parameters (reference point from the previous design cycle). On the other hand, the estimation of the reference point for the current design cycle (to be used in the next iteration) is immediate since the same information used for the estimation of the average and first moments of area of the failure probability function can be used in Equation 21. In this manner, each design cycle requires only one dynamic analysis and the information gathered during the optimization process is utilized in a cumulative manner.

9 Example

A six story reinforced concrete building under stochastic earthquake excitation is considered as an example problem. A top view of the building is shown in Figure 1. Each of the six floors is supported by 64 columns of square cross-section. All floors have a constant height and equal to 3.5 m leading a total height of 21.0 m. It is assumed that each floor may be represented sufficiently accurate as rigid within the $x - y$ plane when compared with the flexibility of the columns. Hence, each floor can be represented by just three degrees of freedom, i.e. two translatory displacements and a rotational displacement. The total mass of the first five floors is given by 1.3×10^6 kg and the mass of the sixth floor is equal to 0.72×10^6 kg. A Young's modulus $E = 3.0 \times 10^{10}$ N/m^2 is considered in this case. A classical damping is assumed in the model so that the modes have 5% of critical damping ($\xi = 0.05$). The Young's modulus E and the damping ratio ξ are assumed to be uncertain and they are modeled by independent Gaussian random variables with coefficient of variation equal to 25% and 40%, respectively. The building is excited horizontally by earthquake excitation $a(t)$ in the y direction.

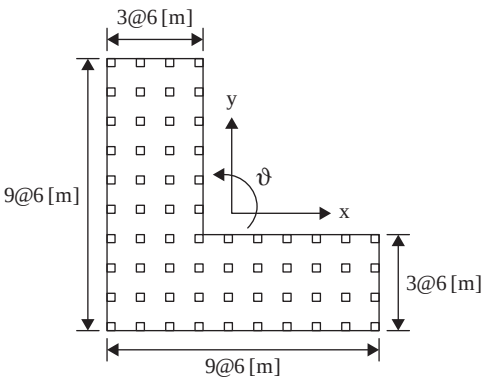

Figure 1 Six-story building. Floor plan.

The acceleration is modeled as stochastic process defined as filtered white noise. With respect to Equation 8,

$$\{\beta\}^T = < \omega_{1g}^2 \; 2\xi_{1g}\omega_{1g} \; -\omega_{2g}^2 \; -2\xi_{2g}\omega_{2g} >, \quad \{b\}^T = < 0 \; 1 \; 0 \; 0 > \tag{22}$$

$$[B] = \begin{bmatrix} 0 & 1 & 0 & 0 \\ -\omega_{1g}^2 & -2\xi_{1g}\omega_{1g} & 0 & 0 \\ 0 & 0 & 0 & 1 \\ \omega_{1g}^2 & 2\xi_{1g}\omega_{1g} & -\omega_{2g}^2 & -2\xi_{2g}\omega_{2g} \end{bmatrix} \tag{23}$$

with envelope function

$$e(t) = \begin{cases} (t/4)^2 & if \; t \le 4s \\ 1 & if \; 4 \le t \le 10s \\ \exp(-0.2(t-10) & if \; 10 \le t \le 15s \end{cases} \tag{24}$$

The values $\omega_{1g} = 15.6$ rad/s, $\xi_{1g} = 0.6$, $\omega_{2g} = 1.0$, rad/s, $\xi_{2g} = 0.9$, and white noise spectral intensity $S = 0.001\,\text{m}^2/\text{s}^3$ are used in this application. The sampling interval is assumed to be $\Delta t = 0.05$ s and the duration of the excitation is $T = 15$ s. The total number of time points, and hence the number of input random variables $\{z\}$ in the discrete representation of the excitation is thus $n_T = 301$.

A deterministic objective function is chosen for the optimization problem, and it corresponds to the total volume of the column elements. To control serviceability and minor damage, the design criterion considered in this example problem is defined in terms of the interstory drift ratio in the x and y direction over all stories of the building, and the relative rotation between consecutive floors. Therefore, the number of response functions involved in the problem is 18 and the system failure event F is defined as

$$F = \bigcup_{i=1}^{18} \bigcup_{k=1}^{301} \{|r_i(t)| > r_i^*\} = \bigcup_{i=1}^{18} \bigcup_{k=1}^{301} F_{ik} \tag{25}$$

where the upper bound values are chosen to be 0.2% of the story height for the interstory drift ratio, and 0.0029% of the story high for the relative rotation. These levels of response are related to low level vibration where the structural response is expected to be dominated by linear elastic behavior. Therefore, the use of the linear model considered in this work is adequate for the current example problem. The design constraint for the optimization problem is written as $P_F \le 10^{-3}$. The design variables are the dimensions of the square cross section of the column elements. Over the height of the building, the columns have six different cross-sections with initial design $y_1 = 0.90$ m, $i = 1, \ldots, 6$ and side constraints $0.50 \le y_i \le 1.60$ m. The final design of the structure using deterministic and uncertain structural parameters is given in Table 1. The probabilities of failure have been estimated with a coefficient of variation of 15% in this case. The corresponding iteration history of the design process in terms of the volume of the column elements is shown in Figure 2. A variable move limit strategy in which all design variables are initially assigned the same move limit value is adopted in this application. As the design process progresses and the optimum is approached the initial move limit value of 30% (percentage of the current design point) is continually reduced

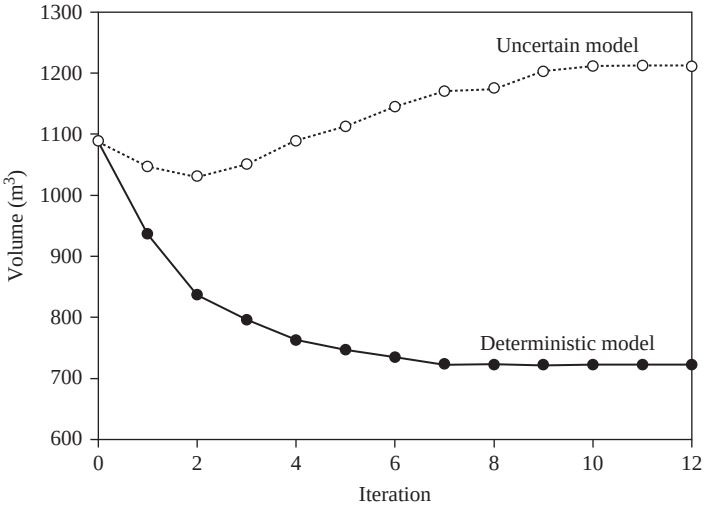

Figure 2 Iteration history in terms of the volume of the column elements.

as the approximations become more critical for convergence. The last iterations are performed with a move limit of 5%. The convergence criterion is defined in terms of the relative change of the objective function between two consecutive iterations (1% in this implementation). The optimization process converges in about 10 design cycles for the case of deterministic structural parameters and in 12 iterations when the parameters are uncertain. The fast convergence leads to a small number of dynamic analyses to be performed during the optimization process. For example, in the case of uncertain structural parameters, only 12 system dynamic analyses are required to obtain the final design by the proposed approach whereas 167000 analyses are required in the direct case. This number is less than 0.02% of the total number of analyses to be performed in the exact case. In this context the exact case solution corresponds to the final design obtained when the system dynamic analyses are evaluated directly for every change of the design variables during the optimization process. The main difference between the approximate and direct solution is in the number of dynamic analyses required for convergence since it was found that both solutions are almost identical.

From Table 1 it is observed that the dimensions of the column elements at the final design of the system with uncertain structural parameters are greater than the corresponding components of the model with deterministic parameters. The volume of the uncertain model increases in about 67% with respect to the volume of the deterministic system. Then, the effect of the uncertainty in the system parameters on the final design is significant. The importance of considering the effects of uncertainty in the structural parameters during the design process can also be illustrated from a constraint violation point of view. The probability of failure of the deterministic model at the initial design is given by 9.90×10^{-7}, and therefore this design is feasible. On the contrary, the initial design of the uncertain system is infeasible since it has a probability of failure equal to 1.45×10^{-2}. The effect of the uncertain system parameters is also evident during the optimization process. For example, the failure probability of the final design obtained

Table 1 Final designs.

		Final design	
Design variables	*Initial design*	*Deterministic model*	*Uncertain model*
y_1 (m)	0.90	0.83	1.06
y_2 (m)	0.90	0.79	1.03
y_3 (m)	0.90	0.77	1.03
y_4 (m)	0.90	0.73	0.95
y_5 (m)	0.90	0.67	0.86
y_6 (m)	0.90	0.57	0.70
Objective function (m^3)	1089	723	1211
Normalized Probability of Failure P_F/P_F^{accept}		50.0*	0.90*
Number of Dynamic analyses		10	12

*considering uncertainties in structural parameters

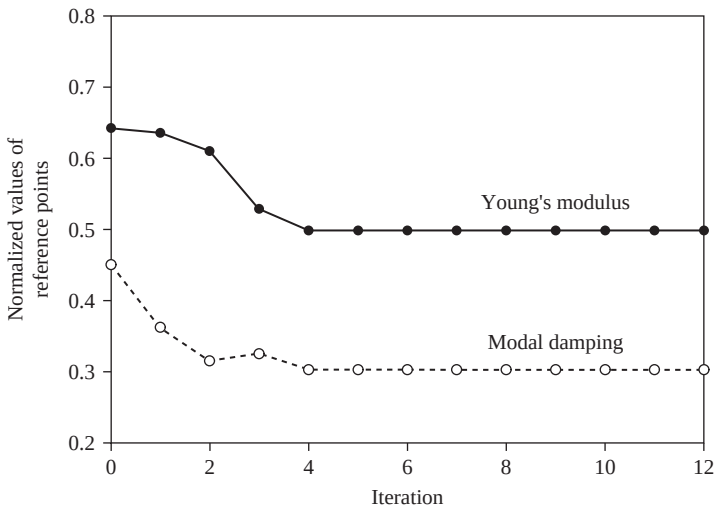

Figure 3 Evolution of reference points.

with deterministic structural properties is 50 times the value of the target failure probability when the uncertainty in the system parameters is considered. Therefore, this design is not even feasible. These results indicate the importance of considering the effect of system parameter uncertainty explicitly during the design process.

As previously pointed out the efficiency of the proposed method depends, among other things, on the selection of the reference point. It is found that the values of the reference points corresponding to the uncertain system parameters ξ (modal damping) and E (Young's modulus) show an important change during the design process. Figure 3 shows the evolution of the values of the reference points during the optimization process.

The values are normalized by their most probable values, i.e. $\bar{\xi} = 0.05$ and $\bar{E} = 3.0 \times 10^{10}\,\mathrm{N/m^2}$. It is seen that the values of the reference points change significantly during the optimization process. At each design cycle, the most probable value of the system parameters ξ and E, given that failure has occurred, is determined by the proposed approach. At the final design the value of the reference point is equal to $(0.3\bar{\xi},\ 0.5\bar{E})$. This result indicates that the most probable value of the system parameters ξ and E, given that failure has occurred with probability 10^{-3}, is substantially different from their most probable values. Then, the main contribution to the probability of failure, in terms of the uncertainty of the damping ratio and Young's modulus, comes from a domain in the vicinity of $(0.3\bar{\xi},\ 0.5\bar{E})$. From these results it is clear that the approximations of the response functions in terms of the uncertain system parameters should be expanded about the reference points and not about their most probable values.

10 Conclusions

A methodology based on approximation concepts for efficient solution of reliability-based optimization problems of uncertain linear systems subject to stochastic loading has been presented. The reduction of the computational effort required for reliability estimation and reliability sensitivity during the optimization procedure is crucial. This is achieved by application of approximation concepts which are used to approximate the system responses and failure probability functions. The system responses are approximated in terms of the design variables and uncertain system parameters while the failure probability functions are approximated with respect to the design variables. The proposed procedure dramatically reduces the number of exact dynamic analyses as well as reliability estimations required during the design process. This is essential especially for large complex systems since the computational efforts are reduced considerably in those cases. Thus, the proposed implementation is expected to be useful in the reliability-based optimal design of real structural systems. Numerical results show that uncertainty in the structural parameters may cause significant changes in the performance and reliability of linear systems subject to stochastic loading. In these situations the uncertainty in the specification of the structural properties should be properly accounted for during the design process.

Acknowledgments

The research reported here was supported in part by CONICYT under grant number 1070903 and the Austrian Science Fund (FWF) under contract number P17459-N13 which are gratefully acknowledged by the authors.

References

Ang, G.L., Ang, H.S. & Tang, W.H. 1992. Optimal Importance Sampling Density Estimator. *Journal of Engineering Mechanics*. Vol. 118:1146–1163.

Au, S.K. & Beck, J.L. 2001. First Excursion Probabilities for Linear Systems by very Efficient Importance Sampling. *Probabilistic Engineering Mechanics*. Vol. 16:193–20.

Au, S.K. 2004. Probabilistic Failure Analysis by Importance Sampling Markov Chain Simulation. *Journal of Engineering Mechanics*. Vol. 103:303–311.

Gasser, M. & Schuëller, G.I. 1997. Reliability-Based Optimization of Structural Systems. *Mathematical Methods of Operational Research*. Vol. 46:287–307.

Lin, Y.K. & Cai, C.Q. 1995. *Probabilistic Structural Dynamic: Advance Theory and Applications*. New York, McGraw-Hill.

Jensen, H.A. & Valdebenito, M.A. 2007. Reliability Analysis of Linear Dynamical Systems using Approximate Representations of Performance Functions. *Structural Safety.* Vol. 29:222–237.

Jensen, H.A. 2005. Design and Sensitivity Analysis of Dynamical Systems Subjected to Stochastic Loading. *Computers and Structures*, Vol. 83:1062–1075.

Nelson, R.B. 1976. Simplified Calculation of Eigenvector Derivatives. *AIAA Journal*. Vol 14:1201–1205.

Valdebenito, M.A. & Schuëller, G.I. 2007. Reliability Based Optimization using a Decoupling Approach and Reliability Approximations. *In Proceedings: 6th International Congress on Industrial and Applied Mathematics (ICIAM)*. Zurich, Switzerland, July 2007.

References

ABAQUS. 2003. Analysis user's manual, Version 6.4, ABAQUS Inc., USA.

Abraham, R., Marsden, J.E. 1978. Foundations of Mechanics. Reading, Mass.: Benjamin/ Cummings.

Adan, S.M. 2006. Reduced beam section moment connections without continuity plates. Ph.D. Dissertation, University of Utah, Salt Lake City, Utah.

Adan, S.M., Gibb, W. 2006. Cyclic behavior of the Kaiser bolted bracket steel moment-resisting connection. Technical Report, KPFF Consulting Engineers, Seattle, Washington.

Agha. G. 1984. Actors: A Model of Concurrent Computation in Distributed Systems. MIT Press.

Ahmed, K.A., Kanda, J., Iwasaki, R. 1996. Estimation of uncertainties in the dynamic response of urban soils in Japan. In Proceedings of the Eleventh World Conference on Earthquake Engineering, Rotterdam. Elsevier Science.

Aiken, I. 1996. Passive energy dissipation hardware and applications. Proceedings, Lo Angeles County and Seaosc Symposium on Passive Energy Dissipation Systems for New and Existing Buildings, Los Angeles.

Akaike, H. 1974. A new look at the statistical identification model, IEEE Transactions on Automatic Control, 19, 716–723.

Allahabadi, R., Powell, G.H., Drain-2DX user guide, University of California at Berkeley. 1988.

American Institute of Steel Construction. 1999. Steel Design Guide Series 12 – Modification of existing welded steel moment frame connections for seismic resistance, Chicago, Illinois.

American Institute of Steel Construction. 2005. Seismic Provisions for Structural Steel Buildings. Chicago, Illinois.

American Institute of Steel Construction. 2005. Specification for Structural Steel Buildings. Chicago, Illinois.

American Institute of Steel Construction. 2006. Prequalified Connections for Special and Intermediate Steel Moment Frames for Seismic Applications. Chicago, Illinois.

American Welding Society. 2006. Structural Welding Code Steel, ANSI/AWS D1.1:12006. Miami, Florida.

Ang, G.L., Ang, H.S., Tang, W.H. 1992. Optimal Importance Sampling Density Estimator. Journal of

Ansal, A., Durukal, E., Tönük, G. 2006a. Selection and Scaling of Real Acceleration Time Histories for Site Response Analyses. Proc. of ISSMGE ETC12 Workshop, Athens, Greece.

Ansal, A., Tönük, G., Demircioglu, M., Bayrakli, Y., Sesetyan, K., Erdik, M. 2006b. Ground Motion Parameters for Vulnerability Assessment. Proceedings of the First European Conference on Earthquake Engineering and Seismology, Geneva, Paper Number: 1790.

Ansal, A., Özaydin, K., Erdik, M., Yildirim, M., Kiliç, H., Adatepe, S., Özener, P.T., Tonaroglu, M., Sesetyan, K., Demircioglu, M. 2005. Seismic Microzonation for Urban Planning and Vulnerability Assessment. Proceedings of the International Symposium of Earthquake Engineering (ISEE2005), Geotechnical Session, Awaji Island, Japan.

ANSYS. 2005. User Manual Version 9.0. ANSYS, Inc., Canonsburg, Pennsylvania.
Antman, S.S. 1991. Nonlinear Problems of Elasticity, Springer-Verlag, 1991.
Antoniou, S., Pinho, R. 2004. Advantages and Limitations of Adaptive and Non-adaptive Force-Based Pushover Procedures, Journal of Earthquake Engineering, 8(4), 497–522.
Applied Technology Council. 1992. Guidelines for the Cyclic Seismic Testing of Components of Steel Structures. Publication No. 24, Redwood City, California.
Armero, F. 2000. On the locking and stability of finite elements in finite deformation plane strain problems, Computers, Structures, 75: 261–290.
Armero, F. 2006. Energy-dissipative momentum-conserving time-stepping algorithms for finite strain multiplicative plasticity, Comp. Meth. Appl. Mech. Eng., 195: 4862–4889.
Armero, F., Romero, I. 2001a. On the formulation of high-frequency dissipative timestepping algorithms for nonlinear dynamics. Part I: Low order methods for two model problems and nonlinear elastodynamics, Comp. Meth. Appl. Mech. Eng., 190: 2603–2649.
Armero, F., Romero, I. 2001b. On the formulation of high-frequency dissipative timestepping algorithms for nonlinear dynamics. Part II: High order methods, Comp. Meth. Appl. Mech. Eng., 190: 6783–6824.
Armero, F., Romero, I. 2003. Energy-dissipative momentum-conserving timestepping algorithms for the dynamics of nonlinear Cosserat rods, Comp. Mech., 31: 3–26.
Armero, F., Zambrana-Rojas, C. 2007. Volume–preserving energy–dissipative momentum–conserving algorithms for isochoric multiplicative plasticity, submitted.
Armstrong, P.J., Frederick, C.O. 1966. A mathematical representation of the multiaxial bauschinger effect. Technical Report RD/B/N/ 731, C.E.G.B.
Arnold, V.I. 1989. Mathematical Methods of Classical Mechanics. New York: Springer-Verlag.
Ashrafi, S.A., Smyth, A.W. 2007. Generalized Masing approach to modeling hysteretic deteriorating behavior, Journal of Engineering Mechanics, 133, 495–505.
Ashrafi, S.A., Smyth, A.W., Betti, R. 2005. A parametric identification scheme for non-deteriorating and deteriorating non-linear hysteretic behavior, Structural Control and Health Monitoring, 13, 108–131.
ATC 40, 1996. Seismic Evaluation and Retrofit of Concrete Buildings, Applied Technology Council.
ATC-13, 1985. Earthquake Damage Evaluation Data for California. Applied Technology Council: Redwood City, CA.
Attolico, A., Biondi, S., Nuti, C., Petrangeli, M. 2000. Influence of Buckling of Longitudinal Rebars in Finite Element Modelling of Reinforced Concrete Structures Subjected to Cyclic loading: Two Case Studies, Proc. of Workshop on Seismic Protection of Existing and New Construction Buildings by means of Unconventional Systems, Prin 97, Naples, 12–13 May.
Au, F.T.K., Cheng, Y.S., Cheung, Y.K. 2001. Vibration analysis of bridges under moving vehicles and trains: an overview. Progress in Structural Engineering and Materials 3: 299–304.
Au, S. 2006a. Critical excitation of SDOF elasto-plastic systems. Journal of Sound and Vibration 296(4–5), 714–733.
Au, S. 2006b. Sub-critical excitations of SDOF elasto-plastic systems. International Journal of Non-Linear Mechanics 41(9), 1095–1108.
Au, S. 2008. First passage probability of elasto-plastic systems by importance sampling with adapted process. Probabilistic Engineering Mechanics 23, 114–124.
Au, S., Beck, J. 2001a. Estimation of small failure probabilities in high dimensions by subset simulation. Probabilistic Engineering Mechanics 16, 263–277.
Au, S., Beck, J. 2001b. First excursion probabilities for linear systems by very efficient importance sampling. Probabilistic Engineering Mechanics 16(3), 193–207.
Au, S., Lam, H., Ng, C. 2007. Reliability analysis of single-degree-of-freedom elastoplastic systems. I: Critical excitations. Journal of Engineering Mechanics 133(10), 1072–1080.

Au, S.K. 2004. Probabilistic Failure Analysis by Importance Sampling Markov Chain Simulation. Journal of Engineering Mechanics. Vol. 103: 303–311.

Au, S.K., Beck, J.L. 2001. First Excursion Probabilities for Linear Systems by very Efficient

Au, S.K., Papadimitriou, C., Beck, J.L. 1999. Reliability of uncertain dynamical systems with multiple design points. Structural Safety, 21(2), 113–133.

Au, S-K., Beck, J.L. 2001. Estimation of small failure probabilities in high dimensions by Subset Simulation. Probabilistic Engineering Mechanics 16: 263–277.

Au, S-K., Beck, J.L. 2003. Subset Simulation and its application to seismic risk based on dynamic analysis. Journal of Engineering Mechanics 129(8): 901–917.

Aydınoğlu, M.N. 2004. An improved pushover procedure for engineering practice: Incremental Response Spectrum Analysis (IRSA). International Workshop on Performance-based Seismic Design: Concepts and Implementation. Bled, Slovenia. PEER Report 2004/05: 345–356.

Aydınoğlu, M.N. 2007. A Response Spectrum-Based Nonlinear Assessment Tool for Practice: Incremental Response Spectrum Analysis (IRSA). Special Issue: Response Spectra (Guest Editor: M.D. Trifunac), ISET Journal of Earthquake Technology 44(1), No. 481.

Aydınoğlu, M.N. 2003. An incremental response spectrum analysis based on inelastic spectral displacements for multi-mode seismic performance evaluation. Bulletin of Earthquake Engineering 1(1): 3–36.

Aydinoglu, A., Polat, Z. 2004. First Level Evaluation and Assessment of Building Earthquake Performance. Report for the Istanbul Master Plan Zeytinburnu Pilot Project, Metropolitan Municipality of Istanbul, Planning and Construction Directorate (in Turkish).

Aydinoglu, A., Polat, Z., Celep, Z., Hancıoglu, B., Kırçıl, M., Önem, G., Tüzün, C. 2004. Second level evaluation and assessment of building earthquake performance. Report for the Istanbul Master Plan Zeytinburnu Pilot Project, Metropolitan Municipality of Istanbul, Planning and Construction Directorate (in Turkish).

Bachmann, H. 2002. Seismic Conceptual Design of Buildings – Basic principles for engineers, architects, building owners, and authorities. Order Number: 804.802e, Swiss Federal Office for Water and Geology, Swiss Agency for Development and Cooperation. BWG, Biel.

Bae, S., Miesses, A.M., Bayrak, O. 2005. Inelastic Buckling of Reinforcing Bars. Journal of Structural Engineering 131(2): 314–321.

Balan, T.A., Filippou, F.C., Popov, E.P. 1998. Hysteretic model of ordinary and high-strength reinforcing steel. Journal of Structural Engineering 124(3): 288–297.

Balay, S., Buschelman, K., Eijkhout, V., Gropp, W.D., Kaushik, D., Knepley, W.G., Curfman McInnes, L., Smith, B.F., Zhang, H. 2004. PETSc users manual. Technical Report ANL-95/11 – Revision 2.1.5, Argonne National Laboratory.

Balay, S., Buschelman, K., Gropp, W.D., Kaushik, D., Knepley, W.G., Curfman McInnes, L., Smith, B.F., Zhang, H. 2001. PETSc Web page, http://www.mcs.anl.gov/petsc

Balay, S., Gropp, W.D., Curfman McInnes, L., Smith, B.F., 1997. Efficient management of parallelism in object oriented numerical software libraries. In E. Arge, A.M. Bruaset, and H.P. Langtangen, editors, Modern Software Tools in Scientific Computing, pages 163–202. Birkhäuser Press.

Balling, R.J., Yao, X. 1997. Optimization of reinforced concrete frames. Journal of Structural Engineering: 123(2): 193–202.

Banverket – www.banverket.se. Latest access 19/2-2007.

Barakat, S., Bani-Hani, K., Taha, M.Q. 2004. Multi-objective reliability-based optimization of prestressed concrete beams. Structural Safety 26(3): 311–342.

Barbat, A.H., Oller, S., Hanganu, A., Oñate, E. 1997. Viscous damage model for Timoshenko beam structures. International Journal for Solids and Structures; 34(30): 3953–3976.

Barbato, M., Conte, J.P. 2005. Finite element response sensitivity analysis: a comparison between force-based and displacement-based frame element models. Computer Methods in Applied Mechanics and Engineering, 194(12–16), 1479–1512.

Barbato, M., Conte, J.P. 2006. Finite element structural response sensitivity and reliability analyses using smooth versus non-smooth material constitutive models. International Journal of Reliability and Safety, 1(1–2), 3–39.

Barbato, M., Gu, Q., Conte, J.P. 2006. Response sensitivity and probabilistic response analyses of reinforced concrete frame structures. Proceedings of the 8th NCEE, San Francisco, April 18–22.

Barbato, M., Zona, A., Conte, J.P. 2007. Finite element response sensitivity analysis using three-field mixed formulation: general theory and application to frame structures. International Journal for Numerical Methods in Engineering, 69(1), 114–161.

Bathe, K. 2002. Finite Element Procedures, Upper Saddle River: Prentice-Hall.

Bayrak, O., Sheikh, S.A. 2001. Plastic hinge analysis. Journal of Structural Engineering; 127(9): 1092–1100.

Beck, J., Au, S. 2005. Reliability of dynamic systems using stochastic simulation. In C. Soize and G.I. Schuëller (eds.), Structural Dynamics EURODYN 2005 – Proceedings of the 6th International Conference on Structural Dynamics,Volume 1, Paris, France, pp. 23–30. Millpress, Rotterdam.

Beck, J.L. 1989. Statistical system identification of structures, 5th International Conference on Structural Safety and Reliability, San Francisco, California.

Beck, J.L., Au, S.-K. 2002. Bayesian updating of structural models and reliability using Markov Chain Monte Carlo simulation, Journal of Engineering Mechanics, 128, 380–391.

Beck, J.L., Katafygiotis, L.S. 1991. Updating of a model and its uncertainties utilizing dynamic test data, 1st International Conference on Computational Stochastic Mechanics, Corfu, Greece.

Beck, J.L., Katafygiotis, L.S. 1998. Updating models and their uncertainties. I: Bayesian statistical framework. Journal of Engineering Mechanics 124(4): 455–461.

Beck, J.L., Muto, M. 2007. Bayesian updating and model class selection of deteriorating hysteretic structural models using seismic response data. ECCOMAS Thematic Conference on Computational Methods in Structural Dynamics and Earthquake Engineering, Rethymno, Crete, Greece.

Beck, J.L., Yuen, K.-Y. 2004. Model selection using response measurements: Bayesian probabilistic approach, Journal of Engineering Mechanics, 130, 192–203.

Belytschko, T., Liu, W.K., Moran, B. 2000. Nonlinear Finite Elements for Continua and Structures. New York: Wiley.

Benedettini, F., Capecchi, D., Vestroni, F. 1995. Identification of hysteretic oscillators under earthquake loading by nonparametric models, Journal of Engineering Mechanics, 121, 606–612.

Benjamin, J.R., Cornell, C.A. 1970. Probability, Statistics, and Decision for Civil Engineers, McGraw-Hill. New York.

Bertero, R.D., Bertero, V.V. 2002. Performance-based seismic engineering: the need for a reliable conceptual comprehensive approach. Earthquake Engineering and Structural Dynamics 31, 627–652.

Bertero, R.D. 1995. Inelastic torsion for preliminary seismic design. Journal of Structural Engineering 121(8): 1183–1189.

Beskos, D.E. 1997. Boundary element methods in dynamic analysis: Part II 1986–1996. ASME Applied Mechanics Reviews, 50: 149–197.

Beyer, H.G., Sendhoff, B. 2007. Robust Optimization. A comprehensive survey. Computer Methods in Applied Mechanics and Engineering doi: 10.1016/j.cma.2007.03.003.

Bielak, J., Loukakis, K., Hisada, Y., Yoshimura, C. 2003. Domain reduction method for three–dimensional earthquake modeling in localized regions. Part I: Theory. Bulletin of the Seismological Society of America, 93(2): 817–824.

Biot, M.A. 1957. The elastic coefficients of the theory of consolidation, Journal of Applied Mechanics, 24, 594–601.
Bode, C., Hirschauer, R., Savidis, S.A. 2002. Soil-structure interaction in the time domain using halfspace Green's functions. Soil Dynamics and Earthquake Engineering 22: 283–295.
Booker, J.R. 1974. The consolidation of a finite layer subject to surface loading, International Journal of Soils and Structures, 10, 1053–1065.
Boore, D.M. 2003. Simulation of ground motion using the stochastic method. Pure and Applied Geophysics 160: 635–676.
Bougacha, S., Tassoulas, J.L., Roësset, J.M. 1993. Analysis of foundations on fluid-filled poroelastic stratum. Journal of Engineering Mechanics 119(8): 1632–1648.
Breitung, K. 1984. Asymptotic approximations for multinormal integrals. Journal of the Engineering Mechanics Division (ASCE), 110(3), 357–366.
Breitung, K. 1994. Asympotic Approximations for Probability Integrals. Lecture Notes in Mathematics, vol. 1592. Berlin: Springer.
Brincker, R., Zhang, L.M., Andersen, P. 2001. Modal identification of output-only systems using frequency domain decomposition. Smart Materials & Structures 10(3): 441–445.
Browning, J. 2002. Proportioning earthquake-resistant RC frames in central/eastern U.S. Earthquake Engineering, Structural Dynamics 31(6): 1267–1280.
BSSC-Building Seismic Safety Council. 2001. NEHRP (National Earthquake Hazards Reduction Program) Recommended Provisions for Seismic Regulations for new buildings and other structures, 2000 Edition, Part 1: Provisions (FEMA 368), Ch. 4, Washington, D.C.
Cadzow, J.A. Discrete Calculus of Variations. International Journal of Control, 11(3): 393–407, 1970.
Capecchi, D., De Angelis, M., Sepe, V. 2004. Modal model identification with unknown nonstationary base motion. Meccanica 39: 31–45.
Carvalho, E.C., Coelho, E. (Editors). 2001. Seismic assessment, strengthening and repair of structures. ECOEST2-ICONS Report No.2, European Commission – "Training and Mobility of Researchers" Programme.
Casciati, F., Faravelli, L. 1991. Fragility Analysis of Complex Structural Systems. Taunton: Research Studies Press Ltd.
C-Core Earthquake Induced Damage Mitigation from Soil Liquefaction, 2004. Centre for Cold Ocean Resources Engineering, Data Report of Centrifuge Test CT1 and CT2, Canada.
CEN. 2005. Eurocode 8: Design of structures for earthquake resistance. Part 3: Strengthening and repair of buildings. Brussels.
Chan, C.-M., Wang, Q. 2006. Nonlinear stiffness design optimization of tall reinforced concrete buildings under service loads. Journal of Structural Engineering 132(6): 978–990.
Chan, C.-M., Zou, X.-K. 2004. Elastic and inelastic drift performance optimization for reinforced concrete buildings under earthquake loads. Earthquake Engineering, Structural Dynamics 2004, 33(8): 929–950.
Charmec- www.charmec.chalmers.se Latest access 19/2-2007.
Chen, C. 2006. Vibration et vibroacoustique des panneaux composites sandwich en presence d'incertitudes – Exp'erimentation et validation du mod'ele. Thesis of the university of Marne la Vall'ee, Paris, France.
Chen, C., Duhamel, D., Soize, C. 2006. Probabilistic approach for model and data uncertainties and its experimental identification in structural dynamics: case of composite sandwich panels. Journal of Sound and vibration, 294, 64–81.
Chen, W.-F., Saleeb, A.F. 1994. Constitutive equations for engineering materials, volume 1: elasticity and modeling. Elsevier.
Chi Chen, M., Penzien, J. 1977. Nonlinear soil–structure interaction of skew highway bridges. Technical Report UCB/EERC-77/24, Earthquake Engineering Research Center, University of California, Berkeley, August.

Chiang, D.-Y. 1992. Parsimonious modeling of inelastic systems, Technical Report EERL 92-02, California Institute of Technology, Pasadena, CA.

Ching, C.Y.R. Finite Element Rail Vibration Dynamics: Multi-body Dynamics of Modern High-speed Trains. Master Thesis 04:15, Department of Structural Engineering and Mechanics, Chalmers University of Technology, Gothenburg, Sweden, 2004.

Ching, J., Au, S-K., Beck, J.L. 2005a. Reliability estimation for dynamical systems subject to stochastic excitation using Subset Simulation with splitting. Computational Methods in Applied Mechanics and Engineering 194: 1557–1579.

Ching, J., Au, S-K., Beck, J.L. 2005b. Hybrid Subset Simulation method for reliability estimation of dynamical systems subject to stochastic excitation. Probabilistic Engineering Mechanics 20: 199–214.

Ching, J., Chen, Y-J. 2007. Transitional Markov Chain Method for Bayesian model updating, model class selection and model averaging. Journal of Engineering Mechanics 133: 816–832.

Ching, J., Muto, M., Beck, J.L. 2005. Bayesian linear structural model updating using Gibbs sampler with modal data, 9th International Conference on Structural Safety and Reliability, Rome, Italy.

Ching, J., Muto, M., Beck, J.L. 2006. Structural model updating and health monitoring with incomplete modal data using Gibbs sampler, Computer-Aided Civil and Infrastructure Engineering, 21, 242–257.

Chopra, A.K. 2001. Dynamics of Structures, Theory and Applications to Earthquake Engineering. Prentice Hall, New Nersey.

Chopra, A.K., Goel, R.K. 2002. A modal pushover analysis for estimating seismic demands for buildings. Earthquake Engineering and Structural Dynamics 31(3): 561–582.

Chopra, A.K., Goel, R.K., Chintanapakdee, C. 2004. Evaluation of a Modified MPA Procedure. Earthquake Spectra 20(3): 757–778.

Chopra, A.K. 2001. Dynamics of structures. New Jersey: Prentice Hall.

Christian, J.T., Baecher, G.B. 1998. Point-estimate method and numerical quadrature. Journal of Geotechnical and Geoenvironmental Engineering 125, 779–786.

Chung, J., Hulbert, G.M. 1993. A time integration algorithm for structural dynamics with improved numerical dissipation: the generalized alpha-method. Journal of Applied Mechanics, Transactions of the ASME 60: 371–375.

Cifuentes, A.O., Iwan, W.D. 1989. Nonlinear system identification based on modeling of restoring force behavior, Soil Dynamics and Earthquake Engineering, 8, 2–8.

Clark, P., Aiken, I., Ko, E., Kasai, K., Kimura, I. 1999. Design procedures for buildings incorporating hysteretic seismic devices. Proceedings, 68th Annual Convention Santa Barbara, California Structural Engineering Association of California.

Clark, P., Frank, K., Krawinkler, H., Shaw, R. 1997. Protocol for fabrication, inspection, testing and documentation of beam-column connection tests and other experimental specimens. Report No. SAC/BD-97/02, Sacramento, California.

Clough, R.W., Penzien, J. 1993. Dynamics of Structures. New York: McGraw-Hill.

Coburn, A., Spence, R. 1992. Earthquake Protection, John Wiley, ISBN 0 471 91833 4.

Coello Coello, C.A., Handling Preferences in Evolutionary Multiobjective Optimization: A Survey, IEEE Neural Networks Council (ed.), Proceedings of the 2000 Congress on Evolutionary Computation (CEC 2000. Vol. 1, IEEE Service Center, Piscataway, New Jersey, pp. 30–37.

Coello, C. 2002. Theoretical and numerical constraint-handling techniques used with evolutionary algorithms: a survey of the state of the art. Computer Methods in Applied Mechanics and Engineering 191(11–12), 1245–1287.

Coleman, J., Spacone, E. 2001. Localization Issues in Nonlinear Force-Based Frame Elements, ASCE Journal of Structural Engineering, 127(11), pp. 1257–1265.

Collins, M.P., Porasz, A. 1989. Shear Design for High Strength Concrete, Proceeding of Workshop on Design Aspects of High Strength Concrete. Comité Euro-International du Béton Bulletin d'Information. CEB. Paris. pp. 77–83.

Combescure, D., Pegon, P. 1997. α-operator splitting time integration technique for pseudo-dynamic testing, Error propagation analysis. Soil Dynamics and Earthquake Engineering. Vol. 16, pp. 427–443.

Connor, J.J., Wada, A., Iwata, M., Huang, Y.H. 1997. Damage-controlled structures. I: Preliminary design methodology for seismically active regions. Journal of Structural Engineering; 123(4): 423–431.

Conte, J.P. 2001. Finite element response sensitivity analysis in earthquake engineering. In Spencer, Hu (eds.), Earthquake Engineering Frontiers in the New Millennium, 395–401.

Conte, J.P., Barbato, M., Spacone, E. 2004. Finite element response sensitivity analysis using force-based frame models. International Journal for Numerical Methods in Engineering, 59: 1781–1820.

Conte, J.P., Vijalapura, P.K., Meghella, M. 2003. Consistent finite-element response sensitivity analysis. Journal of Engineering Mechanics (ASCE), 129: 1380–1393.

Cook, R.D., Malkus, D.S., Plesha, M., Witt, R.J. 2002. Concepts and Applications of Finite Element Analysis. New York: John Wiley, Sons.

Cornell, C.A., Jalayar, F., Hamburger, R.O., Foutch, D.A. 2002. Probabilistic basis for 2000 SAC Federal Emergency Management Agency Steel Moment Frame Guidelines. Journal of Structural Engineering ASCE 128(4): 526–533.

Cosenza, E., Prota, A. 2006. Experimental Behaviour and Numerical Modelling of Smooth Steel Bars under Compression. Journal of Earthquake Engineering 10(3): 313–329.

Craig, R.R., Bampton, M.C.C. 1968. Coupling of substructures for dynamic analyses, AIAA Journal, 6(7): 1313–1319.

Crisfield, M., Shi, J. 1994. A co-rotational element/time-integration strategy for nonlinear dynamics, Int. J. Num. Meth. Eng., 37: 1897–1913.

CSI – Computers and Structures Inc. 2006. PERFORM-3D: Nonlinear Analysis and Performance Assessment for 3D Structures, User Guide. Version 4. August 2006.

Dall'Asta, A., Zona, A. 2004. Comparison and validation of displacement and mixed elements for the non-linear analysis of continuous composite beams. Computers and Structures, 82(23–26), 2117–2130.

de Boer, P., Kroese, D., Mannor, S., Rubinstein, R. 2005. A tutorial on the cross-entropy method. Annals of Operations Research 134(1), 19–67.

De Gersem, H., Moens, D., Desmet, W., Vandepitte, D. 2005. A fuzzy finite element procedure for the calculation of uncertain frequency response functions of damped structures: Part II – numerical case studies, Journal of Sound and Vibration, 288(3): 463–486.

De Gersem, H., Moens, D., Desmet, W., Vandepitte, D. 2006. An automated response surface based optimisation technique for the calculation of fuzzy envelope FRFs of models with uncertain properties, Proceedings of the International Conference on Noise and Vibration Engineering ISMA 2006, pages 4091–4103, Leuven, Belgium.

De Gersem, H., Moens, D., Desmet, W., Vandepitte, D. 2007. Interval and fuzzy eigenfrequency analysis of uncertain substructured FE models, Computer Assisted Mechanics and Engineering Sciences (CAMES), in press.

De Gersem, H., Moens, D., Desmet, W., Vandepitte, D. 2007. On the use of deviatoric component modes for the assessment of uncertainty in Component Mode Synthesis, Proceedings of the 1st International Conference on Uncertainty in Structural Dynamics, Sheffield, June.

De Munck, M., Moens, D., Desmet, W., Vandepitte, D., 2006. An automated response surface based optimisation technique for the calculation of fuzzy envelope FRFs of models with uncertain properties, Proceedings of the International Conference on Noise and Vibration Engineering ISMA 2006, Leuven, September, 4091–4104.

Default vehicle property file: http://www.gensys.se/doc_html/analyse_r_vhe_prop.ins.html – vhe_prop.ins. Latest access 19/11-2006.
Degrande, G., Schillemans, L. 2001. Free field vibrations during the passage of a Thalys high-speed train at variable speed. Journal of Sound and Vibration 247: 131–144.
Deierlein, G. 2004. Overview of a comprehensive framework for earthquake performance assessment, Proceedings of the International Workshop on Performance-Based Seismic Design – Concepts and Implementation, Bled, Slovenia, Fajfar P., Krawinkler H. eds., PEER Report 2004/05: 15–26, Berkeley.
De-la-Colina, J. 2003. Assessment of design recommendations for torsionally unbalanced multi-storey buildings. Earthquake Spectra 19: 47–66.
Demmel, J.W., Eisenstat, S.C., Gilbert, J.R., Li, X.S., Liu. J.W.H. 1999. A supernodal approach to sparse partial pivoting. SIAM J. Matrix Analysis and Applications, 20(3): 720–755.
Dendrou, B., Werner, S.D., Toridis, T. 1985. Three dimensional response of a concrete bridge system to traveling seismic waves. Computers and Structures, 20: 593–603.
Deodatis, D. 1996. Non-stationary Stochastic Vector Processes: Seismic Ground Motion Applications. Probabilistic Engineering Mechanics 11: 145–168.
Der Kiureghian, A. 1996. Structural reliability methods in seismic safety assessment: a review. Journal of Engineering Structures, 18(6), 412–424.
Der Kiureghian, A., De Stefano, M. 1991. Efficient algorithms for second-order reliability analysis. Journal of Engineering Mechanics (ASCE), 117(12), 2904–2923.
Deraemaeker, A., Preumont, Kullaa, J. 2006. Modeling and removal of environmental effects for vibration based SHM using spatial filtering and factor analysis. Proc. IMAC XXIV, S.E.M., St Louis, USA.
Deraemaeker, A., Reynders, E., De Roeck, G., Kullaa, J. 2008. Vibration based Structural Health Monitoring using output-only measurements under changing environment. Mechanical Systems and Signal Processing, submitted.
DiPasquale, E., Cakmak, A.S. 1987. Detection and assessment of seismic structural damage. National Center for Earthquake Engineering Research, Techn. Rep. NCEER-87-0015, State University of New York, Buffalo.
Ditlevsen, O., Madsen, H.O. 1996. Structural Reliability Methods. New York: Wiley.
Dodd, L.L., Restrepo-Posada, J.I. 1995. Model for Predicting Cyclic Behaviour of Reinforcing Steel. Journal of Structural Engineering 121(3): 433–445.
Doebling, S.W., Farrar, C.R., Prime, M.B., Shevitz, D.W. 1996. Damage indication and health monitoring of structural and mechanical systems from change in their vibrations characteristics: A literature review. Technical Report LA-13070-MS. Los Alamos National Laboratory.
Dolšek, M., Fajfar, P. 2004b. Inelastic spectra for infilled reinforced concrete frames. Earthquake Engineering and Structural Dynamics 33(15): 1395–1416.
Dolšek, M., Fajfar, P. 2005. Simplified non-linear seismic analysis of infilled reinforced concrete frames. Earthquake Engineering and Structural Dynamics 34(1): 49–66.
Dolšek, M., Fajfar, P. 2007. Simplified probabilistic seismic performance assessment of plan-asymmetric buildings. Earthquake Engineering and Structural Dynamics, 36:2021–2041.
Dolšek, M., Fajfar, P. 2004a. IN2 – A Simple Alternative for IDA. Proceedings of the 13th World Conference on Earthquake Engineering, Vancouver, Canada, paper 3353.
Dolšek, M., Fajfar, P. 2007. Effects of masonry infills on the seismic response of a four storey reinforced concrete frame – deterministic assessment. Engineering Structures, submitted.
Doltsinis, I., Kang, Z. Robust design of structures using optimization methods. Comput Methods Appl Mech Eng 2004; 193: 2221–2237.
Doltsinis, I., Kang, A. 2004. Robust design of structures using optimization methods. Computer Methods in Applied Mechanics and Engineering 193, 2221–2237.
Doltsinis, I., Kang, A., Cheng, G. 2005. Robust design of non-linear structures using optimization methods. Computer Methods in Applied Mechanics and Engineering 194, 1779–1795.

Donders, S., Vandepitte, D., Van de Peer, J., Desmet, W. 2005 Assessment of uncertainty on structural dynamic responses with the short transformation method, Journal of Sound and Vibration, Vol. 288, No. 3, 523–549.
Dong, W., Shah, H. 1987. Vertex Method for Computing Functions of Fuzzy Variables Fuzzy Sets and Systems, Vol. 24, 65–78.
Driankov, D., Hellendoorn, H., Reinfrak, M. 1996. An introduction to fuzzy control. 2nd edition, Springer Verlag.
Dryden, M. 2006. Validation of simulations of a two-span reinforced concrete bridge. Submitted in partial satisfaction of the requirements for degree od Ph.D.
Duan, X.N., Chandler, A.M. 1997. An optimized procedure for seismic design of torsionally unbalanced structures. Earthquake Engineering, Structural Dynamics 26: 737–757.
Durand, J.-F. 2007. Mod'elisation de v'ehicules automobiles en vibroacoustique num'erique avec incertitudes et validation exp'erimentale. Thesis of the University of Marne la Vall'ee, Paris, France.
Durand, J.-F., Soize, C., Gagliardini, L. 2008. Structural-acoustic modeling of automotive vehicles in presence of uncertainties and experimental identification and validation, J. Acoust. Soc. Am., 124(3).
Durukal, E., Ansal, A., Tönük, G. 2006. Effect of Ground Motion Scaling and Uncertainties in Site Characterisation on Site Response Analyses. Proceedings of the 100th Anniversary Earthquake Conference Commemorating the 1906 San Francisco Earthquake, San Francisco, USA.
EAK. 2000. Greek seismic code, Greek Ministry of Public Works, Athens, Greece.
Eberhard, P. 2000. Kontaktuntersuchungen durch hybride Mehrkörpersystem/Finite Elemente Simulation (in German), Aachen: Shaker.
EC2. 2002. Eurocode 2: Design of Concrete Structures. Part 1: General rules and rules for buildings. CEN, EN 1992-1-1:2002. European Committee for Standardization. Brussels.
EC3. 1992. Eurocode 3, Design of steel structures, Part 1.1: General rules for buildings, European Prestandard ENV 1993-1-1/1992. European Committee for Standardization (CEN): Brussels.
EC8, Eurocode No. 8. 2001. Design of structures for earthquake resistance. European Committee for standardization, 3rd Draft, prEN 1998-1-1.
Ekevid T., Wiberg N.-E. Computational Wave Propagation – by Adaptive Multigrid FE Technique, Keynote paper at the Fifth World Congress on Computational Mechanics, Vienna, Austria, July 7–12, 2002.
Ekevid, T., Li, M.X.D., Wiberg, N.E. 2001. Adaptive FEA of wave propagation induced by high-speed trains. Computers and Structures 79: 2693–2704.
Ekevid, T., Wiberg, N.E. 2002. Wave propagation related to high-speed train A scaled boundary FE-approach for unbounded domains. Computer Methods in Applied Mechanics and Engineering 191: 3947–3964.
Elegbede, C. 2005. Structural reliability assessment based on particle swarm optimization. Structural Safety 27, 171–186.
Ellingwood, B.R., Wen, Y.-K. 2005. Risk-benefit-based design decisions for low-probability/high consequence earthquake events in mid-America. Progress in Structural Engineering and Materials 7(2): 56–70.
Elnashai, A.S. 2002. Do we really need Inelastic Dynamic Analysis?, Journal of Earthquake Engineering, 6, Special Issue 1, 123–130.
Elnashai, A.S., Papanikolaou, V., Lee, D.H. 2002. Zeus-NL – A System for Inelastic Analysis of Structures.
El-Sayed, M.E.M., Marjadi, D., Sandgren, E. 1991 Force Method Formulations Based on Hamilton Principle. Computers, Structures, 38(3): 301–316.
Erdik, M., Aydınoglu, M.N., Barka, A., Yüzügüllü, Ö., Siyahi, B., Durukal, E., Fahjan, Y., Akman, H., Birgören, G., Biro, Y., Demircioğlu, M., Özbey, C., Sesetyan, K. 2002.

BU-ARC, Earthquake Risk Assessment for Istanbul Metropolitan Area, Project Report, Bogazici University Publication.
Erdik, M., Demircioğlu, M., Sesetyan, K., Durukal, E. 2005. Assessment of earthquake hazard for Bakirköy, Gemlik, Bandırma, Tekirdağ, Körfez, WB MEER Project – A3 Component, Microzonation and Hazard Vulnerability Studies For Disaster Mitigation in Pilot Municipalities, Bogazici University, Kandilli Observatory and Earthquake Engineering Research Institute.
Erdik, M., Demircioğlu, M., Sesetyan, K., Durukal, E., Siyahi, B. 2004. Earthquake Hazard in Marmara Region, Soil Dynamics and Earthquake Engineering 24: 605–631.
Erdik, M., Fahjan, Y. 2005. System Analysis and Risk. Assessing and Managing Earthquake Risk – Geo-scientific and Engineering Knowledge for Earthquake Risk Mitigation: developments, tools, techniques, Part 3, Book Series: Geotechnical, Geological, and Earthquake Engineering, V2, Oliveira CS, Roca A, Goula X (eds.).
Fajfar, P. 1998. Towards nonlinear methods for the future seismic codes. In Booth (ed.), Seismic design practice into the next century. Balkema.
Fajfar, P. 1999. Capacity Spectrum Method Based on Inelastic Demand Spectra, Earthquake Engineering and Structural Dynamics, 28, 979–993.
Fajfar, P. 2000. A nonlinear analysis method for performance-based seismic design. Earthquake Spectra 16(3): 573–592.
Fajfar, P. 2002. Structural Analysis in Earthquake Engineering – A Breakthrough of Simplified Non-Linear Methods, 12th European Conference on Earthquake Engineering, London, United Kingdom, Paper 843.
Fajfar, P., Kilar, V., Marusic, D., Perus, I. 2005. The extension of the N2 method to asymmetric buildings, 4th European Workshop on the Seismic Behaviour of Irregular and Complex Structures, Paper No. 41, Thessaloniki, Greece.
Fajfar, P., Dolšek, M., Marušić, D., Stratan, A. 2006. Pre- and post-test mathematical modelling of a plan-asymmetric reinforced concrete frame building. Earthquake Engineering and Structural Dynamics 35: 1359–1379.
Fajfar, P., Marusicì, D., Perus, I. 2005.Torsional effects in the pushover-based seismic analysis of buildings. Journal of Earthquake Engineering. 9(6): 831–854.
Farhat, C. 1987. Muliprocessors in Computational Mechanics. PhD thesis, University of California, Berkeley.
Farhat, C. 1991. Saddle-point principle domain decomposition method for the solution of solid mechanics problems. In Fifth International Symposium on Domain Decomposition Methods for Partial Differential Equations, Norfolk, VA, USA, May 6–8.
Farhat, C., Geradin, M. 1992. Using a reduced number of lagrange multipliers for assembling parallel incomplete field finite element approximations. Computer Methods in Applied Mechanics and Engineering, 97(3): 333–354.
Farhat, C., Roux, F-X. 1991. Method of finite element tearing and interconnecting and its parallel solution algorithm. International Journal for Numerical Methods in Engineering, 32(6): 1205–1227.
Federal Emergency Management Agency. 2000. Prestandard and Commentary for the Seismic Rehabilitation of Buildings, Report 356, Washington, DC: FEMA.
Federal Emergency Management Agency. 2000. Recommended Seismic Design Criteria For New Steel Moment-Frame Buildings, FEMA 350. Washington, D.C.
Federal Emergency Management Agency. NEHRP Recommended Provisions for Seismic Regulations for New Buildings and Other Structures. 2000. Report 368, Washington, DC: FEMA.
FEMA 1997. NEHRP Guidelines for the seismic rehabilitation of buildings. Report 273. Buildings Seismic Safety Council.
FEMA 227. 1992. A Benefit–Cost Model for the Seismic Rehabilitation of Buildings. Federal Emergency Management Agency, Building Seismic Safety Council. Washington, DC.

FEMA 273. 1997. Guidelines for the Seismic Rehabilitation of Buildings. Federal Emergency Management Agency, Washington DC, USA.
FEMA-310. 1998. Handbook for the Seismic Evaluation of Buildings – A Prestandard, prepared by the American Society of Civil Engineers for the Federal Emergency Management Agency, Washington, DC.
FEMA-National Institute of Building Sciences. HAZUS-MH MR1. 2003. Multi-hazard Loss Estimation Methodology Earthquake Model. Washington, DC.
Fenves, G., McKenna, F., Scott, M.H., Takahashi, Y. 2004. An Object-Oriented Software Environment for Collaborative Network Simulation, 13th World Conference on Earthquake Engineering, Paper 1492, Vancouver, B.C. (Canada), 1–6 Augus.
Fenves, G., Dryden, M. 2005. Nees sfsi demonstration project. NEES project meeting, TX, Austin, August.
Filippou, F.C., Constantinides, M. 2004. FEDEASLab – Getting Started Guide and Simulation Examples. NEESgrid Report 2004–22 and SEMM Report 2004–05, p. 42.
Filippou, F.C., Popov, E.P., Bertero, V.V. 1983. Effects of bond deterioration on hysteretic behaviour of reinforced concrete joint, Report No. UCB/EERC-83/19, University of California, Berkeley.
Florian, A. 1992. An efficient sampling scheme: Updated Latin Hypercube Sampling. Probabilistic Engineering Mechanics 7, 123–130.
Fonseca, C.M., Fleming, P.J., Genetic Algorithms for Multi-Objective Optimization: Formualtion, Discussion and Generalization, Genetic Algorithms: Proceedings of the 5th International Conference (S. Forrest, ed.) San Mateo, CA: Morgan Kaufmann, July 1993.
Formas – www.formas.se. Latest access 19/2-2007.
Foschi, R., Li, H., Zhang, J. 2002. Reliability and performance-based design: a computational approach and applications. Structural safety 24: 205–218.
Fourie, P.C., Groenwold, A.A. 2002. The particle swarm optimization algorithm in size and shape optimization. Structural and Multidisciplinary Optimization 23, 259–267.
Fragiadakis, M. 2001. Nonlinear Material Modelling of Reinforcement Steel Bars Under Transient Loading, MSc Dissertation, Department of Civil Engineering, Imperial College London, UK.
Frangopol, D. 1995. Reliability-based structural design. In C.R. Sundararajan (Ed.), Probabilistic Structural Mechanics Handbook, pp. 352–387. New York: Chapman, Hall.
Frangopol, D.M. 1986. Computer-automated design of structural systems under reliability-based performance constraints. Engineering Computations. 3(2): 109–115.
Fredlund, D.G., Rahardjo, H. 1993. Soil Mechanics for Unsaturated Soils. John Wiley, Sons.
Freudenthal, A. 1956. Safety and the probability of structural failure. ASCE Transactions 121, 1337–1397.
Fryba, L. 1996. Dynamics of Railway Bridges. London: Thomas Telford.
Fu, Y., Kasai, K. 1998. Comparative study of frames using viscoelastic and viscous dampers. Journal fo Structural Engineering; 124(5): 513–522.
Fujimura, K., Der Kiureghian, A. 2007. Tail-equivalent linearization method for nonlinear random vibration. Probabilistic Engineering Mechanics 22(1), 63–76.
Fulton, R.E., Su, P.S. 1992. Parallel substructure approach for massively parallel computers. Computers in Engineering, 2: 75–82.
Ganzerli, S., Pantelides, C.P., Reaveley, L.D. 2000. Performance-based design using structural optimization. Earthquake Engineering, Structural Dynamics. 29(11): 1677–1690.
Garcia, M., de la Llera, J.C., Almazan, J.L. 2007. Torsional balance of plan asymmetric structures with viscoelastic dampers. Engineering Structures. 29(6): 914–932.
Gasser, M., Schueller, G.I. 1997. Reliability-based optimization of structural systems. Mathematical Methods of Operations Research 46, 287–307.

Gasser, M., Schuëller, G.I. 1997. Reliability-Based Optimization of Structural Systems. Mathematical Methods of Operational Research. Vol. 46: 287–307.

Ghobarah, A. 2004. On drift limits associated with different damage levels. International Workshop on Performance-Based Seismic Design, 28 June–1 July 2004.

Ghobarah, A., Youssef, M. 1999. Modeling of reinforced concrete structural walls. Engineering Structures. Vol. 21, pp. 912–923.

Gill, P.E., Murray, W., Wright, M.H. 1981. Practical Optimization. London: Academic Press.

Glocker, C. 2001. On frictionless impact models in rigid-body systems. Philosophical Transactions of the Royal Society of London, A359: 2385–2404.

Glowinski, R., Le Tallec, P. 1989 Augmented Lagrangian and operator-splitting methods in nonlinear mechanics, Society for Industrial and Applied Mathematics,

Goel, R.K. 2005. Seismic response of linear and non-linear asymmetric systems with non-linear fluid viscous dampers. Earthquake Engineering, Structural Dynamics 34(7): 825–846.

Goldsmith, W. 1960. Impact, London: Edward Arnold Ltd.

Gomes, A., Appleton, J. 1997. Nonlinear cyclic stress-strain relationship of reinforcing bars including buckling. Engineering Structures 19(10): 822–826.

Gonzalez, O. 2000. Exact energy-momentum conserving algorithms for general models in nonlinear elasticity, Comp. Meth. Appl. Mech. Eng., 190: 1763–1783.

Griffiths, J.B. 1985. The Theory of Classical Dynamics. Cambridge University Press, Cambridge, United Kingdom.

Gu, Q., Conte, J.P. 2003. Convergence studies in non-linear finite element response sensitivity analysis. Applications of Statistics and Probability in Civil Engineering, Proceedings of ICASP9, San Francisco, July 6–9.

Gu, Q., Barbato, M. and Conte, J.P. 2008a. Handling of constraints in finite element response sensitivity analysis. *Journal of Engineering Mechanics*, (ASCE). Submitted for review.

Gu, Q., Conte, J.P., Yang, Z. and Elgamal, A. 2008b. Consistent tangent moduli for multiyield-surface J_2 plasticity material model. *International Journal for Numerical Methods in Engineering*. Submitted for review.

Gu, Q., Conte, J.P., Yang, Z. and Elgamal, A. 2008c. Finite element response sensitivity analysis of multi-yield-surface J_2 plasticity model by direct differentiation method. *Computer Methods in Applied Mechanics and Engineering*. Submitted for review.

Guerra, F. 2005. Optimum layout of building subjected to geometric constraints. Practice Periodical on Structural Design and Construction 10(4): 239–245.

Gull, S.F. 1989. Bayesian inductive inference and maximum entropy. J. Skilling ed. Maximum entropy and Bayesian methods. Kluwer.

Gupta, B., Kunnath, S.K. 2000. Adaptive spectra-based pushover procedure for seismic evaluation of structures. Earthquake Spectra 16(2): 367–392.

Haftka, R.T., Gurdal, Z. 1993. Elements of Structural Optimization. Dordrecht: Kluver Academic Publishers.

Hagen, O., Tvedt, L. 1991. Vector process out-crossing as parallel system sensitivity measure. Journal of Engineering Mechanics (ASCE), 117(10), 2201–2220.

Hajjar, J.F., Abel, J.F. 1988. Parallel processing for transient nonlinear structural dynamics of three-dimensional framed structures using domain decomposition. Computers, Structures, 30(6): 1237–1254.

Haldankar, H. 2007. Studies of high speed train induced vibrations. MS Thesis, University of South Carolina.

Hall, L. 2003. Simulations and analyses of train-induced ground vibrations in Finite Element Models. Soil Dynamics and Earthquake Engineering 2003(23): 403–413.

Hanganu, A., Oñate, E., Barbat, A.H. 2002. Finite element methodology for local/global damage evaluation in civil engineering structures. Computers and Structures; 80: 1667–1687.

Hanson, R.D., Aiken, I.D., Nims, D.K., Ritchter, P.J., Batchman, R.E. 1993. State of the art and state of the practice in seismic engineering dissipation. Procedings, ATC-17-1. Seminar on seismic isolation, passive energy dissipation and active control. Applied Technology Council, San Francisco, California.

Hanss, M. 2003. The extended transformation method for the simulation and analysis of fuzzy parameterized models, International Journal of Uncertainty, Fuzziness and Knowledge-Based Systems, Vol. 11, No. 6, 711–727.

Harr, M. 1989. Probabilistic estimates for multivariate analysis. Applied Mathemathical Modelling 13, 313–318.

Hastings, W.K. 1970. Monte Carlo sampling methods using Markov chains and their applications, Biometrika, 57, 97–109.

Haukaas, T., Der Kiureghian, A. 2004. Finite element reliability and sensitivity methods for performance-based engineering. Report PEER 2003/14, Pacific Earthquake Engineering Research Center, University of California, Berkeley.

HAZUS. 1999. Earthquake Loss Estimation Methodology. Technical Manual, Federal Emergency Management Agency and National Institute of Buildings Sciences, Washington, D.C., USA.

Herle, I. 1997. Hypoplastizitat und Granulometrie einfacher Korngerüste, Dissertation, Institut für Bodenmechanik und Felsmechanik der Universitat Karlsruhe, 142.

Hewitt, C., Bishop, P., Steiger, R. 1973. A Universal Modular ACTOR Formalism for Artificial Intelligence. In Proceedings of the 3rd International Joint Conference on Artificial Intelligence, Stanford, CA, August.

Hibbit, Karlsson, Sorensen, 2001. ABAQUS theory manual. Version 6.2.

Holler, S. 2006. Dynamisches Mehrphasenmodell mit hypoplastischer Formulierung der Feststoffphase, Mitteilungen des Lehrstuhls fur Baustatik und Baudynamik, RWTH Aachen, 11.

Holler, S., Meskouris, K. 2006. Granular Material Silos under Dynamic Excitation: Numerical Simulation and Experimental Validation, Journal of Structural Engineering, 132, 1573–1579.

Hong, H.P. 1998. An efficient point estimate method for probabilistic analysis. Reliability Engineering and System Safety 59, 261–267.

Hu, B., Eberhard, P. 1999. Experimental and theoretical investigation of a rigid body striking an elastic rod. Institutsbericht IB-32, Stuttgart: Institute B of Mechanics.

Hu, B., Eberhard, P., Schiehlen, W. 2003. Comparison of analytical and experimental results for longitudinal impacts on elastic rods. Journal of Vibration and Control, 9: 157–174.

Hughes, T.J.R. 1976. Reduction scheme for some structural eigenvalue problems by a variational theorem. International Journal for Numerical Methods in Engineering 10: 845–852.

Hughes, T.J.R. 1979. A note on the stability of Newmark's algorithm in nonlinear structural dynamics, International Journal for Numerical Methods in Engineering, 11, 383–386.

Hughes, T.J.R. 1980. Generalization of selective integration procedures to anisotropic and nonlinear media, Int. J. Num. Meth. Eng., 15: 1413–1418.

Hughes, T.J.R., Caughey, T.K., Liu, W.K. 1978. Finite-element methods for nonlinear elastodynamics which conserve energy. Journal of Applied Mechanics, Transactions of the ASME 45: 366–370.

Hurtado, J. 2004. Structural Reliability – Statistical Learning Perspectives, Lecture Notes in Applied and Computational Mechanics. 17. Springer Verlag.

Hurtado, J.E. 2004. Structural Reliability. Statistical Learning Perspectives. Heidelberg: Springer.

Hurtado, J.E. 2006. Optimal reliability-based design using support vector machines and artificial life algorithms. In Y. Tsompanakis and N. D. Lagaros (Eds.), Intelligent Computational Paradigms in Earthquake Engineering. Hershey: Idea Group Inc.

Hurtado, J.E. 2007. Structural robustness and its relationship to reliability. In Y. Tsompanakis, N. D. Lagaros, and M. Papadrakakis (Eds.), Structural Design Optimization Considering Uncertainties. Leiden: Taylor and Francis.

Hurtado, J.E., Barbat, A. 1996. Improved stochastic linearization method using mixed distributions. Structural Safety 18, 49–62.

Hurtado, J.E., Barbat, A. 2000. Equivalent linearization of the Bouc-Wen hysteretic model. Engineering Structures 20, 1121–1132.

Iai, S. 1998. Seismic analysis and performance of retaining structures, in Dakoulas, P., Yegian, M., Holtz, R.D. (Eds.), Proceedings of Geotechnical Earthquake Engineering and Soil Dynamics III, Geotechnical Special Publ. No. 75, Vol. 2, ASCE, Reston, Va., pp. 1020–1044.

Ibrahimbegovic, A. 1995. On finite element implementation of geometrically nonlinear Reissners beam theory: three-dimensional curved beam elements. Computer Methods in Applied Mechanics and Engineering; 122: 11–26.

Idriss, I.M., Sun, J.I. 1992. Excerpts from USER'S Manual for SHAKE91: A Computer Program for Conducting Equivalent Linear Seismic Response Analyses of Horizontally Layered Soil Deposits. Center for Geotechnical Modeling Department of Civil, Environmental Engineering University of California Davis, California.

Iervolino, I., Maddaloni, G., Cosenza, E. 2006. Unsealed real record sets compliant with Eurocode 8. First European Conference on Earthquake Engineering and Seismology, Geneva, Switzerland.

Igusa, T., Kiurghian, A.D. 1988. Response of uncertain systems to stochastic excitation. J Engng Mech, ASCE; 114: 812–832.

IKP – Division of Solid Mechanics – www.ikp.liu.se/solid/. Latest access 27/2-2007.

Irschik, H. 2002. A review of static and dynamic shape control of structures using piezoelectric actuation. Engineering Structures, 24(1).

Isakovic, T., Fischinger, M. 2006. Higher modes in simplified inelastic seismic analysis of single column bent viaducts. Earthquake Engineering and Structural Dynamics 35: 95–114.

Iwan, W.D. 1966. A distributed-element model for hysteresis and its steady-state dynamic response, Journal of Applied Mechanics, 33, 893–900.

Iyisan, R. 1996. Correlations between Shear Wave Velocity and In-situ Penetration Test Results, Technical Journal of Turkish Chamber of Civil Engineers, 7(2): 1187–1199 (in Turkish).

Jayakumar, P. 1987. Modeling and identification in structural dynamics, Technical Report EERL 87-01, California Institute of Technology, Pasadena, CA.

Jayakumar, P., Beck, J.L. 1988. System identification using nonlinear structural models. H.G. Natke, J.T.P. Yao eds. Structural safety evaluation based on system identification approaches, Vieweg and Sons.

Jaynes, E.T. 2003. Probability theory: the logic of science. Cambridge University Press.

Jeffreys, H. 1939. Theory of probability. Clarendon Press.

Jensen, H.A. 2005. Design and Sensitivity Analysis of Dynamical Systems Subjected to Stochastic Loading. Computers and Structures, 83: 1062–1075.

Jensen, H.A., Valdebenito, M.A. 2007. Reliability Analysis of Linear Dynamical Systems using Approximate Representations of Performance Functions. Structural Safety. 29: 222–237.

Jeong, S.H., Elnashai, A.S. 2004a. Analytical assessment of an irregular RC frame for full-scale 3D pseudo-dynamic testing, Part I: Analytical model verification. Journal of Earthquake Engineering, 9(1): 95–128.

Jeong, S.H., Elnashai, A.S. 2004b. Analytical assessment of an irregular RC frame for full-scale 3D pseudo-dynamic testing, Part II: Condition assessment and test deployment. Journal of Earthquake Engineering. 9(2): 265–284.

Jeong, S.-H., Elnashai, A.S. 2006. New three-dimensional damage index for RC buildings with planar irregularities. Journal of Structural Engineering 132(9): 1482–1490.

Jeremic, B. 2004. Lecture notes on computational geomechanics: Inelastic finite elements for pressure sensitive materials. Technical Report UCD-CompGeoMech–01–2004, University of California, Davis, 2004. available online: http://sokocalo.engr.ucdavis.edu/~jeremic/CG/LN.pdf.

Jeremic, B., Yang, Z. 2002. Template elastic–plastic computations in geomechanics. International Journal for Numerical and Analytical Methods in Geomechanics, 26(14): 1407–1427.

Jeremic, B., Kunnath, S., Xiong, F. 2004. Influence of soil–structure interaction on seismic response of bridges. International Journal for Engineering Structures, 26(3): 391–402.

Jeremic, B., Sture, S. 1997. Implicit integrations in elasto–plastic geotechnics. International Journal of Mechanics of Cohesive–Frictional Materials, 2: 165–183.

Jeremic, B., Sture, S. 1998. Tensor data objects in finite element programming. International Journal for Numerical Methods in Engineering, 41: 113–126.

José, J.V., Saletan, E.J. 1998. Classical dynamics: a contemporary approach, Cambridge University Press.

Kan, C.L., Chopra, A.K. 1977. Effect of torsional coupling on earthquake forces in buildings, Journal of Structural Division ASCE, 103(4): 805–819.

Kanagasundaram, S., Karihaloo, B.L. 1991. Minimum cost design of reinforced concrete structures. Computers, Structures, 41(6): 1357–1364.

Kane, C., Marsden, J.E., Ortiz, M., West, M. 2000. Variational integrators and the Newmark algorithm for conservative and dissipative mechanical systems. International Journal for Numerical Methods in Engineering, 49: 1295–1325.

Kapania, R.K., Li, J. 2003. On a geometrically exact curved/twisted beam theory under rigid cross-section assumption. Computational Mechanics, 30: 428–443.

Kappos, A.J., Manolis, G.D., Moschonas, I.F. 2002. Sismic assessment and design of R/C bridges with irregular configuration, including SSI effects. International Journal of Engineering Structures, 24: 1337–1348.

Karypis, G., Schloegel, K., Kumar, V. 1998. ParMETIS: Parallel Graph Partitioning and Sparse Matrix Ordering Library. University of Minnesota.

Kasai, K., Fu, Y., Watanabe, A. 1998. Passive control systems for seismic damage mitigation. Journal of Structural Engineering, 124(5): 501–512.

Kasai, K., Bleiman, D. 1996. Bolted brackets for repair of damaged steel moment frame Connections. 7th US-Japan Workshop on the Improvement of Structural Design and Construction Practices: Lessons Learned from Northridge and Kobe, Kobe, Japan.

Katafygiotis, L., Cheung, S. 2006. Domain decomposition method for calculating the failure probability of linear dynamic systems subjected to Gaussian stochastic loads. Journal of Engineering Mechanics 132(5), 475–486.

Katafygiotis, L., Cheung, S. 2007. Application of spherical subset simulation method and auxiliary domain method on a benchmark reliability study. Structural Safety 29(3), 194–207.

Katafygiotis, L., Moan, T., Cheung, S. 2007. Auxiliary domain method for solving multiobjective dynamic reliability problems for nonlinear structures. Structural Engineering, Mechanics 25(3), 347–363.

Katafygiotis, L.S., Lam, H.-F. 2002. Tangential-projection algorithm for manifold representation in unidentifiable model updating problems, Earthquake Engineering and Structural Dynamics, 31, 791–812.

Katsikadelis, J.T., Kandilas, C.B. 1990. A Flexibility Matrix Solution of the Vibration Problem of Plates Based on the Boundary Element Method, Acta Mechanica, 83: 51–60.

Katsikadelis, J.T. 2002. The Analog Equation Method. A Boundary – only Integral Equation Method for Nonlinear Static and Dynamic Problems in General Bodies, Theoretical and Applied Mechanics, 27: 13–38.

Kausel, E. 1974. Forced vibrations of circular foundations on layered media. Research Report R74-11, Department of Civil Engineering, Massachusetts Institute of Technology, Cambridge, Massachusetts.
Kaynia, A.M., Madshus, C., Zackrisson, P. 2000. Ground vibration from high-speed trains: Prediction and countermeasure. Journal of Geotechnical and Geoenvironmental Engineering 126: 531–537.
Kelly, J.M. 1993. Earthquake-Resistance Design with Rubber. London: Springer-Verlag. Kennedy, J. and R. C. Eberhart 2001. Swarm Intelligence. San Francisco: Morgan Kaufmann.
Kicinger, R., Arciszewski, T., De Jong K. 2005. Evolutionary computation and structural design: A survey of the state-of-the-art, Computers and Structures 83: 1943–1978.
Kikuchi, N., Oden, J. 1989. Contact Problems in Elasticity: A Study of Variational Inequalities and Finite Element Methods, Philadelphia: SIAM.
Kilar, V., Fajfar, P. 1996. Simplified Push-Over Analysis of Building Structures. Proceedings of the 11th World Conference Earthquake Engineering, 59–66, Acapulco Mexico.
Kiliç, H., Özener, P.T., Ansal, A., Yildirim, M., Özaydin, K., Adatepe, S. 2006. Microzonation of Zeytinburnu Region with respect to Soil Amplification: A Case Study. Journal of Engineering Geology 86: 238–255.
Kim, J.K., Koh, H.M., Kwon, K.J., Yi, J.S. 2000. A three-dimensional transmitting boundary formulated in Cartesian co-ordinate system for the dynamics of non-axisymmetric foundations. Earthquake Engineering and Structural Dynamics 29: 1527–1546.
Klaas, O., Kreienmeyer, M., Stein, E. 1994. Elastoplastic finite element analysis on a MIMD parallel–computer. Engineering Computations, 11: 347–355.
Kleiber, M., Antunez, H., Hien, T.D., Kowalczyk, P. 1997. Parameter Sensitivity in Nonlinear Mechanics: Theory and Finite Element Computation. New York: Wiley.
Kleiber, M., Hien, T.D. 1992. The Stochastic Finite Element Method. Basic Perturbation Technique and Computer Implementation. New York: Wiley.
Koo, H., Der Kiureghian, A., Fujimura, K. 2005. Design–point excitation for non–linear random vibrations. Probabilistic Engineering Mechanics, 20(2), 134–147.
Koskisto, O.J., Ellingwood, B.R. 1997. Reliability-based optimization of plant precast concrete structures. Journal of Structural Engineering, 123(3): 298–304.
Koyluoglu, U., Cakmak, A., Nielsen, S. 1995. Interval Algebra to Deal with Pattern Loading and Structural Uncertainties, Journal of Engineering Mechanics, 121(11): 1149–1157.
Kramer, S.L. 1996. Geotechnical Earthquake Engineering. Prentice Hall, New Jersey.
Krätzig, W.B. 1997. Multi-level modeling technique for elasto-plastic structural responses, In: D.R.J. Owen, et al. (eds.), Computational Plasticity. Proceedings 5th International Conference, Vol. 1, 457–468, CIMNE Barcelona.
Krätzig, W.B. 2006. Damage Indicators for Estimates of Seismic Vulnerability. In: Topping, B.H.V. et al. (eds.) Innovations in Computational Structures Technologies, 111–132. Saxe-Coburg Publications, Stirlingshire.
Krätzig, W.B., Meskouris, K. 1999. Assessment of seismic structural vulnerability as a low-cycle fatigue process, In: Ph. Bisch, P. Labbé, A. Pecker, (eds.), Proc. of the 11th European Conference on Earthquake Engineering, 161–178, A. Balkema, Rotterdam.
Krätzig, W.B., Petryna, Y.S. 2003. Fundamental tools for structural damage indication and lifetime management, In: F. Stangenberg et al. (eds.), ICLODC 2004, 2nd Int. Conf. on Lifetime-Oriented Design Concepts, SFB 398, Ruhr-University Bochum.
Krätzig, W.B., Petryna, Y.S. 2005. Structural damage and life-time estimates by non-linear FE simulation, Journ. Engg. Struct, 27(12): 1726–1740.
Krawinkler, H., Seneviratna, G.D.P.K. 1998. Pros and cons of a pushover analysis of seismic performance evaluation. Int. Journ. Engineering Structures, 20(4–6): 452–464.
Krenk, S. 2006. Energy conservation in Newmark based time integration algorithms, Computer Methods in Applied Mechanics and Engineering, 195, 6110–6124.

Krenk, S. 2006. State-space time integration with energy control and fourth order accuracy for linear dynamic systems, International Journal for Numerical Methods in Engineering, 65: 595–619.

Krenk, S. 2008. Extended state-space time integration with high-frequency dissipation, International Journal for Numerical Methods in Engineering, 73: 1767–1787.

Krenk, S., Høgsberg, J.R. 2005. Properties of time integration with first order filter damping, International Journal for Numerical Methods in Engineering, 64: 547–566.

Krenk, S., Kirkegaard, P.H. 2001. Local tensor radiation conditions for elastic waves, Journal of Sound and Vibration, 247: 875–889.

Kuhl, D., Crisfield, M.A. 1999. Energy-conserving and decaying algorithms in non-linear structural dynamics. International Journal for Numerical Methods in Engineering 45: 569–599.

Kumar, P., Nukala, V.V., White, D.W. 2004. A mixed finite element for threedimensional nonlinear analysis of steel frames. Computer Methods in Applied Mechanic and Engineering; 193(5): 2507–2545.

Kupfer, H.B., Hilsdorf, H.K., Rusch, H. 1969. Behavior of Concrete under Biaxial Stress. ACI Journal. 87(2): 656–666.

Kurtulus, A., Lee, J.J., Stokoe, K.H. 2005. Summary report – site characterization of capital aggregates test site. Technical report, Department of Civil Engineering, University of Texas at Austin.

Kwon, O.S., Nakata, N., Elnashai, A.S., Spencer, B. 2005. A Framework for Multi-Site Distributed Simulation and Application to Complex Structural Systems. Journal of Earthquake Engineering. 9(5): 741–753.

Lagaros, N.D., Fotis, A.D., Krikos, S.A. 2006a. Assessment of seismic design procedures based on the total cost, Earthquake Engineering Structural Dynamics, 35(11): 1381–1401.

Lagaros, N.D., Fragiadakis, M., Papadrakakis, M., Tsompanakis, Y. Structural optimization: a tool for evaluating seismic design procedures, J. of Engrg. Str., (to appear), 2006.

Lagaros, N.D., Papadrakakis, M. 2007. Seismic design of RC structures: a critical assessment in the framework of multi-objective optimization. Earthquake Engineering, Structural Dynamics. 36(12): 1623–1639.

Lagaros, N.D., Papadrakakis, M., Bakas, N. 2006b. Automatic minimization of the rigidity eccentricity of 3d reinforced concrete buildings. Journal of Earthquake Engineering 10(4): 533–564.

Lagaros, N.D., Papadrakakis, M., Kokossalakis, G. 2002. Structural optimization using evolutionary algorithms. Computer, Structures 80(7–8): 571–587.

Lai, S.P. 1982. Statistical characterization of strong ground motions using power spectral density function. Bulletin of the Seismological Society of America 72: 259–274.

Lallemand, B., Cherki, A., Tison, T., Level, P. 1999. Fuzzy modal finite element analysis of structures with imprecise material properties, Journal of Sound and Vibration, 220(2): 353–364.

Lanczos, C. 1970. The Variational Principles of Mechanics, 4th Edition. Toronto: University of Toronto Press.

Lane H., Ekevid, T., Kettil, P., Ching, C.Y., Wiberg, N.-E. 2007. Vehicle-track-underground modeling of rail induced wave propagation. Computers, Structures, 85: 1215–1229.

Lane, H., Kettil, P., Enelund, M., Ekevid T., Wiberg, N.-E. Absorbing Boundary Layers for Elastic Wave Propagation. Presented at the 8th International Conference on Computational Plasticity, Barcelona, Spain, September 5–8, 2007.

Lane, H., Kettil P., Wiberg, N.-E. Moving Finite Elements and Dynamic Vehicle Interaction. Submitted to European Journal of Mechanics A – Solids.

Lane, H. Computational Railway Dynamics. Ph. D. thesis, Chalmers University of Technology, Gothenburg, Sweden, 2007.

Langley, R.S. 2000. Unified approach to probabilistic and possibilistic analysis of uncertain systems, Journal of Engineering Mechanics, 126(11): November, 2000, 1163–1172.

Latteur, P. Optimisation des treillis, arcs, poutres et câbles sur base d'indicateurs morphologiques – application aux structures soumises en partie ou en totalité au flambement (3 vol.), Ph. D. thesis, Vrije Universiteit Brussel, 2000.

Lee, J.H. & Kim, J.K. 2008. Transmitting boundary for water-saturated transversely isotropic strata based on the u-U formation. Soil Dyn Earthquake Eng, doi:10.1016/j.soildyn.2008.08.003.

Lee, J.H. 2007. 3-D Transmitting Boundary in Cylindrical and Cartesian Coordinate Systems for Soil-Structure Interaction Analysis in Water-Saturated Transversely Isotropic Layered Ground. PhD dissertation, Seoul National University, Seoul, Korea (in Korean).

Lehman, D.E., Moehle, J.P. 1998. Seismic performance of well-confined concrete bridge columns. Technical report, Pacific Earthquake Engineering Research Center.

LESSLOSS. 2006. Risk Mitigation for Earthquakes and Landslides. Integrated Research & Development Project of the European Commission. Deliverable 78 – Applications of probabilistic seismic assessment methods to selected case studies. Sub-Project 9 – Probabilistic risk assessment: methods and applications. http://www.lessloss.org.

Lew, A., Marsden, J.E., Ortiz, M., West, M. 2004. Variational time integrators. International Journal for Numerical Methods in Engineering 60: 153–212.

Lewis, R.W., Schrefler, B.A. 1998. The finite element methods in the static and dynamic deformation and consolidation of porous media. John Wiley, Sons.

Li, J., Widlund, O.B. 2007. On the use of inexact subdomain solvers for BDDC algorithms. Computer Methods in Applied Mechanics and Engineering, 196(8): 1415–1428.

Li, G., Cheng, G. 2001. Optimal decision for the target value of performance-based structural system reliability. Structural, Multidisciplinary Optimization 22(4): 261–267.

Lighthill, J. 1978. Waves in Fluids. Cambridge University Press, MA.

Lin, W.H., Chopra, A.K. 2003. Asymmetric one–storey elastic system with non-linear viscous and viscoelastic dampers: Earthquake response. Earthquake Engineering and Structural Dynamics, 32: 555–577.

Lin, Y.K., Cai, C.Q. 1995. Probabilistic Structural Dynamic: Advance Theory and Applications. New York, McGraw-Hill.

Lin, Y.Y., Chang, K.C. 2003. Study on damping reduction factors for buildings under earthquake ground motions. Journal of Structural Engineering, JEE, 129(2): 206–214.

Liu, P., Der Kiureghian, A. 1986. Multivariate distribution models with prescribed marginals and covariances. Probabilistic Engineering Mechanics, 1(2), 105–112.

Liu, P.-L., Der Kiureghian, A. 1991. Optimization algorithms for structural reliability. Structural Safety, 9(3), 161–177.

Lu, Y. 2002. Comparative study of seismic behavior of multistory reinforced concrete framed structures. Journal of Structural Engineering, JEE, 128(2): 169–178.

Luh G.C., Chuen, C.H. 2004. Multi-Objective optimal design of truss structure with immune algorithm, Computers and Structures, 82: 829–844.

Lutes, L.D., Sarkani, S. 2001. Random Vibrations, Butterworth-Heinemann, Oxford (UK).

Lutes, L.D., Sarkani, S. 1997. Stochastic Analysis of Structural and Mechanical Vibrations. Upper Saddle River: Prentice Hall.

Mace, B.R., Shorter, P.J. 2001. A local modal/perturbational method for estimating frequency response statistics of built-up structures with uncertain properties, Journal of Sound and Vibration, 242(5): 793–811.

MacKay, D.J.C. 1991. Bayesian methods for adaptive models, Ph.D. thesis, California Institute of Technology, Pasadena, CA.

Mackerle, J. 1996. FEM and BEM in geomechanics: Foundations and Soil-Structure Interaction – A bibliography 1992-1994). Finite Elements in Analysis and Design 29: 249–263.

Mackerle, J. 1998. Finite element and boundary element analysis of bridges, roads and pavements – A bibliography 1994–1997). Finite Elements in Analysis and Design, 29: 65–83.

Madshus, C., Kaynia, A.M. 2000. High-speed railway lines on soft ground: Dynamic behaviour at critical train speed. Journal of Sound and Vibration 231: 689–701.
Maeck, J., De Roeck, G. 2003a. Description of Z24 benchmark. Mechanical Systems and Signal Processing 71(1): 127–131.
Maeck, J., De Roeck, G. 2003b. Damage assessment using vibration analysis on the Z24-bridge. Mechanical Systems and Signal Processing 71(1): 133–142.
Maia, N.M.M., Silva, J.S.M., He, J., Lieven, N.A.J., Lin, R.M., Skingle, G.W., To, W.-M. & Urgueira, A.P.V. 1997. *Theoretical and Experimental Modal Analysis*. Research Studies Press Ltd., Somerset, England.
Makris, N., Badoni, D., Delis, E., Gazetas, G. 1994. Prediction of observed bridge response with soil–pile–structure interaction. ASCE Journal of Structural Engineering, 120(10): 2992–3011.
Mander, J.B., Priestley, M.J.N., Park, R. 1984. Seismic design of bridge piers, Research Report 84-2, Department of Civil Engineering, University of Canterbury, New Zealand.
Mander, J.B., Priestley, M.J.N., Park, R. 1984. Seismic design of bridge piers. Res. Rep. 84-2, Dept. of Civ. Engrg., Univ. of Canterbury, Christchurch, New Zealand.
Manson, G. 2003. Sharper eigenproblem estimates for uncertain multi-degree of freedom systems, Proceedings of IMAC XXI CDrom, Orlando, Florida, USA, February.
Marano, G.C., Greco, R., Trentadue, F., Chiaia, B. 2007. Constrained reliability-based optimization of linear tuned mass dampers for seismic control, International Journal of Solids and Structures, accepted for publication.
Marinakis, Y., Marinaki, M., Stavroulakis, G.E. 2008. Particle swarm optimization approach for fuzzy control of smart structures. Sixth Intern. Conference on Engineering Computational Technology ECT2008, Athens, Greece, 2–5 September 2008, Civil-Comp Press.
Marini, A., Spacone, E. 2006. Analysis of R/C Elements Including Shear Effects. ACI Structural Journal, 103(5), 645–655.
Marinova, D.G., Stavroulakis, G.E., Zacharenakis, E.C. 2005. Robust control of smart beams in the presence of damage-induced structural uncertainties. International Conference PhysCon 2005, Saint Petersburg, Russia.
Marsden, J.E. 1992. Lectures on Mechanics, London Mathematical Society Lecture Note Series, 174: Cambridge University Press.
Marsden, J.E., West, M. 2001. Discrete mechanics and variational integrators. Acta Numerica, 10: 357–514.
Marsden, J.E., Hughes, T.J.R. 1983. Mathematical Foundations of Elasticity. Englewood Cliffs, New Jersey: Prentice-Hall, Inc.
Masing, G. 1926. Eigenspannungen und verfestigung beim messing (Self-stretching and hardening for brass), 2nd International Congress on Applied Mechanics, Zurich, Switzerland.
Mata, P., Boroschek, R., Oller, S., Barbat, A.H. 2007a. High damping rubber model for energy dissipating devices, Journal of Earthquake Engineering, 11(2): 231–256.
Mata, P., Oller, S., Barbat, A.H., Boroschek, R. 2006. Numerical code for seismic analysis of structures incorporating energy dissipating devices. First European Conference on Earthquake Engineering and Seismology, ECEES, Geneva, Switzerland.
Mata, P., Oller, S., Barbat, A.H., Boroschek, R. 2008b. Computational models for the seismic response of reinforced concrete buildings with energy dissipating devices, Archives of Computational Methods in Engineering, (DOI 10.1007/s11831-008-9024-z).
Mata, P., Oller, S., Barbat, A.H., Boroschek, R. 2008c. Nonlinear seismic analysis of RC structures with energy dissipating devices, International Journal for Numerical Methods in Engineering, (Submitted).
Mata, P., Oller, S., Barbat, A.H. 2007b. Static analysis of beam structures under nonlinear geometric and constitutive behavior, Computer Methods in Applied Mechanics and Engineering; 196: 4458–4478.

Mata, P., Oller, S., Barbat, A.H. 2008a. Dynamic analysis of beam structures considering geometric and constitutive nonlinearity, Computer Methods in Applied Mechanics and Engineering; 197: 857–878.
Mau, E.T., El-Mabsout, M. 1989. Inelastic buckling of reinforcing bars. Journal of Engineering Mechanics 115(1): 1–17.
Mazzolani, F.M., Piluso, V. 1996. The theory and design of seismic resistant steel frames. E, FN Spon.
Mazzoni, S., Fenves, G.L., Smith, J.B. 2004. Effects of local deformations on lateral response of bridge frames. Technical report, University of California, Berkeley.
McCallen, D.B., Romstadt K.M. 1994. Analysis of a skewed short span, box girder overpass. Earthquake Spectra.
McKenna F.T. 1997. Object Oriented Finite Element Programming: Framework for Analysis, Algorithms and Parallel Computing. PhD thesis, University of California, Berkeley.
Mei, C.C., Foda, M.A. 1981. Wave-induced response in a fluid-filled poroelastic solid with a free surface – a boundary layer theory. Geophysical Journal of the Royal Astronomical Society 66: 597–631.
Melchers, R.E. 1999. Structural Reliability: Analysis and Prediction. Chichester: John Wiley and Sons.
Menegotto, M., Pinto, P.E. 1973. Method of analysis for cyclically loaded RC plane frames including changes in geometry and nonelastic behaviour of elements under combined normal force and bending. Proc. IABSE Symposium, Lisbon, Portugal.
Meng, X.N., Laursen, T.A. 2002. Energy consistent algorithms for dynamic finite deformation plasticity, Comp. Meth. Appl. Mech. Eng., 191: 1639–1675.
Metron – www.metron.se. Latest access 19/2-2007.
Meyer, I.F., Krätzig, W.B., Stangenberg, F. 1988. Damage prediction in reinforced concrete frames under seismic action. EEE-European Earthquake Engineering 3: 9–15.
MIDAS, 2006. Civil Analysis Reference Manual, Civil 2006 (v7.12 Release No. 1) Midas Information Technology Co. Ltd.
Minamoto, H. 2005. Elasto/Visco-plastic impact of two equivalent spheres made of SUJ2 (in Japanese). Transactions of the Japan Society of mechanical Engineers, C71: 51–57.
Moayyad, P., Mohraz, B. 1982. A study of power spectral density of earthquake accelerograms. Technical report, Civil and Mechanical Engineering Department, Southern Methodist University, Dallas, TX.
Moens D., Vandepitte, D. 2004. An interval finite element approach for the calculation of envelope frequency response functions, International Journal for Numerical Methods in Engineering, 61(14): 2480–2507.
Moens, D. 2002. A Non-Probabilistic Finite Element Approach for Structural Dynamic Analysis with Uncertain Parameters, Ph.D. thesis, K.U. Leuven, Leuven.
Moens, D., Vandepitte, D. 2005. A Survey of Non-Probabilistic uncertainty treatment in Finite Element Analysis, Computer Methods in Applied Mechanics and Engineering, Vol. 194, Nos. 12–16, 1527–1555.
Moharrami, H., Grierson, D.E. 1993. Computer-automated design of reinforced concrete frameworks. Journal of Structural Engineering, 119(7): 2036–2058.
Molina-Palacios, S., Lindholm, C.D. 2006. SELENA V1.0 User and Technical Manual. NORSAR, Norway (http://www.norsar.no/seismology/selena.html)
Möller, O. 2001. Metodología para evaluación de la probabilidad de falla de estructuras sismorresistentes y calibración de códigos. Tesis de Doctorado en Ingeniería, Universidad Nacional de Rosario.
Möller, O., Foschi, R. 2003. Reliability evaluation in seismic design: a response surface methodology. Earthquake Spectra. 19(3): 579–603.

Möller, O., Foschi, R., Rubinstein, M., Quiroz, L. 2006a. Momento-curvatura de secciones de hormigón armado sismorresistentes utilizando redes neuronales. Mecánica Computacional XXV: 2145–2162. AMCA.
Möller, O., Foschi, R., Rubinstein, M., Quiroz, L. 2006b. Vulnerabilidad sísmica de estructuras: una aproximación probabilística usando redes neuronales. Memorias XIX Jornadas Argentinas de Ingeniería Estructural, CD, 050, AIE.
Mononobe, N., Matsuo, H. 1929. On the determination of earth pressures during earthquakes, Proceedings of the World Engineering Congress, Tokyo, Japan, Vol. 9, Paper 388.
Montgomery, D.C. 1997. Design and analysis of experiments, Wiley, New York, 4th edition.
Monti, G., Nutti, C. 1992. Nonlinear behaviour of Reinforcing Bars Including Buckling. Journal of Structural Engineering 118(12): 3268–3284.
MSC Software Corporation, MSC. Nastran Basic Dynamic Analysis User's Guide, 2002.
MSC Software Corporation, MSC. Nastran superelement user's guide, Los Angeles, 2001.
MSC/NASTRAN for Windows, 1999. Finite element modeling and postprocessing system. Help System Index, Version 4.0, USA.
Müller, F.P., Keintzel, E., Charlier, H. 1983. Dynamische Probleme im Stahlbetonbau. DAfStB – Deutscher Ausschuss für Stahlbetonbau, Heft 342, Berlin.
Muto, M., Beck, J.L. 2008. Bayesian updating and model class selection for hysteretic structural models using stochastic simulation, Journal of Vibration and Control 14:7–34.
Mylonakis, G., Gazetas, G. 2000. Seismic soil-structure interaction: beneficial or detrimental?, Journal of Earthquake Engineering, 4(3), 277–301.
Naeim, F., Kelly, J.M. 1999. Design of seismic isolated structures – From theory to practice. New York: Wiley.
Nagtegaal, J.C., Parks, D.M., Rice, J.R. 1974. On numerically accurate finite element solutions in the fully plastic range, Comp. Meth. Appl. Mech. Eng., 4: 153–177.
National Building Code of Canada. Part 4 Structural Design. Issued by the Canadian Commission on building and fire codes, Federal Publications Inc. Toronto, 1995.
Nelson, R.B. 1976. Simplified Calculation of Eigenvector Derivatives. AIAA Journal. 14: 1201–1205.
Neuenhofer, A., Filippou, F.C. 1998. Geometrically Nonlinear Flexibility-Based Frame Finite Elements, ASCE Journal of Structural Engineering, 124(6), 704–711.
Newmark, N.M. 1959. A method of computation for structural dynamics. Journal of the Engineering Mechanics Division, ASCE, 85, 67–94.
Niemunis, A., Herle, I. 1997. Hypoplastic model for cohesionless soils with elastic strain range. Mechanics of Cohesive-Frictional Materials, 2, 279–299.
Nigam, N.C. 1972. Structural Optimization in random Vibration Environment, AIAA, 551–553.
Noels, L., Stainier, L., Ponthot, J.P. 2004. An Energy-Momentum Conserving Algorithm for Non-Linear Hypoelastic Constitutive Models, Int. J. Num. Meth. Eng., 59: 83–114.
Noor, A.K., Kamel, A., Fulton, R.E. 1978. Substructuring techniques – status and projections. Computers, Structures, 8: 628–632.
Oberkampf, W., DeLand, S., Rutherford, B., Diegert, K., Alvin, K., 1999. A New Methodology for the Estimation of Total Uncertainty in Computational Simulation, Proceedings of the 40th AIAA/ASME/ASCE/AHS/ASC Structures, Structural Dynamics and Materials Conference, AIAA-99-1612, 3061–3083.
O'Brien, J., Rizos, D.C. 2005. A 3D BEM-FEM methodology for simulation of high speed train induced vibrations. Soil Dynamics and Earthquake Engineering 25: 289–301.
Ohayon, R., Soize, C. 1998. Structural Acoustics and Vibration. Academic Press, San Diego.
Okabe, S. 1926. General theory of earth pressures, Journal of the Japan Society of Civil Engineering, 12(1).

Oliver, J., Cervera, M., Oller, S., Lubliner, J. 1990. Isotropic damage models and smeared crack analysis of concrete. Proceedings 2nd ICCAADCS, Zell Am See, Austria, Pineridge Press, 2: 945–958.

Oller, S., Oñate, E., Miquel, J., Botello, S. 1996b. A plastic damage constitutive model for composites materials. International Journal of Solids and Structures, 33(17): 2501–2518.

Oller, S., Oñate, E., Miquel, J. 1996a. Mixing anisotropic formulation for the analysis of composites, Communications in Numerical Methods in Engineering. 12: 471–482.

OPCM 3431 – Ulteriori modifiche ed integrazioni all'OPCM3274, 2005 (in Italian), Technical Norms for design, evaluation and seismic rehabilitation of buildings.

Ordaz, M. 1988. On the use of probability concentrations. Structural Safety, 5: 317–318.

Ötes, A. 1985. Zur werkstoffgerechten Berechnung der Erdbebenbeanspruchung in Stahlbetontragwerken, Techn. Report No. 25, Inst. f. Reinforced Concrete, TH Darmstadt.

Ottl, G. 2003. A Three-Phase FE-Model for Dewatering of Soils. Innsbruck University press.

Özaydın, K., Ansal, A., Erdik, M., Yıldırım, M., Kılıç, H., Adatepe, S., Özener, P.T., Tonaroglu, M., Sesetyan, K., Demircioglu, M. 2004. Earthquake Master Plan for Istanbul, Zeytinburnu Pilot Project, Report on Geological and Geotechnical Evaluation for Seismic Microzonation and Seismic Microzonation for Ground Shaking, Yıldız Technical Uni., Civil Eng. Geotechnical Dep. (In Turkish).

Palermo, D., Vecchio, F.J. 2003. Compression Field Modeling of Reinforced Concrete Subject to Reversed Loading: Formulation. ACI Structural Journal. Vol. 100, No. 5.

Palermo, D., Vecchio, F.J. 2004. Compression Field Modeling of Reinforced Concrete Subject to Reversed Loading: Verification. ACI Structural Journal. Vol. 101, No. 2.

Panagiotakos, T.B., Fardis, M.N. 2004. Seismic performance of RC frames designed to Eurocode 8 or to Greek Codes 2000. Bulletin of Earthquake Engineering. 2: 221–259.

Panagiotou, M., Restrepo, J. 2007. Computational model for the UCSD 7-story structural wall building slice, SSRP 07-09 Report, Department of Structural Engineering, University of California San Diego, (in press).

Pantelides, C.P., Okahashi, Y., Reaveley, L.D. 2004. Experimental investigation of reduced beam section moment connections without continuity plates. Earthquake Spectra. 20(4): 1185–1209.

Papadimitriou, C., Beck, J.L., Katafygiotis, L.S. 2001. Updating robust reliability using structural test data, Probabilistic Engineering Mechanics, 16, 103–113.

Papadimitriu, C., Beck, J.L., Katafygiotis, L.S. 1997. Asymtotic expansion for reliability and moments of uncertainly systems, Journal of Engineering Mechanics (ASCE), 123(12): 1219–1229.

Papadopoulos, P., Taylor, R. 1992. A mixed formulation of the finite element solution of contact problems. Computer Methods in Applied Mechanics and Engineering, 94: 373–389.

Papadrakakis, M., Tsompanakis, Y., Lagaros, N.D., Fragiadakis, M. Reliability based optimization of steel frames under seismic loading conditions using evolutionary computation, Special Issue of the Journal of Theoretical and Applied Mechanics on Computational Intelligence in Mechanics, 42(3): 585–608, 2004.

Papadrakakis, M., Lagaros, N.D., Thierauf, G., Cai, J. 1998. Advanced solution methods in structural optimization based on evolution strategies. Journal of Engineering Computations 15(1): 12–34.

Papadrakakis, M., Lagaros, N.D., Tsompanakis, Y., Plevris, V. 2001. Large scale structural optimization: Computational methods and optimization algorithms. Archives of Computational Methods in Engineering (State of the art reviews) 8(3): 239–301.

Papageorgiou, A., Halldorsson, B., Dong, G. 2000. Target Acceleration Spectra Compatible Time Histories. University of Buffalo, Dept. of Civil, Structural and Environmental Engineering. NY, http://civil.eng.buffalo.edu/engseislab/

Papagiannopoulos, G.A., Beskos, D.E. 2006. On a modal damping identification model for building structures. Archive of Applied Mechanics, 76: 443–463.

Papagiannopoulos, G.A., Beskos, D.E. 2008a. Use of equivalent modal damping for seismic design of steel structures, Part I: Theoretical aspects. Earthquake Engineering and Structural Dynamics (submitted).

Papagiannopoulos, G.A., Beskos, D.E. 2008b. Use of equivalent modal damping for seismic design of steel structures, Part II: Applications. Earthquake Engineering and Structural Dynamics (submitted).

Papazachos, B.C., Papaioannou, Ch.A., Theodulidis, N.P. 1993. Regionalization of seismic hazard in Greece based on seismic sources. Natural Hazards 8(1): 1–18.

Paraskeva, T.S., Kappos, A.J., Sextos, A.G. 2006. Extension of modal pushover analysis to seismic assessment of bridges. Earthquake Engineering and Structural Dynamics 35: 1269–1283.

Paraskevopoulos, E.A., Talaslidis, D.G. 2004. A rational approach to mass matrix diagonalization in two-dimensional elastodynamics. International Journal for Numerical Methods in Engineering 61: 2639–2659.

Park, Y.J., Ang. A.H-S. 1985. Mechanistic seismic damage model for reinforced concrete. Journal of Structural Engineering. ASCE. 111 (ST4): 722–739.

Parloo, E., Cauberghe, B., Benedettini, F. 2005. Sensitivity-based operational mode shape normalisation: Application to a bridge, Mechanical Systems and Signal Processing 19(1): 43–55.

Pars, L.A. 1965. A treatise on Analytical Dynamics. London: Heinemann Educational Books Ltd.

Parsopoulos, K.E., Vrahatis, M.N. 2001. Particle swarm optimization method for constrained optimization problems. Technical report, Department of Mathematics, University of Patras, Greece.

Paulay, T. 2001. Some design principles relevant to torsional phenomena in ductile buildings. Journal of Earthquake Engineering 5: 273–308.

Paulay, T. 1998. A mechanism-based design strategy for torsional seismic response of ductile buildings. European Earthquake Engineering 2: 33–48.

Paulay, T., Priestley, M.J.N. 1992. Seismic design of reinforced concrete and masonry buildings. John Wiley, Sons, Inc., New York, N.Y.

Pavarino, L.F. 2007. BDDC and FETI-DP preconditioners for spectral element discretizations. Computer Methods in Applied Mechanics and Engineering, 196(8): 1380–1388.

Pearlman, L., D'Arcy, M., Johnson, E., Kesselman, C., Plaszczak, P. 2004. NEESgrid Teleoperation Control Protocol (NTCP), NEESgrid TR-2004-23.

PEER. 1999. Open System for Earthquake Engineering Simulation (OpenSees). Pacific Earthquake Engineering Research Center, University of California, Berkeley, http://opensees.berkeley.edu/

Peeters, B., De Roeck, G. 2001. One-year monitoring of the Z24-bridge: environmental effects versus damage events. Earthquake Engineering and Structural Dynamics 30: 149–171.

Peeters, B., De Roeck, G. 2001. Stochastic system identification for operational modal analysis: A review. Special Issue on the Identification of Mechanical Systems of the ASME J. of Dynamic Systems, Measurement and Control, 659–667.

Peeters, B., Maeck, J., De Roeck, G. 2000. Excitation sources and dynamic system identification in civil engineering. Proceedings of the European COST F3 Conference on System Identification and Structural Health Monitoring, Madrid, Spain, 341–350.

Peeters, B., Van der Auweraer, H., Guillaume, P. 2004. The Polymax frequency-domain method: a new standard for modal parameter estimation? Shock and Vibration 11(3–4): 395–409.

Peruš, I., Poljanšek, K., Fajfar, P. 2006. Flexural deformation capacity of rectangular RC columns determined by the CAE method. Earthquake Engineering and Structural Dynamics 35(12): 1453–1470.

Petal, M. 2003. Research Report: Causes of Deaths and Injuries in the August 17th, 1999 3:02 a.m. Mw 7.4 Kocaeli Earthquake, Bogazici University, Disaster Preparedness Education Project, Istanbul, Turkey.

Petrangeli, M., Pinto, P.E., Ciampi, V. 1999. Fiber element for cyclic bending and shear of R/C structures. I: theory, ASCE Journal of Engineering Mechanics, 125(9), 994–1001.

Petryna, Y.S. 2005. Structural degradation, reliability and lifetime simulations of civil engineering structures. In CD: G. Augusti, G.I. Schueller, M. Ciampoli, (eds.), Proc. ICOSSAR'05, Rome, Italy, Millpress, Rotterdam.

Petryna, Y.S., Krätzig, W.B. 2002. On sensitivity of structural damage measures to stochastic uncertainties. In: H.A. Mang, F.G. Rammerstorfer, J. Eberhardsteiner (eds.), CD-Proc. 5th World Congr. of Comp. Mech., Vienna.

Petryna, Y.S., Krätzig, W.B. 2005. Compliance-based structural damage measure and its sensitivity to uncertainties. Comp., Struct. 83: 1113–1133.

Pettinga, J.D., Priestley, M.J.N., Pampanin, S., Christopoulos, C. 2007. The role of inelastic torsion in the determination of residual deformations. Journal of Earthquake Engineering 11(1): 133–157.

Pfeiffer, F., Glocker, C. 1996. Multibody Dynamics with Unilateral Contacts, New York: Wiley.

PIANC. 2001. Seismic design guidelines for port structures, International Navigation Association (PIANC), Balkema Publishers, Netherlands.

Pierce, A.D. 1989. Acoustics: An Introduction to its Physical Principles and Applications. Acoust. Soc. Am. Publications on Acoustics, Woodbury, NY, USA, 1989 (originally published in 1981, McGraw-Hill, New York).

Pinho, R., Elnashai, A.S., Vaz, C.T. 2000. Experimental observations from shaking-table tests on selective techniques for repair and strengthening of RC walls, Proc. Twelfth World Conference on Earthquake Engineering, Auckland, New Zealand, Paper No. 2245.

Pourzeynali, S., Lavasani, H.H., Modarayi, A.H. 2007. Active control of high rise building structures using fuzzy logic and genetic algorithms. Engineering Structures, 29, 346–357.

Pradlwarter, H., Schuëller, G.I., Koutsourelakis, P., Charmpis, D. 2007. Application of line sampling simulation method to reliability benchmark problems. Structural Safety 29(3), 208–221.

Prakash, V., Powell, S., Campbell, S. 1993. DRAIN 2DX – Base Program Description and User Guide, Version 1.10. Report No. UCB/SEMM-93/17: University of California at Berkeley.

Prevost, J.H. 1977. Mathematical modelling of monotonic and cyclic undrained clay behaviour. International Journal for Numerical and Analytical Methods in Geomechanics, 1(2), 195–216.

Priestley, M.J.N. 1998. Brief comments on elastic flexibility of reinforced concrete frames and significance to seismic design. Bulletin of the New Zealand National Society for Earthquake Engineering. 3, No. 4.

Psarropoulos, P.N., Klonaris, G., Gazetas, G. 2005. Seismic earth pressures on rigid and flexible retaining walls, Soil Dynamics and Earthquake Engineering, 25(7–10), 795–809.

Rackwitz, R. 2006. The effect of discounting, different mortality reduction schemes and predictive cohort life tables on risk acceptability criteria. Reliability Engineering, System Safety 91(4): 469–484.

Rackwitz, R., Lentz, A., Faber, M. 2005. Socio-economically sustainable civil engineering infrastructures by optimization. Structural Safety 27(3): 187–229.

Rao, S.S. 1995. Mechanical vibrations, Addison – Wesley Publishing Company, ISBN 0–201–52686–7.

Rao, S., Sawyer, P. 1995. Fuzzy Finite Element Approach for the Analysis of Imprecisely Defined Systems, AIAA Journal, 33(12): 2364–2370.

Reigles, D.G., Symans, M.D. 2006. Supervisory fuzzy control of a base isolated benchmark building utilizing a neuro-fuzzy model of controllable fluid viscous dampers. Journal of Structural Control and Health Monitoring, 13: 724–747.

Reissner, E. 1973. On one-dimensional large-displacement finite-strain beam theory. Studies inApplied Mathematics; LII, 287–95.
Reynders, E., De Roeck, G. 2008. Reference-based combined deterministic-stochastic subspace identification for experimental and operational modal analysis. Mechanical Systems and Signal Processing, submitted.
Ricker, N. 1960. The form and laws of propagation of seismic wavelets, Geophysics, 18: 10–40.
Rixena, D., Magoulès, F. 2007. Domain decomposition methods: Recent advances and new challenges in engineering. Computer Methods in Applied Mechanics and Engineering, 196(8): 1345–1346.
Rizos, D.C. 1993. An Advanced Time Domain Boundary Element Method for General 3-D Elastodynamic Problems. Ph.D. Dissertation, University of South Carolina.
Rizos, D.C. 2000. A rigid Boundary Element for Soil-Structure Interaction analysis in the direct time domain. Computational Mechanics 26: 582–591.
Rizos, D.C., Karabalis D.L. 1994. An advanced direct time domain BEM formulation for general 3-D elastodynamic problems. Computational Mechanics 15: 249–269.
Rizos, D.C., Loya, K.G. 2002. Dynamic and seismic analysis of foundations based on free field B-Spline characteristic response histories. Journal of Engineering Mechanics 128: 438–448.
Rizos, D.C., Wang, Z. 2002. Coupled BEM-FEM solutions for direct time domain soil-structure interaction analysis. Engineering Analysis with Boundary Elements 26: 877–888.
Robert, C.P., Casella, G. 1999. Monte Carlo statistical methods. Springer.
Robert, C.P., Casella, G. 2004. Monte Carlo Statistical Methods. Springer Texts in Statistics, 2nd edition, Springer and Verlag, New York, 2004.
Roberts, J.B., P.D. Spanos 1990. Random Vibration and Statistical Linearization. Chichester: John Wiley and Sons.
Roesset, J.M. 1977. Soil amplification of earthquakes, in Desai, C.S., Christian, J.T. (eds.), Numerical Methods in Geotechnical Engineering, McGraw-Hill, pp. 639–682.
Romero, I., Armero, F. 2002. Numerical integration of the stiff dynamics of geometrically exact shells: an energy-dissipative momentum-conserving scheme, Int. J. Num. Meth. Eng., 54: 1043–1086.
Rosenblueth, E. 1975. Point estimates for probability moments. Proceedings of the National Academy of Sciences of the USA 72, 3812–3814.
Rosenblueth, E., Mendoza, E. 1971. Reliability optimization in isostatic structures. Journal of the Engineering Mechanics Division ASCE 97, 1625–1640.
Rosenblueth, E., Meli, R. 1986. The 1985 earthquake: causes and effects in Mexico City. Concrete International ACI. 23–34.
Royset, J.O., Polak, E. 2004. Reliability-based optimal design using sample average approximations. Probabilistic Engineering Mechanics 19, 331–343.
Royset, J.O., Kiureghian, A.D., Polak, E. 2001. Reliability-based optimal structural design by the decoupling approach. Reliability Engineering and System Safety 73, 213–221.
Rubinstein, R. 1999. The cross-entropy method for combinatorial and continuous optimization. Methodology and Computing in Applied Probability 1, 127–190.
Rutenberg, A. 2002. EAEE Task Group (TG) 8: Behaviour of irregular and complex structures asymmetric structures-progress since 1998. Proceedings of the 12th European Conference on Earthquake Engineering, London. Elsevier: Oxford, Paper no. 832.
Saiidi, M., Sozen, M.A. 1981. Simple Nonlinear Seismic Analysis of RC Structures. ASCE Journ. Struct. Div. 107: 937–952.
Samuelsson, A., Wiberg, N.-E. 1998. Finite Element Method – Basics, Studentlitteratur, Sweden.
Samyn, P., Latteur, P., Van Vooren, J. Volume of structures: application to classical and harmonic structures, International IASS symposium on Lightweight structures in Architecture, Engineering and Construction, 1998 – October 5–9, Sydney, Australia.

Samyn, P. Etude comparée du volume et du déplacement de structures bidimension-nelles, sous charges verticales entre deux appuis – vers un outil d'évaluation et de pré-dimensionnement des structures (4 vol.), Ph. D. thesis, Université de Liège, 1999.
Samyn, P. Étude de la morphologie des structures à l'aide des indicateurs de volume et de déplacement, Académie royale de Belgique, Classe des Sciences 2004., ISBN 0365–0952.
SAP2000 2004. Linear and Nonlinear Static and Dynamic Analysis and Design of Three-Dimensional Structures, Version 9, Computers and Structures, Inc., Berkeley, California, USA.
Sapountzakis, E.J., Katsikadelis, J.T. 1999. Dynamic Analysis of Elastic Plates Reinforced with Beams of Doubly-Symmetrical Cross Section, Computational Mechanics, 23: 430–439.
Sapountzakis, E.J., Mokos, V.G. 2003. Warping Shear Stresses in Nonuniform Torsion by BEM, Computational Mechanics, 30(2): 131–142.
Sapountzakis, E.J., Mokos, V.G. 2007. Analysis of Plates Stiffened by Parallel Beams, International Journal for Numerical Methods in Engineering, 70: 1209–1240.
Sarma, K.C., Adeli, H. 1998. Cost optimization of concrete structures. Journal of Structural Engineering 124(5): 570–578.
Scheck, F. Mechanics: from Newton's laws to deterministic chaos, ed. 2nd corr. and enl., Springer Verlag, 1994.
Schenk, C.A., Schuëller, G.I. 2005. Uncertainty Assessment of Large Finite Element Systems. Berlin: Springer.
Schiehlen, W., Eberhard, P. 2004. Technische Dynamik, (in German) Wiesbaden: Teubner, 2004.
Schiehlen, W., Guse, N., Seifried, R. 2006. Multibody dynamics in computational mechanics and engineering Applications. Computer Methods in Applied Mechanics and Engineering, 195: 5509–5522.
Schiehlen, W., Seifried, R. 2004. Three approaches for elastodynamic contact in multibody systems. Multibody System Dynamics, 12: 1–16.
Schiehlen, W., Seifried, R. 2005. Impact mechanics in mechanical engineering. Proceedings of the International Conference on Mechanical Engineering and Mechanics2005 (ICMEM), Nanjing, China, October 25–26: 2–10.
Schiehlen, W., Seifried, R. 2006. Impact systems with uncertainty. In H. Hu, E. Kreuzer, Z. Wang (eds.), Proceedings of the IUTAM Symposium on Dynamics and Control of Nonlinear Systems with Uncertainty, Nanjing, China, September 18–22.
Schiehlen, W., Seifried, R., Eberhard, P. 2006. Elastoplastic phenomena in multibody impact dynamics. Computer Methods in Applied Mechanics and Engineering, 195: 6874–6890.
Schloegel, K., Kaypis, G., Kumar, V. 1999. Graph partitioning for high performance scientific simulations. Technical report, Army HPC Research Center, Department of Computer Science and Engineering, University of Minnesota.
Schueller, G.I., Bucher, C.G., Pradlwarter, H.J. 1991. Efficient computational procedures for reliability estimates of mdof systems, Journal of Nonlinear Mechanics, 26(6): 961–974.
Schueller, G.I., Bucher, C.G., Pradlwarter, H.J. 1991. The response surface method – an efficient tool to determine the failure probability of large structural systems, Proceedings of the International Conference on Spacecraft Structures and Mechanical Testing, pages 247–251, Noordwijk, The Netherlands.
Schuëller, G.I., Stix, R. 1987. A critical appraisal of methods to determine failure probabilities. Structural Safety 4, 293–309.
Schuëller, G.I., Pradlwarter, H., Koutsourelakis, P. 2004a. Benchmark Study on Reliability Estimation in Higher Dimensions of Structural Systems. Chair of Engineering Mechanics, Leopold-Franzens University, Innsbruck, Austria, EU, http://mechanik.uibk.ac.at/Benchmark Reliability/.
Schuëller, G.I., Pradlwarter, H., Koutsourelakis, P. 2004b. A critical appraisal of reliability estimation procedures for high dimensions. Probabilistic Engineering Mechanics 19(4), 463–474.

Scott, M.H., Franchin, P., Fenves, G.L., Filippou, F.C. 2004. Response sensitivity for nonlinear beam-column elements. Journal of Structural Engineering (ASCE), 130(9), 1281–1288.
Scott, R.F. 1973. Earthquake-induced pressures on retaining walls, Proceedings of the 5th World Conference on Earthquake Engineering, Vol. 2, pp. 1611–1620.
Scott, M.H., Fenves, G.L. 2006. Plastic Hinge Integration Methods for Force-Based Beam Column Elements, ASCE Journal of Structural Engineering, 133(2): 244–252.
Scott, M.H., Filippou, F.C. 2007. Response Gradients for Nonlinear Beam-Column Elements under Large Displacements, ASCE Journal of Structural Engineering, 133(2): 155–165.
SEAOC. 1995. Vision 2000 – Performance Based Seismic Design of Buildings. Committee Report, Structural Engineers Association of California, Sacramento.
Seed, H.B., Whitman, R.V. 1970. Design of earth retaining structures for dynamic loads, Proceedings of the Special Conference on Lateral Stresses in the Ground and Design of Earth Retaining Structures, ASCE, pp. 103–147.
Seed, H.B., Wong, R.T., Idriss, I.M., Tokimatsu, K. 1984. Moduli and damping factros for dynamic analysis of cohesionless soils. Earthquake Engineering Research Center Report UCB/EERC 84/14, University of California Berkeley.
Seifried, R. 2005. Numerische und experimentelle Stoßanalyse für Mehrkörpersysteme, (in German). Dissertation, Schriften aus dem Institut für Technische und Numerische Mechanik der Universität Stuttgart, Band 2, Aachen: Shaker.
Seifried, R. 2007. Effect of body flexibility on impacts studied on rods and beams. Proceedings of the ASME 2007 International Design Engineering Technical Conferences and Computers and Information in Engineering Conference (IDETC/CIE 2007., Las Vegas, USA, September 4–7, DETC2007-34817.
Seifried, R., Eberhard, P. 2005. Comparison of numerical and experimental results for impacts. D. van Campen, M. Lazurko, W. van der Oever (eds.). Proceedings of the ENOC-2005 Fifth EUROMECH Nonlinear Dynamics Conference, Eindhoven, The Netherlands, August 7–12: 399–408.
Seifried, R., Hu, B., Eberhard, P. 2003. Numerical and experimental investigation of radial impacts on a half-circular plate. Multibody Systems Dynamics, 9: 265–281.
Seifried, R., Schiehlen, W., Eberhard, P. 2005. Numerical and experimental evaluation of the coefficient of restitution for repeated impacts. International Journal of Impact Engineering, 32: 508–524.
Sepe, V., Capecchi, D., De Angelis, M. 2005. Modal model identification of structures under unmeasured seismic excitations. Earthquake Engineering and Structural Dynamics 34: 807–824.
Serfling, R.J. 1980. Approximation Theorems of Mathematical Statistics, John Wiley, Sons.
Sha, D., Zhou, X., Tamma, K.K. 2003. Time discretized operators. Part 2: towards the theoretical design of a new generation of a generalized family of uncondicionally stable implicit and explicit representations of arbitrary order for computational dynamics. Computer Methods in Applied Mechanics and Engineering 192: 291–329.
Shen, K.L., Soong, T.T. 2005. Design of energy dissipation devices based on concept of damage control. Journal of Structural Engineering, 122(1): 76–82.
Sheng, X., Jones, C.J.C., Thompson, D.J. 2003. A comparison of a theoretical model for quasi-statically and dynamically induced environmental vibration from trains with measurements. Journal of Sound and Vibration, 267: 621–635.
Shinozuka, M., Sato, Y. 1967. Simulation of nonstationary random processes. ASCE Journal of Engineering Mechanics, 93(1): 11–40.
Sibilio, E., Ciampoli, M. 2006. Valutazione dell'affidabilità strutturale attraverso tecniche di simulazione Monte Carlo: Subset Simulation e Bayesian Updating. Proc. CRASC'06, Messina, CDRom.

Sibilio, E., Ciampoli, M., Beck, J.L. 2006. Seismic reliability assessment of structures via Subset Simulation and Bayesian updating. 3rd International Conference on Advances in Mechanical Engineering and Mechanics, Hammamet, Tunisia, CDRom.

Siddall, J.N. 1984. A new approach to probability in engineering design and optimisation. ASME J Mech, Transmiss, Autom Des 1984; 106: 5–10.

Simo, J.C. 1985. A finite strain beam formulation. The three-dimensional dynamic problem. Part I. *Computer Methods in Applied Mechanic and Engineering*, 49: 55–70.

Simo, J.C., Govindjee, S. 1991. Non-linear B-stability and symmetry preserving return mapping algorithms for plasticity and viscoplasticity. International Journal for Numerical Methods in Engineering, 31(1): 151–176.

Simo, J.C., Hjelmstad, K.D., Taylor, R.L. 1984. Numerical formulations of elastoviscoplastic response of beams accounting for the effect of shear. Computer Methods in Applied Mechanics and Engineering; 42: 301–330.

Simo, J.C., Tarnow, N. 1992. The discrete energy-momentum method. Conserving algorithms for nonlinear elastodynamics. Journal of Applied Mathematics and Physics, 43: 757–792.

Simo, J.C., Vu-Quoc, L. 1986. A three-dimensional finite-strain rod model. Part II: Computational aspects. Computer Methods in Applied Mechanics and Engineering, 58: 79–116.

Simo, J.C., Vu-Quoc, L. 1988. On the dynamics in space of rods undergoing large motions – A geometrically exact approach. Computer Methods in Applied Mechanics and Engineering, 66: 125–161.

Simo, J.C., Posbergh, T.A., Marsden, J.E. 1991. Stability of relative equilibria. Part II: Application to nonlinear elasticity, Arch. Rational Mech. Anal., 115: 61–100.

Simo, J.C., Taylor, R.L., Pister, K. 1988. Variational and projection methods for the volume constraint in finite deformation elastoplasticity, Comp. Meth. Appl. Mech. Eng., 57: 177–208.

Simpson, B. 1992. Retaining Structures: displacement and design. Geotechnique, 42, 541–576.

Sivaselvan, M.V., Reinhorn, A.M. 2006. Lagrangian approach to structural collapse simulation. Journal of Engineering Mechanics-ASCE, 132(8): 795–805.

Sivaselvan, M.V., Reinhorn, A.M. 2004. Nonlinear structural analysis towards collapse simulation – a dynamical systems approach, Technical Report, Multidisciplinary Center for Earthquake Engineering Research.

Smyth, A.W., Masri, S.F., Chassiakos, A.G., Caughey, T.K. 1999. On-line parametric identification of MDOF non-linear hysteretic systems, Journal of Engineering Mechanics, 125, 133–142.

Socha, L. 1986. The sensitivity analysis of stochastic non-linear dynamical systems. Journal of Sound and Vibration 110, 271–288.

Soize, C. 2001. Maximum entropy approach for modeling random uncertainties in transient elastodynamics, Journal of the Acoustical Society of America, 109(5), 1979–1996.

Soize, C. 2005. Random matrix theory for modeling uncertainties in computational mechanics. Computer Methods in Applied Mechanics and Engineering, 194(12–16), 1333–1366.

Somerville, P., Collins, N. 2002. Ground motion time histories for the Humboldt bay bridge. Pasadena, CA, URS Corporation, www.peertestbeds.net/humboldt.htm.

Sondergaard, R., Chaney, K., Brennen, C. 1990. Measurement of solid spheres bouncing off flat plates. Journal of Applied Mechanics, 57: 694–699.

Soong, T.T. 1990. Active Structural Control: Theory and Practice. Avon: Longman Scientific, Technical.

Soong, T.T., Dargush, G.F. 1997. Passive Energy Dissipation Systems in Structural Engineering; John Wiley, Sons Ltda.

Sousa, M.L., Campos Costa, A., Carvalho, A., Coelho, E. 2004. An Automatic Seismic Scenario Loss Methodology Integrated on a Geographic Information System. 13th World Conference on Earthquake Engineering, Vancouver, B.C., Canada, August 1–6, Paper No. 2526.

Spacone, E., El-Tawil, S. 2004. Nonlinear analysis of steel-concrete composite structures: state-of-the-art. Journal of Structural Engineering, 130(2): 159–168.

Spacone, E., Filippou, F.C., Taucer, F.F. 1996. Fibre beam-column element for nonlinear analysis of R/C frames. Part I: formulation. Earthquake Engineering and Structural Dynamics, 25(7), 711–725.

Spacone, E., Filippou, F.C., Taucer, F.F. 1996. Fibre beam-column model for non-linear analysis of r/c frames 1. formulation. Earthquake Engineering and Structural Dynamics, 25: 711–725.

Spacone, E., Filippou, F.C., Taucer, F.F. 1996. Fiber Beam-Column Model for Nonlinear Analysis ofR/C Frames. I: Formulation, II: Applications. Earthquake Engineering and Structural Dynamics, 25(7): 711–742.

Spence, R., Pitilakis, K., Kakderi, K., Ansal, A., Erdik, M., Costa, A.C., Sousa, M.L. 2006b. Revised Loss Estimates Based on Alternative Mitigation Actions and Evaluation, Deliverable 115, Project LessLoss on Risk Mitigation for Earthquakes and Landslides, Sub-Project 10 – Earthquake disaster scenario predictions and loss modelling for urban areas, Sixth Framework Programme.

Spence, R., Pitilakis, K., Kakderi, K., Ansal, A., Erdik, M., Costa, A.C., Sousa, M.L. 2006a. Report for each city containing reference loss estimates, Deliverable 85, Project LessLoss on Risk Mitigation for Earthquakes and Landslides, Sub-Project 10 – Earthquake disaster scenario predictions and loss modelling for urban areas, Sixth Framework Programme.

Spence, R., Pitilakis, K., Kakderi, K., Ansal, A., Erdik, M., Costa, A.C., Sousa, M.L. 2005. Report on Building Stock Inventory and Vulnerability Data for each case study, Deliverable 84, Project LessLoss on Risk Mitigation for Earthquakes and Landslides, Sub-Project 10 – Earthquake disaster scenario predictions and loss modelling for urban areas, Sixth Framework Programme.

Srinivas N., Deb K., 1994. Multi-objective Optimization Using Nondominated Sorting in Genetic Algorithms, Journal of Evolutionary Computation, 2(3): 221–248.

Stavroulakis, G.E., Foutsitzi, G., Hadjigeorgiou, V., Marinova D.G., Baniotopoulos, C.C. 2005. Design and Robust Optimal Control of Smart Beams with Application on Vibrations Suppression, Advances in Engineering Software, 36, 806–813.

Stavroulakis, G.E., Foutsitzi, G.A., Hadjigeoriou, E.P., Marinova, D.G., Zacharenakis, E.C., Baniotopoulos, C.C. 2007. Numerical experiments on smart beams and plates. In Miara, B. Stavroulakis, G.E. Valente, V. (eds.), Topics on Mathematics for Smart Systems, European Conference, Roma, 26–28 October 2006, 218–236, World Scientific Publishers.

Stern, T.E. Theory of nonlinear networks and systems; an introduction, Addison-Wesley, 1965.

Storaasli, O.O., Bergan, P. 1987. Nonlinear substructuring method for concurrent processing computers. AIAA Journal, 25(6): 871–876.

Stronge, W. 2000. Impact Mechanics. Cambridge: Cambridge University Press.

Sues, R.H., Wen, Y.K., Ang, A.H.S. 1985. Stochastic evaluation of seismic structural performance. Journal of Structural Engineering, 111: 1204–1218.

Sweet, J. 1993. A technique for nonlinear soil–structure interaction. Technical Report CAI-093-100, Caltrans, Sacramento, California.

Tamma, K.K., Sha, D., Zhou, X. 2003. Time discretized operators. Part 1: towards the theoretical design of a new generation of a generalized family of uncondicionally stable implicit and explicit representations of arbitrary order for computational dynamics. Computer Methods in Applied Mechanics and Engineering 192: 257–290.

Tassoulas, J.L. 1981. Elements for the numerical analysis of wave motion in layered media. Research Report R81-2, Department of Civil Engineering, Massachusetts Institute of Technology, Cambridge, Massachusetts.

Teughels, A., De Roeck, G. 2004. Structural damage identification of the highway bridge Z24 by FE model updating. Journal of Sound and Vibrations, 278(3): 589–610.

Teughels, A., DeRoeck, G., Suykens, J.A.K. 2003. Global optimization by Coupled Local Minimizers and its application to FE Model Updating. Computers and Structures, 81(24–25): 2337–2351.

Teughels, A., Maeck, J., De Roeck, G. 2002. Damage assessment by FE model updating using damage functions. Computers and Structures, 80(25): 1869–1879.

Thyagarajan, R.S. 1989. Modeling and analysis of hysteretic structural behavior, Technical Report EERL 89-03, California Institute of Technology, Pasadena, CA.

Tso, W.K. 1990. Static eccentricity concept for torsional moment estimations. Journal of Structural Engineering, 116(5): 1199–1212.

Tso, W.K., Myslimaj, B. 2003. A yield displacement distribution-based approach for strength assignment to lateral force-resisting elements having strength dependent stiffness. Earthquake Engineering, Structural Dynamics, 32: 2319–2351.

Tsompanakis, Y., Avrana, V., Zania, V., Psarropoulos, P.N. 2006. Dynamic interaction between retaining walls and retained structures/geostructures, Proceedings of the 1st European Conference on Earthquake Engineering and Seismology (ECEES 2006., September 3–8, Geneva, Switzerland.

Tsompanakis, Y., Psarropoulos, P.N., Zania, V., Tsimpourakis, S. 2007. Effects of soil nonlinearity on the seismic response of rigid non-sliding retaining walls, Proceedings of the 4th International Conference on Earthquake Geotechnical Engineering, ICEGE 2007. June 25–28, Thessaloniki, Greece.

Utku, S., Melosh, R., Islam, M., Salama, M. 1982. On nonlinear finite element analysis in single– multi– and parallel processors. Computers, Structures, 15(1): 39–47.

Valdebenito, M., Pradlwarter, H., Schuëller, G.I. 2008. The role of the design point for calculating failure probabilities – Part 2: In view of nonlinearities. Structural Safety, Submitted for publication.

Valdebenito, M.A., Schuëller, G.I. 2007. Reliability Based Optimization using a Decoupling Approach and Reliability Approximations. In Proceedings: 6th International Congress on Industrial and Applied Mathematics (ICIAM). Zurich, Switzerland, July 2007.

Vamvatsikos, D., Cornell, C.A. 2002. Incremental Dynamic Analysis. Earthquake Engineering and Structural Dynamics 31: 491–514.

Van den Nieuwenhof, B. 2003. Stochastic finite elements for elastodynamics: random field and shape uncertainty modelling using direct and modal perturbation-based approaches, Ph.D. thesis, Universit'e catholique de Louvain, Louvain-La-Neuve, Belgium.

Van Steirteghem, J. A Contribution to the Optimisation of Structures Using Morphological Indicators: (In)Stability and Dynamics, Ph.D. thesis, Vrije Universiteit Brussel, Mechanics of Materials and Structures, W.P. De Wilde, supervisor, 2006.

Vandenbergh, T., Verbeeck, B., De Wilde, W.P. 2007, Dynamical analysis and op-timisation of statically determinate trusses at conceptual design stage, Compdyn 2007, Rethymnon, June 2007.

Vanmarcke, E. 1976. Structural response to earthquakes. In C. Lomnitz and E. Rosenblueth (eds.), Seismic Risk and Engineering Decisions, pp. 287–337. Amsterdam: Elsevier.

Vanmarcke, E.H., Lai, S.P. 1980. Strong-motion duration and rms amplitude of earthquake records. Bulletin of the Seismological Society of America 70, 1293–1307.

Vecchio, F.J. 1990. Reinforced Concrete Membrane Element Formulations. Journal of Structural Engineering. Vol. 116, No. 3.

Vecchio, F.J. 2000. Disturbed Stress Field Model for Reinforced Concrete: Formulation. ASCE Journal of Structural Engineering. 126(8): 1070–1077.

Vecchio, F.J., Collins, M.P. 1986. The modified compression field theory for reinforced concrete elements subjected to shear. ACI Structural Journal, 83(2): pp. 219–231.

Vecchio, F.J., Emara, M.B. 1992. Shear deformations in reinforced concrete frames. ACI Structural Journal 89(1): 45–56.

Veletsos, A.S., Younan, A.H. 1997. Dynamic response of cantilever retaining walls, ASCE Journal of Geotechnical and Geoenvironmental Engineering, 123(2), 161–172.
von Estorff, O., Firuziaan, M. 2000. Coupled BEM/FEM approach for nonlinear soil/structure interaction. Engineering Analysis with Boundary Elements 24: 715–725.
Von Wolffersdorff, P.-A. 1996. A hypoplastic relation for granular materials with a predefined limit state surface. Mechanics of Cohesive-Frictional Materials, 1, 251–271.
Waas, G. 1972. Linear two-dimensional analysis of soil dynamics problems in semi-infinite layered media. PhD dissertation, University of California, Berkeley, California.
Wang, A.P., Lin, Y.H. 2007. Vibration control of a tall building subjected to earthquake excitation. Journal of Sound and Vibration, 299, 757–773.
Washizu, K. 1975. Variational methods in elasticity and plasticity. Oxford: Pergamon Press.
Wen, Y.K., Kang, Y.J. 2001a. Minimum building life-cycle cost design criteria. I: Methodology. Journal of Structural Engineering, 127(3): 330–337.
Wen, Y.K., Kang, Y.J. 2001b. Minimum building life-cycle cost design criteria. II: Applications. Journal of Structural Engineering, 127(3): 338–346.
Wen, Y.K. 1976. Method for random vibration of hysteretic systems. Journal of the Engineering Mechanics Division 102: 248–262.
Wen, Y.-K. 1976. Method for random vibration of hysteretic systems, Journal of Engineering Mechanics, 102: 249–263.
Wong, C.M., Tso, W.K. 1995. Evaluation of seismic torsional provisions in uniform building code. Journal of Structural Engineering, 121(10): 1436–1442.
Wong, P.S., Vecchio, F.J. 2002. VecTor2, Formworks User's Manual. University of Toronto.
Wood, J.H. 1975. Earthquake–induced pressures on a rigid wall structure, Bulletin of New Zealand National Earthquake Engineering, 8, 175–186.
Wriggers, P. 2002. Computational Contact Mechanics, Chichester: Wiley.
Wright, J.K. (ed.). 1985. Earthquake Effects on RC Structures. US-Japan Research, SP-84, ACI Detroit.
Wu, C., Li, L., Thornton, C. 2003. Rebound behavior of spheres for plastic impacts. International Journal of Impact Engineering, 28: 929–946.
Wu, G., Finn, W.D.L. 1999. Seismic lateral pressures for design of rigid walls, Canadian Geotechnical Journal, 36(3), 509–522.
Wyckoff, R.D., Botset, H.G. 1936. The flow of Gas-liquid Mixtures through Unconsolidated Sands. General and Applied Physics, 7, 325–345.
Xue, Q. 2000. Need of performance-based earthquake engineering in Taiwan: a lesson from the Chichi earthquake. Earthquake Engineering, Structural Dynamics 29(11): 1609–1627.
Yang, J.N., Lin, S. 2004. On-line identification of non-linear hysteretic structures using an adaptive tracking technique, International Journal of Non-Linear Mechanics. 39: 1481–1491.
Yang, Y.B., Hung, H.H., Chang, D.W. 2003. Train-induced wave propagation in layered soils using Finite/Infinite Element simulation. Soil Dynamics and Earthquake Engineering 23: 263–278.
Yazdchi, M., Khalili, N., Valliappan, S. 1999. Dynamic soil-structure interaction analysis via coupled Finite Element-Boundary Element Method. Soil Dynamics and Earthquake Engineering 18: 499–517.
Yoshimura, C., Bielak, J., Hisada, Y. 2003. Domain reduction method for three-dimensional earthquake modeling in localized regions. part II: Verification and examples. Bulletin of the Seismological Society of America, 93(2): 825–840.
Youn, B., Choi, K., Du, L. 2005. Adaptive probability analysis using an enhanced hybrid mean value method. Structural and Multidisciplinary Optimization 29(2), 134–148.
Yuen, K-V., Katafygiotis, L.S. 2005. Model updating using noisy response measurements without knowledge of the input spectrum. Earthquake Engineering and Structural Dynamics 34: 167–187.

Yuen, K-V., Katafygiotis, L.S. 2006. Substructure identification and health monitoring using noisy response measurement only. Computer-Aided Civil and Infrastructure Engineering 21: 280–291.

Yun, S.-Y., Hamburger, R.O., Cornell, C.A., Foutch, D.A. 2002. Seismic performance evaluation for steel moment frames. Journal of Structural Engineering ASCE 128(4): 534–545.

Zadeh, L. 1965. Fuzzy sets, Information and Control, 8(3): 338–353.

Zang, C., Friswell, M.I., Mottershed, J.E. 2005. A review of robust optimal design and its application in dynamics. Computers and Structures, 83: 315–326.

Zenisek, A. 1990. Nonlinear Elliptic and Evolution Problems and Their Finite Element Approximations. London: Academic Press.

Zhang, J., Foschi, R.O. 2004. Performance-based design and seismic reliability analysis using designed experiment and neural networks. Probabilistic Engineering Mechanics. 19: 259–267.

Zhang, Q.W. 2007. Statistical damage identification for bridges using ambient vibration data. Computers and Structures 85: 476–485.

Zhang, X., Vu-Quoc, L. 2002. Modeling of the dependence of the coefficient of restitution on impact velocity in elasto-plastic collisions. International Journal of Impact Engineering, 27: 317–341.

Zhang, J. 2003. Performance-based seismic design using designed experiments and neural networks. PhD. Thesis, Department of Civil Engineering, University of British Columbia, Canada.

Zhao, Y.G., Ono, T., Idota, H. 1999. Response uncertainty and time-variant reliability analysis for hysteretic MDF structures. Earthquake Engineering and Structural Dynamics, 28, 1187–1213.

Zhong, Z.-H. 1993. Finite Element Procedures for Contact-Impact Problems, New York: Oxford University Press.

Zienkiewicz, O.C., Chan, A.H.C., Pastor, M., Schrefler, B.A., Shiomi, T. 1999. Computational geomechanics with special reference to earthquake engineering. John Wiley, Sons.

Zimmermann, T., Truty, A., Urbanski, A., Podles, K. Z-Soil user manual, Zace Services Ltd, 198552007.

Zona, A., Barbato, M., Conte, J.P. 2005. Finite element response sensitivity analysis of steel-concrete composite beams with deformable shear connection. Journal of Engineering Mechanics (ASCE), 131(11): 1126–1139.

Zona, A., Barbato, M., Conte, J.P. 2006. Finite element response sensitivity analysis of continuous steel-concrete composite girders, Steel and Composite Structures, an International Journal, 6(3), 183–202.

Zonno, G., Garcia-Fernandez, M., Jimenez, M.J., Menoni, S., Meronil, F., Petrini, V. 2003. The SERGISAI procedure for seismic risk assessment. Journal of Seismology 7: 259–277.

Author index

Subject index

Structures and Infrastructures ISSN 1747-7735
Series Editor: Dan M. Frangopol

Computational Structural Dynamics and Earthquake Engineering

2

The increasing necessity to solve complex problems in Structural Dynamics and Earthquake Engineering requires the development of new ideas, innovative methods and numerical tools for providing accurate numerical solutions in affordable computing times.

This book presents the latest scientific developments in Computational Dynamics, Stochastic Dynamics, Structural Dynamics and Earthquake Engineering in thirty-five self-contained contributions. The selected state-of-the-art chapters are revised and extended versions of the papers which were presented as plenary, semi-plenary and keynote lectures at the thematic COMPDYN 2007 Conference.

This volume will benefit researchers and engineering professionals working on structural dynamics, earthquake engineering and computational mechanics. Readers will get acquainted with advanced computational methods and software tools, which can assist them in tackling complex problems in dynamic/seismic analysis and design. Moreover, it will raise the awareness of important application areas and the social impact of the scientific and technical fields involved.

CRC Press
Taylor & Francis Group
an Informa business
www.crcpress.com

6000 Broken Sound Parkway, NW
Suite 300, Boca Raton, FL 33487
Schiphollweg 107C
2316 XC Leiden, NL
2 Park Square, Milton Park
Abingdon, Oxon OX14 4RN, UK

ISBN 0415452619
9 780415 452618

an Informa business